ISTITUTO NAZIONALE DI FISICA NUCLEARE
Laboratori Nazionali di Frascati

FRASCATI PHYSICS SERIES

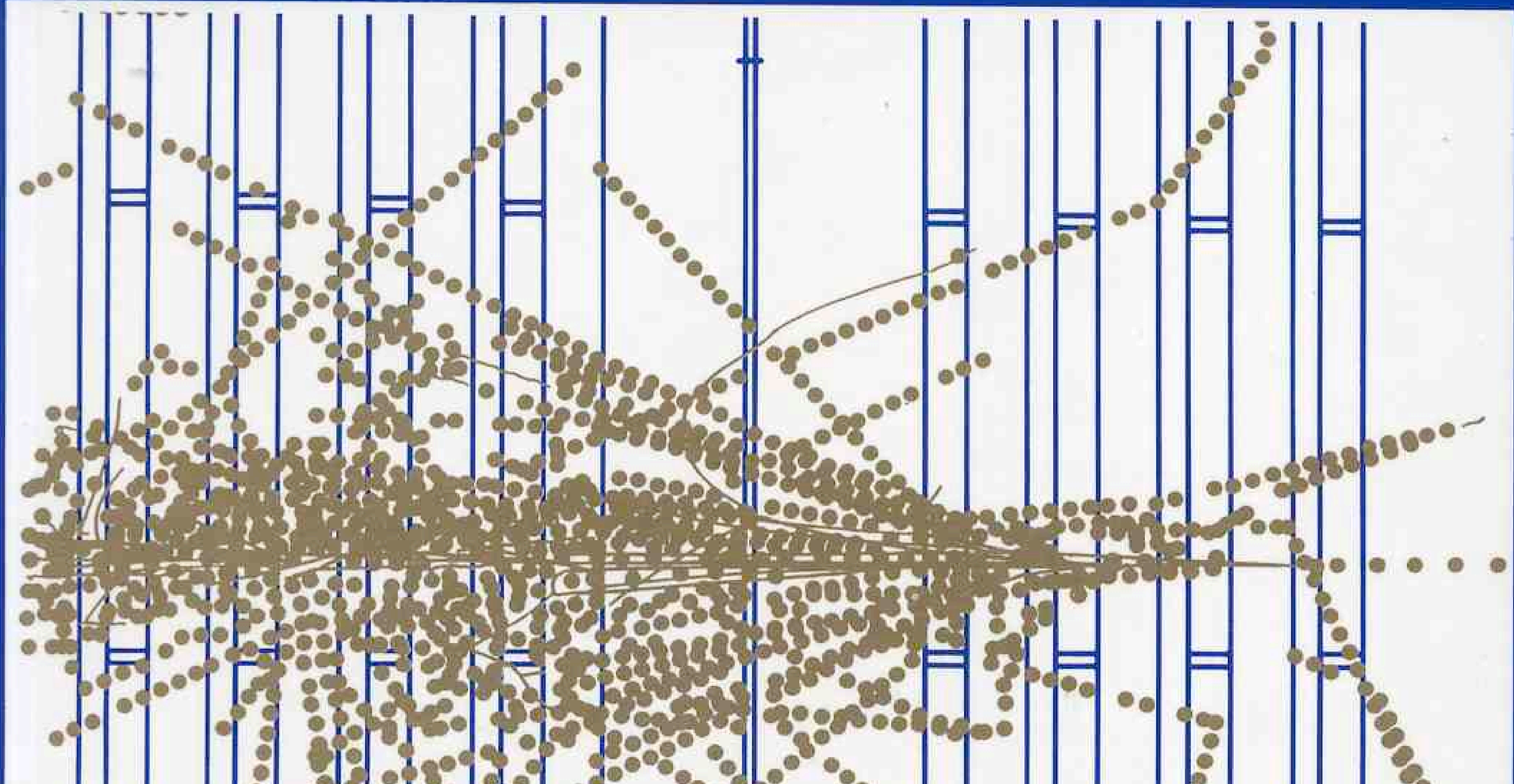

CALORIMETRY IN HIGH ENERGY PHYSICS

A. Antonelli, S. Bianco, A. Calcaterra, F.L. Fabbri

Opening Talk

ascati Physics Series Vol. VI, (pp. 49–64)
[INT. CONF. ON CALORIMETRY IN HEP – Frascati, June 8–14, 1996

THE HERA-B CALORIMETER ALSO IN VIEW OF LHC-B.

Andrei Golutvin
ITEP, B.Cheremushkinskaya 25, 117259 Moscow, Russia

ABSTRACT

ıe main goals, performance requirements and design considerations of the HERA-calorimeter are described in view of the LHC-B calorimeter. The first 360 towers scintillator/lead sandwich type sampling calorimeter "shashlik" of the HERA-B tector have been constructed and tested with electron and proton beams in terms light yield, uniformity of response and energy resolution. The measurements of e phototubes aging and radiation hardness studies of the scintillator and wavegth-shifting (WLS) fibres are also presented.

Introduction

ɔth HERA-B [1, 2] and LHC-B [3] experiments are proposed to detect and study P-violation in the B-meson system. The HERA-B detector is presently under construction. It is foreseen to achieve a phase of efficient data taking in two years ɔm now. LHC-B is planned as a more general purpose B-physics experiment hich should provide the ultimate precision in the field during the LHC operaɔn. Obviously HERA-B will have a long-term impact in developing technology ıd methodology for LHC-B including the calorimetry aspects. The benchmark for ı electromagnetic calorimetry is the detection and tagging of $B \to J/\psi K^0_S$ decays order to observe CP-violating asymmetry.

This paper is outlined as follows. The main goals and performance reıirements of the HERA-B calorimeter are described in section 2 with a reference LHC-B calorimeter requirements. Overall system aspects for both calorimeters e overviewed in section 3. Section 4 contains selected test results obtained for the ERA-B calorimeter.

2 Performance requirements

The calorimetry will play a key role in the electron identification and the formation of the first level trigger. The main goals of the calorimetry are:

- To provide a pretrigger signal for the first level trigger
- To provide the discrimination of hadrons against electrons and positrons at the level of ~ 100.

These major goals define a set of requirements on the calorimeter performance.

2.1 Acceptance

Both HERA-B and LHC-B calorimeters are positioned at rather large distances from the primary vertices. A large geometrical acceptance is of particular importance for the HERA-B experiment due to relatively small cross-section of $b\bar{b}$ pairs production. In order to have high detection efficiency both for the electrons produced in J/ψ decay and for the tagging electrons, the calorimeter should cover the range $|x| < 312$ cm and $|y| < 234$ cm. The resulting angular coverage is 220×160 *mrad*. The calorimeter has an asimmetrical shape because the magnetic field in HERA-B spreads charge particles in horizontal direction. The geometrical acceptance to detect both electron and positron from J/ψ decay is found to be 68%. The corresponding acceptance for the tagging electron is 82%. The acceptance loss is caused mainly by the inner hole of the calorimeter $22.3 \times 22.3\ cm^2$. However the geometrical acceptance of the calorimeter is still higher than that of the tracker system. Showers initiated by the tracks with angles as low as 10 mrad (which is the lower boundary of the tracker system acceptance) will be completely confined in the calorimeter. Therefore the calorimeter itself does not contribute to the loss of geometrical efficiency.

The transverse dimension of the LHC-B calorimeter is $8.1 \times 8.1\ m^2$ corresponding to the angular coverage of 300×300 *mrad*. The resulted geometrical acceptance to recontruct electron and positron from J/ψ decay is $\sim 25\%$. [1]

2.2 Trigger performance

To avoid pile-up and to provide the first level trigger the signal collection time has to be below 100 ns for the HERA-B calorimeter and 25 ns for the LHC-B calorimeter.

LHC-B is planning for more general trigger based on high-P_t electrons and hadrons using both electromagnetic and hadronic calorimeters. A possible use of

[1] To compare with HERA-B geometrical acceptance one has to take into account that half of $B\bar{B}$ pairs produced at LHC collider is lost in the backward hemisphere.

eshower detector, placed in front of the electromagnetic calorimeter, in formation electron pretrigger is presently under consideration.

3 Occupancy

ıe rates of photons and charged particles at the front face of the HERA-B and IC-B calorimeters are shown as a function of x- and y- distances from the centre of e calorimeter in fig.1 and fig.2 respectively. In HERA-B environment one expects ·10 energetic photons per bunch crossing which pass energy threshold cut of the

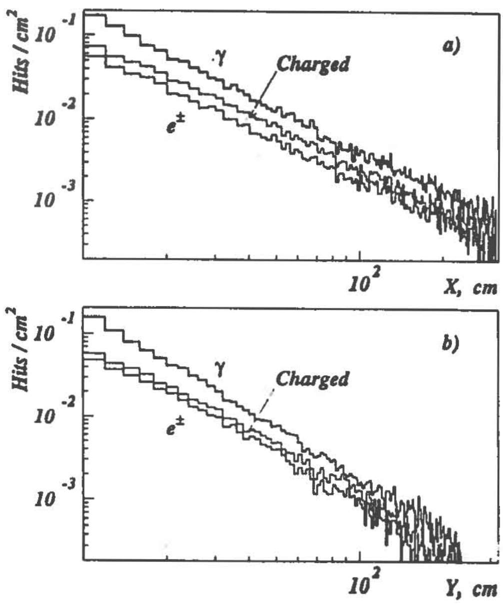

igure 1: The expected rates of particles per 1 cm^2 and bunch crossing at the ERA-B calorimeter front face as a function of x and y.

ılorimeter. These photons can overlap accidentally with charged tracks, thus deteorating the trigger capability of the calorimeter. In order to minimize the number fake electron candidates the occupancy for charged particles per calorimeter cell ıould not exceed the 10% level.

4 Transverse segmentation

he fine transverse segmentation of the calorimeter serves as an essential tool to improve the discrimination of electrons and charged hadrons overlapping with photons

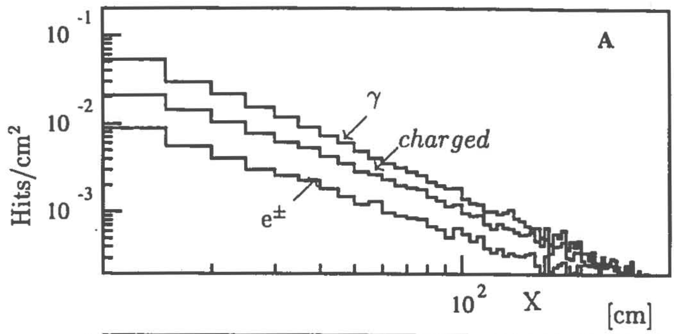

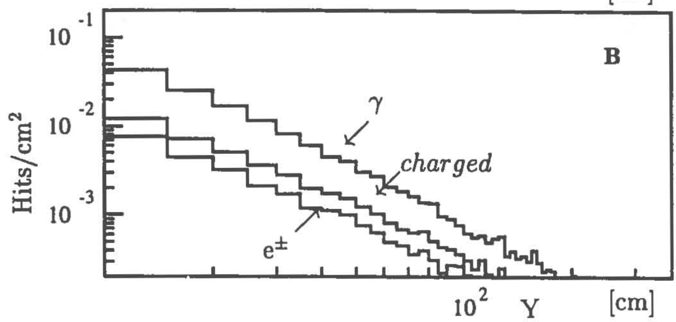

Figure 2: The expected rates of particles per 1 cm^2 and bunch crossing at the LHC-B electromagnetic calorimeter front face as a function of x and y.

from π^0 decays. The latter process represents the main limitation for the electron-pion separation. The transverse segmentation gives also a measure of the spatial resolution and consequently the capability to separate two showers. The following factors favour a small size of the ECAL cell:

- The smaller size of the cell reduces pile-up effects and hence improves electron/pion separation.
- The photons resulting from π^0 decays should hit different cells. This requirement is important to ensure both the π^0 reconstruction and a more efficient rejection of photons at the first level trigger using the energy threshold cut.

On the other hand, the cost considerations and reliability of the system set a limit on the number of calorimeter channels.

The steep radial dependence of the track density requires a variable cell size in order to limit the number of readout channels. In order to minimize occupancy per shower area the Moliere radius of the calorimeter media should be kept at a reasonably small level, varying as a function of the radial distance and the calorimeter cell size.

5 Energy resolution

he energy resolution of the HERA-B calorimeter should be sufficient to provide ·quired electron/pion separation by comparing energy deposition measured in the ılorimeter and momentum of the track measured in the tracking system. The ıergy resolution for electron candidates is determined to a large extent by the pile-p noise from the neighboring tracks, rather than by the intrinsic energy resolution ' the device. Due to that reason the requirements on the energy resolution of the ERA-B calorimeter are rather modest:

$$\frac{\sigma(E)}{E} = \frac{10-15\%}{\sqrt{E}} \oplus 1.5\% \tag{1}$$

HC-B puts more challenging requirements on the calorimeter energy resolution:

$$\frac{\sigma(E)}{E} = \frac{7\%}{\sqrt{E}} \oplus 1\% \; for \; ECAL \quad and \quad \frac{\sigma(E)}{E} = \frac{50\%}{\sqrt{E}} \oplus 2\% \; for \; HCAL \tag{2}$$

. good energy resolution is particularly important at LHC-B for CP-violation search ı B-decays into D mesons in order to reconstruct D mesons in the final states ɔntaining π^0's.

.6 Radiation environment

'he expected radiation dose for the calorimeter depends drastically on the distance ·om the beam pipe. The annual radiation load of the HERA-B calorimeter accu-ıulated at the shower-max position is shown in fig.3 as a function of the distance ·om the beam. For the innermost part peak doses of up to 5 Mrad can be accumu-ıted within one year of HERA-B operation. According to radiation damage studies [, 5] (see section 4.3), a perforated injection molded polystyrene based scintillator nd standard WLS fibres such as Kuraray Y-11 show no substantial degradation of ght conversion efficiency and transparency after irradiation with such a dose. Nev-rtheless a few (up to 16) innermost HERA-B calorimeter modules are considered ɔ be replaced after each year of HERA-B operation at nominal luminosity. The HC-B calorimeter is planned to operate during 10 years without any replacement f its components. The expected radiation dose, which innermost modules have to ·ithstand, is $\sim$ 20 Mrad.

The maximum radiation dose accumulated by the phototubes in the vicin-:y of the beam pipe is expected to reach up to 1.5 Mrad per year. The dose is ecreasing rapidly with the increase of the distance between PM and the beam ipe. Since the conventional borosilicate glass window of a PM looses its trans-arency in the light wavelength range of 480-500 nm after an irradiation up to such dose, HAMAMATSU-R760 with radiation hard silica window will be used for the ınermost calorimeter modules (see section 4.3).

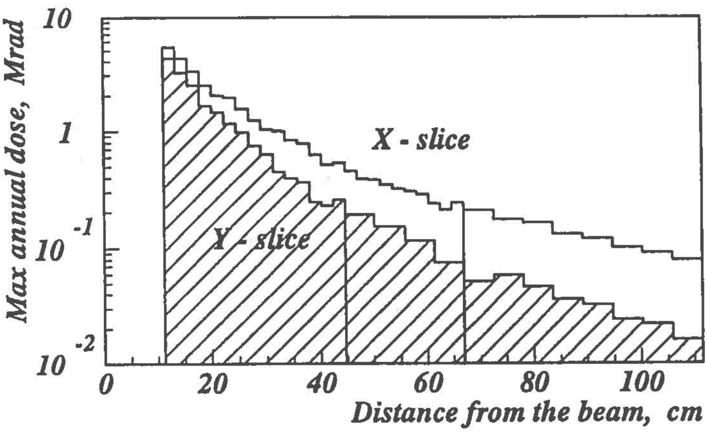

Figure 3: Expected annual radiation dose collected at the shower-maximum position of the HERA-B calorimeter.

3 Design considerations

The main parameters of the HERA-B electromagnetic calorimeter are summarized in tab.1 (see table at the end of the text). An isometric view of the HERA-B ECAL is shown in fig.4. The calorimeter consists of inner, middle and outer sections. All sections employ the same technology of sampling scintillator/absorber sandwich structure read out by plastic WLS fibres ("shashlik"). This is a well proven technology which offers the combination of ease of assembly and integration, possibility to adjust variable cell size and Moliere radius, good time characteristics and adequate energy and spatial resolution. Moreover the "shashlik" technology represents a cost-effective solution simple in production.

The basic ECAL unit is a module (shown in fig.4 as a rectangular block) with transverse dimensions of $11.15 \times 11.15\ cm^2$. The middle and outer calorimeter modules use standard lead absorbers while the inner modules use tungsten alloy absorbers in order to reduce the Moliere radius. The steep radial dependence of the track density requires a variable ECAL granularity in order to limit the number of readout channels. Thus the inner, middle and outer modules comprise 25, 4 and 1 cell respectively. The cell sizes, as well as the numbers of readout channels, are presented in tab.1 separately for each part of the calorimeter. The modular geometry allows straightforward integration into the HERA-B detector. Mechanically the modules form a self-support structure with 42 horizontal rows, each containing 56 modules neglecting the cut-outs for the proton and electron beam pipes. The actual

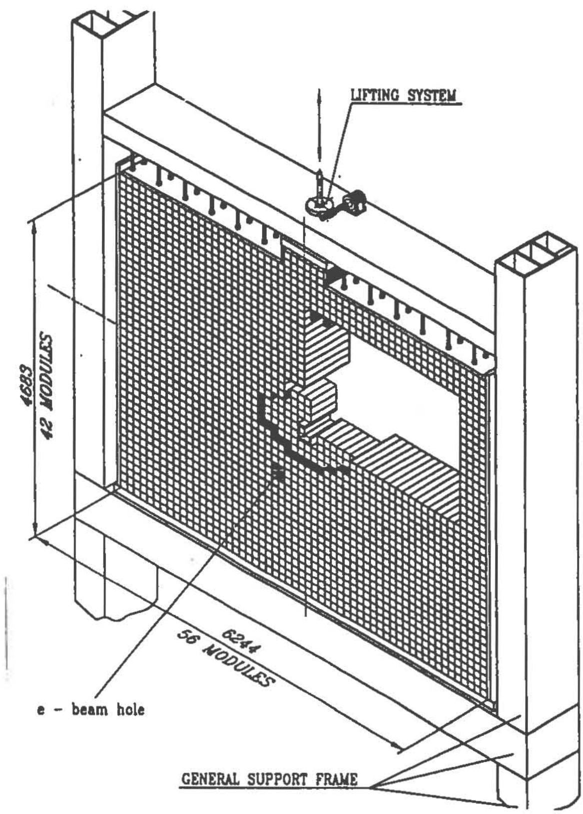

'igure 4: An isometric view of the HERA-B calorimeter. Inner, middle and outer ɜgions are separated by the bold plotted lines. The numbers are in mm.

ʼeight carried by a single module in the bottom row is about 800 kg. In total, there re 2344 calorimeter modules. The total length of the calorimeter in the z-direction ; 86 cm.

The LHC-B calorimeter system comprises electromagnetic and hadronic ıarts. The hadronic component is required to provide a hadron transverse energy neasurement for selection of high-p_t pions and to improve particle identification by .sing longitudinal segmentation of the hadron calorimeter.

Analogous to the HERA-B calorimeter the electromagnetic calorimeter for he LHC-B detector is also subdivided into the inner and outer part. The summary f its parameters is presented in tab.2 (see table at the end of the text). The outer ›art has a modular structure of the shashlik-type calorimeter modules of identical xternal dimension. There are three types of modules differing by the transverse egmentation which can be determined by the different grouping of WLS fibres onto he photodetector.

In contrast to HERA-B, the innermost part of the LHC-B calorimeter is

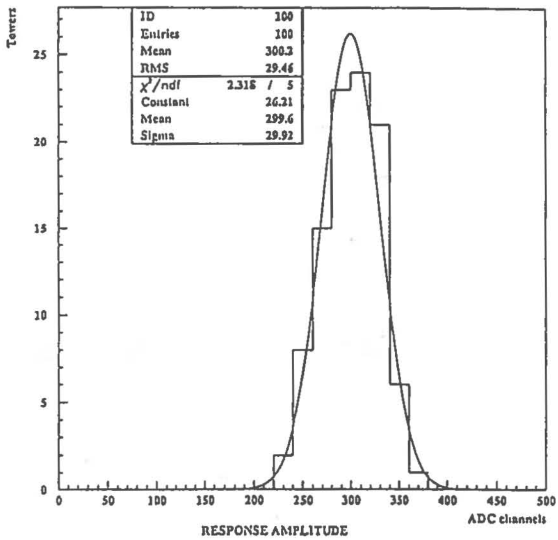

Figure 5: Cell-to-cell uniformity in light response measured at ITEP 3 GeV proton beam.

not considered to be replaced during the operation. Therefore the inner module has to be made of more radiation hard material than plastic scintillator and WLS-fibres. The recently developed $PbWO_4$ scintillating crystal [6, 7] is considered as a possible solution.

4 Selected test results of the HERA-B calorimeter modules

The "shashlik" technology has been extensively studied within the CMS Collaboration at CERN [8, 9, 10] and the PHENIX Collaboration at BNL [11]. Beam tests of several prototypes, including HERA-B modules, demonstrated a good agreement between measured and calculated energy and spatial resolution. In this paper only selected test results are presented specific to the HERA-B case.

4.1 Measurement of the light yield and energy resolution of the HERA-B modules

A total of 360 towers of the middle calorimeter section have been constructed and tested in terms of uniformity of the light yield and energy resolution achieved in mass production.

The light response of the calorimeter tower to 3 GeV protons was measured at ITEP test beam using a single phototube for the readout. The resulting response amplitude distribution (shown in fig.5) has a mean value corresponding to 250 p.e. per MIP which is in a good agreement with Monte Carlo prediction. The observed

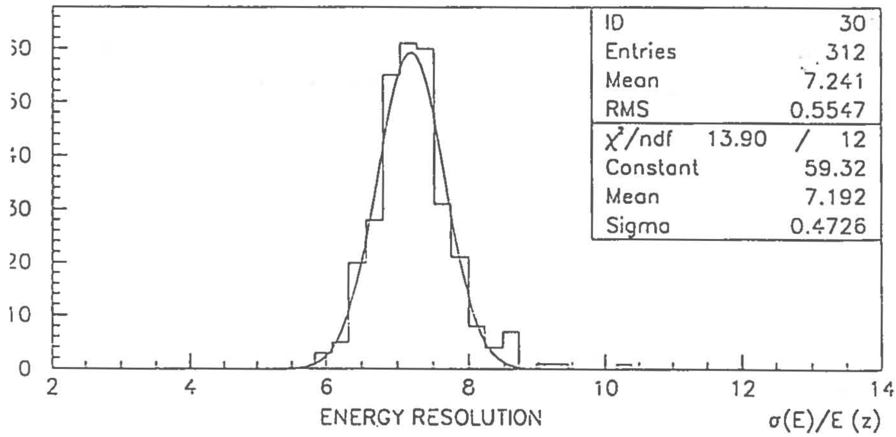

igure 6: Cell-to-cell uniformity in energy resolution measured for 3 GeV electrons the DESY test beam. The energy resolution is given in percents.

)% cell-to-cell variation is explained mainly by the fibre polishing procedure and ore-to-fibre response variation.

The uniformity in cell-to-cell energy resolution was measured using 3 GeV ectrons at DESY electron test beam. The on-line data (see fig.6) for 360 calorime- r towers show 6.5% non-uniformity.

.2 Measurement of the long-term drift of the phototube gain

'he measurement of the long-term gain degradation is of particular importance r the phototubes reading out the scintillating light in the innermost HERA-B alorimeter modules. An average energy deposition in the innermost calorimeter egion is expected to be as large as 1.6 GeV per cell per bunch crossing. This value orresponds to the total charge delivered to the photocathode per one year of HERA- operation of $\sim$ 3 mC. The phototube gain degradation can be caused by either hotocathode or dynode system fatigue. In order to perform aging test FEU-68, nvisaged for the readout of the inner calorimeter section, was exposed by the light rom a green LED. The photocathode response is shown in fig.7(a) as a function f the charge collected at the first dynode of FEU-68. No degradation is observed or collected charges up to 0.3 C. This amount is equivalent to the operation in the IERA-B environment during 30 years. A relative variation of the FEU-68 gain is hown in fig.7(b) as a function of the charge passed through the anode. The shown nterval of the x-variable corresponds to 30 years of HERA-B operation. A total ain degradation of FEU-68 after this time is expected to be at 10% level. A sharp

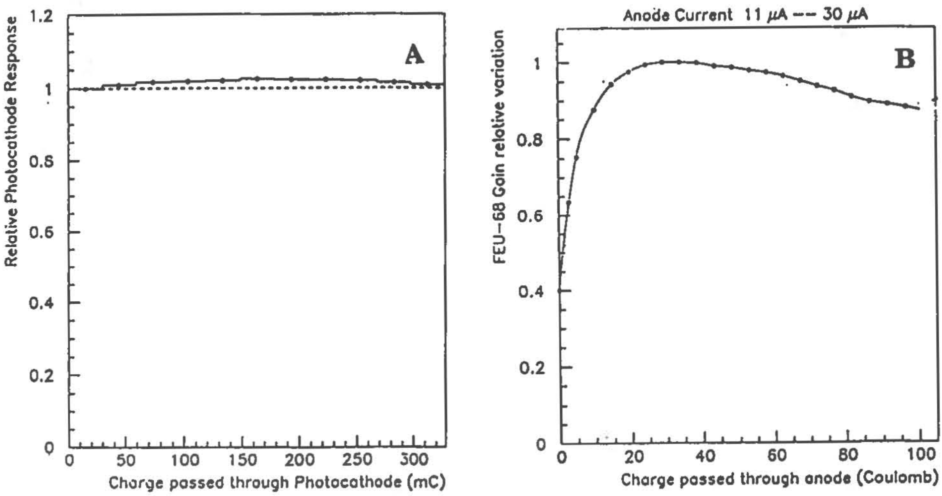

Figure 7: (a) Relative photocathode response of FEU-68 as a function of the charge collected at the first dynode. (b) Relative variation of the FEU-68 gain as a function of the charge passed through the anode.

rise of the phototube response at the beginning of exposition is explained by the training effect of FEU-68.

4.3 Study of radiation hardness of the calorimeter components

The innermost modules of the HERA-B calorimeter will encounter a considerable amount of radiation. According to the HERA-B requirements the detector components must withstand radiation doses collected after one year of operation without any significant degradation of performance. The predicted maximum annual doses for the calorimeter module components are as follows:

- Up to 5 Mrad for the plastic scintillators and WLS fibres (at the shower maximum position);

- Up to 1.5 Mrad for the HAMAMATSU-R760 phototubes installed at the modules in the vicinity of the beam pipe;

- Up to 1.5 Mrad for the PM dividers and preamps;

- Up to 0.1 Mrad for the FEU-68 phototubes.

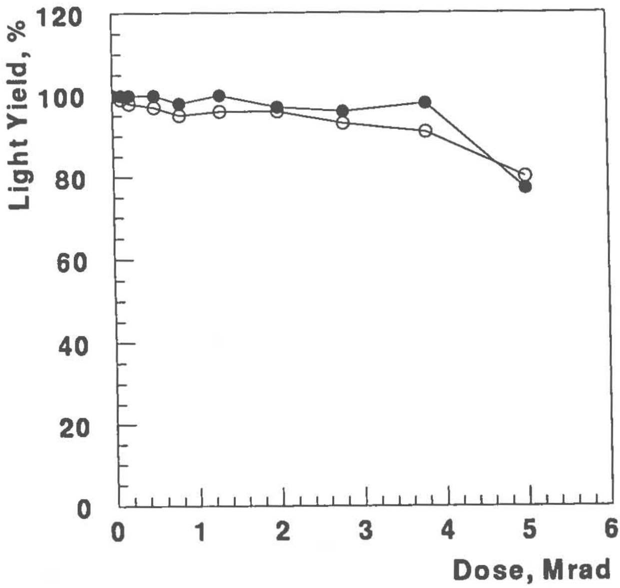

'igure 8: The relative light output as a function of collected dose for the BICRON closed circles) and Vladimir (open circles) scintillators.

3.1 Radiation hardness of plastic scintillators and WLS fibres

he irradiation of fibres and plastic scintillators was performed using calibrated *Co* γ-source. The dose map in the vicinity of the source was measured with $\sim 2\%$ ccuracy. An irradiation was possible with dose delivery rate in the range from to 50 krad/hour depending on the position of irradiated sample relative to the -source. The dose rate profile along the sample can be well approximated by the niform distribution. Measurements of the light output of irradiated scintillators nd fibres with respect to the non-irradiated ones were made using MIPs at ITEP est beam and blue LEDs correspondingly. In order to reproduce the conditions f light collection in the calorimeter module the tested scintillator tiles of 2×2 m^2 size and 1 mm thickness were assembled into the stack identical to the inner alorimeter cell without absorber plates. The scintillating light was read out via 9 VLS fibres of 1.2 mm diameter penetrating the entire body of the stack. The fibres vere bounded together, polished and coupled to the phototube as in the calorimeter nodule. The light output as a function of collected dose is presented in fig.8 for he BICRON scintillator (shown with closed circles) and polystyrene based moulded cintillator (shown with open circles) produced in Vladimir (Russia) for the HERA-3 calorimeter. The dose delivery rate was 50 krad per hour which is 25 times higher

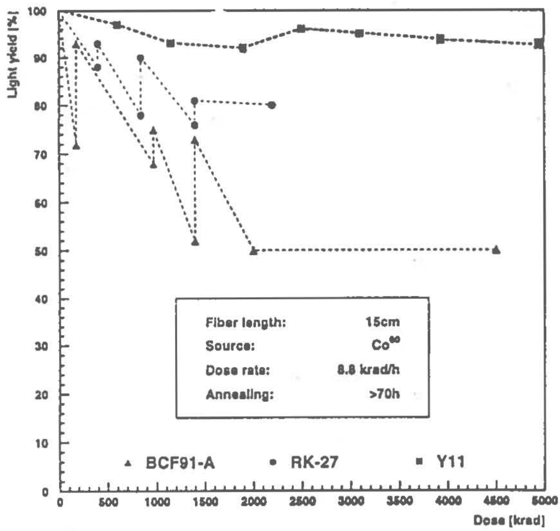

Figure 9: The relative light output of various WLS fibres after irradiation.

than expected in HERA-B environment. Even at such high dose rate the scintillating plastics of small transverse size and thickness, used in the HERA-B inner modules, can stand up to 5 Mrad with less than 20% degradation of initial light yield.

In order to select the most radiation hard candidate we have performed a comparative study of various WLS fibres. Since the length of the inner HERA-B module is rather short small worsening in the attenuation length should not affect much the performance. Samples of 15 cm length WLS fibres were irradiated and measured with respect to the non-irradiated sample using blue LED for the excitation. Each sample consisted of 5 fibres bound together into the bundle and coupled to the phototube. The results of this study are summarized in fig.9. For each collected dose the light output was measured right after and in more than 70 hours after the irradiation. [2] The upper set of data points in fig.9 for the BCF91-A and RK-27 WLS fibres corresponds to the light output after annealing. The KURARAY Y-11 WLS fibres choosen for the HERA-B inner modules show only minor decrease in the light yield after irradiation up to 5 Mrad.

4.3.2 Radiation hardness of the phototubes and dividers

The darkening of the PM window was measured as a function of collected dose using a ^{60}Co γ-source. The relative PM signals after irradiation are presented in fig.10 for

[2] According to our dedicated study some of the tested fibres show a substantial annealing which saturates in 50 to 100 hours after irradiation depending on the dose delivery rate.

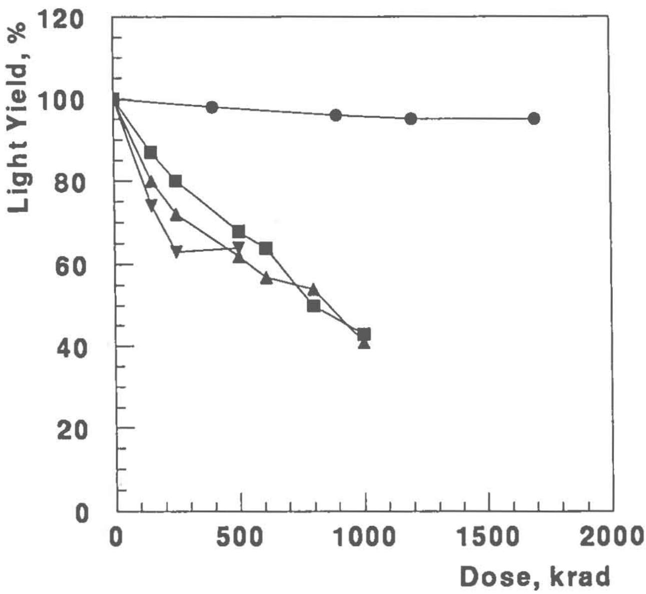

gure 10: The output current as a function of collected dose for a sample of the ΞU-68 (triangles and squares) and HAMAMATSU-R760 (circles) phototubes.

sample of FEU-68 (shown with triangles and squares) and HAMAMATSU-R760 ıown with circles) equipped with a silica fused window. The output current of ΞU-68 drops by 50% after 500 krad while HAMAMATSU-R760 stands up to at ıst 1.7 Mrad without noticeable degradation of the signal.

The HV supply system of the HERA-B calorimeter phototubes is based the Cockroft-Walton solution [12]. The HV distribution on the Cockroft-Walton vider stages was measured to be stable within 1% accuracy after irradiation of up 5 Mrad.

Acknowledgements

would like to thank the organizers of this conference for providing support. I also ank Sergey Semenov, Sergey Shuvalov, Vladimir Rusinov and Evgueny Tarkovsky r many helpful and stimulating discussions.

References

1. HERA-B Collaboration, HERA-B Proposal, DESY-PRC 94/02, May 1994.
2. HERA-B Collaboration, HERA-B Design Report, DESY-PRC 95/01, January 1995.
3. LHC-B Collaboration, LHC-B Letter of Intent, CERN/LHCC 95-5, August 1995.
4. SDC Collaboration, SDC Technical Design Report, SDC-92-201, SSCL-SR-1215, 1992.
5. V.G.Vasilchenko, New results on plastic scintillator radiation damage, CMS TN 94-220, 1994.
6. V.A.Kachanov et al., Study of characteristics of real size $PbWO_4$ crystal cells for precise EM-calorimeters to be used at LHC energies, Report at the Int. Workshop CRYSTAL-2000, Chamonix, France, 1992.
7. O.V.Buyanov et al., Beam studies of EM-calorimeter prototype built of heavy fast-scintillating $PbWO_4$ crystals, ALICE/93-25, CERN, Geneva, 1993.
8. J.Badier et al., NIM **A344** (1994) 57.
9. J.Badier et al., NIM **A348** (1994) 74.
10. J.Badier et al., Multi-Bundle Shashlik calorimeter prototypes, CMS TN/94-197.
11. Workshop on PHENIX PbSc EM Calorimeter, IHEP, Protvino, 1993.
12. J.D.Cockroft and E.T.S.Walton, Proc. R. Soc. London **A347** (1932) 229.

Table 1: Parameters of the HERA-B calorimeter.

	Inner	Middle	Outer
Outer size	$156 \times 89\ cm^2$	$446 \times 268\ cm^2$	$624 \times 468\ cm^2$
Type	Shashlik	Shashlik	Shashlik
# of channels	2100	2128	1728
Absorber	Tungsten	Lead	Lead
Volume ratio	W/Scint = 2/1	Pb/Scint = 3/6	Pb/Scint = 3/6
Moliere radius	1.4 cm	4.2 cm	4.2 cm
Radiation length	0.56 cm	1.68 cm	1.68 cm
Cell size	$2.23 \times 2.23\ cm^2$	$5.575 \times 5.575\ cm^2$	$11.15 \times 11.15\ cm^2$
Depth	12.8 cm (23 X_0)	34 cm (20 X_0)	34 cm (20 X_0)
Weight	2.1 tons	11 tons	36 tons
Absorb. weight	1.63 tons	8.5 tons	27.6 tons
Scint. weight	52 kg (1 mm plates)	1600 kg (6 mm plates)	5180 kg (6 mm plates)
WLS fibres	Y-11 (3.8 km)	BCF-91A (42 km)	BCF-91A (137 km)
Phototube	FEU-68 R760	FEU-84-3	FEU-84-3

Table 2: Parameters of the LHC-B electromagnetic calorimeter.

	Inner
Radiator	$PbWO_4$ crystal
Dimensions	$80 \times 80 \times 40\ cm^3$
Beampipe hole	$30 \times 30\ cm^2$
Depth	25 X_0
Moliere radius	2 cm
Module size	$7.5 \times 7.5 \times 40\ cm^3$
Channels per module	16
# of modules	128
Crystal size	$18.75 \times 18.75 \times 225.0\ cm^3$
Phototube	Hamamatsu R5189 or FEU-68 with amplifier
# of channels	1824
	Outer
Type	Shashlik
Dimensions	$8.1 \times 8.1 \times 0.5\ m^3$
Average thickness	22.5 X_0
Moliere radius	34 mm
Module size	$15 \times 15 \times 50\ cm^3$
Sampling structure	125 layer (1 mm Pb+ 2 mm Scint. + 0.2 mm paper)
Holes per module	20×20, 7.5 mm spacing, 1.2 mm dia, 2.9%
Fibre per module	$\sim$ 200 m
Module weight	42.4 kg
16 cell modules	$3.75 \times 3.75 cm^2$, 220 (3520 cells)
4 cell modules	$7.5 \times 7.5 cm^2$, 768 (3072 cells)
1 cell modules	$15 \times 15 cm^2$, 1892 (1892 cells)
Phototube	Hamamatsu R5600 or FEU-115M
# of channels	8484

ascati Physics Series Vol. VI, (pp. 65–84)
[INT. CONF. ON CALORIMETRY IN HEP – Frascati, June 8–14, 1996

ELECTROMAGNETIC CALORIMETRY REQUIREMENTS FOR LHC PHYSICS. POTENTIAL OF THE ATLAS ELECTROMAGNETIC CALORIMETER

Fabiola Gianotti
PPE Division, CERN, 1211 Geneva 23, Switzerland
and
Dipartimento di Fisica dell' Università di Milano,
Via Celoria 16, 20123 Milano, Italy

ABSTRACT

Electromagnetic calorimeters will play a crucial role at the CERN Large ıdron Collider (LHC). The numerous requirements coming from physics are dis- ssed in this paper. In particular, the physics potential of the electromagnetic lorimeter of the ATLAS experiment is described.

Introduction

ıysics requirements for the LHC electromagnetic (EM) calorimeters have been dis- .ssed for more than ten years [1]. Today, a vast R&D activity has been completed, ıd several prototypes of the future calorimeters have been built and tested with :ams. Detailed simulation studies of the most interesting physics channels have :en performed, and the detectors optimised accordingly [2, 3]. The design of the HC calorimeters, both for the ATLAS and CMS experiments, is well advanced or 'en frozen. For instance, the construction of the so-called "module zero" of the TLAS EM calorimeter has started.

Therefore, we have today a much deeper understanding of how an EM ılorimeter should operate at the LHC, and revisiting the physics requirements in ıe light of our present experience is not a mere repetition.

LHC physics requirements

he role of the EM calorimeters at past and present hadron colliders has been and : to measure the energy and the position of electrons and photons; to measure, together with the hadronic calorimeter, the energy of jets and the event missing transverse momentum ($\not{p}_T$); to identify particles, namely recognise electrons and photons from hadrons and jets.

These will be the principal calorimeter tasks also at the LHC, made more difficult, however, by the two main parameters of the machine: the large centre-of-mass energy (16 TeV), which requires good performance over an energy range extending from 1–2 GeV up to the TeV scale and demands a much larger dynamic range of the readout electronics than in existing calorimeters; and the high luminosity. At the LHC design luminosity ($10^{34}\,\mathrm{cm}^{-2}\mathrm{s}^{-1}$), twenty soft collisions will be produced, on average, every bunch crossing (i.e. every 25 ns), giving rise to the so-called "pile-up" both in space and in time. Fast detector response (< 50 ns) and fine granularity are required to minimise the impact of the pile-up on the physics, as well as high radiation resistance given the huge particle fluxes expected over a period of operation of at least ten years.

The LHC physics goals set challenging detector performance specifications. This is the subject of the next sections.

2.1 Benchmark physics channels

Although the LHC EM calorimeters will be involved in a variety of measurements, the most stringent performance specifications come from a few channels: the search for a Higgs boson through the decays H$\rightarrow \gamma\gamma$ and H$\rightarrow 4e$; the search for heavy Vector Bosons (W', Z') with masses up to 5–6 TeV decaying into W'$\rightarrow e\nu$ and Z'$\rightarrow e^+e^-$; the detection of inclusive electrons with $p_T \geq 20$ GeV. These channels set the most severe requirements in terms of energy resolution, position/angle resolution, particle identification capability and dynamic range.

Figure 1 shows the LHC discovery potential of a Standard Model Higgs boson for masses up to the upper limit set by the theory (1 TeV). It can be seen that if the Higgs mass is larger than two times the mass of the Z, Higgs discovery at LHC is relatively easy, thanks mainly to the "gold-plated" decay mode H$\rightarrow$ ZZ $\rightarrow 4\ell$. On the other hand, the most difficult region (lowest significance) is for Higgs masses between the expected LEP2 limit of 98 GeV and $\sim$ 180 GeV, where decay channels with large branching ratios (H$\rightarrow b\bar{b}$) are difficult to extract from the background, while channels with clear signatures (for instance H$\rightarrow \gamma\gamma$) have small rates. This region is mainly covered by two decay modes, H$\rightarrow \gamma\gamma$ and H$\rightarrow 4\ell$, and the possibility of observing the Higgs in this mass window through these two channels sets very stringent requirements on the EM calorimeter performance in terms of energy resolution and particle identification capability. As an example, the H$\rightarrow \gamma\gamma$ channel is discussed in more detail in the next section.

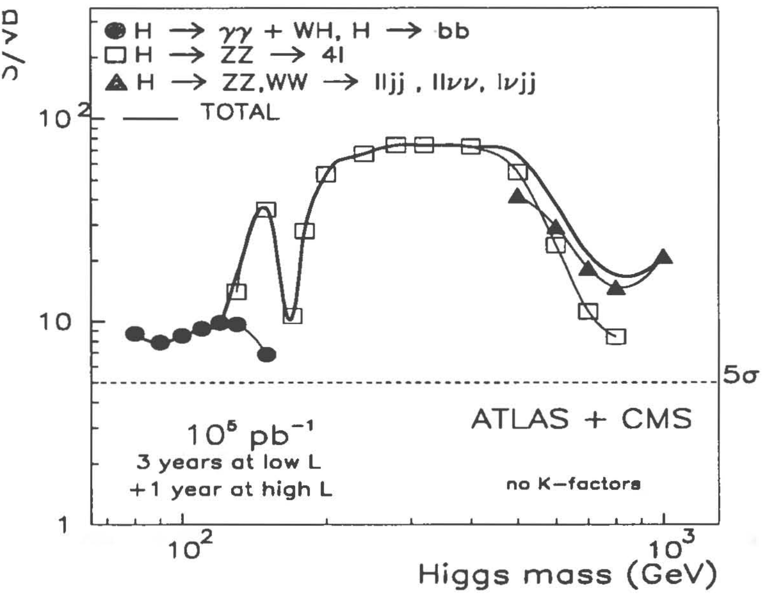

gure 1: Expected significance of a Standard Model Higgs signal over background the LHC as a function of the Higgs mass for an integrated luminosity of 10^5 pb^{-1}. ıe two experiments ATLAS and CMS are combined. Different symbols refer to fferent decay channels.

.1.1 $H \rightarrow \gamma\gamma$

his decay [4] gives rise to two high-p_T photons ($p_T \simeq 50$ GeV) in the final state. he signal cross-section is about 50 fb, while the backgrounds have much larger ıtes:

- The $\gamma\gamma$ irreducible background has a cross-section 30 times larger than the signal cross-section. Since the intrinsic width of the Higgs is a few MeV in this mass region, the possibility of observing a signal peak in the $\gamma\gamma$ invariant mass distribution over the background continuum depends crucially on the energy and angular resolution of the EM calorimeter. A mass resolution of the order of 1% or less is needed.

- The γ-jet and jet-jet production is more than six orders of magnitude larger than the $\gamma\gamma$ continuum, and is affected by large theoretical and experimental uncertainties. Therefore, a rejection of the order of 5000 against jets faking photons is needed, with high efficiency for isolated photons, in order to reduce this background safely below (<20%) the $\gamma\gamma$ rate. This requires adequate transverse and longitudinal segmentation of the EM calorimeter (better than $\Delta\eta \times \Delta\phi = 0.05 \times 0.05$), and a fine-grained preshower-like detector to reject photon pairs from high-p_T π^0's produced among the jet fragments.

2.2 Summary of the physics requirements

The main EM calorimeter requirements set by the LHC physics are listed below. These requirements have guided the design of the ATLAS and CMS calorimeters.

- Rapidity coverage over at least $|\eta| \leq 2.5$. A coverage limited to the region $|\eta| \leq 2$ would decrease the significance of a H$\rightarrow \gamma\gamma$ signal over the background by $\sim$ 10%. The loss would be even larger for the H$\rightarrow 4e$ channel. For the same reason, regions of the acceptance with deteriorated energy response (transition between barrel and end-cap, border between calorimeter modules, etc.) should be kept smaller than 10% of the total coverage.

- Electron reconstruction and identification capability from 1–2 GeV up to 3 TeV. The lower limit comes from the possibility of reconstructing low-p_T electrons produced in the semileptonic decays of b-quarks, which would allow to increase the total b-tagging efficiency by 10%. This lower limit is therefore important for the search for a possible H$\rightarrow b\bar{b}$ decay [2], and for many aspects of B-physics [5]. The upper limit is set by electrons from Z' and W' decays.

- Excellent energy resolution over the range 10–300 GeV, in order to achieve a mass resolution of 1% for the H$\rightarrow \gamma\gamma$ and H$\rightarrow 4e$ channels in the mass region 90–180 GeV (see section 3.1). In particular, the constant term of the energy resolution must be kept smaller than 1%, which is not an easy task since the LHC EM calorimeters will be equipped with more than 10^5 readout channels. A small constant term is needed not only for Higgs physics, but also for the search of a heavy Z'. This is because the constant term dominates the calorimeter resolution at high energy, and the contribution of the detector resolution to the width of the reconstructed Z' mass should be kept smaller than the Z' intrinsic width ($\Gamma_{Z'} \simeq 10$ GeV for $m_{Z'} \simeq 1$ TeV according to Extended Gauge Theories).

- Total thickness of at least 24 radiation lengths, in order to keep the contribution to the energy resolution coming from longitudinal fluctuations of high-energy showers ($E > 500$ GeV) not fully contained in the calorimeter to an acceptable level (<0.4%).

- Dynamic range between 30 MeV and 3 TeV, where the lower limit corresponds to the typical electronic noise per channel and the upper limit to the maximum energy deposited per cell by electrons produced in the decays of Z' and W' with masses 5–6 TeV.

- Response linearity of better than 0.5% in the energy range up to 300 GeV, to preserve the mass resolution for the H→ $\gamma\gamma$ and H→ $4e$ channels. A linearity at the level of 1% is adequate at higher energy.

- Capability of measuring the shower direction in θ with a resolution of ~ 50 mrad$/\sqrt{E(\mathrm{GeV})}$. The energy resolution is not the only contribution to the width of the reconstructed $\gamma\gamma$ invariant mass in the case of the H→ $\gamma\gamma$ channel. There is also a contribution coming from the measurement of the photon direction in θ. This is because at the LHC the position of the interaction vertex along the beam axis will have a spread of 5.6 cm. At low luminosity, charged tracks belonging to the underlying event associated with the H→ $\gamma\gamma$ event can be used to determine the vertex position with high accuracy. But at the design luminosity, the pile-up will significantly reduce the efficiency of this method, so that in most cases the directions of the two photons will be known with poor accuracy, which would spoil the $\gamma\gamma$ mass resolution. Therefore the EM calorimeter has to provide an independent measurement of the photon direction in θ. This requires good transverse and longitudinal segmentation of the calorimeter (see section 3.2) or, in the absence of longitudinal segmentation, the use of a preshower detector [3].

- γ/jet separation capability. As discussed in section 2.1.1, a jet rejection of 5000 (for a photon efficiency of 80% or more) is required for $p_T \simeq 50$ GeV in order to suppress the γ-jet and jet-jet backgrounds to the H→ $\gamma\gamma$ channel. In particular the calorimeter, or a dedicated preshower detector, must be able to reduce the rate of isolated π^0's produced in the quark fragmentation by a factor of at least three (see section 3.5).

- e/jet separation capability. At the LHC, the rate of isolated electrons with $p_T = 20 - 50$ GeV, coming for instance from W, Z and heavy flavour decays, is five orders of magnitude smaller than the rate of QCD jets of the same p_T (e/jet$\sim 10^{-5}$). For comparison, the same ratio is e/jet$\sim 10^{-3}$ at the Tevatron $p\bar{p}$ collider. As a consequence, the electron identification capability of the LHC experiments has to be two orders of magnitude better than at present hadronic machines. In particular, a jet rejection factor of about 10^6 will be needed to extract a signal due to genuine electrons. This rejection will be based on the information of the EM and hadronic calorimeters, combined with the information from the inner detector (see section 3.5).

- τ/jet separation capability. For a large part of the parameter space of the Minimal Supersymmetric extension of the Standard Model (MSSM [6]), the heaviest Higgs bosons (A, H, $H^\pm$) decay preferentially to τ's. Therefore, powerful separation of τ jets from QCD jets is mandatory to fully explore the MSSM. Simulation studies [2] have shown that a rejection of at least 400 against QCD jets, for a τ efficiency of 30%, is needed to achieve this goal. This rejection may be obtained by combining the information of the EM calorimeter (identification based on the shower shape), of the hadronic calorimeter and of the inner detector.

- Fast response. The detector integration time should be as short as possible, in order to minimise the impact of the pile-up on the detector performance issues listed above.

- Coherent noise per channel smaller than $\sim$ 3 MeV. A larger coherent noise would spoil the measurement of the event missing-p_T, as it is demonstrated in section 3.4. Good $\not{p}_T$ resolution is needed at the LHC to observe, for instance, the already mentioned decays of the MSSM Higgs bosons into pairs of τ's, since the $\not{p}_T$ resolution determines in most part the width of the reconstructed $\tau\tau$ invariant mass.

- Bunch-crossing identification capability down to 1 GeV of deposited energy in a trigger tower[1], in order to identify electrons and photons at the trigger level by applying isolation cuts in the trigger towers surroundig the electromagnetic shower. This requires a calorimeter time resolution of a few nanoseconds at 1 GeV.

This unprecedented list of requirements is complicated by several additional difficulties: the LHC EM calorimeters will be very large systems ($> 10^5$ channels); they will have to stand neutron fluences of up to 10^{15}n/cm^2 and radiation doses of up to 200 kGy (integrated over ten years of operation); they must be built within reasonable cost constraints.

The solution to the above list of requirements is not unique, since the ATLAS and the CMS calorimeters are based on two completely different technologies. The main design features, the expected performance and the physics potential of the ATLAS calorimeter are discussed in the next sections.

3 The ATLAS electromagnetic calorimeter

A view of the ATLAS calorimetry is presented in fig. 2. The electromagnetic section is a lead-liquid argon calorimeter with Accordion geometry, covering the rapidity

[1]The size of a trigger tower is $\Delta\eta \times \Delta\phi = 0.1 \times 0.1$ in ATLAS.

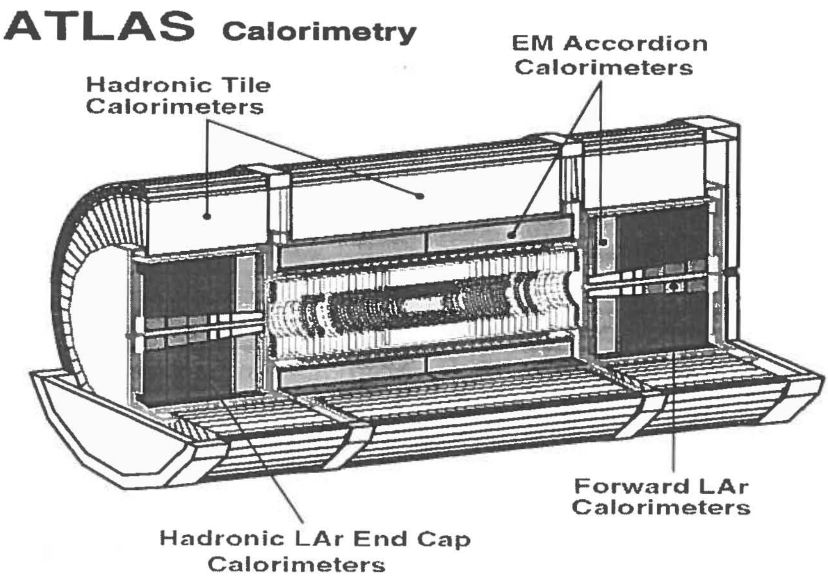

igure 2: Three-dimensional view of the ATLAS calorimeters. The inner detector also visible.

ange $|\eta| \leq 3.2$. It surrounds the inner detector (also shown in fig. 2), which is inside 2 T solenoidal field. The superconducting coil producing this field is located in ront of the EM calorimeter, and will be integrated in the vacuum of the barrel ryostat in order to reduce the amount of material and the dead space in front of he calorimeter.

Over the region $|\eta| < 2.5$, which is devoted to precision physics (Higgs earches, etc.), the EM calorimeter is divided into three longitudinal compartments. he first compartment is segmented in narrow strips in the η direction (4 mm pitch), hich are used to separate single photons from $\pi^0 \to \gamma\gamma$ decays and contribute to he measurement of the shower direction (see section 3.2). The second compartment as a granularity $\Delta\eta \times \Delta\phi = 0.025 \times 0.025$ (corresponding to a 4 cm cell size in both irections), while the third compartment has a granularity $\Delta\eta \times \Delta\phi = 0.05 \times 0.025$. This segmentation, which is finer than in most of the existing calorimeter systems, ives rise to a total of 170000 channels, which are read out by electronic chains ocated outside the cryostats.

The lead thickness in the absorber plates changes from 1.1 mm to 2.2 mm s a function of rapidity, so as to optimise the calorimeter performance in terms f energy resolution [7]. The liquid argon (LAr) gap is 4 mm thick in the barrel art ($|\eta| < 1.47$) and smaller in the end-cap. More details about the calorimeter eometry and mechanics can be found in [7, 8, 9].

In the barrel part the EM calorimeter is preceded by a presampler detector. The presampler is a LAr active layer with independent readout, located behind the cryostat cold wall. Its main purpose is to recover the energy lost by electrons and photons in the material in front of the EM calorimeter (see section 3.1.1). A presampler is probably not needed in the end-cap region, where the amount of material in front of the calorimeter is less (no coil) and the shower energy larger for a given transverse momentum.

3.1 Energy resolution

The energy resolution of a generic calorimeter can be parametrized as

$$\frac{\sigma}{\mathrm{E}} = \frac{a}{\sqrt{E}} \oplus \frac{b}{E \cdot sin\theta} \oplus c \tag{1}$$

where the first term on the right-hand side is the sampling term, the second one is the noise term (which includes also the contribution of pile-up at the LHC design luminosity), the third one is the constant term, and θ is the particle polar angle with respect to the beam axis. In the energy range 10–300 GeV, where excellent resolution is required at the LHC, none of these terms is negligible, so all of them have to be kept as small as possible.

3.1.1 Sampling term

A liquid argon sampling calorimeter has a typical sampling term of $10\%/\sqrt{E(\mathrm{GeV})}$. This is what has been measured with barrel and end-cap prototypes of the ATLAS Accordion calorimeter (see fig. 3 left).

Although homogeneous calorimeters, such as the CMS crystal calorimeter, have better sampling terms [10], ATLAS has chosen a LAr calorimeter in order to satisfy, in a balanced way, several requirements at the same time: the LAr technique is intrinsically radiation hard; it allows for a fine longitudinal and lateral detector segmentation (which improves particle identification); it is uniform, stable and relatively easy to calibrate (which improves the constant term in the energy resolution).

Furthermore, when operating at the LHC the EM calorimeter will be preceded by several layers of material: by the coil and the cryostat walls in ATLAS, by a preshower detector in CMS, by the inner detector (inside a magnetic field) in both experiments. This environment will unavoidably spoil the calorimeter performance, thus reducing the advantage of the calorimeter with the better resolution.

The effect of the upstream material on the calorimeter energy resolution has been studied with test beam data. The result is shown in fig. 3 (right) and indicates that the r.m.s. of the energy lost in 3.5 X_0 of material, which is much

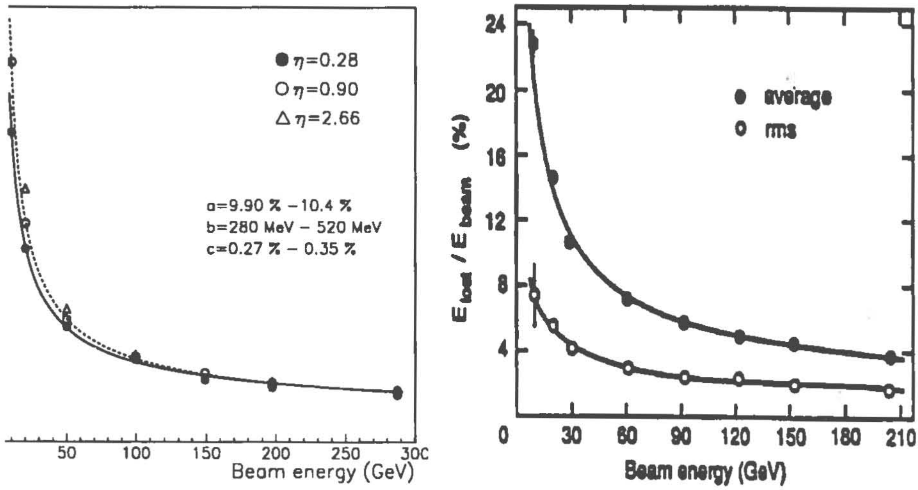

gure 3: Left: Energy resolution as a function of the incident beam energy for test ectrons incident at three rapidities: η=0.28 and η=0.9 (barrel prototype), and =2.66 (end-cap prototype). The three terms of the energy resolution (see text) easured at these rapidities are also indicated. Right: Average and r.m.s fraction energy lost by test electrons in 3.5 X_0 of passive material in front of an Accordion ototype, as a function of the incident beam energy.

ore than the material in front of the ATLAS EM calorimeter over most of the pidity coverage, can be parametrized as $\sim 20\%/\sqrt{E(\mathrm{GeV})}$. These fluctuations, hich are a factor of two larger than the intrinsic sampling term of the Accordion ee fig. 3 left), would ruin the calorimeter resolution if these energy losses were not easured. Both simulation studies and test beam results [11] have demonstrated at an almost complete recovery is possible, for instance by using a massless gap a presampler, if the upstream material does not exceed 2.5–3 X_0. With more aterial, the resolution of the calorimeter is fully dominated by the fluctuations of e energy lost in front of it.

Furthermore, the layers of the inner detector, which are located at a large stance from the EM calorimeter and are inside a magnetic field, contribute to the rmation of low-energy tails in the electron and photon energy spectra reconstructed the calorimeter. This is because electrons and photons interacting in the inner etector produce secondary particles (for instance e^+e^- pairs in the case of photon onversions). These secondaries are opened up in ϕ by the magnetic field and reach e EM calorimeter at a distance of a few centimetres from each other. In order collect the full energy of these secondaries, and therefore of the original particle, usters of many calorimeter cells should be used. On the other hand, clusters of w cells are required in order to minimise the contribution to the energy resolution coming from the pile-up and electronic noise, which scales approximately as the square root of the cluster size. The best compromise between these two competing factors consists in using asymmetric clusters, larger in the ϕ than in the η direction. Clusters of 3×5 cells in $\eta \times \phi$ are used in ATLAS, corresponding to a calorimeter area of 11×20 cm^2. Even with such large clusters, low-energy tails at the level of a few percent persist. At the test beam (no inner detector in front, no magnetic field, no coil) an electromagnetic shower in the Accordion calorimeter is contained in 8×8 cm^2 and no tails are observed. The problem of tails is more serious in CMS than in ATLAS (see section 3.3) because of the stronger magnetic field of CMS (4 T, as compared to 2 T in ATLAS) and of the better intrinsic resolution.

A lot of effort has been invested in ATLAS to minimise the amount of material in front of the EM calorimeter [7]. In the present layout (fig. 4 left), the total material seen by an incident particle from the interaction vertex up to the calorimeter front face is 1.7 X_0 at $\eta = 0$, increasing to 3.5 X_0 at the end of the barrel ($\eta = 1.47$) due to the effect of the angle. On the other hand, the material in front of the presampler never exceeds 2.5 X_0, which allows for an almost complete energy resolution recovery.

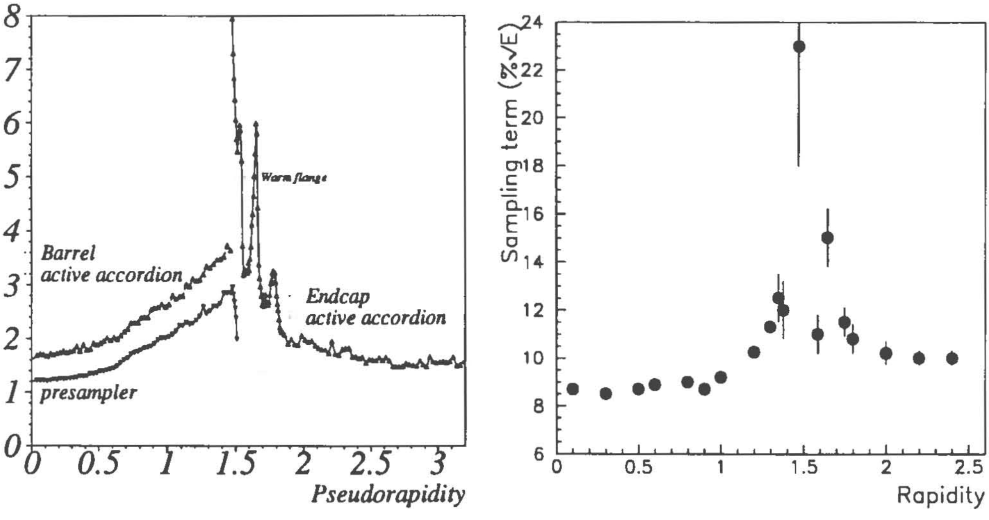

Figure 4: Left: Total material (in radiation lengths) seen in ATLAS by an incident particle before reaching the presampler detector (closed symbols) and the EM calorimeter (open symbols), as a function of rapidity. Right: Sampling term of the energy resolution of the ATLAS EM calorimeter as a function of rapidity for photons of transverse energy $E_T = 50$ GeV.

At the transition between the barrel and the end-cap region, the presence two cryostats (housing the barrel and the end-cap EM calorimeters), of the coil, ıd of cables and services of the calorimeter and inner detector, produces spikes of aterial reaching 6–8 X_0. At larger rapidity in the end-cap, the material goes down a more acceptable level of 2 X_0 or less.

The sampling term of the energy resolution, as obtained from a full simution of the ATLAS calorimeter and of the inner detector, is shown in fig. 4 (right). his term is about $9\%/\sqrt{E(\mathrm{GeV})}$ in the barrel and $10\%/\sqrt{E(\mathrm{GeV})}$ in the end-cap, ıe difference being due mainly to the larger lead thickness in the absorber plates the end-cap calorimeter. A strong deterioration of the resolution is visible at the ansition between barrel and end-cap, reflecting the increased amount of material. ptimisation studies are still going on to improve this region.

The expected contribution of the sampling term to the reconstructed $\rightarrow \gamma\gamma$ mass resolution is 820 MeV for a Higgs mass of 100 GeV.

.1.2 *Noise term*

'he contribution of the electronic and pile-up noise to the energy resolution depends n the detector technique and on the performance of the electronic chain.

The expected noise in the ATLAS EM calorimeter is shown in fig. 5. The lectronic noise decreases with the shaping time as $\sim t_p^{-3/2}$, while the pile-up noise ıcreases as $\sim t_p^{1/2}$. There exists therefore an optimum shaping time at which the otal noise (sum of the electronic and pile-up contribution) is minimised. This ptimum shaping is 45 ns in the ATLAS calorimeter at high luminosity, which is quivalent to integrating over two bunch crossings. At the optimum shaping, the otal noise in a calorimeter region of 3×5 cells is expected to be 350 MeV, and the ıoise contribution to the reconstructed H$\rightarrow \gamma\gamma$ mass resolution is expected to be 80 MeV for a Higgs mass of 100 GeV.

!.1.3 *Constant term*

\s already mentioned, the constant term of the energy resolution must be smaller han 1%, since otherwise it would become the dominant contribution to the recontructed mass resolution for a Higgs decaying to two photons or to four electrons in he mass region 90–180 GeV. ATLAS aims at a constant term of 0.7% over the full apidity coverage of the EM calorimeter. The strategy to achieve this goal is the ollowing:

- With a 2 m long prototype of the Accordion calorimeter [12], a position scan over a region of 150 cells has been collected with test electrons of 287 GeV.

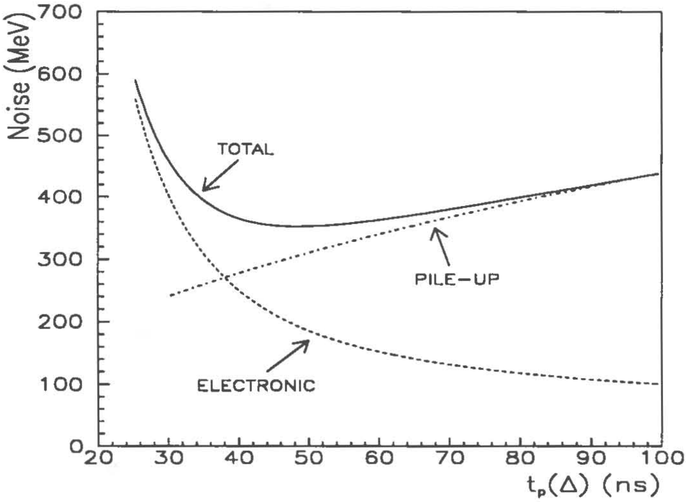

Figure 5: Electronic, pile-up and total noise (r.m.s.) expected in a region of 3 × 5 cells in the ATLAS EM calorimeter at the LHC design luminosity, as a function of the shaping time of the electronic chain.

The response variation from cell to cell had an r.m.s. of 0.6%, which translated into a constant term of 0.7%. Instrumental sources contributing to this constant term were identified: they are listed together with their estimated contributions in tab. 1. As it can be seen, they can explain to a large extent the origin of the measured constant term.

- Based on the experience gained in the construction and test of the 2 m prototype, it is expected that in the ATLAS EM calorimeter, over a region with a similar number of cells as scanned in the prototype ($\Delta\eta \times \Delta\phi = 0.2 \times 0.4$), the various contributions to the constant term listed in tab. 1 reduce to the values given in the third column:

  1. Residual ϕ-modulation. Due to the Accordion geometry, the calorimeter density changes as a function of ϕ, giving rise to a periodical modulation of the response. This modulation can be corrected for. In ATLAS, an optimisation of the Accordion geometrical parameters will allow to reduce the residual modulation after correction, and therefore the contribution to the constant term, from 0.3% (2 m prototype) to 0.2% (ATLAS).
  2. Absorber non-uniformity. The sensitivity of the calorimeter response to the lead thickness in the absorber plates has been studied with test beam data [8]. It was observed that 1% more lead produces a response drop of

.ble 1: Contributions to the constant term of the energy resolution measured with e 2 m prototype and expected in the ATLAS calorimeter over a region of about 0 cells.

Source	2 m prototype	ATLAS
Residual ϕ-modulation	0.3%	0.2%
Absorber non-uniformity	0.3%	0.2%
Gap non-uniformity	0.15%	0.15%
Calibration accuracy	0.25%	0.25%
Timing accuracy	0.2%	0
Cross-talk problem	0.15%	0
Total	0.57%	0.4%

0.7%, mainly due to the decrease of the sampling fraction. This result allowed to determine the tolerances required on the absorber uniformity and the best way for assembling the plates [8], in order to achieve a contribution to the constant term as small as 0.2%.

3. Gap non-uniformity. In a slow LAr calorimeter, with integration time equal or larger than the electron drift time in the gap ($\sim$ 400 ns), the detector response depends linearly on the gap thickness. With fast shaping, the response sensitivity to the gap thickness is largely reduced: a 1% thicker gap produces a response increase of only 0.3%.

   The gap uniformity achieved with the 2 m prototype is shown in fig. 6 (left). Away from the boundary between two calorimeter modules the measured gap dispersion was 50 μm, which translated into a contribution to the constant term of 0.15%. This contribution is acceptable, therefore 50 μm was chosen as the requirement on the gap uniformity for ATLAS. At the module boundary the gap is 7% larger (7% drop in the gap capacitance in fig. 6), hence one expects a response drop of 2–2.5% with fast shaping in this region. This is what has been observed with test beam data (see fig. 6 right).

   The support system of the ATLAS EM calorimeter [8] has been designed in such a way as to obtain an inter-module gap similar to all other gaps in the rest of the calorimeter, in order to eliminate this problem.

4. The calibration system of the ATLAS calorimeter has been designed to deliver uniform pulses within 0.2%. However, a contribution to the constant term of 0.25% from calibration inaccuracies (as in the prototype, where the system was not fully optimised) has been assumed conservatively.

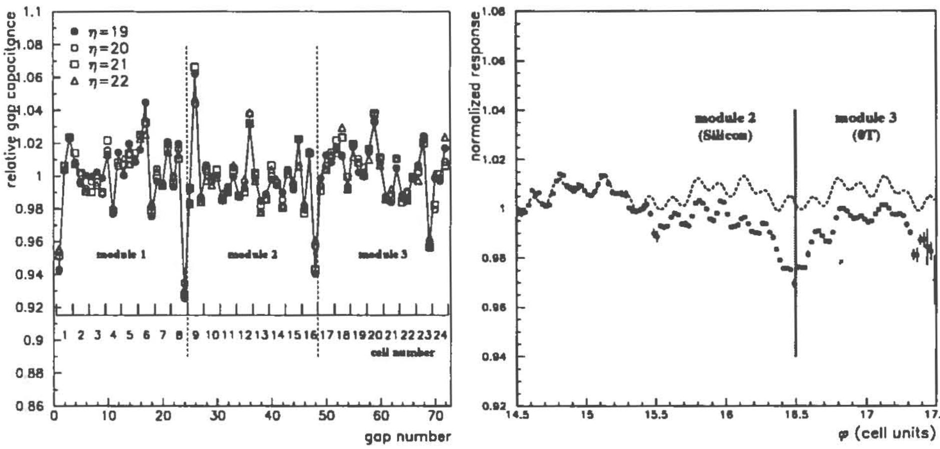

Figure 6: Left: Double-gap capacitance, normalised to the average, as a function of the gap position in the stack, measured with the 2 m prototype at four different η positions. Right: Normalised calorimeter response, as a function of ϕ, to 287 GeV electrons hitting the 2 m prototype at the boundary between the two upper modules of the stack. The dashed curve is a fit to the energy response away from the boundary region.

- In conclusion, a constant term of 0.4% is expected, by construction, over a region of size $\Delta\eta \times \Delta\phi = 0.2 \times 0.4$ of the ATLAS calorimeter. However, long-range non-uniformities, due for instance to temperature effects, mechanical deformations, variation in the material in front of the calorimeter, cannot be *a priori* excluded. These can be controlled with the following tools:

  1. Several calorimeter modules will be tested with beams before being assembled. This will allow to check the uniformity within a module, and to control the module-to-module reproducibility.
  2. *In situ* calibration at the LHC by measuring the E/p ratio (the ratio between the energy reconstructed in the calorimeter and the momentum measured in the inner detector) for electrons. This method, which has been demonstrated by CDF [13] to be a powerful tool for the calorimeter calibration, consists in determining first the momentum scale in the inner detector (by using for instance $J/\psi \rightarrow \mu^+\mu^-$ decays), and then in transferring the momentum scale from the inner detector to the EM calorimeter by requiring that the E/p ratio for electrons be equal to one.
  3. *In situ* calibration by using $Z \rightarrow e^+e^-$ decays, which are abundantly produced at the LHC: one event per second is expected in the initial phase at low luminosity (10^{33} cm^{-2}s^{-1}). Using the Z-mass constraint has the advantage of being a standalone calorimeter method independent of the

inner detector, but the disadvantage that correlations between the two electrons from the Z complicate the procedure. Simulations studies have shown that with 60000 Z$\rightarrow e^+e^-$ decays, which will be collected in about four days of data taking at low luminosity, an overall constant term of 0.6% can be achieved over the ATLAS barrel calorimeter.

The expected contribution of the constant term to the reconstructed $\rightarrow \gamma\gamma$ mass resolution is 490 MeV for a Higgs mass of 100 GeV.

[.4 *Total energy resolution*

ıe total energy resolution for photons of $E_T = 50$ GeV, which is the typical ınsverse energy of photons produced in H$\rightarrow \gamma\gamma$ decays, is about 1.5% in the ırrel region and 1.1% in the end-cap region [7]. Since the constant term does not ange with rapidity, and the total noise is constant with η for a fixed E_T, the tal resolution improves at large rapidity because the sampling term improves (the ower energy increases with rapidity for fixed E_T).

2 Angular resolution

he good longitudinal and lateral segmentation of the ATLAS EM calorimeter allows r an accurate measurement of the photon direction in θ (see section 2.2). This tter is determined by measuring the shower centroid in z at two positions in depth: the strip compartment (with a precision of 3 mm$/\sqrt{E(\mathrm{GeV})}$) and in the second ımpartment (with a precision of 8 mm$/\sqrt{E(\mathrm{GeV})}$). The angular resolution which ın be obtained in this way is shown in fig. 7 (left).

For a fixed transverse energy of the photon, the precision of the angle meaırement improves with rapidity, because the shower energy increases. The points in g. 7 can be parametrised as $\sigma_\theta \sim 45$ mrad$/\sqrt{E(\mathrm{GeV})}$, which satisfies the resolution equirement discussed in section 2.2. On the other hand, the resulting accuracy on ıe vertex position along z, obtained by extrapolating the photon direction from the alorimeter back to the beam axis, deteriorates from 1–2 cm in the barrel to 5–6 cm ı the end-cap (fig. 7 right), mainly because of the larger distance of the calorimeer from the interaction centre. Therefore in the end-cap the vertex measurement rovided by the EM calorimeter is not more accurate than the vertex spread itself. [owever, most H$\rightarrow \gamma\gamma$ decays are expected to contain at least one photon in the arrel calorimeter.

The expected contribution of the photon direction measurement to the econstructed H$\rightarrow \gamma\gamma$ mass resolution is 590 MeV for a Higgs mass of 100 GeV.

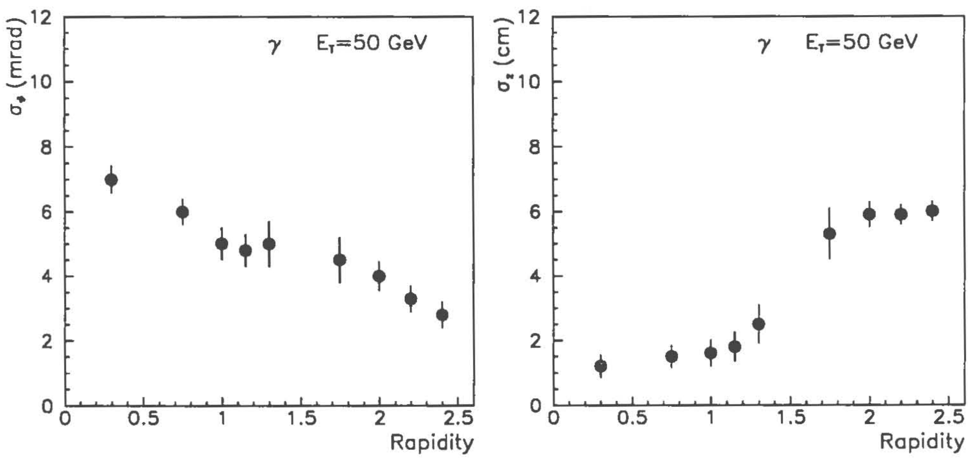

Figure 7: Angular resolution (left) and vertex position resolution in z (right) as a function of rapidity, obtained with the ATLAS EM calorimeter for simulated single photons of $E_T = 50$ GeV.

3.3 Higgs mass resolution

The reconstructed mass spectra for the decays H$\rightarrow \gamma\gamma$ ($m_H = 100$ GeV) and H$\rightarrow 4e$ ($m_H = 130$ GeV), obtained with a full simulation of the ATLAS detector, are shown in fig. 8. The mass resolution is 1.24 GeV (1.02 GeV) at high (low) luminosity for the H$\rightarrow \gamma\gamma$ channel, and 1.67 GeV (1.52 GeV) for the H$\rightarrow 4e$ channel. The dominant contribution comes from the sampling term.

Tails in the mass spectra due to detector effects (material in front of the calorimeter) are at the level of 2% in both cases. The H$\rightarrow \gamma\gamma$ spectrum includes unconverted photons, but also photons which converted in the inner detector.

With the CMS crystal calorimeter, the mass resolution for H$\rightarrow \gamma\gamma$ events with $m_H = 100$ GeV is 775 MeV [3], however when only unconverted photons are considered. In fact the energy measurement for converted photons is significantly spoiled, in CMS, by the effect of the 4 T field (see section 3.1.1). Part of the converted photons have been recently recovered by an improved analysis [14]. The mass resolution for the H$\rightarrow 4e$ channel in CMS [3] is similar to the ATLAS resolution, despite the better sampling term of the CMS calorimeter, because of the effect of electron bremsstrahlung in the 4 T field. This effect is responsible also for more low-energy tails in the reconstructed spectrum than in ATLAS.

In ATLAS, the expected signal significance over background is 4.8 for a H$\rightarrow \gamma\gamma$ signal with $m_H = 100$ GeV and an integrated luminosity of 10^5 pb^{-1}, and 5.2 for a H$\rightarrow 4e$ signal with $m_H = 130$ GeV and an integrated luminosity of $3 \cdot 10^4$ pb^{-1}.

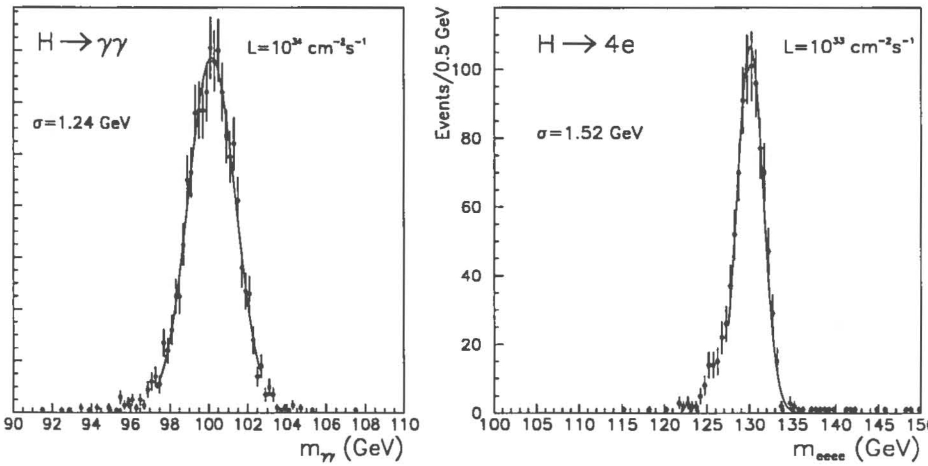

ıgure 8: Reconstructed $\gamma\gamma$ invariant mass for H→ $\gamma\gamma$ events with m_H = 100 GeV ɜft), and reconstructed four-electron invariant mass for H→ $4e$ events with m_H = ı0 GeV (right), obtained with a full simulation of the ATLAS EM calorimeter and ner detector.

4 Missing p_T measurement

he quality of the $\not{p}_T$ measurement in ATLAS has been studied with a full detector mulation and is shown in fig. 9 (left).

The $\not{p}_T$ resolution is dominated by the energy resolution of the hadronic ılorimeter. However, LHC EM calorimeters will have many more channels than ədronic calorimeters, and the presence of coherent noise (which scales linearly with ıe number of channels involved in the energy measurement) in the readout elec- onics of the EM calorimeter could have a serious impact on the $\not{p}_T$ measurement. he effect of the coherent noise has been studied in ATLAS and is shown in fig. 9 ight). It can be seen that a coherent noise of 5 MeV per channel deteriorates the $_T$ resolution by a factor 1.5 and the significance of a possible $A \rightarrow \tau\tau$ signal with $_A$ = 150 GeV by 20%. Therefore, the coherent noise in the EM calorimeter has to e kept below 3 MeV per channel.

.5 Particle identification

'wing to a good lateral and longitudinal segmentation, and in particular to the resence of a strip compartment, the ATLAS EM calorimeter is expected to provide xcellent performance for particle identification. This is complemented by the inner etector which has also been designed for powerful particle identification, and which ıcludes, in particular, a Transition Radiation Tracker. Therefore, when combined

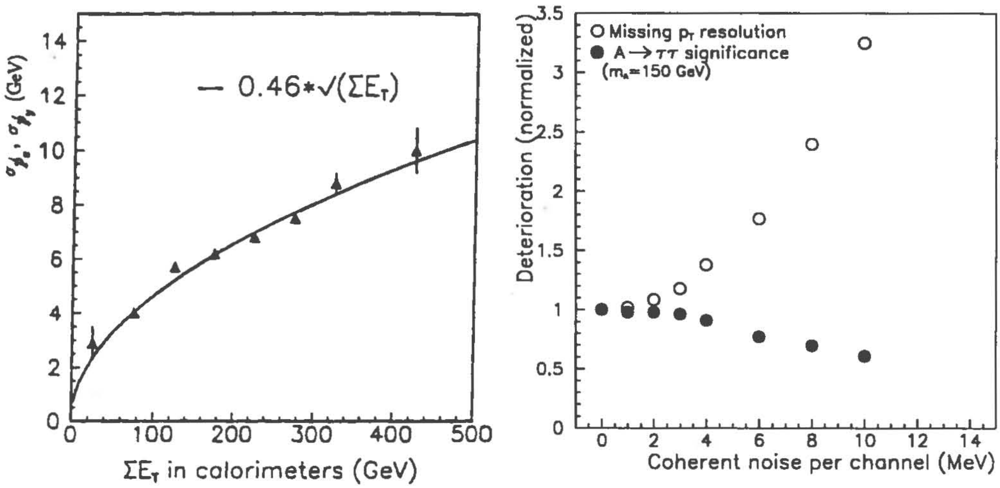

Figure 9: Left: Resolution of the two components of the $\not{p}_T$ vector ($\not{p}_x$, $\not{p}_y$) at low luminosity, as a function of the total transverse energy in the ATLAS calorimeters. Right: Deterioration of the $\not{p}_T$ resolution and of the significance for a $A \to \tau\tau$ signal with $m_A = 150$ GeV, as a function of the coherent noise per channel in the EM calorimeter.

together, the EM calorimeter, the hadronic calorimeter and the inner detector are expected to be able to achieve the desired rejection of the jet background (see section 2.2) for high electron and photon efficiency.

Electron and photon identification in ATLAS is discussed more extensively in [7, 15]. Here the main aspects of the expected performance are only briefly summarised.

Figure 10 (left) shows the residual jet-jet and γ-jet backgrounds to the H→ $\gamma\gamma$ channel at different levels of the γ/jet separation procedure.

After cuts in the hadronic calorimeter and in the second and third compartments of the EM calorimeter (dashed line), based on the different lateral and longitudinal shape of showers produced by jets and by single photons, the total jet background (jet-jet plus γ-jet), which at this level consists mainly of isolated π^0's, is of the same order as the $\gamma\gamma$ irreducible background. It can be further reduced to below 20% of the $\gamma\gamma$ rate (see section 2.2), provided that the surviving π^0's are rejected by a factor of three. This is achieved in ATLAS by using the information of the strip compartment (full line). The efficiency of these γ/jet identification criteria for single photons is 80%.

The e/jet separation capability of ATLAS in the p_T range 20–50 GeV is shown in fig. 10 (right). It can be seen that the EM and hadronic calorimeters alone provide a jet rejection of 1000, for more than 90% electron efficiency. Another factor

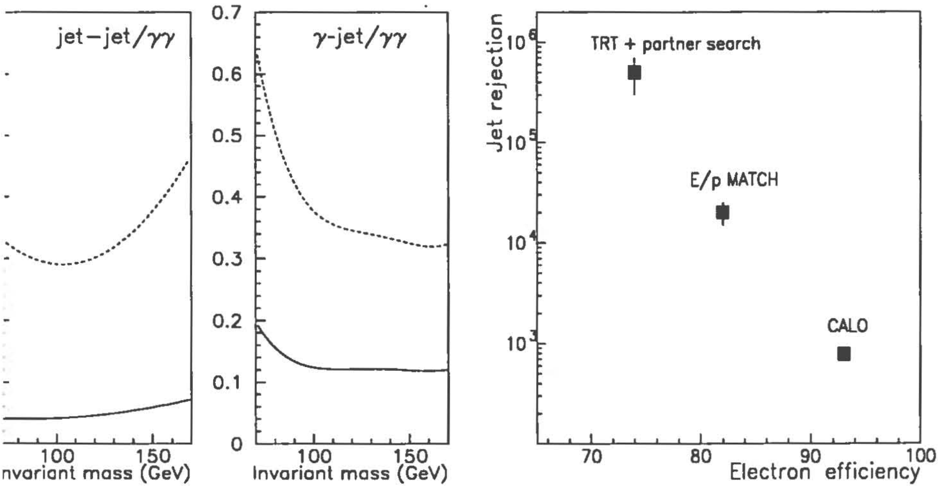

ıgure 10: Left: Expected ratio between the residual jet background and the $\gamma\gamma$ reducible background, as a function of the invariant mass of the pair of photon ındidates, before (dashed line) and after (full line) π^0 rejection in the strip comırtment. Right: Jet rejection as a function of the electron efficiency, obtained with ıe calorimeters and inner detector (see text) at high luminosity.

ten in the rejection is obtained by combining the EM calorimeter information with ıe inner detector, that is by requiring a track in the inner detector pointing to the ıower in the EM calorimeter, with momentum matching the shower energy. A ıal rejection of more than 10^5 (see section 2.2) is achieved by using the Transition adiation Tracker to recognise charged hadrons faking electrons, and by rejecting ›nverted photons. The overall electron efficiency for these selection criteria is 75%.

Figure 10, which was obtained from a full simulation of large samples of vo-jet events in the ATLAS detector, shows that ATLAS has the capability to ›ject the hadronic backgrounds to the desired level.

Conclusions

lectromagnetic calorimeters will play a very important role at the LHC. They will e used for a variety of measurements, involving electrons, photons, jets, neutrinos, 's, b-jets, etc. They will also play a crucial role in the search for channels of prime ıterest, such as H→ $\gamma\gamma$, H→ $4e$ and Z'→ e^+e^- decays.

Their task will be more difficult than at present colliders. Most of the ew channels are expected to have low rates, and even standard processes will often ave smaller signal-to-background ratios than at present machines. Furthermore the detectors will operate in an extremely harsh environment (radiation, pile-up), which demands challenging technical specifications (speed, radiation hardness, dynamic range).

The ATLAS LAr EM calorimeter is based on a robust and stable technique, well suited to this difficult environment. It is a versatile detector, allowing for good energy resolution, excellent response uniformity, powerful particle identification and accurate position and angle measurements.

References

1. See for instance Ph. Bloch, Electron and photon identification, in: Proc. of the LHC ECFA-CERN Workshop (Lausanne, March 1984), ECFA 84/85, CERN 84–10, **2**, 369 (1984).
2. ATLAS Collaboration, Technical Proposal for a general-purpose *pp* experiment at the Large Hadron Collider at CERN, CERN/LHCC/94–43, LHCC/P2 (1994).
3. CMS Collaboration, Technical Proposal, CERN/LHCC/94–38, LHCC/P1 (1994).
4. V. Tisserand, these Proceedings.
5. ATLAS Collaboration, CERN/LHCC/93–53.
6. Z. Kunszt and F. Zwirner, Nucl. Phys. **B385**, 3 (1992).
7. M. Seman, these Proceedings.
8. B. Mansoulié, these Proceedings.
9. P. Fassnacht, these Proceedings.
10. C. Seez, these Proceedings.
11. D.A. Lissauer, Performance of an Accordion electromagnetic calorimeter with liquid krypton, in: Proc. of fifth International Conference on Calorimetry in High Energy Physics, Brookhaven National Laboratory (New York), 1994.
12. D.M. Gingrich et al., Nucl. Instr. and Meth. **A364**, 290 (1995).
13. F. Abe et al., Phys. Rev. Lett. **75**, 11 (1995).
14. K. Lassila-Perini, these Proceedings.
15. I. Vichou, these Proceedings.

'ascati Physics Series Vol. VI, (pp. 3–12)
I INT. CONF. ON CALORIMETRY IN HEP – Frascati, June 8–14, 1996

THE DOMINANT ROLE OF TECHNICAL PROGRESS (FROM THE ELECTROSYNCHROTRON TO DAΦNE)

Giorgio Salvini

ABSTRACT

One specific point of my opening address to this conference dedicated to alorimetry is to recall the primary importance of instruments, detectors and laboratories the progress of physics. This has been particularly evident in these last fifteen years, ır technical progress has succeeded in clarifying and deeply renewing our general eas. The fact is that, in the past, we have never been so modest (or conscious of the nits of our understanding) as in this period. In the following we recall some present ·oblems connected to the limits of our detectors (part I) and the contribution of Frascati ›art II), from past results to present expectations for the measurements of DAΦNE.

ıtroduction

I would like on this occasion to recall the importance of experiments, instruments ıd laboratories in the progress of physics. This is obvious, and none of us believes that ıe progress of physics can remain too long in the beautiful "octopus-like" hands of ıeoretical ideas. But I think that the present period of our research is particularly ıteresting in riveting the importance of technical progress and new instruments in arifying or deeply renewing our general ideas.

At the same time I would like to remember the contribution of our Frascati ıboratories during the last thirty years to the progress of our techniques and to the eneral scientific knowledge in physics. So, let me start with some general onsiderations, and after I will concentrate on some of the Frascati results.

his period of physics research is in my opinion very interesting, and I am rather nvious of the younger physicists today for what they will know in the future. Let me be ıore specific.

In 1982, on the wave of the discovery of heavy bosons $W^{\pm}$, Z^0, I thought that we ad understood the basic structure of our Universe. Now we are less sure and we know ıat we must still search and wait. Let me give a glance with you at our present roblems, at our present uncertain replies, and at the technical progress we need to be ıore certain in the future.

The main (formidable) questions are:

1. What are the particles that form our Universe?
2. What is the mass and the presence of neutrinos in our Universe?
3. We are searching for new particles on Earth, Higgs particles, etc. What are our perspectives?
4. What is the density of our Universe? How sure are we of the Big Bang model, the Hubble constant?
5. What is the symmetry of the laws which govern our Universe? (We shall see more of it in the next paragraph).

1. Some general remarks

1.1 What are the particles that form our Universe?

This, as you know, is a fascinating problem. As I said, most of us were more sure in the eighties. Now we know that there must be some other particles other than protons (neutrons, nuclei), electrons, neutrinos and gammas.

Mathematical arguments applied to the laws of gravity, well known to us, and experimental observations on the structure of the galaxies and the evidence of non-luminous bodies wandering throughout the Universe lead us to think that 9/10 of the mass that forms the Universe is an ensemble of particles, perhaps not hadronic, which, however, we cannot clearly identify. It is the so-called dark matter in whose existence we must now believe. There are several possible hypotheses, which we will come across again later when speaking of the particles present on Earth.

One of the most interesting hypotheses is that neutrinos have a mass different from zero, like photons. A good part of dark matter may be composed of neutrinos. However, these alone are not enough. These uncertainties lead us to a clear conclusion: we must study more deeply our galaxies to understand the total mass and not only its luminous mass. In short, where and how is this excess of mass hidden in the Universe?

During the last decades this problem has led almost to a revolution in the theory of the galaxies. Galaxies are masses of stars which formed and compacted through the action of gravity. But near the centre of the galaxy there may be a central vortex, an enormous accumulation, the famous black hole. This enormous central oven attracts stars and swallows them. Yes, it swallows them. A certain evidence - perhaps not yet entirely certain - may be found in recent observations with the HUBBLE telescope (HST) carried out by a group of astronomers[1]. They have observed the presence of an intense source of radiation, for the most part ultraviolet, about a million times more intense than our sun, for a diametric dimension less than fifteen light years (this being e limit of the spatial resolving power of the HUBBLE at that distance). This source is cated at the centre of the galaxy under observation. It is a very interesting result.

The matter captured from the star began to rotate rapidly around the black hole like ather thin disc of gas which emits ultraviolet radiation due to intense heating as it nears e black hole. These are enormous phenomena, fantascientific, which however had eady been predicted several years ago, but which have now been experimentally served.

I have recalled this episode in order to provoke one obvious question: so, when ill we know what the Universe is made of? The reply is: when we have adequate struments to understand the mass of the galaxy, its dark centre, its vortices.

Progress over the last few years has been enormous. The adventure of the UBBLE telescope, its death and resurrection, is fantastic. But it will take time (at least ree more years) and it will be necessary to build larger antennas and telescopes and - me say - an observatory on the Moon, perhaps sooner than one thinks.

2 What is the mass and the presence of neutrinos in our Universe?

My next curiosity regards neutrinos. What is their mass? This, as you know, is an en question.

We do not know yet if the electron neutrinos have zero mass, or something like ·10 eV. The problem is fundamental. We know how to describe the birth and death of a ar, we know how the Sun proceeds in its nuclear reactions and how it sends us a well reseen flux of neutrinos. But you know also that the neutrinos emitted by the Sun em to be, by a factor 1.5 at least, less than expected[2)].

Yes, the problem is relevant. It excites our interest to discover possible neutrino scillations, to measure the possible mass of the neutrino, and to analyse the interpretation of the evolution of the stars, the Sun being a rather calm commoner in e stellar population of the Universe[3, 4)].

When will this problem be resolved? We need new techniques and experiments nd this will not be resolved before the end of this century.

It is a question of:

purity (10^{-18} in U, Thorium content) [Borexino liquid]

quantity of matter (Kamiokande etc.)

Study of oscillations with new large courageous initiatives.

We will have to be patient until the end of the year 2000.

1.3 New particles on the Earth?

In this field, it is wonderful to see how we jump in our catalogues from sure knowledge to an obscure future. You know very well that the questions that the experts face are: How sure are we that the Higgs particle exists, and that it will eventually be discovered? Here too the solutions are bound to our technical progress:

- the luminosity of the accelerating machines;
- the resolving power of the detectors, which is an important challenge for all coming accelerators, from LHC to DAΦNE;
- the year in which the large LHC machine will start recording data.

What is rather probable is that astrophysics will not directly help us in their identification, and we must observe them in the laboratory. (The dark matter problem[4]).

When we put all these parts together, we end with experiments which cannot be ready before the end of the century, perhaps eight years from now, with a battalion of physicists and engineers working at the same experiment.

Let me add that, when speaking of new particles, there are some secret ones which could be discovered only with more advanced calorimeters, for instance cold bolometers, as studied by E. Fiorini[5].

1.4 What is the density distribution of matter in our Universe?

This is a growing problem which needs new observations and will soon present a general challenge. In fact, on the next June 24th, in Princeton (USA), experts will discuss the distribution of matter in our Universe: if we should conceive an isotropic and homogeneous distribution of the stars (the galaxies) in our Universe[6], or an inhomogeneous structure, for instance density decreasing from any point of observation. The question is extremely important. It is clear that the description of our Universe if we assume it as homogenous is in agreement with our easiest representation: an initial big bang, with a Hubble dynamic expansion. This classical rather pleasant structure could be today in serious trouble, for the simple reason that the Universe does not seem to be homogeneous even if isotropic. An inhomogeneous world will imply a different explanation of the Hubble constant, and the simple big bang interpretation could encounter some problems. Many symptoms seem to indicate that the Hubble constant is not so simple and "constant", and the definition of the age of the Universe could have difficulties.

But this is not the main puzzle: it seems (L. Pietronero and co-workers[6]) that the analysis of recent density distributions of the galaxies is rather more fractal than homogeneous. This comes from the subtle analysis of the time-space maps representing ır galaxy distribution. The material is very controversial, and some fierce battle will ppen on that June 24th 1996 in Princeton.

So, let's ask as usual: why can't we solve these doubts on the density and ustering of the Universe in these years? The reply is again: be patient, and it may be at the next century will bring you the reply. In fact the statistics we have now are not t decisive. We will arrive at the systematic exploration of the galaxies up to magnitude), and with poor statistics. New powerful instruments are necessary and are in eparation: one is the 8 metre diameter telescope KEW; it will be possible to explore to agnitude 22-24 and determine red shifts with z values up to $z \approx 2$ [1,7].

An analysis within these limits, with one million galaxies examined, could decide e problem of homogeneity or not. These new limits shall be achieved at the very end of is century. In this period, we do not really know what the structure of the Universe is: ke living in a hotel where you don't know where the windows, the doors, the roof are.

Another open field is the distribution of Radio Galaxies: they are still in a confused ate. But soon Radio Galaxies will contribute to the problem of distinguishing the stribution of dark matter from luminous objects. You understand that until we separate f they are separate) the luminous part of our Universe from the dark matter (which, otice, seems to be 95% of the whole) we will really have no certainty in understanding ıe Universe.

The next century will also bring a contribution from another point of view: the udy of cosmic background radiation. The photons of the cosmic background at 2.72°K ome from a distance which goes well beyond the remotest galaxies. This photosphere f cosmic primeval radiation represents the conditions at about 300.000 years, since the eginning our Universe. In that period the temperature had descended to 3000°K and ɔrmation of neutral atoms (electrons and nuclei) had become possible. The Universe ıen became transparent to light and the thermal photons emitted could travel undisturbed ɔ us.

Well, the careful analysis of the cosmic background radiation[8] has become very ıteresting: in fact density fluctuations should exist, which later gave origin to galaxies, lusters of galaxies and possible other bodies. Present data do not allow the drawing of ure consequences on the nature and distribution of dark matter. Yes, it will take a few ears. We have only candidates like neutrinos for the hot dark matter, and other nknown particles (neutralinos) for the cold one.

It is rather obvious that all the general (philosophical) conclusions on the structure f the Universe, and our present understanding, depend in a breathtaking way on the technical progress of our instruments, calorimeters, balloons, satellites, that is on those too obscure persons, our splendid technicians, that, with their subtle preparation, make the fundamental discoveries possible.

In figure 1 we give some numbers to indicate the limits of our personal knowledge. By M I mean the relative Magnitude; L is the collider luminosity.

LIMITS TO OUR CURIOSITY: WAIT FOR THE NEXT CENTURY!

	1985	1996	What is needed	When?
1 Which particles in our Universe?	e, p, n, g	more, but which?	gravitational optics M=22, ; Z→3 8 metres diameter	2000, hopefully
2 Mass of neutrinos in the Universe	Deficit from sun m_n uncertain	Deficit confirmed N_n, m_n doubtful ~1.5	Borexino etc. Oscillations	2000
3 New particles on Earth; Higgs	$M_H > 600$ GeV Supersymmetry?	$100 < m_H < 600$ Other particles and bodies	LHC $L > 10^{35}$ fast detectors (<10ns)	2003
4 Density of our Universe	Homogeneous Hubble O.K. Big Bang	Inhomogeneous? Is Ho constant? N ~ 4000 (number of measured galazies)	Galaxies/analysis $N > 10^6$ M> 22 $Z \geq 3$	8 metres; Hubble, statistics 2000
5 Symmetry of Universe	CP non conservation e' unknown	$0 < e'/e < 3.10^{-3}$	Daphne etc. $>10^{10}$ events ⇒ $10^7 K_L$ (2P) ⇒ 10^{-3} resolution	1998-2002 D(e'/e) ~ 10^{-4}

Figure 1

2 The contribution of the Frascati laboratories to that technical progress which resulted so decisive to our knowledge

I will now concentrate on our results in Frascati and Rome, and conclude with number 5 of our initial questions.

What follows is far from being the history of Frascati, it is only the memory of a few technical achievements.

When we go back to the beginning of our history, we can recall that our 1.1 Gev Electrosynchrotron had, for a certain period, the highest intensity electron beam. This allowed our analysis on the excited states of protons, the famous 3/2 3/2, 1/2 ... resonances. But there is one point I must recall between 1959 and 1960: the preparation and creation of polarised monochromatic photon beams.

Frascati and its school became masters of fine optical measurements in 1955-59. Along these lines the same persons working on the measurements of magnetic gradients for the machine (I recall G. Diambrini and the school he started), developed the art of getting monochromatic polarised photons through interference with mono crystals, a technique which spread from Frascati all over the world[9)].

When we go to the e^+e^- epoch, which started in Frascati and Novosibirsk in 1960, nust remember ADA. It is too well known to be recalled again now, but I think that ıe historical mark must remain: we were able, through the discovery of new effects and culiar behaviour of electrodynamics, to demonstrate the long life circulation of positive d negative electrons colliding in the same donut. We succeeded[10)] in observing, with ır naked eyes, a single electron circulating in the donut (by its synchrotron radiation).

ADA started the technique of preparing e^+e^- rings of high luminosity. With its ılp, we arrived at ADONE, the 2 x 1500 MeV machine. We will, we must, remember r ever the hard fight, with the discovery of new effects, to achieve the best luminosity. 'e must know that it was the school of Amman[11)], Ritson, Touschek and co-workers, hich permitted the discovery of multihadronic production and of the coloured quarks, ıd collaborated in the SLAC ring for the manipulation of the beams, intensity and size, hich led to the discovery of J/Ψ at SLAC.

Among the technical progress in Frascati, let me remind you of two large detectors hich could possibly be replaced by other instruments, but at a very high, perhaps ·ohibitive, cost.

Iarocci Tubes

One is the device which goes under the name of "Iarocci tubes". In 1987 it was ritten [Wit Busza, MIT Tech. Report, 160, April 1987]: "To date, close to half a ıillion Iarocci tubes have been built." Let me specify what they are: Iarocci tubes are gas nplification detectors, in which the cathode consists of an isolated material coated on ıe inside with high resistant carbon paint. The cathode is transparent to fast signals, and ıus they can be read out by means of strips or pads placed on the outside of the tubes. hey are normally used with highly quenched gases and operated in the limited streamer ıode.

You know all this. Let me recall the main attraction of the Iarocci tubes:
they allow simultaneous X and Y or strip and pad read outs
they lend themselves to mass production techniques
the production costs are very reasonable, \$~500 per square metre, including salary and electronics
the signals are comfortably large.

I cannot quote here the experiments where they have been used, from Charm II, to)elphi to Aleph to UA1 to SLD.

After this, Busza raises a number of interesting concerns. He says, in a subtle jocose way, Iarocci tubes have a Jekyll and Hyde nature. They can be easily constructed on a very large scale with good longevity. At the same time they show, if not carefully built, many nasty characteristics.

This maintains Iarocci in the blue sky, and invites every "tubist" to study more and to wash his hands.

- The R.P.C.s

R.P.C.s go under the name of R. Santonico, the main inventor[13]. They consist of two plates of resistive electrodes, spaced by spacers. In many chambers, plates of 2mm thick window glass are used (see fig. 1).

What is remarkable is that these instruments could have been used many years ago in experiments during the 1960s and 70s. But they were not necessary in their tremendous quality, that make them successful: the signal (the avalanche) due to a traversing particle arises in about 10 n seconds, with a jitter or fluctuation close to 1 n second. This makes them very convenient for L3 and some experiments of the new LHC generation, which require fast triggers and fast resolutions.

The history of the techniques invented and improved in Frascati in these years is really large. Let me only recall the techniques developed by R. Baldini, M. Spinetti and others in the last Adone experiment, the Proton Neutron Form Factor[14].

3 DAΦNE

Now I shall talk about DAΦNE (my question number 5) and about what news and new developments will be necessary from a technological point of view.

I do not have to comment on DAΦNE[15] and KLOE here in the presence of great experts. I only wish to put the DAΦNE enterprise on top of our technical challenges in these years for two reasons.

One, very severe, is the luminosity required. As you know one must have, at the φ resonance, a final luminosity $L=10^{33}cm^{-2}s^{-1}$, which is 100 times larger than what has been achieved so far. This again underlines our point that our philosophy is speared on the spikes of our technical capacity. It is a very hard number. The second point is a more artisan difficult point, which is a great challenge at any age of physics. The fact is that when comparing the decay modes of K_S and K_L, we must refer mostly to the rare cases (a few per thousand) of the decay of K_L in two pions, and we must compare the $\pi^o \pi^o$ and $\pi^+\pi^-$ decay with a precision of, let's say, less than 1‰, which means that you need one year $5x10^{10}$ φ's. This will give the measurement of the famous ε'/ε effect with me 10^{-4} precision, that is the registration of at least 10^7 K_L decaying into 2 pions, parating $\pi^o \pi^o$ from $\pi^+ \pi^-$ with a 1‰ precision. These are just statistics; but the allenging experimental point in the apparatus will be to measure carefully the ficiency of detection of those two different decays, like $\pi^o \pi^o$ and $\pi^+ \pi^-$.

Still the prize on top of this effort, which will again show definite success only at e end of this century, is very high. If ε'/ε is clearly different from zero, then we can eatly contribute to explaining the asymmetry of our Universe (why only one type of atter?) in the ways proposed in recent years. Should ε'/ε be confirmed to be about zero, en the hope of explaining our Universe will fade away. Other experiments will be eded (decay from the B mesons, the Beauty factories), and our curiosity to understand ur Universe tends to remain unsatisfied for many years to come.

Conclusions

So, I come to my conclusion: please, experimental physicists and technicians, ork hard on the subtle, fine details: your work, if systematic and precise, will be the nly way toward what is new and unexpected, and toward the highest philosophical uestions of our world. We really do not know the replies to the list of questions I gave t the beginning. The fact is that those questions are the main questions of basic physics day. A scientist who discovers the replies to those questions will be by far more dvanced than today. This will be the legacy for the next century. And your technical rogress will be the real way to open a new and still unknown world to all men.

Let me thank all the members of the international advisory committee and the rganizing committee for this timely Conference, in particular Profs. F. L. Fabbri, . Murtas, V. Valente.

References

1. I am grateful to G. Setti for recent news regarding the observations with HST, the Hubble Space Telescope.
2. Gallex collaboration: Phys. Lett. B 357, 237 (1995); SAGE collaboration Nucl. Phys. B (Proc. Suppl.) 38, 60 (1995).
3. G. Ranucci e R. Tartaglia, Il Nuovo Saggiatore, Bollettino della S.I.F. 11, 62 (1995). Clear syntheses of the Borexino Experiment and of preceeding results are presented.
4. J.K. Rowley, B.T. Cleveland and R. Davis Jr.; edited by M. Cherry and K. Landes, AIP, Conf. Procs. 126, 1 (1985).
5. E. Fiorini, Underground Cryogenic Detectors, Europhys. News, 207 (1992).
6. L. Pietronero, M. Montuori and F. Sylos Labini, Lecture to be presented at the meeting "Critical Dialogues in Cosmology" June 1996.
7. G. Vettolani et al, Preliminary results from the ESO Slice Project, BAP 12 - 1993-O42 - JRA.
8. B. Melchiorri and F. Melchiorri, The Cosmic Background Radiation, Riv. Nuovo Cimento, 17, 1-101 (1994).
9. G. Barbiellini, G. Bologna, G. Diambrini Palazzi, G.P. Murtas, Phys Rev. Letts. IX, 9 396 (1962) and IV, 3 134 (1960).
10. C. Bernardini, G.F. Corazza, G. Ghigo and B. Touschek, Nuovo Cimento, 18, 1293 (1960).
11. F. Amman et al, Proc. Intern. Conference on High Energy Accelerators, 309 (Dubna, 1963).
12. E. Iarocci et al, Nucl. Instr. and Methods, 152, 423 (1978), 202, 459 (1982), 217, 30 (1983).
13. R. Santonico and R. Cardarelli, Nucl. Instr. and Methods, 187, 377 (1981).
14. A. Antonelli et al, Phys. Lett. B 313, 283 (1993), B 301, 317 (1993).
15. Workshop on Physics and Detectors for Daphne 1995, Frascati, 4-7 April 1995.

I – Overview

Convener E. Iarocci
Secretary L. Benussi

R. Sulak	Quartz Cherenkov Calorimetry for High Rate Radiation–Tolerant Forward Physics
Rutherfoord	The ATLAS Forward Calorimeters
Golutvin	The HERA–B Calorimeter, also in view of LHC–B
Gianotti	Electromagnetic Calorimetry Requirements for LHC Physics. Potential of the ATLAS Electromagnetic Calorimeter
Denes	New Crystal Calorimeters for Colliders
. Barbiellini	Calorimetry for Astroparticle Physics

ascati Physics Series Vol. VI, (pp. 15–33)
[INT. CONF. ON CALORIMETRY IN HEP – Frascati, June 8–14, 1996

QUARTZ CHERENKOV CALORIMETRY FOR HIGH RATE RADIATION-TOLERANT FORWARD PHYSICS

L.R. Sulak
Boston University, Boston, MA 02215
for the CMS VFCal Collaboration

ABSTRACT

nlike at previous, lower energy colliders, the physics at the LHC demands excep-onal calorimetry in the very forward region. The missing E_t signature of supersym-ıetry requires good spatial and energy resolution down to within 0.5° of the beam ne. The pseudorapidity region that must be covered, from 2.75 to 5.25, includes lmost half of the phase space observed by calorimetry at the LHC. The production f high mass Higgs particles ($> 500\,\mathrm{GeV/c^2}$) is severely suppressed. They can only e detected via high rate decay modes with jets and neutrinos, again demanding xcellent hermeticity. In addition, the tagging of leading quark jets, which go into he forward calorimeter, is a critical signature. Sensing these jets requires supe-ior spatial resolution and high speed. Lastly, the forward region presents a hostile nvironment of high neutron fluence and gigarad radiation levels.

Tests of quartz fiber prototypes, based on the detection of Cherenkov light rom showering particles, demonstrate a detector possessing all of the desirable char-ıcteristics for a forward calorimeter. A prototype for the CMS experiment consists of 0.3 mm diameter fibers embedded in a copper matrix. The response to high en-ergy (10–375 GeV) electrons, pions, protons and muons ... the light yield, energy ınd position resolutions, and signal uniformity and linearity ... are discussed. The signal generation mechanism gives this type of detector unique properties, especially for the detection of hadronic showers: Narrow, shallow shower profiles, hermeticity ınd extremely fast signals. The implications for measurements in the high-rate, high-radiation LHC environment are discussed.

1 Introduction

The primary goal of the LHC research program is the search for the Higgs particle [1)] and the associated search for supersymmetry. If neither is found, the task is to uncover the unexpected new physics that must be in the region below 1 TeV. If the Higgs or supersymmetric particles are discovered, we must determine their characteristics. For all of these goals the very forward calorimeter is a critical detector system.

As at the SSC, a very forward calorimeter (VFCal) at the LHC must cover the pseudo-rapidity range from $\eta = 2.5$ to $\eta = 5$, allowing both measurement of missing transverse energy and forward jet tagging [2)]. Operation at such high rapidity requires the use of a calorimetry technique that is radiation-resistant to gigarads, faster than bunch crossing time, and insensitive to high ambient radioactivity. These requirements can be achieved with quartz optical fibers embedded in a heavy absorber. Shower particles produce light by the Cherenkov effect, generating a signal at the speed of light ($\sim$ 3 ns duration). The quartz VFCal meets the challenge of operating in the extremely hostile radiation environment with event rates up to 16 per bunch crossing [3)].

The quartz fibers are inserted into grooves in a copper or iron matrix, as in scintillating-fiber calorimeters. The quartz VFCal is only sensitive to relativistic charged particles. Hence, it does not see low-energy neutrons, which will traverse it in large numbers. Furthermore, high-purity quartz is one of the most radiation-hard substances known. Hence, this detector is largely insensitive to the effects of induced radioactivity [4)].

The quartz technology has been prototyped by the Boston group for over six years, first for the SSC [5)] and now as the CMS detector at the LHC [6)]. The conceptual design for one arm of this detector is shown schematically in Figures 1 and 2. Figure 3 shows the location of the detector in a half view of the overall CMS detector.

Our construction experience and test beam work confirm the anticipated unique properties of a passive, optical quartz detector:

1. inherently high spatial and temporal resolution.
2. blindness to neutrons and to heavily-ionizing particles.
3. simple construction that is totally hermetic, i.e., with no dead areas and no cracks.
4. inherent hardness to gigarads of radiation and high neutrons fluences.

In 1994 we conceptually designed the detector and built the first prototype tower to fully contain a hadronic shower. In test beam studies at CERN [7)], the

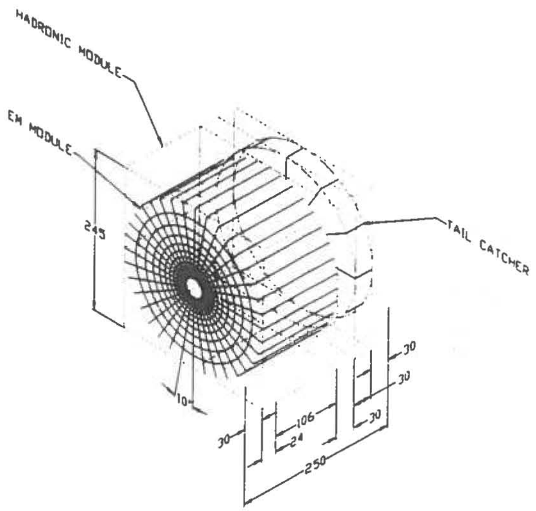

ƺure 1: Conceptual engineering design of one arm of the CMS quartz fiber VFCal ɔwing four 20 ton modules with both EM and hadronic compartments. A tail ;cher (TC) is similarly split into 4 blocks. Optical fiber readout groups in $\Delta\eta\,\Delta\phi$ ꞓ superposed on the iron blocks. There are 36 wedges in ϕ, and 12 rings in η. Each ver subtends 0.175×0.175 of phase space. The TC has 1/3 as many towers in ꞓh dimension as the EM and HAD compartments. All dimensions are in cm. The cm gaps in front of the EM, between the hadronic module and the tail catcher, d after the TC contain the optical readout packages. The four blocks fit together a hermetic, pinwheel fashion about the beam pipe to avoid projective cracks.

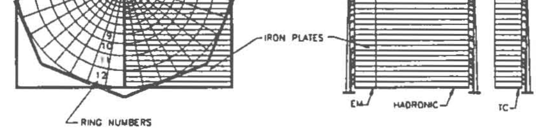

gure 2: End (left) and side (right) views of the CMS VFCal showing the light llection scheme. A few of the fiber ribbons are depicted in one wedge. The inner 4 5 rings have quartz-clad fibers, to match the required radiation hardness, readout air cone light guides (see side view). The outer rings use plastic-clad fibers in ɔbons which run to the PMTs on a plate at the periphery of the calorimeter. The ɔn absorber plates are shown schematically in the lower portions of each figure. ɔe plates that intersect with the beam hole are sheared to form a near-conical ꞓam channel at $\eta = 5.5$.

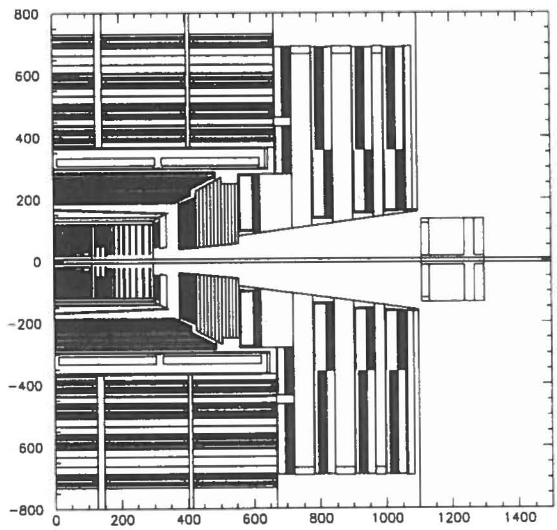

Figure 3: Side view of one half of CMS, showing the VFCal placement (center right) ignoring its shielding. The absorber of VFCal extends only 1.9 m in z and consequently only to 1.4 m in radius to cover 10cm farther from the beam line than the $\eta = 3$ radius overlap with the endcap hadronic calorimeter. This figure shows the geometry we use in CMSIM physics simulations of the detector performance.

sampling in that detector (1 mm fibers spaced at 8 mm) was too coarse, leading to tails at the1% level in the hadronic energy resolution. Extrapolations led us to build in 1995 the first fine grained (0.3 mm fibers spaced at 2.3 mm) hadronic prototype, with 10 towers comparable to those planned for $\eta = 4$ operation at the LHC. In 1996 we built an EM prototype and tested it CERN.

2 The Physics Promise of the Forward Calorimeter

At the LHC, three energy regions require different detection strategies for the Higgs; all three benefit from the very forward calorimeter:

1. Below $2m_Z \sim 80$–150 GeV, search for $H \to \gamma\gamma$.
2. Near and above $2m_Z \sim 150$–600 GeV, the favored channel is $H \to Z^0Z^0 \to \ell^+\ell^-\ \ell^+\ell^-$.
3. From 600–1000 GeV, one must optimize with $H \to \ell^+\ell^-\nu\bar{\nu}$ or $H \to \ell^+\ell^- jj$.

In regions 1 and 2, the VFCal will be critical to determine what is the nature of that Higgs, e.g. is it supersymmetric? Supersymmetry should expose itself by having as lightest manifestation a "neutrino-like" particle $\tilde{\chi}_1^0$ as the product of $\tilde{p}$ decay. :ge production cross sections are expected for $pp \to \tilde{g}\tilde{g} + X$. The number of :nts per year at the initial luminosity ($\mathcal{L} = 10^{33}$ cm^{-2}s^{-1}) ranges from $\sim 10^7$ for) GeV to $\sim 10^4$ for 1000 GeV.

Extraction of this SUSY signal requires detection of $\not{E}_T$ and *jets*, for which f of the phase space lies beyond $\eta = 3$, the zone of the VFCal. This places illenging constraints on the apparatus: i) good calorimeter position and modest ergy resolution up to $\eta = 5$, which means sensitivity to 5.5, and ii) nearly perfect :meticity to avoid false signals in a high background situation. Hence, for the low iss and supersymmetric Higgs searches, the VFCal is essential.

Below 600 GeV the leading mechanism for Higgs production is gg fusion. the 600–1000 GeV energy region WW or ZZ fusion is dominant, leading to :ompanying "tagging jets" in the two forward regions. However, in the high-iss region the cross section decreases. Even at a final luminosity of 10^{34} cm^{-2}s^{-1}, ly 10^4 Higgs a year are expected. Furthermore, the background due to WW pair oduction and decay is extremely high.

The Higgs total width Γ_H is a rapidly increasing function of m_H. Although e experimental mass resolution plays a dominant role for $\Gamma_H < 0.2$ TeV, for large asses ($m_H \gg m_W$), the Higgs width broadens and the peak eventually disappears ;o the background above 1 TeV. Hence, superior energy resolution is not a major quirement in the high mass region.

At high Higgs masses, the $H \to ZZ \to \ell^+\ell^-\nu\bar{\nu}$ channel is important cause its cross section is six times larger than the $H \to 4\ell$ channel. However, is is a difficult mode to discern due to the undetectable neutrinos. A critical servable is missing-p_t, the distribution of which would show a significant bump if e Higgs were present. The decisive issue is calorimetric performance, which allows e missing energy to be measured. Nearly perfect hermeticity and calorimeter verage up to at least $\eta = 4$ is required.

Another channel expected to produce a significant enhancement above the ckground is $H \to WW$ or $ZZ \to \ell\ell jj$. This channel has the drawback of a high te of jet background. The W or Z branching ratio into jj is about 70%. We use e two-forward tagging jets to suppress the W, Z + *jets* and $t\bar{t}$ backgrounds. The gging jets lie between $\eta = 2$ and 4, i.e. in the very small angle region between 1° id 5° with respect to the beam axis.

At VFCal, 11 downstream from the interaction region, the tagging-jet fragents are well collimated. More than 95% of the jet energy is contained within 20 cm the jet axis. The hermeticity requirements are not as stringent as in the previous ode. However, in this region of high pileup from multiple events per crossing, *jet-*

jet separation capability is essential. This mode places two additional constraints on the technology: 1) very fast response to the collect separately the signals in each bunch crossing, and 2) unusually fine granularity at large η to respond to small transverse signal size and to close nearby background jets.

The VFCal is a key subsystem for Higgs searches above 600 GeV. The calorimeter must be hermetic and must tag jets at pseudorapidities up to 5 with a total signal collection time much less than the 25 ns bunch spacing, especially to distinguish in-time signals from quadrupole halo and other out-of-time beam-generated background. Further, the VFCal must have a lateral response to high energy hadronic jets that is comparable to the jet size itself, which is much smaller than the ionization signal produced by a showering jet.

3 A Status Report on the Development of Quartz Fiber Calorimeter

Unique to quartz fiber technology, the observed Cherenkov signal from the electromagnetic core of a hadronic shower has a transverse dimension three to four times smaller than that in conventional calorimeters that sample ionization energy only. Since most radioactive decays and neutron interactions produce particles below the Cherenkov threshold, the calorimeter is intrinsically insensitive to the broad and time-delayed signals from these sources. Fortuitously, the geometric size of the Cherenkov response to the leading particles of the shower is the same size as a quark jet in the $\eta = 5$ region. This enables precise spatial resolution, sharp isolation cuts, and good single and dijet recognition above the minimum bias background.

These characteristics allow a quartz fiber calorimeter to be operated in the extreme working conditions of a forward detector for the LHC. Our R&D work includes in-depth study of the performance of fibers with different manufactures, diameters and cladding (plastic vs. fluorine-doped quartz) of silica fibers in the presence of radiation load. We have also studied potential photodetectors and optical transmission systems. We have constructed and beam tested of full-containment EM, hadronic and tailcatching calorimeter modules. These modules have validated all the features required for a forward calorimeter: transverse shower size, radiation resistance, speed, spatial resolution, transverse energy measurement and implementation of an E_t trigger.

The hadronic (HAD) prototype optimized for the $\eta = 4$ regions, fully satisfies the baseline design of the CMS Technical Proposal [8]. It is 1.35 m ($8.8\lambda_{int}$) long and contains 1.5% by volume of quartz optical fibers with 300 μm diameter. The fibers are clad with fluorine-doped quartz, and are therefore radiation-tolerant to gigarad levels, enough to last for a decade at the full LHC design luminosity of 10^{34}. The fibers are embedded in a stack of copper plates with lithographically

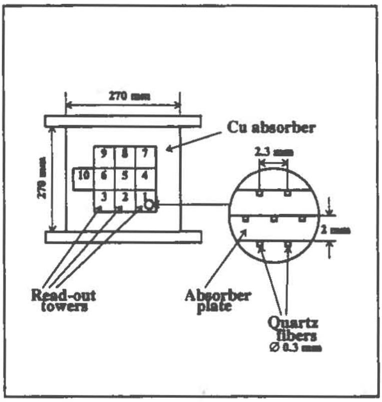

gure 4: Lateral cross section of the VFCAL prototype calorimeter. The detector nsists of 2.0 mm thick copper sheets and 0.3 mm core diameter quartz fibers.

ched grooves to form a hexagonal matrix with a spacing of 2.3 mm. The mass .3 ton) and cross section $(27\,\mathrm{cm})^2$ are sufficient to fully contain the ionization from hadronic shower.

The fibers were laid three by three array of 5.3 cm^2 towers in the central gion were stuffed with fibers (see Figure 4), corresponding to actual towers at $\cong 4$ with a segmentation of $\Delta\eta = \Delta\phi = 0.175$. This region is large enough to ntain the narrow Cherenkov emission from the core of a hadronic shower. A tenth wer sampled the region of the next nearest neighbors for showers. Since the fibers ere initially mirrored at their far end, the module could be turned 180° in the beam simulate a long version of an EM compartment with read out by PM's upstream the EM section (see Figure 2).

The design of this hadronic prototype follows an extrapolation from the sults obtained from CERN beam tests of the tail catcher (TC) prototype. The TC as built as the SSC close-out project for the GEM forward calorimeter of similar esign. In the 1995 tests, the TC module was placed either in the beam immediately ehind the hadronic module (the normal position of the tail catcher) or at 90° to ie beam in front of the HAD prototype as a crude EM compartment.

In 1996, we tested a baseline (1.5 absorption length, 15 radiation length) M compartment to demonstrate the expected longitudinal correlation between ie two compartments. A total of 12 towers were instrumented, three with fluorine oped quartz cladding, and 9 with inexpensive plastic clad quartz fibers, the baseline ber for the small η regions where radiation tolerance is less of a challenge. A iass assembly technique, stuffing the fibers into the holes of a complete block was emonstrated.

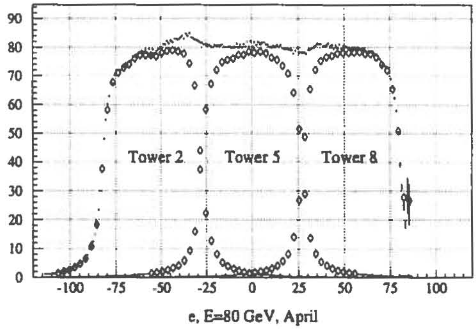

Figure 5: Detector uniformity measured with a vertical scan across three towers using 80 GeV electrons incident at 0°. The response of individual towers is shown by diamonds; the summed response by dots and error bars. The variation is ±2%.

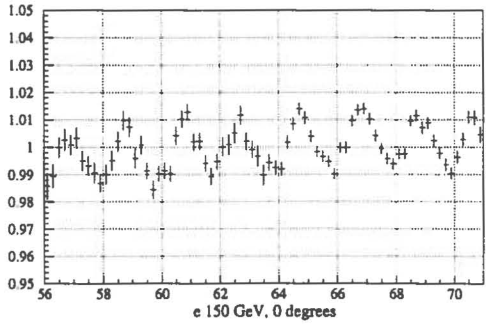

Figure 6: Detector uniformity measured with a a vertical scan using 150 GeV electrons incident at 0°. The 2 mm spacing between fiber planes is apparent.

4 FY96 Prototype Test Beam Results

The test beam program included the following, all of which were accomplished [9]:

4.1 Evaluation of detector uniformity and hermeticity

The small dots in Figure 5 represent the summed single of the entire calorimeter for a vertical scan with electrons. The signal is uniform to ±2% across the tower boundaries. As is seen in the blow up of Figure 6, where the response to electrons is modulated by whether the shower starts in a plate (lower signal) or in a plane of fibers. The spatial resolution is better than the 2 mm vertical spacing of fiber planes, and the variation is ±1%.

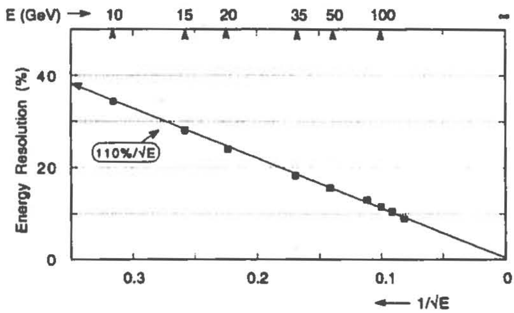

ʒure 7: Resolution response (rms width divided by signal amplitude) to electrons a function of energy. Note that the electron resolution falls as $E^{-0.5}$, showing at it is dominated by photoelectron statistics.

‽ Energy linearity and resolution measurements.

ith electron beams from 15 to 150 GeV, Figure 7 shows the resolution to electrons photostatistics dominated at $110\%/\sqrt{E}$. With pion and proton beams from 15 375 GeV, Figure 8 shows that the hadronic resolution response appears to fall ʒarithmically, i.e. it is dominated fragmentation fluctuations into neutral pions. /aluation of non-Gaussian tails in the resolution function showed none are observed the level of one per thousand, as anticipated by sampling a factor of ten finer in e tail catcher prototype. Compensation for $\pi^0/\pi^{\pm}$ fluctuations was accomplished ʳ weighting the longitudinal (or transverse) development of a hadronic shower a compartmentalized detector. The energy resolution for 300 GeV protons is '%, before any corrections to compensate for the observed e/π ratio of 1.7. This solution improves to 14% after corrections for lateral size: the broader the shower, ιe higher the charged π component and the lower the light yield. Three independent gorithms — linear, quadratic, and the H1 technique from HERA — give similar ıhancements of resolution by weighting.

A similar improvement is anticipated with longitudinal segmentation. Usıg an interaction trigger, 300 GeV pions entered a trial EM compartment (the TC ıodule at right angles to the beam) in front of the HAD. The anticipated corre-.tion between the energy deposited in the EM and that in the HAD is shown in igure 9. Data with the prototype EM module in front of the HAD was taken in uly 1996 and data is currently being analyzing.

For a VFCal, the important observable is the E_t resolution, a convolution f the total energy resolution with the spatial resolution. Due to the Lorentz boost, his significantly relaxes the requirement on total energy resolution. Indeed the bserved 14% resolution implies an E_t jet resolution in the VFCal of 7%, better han the E_t resolution of the barrel and endcap hadron calorimeters.

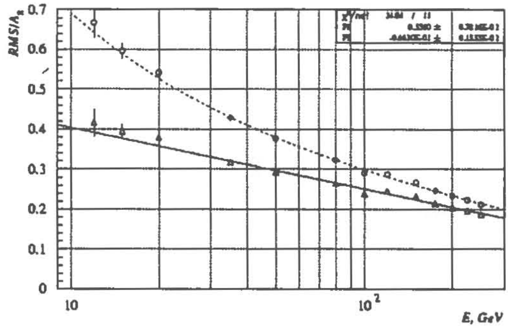

Figure 8: Resolution response to pions as a function of energy. The hadronic resolution appears to fall logarithmically, showing that it is dominated by fragmentation fluctuations.

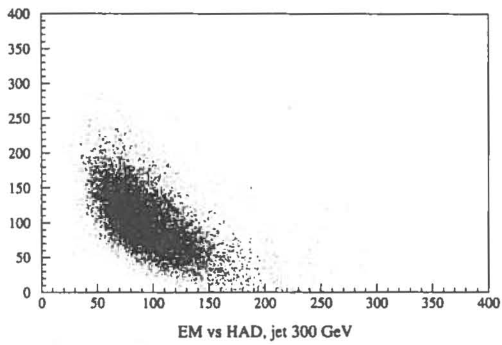

Figure 9: Signal correlation in a trial EM (the TC module at 90°) versus that in the HAD prototype for 300 GeV "interaction jets."

4.3 Shower size evaluation.

The lateral shower development is shown by the solid line in Figure 10, where it is compared with the dashed line response of a scintillating fiber calorimeter (SPACAL). The Cherenkov response is a factor of two narrower in one dimension than that of the device sensitive to ionization losses.

The hadronic shower core, as observed by Cherenkov light produced mainly by low energy $e^{\pm}$, is shown in a typical "lego" plot in Figure 11. A lateral size of only ± 5 cm contains 80% of the shower, showing that this technique is blind to the broad glow caused by neutrons, heavily ionizing particles, nuclear breakup, and other low energy end products amplified in dE/dx counters.

The inherent spatial resolution drops as $1/\sqrt{E}$, as is shown in Figure 12, and is only a factor of 2 larger for pions than for electrons. A resolution of 7 mm is measured for high-energy pions. This should imply good *jet-jet* separation, good signal-to-noise ratio in a high-radiation environment, and sufficient E_t resolution

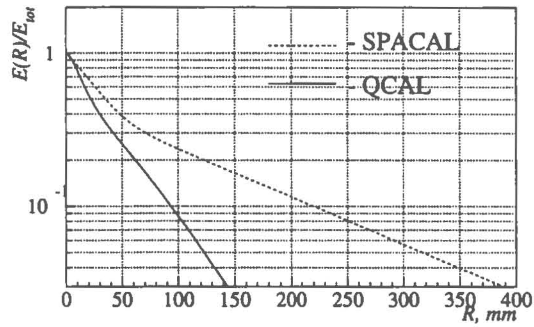

gure 10: Lateral shower profiles for 80 GeV pions in Cherenkov and ionization
tectors.

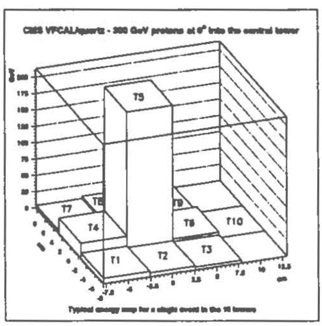

igure 11: A typical shower profile (a lego plot) for a 300 GeV proton incident at degrees into the central tower of the hadronic prototype. Typically 80% of the iergy is contained in one $5 \times 5\,\mathrm{cm}^2$ tower.

hen convolved with the total energy resolution.

The longitudinal shower development was measured by placing iron bricks front of the hadron calorimeter. The response is displayed in Figure 13 for four adron energies. Note that in contrast with ionization detectors, high energy showers e fully contained after only 120 cm (7 absorption lengths) of solid iron. A depth $8\lambda_{int}$ is sufficient for 97% containment of the Cherenkov signal from a shower in opper. This translates to more than a 50% decrease in the overall detector mass r a Cherenkov shower detector compared with an ionization detector.

Temporally, the Cherenkov device produces a signal with a full width at alf maximum of 3 ns (see Figure 14). The insensitivity to the late radioactive ortion of the shower implies fast performance in the high-rate forward region. n particular, sub-bunch temporal discrimination against beam background from craping on the quadrupoles, etc., should prove invaluable, as suggested by DØ [10].

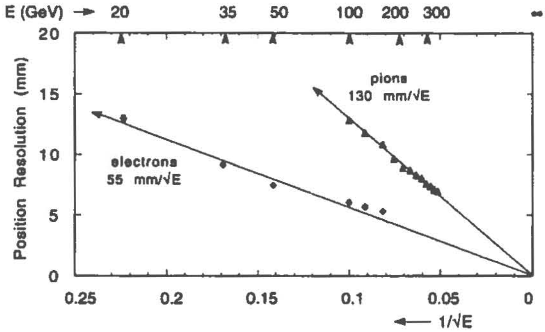

Figure 12: Position resolution for electrons (diamonds) and pions (triangles) as a function of energy.

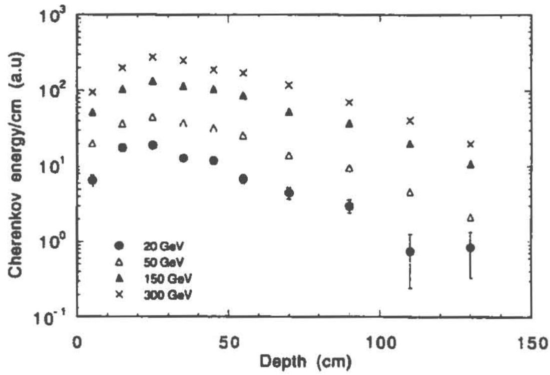

Figure 13: Longitudinal shower development in a Cherenkov calorimeter made of iron.

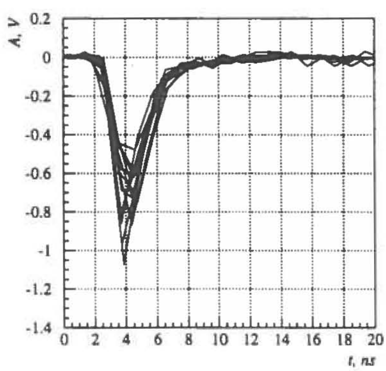

Figure 14: Digital waveforms for the Cherenkov signal from high energy pions incident at 0 degrees. The signals from electrons are similar. Notice how reproducible hadronic signals are in this detector.

Angular response as a function of the beam angle

: electrons incident at 0, 3, and 6 degrees, we showed that particle channeling eliminated (even at 0 degrees) with fibers this fine (0.3 mm) and at this close ιcing (2 mm) relative to the Moliere length (6 mm). with beams incident at 0 d at 180 degrees, we tested the readout for both the hadronic compartment (0 grees, with readout at the back) and the EM (180 degrees, with readout from the nt using the mirrors at the ends of the fibers). With the beam at 90 degrees, we easured the attenuation length of Cherenkov light in the fibers to be 5 m.

Optimization of optical readout.

coiling a fiber ribbon behind the HAD, we showed that shower leakage into the er ribbons coming out the back of the module was negligible. We tested the light ınsmission through air light guides with front surface aluminization from a tower a PM. This readout technique for the $\eta > 4$ region was shown to be feasible th transmission better than 65%. Nevertheless, the baseline design is readout a fiber ribbon that transmits the light through the concrete shield to the PM's d electronics in the shielded region at low η. We tested light concentration using nple Winston cones for towers at $\eta \cong 3$, where the fiber bundle cross-section om the physically large tower sizes (for fixed $\Delta\eta$, $\Delta\phi$ sampling) is larger than e area of the baseline R5900 PMs. It is feasible with only a 20% loss in light. 'e observed negligible pickup from stray particles passing through the mini-metal Ms was demonstrated. A comparative measurement of the uniformity of reflection om the aluminized mirrors used for the readout of the EM section was made. The solution with the beam incident both at 0 and at 180 degrees showed a reflecting 90%.

Fast Timing and Electronics for the Forward Region

he unique environment of the very forward region poses significant readout chalnges. The specifications for the VFCal readout are summarized in Table 1. The ırrent status of the readout system design is reviewed here; the primary goal is develop a proof-of-principle system to test under high-rate conditions at a new ERN test beam in 1997. This beam will have a hot radioactive source in a high rate ıuon beam line. We must choose a baseline photo-detector, preamp, and ADC sysem (most likely the FERMI system being developed at CERN), and then prototype custom front-end circuit to interface between the two.

The proposed readout system takes advantage of the inherent signal speed f the Cherenkov technique. It attempts to enhance the background rejection by

Table 1: Electronics specifications for the CMS VFCal.

Light collection	0.8 pe/GeV (π); 1.2 pe/GeV (e)
Noise (design goal)	$\frac{1}{4}$ pe
Least-count and threshold	$\frac{1}{2}$ pe (HAD, to see μ 30 GeV (EM, TC)
Dynamic range/tower	10^4 (0.5 GeV - 5 TeV)
Resolution consistent with	$\frac{1.8}{\sqrt{E}} + 5$

simple pulse shape analysis. For each calorimeter channel, we will digitize two charge measurements during each 25 ns bunch crossing period, one in time with the IR crossing and one out-of-time, e.g. at the time of beam-induced background. Presumably this second gate will be set for the time of quadrupole crossing, as has been found to be necessary at DØ. Figure 15 illustrates the VFCAL location and expected signals from the IR and from quadrupole halo. A proposed block diagram of the VFCal readout is shown in Figure 16, each element of which we discussed briefly:

5.1 Light Pulser and Photodetectors

Light detectors are being evaluated on the bench and in the test beam The new, fast blue LED's [11] mimic the hostile high-rate conditions in the forward region of the LHC. This system will eventually be used in quality assurance and in monitoring during the experiment. We are evaluating three candidates for the photodetector:

1. Hamamatsu R5600 (R5900) Phototubes: These 15 mm round (25 mm square) PMTs are the baseline photodetectors for the high (low) rapidity regions. They have the advantage of ultra-compact design, low cost, fast risetime, radiation hardness, and immunity to local Cherenkov light generation due to the metal envelope and thin ($<$ 1 mm) window. The limitations we are evaluating include low-end non-linearity due to mesh dynode structure and limited dynamic range.
2. Philips XP2012 PMT: This 34 mm PMT is a conventional 10-stage PMT. It has a linear focus dynode structure and significantly wider dynamic range. It can be manufactured with a black glass envelope to suppress background from local Cherenkov light production. However, the window is large and thick.
3. DEP Proximity-Focused Hybrid Photodiode: The main advantage is a wider dynamic range than that of PMTs, and the possibility of use by the CMS hadronic calorimeter, which would mean cost savings both initially and during maintenance.

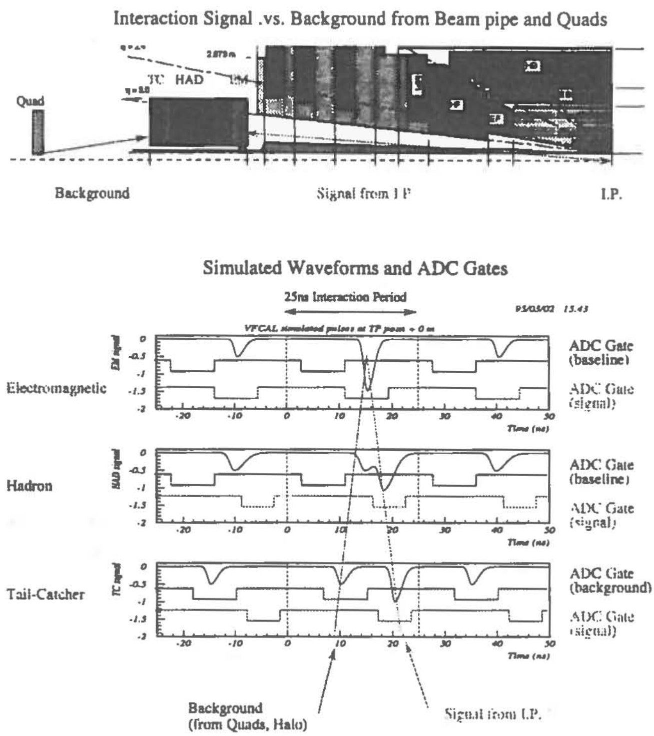

gure 15: VFCAL Location, Expected Signal and Background. Simulated relative ning of signal and background in the three detector compartments. Two ADC .d one DC sample are taken for each tower in each compartment every 25 ns. A nple "level 0" trigger logic should reject out-of-time background.

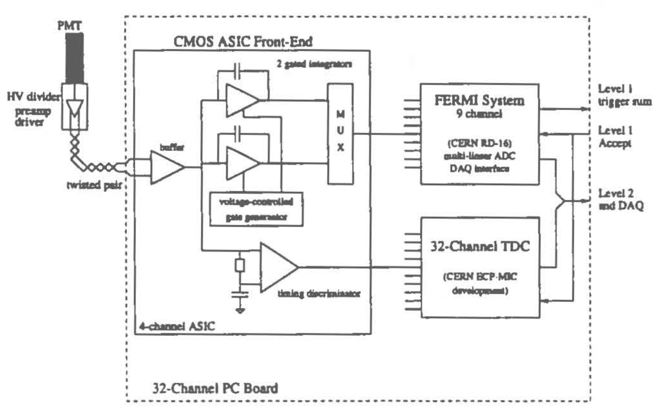

Figure 16: Preliminary VFCal Readout Diagram

5.2 Preamplifier

This will almost certainly be required to get the required 10^4 dynamic range. The PMTs will have to be operated at low gain; photo-diodes are inherently low-gain devices. We will evaluate at least one of the existing preamplifier designs being developed by the CMS ECAL group. We will either choose one and modify the input to be appropriate for a PMT, or, if absolutely necessary, develop a new device which meets our requirements.

5.3 Front-End Readout Interface

This provides the two sub-25 ns gated charge measurements and the TDC measurement which are not needed for the low rate subdetectors. Digital traces recorded in the test beam from hadronic showers have allowed us to simulate the required gates, etc., as shown in Figure 15. This may be either a hybrid circuit or a custom IC, depending on considerations of space, power and radiation hardness.

5.4 ADC and Readout System

The FERMI readout system being developed by RD16 at CERN is the current baseline for CMS. Alternative candidates are a switched-capacitor array based system and the digital photo-multiplier chip system [12)] developed at Fermilab. Whichever system is adopted for use in CMS calorimetry, we will modify its input to suit our needs, thereby saving the significant costs of developing a custom system.

5.5 High Voltage

A high-voltage supply with last dynode boosters will be required to maintain linearity despite the high peak currents. Since we must minimize the number of cables, we plan to pipe low voltage to the detector and to multiply to the required voltage there.

A standard technique for generating high voltage on the detector uses a Cockroft-Walton voltage multiplier [13)]. Several such systems have been successfully deployed. We plan to use a similar system, which will provide sufficient current to each dynode of the PMT to prevent sagging at high rates. A remote-controlled system, like those cited above, will be used to provide voltage control and current monitoring of each VFCal channel.

Summary

:onclusion, the quartz fiber calorimeter seems to be eminently suited to calorime- [14] in the forward region of hadron colliders. It is gratifying to see that another up [15] at this conference has come to the same conclusion, and that several other ups are designing forward fiber calorimeters for heavy ion experiments [16].

Acknowledgments

m particularly indebted to my colleagues on this project since the early SSC days, Winn and Y. Onel, as well as R. Webb. Early in the game I learned much from Salvo, P. Gorodetzky, and M. Lundin. Nonetheless, each of my current colleagues CMS plays an absolutely critical role in obtaining the results described here [17]. ey include S. Doulas, J.-P. Merlo, D. Osborne, A. Rosowsky, and J. Sullivan oston); D. Winn (Fairfield); N. Akchurin and Y. Onel (Iowa); V. Gavrilov, Y. rshtein, V. Kolosov, V. Kuleshov, D. Litvinsev, and V. Stolin (ITEP); and O. nel and R. Wigmans (Texas Tech).

Currently, Antonio Ferrando (CIEMAT), is VFCal spokesperson and Nural :churin (Iowa) is project manager. The VFCal system is a part of the hadron lorimeter subdetector. Its spokesperson is Dan Green (FNAL) and the chairman of collaboration council is Andris Skuja (Maryland). I thank all these collaborators : uncommon good judgment, civility, and support in developing this technology : CMS.

eferences

. D. Denegri, "Standard Model Physics at the LHC (pp COLLISIONS)," ECFA, Aachen, October 1990, CERN PPE/90-181.

:. The forward calorimeters were an integral part of the detector design and essential for the discovery of the W and Z bosons. G. Arnison et al., "Further Evidence for Charged Intermediate Vector Bosons at the SPS Collider," Phys. Lett. **129B**, 273 (1983).

}. The SSCintCAL Collaboration (D. Winn et al.), "Cherenkov Fiber Sampling Calorimeters," IEEE Trans. Nucl. Sci., (1993). D. Winn and W. worstell, "Compensating Hadron Calorimeters with Cherenkov LIght".

1. I. Azhgirey et al., Simulation of the VFCAL/QF Irradiation During the LHC Operation, CMS TN/95-063. V. Gavrilov et al., Study of Quartz Fiber Radiation

Hardness, CMS TN/94-324. A. Ulianov et al., Neutron Sensitivity of Quartz Fiber Calorimeter, CMS TN/95-145.

5. The SSCINTCAL Collaboration (D.H. Brown et al.), "Copper / Scintillating Fiber Hadron Calorimeter Prototypes," IEEE 1992 NSS Conf. Record, IEEE Pub. 0-7803-2/93, 274(1993). The SSCINTCAL Collaboration (W. Worstell et al.), "Performance of a Copper / Scintillating Fiber Hadron Calorimeter Prototype," Dec, 1994 (to be submitted to NIM). The SSCINTCAL Collaboration (W. Worstell et al.), "Design and Performance of Compact Scintillating Fiber Calorimeters Cast in Eutectic Lead Alloy," Dec, 1994 (to be submitted to NIM). SSCintCAL Collaboration, "Copper-Scintillating Fiber Hadron Calorimeter Tower Prototypes," submitted to IEEE Nuclear Science Symposium.

6. "The HV Decision for CMS: Requirements and Detector Performance of the Quartz Fiber Calorimeter," CERN, November 1995; CMS HV-QF Collaboration Q & A and Addendum, December 1995. J. Sullivan, CMS Cost Review 6, HV-QF Supplement, CMS/CRWG/95-03.

7. K. Arrington, D. Kefford, V. Podrasky, C. Sanzeni, D.R. Winn, A. Rosowsky, L. Sulak, J. Sullivan, N. Akchurin, A. Bravar, Y. Onel, "1994 CERN Test Beam Results of a 0° Fiber Cherenkov Sampling Hadron Test Calorimeter: A Preliminary Study for CMS Very Forward Calorimetry," CMS TN/94-327.

8. The CMS Collaboration: "Technical Proposal," CERN/LHCC 94-38.

9. S. Doulas et al., "Beam Test Results from a Fine-Sampling Quartz Fiber Calorimeter for Lepton, Hadron, and Jet Detection", CMS TN/95-144 (to be submitted to NIM).

10. John Butler and Dan Green, private communication.

11. A new family of InGaN/AlGaN LEDs with peak emission at 450nm has been developed by he Japanese Nichia Chemical Company. Recent tests by the g-2 group at Minnesota have shown that one can achieve <10ns risetime and 50MHz rates with very low-voltage pulsers.

12. "A Pipelined Multi-ranging Integrator and Encoder ASIC for Fast Digitization of Photo-multiplier Tube Signals," proc. of the International Conference on Electronics for Future Colliders, 1992, LeCroy

13. CERN-EP Internal Report 78-5. "A Remote Controller High Voltage Supply System for Photo Multipler Tubes," NIKHEV ETR 94-11, M. Gospic,

H. Groenstege. "A New High Voltage Supply for Large Photomultiplier Systems," M.L. Purschke *et al*, Third International Conference on Electronics for Future Colliders, 1993, LeCroy

these proceedings: V. Gavrilov, "CMS Quartz Fiber Calorimetry". R. Wigmans, "The benefits of extreme non-compensation: quartz fiber calorimetry for CMS".

A. Musso, "The Quartz Fibre Zero Degree Calorimeter of NA50 Experiment at CERN SPS", these proceedings.

G. Anzivino et al., "Recent developments in quartz fibre calorimetry", NIM A 357 (1995) 369-379. P. Gorodetzky et al., "Quartz fiber calorimetry", NIM A 361 (1995) 163-179. E. Chiavassa et al., "A position sensitive, highly radiation hard and fast hadron calorimeter for a lead ion experiment at CERN SPS", Vienna Wire Chamber Conference, Vienna, Austria, February 1995. ALICE technical proposal, "Zero-degree Calorimeters", CERN/LHCC 95-71 (chapter 7).

Yu. Gershtein, Impact of Single Particle Resolution on Very Forward Physics, CMS TN/95-075. Yu. Gershtein, Pattern Recognition in the Quartz Fiber Very Forward Calorimeter, CMS TN/95-099. V. Gavrilov, Sensitivity of Photomultipliers to Protons and Gammas, CMS TN/95-146. N. Akchurin et al., Calibration and Monitoring of Quartz Fiber VFCAL, CMS TN/95-149. D. Litvintsev, Detailed Monte Carlo Program for Quartz Very Forward Calorimeter for CMS Detector, CMS/TN95-098. E. Hazen, A Readout System Based on FERMI for the CMS HV/QF Calorimeter, TN/95-169, in preparation. O. Ganel and R. Wigmans, NIM A365,104. Yu. Gershtein, Simulation of the Signal and Background, Talk at CMS Week, September 1994. L. Sulak, "HV-QF Status Report", and A. Rosowsky, Quartz VFCAL - Analysis with GEANT, CMS Week, Tahoe, California, September 1995, and TN/95-169; CMSIM-CMANA CMS Simulation Facilities, MCS TN/93-63.

ascati Physics Series Vol. VI, (pp. 35–47)
[INT. CONF. ON CALORIMETRY IN HEP – Frascati, June 8–14, 1996

THE ATLAS FORWARD CALORIMETERS

John Rutherfoord
University of Arizona, Tucson, Arizona, USA

ABSTRACT

rward calorimetry completes the nearly 4π coverage for high p_T hadronic events the ATLAS detector at the LHC. Both the deployment and the technology of e forward calorimeters (FCal) in ATLAS are novel. The FCal physics goals and rformance requirements focus on missing E_T and tagging jets. The placement of e FCal relatively close to the interaction point provides many advantages includ- g nearly seamless calorimetry and natural shielding for the muon system. The uid argon rod/tube electrode structure for the FCal was invented specifically for plications in high rate environments. Recent electron test beam results of an EM ototype show linearity of response better than 1% with energy and angle, en- gy resolution with a constant term less than 4% with Gaussian tails, and position solution of order 1 mm.

The Role of Forward Calorimeters

t a high luminosity hadron collider such as the LHC at CERN the particle densities id energies are largest at high $|\eta|$, i.e. near the forward and backward directions. alorimetry is the only useful detector technology which can survive in this envi- nment. Furthermore many compromises are imposed on the calorimeter design in der to meet all the stringent requirements.

In the ATLAS detector at the LHC [1] the inner detector coverage extends p to $|\eta|$=2.5, the muon coverage up to $|\eta|$=2.7, and the precision calorimetry for ectrons and gammas up to $|\eta|$=2.5. Beyond this the only coverage is calorimetric id extends to $|\eta|$=4.9. In this region ATLAS focuses on jets. The ATLAS forward ilorimeters cover the region $3.1 < |\eta| < 4.9$.

A major objective of forward calorimetry is physics with missing E_T. Events with high p_T neutrinos or other weakly interacting particles will escape detection but their presence can be inferred by observing events with large momentum imbalance in the transverse direction. Such events can be quite interesting. A major background comes from ordinary events where a jet escapes detection, often down the beam hole. Forward calorimeters close as much of this beam hole as is practical thereby completing the hermetic calorimeter system. Benchmark processes which have guided our performance goals include heavy (500 to 800 GeV) Higgs production with subsequent decay to Z pairs with one Z decaying to charged leptons (electrons or muons) and the other decaying to unobserved neutrinos. The search for Supersymmetry (SUSY) will have pushed the gluino mass limit to 300 GeV at LHC turn-on so missing E_T greater than 100 GeV will set the scale. Sensitive to the missing E_T resolution (dominated by calorimetric coverage) is the decay $A/H \to \tau^+\tau^-$.

Longitudinal WW, WZ, and ZZ scattering processes leave two recoil jets near the forward and backward directions which can be used as tags to enhance the signal over background. If the Higgs is heavy such processes will act as probes of a poorly understood, strongly interacting, electroweak sector. Many of these tagging jets will fall in the forward calorimeters and it will be a challenge to pick up these above the pileup noise.

2 Performance Requirements

The forward calorimeters primarily detect jets, either tagging jets or jets which would otherwise escape detection and lead to false E_T signatures. This sets the segmentation of the readout to be of order $\Delta\eta \times \Delta\phi = 0.2 \times 0.2$.

We set the E_T resolution to be $\delta E_T/E_T < 10\%$ for $E_T > 100$ GeV. This requires the FCal energy resolution to be $\delta E/E < 7\%$ and and the jet angle resolution to be $\delta\theta/\theta < 7\%$ typically. At the highest $|\eta|$ it is the angle resolution which dominates.

Physics pileup, measured in terms of E_T, is about the same as at lower $|\eta|$. In order to minimize this pileup fast response, of order a beam crossing interval of 25 ns, is required.

The forward calorimeters must be especially radiation hard to insure long-term stability. To set the scale, at every 25 ns beam crossing 7 TeV of energy is deposited in each FCal [2]. The ionization dose varies throughout the FCal from a low of about 10 kRad to values approaching 1 GRad per LHC year. And the flux of neutrons with kinetic energies above 100 keV ranges from 10^4 to 10^6 kHz/cm^2.

Integrating the FCal into ATLAS

e severe environment near the beam line, dominated by products of collisions at interaction point (IP), suggests locating the forward calorimeters as far from IP as possible. This reduces the particle densities and therefore the radiation nage. The original ATLAS design placed the FCal at about 15 m from the IP. t further study [3, 4, 5, 6] showed that there were many advantages to locating FCal at roughly the same place as the endcap calorimeters, i.e. *integrated* into endcap. The distance of the ATLAS FCal from the IP is now about 5 m where density of particles is approximately 9 times greater. Despite the punishment in liation damage there are many advantages to this design strategy [7].

The calorimetry system is now manifestly *hermetic.* A deep calorimeter stem continuously surrounds the IP (with non-projective gaps to route signals d services for the inner detector). A key feature is that *transitions* are minimized. e edges of transitions can be problematic in that hadronic showers near the edges n spray into remote calorimeters with no hint that the energy did not come from IP. This leads to false reconstruction of the energy flow. The endcap-forward nsition in ATLAS now suffers little of this effect.

ATLAS has an *open* muon system, i.e. the muon chambers are not embed-d between magnetized iron slabs which would provide natural shielding. So the TLAS muon chambers are fully exposed to backgrounds (particularly neutrals) in e collision hall. In the early far forward FCal design ATLAS had deployed massive ielding in order to reduce the backgrounds to manageable levels. The newer *inte-ated* design allows for much more flexibility in optimizing the muon shielding [8, 9] elding important reductions in the background rates.

With a far forward calorimeter ATLAS was required to leave a clear space m the IP to the FCal so as not to obstruct the particles. This clear space, the ed to deploy massive shielding, the desire by the muon people to cover to as high lues of $|\eta|$ as possible, and the beam line appurtenances were all in conflict. The ace was oversubscribed. The *integrated* design greatly ameliorated this conflict.

There is unavoidable material upstream of all the ATLAS calorimeters. is material is particularly troublesome near the beam line in front of the FCal. camples include the beam pipe itself which is crossed as shallow angles by the rticles but in addition includes flanges, valves, vacuum pumps, vacuum backout pliances, support structures, and, in the case of ATLAS, cryostat walls. With the *tegrated* FCal there is less of this material but, more importantly, the *lever arm* om the material to the FCal is much smaller. For particles which shower in the stream material, that shower cannot spread much over the short distance to the Cal so the energy flow is well collimated along the original direction. For a far forward calorimeter, on the other hand, the far upstream material causes the energy to spread over so large an area of the FCal that much of it is lost in the pileup.

Finally the smaller physical size of the *integrated* FCal leads to a savings, some of which can be used for a higher quality device.

4 The Liquid Argon Technology

The ATLAS FCal is a liquid argon, ionization, sampling calorimeter. Because liquid argon and the absorber metals are radiation hard it is anticipated that the FCal performance will be stable over the life of the detector. Care will be required in selecting the several additional materials (e.g. readout cables) which go into the construction in order to ensure they also will not degrade with the expected exposure. The choice of liquid argon is natural because the FCal lies within the ATLAS Hadronic Endcap Calorimeter (HEC) which is a liquid argon parallel plate design. Along with the EM endcap 'Spanish Fan', the HEC and FCal will all sit within the same cryostat.

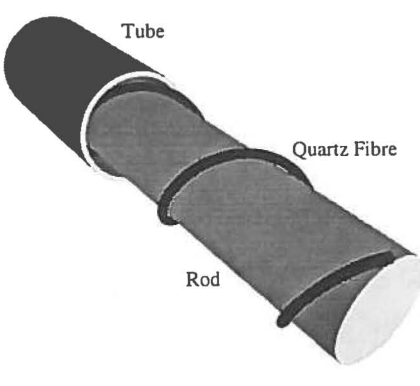

Figure 1: Tube electrode with the inner rod pulled out to expose the spiraled quartz fiber holding the rod coaxially within the tube. Liquid argon fills this gap between rod and tube which, for the EM module, is 250 μm across. The rod is held at positive high voltage while the tube is grounded.

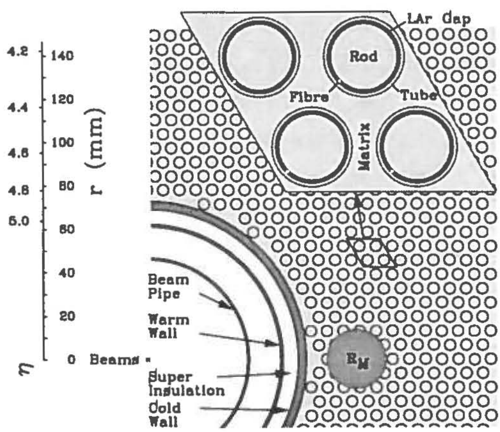

Figure 2: Front face of the EM forward calorimeter module in the region of the beam pipe. The circle labelled R_M indicates the Molière radius for e.m. showers. The insert at the upper right shows the detail of four tube electrodes embedded in the absorber matrix. On the left is a scale in mm and η.

But the ATLAS FCal is not a conventional liquid argon calorimeter. The liquid argon gap in the EM FCal module is chosen to be 250 μm to avoid the ion ildup problem 10) resulting from the low mobility of the positive charge carriers the argon. At sufficiently high ionization rates (due to pileup events) a threshold :eached above which the electric field distortion significantly degrades the electron nal. Smaller gaps allow the FCal to stay below this threshold. The smaller gaps o lead to a much faster signal. The triangular current pulse at the electrode s a full drift time of 50 ns as opposed to the 400 ns of more conventional 2 mm ps in many liquid argon sampling calorimeters. After 25 ns 75% of the signal s already accumulated on the electrode. The readout and electronics shape this rrent pulse to a peaking time of about 40 ns. This leads to an *rms* pileup noise ιich is about 30% larger than the irreducible pileup from an ideal detector which s an integration time of one bunch crossing. We say the actual pulse leads to a eup penalty of a factor 1.3.

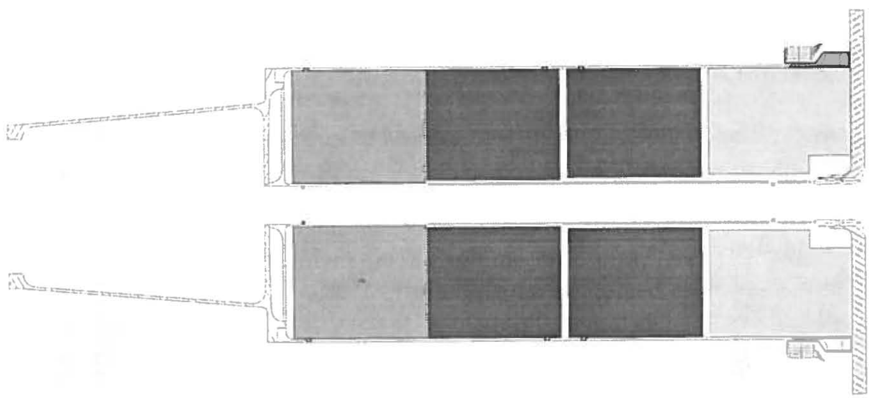

gure 3: Slice along the beamline of the FCal modules housed in their support be. The EM module in medium gray is on the left, followed by the two hadronic odules in dark gray. The light gray module at the right is the copper 'plug' which ovides extra shielding for the muon system.

Precision small gaps are difficult to maintain in a parallel plate design so e have chosen an electrode structure based on tubes and rods as shown in Figure 1. he gap between the inner solid rod and the outer tube is maintained by a spiraled ıartz fiber of 250 μm diameter. Liquid argon, the ionizing (sensitive) medium, fills ıe rest of the gap not occupied by the fiber (98.7% of the volume of the gap). The ırrent of electrons drifting toward the rod constitutes the signal. Note that the ;ure is an *exploded* view, i.e. the rod has been pulled out to expose the fiber. The ›d and tube are made of the same material as the absorber matrix in which these ectrodes are embedded in a hexagonal array as shown in Figure 2.

The rods, tubes, and absorber matrix of the EM modules are made of copper. Copper was chosen because the Molière radius (14 mm) is not too small (in contrast to Tungsten). This makes the response across the front face of the module reasonably uniform [11]. The rods and matrix in the two (at each end) hadronic modules are Tungsten. The liquid argon gap in the first hadronic module is 375 μm while that in the second is 500 μm. These larger gaps deeper in the calorimeter are allowed because the ionization density from showers is lower here than in the EM module. All modules are 450 mm in depth with an outer radius of 450 mm. The EM modules are 25 X0 deep or 2.5 λ. The hadronic modules are each 3.4 λ deep for a total active depth of 9.3 λ. Behind the second hadronic module at each end is a 'plug' of passive copper to help shield the muon system. The three modules at one end of ATLAS are shown in their support tube in Figure 3. The nearest-neighbor spacing of electrodes in the EM section is 7.5 mm center-to-center and increases in the hadronic modules so that they are pseudo-projective.

5 Electron Test Beam Results

We have built and tested a prototype of the EM FCal module [12, 13]. The prototype has the full 450 mm depth of the actual device but is only 180 mm in diameter. Four tube electrodes are ganged together at the module to form a readout channel with total capacitance of 1.45 nF. The prototype has 91 such channels. The signals are transferred from the electrodes to the electronics via 20 Ω coax cables with polyimide dielectric and insulation for radiation hardness. The cable in the cryostat is 4.5 m long and 1 m outside the cryostat to simulate the actual cable lengths. The preamps, located outside the cryostat, are the so-called ØT type [14, 15]. Modified Sallen-Key (equivalent to CR-RC) shapers give a peaking time for the liquid argon pulses of about 40 ns. Track & Holds convert the peaks of the pulses to voltage levels which are fed to 11-bit FERA ADC's read by CAMAC into a PC and onto a disk co-mounted with a VAXStation. Incoherent noise per channel was under 80 MeV with a coherent noise contribution of about 20% of this. The coherent noise appears to have a coherence length limited to 16 channels. Our preamps, shapers, and Track & Holds were all mounted on motherboards with 16 channels each and cables interconnecting these came in groups of 16. We have not yet isolated the source of the coherent noise but it is not significant for the energies and cluster sizes used in this test.

The high voltage (only 250 V to give 10 kV/cm electric field) is applied near the preamp input (separated by a blocking capacitor on the preamp board) and reaches the electrodes via the readout coax cable. The calibration pulse is also injected at the preamp input. None of the results presented below use the calibration. Those preamps corresponding to channels which are struck by beam ctrons (17 in all) are calibrated by beam and are uniform to better than 0.5% ng the same calibration constant for all channels.

Three scintillators form the trigger with the defining size of 5 by 5 cm. e electron beam is defocussed to fill this area uniformly. A veto wall eliminates ggers with additional charged particles outside this area. Ten planes of 1 mm ıcing MWPC's (5x and 5y) allows good tracking of the electron. Optional dead ıterial (Aluminum blocks) can be placed upstream of the prototype to simulate anticipated situation in ATLAS. Rohacell^{TM} displaces liquid argon upstream and wnstream of the prototype inside the cryostat. Downstream of the prototype is a ıde hadronic tail catcher consisting of iron-scintillator layers. After 10 λ a small ntillator centered on the beam tags muons. An argon purity monitor [16, 17] d oxygen analyzer ensure that contamination is at or below the 0.5 ppm oxygen uivalent level.

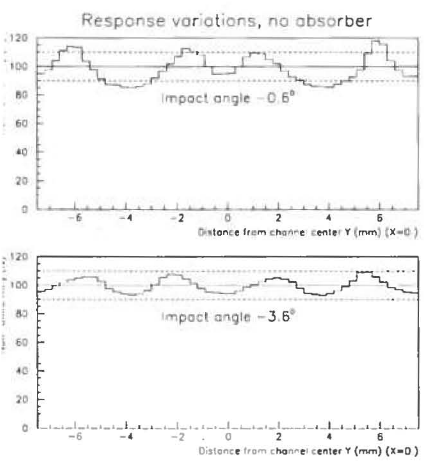

'igure 4: Normalized energy response ersus position at two incident electron ıngles.

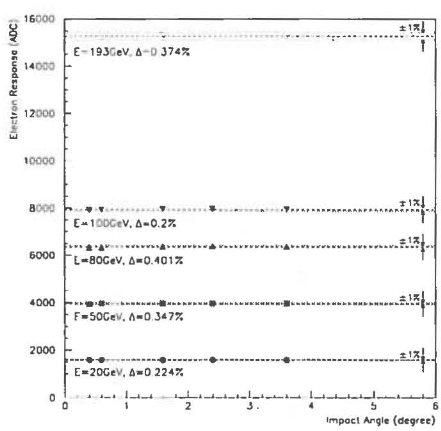

Figure 5: Prototype response to electrons versus angle to the normal for different electron energies.

In the actual FCal particles enter at angles between 0.8° and 4.7° to the ormal. Channeling effects are a potential problem as evidenced by a position ependence to the response. Electrons which strike the prototype at small angles the normal and near the argon gap give a response of order 15% above average hile electrons which strike the center of a rod give a response about 15% below erage. At larger angles to the normal this position dependence of the response ashes out. At a typical angle of 3.6° the peak variation is of order ±8%. For most of the angular range the *rms* position response variation is under 5% as shown in Figure 4.

Averaging over position the response variation with angle is very uniform, within $\pm1\%$ full width. Figure 5 shows that all the data points lie within this range over a spread in angles beyond that covered by the FCal.

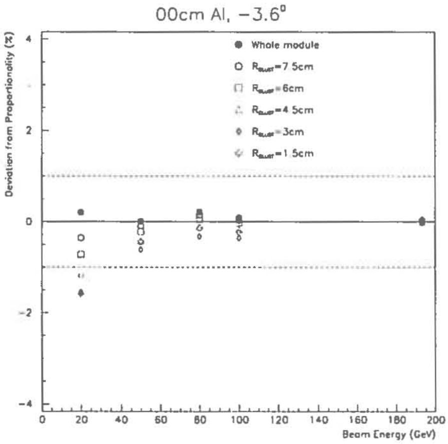

Figure 6: Deviation of the energy response from a straight line constrained to the origin for different clustering radii.

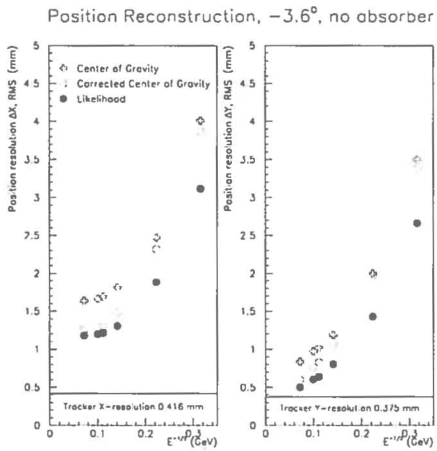

Figure 7: Position resolution versus $1/\sqrt{E}$ using different algorithms.

When analyzing the data we include only those channels within a 'cluster radius' of the center-of-energy. This center is determined by a clustering algorithm (not by the MWPC's). Various cluster radii will be used in the following results. A cluster radius of 35 mm generally contains 95% of the energy (at 3.6°) except at our lowest energy point at 20 GeV where the 95% containment radius jumps to 40 mm.

Figure 6 shows the deviation from a straight line (constrained to the origin) of the energy response of the prototype EM module for different clustering radii. For large radii the linearity is well under $\pm0.5\%$. Smaller clustering radii show the small but discernible energy dependence of the transverse shower size confirming that lower energy electromagnetic showers spread a bit more.

The fine readout channel granularity allows a good position determination from shower sharing. Three reconstruction techniques have been used. When compared to the position determined from the MWPC's an *rms* position resolution can be determined. These data are shown in Figure 7 versus $1/\sqrt{E}$. The beam lies in

: x-z plane making an angle of 3.6° to the z axis. Longitudinal shower fluctua-ns couple into the position determination in this plane so the position resolution worse than in the y-z plane where the beam angle is normal to the prototype. The WPC resolution (which is not subtracted in this analysis) limits the determination the position resolution to about 0.4 mm. The excellent position resolution seen re allows us to remove most of the position dependence of the response from the st beam data. We will show this below.

The *rms* percent energy resolution for electrons is plotted versus cluster dius for different electron beam energies in Figure 8. Correcting for the variation response due to position improves the energy resolution substantially at the higher ergies. Note that at the lower energies the electronics noise is not negligible for ger cluster radii.

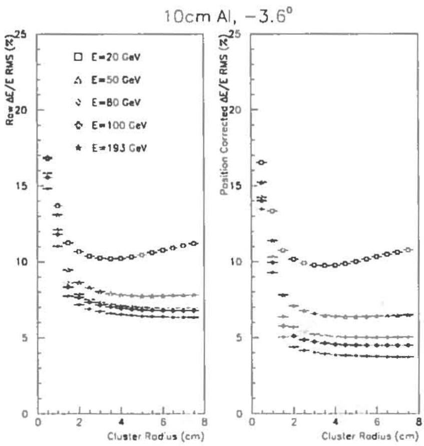

Figure 8: Percent energy resolution versus cluster radius for different elec-tron beam energies without and with position correction.

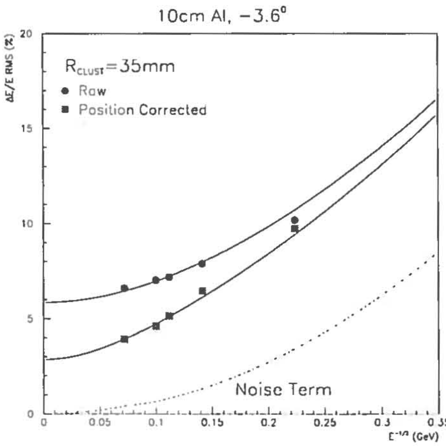

Figure 9: Percent energy resolution for electrons versus $1/\sqrt{E}$ for fixed cluster radius of 35 mm without and with position correction.

Choosing a cluster radius of 35 mm we have plotted in Figure 9 the *rms* ercent energy resolution versus $1/\sqrt{E}$ without and with a correction for response uriations due to position. A fit to this data of the form $\Delta E/E = a \oplus b/\sqrt{E} \oplus c/E$ elds the usual summary energy resolution terms. The so-called constant term is a, hile the stochastic term is b, and the noise term (in this case due only to electronics) c. The noise term for a cluster radius of 35 mm is plotted at the bottom of the gure. Repeating this fit for different cluster radii yields the data of Figure 10. Note that the response variation due to position contributes to the constant term.

As noted earlier the FCal measures jets. The EM module, a prototype of which we have exposed to the testbeam, measures the EM components of such jets and the early parts of the hadronic components. Jets typically contain several EM components spread over the front face of the FCal into an area large compared to a unit cell. (A unit cell contains one tube electrode.) So the response variations due to position are averaged over. To evaluate the effect of this averaging we have taken tagging jets generated via Pythia for the process $pp \to HX \to ZZjjX$. We then decayed each Z into neutrinos to avoid dealing with the decay products. We next picked out the EM components of each tagging jet and, using our testbeam data as a lookup table, simulated the response of the FCal. The results, shown in Figure 11, yield a constant term of about 3%, approximately what we determined after position correction of the electron data as seen in Figure 10.

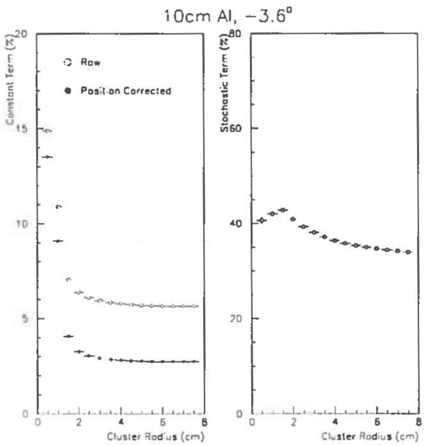

Figure 10: Constant term and stochastic term in the energy resolution parameterization versus cluster radius without and with position correction.

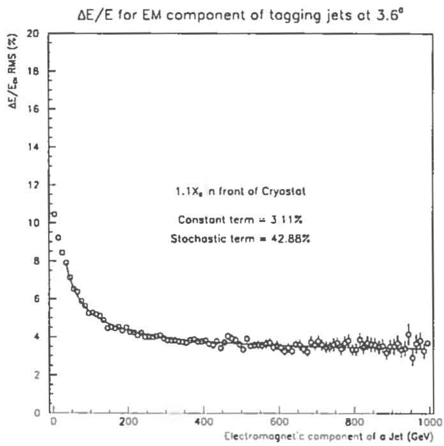

Figure 11: Calculated percent energy resolution for the electromagnetic component of tagging jets from 800 GeV Higgs production versus the energy of that electromagnetic component.

Up to this point we have concentrated on the prototype performance at a typical angle of incidence to the normal of 3.6°. Figure 12 shows how the energy resolution varies with incident angle after the correction for the response variation due to position. While the energy response is quite constant with angle (see Figure 5) the *rms* energy resolution improves with angle as is shown in Figure 12. At the nallest angles relevant to the FCal, of order 1°, the angle resolution dominates ıe E_T determination so the energy resolution, if under control, is not the critical ırameter. Figure 12 shows that the energy resolution for EM energy deposits is ell within our requirements.

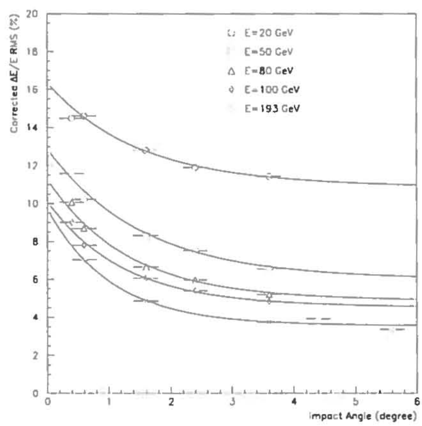

Figure 12: Percent energy resolution versus angle for different electron beam energies with position correction.

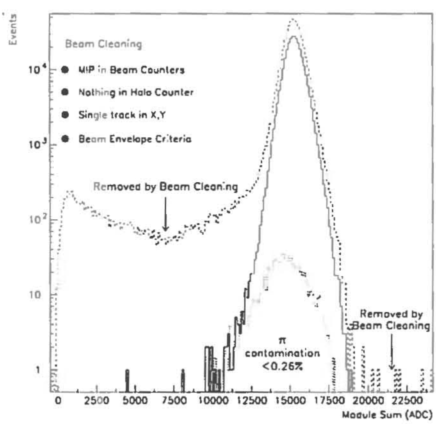

Figure 13: Electron energy resolution function without beam cleaning (dashed), with beam cleaning (solid), and pion contamination (dotted) for 193 GeV beam at 3.6°.

Tails on the energy resolution function can be a problem. Figure 13 shows the energy resolution function for 193 GeV electrons over almost five orders of magnitude. With only simple cuts to eliminate pions there is a large tail on the low energy side (approximately 1% of the peak height) and a few events on the high side outside the peak. After examination of single events we could see rare instances of a low energy cluster centered on the MWPC track projection but another neutral cluster elsewhere in the prototype. This was clear evidence for electron bremsstrahlung upstream in the beam line. The events with low pulse height occur when the bremsstrahlung photon misses the prototype. A severe cut on the beam angle appears to eliminate all such events with a concomitant loss of about 50% of the good events. The cut has the virtue that it is completely unbiased. An estimate of the pion contamination surviving the cuts, obtained from separate pion runs, appears to explain the remaining low energy tail well below the 10^{-4} level.

6 Summary

ATLAS has elected an unconventional location for its forward calorimeters resulting in many benefits. The chosen technology employs a novel liquid argon electrode structure. Test beam results with electrons show performance exceeding the requirements.

References

1. The ATLAS collaboration, *Technical Proposal for a General-Purpose pp Experiment at the Large Hadron Collider at CERN*, CERN/LHCC/94-43 (1994).
2. J. Rutherfoord, *Heating and Cooling a Forward Calorimeter*, ATLAS Internal Note CAL-NO-056, 21 June 1994.
3. J. Rutherfoord, L. Shaver, and M. Shupe, *The ATLAS Forward Region*, ATLAS Internal Note CAL-NO-035, 1994.
4. M. Shupe and J. Rutherfoord, *Three Options for the ATLAS Forward Region: Particle and Jet Response and Fluence Results from a GEANT Mixture Description of the Detector*, ATLAS Internal Note CAL-NO-036, 1994; M.Shupe, *Using GEANT Mixtures for the Precise Simulation of Particle and Jet Response, and Particle Fluxes in ATLAS*, ATLAS Internal Note CAL-NO-037, 1994.
5. J. Rutherfoord, A. Savin, L. Shaver, M. Shupe, *The ATLAS Integrated Forward Calorimeter, Progress on Answers to Calorimetry Panel Questions*, ATLAS Internal Note CAL-NO-055, 27 May 1994.
6. Laurie Waters and William B. Wilson, *LAHET/MCNP/CINDER'90 Activation Calculations for the ATLAS Integrated Forward Calorimeter Concept*, ATLAS Internal Note CAL-NO-047, 19 July 1994.
7. J. Dowell *et al.*, *Report of the ATLAS Review Panel on Forward Calorimetry*, ATLAS Internal Note GEN-NO-007, 26 August 1994.
8. M. Shupe, *ATLAS Muon Region Background Fluxes in Four Forward Configurations*, ATLAS Internal Note GEN-NO-011, 7 November 1994.
9. G .Battistoni, A. Ferrari, and P.R. Sala, *Background calculations for the ATLAS detector and hall*, ATLAS Internal Note, GEN-NO-010, 13 October 1994.
10. J. Rutherfoord, *Ion Loading in Liquid Ionization Calorimeters*, GEM TN-91-27, 25 October 1991; J.Rutherfoord, *Testing for Effects of Ion Loading in Liquid Ionization Calorimeters*, GEM TN-93-410, 18 May 1993.

1. P. Loch, *Tube Radius Optimization for the Electromagnetic Forward Calorimeter in ATLAS*, ATLAS Internal Note LARG-NO-039, 12 April 1996.

2. ATLAS members contributing to the test beam run reported here are J.C. Armitage (Carleton University, Ottawa), A. Artamonov, V. Epchtein, V. Jemanov, V. Khovansky, M. Ryabinin, P. Shatalov (ITEP, Moscow), L. Austin, K. Johns, P. Loch, R. Norton, J. Rutherfoord, A. Savin, L. Shaver, M. Shupe, J. Steinberg, D. Tompkins (University of Arizona), J.K. Mayer, R.S. Orr, and G. Stairs (University of Toronto).

3. Earlier test beam results are reported in M.I. Ferguson *et al.*, *Electron Testbeam Results for the ATLAS Liquid Argon Forward Calorimeter Prototype*, accepted for publication in Nucl. Instrum. and Methods **A**, July 1996; A. Savin, *Beam Test of Liquid Argon Tube Calorimeter Prototype*, Proc. of the 5th Int. Conf. on Calorimetry in High Energy Physics, Brookhaven, New York Sept 25 – Oct 1, 1994, ed. Howard A. Gordon and Doris Rueger, World Scientific 1995; M.I. Ferguson *et al.*, *A liquid argon forward calorimeter prototype: beam test results*, ATLAS Internal Note CAL-NO-042, 18 January 1994.

4. R.L. Chase, C. de La Taille, S. Rescia, and N. Seguin-Moreau, *Transmission lines connection between detector and front end electronics in liquid argon calorimetry*, Nucl. Instr. and Meth. **A330** (1993) 228-242; R.L. Chase, C. de La Taille, and N. Seguin-Moreau, *Experimental results on cable-coupled preamplifiers (∅T)*, Nucl. Instr. and Meth. **A343** (1994) 598-605.

15. J. Rutherfoord, *The Electronics Choice for the ATLAS FCal*, ATLAS Internal Note CAL-NO-087, 6 November 1995.

16. G.C. Blazey, *Monitoring Liquid Argon Purity at DZero*, in Proc of Int. Conf. on Calorimetry in High Energy Physics, Batavia, IL Oct. 29 – Nov. 1, 1990 (1991).

17. A. Attard, J.K. Mayer, R.S. Orr, G.S. Stairs, and J.C. Armitage, *Development of a Portable Liquid Argon Purity Monitor System*, ATLAS Internal Note LARG-NO-032, 15 December 1995.

ascati Physics Series Vol. VI, (pp. 85–97)
: INT. CONF. ON CALORIMETRY IN HEP – Frascati, June 8–14, 1996

NEW CRYSTAL CALORIMETERS FOR COLLIDERS

Peter Denes

Physics Department, Princeton University

ABSTRACT

'hree new crystal calorimeters are under construction for use at colliders. BaBar and 3elle at asymmetric B factories will each use $\sim 10^4$ CsI(Tl) crystals, and CMS at the ,HC will use $\sim 10^5$ $PbWO_4$ crystals. This paper outlines certain technical aspects of rystal calorimetry, with emphasis on selected properties of crystals and issues with he electronic readout.

. Introduction

'or decades now, calorimeters composed of large numbers of scintillating crystals ıave consistently provided high-resolution measurements of the energies of :lectromagnetically interacting particles. In the future, three large collider :xperiments (as well as other smaller and fixed-target experiments) will use crystals 'or their electromagnetic calorimeters. BaBar (SLAC) and Belle (KEK) will each :mploy $\sim 10^4$ CsI(Tl) crystals, and CMS (LHC) will use $\sim 10^5$ $PbWO_4$ crystals. 3etween the B-factories and the LHC, there is a factor of 1000 in beam energy and a arge difference in interaction rates, yet all three experiments wish to perform precision measurements of a dynamic range of roughly 18 bits.

A successful calorimeter requires careful attention to numerous details, but the key problems for the construction of a crystal calorimeter are the crystal itself, conversion of the optical signal into an electrical one, and the capture of that electrical signal with the dynamic range and precision that are required. After that point, a crystal calorimeter is like any other, only more precise. Once built, the key problem is, of course, maintaining the detector calibration at a level consistent with the resolution desired.

All three of the new collider detectors (see Table 1) operate in a magnetic field. The presence of a magnetic field influences the choice of photodetectors, as conventional vacuum devices are difficult to use in 4π detectors with magnetic field. At low fields, shower development is not strongly influenced by the magnetic fields, however the 4T field of CMS will cause distortion in both directions of the shower. (Shower shape, for example the pulse height in the "core" of the shower divided by the pulse height in a wider region, is important to determine the "electromagneticity" of the particle. In addition, impact point determination depends on the center of gravity of the shower in the crystals.)

For BaBar and Belle, the crystal is well developed, although special care is needed due to the high rate. Silicon photodiode readout is well established, so that the novelty is to cover the dynamic range in what is effectively a DC (non-synchronous) environment. CMS is a bit more ambitious. First, a factor of ten times more crystals than any other detector are required, and these crystals must survive the radiation environment of the LHC. Next, the low light yield, combined with the high magnetic field, precludes the use of conventional photodiodes, thus avalanche photodiodes are used. Finally, the usual precision and wide dynamic range must be obtained at 40 Mhz sampling rates.

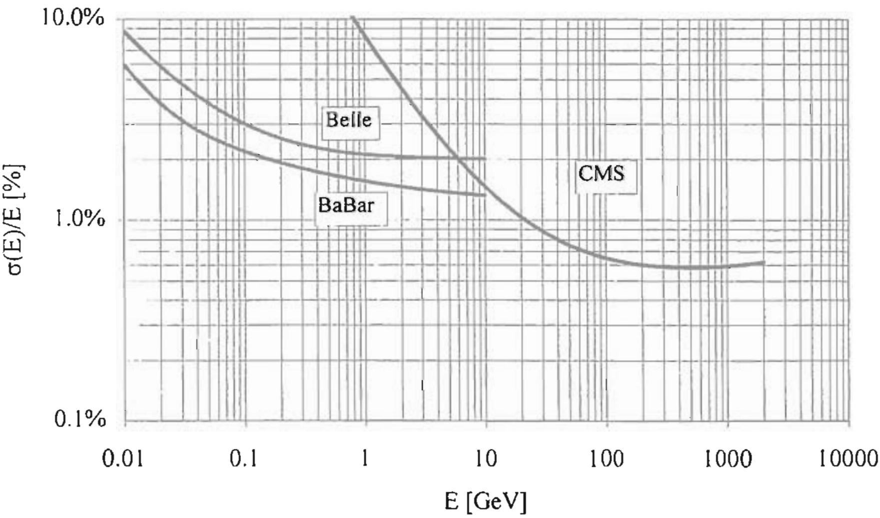

Figure 1 Proposed energy resolution for Belle, BaBar and CMS. Belle and BaBar have differing assumptions about intrinsic resolution and constant terms.

Table 1: Some existing and proposed crystal calorimeters. New collider detectors clude BaBar and Belle at asymmetric B-factories, and CMS at the LHC. In the table below N is the number of crystals in the detector (in thousands), X_0 is the radiation length of the crystal and f_{BC} is the bunch crossing frequency. *Photo* refers to the photodetector: photomultiplier tube (PMT), Silicon *p-i-n* photodiode (Si PD), vacuum phototetrode (V4T) or Silicon avalanche photodiode (APD)

Crystal Ball	**CLEO II**	**L3**	**BaBar**	**Belle**	**KTeV**	**L* EoI**	**GEM EoI**	**CMS EoI**	**L3P EoI**	**CMS TP**
SPEAR	CESR	LEP	SLAC	KEK	FNAL	SSC	SSC	LHC	LHC	**LHC**
$e^\pm$ 4 GeV	$e^\pm$ 6 GeV	$e^\pm$ 100 GeV	$e^\pm$ 9+3.1 GeV	$e^\pm$ 8+3.5 GeV	$p^\pm$ 1 TeV	p 20 TeV	p 20 TeV	p 8 TeV	p 8 TeV	**p 7 TeV**
NaI(Tl)	CsI(Tl)	BGO	CsI(Tl)	CsI(Tl)	CsI	BaF_2	BaF_2	CeF_3	CeF_3	$\mathbf{PbWO_4}$
0.672	7.8	11.4	6.8	8.8	3.3	26	15	45	100	**100**
16	16	21.5	16	16	27	24.5	24.5	25	25	**25**
PMT	Si PD	Si PD	Si PD	Si PD	PMT	V4T	V4T	Si PD	VPD	**APD**
0	1.5	0.5	1	1	0	.75	.8	4	1	**4**
1.3	2.8	0.091	238	10-508	0.29	60	60	67	67	**40**

Anticipated energy resolutions for the new collider detectors are shown above in Figure 1. For CMS, energy resolution in the 50 - 100 GeV region ($H \rightarrow \gamma\gamma$) is crucial, and must be ensured by maintaining calibration precision.

2. Crystal Properties

Crystals are characterized by several parameters, some of which are shown for selected crystals in Table 2. The mechanical parameters determine the dimensions that the crystal must have, and the scintillation parameters influence the readout. In detail:

- High density (ρ) ensures a compact calorimeter.

- In order to achieve a certain energy resolution, the crystals must be long enough to contain the electromagnetic shower at that energy. The radiation length (X_0), is a measure of longitudinal shower development. As energies increase, the position in the crystal of the shower maximum (in X_0) moves further back lograithmically, so that at very high energies longer crystals are needed. A short radiation length thus also ensures a compact calorimeter.

- The transverse size of the shower is traditionally parameterized by the Molière radius R_M. The typical cross-section of the crystals is one R_M, in which case for a particle striking the center of a crystal, roughly ¾ of the energy is deposited in that crystal, and a sum of that crystal along with its eight closest neighbors contains over 90% of the energy. Granularity is important for position reconstruction, and crucial for particle identification and isolation, as narrow showers are signatures of electrons or photons.

- The scintillation decay (or, more usually, decays) is characterized by an emission spectrum with a certain peak wavelength, decay time constant and light yield. The light yield, traditionally quoted as a percentage of that of NaI(Tl) depends on numerous particularities of the crystal, its shape, reflective wrapping, and so on, thus often fluctuating from publication to publication. Further, light yields tend to be quoted as the integral of the total photocurrent, and may thus be strongly influenced by long decay tails.

- Mechanical hardness, the presence of cleavage planes, the melting point and other similar parameters are important for the growth of the crystal, and the construction of the calorimeter. Hermetic detectors require non-rectangular crystals, hence relatively precise machining of the crystal faces is required.

- The light yield of all crystals is temperature-sensitive to some degree. $PbWO_4$, like BGO, has a strong sensitivity at room temperature, on the order of -1.5% per degree.

Гable 2: Properties of crystals used of proposed for certain crystal detectors. X_0 is ıe radiation length, ρ the density, τ the principal decay time constant, λ the principal emission peak wavelength, *n* the index of refraction, and *LY* the light yield as a percentage of NaI(Tl).

	NaI(Tl)	BaF_2	CsI(Tl)	CeF_3	BGO $Bi_4Ge_3O_{12}$	$PbWO_4$	
X_0	2.59	2.03	1.86	1.66	1.12	0.92	cm
ρ	3.67	4.89	4.53	6.16	7.13	8.2	g/cm^3
τ	230	0.6/620	1050	30	340	~10	ns
λ	415	230/310	550	380	480	~500	nm
n	1.85	1.56	1.80	1.68	2.15	~2.3	
LY	100%	5%/16%	85%	5%	10%	0.2% [23 cm]	%NaI

ı obtain high resolution, the crystal must also provide a uniform scintillation

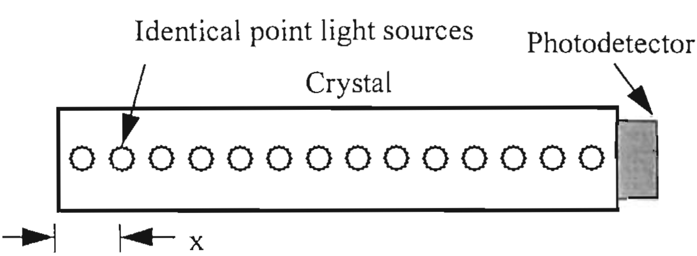

gure 2: Longitudinal uniformity of response. The non-uniformity is the variation in light yield as a function of position, for an ideal light source at that location.

sponse. The uniformity, as indicated in Figure 2, is measured by observing the ıriation in light produced as a function of position. A non-uniformity influences ıergy resolution in two ways. Because the longitudinal deposition of energy from ıowers fluctuates, non-uniformity spoils the resolution. Also, as the shower aximum moves with energy, non-uniformity gives an energy dependent non-ıearity in the calibration.

The new calorimeters all have non-rectangular crystals, which automatically introduces a non-uniformity due to the "focusing effect": For a rectangular crystal with a given index of refraction, the probability for a scintillation photon to escape the crystal and enter the photodetector is independent of position (depending only on the initial angle of the photon). In a tapered (and particularly high index of refraction) crystal, the tapering favors photons produced at the front of the crystal. This effect is either balanced by light attenuation in the crystal (if the attenuation length Λ is short) or by modifying the reflective coating.

Measuring the uniformity of response for most crystals, such as CsI, is in principle straightforward, but low-light yield crystals, in particular $PbWO_4$, present special problems. Scanning the crystal with a typical radioactive source (energies ~ 1 MeV) becomes imprecise as the light yield diminishes. The position of the energy deposition in the crystal is hard to know, as sources are hard to collimate and low energy particles either deposit their energies on the surface or travel some distance in the crystal. Use of correlated tagging (i.e. a ^{22}Na source where an e^+e^- pair are produced, and one of the pair is detected in a tagging counter) can simplify source measurements. Cosmic rays deposit more energy in the crystal, however precise position measurements are needed to reconstruct uniformities. For CMS a technique using a beam of stopping protons at 405 MeV/c has been developed. Such a beam penetrates roughly 15 mm into the crystal, and produces well defined energy deposition with dE/dx roughly 5 times minimum ionizing (except for the Bragg peak in the last microns). This technique has been shown to produce accurate and reproducible measurements of light yield and uniformity.

3. Photodetectors

For detectors without magnetic field, conventional vacuum photodetectors are employed. Vacuum photodetectors with few stages can be employed in magnetic fields, provided that the angle between the field and the photodetector axis is not so large as to cut off the photocurrent. Silicon *p-i-n* photodiodes have been used successfully with crystals (see Table 1). *p-i-n* photodiodes have high quantum efficiencies and a stable gain of 1. For CMS, the small light output of $PbWO_4$ crystals requires additional gain, thus silicon avalanche photodiodes are used.

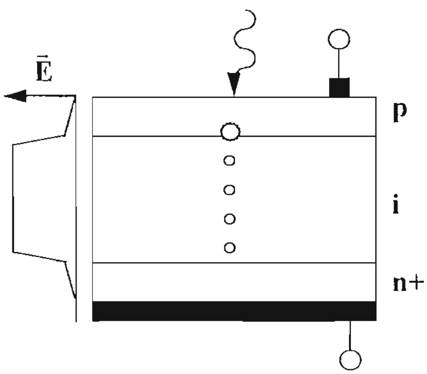

Figure 3 *p-i-n* photodioide

A *p-i-n* photodiode consists of a thin p-region which acts as a photocathode and an n^+- region, positively biased with respect to the p-region, which serves to collect the charge. These two regions are separated by 100-500 μ of intrinsic semiconductor, which reduces the capacitance between p- and n^+-regions. Visible light passes through a transparent protective window, enters the p-region, and creates an electron-hole pair. The electron drifts at constant velocity through the i-region and is then collected.

The *p-i-n* photodiodes used with crystals typically have areas ≥ 1 cm^2, leakage currents of a few nA, and capacitances of 25-75 pF/cm^2. (For large-area crystals, such as CsI, wavelength shifter bars coupled to narrow photodiodes are also used.)

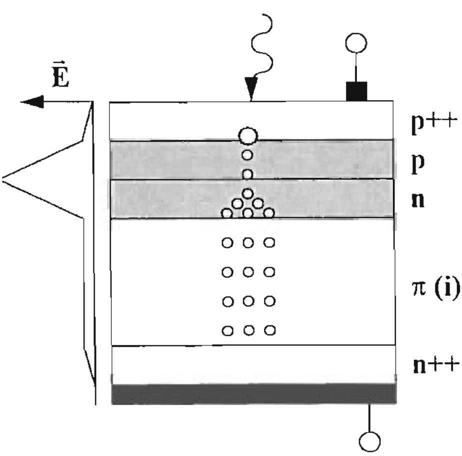

Figure 4: Avalanche photodiode.

An avalanche photodiode (of the type suitable for crystal readout) is similar to a *p-i-n* photodiode, but includes a p-n junction buried beneath the "photocathode". As before, the photon converts in the thin "photocathode", but unlike the *p-i-n* structure, the electron is accelerated by the high field across the buried p-n junction, and undergoes avalanche multiplication, thus providing gain.

Unlike *p-i-n* diodes, APDs are new to high-energy physics. The APD gain, M, is a sensitive function of voltage and temperature. (Typical APDs currently being developed for CMS have gain sensitivities dM/dV and dM/dT that are a few percent of the gain.) In addition, the statistics of the gain mechanism influence both the observed photostatistics as well as the noise.

If the crystal has a light yield of N_γ photons/MeV deposited, then for energy E deposited, $N_\gamma \cdot E$ photons arrive at the entrance of the APD. For a quantum efficiency ε_Q (which can easily be 85%) $N_{pe} = N_\gamma E \varepsilon_Q$ photoelectrons are created. As the photons are produced with Gaussian statistics in the crystal (i.e. if in a time window Δt, N photons are produced on average, the rms fluctuation is $\sqrt{N}$) $N_{pe} \pm \sqrt{N_{pe}}$ photoelectrons enter the amplification region. As a gain of M is applied, if there were *no* fluctuations in the gain, $M \cdot N_{pe} \pm M\sqrt{N_{pe}}$ electrons would be collected.

Avalanche photodiodes, however, have strong multiplication statistics. If we imagine that we are able to create exactly one photoelectron at the entrance of the amplification region, then we would experimentally observe $M \pm \sigma(M)$ electrons are collected, where σ(M) is the rms fluctuation of the gain (which, in APDs is a function of the gain, M). Because of this gain fluctuation, the actual number of electrons we collect is given by $M \cdot N_{pe} \pm \sqrt{M^2 + \sigma^2(M)}\sqrt{N_{pe}}$. As a consequence, the *photostatistical* contribution to the energy resolution is

$$\frac{\sigma_{photo}(E)}{E} = \frac{1}{\sqrt{N_\gamma \varepsilon_Q E}}\sqrt{\frac{M^2 + \sigma^2(M)}{M^2}} \equiv \frac{1}{\sqrt{N_\gamma \varepsilon_Q E}}\sqrt{F}\,.$$

The quantity F is referred to as the *excess noise factor*, and expresses the degradation in photostatistical resolution due to fluctuations in the amplification mechanism. (Typical APDs currently being developed for CMS have excess noise factors on the order of F=2.)

The excess noise factor also plays a role in the noise generated by leakage currents in the APD. Unlike a *p-i-n* diode, two sources of leakage current exist in the APD: those electrons which flow from the p^{++} to the n^{++} region without undergoing multiplication (called *surface* leakage, even though it may occur within the bulk of the device) and those electrons which undergo amplification (called bulk leakage). For surface leakage, electrons flow at an *average* rate I (electrons/second), but arrive at random times, thus creating an rms fluctuation of $\sqrt{qI}$. This is also true for the bulk leakage, however because of amplification the rms fluctuation becomes $M\sqrt{qI}$. Incorporating the effect of gain fluctuations, the observed rms fluctuation increases to $\sqrt{M^2 + \sigma^2(M)}\sqrt{qI}$.

With all effects included, the energy resolution that may be obtained with a crystal calorimeter employing APD's becomes

$$\frac{\sigma(E)}{E}=\frac{\sigma_{stoch}}{\sqrt{E}}\oplus\frac{\sigma_{cal}}{E}\oplus\sqrt{\frac{F}{N_\gamma\varepsilon_Q E}}\oplus\alpha\frac{"C"\sqrt{"R"}}{MN_\gamma\varepsilon_Q E\sqrt{\tau}}\oplus\beta\frac{\sqrt{I_S+M^2FI_B}\sqrt{\tau}}{MN_\gamma\varepsilon_Q E}$$

'he first two terms in the resolution are arise from the calorimeter: σ_{stoch} refers to the stochastic" term (borrowing a phrase from sampling calorimeters. The "stochastic" ɜrm in fact represents fluctuations in energy leakage out of the calorimeter, a large art of which just happens to be $\propto\sqrt{E}$), and σ_{cal} is the "constant" term (due to alibration errors). The third term is the photostatistical term, which reduces to ormal photostatistics for F=1. The fourth term represents the contribution from reamplifier "series noise" (see below). The term "C" represents (essentially) the otal capacitance at the input, the term "R" represents (essentially) the input ransconductance and any photodetector series resistance. τ is meant to represent the shaping time" of the complete system, and α is a constant (which conveniently llows noise to be calculated even if there is more than one "τ" involved). The fifth erm represents the contribution of preamplifier "parallel noise" and detector leakage urrent. The two noise terms are similar for *p-i-n* or APD, with the exception of the dditional bulk term (M^2FI_B) for APDs.

Preamplifiers

'he signal from solid state photodetectors used with crystals is sufficiently weak that preamplifier is required. Belle, BaBar and CMS run the full spectrum from fully liscrete (Belle), integrated circuit with external JFET (BaBar) to fully integrated CMS). Some of the characteristics of the different designs are listed below in Table 3.

Table 3 Preamp and photodetector combinations

	Belle	BaBar	CMS
Photodetector	Si PD 2 x 2 cm^2	Si PD 2 x 2 cm^2	Si APD 0.25 cm^2
Noise (e^-)	600-700 (μs shaping times)	600-700 (μs shaping times)	3000-5000 (~30 ns shaping times)
Type	Discrete	Discrete + IC	IC
Dynamic Range	17 - 18 bits		

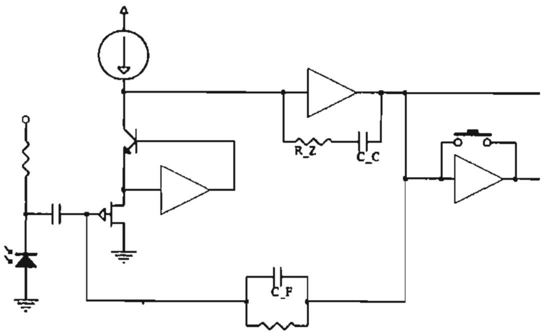

Figure 5 CMS Full Range Preamplifier

For CMS, a preamplifier covering the full dynamic range has been constructed, and is shown schematically in Figure 5. This preamp, designed in 0.8 μ BiCMOS technology, consists of a large PFET input stage, followed by a class A-B output buffer. In addition, a clamping amplifier with gain 8 is also included, for use with a floating-point acquisition system as described below. The preamp outputs are additionally buffered by a bipolar emitter-follower to provide the required drive for a 50 Ω cable. This preamp operates at 5 Volts, and consumes roughly 50 mW.

5. Signal Acquisition

Covering a dynamic range on the order of 17 bits presents a daunting challenge to the electronics design. As a single digitizer with such a dynamic range is usually not practical, the chief obstacle to be overcome is to find a way to compress the dynamic range at the input to that of the ADC. Such approaches are possible in calorimetry because although the dynamic range required is'17-18 bits, the precision required is not. If the detector has a particular energy resolution (generally higher in resolution as the energies increase) the compression scheme must simply be arranged in such a way that the degradation in resolution is small compared to the intrinsic resolution at low energies. This means in particular that the noise contribution must be small, and that the linearity (or calibration stability) of the system must be quite high.

Several schemes are candidates for compression of dynamic range:

- **Non-linear amplifiers**: A preamplifier with a non-linear feedback element (such as a FET), or a linear preamplifier followed by a non-linear amplifier can be arranged to provide large gain for small signals, and lower gain for large signals. Theoretically, if one were able to construct an ideal non-linear amplifier, one could even tune the gain curve so that the quantization error of the ADC would become a fixed fraction of the detector resolution. The principle drawback of this technique is the difficulty of precision knowledge and stability of the gain curve, which often depends on individual transistor parameters, or requires clamping circuitry that performs at high levels of perfection. Further, finite bandwidth (anywhere in, or following the non-linear element) gives rise to non-linear distortion of the signal. Thus, whereas this technique has been successfully used for decades for wide dynamic range, relatively low precision applications, its use at the level of precision required for crystals remains to be demonstrated.

Switched-Capacitor arrays: The popularity of SCA's surged at the time of the SSC. One could arrange parallel banks of SCA's with different gains before each bank, and later on select the appropriate bank to digitize. None of the three new collider crystal calorimeters are considering such an approach.

Floating Point approaches: In this approach, the signal to be captured is acquired with multiple (different) gains, and then the appropriate gain range is used for digitization. The resulting data includes the ADC reading (the mantissa) and a digital code for which gain was used. The voltage at the input is reconstructed by a linear relation $V = g_i \cdot ADC + O_i$ where g_i is the gain for the ith range, and O_i is the offset (these constants are determined in advance, and ideally remain unchanged).

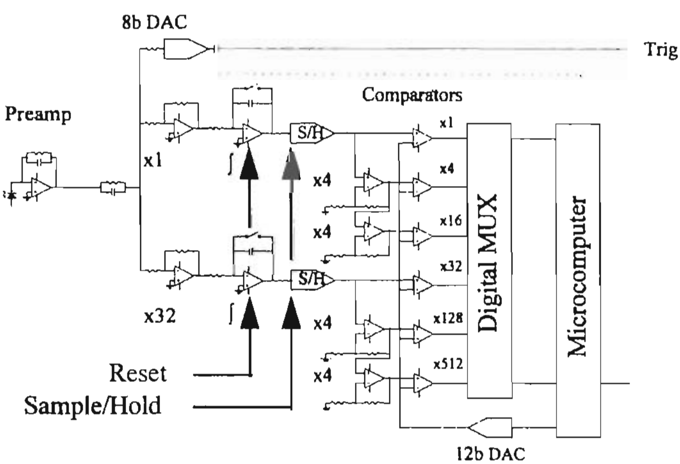

Figure 6: L3 BGO Floating-Point ADC

n early example of floating-point digitization for crystals is the L3 BGO readout hown in Figure 6. The preamplifier output covers the full 18-bit dynamic range (50 V to 10V). The preamplified signal, after shaping, is acquired by two gated ntegrators, one with unity gain and one with a gain of 32. The same preamplified ignal is converted into a calibrated current, which is used to form trigger sums. tarting slightly before the bunch crossing, the integrators become active, and the ample/hold amplifiers sample the integrator outputs. At a fixed time after the bunch crossing, the sample/hold holds the integrator level (thus completing the integration of the signal) and the integrators are reset to zero. If no trigger occurs, this cycle repeats. When a trigger does occur, the microcomputer sets the 12-bit DAC to 7/8 full scale and examines the outputs of the amplifiers after the sample/hold amplifiers. With the two gain-4 amplifiers after each sample/hold, the integral of the input is available with a gain of 1, 4, 16, 32, 128, 512. The microcomputer selects the gain range with the highest gain that is below 7/8 full scale, and proceeds to perform a successive-approximation digitization.

The data format

P	*G*	*G*	*G*	*D*	*D*	*D*	*D*	*D*	*D*	*D*	*D*	*D*	*D*	*D*	*D*

consists of the 12 bits of ADC information (D), a 3-bit code identifying the gain used during digitization (G) and a parity bit (P) for error-checking.

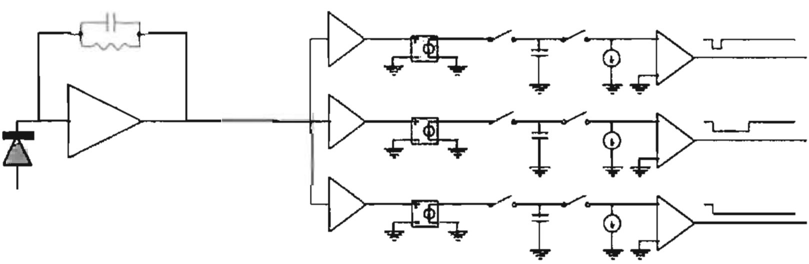

Figure 7 "Wilkinson" floating point for Belle

For Belle, an interesting approach (see Figure 7) is used. The preamplifier signal is acquired by three gated integrators with different gains. The digitization is performed by running down the storage capacitor (i.e. a Wilkinson ADC) and the information is sent as a digital pulse whose duration (as measured by a TDC) is proportional to the pulse height.

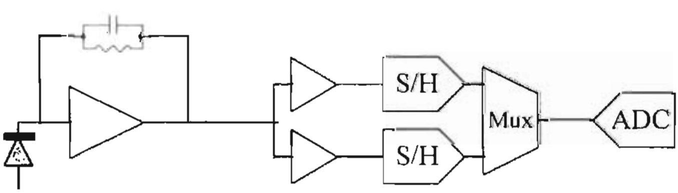

Figure 8 "Multi-slope" floating point for BaBar and CMS

For BaBar and CMS, a more conventional multiple slope approach is envisaged. In this scheme, the preamplifier signal is amplified by separate amplifiers (4 slopes for both BaBar and CMS), and synchronously sampled with Sample/Hold amplifiers. Comparators after the Sample/Holds along with digital logic determine which gain range to use, and an output multiplexer sends this signal to the ADC. For CMS, such a circuit, operating

. 40 MHz, has been constructed in both 0.8 μ BiCMOS and 0.7 μ CHFET :*omplementary* GaAs).

. Conclusions

'he design of each of the new crystal calorimeters for colliders presents specific :chnical problems to be overcome, only a few of which have been outlined above. 'he growth of high-quality reproducible crystals is clearly fundamental to the success f the calorimeter. After that, the key challenge is most often in the readout. Jnmentioned in this survey are the problems associated with radiation hardness, :quired for all three calorimeters (and particularly for CMS) as well as numerous ıechanical issues. In conventional sampling calorimeters, mechanical precision plays major role in the precision, whereas for homogenous crystal calorimeters the ıechanical challenge is more to find a mechanism of supporting the crystals that ıtroduces the minimum of dead material. Despite the challenges faced during the esign and construction of crystal calorimeters, they have always in the past provided ıe excellent resolution and performance that one expects with crystals. For the new alorimeters, although there is much work to be done, we can hope that the use of rystal calorimeters will enable exciting discoveries.

₹eferences

'or further and more up-to-date information, the best sources are the technical ıroposals and accompanying notes from the different experiments easily found on ⱱWW.

ıscati Physics Series Vol. VI, (pp. 99–110)
INT. CONF. ON CALORIMETRY IN HEP – Frascati, June 8–14, 1996

CALORIMETRY FOR ASTROPARTICLE PHYSICS

Guido Barbiellini
Università degli Studi di Trieste
and
Istituto Nazionale di Fisica Nucleare, Sezione di Trieste, Padriciano 99
I–34012 Trieste, Italia

ABSTRACT

The experimental tools to investigate the cosmic rays particles composition are optimized :ording the energy range of the particles under study. In this note are described "Calorimeters", total sorption devices, for charged and neutral particles in the energy interval from few tenths of MeV to the :v range.

After some general consideration on particles detectors for space application, few examples of :ently realized calorimeters for satellites and balloon flights will described, and the recent experimental ;ults, obtained with detectors that include Calorimeters, will be presented.

Conventional Calorimeters and flying Calorimeters

A typical detector for particles physics in the energy range from one GeV to few ındred GeV is usually consisting of three main components;

- the tracking region (devoted to momentum measurement);
- a particle identification section (I.D.) (a velocity or a energy over mass measurement device);
- a total absorption energy measurement device, the "Calorimeter".

The first two componet are as transparent as possible absorbing a very small action of the energy of the particles to be detected. The second task is some time :complished partly in the first and in the third section.

The third component, the total absorption Calorimeter is subdivided in the ectromagnetic and hadronic sector. The electromagnetic component is caracterized by very high Z material to reach a large value of bremstrahalung and pair production ·oss sections for incoming electron, positron or photons.

The hadronic showering material in the second sector is chosen to emphasize adronic cross section and also on the basis of geometrical convenience. The depth of ıe electromagnetic and hadronic calorimeter is given in unit of radiation (X_0) and ıteraction (λ) length respectively. In the energy range considered the typical depths are 25 X_0 and $\geq 20\ \lambda$, in the experiment at accelerating machines in the GeV region.

2 Calorimeter for Space Experiments

The Calorimeters for particles detection in astroparticles experiments carried out on space should follow in principle to the same rules applied to calorimeter of ground based experiments.

The physical laws are universal but .... The space environment and some practical aspects look quite different.

The particles accelerated in the Galaxy by explosions or and by stocastic processes are isotropicaly distributed, their energy spectra have a typical power law ($E_{GeV}^{-\alpha}$) where α varies between 1-3 depending on the particle. The dominant component of the cosmic rays are proton and alpha particles.

Other component like nuclei or electrons and photons (γ) are a small fraction, e/p $\sim 10^{-2}$, γ /p $\sim 10^{-4}$. The presence of antiparticles like positron (e^+) or antiproton ($\bar{p}$) are compatible with secondary production from primary cosmic rays (p) interacting in the interstellar medium (I.S.M.) and also represent a small fraction of cosmic.

The relative abundance of e^+ and $\bar{p}$ to the main components $\sim 10^{-3}$ (e^+/p) and 10^{-4} ($\bar{p}$/p).

As result of the decreasing flux with energy the study of the high energy component of the cosmic rays requires large area detector to reach a reasonable statistic but the unavoidable restriction coming from the limited weigth and power budget on board of satellites impose some compromise between the desired large area calorimeters and the depth.

The calorimeters that will be presented in this talk have a depth limited to 8 X_0. The weigth limitation of the past space experiment did not allow until now the flight with calorimeters having both the electromagnetic and hadronic sector. The solution adopted is the one with high Z material producing with high probability an electromagnetic cascade when the incoming particle is an $e^{\pm}$ or a γ. Consequently the hadronic particles interact in the calorimeter as minimum ionizing particle (MIP) or eventually initiate the beginning of a hadronic cascade.

Other requirements for the calorimeter in space experiments are:

1) Mechanical resistence to strong acceleration (some ground tests are done until 50 g $\cong$ 500 m/s^{-2}).
2) Long duration (5-7 years).
3) High gain stability of the sensor and self calibration with the most frequent MIP (no interacting protons).

) It is a good precaution to avoid consumable material like circulating gas or cryogenic components.

The weight limitation and the requirement of a large surface acceptance implies a :duced containement of the showers initiated by energetic (E > 10 GeV) electrons or $^{+}$ or γ.

The fluctuations in the deposited energy due to the fluctuations in the beginning f the showers deteriorate the energy resolution.

A calorimeter with 8 X_0 has an energy resolution dominated by fluctuations of the nergy leaking of ~6% at 5 GeV. So even the high resolution of the omogeneous crystal alorimeters can be fully esploited only at low energy. The high energy component of ıe particles spectrum can be measured by a sampling calorimeter with a sampling step s course as 1 X_0.

If the calorimeter is part of a more complete detector with momentum ıeasurement (magnetic field B) and particle identification, the incomplete energy ontainement partly spoils one of the important criteria for $e^{\pm}$ identification the energy E) and momentum (p) equal value: E/p = 1 where E is the energy deposited in the lectromagnetic calorimeter and p is the momentum measured in the tracking system ıside the magnetic field B.

To compensate this lost of $e^{\pm}$ identification the space el. m. calorimeter are built /ith high granularity and fine longitudinal segmentation.

Calorimeters with high granularity and longitudinal segmentation are also called maging calorimeters. An elegant realization of an imaging calorimeter will be .escribed in detail at this Conference by M. Ricci as representative of the WIZARD Collaboration.

Some general features and few experimental results obtained with the 7 X_0 maging calorimeter of silicon detectors and Tungsten absorber used in the CAPRICE light will be mentioned also in this note.

3 The CAPRICE Mission

The CAPRICE balloon flight is part of the general program CAPRICE flight on .ntimatter search in cosmic rays carried out by the WIZARD Collaboration. The ıalloon launch has been done the August 8, 1994 from a North based area (Lynn Lake Manitoba Canada) in order to obtain a low energy geomagnetic cut-off. The NMSU-WIZARD/ CAPRICE (1) spectrometer is shown in Fig. 1 and from top to bottom it ncludes a Ring Imaging Cerenkov Counter (RICH) a time of flight (TOF) i.e. two sets ıf scintillator conunters with photomultiplier read out separated by ~1 m.

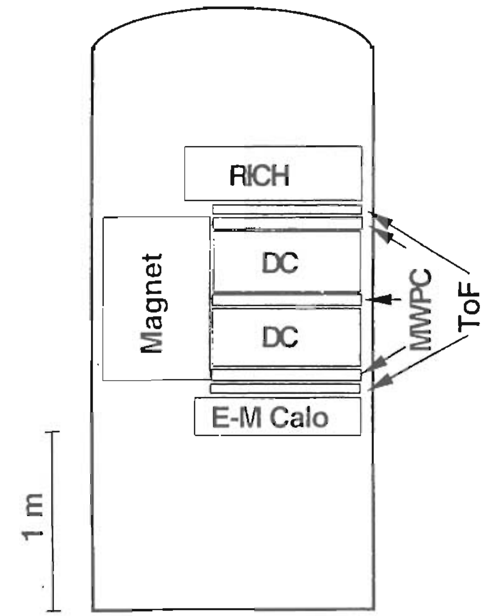

Fig. 1 - Schematic diagram of the CAPRICE apparatus.

The magnetic spectrometer comprese multiwire proportional chambers (MWPC) and drift chambers in a magnetic field produced by a superconducting coil.

At the end of the detector (for particles arriving from the top) there is a 7 X_0 Si W absorbing Calorimeter.

The electromagnetic Calorimeter is composed of eight planes with dimension 50x50 cm^2 of Silicon deterctors with strip read out in to two ortogonal directions (x,y read out). Each plane is formed connecting 8x8 X tiles and an equal number of y tiles. The single tile is composed of two one X one y 6x6 cm^2 wafer mounted on support inspered to microchips technology (Fig. 2).

The tiles interconnection is done by a G10 printed circuit planes.

The Calorimeter energy resolution as measured on a single column of 6x6 cm^2 tiles in a test beam is ~17% $/\sqrt{E(GeV)}$ until 2 GeV and stay almost constant reaching $20\%/\sqrt{E(GeV)}$ at the maximum energy measured in the flight E_{max} ~50 GeV.

The imaging calorimeter has a powerfull separation of electromagnetic versus hadronic shower based on the narrow and regular energy deposition inside 4 Molière radius around the track measured by the tracking system.

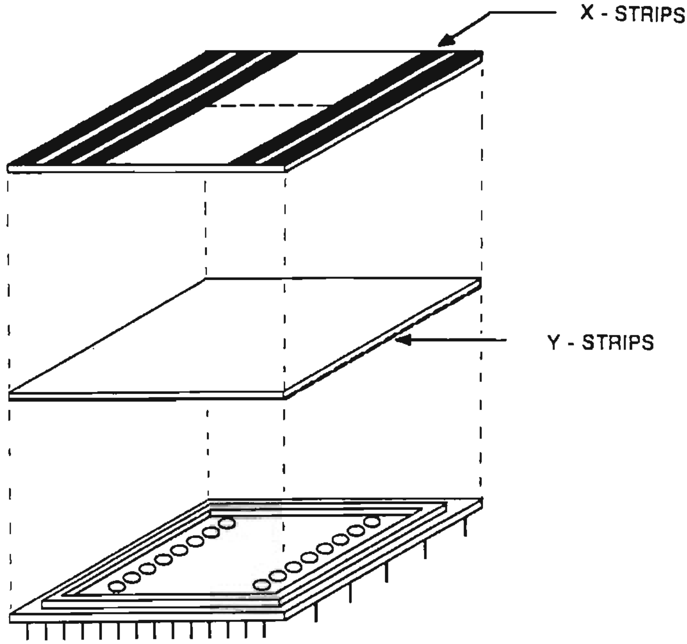

Fig. 2 - Exploded view of the lay-out of the packaging of two detectors with perpendicular strips.

Additional cuts based on the match of the measured momentum to the deposited energy and on the longitudinal shower development being an overall reduction of 10^3 of the proton leaving an efficiency for electron and positron $\varepsilon_{e\pm} \sim .8$.

The displays of a positron crossing the CAPRICE detector are shown in Fig. 3.a. Fig. 3.b gives an expanded view of the Calorimeter response to a positron.

The imaging SW calorimeter is able to measure the electron direction by connecting the x,y center of granty of the energy deposition. A comparison of the Calorimeter measured direction with that measured by the tracking system shows an angular resolution $\Delta\vartheta$ at 4 GeV of 2^0 and the expected energy dependence of $\Delta\vartheta$ is $\Delta\vartheta \sim \Delta\vartheta(1)/\sqrt{E(GeV)}$.

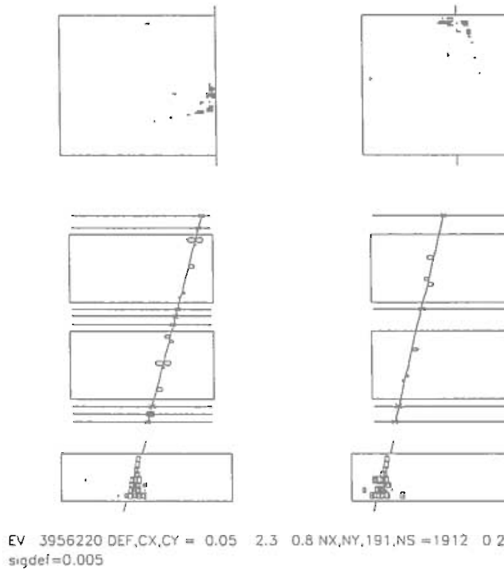
EV 3956220 DEF,CX,CY = 0.05 2.3 0.8 NX,NY,191,NS =1912 0 2
sigdef=0.005

Fig. 3.a

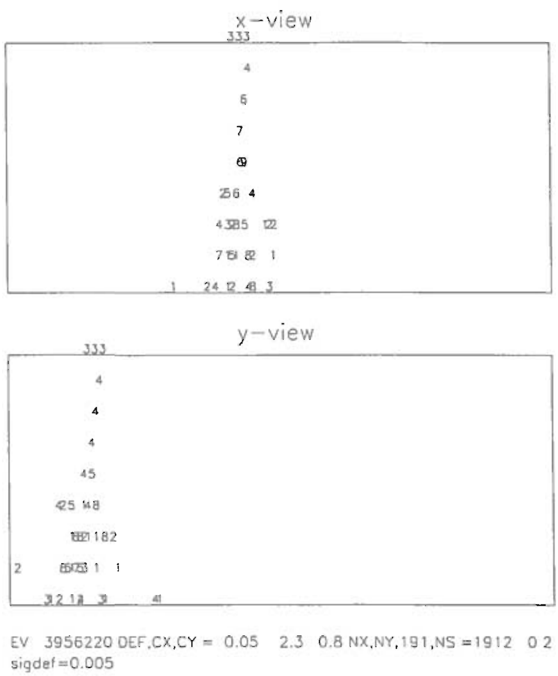
x–view
y–view
EV 3956220 DEF,CX,CY = 0.05 2.3 0.8 NX,NY,191,NS =1912 0 2
sigdef=0.005

Fig. 3.b

Calorimeters for gamma ray Telescope

The principle of the γ-rays direction measurement for hard γ is illustrated in Fig. 4 hat is a schematic diagram of the very successfull detector EGRET now flying on the C.G.R.O. (Compton, Gamma, Ray Observatory).

The detection of the e^-e^+ angle is obtained in the spark chamber and the energy is neasured by a total absorption shower counter (TASC) realized with 8 radiation lenghts of NaI.

The C.G.R.O. has been very successfull in astrophysic results and the high energy 20 MeV< Eg <20 GeV) detector has discovered many new point like sources in our Galaxy and extragalactic emitting very energetic photons.

The EGRET detector can operate for near two more years before the end of the park chamber gas.

New projects have been already prepared to mantain the new observational capability in high energy gamma astronomy.

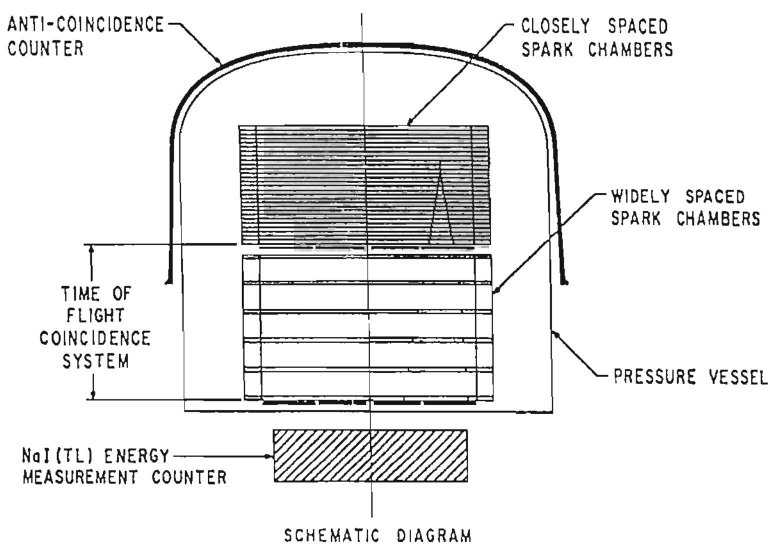

Fig. 4 - EGRET DETECTOR

5 Future detectors for γ-rays astronomy

The very successfull data-taking of the EGRET detector will last no more than two or three years from now, the main reason being the total consumption of the gas for the spark chamber.

Due to variability of the γ emission of different sources and the possibility of improving the already good features of EGRET, new project are in progress for the future of hard γ-rays astronomy.

In the following are described two of such projects.

The first one named GILDA and the second GLAST.

GILDA is a part of a Russian Italian collaboration included in the larger program of the RIM (Russian Italian Mission) project. wich cosist of three successive steps.

The first one already funded and named NINA is a silicon detectors telescope to study solar activity in the emission of medium energy proton and ions. NINA flight is scheduled for the end of 1996.

The second step of RIM, PAMELA is a search for the antimatter component in the cosmic ray flux.

The third step GILDA is a large acceptance γ-ray telescope .

5.1 The GILDA apparatus

The core of the GILDA telescope is a modified space version of the silicon calorimeter presently used in the Wizard balloon flights program, to be installed on a future version of the Resource-01 satellite, scheduled to fly at the beginning of the next millennium. This detector is a fine-grained imaging electromagnetic calorimeter conceived for the Wizard experiment to investigate, in a planned space mission, the antimatter component of the primary cosmic radiation .

Detectors based on the silicon technology have many advantages for space applications: no gas refilling system or high voltages, no need of photomultipliers (low consumption), short dead time, possibility of self triggering. During the project phase, the calorimeter has been extensively studied with Monte Carlo simulations, and a prototype, containing 20 XY samplings of silicon wafers with strips 3.6 mm wide interleaved with 19 showering tungsten planes (for a total of 9.5 X_0), has already been built and tested at the CERN Proton Synchrotron (PS). The five planes (50 x 50 cm^2) have flown in a balloon experiment from the NASA base at Fort Sumner (New Mexico) in September 1993; the Si-W calorimeter with 8 planes has also successfully operated in the flight from Lynn Lake (Canada), of July 1994.

The basic element of the GILDA telescope is a 6 x 6 cm^2 module composed by vo Si detectors, each with a thickness of 380 μm, mounted back to back with erpendicular strips to give the X and Y coordinates (Fig. 2). In this experiment, two ifferent strips widths are considered. For the 3.6 mm strips, each module contains 16 rips, while for the 125 μm ones it is possible to arrange 500 strips in each wafer. The etectors are held in a special package which, when patched to form large surfaces, llows a minimal dead area for the sampling planes of the calorimeter. All the used naterials are approved by NASA for space applications. The principal constraints are nposed by the satellite in terms of volume, weight and available electric power. The ree volume on the satellite is a cylinder 110 cm diameter and 70 cm in height, the vailable mass and electric power are respectively 700 kg and 350 W.

The baseline configuration of GILDA has a height of 40.8 cm, an area of 50 x 50 m^2 and a total showering length of 10 X_0 (radiation lengths). A suitable arrangement f the electronics coupled to the calorimeter and of the anticoincidence system allows to natch the 110 cm diameter of the available cylindrical volume. In the volume under the letector, the remaining digital electronics, interfaces and services can be located.

The stratigraphy of the instrument is shown in Fig. 5. The γ detector can be eparated into two sections: the converter (or tracker) and the absorber. The first twenty lanes form the converter zone, in which the silicon layers, made of 125 μm strips, are eparated by tungsten plates of thickness 0.07 X_0. The distance between two contiguous lanes is 1.0 cm. In each plane, 4000 silicon strips per view allow a very precise neasurement of the direction of the incoming gamma ray. The granularity of the silicon nd the thickness of the tungsten have been decided by detailed Monte Carlo studies nd hardware developments and they represent the compromise between number of ecessary electronic channels, distance between planes, power consumption (1.5 nW/ch), efficiency and angular resolution.

The last ten planes E_1...E_{10} constituting the absorber, are composed of 3.6 mm silicon strips and separated by layers of active scintillating lead fibers, 1 X_0 total hickness. Between the converter and the absorber, an aluminum plate of 0.2 X_0 is placed in order to reduce the back scattering of particles from the bottom of the calorimeter. Each silicon plane is 1.6 cm far from the following.

The structure of the scintillating fibers lead calorimeter has been built embedding polystyrene fibers (emitting in the blue), 1 mm of diameter, between plastic deformations of lead foils 0.5 mm thick. Fibers are glued to the foils and run parallel to each other with a pitch of 1.35 mm. The overall structure has a fiber:lead:glue volume ratio of 48:42:10 and a sampling fraction of ~14% for a minimum ionizing particle;

moreover, it has a density of ~5 g cm^{-3} and a X_0 of ~ 1.5 cm. This means that, in one radiation length, ten lead foils are interleaved with the same number of fibers.

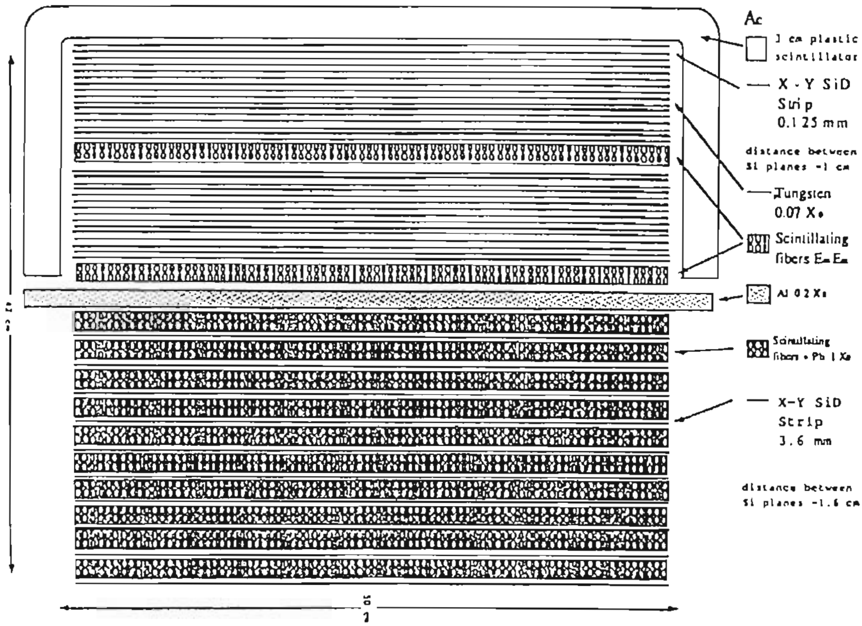

Fig. 5 - The GILDA configuration.

Prototypes have already been extensively tested with accelerator beams, showing that the lead scintillating fibers calorimeter has an energy resolution for γ of the order of $5\%/\sqrt{E(GeV)}$ for total containment. The solution of adopting these fibers is particularly attractive because HPK has developed compact PM's (PMT R5600 series) reduced to the same dimensions as a solid state detector and housed in a robust metal package 15 mm in diameter and 10 mm in length, while maintaining the same performances, high sensitivity and high; peed as a conventional PM. The very low mass and the power consumption of the PMT R5600 (~100 mW) allow the use of the large number of PM needed for a fast trigger.

The configuration is completed with a plastic anticoincidence scintillator A_c (3 cm thick) around the converter zone of the calorimeter, and with two fibers scintillators (without the lead), one, E_{01}, after the first seven planes (that is after 0.49 X_0) and the other, E_{02}, after fourteen planes from the top of the detector. The introduction of the first one allows to obtain a threshold for gamma ray detection of 25 MeV.

.2. The GLAST Detector

The GLAST (Gamma ray Large Area Silicon Telescope) R & D program's goal is) produce a proposal for the next instrument in this series. GLAST was started a year go in response to a NASA request for R & D proposals. The Stanford side of the Egret ollaboration had strong ties to close-by SLAC where interest in Astro-Physics already xisted. Particle detection technology has progressed a long way from triggered spark hambers, and the silicon strip detector technology might be a good solution to the :gret problem. A proposal was submitted and subsequently funded by NASA for one 'ear in which a more detailed design study could be accomplished.

The adopted principle design that GLAST technology has followed is an ιdaptation of existing HEP detectors. Silicon strip detectors would provide tracking vith a modern crystal calorimeter (read out using silicon diodes) to provide the energy neasurement. The maximum size of presently available silicon detectors is only 6 cm x) cm, but by ganging together three (possibly four) such "tiles," the channel count may)e kept to a reasonable level. A large device is easier to build if it can be made modular, ınd we opted to arrange GLAST as a mosaic of semi-autonomous tower modules. The 'est of the design concept followed logically from Egret and is shown in Fig. 6.

The proposed GLAST calorimeter is an array of Csl crystals for a total depth of ~10 X_0.

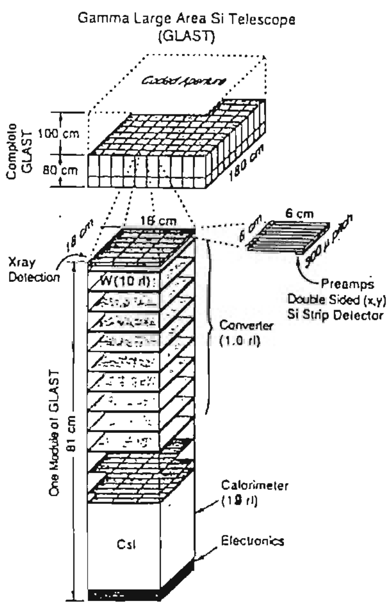

Fig. 6 - The GLAST configuration.

Recently in the GLAST collaboration the use of an imaging calorimeter with Scintillating fibres and Lead based on the technology developed by the KLOE collaboration. The main reason for this proposal being the measurement of the direction of high energy γ not converted in the tracking region (60% of the total γ flux). The quality of this calorimeter are presented at this conference by A. Morselli.

6 Conclusion

High energy astroparticle is introducing more and more sophysticated technique developed in experiment at accelerating machine. The quality of the new data from many new mission and for from the WIZARD Collaboration CAPRICE flight where two innovative detectors like the Ring Imaging Cerenkov (RICH) detector and a Si W imaging Calorimeter have complemented the existing spectrometer, indicate that this introduction of particles physic experimental tools in the astrophysic domain is giving the good results. GLAST or GILDA contain many concept from high energy particle experiment and I hope in their future success.

7 References

(1) G. Barbiellini et al.: Astronomy and Astrophysics 23.3.96.

II – Non Conventional Calorimeters

Convener B. Aubert
Secretary L. Benussi

Aubert	Convener's Report
. Ricci	The Wizard Program on Calorimeters for Space Applications
. H. Mielke	A Calorimeter for Cosmic Ray Hadrons up to 10 TeV
P. Denisov	Energy Loss Measurements of Cosmic Ray Muons in the LAr Calorimeter BARS
. Gemmeke	Upgrade of Karmen Neutrino–Calorimeter
. Giuliani	Phonon Mediated Particle Detection: Results and Prospects
Pietropaolo	The Liquid Argon TPC for the ICARUS Experiment
P. Denisov	Use of Heavy Freons in Gas Ionization Calorimetry

scati Physics Series Vol. VI, (pp. 113–114)
INT. CONF. ON CALORIMETRY IN HEP – Frascati, June 8–14, 1996

(Convener's Report)

NON CONVENTIONAL CALORIMETERS

Bernard Aubert
LAPP–CNRS/IN2P3–Annecy le Vieux

When you did ask Yourself "What is a non conventional calorimeter?", it is ry instructive to compare the scientific program of this meeting with the evolution calorimeter's technology: Non Conventional yesterday is today Conventional. Let review briefly some recent idea in different field.

- Sampling Calorimetry

1. with liquid detecting medium:
   The use of Liquid Argon proposed by W.J.Willis in the early sixties has been followed by several other cryogenics liquid proposal like the use of liquid Krypton, and the proposition to use room temperature liquid, like tetramethylsilane or tetrametylpentane. The most recent idea is a change of the classical set up. The electrodes, instead to be flat and perpendicular to the particle path, becomes accordeon shaped following the particle axis. This improvement provide a faster response and a better hermeticity for the charge collection.

2. with solid detecting medium:
   The most common technology, plastic scintillator, have been greatly improved by the use of scintillating fiber. Here the fiber could be used or like detecting material or like optical component with the use of wave lenght shifter. As for the Liquid Argon calorimeter, new geometry with detecting plate parallel to the particle direction, are now under construction.

- Homogeneous Calorimeter

  The lead glass technology has open up a field where crystal calorimeters experts develop high precision detectors using large volume of crystal material. The innovation be here on the search of low cost component. Recently the BGO has been followed by $PbWO_4$, and room remain for futur development.

All those new contributions to calorimetry, non conventional little time ago, are now include in other sessions. Where could be innovation and creativity? We can identify three domaine partly covered in our session or completely missing:

1. The non conventional application of conventional technics. We will get presentations of calorimeters used in space research, in cosmic ray physics, in double beta decay experiment.
2. The gas-discharge technology. Large improvements are needed in order to be able to build a competitive detector with gas calorimeter.
3. The integration of large system. Building smaller and smaller size detecting cell, to improve the spatial resolution, and read out a calorimeter without loss of detection power is a challenge for the actual experiment.

In conclusion, we will listen the presentations, but bear in mind that regarding non conventional, the "no show" is almost as instructive as the show.

I would like to thank Alessandro Calcaterra for his very valuable help before and during the conference, as well as the conference organizers for a very effective meeting.

THE WIZARD PROGRAM ON CALORIMETERS FOR SPACE APPLICATIONS

M. Ricci
INFN - Laboratori Nazionali di Frascati, P.O. Box 13, I–00044 Frascati (Roma) Italy

Written contribution not received

scati Physics Series Vol. VI, (pp. 117–124)
INT. CONF. ON CALORIMETRY IN HEP – Frascati, June 8–14, 1996

CALORIMETER FOR COSMIC RAY HADRONS UP TO 10 TEV

H.H. Mielke, M. Locher, H. Kornmayer, J. Engler, and J. Knapp
Forschungszentrum und Universität Karlsruhe, P.O. Box 3640, D 76021 Karlsruhe

ABSTRACT

ι iron calorimeter for cosmic ray hadrons to be used in the large air shower ex- ɾiment KASCADE is described. The iron absorber is interspersed with ionization ambers filled with the room temperature liquid tetramethylsilane. Experiences th a prototype of the calorimeter, its performance and long-term stability are esented. For energies in the TeV region shower profiles and transition curves have en measured and are compared with Monte Carlo (MC) calculations using the ,UKA and GHEISHA option within the GEANT code.

Introduction

ithin the extensive air shower experiment, KASCADE [1] at Karlsruhe, the central re of hadrons is investigated using a totally absorbing sampling calorimeter. The n of the experiment is to determine the mass composition of primary cosmic ys in the energy domain of 10^{14} to 10^{16} eV and to measure reliably the cosmic y energy spectrum. The hadron content of an air shower at sea level decisively pends on the mass of the primary particle. Roughly speaking, iron nuclei initiate scades with less hadrons and hadronic energy at sea level than primary protons of e same total energy. Cascades initiated by high-energy photons should contain no dronic energy at all. A hadron calorimeter, therefore, is well suited to distinguish ɾ showers initiated by different primaries.

Such a calorimeter should be able to detect hadrons of 10 TeV and more. ɪr a good energy reconstruction it should be deeper than 10 nuclear interaction ngths λ_I. In order to distinguish individual hadrons within the core and to deter- ine their energy separately, a relatively fine lateral segmentation is desirable. For instance, it is of interest to know the energy of the most energetic hadron, since it is a parameter closely related to the primary's mass. A major challenge of cosmic rays at the highest energies is their small particle flux requiring large detector surfaces. To accumulate 100 particles per annum at 10 PeV, a calorimeter surface of 300 m^2 is needed. This is the size of the KASCADE calorimeter with 8 active layers leading to a total of 2400 m^2 detector area.

A prototype of this calorimeter having an identical longitudinal configuration but 5% of its lateral size only and the original instrumentation has been set up and has collected data for nearly three years [2)]. It is the intention of this article to report about the experience gained with this prototype, especially with the new type of liquid ionization chambers chosen as active elements. They use the liquid tetramethylsilane (TMS) as dielectric medium. It is also of interest how well existing shower simulation codes such as GHEISHA [3)] and FLUKA [4)] describe hadronic cascades in the TeV region. We cannot test the absolute amount of energy deposition due to the lack of calibration possibilities at accelerators, but we can compare the longitudinal and lateral profiles of the energy deposition with predictions of the MC codes and thereby examine their reliability.

2 Calorimeter Configuration

A setup of the prototype calorimeter is shown in fig. 1. It is constructed from casted Fe slabs, 12 cm thick, leaving eight slots for active elements. Seven slots are filled with liquid ionization chambers, whereas scintillation counters for fast trigger purposes are inserted into the space behind the second iron layer where hadron showers of 100 GeV have their maximum of energy deposition. On top of the calorimeter a plane of scintillators serves to measure the particles' dE/dx and separate charged from neutral hadrons. Its longitudinal structure is almost the same as for the KASCADE calorimeter only the last layer - a tail catcher of 2.5 λ_I concrete - is missing. The total depth of the prototype calorimeter corresponds to 9 interaction lengths, ensuring a reasonable shower containment up to 10 TeV hadrons. At this energy approximately 96% of the energy are deposited in the calorimeter. As can be seen from fig. 1, sampling is constant at the top and becomes coarser in deeper layers where the mean transition curve drops exponentially. For cosmic ray hadrons a very good energy resolution is not mandatory at the highest energies. We, therefore, deliberately renounce on the $1/\sqrt{E}$ improvement with rising energy in case of a calorimeter with constant sampling steps. Yet, the energy resolution is a critical parameter when dealing with a flux spectrum that is steeply falling with energy. Due to a limited resolution, the incident energy is systematically reconstructed too high. To keep the correction for this shift small, a reasonably good resolution is desirable.

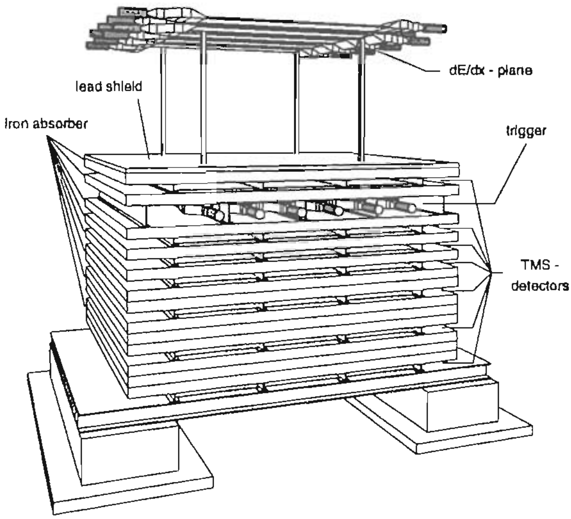

Figure 1: Schematic view of the KASCADE prototype calorimeter

cording to MC calculations, the calorimeter has a resolution of $\sigma(E)/E = 20\%$ at GeV which improves to 10% at 10 TeV. The systematic bias of the reconstructed ergy has been calculated to amount to 20% in the TeV region.

The trigger plane of the prototype calorimeter consists of eight scintillators) × 220 cm) viewed by photomultipliers from both ends. The thresholds are justed to ensure a coincidence between the two ends of the scintillator with an iciency of almost 100% for a passing muon. The trigger threshold for hadrons set to 30 particles. The trigger layer is located behind a material corresponding 1.6 interaction lengths. This position has been chosen as a compromise between good efficiency at high energies and a threshold that is as low as possible. The igger efficiency reaches 80% for 120 GeV hadrons.

Liquid Ionization Chambers

he structure of the ionization chamber is sketched in fig. 2. It consists of a) × 50 × 1 cm^3 steel box containing four electrodes (25 × 25 cm^2) positioned in ie midplane of the box by ceramic spacers. A ceramic feedthrough allows to apply gh voltage to the electrodes and read out their signals independently, ensuring fine spatial segmentation of the calorimeter. As liquid TMS has been chosen. everal high-mobility liquids suitable for particle detection in calorimeters exist [5]. hese liquids show electron conduction, i.e. free electrons from ionization processes

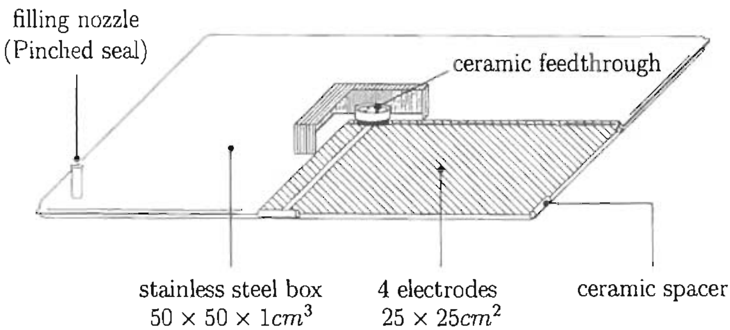

Figure 2: Schematic view of a TMS ionization chamber.

move under the influence of the electric field in a conduction band similar to those in semiconductors. For the present purpose a high signal yield and low costs for the 17000 l liquid were the decisive criteria whereas a fast signal generation, hence, a high drift velocity was of minor importance. Tetramethylpentane (TMP) is too expensive for such a large calorimeter, but hexamethyldisilane (HMDS) despite of its lower charge yield would have been an alternative solution [6] due to its low price. TMS recommends itself by its easy process of purification. The costs of a chamber being mainly determined by the price for the liquid, the thickness was chosen as a compromise between affordable costs and a reasonable signal/noise ratio for minimum ionizing particles. A ratio of 2/1 was taken to be sufficient to recognize the pattern of a muon passing through the eight active layers of the Fe absorber.

An important quantity which determines the operational capability of an ionization chamber is the lifetime τ of free electrons in the liquid. It should be much greater than the electrons' drift time in order to collect the total charge produced. The lifetime is limited by the presence of electron-attaching impurities. For the most frequent impurity, oxygen, a concentration of 1 ppm in molar units limits already the lifetime to approximately $\tau = 1\mu s$. Therefore, all parts of the chamber and the liquid have to be cleaned carefully before assembly.

4 Signal Stability

One of the principal motivations to use liquid ionization chambers for a ten-year cosmic ray experiment is their long-term stability. The electronic feed-back amplifier chain fulfills this requirement. For the actual chamber signal, however, this remains to be proven. Individual chambers, therefore, have been tested repeatedly in a triton beam at the Karlsruhe cyclotron [7] and with cosmic ray muons [8], where the signal of penetrating particles has been monitored. No signal decrease has been observed.

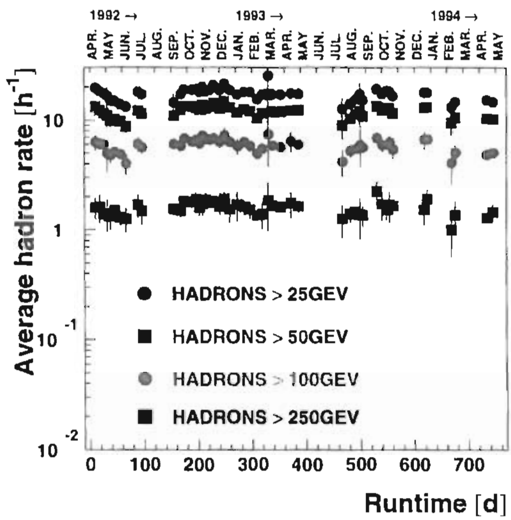

;ure 3: Average hadron rate in the calorimeter. The different symbols represent : indicated threshold energies.

ı the contrary, a slight improvement can be noticed in some of the chambers as has ən reported amongst others by the WALIC collaboration [9]. This signal increase ı be attributed to adhesion of rest impurities present in the liquid onto the metal rfaces, which - if extremely clean - have a very polar character.

The behavior under constant electric field strength has been studied with ə prototype calorimeter and is documented in fig. 3. It shows the average rate · hadrons with an energy above the indicated threshold. As the flux of cosmic ray drons and the energy spectrum are known to be stable with time, the constant te immediately reflects the signal stability of the chambers. So we can conclude at neither impurity molecules diffuse from the bulk of the chamber material into e liquid nor the liquid associates or dissociates under electrical stress. A very ıble and reliable performance of the calorimeter for many years can be anticipated, quiring only occasional calibrations of the amplifier chain by charge injection.

Results

order to gain confidence in the simulation codes we compare the longitudinal and teral distributions of energy deposition of showers with the same reconstructed ergy.

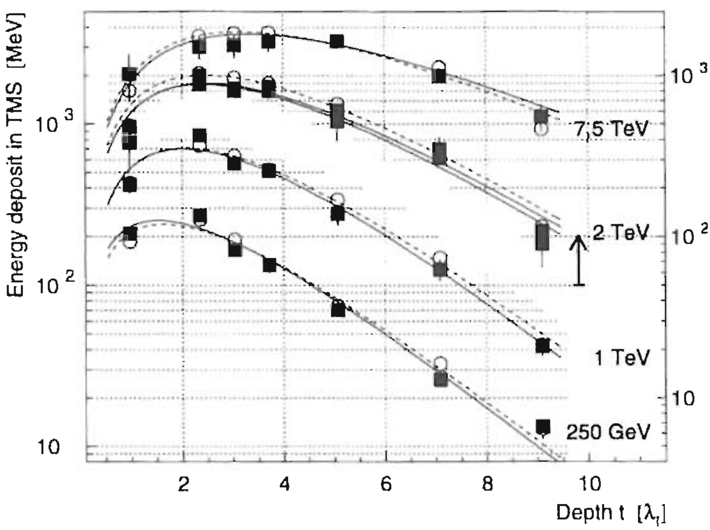

Figure 4: Measured (full squares) and simulated (open dots) transition curves for different reconstructed energies. The curves are fits of the form $dE/dt \propto t^a e^{-bt}$ to the data points. (Read the lower two curves at the left and the upper two at the right scale.)

5.1 Transition curves

The longitudinal development is shown in fig. 4. From 250 GeV to 7.5 TeV the simulations with the FLUKA code reproduce the experimental data quite well. The flattening in the experimental data due to electronics limitations are well reproduced by the MC calculations. The largest discrepancy between data and simulation occurs in the first layer at 2 TeV and 7.5 TeV. It is due to the fact that very high energy hadrons are likely to be accompanied by low energy electromagnetic radiation being created somewhere in the air above the detector, an effect which is not taken into account in the simulations. Simulations with the GHEISHA code are not shown but reproduce experimental results with a comparable precision as FLUKA.

5.2 Lateral Energy Deposition

A comparison of the lateral energy distribution between data and FLUKA simulation is done in fig. 5. It shows the energy density as an example in the third layer. As function of the radius it exhibits an exponential shape with a change in the slope at 30 cm. The observations show that the width of the lateral distributions does not vary significantly with energy. The experimental findings are well reproduced

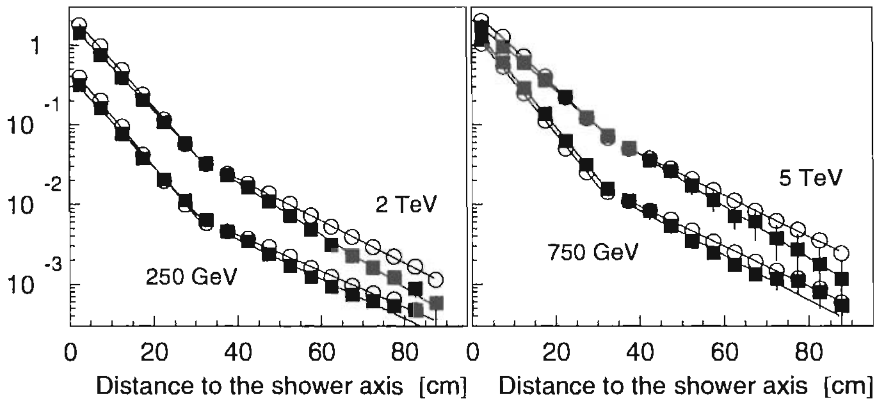

ure 5: The lateral shower development in the third layer for different energies. : energy density versus distance to the shower axis. Experimental results are ɜn as full squares and simulations as open dots. The lines represent fits with two ıbined exponential distributions.

the simulations that are represented by the open symbols. Near to the shower ; one recognizes for the 5 TeV showers the effect of electronics saturation and of ɔnstruction on the form of the distributions. The kink in the exponential fall- can be noticed in the simulations as well. It indicates the existence of a halo ɿponent emerging to larger core distances. Low energy neutrons and photons ıetrate the absorber of the calorimeter better than charged particles due to their · interaction cross-section and are, thus, good candidates for the origin of the o. TMS with its large fraction of hydrogen is sensitive to neutrons and detects ciently their recoil protons. MC studies showed that indeed neutrons and photons ninate the energy deposit at large radii. The calculations, however, seem to :restimate the halo component. The exponential slope in the halo region is higher ın in the simulations by about 30%. This is a small effect not influencing the ɜrgy determination. However, being observed in all the layers and at all energies ɹffects the capability to separate individual hadrons in dense jets of particles or cosmic ray shower cores. Again GHEISHA and FLUKA give comparable results.

Conclusions

ɹrm liquid calorimetry with TMS detectors has proven to be feasible for large tector systems. The prototype of the large hadron calorimeter for the KASCADE periment has exhibited stable performance during three years of operation and registered hadrons up to 10 TeV. FLUKA and GHEISHA simulations describe the experimental findings in this energy range equally well. First results on the cosmic ray energy spectrum and the p-air inelastic cross section at high energies [10] could be obtained. The large hadron calorimeter with 300 m^2 surface has started operation and will deliver a large amount of data within the next years. With high statistics more precise measurements can be done allowing to investigate the performance of the calorimeter and the simulation programs at even higher energies.

7 Acknowledgment

It is a pleasure to acknowledge the enthusiastic assistance of many colleagues who helped to make the prototype calorimeter work successfully, in particular H. Keim, P. Ziegler, B. Peter, M. Föller, and M. Riegel.

References

1. P. Doll et al., (KASCADE Collaboration), The Karlsruhe Cosmic Ray Project KASCADE, KfK-Report **4686**, Kernforschungszentrum Karlsruhe (1990)
2. H.H. Mielke et al., Nucl. Instr. and Meth. **A360** (1995) 367
3. H. Fesefeldt, The Simulation of Hadronic Showers - Physics and Application -, Report **PITHA 85/02**, RWTH Aachen (1985)
4. P.A. Aarmio et al., FLUKA User's Guide, Technical Report, **TIPS-RP-190**, CERN (1987 & 1990)
FLUKA: Hadronic benchmarks and applications, Proc. MC 93 Int. Conf. on Monte-Carlo Simulation in High Energy and Nuclear Physics, Tallahassee, Florida (1993)
5. J. Engler, J. Phys. G.: Nucl. Phys. **22** (1996) 1
6. J. Engler, J. Knapp and G. Vater, Nucl. Instr. and Meth. **A327** (1993) 102
7. J. Engler et al., Nucl. Instr. and Meth. **A311** (1992) 479 and **A327** (1993) 128
8. J. Hörandel, Kalibration von TMS-Ionisationskammern mit Myonen der Höhenstrahlung und Messung des Myonflusses, KfK-Report **5320**, Kernforschungszentrum Karlsruhe (1994)
9. B. Aubert et al., Nucl. Instr. and Meth. **A316** (1992) 165
10. H.H. Mielke et al., J. Phys. G: Nucl. Part. Phys. **20** (1994) 637

ıscati Physics Series Vol. VI, (pp. 125–132)
INT. CONF. ON CALORIMETRY IN HEP – Frascati, June 8–14, 1996

ENERGY LOSS MEASUREMENTS OF COSMIC RAY MUONS IN THE LAr CALORIMETER BARS

S. V. Belikov, S. N. Gurzhiev, Yu. E. Gutnikov, A. G. Denisov, S. P. Denisov, A. Yu. Dushkin, A.V. Ekimov, V. I. Kochetkov, V. Lipaev, S. V. Los, E. A. Melnikov, V. S. Mikhailov, I. V. Shein, A. P. Soldatov, A. N. Sytin
Institute for High Energy Physics, Protvino, Russia
G. Gennaro, F. Sergiampieri, G. Spandre
INFN – Sezione di Pisa, Italy
M. Lanfranchi, A. Marchionni
INFN – Sezione di Firenze, Italy
G. Conforto, F. Martelli
INFN – Sezione di Firenze and University of Urbino, Italy
T. M. Kirina, R. P. Kokoulin, A. A. Petrukhin, M. A. Reznikov
Moscow Engineering Physics Institute, Moscow, Russia

ABSTRACT

Big liquid ARgon Spectrometer BARS was used to detect horizontal cosmic ray ɹons. The large thickness and fine granularity of BARS make it possible to measure ɹon energy losses due to ionization, bremsstrahlung and e^+e^- production with high ecision. The estimation of muon energy by the energy loss measurements is discussed. eliminary results of experimental data analysis are presented.

Introduction

Investigation of energy distribution of horizontal cosmic ray muons in multi-TeV gion can provide an important information on primary cosmic ray spectrum and ımposition. Conventional methods of muon energy measurements (magnetized steel ıectrometers, TRD's) have a practical limit of 5-10 TeV. Another technique of HE uon spectrometry which is free of limitations of the above mentioned methods was ·oposed by Alekseev and Zatsepin in 1959[1].

The idea of this technique is rather simple. In the TeV energy range the average uon energy loss is determined mainly by e^+e^- production and bremsstrahlung and is ·oportional to E (fig.1). But the losses due to e^+e^- and γ emissions are different: ⁄erage energy transferred to e^+e^- is about 1% of muon energy while the average energy ˜ γ is much higher (fig.2). So when passing through a thick layer of matter a high ıergy (> 1 TeV) muon produces a set of EM showers mainly due to e^+e^- production ig.3) and it is possible to estimate the muon energy by counting of the number of ıowers and by measurement of their energies. Because of the important role of e^+e^- ᵣoduction this method is often called the pair meter technique.

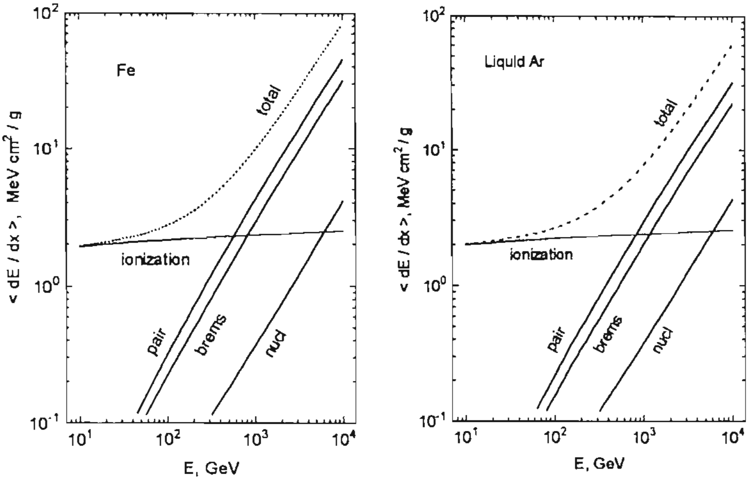

Figure 1. The average energy loss of muons in iron and liquid argon as a function of energy.

Theoretical consideration of the pair meter technique and a review of early works can be found in refs[2,3]. The most important advantage of this technique is the absence of upper limit on muon energy measurements. Asymptotically, the pair meter energy resolution is given by the formula

$$\frac{\sigma}{E} = \sqrt{\frac{9\pi}{28\alpha T}} \approx \sqrt{\frac{1}{\alpha T}}, \tag{1}$$

where T is the pair meter thickness in r.l. and $\alpha = 1/137$ is the fine structure constant. From (1) it follows that the spectrometer should be thick (T > 137 r.l.). On the other hand it should have a fine granularity to measure low energy (ε < $10^{-3}E$) EM showers and a large acceptance to detect the low flux of HE cosmic ray muons.

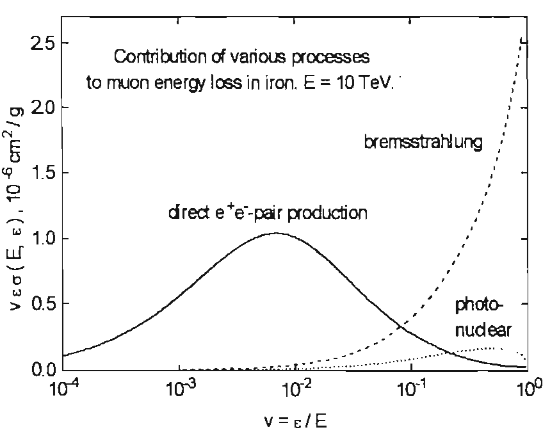

Figure 2. Energy loss distributions of 10 TeV muon for e^+e^- production, bremsstrahlung, and photonuclear interaction.

Though the physical grounds of the pair meter technique seem to be well understood, it has not been properly tested experimentally, mainly due to

: small thickness and/or coarse granularity of the detectors used.

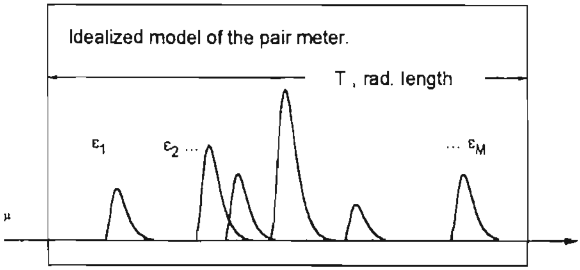

gure 3. Longitudinal energy distribution in the ideal pair meter.

In February 1996 we started experiments with the Big liquid ARgon Spectrometer BARS to study the pair meter technique and to measure the flux of horizontal cosmic ray muons. Although BARS was designed for tagged utrino experiments at the IHEP accelerator its size and structure are quite adequate for e pair meter technique and its acceptance is sufficient to obtain high statistics of muon ents in the TeV energy range.

Detector BARS

The detector BARS consists of two identical LA calorimeters BARS1 and ARS2 (fig.4). Each calorimeter contains 216 t of LA, 154 t of those being in the lucial volume. There are two types of detectors inside the cryostat: ionization ambers and scintillation hodoscopes.

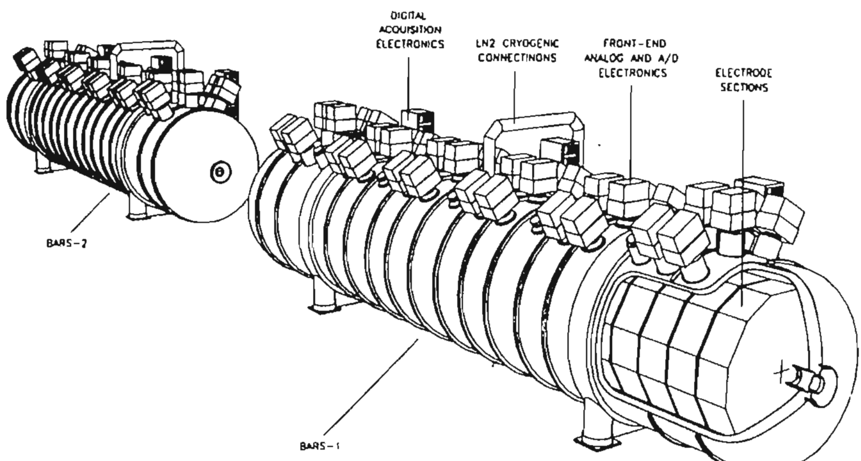

Figure 4. BARS calorimeters.

Signal electrodes of ionization chambers are made of Al strips, 3 mm thick and 1 mm wide. Grounded Al electrodes are 6 mm thick. The gap width is 24 mm. Each signal plane consists of 48 strips. The strips in adjacent planes are rotated by 120° thus forming u, v, and x coordinates. 12 signal planes are combined into a section. There are 24 sections in the calorimeter. Total calorimeter thickness is 18 m (137.4 r.l., 25 i.l.). The diameter of electrode system is 3 m.

A plane of 8 scintillation counters is positioned in front of each section. Scintillation light is collected by the WLS bars placed between the counters. The WLS bars are viewed from both ends by FEU-84 PM's. Both counters and PM's with bases are in the LA.

The electronics for ionization signals includes low-noise charge preamplifiers with matching transformers at inputs, $(\text{CR-RC})^2$ bipolar shaping amplifiers with a shaping time of 15 μs and a peaking time at 2 μs, peak sensitive 20 MHz 12 bit ADC's. The total number of channels in each calorimeter is 13824.

The signals from PM's viewing the same WLS bar after amplification and shaping are transmitted to "mean timer" units with a guaranteed 5 ns time resolution.

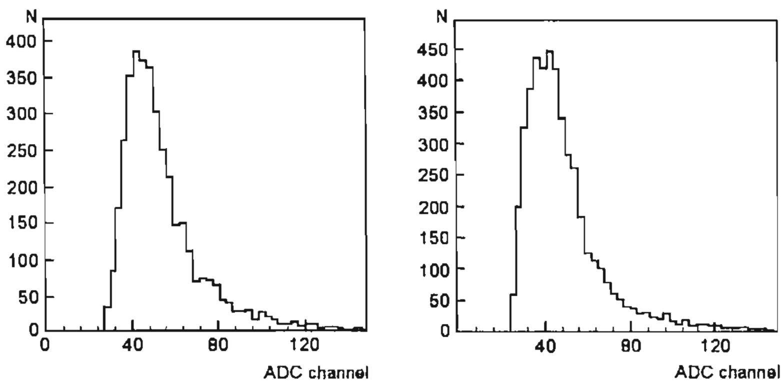

Figure 5. Typical pulse height distributions for relativistic muons.

DAQ electronics sends to the host computer only signals with pulse heights above preprogrammed thresholds $k\sigma_n$ where k is in the range from 2 to 3 and σ_n is a RMS of the noise signal distribution. For the most of channels σ_n is close to 10 counts of ADC while the average pulse height of a relativistic muon signal is about 50 counts (fig.5).

BARS energy resolutions for EM and hadron showers are $0.04/\sqrt{E} \oplus 0.08/E$ and $0.55/\sqrt{E} \oplus 0.02$ correspondingly. The e / h rejection factor is less than 0.04 at 99% electron detection efficiency, using the RMS of the transverse energy distribution as the only discriminating parameter. More information about BARS parameters and characteristics can be found in ref.[4)]

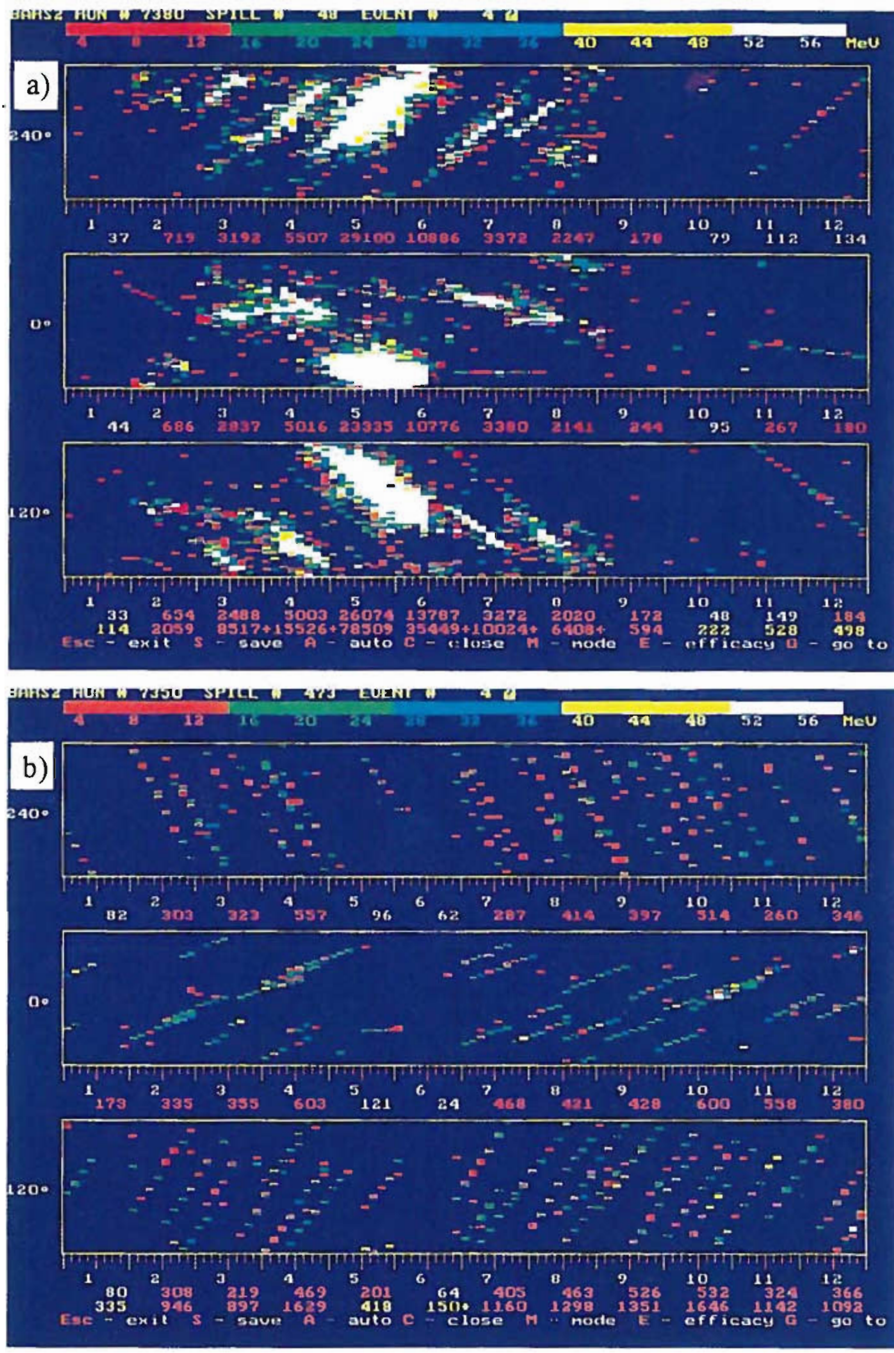

Fig.6. Background events from EAS(a) and a group of muons(b). Scale of energy deposited in the cells is shown at the top of figs.

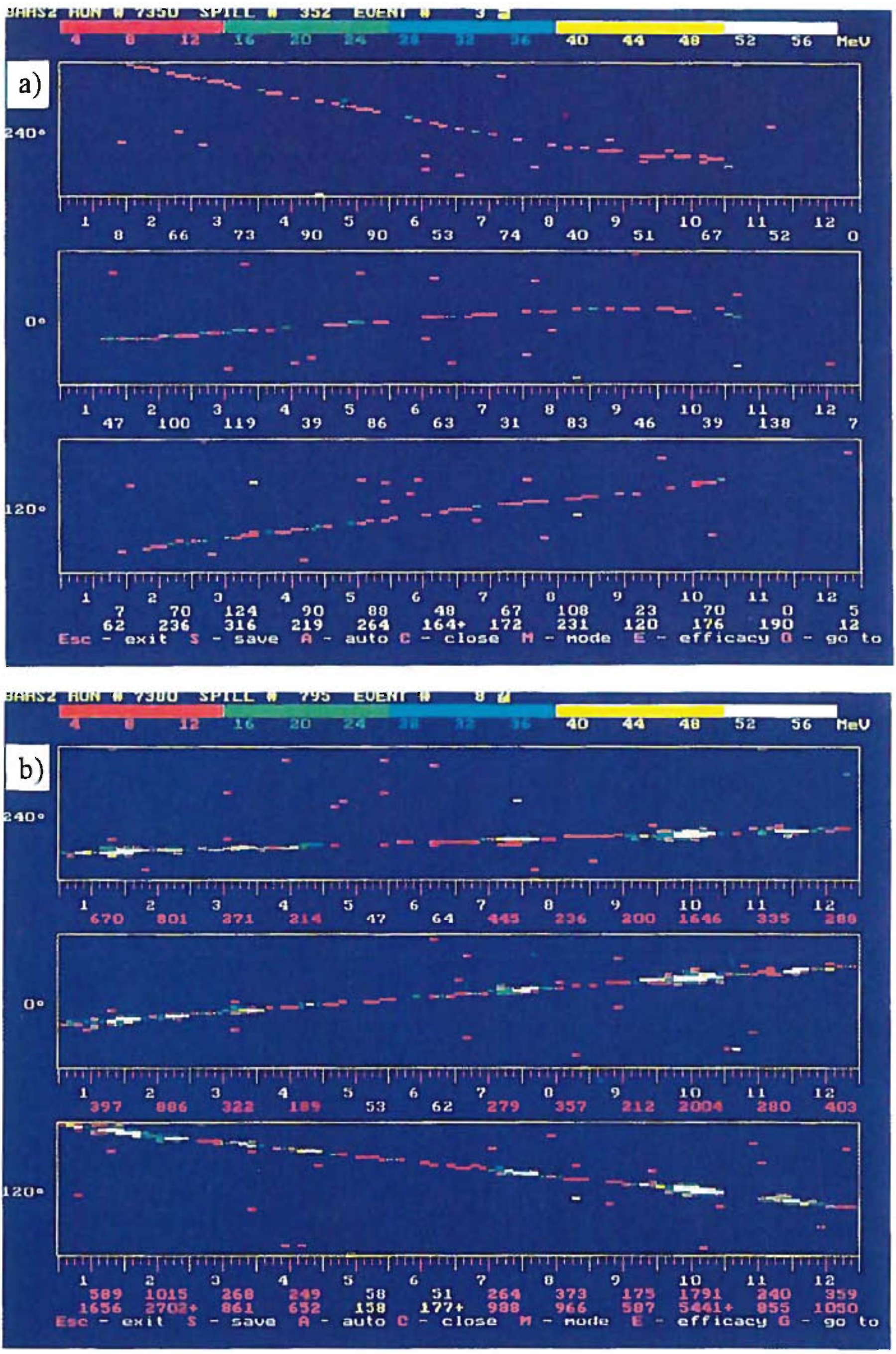

Fig. 7. Muon tracks Scale of energy deposited in the cells is shown at the top of figs.

Measurements and results

Measurements were performed during a two-week run in February, 1996. ıble coincidences between the following scintillation planes were used as a trigger: 1 18, 2 and 19, 3 and 20, 4 and 21. Geometric acceptance for this trigger figuration is equal to 0.26 m^2·sterad, zenith angle interval is 78° to 90°. Trigger ciency did not depend on the muon direction and was as high as 99% for muons ssing all trigger planes. Trigger rate was about 0.4 Hz. About 1/3 of detected events due to horizontal muons and 2/3 are due mainly to random coincidences, to EAS .6a) and to groups of vertical muons (fig.6b).

About 10^5 horizontal muons were detected. Preliminary results presented below based on 1/15 of the collected statistics. Fig.7a shows a track of low energy muon pped in the BARS which lost its energy due to ionization. The track shown in fig.7b ongs to a high energy muon. It produced as many as 7 EM showers (see fig.8). The mated energy of this muon is about 2 TeV.

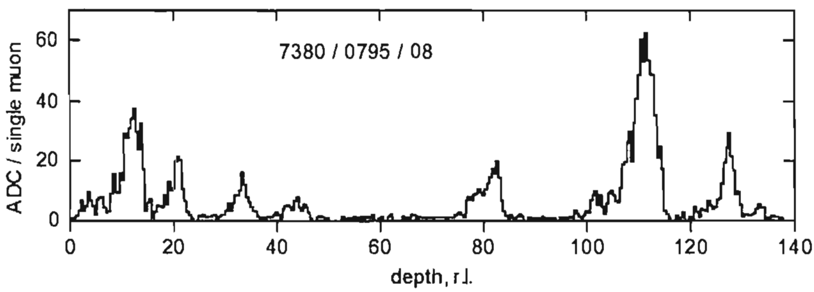

Figure 8. Energy distribution along the BARS for the event shown in fig.7b.

The distribution of EM shower multiplicities for different values of the energy eshold ε_0 are presented in fig.9. The dashed lines are calculations based on existing a on muon energy spectrum[5)] and commonly used formulas for cross sections of e^+e^- l γ production by HE muons. The agreement of experimental results with expectation ather good. Further analysis of available data is in progress.

Fig.10 demonstrates the expected muon flux per year through one BARS. More n $2 \cdot 10^4$ muons in the energy range above 1 TeV can be detected in two BARS orimeters during one year.

Conclusions

The pair meter method of muon energy measurements was tested using the ιRS spectrometer. It is shown that this technique is promising for the study of the smic ray muon energy spectrum in the multi-TeV region. Due to fine granularity, large

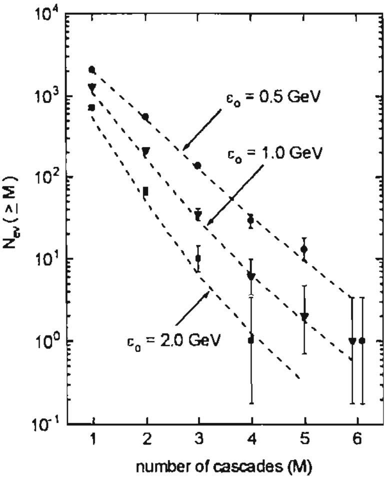

Figure 9. Distribution of EM shower multiplicities for different values of the energy threshold ε_0.

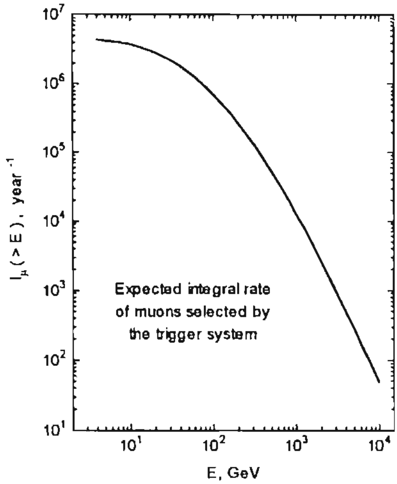

Figure 10. Expected muon flux per year through one BARS.

thickness and high acceptance, BARS can be also used to search for new phenomena and to study rare processes (for example, narrow muon bundles) connected with horizontal cosmic rays.

Acknowledgements

We wish to thank L.Beretta, U.Cazzola, L.Corucci, N.Filimonov, R.Franceschini, A.Godov, V.Kostjuchenkov, C.Magazzu, O.Romashov, R.Ruberti, and V.Volkov for their help in BARS assembling and testing. This work was partially supported by Russian Fund for Basic Research (grant N96-02-16857).

References

1. I.S.Alekseev, G.T.Zatsepin, in: Proc. Intern. Conf. on Cosmic Rays (Moscow, 1960), **vol.1**, 324.
2. R.P.Kokoulin, A.A.Petrukhin, NIM **A263,** 468 (1988).
3. R.P.Kokoulin, A.A.Petrukhin, Sov. Journ. Part. and Nucl. **21,** 332 (1990).
4. F.Sergiampietri, in: Proc. IV Intern. Conf. on Calorimetry in High Energy Physics (La Biodola, 1993), 357.
5. O.C.Allkofer e.a., Nucl. Phys. **B259,** 1 (1985).

scati Physics Series Vol. VI, (pp. 133–142)
INT. CONF. ON CALORIMETRY IN HEP – Frascati, June 8–14, 1996

UPGRADE OF KARMEN NEUTRINO-CALORIMETER

H. Gemmeke, G. Drexlin for KARMEN Collaboration*

Forschungszentrum Karlsruhe, Postfach 3640, D-76021 Karlsruhe, Germany

ABSTRACT

e KARMEN neutrino-calorimeter is in the state of upgrading for the verification refutation of the $\bar{\nu}_\mu \rightarrow \bar{\nu}_e$ oscillation claim of the LSND experiment [1]. The ysical goal of increasing the sensitivity of KARMEN by a factor 5 to 7 will be iieved by an additional active shield layer of plastic scintillator slabs covering area of 300 m^2 inside the walls and the roof of the passive iron shielding of RMEN. This approach will reduce the cosmogenic background by a factor of 40 d is the most effective solution without an expensive improvement of the central lorimeter. The technical design and simulation results are presented.

Introduction

ie KARMEN neutrino-experiment uses the neutron spallation source ISIS at the utherford Appleton Laboratory (Chilton, England) as ν-source. The 800 MeV otron beam of the rapid cycling synchrotron with an averaged beam current of 0 μA is an intensive source of pions in the TaD_2O target with a π^+ /p-ratio of

*B. Armbruster, T. Csabo, V. Eberhard, K. Eitel, S. Faion, A. Grindler, R. Gumbsheimer, Hucker, T. Jannakos, M. Kleifges, J. Kleinfeller, C. Oehler, P. Plischke, J. Rapp, I. Rednic, Reichenbacher, A. Rininsland, P. Schirrmann, F. Schnürer, M. Steidl, J. Wolf, B. Zeitnitz *rschungszentrum Karlsruhe, Institut für Kernphysik I, Institut für experimentelle Kernphysik, niversität Karlsruhe, D-76021 Karlsruhe, Postfach 3640, Germany.* B.A. Bodmann, E. Finckh, Hößl, W. Kretschmer, O. Stumm, *Physikalisches Institut, Universität Erlangen-Nürnberg, Erwin ommel Straße 1, D-91058 Erlangen, Germany.* C. Eichner, R. Maschuw, C. Ruf *Institut für rahlen- und Kernphysik, Universität Bonn, Nußallee 14-16, D-53115 Bonn, Germany.* I.M. Blair, A. Edgington, B. Seligmann, *Physics Department, Queen Mary and Westfield College, Mile End oad, London E1 4NS, United Kingdom.* N.E. Booth *Department of Physics, University of Oxford, eble Road, Oxford OX1 3RH, United Kingdom.*

0.046. The decay of the stopped pions in the target provides an equal flux of three types of neutrino's ν_μ ,$\bar{\nu}_e$ and $\bar{\nu}_\mu$. The time structure of ISIS and the time and energy structure of π-decay at rest allows for ν-type identification in KARMEN [2].

The KARMEN detector is a 56 t high resolution scintillation calorimeter (see fig.2) and has been continuously in operation since summer 1990. In the last five years approx. 2000 neutrino interactions with ^{12}C were identified and analysed. In particular, the experiment has measured the energy dependence of the $^{12}C(\nu_e, e^-)^{12}N_{g.s.}$ cross section with a signal to background ratio of 35:1 and made the first observation of the neutral current process $^{12}C(\nu, \nu')^{12}C^*$ $(1^+ 1)$ with $(\nu_e, \bar{\nu}_\mu)$. Recently the statistics were sufficient to deduce for the first time the cross section for the reaction $^{12}C(\nu_\mu, \nu_\mu{}')^{12}C^*$ and to extract the first reliable cross section for the astrophysically interesting reaction $^{12}C(\nu_e, e^-)^{12}N^*$. In general, one can conclude that for all cross section measurements on ^{12}C the systematic errors due to the flux normalisation are now larger than the statistical errors. A notable exception are the cross sections for ν_e - absorption on ^{13}C and ^{56}Fe. Here an increased neutrino statistics and background reduction would be helpful. The main emphasis of the future measurements of KARMEN will however be focused on the search for **neutrino oscillations** [3] and the investigation of the **time anomaly** [4].

LSND found a **positive** evidence for neutrino oscillation but KARMEN saw no evidence for neutrino oscillation at all in the measuring period from 1990 to 1995. To allow a verification or refutation of LSND results KARMEN is now upgraded to suppress backgrounds that limit the sensitivity.

2 Cosmic Background for Oscillation and Single Prong Events

Over the last years the signatures of cosmic ray induced background in the KARMEN detector have been studied in great detail. Comparison of experimental signatures with Monte Carlo simulations based on GEANT 3 has revealed the nature and the origin of all important background processes. In the following a detailed discussion of all relevant background sources is given.

2.1 Background for Oscillations

In the search for $\bar{\nu}_\mu \rightarrow \bar{\nu}_e$ appearance the experiment looks for the characteristic delayed coincidence induced by the inverse β - decay reaction on the free protons of the liquid scintillator:

$$\begin{array}{lcl} \bar{\nu}_e + p & \rightarrow & n + e^+ \\ & & \downarrow \quad \tau = 105\ \mu s \\ & & Gd(n, 3\gamma) \qquad (\Sigma E_\gamma = 8\ \mathrm{MeV}) \end{array}$$

The signature of $\bar{\nu}_e$ is thus an energetic positron with energies in the range ·om 10-50 MeV followed by capture gamma rays (energies up to 8 MeV) from ab- ɔrption of the thermalized neutron in Gd or ^{1}H. The coincidence time interval is ɜquired to be in the range from 5-500 μs. Although this delayed coincidence sig- ature is very stringent, there is a significant background from cosmic rays of up ɔ **10 coincidences per μs** accumulated from july 1990 to february 1995, which ; a rather high level of background as compared to the few oscillation events one xpects if LSND is correct. The data analysis makes use of the expected time distri- ution of the oscillation signal (a 2.2 μs decay time constant on top of a flat cosmic ackground) as well as on the known energy distributions of background and the scillation signal (i.e on the prompt energy signal). In the framework of a likelihood nalysis independent for all oscillation parameters Δm^2 one obtains the oscillation xclusion plot of fig.6,. Would there be no background at all, the sensitivity of ⟨ARMEN will be improved by a factor of four. The KARMEN experiment is thus learly *background limited.*

The main background source for the oscillation search are high energy (HE) ıeutrons in the energy range up to 200 MeV. HE neutrons can penetrate deep into he liquid scintillator volume without giving a signal in the veto counter system neutral background). The recoil proton from (n,p) scatterings gives a prompt ignal, the delayed signal is produced after thermalization and n-capture by the ɜd(n,γ) or the ^{1}H(n,γ) process. Fig.1 shows the measured energy distribution of he **sequential background**. There are two components: a hard component with ın exponential slope parameter $E_0 = 39.5$ MeV and a soft component with $E_0 = 2.1$ ⁄IeV. The soft component originates from neutrons following nuclear capture of topped μ^- in iron and is only relevant in the low energy regime $E_{vis} < 20$ MeV.

The hard component is generated by muons which undergo a **deep inelas- ;ic scattering (DIS)** in the blockhouse without giving a hit in any of the existing ʼeto systems. High energy neutrons from μ-DIS can easily penetrate the inner pas- ıive shield of KARMEN and their interactions in the liquid scintillator give rise to ıequential event patterns (see fig.2) which deteriorates the oscillation signal. Up to ıow the KARMEN central dectector was 'only' shielded by 18 cm of iron against ıeutrons produced outside the outmost active shield detector. Neutrons from DIS ɜvents of near-miss muons are therefore only suppressed by a factor of 3 (the inner ɔassive shielding roughly corresponds to one neutron absorption length of $\lambda_n = 21.6$ ːm).

On the other hand the **random background** is very small compared to ;he sequential background and amounts to only 7 % of the total background for ɔscillations.

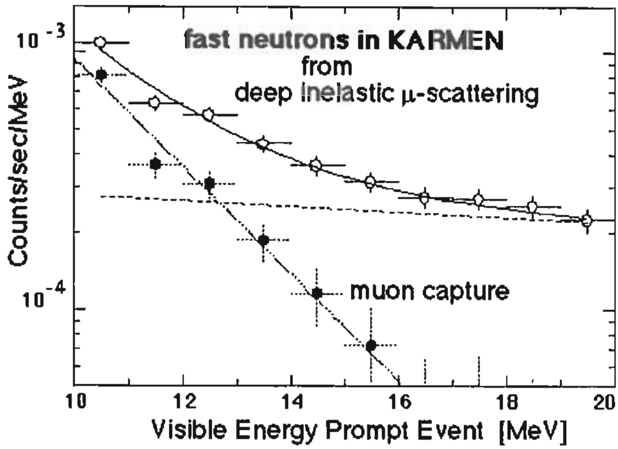

Figure 1: Sequential background in KARMEN from deep inelastic μ-scattering and μ^-capture.

2.2 Background for Single Prongs

As the investigation of the anomaly in the time distribution of single prong events [4] is the second major topic of KARMEN, one has to look carefully for the background also for single prong events. The neutrinos and the anomaly sit on a constant cosmic background level which amounts to 140 background events per μs. At present the event ratio *anomaly : neutrinos : cosmic background* is *1 : 2.4 : 2.2* in the relevant time window from 2.6 - 4.6 μs after beam-on-target. Interestingly the major background component is the same as for the neutrino oscillation search: HE neutrons from DIS. Furthermore Bremsstrahlung of cosmic muons and their decay products not detected by the existing veto system contribute to the single prong background.

A significant reduction of the cosmic background will improve the signal to background ratio for the anomaly by a *factor 2.* Also for the ν_e - reaction on ^{13}C and ^{56}Fe a dramatic improvement is expected.

3 Hardware Requirements

The only way to reduce the background for both neutrino oscillations and the time anomaly is thus to *actively* detect the primary muon in the iron blockhouse. If the muon is detected and then undergoes DIS, a very short hardware-veto of $< 1\,\mu$s will inhibt the HE neutron interactions in the central detector. The tagging of the primary muon requires the implementation of a second active shield layer of plastic scintillator slabs **inside** the walls and the roof of the blockhouse. The optimised position (see fig.2) requires a minimum amount of about 90 cm of iron or 4.3 neutron

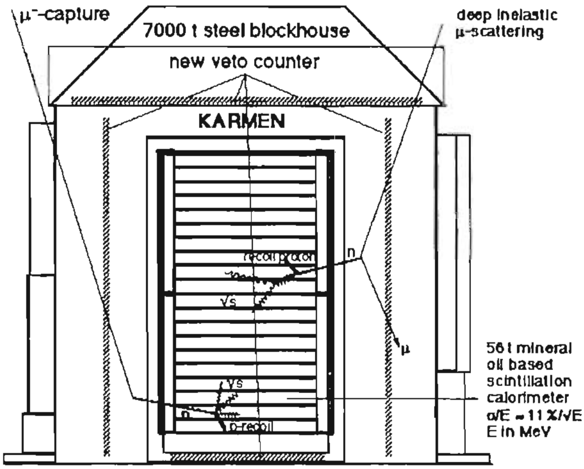

;ure 2: Effect of new veto counter in KARMEN on μ-scattering and μ^-capture.

enuation lengths λ_n (reduction of primary intensity to $\exp(-90\,\mathrm{cm}\,/\,21.6\,\mathrm{cm})$ = 5 %). The structure of the blockhouse, consisting of 18 cm thick iron slabs, allows : removal of slab layers and the reconstruction of the structure.

The removed steel can be moved to the outer layers to guarantee identical .elding conditions for beam correlated background. The new shield will be sup- :mented at the downstream side by an additional 0.7 m thick steel wall (230 t) ;ached inside the blockhouse.

[Veto Detector

ıe new veto system will have a surface area of approximately 300 m^2. All individual .ntillator modules will have a width of 0.65 m, which is the maximum production dth of the manufacturers for long bars. This width sets the total number of to counters to 136 modules. Each module will have 50 mm thickness for efficient scrimination of low energy background γ's.

Of crucial importance for the veto upgrade is the choice of the scintillator aterial. In general one requires a material with high light output, very long at- nuation length (several meters) and fast decay constant. BC412 from Bicron and E110A from Nucl Enterprises Ltd. are solid plastic scintillators with comparable ;htoutput (60 % Anthracen) and light attenuation length (6 m). From tender :ercise the BC412 material was selected.

Samples of the scintillator were tested with a laser photometer. In addition, ur scintillator slabs of 4 m and 3 m length (thickness 50 mm and width 650 mm)

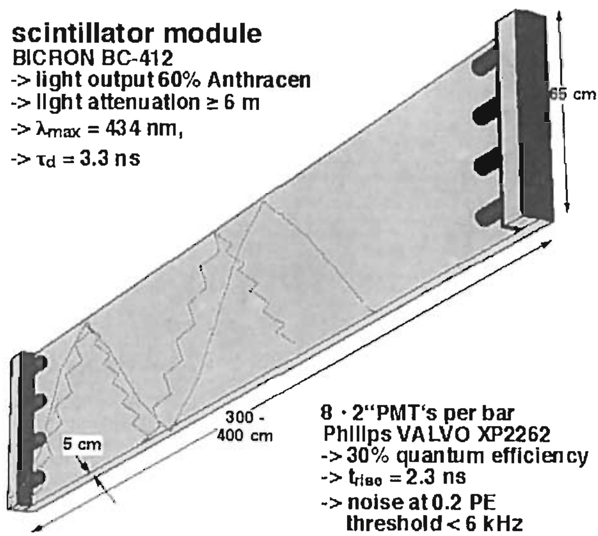

Figure 3: Structure and geometry of a scintillator module.

have been tested with various PM read-out configurations, see fig.4. The light output of cosmic muons (10 MeV) and gammas summed up on one side is shown against the position measured by the time difference of both ends. The Landau-distributed muons exhibit, by their position dependency, the light attenuation of the scintillator. Due to the sufficient scintillator thickness of 50 mm muons and γ's may be well separated by an integral threshold.

These investigations have been preceded by extensive simulations with a three dimensional light tracking code to optimize the scintillator layout, PMT's and light readout geometry. To minimize gaps between adjacent scintillator modules the light readout at the module ends is bended around 180^o by the help of Lucite blocks glued to the scintillator. The end cuts of scintillator and light guide have an angle of 7^o and 12^o and are covered by an aluminum mirror to optimize light transport. The area between the PM tubes is also coated by an aluminium mirror improving the light output. This set-up has the advantage of a relatively easy construction and provides an 80% efficiency against a straight readout scheme (PM's directly attached to the schintillator ends) and a homogeneous detection efficiency at the far ends of the modules. As photomultiplier, the Philips VALVO 2" XP2262 is selected because of its superior price performance ratio. They allow a good quantum efficiency of 30 %, a fast rise time of 2.3 ns together with a dark noise behaviour of < 6 kHz at a threshold of 0.2 photoelectrons obtained at a gain of 2×10^7.

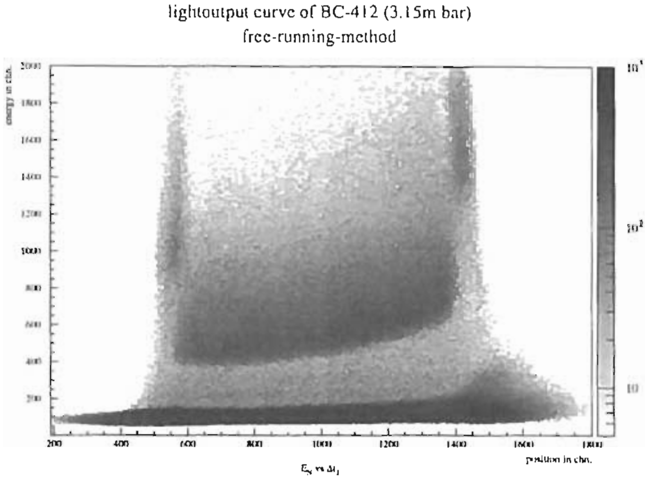

igure 4: (μ , γ)-discrimination of the scintillator modules in fig.3. For cosmic μs nd background-γs the visual energy on one end of the module against the time ifference (position) is shown. .

In the progress of the upgrade project, momentaryly 3/4 of the blockhouse ɔof is dismanteled and the wall layers over 2/3 of the rear part of the blockhouse re removed, see fig.5. Covering the shield by at least 60 cm of steel still suppress he hadronic and electromagnetic component of cosmic radiation. Muon induced eutron background in the steel enclosed by the new shield (thickness: 0.72 m roof, .9 m walls) will be tagged and suppressed.

Physics Potential

'he physics potential that arises for neutrino oscillation from the new shield layer ave been investigated with extensive Monte Carlo simulations on the basis of EANT 3. The simulations suggest a three year measuring period up to the end f 1999. By then the experiment will have accumulated 7000 C of protons with ignificantly reduced background levels. The sensitivity for neutrino oscillations depends strongly on two parameters: the **neutron detection efficiency** ε_n and the **osmic ray induced background** level.

.1 Neutron Detection Efficiency

n the last months the neutron detection efficiency ε_n was increased significantly by owering the thresholds on the front-end ASTERIX cards. The analog thresholds vere lowered from 15 mV to 10 mV corresponding to an increase of the neutron

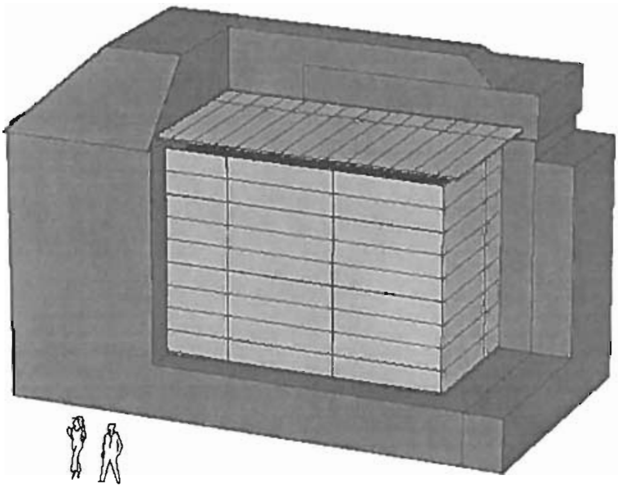

Figure 5: Geometry of veto counter within blockhouse.

detection efficiency from $\varepsilon_n = 20\,\%$ to $\varepsilon_n = 53\,\%$. Together with some hard- and software upgrades the experiment is now able to clearly identify the 2.2 MeV gamma-rays from the $p(n,\gamma)$ capture reaction.

4.2 Oscillation Plots

The estimated oscillation sensitivities are derived from the enhanced neutron efficiency and the following experimental conditions:

- The sequential background from HE neutrons originating from DIS μ-events is reduced by a factor of 40 to 2.6 sequential background events per year in the energy range from 10-50 MeV.
- The random background, which is a mixture of bremsstrahlungs γ's and HE neutrons is reduced accordingly. The random background then amounts to 0.5 events per year.
- There are 2.3 exclusive CC events per year of the type $^{12}C(\nu_e, e^-)^{12}N_{g.s.}$ in the data.

The expected background events were allowed to fluctuate following a Poisson distribution. Then these data were analysed with a maximum likelihood procedure, which requires that possible oscillation events follow the 2.2 μs time dependence with respect to beam-on-target whereas cosmic background is flat in

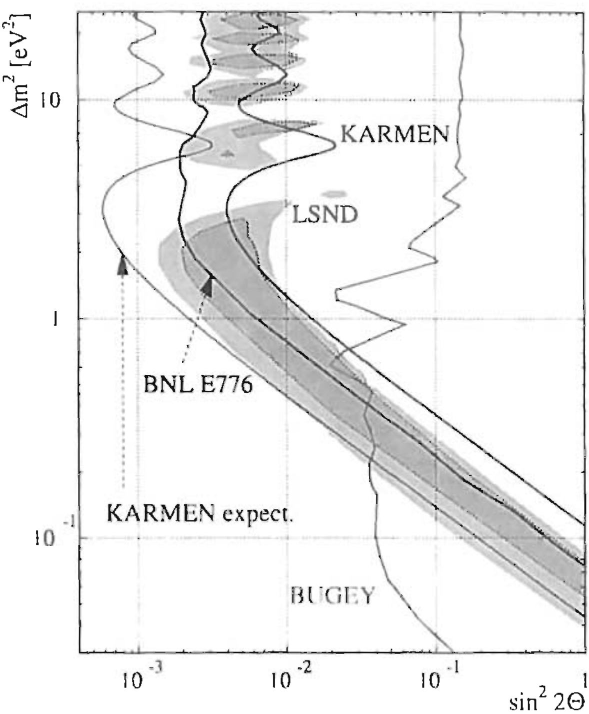

Figure 6: Oscillation exclusion plot for KARMEN (now) and expected (after 3 years). Bugey, BNL E776 limits and LSND oscillation evidence region.

ime and making use of the energy information of prompt events for each Δm^2 - parameter seperately. Furthermore in a reasonable approximation for the remaining background the measured energy distribution of the HE neutron background is used. In the framework of a two parameter energy-time likelihood one obtains oscillation limits (90 % CL) of $\sin^2 2\Theta = (1.9 \pm 0.5) \times 10^{-3}$ after one year and after three years $\sin^2 2\Theta = (0.9 \pm 0.2) \times 10^{-3}$, as shown in fig.6. After one year of data taking most of the LSND parameter space will be covered. After three years the experiment will have a sensitivity to mixing angles close to the limit of the $\bar{\nu}_e$ - contamination at ISIS which amounts to 4×10^{-4} in the time interval from 0.6 - 10 μs.

Apart from discussing the search for neutrino oscillations in terms of exclusion limits only (i.e. assuming that no signal is seen), one should have in mind the distinct possibility that the LSND findings are a real effect. Therefore one should discuss the *discovery potential* of KARMEN. Here the background reduction will also be most powerful- the experiment will be able to pin down the neutrino mass parameter Δm^2 with an L / E_ν likelihood fit. This is due to two unique facts:

- KARMEN is able to determine the neutrino flight path L (from target to detector) with a relative precision of $\Delta L / L \leq 1\,\%$ (assuming a ΔL of 17 cm over a mean flight path of 17 m). No other experiment can do this with a similar precision. A typical high energy experiment usually has a much too long π^+ decay chain and achieves a resolution of $\Delta L / L \approx$ 30-40 %.

- The ability of KARMEN to measure the neutrino energy E_ν via the inverse β-decay on the proton (*neutrino spectroscopy*). A comparison of the energy resolution of KARMEN ($\Delta E / E = 11.5\,\% / \sqrt{E(MeV)}$) and LSND ($\Delta E / E = 42\,\% / \sqrt{E(MeV)}$) shows the better calorimetric properties of KARMEN. Even a few events would be sufficient to get a rough estimate on Δm^2 .

5 Conclusion

In conclusion it can be stated that the KARMEN experiment will significantly improve its physics potential at the end of 1996 when the veto system with a surface area of 300 m^2 is implemented inside the walls and the roof of the blockhouse. This leads to a substantial reduction of HE neutrons from spallation reactions of cosmic muons in the iron shielding. For neutrino oscillations this will result in a sensitivity to extremely small mixing angles $\sin^2 2\Theta = 1 \times 10^{-3}$ and will allow investigations of the whole parameter space allowed by the LSND experiment. In any case KARMEN will then be able to deduce the best oscillation limits in the channel $\bar{\nu}_\mu \rightarrow \bar{\nu}_e$. In addition, the reduced background level for single prong events will allow investigations of the time anomaly in great detail and measurements for the first time of the ν_e-absorption rates on ^{13}C and ^{56}Fe with high precision.

References

1. C. Athanassopoulos *et al.*,(LSND Collaboration), Los Alamos preprint LA-UR-96-1582, acc. for publ. in Phys. Rev. Letters.

2. H. Gemmeke *et al.*,(KARMEN Collaboration), Nucl. Instr. & Meth. A **289**, 490 (1990)

3. B. Armbruster *et al.*,(KARMEN Collaboration), Nucl. Phys. B (Proc. Suppl.) **38**, 235 (1995); G. Drexlin, Prog. Part. Nucl. Phys. Vol. **32**, 375 (1994).

4. B. Armbruster *et al.*,(KARMEN Collaboration), Phys. Lett. B **348**, 19 (1995).

;cati Physics Series Vol. VI, (pp. 143–152)
NT. CONF. ON CALORIMETRY IN HEP – Frascati, June 8–14, 1996

HONON MEDIATED PARTICLE DETECTION: RESULTS AND PROSPECTS

A. Giuliani
Dipartimento di Fisica dell'Università and Sezione dell'INFN, Via Celoria 16, I-20133 Milano, Italy

ABSTRACT

ɔnon-mediated detection of particles is briefly presented and discussed. Its pos- :e impacts on crucial aspects of non accelerator particle physcics, such as neu- ıoless double beta decay, neutrino mass, low energy neutrino detection and dark tter searches, are considered. In particular, the status of the most advanced ex- ·imental work in some of these fields is described and the future prospects are sented.

The principles of phonon-mediated detection of particles

e operation of every particle detector exploits the production of elementary exci- ions in a proper material caused by the interaction of the particle to be detected. .e lower the energy necessary on the average to produce an elementary excitation, ꞓ better the detector performance in terms of energy resolution and threshold. ɔm this simple consideration, it is clear that great advantage could be taken if one re able to observe the phonons produced by particle interactions, as these lattice citations have typical energies around at most the Debye energy (a few tens of ꞓV in ordinary solid materials), much lower than the energy associated to the ·mentary processes in conventional detectors. Of course, in order to prevent the ermal population of the relevant phonon states, low temperatures are required; in ·ne cases, it is necessary to operate in the ~ 10 mK range.

Historically, the first proposed phonon-mediated particle detectors were rfect calorimeters [1], i.e. devices where the energy deposited by an elementary rticle in a suitable material leads to a new thermal phonon distribution and the ;nal consists of a temperature rise of the energy absorber.

1.1 Low temperature calorimeters

The principle at the base of the quoted paper [1)] is very simple: when a dieletric diamagnetic crystal (for which only the lattice contribution to the specific heat is important) is kept at temperatures in the few mK range, the Debye law (1) predicts a specific heat so low that appreciable temperature increases can be induced in macroscopic amounts of material even by the tiny energy released by a single particle:

$$C = 1944 \cdot n \cdot N_{at} \cdot \left(\frac{T}{\Theta_D}\right)^3 J/K. \tag{1}$$

In this equation n is the number of moles, N_{at} is the number of atoms per molecule, T the crystal temperature and Θ_D the material Debye temperature. Therefore, materials with high Θ_D are preferred.

Normal metals are ruled out because free electrons contribute to specific heat with a term proportional to T at low temperatures, usually too high in macroscopic absorbers. Even materials with atomic or nuclear magnetism are not ideal, due to the appearance of Schottky anomalies in the low temperature specific heat behaviour.

A longer discussion is required for superconductive absorbers. In principle, well below the critical temperature T_c only the lattice should contribute to the specific heat, again ruled by 1. Actually, the time required for the complete conversion into phonons of the deposited energy can be very long (ms or tens of ms even in small samples) because a large fraction of the deposited energy can be trapped in quasiparticle states. In the experimental tests, contradictory results were up to now obtained [3)].

If the specific heat of a material is given simply by (1), it is easy to check that in macroscopic amounts of material kept at temperatures as low as a few mK or a few tens of mK, the deposition of "nuclear" energies gives rise to measurable temperature variations.

A low temperature calorimeter can be schematized as a particle absorber, whose crucial parameter is the the heat capacity C, a sensitive thermometer in good thermal contact with it, and a weak thermal link, characterized by a thermal conductance G, which connects the detector to a heat bath. After a temperature pulse, the detector recovers to the operation temperature in a characteristic time τ given by C/G.

1.2 Non thermal phonon assisted detection

Complete and fast thermalization of the energy deposited by the impinging particle is a naive assumption. Thermalization is a delicate, complicate process, depending the type of interacting particle and absorber material [2]. Generally, the particle ,eraction produces on a faster time scale ($< 1\mu s$) "high energy" (tens of meV) onons, which down-convert to low energy and thermal phonons on a much slower ne scale (ms or tens of ms).

The use of fast phonon sensors, such as superconductive films or supercon- ctive tunnel junctions [3, 4] enables the detection of the fast phonon component, iich in principle contains much information on the particle interaction: not only ergy, but also position, momentum and type of interacting particle. Only if the onon sensor response is slower than the thermalization process, are we authorized speak in terms of "thermal" detectors and of low temperature "calorimeters".

3 Advantages of phonon-mediated detectors over conventional detectors

several aspetcs, phonon-mediated particle detectors present some advantages over nventional techniques.

ıergy resolution. In perfect calorimeters it can be shown that the intrinsic energy solution is approximately given by the following equation:

$$\Delta E_{rms} \simeq \sqrt{k_b T^2 C} \tag{2}$$

which measures the fluctuations of the internal energy of the detector [5]. macroscopic amounts of materials, it turns out that the intrinsic energy resolution as low as a few eV. The fundamental reason of the superior energy resolution of a ermal device is that all the deposited energy is converted into heat and measured, e only sources of uncertainty being the fluctuations associated to a dissipative ad-out and those of the internal energy itself of the device [5]; in conventional tectors the intrinsic inevitable limit to resolution is connected to the fact that only fraction of the deposited energy is actually measured (the one going to ionization) ıd this fraction is subjected to statistical fluctuations.

Most of the thermal detectors operated up to now exhibit an energy reso- tion worse than the theoretical one, both for intrinsic (non complete thermaliza- on) and experimental reasons (disturbances coming from spurious noise sources, ce microphony which is particularly annoying in thermal detectors, whose signal ındwidth sometimes does not exceed the few tens of Hz).

ıergy threshold. It is in principle given by a few times ΔE_{rms}: therefore it is much wer than for conventional devices.

ensitivity to low- or non-ionizing events. Unlike detectors based on ionization or omic excitations, even low ionizing events, such as low energy nuclear recoils, ın be detected with high efficiency [6, 15]. This characteristic, joined to the low threshold, makes phonon-mediated detectors ideal devices for WIMPs search [7] (section 2.3).

Material flexibility. The only constrain for a material to be used as an energy absorber in a low temperature detector is the ability to convert with high efficiency into phonons the energy deposited by an elementary particle. For thermal devices, this property is assured if the energy absorber is dielectric and diamagnetic. This makes the spectrum of the materials that can be used to build a particle detector very wide. There are many applications where the sensitivity of the experiments can be enormously increased if one has the freedom to choose the detector composition: a typical example, as pointed out in section 2.1, is offered by the search for 0ν-DBD.

1.4 Experimental results

It is impossible to review in a few lines the large amount of interesting technical results obtained up to now in phonon-mediated particle detection. Therefore we recommend the interested reader to refer to the copious literature on this topic [2, 3, 4, 7]. Here we shall give a short presentation of three emblematic results, concerning low energy X-ray spectroscopy, γ-ray spectroscopy and mass to threshold ratio.

1.4.1 X-ray spectroscopy

Outsanding results were obtained in this field by an american collaboration [11]. This group uses semiconductor thermistors as temperature sensors [2] based on silicon chips doped by implantation using standard silicon technology. They have developed very small mass bolometers ($\sim 10\mu$g) devoting particular care to the material choice for the absorber, in order to push energy resolution as close as possible to the theoretical limit. Even if so small, these detectors are able to absorb completely and with efficiency close to 1 low energy photons (up to a few tens of keV).

Materials which exhibit an energy gap are always affected by impurities or defects which behave as trapping centres for the electrons and holes initially produced by the X-ray photons. This leads to incomplete or delayed thermalization; this phenomenon being subjected to statistical fluctuations, the energy resolution is consequently deteriorated. Zero-gap semiconductors and superconductive metals are in general materials which minimize this trapping phenomenon. For this reason, the best results in terms of energy resolution were obtained with tin (a superconductor) and TeHg (a zero-gap semiconductor).

An impressive energy resolution of 7.3 eV FWHM was achieved with a

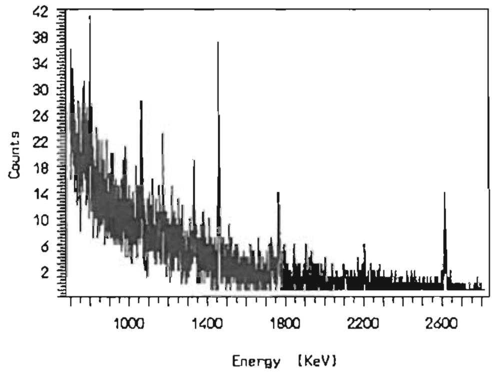

Figure 1: Background γ spectrum obtained with a TeO_2 340 g detector in the Gran Sasso Laboratories [17].

Te detector on the Mn K_α line (5.9 keV) of an ^{55}Fe source [11]: this result is times better than that achievable with conventional Si(Li) detectors. A similar ergy resolution was recently obtained by an other collaboration [7] with a tin sorber and a doped germanium temperature sensor.

[.2 γ-ray spectroscopy

ie most interesting results in this field, considering both energy resolution and tector efficiency, were up to now obtained by a group (to which the author belongs) erating at the University of Milano and at the Gran Sasso National Laboratory in ıly. The goal is the realization of large mass calorimeters for Double Beta Decay 'BD) search (section 2.1).

The typical calorimeter realized by this collaboration consists of a single ystal acting as an absorber and of a small neutron transmutation doped Ge ther-istor as a temperature sensor, epoxied onto the absorber. The best results were to now achieved with TeO_2 low temperature calorimeters [14]. This compound ıs chosen for its interest in DBD search. The largest detectors, operated at about mK, have masses of 340 g, which is a record for low temperature calorimeters. ermanium quality γ-spectrum were obtained, as can be appreciated in fig. 1. With ese detectors it was clearly demonstrated that thermal devices are sensitive even low energy nuclear recoils [15].

1.4.3 Mass to threshold ratio.

Impressive results in this field were obtained by two groups in Munich [25, 26]. Their typical detectors consist of sapphire crystals on which a tungsten film is deposited and kept across the critical temperature ($\sim$ 11 mk): in this region of course the film exhibits a very steep dependance of the resistance on the temperature and therefore works as a very sensitive thermometer. Thresholds of the order of 50 eV and 600 eV were achieved with crystal masses of respectively 32 and 262 g.

2 Application to non accelerator particle physics

There are several potential applications of phonon mediated particle detectors in different fields of physics, such as Dark Matter search, x-ray astrophysics, measurements of rare nuclear processes, heavy ion physics, neutrino physics, measurement of radioactive components in bulk materials: probably there are many other not yet proposed. I will limit here the discussion to those applications relevant to non accelerator particle physics.

2.1 Search for neutrinoless Double Beta Decay

Search for neutrinoless DBD (0ν-DBD) is a powerful tool for the investigation of lepton number non conservation and neutrino properties: its observation would imply new physics beyond the Standard Model [8]. The most sensitive method to investigate 0ν-DBD is to build a high energy resolution detector which contains the candidate nuclei. This technique has produced the longest life time limit for the candidate nucleus ^{76}Ge, essentially because it is possible to realize high resolution large germanium semiconductor detectors [9]. In this approach, the signature for the neutrinoless process is a peak in the background energy spectrum of the detector corresponding to the transition energy of DBD.

Thermal detectors allow to extend this technique to many other candidates, often more promising than ^{76}Ge, both for the transition energy and for the nuclear matrix elements. The Milano group has chosen to develop most of all the search on ^{130}Te, which is an interesting candidate to 0ν-DBD because of its large natural isotopic abundance (33.87 %), its reasonably high transition energy (2528 keV, outside all the natural γ background except the ^{208}Tl 2614 keV line) and the favourable neutrinoless decay rate [8]. As shown is section 1.4.2 large single crystals of TeO_2 can be grown, with excellent features as thermal detectors. A preliminary experiment performed in Gran Sasso Laboratories with a 334 g [16] detector, operated for 10,508 hour live time, has allowed to set a limit of $2.1(3.4)\times10^{22}$ y at the 90 %(68 %) confidence level for the half life of ^{130}Te 0ν-DBD. The corresponding

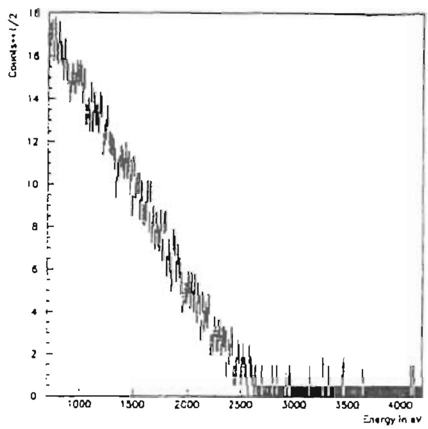

Figure 2: Kurie plot of ^{187}Re β decay measured with 125 eV FWHM energy resolution [10].

nit on neutrino Majorana mass ranges between 2.8 and 5.5 eV, according to the ırious nuclear matrix element calculations [8]. The half life limit excludes a rel- 'ant contribution of the 0ν-channel to the ^{130}Te DBD observed with geochemical ethods [8].

This experiment is a very preliminary step toward a large mass detector ray, which is now in preparation. Substantial improvements are possible also in rms of energy resolution and background. The possibility to realize detector arrays as tested succesfully with a four element device operated for $\sim$ 3,000 h [17]: the ackground specrum from one element is shown in fig. 1 as an example of high solution γ detection.

.2 Search for neutrino mass

nother possible application of thermal detectors to neutrino physics consists of n accurate calorimetric measurement of low energy β spectra, such as those of H (Q = 18.6 keV) and ^{187}Re (Q = 2.6 keV), in order to investigate a possible on vanishing value of the electron antineutrino mass. The thermal technique is omplementary to the conventional spectrometer technique. It allows in principle ɔ achieve similar energy resolution (a few eV), but is much less affected by the ystematics associated to molecular excited final states and to any mechanism that nplies some energy loss in the source, since thermal detectors are sensitive to the hole decay energy, except of course the one carried away by the neutrino itself. A drawback is the intrinsic slowness of thermal devices: severe limits on the source decay rate are set by the necessity to avoid pulse pile-up which could dangerously affect the spectrum shape in the high energy region.

An interesting approach was proposed: with the technique introduced in section 1.4.1, a high resolution detector can be realized with a superconductive Re absorber, which contains naturally the beta active isotope. It turns out that a few mg of natural rhenium would give a counting rate of a $\sim$ 10 Hz: such a detector, with an energy resolution of 10 eV, would allow to achieve 5 eV sensitivity to the antineutrino mass in one year running time.

Re spectra were already collected by the Genoa [10)] (fig. 2) and the Milano [18)] groups, with a resolution still far from the required one: much work is in progress to push the detector performances close to the theoretical limits.

2.3 Search for Dark Matter

Due to their sensitivity to low energy nuclear recoils, phonon-mediated detectors are ideal devices for WIMPs search [20, 7)]; two preliminary experimental results were already obtained in this field [15, 21)], while an experiment with a four element detector based on the results described in section 1.4.3 is in preparation in the Gran Sasso Laboratories [19, 25)].

A good background suppression [23, 24)] can be obtained if the phonon signal is measured simultaneously with a ionization signal in a proper semiconductor or with a light signal in a scintillator, because nuclear recoils give pulses with an enhanced phonon component with respect to ordinary β or γ background events.

2.4 Solar neutrino spectroscopy

The Milano group has proposed the realization of a large scale array of low temperature NaBr calorimeters (about 100 tons of total mass) to detect with high energy resolution solar neutrinos [12)], in particular those belonging to the higher energy line of ^{7}Be. The abundance of these neutrinos is strictly connected to the solar neutrino puzzle, and the shape and position of this line would provide a direct measurement of the central temperature of the sun [13)].

The principle of the experiment is the following: solar neutrinos induce the nuclear reaction ^{81}Br(ν,e$^-$)^{81}Kr*, with a threshold of 471.2 keV. The transition to the ground state of ^{81}Kr is forbidden. ^{81}Kr* decays to the ground state emitting a 190 keV photon or internal conversion electron, with a life time of 13 s. The prompt electron energy (which is equal to the neutrino energy minus the threshold) would be measured by the NaBr crystals with high resolution, while the delayed 190 keV energy deposition would provide a powerful signature of the neutrino interaction. A

;nal of 0.3 events/day was estimated, versus a background of only 10^{-3} events/day. one year, the higher energy ^{7}Be line would be observed with a statistics of $\simeq$ 0 events and with a resolution of a few keV. Unfortunately, the first tests on ıBr crystals as thermal detectors are not encouraging [12], but a more systematic vestigation is required.

Other proposed reactions to detect solar neutrinos with thermal methods e ^{115}In(ν,e$^-$)^{115}Sn* and ^{7}Li(ν,e$^-$)^{7}Be [4].

5 Detection of neutrino induced nuclear recoils

he coherent interaction of low energy neutrinos with atomic nuclei is a process ·edicted by the Standard Model of Weak Interactions, but never observed. The oss section of this process is enhanced, due to the coherence effect, by a factor N^2 ith respect to the typical weak cross sections, where N is the number of neutrons in ıe nuclide [22]. Unfortunately, neutrinos in the MeV energy range which elastically ffuse off heavy nuclei determine a few tens of eV nuclear recoils or even less: ıerefore, the only devices which could detect this process are phonon-mediated etector arrays with an energy threshold close to the theoretical limit (section 1.4.3) [9].

Conclusions

)utstanding technical results have been obtained with phonon mediated particle etectors. Physics results were already achieved in the search for 0ν-DBD and VIMPs interactions. For other aspects of non accelerator particle physics, sensitive xperiments can be designed: test devices are under development to prove their easability.

References

1. E. Fiorini and T.O. Niinikoski, Nucl. Instr. Meth. **224**, 83 (1984)
2. A. Giuliani and S. Sanguinetti, Mater. Sci. Eng., **R11**, 1 (1993)
3. D. Twerenbold, Rep. Pro. Phys. **59**, 349 (1996)
4. N. Booth, B. Cabrera and E. Fiorini, to be published in Ann. Rev. Nucl. Part. Sci. **46**
5. S.H. Moseley et al., J. Appl. Phys. **59**, 1257 (1984)
6. A. Alessandrello et al., Phys. Lett. **B202**, 611 (1988)

7. H.R. Ott and A. Zehnder (eds), Proc. 6th Int. Workshop on Low Temperature Detectors, Nucl. Instr. Meth **A370**, 1996

8. M. Moe and P. Vogel, Annu. Rev. Nucl. Sci. **44**, 247-283 (1994), and references therein

9. H.V. Klapdor-Kleingrothaus, Double β decay, review, in: Neutrino 96, June 13-19, 1996, Helsinki, Finland, and to be published in the proceedings

10. E. Cosulich et al., Nucl. Phys. bf A592, 59 (1995)

11. D. MacCammon et al., Nucl. Phys. **A527**, 821c (1991)

12. A. Alessandrello et al., Astropart. Phys. **3**, 239 (1995)

13. J.N. Bahcall, The Central Temperature of the Sun can be Measured via the ^{7}Be Solar Neutrino Line, Astrophysics Preprint Series, IASSNS-AST 93/41, Sep. 93, Princeton

14. Nucl. Instr. Meth. **A320**, 388 (1992)

15. A. Alessandrello et al., Preliminary results on the performance of a TeO_2 thermal detector in a search for direct interactions of WIMPs, to be published in Phys. Lett. B

16. A. Alessandrello et al., Phys. Lett. **B335**, 519 (1994)

17. A. Alessandrello et al., Nucl. Phys. (proc. suppl.) **B48**, 238 (1996)

18. A. Alessandrello et al., Construction and characterization of Si thermistors for high resolution X-ray detectors, to be presented in: LT16, Praha, August 1996, and to be published in Czechoslovak Journal of Physics (Proc. Suppl.)

19. M. Buehler et al., Nucl. Instr. Meth. **A370**, 237 (1996)

20. R. Bernabei, Riv. Nuovo Cimento **18** n. 5 (1995)

21. A. de Bellefon et al., Nucl. Instr. Meth **A370**, 230 (1996)

22. A. Drukier and L. Stodolsky, Phys. Rev. **D30**, 2295 (1984)

23. T. Shutt et al., Phys. Rev. Lett. **69**, 3531 (1992)

24. A. Alessandrello et al., Nucl. Phys. (proc. suppl.) **B28A** 233 (1992)

25. P. Colling et al., Nucl. Instr. Meth. **A354**, 408 (1995)

26. P. Ferger et al., Phys. Lett. **323B** 95 (1994)

ascati Physics Series Vol. VI, (pp. 153–164)
: INT. CONF. ON CALORIMETRY IN HEP – Frascati, June 8–14, 1996

THE LIQUID ARGON TPC FOR THE ICARUS EXPERIMENT

Francesco PIETROPAOLO
Dipartimento di Fisica e INFN, Università di Padova, Via Marzolo 8, I–35131, Padova, Italy

ABSTRACT

ıe ICARUS project aims at the realisation of a large liquid argon TPC to be run at e underground Laboratories of Gran Sasso in Italy. An intense R&D activity has ıt on firm grounds this novel detector technology and experimentally confirmed, on few ton scale, its feasibility. Based on these solid achievements, the collaboration now confident of being capable to build and safely operate a multi-kton detector. he research program of the experiment involves the systematic study of a large ectrum of physical phenomena that covers many orders of magnitude in the energy posited in the detector: from the few MeV of solar neutrino interactions, to the out one GeV of the proton decay and atmospheric neutrinos, up to the higher ıergies of long baseline neutrinos from accelerators.

Introduction

HC is the main new enterprise in high energy physics, however its indent on the andard Model of Fundamental Interactions is necessarily limited by the proton nstituent energy $\simeq 1TeV$. In addition, the answers to some of the most funamental physics issues such as Grand Unification, new Symmetries (SUSY, etc.), osmology, lie beyond the Standard Model at an energy scale so high ($\simeq 10^{16}GeV$) be experimentally inaccessible to direct exploration.

A different experimental methodology must be introduced: propagator hysics has to replace direct observations. The detection of nucleon instability is robably the only way to explore experimentally the energy scale of Grand Unifiation. The situation is somehow analogous to the one of weak interactions. The ıasses of the W and Z gauge bosons are of the order of 90 GeV and we could observe them directly only at the big colliders during the eighties. Nevertheless almost all the properties of weak interactions were predicted in the first part of the century through the study of β-decay. Nucleon decay is likely to occur at some level; if experimentally observed it can be used to determine fundamental properties of Nature and the structure of the Unifying Gauge Theory at a scale of $\simeq 10^{-32} cm$.

From the experimental point of view, the challenge matches the importance of the issue. Because of the already very high limit on the núcleon lifetime ($\geq 10^{32} years$ in most of the decay channels), a modern proton decay detector should have a large sensitive mass (at least few kton). In addition, in order to separate efficiently the signal from the cosmic radiation induced background, this detector has to be operated underground and should have performances very similar to those of traditional bubble chambers. Namely: 1) it has to be able to provide high resolution, unbiased, three dimensional images of ionising events; 2) it has to accomplish simultaneously the two basic functions of target and detector. Unlike bubble chambers which were triggered blindly, were slow and for which the data analysis was difficult and fastidious, this detector should be fully and continuously sensitive, self-triggering and read-out without dead time.

We believe that the ICARUS Liquid Argon Time Projection Chamber represents the ideal detector for rare event search such as proton decay and neutrino interactions. In fact, this novel detector technology, first proposed by C. Rubbia [1] in 1977, combines the characteristics of a bubble chamber with the advantages of the electronic read-out: it is fully and continuously sensitive, self-triggering, able to provide three dimensional views of ionising events with particle identification from dE/dx and range measurement and can be operated over large active volumes. This detector is also a superb calorimeter of very fine granularity and high accuracy.

2 The ICARUS Liquid Argon Time Projection Chamber

2.1 The three ton Prototype

The first phase of the ICARUS program has been an intensive R&D program based on a reasonable scale prototype detector ($\simeq 3ton$) where the feasibility of the LAr TPC has been successfully verified by solving the main technological problems [2].
a) Argon purification. Liquid argon must be ultra pure even in the presence of a large number of feed-throughs for the signals and the high voltage and with wire chambers, cables, etc. in the clean volume. The contamination of electronegative molecules must be kept to around 0.1 ppb to allow drifts on long distances (metres) without capture of the ionisation electrons. This has been achieved using commercial gas purification system to remove oxygen and polar molecules (H_20, CO_2, fluorinated

ıd chlorinated compounds) combined with ultra-high-vacuum techniques to avoid contamination of the liquid through leaks and with the use of low degassing mate- ıls for the detector components. Electron lifetime higher then 3 ms ($\simeq 0.1 ppb$) are .sily and constantly reachable. Liquid phase purification allows fast filling of large :tectors. Continuous recirculation of the liquid through the purifier during normal)eration is used to keep the lifetime stable (against micro-leaks and degassing).

) Wire chambers. The wire chambers must be able to perform non-destructive ad-out with several wire planes with a few mm pitch; they must be built out of on-contaminating materials and must stand the thermal stress of going from room liquid argon temperatures; the precision and the reliability of the mechanics must e high and a good knowledge of the electric field in the detector must be granted.

) Analogue electronics. In order to obtain a good signal to noise ratio, very low noise ectron preamplifiers must be developed. Since the signal is very small ($\simeq$ 10.000 ectrons for a minimum ionising track in a 2 mm wire pitch) the equivalent noise ıarge must be less than 1000 electrons. This has been reached by means of j-FET :chnology. Since the noise depends on temperature and input capacitance, a further nprovement can been obtained placing the preamplifiers in liquid argon near the :nse wires.

) Data Acquisition. The ICARUS detector readout system behaves as a large ıulti-channel wave form recorder. The digital conversion is performed by means of 'AD's continuously active sampling at a rate 5 MHz. The system effectively stores he charge information collected by each sense wire during a time corresponding t least to the maximum drift time of the electrons (few milliseconds). The high esolution that has to be achieved, both in space and time sampling, brings the size f a single event to over hundreds of kilobytes. The useful signal occupies only a mall fraction of the data sample. Although in the initial phases of the experiment he complete information is useful for trouble shooting and debugging purposes, this ; the real bottleneck of the whole data taking system, overloading both the on-line nd off-line processing. To speed up the performances of the detector and reduce he dead times, a great effort has been devoted in the development of the software ırchitecture and the algorithms for data reduction.

The three ton prototype detector consists of a cylindrical dewar filled with iquid argon split vertically into two sections by a frame running along a diameter and ıolding two wire chambers. Each chamber supports two orthogonal read-out views vith 2 mm pitch and a total of 2000 electronic channels. They face, in opposite lirections, the active volume where a uniform electric field (max. 1 kV/cm) is ıpplied by means of field shaping electrodes. The maximum drift distance is 42 :m. A large amount of data has been collected with the 3 ton prototype, during

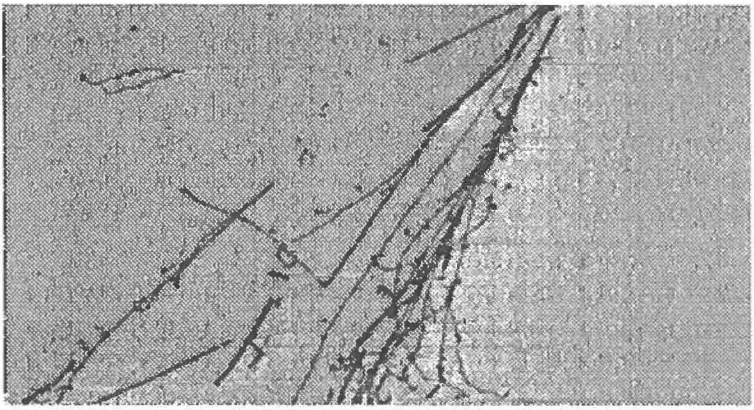

Figure 1: Electronic image of a cosmic ray shower as observed in the ICARUS 3-ton prototype at CERN. The drift direction is along the horizontal axis spanning a distance of about 40 cm. The vertical axis corresponds to 192 sense wires with a 2 mm pitch.

more than four years of operation, using cosmic rays and gamma rays sources to study the response of the detector to a wide range of energies (from a few MeV to several GeV). A good overview of the imaging capability of the LAr TPC is given by the cosmic ray electromagnetic/hadronic shower recorded with the 3 ton prototype and shown in figure 1. The quality of the image (approximately $40 \times 60cm^2$ wide) is of bubble chamber grade. The grey level of the pixels codes the pulse height, proportional to the collected charge. Very fine details of the event are noticeable: the electromagnetic shower is initiated by a γ ray, its conversion vertex is visible in the upper-right corner of the picture; a stopping pion decaying into a muon (whose kinetic energy of 3 MeV is deposited within one wire) that in turn decays into an electron are also visible, the increase in ionisation near the pion stopping point is evident; heavily ionising particles, probably low energy protons produced by neutron interactions, accompany the shower; a low energy pair is easily identifiable and measurable (top left); finally, the small black dots are not noise but real part of the event: they are Compton electrons with energy around 1 MeV.

The physical parameters characterising the detector have been found to be consistent with the expectation; their stability in time has been also extensively verified.

a) The electron lifetime was always above 4 ms corresponding to an attenuation length of more than 8 metres. As a consequence, drift distances of about two metres are reachable without major loss of drifting charge.

The electron diffusion coefficient, estimated from the width of signal rise time, is nsistent with the value foreseen for thermalised electrons ($4cm^2s^{-1}$). This means at a point-like charge, after two meters of drift, is spread over less than 1 mm mely less than the wire pitch. Hence the space resolution should not be seriously ected by this factor.

The electron drift velocity have been measured as a function of the electric field om 50 to 1000 V/cm. It is linearly dependent on the field up to 200 V/cm ($\mu =$ $E \simeq 500cm^2V^{-1}s^{-1}$) then it starts saturating ($v \simeq 2mm/\mu s$ at 1 kV/cm). The ee electron yield (i.e. the fraction of free electrons remaining along a minimum nising track after the electron-ion recombination) shows as well a slight dependence the fields (from 50 to 75% in the measured range). Both measures indicate that e working electric field can be chosen quite low with clear advantage for the high ltage system when drift of 2 metres are considered ($HV \simeq 100kV$).

2 Performance of the LAr TPC

he main results concerning the performance of the LAr TPC have been obtained rough the analysis of the wide variety of events occurring in the detector [3]. They n be summarised as follows.

) Space resolution. Through-going cosmic muons have been used to evaluate the ngle point space resolution along the drift co-ordinate (σ_z). Values of about $150\mu m$ re the norm and appear to be independent on the field in our range of intensities. nstead σ_z strongly depends on the signal to noise ratio ($\simeq 10$ in our case). Specific ests on small scale detector have shown that resolutions of less that $50\mu m$ are eachable with a signal to noise ratio of $\simeq 20$. The space resolution on the other wo co-ordinates are strictly related to the wire pitch (p): $\sigma_{x,y} \simeq \sqrt{12}p$.

) Energy resolution. Always by means of through-going minimum ionising muons e measured the distribution of the charge deposited over 2 mm. Its width is the onvolution of a Landau function with the gaussian electronic noise and is directly elated to resolution on the energy deposited by ionisation. A comparison with a est pulse distribution shows that the noise is the main contribution to the width. Hence an energy resolution of $\simeq 10\%$ over 2 mm track is the typical value in the 3 on prototype.

:) Energy resolution in the MeV range. It has been evaluated by studying the Comp- on spectrum and the pair production peak produced by a 4.43 MeV monochromatic gamma ray source placed outside the dewar. This spectrum has been fitted with a Monte Carlo simulation including, as a free parameter, a smearing caused by the detector response. The best fit gives a resolution of 7% at 4 MeV in agreement with the calorimetric measurement found in the literature.

d) Particle identification. This very important feature is directly related to the ability of measuring the dE/dx along the range of a stopping particle. A study of cosmic muons and protons stopping in the 3 ton prototype has shown that the charge deposited along the track is not proportional to the energy deposited because of the recombination effect that strongly depends on the ionisation density. This non-linear response may degrade the particle identification capability of the LAr TPC. A solution to recover linearity has been found and consists in dissolving in liquid argon a photosensitive dopant able to convert back the scintillation light (due to electron-ion ricombination) into into free electrons [4]. We chose tetra-methyl-germanium (TMG) as dopant mainly because it has a large photo-absorption cross section (62 Mbarn) and large quantum efficiency (close to 100%); this implies that small quantities of TMG will be enough to convert all the de-excitation photons into electrons in the vicinity of the ionising track (without spoiling the space resolution). Few ppm of TMG are required to linearize completely the dQ/dx vs. dE/dx relation.

3 The ICARUS Physics Program

The successful completion of the ICARUS R&D program demonstrating the feasibility of a large volume LAr TPC allows the collaboration to proceed to the following phases namely the engineering and the construction of a multi-kiloton detector to be run at the Gran Sasso underground laboratories optimised to study the wide class of events foreseen by the ICARUS scientific program [5]. Figure 2 is an artist's view of the detector principle. In the following the physics program addressed with the final 5 kton ICARUS detector at Gran Sasso will be reviewed. The priority goes to two main fundamental issues: the stability of the nucleon and the nature of neutrinos.

3.1 Proton Decay

Proton decay experiments with dedicated detectors started in the early 1980's, mainly motivated by the SU(5) GUT which predicted a lifetime of $10^{31} years$ for the dominant decay mode $p \rightarrow e^+\pi^0$. Being this channel easily identifiable, few years of data taking were sufficient to extend the proton lifetime limit to a few times $10^{32} years$ thus ruling out the SU(5) model and, at the same time, exhausting the range of the experiments. A new generation of experiments is therefore needed to explore the region of interest as predicted by SUSY GUT. This may start as low as $10^{31} years$ if channels such as $p \rightarrow e^+\nu\bar{\nu}$ exist and extend up to $10^{35} years$ if the dominant decay mode is $p \rightarrow \bar{\nu}K^+$.

ICARUS seems to be the ideal device for nucleon decay detection in particular for those channels that are not accessible to Cerenkov detectors due to the

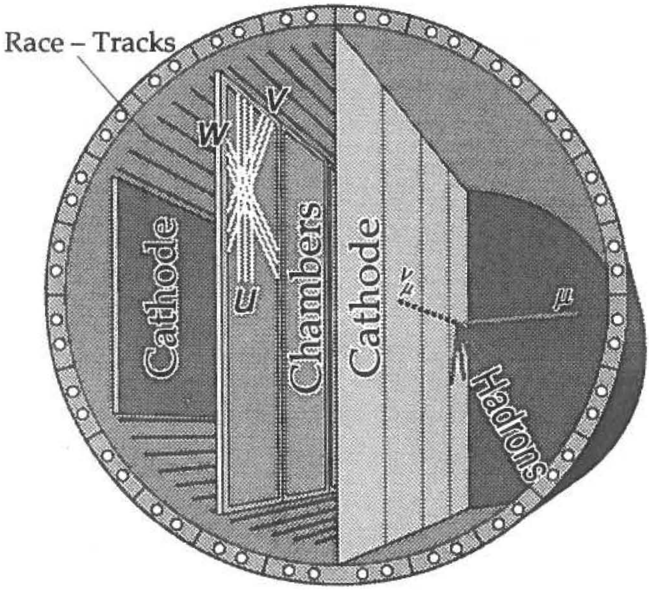

Figure 2: Artist's view of the ICARUS LAr TPC at Gran Sasso.

omplicated event topology or because the emitted particles are below the Cerenkov hreshold (e.g. charged kaons). Unlike the other large detectors for proton decay, CARUS can perform exclusive measurements thanks to its excellent tracking and article identification capabilities, thus providing a much more powerful background ejection. In particular it is possible to distinguish between atmospheric neutrino vents and true nucleon decays. See for instance the spectacular simulation of the USY preferred decay mode of the proton $p \rightarrow \bar{\nu}K^+$ displayed in figure 3. We can bserve the increase in ionisation density by the K^+ as it comes to rest. There is o ambiguity in the direction of the particles along their trajectory. The energy of ach particle is precisely measured. The K^+ identification is unambiguous due to he ability of measuring dE/dx vs. range.

It is easy to understand that, under such conditions, proton decays can clearly be identified event per event and it is not necessary to rely on statistical nethods to extract a signal.

In ten years of operation, ICARUS (5 kton) will be able to reach a proton ifetime limit of $5 \cdot 10^{33} years$ for the $p \rightarrow \bar{\nu}K^+$ decay mode. This will increase the present limit by nearly two order of magnitude. However, since for this particular channel the discovery requires only one event, because of the negligible background,

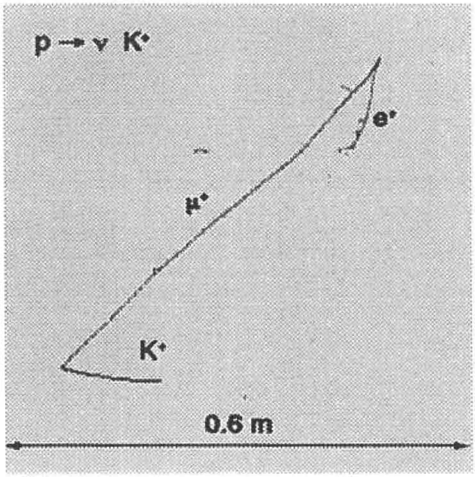

Figure 3: Simulated proton decay in the SUSY preferred channel $p \rightarrow \bar{\nu}K^{+}$ as it will be observed in the ICARUS LAr TPC.

a lifetime of $10^{34}years$ is accessible. In a similar way, many other exclusive channels can be searched for, both for proton and neutron decays; for most of them the present limit will be exceeded after only one year of data taking and in ten years the unexplored region between 10^{33} and $10^{34}years$ will be reached.

3.2 Atmospheric Neutrino Studies

The search for neutrino oscillation using the flux of atmospheric neutrinos has been pioneered by the Kamiokande experiment. These neutrinos are produced in the atmosphere by the interaction of primary cosmic rays with air nuclei, via the subsequent decay of $\pi's$, $K's$ and $\mu's$ (ν_e are twice as abundant as ν_μ). Kamiokande II and IMB (both water Cerenkov detectors) observed an anomaly in the contained charged current neutrino event samples. The ratio of muons to electron, measured by both experiments, is smaller by $\simeq 40\%$ than what is predicted by several theoretical calculations. The simplest and often made hypothesis is that the contained events anomaly is explained through ($\nu_\mu \leftrightarrow \nu_{\tau,e}$) oscillations. Other experiments such as Nusex and Frejus, adopting a different experimental technique, do not see this effect.

ICARUS can contribute to clarify this crucial issue. The LAr TPC technique is perfectly suited to provide high electron to muon discrimination, precise energy measurement and good neutrino direction reconstruction especially at the

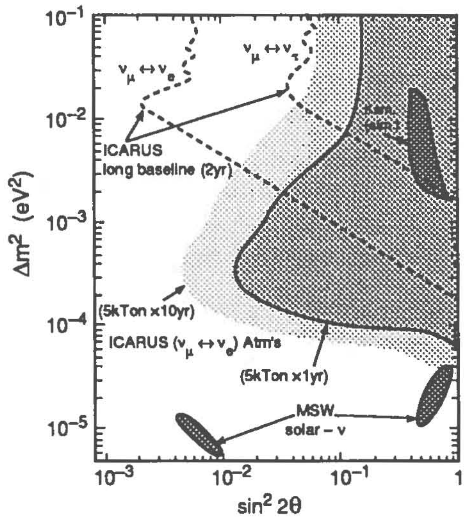

gure 4: ICARUS sensitivity to neutrino oscillation using atmospheric neutrinos. ıe shaded regions are escluded at 90% CL and correspond to 1 and 10 years of posure of ICARUS 5 kton. Long baseline sensitivity is also shown for 2 years of posure.

ergy scale of atmospheric neutrinos (less than few GeV) where the event topology nsists mainly of isolated, contained tracks. The unambiguous separation between ›ward-going neutrinos and downward-going neutrinos will allow to exploit effec- vely the long baseline range (up to 12000 km) provided by the earth to study $\leftrightarrow \nu_e$, $\nu_\mu \leftrightarrow \nu_\tau$ and $\nu_e \leftrightarrow \nu_\tau$ oscillations.

ICARUS can detect neutrino interactions down to the energy threshold for ıarged current reactions on argon nuclei (about 25 MeV for ν_e and 120 MeV for ν_μ). his allows to collect the full atmospheric neutrino statistics of about 1200 event ɜr year per 5 kton in 4π steradians, assuming no oscillations. The corresponding nsitivity to neutrino oscillations extends to Δm^2 values as low as $\simeq 10^{-4} eV^2$, ›vering abundantly the region in the parameter space allowed by Kamiokande and ΛB (figure 4).

3 Long Baseline Neutrino Oscillations

ne interesting complementary way to study neutrino oscillations is to use an arti- cial neutrino beam and to extend the baseline outside the limits of the laboratory. feasibility study [6] has shown that it is possible to send a CERN ν_μ beam to ran Sasso which happens to lie in a favourable azimuthal direction, at a distance 732 km, taking advantage of a planned LHC beam transfer gallery.

The configuration of the CERN neutrino beam pointing to Gran Sasso will be similar to the one presently working for short baseline. Namely, it will be a wide band ν_μ beam with mean energy of about 30 GeV and a ν_e contamination lower than 1%. The number of charged current neutrino events in ICARUS 5 kton has been calculated to be around 13000 per year. Given this sufficiently high statistics, several independent methods can be used to test neutrino oscillations.

The most sensitive and better suited to the ICARUS LAr TPC technology is an appearance method that consists in identifying only the quasi-elastic events with an electron and a proton in the final state. In two years of data taking only 1 event from the ν_e contamination is foreseen against about 280 ν_μ events. Hence an excess of interactions with the above topology could be explained as $\nu_\mu \leftrightarrow \nu_e$ or $\nu_\mu \leftrightarrow \nu_\tau$ oscillations. Since these events are completely reconstructible, their kinematics can be exploited to distinguish unambiguously between the two hypotheses: in the ν_e case the kinematics is quasi-elastic, in the ν_τ case there is transverse momentum unbalance due to the two missing neutrino from the decay $\tau \rightarrow e\nu\bar{\nu}$. The sensitivity that can be reached with this method is shown in figure 4. The Kamiokande allowed area is covered with a tool that leaves no space to possible ambiguous interpretations. Moreover disappearance methods, like the NC to CC ratio, can be used to confirm the result because they also reach similar level of sensitivity.

3.4 Solar Neutrinos

Solar neutrinos are particularly interesting because the study of their flux and flavour composition is up to now the most effective way to test the theory of resonant flavour mixing in dense matter (the so-called MSW effect). The four existing solar neutrino experiments (GALLEX, SAGE, Homestake, Kamiokande) claim a deficit in the solar neutrino flux respect to the predictions of the most popular solar models but at different levels. Their data could be interpreted in terms of flavour oscillations if one assumes the MSW effect.

Two solutions are at present allowed in the oscillation parameters space: both have a central value of $\Delta m^2 \simeq 10^{-5} eV^2$ but one is at small mixing angle (non-adiabatic solution at $sin^2(2\theta) \simeq 7 \cdot 10^{-3}$) while the other prefers a large vacuum mixing (adiabatic solution at $sin^2(2\theta) \simeq 0.6$). The non-adiabatic solution has a better χ^2.

ICARUS will detect solar neutrino interactions in real time with two different reactions: elastic scattering and absorption on Ar nuclei. The signatures are quite clear: an electron pointing in the forward direction for the first and an electron accompanied by few MeV $\gamma's$ from the de- excitation of the remnant nucleus (^{40}K) for the second. The detection threshold is likely to be around 5 MeV depending on the level of the radioactive background (detailed study are underway); for this ιson ICARUS will be sensitive only to ^8B neutrino in the same energy range where ιmiokande claims a flux deficit of about 50%.

Since the absorption process is allowed only to ν_e, while the elastic scat- :ing is permitted also to ν_μ and ν_τ (although with smaller cross sections), we have e possibility to measure simultaneously total flux and flavour composition of the utrinos from the sun. In particular the ratio (R) of the two reactions will be solar model independent tool to test neutrino oscillations. In one year of data king, ICARUS 5 kton should collect about 3000 events from both reactions. This ll be statistically sufficient to distinguish between the presently allowed solution the oscillation parameters space.

Conclusion

ıe R&D phase of ICARUS was extremely successful, demonstrating that a new ol for detecting cosmic and rare underground signals is available. The ICARUS Ar TPC is a truly modern version of the bubble chamber. The device can be iggered from the event information itself, it is continuously sensitive and a precise nisation measurement is improving the particle identification capability and is aking it possible to determine, in addition, the direction of particles.

The physics program, based on a multi-kiloton detector, is unique in that addresses, in an original way, several fundamental issues of modern high energy ıysics like proton decay and neutrino physics. The present strategy to reach the quired sensitive mass consists in proceeding through an intermediate size detector. his will allow to develop progressively at Gran Sasso the infrastructure needed to ıild and operate a large detector, the in situ experience needed in terms of safety, ιe definitive and practical evaluation of the engineering choices for the final phase. he most efficient and economical way to have this module operative is to assemble ıd test it outside the Laboratory and after move it inside. For this reason the .odule has to be transportable; this limits its size to about 600 ton.

The conceptual design of such a module is a straight forward extrapolation › larger volumes of the 3 ton prototype both from the mechanics and the electronics oint of views. Nevertheless great effort has been spent on the safety issues in order › foresee and minimise all possible accidents involving argon spills during filling ıd operation underground. Table 1 gives an overview of the main parameters of ıe 600 ton module [7].

Even if some interesting physics subjects will be studied with the 600 ton ıodule like proton decay in exotic channels or solar neutrinos (the detector mass similar to that of Kamiokande), the most important feature of this intermediate :ep is that it opens the possibility to explore an alternative route towards a larger

Table 1: Main parameter list of the 600 ton module.

Overall dimensions	$9.0 \times 6.2 \times 20.0m^3$
Total LAr mass	$600ton$
Sensitive mass	$530ton$
Number of independent drift volumes	4
Maximum high voltage (at 500 V/cm)	$82.5kV$
Number of co-ordinates per read-out plane	3
Pitch of the read-out electrodes	$3mm$
Total number of read-out channels	55000

detector: the construction of a number of identical modules installed next to each other to reach a final fiducial mass of $\simeq 5kton$. Equipped with such a powerful tool, we expect the ICARUS experiment to give, in the next few years, spectacular progress in the field of underground physics.

Acknowledgments

I am particularly grateful to the organisers of the ICCHEP '96 for giving me the opportunity to review the status of the ICARUS experiment.

References

1. C. Rubbia, CERN-EP Internal Report **77-8**, (1977).

2. A. Bettini *et al*, *Nucl. Instrum. Methods* A **305**, 177 (1991).
   A. Benetti *et al*, *Nucl. Instrum. Methods* A **331**, 395 (1993).
   A. Benetti *et al*, *Nucl. Instrum. Methods* A **333**, 567 (1993).
   A. Benetti *et al*, *Nucl. Instrum. Methods* A **346**, 550 (1994).

3. A. Benetti *et al*, *Nucl. Instrum. Methods* A **345**, 230 (1994).

4. A. Benetti *et al*, *Nucl. Instrum. Methods* A **355**, 660 (1995).

5. ICARUS Collaboration, *ICARUS II: A second generation Proton Decay Experiment and Neutrino Observatory at the Gran Sasso Laboratory*, Proposal, (LNGS-94/99 vol. I & II, 1994).

6. A.E. Ball, CERN-SL Internal Report **92-75**, (1992).

7. ICARUS Collaboration, *A first 600 ton ICARUS Detector installed at the Gran Sasso Laboratory*, Addendum to Proposal, (LNGS-95/10, 1995).

cati Physics Series Vol. VI, (pp. 165–170)
NT. CONF. ON CALORIMETRY IN HEP – Frascati, June 8–14, 1996

USE OF HEAVY FREONS IN GAS IONIZATION CALORIMETRY

.P. Denisov, A. Dushkin, Yu. Gilitsky, V. Mikhailin, V. Onuchim, I. Shein, A. Soldatos, V. Sytnik

Institute for High Energy Physics, Protvino, Russia.

ABSTRACT

e results of the first study of a gas ionization calorimeter filled with heavy freon C_3F_8 reported. C_3F_8 is a fast gas. Its density is 4.4 times higher than the density of the %Ar+10%CF_4 mixture previously used. The dependence of the calorimeter response C_3F_8 pressure is presented.

Introduction.

During the last 4 years extensive developments in gas ionization calorimetry have en made.[1)] In particular it was shown that hadron gas calorimeters with a planar ectrode geometry filled with 90%Ar+10%CF_4 gas mixture have a number of important vantages like good energy and time resolutions, high uniformity and stability, fine anularity, simple calibration, high intrinsic radiation resistance and low cost. The only sadvantage of these calorimeters is a high gas pressure necessary to reach a low enough vel of S/N ratio. One possible way to reduce the pressure is to use gases with higher nsities.

In this paper the results of the first study of a gas ionization calorimeter filled ith heavy freon C_3F_8 are reported. There are several reasons for the choice of C_3F_8 :

- its density is 4.4 times higher than the density of the 90%Ar+10%CF_4 mixture previously used,
- C_3F_8 is a fast gas; its electron drift velocity is close to those for a 90%Ar+10%CF_4 mixture and pure CF_4 ,
- C_3F_8 is nontoxic and nonflammable.

s saturated density and pressure at 20^0C are 0.075g/cm^3 and 7.57 atm.

Calorimeter.

The calorimeter tested consists of a stack of 12 ionization chambers interleaved vith a 30 mm thick steel absorbers (fig. 1). Signal pads of 1 mm steel were placed etween the absorbers forming two 3 mm drift gaps. There are 4 x 4 pads in the signal lane. Pad size is 76 x 76 mm^2 . The total calorimeter thickness is 21 r.l. The average r.l. s 2.1 cm and Molière radius is 1.5 cm.

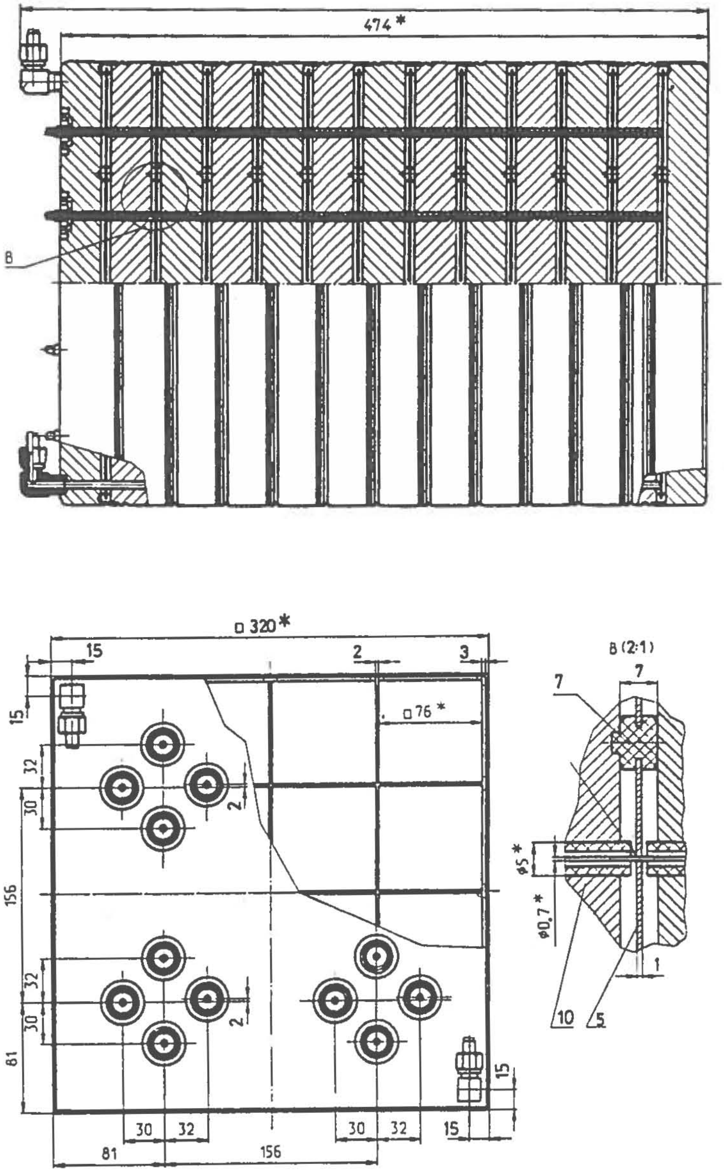

Fig.1. The calorimeter design.

Six consecutive pads were connected to each other forming two sections in each gitudinal tower. The absorbers were grounded and HV was applied to signal ctrodes. The ratio of HV to C_3F_8 pressure was 830 V/atm which gives an electron ft velocity of 0.07mm/ns. For comparison, a gas mixture of 90%Ar+10%CF_4 was o used at V/P = 185 V/atm (v_d=0.1 mm/ns). The calorimeter was designed to operate pressure up to 16 atm.

Signals from each section were connected to low noise amplifiers and then to)C's. ADC gates of 30, 59, 100 and 145 ns were used. A dependence of the noise 'el for one tower on the gate width is shown in fig. 2. The RMS of noise distribution : all 16 towers at t_g=59ns is equal to 80KeV which is to be expected for uncorrelated ise.

Measurements and results.

Measurements were performed with a 26.6 GeV/c electron beam at the 70 GeV IEP accelerator. The beam momentum spread was about 3% and hadron and muon ntamination was less than 4%. Five scintillation counters placed along the beam line ere used to measure the electron flux. The last counter of Ø 2 cm was positioned in ont of the calorimeter at the center of one of the towers. An anticoincidence counter ith Ø 3 cm hole was used to reject the background from beam halo.

The studies consisted in measuring a pulse height spectra at different values of V, ADC gate width and gas pressure. The gate delay was set at the signal maximum oise and calibration measurements were taken periodically.

The events satisfying the following criteria were selected for analysis :

- signals in any tower around the tower hit by beam electrons (beam tower) had to be less than 10% of the signal in the beam tower,
- signals in the forward section of the beam tower had to be higher than the signal in the backward one and the noise signal.

These criteria allow one to reject the events connected with muons, hadrons and eam halo.

In average more than 98% of energy of selected events were released in the beam ower. As most of the signals in the other channels were less than noise, only beam ower signals were used in data analysis.

Typical distribution of noise and EM shower pulse heights are presented in fig. 3. ll the spectra measured were fitted well by a Gaussian.

The dependencies of average pulse height A, on gas pressure P, and HV are hown in fig. 4,5. From fig. 5 it follows that for 90%Ar+10%CF_4 gas mixture, A is roportional to P up to 11 atm while for C_3F_8, A approaches plateau at pressures above l atm. The nonlinearity of the A vs P (C_3F_8) can be explained either by electronegativity of the C_3F_8 itself or by the electronegativity of the contaminations in the C_3F_8 .

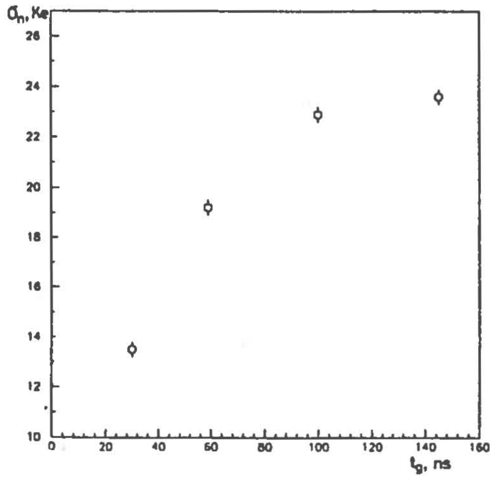

Fig.2. The RMS of noise distribution for one tower vs gate width.

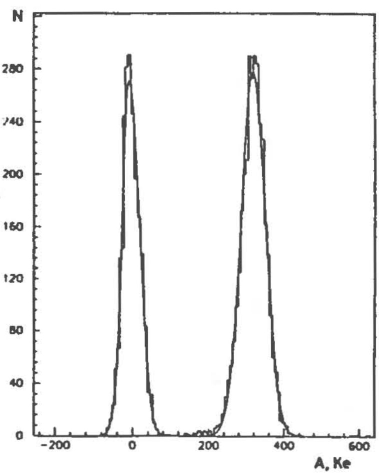

Fig.3. Noise and signal spectra measured at $t_g = 100$ ns and C_3F_8 pressure of 6 atm.

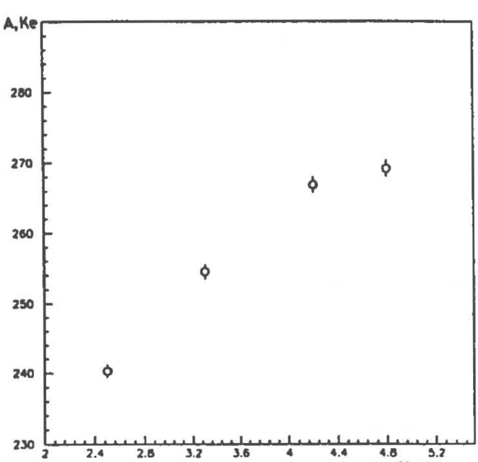

Fig.4. The average pulse height vs HV.

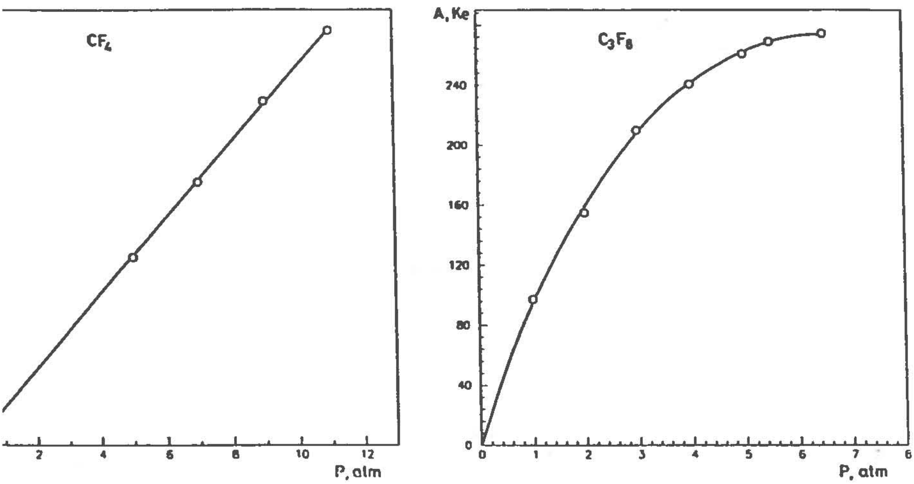

Fig.5. The average pulse height as a function of CF_4 and C_3F_8 pressure.

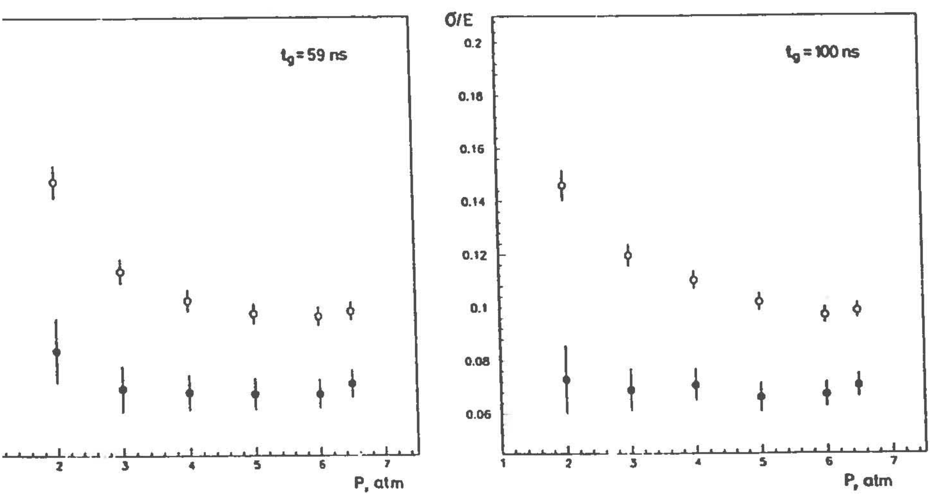

Fig.6. The dependence of the energy resolution on C_3F_8 pressure with (•) and without (○) noise subtraction for t_g =59 ns and 100 ns.

Fig.6. demonstrates that the energy resolution (after noise subtraction) does not depend on the C_3F_8 pressure in the range from 2 to 6.5 atm.

4 Conclusions

The first study of a gas ionization calorimeter filled with heavy freon C_3F_8 has been performed. The equivalent noise energy is equal to 2 GeV per tower at 4 atm of C_3F_8 pressure. The stochastic part of energy resolution is independent on gas pressure in the range of 2 to 6.5 atm. We plan to study the origin of the signal saturation at C_3F_8 pressures above 4 atm.

A detailed study of the gas ionization calorimetry performed during the last few years shows that this technique can play an important role in future experiments in high energy physics.

5 Acknowledgements.

We wish to thank N.Filimonov, A.Godov, V.Kostjuchenkov, O.Romashov and V.Volkov for their help in BARS assembling and testing. This work was partialy supported by Russian Fund for Basic Research (grant N 96-02-16856).

References.

1. S.P.Denisov et al., Nucl.Instr. and Meth. A335 (1993) 106
   N.D.Giokaris et al., Nucl.Instr. and Meth. A333 (1993) 364
   D.M.Khazins et al., Nucl.Instr. and Meth. A333 (1993) 372
   S.P.Denisov et al., in: Proc. fifth Intern.Conf. on Calorimetry in High Energy Physics (ed. H.A.Hordon and D.Rueger, BNL, September-October 1994) 380 (World Scientific, Singapore, 1995).
   S.L.Bagdasarov et al., in: Proc. fifth Intern.Conf. on Calorimetry in High Energy Physics (ed. H.A.Hordon and D.Rueger, BNL, September-October 1994) 388 (World Scientific, Singapore, 1995).

III – Sampling Calorimeters

Convener U. Goerlach
Secretary G. Cabibbo

ȝoerlach	Convener's Report
ouz	The Performance of the DELPHI Stic Detector at LEP
J. Llope	The Electromagnetic Calorimeter for the Solenoidal Tracker at RHIC
₹usack	A Lead–Liquid Scintillator "Shashlik" e.m. Calorimeter Prototype
Γaiuti	The CLAS Large Angle Calorimeter
J. Grabosch	The Presampler for the Forward and Rear Calorimeter in ZEUS
⁄Iaio	WLS Fibers for Calorimetry: Comparative Studies
. Gorelov	Recent Experience with the H1 Lead/Scintillating–Fibre Calorimeter
Incagli	Status Report on the Construction of the KLOE Calorimeter
⁄Iigliozzi	The CHORUS Calorimeter: Test Beam Results and Operation with Neutrino Beams
A. Pruneau	The E864 Lead/Scintillating Fiber Hadronic Calorimeter
Ɜavrilov	CMS Quartz Fiber Calorimetry
Wigmans	The Benefits of Extreme Non–Compensation
Musso	The Quartz Fibre Zero Degree Calorimeter of the NA50 Experiment at the CERN SPS
Bosman	The ATLAS Hadronic Tile Calorimeter
Henriques	Response of the ATLAS Tile Calorimeter to Muons
'reeman	The CMS Central Hadron Calorimeter

scati Physics Series Vol. VI, (pp. 173–175)
INT. CONF. ON CALORIMETRY IN HEP – Frascati, June 8–14, 1996

(Convener's Report)

SAMPLING CALORIMETERS

Ulrich Goerlach
Université Louis Pasteur et Centre de Recherches Nucléaires
23, rue du Loess, F-67200 Strasbourg, France

The technique of sampling calorimetry is today very well established within ɜ High Energy Physics community. In particular the non-cryogenic variant which the subject of the following session is the most commonly used concept for the nstruction of large-scale calorimeters.

Amongst the features which make this technique so attractive are its large xibility and variety to adopt the calorimeter to different geometries and perfor-ınces required by the experiment, and last but not least to the available funding. ıe choice of sampling fraction and frequency together with the characteristics of e passive and active materials allows to tune energy, spatial and time resolution thin a very wide range. This is equally true for both electromagnetic and hadronic lorimeters. Compensation, important for high resolution hadronic calorimetry can achieved by the proper choice of materials. Appropriate transverse and longitu-nal segmentation is relatively easy to achieve and allows powerful electron-hadron paration. The absence of bulky cryostats allows to master complicated geome-ies. A further attractive feature is also certainly, that much of the technological ıow-how can easily be managed even by small laboratories.

The active medium of a sampling calorimeter can be solid or liquid scin-lator, but also a gaseous detector. The latter variant has been used for example the DELPHI and ALEPH detectors at LEP, however no contribution along these ıes was submitted to this conference. The historically very successful concept of intillator plates, read-out with bars of wave-length-shifters is still used in many ɜtectors. However, during the last 10 years other schemes have been developed ısed on the progress made in the fabrication of optical fibers: The use of scintil-ting fibers as active medium, coupled directly to the light detection system (type

SPACAL) or the use of wave-length shifting fibers embedded into the scintillator to transport the light to the photon detector (tile- and shashlik-type calorimeters).

These technologies are well-established and under control. They play a fundamental role in nowadays High Energy Physics experiments. Today, the focus of interest is concentrated on the refinement of the technologies, the system performances achieved, and to explore the limits of the technology. Not too surprisingly, the larger fraction of contributions submitted to this session fall in this category: reports on experiences with running detectors, the special optimisation for a given experiment (STAR and CLAS) and physics goal. Scintillating fiber calorimeters for H1(DESY), CHORUS(CERN), E864(BNL) and KLOE(DAΦNE), shashliks for DELPHI(LEP) and LHC, even a liquid shashlik, so far impossible to order in a restaurant.

With the upcoming large experiments at LHC a new aspect entered the engineering of calorimeters, in particular for the hadron calorimeters: size! Both, the ATLAS and the CMS collaboration, use scintillating tiles read by wave-length shifting fibers, but in different mechanical arrangements. The challenge is to construct many large modules several meters in length and to control their parameters like uniformity, resolution and calibration to sufficient precision.

The particular problem of very high particle densities and radiation levels in the forward region of the future LHC detectors leads to an interesting case of spaghetti calorimetry: quartz-fiber calorimeters. Pioneered by the RD40 and NA50 collaborations this type of calorimeter found its place as the forward calorimeter of the CMS detector.

Exploiting only the Cerenkov light induced inside the quartz fibers the effective electromagnetic and hadronic shower size becomes very small; only the very relativistic shower particles produce sufficient light to contribute. The loss of photon statistics is not a problem at these high energies. Interesting enough, compensation, once by some of us advocated as the MUST in calorimetry, is not a feature of quartz fiber calorimeters; they are extremely non-compensating! A Paulus (at least one) became a Saulus!

Frequently the very good test beam performance of calorimeter-builders is "sabotaged" by their colleagues of inner tracking detector systems being forced to place mechanical supports, cooling pipes and cables in front of the calorimeters. Additional devices have been invented to overcome these hazards; for example the pre-sampler of the ZEUS detector. Not only could they recover to a large extent their energy resolution, but also could they reconstruct from the data the location of supports, cable bunches etc..

In summary, the papers you will find on the following pages and to which I 'er with my remarks above, address todays problems in constructing (large) non-/ogenic sampling calorimeter systems: adaptation to the specific requirements of eir experiment, achieved performances and their control in the experiments. Fur-er topics are the new aspects related to the large dimensions of LHC experiments d the particularities of the very forward rapidity regions mastered by the now dolescent" technology of quartz-fiber calorimeters.

You'll find many interesting discussions of todays performances and chal-iges in building calorimeters. You will not find revolutionary, unheard of, inven-ns of new technologies. Today, the progress is in the direction of mastering large lorimeter systems.

cknowledgments

is a pleasure to thank Stefano Miscetti for helping me efficiently to organize this ssion on sampling calorimeters. I would also like to thank Franco L. Fabbri and his lleagues for smoothly organizing this enjoyable conference at Frascati.

ıscati Physics Series Vol. VI, (pp. 177–186)
INT. CONF. ON CALORIMETRY IN HEP – Frascati, June 8–14, 1996

ΗΕ PERFORMANCE OF THE DELPHI STIC DETECTOR AT LEP

Presented by I.Gouz[1]
INFN Turin, Italy

ABSTRACT

ıe STIC detector, installed in DELPHI during 1994, is a lead-scintillator calorime-·, segmented into towers projective to the interaction point. The light is collected WLS fibers running perpendicularly to the sampling planes and it is read out by ototetrodes (Hamamatsu R2149), which can operate inside the magnetic field of ! T. The main goal of the calorimeter is to measure the luminosity with an accu-:y better than 0.1% and to obtain this, the detector had to be built with a very ʒh mechanical precision. The detector is equipped with two planes of the silicon ower maximum detectors, placed at a depth of 4.0 and 7.4 radiation lengths. The rformance of the calorimeter during the 1994-95 data taking is discussed in detail. rst results from silicon detectors operation at LEP are also presented.

[1]S.J. Alvsvaag, O.A. Maeland, A. Klovning
Department of Physics, University of Bergen, Bergen, Norway
A.C. Benvenuti, V. Giordano, M. Guerzoni, F.L. Navarria, A. Perrotta
Dipartimento di Fisica, Università di Bologna and INFN, Bologna, Italy
T. Camporesi, V. Obraztsov*, M. Paganoni, E. Vallazza
CERN, European Organization for Nuclear Research; Geneva, Switzerland
M. Bozzo, R. Cereseto
Dipartimento di Fisica, Università di Genova and INFN, Genoa, Italy
G. Barreira, M.C. Espirito Santo, A. Maio, A. Onofre, L. Peralta, M. Pimenta, B. Tome
LIP and IST-FCUL Coimbra and Lisbon, Portugal
H. Carling, E. Falk, V. Hedberg, G. Jarlskog, I. Kronkvist
Department of Physics, University of Lund, Lund, Sweden
M. Bonesini, F. Chignoli, P. Ferrari, S. Gumenyuk*, R. Leoni, R. Mazza, P. Negri, L. Petrovykh*, F. Terranova
Dipartimento di Fisica, Università di Milano and INFN, Milan, Italy
D.R. Dharmasiri, B. Nossum, A. L. Read, B. Skaali
Physics Department, University of Oslo, Oslo, Norway
L. Castellani, M. Pegoraro
Dipartimento di Fisica, Università di Padova and INFN, Italy, Padua,Italy
A. Fenyuk, I. Ivanyushenkov, A. Karyukhin, A. Konopliannikov, N. Shalanda, V. Sen'ko, E. Vlasov, A. Zaitsev
Institute for High Energy Physics, Protvino, Russian Federation
M. Bigi, V. Cassio, D. Gamba, I. Gouz*, E. Migliore, A. Romero, L. Simonetti, P.P. Trapani
Dipartimento di Fisica, Università di Torino and INFN, Turin, Italy
M. Bari, G. Della Ricca, L. Lanceri, P. Poropat, M. Prest
Dipartimento di Fisica, Università di Trieste and INFN, Trieste, Italy

* On leave of absence from IHEP, Protvino, Russian Federation

1 Introduction

At the beginning of 1994 the DELPHI collaboration installed a new electromagnetic calorimeter named STIC (Small angle TIle Calorimeter) [1], with the aim of providing a luminosity measurement with an accuracy of 0.1% at LEP I, and improving the hermeticity and energy resolution in the very forward region for the LEP II phase. The STIC detector consists of 3 subdetectors: the calorimeter itself [2], the silicon shower maximum detector [3] and the scintillator hodoscope (VETO) [2]. This paper reports on the operation of all the three subdetectors during the 1994-95 data taking.

The precision of the mechanical structure, a good energy and position resolution, and a uniform response are the most relevant features of the STIC in order to select, with high efficiency and well known acceptance, the sample of Bhabha events at low angles.

Up to now about four million Bhabha events were detected inside the STIC acceptance (2.4 million in 1994 and 1.6 million in 1995). The calorimeter was very stable and reliable and met all the requirements necessary for achieving the design accuracy in the luminosity measurement.

The silicon shower maximum detector started operating at the end of 1995 LEP run. Its performance is in agreement with design requirements.

2 The STIC calorimeter

The STIC calorimeter (see Fig.1) is made of two independent cylinders (called A and C) located at $\pm$ 2.2 m from the interaction point, covering the regions from 29 to 185 mrad around the two arms of the beamline. Each cylinder in turn consists of two independent half-cylinders around the beam pipe.

The calorimeter is composed of 47 layers, each made of a 3.4 mm thick continuous converter plane (lead reinforced by 100 μm steel foils) followed by 3 mm thick scintillator tiles, for a total depth of 27 X_0. The tiles are optically isolated from each other by 120 μm thick white Tyvek[1] and mounted on the converter planes by precision pins with a mechanical accuracy of 50 μm. The tiles form a radial structure (10 rings of 3 cm width[2] and 16 sectors), which is projective to the interaction point. The light readout is done by WLS fibers running perpendicularly to the planes through the holes drilled (punched) in the tiles (converter) [4, 5]. The density of the fibers is about 0.8 per cm^2. The towers are twisted in the ϕ direction by $\approx 3°$ in order to avoid pointing cracks to the interaction point and channelling of particles

[1] *Tyvek*® is Du Pont's registered trademark.
[2] Except for the first, 3.5 cm, and last, 7.8 cm

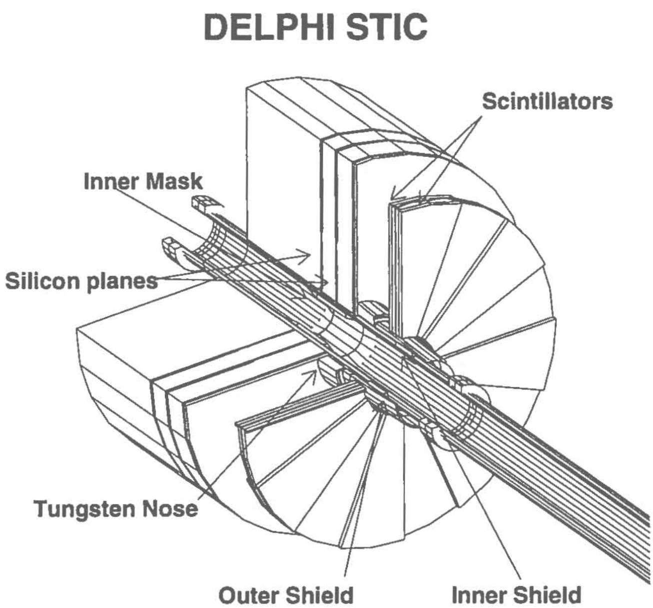

Figure 1: The general view of one arm of the STIC calorimeter

the WLS fibers.

The light readout inside the DELPHI magnetic field (1.2 T) is performed ing Hamamatsu 1" R2149-03 tetrodes. Their behaviour was studied in detail at e superconducting solenoid SOLEMI-1 (LASA laboratory, INFN-Milano), showing average gain of about 19 in the magnetic field and about 30 outside the magnetic ld [6]. For details of the calorimeter construction and components see [7] and ferences therein.

In order to achieve a good energy resolution, a precise knowledge of the lorimeter characteristics is required, including a follow-up of their possible changes th time. The time dependence of the energy response of the calorimeter to Bhabha ectrons, obtained by using the same set of calibration coefficients for all the data, shown in Fig.2. A reduction of about 2 % per year is observed. The origins of is ageing effect are currently under investigation. A possible explanation is the diation damage of the scintillator and/or fibers due to the synchrotron radiation. order to correct for the ageing effect, the calorimeter was calibrated approximately ice per month, using a sample of non-radiative Bhabha events, which deposit

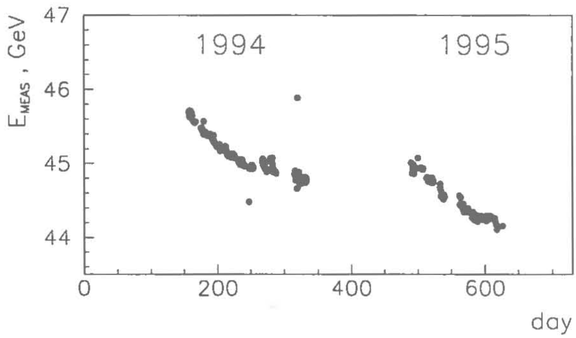

Figure 2: The calorimeter energy response to Bhabhas at LEP I versus time.

known amount of energy in the calorimeter [8].

The energy response of shashlik-type calorimeters usually depends on the impact point of the incoming particle. The R-ϕ dependence of the energy response of one STIC tower to non-radiative Bhabha events is shown in Fig.3 as a function of reconstructed position of the shower. The bumps at the picture correspond to the positions of WLS fibers. The size of the position dependence of energy response varies from $\pm 2\%$ in the inner part of the calorimeter to $\pm 8\%$ in the outer part, where, due to the radial structure of the calorimeter, towers are large in the ϕ direction. For the purpose of the energy reconstruction, these non-uniformities can be easily corrected for by mapping. The correction function E(R,ϕ) was calculated by averaging over the 8 sectors of each half-cylinder of STIC.

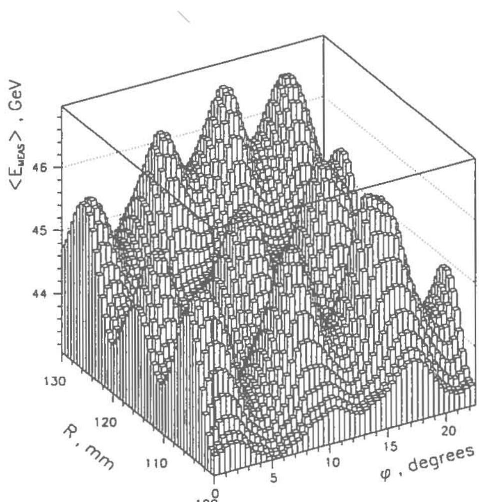

Figure 3: Energy response to 45.6 GeV electrons versus impact point.

During 1994 and 1995 both sides of the STIC calorimeter were affected common mode noise due to electromagnetic disturbances caused mainly by the ɔtors of the LEP collimators. The direct calculation of the correlation coefficients · the common noise showed that it is almost fully correlated for all the 80 towers a half-cylinder module. As the electromagnetic showers occupy, on average, 10- towers, we were able to measure for each module, on an event by event basis, e value of the common noise to be subtracted. This procedure of common noise btraction improves by 10% the energy resolution for 45 GeV showers and, what is ɔre important, it strongly reduces the non-gaussian tails in the energy distribution.

The dependence of the energy resolution on the radial position, before and ;er non-uniformity correction and coherent noise subtraction, is shown in Fig.4. ɪe average energy resolution for non-radiative Bhabha events, distributed as $1/R^3$, ɪs measured to be 2.7%.

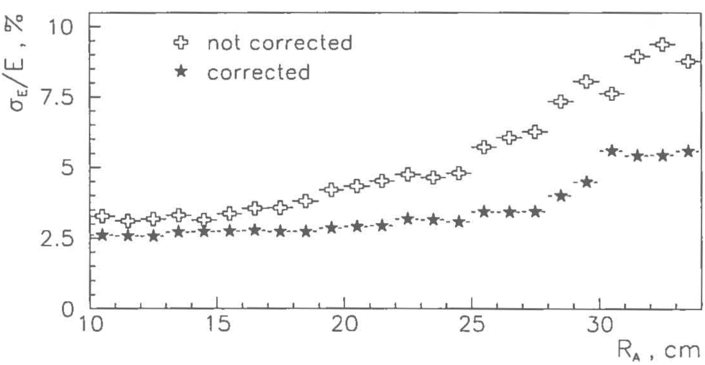

igure 4: Energy resolution vs radius (side A) before and after corrections, for habha events at LEP I .

Both the radius (R) and the azimuthal angle (ϕ) of the impact point of ɪe shower can be measured on the basis of the sharing of the deposited energy ɜtween nearby calorimeter towers. The precision of the radius reconstruction is ɜry important for the luminosity measurement.

The Bhabha events are particularly well suited for achieving a good ra- ial resolution, because all the particles have approximately the same energy and riginate from the interaction point, so that at each radius the angle at which the articles hit the calorimeter is always the same. Consequently, all the events at the ɪme radial position have similar shower profiles. Furthermore, due to the projec- vity of the STIC towers, the reconstructed radius is not sensitive to longitudinal uctuations in the development of the shower. The measurement of the radial position of the shower was performed by means of the reconstruction of its distance from the nearby border between rings of calorimeter towers. The distances d_k with respect to the border between rings k and $k+1$ were parametrized as function of the estimator

$$\epsilon = \ln \frac{\sum_{i=1}^{k} E_i}{\sum_{i=k+1}^{N_{rings}} E_i} \tag{1}$$

where E_i are measured energy depositions in the ring i. The functions $d_k(\epsilon)$ were calculated for each border by using data taken at a testbeam where the point at which the particle was entering the STIC was precisely measured by means of a silicon microstrip telescope. In order to achieve better resolution in the middle of the ring, we combined the two measurements with respect to the two ring borders delimiting the ring with the maximum energy deposition.

The resolution of the radial reconstruction, calculated for the testbeam data (see Fig.5), is not uniform and varies from 0.25 mm in the narrow region (± 2 mm) around ring borders up to 1.2 mm in the central regions of the rings.

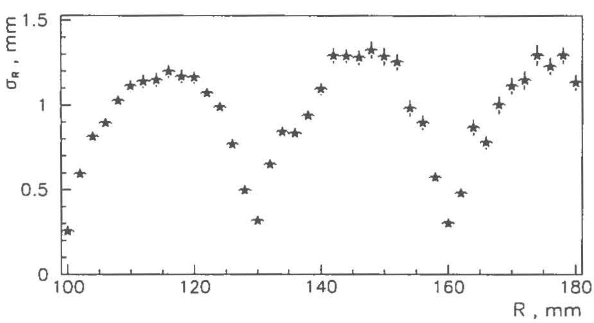

Figure 5: The radial resolution of the calorimeter vs radius.

The ϕ reconstruction algorithm is based on the shower energy sharing at the border between nearby sectors. We calculated the linear distance from the impact point to a border between sectors k and $k+1$ on the basis of an estimator similar to (1). Then, using the radius measured for this shower, we calculated the ϕ coordinate.

3 Interaction point measurement by STIC

The possibility of an independent determination of the IP position by STIC is important for reducing the systematic error in the luminosity measurements.

The IP position is reconstructed, on a fill by fill basis, by minimizing the quantity $\sum_{k=1}^{N_B} d_k^2$, where d_k is the distance from the IP to the straight line

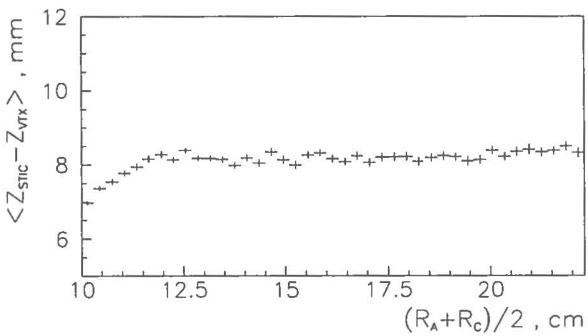

igure 6: The difference between z position of IP measured by STIC and the mi-overtex detector versus $\bar{R}$.

onnecting showers on both sides and N_B is the number of Bhabhas from one fill. sample of nonradiative Bhabha events selected by a tight energy cut was used for ie calculations. A small correction is applied to take into account the effect of the iagnetic field.

The comparison of the IP coordinates measured by STIC and the DELPHI iicrovertex detector gives:

$$\begin{aligned} \sigma(X_{IP}^{STIC} - X_{IP}^{MVTX}) &= 20\ \mu m \\ \sigma(Y_{IP}^{STIC} - Y_{IP}^{MVTX}) &= 60\ \mu m \\ \sigma(Z_{IP}^{STIC} - Z_{IP}^{MVTX}) &= 280\ \mu m \end{aligned} \tag{2}$$

'he most significant for the luminosity measurements is to reduce the systematic rror im z_{IP}, which means an accurate control of systematics in the radial reconstruc-on over the full STIC surface. In order to check this, we performed z_{IP} calculations electing Bhabha events in narrow intervals in the variable $\bar{R} = (R_A + R_C)/2$. Fig.6 iows the dependence of $z_{IP}^{STIC} - z_{IP}^{MVTX}$ on $\bar{R}$. It can be seen that for the region $\bar{R} > 12$ cm the systematics are below $\pm$ 0.3mm, corresponding to the systematics i the radius measurements of $\pm 40\ \mu$m.

The VETO hodoscope

'he scintillation hodoscope is installed in front of the STIC calorimeter, with the im of separating charged and neutral particle, and in particular of triggering the adiative return ($e^+e^- \rightarrow Z^0\gamma$) events at LEP II.

The STIC Veto System consists of 64 trapezoidal counters assembled into our planes, two on each side (Fig.1). The counters are made of 10 mm thick plastic scintillator. The light is collected by 8 WLS fibers glued in a groove machined on each side of the scintillator. The type of WLS fibers is the same as for the calorimeter. The top and bottom edge of the counter are coated with a reflector paint. The scintillator is wrapped with Tyvek to improve light collection. The light is read out by a 10 stage Hamamatsu H3165 photomultiplier located outside the DELPHI magnetic field. The photomultiplier is coupled to the counter via a 10 m long fiber optic cable made of 16 Kuraray clear PST 1 mm diameter fibers. The average response of a counter is ~ 32 photoelectrons/MIP (~ 20 p.e./MIP after the optical cable).

The efficiency of the hodoscope to charged particles was measured to be better than 96%, with the noise rate of less than 2% for all the 64 counters. The photon tagging efficiency is determined by the material in front of the detector (mainly in the vacuum pipe which is crossed at low angle) and was measured to be $\sim 55 \pm 10\%$ during the 130 GeV run in 1995.

5 The silicon shower maximum detector

For mechanical reasons, it is difficult to have longitudinal segmentation in shashlik-type calorimeters. Each arm of the STIC calorimeter is instead equipped with two planes of silicon shower maximum detectors [3], for the following reasons:

- it gives a shower axis reconstruction with ~10 mrad accuracy, which is important for the off-momentum background rejection at LEP II;
- improved $e - \pi$ separation;
- improved coordinate resolution and two shower separation;
- cross-check of the STIC calorimeter in the definition of the acceptance for the luminosity measurements.

The silicon planes are positioned at a depth of 4 and 7.4 radiation lengths inside the calorimeter and cover the angular region between 32.5 and 79 mrad. The two planes are slightly different to match the projective geometry of the STIC calorimeter. The most unusual feature of their mechanical design is the presence of laser cut holes, to let the WLS fibers of the STIC calorimeter go through.

Each silicon detector is made of 300 μm thick, high resistivity n-type silicon, with p-type strips implanted on the front and a n^+ layer on the back. The strips cover 22.5^o in ϕ and have a radial pitch of 1.712 mm (1.754 mm) for the first (second) plane. Each sector has 60 strips. The strips are biased by means of a

XFET scheme and AC coupled to the readout. Signals are carried to the front-
l electronics by 35 cm long flat Kapton cables. Every two sectors are read out
MX4 Microplex chip 9) which consists of a 128 channels charge amplifier array
h multiplexed output [3].

A sample of non-radiative Bhabha events was selected for the studies of
silicon detector performance. A signal/noise ratio of about 40 was obtained for
GeV electrons in the strip with the maximum signal.

Fig.7 shows, for the Bhabha sample, the distribution of the difference be-
een the asimuthal angle of the shower axis calculated by means of the silicon
nes and the azimuthal angle of the track calculated with the assumption that it
ginates at the beam interaction point, as expected for Bhabha events. The fit
es a precision of the shower axis reconstruction of $\simeq$ 13 mrad.

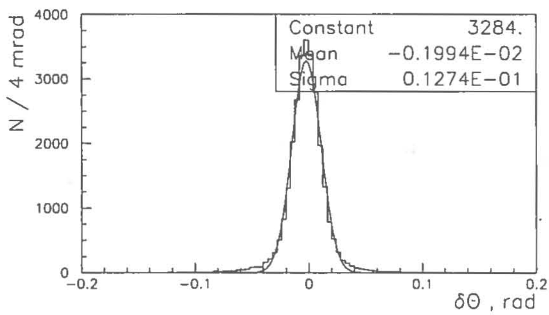

Figure 7: The resolution of the shower axis reconstruction by silicon planes.

An example of two shower separation in the silicon detector is given in
g.8. In this radiative Bhabha event ($e^+e^- \rightarrow e^+e^-\gamma$), the two showers, from the
and the γ, are well separated in the silicon plane, while merged to one cluster in
calorimeter.

Conclusions

e STIC calorimeter has been operating at LEP since 1994 and satisfied the design
quirements with a radial position resolution between 250 μm and 1.2 mm and
energy resolution of 2.7% for 45 GeV electrons at LEP. The first results from
e silicon shower maximum detector at LEP show the precision of the shower axis
construction of $\simeq$ 13 mrad.

[3]manufactured by Rutherford Appleton Laboratories (UK)

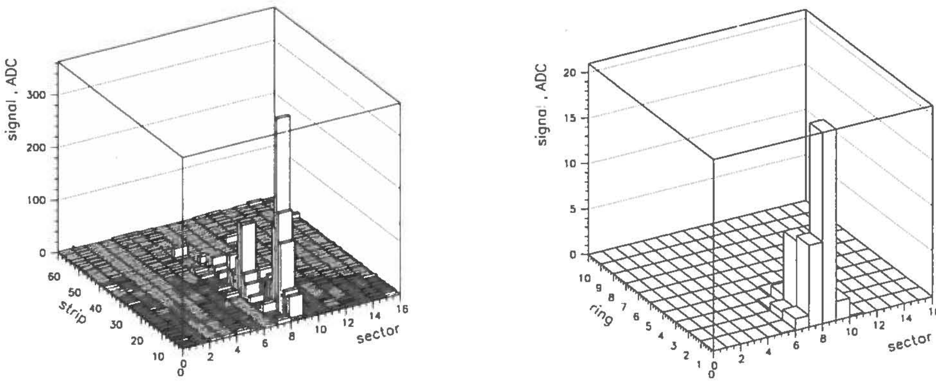

Figure 8: The two close showers are well separated in the silicon plane (left) and not separated in the calorimeter (right).

References

1. The DELPHI Collaboration, preprint CERN-LEPC/92-6

2. S.J.Alvsvaag et al., IEEE Trans. Nucl. Sci. **42** (4), 478 (1995).

3. S.J.Alvsvaag et al., IEEE Trans. Nucl. Sci. **42** (4), 469 (1995).
   S.J. Alvsvaag et al., Nucl. Instr. and Meth. **A360**, 219 (1995)

4. H.Fessler et al., Nucl. Instr. and Meth. **A240**, 284 (1985).
   B.Loher et al., Nucl. Instr. and Meth. **A254**, 26 (1987).

5. G.Atojan et al., Nucl. Instr. Meth. **A320**, 144 (1992).

6. M.Bonesini et al., Preprint INFN/AE-94/14, Milano, May, 1994.

7. S.J.Alvsvaag et al., Proceedings of *The 5th International Conference on Calorimetry BNL, New-York, USA, September 1994.*
   S.J.Alvsvaag et al., Proceedings of *The Beijing Calorimetry Symposium, Beijing, China, October 1994, Ed. by H. S. Chen, IHEP, Beijing, 1995.*

8. L.Bugge et al, NIM **A327**, 539–543 (1993).

9. J.Santon et N.Kurtz, An introduction to the MX Chip, preprint RAL-89-028.
   J.T. Walker et al., Nucl. Instr. Meth. **A226**, 243 (1990).

:ascati Physics Series Vol. VI, (pp. 187–197)
I INT. CONF. ON CALORIMETRY IN HEP – Frascati, June 8–14, 1996

THE ELECTROMAGNETIC CALORIMETER FOR THE SOLENOIDAL TRACKER AT RHIC

W.J. Llope for the STAR-EMC Collaboration [1)]
T.W. Bonner Nuclear Laboratory, Rice University, Houston, TX 77005-1892

ABSTRACT

he ElectroMagnetic Calorimeter (EMC) of the Solenoidal Tracker at RHIC (STAR) a stack of 5 mm lead and 4 mm plastic scintillator layers in the shape of a 4800 ›wer ~18 X_0 barrel and at least one 540 tower ~25 X_0 endcap. A Shower Maximum etector (SMD) is placed inside the stack at a depth of ~4.5 X_0. The design of ıis calorimeter, and the status of the effort to build it, will be described. The ›nstruction and performance on the bench of the optical read-out chain will be scussed; particular attention is paid to aspects of the thermal splicing of the plastic ›tical fibers. A Small Prototype EMC (SPEMC) was constructed and tested in the NL-AGS B2 line in two runs, resulting in about 1.4 billion events on tape. Five ifferent configurations of the SPEMC were studied systematically for $e^{\pm}$, $h^{\pm}$ (π and), and $\mu^{\pm}$ at 5-7 momenta in the range from 0.3 to 8 GeV/c and at 12-20 positions ı the face of the stack. The configurations differ in the depth segmentation (none, /15, or 10/10 in layers) and the angle of incidence (zero or 15°). Selected results om these comprehensive beam tests, both for the stack and the SMDs, will be escribed.

Calorimetry in STAR

'he detectors at the Relativistic Heavy-Ion Collider (RHIC) must make sensitive ıeasurements of hadron collisions provided by an extremely flexible machine. RHIC an be tuned to collide two heavy ions of mass A up to ^{197}Au ($\sqrt{s}$=200A GeV), wo polarized protons ($\sqrt{s}$=60-500 GeV), or protons and nuclei. This very wide ange of entrance channels results in a similarly wide range of final states, each f which may contain fundamental information or signatures of novel phenomena. 'he first experiment approved at RHIC, called STAR (for the Solenoidal Tracker ıt RHIC), is a capable detector for all of the RHIC beams and is presently under onstruction. [2)] This experiment will search for signatures of Quark-Gluon Plasma formation, investigate the behavior of strongly interacting matter at high energy density, and study parton structure functions, Drell-Yan, W and Z production, and other spin-dependent phenomena. Like all other major collider experiments throughout the world, calorimetry is an essential component [3] of STAR.

Proceeding outward from the primary vertex, STAR will consist of a Silicon Vertex Tracker (SVT), a large cylindrical Time Projection Chamber (TPC), a Central Trigger Barrel/Time-of-Flight array (CTB/TOF), an Electromagnetic Calorimeter (EMC), and a room temperature 0.5 T solenoidal magnet. Also included in the design of the apparatus are Forward Time Projection Chambers (FTPCs), Vertex Position Detectors (VPD), as well as forward calorimetry. The Electromagnetic Calorimeter will be a Lead/plastic scintillator sampling calorimeter consisting of a barrel calorimeter (BEMC), barrel Shower Maximum Detectors (BSMDs), two endcap calorimeters (EEMCs), and endcap shower maximum detectors (ESMDs). The BEMC(EEMC) is an $\sim$18(25) radiation length stack of 5 mm thick Lead sheets and 4 mm thick plastic scintillator plates which are read out by 1 mm diameter wavelength-shifting fibers (WSFs). These WSFs are thermally spliced to longer 1 mm diameter clear fibers (CFs), which route the shifted scintillation light out through the magnet coils to externally mounted photo-multiplier tubes (PMTs).

There are 4800(540) projective towers in the BEMC(EEMC). Each tower in the BEMC subtends $(\Delta\eta,\Delta\phi)\sim(0.05, 0.05)$. The initial configuration of the BEMC will likely have the towers that are adjacent in η and ϕ in each module ganged pairwise, resulting in 1200 "instrumented" towers, each subtending $(\Delta\eta,\Delta\phi)\sim(0.1, 0.1)$. Each tower will be segmented in depth to improve the electron/hadron discrimination of the device. The SMDs are wire/strip chambers that are positioned after 5 Lead/scintillator layers ($\sim$4.5 X_0). The pixel size in the SMDs will be on the order of $\sim$1.5cm$\times$1.5cm.

A Small Prototype EMC (SPEMC) was constructed [4] to optimize the construction techniques and study the performance of the stack and several SMD prototypes in test beams appropriate for the RHIC environment. The design of this prototype is based on the design of the BEMC. Results on the optimization of the fiber splices that are part of the stack's optical read-out chain, and the SPEMC/prototype SMD performance in beam will be presented below. Further information on the scintillator wrapping, scintillator/WSF coupling[1], full simulations, and test beam studies have been presented [3, 5, 6] in the preceding conferences in this series.

[1]We note that a different approach for the scintillator/WSF coupling (an "α-groove") will be studied in prototype BEMC and EEMC modules that are presently under construction.

Optical Fiber Splicing

ıe to space limitations and the relatively high cost of magnetic field-insensitive ⁄ITs, the scintillation light is to be shifted and carried outside of the magnet coils externally mounted PMTs. Round 1 mm diameter plastic optical fibers will be :cuitously routed over a path that's $\sim$3 m long, which is large compared to the pical attenuation length of WSFs. We have therefore adopted a design similar to at used in the CDF calorimeters, [7] which involves the thermal splicing of 20-35 n long WSFs to $\lesssim$3 m long CFs. If this method is to work, one must simultaneously aximize the optical transmission efficiency at each splice, minimize the splice-to-lice variation in this transmission, and maximize the mechanical strength of the lice joint. The fibers used in this study and in the SPEMC are Bicron BCF-91A.

The thermal splicing was done using an automated device [8] developed , the Michigan State University - High Energy Physics group for use in the con-ruction of CDF calorimeters. [7] As the optical fibers for the STAR-EMC differ om those used in the CDF calorimeters, it is important to re-explore the parame-r space of this fiber splicer for the present application. The mechanical strength ıd optical transmission efficiency of the splices can depend strongly (and often versely) on the various splicer settings.

The operation of the MSU-HEP fiber splicer is highly automated, which sults in very consistent splices. Four time intervals and two pressures are ad-ıstable, but in general the most important parameter is the heating time. This is ıe time interval over which a modified projector lamp melts the two fibers where ıey meet. The fibers are held inside a short section of preshrunk FEP tubing (the acket"), which is enclosed by a pair of precision milled glass half tubes.

A side view of a typical splice is shown in Figure 1. The splices obtained om this device look similar to those obtained from other optical fiber splicers. [9] 'he jacket increases the splice width, but it also adds a considerable amount of rain relief to the joint.

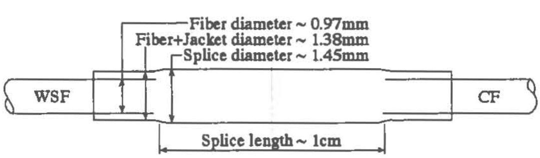

Figure 1: A dimensioned side view of the typical splice used in the SPEMC.

The mechanical strength of the splices were studied versus the heating time and the other splicer parameters in two different ways. The strength longitudinally was studied using a machine provided by the MSU-HEP group which held the fiber on both sides of the splice and pulled by increasing amounts. Undeformed splices typically had longitudinal strengths within ~20% of that for lengths of the same fiber without a splice, supporting more than 10 lbs. of force along the fiber. The "transverse" strength is a somewhat more critical attribute, as the fibers may be bent over radii of curvature $\gtrsim$3.0 cm near the splice. This bending strength depends more strongly on the splicer parameters than the longitudinal strength. It was evaluated by bending spliced fibers in a circle at the splice and measuring the radius of this circle that results in the breaking of the splice joint.

The strongest splices have minimal break radii, while Liouville's theorem [10)] demands light losses of an amount increasing with the splice length[2]. The best heating time thus results in a minimal break radius and a minimal splice length. The break radius and the splice length are shown versus the heating time in Figure 2. The splice length increases linearly with the heating time in the range from 5 to 15 s. As the heating time is increased, however, the break radius of the splice decreases, *i.e.* the splices become mechanically stronger. For heating times in the range from 10 to ~14 seconds, the splice joints do not break for radii of curvature that are $\gtrsim$0.5 cm. Here the splice joint is stronger than the fiber itself, as for radii $\lesssim$1.5 cm, the fibers themselves more often break where they enter the jacket.

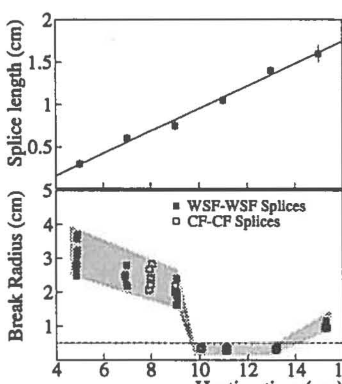

Figure 2: The splice length (upper frame) and the break radius (lower frame) versus the heating time.

We therefore set the heating time at 11 s for the SPEMC fibers. This safely results in the shortest possible splice lengths for essentially unbreakable splices. The focus was then directed onto maximizing the optical transmission efficiency of the

[2]Increasing the splice diameter relative to the fibers also increases light loss at the splice according to this theorem, but the splice diameter is held constant to ~1 mil by the splicer.

lices over the more limited range of splicer parameters leading to unbreakable lices. However, unlike the mechanical properties, the optical transmission efficiency can be significantly affected by the quality of the fiber preparation before the licing.

A linear scanner including a collimated UV light source and reference meaurements was used to measure the shifted light transmission as a function of the osition along unspliced WSF fibers and spliced WSF+WSF fibers. These measureents were used to extract the optical transmission efficiency for shifted light across ach splice, which was tabulated versus different splicer settings following different ethods used to prepare the fibers before splicing.

Besides the optical transmission from the linear scanner, there are two plice properties that can be evaluated visually with a hand-held UV light source. he first is splice deformation (either along the splice or azimuthally), which results om the occasional uneven heating of the joint producing a mechanically weak and ptically inefficient splice. The second is by far the most important contributor of ptical transmission inefficiencies. If the cladding on one or both fibers is damaged uring the cutting of these fibers, a break in the cladding exists where the (spliced) bers meet, which allows a significant amount of light to escape. The splices were herefore classified into three categories ("gold", "silver", and "bronze") on the basis f the visual inspection with a hand-held UV source. The best splices ("gold") were ndeformed and showed no cladding breaks. The next best class of splices ("silver") ere either slightly deformed, or showed small cladding breaks (typically less than ~1/3 of the circumference of the splice). The apparently worst splices ("bronze") ere either very deformed or had large cladding breaks, or both.

The typical results from the linear scanning is shown in Figure 3. The eft frame shows the dependence of the shifted light output on the linear distance etween the collimated UV source and a PMT which are "connected" by a straight nspliced WSF fiber. The core attenuation length was consistently measured to be .8 m. Exponential fits to the transmission curves for spliced fibers were employed vith fixed attenuation lengths to extract the transmission efficiency of shifted light across each WSF to WSF splice. Examples of these fits for typical gold, silver, and bronze splices are shown in the right frame of Figure 3.

The attributes of the splices evaluated by the visual inspection under a UV light source (*i.e.* splice deformation and/or cladding breaks) were strongly correlated with the transmission efficiencies measured by the linear scanner. This is because the splice dimensions are fixed at the constant values appropriate for the final set of splicer parameters. Thus, Liouville's theorem contributes much less to the splice-to-splice variations in the transmission as compared to sloppy fiber preparation, which

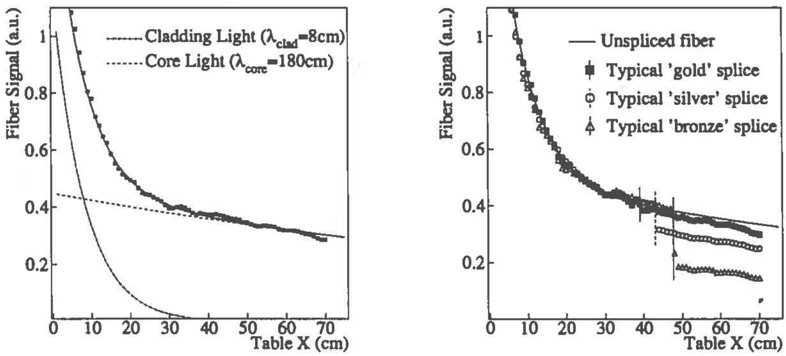

Figure 3: The light output at the end of unspliced (left frame) and spliced fibers of various qualities (right frame).

results in visually apparent cladding breaks, and rarely, splice deformation. The optical efficiencies obtained were (92±4)%, (80±10)%, and (65±20)% for the gold, silver, and bronze splices, respectively. The optical efficiency of our gold splices is consistent [8] with that obtained by the CDF group for their best splices, although our fibers have a larger diameter and different manufacturer, and our set of splicer parameters are different.

The 240 spliced fibers needed for the SPEMC were then produced. As the fiber preparation is by far the most important aspect of the production of consistently high quality splices, considerable care was taken to cut the WSFs and CFs using a jig that minimized damage to the fiber cladding. During the final production, approximately 14/15 of the splices were visually classified as golden. Loading the fibers in the preshrunk jacket, inserting these into the splicer, and running the splicer takes about 90 seconds per splice. Cladding breaks are essentially eliminated altogether by polishing the two ends to be spliced using another automated device (also developed for the construction of the CDF calorimeters). This polishing takes about 60 s/splice, but it leads to gold splices essentially every time.

The SPEMC was then assembled using a scintillator wrapping and scintillator/WSF coupling technique involving Tyvek paper and Aluminized mylar that results in an average of 1.75 photoelectrons [5] per minimum ionizing particle for WSFs(CFs) that were 18(200) cm long. In the SPEMC, the scintillator was Kurrary SCSN38 and the Lead was unclad and unalloyed. The scintillators were arranged in six towers, four(two) of which were the same size as the BEMC towers at $\eta\sim0(1)$. An aluminum box was placed in the stack after 5 lead/scintillator layers ($\sim$4.5 X_0) to allow the insertion of different prototype SMDs. Selected results from the in-beam tests of the SPEMC and the prototypical SMDs are described in the next section.

SPEMC and SMD Performance

he SPEMC was studied in beam at the Brookhaven AGS B2 line in two runs in ay 1994 and July 1995. Five different configurations of the SPEMC were studied stematically for $e^{\pm}$, $h^{\pm}$ (π and p), and $\mu^{\pm}$ at 5-7 momenta in the range from 0.3 to GeV/c and at 12-20 positions on the face of the stack. The configurations differ in ıe depth segmentation (none, 5/15, or 10/10 in layers) and the angle of incidence ero or 15°). Three different prototype SMDs were inserted into the SPEMC stack study their performance as well. A high speed transputer data acquisition system as used, which allowed event rates to tape approaching 15 kHz, and resulted in ver 1.4 billion events on tape in total.

The SPEMC energy resolution and linearity for electrons is shown in Figure This resolution is consistent with that from similarly designed EMCs in other xperiments, and better than the $\sim 20\%/\sqrt{E}$ design goal for the STAR-EMC. The PEMC is linear to better than 1% for electron energies below ~6 GeV/c after the orrection [11] for the electron energy loss in the beam-line.

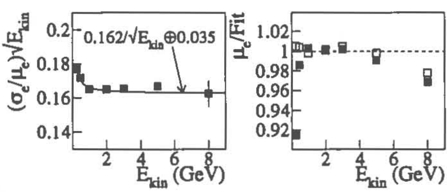

igure 4: The energy resolution (left frame) and the linearity (right frame) of the ɔtal signal from the SPEMC stack for electrons. The linearity is shown before ;olid points) and after (open points) the correction for the electron energy loss in ıe beam-line.

Of the three SMDs that were studied in beam, one was a scintillator/fiber/-MT design ("SciFi") and the other two were wire/strip chambers. The SciFi SMD ɔnsists of two layers, each of which consists of a 2 mm thick Lead plate and 5mm ıick by 1.4 cm wide scintillator strips. It is just under one X_0 in thickness, which considerably thicker in radiation lengths than either of the prototype wire/strip hamber SMDs. This will be apparent in the results shown below.

Due to significant differences in the cost, wire/strip chambers will be the MD technology used in the STAR-EMC. The design of the two different wire/strip MD prototypes that were studied in the SPEMC is similar to that for the SMDs ı CDF. The following will concentrate on the results obtained from one of these hambers, called "ASMD"; the data from the other SMD is being analyzed indepen-ently. The wire(strip) pitch in the ASMD was (0.725)1.56 cm, and the wires were anged in two per read-out channel. The gas was 5% CO_2 and 95% Argon, while the

Voltage was ~1400 V. There were transresistance amplifiers on the chamber itself, all of which where within ~2 cm of the wires or strips.

The ASMD gas volume was inside an aluminum foil EM shield which was isolated from both the ASMD ground and the SPEMC ground. This ground was connected to the cable shield. On the basis of SPICE simulations (see below), the twisted-pair signal cables were shielded with aluminum foil and an outside insulator. On the other end of these ~20 meter signal cables, there were MAX436 differential receiver chips before the ADCs. The cable shield was connected to ground only at the receiver end.

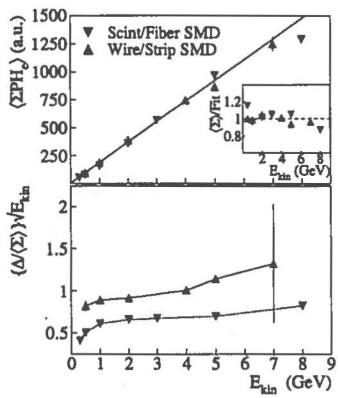

Figure 5: The SMD summed pulse height response (upper frame) and pulse height resolution (lower frame) versus the energy of electrons incident on the SPEMC for the SciFi SMD (down triangles) and the ASMD (up triangles). The inset depicts the linearity of the SMD total pulse heights without any constraint on the depth of the shower maximum (see text).

The average values of the total pulse height distributions from the SciFi SMD and the ASMD are shown versus the electron energy in Figure 5. Without any constraint on the depth of the shower maximum via a cut on the front/back energy sharing in the depth segmented SPEMC, the average total pulse heights from both SMDs is linear to ~15%. Employing such a gate to select showers with maxima near the SMD layer, the SMD signal linearity can be improved by a factor of two. The lower frames of Figure 5 depict the energy weighted SMD pulse height resolution, $\Delta\sqrt{E}/\Sigma$, where Σ and Δ are the average and standard deviation of the pulse height distribution for electrons of an energy E. The ratio Δ/Σ for the SciFi SMD thus behaves like $\sim 0.6/\sqrt{E}$, while the ASMD resolution goes like $\sim 1/\sqrt{E}$. The considerably better pulse height resolution obtained from the SciFi SMD is the natural result of its much larger thickness in radiation lengths.

Like the optical fibers for the stack, the signal cables for the (wire/strip amber) SMDs in STAR are routed out radially through the magnet coils. The 'AR magnet coils could potentially have a voltage ripple of a few hundred Volts, t this could be reduced to ~20 V with some filtering of the magnet power. A test s therefore performed to evaluate the performance of the SMD with and without e presence of a (simulated) capacitively coupled noise signal from a magnet coil.

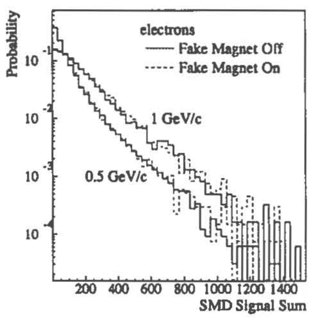

gure 6: The total pulse height distributions obtained from a prototype wire/strip ΛD in the SPEMC for 0.5 GeV/c and 1.0 GeV/c electrons, as labelled, with the nulated magnet noise signal off (solid lines) and on (dashed lines).

To simulate the magnet noise, a 20 V square wave (1 kHz rate, 1 μs rise ne) was added though ~500 pF to the ASMD cable shield. The summed pulse ight distributions obtained from the ASMD when low energy electrons are directed the SPEMC are shown in Figure 6. The solid and dashed histograms show what obtained with the fake magnet off and on, respectively. No modification of the mmed pulse heights, or the signals from individual ASMD channels (not shown), apparent. The shielding of the ASMD and its cables that was described above us provides the necessary protection from ~20 V magnet noise that is coupled rough ~500 pF.

Electron/hadron Discrimination

he direct identification of electrons with momenta above a few GeV/c in STAR is ossible only with the information provided by the EMC. As the SPEMC and all ree prototype SMDs worked well in the test beam, it is relevant to explore the ectron/hadron discrimination that is possible using a variety of cuts on both stack d SMD observables.

For SMD-equipped EMCs that are segmented into two depth sections, the x observables shown in Figure 7 support cuts that provide e/h discrimination for ts of known momentum.[3] The stack observables are the total energy ("SPEMC

[3]In the test beam, this was controlled via the beam line magnets, while in STAR, track momenta

ΣPH"), the front, F, to back, B, energy sharing quantified by $Z=(B-F)/(B+F)$ ("Cal-Z"), and the ratio of the struck tower energy to the total ("isolation"). The SMD observables are the total pulse height ("SMD ΣPH"), the pulse-height weighted shower width in both the X and Y directions in centimeters ("SMD $\Delta X \oplus \Delta Y$"), and the difference between the expected location of the shower centroid and the measured shower centroid ("$\vec{X}_{smd}-\vec{X}_{pred}$").

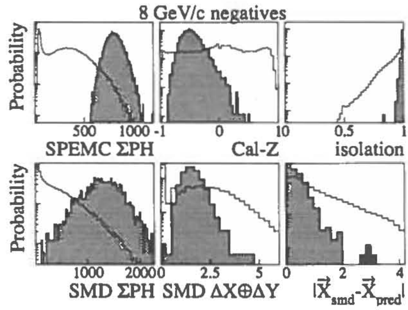

Figure 7: Three stack observables (upper frames) and three SMD observables.(lower frames) that support cuts leading to e/h discrimination, shown for 8.0 GeV/c electrons (shaded histograms) and hadrons (open histograms).

The geometry of the actual STAR-EMC is somewhat different from the SPEMC geometry, while the test beam data cannot include the tower and SMD channel occupancy expected in RHIC events. We have thus concentrated only on simple and approximately located cuts to get a feel for the general trends.

At momenta below ~1.5 GeV/c, the most effective cuts are the E/p cut and the front/back energy cut. For larger momenta, the front/back energy cut becomes less effective, while the E/p cut and all of the SMD-based cuts become more effective. Using reasonable but unoptimized cuts on these two combinations of observables, the discrimination is roughly 6:1 at electron efficiency of ~80% for momenta below ~1 GeV/c. In this range of momenta, however, other detectors in STAR, primarily the STAR TOF, also provide e/h discrimination capabilities. At momenta above 2 GeV/c, the discrimination is $\gtrsim$100:1 and the electron efficiency is between 60 and 80%.

5 Outlook

This contribution described results obtained during the construction and in-beam tests of a small calorimeter composed of BEMC towers and several prototype SMDs. At present, a mechanical prototype of a BEMC module is being studied to optimize

are provided by the TPC and the SVT.

: module construction techniques and fiber routing. A fully functional module the EEMC is also under construction. The development of prototype electronic nponents and the detailed simulation of the EMC as a part of STAR continues we prepare to be ready for the first day of RHIC beams in the Fall of 1999.

Acknowledgements

ιis work was supported by the U.S. Department of Energy under the Grant No. Σ-FG03-93ER40772. We are grateful to R. Richards, J. Huston, D. Shooltz, J. ansour, and B. Tannenbaum (MSU-HEP group) for helpful discussions and the e of their fiber splicer, polisher, and linear scanner.

eferences

. Argonne National Laboratory, Brookhaven National Laboratory, IHEP - Protvino, JINR - Dubna, Lawrence Berkeley Laboratory, Michigan State University, Penn State University, Rice University, Wayne State University, University of California - Los Angeles, and University of New Mexico.

:. http://rsgi01.rhic.bnl.gov/star/starlib/doc/www/star.html

;. G.D. Westfall, published in the Proceedings of the V International Conference on Calorimetry in High Energy Physics, Brookhaven, N.Y. (1994).

:. http://bonner-mac8.rice.edu/

). D.G. Underwood, published in the Proceedings from the IV International Conference on Calorimetry in High Energy Physics, La Biodola, Elba (1993).

;. D.G. Underwood, published in the Proceedings of the V International Conference on Calorimetry in High Energy Physics, Brookhaven, N.Y. (1994).

7. http://www-cdf.fnal.gov/

3. R. Richards, private communication; B. Tannenbaum, Masters Thesis, Michigan State University, unpublished (1994); J.P. Mansour *et al.*, /CDF/DOC/PLUG_UPGR/PUBLIC/2562.

9. G. Apollinari *et al.*, Nucl. Inst. and Methods **A311**, 520 (1992).

0. K.G. Steffen, *High Energy Beam Optics*, pgs. 161-172 (Interscience Publishers, New York, N.Y.).

1. A. Patwa *et al.*, PHENIX Technical Note 181 (1995).

A LEAD-LIQUID SCINTILLATOR "SHASHLIK" E.M. CALORIMETER PROTOTYPE

R. Rusack
University of Minnesota, Minneapolis MN 55455, USA

Written contribution not received

.cati Physics Series Vol. VI, (pp. 201–208)
NT. CONF. ON CALORIMETRY IN HEP – Frascati, June 8–14, 1996

THE CLAS LARGE ANGLE CALORIMETER

presented by M.Taiuti for the AIACE Collaboration*

ABSTRACT

: present a description of the modules of the Large Angle Calorimeter for CLAS, owing the Monte Carlo results and the response to minimum ionising particles. In rticular the results of the measurement of the light attenuation length in the orimeter, the light output and the resolution of the interaction point reconstruction are scussed. The performance of the detectors was found equal or even better than pected.

- Introduction

The AIACE collaboration[1)] participates to the TJNAF (formally CEBAF)[2)] Hall experimental activity. Hall B is equipped with a Large Acceptance Spectrometer LAS)[3)] based on a toroidal magnetic field. The field is generated by six perconducting coils arranged around the beam line to produce a magnetic field that is imarily in the ϕ-direction. Each region between two coils is equipped with a) three yers of drift chambers to track the charged particle, b) a Cherenkov detector to scriminate electrons from pions, c) scintillation counters for time-of-flight easurements and d) an electromagnetic calorimeter to detect electrons and photons. ie AIACE collaboration realised two modules of the Large Angle Electromagnetic iower Calorimeter (LAEC) to detect particles at θ angles larger than 45° in the boratory. The LAEC is used for a) the π/e separation, b) the detection of photons om the decay of mesons (π^0, η, η' ...), c) the measurement of neutron momentum ing time-of-flight. In fig.1 the CLAS layout with the position of the LAEC modules is ported.

In this paper, after a description of the detector and a discussion of the effects of e light collection efficiency on detector performances obtained from Monte Carlo

M.Anghinolfi[1], H.Avakian[2], M.Battaglieri[1], N.Bianchi[2], G.P.Capitani[2], P.Corvisiero[1], .Deppman[2], E.DeSanctis[2], V.Giourjian[2], P.LeviSandri[2], A.Longhi[1], S.Mansanta[2], .I.Mokeev[3], V.Muccifora[2], M.Olcese[1], E.Polli[2], A.R.Reolon[2], G.Ricco[1], M.Ripani[1], .Rossi[2], M.Sanzone[1], V.Sapunenko[3], M.Taiuti[1], A.Zucchiatti[1]

Dipartimento di Fisica dell'Università di Genova or I.N.F.N.-Sezione di Genova, I-16146, Genova, Italy.
.N.F.N.-Laboratori Nazionali di Frascati, P.O.Box 13, I-00044, Frascati , Italy.
nstitute of Nuclear Physics, Moscow State University.

simulations, we discuss the results of the tests performed with cosmic rays. Both energy and timing properties were studied. We measured the light propagation in scintillators, the number of photoelectrons/MeV collected and the position reconstruction resolution. The tests showed that the module properties well agree to the initial specifications.

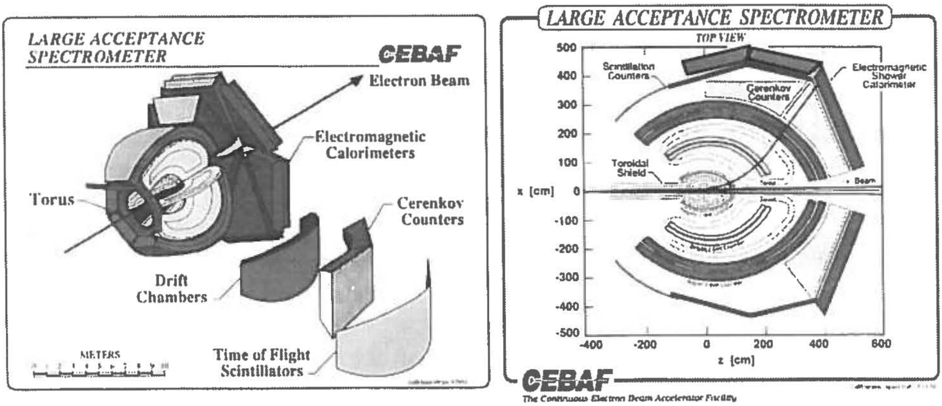

Figure 1: The CLAS layout.

2. - Detector description

Each LAEC module has a multi-layer structure with lead sheets and scintillator bars, a configuration that provides the best agreement between good energy resolution and high neutron detection efficiency requirements. It consists of 33 layers, each composed by a 0.20 cm thick lead foil and NE110A plastic scintillator bars with average width 10 cm and constant thickness 1.5 cm.[4,5] The module thickness corresponds to 12.9 radiation lengths and 1.0 absorption length. Teflon sheets with 0.2 mm thickness separate scintillators from lead while 0.2 mm thick Teflon strips between each pair of contiguous scintillator bars avoid optical cross-over. Each layer is rotated by 90° to form a 40x24 matrix of $\approx$10x10 cm^2 cells. The bar width increases going from the inner side toward the outer to guarantee the tapering required by the CLAS geometry. The surface exposed to particle fluxes is 217x400 cm^2.

The module is vertically divided into an inner and an outer part to improve the electron-pion discrimination. Scintillators lying (for the inner and outer part separately) one on top of the other with the same orientation form 128 different stacks. In fig.2 a conceptual drawing of the calorimeter shape and its internal structure is reported. The electromagnetic showers originate in the lead sheets and propagate through the layers; the energy absorbed in the active material produces a light pulse that is collected at both ntillator ends with Lucite light guides coupled to scintillators with an air gap on a)x0.4 cm^2 area.[6] Being the coupling area smaller than the scintillator cross section, : remaining scintillator surface was protected with Teflon to prevent scratches from : aluminium external structure. The collected light is summed, separately for each ıck, before a EMI 9954A photomultiplier. Therefore light pulses emitted from 8 ferent scintillators are summed up on a single photomultiplier that is placed on the ɔ surface of the LAEC module several centimetres away from the scintillators. To luce photocathode non-homogeneity effects, the light guides are glued together before upling to photomultiplier. Scintillators placed in the inner and the outer parts are upled to different photomultipliers.

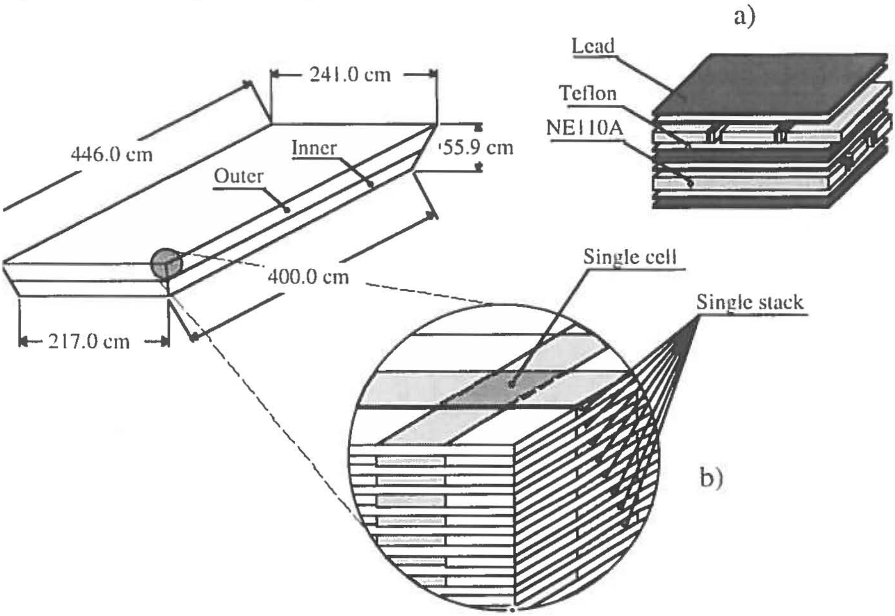

Figure 2: Conceptual drawing of the calorimeter volume showing in detail: a) the composite internal structure and b) the plastic scintillators stack structure (light grey area) with the crossing of two orthogonal stacks that defines a cell (dark grey area).

. - The Monte Carlo simulations

Monte Carlo simulations with GEANT give the detector characteristics estimated ; follows:

linearity up to 2 GeV incoming electron energy;

energy resolution $\sigma_E / E \approx 7.5\% / \sqrt{E}$;

- pion/electron rejection factor > 50 at momenta higher than 0.5 GeV/c;
- π^0 mass reconstruction resolution $\sigma_M/M \simeq 10\%$;
- η mass reconstruction resolution $\sigma_M/M \approx 7\%$;
- neutron detection efficiency $\varepsilon_n \approx 50\%$.

Monte Carlo simulations showed that these performances are strongly affected by the efficiency of light transmission and collection. For comparison in fig.3 the effects of the number of the collected photo-electrons on the energy resolution for 100 MeV electrons (left) and on the neutron efficiency (right) are reported. For this reason special attention was devoted to the production of high quality scintillators and light guides whose results have been already reported in previous papers:[4-6] in particular we selected scintillators with a light attenuation length equal to 410 cm in average with a light output of 60 photoelectrons/MeV in average when coupled to EMI 9954A photomultipliers and light guides that provide a ≈8% transmission efficiency.

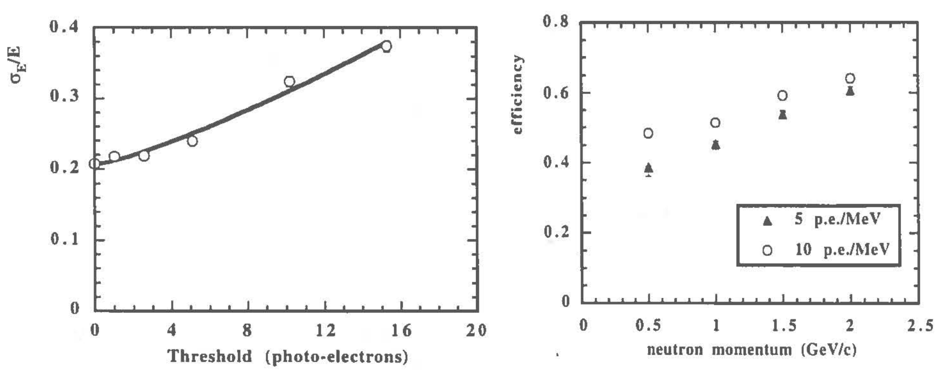

Figure 3: Effects of the collected number of photo-electron: energy resolution for 100 MeV electrons (left); neutron detection efficiency (right).

4. - The cosmic ray test

To perform the cosmic ray measurements we took advantage from the module projecting geometry: the module was horizontally positioned with a trigger detector, realised with a 10x10x2 cm^3 plastic scintillator placed in the detector focus. In this configuration a cosmic muon, after interacting in the trigger scintillator, crosses the calorimeter mostly through a single cell.

- The energy resolution

The single cell energy deposition spectra showed the typical Landau energy ıtribution convoluted with the fluctuations of the collected light. Fitting the energy ectra with gaussian functions we produced for each photomultiplier two plots as those ported in fig.4 showing the position dependence of mean and sigma of the deposited ergy. The spectra were analysed to extract the average scintillator attenuation length λ d the collected number of photoelectrons/MeV $N_{p.e.}$ using the following equations:

$$Q(x) = Q_0\left(e^{-x/\lambda} + \alpha e^{-(2L-x)/\lambda}\right) \qquad 1)$$

$$\frac{\sigma_E}{E}(x) = \left(0.01 + \frac{1}{N_{p.e.} E_d\left(e^{-x/\lambda} + \alpha e^{-(2L-x)/\lambda}\right)}\right)^{1/2} \qquad 2)$$

ıere α represents the reflection coefficient that takes into account the contribution of flected light at opposite end of scintillators, L is the scintillator length and $_d = 25$ MeV is the average deposited energy in one stack.

Two effects contribute to energy resolution: a) the Landau fluctuations that ovide a constant contribution that in our configuration is 10% as obtained from Monte arlo simulations and b) the fluctuations in light collection statistics that provide a ontribution proportional to the deposited energy and to the attenuation length λ of the ack. Equation 2 represents the fit with these contributions quadratically summed.

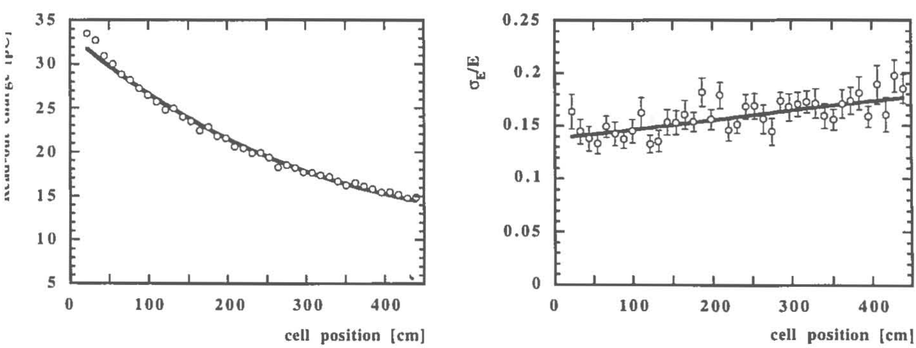

Figure 4: Position dependence of muon deposited energy: average energy (left) and relative width (right). Curves are described in the text.

The summary for all scintillators is reported in fig.5. The distribution of attenuation lengths obtained fixing $\alpha = 0.4$ as most probable value is comparable to that measured in single scintillators[5] showing that the adopted light read-out system did not affect the scintillator properties. Concerning $N_{p.e.}$ the sigma of the distribution, equal to 17%, is comparable to that measured in single scintillators[5] while the average value $N_{p.e.} = 4.7$ is very close to the value $N_{p.e.} = 5.0$ resulted to be the optimal from Monte Carlo simulations. Considering that the average measured light output for single scintillator is 60 photoelectrons/MeV[5] we can say that the attenuation factor in light guides is ≈ 12.5 instead of 8 as measured on few prototypes.[6] This difference could be explained considering that the final light guides resulted to be longer than prototypes and with a third bending introduced to fit the module geometry. The reduced values is however compensated by the improved amount of transmitted light in scintillator as previously discussed.

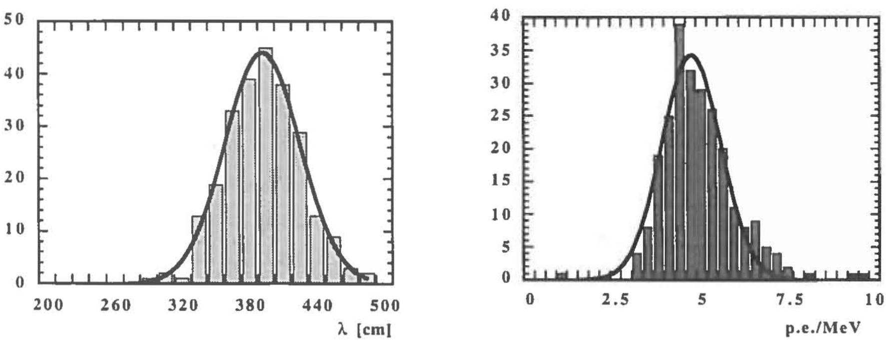

Figure 5: Summary of first module properties: attenuation length (left) and number of photoelectrons/MeV (right). The solid lines are fits with a gaussian distribution.

4.2 - The timing resolution

We also analysed the timing properties studying in particular the effect of the fluctuations on the position reconstruction. With the same criteria adopted to select deposited energy in single cell, we measured the single cell timing distribution for the semi-difference

$$\Delta t = \frac{1}{2}\left(t'_L - t'_R\right) \qquad 3)$$

:tween the two photomultipliers coupled to opposite ends of the same stack.[6] Fitting e timing spectra with gaussian functions we produced for each photomultiplier two ots showing the position dependence of mean and sigma of Δt respectively.

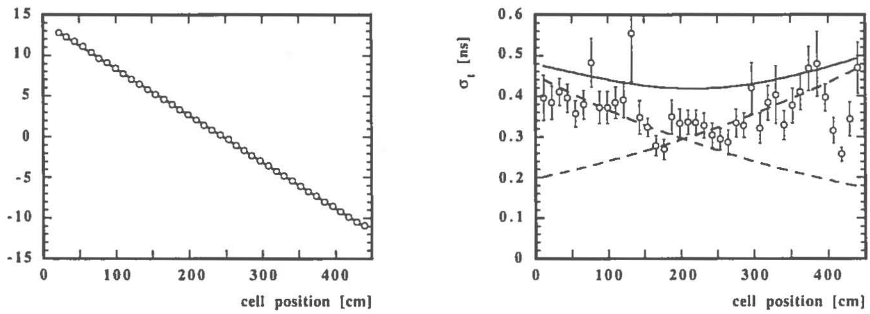

Figure 6: Position dependence of muon detection timing: Δt average (left) and relative width (right). Curves are described in the text.

In fig.6 the position dependence of timing properties are reported: the average Δt ıows a typical linear behaviour and the curve represents the fit performed to extract the ɜlocity of light c in the scintillator; the sigma of the Δt distribution shows a minimum ı the middle of the scintillator that can be easily explained taking into account the ming fluctuations due to light propagation in scintillators and photomultiplier jitters.[6] he dashed lines represent the contribution of single photomultiplier as extracted from ıeasurements with some prototypes; the overall result reported as continuous line ıows that the calorimeter timing resolution well agrees with what expected.

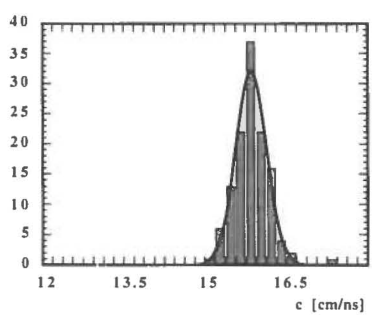

Figure 7: Summary of first module properties: distribution of the velocity of light c in scintillator. The solid line is the fit with a gaussian distribution.

The summary of extracted *c* is reported in fig.7. The distribution shape and the absolute value 16.0±0.3 agree with those measured in single scintillators.[5]

The sigma of timing distribution can be related, through the velocity *c*, to the resolution in reconstruction of the interaction point. From the present measurements and considering that the non negligible size of the selected cell introduces an extra 1 cm uncertainty we could conclude that the resolution could be as better as 5 cm in sigma.

5. - Conclusions

We realised two module of the CLAS Large Angle Calorimeter. The calorimeter was designed to detect electrons up to 2 GeV incoming energy and neutral particle like photons and neutron. Being the module performances strongly affected by the light collection efficiency we used high quality scintillators and light guides. The module response to minimum ionising particles has been studied considering the contribution of light propagation and collection efficiency. We measured a) the light output, b) the light transmission and c) the timing selecting only the particles that crossed the module through a single cell taking advantage of the projecting geometry of the detector.

The measurements showed that the module performances are very close to those expected or even better as in the case of timing resolution and light transmission efficiency. In particular the improved transmission efficiency would compensate the reduced transmission efficiency in light guides.

References

1. M.Anghinolfi et al., Proceedings of the *International Workshop on Flavour and Spin in Hadronic and Electromagnetic Interactions*, Torino September 21-23, 1992, ed. by F.Balestra, R.Bertini and R.Garfagnini, Italian Physical Society vol.39 (1993) p.237.

2. J.J.Domingo, Proceedings of the *5th Workshop on Perspectives in Nuclear Physics at Intermediate Energies*, Trieste May 6-10, 1991, ed. by S.Boffi, C.Ciofi degli Atti and M.Giannini, World Scientific (1992) p.260.

3. V.D. Burkert and B.A. Mecking, Modern Topics in Electron Scattering, ed. by B. Frois & I. Sick, World Scientific Publishing Co., 1991.

4. M.Taiuti et al., Nucl. Instr. and Meth. A357(1995)344.

5. P.Rossi et al., Nucl. Instr. and Meth. in press.

6. M.Taiuti et al., Nucl. Instr. and Meth. A370(1996)429.

ascati Physics Series Vol. VI, (pp. 209–218)
. INT. CONF. ON CALORIMETRY IN HEP – Frascati, June 8–14, 1996

THE PRESAMPLER FOR THE FORWARD AND REAR CALORIMETER IN ZEUS

H.–J. Grabosch
DESY–IfH– Zeuthen
for the ZEUS–Presampler–Group[1)]

Abstract

The ZEUS detector at HERA has recently been supplemented with a pre- mpler detector in front of the forward and rear calorimeters. It consists of a gmented scintillator array, read out with wavelength-shifting fibers. We discuss ; design, construction and performance. Testbeam data obtained with a prototype esampler and the ZEUS prototype calorimeter demonstrate the main function of is detector, the correction for the energy lost by a particle interacting in inactive aterial in front of the calorimeter.

Introduction

he material situated between the electron-proton interaction point and the front ce of the uranium-scintillator calorimeter within the ZEUS detector at HERA leads to a degradation of the calorimetric energy measurement of the particles ·oduced in the interaction. In order to measure the energy loss, we have constructed presampler detector, which is installed directly in front of the forward and rear EUS calorimeter sections. The detector consists of a layer of scintillator tiles, avelength-shifting fibers, embedded in the scintillator and light guide fibers to ıotomultipliers. Particles which shower in the material in front of the presampler ad to an increased particle multiplicity which is measured by the presampler. The ›mbined information from the presampler and the calorimeter allows an event-by- ⁄ent measurement of the energy loss in front of the calorimeter and thus allows to :cover the energy scale and energy resolution of the ZEUS calorimeter.

Scintillator/fiber combination

he segmentation of the presampler matches that of the ZEUS calorimeter [3)] adronic sections, 20 x 20 cm². The scintillation light is read out by wavelength- ıifting fibers embedded in the scintillator and transported by clear fibers to a hotomultiplier. Since the calibration of the presampler is performed with minimum ›nizing particles(MIP) we require a photoelectron yield of at least 5 photoelectrons er MIP at the photocathode of the photomultiplier (PMT). We aim for a response niformity of about 10% over the tile area.

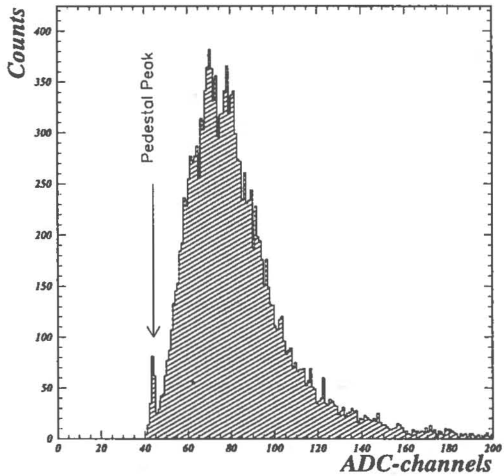

Figure 1: *Response of a scintillator tile to cosmic muons. The peak around the pedestal value of 45 ADC counts is due to false triggers and zero response due to photostatistics.*

We have investigated several combinations of scintillator material, fiber material and fiber layout to optimize light yield and response homogeneity, resulting in the following choice:

- scintillator material SCSN38 (Kuraray Co. Ltd), 5 mm thick with dimension 203 x 198.5 mm^2; tiles are cut and diamond-polished. Six grooves, parallel to the long edge, are machined in the tiles with an ordinary saw blade
- six fibers read out one tile; they are glued in the grooves
- WLS fiber material Y11 (Kuraray Co. Ltd), double clad, 1 mm diameter, 23 cm long with a sputtered Al mirror at one end.
- a 1 mm diameter double clad transparant polystyrene fiber DCLG (Kuraray Co. Ltd) guides the light to the photomultiplier; the fiber is 3 m long and is glued to the WLS fiber.
- wrapping of the tile in Tyvek paper (quality Q173-D, DuPont) paper.

2.1 Light yield measurement

The absolute light yield for minimum ionizing particles was measured in a cosmic ray telescope with an effective area of 12 x 12 cm^2. The PMT pulse was integrated by a LeCroy 2249A ADC, triggered by a threefold coincidence of the signals from the cosmic trigger. Figure 1 shows the response to cosmic ray particles for the final tile/fiber/PMT layout.

The ratio of triggers with no signal in the pedestal region to the total number of triggers is equal to (0.37$\pm$0.03%), taking into account the trigger efficiency of 98.9%. From this we obtain an absolute light yield of 5.6$\pm$.1 photoelectrons.

Mechanical layout

1 Tile assembly

he scintillator tiles are assembled in cassettes, made of 0.4 mm thick stainless steel; ey are 20 cm wide and vary in length, containing between 1 and 10 tiles. The tal thickness of the cassette is $\sim$ 11 mm and represents about 5 % of a radiation ngth. The six readout fibers of one tile are glued together in a connector which fixed to the PMT housing. In addition to the six fibers a seventh clear fiber is lded to guide the light from a Laser/LED monitor system to the PMT.

2 Detector assembly

he forward and rear calorimeters are split in two halves, such that they can be ithdrawn from the beampipe region during injection of the electrons and protons . HERA. A group of 19 cassettes, which covers one half of each calorimeter face, is ued on a 2 mm thick aluminium plate (0.02 radiation lengths) of 2 x 4 m^2.

Figure 2 shows the coverage of the calorimeter by the presampler. Shown the segmentation of the electromagnetic sections, which is finer in the region ot shadowed from the nominal interaction point by the barrel calorimeter. The) x 20 cm towers covered by the presampler tiles are shaded.

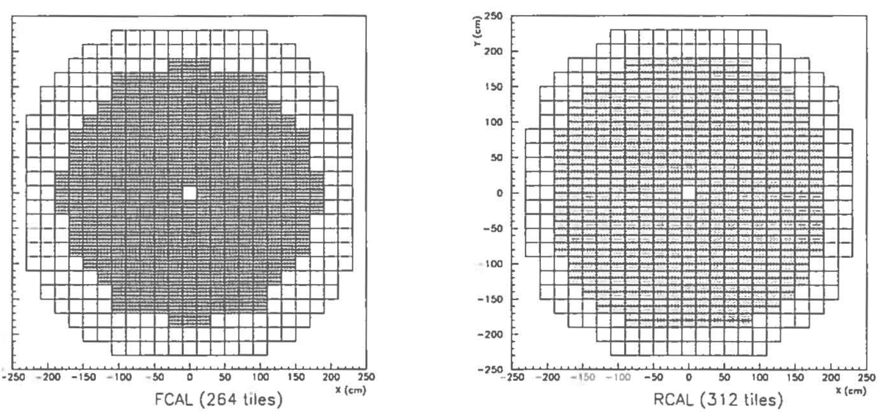

Figure 2: *Front view of the forward (FCAL) and rear calorimeter (RCAL).*

A 2.5 mm diameter tube is glued over the full length on the outside of each assette, positioned at the center of the tiles. The tube guides a radioactive source or calibrating the light output of the individual tiles and the gain of the PMT hannels (see section 6.2).

4 Photomultiplier tests

Due to the limited space available in the ZEUS detector it was decided to use multichannel PMT's. The Hamamatsu R4760 16-channel photomultiplier has been extensively tested for our application (see also [4]). This is a 4 x 4 multichannel PMT with a front face of 70 mm diameter. Each of the 16 channels has a 10 stage dynode chain but they all share the same voltage divider. The diameter of the photocathode for each channel is 8 mm. Our PMT fulfills the following requirements:

- cathode sensitivity $> 45\ \mu$A/lm
- minimum gain at 1000 V: 1×10^6
- gain spread between the 16 channels of one PMT assembly less than a factor of 3

The cross talk between adjacent channels has been measured to be less than 3% and can be neglected for all non-adjacent channels.

5 Readout system

The readout system is a copy of the existing ZEUS calorimeter readout system with some minor modifications [5]. The modifications consist of upgraded versions of the shaping/amplifier [6] and the digital signal processor. The PMT pulses are amplified and shaped by a pulse shaper circuit mounted at the detector. The shaped pulse is sampled every 96 ns (the bunch crossing rate of the HERA storage ring) and stored in a switched capacitor analog pipeline. After receipt of a trigger from the ZEUS detector, eight samples are transferred from the pipeline to an analog buffer and multiplexed to ADCs. The data are sent to a location outside the detector where the digitisation and signal processing takes place.

6 Calibration tools

We use an LED/Laser system to monitor the gains of the PMT's and a source system to monitor the combined response of tile, fiber and PMT. During the operation of ZEUS, halo muons and charged hadrons are used to determine the response to single particles for each individual channel. The use of the multichannel PMT makes it impossible to equalize individual channel responses via the HV setting, since 16 channels share a common HV supply.

6.1 Results from cosmic ray measurements

A cosmic ray test was performed in the laboratory to measure the light yield of the 576 tiles (264 FCAL and 312 RCAL tiles) assembled in 76 cassettes. The trigger system consists of eight cosmic ray telescopes which allows to measure 16 tiles simultaneously. The readout PMT was a 16-channel R4760 as used in the final

·esampler design. To compare the light yield of different tiles, all 16 channels of ιe PMT were calibrated with a reference tile to correct for differences in quantum ficiency(QE) and gain between the 16 PMT channels. Figure 3 shows the mean ılue for all 576 tiles normalized to one. From the RMS value of the distribution ıe can conclude that the responses of all tiles are equal to within 12%.

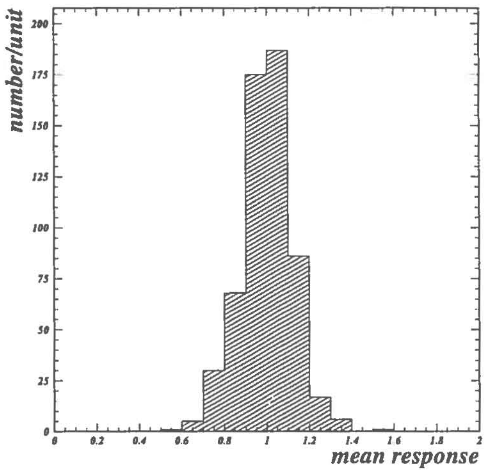

'igure 3: *Average pulse height for cosmic muons normalized to one after having orrected for the gain differences between individual PMT channels.*

.2 Source system

:he response to a ^{60}Co source provides a relative calibration and quality control f the individual channels of the presampler. The source scans take place during hutdowns of HERA and provide information on the long term behaviour of the ght output of the combination of scintillator and wave-length-shifting fiber.

' Results from beam tests of the presampler and forward calorimeter prototypes

[he influence of material in front of the ZEUS calorimeter on its energy measurenent has been studied previously in several test beam runs with the ZEUS forward :alorimeter (FCAL) prototype [8]. The corrections of the calorimetric measurenents that can be derived from the signals of a presampler have been studied in [9]. n the following we give a brief summary of the most recent results obtained with he final presampler layout [10].

7.1 Setup

The presampler prototype consists of an array of 4 x 4 scintillator tiles covering an area of 800 x 800 mm^2. The presampler is positioned directly in front of the ZEUS FCAL prototype which has the same lateral size. The depth of the calorimeter is 7 interaction lengths [8]. Beam tests were performed in the X5 test beam of the CERN SPS West Area. The prototype presampler detector is read out via a R4760 multichannel photomultiplier. Furthermore, the final readout electronics was used for both the presampler and the FCAL prototype modules.

The uranium radioactivity was used to calibrate the calorimeter and single beam muons were used to calibrate the presampler. The combined response of the presampler and calorimeter was determined for electrons in the energy range from 3-50 GeV. The amount of material installed in front of the presampler was varied between 0 and 4 X_0. During these studies, the position of both calorimeter and presampler relative to the beam was fixed.

7.2 The presampler response uniformity to incident muons

Figure 4 shows the mean presampler response to 75 GeV muons. The position information was provided by the delay wire chamber with a resolution of 0.5 mm. The presampler signals for the incident muons are normalized to the response at the

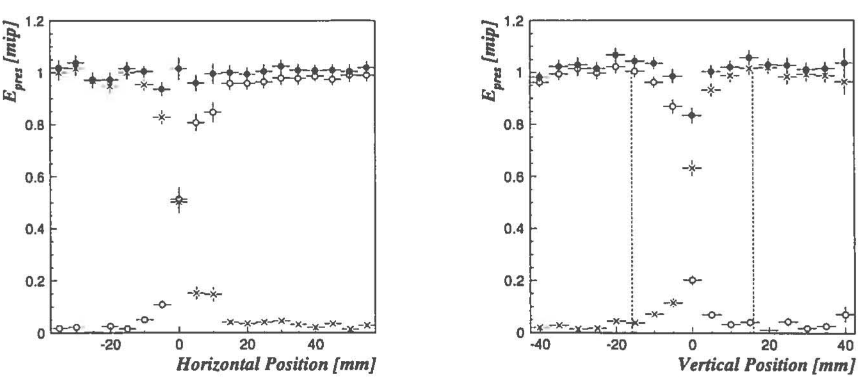

Figure 4: *The response uniformity of the presampler across tile borders to muons. a) a horizontal scan in x-direction (* represents response of tile 1, o for tile 2 and • sum of both), b) a vertical scan in y-direction, perpendicular to the embedded fibers. The dashed lines indicates the fiber position.*

center of the tile and averaged over uniformly populated rectangles of 90 x 5 mm. The nonuniformity in the sum of the two bordering tiles is a few percent in the regions of the fibers; horizontally (figure 4a) the tiles are mounted within one cassette, not allowing any gap in between. Vertically (figure 4b) a signal drop is observed etween the cassettes due to the 1.4 mm gap between the scintillator tiles. The onuniformity averaged over the surface of a tile is less than 1%.

.3 Electron energy correction

igure 5 shows the correlation between the presampler signal (normalized to the verage signal of a minimum-ionising particle) and the calorimeter signal for 25 ;eV electrons as a function of the amount of absorber material.

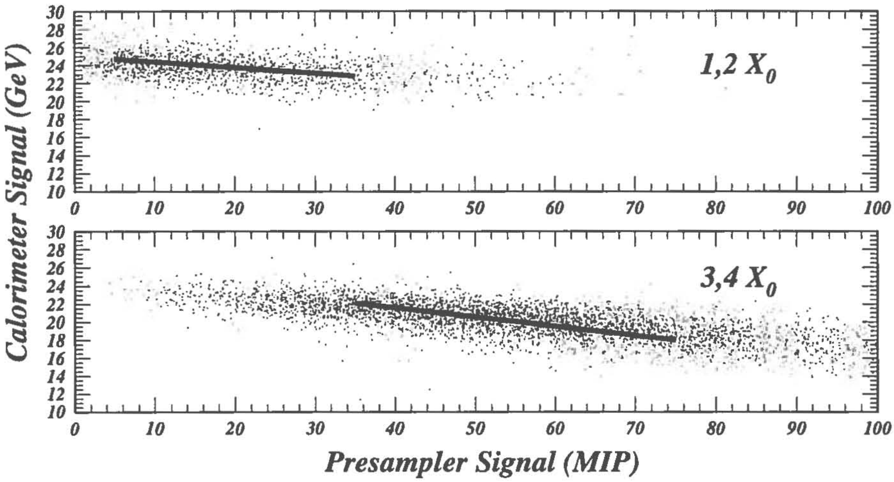

'igure 5: *Calorimeter versus presampler response for 25 GeV electrons and absorber naterial ranging from 1 to 4 X_0. The line represents the fit to the data according 'ormula (1).*

We have considered a variety of parametrisations for the relationship between :alorimeter and presampler responses. In the well-defined environment of a test ›eam the correction is straightforward and depends on the incident energy and the ımount of absorber material, both of which are precisely known.

In a detector environment the amount of absorber material in front of the :alorimeter is not uniformly distributed, arising from cables, support structures, etc. Ͻne can, however, identify regions where the average amount of absorber material s roughly known. For this reason we show here the result obtained with one set of :orrection constants common to the 1 and 2 X_0 data set and one for the 3 and 4 X_0 data set. The relation between the measured mean values of E_{cal} and E_{pres} has ›een parametrised in a linear approximation:

$$E_{cal} = a_0 + a_1 E_{pres} \tag{1}$$

Ꮖhe result for the two data sets for 25 GeV electrons is shown in figure 5. The ›arameters a_i depend on the amount of material and on the electron beam energy.

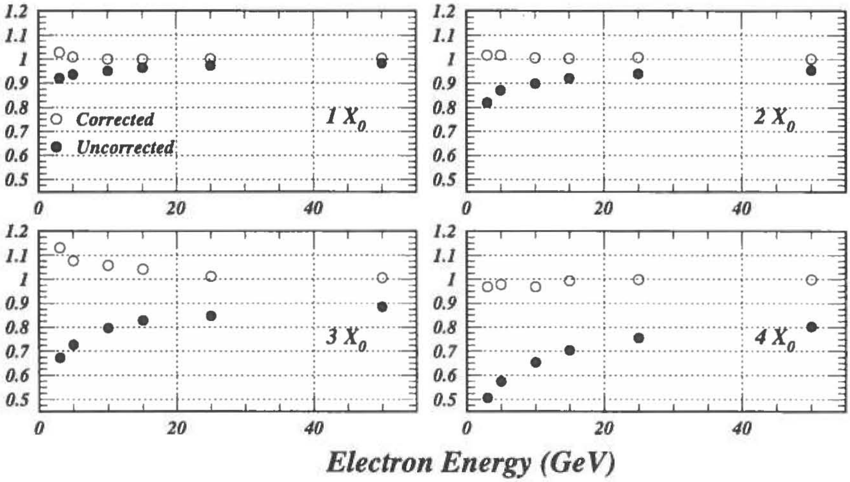

Figure 6: *Average calorimeter response normalized to the electron energy versus the electron energy before and after correction*

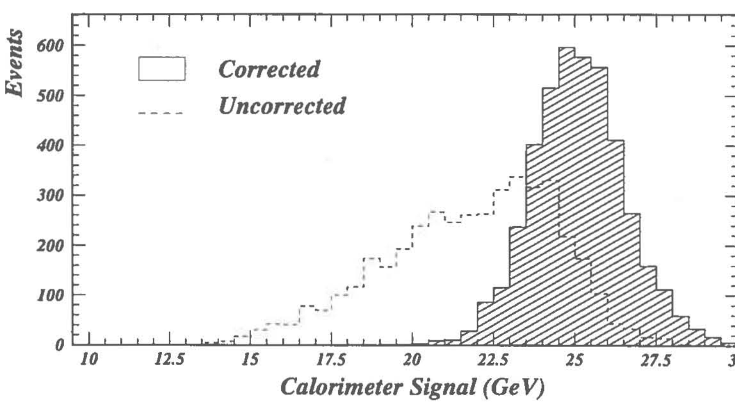

Figure 7: *Reconstructed energy distributions for 25 GeV electrons for a mixture of the 1-4 X_0 data before and after application of the correction algorithm*

his correction algorithm allows for a linear energy dependence of the parameters a_i: $= \alpha_i + \beta_i E_{beam}$. We neglect the dependence on the amount of absorber material order to estimate the success of the algorithm when the amount of absorber varies ithin the data sample. The parameters α_i and β_i are determined by minimising ıe difference of the beam energy and the corrected calorimeter signal. The results ır the corrected calorimeter response for electrons in the energy range 3-50 GeV, e shown in figure 6. This procedure provides a correction accurate to 3% for the ıergy range studied here, but for an overcorrection of about 10% for the 3 X_0 data əints at low energy. For electron energies greater than 5 GeV and for absorber ıickness less than 2 X_0, the values relevant to the operation of the ZEUS detector, ıis simple correction algorithm yields a systematic precision of 2%.

he improvement in the energy resolution as well as in the energy scale is shown in gure 7. The energy distribution of 25 GeV electrons for a merged 1-4 X_0 data set shown before and after correction.

Summary and conclusions

/e have described the presampler which is in use for the ZEUS calorimeter. It is ıade of scintillator tiles, read out with wavelength-shifting fibers embedded in the cintillator. The efficiency to identify single charged particles is above 99%. The esponse over the tile is uniform within 5%. The performance of the presampler ı combination with a prototype ZEUS calorimeter is measured for electrons in the nergy range 3-50 GeV, with various amounts of absorber material (up to 4X_0) positioned in front of the presampler/calorimeter. There is a linear dependence between ıe energy lost and the presampler signal. This dependence is a function of the mount of absorber material and the incident energy, which allows the calculation f the energy lost in the absorber material.

References

1. A.Bamberger[4], A.Bornheim[1], J.Crittenden[1], H.-J.Grabosch[3], M.Grothe[1], L.Hervas[7], E.Hilger[1], U.Holm[5], D.Horstmann[5], V.Kaufmann[4], A.Kharchilava[3], U.Kötz[2], D.Kummerow[5], U.Mallik[6], A.Meyer[3], M.Nowoczyn[5], R.Ossowski[1], S.Schlenstedt[3], H.Tiecke[8], W.Verkerke[8], J.Vossebeld[8], M.Vreeswijk[8], S.M.Wang[6], J.Wu[6]

   [1] Physikalisches Institut der Universität Bonn, Bonn, Germany
   [2] Deutsches Elektronen-Synchrotron DESY, Hamburg, Germany
   [3] DESY-Zeuthen, Zeuthen, Germany
   [4] Fakultät für Physik der Universität Freiburg i.Br., Freiburg i.Br., Germany
   [5] Hamburg University, II. Institute of Exp. Physics, Hamburg, Germany
   [6] University of Iowa Physics and Astronomy Dept, Iowa City, USA
   [7] Univer. Autonoma Madrid, Depto de Fisica Teorica, Madrid, Spain
   [8] NIKHEF and University of Amsterdam, Netherlands.

2. ZEUS, A Detector for HERA, DESY, February 1993.

3. A. Andresen et al. NIM A309 (1991)101-143.
4. A.Weisenberger et al., NIMA327 (1993)500-508.
5. A.Caldwell et al., NIM A321(1992)356.
6. Shaping Amplifier for PMT signals for ZEUS, P.Rewiersma, I.Weverling, NIKHEF-ETR 94-12.
7. B.Krebs et al., NIM A323(1992)611.
8. U.Behrens et al. NIM A289 (1990), 115.
   A.Andresen et al. NIM A290 (1990), 95.
   W.Kröger, Studies of particle Jets with an Interaction Trigger, PhD Thesis, University of Hamburg, 1992.
9. A Prototype Presampler for Uranium-Scintillator Calorimeter in ZEUS, H.Grabosch et al., NIKHEF-H/93-11.
10. A. Bornheim, Diploma Thesis, Bonn IB 95-24 (1995) (in German).

·ascati Physics Series Vol. VI, (pp. 219–224)
I INT. CONF. ON CALORIMETRY IN HEP – Frascati, June 8–14, 1996

WLS FIBERS FOR CALORIMETRY: COMPARATIVE STUDIES

A. Maio, M. David, A. Gomes and A. Henriques
LIP and FCUL, Av. Elias Garcia 14 1°, 1000 Lisbon, Portugal

ABSTRACT

Optical properties of polystyrene WLS fibers with different cladding, con-entration and UV absorber are compared. Typical results for fibers from Bicron, ʿuraray and Pol.Hi.Tech are presented.

Introduction

n this paper we will report on our experience on polystyrene WLS fibers developed ɔr electromagnetic and/or hadronic calorimeters. This work is still in progress ,nd it is essentially developed to optimize the performance of the Barrel Hadronic ʾalorimeter of ATLAS (TILECAL/ATLAS) [1] [2] [3] [4]. Fibers from BICRON, ‹URARAY and POL.HI.TECH companies are being tested and used to build proto-ypes and the final ATLAS calorimeter. Tests have been also made in order to select VLS fibers for the upgraded DELPHI Scintillator TIle and WLS fiber Calorimeter STIC) [5].

! Experimental results

Ꮁhe general requirements for electromagnetic and hadronic calorimeters are not ıecessarily the same. Fibers for electromagnetic calorimeters are about 50 cm long as it is the case when the absorber is lead) and for hadronic calorimeters the typical engths are of the order of 200 cm. The density of fibers can also change drastically 'rom one calorimeter to another, making light yield very critical.

In this paper we will report on the optimization of some properties of he optical fibers: light yield, attenuation length, response to charged particles and nechanical flexibility. This work was developed in close collaboration with BICRON, ‹URARAY and POL.HI.TECH. Experimental results for the optical properties of ibers measured as function of cladding type, dopant or UV absorber concentration ınd mechanical properties are presented.

Fiber response to the blue TILECAL scintillator [6] is measured using a ɔi-alkali photomultiplier tube (PMT) and integrating the current I(x) with a digital nultimeter. The light in the scintillator is excited by electrons from a ^{90}Sr β-source.

The same β-source was used to evaluate the WLS fiber response to charged particles. Position of the source, movement of the scanning table and measurement of current,

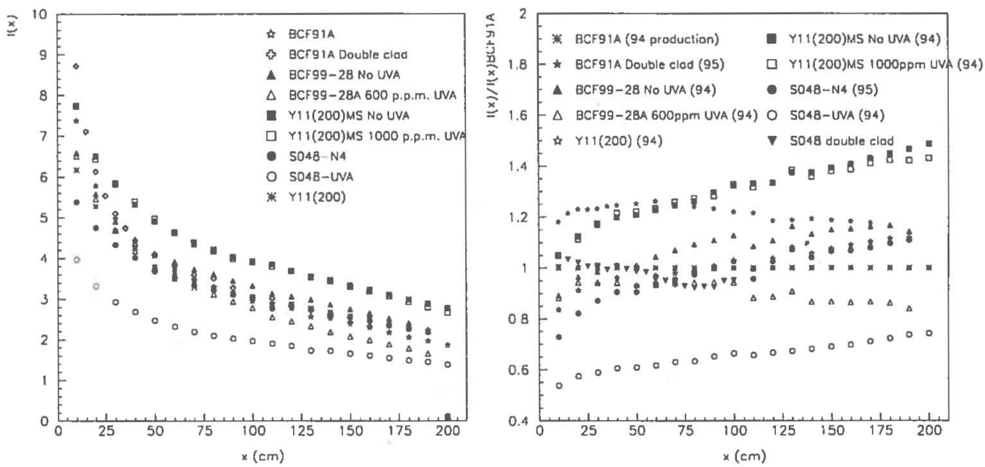

Figure 1: Light output $I(x)$ for some typical 200 cm long WLS fibers as a function of distance x to the PMT (left). Light output of WLS fibers normalized to the BCF91A fiber $*$ (right).

is computer controlled by a Macintosh equipped with LABVIEW software [7]. The fibers light output can be described satisfactorily (see Fig.1-left) by the sum of two exponentials with attenuation lengths L_1 (short) and L_2 (long).

2.1 Effect of the dopant concentration

Since 92 that fibers with various dopant concentrations have been systematically tested. Optimal concentrations for each of the selected type of fibers were found. Till a certain limit, the light yield increases with increasing dopant concentration. First, the light transmitted through the fiber is not attenuated, but after a certain dopant concentration, the increase in light yield is obtained at expenses of decreasing the attenuation length.

In Fig.1-left are shown the lightoutput I(x) of the several typical fibers tested for the TILECAL calorimeter: Bicron BCF91A and BCF99-28, Y11 from Kuraray (the number in parentheses stands for the dopant concentration, M for multicladding and S means that the fibers are produced to be flexible), and S048-100 from Pol.Hi.Tech. In Fig. 1-right the same experimental results are shown but with the I(x) values normalized to the correspondent values for the BICRON BCF91A fibers used to instrument the first TILECAL prototype. For each of those fibers, optimized in dopant concentration, the optical characteristics are shown in table 1.

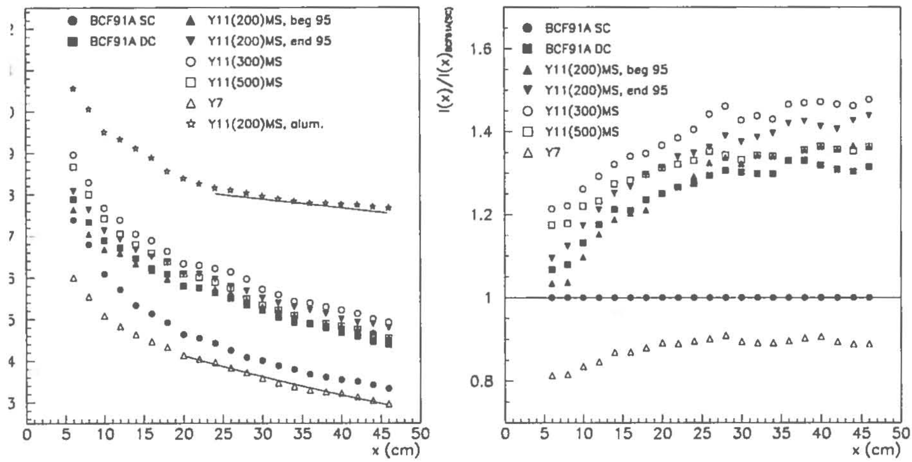

igure 2: Light output $I(x)$ for some typical 50 cm long WLS fibers as a function f distance x to the PMT (left). Light output of WLS normalized to the BCF91A iber • (right).

ll three producers can offer WLS fibers with light output and attenuation length L_2 that are compatible with the minimal requirements of the TILECAL calorimeter about 150 cm for non aluminized fibers). However for some of these fibers other parameters need also to be optimized, such as mechanical fragility and radiation hardness [3) 9)].

Fig.2-left and 2-right shows recent experimental results from studies to optimize the light yield response of short fibers (50cm long) to instrument the upgrade DELPHI STIC calorimeter. Fibers with 300 ppm of dopant concentration can be adequate for this detector by increasing the signal/noise ratio improving the detection of particles depositing little energy in the calorimeter as it is the case of muons. Since the fibers are short, it can be possible to increase the light yield without appreciate deterioration of the effective attenuation length. This value, when measured between 20cm and 40cm from the PMT is $\sim$ 100 cm without mirror and about 350 cm with an aluminised mirror (reflectivity of 0.7) at one fiber end.

In Fig.2 it can be seen the gain in light output, when using Y11 fibers instead of the Y7. Y11 fibers were not available when the STIC was designed and material commissioned. Typical values for lightoutput and attenuation length are shown in table 2.

Company	Fiber type	UVA conc (ppm)	L_2 (cm)	I (90) (a.u.)	I (140) (a.u.)
Bicron	BCF91A		262 (4.7%)	2.09 (1.3%)	1.69 (2.8%)
	BCF99-28	0	261 (4.0%)	3.45 (1.7%)	2.86 (1.4%)
	BCF99-28A	600	186 (2.2%)	2.94 (2.6%)	2.18 (2.7%)
Kuraray	Y11(200)MS	0	310 (6.2%)	4.03 (1.4%)	3.46 (1.1%)
	Y11(200)MS	1000	280 (1.9%)	3.99 (1.9%)	3.43 (2.4%)
Pol.Hi.Tech	S048-100 N4		291 (9.2%)	3.11 (2.8%)	2.63 (3.3%)
	S048-100 UVA	not spec.	303 (3.7%)	2.03 (1.9%)	1.72 (1.9%)

Table 1: Typical values for lightoutput $I(90cm)$, $I(140cm)$ and attenuation length L_2 (long component), of 200 cm long fibers. In () are shown the fiber to fiber fluctuations, for an average of 5 fibers.

2.2 Fiber cladding

In Fig.1 it is shown the optical improvement by using a multiclad instead of a single clad fiber. KURARAY Multiclad fibers are available since last few years [8]. When compared with single clad fibers they show an increase of about 40%. BICRON and POL.HI.TECH are also developing this technique but the results are not still satisfactory, as it can be seen in Fig.1.

2.3 Fibers with UV absorber

Experimental tests on the first TILECAL prototype [10], have shown that muons or pions impinging on the crack region between scintillators (where the fibers sit) produce an enhancement of the calorimeter signal, leading to appreciable nonuniformities. This effect can be reduced with the addition of small concentrations of UV absorber (UVA) to the mixture used in the commercial standard fibers. In Fig. 3 it is shown the ratio of the light output at 140 cm, for fibers doped with and

Fiber type	L [20-40 cm] (cm)	I (20) (a.u.)	I (40) (a.u.)
Y11(200)MS	100.9	6.08	5.00
Y11(200)MS alum	366.0	8.56	7.76
Y7(250)	76.5	4.13	3.21

Table 2: Typical values for lightoutput $I(20cm)$, $I(40cm)$ and attenuation length L between 20 and 40 cm, for 50 cm long fibers.

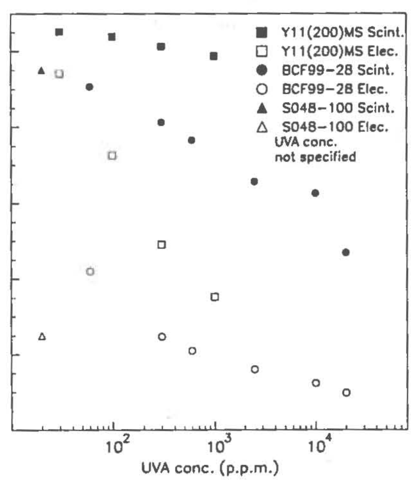

igure 3: Ratio [I(140) with UVA] [I(140) no UVA] for Bicron, Ku-ıray and Pol.Hi.Tech fibers, as func-on of UV absorber concentrations. 'he S048-100 UV absorber concentra-on was not specified. Scintillator ɔlack points) and electron response ɔpen points).

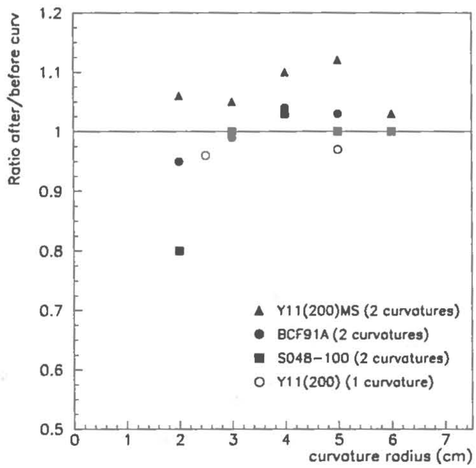

Figure 4: Ratio of lightoutput after/before bending as a function of curvature radii. The Y11(100) fiber has one curvature and the others have two curvatures.

/ithout UVA as function of the UVA concentration. For the TILECAL calorimeter he 600ppm UVA, results in a optimal uniformity of the calorimeter.

:.4 Mechanical stress

ʾlexibility of the WLS fibers for TILECAL calorimeter is mandatory. The fibers ıeed to be curved to diameters of about 10cm or less and they should survive during .0 years. Mechanical fragility of fibers can be considerable [3]. Presently, the plas-icity of the fibers can be optimized to reach the calorimeter required performance ıs it is shown in Fig.4. Some of the fibers can be bended to diameters of 5 cm vithout appreciable degradation of the attenuation length. Tests are underway.

3 Conclusions

Bicron, Kuraray and Pol.Hi.Tech produce WLS fibers with adequate light yield and attenuation length to be used in electromagnetic and/or hadronic calorimeters. Plasticity of fibers allows curvatures with diameters of the order of 10 cm and WLS dopant and UVA absorber concentration can be tuned to specific requirements. For calorimeters using a small density of WLS fibers, as the case of TILECAL, multiclad fibers with light yield similar to the Y11 KURARAY fibers will improve considerably the calorimeter performance. Radiation hardness of fibers was presented in another paper of this Conference, but should not be forgotten when selecting WLS fibers.

4 Acknowledgments

We gratefully acknowledge M. Mishina, B. Miller and J. Huston for helping us with the fiber cutting machine, and the financial support of JNICT/Portugal.

References

1. O. Gildemeister, F. Nessi-Tedaldi and M. Nessi, Proc. 2nd Int. Conf. on Calorimetry in HEP, Capri 1991
2. ATLAS Technical Proposal, CERN/LHCC/94-43, 15 December 94
3. M. David et al., Comparative Measurements of WLS Fibers, ATLAS Internal Note, TILECAL-NO-034, 28 November 1994 M. David et al., Systematics of WLS fibers with UV absorber, to be published as TILECAL internal note
4. A. Ariztizabal et al., Construction and Performance of an Iron-Scintillator Hadron Calorimeter with Longitudinal Tile Configuration, NIM A349 (1994) 384-397
5. A. Benvenuti et al., Prototype design, construction and test of a Pb/scintillator sampling calorimeter with wavelength shifter fiber optic readout, IEEE Transactions on Nuclear Science, Vol. 40, No. 4, 1993
6. V. K. Semenov, Proc. IX Conference on Scintillators, Kharkov 1986, p. 86
7. B. Tome et al, Test bench for quality control of scintillating and WLS fibers, LIP note 5-10-94
8. S. Buontempo et al., An instrument for the high statistics measurement of plastic scintillating fibers. NIM A348 (1994), 131-138
9. M. David et al., Dose rate effects in WLS fibers, to be published as TILECAL Internal note, and in this proceedings.
10. A. Henriques, Response of the ATLAS Tile Calorimeter Prototype to Muons, these proceedings

ıscati Physics Series Vol. VI, (pp. 225–236)
INT. CONF. ON CALORIMETRY IN HEP – Frascati, June 8–14, 1996

RECENT EXPERIENCE WITH THE H1 LEAD/SCINTILLATING FIBRE CALORIMETER

Igor V. Gorelov
ITEP (Moscow) representing the H1 Collaboration (DESY)

ABSTRACT

ıe backward region of the H1 detector has been upgraded in winter–shutdown 94/95 with a new lead/scintillating-fibre calorimeter SPACAL consisting of two parate parts – a closest to an interaction point electromagnetic section followed by hadronic section. Later in winter shutdown 1995/96 a volume around the beam pe in the iron return yoke has been instrumented with a small backward plug lorimeter worked out with the same technology. The purpose of these detectors a precise measurement of the energy and position of the scattered electron in *ep* llisions at HERA up to tiny angles w.r.t. the beam pipe corresponding to low Q^2 nematic domain. SPACAL also determines the hadronic energy flow and provides precise time information to suppress beam-related out–of–time background events the first trigger level. The recent experience with the data taken is presented.

Introduction

winter–shutdown 1994/95 the backward region of the H1 detector at the *ep* stor-e ring HERA has been equipped with a high–resolution lead/scintillating–fibre lorimeter SPACAL [1]. The calorimeter comprises an electromagnetic and a dronic section. In 1995/96 the acceptance near the beam pipe has been fur-er increased by adding a backward plug calorimeter BPLUG. The position of the lorimeters inside the H1 detector is illustrated in Fig. 1.

The main physics motivation for the construction of a high–resolution lorimeter is the measurement of the proton structure function which implies a pre-se reconstruction of the kinematic variables in deep inelastic scattering events [1]) to very low x values of the order of 10^{-5} with low Q^2 values of 0.1 GeV^2.

The aim for a good energy resolution which directly affects the x resolution led to the choice of 0.5 mm diameter fibres in combination with a lead–to–fibre ratio of 2.3:1 for the electromagnetic section [2, 3]. The large acceptance up to angles as large as 177.5° and the need of a good Q^2 resolution requires the angular resolution to be of 1–2 mrad which corresponds to a position resolution of a few millimeters [1]. This fact in turn requires the fine granularity of the electromagnetic SPACAL.

The hadronic section of SPACAL [3] aims to measure electromagnetic energy leakage from the electromagnetic section and, in combination with it, to measure hadronic energy flow in the backward region. The extra $\sim 1\lambda$ depth of the hadronic section, together with $\sim 1\lambda$ of the electromagnetic part, provides longitudinally- segmented calorimetry which enhances the e/π separation capabilities [4] and improves the measurement of hadronic jets.

The special innermost 16-cell module of electromagnetic section, so called insert, measures electrons scattered to small angles and controls the energy leakage into the beam pipe.

To suppress the background induced by the proton beam the calorimeter is exploiting the 9 ns (for the electromagnetic section) or 12 ns (for the hadronic one) time–of–flight (*ToF*) difference of particles originating at the *ep* collision vertex compared to those from upstream proton beam background events. Based on precise timing, SPACAL provides the H1 detector with a veto on this background at the first level trigger.

A summary of the basic design requirements and construction parameters is given in Table 1.

The backward plug calorimeter BPLUG extends the acceptance of the electromagnetic and hadronic calorimeter to polar angles of 178.7°, covering a Q^2 range of approximately 0.1 – 0.5 GeV^2 for events at the nominal ep interaction vertex. This kinematic domain is particularly interesting as the transition region between deep inelastic scattering and photoproduction processes. All 12 modules of BPLUG [3] have a lead–to–fibre ratio of 3.4:1 with 1 mm thick fibres similar to the hadronic section. Being placed a larger distance from the ep collision vertex BPLUG provides additional veto information to the H1 first level trigger.

Since all sections of SPACAL are situated in a strong magnetic field of 1.0 Tesla, they are equipped with fine–mesh photomultipliers from Hamamatsu (for details see [5]).

A precise energy measurement requires the effective monitor of any short–term fluctuations and long–term drifts of the photomultiplier gains with a precision of a few per mil. This task is fulfilled by means of a light–emitting diode (LED) monitoring system [6].

The calorimeter electronics comprises three parallel branches for energy easurement, time measurement and trigger information [7].

Table 1: Construction parameters of the calorimeter.

	Electromagnetic section	Hadronic section
Acceptance	$153° < \theta < 177.5°$	$160° < \theta < 178°$
Energy resolution	$\leq 2\%$ at 30 GeV (electr.)	$\sim 40\%$ (hadr.) [4]
Angular Resolution	1–2 mrad	–
Time resolution	< 1 ns	< 1 ns
e/π Rejection	> 100 [4]	–
Lead/fibre ratio	2.3 : 1	3.4 : 1
Fibre diameter	0.5 mm	1.0 mm
Number of channels	1192	136
Size of standard cell	40.5×40.5 mm^2	119.3×119.0 mm^2
Active length	250 mm	250 mm
Radiation length	9.0 mm	8.5 mm
Interaction length	250 mm	246 mm
Molière radius	25.5 mm	24.5 mm
Lead–fibre–density	7.3 g/cm^3	7.7 g/cm^3

Performance of the electronics

he signals from an integrating preamplifier situated directly on the base of every ıototube arrive through coaxial cables to the energy, time and trigger branches. he slow energy branch signal is bipolar and peaked at 300 ns. It is delayed by an ljustable delay line, stored in a sample/hold circuit and then digitized by two 12 ts ADCs through a 128-channel multiplexer with 2 outputs with a gain ratio of 7. Thus the effective dynamical range of 14 bits is reached and covers the energy ınge from few tens MeV (as deposited by minimum ionizing particle) up to 40 GeV. he noise level in this branch was observed to be $\sigma_{noise} \simeq 3\ MeV$.

To provide a time resolution of better than 1 ns, the calorimeter signals are d into fast shaping units with a peak time of 6 ns followed by Constant Fraction iscriminators (CFD). One CFD output is sent to a 6–bit TDC, the other is put in ›incidence with the in–time *ToF* window gating the signals from the nominal vertex *ep* collisions. In the first year of running we achieved the desired time resolution better than 1 ns for particle energies ranging from a few hundred MeV up to) GeV. The typical TDC time distribution for electron candidates with an electron uster energy above 4 GeV is illustrated in Fig. 2. The fit with the Gaussian yields $_{TDC} \simeq 0.6\ ns$ which is in agreement with test beam results [2].

The trigger branch [7] signals are peaked at 30 ns and are directed according to the *ToF* coincidence into the in–time *ToF* or out–of–time *AToF* channel. The noise level was found to be $\sigma_{noise} \simeq 3\ MeV$. An analog adding tree produces various *ToF* and *AToF* energy sums and the Inclusive Electron Trigger (*IET*). The *IET* system provides a high granularity of 320 16 $\times$ 16 cm^2 overlapping trigger windows with three different *ToF* energy threshold levels. The three levels may be set to 15 GeV for high–energetic electrons to be used for calibration, to 2–6 GeV for a low–x physics trigger and to $\sim$ 100 MeV as a minimum–bias trigger. In addition, the thresholds may vary over detector area. For the first year of data taking, we decided to divide the detector into three regions of different thresholds. The lowest threshold was set to 4 GeV for the central detector region and to 1 GeV for the outer region.

The threshold curves for the central area of electromagnetic section corresponding to second (physical) and third (calibration) thresholds are shown in Fig. 3. The 100% trigger efficiency is reached for electron energies larger than 9 GeV in genuine deep inelastic scattering events. Excluding a small number of not yet fully optimized detector channels full efficiency is reached at lower electron energies of about 4 GeV. This allows us to extend the kinematic range of structure function measurements [8] compared to previous H1 results [9].

3 Monitoring and Energy calibration

To be able to fully exploit the intrinsic energy resolution of the calorimeter, the precision of the energy calibration is of major importance. Therefore the gains of photomultipliers are carefully monitored in time with a special light pulser based on LEDs illuminating via the optical fibers the phototubes. The system is also used for initial HV setting and rough timing adjustments. The response of every LED is monitored with photodiodes to be read out in the same way as the signals from photomultipliers.The LED Trigger rate was set to 1Hz in 1995. The response of the phototube normalized to the response of the corresponding photodiode is shown as a function of time in Fig. 4. The upper picture illustrates the bad phototube to be replaced during 1995/96 winter shut-down, while the other one is the typical behavior of the gain with the instabilities of less then 1%.

The relative calibration of the electromagnetic section is based on three main methods: calibration with high–energetic electrons in deep inelastic scattering events, with cosmic muons and with muons of the proton beam halo. For the inter-calibration of the hadronic section, cosmic muons and halo muons are used.

The scattered electron spectrum shows a steep peak at energies close to the incoming electron beam energy. The position of the peak is well known by ton structure measurements of fixed-target data and can thus be used to calibrate detector cells [10]. The calibration procedure constrains the energy sum of ically 3–4 cells. In Fig. 5 calibrated data and simulation spectra are shown for ee detector regions of different radial distance to the beam line. The excellent eement of data and simulation is clearly visible. For the inner region of the ector we obtain a precision of 1–2% in the relative energy calibration. Analyzing detailed peak shape we derive a stochastic term for energy resolution of $\sigma/E =$ % consistent with our test beam measurements [2]. The outer and partially ermediate regions are calibrated with cosmic and halo muons as the electron ctrum suffers from poor statistics in that areas (see Fig. 5). The hadron section calibrated with cosmics.The size of cosmic muons and halo muons signals in the ronic calorimeter corresponds to $\sim$ 150 MeV and $\sim$ 400 MeV, while for the ctromagnetic section the numbers are $\sim$ 50 MeV and $\sim$ 400 MeV respectively. e signals are well above noise level. The precision of the relative energy calibration h muons was determined to be 2–3% .

Using the data taken in 1995 we directly determined the spatial resolution king at the difference between the position of electron cluster calculated as centre gravity for cells weighted as a logarithm energy and the respective measurement m a backward drift chamber BDC (see Fig. 1). For electron clusters with the ergy above 15 GeV and the distance w.r.t. the beam pipe of less than 15 cm an *IS* of position resolution was measured to be (4.0 ± 0.2) mm .

To understand our absolute energy scale we used several methods. One of em is the electron proton scattering with radiative Compton photons in the final te [11]. These events have very simple topology with only one or two tracks in the ckers and two coplanar and distinct electromagnetic clusters in electromagnetic tion. Then the energy of every cluster is constrained by the kinematics of an ent and can be easily calculated from the initial electron beam energy and angle asurements in trackers. To estimate the linearity of the absolute energy scale we the expression 1.

$$\frac{E^{clus}_{meas} - E^{clus}_{calc}}{E^{clus}_{calc}} \tag{1}$$

the Fig. 6 the difference of eq. 1 in MC calculations and data is drawn against e cluster energy as measured in the calorimeter. The linearity of the energy scale lows the Monte Carlo calculations within $\sim$ 1% for the clusters above 10 GeV. other similar approach, the 'Σ–method', makes use of the 4π acceptance of the detector which enables to reconstruct the kinematic variables in deep inelastic attering using measured quantities from the hadronic final state (calorimetric and ack information) [12]. The comparison of the calculated energy with the energy at is directly measured in the SPACAL calorimeter serves as a powerful test for the understanding of the absolute energy scale. In Fig. 7, the distribution of the ratio of the kinematical variable y measured using the 'Σ-method' and the scattered electron, y_Σ/y_e, and the distribution of the ratio for the transverse momenta, $p_{t,h}/p_{t,e}$, are shown. Good agreement with Monte Carlo is seen for both distributions. Finally we estimate the uncertainty of our absolute electromagnetic energy scale to be 2%

4 Summary

The first year of data taking has proved that the new H1 lead/scintillating-fibre calorimeter SPACAL is working according to the design specification.

The noise in energy and trigger branches was observed to be $\sigma_{noise} \simeq 3\ MeV$. A time resolution of better than 1 ns was reached for energies as small as a few hundred MeV. The trigger performance and its thresholds have been understood. The typical gain deviations of phototubes of less than 0.5% were observed with the LED monitoring system. A stochastic term of energy resolution of 1.5% for 30 GeV electrons was confirmed by real data. The first relative calibration with high-energetic electrons reached a precision of 1–2 %. The calibration of the hadronic calorimeter section was performed with cosmic and beam halo muons leading to a precision in the order of 2%. The uncertainty of the absolute electromagnetic energy scale was estimated to be 2%. Using the data taken an *RMS* of position resolution of the order of 4 mm for clusters at a radial distance below 12 cm w.r.t. the beam pipe was measured. Our Monte-Carlo simulations reasonably describe data.

We conclude that H1 SPACAL became a working detector which was able to record a large first set of high-quality data in its first running period.

5 Acknowledgments

It is a pleasure to thank our colleagues and the many engineers and technicians from the participating institutes for their permanent interest in the project and their good team spirit. Without their outstanding commitment this calorimeter would not be. Many thanks to the organizers of the 'VI International Conference on Calorimetry in High Energy Physics' for an excellent organization of the Conference and for a warm south hospitality.

ferences

H1 Collaboration, *Technical Proposal to Upgrade the Backward Scattering Region of the H1 Detector*, PRC 93/02, March 8, 1993.

The H1 Spacal Group, DESY–95–165, Sept. 1995, to appear in Nucl. Instr. and Methods **A 374** (1996).

H1 Spacal Group, *The H1 Lead/Scintillating–Fibre Calorimeter*, to be submitted to Nucl. Instr. and Methods;
H1 Spacal Group, DESY–96–013, Jan. 1996.

H1 Spacal Group, DESY–95–250, Sept. 1995, submitted to Nucl. Instr. and Methods.

Hamamatsu Photonics Data Sheet;
R.D. Appuhn *et al.*, *Performance Tests with a Large Sample of Fine Mesh Photomultipliers for Use at 1.2 Tesla*, Proceedings of the IV International Conference on Calorimetry in High Energy Physics, La Biodola, Elba, Italy (1993) 118;
J. Janoth *et al.*, Nucl. Instr. and Meth.**A350**(1994) 221;
H1 SPACAL GROUP, *Test of a Large Number of Fine-Mesh Photomultiplier Tubes for Usage in a Magnetic Field of 1.2 Tesla,* to be submitted to NIM.

. H1 Spacal Group, *The LED based Calibration System of the H1 Lead/Scintillating–Fibre Calorimeter*, to be submitted to Nucl. Instr. and Methods.

. H1 Spacal Group, *The Electronics of the H1 Lead/Scintillating–Fibre Calorimeter*, to be submitted to Nucl. Instr. and Methods.
V. Boudry *et al., The Inclusive Electron Trigger for the SPACAL: Design and CERN-test Results*, H1 internal note, H1-03/95-430.

. V. Chekelian(Shekelyan), *New Results from H1 on Structure Functions*, to be published in Proceedings of the 28th International Conference on High Energy Physics ICHEP'96, Warsaw, Poland, July 1996.

. H1 Collaboration, DESY–96–39, submitted to Nucl. Physics.

. H1 BEMC Group, DESY–95–177, Sept. 1995.

. A. Courau and P. Kessler, Phys. Rev. **D7** (1986) 2028.

. S. Bentvelsen *et al.*, Proc. of the Workshop *Physics at HERA*, Vol. 1 (1991) 23.
H1 Collaboration, T. Ahmed *et al.*, Nucl. Phys. **B439**(1995) 471

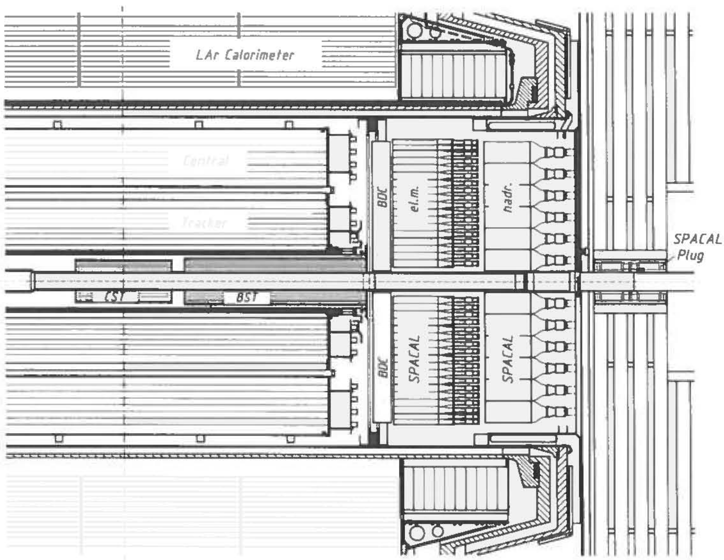

Figure 1: Side view of the H1 detector showing the new calorimeters.

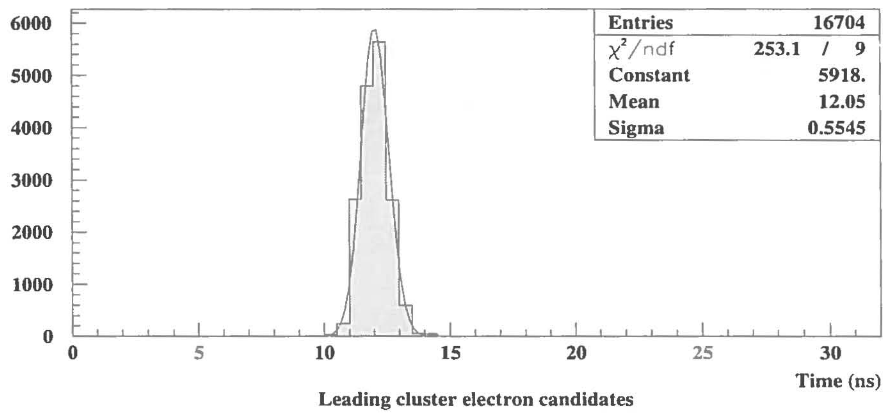

ure 2: The TDC time distribution for electron candidates with an energy above ;eV.

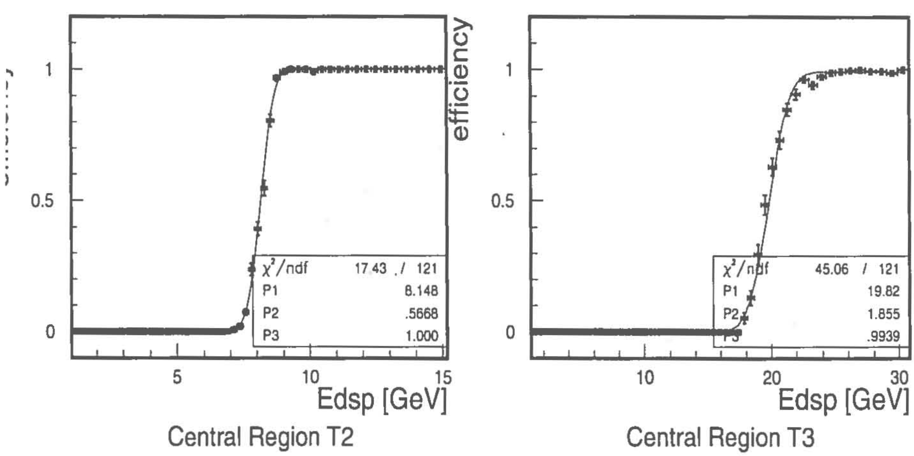

;ure 3: The threshold curves for central physical area of electromagnetic section d second threshold T2, physical trigger (left picture), and third threshold T3, ;h energy electron trigger for calibration purposes (right picture). Points corre- ond to data, solid lines show fit with probability function. The trigger energy is :onstructed using the information from the energy branch.

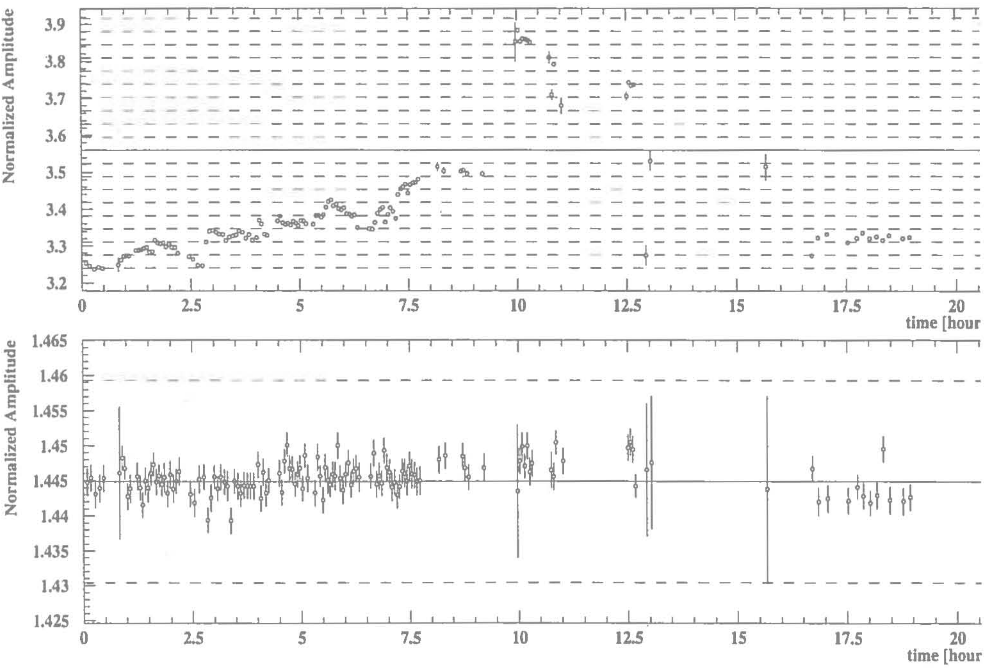

Figure 4: The response of PMT to LED normalized to the response of photodiode to LED as a function of time. The gap between dashed lines corresponds to 1% deviation. The upper picture shows the bad PMT replaced this winter shutdown, while the lower one displays the typical instabilities.

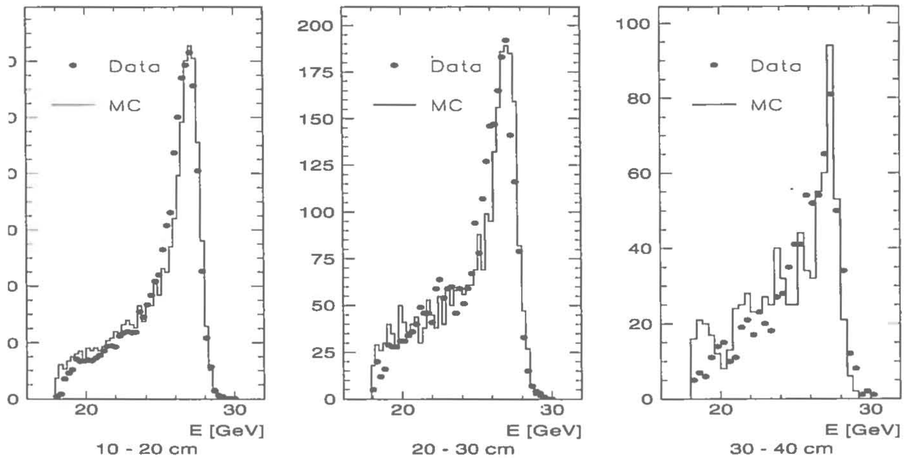

ure 5: Scattered electron energy spectra for inner, intermediate and outer areas of :tromagnetic section. The spectra suffer from poor statistics as the cross section ps towards outer cells.

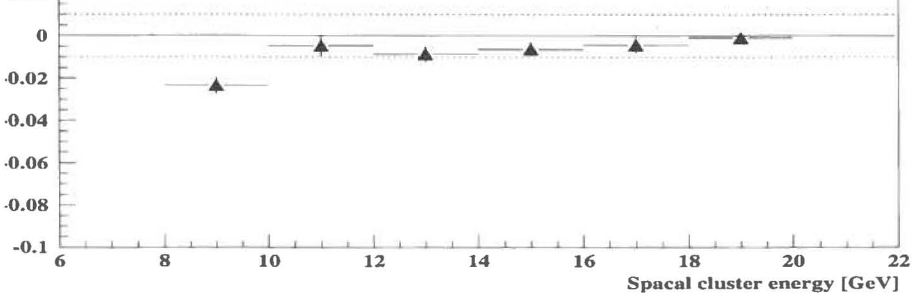

;ure 6: The electromagnetic cluster energy for Compton events - check of linearity comparison with Monte-Carlo calculations.

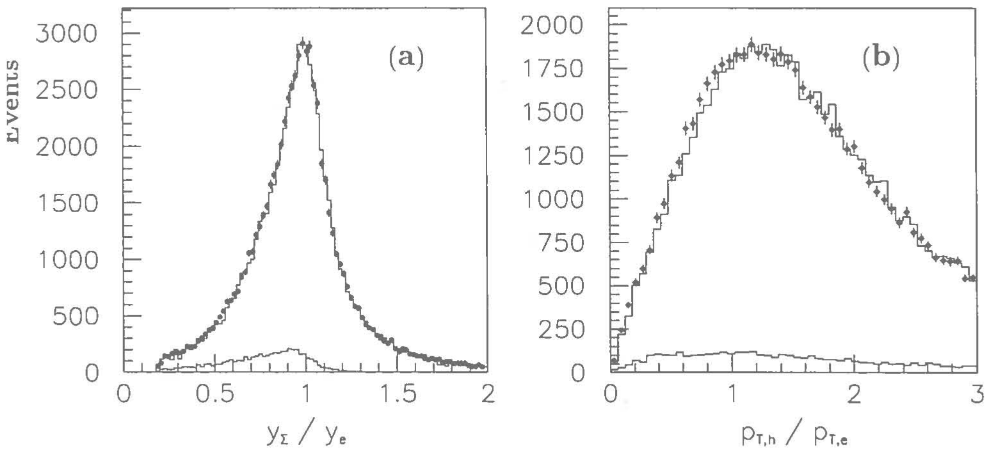

Figure 7: Experimental (points) and Monte Carlo (solid lines) distributions for $y_\Sigma > 0.05$ of the ratio of a) the y values measured with the Σ, and Electron method y_Σ/y_e, and b) the transverse momentum of the hadronic system and the electron $p_{t,h}/p_{t,e}$. The Monte Carlo curve is the sum of DIS and photoproduction background events (shown separately by the lower curve)

scati Physics Series Vol. VI, (pp. 237–246)
INT. CONF. ON CALORIMETRY IN HEP – Frascati, June 8–14, 1996

STATUS REPORT ON THE CONSTRUCTION OF THE KLOE CALORIMETER

M. Incagli
INFN – Sezione di Pisa, Pisa Italy

For the KLOE Calorimeter Group

ABSTRACT

e design and status of construction of the KLOE electromagnetic calorimeter are ;cribed in this report. A particular accent is put on the physics motivations that /e driven the calorimeter parameters. At this moment 19 out of 24 *Barrel* (central) ›dules and 42 out of 64 *End Cap* (forward) modules have been built. A full e prototype module has been tested at PSI beam (Zurich) showing performances ;hin specifications. All modules are tested, as they are built, at the Cosmic Ray st Stand facility set up in Laboratori Nazionali di Frascati. The results of these ts show a time resolution of 55 ps/$\sqrt{E(\mathrm{GeV})}$, a spatial resolution along the fiber 0.9 cm/$\sqrt{E(\mathrm{GeV})}$ and an energy resolution of 4.7% /$\sqrt{E(\mathrm{GeV})}$.

The KLOE calorimeter group is composed by:

M. Antonelli,[c] F. Anulli,[c] G. Barbiellini,[j] S. Bertolucci,[c] C. Bini,[f] C. Bloise,[c] R. Caloi,[f] G. Cabibbo,[g] P. Campana,[c] F. Cervelli,[e] G. De Zorzi,[f] G. Di Cosimo,[f] A. Di Domenico,[f] '. Erriquez,[a] S. Di Falco,[e] A. Farilla,[a] A. Ferrari,[f] P. Franzini,[f,d] P. Gauzzi,[f] S. Giovannella,[c] E. Graziani,[h] S. W. Han,[c,b] M. Incagli,[e] W. Kim,[i] G. Lanfranchi,[f] J. Lee-Franzini,[c,i] T. Lomtadze,[e] S. Miscetti,[c] F. Murtas,[c] F. Scuri,[j] E. Spiriti,[h] L. Tortora,[h] G. Venanzoni,[e] S. Wölfle,[c] J. Q. Zhang.[c,b]

ɔartimento di Fisica dell'Università e Sezione INFN, Bari
ititute of High Energy Physics of Academica Sinica, Beijing, China
boratori Nazionali di Frascati dell'INFN, Frascati
ıysics Department, Columbia University, New York
partimento di Fisica dell'Università e Sezione INFN, Pisa
partimento di Fisica dell'Università e Sezione INFN, RomaI
partimento di Fisica dell'Università e Sezione INFN, RomaII
ituto Superiore di Sanità and Sezione INFN, ISS, Roma
ysics Department, State University of New York at Stony Brook
partimento di Fisica dell'Università e Sezione INFN, Trieste/Udine

1 CP Physics at KLOE: the role of the EMC

The main goal of the KLOE [1] experiment at the DAΦNE ϕ factory is to study CP violation in the Kaon system, in particular by measuring $\Re(\varepsilon'/\varepsilon)$with an accuracy of $O(10^{-4})$. The *golden channel* in which to perform this measurement is the decay chain $\phi \to K_S K_L \to (\pi\pi)(\pi\pi)$. The electromagnetic calorimeter (EMC) has to be able to reconstruct the neutral decay vertex $K_{L,S} \to \pi^0\pi^0$. In the ϕ two body decay,the neutral Kaons are emitted at low speed ($\beta \simeq 0.2$) and the energy spectrum of photons from pion decay ranges from 20 to 280 MeV. Therefore the EMC has to able to detect photons with very high efficiency down to 20 MeV. Moreover the EMC has to measure the K_L decay point (*neutral vertex*) with a precision of $\simeq 1\,cm$, to define with sufficient precision the Fiducial Volume. This can be accomplished by measuring the γ conversion point, with an accuracy of $\simeq 1\,cm$ and its arrival time on the calorimeter, with an accuracy of $\simeq 150\,ps$ (the algorythm used to reconstruct the neutral vertex is discussed, for example, in [1]). This implies that the EMC has to have excellent time and position performances. Note also that, given the K_L mean fly path of 343 cm, the photons will impact on the calorimeter face from all directions, making useless a projective geometry.

The main background to the neutral channel is the CP conserving decay $K_L \to \pi^0\pi^0\pi^0$, in which two of the final pions are missed. This channel is $\simeq$ 200 times the *golden channel*, so, in order to get the required accuracy on $\Re(\varepsilon'/\varepsilon)$, it has to be suppressed at the level of 10^{-4}. In order to reach this rejection factor the calorimeter has to be as hermetic as possible.

The requirements on KLOE EMC can be summarized as follows:

- Full efficiency in the range $20 - 240\,MeV$
- Excellent time resolution ($\simeq 70\,ps\sqrt{E(\mathrm{GeV})}$)
- Determination of γ conversion point with an accuracy of $\simeq 1\,cm$
- Good energy resolution ($\simeq 5\%\sqrt{E(\mathrm{GeV})}$) to apply kinematical constraints
- Hermeticity to reject $K_L \to \pi^0\pi^0\pi^0$
- Fast response for trigger purposes, mainly to reduce the Bhabha rate ($\simeq$ 50 $Khertz$)

All of the above has to be accomplished by a calorimeter having dimensions of $\simeq 4\,m$!

The KLOE calorimeter

'en the above requirements, the choice has been made to use a fine sampling 1-scintillating fibers calorimeter with 1 mm fibers and 0.5 mm thick lead foils t together by optical glue (Bycron BC600). The ratio fiber:lead:glue is 48:42:10 allowing for a very high sampling fraction of 13%. It is very important to note t the fibers run *perpendicular* to the incident particle (at least for particles from Interaction Point), differently from the standard Spaghetti calorimeters.

The calorimeter density is $\rho = 5\,gr/cm^3$ and its equivalent interaction gth is $X_0 = 1.5\,cm$.

The KLOE electromagnetic calorimeter [1] consists of a central part, the *rel* and two *end-caps* (see fig.1). The *barrel* covers the angular region $43^o < \theta <$ and it is organized in 24 modules of trapezoidal cross section 4.3 m long and 23 thick ($15X_0$), approximating a cylindrical shell of 4 m inner diameter. Fibers ı parallel to the beam. Each *end-cap* consists of 32 modules of different lengths ich run parallele to the vertical (y) axis. They also are 23 cm thick and are bent wards at the two ends, becoming parallel to the *barrel*. The resulting C shape vides a hermetical coverage of the calorimeter.

Kuraray SCSF-81 and Pol.Hi.Tech. 0046 fibers, both emitting in the blue ion, are used: measurements carried on samples of fibers shows that they satisfy requirement for light yield, scintillation decay time and attenuation length [3].

Modules construction

Mechanical assembly

e mechanical assembly of *barrel* modules is being carried out at Pol.Hi.Tech. with peed of construction of 3 weeks/module. First of all, (450×65) cm^2 lead foils 0.5 n thick are machined to the proper grooved shape by our *lead-o-matic*. Tolerances foil construction are kept tight in order to facilitate the assembly: grooves do t deviate by more than 0.5 mm from a straight line, while the pitch is precise to evel of $20 \div 30$ μm. The assembly starts by glueing the first lead foil on the 3 cm ck aluminum supporting plate. After the first layer is set, non aggressive epoxy ıe (Bicron BC600) is distributed on the plane, a layer of fibers is positioned in the oves and glue is spread again before positioning next lead foil. This procedure is eated until a stack of 7-8 planes is formed. Before the glue starts curing, a uniform essure of 1 Ton is applied for 2 hours on the calorimeter surface to allow a more iform glue distribution. The procedure of stacking is repeated until a thickness 23 cm, which corresponds to $\sim$ 200 lead-fibers planes, is reached. The thickness the growing stack is surveyed during the construction in 30 specific points along

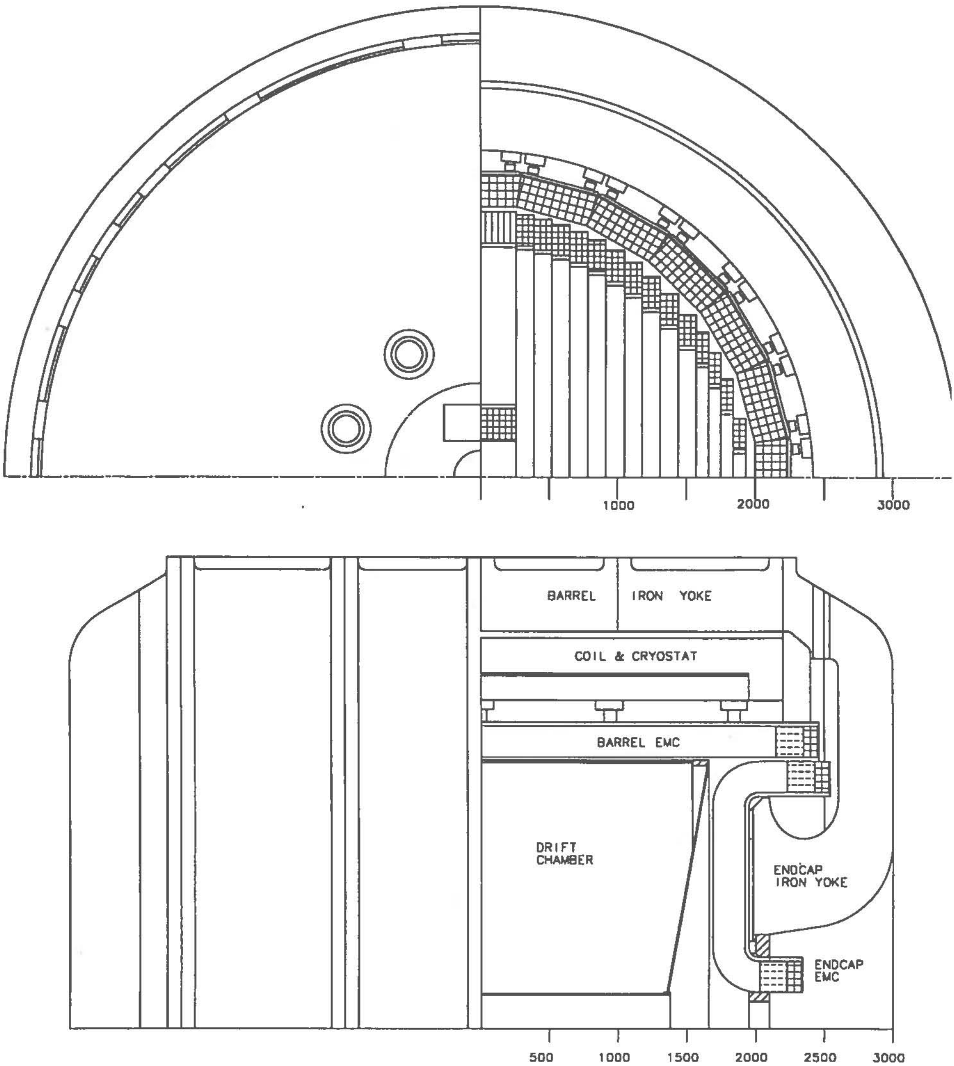

Figure 1: Partial KLOE views: (top) front view of upper half KLOE detector, the part on the right is shown without the return iron yoke; (bottom) side view of upper half KLOE detector, the part on the right is a cross section in the vertical plane including the beam pipe. Length scales are expressed in mm.

ɜ module surface. Maximum deviation from nominal values are around 2 mm.

A similar technique is used also for *end-cap* modules, the only relevant ference being the treatment of the curved sections. The growing stack is assembled t on a special platform with removable ends. After one hour of stacking these tensions are removed and the lead-fibers composite is laid with a special tool on ɜ curved aluminum supporting plate. Pressure is then applied on the straight and rved sections for ~ 2 hours. Since we have 64 modules of different dimensions, we ɜ building them in three parallel assembly stations in Frascati, Pisa and RomaI, ch one being specialized for different module sizes. Speed of construction is ~ 2 eks/module.

2 Fibers quality monitoring

fundamental requirement of our calorimeter is to maintain the excellent time solution shown by module 0 for all the other modules. Since σ_T depends on the ht yield as $1/\sqrt{N_{pe}}$, we monitor the fibers quality by randomly testing two fibers r batch. The set-up consists of a β source (Sr^{90}), which can be positioned in ference points along the fiber, and a PM optically air-coupled. The intensity of e current is registered on each point and then fitted with a sum of two exponentials nctional form. The longest attenuation length, λ, and its corresponding current, are reconstructed with a reproducibility of 2% and 4% respectively.

Values obtained for Pol.Hi.Tech. fibers have a wider spread in the I-λ plane ıd show on average worse characteristics respect to the Kuraray ones. Still, the ɔl.Hi.Tech. production has gone through a continuous improvement in 1994 and ıce 1995 the two kind of fibers are practically equivalent.

In order to guarantee a uniform response among calorimeter modules of fferent lengths, we select fibers which give the same amount of current when illuinated at their farthest end. Therefore the older Pol.Hi.Tech. production is used r the construction of short *end-cap* modules.

3 Modules final coverage

nce the modules are mechanically assembled and milled, they are sent to LNF for ıe final mounting. Each of them is wrapped with 0.1 mm thick aluminium tape r light tightness and then the read-out system is mounted on the two ends: light ıides are glued and PM's holders are mounted in an aluminum box.

4 Status of construction

t the moment we have 19 out of 24 *barrel* modules fully assembled and 42 out of 64 ıd-cap modules mechanically built. The end of mechanical construction is foreseen

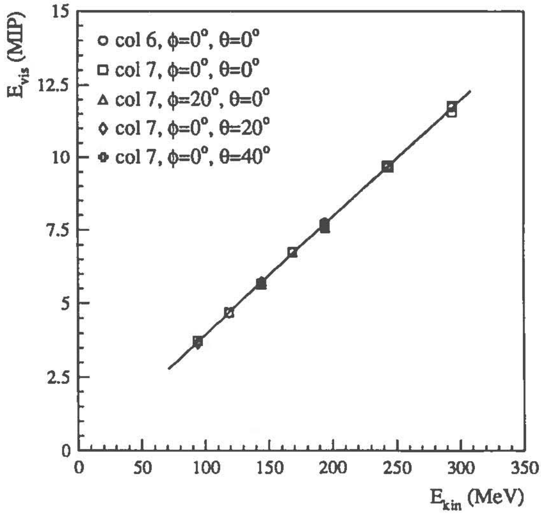

Figure 2: Energy response for electrons.

for November 1996; all modules will be equipped within March 1997.

3.5 Modules readout

The modules are read-out in both ends, in order to reconstruct the coordinate along the fibers using time differences, by collecting the signal of group of fibers and reading it with a photomultiplier (PM). The fibers are coupled to the PMs by light guides; the resulting granularity is around $(4.4 \times 4.4)\ \mathrm{cm}^2$.

Each light guide consists of a mixing part and a Winston cone concentrator. This system allows for an area reduction up to 4 still mantaining a a high efficiency in light collection ($\simeq 87\%$) and a good uniform distribution on photocathode.

The calorimeter is inside the superconducting coil that provides a magnetic field of $0.6\,T$. In the PM area the residual magnetic field is up to $2\,Kgauss$, with an angle with respect to the PM axis up to 25^o. Because of this fine mesh Hamamatsu R5946 PM's, specially designed for KLOE, are used. They have been tested [4] within a solenoid showing a response indipendent from the magnetic field, in the KLOE working region.

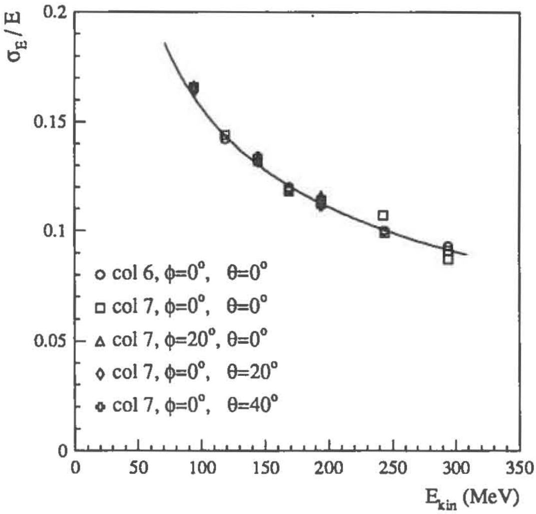

Figure 3: Energy resolution for electrons.

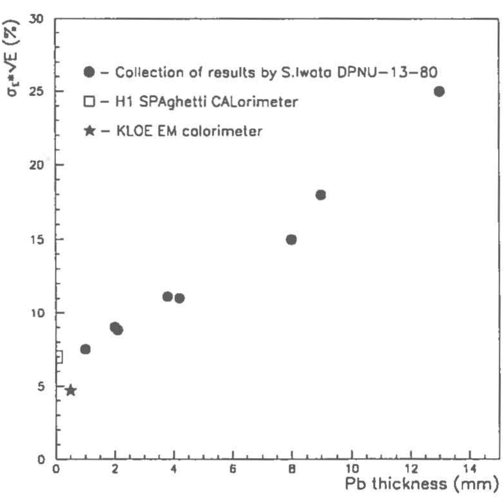

gure 4: Energy resolution of lead/scintillator sampling electromagnetic calorime-
:s as a function of the lead thickness.

4 Test of Module 0

At the beginning of 1994 the first full size *barrel* module has been built, equipped with the final light guides, PM's and front-end electronics. It was taken to the Paul Scherrer Institut, Zurich, in July to be tested with electron, muon and pion beams in a momentum range $100 \div 450$ Mev/c. In the following, results for electrons are discussed.

4.1 Energy response and resolution

The module was calibrated using *m.i.p.*s: the energy released in each cell from particles impinging perpendicularly to the calorimeter (MIP) is the unit of energy. The distributions of total energy, that is the calibrated sum over all channels, are gaussian with almost no tails. The energy response is linear, independently of the incidence angle (see Fig. 2). The slope of 31 MIP/GeV corresponds to a sampling fraction of 13% and to a light yield of $\sim$ 1660 N_{pe}/GeV for Kuraray fibers and $\sim$ 1075 for Pol.Hi.Tech. ones. The energy resolution (Fig.3) is $\sigma_E/E = 5\%/\sqrt{E(\mathrm{GeV})}$ and is fully dominated by sampling fluctuations.

This excellent resolution is mainly due to the very fine sampling. Also the usage of scintillating fibers, instead of scintillator slabs, allows for the construction of homogeneus devices. Figure 4 shows a collection of results, taken from [6], of the energy resolution as a function of lead thicknes for standard electromagnetic calorimeters. In the same plot the resolution found in H1 calorimeter, described in another report of these proceedings, is plotted, too.

The H1 SPACAL calorimeter uses scintillating fibers of 0.5 mm diameter. These fibers point toward the Interaction Point, and this causes channeling effects that worsen the resolution, as compared to KLOE EMC.

4.2 Time resolution

The event time is defined as the mean time obtained using all the cells belonging to the shower, weighted with their own energy:

$$T = \frac{1}{2}\frac{\sum_i (T_A + T_B)_i\,(E_A + E_B)_i}{\sum_i (E_A + E_B)_i}$$

A simple gaussian fit nicely reproduces the time distribution. After quadratically subtracting the jitter of the trigger ($\sim$ 180 ps), we parameterize the time resolution (Fig. 5) as: $\sigma_T = 72\,\mathrm{ps}/\sqrt{E(\mathrm{GeV})}$ showing its dependence on the number of photoelectrons N_{pe}.

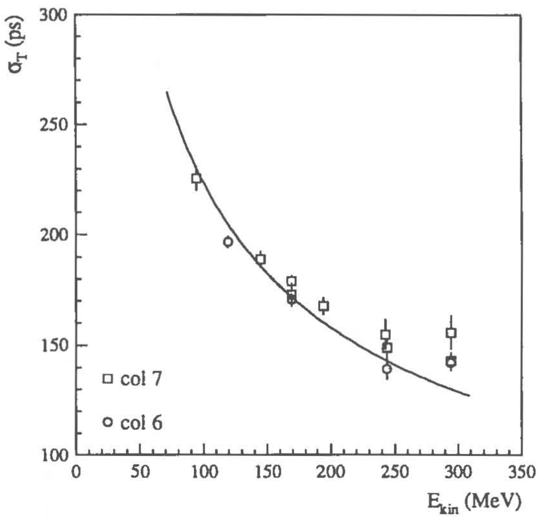

Figure 5: Time resolution for electrons.

Test with cosmic rays

order to perform a quick and simple test of all EMC modules, a Cosmic Ray Test and (CRTS) was assembled at Frascati Laboratory. The CRTS will be described detail by P.Gauzzi in a separate report of these proceedings.

The Test has shown that the "real" modules have preformances that are en better than the one observed for prototype 0. This mainly because of two ctors:

- the performances of PHT fibers have definitely improved with time, passing from an average attenuation length $\lambda_0 \simeq 2.5\,m$ to $\lambda \simeq 3.5\,m$;
- the Kuraray fibers have shown a big sensitivity to blue light; screening with yellow filters the halls where modules are built, has resulted in a reduction of light damage and in an improvement of performances.

ue to these improvements, the time resolution of the calorimeter modules has gone own to $\sigma_t = 55\,ps/\sqrt{E}$ and the resolution on the coordinate along the fiber is $= 0.9\,cm/\sqrt{E}$.

6 Conclusions

The CP violation physics program of KLOE experiment at DAΦNE requires excellent e.m. shower detection performances. A hermetic, fine sampling calorimeter is under construction. A full size barrel module prototype was tested on e,π,μ beams at PSI (Villigen, Switzerland), while the final modules are tested at a Cosmic Ray Test Stand in Frascati before the final assembling. Energy resolution $\sigma_E/E \sim 4.7\%/\sqrt{E\ (\mathrm{GeV})}$ and time resolution $\sigma_T \sim 55\ \mathrm{ps}/\sqrt{E\ (\mathrm{GeV})}$ are the most significant characteristics of this detector.

References

1. The KLOE Collaboration, The KLOE Detector Technical Proposal, LNF-93/002 (1993).

2. A. Antonelli et al., Nucl. Instr. and Meth. A 354 (1995) 352.

3. A. Antonelli et al., Nucl. Instr. and Meth. A 370 (1996) 367.

4. A. Antonelli et al., Nucl. Instr. and Meth. A 368 (1996) 628.

5. A. Anelli et al., Damage induced by light irradiation on blue scintillating fibers, KLOE Note 136 (1995).

6. S.Iwata, *Calorimeter*, DPNU-13-80, report of the TRISTAN *ep* working group (May 1980)

'ascati Physics Series Vol. VI, (pp. 247–259)
I INT. CONF. ON CALORIMETRY IN HEP – Frascati, June 8–14, 1996

THE CHORUS CALORIMETER: TEST BEAM RESULTS AND OPERATION WITH NEUTRINO BEAMS

.Di Capua, M.Ferroni, C.Luppi, S.Ricciardi, B.Saitta[1] and P.Zucchelli[2]
Università di Ferrara and INFN Sezione di Ferrara, Italy
S.Buontempo, A.G.Cocco, A.Ereditato, G.Fiorillo, F.Garufi, F.Marchetti-Stasi, M.Messina, P.Migliozzi, V.Palladino and P.Strolin
Università "Federico II" and INFN Sezione di Napoli, Italy
.Capone, D.Depedis, U.Dore, P.F.Loverre, D.Macina[2], M.A.Mazzoni, G.Piredda, P.Righini and R.Santacesaria
Università "La Sapienza" and INFN Sezione di Roma, Italy

ABSTRACT

'e report on the performance of the high energy resolution calorimeter of the *HORUS* experiment, which searches for ν_μ-ν_τ oscillations in the *CERN* Wide and Neutrino beam. This calorimeter is longitudinally divided into three sectors: ıe electromagnetic and two hadronic. The first two upstream sectors are made of ad and plastic scintillating fibers in the volume ratio of 4/1, and they represent ıe first large scale application of this technique for combined electromagnetic and ıdronic calorimetry. The third sector is made of a sandwich of lead plates and intillator strips and complements the measurement of the hadronic energy flow. ı this paper, we briefly describe the calorimeter design, we show results on its re- ›onse to electrons and pions, obtained from tests performed at the *CERN* SPS ıd PS and we present some results obtained with the operation in the neutrino ɜam. An energy resolution of $\sigma(E)/E = (32.3 \pm 2.4)\%/\sqrt{E(GeV)} + (1.4 \pm 0.7)\%$ as achieved for pions, and $\sigma(E)/E = (13.8 \pm 0.9)\%/\sqrt{E(GeV)} + (-0.2 \pm 0.4)\%$ for ectrons.

Calorimeter design

he calorimeter described in this paper, a component of the *CHORUS* detector, the first large scale application of the technique, developed in the past few years ⁾, of embedding plastic scintillating fibers into a lead matrix. The fiber sectors ›nsist of about 1500 km of 1 mm diameter fibers in the lead to scintillator volume ıtio of 4/1, that allows for compensation and provides good energy resolution in ıe detection of hadrons.

[1]Now at Università di Cagliari and Sezione INFN, Cagliari, Italy
[2]Now at CERN, Geneva, Switzerland

The $CHORUS$ experiment [2] searches for ν_μ-ν_τ oscillations in the $CERN$ SPS Wide Band Neutrino Beam. It uses nuclear emulsions to detect τ decays, produced by charged current interactions of ν_τs, to be extracted out of a large background of ordinary ν_μ interactions. The events to be scanned in the emulsions are selected on the basis of kinematical variables, measured by means of electronic detectors. Such a selection is more efficient if the hadron shower following the neutrino interaction is measured with high angular and energy resolution. In order to detect the τ muonic decay, it is also necessary to efficiently track throughgoing muons in the calorimeter and to match their trajectories with those determined by the other detectors of the apparatus.

A description of the design and construction of the calorimeter for the $CHORUS$ experiment can be found in Ref. [3]. In this paper, we simply outline here the main design features. A view of the detector is shown in Fig. 1.

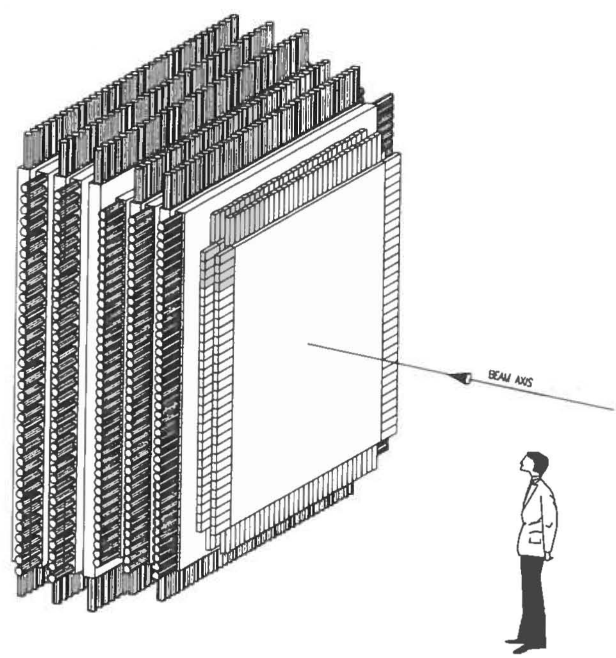

Figure 1: View of the calorimeter.

The calorimeter is arranged in modules to form planes oriented normally to the beam, alternately with horizontal and vertical directions. This structure is mainly motivated by the necessity of providing muon tracking. This is the main difference with respect to the original $SPACAL$ geometry [1], where the modules ve fibers parallel to the beam direction, and the signals are collected at the back the calorimeter.

The calorimeter consists of three sectors with decreasing granularity (EM, AD1 and HAD2). The first one measures the electromagnetic component of e events, while the other two complete the measurement of the hadron show-s. The average interaction length [4] of the calorimeter is 21 cm, its radiation ıgth 0.72 cm; the effective Moliere radius is 2 cm and the density of the mod-es 9 g/cm^3. The total calorimeter thickness is about 5.2 interaction lengths (144 diation lengths), sufficient to contain showers produced in the neutrino interac-ons. The EM and the HAD1 sectors (2.8 interaction lengths altogether) are made scintillating fibers and lead, while HAD2 is a sandwich of lead and scintillating rips. The transverse structure of the calorimeter allows light collection through ıotomultipliers (PMs) on both sides of the module, thus reducing the effects of ht attenuation in the scintillator [3]. Sets of limited streamer tube planes are serted between the horizontal and the vertical planes for tracking purposes; they e arranged in pairs with horizontal and vertical wires.

EM modules are built by piling-up extruded layers of grooved lead and astic scintillating fibers positioned in the grooves. The groove diameter is 1.1 mm ıd the layer thickness 1.9 mm; the material, the same as for the HAD1 and HAD2 odules, is 99% lead and 1% antimony. A module consists of a pile of 21 layers, 20 mm long and 82.4 mm wide, and 740 fibers of 1 mm diameter and 3050 mm ng. On either side of the module, fibers are assembled in two hexagonal bundles, fining two different read-out cells with about 40×40 mm^2 cross-section. Each of e fiber bundles is coupled to a 1" PM via a plexiglas light guide.

Each HAD1 module is made of 43 extruded layers of lead identical in width ıd groove size to those used for the EM sector, but with a length of 3350 mm. The intillating fibers have 1 mm diameter and 3810 mm length, for a total of 1554 ers per module. Fibers are collected at both ends in a hexagonal bundle coupled a a light pipe to a 2" PM.

Each HAD2 module is constructed by superposing five alternate layers of ıe lead bar ($3690 \times 200 \times 16$ mm^3) and two adjacent scintillator strips ($3714 \times$ 10 $\times 4$ mm^3 each). Each of the two groups of five scintillators is coupled to 2" Ms at both ends via plexiglas light guides; therefore, a single module is seen by a tal of four PM tubes, and contains two cells.

Test beam data and calibration

he main measurements with electron and pion beams were performed in the X9 st beam at the *CERN* SPS. The beam line is almost parallel to the neutrino

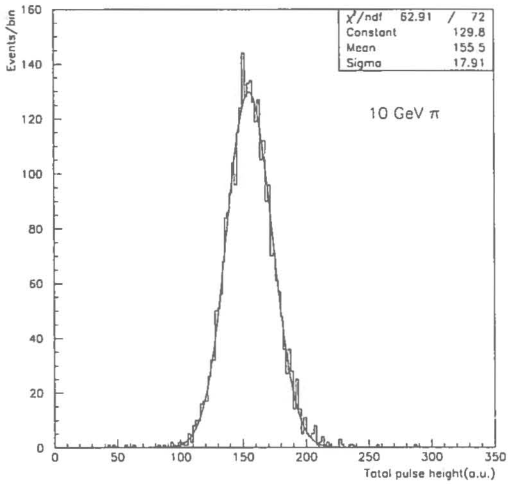

Figure 2: Calorimeter response to 10 GeV/c pions.

beam axis. The calorimeter, mounted on rails, can be shifted about four meters sideways from its nominal position to meet the test beam. Electron data were taken with pure beams from 2.5 to 10 GeV/c, while pions came from mixed electron/pion beams from 3 to 20 GeV/c.

Three sequential steps are needed for the determination of the calorimeter response: first, within each sector, the *equalization* of the signals from each individual PM, then the *intercalibration* among different sectors, and, finally, the overall energy calibration. The *equalization* of signals from modules of the same type is performed by means of penetrating cosmic rays. An *equalization* constant is computed for each PM by selecting cosmic muons crossing the central region of the modules ($\pm 10\ cm$), and correcting for the effective track length. Systematic effects due to the time dependence of the PM gain and to the position dependence of the energy spectra for the selected muons were also studied, the latter being due to the different amount of material crossed by the muons before entering the module.

To combine the signals of the three different sectors, two *intercalibration* constants are needed, namely those of HAD1 and HAD2 relative to EM. These constants are determined experimentally using pions interacting at different calorimeter depths. The details of the equalization and intercalibration procedures are given in [5].

Response to electrons

'he calorimeter response to the incoming particle is determined by adding up the nergy deposited in all the modules, once the *equalization* and *intercalibration* proedures have been performed. As noted before, each read-out cell is equipped with a 'M at each fiber (strip) end, in order to reduce the influence of the light attenuation n the scintillator. This leads to different possible definitions of the module signal, ccording to the way the two PM signals (L and R) are combined. In our case we se the geometric mean: $S_g = \sqrt{S_L \times S_R}$. Under the assumption of single hit per nodule and exponential light attenuation in the fibers (strips), as found in Ref. [3], he geometric mean yields a value for the module response which is independent of he hit position x along the module with length L :

$$S_L = Ae^{-\frac{x}{\lambda}} \quad , \; S_R = Ae^{-\frac{L-x}{\lambda}} \quad \rightarrow \quad S_g = Ae^{-\frac{L}{2\lambda}}$$

In Fig. 2 we show the calorimeter signal distribution produced by 10 GeV/c legative pions. The shape is gaussian, indicating that both the *calibration* and *ntercalibration* procedure do not introduce any appreciable bias in the determinaion of the overall calorimeter response.

The electron response was studied for different SPS beam momenta, in he range from 2.5 to 10 GeV/c, relevant for the $CHORUS$ experiment. For each nomentum, a gaussian fit is performed to the distribution of the calorimeter signal.

The measured points lie on a straight line up to 10 GeV/c, where electronics aturation tends to reduce the calorimeter signal. This effect is due to the small pace dimensions of the electromagnetic showers, such that a large fraction of the nergy can be released in a single EM module. This does not happen for hadron or neutrino induced events, where many modules share the incident energy. The esult of a linear fit performed in the interval from 2.5 to 5 GeV/c indicates that xtrapolation to zero pulse height leads to a *negative* value of the momentum:

$$S \;=\; (17.2 \pm 0.3) \;\times P(GeV/c) \;+\; (6.4 \pm 0.9) \tag{1}$$

The above result is in agreement with our previous analysis on the electromagnetic esponse of single calorimeter modules, tested on the same beam line [3]. It is onsistent with the actual value of the beam momentum being 370 $\pm$ 50 MeV/c higher than the nominal value.

The electromagnetic response of the calorimeter and its linearity have been nvestigated by simulation. Montecarlo predictions give a linear response of the letector to electrons, as well as to photons, and no offset is expected.

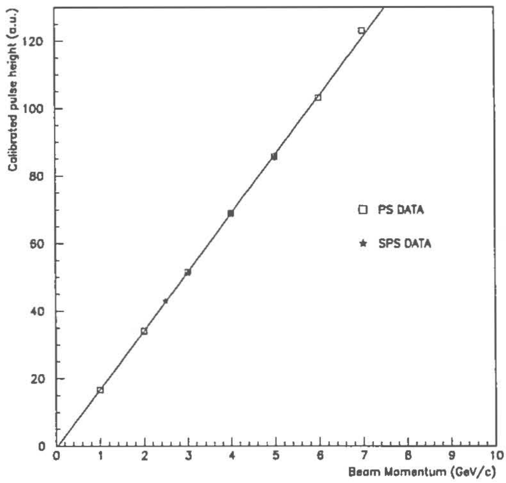

Figure 3: Electron response for the PS set-up. The SPS points are also shown, corrected for the 370 MeV/c momentum shift.

In order to solve this problem, independent measurements were done at the $CERN$ PS. The results indicate that the extrapolation to zero calorimeter pulse height leads, indeed, to a momentum compatible with zero (intercept equal to +40 $\pm$ 20 MeV/c), supporting the conclusion of a calibration shift of the SPS X9 beam momentum. These results are shown in Fig. 3, together with the the SPS points corrected for the 370 MeV/c offset; the agreement between the two sets of data is excellent. The following (corrected) relation is then obtained for the energy dependence of the electromagnetic response:

$$S \; = \; (17.2 \pm 0.3) \; \times P(GeV/c) \; - \; (0.14 \pm 0.96) \tag{2}$$

The energy resolution $\sigma(E)/E$, is plotted in Fig. 4 as a function of the electron energy. The energy dependence of the resolution is well fitted by the usual function:

$$\frac{\sigma(E)}{E} = \frac{(13.8 \pm 0.9)\%}{\sqrt{E(GeV)}} + (-0.2 \pm 0.4)\%$$

This result fulfills the design requirements and agrees with the Montecarlo predictions. By studying electron showers developing in different calorimeter zones we estimated the disuniformity in the electromagnetic response to be of the order

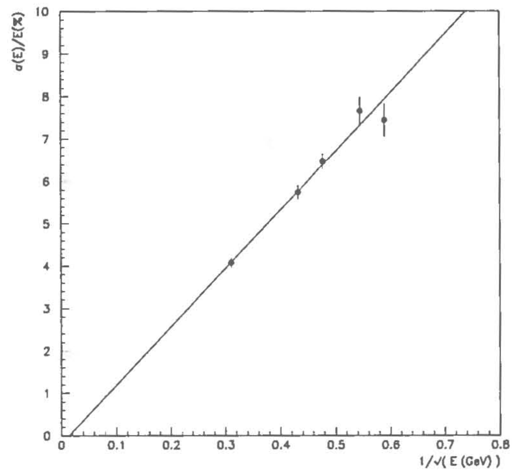

Figure 4: Energy resolution for electrons as a function of the energy.

$\pm 5\%$, in agreement with the design requirements.

Response to pions

he pion response was studied for different beam momenta, from 3 to 20 GeV/c. he mean value S of the signal distribution, which is gaussian as in the electron ıse, is plotted in Fig. 5 as a function of the nominal momentum P, corrected for ıe shift of 370 MeV/c, found with the electron data.

The measured pion momentum dependence may be parametrized as:

$$S = (15.3 \pm 0.2) \times P(GeV/c) - (5.8 \pm 1.0) \tag{3}$$

'hich corresponds to a *positive* intercept of $380 \pm 65\ MeV/c$. A different value of his quantity for electrons (compatible with zero) and pions is expected and can be nderstood on the basis of the following considerations:

- a comparison of the response to electrons and pions of the same energy hows deviations from exact compensation ($S_{electron} > S_{pion}$). Therefore, at high ıomenta, the increase of the electromagnetic energy content in the hadron showers $\frac{E_{EM}}{E_{TOT}} \propto ln(E_{TOT})$) induces an energy dependent enhancement of the signal.

- At low momenta ($\sim 1\ GeV/c$), the contribution from neutral pions be-

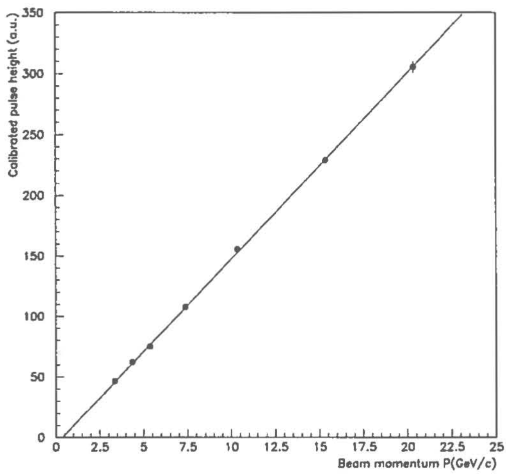

Figure 5: Calorimeter response as a function of the pion momentum.

comes negligible and small multiplicity processes dominate. In this case, the effect of the particle masses not converted into visible energy in the read-out gate becomes visible.

Both the above effects indicate that a straight line fit to the data taken in the mentioned momentum range, should have an intercept at a positive value of the abscissa. This is confirmed by the Montecarlo simulation, which predicts an intercept of $340 \pm 50\ MeV/c$. The calorimeter turns to be linear within 2%.

From the gaussian fit to the response distributions one determines the energy resolution $\sigma(E)/E$, which is plotted in Fig. 6 as a function of the pion energy. The errors assigned to each point include a systematic uncertainty of about 2% determined applying different event selection criteria to the data, and studying pions hitting different calorimeter positions. The above uncertainty is lower than the one for the electron case ($\pm 5\%$). The main reason for this is that more calorimeter modules are involved in a hadron shower. The energy dependence of the resolution is parametrized as:

$$\frac{\sigma(E)}{E} = \frac{(32.3 \pm 2.4)\%}{\sqrt{E(GeV)}} + (1.4 \pm 0.7)\%$$

The predictions of a Montecarlo simulation are also shown in Fig. 6. The

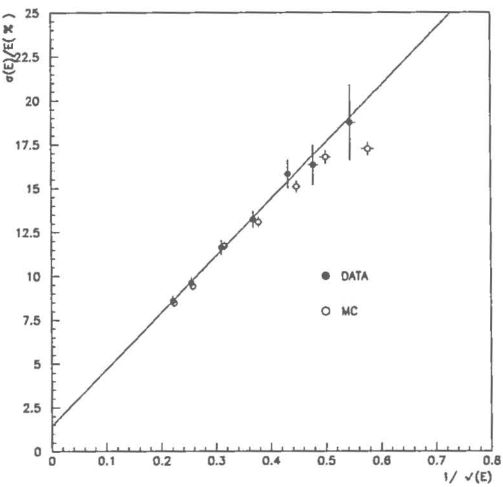

igure 6: Pion energy resolution as a function of the energy. The open circles show ıe Montecarlo predictions.

ɔngitudinal and transverse shower development in the calorimeter have been studːd. Fig. 7a shows the projection of hadron showers onto the calorimeter transverse lane. In Fig. 7b it is shown that a cylinder containing 95% of the shower energy as a radius of about 25 *cm*, almost constant in the energy range explored by our ıeasurements. This result is in excellent agreement with the Montecarlo prediction, lso shown in the figure.

From the electron and pion response of the calorimeter we can determine he experimental e/π ratio. In Fig. 8 we plot the ratio of the average electron and ıion calorimeter signal as a function of the momentum. The systematic error, due o the response disuniformity, has been added to the statistical. In the same figure, ve also plot the ratio of the functions (2) and (3), describing the signal momentum lependence for electrons and pions.

; Neutrino events

As previously discussed one needs a high resolution calorimeter to efficiently perform he kinematical preselection of neutrino interactions. The kinematical variables used or this selection are: the energy, the visible P_T, and the shower angle with respect o the neutrino direction. In the following we shall describe the procedure used to

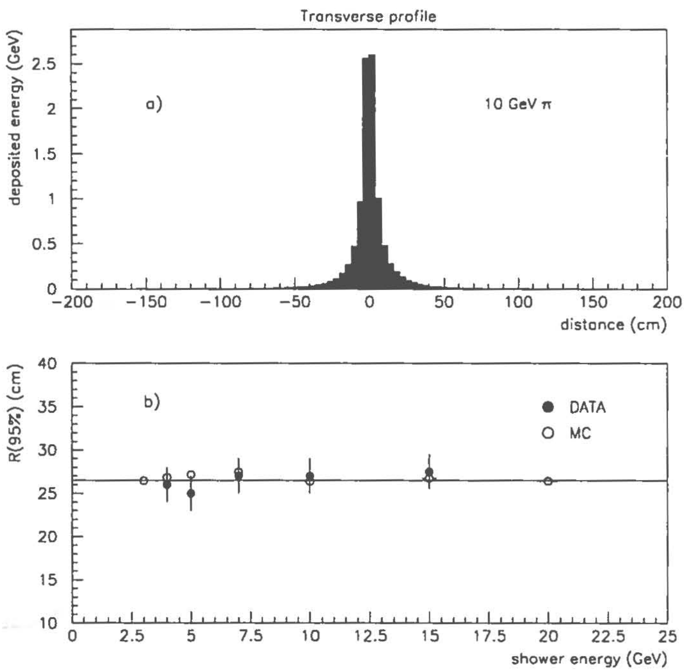

Figure 7: (a) Shower projection onto the transverse plane orthogonal to the beam direction for 10 GeV/c pions; (b) transverse dimensions of the pions shower as a function of the energy: the black circles represent the radius around the shower axis which contains 95% of the energy. The open circles show the Montecarlo predictions.

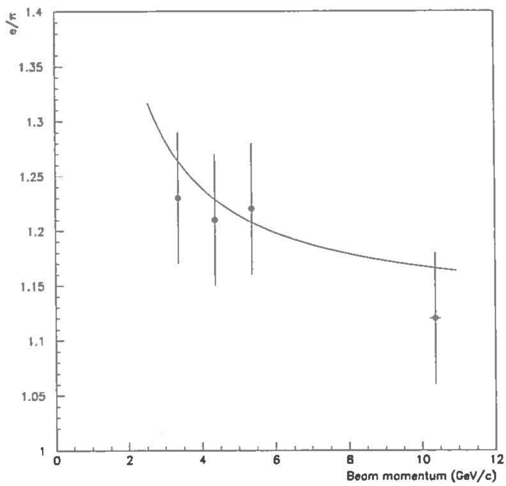

gure 8: $\frac{e}{\pi}$ ratio as a function of the beam momentum. The continuous line represents the ratio of the electron and pion momentum-dependence functions.

mpute the kinematical variables and some results.

clustering algorithm is needed to define showers in the calorimeter produced by dividual particles. The algorithm uses the information on the interaction vertex constructed in the target and on the calorimeter module pulse height in each plane. he output of the algorithm (the details are given in [6]) is a list of bidimensional usters each with its own energy, width and depth. These variables allow us to assify the clusters as due to a minimum ionizing particle, to a hadronic or to ι electromagnetic shower. In order to reconstruct tridimensional clusters in the ılorimeter we also use the 3D informations from the upstream target tracker made scintillating fibers [2].

1 Results

figure (9) the energy and the P_T (visible transverse momentum of the event) solution for neutrino induced neutral current events are shown. Note that the ıantity ($E_{MC} - E_{meas}$) (where E_{MC} is the visible energy produced at the vertex ıd E_{meas} is the energy measured in the calorimeter) is not centered at zero and ıere is a tail on the right side of the distribution. This is due to the energy lost efore the calorimeter. Nevertheless the gaussian part of the distribution gives a energy resolution compatible with the one measured in the test beam. The resolution on the visible P_T is about $500 MeV/c$. Using these kinematical variables we are able to apply cuts that reduce by more than a factor 2 the number of neutral current events to be scanned in the emulsion, with an efficiency on the $\tau \rightarrow 0\mu$ channel of about 90%.

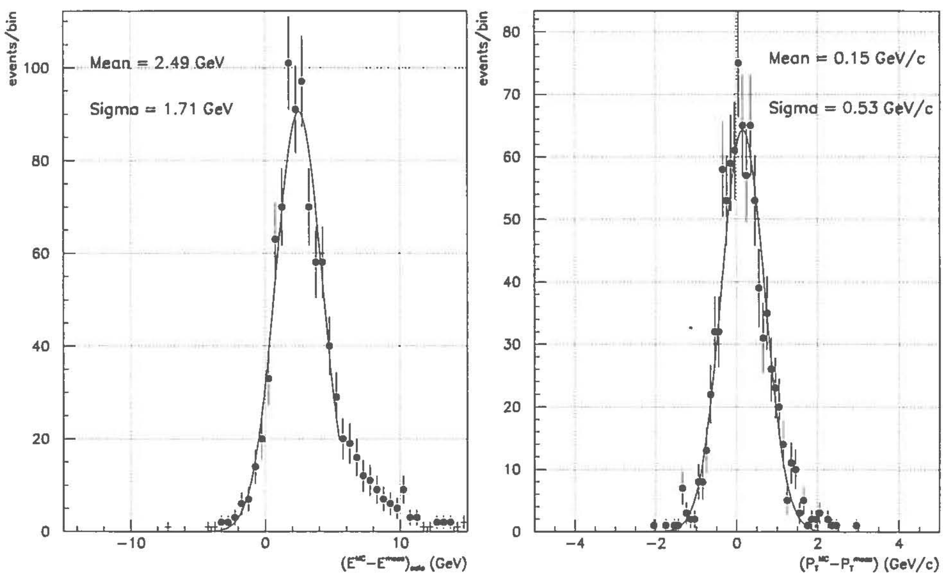

Figure 9: Distribution of: (left side) difference between the visible energy produced at the vertex (MC) and the energy measured in the calorimeter. The mean energy in neutral current neutrino interaction is $\sim 21 GeV$; (right side) difference between the transverse visible momentum (MC) with respect to the neutrino direction, and the one measured in the calorimeter.

6 Conclusions

The *CHORUS* calorimeter, the first large scale application of the scintillating fiber/lead technique for integrated electromagnetic/hadronic calorimetry, was exposed to electron and pion beams in the momentum range from 2.5 to 20 GeV/c at the *CERN* SPS.

The calorimeter response to electrons was found to be linear with the ›mentum, after applying a correction to its nominal value, as indicated by mea- :ements performed at the *CERN* PS. The energy dependence of the resolution s parametrized as

$$\sigma(E)/E \; = (13.8 \pm 0.9)\%/\sqrt{E(GeV)} + (-0.2 \pm 0.4)\%$$

ιe calorimeter response to pions is also linear in the momentum range explored by ɜ measurements, and we achieved an energy resolution of

$$\sigma(E)/E \; = (32.3 \pm 2.4)\%/\sqrt{E(GeV)} + (1.4 \pm 0.7)\%$$

ιis result is in agreement with the design features and the Montecarlo predic- ›ns. We also show Montecarlo results obtained with neutrino events concerning e transverse momentum resolution. The calorimeter has been successfully op- ational during the 1994, 1995 and 1996 data taking periods of the *CHORUS* periments in the *CERN* Wide Band Neutrino beam.

Acknowledgements

ıis work was carried out with the financial support of the italian Istituto Nazionale Fisica Nucleare. We gratefully acknowledge the skill of our technical collaborators .d engineers. The kind help of many *CHORUS* colleagues during the calorimeter nstruction and test is also warmly acknowledged.

eferences

.. D. Acosta et al., NIM **A308**, 481 (1991).

!. M. de Jong et al., CERN-PPE/93-131.

!. S. Buontempo et al., NIM **A349**, 70 (1994).

!. Particle Data Group, Phys. Lett. **B239**, page III 5,6 (1990).

!. E. Di Capua et al., CERN-PPE/95-188.

!. P. Migliozzi, Ph.D. Thesis, in preparation.

ascati Physics Series Vol. VI, (pp. 261–268)
INT. CONF. ON CALORIMETRY IN HEP – Frascati, June 8–14, 1996

HE E864 LEAD/SCINTILLATING FIBER HADRONIC CALORIMETER

Claude A. Pruneau
)epartment of Physics and Astronomy, Wayne State University, Detroit MI 48201
for the E864 Collaboration
Ames Lab, BNL, Iowa State U., MIT, Penn State U.,
Purdue U., U. Bari, UCLA, Vanderbilt U., Wayne State U., Yale U.

ABSTRACT

iis contribution describes the design and construction of a large lead scintillating ›er hadronic calorimeter integrated to the AGS E864 forward magnetic spectrom- er for the search of strangelets and the study of light nuclei and anti-matter pro- ıction in heavy ion reactions. Selected results obtained from the 1995 AGS heavy n runs are presented. The energy resolution of the calorimeter is found to be $\sigma/E = 0.047(\pm0.006) + 0.34(\pm0.01)/\sqrt{E}$ in very good agreement with a FLUKA .lculation. The time resolution is measured to be 400 ps.

Introduction

large lead-scintillating fiber calorimeter has been built for the AGS experiment 864 [1], a heavy ion experiment primarily designed to search for strangelets but also ıpable of studying a variety of particle production in connection with the heavy n reaction dynamics and the possible production of a Quark Gluon Plasma.

A prototype of this calorimeter was built and tested with the AGS test eam during the summer of 1993 [2]. A partial implementation of the E864 calorime- :r was completed for the 1994 heavy ion run. The full detector and calibration /stems were completed and used during the 1995 run. This paper discusses the de- gn, construction technique, and performance of the calorimeter. Motivations and alorimeter design considerations are outlined in Sec.2. The construction technique nd implementation are described in Sec.3. An analysis of data from the 95 AGS eavy ion run illustrating the calorimeter performance in terms of energy linearity nd resolution as well as time of flight (TOF) resolution is presented in Sec.4.

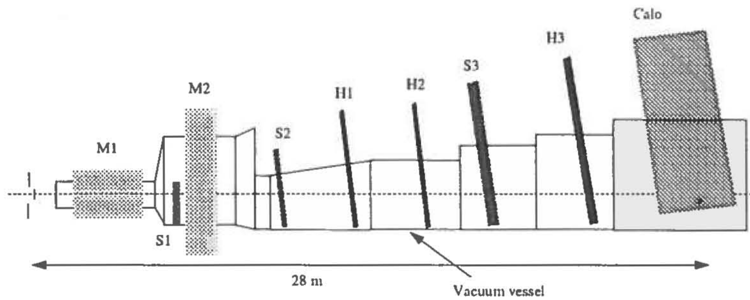

Figure 1: Top View of the E864 Apparatus.

2 Design Considerations

Experiment E864 was primarily conceived to improve upon the inconclusive strangelet searches conducted by previous experiments [3, 4, 5] by reaching a level of sensitivity of 10^{-11} per Au+Au collision. Strangelets are thought to be massive objects, containing more than three quarks within a single bag (in the sense of the MIT bag model) with a large fraction of strange quarks. They are expected to have a charge to mass ratio smaller than 1/3 and should be produced roughly at half the beam rapidity in central Au+Pb reactions. The E864 detector, illustrated in Fig.1, is an open geometry magnetic forward spectrometer with a high rate capability. The apparatus includes a large vacuum vessel surrounding the target area and extending all the way to a beam dump in order to minimize background production through the apparatus. There are two magnetic dipoles (M1, M2) that can be operated with fields up to 1.5 Tesla for momentum analysis and to sweep away light particles. The detection system, located below the vacuum vessel, features three TOF hodoscopes (H1, H2, H3) as well as 3 straw tube planes (S1, S2, S3) for accurate tracking and particle momentum determination. The combination of the TOF hodoscopes and tracking detector provides for particle's mass determination with a resolution of the order of 4% or better [8].

The apparatus was completed with a large hadronic calorimeter to provide independent measurements of the particle's TOF and energy used for identification. An innovative trigger system based on the calorimeter energy and TOF measurements has also been included in the experiment. As strangelets are expected to be massive and produced at mid-rapidities, the triggering scheme consists of using the calorimeter to identify slow moving objects with a large energy, and is dubbed the Late Energy Trigger (LET) to refer to high energy particles arriving late relative to ding speed of light particles.

The calorimeter is required to measure energy and TOF with resolutions tter than $40\%/\sqrt{E}$ and 500 ps respectively [1]. Also, to minimize ambiguities in e identification of particles, an hermetic design with no seams, gaps and cracks s desired. Moreover, the calorimeter must operate at high rate and within a gh particle multiplicity environment typical of heavy ion reactions. Such require-ents are readily fulfilled with a lead–scintillating–fiber–spaghetti calorimeter. The 'ACAL collaboration has shown [6] that good compensation and linearity can be tained with such a device. Other interesting aspects of this technology are uni-mity, speed, good energy resolution and the expectation of good TOF resolution view of the fast response.

The E864 calorimeter, illustrated in Fig. 2, comprises 58 by 13 towers. The wer design is quite similar to that of SPACAL [6]. However, as the calorimeter ould match the rectangular fiducial acceptance of the E864 spectrometer, the wers were designed with a square section rather than a hexagonal layout as in e SPACAL design. The absorber is lead with a 1% admixture of antimony to hieve the desired mechanical properties. BCF-12 fibers, from BICRON, are used r sampling and readout. They were selected for their fast response (decay time $\sim$ 2 ns), long attenuation length ($1/e \sim 2.2$ m), high light yield (50% of anthracene), nd relatively low cost. The fibers have a diameter of 1 mm and are spaced regularly, 13 mm apart, on a square lattice as illustrated in Fig.3. This yields a lead to fiber tio of 4.55. The effective nuclear interaction length and effective radiation length re 22.15 cm and 7.2 mm respectively. Each tower contains 47×47 fibers. They ave a square section of 10×10 cm and are 117 cm long. A UV absorbing lucite light uide, coupled at the back, as illustrated in Fig.3, is used to funnel the scintillation ght into a two inch diameter Philips XP2262 photo-multiplier tube.

Construction Technique and Implementation

pecial care was devoted to select a construction technique that could guarantee regular fiber to fiber spacing in order to ensure a good response uniformity and nergy resolution. Of the many construction techniques reported in the literature [6], he lamination technique described below was found to be the best for our purpose.

Flat extruded lead plates were rolled with a custom made rolling machine to produce plates with an imprinted semi-circular groove pattern. Stringent tolerances of 0.0005 inches were used in the design of the rolling dyes to insure uniform fiber o fiber spacing in the lattice and ease the laminating process. Once the imprinted plates were cleaned and deburred, the lamination proceeded as follows: A lead sheet was placed on a flat metal base and BC600 epoxy was liberally applied on its surface.

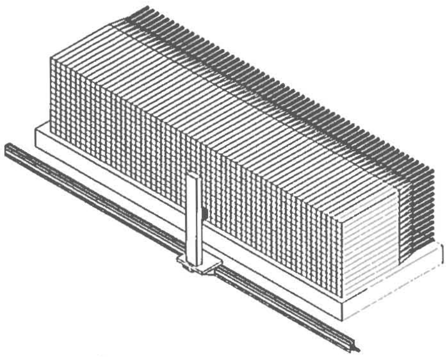

Figure 2: View of the E864 Calorimeter and ^{60}Co Transport System.

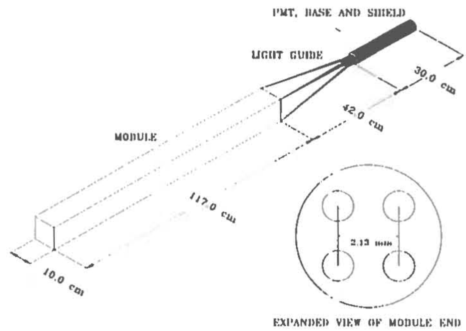

Figure 3: Calorimeter Tower Design.

Next, a pre-assembled ribbon of 47 fibers was smoothed into the grooves. A new plate was then gently keyed into place. This was repeated until 47 layers were stacked. At this point, the towers were typically too thick due to an excess of epoxy. Top and side steel plates were thus clamped on the tower to form a rigid mould used to constrain it to the correct cross-sectional size and straighten any residual bowing. The tower was tilted by 90° to a vertical position. BC600 epoxy was poured through the open top of the mould. The assembly was placed in an oven to cure the epoxy. Once the epoxy had cured, the mould was removed, and the excess epoxy at this one end was machined off almost down to the lead to provide a smooth surface to which the lucite light guide was glued. Finally the tower surfaces were coated with a thick black epoxy paint and the light guide was wrapped with a non wetting aluminized mylar and tape in order to insure light tightness.

Rather than using conventional resistive bleeder chain bases, Cockroft Walton voltage generator bases designed and built by Nanometrics were used to bias the PMTs. An on-tube leading edge discriminator was also included in the bases to provide fast and accurate timing signals. The signal readout was performed with FASTBUS 1881M ADC and 1875A TDC from Lecroy. A dual calibration system based on a ^{60}Co radioactive source and a nitrogen Laser system was used to equalize the 754 tower gains and monitor their variation.

4 Performance during the 1995 Run

The calorimeter performance in terms of energy response linearity, resolution, and time resolution was studied on the basis of the 1995 Au beam run data.

The calorimeter absolute energy calibration and the performance evalua-n are based on well reconstructed and identified tracks produced with the 11.6 :V/A Gold beam impinging on a Pb target. The reconstruction relies on the :cessful performance of the E864 charged particle tracking system consisting of э three TOF hodoscopes planes H1,H2,H3 as well as the two straw tube tracking ambers, S2, S3, and proceeds along an algorithm presented in detail in ref. [7, 8]. ıe momentum resolution achieved, roughly 3%, is limited by multiple scattering. ıe time of flight (TOF) resolution is also excellent and the combined momentum d TOF information permit mass reconstruction with a resolution of the order of 5% for particles with $\beta < 0.975$. Data obtained from various field settings (0.45, 75, and 1.5 Tesla) were used in order to provide samples of different particle species rotons, deuterons, and tritons) and maximize the examined energy range. Also, the calorimeter was built specifically to search for heavy particles, it is imperative evaluate its performance for heavy particles.

The calorimeter tower gains are first equalized according to gain measure-ents performed with the ^{60}Co calibration system [10]. Minor corrections derived om the laser system are also applied. The absolute energy calibration coefficient thus determined by comparing the (uncalibrated but gain equalized) energy mea-red with the calorimeter with the kinetic energy of proton, deuteron, and triton acks. The kinetic energy of the tracks, E, is evaluated from the reconstructed track omentum and the mass of the identified particles. To avoid ambiguities, a number stringent cuts are applied to ensure good particle identification and purity. The acks thus identified are extrapolated to the calorimeter front face in search of a atching energy cluster. We use the sum of energies in an 5×5 array of towers rrounding the leading towers as a measure of the deposited energy, $E_{5\times5}$, and to etermine the energy calibration coefficients (ECC). The energy response is slightly on-Gaussian, with a high side tail. Moreover, the non-Gaussian contribution is a nction of the particle's energy. We thus use the mean of the distributions rather ıan the peak position to determine the ECC. The ECC values, listed in Table 1, ere determined independently for identified protons, deuterons, and tritons under vo field settings (0.45- and 1.5 Tesla) of the spectrometer magnets. The ECC val-es determined for deuterons under the two different field settings differ by 3% only ıd are within a few per cent of the coefficients obtained with protons and tritons: first indication that the calorimeter response is linear in spite of its non Gaussian ıaracter at low energy.

To further investigate the response linearity, we plot in the top part of ig.4 the relative difference, $\Delta E_{diff} = (E_{5\times5} - E)/E$, between the energy measured ith the calorimeter, $E_{5\times5}$, and that measured with the tracking system, E, as a

Table 1: Energy Calibration Coefficients evaluated with different particle species.

Species	ECC (0.45 Tesla) MeV/ADC channel	ECC (1.5 Tesla) MeV/ADC channel
protons	5.40 ± 0.02	-
deuterons	5.43 ± 0.03	5.25 ± 0.03
tritons	-	5.19 ± 0.03

function of E. The response is found to be linear to better than $\pm 1\%$.

In order to investigate the hadronic energy resolution of the calorimeter, the width of the relative difference $\delta E/E$ has been studied as a function of the particle energy and is shown in the bottom part of Fig. 4. The data (dark circles) have been fitted (solid line) with the usual expression: $\delta E/E = a + b/\sqrt{E}$. The constant and stochastic terms have values of 0.047 ± 0.006 and 0.34 ± 0.01 respectively.

The measured resolution is in good agreement with a calculation, shown as open squares in Fig. 4, of the expected energy resolution based on the GEANT (3.21) / FLUKA program. The calculation features a complete description of the tower geometry including a detailed parameterization of the scintillation fiber core and cladding to properly evaluate the photon production. The attenuation of the fiber was also taken into account [9, 10]. The agreement between the data and the GEANT prediction is excellent especially at the higher energies. At the lowest energy measured, FLUKA slightly underestimates the fluctuations possibly owing to an excessive neutron production.

Overall, the energy resolution achieved during the 1995 physics run with the full calorimeter implementation is well within the design specifications of E864 [1].

Fig.5 illustrates the time of flight (TOF) resolution performance of the calorimeter evaluated with deuterons and tritons. The TOF measured with the three hodoscopes H1, H2, and H3 was used to extrapolate the track TOF at the calorimeter front face. The TOF measured with the calorimeter (leading) towers, t_c is then compared to this calculated value, t_t, to evaluate the calorimeter TOF resolution. The difference $\Delta t = t_c - t_t$ is found to have a nearly Gaussian distribution. Fig.5 shows a plot of the width of the distribution of the time difference, Δt, as a function of the particle's energy. Unlike the energy resolution, the TOF resolution is nearly constant, with a value of the order of 450 ± 10 ps, in the energy range examined and does not manifest the $1/\sqrt{E}$ behavior seen in other studies. The considerable fluctuations in the shower developments and the limited photon yield might contribute to complicate the situation at low energies.

The TOF resolution of the three hodoscopes has been estimated to be of the order of 200 ps or better [8]. This then entails that the calorimeter TOF

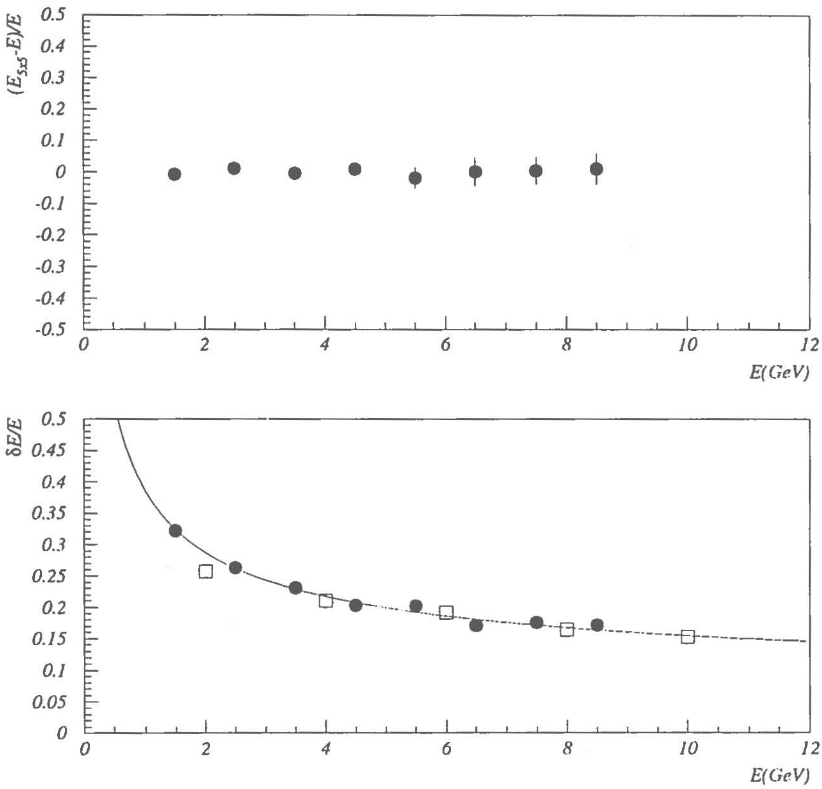

gure 4: Top: Energy response Linearity, Bottom: Resolution vs Particles Energy. ›lid circles - data, Open squares - Geant calculation.

solution is of the order of 430 ps. The TOF performance of the calorimeter is thus so found to satisfy the design requirements set forth for the E864 experiment [1].

Summary and Conclusions

'e have described the design and construction technique of a new hadronic lead intillating fiber spaghetti calorimeter for AGS experiment E864. The performance this calorimeter during the heavy ion run of Fall 95 was studied in detail. The lergy resolution is measured to be $\delta E/E = 0.047(\pm 0.006) + 0.34(\pm 0.01)/\sqrt{E}$ in ›od agreement with a calculation with the FLUKA package. The TOF resolution as found to be of the order of 430 ps and constant in the 2-12 GeV energy range.

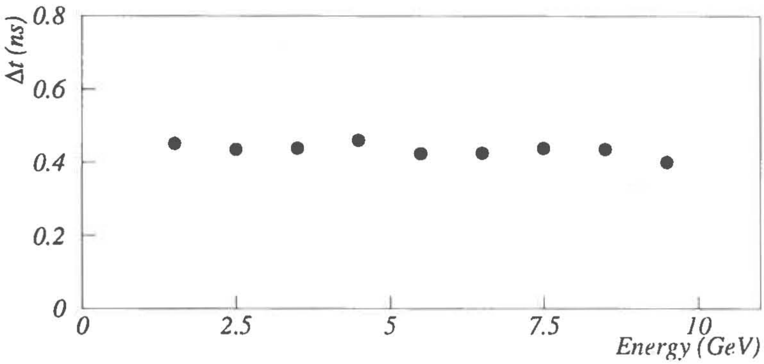

Figure 5: TOF Resolution vs Particle's Energy.

References

1. J. Sandweiss *et al.*, *E864 Collaboration, Proposal for funding - Measurements of rare composite objects and high sensitivity searches for novel forms of matter produced in high energy heavy ion collisions* (1991).
2. S. J. Bennett, *et al.*, Proc. 5th Int. Conf. on Calorimetry in High Energy Physics, BNL, H.A.Gordon and D. Rueger Eds., World Scientific (1994) 361.
3. J. Barrette, *et al.*, Phys. Lett. **B252** (1990) 550.
4. M. Aoki, *et al.* Phys.Rev.Lett. **69** (1992) 2345, B. S. Kumar, *et al.*, Nucl.Phys. **A566** (1994) 439c.
5. D. Beavis, *et al.* Phys.Rev.Lett. **75** (1995) 3078.
6. D. Acosta, *et. al.* , NIM **A294** (1990) 193.
7. J. Sandweiss, *et al.*, to be published in NIM.
8. J. G. Lajoie, Ph.D. Thesis Dissertation, Yale University, 1996.
9. R.Bellwied, *et. al.*, Proc. III Int. Conf. on Calorimetry in High Energy Physics, Corpus Christi, TX, P. Hale and J. Siegrist Eds., World Scientific (1992) 604.
10. S. J. Bennett, *et al.*, to be published in NIM.

:ati Physics Series Vol. VI, (pp. 269–280)
ıT. CONF. ON CALORIMETRY IN HEP – Frascati, June 8–14, 1996

CMS QUARTZ FIBER CALORIMETRY

V.Gavrilov, Y.Gershtein, V.Kolossov, S.Kuleshov, D.Litvintsev, A.Nikitin, V.Rusinov, V.Stolin, A.Ulyanov
ITEP, Moscow
E.Booth, R.Carey, S.Doulas[1], E.Hazen, O.C.Johnson, F.Krienen, J.Miller, D.Osborne, B.L.Roberts, J.Rohlf, A.Rosowsky[2], L.Sulak, J.Sullivan, W.Worstell
Boston University, USA
C.Arrington, C.P.Beetz, D.Kefford, V.Podrasky, C.Sanzeni, D.Winn
Fairfield University, USA
N.Akchurin, A.Braver, M.Kaya, J.Langland, J.McPherson, M.Miller, Y.Onel, E.Ozel, S.Ozkorucuklu, E.Ruth
University of Iowa, USA
O.Ganel, R.Wigmans
Texas Technical University, USA

ABSTRACT

.e expected performance of the CMS Very Forward quartz fiber Calorimeter is cussed

The Large Hadron Collider (LHC) will operate at such high energies and ninosities that the environment in which detector components need to operate will difficult in the extreme. This is especially true in the very forward region ($|\eta| > 3$, $\theta < 5.7°$) where the most hostile environment is expected. The calorimeter will the only detector which will operate at this angular region. This Very Forward ALorimeter (VFCAL) will be required for hermetic calorimetry coverage needed for tection of missing E_t and so called tagging hadron jets [1]. Finding an adequately ecise and robust detection method for this region is truly a challenging exercise detector R&D. The main constraints and conditions that apply to this region are follows:

1. High radiation level. The radiation expected [1, 2] is measured in mega-Grays. Radiation damage of detector components is a major concern.
2. High occupancy. Minimum-bias events deposit substantial amount of energy in the very forward calorimeter (VFCAL), so that resulting occupancy problems are expected to be extremely serious for jet recognition.

[1]Now at Northeastern University, Boston, MA
[2]Now at CE Saclay, DAPNIA, Gif-sur-Yvette, France

3. Fast signal collection. The high particle densities and the high frequency of bunch crossings (25 ns) also constraints the acceptable signal duration.

4. Insensitivity to neutrons and activation products. The neutron fluxes up to $10^9 n/cm^2/sec$ are expected in the very forward calorimeter. Induced radioactivity may also have a large impact on measurements to the extent that it may give rise to a calorimetric signal. It is therefore important that VFCAL signals be as immune as possible to neutrons and to induced radioactivity.

5. Reliable operation with limited maintenance. The very forward region require extremely robust and reliable device because detector will be radioactivated after few years of operation and consequently the manual access to its hottest part will not be allowed.

The calorimeter that was proposed as an optimal design to the concerns raised above consists of quartz fibers embedded in an absorber matrix. Both copper and iron are considered as possible absorber material. The fibers run longitudinally, i.e. in the same direction as the incoming particles, as in many scintillating-fiber calorimeters. In this calorimeter, the signals are caused by Cherenkov light produced in the quartz optical fibers. Quartz is transparent to a large fraction of this light.

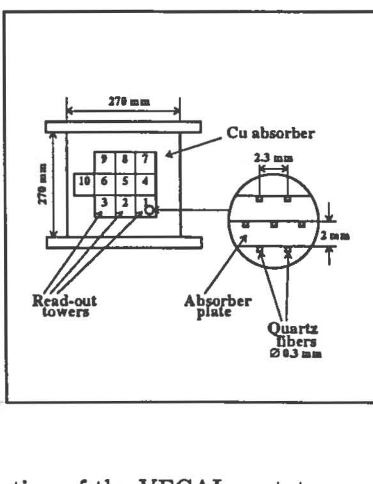

Figure 1: Lateral cross section of the VFCAL prototype calorimeter. The detector consists of 2.0 mm thick copper sheets and 0.3 mm core diameter quartz fibers.

The existing results on radiation hardness of silica core and F-doped silica clad optical fibers (see e.g. [3, 4]) show that such fibers keep their transparency for visible light after irradiation up to doses of 10 MGy.

The emission of Cherenkov radiation is a directional process. For particles h $\beta \approx 1$ travelling in quartz, Cherenkov light is emitted in a cone at an angle about 46° to the direction of the particle [5]. However, the shower particles ıtributing to the calorimeter signal are to a large extent isotropically distributed, they have "forgotten" the direction of the incoming particle that created the ›wer. It has been shown experimentally [6] that the response at very small angles ween the incoming beam particles and the fibers is only a factor of about 2 aller than the maximum value (measured as expected at 46°).

The spaghetti structure allows for a perfectly hermetic detector and for a ver structure with a transverse granularity that can be easily adapted and modified match the needs of an experiment. The signals can be conveniently extracted and nsported to a shielded location for the readout electronics.

The VFCAL is intended for the $3 < \|\eta\| < 5$ region of the CMS experiment. is means that the particles enter it at angles between $\sim 0.7°$ and $\sim 6°$ with the am line. If all fibers are oriented parallel to this beam line, the angles between particles and the fibers are in the same range. The geometrical structure of the CAL design was chosen as an optimal from the cost/performance considerations. avoid angular effects in the calorimeter, we chose a very-fine-sampling design, sed on quartz fibers with a core diameter of 0.3 mm, separated 2.3 mm. The ısitive part of fibers is only 1.5% fraction of total calorimeter volume making the al cost acceptable.

In order to evaluate the expected performance of the VFCAL, an 8.5 λ_i ıg prototype has been built and tested with high energy pions and electrons. ıe prototype has the same absorber/fibers geometrical parameters as proposed [1]. It is equipped with quartz fibers consisting of a 0.3 mm diameter core rrounded by 0.015 mm thick F-doped silica cladding. The front faces of fibers re mirrored. The absorber is copper. The total active depth of this calorimeter ıs 135cm, corresponding to 8.5 nuclear interaction lengths ($\lambda_{int} = 15.8cm$). The lorimeter contained in total 6000 quartz fibers, which were arranged in a pattern own in Fig.1. The fibers were grouped to form 10 towers. Each tower measured $\times 54mm^2$ and contained 600 fibers. The fibers sticking out at the back end of the wer were bunched together, machined, polished and coupled through a hexagonal r light guide to a photo-multiplier (HAMAMATSU R329-02, 2", 12-stage PMT ith Borosilicate glass window).

The measurements were performed in the H4 beam line of the SPS at ERN. The prototype was mounted on a platform that could move vertically and deways with respect to the beam, thus allowing to change the y and x coordinates the impact point of the particles, respectively.

The PMT gains were chosen in such a way that the average signal for 50 GeV electrons in the hit prototype cell corresponded to about 300 ADC counts above the pedestal value ($\sim 1.5pC/GeV$). Such a high gain was chosen to make a single photo-electron peak clearly observable.

As the calorimeter is strongly non-compensating the response depends on the type of incident particles. Throughout the analysis we used electro-magnetic energy scale. The response of each tower was calibrated by using electron beams with energies from 15 to 150 GeV directed into the center of that tower. Such a calibration procedure does not allow to unfold the potential non-linearity of QFCAL response for electrons and non-linearity of PMTs and read-out electronics channels. The systematic uncertainties of this procedure are currently under study, thus the results concerning energy resolution and pion response linearity presented here, have to be considered as preliminary.

The light response of the VFCAL prototype was found to be of 0.6-0.8 p.e./GeV. The sum of signals from 3×3 QFCAL module towers was used as a measure of the calorimeter response. The energy resolution for the detection of electro-magnetic (EM) showers was measured as a function of the electron beam energy. There are no significant deviations from a Gaussian line shape for 150 GeV electrons and the value of σ from a Gaussian fit is almost the same as the RMS for the signal distribution.

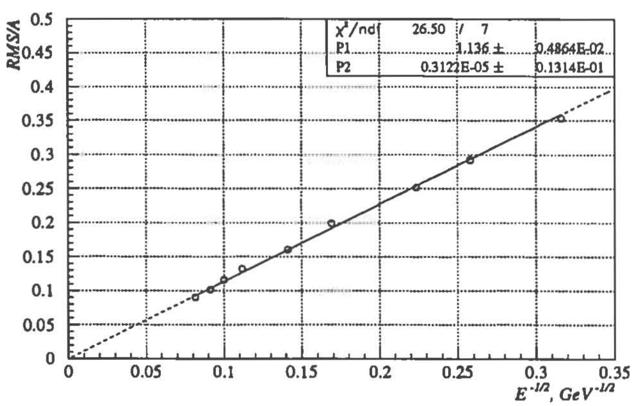

Figure 2: The QFCAL energy resolution for electrons as a function of the electron energy, which is plotted on a scale linear in $E^{-1/2}$.

Fig.2 shows the electron energy resolution as a function of $1/\sqrt{E(GeV)}$. We have fitted the data to the form: $\sigma_E/E = A/\sqrt{E} \oplus B$ and obtained $A = 1.136 \pm 0.005$, $B = 0 \pm 0.012$.

Angular effects were studied in the range from 0° to 6°. Electrons of GeV were steered into the centre of the VFCAL module at angles $\phi = 0°, 3°$. 6°. The signal distributions are shown in Fig.3 No significant differences were erved in the calorimeter response or in the energy resolution.

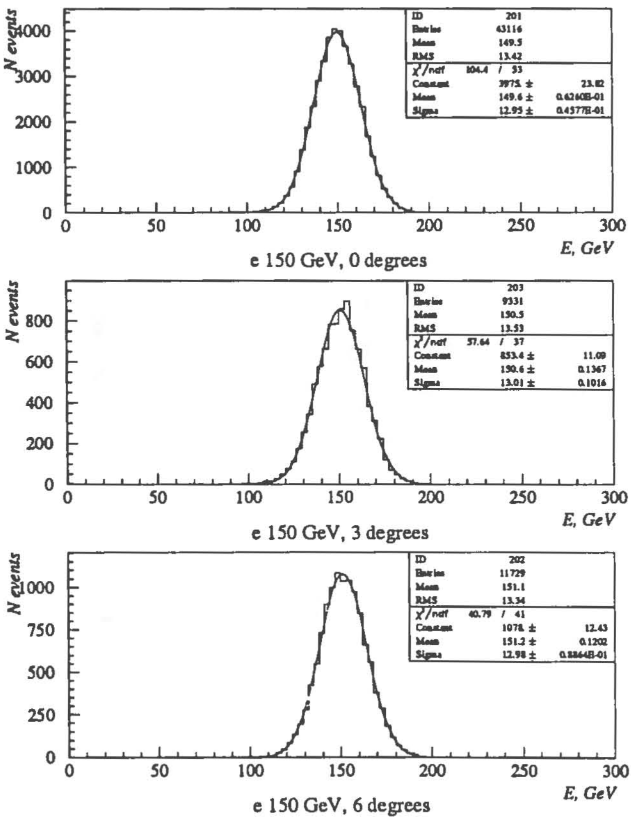

gure 3: Prototype signal distributions for 150 GeV electrons at different angles.

The mean hadronic response is smaller than the EM one and nonlinear (see g.4). As far as the scale calibration is valid up to EM scale energy of 150 GeV, ıich corresponds to the maximum response at the centre of the prototype to 250 eV pions. Data for higher pion energies are not presented. A 10% correction for complete hadronic shower containment was applied. This correction was measured a pion energy of 80 GeV and was found to be energy independent.

The pion energy resolution is described by a logarithmic energy dependence 'ig.5). The open circles in this figure show measured values while the triangles

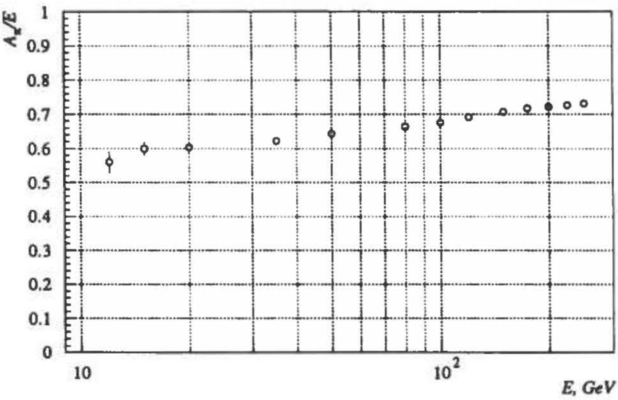

Figure 4: Mean hadronic response measured in EM scale

show the result of a quadratic subtraction of the photo-statistics contribution to the energy resolution. One can see that the hadron energy resolution of QFCAL can be described as a quadratic combination of two major terms: a photo-statistics term varying as $1/\sqrt{N_{pe}}$ and a shower fluctuation term with a logarithmic energy dependence. This is in agreement with the prediction of O.Ganel and R.Wigmans [7].

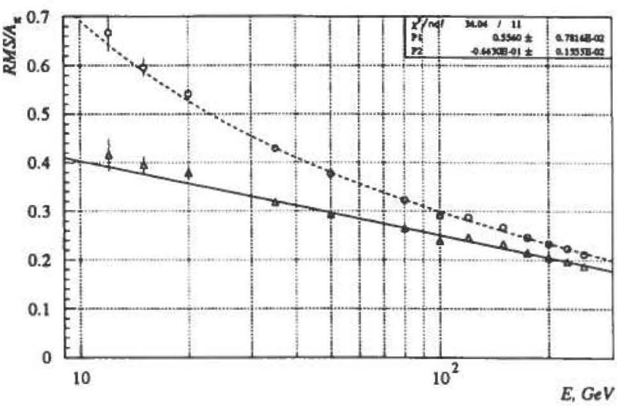

Figure 5: RMS/E dependence for pions measured in EM scale

The lateral uniformity of the detector and the lateral profiles of its response to electrons and pions were measured using a transverse scan. To study the signal uniformity of th: QFCAL module, we mapped the signals from 80 GeV electrons over an area of $2 \times 15cm^2$. The detector was moved vertically across the beam spot ($2 \times 2cm^2$). Drift chambers installed upstream of the calorimeter allowed the impact nt of each individual electron to be determined with a precision of $\pm 0.2mm$. sults are given in Fig.6, which shows the average value of the total calorimeter nal as a function of the impact point of the electron. Apart from the obvious :rease of the mean signal near the edge of the instrumented volume due to leakage, :re is no indication of edge effects in the border areas between different towers. is is one of the advantages of the spaghetti structure, which allows for a perfectly rmetic detector. The average signals in the three calorimeter towers traversed by : beam in these measurements are also shown in Fig.6.

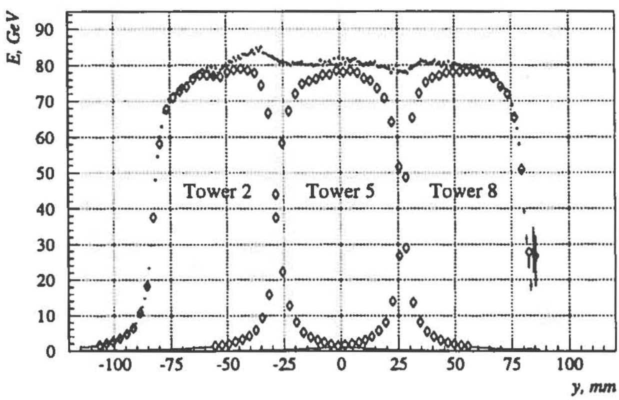

Figure 6: Spatial uniformity for 80 GeV electrons.

When we took a closer look at the similar high statistics data for 150 GeV :ctrons, it turned out that there was a very regular fine structure in the position :pendence of the calorimeter response (Fig.7). The response oscillates with an nplitude of $\sim 1\%$ around the central value. The period of the oscillation, 2.0 mm, rresponded exactly with the absorber layer thickness. It is caused by the fact that .e effective sampling fraction (and thus the calorimeter response) is slightly larger r electrons entering the calorimeter in a fiber plane than for electrons entering in ι absorber plane separating the fiber planes.

One of the main advantages this type of calorimeter as expected to offer the small width of hadronic showers [1]. Therefore special attention was paid to ıe measurement and the analysis of lateral shower profiles for electrons and pions.

To analyse the transverse response of the QFCAL module to 80 GeV pions ıd electrons we used the same data as for the transverse uniformity study, namely ıe runs in which beam particles entered the calorimeter at different impact points. he sum of signals from the towers in a row of 3×1 towers was measured with respect ı the distance of particle's icident point from The results obtained in this way are

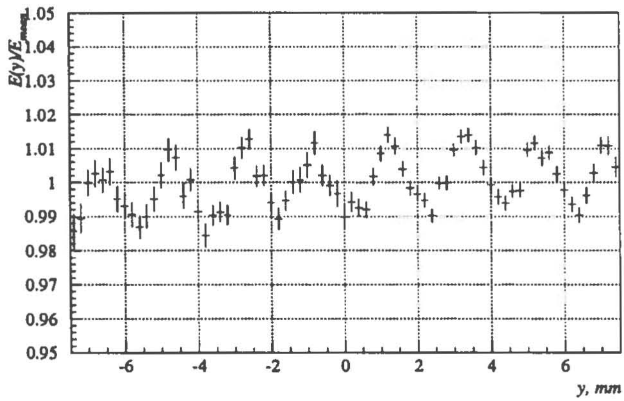

Figure 7: Spatial structure for 150 GeV electrons.

shown in Fig.8 and Fig.9. To approximate these profiles the following function was used:

$$F(x) = \int_S \Phi(r)dxdy$$

Where S is the area of a row of 3×1 towers and $\Phi(r)$ is the function which describes the lateral shower profile. The function

$$\Phi(r) = \exp(p1 + p2 \cdot r) + \exp(p3 + p4 \cdot r)$$

was used to fit the distribution. The experimental profiles are well described by this function. The results of the fit are shown in the Fig.8 Fig.9 by solid lines. The results of these fits are thus used to describe the shower profiles.

Fig.10 and Fig.11 show the leakage from the cylindrical volume with respect to the radius of this volume. The shower profiles for lead and scintillating fiber Spaghetti Calorimeter (SPACAL) are also shown in these figures for comparison with the quartz fiber calorimeter. This figure indicates that hadronic shower profiles in the QFCAL are considerably narrower than in the SPACAL. EM shower profiles in the QFCAL have almost the same profiles as in the SPACAL up to a shower containment level of 99%.

The emission of Cherenkov light is intrinsically a very fast process, with a time constant that is much smaller than the 1 - 10 ns typical for fast scintillators. Also, tails in the time structure of the calorimeter signals which may be produced by slow shower neutrons in other types of calorimeter are expected to be absent in a detector based on detection of Cherenkov light. Instrumental effects (e.g. those caused by the light detection devices or by the mirrors) broaden the calorimeter

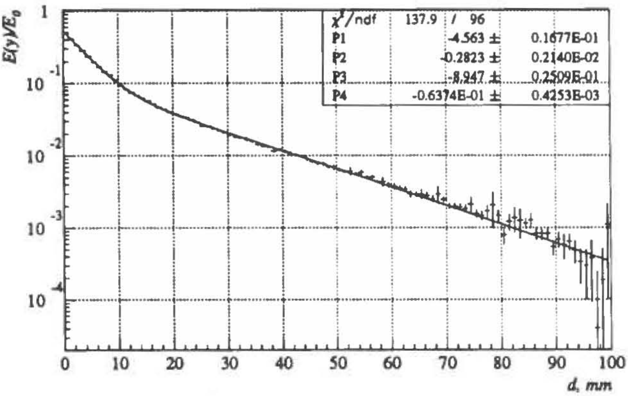

ure 8: Distribution of the signal in the 3 × 1 slice vs the distance to the beam 80 GeV electrons.

nals. In this study, we have investigated if, in spite of such effects, the charge lection time of a quartz-based calorimeter may still be sufficiently short for LHC rposes (25 ns bunch spacing).

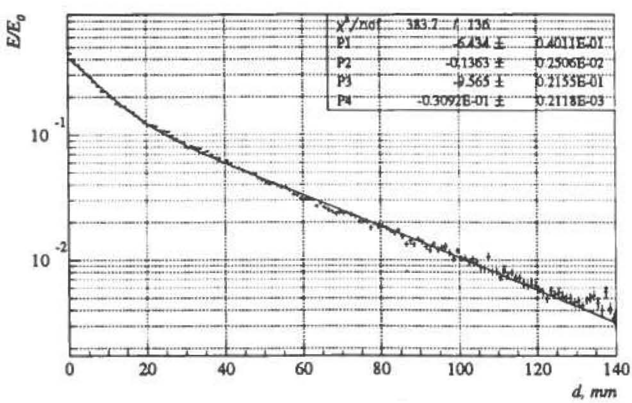

gure 9: Distribution of the signal in the slice 3 × 1 vs the distance to the beam : 80 GeV pions.

Signal traces of 375 GeV pions traversing a QFCAL tower equipped with fast PMT were recorded using a fast digital oscilloscope (LC7200) operated in e self-triggering mode. 10 m long RG-58 cable was used to link with the cilloscope. The beam was steered at the edge of the QFCAL tower. Fig.12 shows sample of such traces in order to illustrate that the FWHM of pion signal from FCAL is 2-3 ns and the full charge collection time does not exceed 10 ns if a fast PMT is used and the front-end electronics is placed near it. Very fast signal from QFCAL will allow not only a full suppression of pile-up from different bunch crossings, but also the use of timing information to suppress background signals caused by high energy particles coming e.g. from the low beta quad shield.

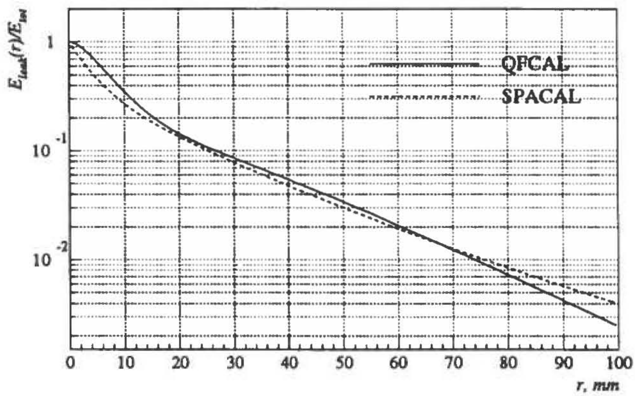

Figure 10: Shower profile for 80 GeV electrons.

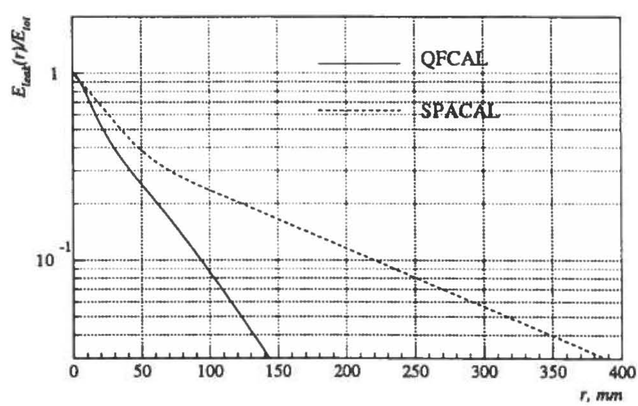

Figure 11: Shower profile for 80 GeV pions.

We conclude that the quartz fiber calorimeter is a truly exceptional device. It has some unique properties which make it eminently suitable for its tasks and which we briefly summarise below:

- The detector is, for all practical purposes, mainly sensitive to EM showers. This makes all showers very narrow in the transverse plane, which has major

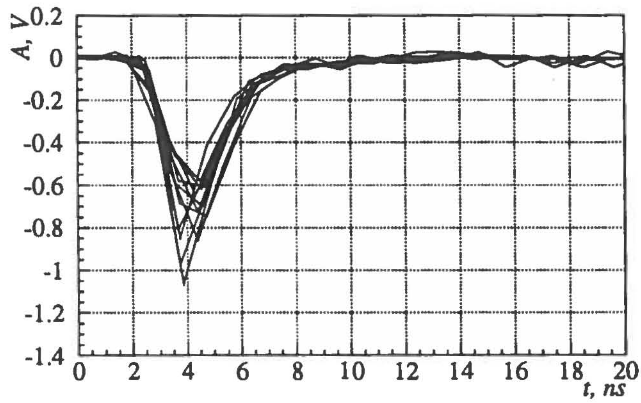

Figure 12: Oscilloscope traces for 375 GeV pions.

advantages for jet identification and for jet position measurements up to very large pseudorapidities.

- The response to electrons and hadrons is practically independent of the incident angle in the range from 0° to 6°
- Based on the detection of Cherenkov light, it is the fastest conceivable detector.
- The detector can be made perfectly hermetic. Granularity can be chosen as needed, all the way to the beam pipe, providing the maximum possible effective η-coverage.

Looking at potential drawbacks of this type of calorimeter, one is struck rst by the very low light-yield, ~ 0.7 photoelectrons/GeV in our prototype. Whereas iis feature dominates the energy resolution for isolated EM showers, one should reize that for 1 TeV jets, the contribution of statistical fluctuations in the number of hotoelectrons to the energy resolution is, even for this very low level of light yield, t maximum $\sim 4\%$. This is negligible compared to other sources of fluctuation. irst and foremost among these are the event-by-event fluctuations in the energy action carried by the EM component of jets, since the detector mainly responds these components. The effect of these fluctuations decreases logarithmically with nergy [7], in contrast with those governed by Poisson statistics, which scale with $/\sqrt{E}$. The logarithmic energy dependence of the hadronic energy resolution was emonstrated to be valid for our prototype and extrapolates to resolutions of better han 12.5% at 1 TeV, adequate for the envisaged experimental goals.

Acknowledgements

We would like to thank our colleagues from CMS, and in particular A.Ferrand D.Green and T.Virdee for many fruitful discussions, J.Bourotte and M.Haguenauer, who made the described beam tests possible. We are grateful to N.Doble and the entire SPS team, who provided us with particle beams of excellent quality. This project was carried out with financial support from the U.S. Department of Energy, from the International Science Foundation (grant No: M82000 and No: M82300), from the Russian Ministry of Science and Technical Policy, and from the Russian Fundamental Research Foundation (grant No:95-02-04815a).

References

1. The CMS Collaboration. Technical Proposal. CERN/LHCC 94-39, 1994.
2. I.Azhgirey et al. Simulation of the VFCAL/QF Irradiation During the LHC Operation, CMS TN/95-063, 1995.
3. J.B.Chesser, Radiation Testing of Optical Fibers for a Hot-Cell Photometer, IEEE Transactions on Nuclear Science, v.40, No.3, p.307, 1993.
4. V.Gavrilov et al., Study of Quartz Fiber Radiation Hardness, CMS TN/94-324, 1994.
5. G.Anzivino et al., Recent developments in quartz fiber calorimetry, NIM, v.A357, p.369, 1995.
6. G. Anzivino et al., Angular Dependence of Quartz Fiber Calorimeter Response. NIM, v.A360, p.237, 1995.
7. O.Ganel and R.Wigmans, NIM v.A365, p.104, 19^^.

:cati Physics Series Vol. VI, (pp. 281–288)
ᴺT. CONF. ON CALORIMETRY IN HEP – Frascati, June 8–14, 1996

THE BENEFITS OF EXTREME NON-COMPENSATION

Richard Wigmans
Texas Tech University, Lubbock TX 79409, U.S.A.

ABSTRACT

ırticle detection in the very forward regions of LHC experiments is an extremely allenging task. The CMS Collaboration has chosen a Quartz Fiber Calorimeter : this purpose. The basic principles of this type of calorimetry, and their conseıences for the detection of particles and jets in the LHC environment are briefly scussed.

ıe of the most challenging tasks in designing experiments for the Large Hadron ɔllider is to find adequate detectors for the very forward regions ($|\eta| > 3$, $\theta < 5°$). The radiation conditions in this corner of phase space are similar those at ground zero in the Hiroshima nuclear explosion, which implies staggring particle rates. As was pointed out by J. Rutherfoord this morning, the ergy flow in the ATLAS Very-Forward Calorimeter is estimated to be 7 TeV per ınch crossing (25 ns). If I am not mistaken, this is equivalent to about 10 calo-s per second! This device (and its counterpart in CMS) will therefore become *lorimeters* in the true sense of the word.

this talk, I will discuss the basics of the detector chosen by CMS to meet is challenge, the Quartz Fiber Calorimeter (QFCAL). This device, originally oposed because of its excellent radiation hardness, turns out to have some very ıconventional calorimetric characteristics, which seem to be taylor-made for this ırticular type of application.

ɔ appreciate these characteristics and their implications, it is good to realize hat a calorimeter is. In particle physics experiments, we have come to consider lorimeters as devices that measure energy deposition. However, what is really easured in practice is light (γ's) or ionization charge (e^-), the amount of which **presumed** to be proportional to to the energy deposited in the area from which ıe photons or electrons are collected. This basic assumption of proportionality is general an oversimplification.

particle that showers in a sampling calorimeter structure deposits a certain fraction of its energy in the active layers of the calorimeter, usually referred to as the *sampling fraction*. In general, this sampling fraction depends on the type of particle. For example, in noncompensating calorimeters, it is different for electromagnetic (e.m.) showers and hadronic showers. The sampling fraction for muons is again different from that of electrons, photons and hadrons. The situation is further complicated by the fact that the sampling fraction also depends on the type (and energy) of the particles produced in the shower development. And since the composition of the shower is a function of its "age" (or the distance over which the shower has developed), so is the sampling fraction [1]. This is true for both e.m. and hadronic showers.

These deviations from proportionality cause well-known problems with the calibration of longitudinally segmented calorimeter systems, such as the impossibility to optimize the energy resolution and the signal linearity simultaneously. This is a very interesting topic in its own right, but outside the scope of my present contribution to this Conference.

If the calorimeter signal consists of Čerenkov photons, as in the QFCAL considered here, the proportionality assumption mentioned above is *extremely incorrect*. Čerenkov light is only produced by relativistic, charged shower particles. Therefore, the response of the QFCAL to hadronic showers is extremely dependent on the extent to which such particles are produced in the shower development. Hadronic showers deposit their energy through various processes, each with very different rates of Čerenkov-capable particle production:

- π^0's produced in hadronic shower development give rise to e.m. showers, in which the energy is deposited through electrons and positrons. These shower particles produce Čerenkov light when their energy is larger than about 700 keV.
- Of the energy carried by the non-e.m. shower component, on average 15% is deposited by charged pions. These particles are relativistic above 190 MeV.
- The rest of the non-e.m. energy is deposited by protons and neutrons (relativistic above 1.3 GeV), most of which are coming from nuclear evaporation processes (few MeV), and through release of nuclear binding energy, which leaves no directly measurable signal.

As a result, the QFCAL is extremely non-compensating. The ratio of its response to e.m. and non-e.m. energy deposit is believed to be very large [2]: $e/h > 7$. This has important consequences. Since electrons and positrons produced in the showers dominate the signals from this calorimeter, hadron showers register predominantly through their electromagnetic shower core. This has a two–fold benefit. First, the

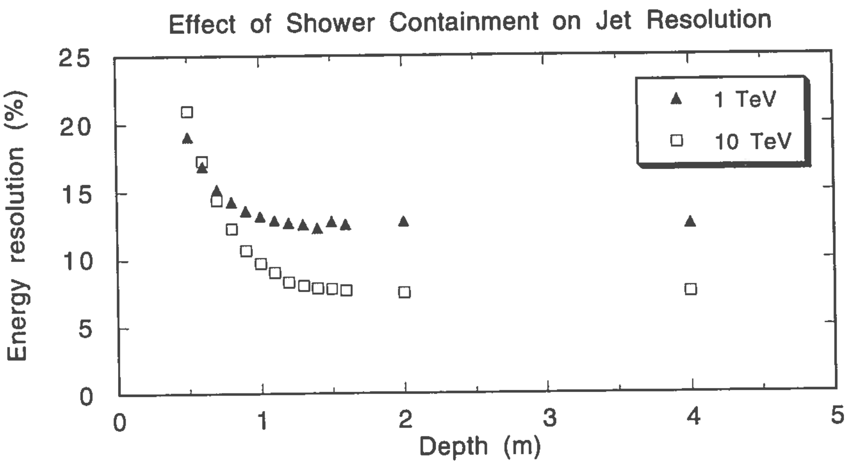

Figure 1. The energy resolution for 1 and 10 TeV jets in a QFCAL with copper absorber, as a function of the instrumented depth of the calorimeter. Results from Monte Carlo simulations[1)].

strumented depth needed is substantially less than that required for full containent of the hadron showers (see figure 1). Second, the lateral dimension of the ıower signals depends on the Molière radius (ρ_M) and is much less determined y the nuclear interaction length, λ_{int}, which governs the lateral development of adron showers in calorimeters based on dE/dx measurements. These two quanties typically differ by an order of magnitude and, therefore, hadron showers in ıis type of calorimeter appear to be considerable narrower than in other types of alorimeter. This is an important advantage when particle densities are as high as ı the very forward region of LHC experiments, since it reduces shower overlap.

'hese characteristics favor the use of absorber materials like copper or iron in uartz fiber calorimeters. Relevant parameters such as ρ_M or λ_{int} are actually maller for these materials than for lead. By using relatively low-Z absorber ıaterial, a considerable reduction in the total weight of the calorimeter is achieved. Iore importantly, the rate of neutron production (of which the Very Forward Calorimeter is one of the main sources) is reduced by as much as a factor of 3, ompared to high-Z alternatives.

'he nature of Čerenkov light gives rise to several other important benefits for the QFCAL:

- In contrast with molecular fluorescence processes, Čerenkov radiation is an intrinsically *very fast* process with a typical time constant of less than 1 ns. Instrumental effects (*e.g.* those caused by the light detection devices) may broaden the signals, but still the charge collection time is more than adequately short for LHC purposes. The signals are even so fast that they might be used to distinguish particles coming from the interaction vertices from those generated in the downstream quadrupoles [3].
- Neutral particles (*e.g.* neutrons) and non-relativistic charged particles (*e.g.* most particles produced by induced radioactivity) do not produce Čerenkov light and thus do not give rise to noise.
- The fibers only collect light emitted by shower particles traveling at angles close to the characteristic Čerenkov angle (46°) with respect to the fibers. Small angle effects, observed in scintillating fiber calorimeters and caused by shower particles traveling long distances through the fibers [4], are therefore absent in this detector.

Talking about the Čerenkov angle, one may actually wonder why this calorimeter produces signals at all, with the fibers oriented in the same direction as the incom-

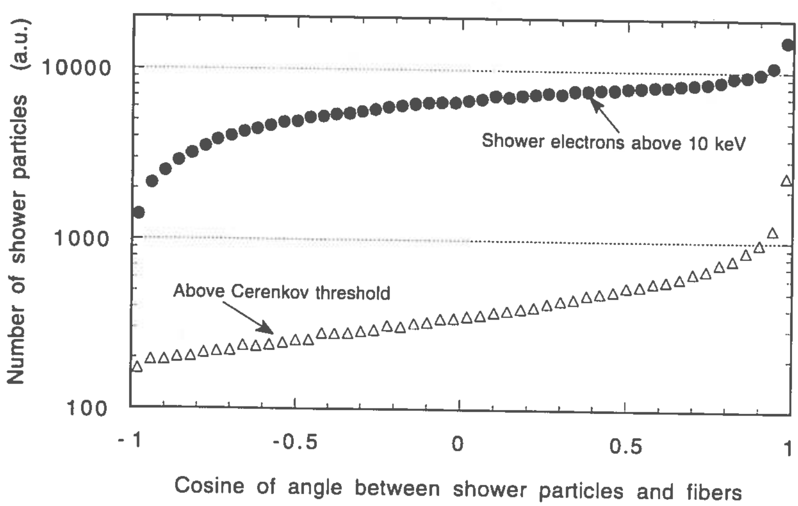

Figure 2. Angular distribution of shower particles (e^+ and e^-) through which the energy of a high-energy electron or photon showering in copper is absorbed. Shown are the results (of Monte Carlo simulations [2]) for all shower particles with kinetic energies larger than 10 keV and for shower particles capable of emitting Čerenkov light ($E_{\text{kin}} > 200$ keV).

g particles. The explanation lies in the fact that a large fraction of the shower ıergy is deposited through electrons produced by Compton scattering. Such ectrons are isotropically distributed with respect to the direction of the incomg photon and, therefore, give rise to an angle independent contribution to the ılorimeter signals. As a result, the signals are only a factor 2 - 3 smaller than ıose in a device with the fibers oriented at 46° with respect to the incoming parcles. Such a device would be sensitive to the fast e^+e^- pairs, produced in the ırly stages of the shower development, and traveling in (approximately) the same irection as the incoming particles.

'hese arguments are made quantitative in figure 2, in which the angular distriutions of electrons contributing to the signals from calorimeters based on dE/dx ıeasurements (full circles) and Čerenkov light detection (triangles) are shown. As ı so many other calorimeters, processes occurring (abundantly) in the later stages f the shower development determine the calorimeter characteristics.

)nce we understand the origin of the signals from this calorimeter, its perforıance can be reliably predicted. Not on the basis of the usual, CPU-devoring lack-box Monte Carlos which, as far as I know, have never made any meaningful ·rediction concerning fundamental calorimetry issues, but on the basis of existing xperimental data, like the ones from the fine-grained SPACAL [5] detector.

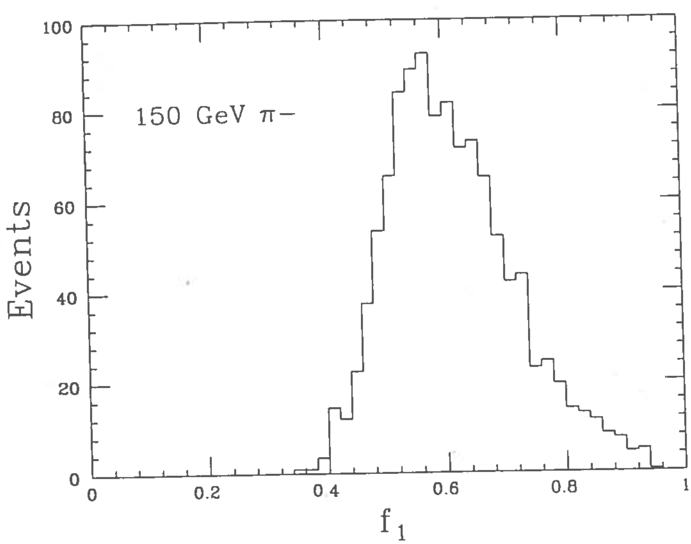

Figure 3. Signals from 150 GeV π^- showering in the SPACAL detector. Shown is the signal distribution in the central tower (effective radius $\sim 2\rho_M$) of the detector [5].

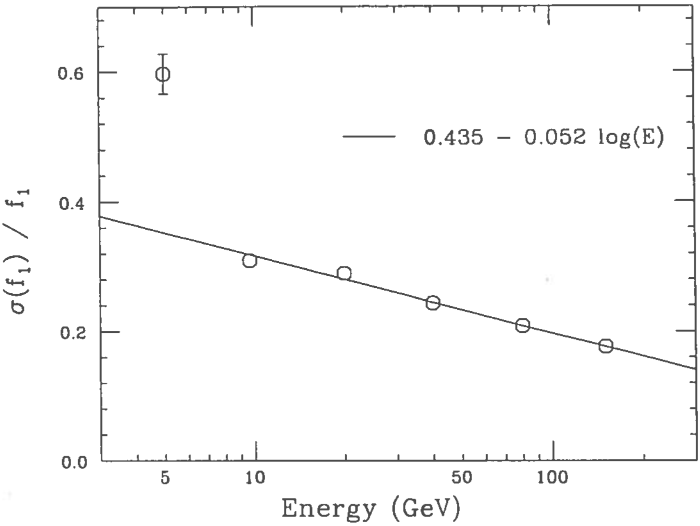

Figure 4. The energy resolution as a function of energy for pions showering in the SPACAL calorimeter, considering only the signals produced in the central tower (effective radius $\sim 2\rho_M$) of this detector. Data from ref. 5.

By considering only the signals produced in the central tower of this calorimeter, in which almost the entire energy of electromagnetic shower core is deposited, and little else, we can get a rather accurate idea of the characteristics of a calorimeter in which this core is the *only* shower component that leads to a signal. Figure 3 shows a typical signal distribution in this tower, produced by 150 GeV π^-. Figure 4 shows the energy resolution of distributions such as the one from figure 3, as a function of energy. These figures exhibit some very characteristic features, which are also typical for hadronic quartz fiber calorimetry. The asymmetric signal distribution in fig. 3 is a result of the peculiarities of π^0 production in shower development. Charged pions may produce neutral ones, but the reverse process does not occur. A large calorimeter signal may be the result of the production of a leading π^0 in the first interaction of the showering particle. However, when a leading charged pion is produced in the first interaction, there is no guarantee that the resulting calorimeter signal will be small, since this leading charged pion may produce a very energetic π^0 in its next interaction. There is no symmetry in the conditions needed for very large and very small calorimeter signals and, therefore, the signal distribution is skewed.

In most other calorimeters, the number of shower particles contributing to the sig-al is (approximately) proportional to the shower energy. Gaussian fluctuations the number of particles contributing to the signals thus lead to the familiar $^{-1/2}$ energy dependence of the energy resolution. In this case, the resolution determined by fluctuations in the numbers of π^0's produced in the shower de-elopment and the fraction of the shower energy carried by these particles. The umber of π^0's produced in hadronic showers increases much more slowly with nergy. Logarithmic [1] and power-law [6] scaling have been proposed to describe his. The SPACAL data (fig. 4) showed that the hadronic energy resolution in he range 10 - 150 GeV scaled indeed with the logarithm of the energy.

ince the average fraction of the shower energy carried by the e.m. core rises approximately logarithmically) with energy, the response is nonlinear: The signal er GeV increases with energy. All these phenomena (skewed lineshape, energy ependence of hadronic resolution, hadronic signal nonlinearity) were experimen-ally observed by analyzing the hadronic signals from the central tower (effective adius 39 mm) of the SPACAL calorimeter, thus selecting the e.m. shower core elieved to be almost entirely responsible for generating the signals in the quartz ber calorimeter.

n 1995 and 1996, a hadronic prototype QFCAL was extensively tested at CERN nd the results are in excellent agreement with these predictions. In particular, the rediction that the hadronic energy resolution in this type of calorimeter scales vith the logarithm of the energy (as opposed to the $E^{-1/2}$ scaling typical for lmost all other calorimeters) was experimentally confirmed [7]. Also, hadronic ignal nonlinearities and lineshapes as discussed above were observed in these ests.

Another crucial prediction concerned the hadronic shower profiles. Since this Čerenkov calorimeter is, for all practical purposes, only sensitive to the electro-magnetic shower cores, these profiles were expected to be much more narrow and shallow than those measured by other types of calorimeter [5]. Also these proper-ties were experimentally confirmed. As argued before, such pencil-shaped showers, and the related insensitivity to neutrons, are very attractive features for a detector in the high-η region of an LHC experiment.

The tests also showed that this type of calorimeter works fine at all angles (including 0°, 90° and 180° between the fibers and the incoming particles), and not exclusively at the Čerenkov angle of 46°.

The CMS Very Forward Calorimeter will be one of the most non-compensating calorimeters ever built. I have tried to describe to you some of the advantages that I see resulting from the very unique properties of this device: Ultrafast signals, pencil-shaped showers, low neutron production. The energy resolution is not going to be excellent, but most likely adequate for the tasks of a calorimeter in this corner of phase space. The question may arise to what extent the smaller e/h value of the ATLAS Very Forward Calorimeter will turn out to be an advantage. In my opinion, this advantage will be minimal. Compensation is achieved through detection of the shower tails. In SPACAL, we had to integrate the signals over a calorimeter surface of about 1 m^2 to get an e/h value close to 1.0 [8]. Almost all prototypes of dE/dx based calorimeters that have been built in the past turned out to be too small to contain hadron showers at a sufficient level to make fluctuations in shower leakage negligible. Given the particle densities typical for the high-η region of LHC experiments, one will have to limit the integration cones in practice to small surface areas. Even with a perfectly compensating calorimeter, one would have to live with the measurement precision provided by a small fraction of the area in which the shower energy is deposited.

Therefore, as I see it, the difference between the ATLAS and CMS Very Forward Calorimeters can be summarized as follows: ATLAS showers do have tails outside the e.m. cores, CMS showers don't have such tails. However, in practice, these tails will will be irrelevant for the energy measurement precision, they will just increase the general "noise" level.

REFERENCES

1. R. Wigmans, Nucl. Instr. and Meth. **A259**, (1987) 389.
2. O. Ganel and R. Wigmans, Nucl. Instr. and Meth. **A365**, 104 (1996).
3. L. Sulak, contribution to these Proceedings.
4. D. Acosta *et al.*, Nucl. Instr. and Meth. **A294**, 193 (1990).
5. D. Acosta *et al.*, Nucl. Instr. and Meth. **A316**, 184 (1992).
6. T.A. Gabriel *et al.*, Nucl. Instr. and Meth. **A338**, 336 (1994).
7. V. Gavrilov, contribution to these Proceedings.
8. D. Acosta *et al.*, Nucl. Instr. and Meth. **A308**, 481 (1991).

scati Physics Series Vol. VI, (pp. 289–298)
INT. CONF. ON CALORIMETRY IN HEP – Frascati, June 8–14, 1996

'HE QUARTZ FIBRE ZERO DEGREE CALORIMETER OF THE NA50 EXPERIMENT AT THE CERN SPS

E. Chiavassa, N. De Marco, G. Dellacasa, M. Gallio, P. Guaita, A. Musso, M. Pezzetta, A. Piccotti, E. Scomparin, C. Soave, E. Vercellin

NFN – Sezione di Torino, Dipartimento di Fisica Sperimentale, Università di Torino, Via P. Giuria 1, 10125 Torino

ABSTRACT

: describe the performance of the zero degree hadron calorimeter (ZDC) operating in : NA50 experiment at the CERN SPS. This detector, based on the "quartz" fibre tech- que, must measure the energy of beam fragments after a 20% interaction length target in 'b-Pb reaction at 158 GeV per nucleon. Despite its very small overall dimensions (5x5cm ^{2} ›nt face and 65 cm length, divided in four longitudinal towers) the energy resolution is od ($\sigma/E = 6.5\%$ on the lead ion) whereas its radiation hardness and velocity are excel- ıt (30% loss after an irradiation of 1.8 Grad, signal width of less than 10 ns). Localiza- n properties for the measurement of the coordinate of the beam on its front face are also ectacular in this energy range (r.m.s. of 0.2 mm). The excellent results obtained in NA50 shed two of the forthcoming LHC experiments (ALICE and CMS) to include detector sed on this new technique in their experimental apparatus.

Introduction

ıe physics goal of the NA50 experiment is the study of the production of muon pairs and ctor mesons (ρ, ω, ϕ, J/ψ and ψ') with special emphasis on the charmonium (J/ψ, ψ') oduction attenuation[1]. The vector mesons are produced in Pb-Pb interactions at 158 eV per nucleon on fixed target and are identified by their decay into two muons in a agnetic spectrometer made by MWPCs, scintillator hodoscopes and a toroidal magnet. ıe very low cross-sections of the charmonium production implies the use of a very high tensity beam: $\sim 5\times10^7$ ions per burst with a burst duration of about 5 s and a repetion 'cle of 20 s.

nce vector meson production has to be correlated with the centrality of the ion-ion col- ;ion, three centrality detectors, which cover different pseudorapidity ($\eta = -\ln(\tan(\vartheta/2))$) tervals, are included in the NA50 experimental apparatus:

ı silicon strip multiplicity detector ($1.6 < \eta < 4.0$);

ın electromagnetic calorimeter ($1.1 < \eta < 2.3$);

- a zero degree hadron calorimeter (ZDC) ($\eta \geq 6.2$).

The hadron calorimeter (ZDC) that we describe in this paper measures the residual energy of the impinging Pb after the interaction to obtain the energy (E_{dep}) released in the target

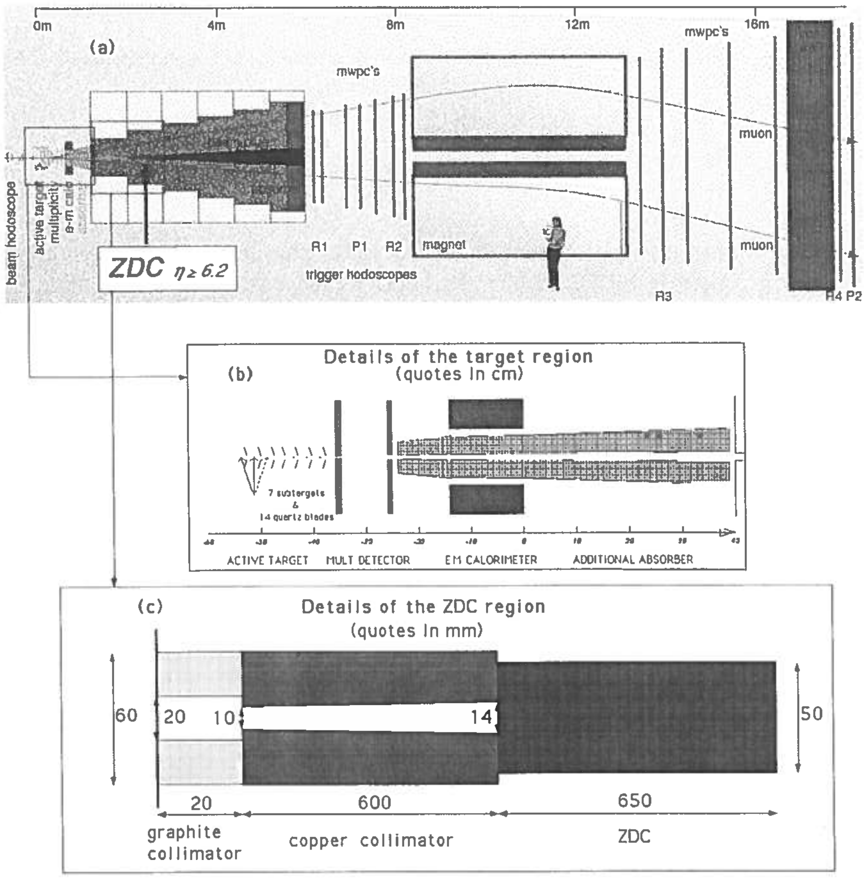

Fig. 1: NA50 experimental set-up with details of the target region (b) and of the ZDC region (c).

from the simple relation $E_{dep}=E_{beam}- E_{ZDC}$: this quantity is directly related to the impact parameter of the Pb-Pb reaction. Since the ZDC is the only detector placed on the beam axis, it also monitors the incoming beam position during the run.

shown in fig. 1 the ZDC constitutes the first element of the 5 m long beam dump, being ated on the beam axis 1.8 m downstream the target; this fact implies that it is particu- y affected by the high intensity beam, which deposes in the detector almost $5x10^7x33$ V/burst since we work with a thin target (20% of lead interaction length) and that the ilable space is very small. Therefore the ZDC should work in a high radiation environ- nt (more than 1 Grad/month of absorbed dose) giving a stable response over a long run iod and it should produce very short signals (about 10 ns width) to reduce pile-up ects. These requirements can only be fulfilled by a "quartz" fibre calorimeter[2, 3] which ers the advantage of being highly radiation resistant, insensitive to induced radioactiva- n and very fast. A fourth advantage of this technique is the reduced lateral size of the ectable shower which permits to build small calorimeters with reasonable energy reso- ion.

veral hadronic and electromagnetic prototypes of quartz fibre calorimeters were al- dy extensively tested[4-10].

e response of our detector has been studied with a Monte Carlo program based on the ITIOF [11] code, which simulates the heavy ion interactions, and the GEANT code[12], ich handles the tracking of the shower particles. Before the final design a prototype of ZDC was tested on the H6 beam of the CERN SPS with hadrons and positrons of ergy ranging from 100 to 200 GeV. Results of these tests are described elsewhere[9]. The ergy resolution measured with 200 GeV protons was 30% (σ/E) and the e/π ratio was out 2. This non-compensation effect does not pose problems in the NA50 experiment, ce the ZDC has to discriminate between impinging nuclear fragments made of nucle- s of the same energy.

Description of the ZDC

e calorimeter structure is similar to that of the spaghetti calorimeters[13] with Tantalum showering material and "quartz" optical fibres, where the light is produced by Cher- kov effect, as active medium. Since the ZDC has to be outside the acceptance of the ectrometer (the graphite region in fig. 1a), its transversal size is limited to 5x5cm ^{2}; ier geometrical constraints limit its length to 65 cm (corresponding to 5.5 nuclear inter- tion lengths). It is made by 30 grooved tantalum slabs (each of them 1.5 mm thick) in ich are uniformly distributed 900 fibres of the type HCG-M-365-U ("Silica-Silica") oduced by SpecTran (USA). Fibre core diameter is 365 μm and the numerical aperture 22; the fibre spacing is 1.5 mm, corresponding to a quartz/tantalum volume ratio of out 1/17. The total length of each fibre is 180 cm: the first 65 cm, placed inside the ntalum slabs at 0° with the beam direction, is the "active" part of the calorimeter, the st, bend at 90°, acts as a "light guide" which transmits the light to the photomultipliers

(Philips XP-2242B) situated in the iron absorber at 1m from the beam axis (see fig. 2). To obtain a position sensitive device the calorimeter is divided in four towers of 225 fibres

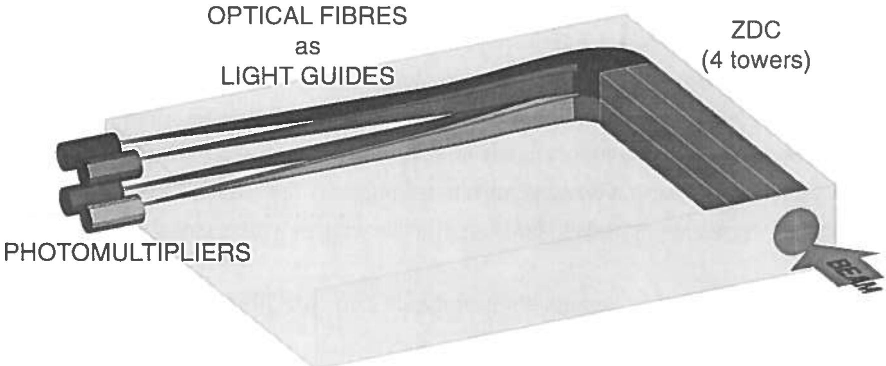

Fig. 2: the ZDC "box".

each, corresponding to the four quadrants of its front face. To permit a fast access for maintenance, the detector is contained in a sliding box, that can be easily moved out of the absorber and is filled with the same material of the absorber. The ZDC acceptance is delimited by a copper collimator 60 cm long with a conical aperture of 0.2°, corresponding to a 7 mm radius hole on the front face of the ZDC (see fig. 1c).
It has been shown that in this kind of detectors the highest light yield is obtained with fibres at 45° with respect to the beam direction; with fibres parallel to the beam direction, as imposed by mechanical constraints in this experiment, the light yield is reduced of about 50% [2, 3, 8)], but the energy resolution is not strongly affected. Moreover this arrangement makes it easier to obtain a localising and hermetic device.

3 Performance with lead beam

The ZDC was operated during 1994 and 1995 Pb ion runs with some differences in the read-out setup. We will describe here the results obtained with the 1995 setup, the former one having been already described [9)].
The Philips XP-2242B photomultipliers were operated at a gain of $5x10^4$ to keep the mean anode current during the burst under the limit suggested by the manufacturer. The signals, after 45 m of C-50-11-1 cables, were amplified by a factor of ten in a fast linear amplifier (LeCroy 612A), passed through a linear fan-in/fan-out (LFIFO - LeCroy 428F) and send to the trigger circuit to produce a minimum bias trigger, see fig. 3a. A second

tput from the LFIFO was sent to the linear gate through 155 m of coaxial cable and a ;ond amplifier-LFIFO stage. Gated signals were then digitised in a VME CAEN V465)C module. After the first 45 m of cable the signals were very narrow, less than 10ns, as

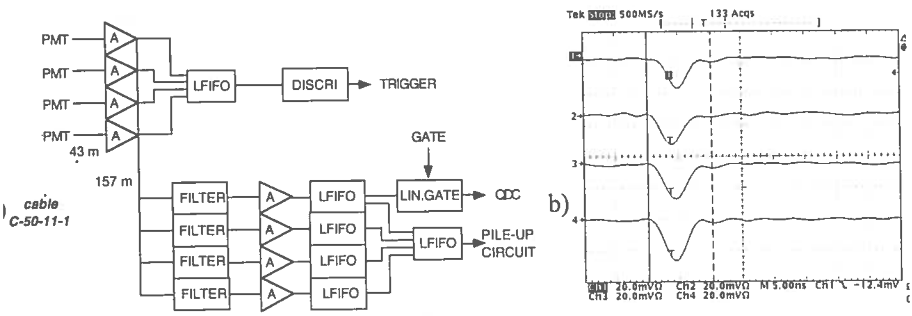

g. 3: General scheme of the ZDC electronic circuit (a) and signal shape at the input of e first amplifier stage (b).

ıown in fig. 3b; unfortunately the second part of coaxial cable (155 m), imposed by the igger formation time, widened them to 18 ns and a T-bridge filter had to be used to keep ıe signal in the 12 ns wide gate.

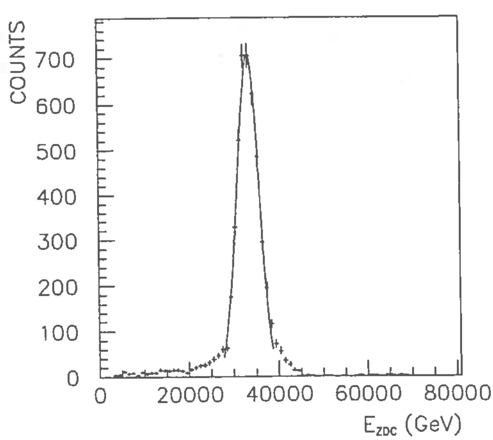

'ig. 4: ADC spectrum obtained from the ZDC with a minimum bias trigger generated by he ZDC itself ; the lead peak is clearly separated from the fragments contribution on its eft side and from pile-up traces on its right side.

n fig. 4 we present the ZDC energy spectrum obtained with minimum bias trigger: we can easily distinguish between the leftmost region with signals produced by beam fragments after interaction in the target and the lead peak, produced by non interacting lead ions (the target thickness is 20% of the lead interaction length). The resolution on the peak (σ/E) is 6.5% , good enough to satisfy the physics request to divide the events into four impact parameter classes. Small traces of the pile-up of two ions in the same gate can be observed on the rightmost spectrum region around 66 TeV. Nevertheless the pile-up affects about

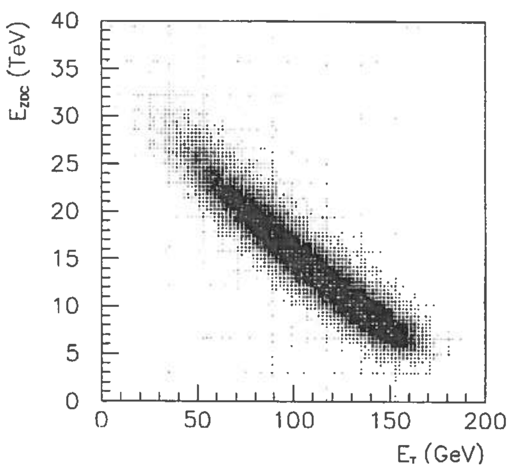

Fig. 5: correlation between the energy measured in the ZDC and the neutral transverse energy measured in the electromagnetic calorimeter.

25% of the events collected with dimuon trigger. A dedicated circuit, based on the use of 24 ADC channels with gates delayed in steps of 2 ns around the central one, permits to recognise with 97% efficiency the events in which the pile-up is produced by two signals having a relative delay larger than 2 ns. A software algorithm for the correction of the ZDC measured energy is under study.

It was not possible to calibrate the ZDC with ions of mass lower than the lead mass; anyway the correlation between the energy measured in the ZDC and the neutral transverse energy measured in the electromagnetic calorimeter observed in fig.5, makes us confident on the ZDC response linearity.

3.1 Position measurement

The ability of the ZDC to measure the beam impact point on its front face was tested with the proton beam [9] using a MWPC to measure the beam position. In fig.6a we present the sults obtained plotting the difference between the coordinate measured with the MWPC d that obtained from the calculation of the centroid of the shower distribution in the four wers of the ZDC. We use the formula:

$$X_{ZDC} = \frac{\sum_{i=1}^{4} ADC_i^{\alpha} \cdot x_i}{\sum_{i=1}^{4} ADC_i^{\alpha}} \qquad (1)$$

here x_i is the coordinate of the centre of the i-th tower, ADC_i is the ADC response of the th tower and α is a parameter obtained fitting simulated data. The resolution on the

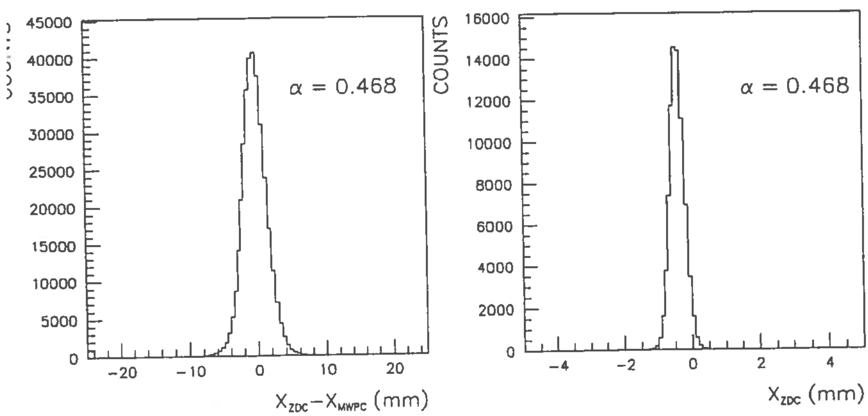

(a) (b)

'ig. 6: (a) difference between the incident proton position measured respectively by the :DC and the MWPC; (b) lead beam profile measured by the ZDC on its front face.

osition measurement is 1.7 mm (σ) in the central region of 7 mm diameter.

n the case of the lead beam, where we use the ZDC to monitor the stability of the beam osition during the run, the response of the ZDC cannot be compared with others position ensitive devices. The horizontal beam profile calculated with formula (1) is presented in ig.6b and the width of the distribution, 0.21 mm r.m.s., can be considered as an upper imit for the position resolution. This improvement with respect to the proton case is due o the better energy resolution that we have with the ion beam.

3.2 Radiation damage

In fig.7 we plot the relative position of the lead peak obtained from the spectrum of fig.4

as a function of the absorbed dose. Raw data are represented by full circle; the step at 1.3 Grad corresponds to an increase of PM voltage of about 100 V. The open circles refer to the lead peak position corrected for the PM gain variation monitored with a laser diode.

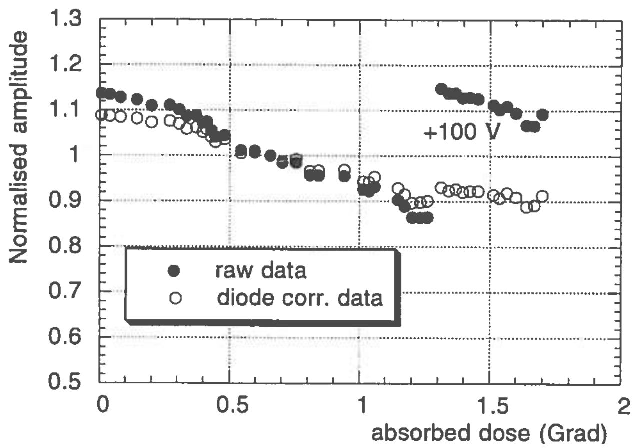

Fig. 7: ZDC response (normalized position of the lead peak in the ADC spectrum) versus absorbed dose during 1995 run.

During the run of November 1995, performed with an almost constant intensity of 4×10^7 ions per burst, the dose absorbed by the central part of the ZDC was estimated to about 1.8 Grad which produced a loss in the response of the detector of about 30%, probably due to a radiation damage of the fibre cladding. Nevertheless, no effect due to induced radioactivation was observed: the ADC pedestals, measured with a randomly generated gate, remained unchanged over the whole run period.

4 Conclusions

A ZDC based on quartz fibre technique was successfully operated in the lead ion runs in the NA50 experiment. Despite its very small physical size, it provides a satisfactory energy resolution whereas its resistance to radiation damage can be considered excellent. This detector also offers very good localising properties.
We can finally emphasise that this technique seems the ideal choice for radhard calorimeters at LHC. ZDCs based on the same design as that of the NA50 experiment are in fact already foreseen in the ALICE experimental setup [15] whereas CMS is also planning to use quartz fibres for its very forward calorimeters [16].

Acknowledgements

ɜ would like to thank all the members of the NA50 collaboration and especially P. ›rodetzky, who first proposed this technique. We are indebted to G. Alfarone, F. Callà d F. Daudo (INFN - Torino), for their valuable technical support in the calorimeter nstruction. A big effort was also produced by C. Ferrari and M. Heuzey (CERN) to lve the problems related to ZDC installation.

References

M.C. Abreu, et Al., Proposal CERN/SPSLC 91-55, Nov. 6, 1991

P. Gorodetzky et Al., Nucl. Instr. and Meth. in Phys. Res. A **361**, 161 (1995)

O. Ganel, R. Wigmans, Nucl. Instr. and Meth. in Phys. Res. A **365**, 104 (1995)

E. Chiavassa et Al., The Zero Degree hadronic sampling calorimeter for the NA50 experiment at the CERN SPS, in: Proc. of the Fourth International Conference on Calorimetry in High Energy Physics, (eds. A. Menzione and A. Scribano, La Biodola, September 1996), 457 (World Scientific Pub. Co., Singapore, 1994)

K. Johnson et Al., Quartz fibers for very forward calorimetry: ultra-fast, infinitely rad-hard and shower core sensitive, in: Proc. of the Fourth International Conference on Calorimetry in High Energy Physics, (eds. A. Menzione and A. Scribano, La Biodola, September 1996), 438 (World Scientific Pub. Co., Singapore, 1994)

G. Anzivino et Al., Nucl. Instr. and Meth. in Phys. Res. A **357**, 369 (1995)

G. Anzivino et Al., Nucl. Instr. and Meth. in Phys. Res. A **357**, 380 (1995)

G. Anzivino et Al., Nucl. Instr. and Meth. in Phys. Res. A **360**, 237 (1995)

E. Chiavassa et Al., Nucl. Instr. and Meth. in Phys. Res. A **367**, 267 (1995)

). A. Contin et Al., Nucl. Instr. and Meth. in Phys. Res. A **367**, 271 (1995)

1. B. Anderson et Al., Phys. Rep. **97**, 31 (1983)

12. R. Brun et Al., "GEANT", CERN Program Library, W5013, version 3.14

13. D. Acosta et Al., Nucl. Instr. and Meth. in Phys. Res. A 294, 193 (1990)

14. R. Wigmans, Ann. Rev. Nucl. Part. Sci. **41**, 133 (1991)

15. ALICE, Technical Proposal, CERN/LHCC 95/71, p. 107 & 129

16. CMS, Technical Proposal, CERN/LHCC 94/38, p. 86

ascati Physics Series Vol. VI, (pp. 299–310)
INT. CONF. ON CALORIMETRY IN HEP – Frascati, June 8–14, 1996

THE ATLAS HADRONIC TILE CALORIMETER

M.Bosman
Institut de Física d'Altes Energies, Universitat Autònoma de Barcelona, Spain
representing the TILECAL collaboration

ABSTRACT

ıe ATLAS hadronic barrel calorimeter is an iron-scintillating tile calorimeter with innovative geometry. Its mechanical design and optical components are described. ıe results of serie of beam tests are presented.

Introduction

ıe design of the Tilecal calorimeter was initiated at the beginning of 1993 in e framework of the RD34 project [1] with the aim of exploring new concepts of intillating hadron calorimetry while developing a suitable hadronic device for the ΓLAS experiment at LHC. The starting point was to build a simple state-of-the-t sampling calorimeter based on steel absorber and plastic scintillator tiles, read ıt by wavelength shifting (WLS) fibers. The choice of steel was driven by cost and the need to return the magnetic flux of the ATLAS inner solenoid.

New to this approach is the orientation of the scintillator tiles within the ›sorber (see fig.1a). To allow a simple, economical and modular assembly, tiles ; in planes perpendicular to the colliding beams; for better sampling homogeneity, les are staggered in the radial direction (corresponding to the shower axis for small ı. Radially oriented WLS fibres collect light from the tiles at both of their open lges and bring it to photomultipliers (PMTs) at the periphery of the calorimeter. ach PMT views a specific group of tiles, through the corresponding bundle of fibers; ith this readout scheme three-dimensional segmentation is immediately obtained.

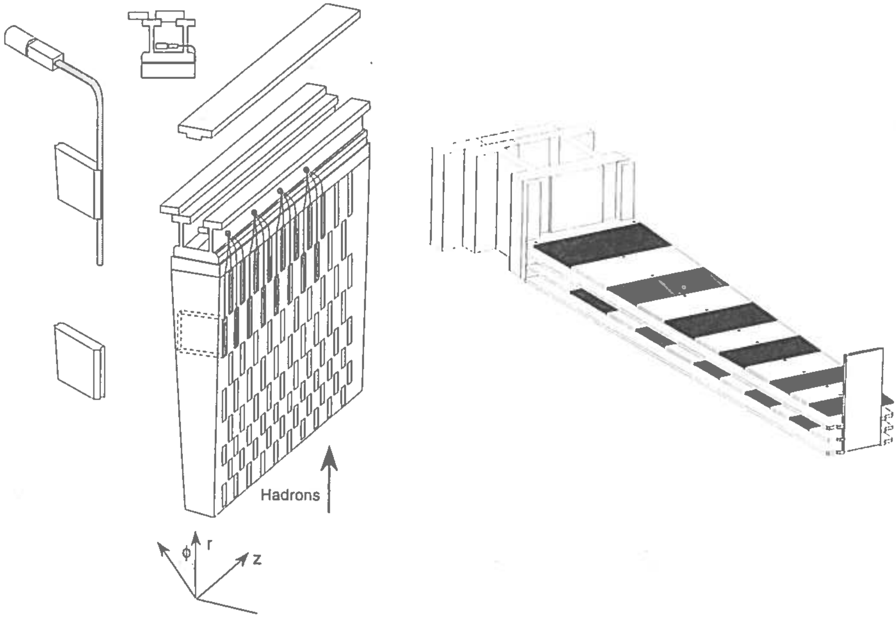

Figure 1: (a):Principle of the Tile hadronic calorimeter; (b):Exploded view of an assembled basic period of masters and spacer plates.

2 Construction and test of 5 prototype modules of the Tile calorimeter

2.1 Prototype Construction

Five 1 m long prototypes have been constructed, each one spanning $2\pi/64$ in azimuth, with a front face of 100×20 cm^2. The radial depth is 180 cm, going from an inner radius of 200 cm to an outer radius of 380 cm ($\sim 9\lambda$). Mechanically the construction consists of a stack of laminated steel plates of different precut shapes (master and spacer plates) (see fig.1b). Each period is 18 mm thick and consists of four layers. The first and third layer are composed of large trapezoidal plates (masters), the second and the fourth layers alternate small steel plates (spacers) and scintillator tiles.

2.2 Scintillator tiles

The main considerations in the choice of scintillating tiles are photoelectron yield, uniformity of response within a tile, tile to tile fluctuations and cost. Due to the large number of tiles foreseen in the ATLAS calorimeter ($\simeq$ 423 000 of 11 different sizes), an important effort was made to efficiently construct them. The tiles were produced in one of the collaborating institutes [3)] by injection molding, which einates operation such as machining to size and polishing edges, at the cost of)ut 1 CHF per tile and at a rate of 2 min per tile. Over the last 3 years the ·formance of the technique have been optimized. The basic material is commer- lly available optically transparent granulated polystyrene mixed with a primary l secondary WLS dyes (1.5% PTP and 0.04% POPOP) and injected in the mold. es are wrapped in Tyvek and air-coupled to WLS fibers. The attenuation length ıbout 40 cm. Improvement in scintillator quality and wrapping allowed to reach level of light yield of 1 photoelectron/mip/tile which ensures that no additionnal ıtribution to the intrinsic calorimeter resolution will result from the light yield: number of photoelectrons per Gev per cell (2 PMTs) is about 60.

A 10% non uniformity of the tile response would contribute 1% to the ıstant term of the resolution. To improve the uniformity of the response black ips are printed on the Tyvek at the edges of the tile. The measured uniformity ·oss the full surface with wrapping optimized is typically $\lesssim$ 5%. Tile to tile ctuation at the production level is better than 5%.

WLS fibres

LS fibres of 1 mm diameter with a decay time of the order of 10 ns are used read out the scintillating tiles. The blue light of the scintillator is absorbed the WLS fibres, shifted to the green and then transmitted along the fibres to e PMTs. Several companies [1] produce fibers with the necessary performances. ulticlad fibres present a better light yield, about 1.2-1.5 the yield of single clad ·res. Typical attenuation length is of the order of 3m. The fibre end is aluminized sputtering, giving a reflectivity of $\sim$ 85%. UV absorber is added to the fiber to oid direct light production by ionizing radiation.

4 Photomultipliers

ıe RD34 prototypes have been tested using Philips XP2020 PMTs recuperated ɔm the UA2 experiment (gain 10^6, noise few nA). For ATLAS, new types of ultra ·mpact PMTs are being tested.

5 Radiation hardness

he maximum expected peak dose in the Tile calorimeter in ATLAS, including ıe dose from charged particles and neutron flux, is about 40 kRad in ten years of ınning at full luminosity. Irradiation tests [1] have showed that the maximum light ss, at the inner radius, should be less than 5% in 10 years.

2.6 Calibration and monitoring

Calibration of the calorimeter is done by means of a Cs^{137} movable source system [4] providing intercalibration of cells and long term monitoring. Short term monitoring is provided by a laser driven light source system [5].

3 Standalone Tilecal prototype test beam results

The standalone Tile prototype was composed of five modules each one spanning $2\pi/64$ in azimuth and segmented radially in 4 samplings 1.5, 2, 2.5 and 3 λ respectively. The segmentation along Z was $\sim 20cm$. The cell size, non-projective, was $\Delta\eta \times \Delta\phi \sim 0.1 \times 0.1$. The prototype has been exposed to high energy pion beams at the CERN SPS. The energy resolution has been studied in the energy range 20 to 300 GeV and at an angle of incidence in Θ from 0° to 30°. Uniformity of response in Θ, ϕ and Z has been studied.

3.1 Resolution for incident pions at various energies

The energy spectra [1] [2] are directly obtained from the raw data, just adding the charge measured in each cell. They are symmetric at low energies and develop small high energy tail at high energies (due to $e/h > 1$) as well as small low energy tail due to longitudinal and transversal leakage. Peak and σ values are obtained from the raw energy spectra by Gaussian fits over a $\pm 2\sigma$ range. Fig.2a shows the resulting σ/E as a function of $1/\sqrt{E}$ at $\Theta = 20°$ and $\Theta = 30°$ for data taken in 1993 and 1995. The energy dependence is well fitted by a linear sum of a sampling and a constant term

$$\sigma/E \sim 50\%/\sqrt{(E)} + 2\%.$$

An iron-scintillator calorimeter is non-compensating, $(e/h > 1)$. The fraction of electromagnetic energy in the shower increases logarithmically with energy causing non-linearity in the pion response. Fig.2b shows the pion response at 20° fitted to the function [6]
$\mathrm{c} \times (1 + (\mathrm{e/h} - 1) \times 0.11 \times \ln \mathrm{E})$ giving $e/h = 1.36 \pm 0.11$.

Weighting techniques can be applied to improve the resolution and the linearity of non-compensating calorimeter. An algorithm that corrects downwards cells with large energy deposit (due to local em shower from π^0 decays) has been developed [2]. The charge in a cell Q_i is corrected by a factor depending on the longitudinal sampling

$$Q_i^{corr} = Q_i(1 - w_{samp}\frac{Q_i}{Q_{samp}})$$

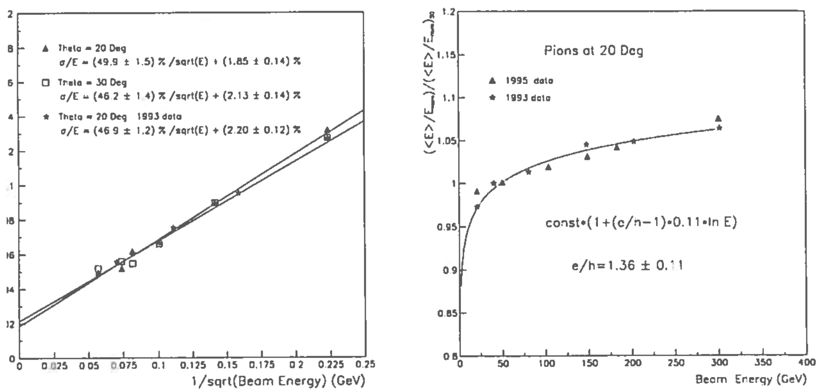

ɡure 2: (a):Energy resolution as a function of the pion energy. (b):Linearity of ɛ calorimeter response in the range 20-300 GeV. The values are normalized to the geV point.

solution and linearity were optimized. The resulting parameters, kept indepen- nt of energy, were $w_1 = 0.15$, $w_2 = w_3 = 0.25$ and $w_4 = 0$. This correction wnwards leads to a systematic underestimate of the incident energy. The final ergy is then obtained by adding an offset (1.7 GeV) and multiplying by a scaling :tor f :

$$E_{rec} = (q + \sum Q_i^{corr}) \times f$$

ıe resulting linearity is better than 1% and the constant term describing the res- ıtion was improved by 1%.

2 Uniformity Scans over Wide Ranges of Θ, Z and y

fine theta scan from 0° to 30° has been performed with 50 GeV pions. Fig. 3 ːft) shows the variation of the measured energy with respect to the 20° point. The ɜponse is very uniform except in a range of a few degrees around 6° where the ɜponse of the calorimeter is 2 % lower. This is due to alignment of scintillators in e staggered tile/iron geometry. The dispersion in the range from 0° to 30° is 0.8%. ıis effect appearing in the standalone Tile calorimeter geometry will be substan- ılly attenuated with the LAr em compartment in front (ATLAS configuration). addition, the tile sizes in ATLAS have been studied to minimize such alignment fects. Fig. 3 (left) shows the resolution: almost constant above 15°, increasing by % below as a result of the effect mentioned above.

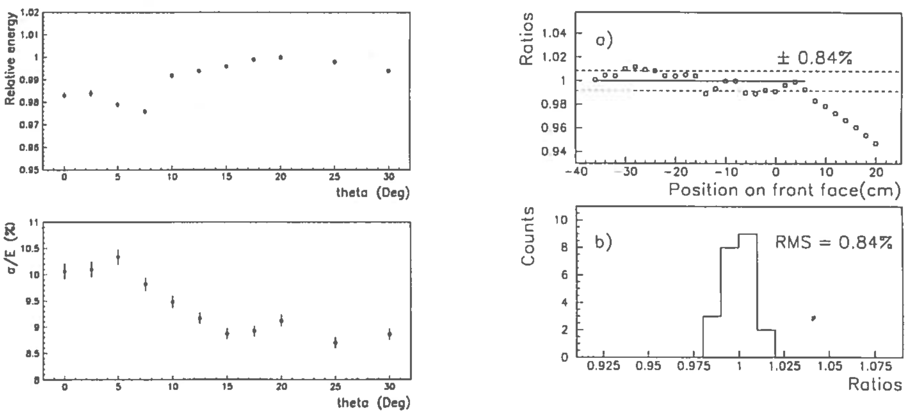

Figure 3: Top left: mean energy of 50 GeV pions for different Θ angle, the values are normalized to the value at $\Theta = 20$ deg; Bottom left: the corresponding relative resolution σ/E in %; Top right: Uniformity scan with 100 GeV pions at 10 deg. The ratios are calculated with respect to the mean signal. Bottom right: The distribution of the ratios in the range -40 cm to 6 cm.

A very fine vertical (y) and horizontal (Z) grid scans have been performed with 100 and 180 GeV pions at $\Theta = 10°$. Fig. 4 (right) shows the response to 100 GeV pions as a function of the impact point Z on the face of the calorimeter from -40 cm to 20 cm. The points are obtained fitting the energy spectrum at each impact point to a Gaussian and then are normalized to the mean value over the scan. At about 6 cm, lateral leakage becomes evident. The uniformity in the range -40 cm to 6 cm is good to 0.84 %.

The five prototype modules have also been scanned across y testing in this way the effect of the physical crack between modules. This crack is mainly due to space needed to extract the fibres to the PMTs. Fig. 4 shows, as a function of y, the sum of the signals in the modules on one side (modules 1, 2 and 3) and on the other side (modules 4 and 5) of the crack, as well as the total sum, normalized to the signal at the center of the module 3. The y coordinate is measured from the crack, in a line perpendicular to the crack plane, extrapolated to the depth of maximum energy deposition. The crack is visible as a small drop of 5 % in the signal at $y = 0$. The dispersion over the full range is $\sigma = 1.7$ %. There is only a marginal increase in the low energy tail.

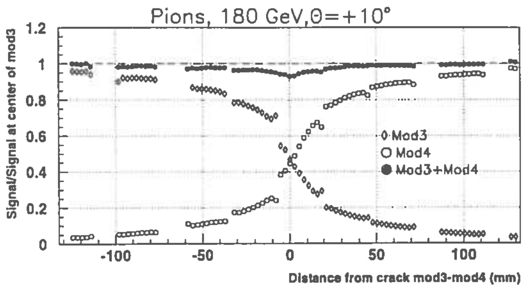

ȝure 4: Response of the calorimeter to 180 GeV pions as a function of the vertical ›rdinate y. The scan covers the region from the center of the central module to ː center of the next module.

Combined test of the ATLAS Electromagnetic Liquid Argon Calorimeter with the Tile calorimeter

.e barrel calorimeter system of the ATLAS [7] is composed of a Liquid Argon .Ar) electromagnetic (EM) calorimeter [8] with hermetic accordion geometry and ᴈ Tile calorimeter. A combined test of the two calorimeters has been carried out. .e setup is shown in fig.5. The total thickness of the EM compartment is 1.2λ ¡X_0) segmented in three compartments $9X_0$, $9X_0$ and $7X_0$ respectively. A $3X_0$ ᴈshower device is placed directly in front of the EM. Both devices were placed wnstream of the 2m radius cylindrical cryostat. The Tile calorimeter was placed ·ectly behind the cryostat. Signals from the preshower were used in the analysis reject early interactions identified as events with more than one track entering ᴈ EM. The distance between the two active parts was $\sim 50cm$, a factor two larger an in ATLAS. The total material before the Tile calorimeter is $\sim 1.5\lambda$, close to ᴈ ATLAS value however the test beam cryostat is mostly steel while in ATLAS will be aluminium. This setup was exposed to pions of various energies ranging ›m 20 to 300 GeV at a fixed angle of 11.3^0.

To reconstruct the hadron energy, various algorithms were developed [9]. the "benchmark approach" the incident energy is reconstructed with a minimal mber of energy-independent parameters in a two step procedure. First, the energy the particle is obtained as the sum of several terms:

$$E_0 = E_{em} + a \cdot Q_{had} + b \cdot E_{em}^2 + c \cdot \sqrt{|E_{em_3} \cdot a \cdot Q_{had_1}|} \tag{1}$$

$_{m}$ is the sum of the signals in the electromagnetic calorimeter, expressed in GeV ing the calibration from electrons. Q_{had} is proportional to the charge deposited

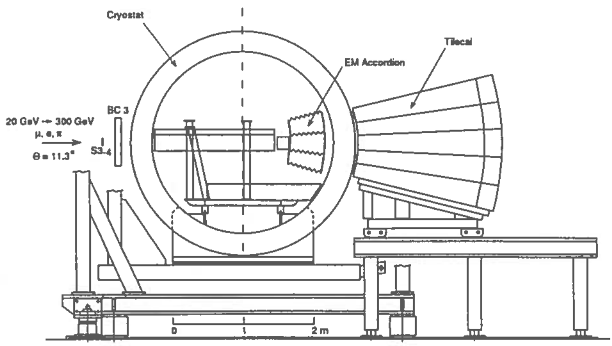

Figure 5: Test beam setup for the combined LAr and Tile calorimeter run.

in the hadronic calorimeter. The last term (E_{cryo}) accounts for the energy lost in the cryostat. It is taken to be proportional to the geometric mean of the energy released in the last EM compartment (E_{em_3}) and the first hadronic compartment (Q_{had_1}). Monte Carlo (MC) studies showed agreement with this *ansatz*. A negative correction term, proportional to E_{em}^2, is added. For showers that begin in the EM calorimeter, this term crudely accounts for its non-compensating behaviour. The parameters a, b and c were determined by minimizing the fractional energy resolution of 300 GeV pions. The values of the three parameters are a = 0.17 GeV/pC, b = -0.00038 GeV^{-1} and c = 0.44. Fig. 6 shows the effect of the successive corrections. This procedure, due to the negative quadratic correction, leads to a systematic underestimate of the incident energy. An additional step of rescaling is necessary: $E_{rec} = (q + E_0) \cdot r$. The rescaling factor r has been fitted to be 1.12 ± 0.01 and the offset q = 1.9 ± 0.1 GeV.

A sampling correction technique, similar to the one described in section 3.1, has been applied to the seven samplings of the combined calorimeter, in addition to the cryostat correction. Weights are adjusted in an iterative procedure minimizing resolution and linearity. The reconstructed energies have to be rescaled upwards. The parameters are fitted by a linear function of the beam energy. The total number of parameters is 15. The energy resolution is plotted in Fig.7 together with the "benchmark" result. The resolution obtained with the weighting technique can be fitted by the function :

$$\frac{\sigma}{E} = [\frac{(49.7 \pm 3.7)\ \%}{\sqrt{E}} + (1.1 \pm 0.2)\ \%] \oplus \frac{(3.1 \pm 0.2)\ GeV}{E}, \qquad (2)$$

The last term has the form expected from electronic noise, although noise studies

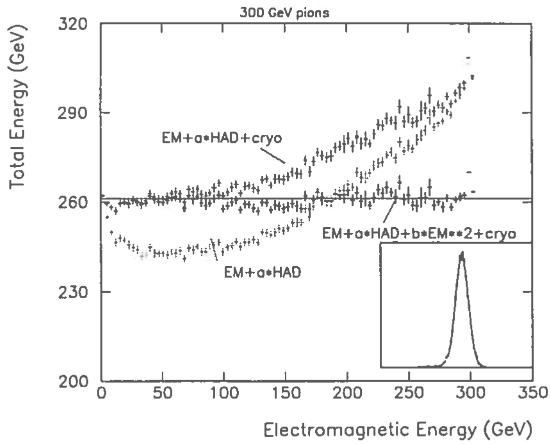

igure 6: Components of the first pass energy E_0 vs. energy in the EM calorimeter sing the "benchmark" energy reconstruction method for 300 GeV pions.

ave shown that the expected contribution should be 1.5 GeV. The value of 3.1 GeV driven by the 20 GeV point and may be an experimental problem at that energy.

Another approach to weighting [10], inspired from a technique developed y the H1 collaboration [11], was applied to the data. Cells with relatively small gnals are corrected upwards to equalize their response to that of cells with large ypically electromagnetic) deposited energy. Cells energy spectra are divided in qually populated intervals (7 in the EM and 13 in the Tile). Weights for each itervals are fitted optimizing simultaneously resolution and linearity. The weights re fitted by the function $w_i = a + b/Ecell$. In turn the energy dependence of the arameters a and b is fitted to a linear function. The total number of parameters 8. No a priori knowledge of the beam energy is needed to calculate the energy ependent correction; instead, the particle energy is calculated from the raw data ith a simple iterative procedure.

The resulting resolution is fitted by

$$\frac{\sigma}{E} = [\frac{38.3\ \%}{\sqrt{E}} + 1.62\ \%] \oplus \frac{3.1\ GeV}{E}, \qquad (3)$$

ig.7 shows the result : further improvement in the resolution compared to the other iethods is obtained. The linearity is better than 0.4%.

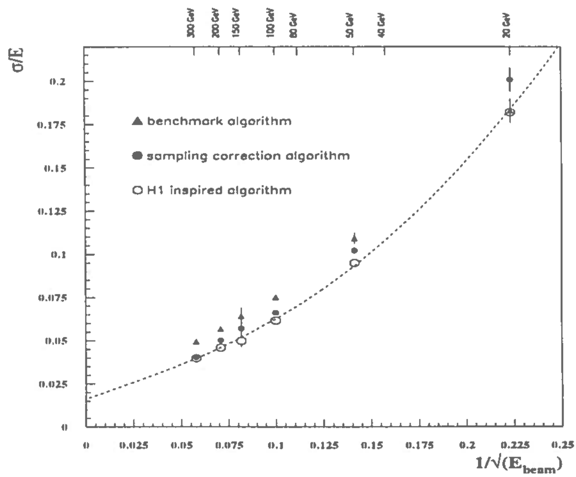

Figure 7: Resolution obtained with various reconstruction algorithms.

5 Shower leakage studies

In the combined calorimeter test beam setup, particles incident at an angle of 11.3^0 traverse about 11 interaction lengths, including passive materials at the back of the Tile calorimeter. Punchthrough particles can be muons from π and K decays in a hadronic cascade or charged particles (mainly soft electrons and hadrons) from showers not fully contained in the calorimeter. The leakage for pions of 50, 100, 200 and 300 GeV has been studied with a "Muon Wall" [12], a set of 10cm thick scintillators located 1m behind the calorimeter and covering an array of $73cm \times 96cm$. The probability of longitudinal shower leakage was defined as the fraction of events with a signal in at least one of the muon wall counters. Figure 8a shows the probability of longitudinal shower leakage (corrected for our limited acceptance) as a function of the beam energy, compared to the results obtained by the RD5 [13] and CCFR [14] collaborations for an iron equivalent thickness of 1.85 m as in the combined calorimeter setup. At 100 GeV this probability is about 15%. The measurements are in agreement with those of the CCFR collaboration. The RD5 collaboration punchtrough probability is smaller, due to their smaller acceptance. The dashed line shows the expectation for the ATLAS configuration (10.6 λ at η=0). Figure 8b shows the average energy loss from leakage, defined as the difference between the energy mean values of events with and without a signal in the muon wall, for several beam energies. The energy loss for events with longitudinal leakage

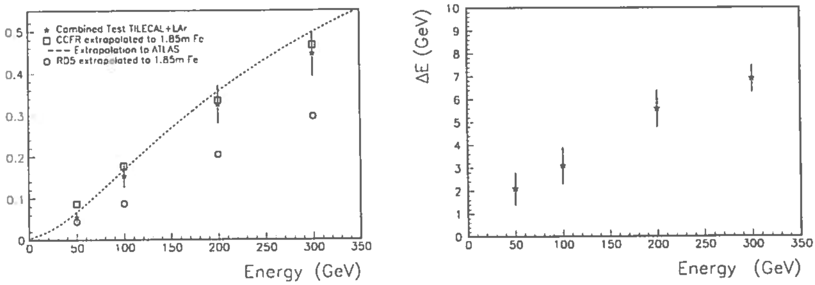

ʒure 8: (a) Punchthrough probability for pions. Results from RD5 and from ƆFR (recalculated for 1.85 m of iron) are also plotted. The dashed line shows the pectation for the ATLAS configuration. (b) Average energy loss vs. beam energy · events with longitudinal leakage.

about 3% at 100 GeV.

Conclusion

ototypes of the Tile calorimeter, an iron-scintillator sampling calorimeter with an novative longitudinal tile configuration have been constructed. An extensive program of beam tests has been carried out demonstrating the good performances of the lorimeter that fulfill the requirements for the ATLAS hadronic barrel calorimetry.

eferences

. Construction and Performance of an Iron-Scintillator Hadron Calorimeter with Longitudinal Tile Configuration, RD-34 Collaboration, CERN/LHCC 95-44, LRDB status report /RD34,1995.

2. F. Ariztizabal et al. (RD34 Collaboration), Nucl. Instr. and Meth. **A349** 384 (1994).

3. V.K.Semenov,in: Proc. of the ninth Conference on scintillator, Kharkov, 1986.

4. G.Blanchot et al., ATLAS Internal Note TILECAL-NO-45 (1994).

5. Z.Ajaltouni et al., ATLAS Internal Note TILECAL-NO-39 (1994).

6. R. Wigmans,Nucl.Instr. and Meth. **A 259**, 389 (1987).

7. ATLAS Technical Proposal, CERN/LHCC/94-43 LHCC/P2.

8. D.M. Gingrich et al. (RD3 Collaboration), Nucl. Instr. and Meth. **A 364**, 290 (1995).

9. M. Cobal et al., ATLAS Internal Note, TILECAL-NO-67 (1995).

10. M.P. Casado et al., ATLAS Internal Note, TILECAL-NO-75 (1995).

11. W Braunschweig et al., DESY Internal Report, DESY 89-022 (1989).

12. M. Lokajicek et al., ATLAS Internal Note, TILECAL-NO-63 (1995);
    M. Lokajicek et al., ATLAS Internal Note, TILECAL-NO-64 (1995).

13. M. Aalste et al. (RD5 Collaboration), Z. Phys. **C60** 1 (1993)
    M. Aalste et al. (RD5 Collaboration), CERN-PPE/95-61

14. F.S. Merrit et al. (CCFR Collaboration), Nucl. Instr. and Meth. **A245** 27 (1986).

scati Physics Series Vol. VI, (pp. 311–322)
NT. CONF. ON CALORIMETRY IN HEP – Frascati, June 8–14, 1996

RESPONSE OF THE ATLAS TILE CALORIMETER TO MUONS

presented by Ana Henriques
CERN, Geneva, Switzerland and LIP, Lisbon, Portugal
(In the framework of the ATLAS/Tile collaboration)

ABSTRACT

study of high energy muons traversing the ATLAS hadron Tile calorimeter in barrel region in the energy range between 10 and 300 GeV is presented. Both perimental data and Monte Carlo simulations are given and show good agreement. e Tile calorimeter capability of detecting isolated muons over the above energy ige is demonstrated. A signal to background ratio of about 10 is expected for nominal LHC luminosity ($10^{34} cm^{-2} sec^{-1}$). The photoelectron statistics effect the muon shape response is shown. The energy loss of a muon in the calorimeter, minated by the energy lost in the absorber, can be correlated to the energy loss the active material. This correlation allows one to correct on an event by event sis the muon energy loss in the calorimeter and therefore reduce the low energy ls in the muon momentum distribution.

Introduction

the ATLAS detector muons with energies greater than 2 GeV will be measured th a system of chambers placed inside an air core toroid after crossing more than 0 radiation lengths of electromagnetic and hadronic calorimetry [1]. The muons ll lose some fraction of their energy in the calorimeter material preceding the ion spectrometer. This fraction will fluctuate from event to event and therefore achieve high precision on the muon momentum measurement it is important to asure this energy loss. Although the major goal of the ATLAS hadron calorimeter ile calorimeter) will be to identify particles and jets and to measure their energy d direction, as well as to measure the total missing transverse energy, it can also asure the muon energy loss. Since the light yield produced by muons in a scintil- or is small compared to signals from hadron showers, the additional requirement identify muons with the Tile calorimeter puts further constraint on the read- t system. Low noise and high photoelectron statistics are additional important rameters to measure the energy deposited by muons.

The ATLAS Barrel calorimeter [1] will include a Pb-Liquid Argon (LAr) ctromagnetic calorimeter with accordion-shaped electrodes, and a large scintillat- ; Tile hadronic calorimeter, with iron as absorber material and scintillating plates read out by wavelength shifting fibres. The momentum resolution of the muon spectrometers in ATLAS are specified as $\Delta p_T/p_T = 2\%$ at 50 GeV and about 10% at 1000 GeV.

The fluctuations of the energy loss from the absorber material in the calorimeter in front of the muon spectrometer will limit the precision of the muon momentum measurement for muon p_T below 30 GeV. In general these fluctuations are reduced when the calorimeter absorber is made out of a relatively low Z material, like iron, as it is the case for the ATLAS Tile calorimeter. Above 30 GeV multiple scattering in the muon chambers and measurement errors will dominate. In the momentum range of 10 to 100 GeV, the correlation between the energy loss in the active and passive material of the Tile calorimeter (plastic scintillator tiles and iron, respectively) can be used to correct the measurement for the energy loss of a muon traversing the full calorimeter depth. This would allow us to improve the muon momentum measurement in the spectrometers or at least to reduce the tails in the muon momentum distribution. The capability to detect the Higgs boson in its intermediate mass range via the decay channel $H \rightarrow ZZ^* \rightarrow 4\mu$ could profit from such an improved muon momentum measurement. These aspects were investigated with data obtained in a test beam at the CERN-SPS have been compared with extensive Monte Carlo (MC) simulations.

The present paper is organized as follows. Section 2 describes the calorimeter prototype and the test beam setup. The test beam results are discussed in Section 3 and compared to our simulation. Results on the energy dependence of the muon signals are given. We use the simulation results in Section 4 to show the accuracy on the muon energy loss measurement and the extent of tails in the muon momentum distribution in the ATLAS spectrometer when such energy loss corrections are applied on the event by event basis. Conclusions are given in Section 5.

2 Test Beam Setup

The data discussed here were taken with a calorimeter prototype consisting of five modules, each spanning $2\pi/64$ in azimuth [1, 2, 3], with a front face of 100×20 cm^2. The longitudinal depth is 180 cm, corresponding to 8.9λ at $\eta = 0$ or to $80.5X_0$. The Tile calorimeter uses iron as absorber and scintillator plates, read out by wavelength-shifting fibres, as the sampling material. An innovative feature of this design is the orientation of the tiles which are aligned parallel to the $\eta = 0$ plane and staggered in depth. Fibres running radially collect light from the tiles at both of their open edges. Readout cells are then defined by grouping together a set of fibres into a photomultiplier (PMT). Thus each calorimeter cell is read out by 2 PMTs. The calorimeter is radially segmented into four depth samplings (corresponding to

, 2, 2.5 and 3 λ at η=0) and five transverse segments, thus providing for a ›jective geometry in azimuth, but not in polar angle. The gain of the PMT's was to deliver $\simeq$ 6 pC/GeV. In the following the conversion of muon response (in) to energy (in GeV) was made on the basis of the calibration constant found :h electrons (α_e = 5.59 pC/GeV at θ = 10°). A detailed simulation code of : calorimeter prototypes, based on GEANT 3.21, was produced and extensively ted. Besides giving a precise description of the geometry of the detector, the code ıulates all known instrumental effects such as PMT noise, tile attenuation and nuniformity, fibre attenuation and photoelectron statistics.

Results

Muon signal

ıe energy lost in the Tile calorimeter by 150 GeV muons at a polar angle of θ = 10° shown in Fig. 1a for the full calorimeter depth (8.9 λ) and in Fig. 1b for the first ıgitudinal sampling (1.5 λ) only. The energy loss spectrum approximately follows Landau distribution, but with large tails at high energies caused by radiative ocesses (Bremsstrahlung, electron-positron pair production) as well as energetic rays.

The simulated energy losses in the Tile calorimeter are also shown in Fig. 1 th and without instrumental effects. The spectra normalization to the data is ade to obtain the same most probable value (MOP) of energy loss at 50 GeV. The mulations incorporating the instrumental effects agree well with the experimental ıta. The broadening of the distribution due to fluctuations in instrumental effects nostly photoelectron statistics) is most evident in the first sampling, which is the ıinnest longitudinal compartment (30 cm or 1.5 λ).

The pedestal distribution after subtraction of its average value is also shown . Fig. 1. The width of this distribution corresponds to a noise of about 40 MeV/cell. his value contains a high amount of correlated noise contribution, unlike data taken n a previous beamline and with different readout electronics wherein the noise per ell was much lower (about 20 MeV/cell). Even in these less-than-optimal conditions ıe pedestal is well separated from the muon signal.

In the last three years an extensive R&D program was carried out to optiıize the light yield of the Tile calorimeter. The combined effect of the tiles' quality, he use of double clad fibres and better geometry on the tile/fibre coupling has ıcreased the photoelectron yield by an overall factor of about 2.5 between 1993 o 1995, from 24 pe/GeV to 64 pe/GeV [3]. In Fig. 2 experimental data on the ıuon lineshape from the three generations of Tile calorimeters yielding 24 pe/GeV,

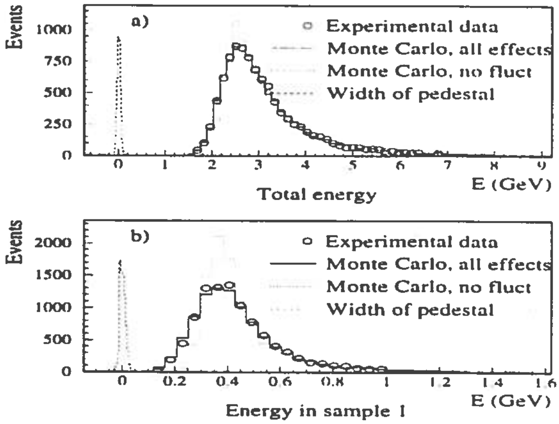

Figure 1: Energy loss of 150 GeV muons traversing (a) the full Tile calorimeter depth (9 λ), (b) the first sampling (1.5 λ). The simulation results are given with and without instrumental fluctuations. The pedestal width is also shown.

48pe/GeV and 64 pe/GeV [4] are shown in the entire calorimeter and in the first sampling. A broadening of the spectrum is visible in the first sampling but not in the full calorimeter; only a small broadening of the muon line shape is observed in the full module with 24 pe/GeV. This indicate that a light yield as low as 48 pe/GeV will not significantly deteriorate the quality of the muon measurements.

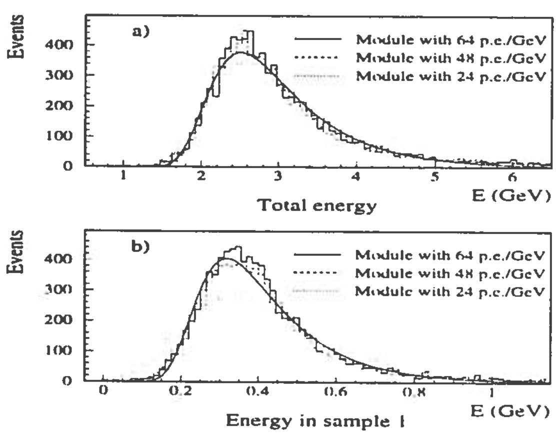

Figure 2: Experimental data on the energy loss of 150 GeV muons at $\theta = 10^\circ$ traversing (a) the full calorimeter length (9 λ), (b) the first sampling (1.5 λ). Data from three prototypes with 24, 48 and 64 pe/GeV per cell are shown. A Moyal fit applied on the module with the highest light yield is shown as the full curve.

Energy dependence of the muon response

e energy loss in the calorimeter as a function of incident energy was studied with ons traversing the Tile calorimeter prototypes at a polar angle of $\theta = 10^o$ using h experimental data and MC simulations with all instrumental effects properly luded. The most probable values of the energy loss in the calorimeter were ained from a fit to a Moyal function. The most probable energy loss grows wly with incident energy as well as an enhancement in the tail of the distribution. th effects are well reproduced by the simulation. This asymmetric distribution is racterized by a width parameter σ_M which is the rms deviation of the function m its peak value. A truncated mean value of energy loss is found by calculating mean of these distributions at values less than 5 σ_M. The mean and the most bable values of the energy losses measured at $\theta = 10^o$ at several beam energies are wn in Fig. 3. The most probable values vary from 2.26 to 2.85 GeV for incident rgies between 10 and 300 GeV.

The peak muon energy deposition of 2.5 GeV can be compared to the ected energy deposition of minimum bias events per bunch-crossing for nominal ninosities ($10^{34} cm^{-2} sec^{-1}$) at LHC, which amounts to $\sim$ 0.2 GeV in a $\Delta\eta \times \Delta\phi$ = $\times$ 0.1 calorimeter cell. This gives a comfortable margin for detecting isolated ions even at the highest luminosity (S/B $\sim$ 10).

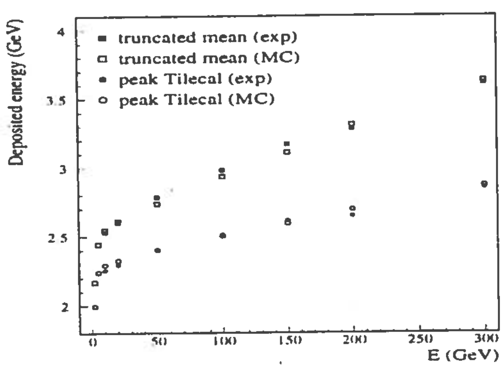

gure 3: The truncated mean energy loss and the energy lost at the peak of the stribution (most probable value), for the Tile calorimeter as a function of the muon ergy at a polar angle $\theta = 10^o$.

Monte Carlo study of the muon energy losses

s mentioned in the Introduction, fluctuations in muon energy losses can be an portant source of error in measuring the muon momentum, and in fact dominate e ATLAS muon momentum resolution below 30 GeV/c. The larger fluctuations, hich are due to hard radiative processes and energetic δ–rays, are characterized by secondaries which are rather effectively sampled in the Tile calorimeter because they typically traverse several iron-scintillator interfaces. This leads to a high degree of correlation between the energy deposited in the iron (about 97% of the total) and the signal in the scintillators. Using our simulation to calculate the energy loss in both the iron absorber and the scintillator, we show in Fig. 4 this correlation for several incident muon energies. The correlation is already evident in the high-energy end of the signal produced by 10 GeV muons, while for lower incident energies softer ionization secondaries dominate and no correlation exists. Consequently for $E_\mu > 10$ GeV the muon energy loss in the calorimeter can be estimated, event by event, from the energy loss in the scintillator.

A detailed study of the correlation, using the prototype's simulation and applying it to the ATLAS configuration when appropriate, is described in this section. The possible improvement in measuring momenta of isolated muons is discussed.

4.1 Correlations between energy losses in the iron and scintillator

To study the correlation between the energy lost in the absorber and active material, the energies lost event by event in iron and scintillator were calculated and divided each by the corresponding sampling fractions, 1-S_μ and S_μ. The distributions of the differences of the scintillator and iron values were fitted with a Gaussian fits within $\pm 2\sigma$. The mean values of the differences are very close to zero as expected. The

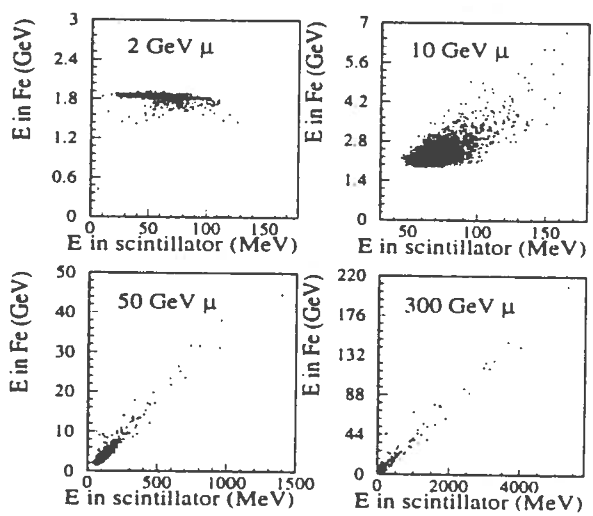

Figure 4: The simulated (MC) energy loss in the scintillator (in MeV) as a function of the energy lost in the Tile calorimeter absorber (in GeV) for 2, 10, 50 and 300 GeV incident muons.

read of the distribution of the differences, measured by σ, is a good representation the error in reconstructing the energy loss in the calorimeter using the scintillator ;nal. Plots of σ *vs.* muon energy are given in Fig. 5 (black dots) and contrasted th the widths σ_M obtained from a Moyal fit to the total energy losses in the lorimeter (stars).

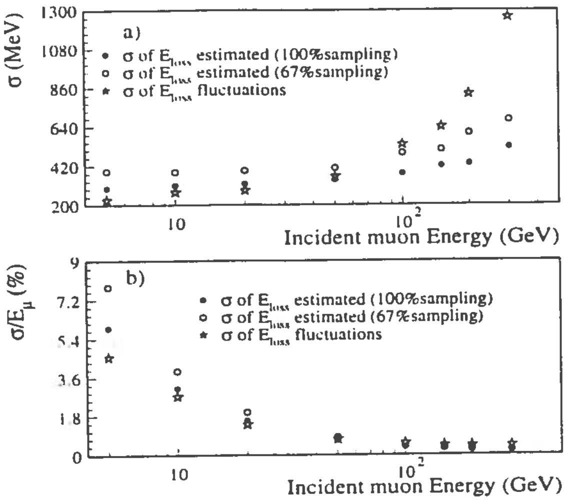

igure 5: Spread of the MC correlation (EFe.vs.Escint. as a function of the muon ıergy. The σ, obtained from a Gaussian fit within $\pm 2\ \sigma$, is given in (a) as MeV, nd in (b) relative to the incident muon energy (σ/E_μ). See text for details.

For muon momenta above 100 GeV the energy loss fluctuations can be econstructed rather precisely using the scintillator signals. The σ of the difference istribution is about 400-500 MeV (0.2-0.3%) whereas, in contrast, σ_M of the enrgy loss distribution is larger and is about 500-1300 MeV. At muon energies $\lesssim$ 20 ;eV the σ of the difference distribution rapidly increases from 1.6% (318 MeV) at 0 GeV/c to 5.9% (295 MeV) at 5 GeV/c. For muon energies $\lesssim$ 20 GeV the average nergy loss has better resolution than does the difference distribution, and thus is a etter approximation to the true energy loss than an event-by-event estimate based n the scintillator information. In this energy range the fluctuations of the energy ɔss in the calorimeter are the dominant factor in the ATLAS muon momentum esolution. Above 100 GeV the momentum resolution of the ATLAS muon spectrometer is increasingly dominated by tracking and alignment errors [1]; therefore ırecise reconstruction of the muon energy loss in the calorimeter is only useful for vents with large or even "catastrophic" energy losses.

4.2 Extension to the ATLAS configuration

In the ATLAS configuration, the total amount of material in front of the muon spectrometer will be 107 X_0 (10.6 λ) at $\eta = 0$. Of the materials in ATLAS, the active parts of Lead-LAr em calorimeter and the Tile calorimeter represent 25 X_0 and 68.7 X_0 respectively. Thus if both the LAr and Tile calorimeters can be used to identify muons, 88% of the total 107 X_0's is sampled while if only the Tile calorimeter is used, then only 64% of the volume is sampled.

The effect of sampling the muon energy loss over only part of the volume has been studied using the MC simulation of the Tile calorimeter prototype. Using only the information from the first three depth samplings only 67% of the total energy loss is sampled (see section 2), a situation which is not too far from that of ATLAS at $\eta = 0$. The results of the simulation are shown (open circles) in Figs. 5a, 5b. The precision in the correlation degrades by about 30% at all muon momenta. If no information is available from the LAr calorimeter, we estimate the degradation at about 30-35%. But if isolated muons are detected in both the LAr and Tile calorimeters, the resulting degradation becomes only about 3%.

4.3 The muon momentum resolution after event-by-event corrections

Several algorithms to calculate the muon energy loss on an event-by-event basis have been considered. Fig. 6 shows energy losses in the iron versus losses in the scintillator for several incident muon energies. The correlation can be parameterized in the form: $E_{Fe} = a_1 \times E_{scint}^{-a_2} + p_1 \times E_{scint}^{p_2}$, where p_1 and p_2 are polynomials with $p_1 = a_3 + a_4 \times E_\mu$ and $p_2 = a_5 + a_6 \times E_\mu + a_7 \times E_\mu^2$. E_μ is the incident muon energy in GeV and a_n ($n = 1 \ldots 7$) are constants. The function is drawn in the figure for E_μ = 300 GeV. This form adequately describes the correlation for muons between 10 and 300 GeV. For relatively large scintillator signals ($E_{scint} \gtrsim 100$ MeV) the slope of the correlation E_{Fe} versus E_{scint} is independent of the incident muon energy and is approximately equal to the sampling fraction of electrons ($S_e = 2.9\% \pm 0.1\%$). On the other hand, at smaller scintillator signals ($E_{scint} \lesssim 100$ MeV) the correlation is somewhat dependent on incident muon energy. This parameterization is used to correct the muon momenta for the energy losses in the calorimeter on an event-by-event basis. The result is compared to the distribution obtained by correcting simply for the most probable value of the total energy loss of muons in the calorimeter.

The case of 50 GeV/c muons will be illustrated in some detail. The effect of the simpler approach is shown in Fig. 7a. The momentum peaks at the correct energy value but has a large low-energy tail. In ATLAS, the multiple scattering and the measurement/alignment error in the muon chambers give additional contributions to the momentum resolution. The distribution in Fig. 7a has been smeared by an ɜrgy-dependent function to include the latter contributions. The result is shown in ʒ. 7b. A gaussian fit between $\pm 2\sigma$ is also shown in the figure. It gives σ=782 MeV $/p$=1.6%), with 4.7% of the events in the low-energy tail which is defined as 3σ or ɔre below the peak. The muon momenta reconstructed with the parameterization

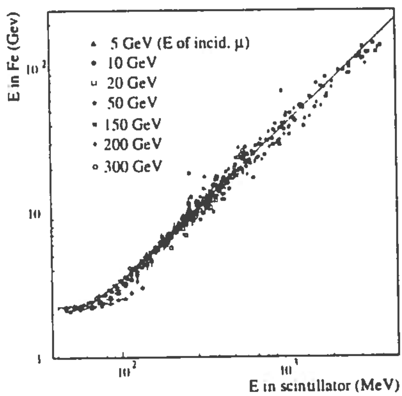

'igure 6: Simulation result showing the energy loss in the scintillator (in MeV) as function of the energy loss in the Tile calorimeter absorber (in GeV) for incident ıuon energies between 5 and 300 GeV. The full curve is a parameterization to the ata for 300 GeV muons.

ˌescribed above are shown in Fig. 7c. After smearing (see Fig. 7d), the Gaussian fit ˌives a slightly lower σ than that obtained with the first method (723 MeV or 1.4% nstead of 782 MeV). The percentage of events in the low-energy tail is substantially educed to 1.7% .

A third method, based on a combination of the first two, has been conˑidered: events which deposit little energy in the scintillator($E_{scint} \leq 80$ MeV, see 'ig. 6) are corrected with the most probable energy loss (first method), while the ɜvents with $E_{scint} > 80$ MeV are corrected by the energy loss estimated event by ɜvent (second method). The results are shown in Fig. 7e before smearing. An imɔrovement is seen in the value of σ while after smearing (Fig. 7f), the result is similar ;o that obtained with method 2.

The same study was carried out with 20 and 300 GeV muons; the results ɜre given in Table 1. At 300 GeV, the contribution from the errors in the muon ʂpectrometer dominates the muon momentum resolution and does not allow to profit from the precise reconstruction of the muon energy loss obtained using the scintillator information. The advantage of the method is limited to a significant reduction of the low-energy tail. At 20 GeV the correlation between the energy loss in the iron and in the scintillator is not good enough to reduce the width of the error distribution; however a reduction in the low-energy tails is still seen.

These results were obtained by sampling the entire thickness of the calorimeter. Reducing the sampled fraction to 67% does not affect the width of the reconstructed momentum distributions but increases the fraction of events in the low-energy tails (from 1.4% to 4.1% at 20 GeV using method 3).

In conclusion, using the calorimeter information to reconstruct the ATLAS

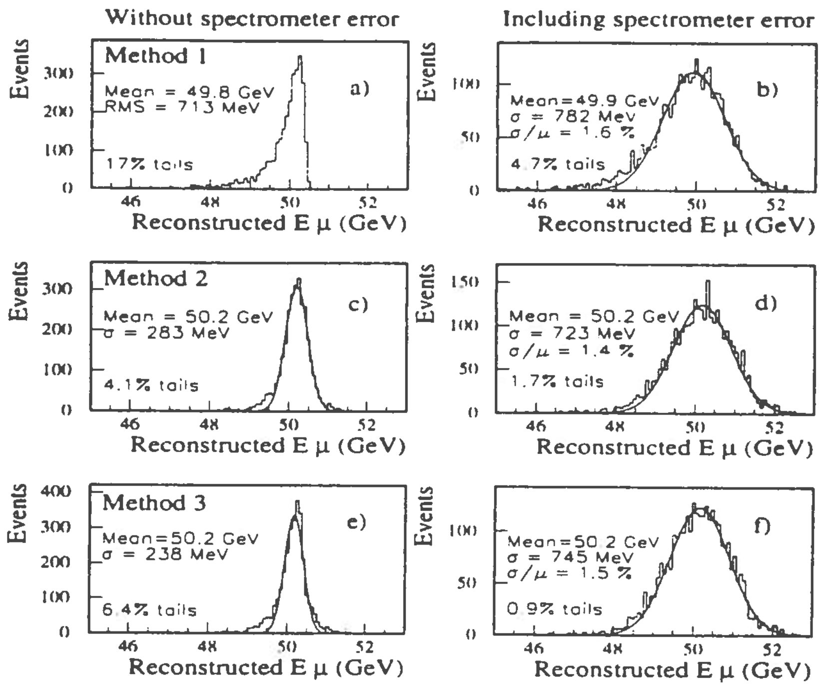

Figure 7: The expected energy distribution for 50 GeV muons after traversing the Tile calorimeter prototype using different methods to correct for the energy losses in the calorimeter (see text for details).

muon momenta will reduce tails in the momentum error distribution at all muon energies. A small improvement of the width of the error distribution can only be obtained at intermediate muon momenta (around 50 GeV). At lower momenta the information from the scintillator is typically not useful, while at high momentum the measurement/alignment error in the muon chambers, together with the multiple scattering, dominates the resolution.

Summary and Conclusions

closing, it may be worth to briefly restate the main results of this study:

With the last generation of calorimeter prototypes a light yield of about photoelectrons per GeV deposited in the calorimeter has been obtained. This eld (or even a slightly lower one) is sufficient to observe isolated muons traversing e thinnest calorimeter segment with no degradation of the spectrum of the signal.

The most probable muon signal in the calorimeter is about a factor of 10 gher than the expected noise from min. bias events at the nominal luminosity of HC. Therefore isolated muons down to approximately 2 GeV should be visible in TLAS using just calorimeter information.

The observed energy loss spectra of muons from 10 GeV/c to 300 GeV/c e seen to be in excellent quantitative agreement with Monte Carlo simulations iich account in detail for all muon energy loss processes and for instrumental fects. The observed agreement is useful to precisely calculate the muon energy sses at each muon energy, both on the average and on an event-by-event basis.

ıble 1: The expected muon momentum resolution and fraction of events in tails low 3 σ for 20, 50 and 300 GeV muons after traversing the Tile calorimeter protope. The results take into account the contribution of the multiple scattering and e measurement/alignment error in the muon chambers. Three different methods ere used to correct for the energy losses in the calorimeter. See text for details.

Muon momentum resolution with all effects included									
	20 GeV			50 GeV			300 GeV		
Correction Method	σ_p MeV	σ_p/p (%)	tail$\leq 3\sigma$ (%)	σ_p MeV	σ_p/p (%)	tail$\leq 3\sigma$ (%)	σ_p MeV	σ_p/p (%)	tail$\leq 3\sigma$ (%)
1) Mean E_{loss}	349	1.8	7.0	782	1.6	4.7	8470	2.8	1.53
2) $E_{loss\ evt-evt}$	356	1.8	1.7	723	1.4	1.7	8450	2.8	0.3
1)$E_{Sc}\leq$80MeV 2)$E_{Sc}\geq$80MeV	356	1.8	1.4	727	1.5	0.9	8450	2.8	0.3

The fluctuations of the energy losses suffered by muons in the calorimeter n be rather precisely recovered using the scintillator signals. After accounting for measurement errors, the resolution on the muon momentum obtained by an event event correction algorithm is not appreciably better than can be obtained just by rrecting for the most probable energy loss; however the event by event correction recovers most of the "catastrophic" energy losses and thereby significantly improves the losses and biases due to "low-energy tails".

In summary, it is shown in this paper that the Tile calorimeter is capable of providing useful information on muon recognition, which constitutes one of the crucial signatures for many physics channels at the LHC.

References

1. ATLAS Technical Proposal, CERN/LHCC/94-43 LHCC/P2.
2. F. Ariztizabal *et al.*, Nucl. Instr. and Meth. **A349** (1994) 384.
3. E. Berger *et al.*, CERN/LHCC 95-44, LRDB status report/RD34, 1995.
4. A. Henriques, G. Karapetian and A. Solodkov, ATLAS Int. Note, TILECAL-NO-068 and references therein.

:ati Physics Series Vol. VI, (pp. 323–334)
IT. CONF. ON CALORIMETRY IN HEP – Frascati, June 8–14, 1996

THE CMS CENTRAL HADRON CALORIMETER

Jim Freeman
Fermi National Accelerator Laboratory, Batavia, Illinois 60510
Representing the CMS Hadron Calorimeter Group

ABSTRACT

e CMS central hadron calorimeter is a copper absorber/ scintillator sampling ıcture. We describe design choices that led us to this concept, details of the chanical and optical structure, and test beam results. We discuss calibration hniques, and finally the anticipated construction schedule.

Overview

e CMS detector is a general purpose experiment that will operate at the Large dron Collider at CERN. It places an emphasis on electron and photon energy olution and muon identification. A key to achieving these goals is to have very ge very strong magnetic field volume for momentum measurement, and to have a h precision electromagnetic calorimeter. The heart of the CMS detector is a large ume 4T superconducting solenoid. The solenoid is 13 meters long with an inner lius of 3 meters. Inside the solenoid are placed tracking detectors, followed by an ctromagnetic calorimeter (ECAL) made of lead tungstate crystals and finally the dron calorimeter (HCAL). Among the reasons for placing the HCAL inside the enoid was the desire to continue muon bending through the hadron calorimeter to prove muon momentum measurement and triggering. Placing the HCAL behind a :ater than 1 λ thick solenoid would have also seriously degraded the performance. ;ure 1 shows a quarter section of the CMS detector design.

A major function of the HCAL is missing transverse energy measurement. r this measurement, gausssian resolution is not as important as elimniation of low ergy tails in the response function. With this in mind, the CMS HCAL design ives to eliminate dead material that causes energy loss, and to maximize the orimeter λ.

The location of the HCAL inside the magnetic field required that the orimeter be non-magnetic. In addition, the constrained space inside the solenoid inted toward a design that had a compact interaction length. Two reasonable ɔices for absorber were stainless steel and copper. Copper, with its approximately % shorter interaction length was chosen for the absorber.

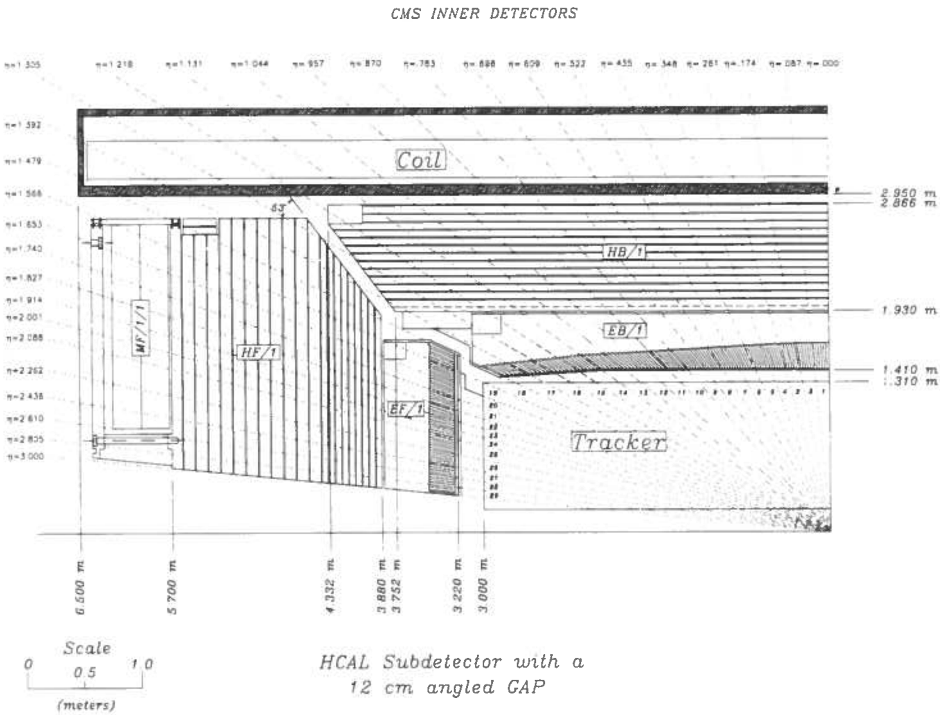

Figure 1: Quarter-section of the CMS central detector.

The central HCAL covers the η range of $-3 < \eta < 3$ and $0 < \phi < 2\pi$. The central HCAL is physically composed of 2 regions, the barrel ($|\eta| < 1.4$) and the endcap, which extends to $|\eta| = 3.0$. The very forward region of CMS , $3 < |\eta| < 5$, is covered by a quartz fiber calorimeter, discussed by V. Gavrilov in these proceedings [1]. The tower granularity is chosen to be $\Delta\eta \times \Delta\phi$=0.087 × 0.087. The segmentation is commensurate with the granularity of ECAL, and is also sufficient for jet reconstruction. [2]

The tile/fiber sampling technique was chosen for calorimeter design. This technique uses scintillator tiles to sample the shower. Wave-shifting fiber imbedded in the tile traps the scintillator light and clear fiber spliced to the WLS fiber carries the light to photo-transducers. First developed at Protvino and CERN [3], the technique has been enhanced and applied to the CDF endcap upgrade calorimeter at Fermilab [4]. In this design, the samples are thin. They require only 0.9 cm

' thickness between absorber plates, so a high density calorimeter is maintained. he choice of scintillator for readout provides a calorimeter that is fast, stable and liable, and radiation-resistant. More than 90% of the scintillation light will be ›llected within a 50 ns time window. Scintillators have been developed that survive ıe radiation exposure that 10 years of operation at the LHC will create (2 - 4 Mrads, ; the worst location, the $|\eta| = 3$ corner of the endcap hadron calorimeter).

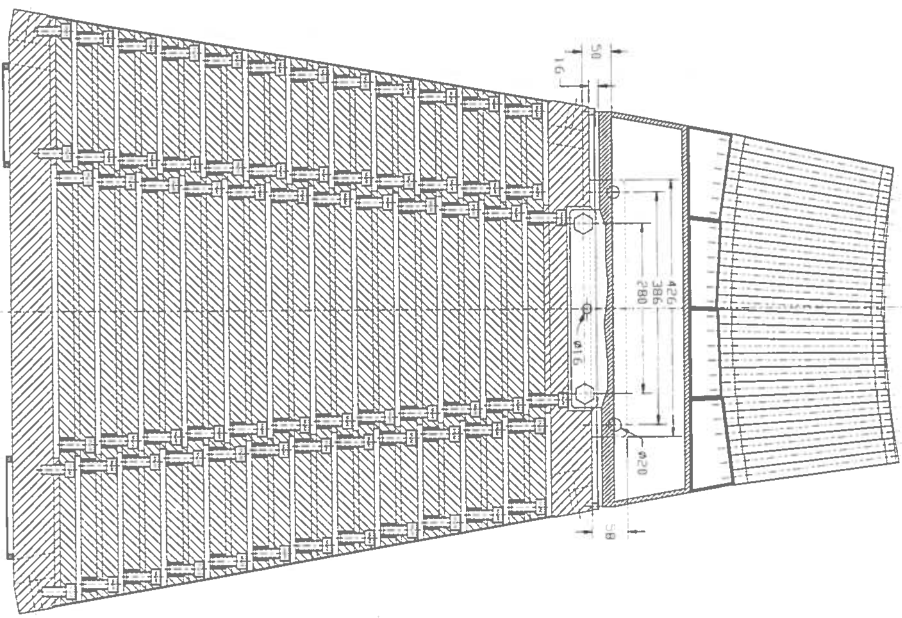

Figure 2: Barrel wedge mechanical construction.

Mechanical Design

'igure 2 shows the mechanical structure of a module of the central HCAL barrel. 'he barrel HCAL is made of $\delta(\phi) = 20°$ wedges. Each wedge extends from $\eta = 0$ to he high η boundary, $\eta \simeq 1.4$. A wedge is about 4.5 meters long, and weighs about :7 metric tons. A wedge is composed of 6 cm thick inner and outer stainless steel ›lates (for mechanical strength), with 6 cm thick copper absorber samples inside. 'he entire structure is bolted together. Figure 2 also shows the $\delta(\phi) = 20°$ ECAL nodule attached to the front of the HCAL wedge.

The absorber structure is designed with alternating "staggered" slots for the scintillators. Thus the (4 tower wide in ϕ) wedge starts with a slot to accommodate scintillators the middle 2 towers, then 1/2 of an absorber sample later in depth, have separate slots for the outer 2 towers. The staggering of the absorber plates provides a rigid mechanical structure, with no projective dead regions. Each slot runs the full length (in η) of the wedge. Long thin scintillator "tile trays" will be inserted from the high η end, and optical cables will carry the scintillation light to the photodetectors. 18 wedges are bolted together to form a half-barrel ring. Tight mechanical tolerances on the plates (and lack of distortion because of bolting) allows the design to have ≤ 2 mm of air gap between adjacent wedges. In addition, only a 9 mm high slot is needed to accommodate the 7.5 mm thick scintillator packages.

The construction endcap hadron calorimeter is logically similar to the barrel. Each endcap is a monolithic structure, bolted together from "pizza slice" shaped plates of copper. Again the plates are staggered to provide alternating slots for the scintillator tile trays. The endcap HCAL is anticipated to have ~ 10 cm thick copper sampling.

Figure 3 shows the total number of interaction lengths of material provided by the ECAL (1.1 λ) and the HCAL. We see that at $\eta = 0$, the combined calorimeter is somewhat thin, 6.2λ. Therefore our design places 2 additional scintillator samples outside the solenoid, the Late Shower Sample. Figure 3 also shows the resulting total number of interaction lengths in the calorimeter.

3 Optical System

The CMS HCAL optical system contains of approximately 70,000 individual scintillator tiles. Since the optical systems for the barrel and endcap HCAL's are very similar, we will concentrate on the description of the barrel.

The scintillators are organized into tile trays, as shown in Figure 4 for the barrel calorimeter. The trays are either 1 or 2 tiles wide in ϕ, and the full length of the barrel (16 tiles) in η. The cross section of the tile tray is shown in Figure 5. The 4 mm thick scintillator tiles are covered with white reflective Tyvek plastic and then sandwiched between top and bottom cover plates. The entire package is connected together by small through-bolts. The thin bottom cover plate provides mechanical protection. The 2 mm thick top plate protects the tiles as well as supplies a path for the fibers from the tiles to travel to the high η end of the tile tray. There, the fibers are terminated into multi-fiber optical connectors. Optical cables carry the light onward to photodetector decoder boxes where the light from each tile is organized into readout towers.

Our baseline choices for optical materials are Kuraray SCSN81 for the scintillator, Kuraray multi-clad Y-11 (K-27 fluor) for the wave-shifting fiber, and

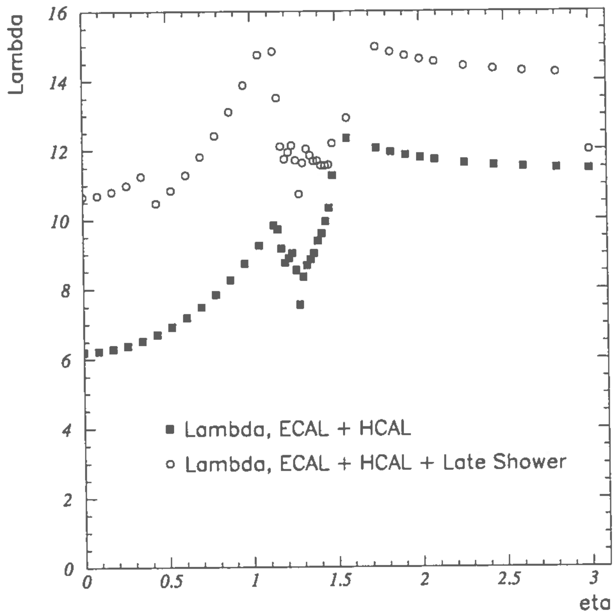

igure 3: Number of interaction lengths inside the solenoid (ECAL + HCAL), and ›tal number of interaction lengths sampled, including the Late Shower Sample.

.uraray multi-clad clear fiber. With these materials, typical light-yields are of rder 2 photoelectrons per minimum-ionizing particle per scintillator layer. Optical ıaterials evaluation will continue for the next several months before the final choices re made.

Quality Control and Calibration

}uality control and calibration schemes are built into the optical system from the eginning. After assembly of the tile trays a collimated Cs^{137} source is used to test he tiles. By measuring the induced radioactive source current after a photodetector, he collimated source measurement establishes the absolute response of the tiles. At he same time a moving wire source is used for cross calibration. Figure 5 shows he 2 mm top cover plate carrying "source tubes". The source tubes are stainless teel tubes that terminate into source-tube connectors that allow them to be to plumbed" to tubes from a moving wire source system. In the moving wire source ystem, a point source at the end of a wire moves through the source tubes to excite he scintillators. The source position relative to the tile is well controlled by the

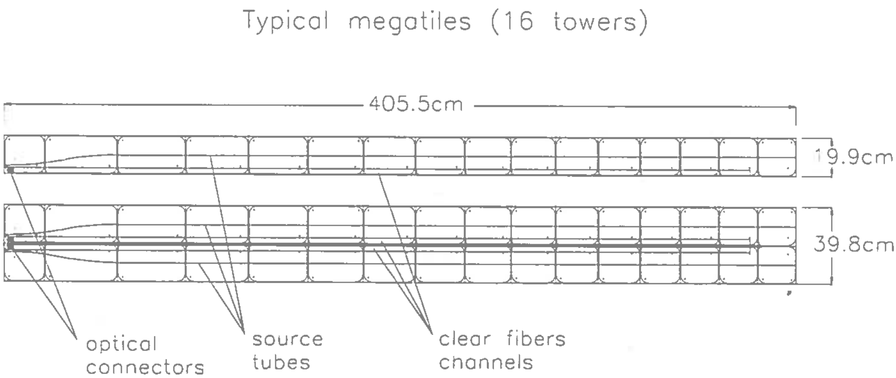

Figure 4: Schematic drawing of a scintillator tile tray. The tray is 16 tiles long in η and either 1 or 2 tiles wide in ϕ.

permanently attached source tube. Because of the fixed geometry of the source tube relative to the tile, the ratio of response of collimated to wire source is stable. The moving wire source (Cs^{137}) is basically an isotropic source. The scintillator response changes by approximately 1% per 0.1 mm of separation between the scintillator and the source. Thus meaningful measurements with the wire source require that the stability of the placement of the wire source relative to scintillator must be controlled to order 0.1 mm. This is achieved by permanent attachment of the source tubes on the tile trays.

After the tile-trays have been installed into the absorber, the wire source is again used to test for system stability. Since the geometry of the wire source tube to scintillator is unchanged, the measurement of wire-source response allows for reference back to the original QC test using the collimated source. A small number of the source tubes will be accessible during operation of CMS. These tubes will be periodically retested to verify stability.

A laser flasher system will also be used to directly excite the photodetectors. This system will be used on a periodic basis to track the gain of the photodetector/amplifier/digital readout system.

The stability of ratio of wire source measurement to collimated source measurement (ie to the true tile absolute response) provides convenient way to carry test beam calibrations to the actual CMS detector. A subset of the barrel wedges will be extensively studied in test beam. A set of calorimeter towers will have their pion response measured with test beams. In addition the wire-source system will measure

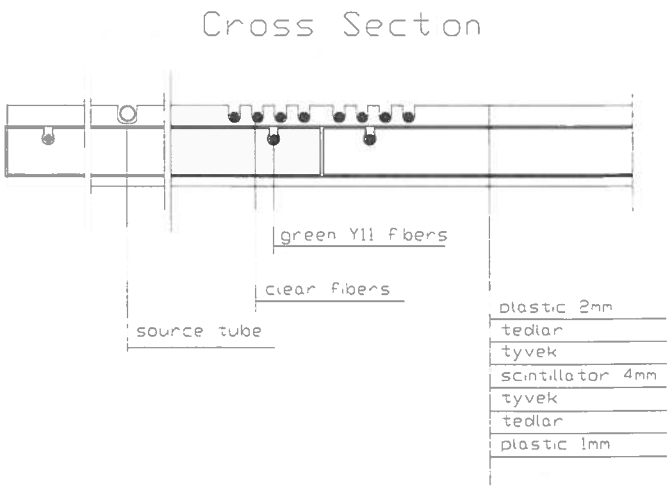

Figure 5: The cross section of the scintillator tile tray.

e "fingerprint" of each tower's optical longitudinal uniformity. An effective "pion-ighted source response" will be formed by convoluting the longitudinal optical ofile with an average pion longitudinal profile. Then the ratio of actual test beam sponse to pion-weighted source response will be used to carry test beam calibration wedges in CMS that were not exposed to beams. From past experience on CDF, initial absolute calibration of 2 - 3% is expected.

The HCAL group has started a program to understand how the intial solute calibration can be improved by using in-situ physics calibrations while MS is operating [5]. One likely signal is $t\bar{t}$ production, where the top quarks en decay into W+b. One W is required to decay into jets, while the other is quired to decay into lepton + neutrino to provide a trigger. For events that have tagged b-jet's, CDF has shown that it can readily reconstruct the W boson that cays into jets. They measure a rms/mean of about 9.1 GeV / 81.4 GeV for 8 constructed top events in $100pb^{-1}$ of data. A similar analysis has been performed ing a simulation of the CMS detector. There, even in the presence of the ~ 30 inimum-bias events anticipated at the ultimate luminosity of 10^{34}, the W into jet decay can be reliably reconstructed. The results expected for one month of IC running at 10^{33} is shown in Figure 6. At the LHC, $t\bar{t}$ production will supply ready source of di-jet events that reconstruct into a fixed mass and will help with libration as well as understanding systematics of jet clustering.

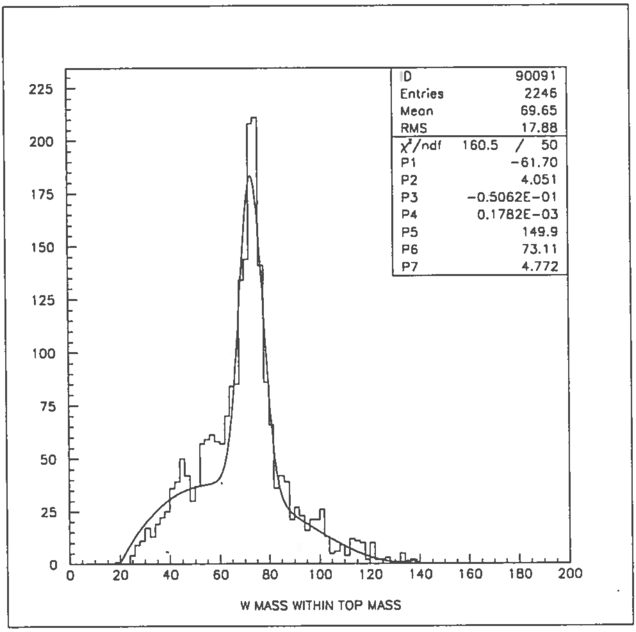

Figure 6: Simulated reconstruction of W decaying into 2 jets for double-b-tagged $t\bar{t}$ events in CMS. The statistics represent one month of low-luminosity running at the LHC.

5 Photodetectors

The barrel photodetectors are positioned at the high η / large radius of the barrel HCAL, inside the 4T magnetic field. (The corresponding location for photodetectors for the endcap calorimeter is at the large radius, large z corner. The photodetectors were placed at these points for several reasons: The next place where they could be located was after about 18 meters of cable length, resulting in substantial light loss. In addition, a design goal was the desire for the calorimeters to be completed and tested at the CMS surface assembly building before being lowered into the collision hall. The calorimeter design should therefore be self-contained and robust.

Because of the placement of the photodetectors, conventional photomultiplier tubes were unusable. Instead a recent development, hybrid photodiodes, HPD's, was adopted. The HPD is a proximity-focused device consisting of a vacuum envelop, a conventional photocathode, and a reverse-biased silicon diode. A high accelerating voltage (of order 10kV) is supplied between the photocathode and the silicon diode. Photoelectrons emitted by the photocathode gain kinetic energy lling through the electric field. This kinetic energy is converted into electron-hole ıirs when the photoelectron impacts the diode. The generated electric pulse is read f the diode, amplified, and sent to digitizing electronics. Typical gains for the HPD 'e from 1000 to 2000. Figure 7 shows the internal design of a HPD. Because the

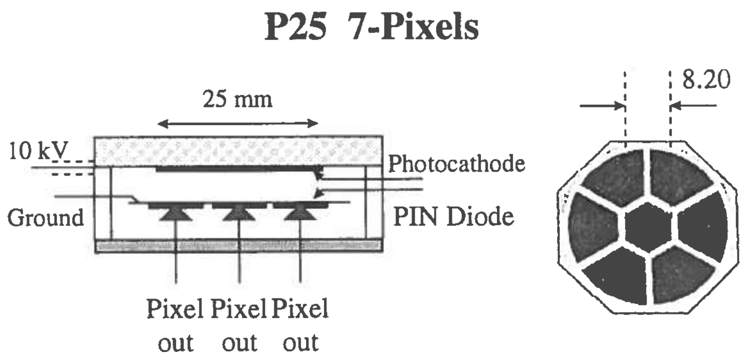

Figure 7: Internal design of a 7 pixel HPD.

ıw gain of the HPD requires the use of an associated amplifier, they are effectively oisier than conventional photomultiplier tubes. However HPD's are able to clearly etect minimum-ionizing particle transits of the calorimeter. Figure 8 shows a test eam measurement of the muon signal through 8 layers of scintillator using a HPD ɔr readout [6].

Because of our reliance on radioactive sources for quality control and cali- ration, the HPD must be able to accurately measure DC currents (supplied by the adioactive sources). The HPD has a typical leakage current of about 1 - 5 nA, with jitter in the current of only order 10 pA. The source-induced currents are of order nA. With these conditions, the HPD's have been shown to make source current ıeasurements of accuracy 1%. [6]

Test Beam Studies

'here were a number of issues requiring exploration before the HCAL design could be ptimized. Performance of hadron calorimeters operation in magnetic fields needed o be understood. Techniques for carrying calibrations from test beam conditions B=0) to operating conditions (B=4T) needed to be developed. Photodetectors ⁊hich operate in high magnetic fields needed to be studied.

To understand these and other issues, a set of test beam measurements

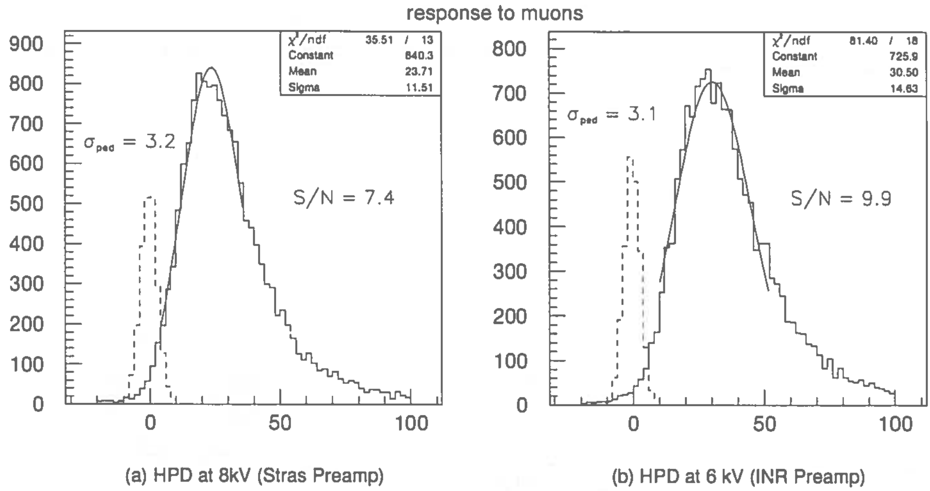

Figure 8: Test beam response for muons when viewed by an HPD. Light yield is approximately 10 photoelectrons. The dotted histograms are superimposed pedestal distributions.

were performed during 1995 and 1996. A "hanging file" calorimeter was constructed. This calorimeter could be easily reconfigured to study different absorber sampling and different scintillator arrangements. Copper absorber thickness of 2 cm or larger were available. The device had an active area of 64 X 64 centimeters, and could be arranged to be up to 10 λ deep. The transverse size was limited by the requirement to place it inside the EHS magnet in the CERN H2 beam line. This superconducting magnet has a cylindrical bore of 1.5 meters diameter and can supply magnetic fields of up to 3T. The test calorimeter could be exposed to magnetic fields either transverse or parallel to the beam.

Several sets of scintillators were built in 2 basic designs: One large tile of approximately 64 X 64 cm, read out by many WLS fibers; or 3X3 arrays of $\sim$ 22X22 cm tiles, each read by one WLS fiber. The light from each tile could be ganged together with the other tiles in the same layer to form individual longitudinal layers (to explore longitudinal shower development) or summed with other tiles in depth to form towers (to study transverse aspects and photodetector performance). The design of the test beam apparatus can be found in ref [7].

The 1995 exposure had the magnetic field parallel to the beam direction

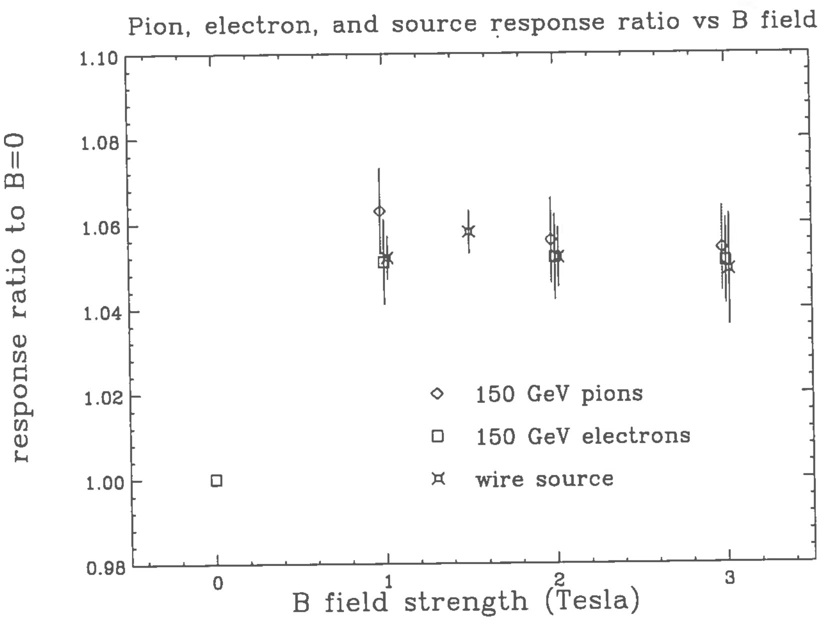

gure 9: Normalized response for electrons and pions vs magnetic field. The field parallel to the beam.

he endcap configuration), while the 1996 orientation had the magnetic field per- :ndicular to the beam direction (the barrel configuration). Figure 9 shows results r the endcap configuration. Shown here are the normalized responses for pions and ectrons as a function of magnetic field. There is about a 6% increase relative to =0. Also shown is the response of the moving wire source. We conclude that the)served change in response is simply the well known brightening of scintillator in a agnetic field. The response in the barrel configuration seems to be more complex. arlier results [8], [9] indicate that there are fundamental differences in pion and ectron showers for transverse fields, and that e/pi changes for $B \neq 0$. Monte Carlo :sults indicate that in the transverse configuration, electron showers in particular :e sensitive to exact details of the transition between absorber and scintillator. reliminary results from 1996 test beams agree with this conclusion. First results re arriving from analysis of the extensive sets of measurements taken in the summer f 1996. This analysis should be completed in the next several months.

7 Schedule

The HCAL design will be finalized during fall 1996 and winter 1997. A full size pre-production prototype will be built during 1997, and tested at CERN test beams in 1998. In 1999 the production factory for HCAL will commence, with completion targeted for 2002.

References

1. V. Gavrilov, et al, CMS Quartz Fiber Calorimeter, these proceedings.

2. Compact Muon Detector Technical Proposal, CERN/LHCC 94-38 , p73

3. V.I. Kryshkin and A.I. Ronzhin, Nucl. Instrum. Methods, **A247** (1986) 583

   M.G. Albrow et al., Nucl. Instrum. Methods, **A256** (1987) 23

4. G.W. Foster, J.Freeman and R.Hagstrom, Nucl. Phys. B, **A23** (1991) 93

   J. Freeman, et al., The CDF Upgrade Calorimeter, Proc. 2nd Int. Conf on Calorimetry in HEP, Capri, Italy, 1991

   P. de Barbaro et al., Nucl. Instrum. Methods, **A315** (1992) 317

   P. de Barbaro and A. Bodek, A Compilation of Tile/Fiber R&D Results, University of Rochester Preprint UR-1389 (1994)

5. J. Freeman and W. Wu, In situ Calibration of the CMS HCAL Detector, FNAL-TM-1984

6. P. Cushman, et al., Comparison of Hybrid Photodiodes and Avalanche Photodiodes as candidate transducers for CMS HCAL, CMS/TN 96-141, Proc. First Conference on New Developments in Photodetection, Beaune96, Beaune, France, June 24-28, 1996

7. H. Budd, CMS Central Hadron Calorimeter, Proc. 6th Topical Seminar on Experimental Apparatus in HEP, San Miniato al Todesco, Italy, May, 1996

8. J. Mainusch et al., Nucl. Instrum. Methods, **A312** (1992) 451

9. V. Kryshkin, private communication.

Not Orally Presented

G. Boca A Tile Calorimeter for the Focus Experiment at FERMILAB

scati Physics Series Vol. VI, (pp. 337–343)
INT. CONF. ON CALORIMETRY IN HEP – Frascati, June 8–14, 1996

A TILE CALORIMETER FOR THE FOCUS EXPERIMENT AT FERMILAB

Gianluigi Boca[1]

*Dipartimento di Fisica Nucleare e Teorica and INFN,
Via Bassi 6, Pavia, Italy*

ABSTRACT

e design and construction of a new calorimeter for the experiment Focus (E831) Fermilab is presented. It is a sampling calorimeter, with 28 iron (passive) and ntillator (active) planes. The active planes are composed of tiles read out by aveLength Shifter fiber spliced to clear fibers.

Purpose of the hadronic calorimeter in Focus

ie fixed target experiment Focus (E831) studies photoproduction of charm at rmilab using a wide band photon beam (average energy is 220 GeV, see in fig.1 the perimental layout) and it is presently running (1996). The hadronic calorimeter ovides the first level trigger necessary to select events with a large (charm) hadron ntent and to reject purely electromagnetic events (mainly e^+e^- pairs). Both a total ergy and a transverse energy triggers are provided. It must give a fast response ithin 40 nsec) and be large enough to cover the desired solid angle (approximately mrad). The reconstruction of the point of impact on the calorimeter upstream rface of neutrons and K_L through the shower energy realease is also possible in der to study particular physics channels (for instance strange baryons decaying to neutron or D mesons decaying into K_L). These goals were achieved building a mpling calorimeter (see fig.1 for a view from the top of the hadronic calorimeter)

[1]co-authors are : S.Gourlay, *Fermilab, Batavia, IL 60510, USA*; Yeon Sei Chung and 'oung-Beom Lee, *Korea University, Seoul 136-701, Korea*; S.Malvezzi and A.Sala, *Dip. di sica dell'Universitá and INFN - Milano, I-20133 Milan, Italy*; V.Arena, G.Bonomi, G.Gianini, Liguori, M.Merlo, M.Marchesotti, S.Ratti,C.Riccardi, P.Torre, L.Viola, P.Vitulo, *Dip. di Fisica icleare e Teorica dell'Universitá and INFN - Pavia, I-27100 Pavia, Italy*

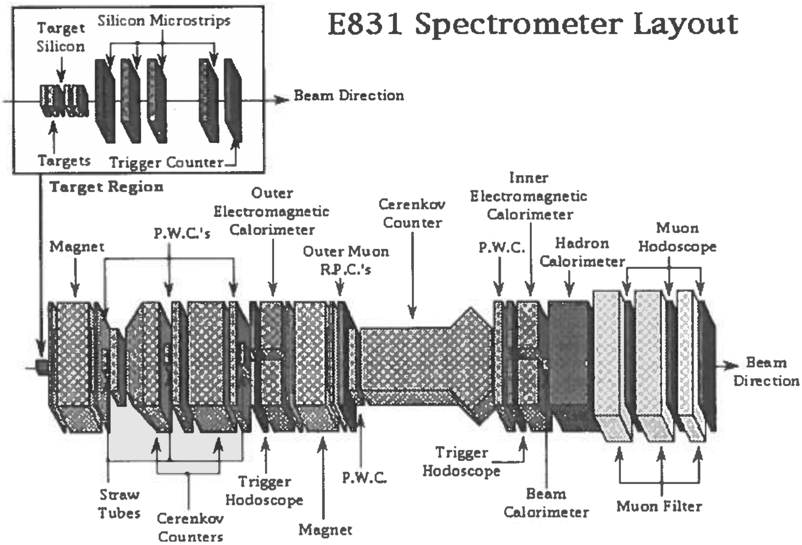

Figure 1: The experimetal layout of Focus (E831), seen from the top. The hadron calorimeter is a parallelepiped placed just upstream of the muon filter.

with 28 planes of iron as absorber and scintillator as sensitive material and dividing each scintillator plane in 66 tiles. The dimensions of the iron plates are 305 cm $\times$208 cm $\times$4.4 cm except the first two planes that have thickness 6 cm. The thickness of each scintillator plate is 0.7 cm (Kuraray SCSN-81 polistyrene scintillator). The total thickness of the calorimeter in the beam direction is 7.8 interaction lengths (the physical length is 219 cm).

2 Description of the sensitive planes

Transverse energy trigger and shower reconstruction are achieved with the segmentation of each active plane in 66 tiles of various dimensions : 20 cm $\times$20 cm in the central region and either 40 cm $\times$ 40 cm or 50 cm $\times$ 50 cm in the outer region (fig.2). Each sensitive plane is encased in an aluminium frame and two white plastic foils that ensure mechanical stability (fig.3). In this frame all 66 tiles are laid side by side to form the sensitive plane. Each tile is painted on the side edge with white

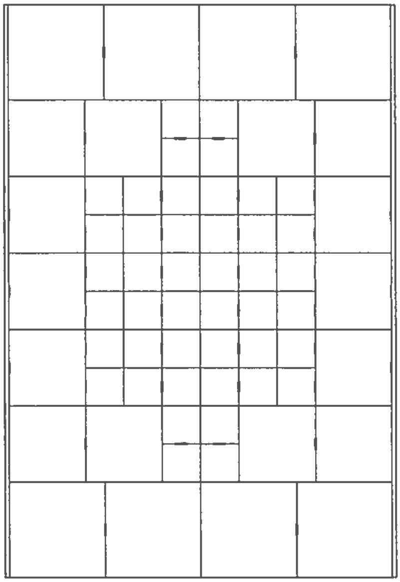

gure 2: Tiles by which each scintillator plane is composed. The three different ;es are 20cm×20cm, 40cm×40cm and 50cm×50cm.

lective paint to avoid light leakage to the neighbouring tile, while the front and ar surfices are covered with a white tyvek plastic thin foil. Each tile is read out two WLS plastic fibers (Kuraray, Y11, 0.89 mm diameter) laid one on top of e other in a groove carved in the scintillator with an alpha shape [1]. The fibers nvert the blu or ultraviolet light emitted by the tiles into the green. The four er ends run outside each tile and go to the outer side of the sensitive plane into a nnector fixed in the aluminium frame. Another fiber is inserted on the other side this connector and goes to a phototube that produces the analog output signal. ıe WLS fiber has an attenuation length of about 3 meters. In order to improve e light transmission clear plastic fiber with double cladding (attenuation length meters) is used from just outside each tile to the phototube. The connection be- een WLS fiber and clear fiber is made splicing them thermically [2]. The light ss due to the splicing is typically 10%. The total length of WLS and clear fiber the same for each tile in order to equalize the time of arrival of the ligth to the ıototube. Since the 20 cm × 20 cm and the 40 cm × 40 cm tiles have a longer ear fiber length, the latter had to be routed in winding grooves carved in the white astic covering the scintillator planes (see fig.4) before reaching the side connector. ıe phototubes used to detect the tile light are EMI 9902 KB. We tested that this pe of tube has a light yield of at least 3 photoelectron/mip in the worst case (with 50 cm × 50 cm tile). A total of 66 × 3 = 198 analog signals are available. In

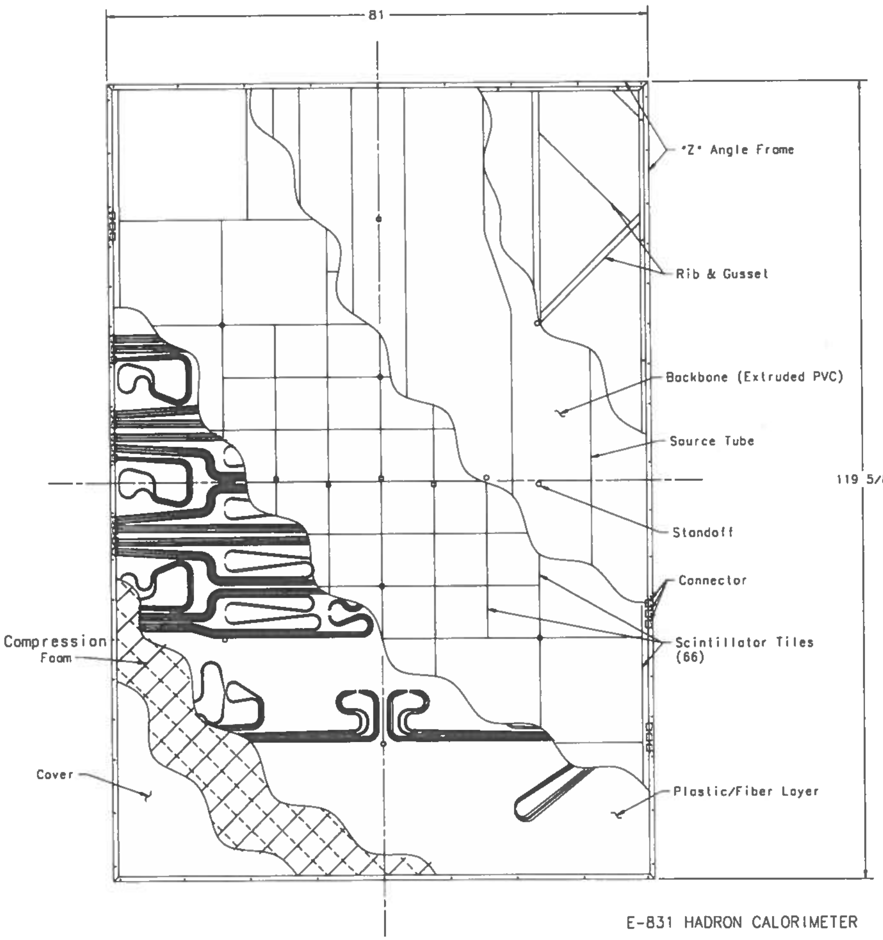

Figure 3: Layers compounding each sensitive plane of the calorimeter.

fact all tiles occupying the same position ('corresponding' tiles) of the first 9 planes (defined as the first section of the calorimeter) are connected to the same phototube. We call 'tower' a set of corresponding tiles. In a similar manner corresponding tiles from plane 10 to 24 (second section) are connected to the same phototube and the same for corresponding tiles belonging to plane 25 to plane 28 (third section). In this way signals of corresponding towers from three sections of the calorimeter are available : the first section is the most useful for shower position reconstruction, the last one for muon identification. The phototube anode signal of each tower is sent to an ADC channel while the dynode signal is sent to the electronics that weights and sums the analog signals to produce the total energy and the transverse energy signal.

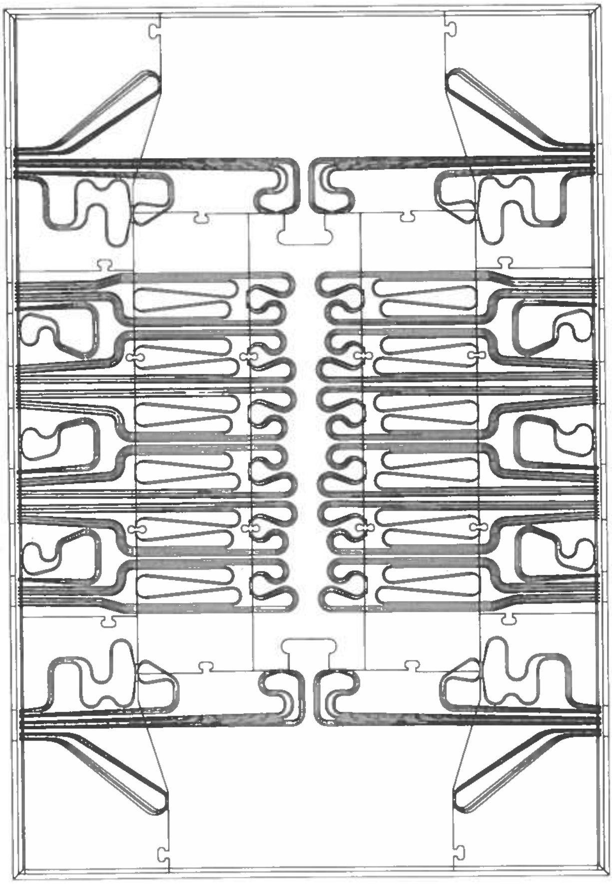

Figure 4: Routing of the clear fibers of each sensitive plane

Monitoring systems

ɪo monitoring systems are implemented : a ^{60}Co source that can illuminate every ɜ with γ rays and check the status of tile and corresponding phototube, and a laser ɜtem to check the phototube gain. The source consist of a thin steel wire with a ıall ^{60}Co source on its tip. This wire can be unrolled from a supporting cilynder d driven by a step motor into thin metal tubes that go through each scintillator ıne aluminium frame and are laid across the plane on top of each tile (see fig.3 ɜ source tubes). There are 8 metal tubes for each of the 28 scintillator plane. The ute the source wire will follow and the length the metal wire will extend can be ogrammed remotely by computer and in this way the center of each tile can be

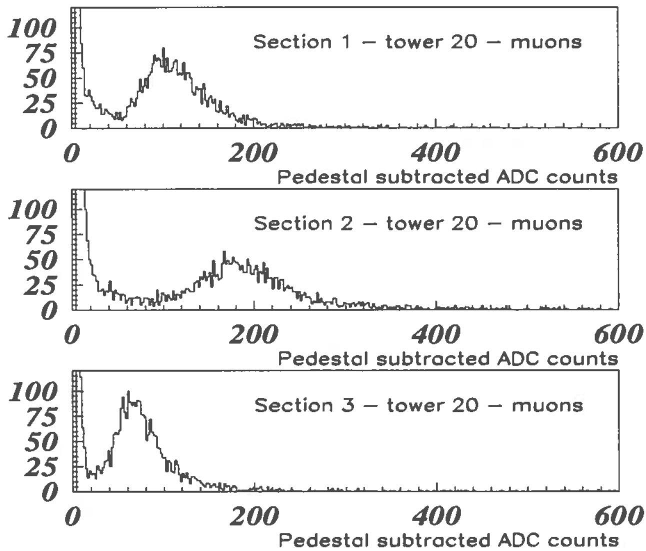

Figure 5: a) muon peak of a central tower of the first section of the calorimeter; b) muon peak for the same tower of the second section; c) muon peak for the same tower of the third section.

illuminated by the source. Since the source is intense, a current can be measured in the phototube connected to the illuminated tile. This gives a measure of the detection efficiency of both tile and corresponding phototube.
The laser system consists of a UV laser whose light beam impinges on a bit of the same plastic scintillator as the one used in the sensitive planes. The light is optically diffused by a lucite cone and transported by 198 glass fibers to 4 different boxes in which they illuminate plastic WLS fibers of the same type used in the calorimeter tiles. The WLS fibers then go to the 198 calorimeter phototubes. In this way when the laser is operated each phototube is illuminated by the same spectrum of light that comes from the tiles. Also two fibers are sent to a pair of thermostatated phototubes used as reference in order to measure the laser light output variations. This allows to calculate the relative gain : (calorimeter phototube)/(reference phototubes) and to track variations under the assumption (verified at least for the time being over a period of couple of months) that the reference tubes are stable.

4 Preliminary results

Preliminary results has been obtained with muons and pions. In fig.5 a typical muon distribution with the characteristic Landau shape is shown for a central tower (tower # 20) of the first section, second and third section of the calorimeter. The ratio of

ADC counts corresponding to the muon peaks of a tower in section 1, 2, 3 is set
proximately at 9:15:4 (the same ratio of the number of scintillator planes forming tion 1, 2 and 3 respectively of the calorimeter).

ferences

V.Arena *et al.*, 'Tile Fiber Calorimeter', Conference 'SCIFI 93', October 24-28, 1993, Notre Dame, Indiana, USA; page 329 of the proceedings ('SCIFI 93, workshop on Scintillating Fiber Detectors') published by World Scientific.

G.Apollinari, D.Scepanovic and S.White, Nuclear Ins. & Meth. A311 (1992).

IV – Calibration

Convener B. Borgia
Secretary M.C. Spitalieri

Borgia	Convener's Report
Kehoe	Hadronic Calibration of the DØ Calorimeter
Gauzzi	Calibration of KLOE e.m. Calorimeter Modules with Cosmic Rays: Test Setup and Preliminary Results
Cauz	A Stability Monitor for CDF Plug Upgrade Calorimeters

ıscati Physics Series Vol. VI, (pp. 347–348)
INT. CONF. ON CALORIMETRY IN HEP – Frascati, June 8–14, 1996

(Convener's Report)

CALIBRATION

Bruno Borgia

Department of Physics, University of Roma "La Sapienza" and INFN Sezione di Roma

The importance of calibration methods in high energy particle detectors doesn't ed to be emphasised. However most of the attention is dedicated to progress in new tectors rather than to their calibration. It is a fact that advances in calibration methods ɜ rare.

Nevertheless the understanding of calorimeter performances and most of all the ıysics interpretation of energy measurements are crucial and deserve constant :ention and effort.

A good example of physical interpretation of energy measurements is the ntribution of R. Kehoe on the calibration of DØ calorimeter where he presents not ıly the single particle calibration to derive resolutions, linearity and absolute energy ale, but the details of reconstructing the jet energy and energy scale.

Only through similar study that relevant physics results can be based.

The DØ calorimeter is made of Lq Argon and Uranium plates, achieving a solution of $\frac{14.8\ \%}{\sqrt{E}} \oplus 0.3\ \%$ in the electromagnetic compartment and $\frac{47\ \%}{\sqrt{E}} \oplus 4.5\ \%$ ı the hadronic section. The absolute e.m. energy scale is derived from particles variant mass reconstruction as the Z decaying in two electrons.

Systematic errors in jet energy reconstruction are estimated to be of the order of :w percent enabling a good agreement between data and theory on the inclusive jet ·oss section up to.

The contribution by D. Cauz on the stability monitor for the CDF calorimeter lug addresses the requirements for such a system. The main parameters to consider in ıe design of a calibration monitor are

) light spectrum of artificial source reproducing the calorimeter signal
) redundance of reference detectors
) variable light output to explore the calorimeter energy range
) radiation hardness of components

5) reliability of components to insure overall stability of the order of a fraction of calorimeter resolution.

The aim of similar monitoring systems is a challenging one considering the performances of projected e.m. calorimeters for Higgs search in the $\gamma\gamma$ decay channel.

A third aspect of calibration methods is presented by P. Gauzzi, discussing the Kloe e.m. calorimeter calibration by a cosmic ray test set up. The availability of cosmic rays allows the systematic testing of detector components. One of the main aim of the test was the verification of time resolution in the time difference between the two phototubes viewing the same module.

In fact the position reconstruction of $\pi^\circ \rightarrow \gamma\gamma$ decay is based on these measurements. Comparison with test beam calibration confirms the calorimeter performances on time, position and energy resolution achieving

$$\sigma_t = 55 \text{ ps} /\sqrt{E} \text{ (GeV)}$$
$$\sigma_{E/E} = 4.5 \%/\sqrt{E}$$

In conclusion, behind the excellent performances and the physics results achieved through calorimetric measurements we always find a thorough proven calibration procedure and stability monitor. In the prospect of several ten thousands of calorimeter towers, even a small channel to channel calibration error will impair the best detector.

ıti Physics Series Vol. VI, (pp. 349–358)
·. CONF. ON CALORIMETRY IN HEP – Frascati, June 8–14, 1996

HADRONIC CALIBRATION OF THE DØ CALORIMETER

Robert Kehoe
(representing the DØ Collaboration)
University of Notre Dame
Notre Dame, Indiana 46556, USA

ABSTRACT

'he DØ detector is used to study $\bar{p}p$ collisions at the 1.8 TeV center-of-momentum nergies available at the Fermilab Tevatron. The heart of the detector is a hermetic alorimeter employing uranium absorber and liquid argon for sampling. Several nalyses require a well-understood jet energy scale. This paper describes how this alibration is obtained.

. Introduction

Jets are now an important part of many analyses and their proper energy calibration n the detector is crucial. At DØ, the jet energy scale is currently the limiting ystematic error in our measurements of the inclusive jet cross section and top quark mass. In this paper, we discuss the DØ jet energy scale determination and outline its verification.

The U/LAr sampling calorimeter is the primary subdetector of DØ [1] used to identify e, γ, jets and missing transverse energy ($\not\!\!E_T$). Since there is no magnetic field in the inner tracking volume, the calorimeter is also used for their energy measurement. The calorimeter readout is segmented transversely into 'towers' projective to the center of the detector which cover an area of 0.1×0.1 in $\eta - \phi$. The pseudorapidity, η, is defined as $-\ln(\tan(\theta/2))$ where θ is the angle with respect to the proton direction, and ϕ is the azimuthal angle. Longitudinally, each tower is segmented into 'cells' in three sections: electromagnetic (EM), fine hadronic (FH), and coarse hadronic (CH). A central cryostat (CC) covers $|\eta| < 1.0$ and two end

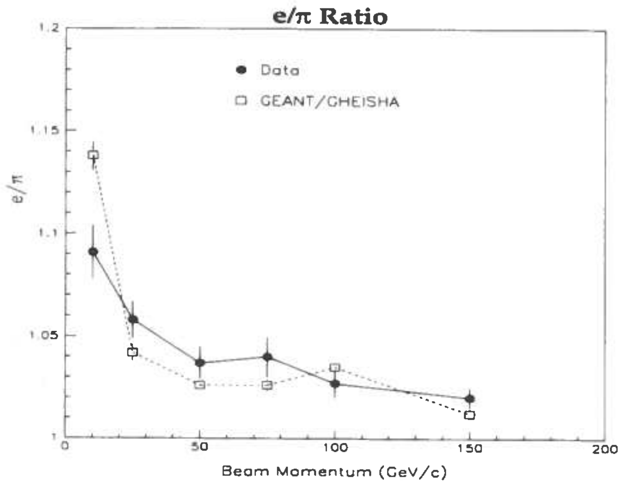

Figure 1: Energy dependence of e/π in EC for GEANT and test beam.

cryostats (EC) cover $1.0 < |\eta| < 4.0$. At DØ, $\not\!\!E_T$ is defined as the negative of the vector sum of the calorimeter cell transverse energies (E_T's).

It is important that the detector is uniform and hermetic, and that the responses to charged hadrons and electrons are similar ($e/\pi \sim 1$). Test beam studies indicated that the linearity of electron and pion response is within 0.5% for energies from 10 GeV to 150 GeV. The e/π ratio of the detector, shown in Figure 1 for the EC [2], is close to unity. For *in situ* studies described later, it is also important that the energy resolution of electrons and photons is good, and that their response is well-known. The test beam analyses indicate the resolutions for single particle showers are $0.148/\sqrt{E} \oplus 0.003$ for electrons and $0.470/\sqrt{E} \oplus 0.045$ for charged pions. The electromagnetic energy scale is determined *in situ* from the ratio of the Z mass as measured at LEP [3] to that measured at DØ using dielectron final states ($M_Z^{LEP}/M_Z^{D\emptyset}$) [4, 5]. The linearity for electrons has also been verified *in situ* using π^0 and J/ψ decays [4].

It is useful to briefly note the nature of jets to help define the calibration goal. The fact that most events display a dijet structure intuitively connects the observed jets to an underlying simple parton interaction. However, it is not easy to associate the jet energy with a specific underlying parton energy (see Figure 2a). The concept of an isolated parton does not exist in the theory of QCD – partons radiate gluons, fragment into hadrons and interact with one another via color flow. This complexity makes jet physics very dependent on the jet definition. The fixed-cone algorithm, which is most commonly used at DØ, clusters energy around a precluster

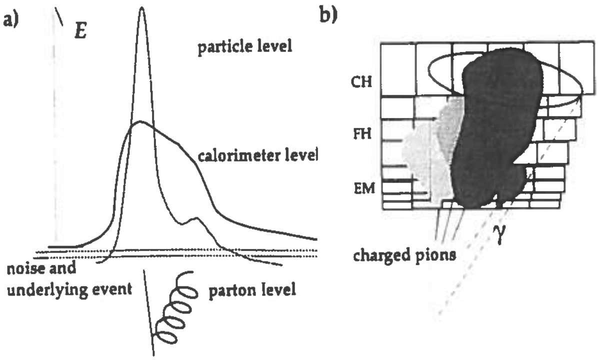

igure 2: a) Sketch of jets at parton, particle, and calorimeter levels. At the particle vel, there is not a clear association of energy to each parton. At the calorimeter vel, showering and noise further alter the energy profile. Sketch b) shows a section : calorimeter with individual particle showers. Charged hadrons, in particular, roduce wide showers which can spill outside of a jet cone.

xis in a cone of size, $\Delta R = \sqrt{(\Delta\phi)^2 + (\Delta\eta)^2}$, calculates an E_T weighted centroid, nd reclusters around that centroid [6]. 'Calorimeter jets' are those jets found with his algorithm after all gluon radiation, fragmentation, and detector effects. We efine our jet calibration to compensate only for detector effects so that we attempt o obtain the 'particle level' energy of a jet (E^{jet}_{ptcl}) from its measured calorimeter nergy (E^{jet}_{meas}). This particle level energy is found with the same algorithm as a natching calorimeter jet but from final state particle energies before detector effects. Ve could also define a 'parton level' jet and attempt to correct back to this but leave hat to individual physics analyses.

Our calibration obtains E^{jet}_{ptcl} from E^{jet}_{meas} by correcting for the following ffects:

I. An energy offset, O, which includes both detector noise and energy from the underlying event.

II. A change in energy due to showering, S, in the calorimeter which is specific to each jet algorithm.

III. A change of the energy scale, R (response), due to e/π [2, 5] and energy lost in readout cracks.

Algebraically, we calculate E^{jet}_{ptcl} for a found jet by,

$$E^{jet}_{ptcl} = \frac{(E^{jet}_{meas} - O)}{R(1-S)}. \tag{1}$$

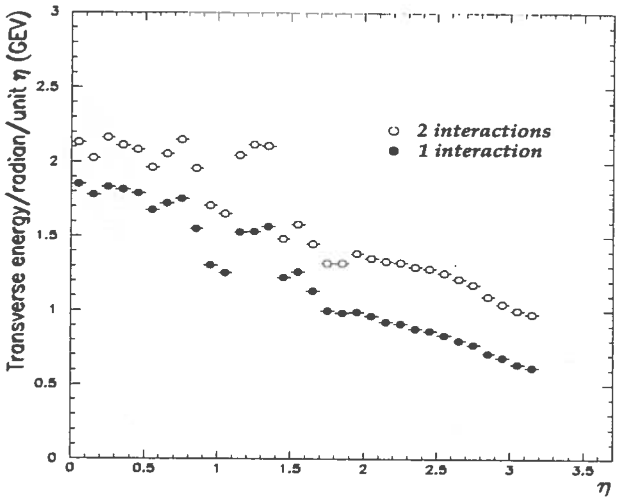

Figure 3: Average E_T density in GeV as a function of calorimeter tower η, for single interaction and double interaction events.

2 Estimation of Offset

Two processes result in measured jet energy not originating from the particles making up the corresponding particle jet. The absorber plates in the EM and FH portions of the DØ calorimeter are made of depleted uranium whose decay results in a measurable signal. The resulting asymmetric pedestal distribution leaves a net positive energy contribution after a symmetric zero suppression cut which we label 'noise' (N). Additional energy comes from beam remnants and additional $\overline{p}p$ interactions and is termed 'underlying event', denoted U.

Figure 3 shows the average E_T density as a function of calorimeter tower η from events satisfying a minimum bias (MB) trigger. The solid circles are from events where only one interaction occurred in each beam crossing. The open circles are from events where two interactions occurred. If the underlying event contribution for two interactions is twice that for single interactions, then the difference between the two histograms in Figure 3 is a measure of the underlying event contribution for a single interaction:

$$U = O_{MB}^{2int.} - O_{MB}^{1int.}. \tag{2}$$

The removal of the underlying event contribution from the single interaction energy density gives the noise contribution,

$$N = O_{MB}^{1int.} - U. \tag{3}$$

The systematic error on the underlying event is 0.2 GeV$/rad/unit - \eta$ and for noise it is 0.1 GeV$/rad/unit - \eta$.

Showering

cording to our definition of E^{jet}_{ptcl}, no correction is needed when an algorithm is plied at the particle level. Once the fragmentation products strike the calorimeter, wever, the observed jet broadens due to the resultant showers and some energy n leak out of, or into, a jet cone (see Figure 2b). To quantify this, central jets e generated with HERWIG [7], and the energies of the fragmentation particles e deposited in the first calorimeter cells intercepted by their momentum vectors. t reconstruction is then performed on these cells to produce 'unshowered' jets. To oduce 'showered' jets, the hadrons/photons in the jet are replaced with test beam ons/electrons of the same energy. The particle's energy is then distributed relative the intercepted cell as observed in the test beam and jets are reconstructed from ese showers. The showered and unshowered jets are matched and the ratio of owered energy to unshowered energy ($= 1 - S$) is calculated. For a cone size of $R = 0.7$, S is 0.01 to 0.0 depending on particle jet energy, while smaller cone sizes ve somewhat larger corrections. The systematic error is about 1%.

Jet Response

y 'jet response' we refer to the collective response of the calorimeter to all the rticles comprising a jet. We use the $\not\!\!E_T$ to determine the relative response be-een two objects. Direct photon plus jet events then allow us to anchor the jet an absolute energy scale as a function of the measured jet energy. Finally, the lorimeter's uniformity is used to extend the energy reach of this analysis.

1 Method

et us consider a dijet event in which one jet is triggered on ('trigger jet') and the her is unbiased ('probe jet') (see Figure 4a). In order to obtain the response of e probe jet in terms of the $\not\!\!E_T$, let us consider the three vectors at the particle vel: $\vec{E_T}^{trig}$, $\vec{E_T}^{had}$, and $\vec{E_T}^{\nu}$. $\vec{E_T}^{had}$ is the vector sum of all interacting particles in e event outside of the trigger jet ($= \vec{E_T}^{probe} + \vec{E_T}^{jet2}$ of Figure 4b), and $\vec{E_T}^{\nu}$ is the ctor sum of all non-interacting particles in the event. In the transverse plane we ve

$$\vec{E_T}^{trig} + \vec{E_T}^{had} + \vec{E_T}^{\nu} = 0. \tag{4}$$

his becomes

$$R^{trig}\vec{E_T}^{trig} + R^{probe}\vec{E_T}^{had} = -\vec{\not\!\!E}_T \tag{5}$$

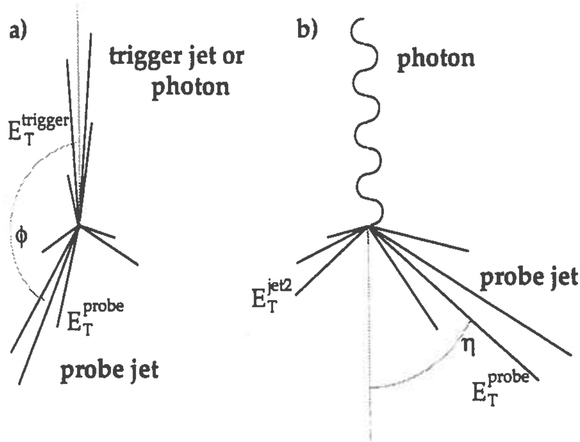

Figure 4: Sketch of the $\not{E}_T$ Projection Fraction method showing a) the trigger jet and the recoiling hadronic system. Photon plus jets events, shown in b), are used to absolutely calibrate jets.

at the calorimeter level, where R^{trig} (R^{probe}) is the response to the trigger (probe) jet. Defining the relative response, $r = R^{probe}/R^{trig}$, and assuming $\vec{E_T}^{\nu}$ is negligible, we obtain

$$r = 1 + \frac{\vec{\not{E}}_T \cdot \hat{n}_T^{trig}}{E_T{}^{trig}} \tag{6}$$

where $\hat{n}_T^{trig}$ is the unit vector in the direction of the trigger jet. When the trigger jet is a calibrated photon, r becomes R^{probe}. We only consider such events in what follows.

If a measured quantity, X, has a poor resolution, the determination of response in terms of X can be biased if one tries to directly plot R^{probe} *vs.* X. This 'resolution bias' arises because, in the case of $X = E^{jet}_{meas}$ or E_T^{jet} for instance, the parent distribution is strongly dependent on X at the parton level. However, both the E_T of the photon (E_T^{γ}) and the direction of the probe jet are well-measured so we define the energy estimator, E', as

$$E' = E_T^{\gamma}\cosh(\eta_{jet}). \tag{7}$$

Using E' to classify the probe jet, we plot the average E^{jet}_{meas} in E' bins *vs.* the average R^{probe} in the same bins. For example, if R^{probe}= 0.83 when E' = 150 GeV, and E^{jet}_{meas}= 120 GeV when E' = 150 GeV, then R^{probe}= 0.83 when E^{jet}_{meas}= 120 GeV. With this procedure we are able to extract response functions with negligible error in a parametric Monte Carlo with jet resolution, photon resolution, falling cross section, and trigger and reconstruction thresholds simulated. Therefore, we assign no systematic error for resolution bias.

Extending the Jet Energy Reach

: CC jets, we are limited to energy < 150GeV by the rapidly falling photon ss section. Also, there are large systematic errors involved in the collider data alysis at low E_T. To overcome these limitations, we first exploit the uniformity the detector by using the EC which has higher energy jets. Comparison of the ponse of jets in CC and EC in the kinematic region in which they overlap indicates isistency of energy scale to within a normalization factor. We use the normalized ! jets to establish the CC response at large energy (up to 350 GeV). To further end the energy reach, we compare jets in data and an ISAJET [8] direct photon nple with full GEANT detector simulation. In the kinematic region where they erlap we find consistency to within a scale factor and renormalize the Monte Carlo nts. The total energy range covered is from 10 GeV to 500 GeV.

Systematic Errors

tial and final state radiation are sources of uncertainty in the method. When a ondary jet is present and hits the calorimeter, Equation 6 is an approximation the probe jet's response. This 'topological' error is determined by measuring the ponse in a subset of the ISAJET direct photon events generated with only one itral jet, and comparing with an inclusive ISAJET sample. Detector simulation s performed for both samples. The estimated bias in measured response is 1% to), depending on jet energy. Significant initial state radiation may be lost down the ampipe. From parametric Monte Carlo studies, the estimated bias in measured ponse is about 3% when $E_T^\gamma < 20$ GeV, and negligible above 30 GeV.

Backgrounds to direct photons are a source of error for this analysis. We t on longitudinal and transverse isolation to remove EM jets with significant ociated hadronic activity. The residual bias to the measurement is estimated be ~1.4%. We also use the transition radiation detector and dE/dx in tracking ambers to remove $W, Z+$ jets background. The remaining W background affects ^{robe} by ~0.5%.

Some systematic errors arise from in extending the energy reach of the alysis. For the EC data, sensitivity to the number of multiple interactions in event results in a 2% systematic error. The systematic error on the Monte rlo/data normalization is about 3.5%.

l Response Curves in Data and Monte Carlo

choose a function for fitting our response curve, we consider models of hadron owering which give $e/\pi = [F_{EM} + (1 - F_{EM})R_h]^{-1}$, where R_h is the response of

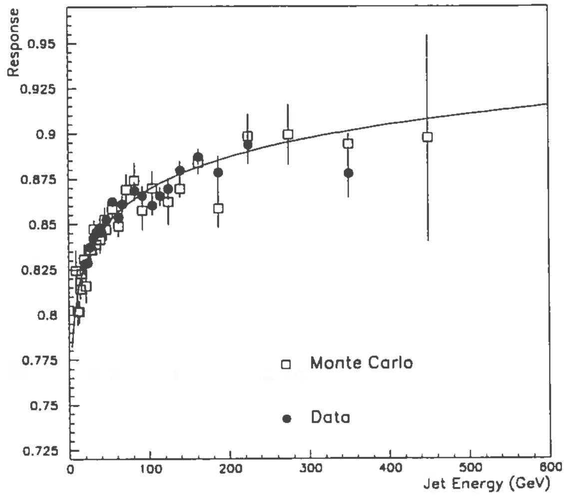

Figure 5: Response, r, of the probe jet relative to the photon *vs.* mean jet energy for Data (solid circles) and Monte Carlo (open squares).

the calorimeter to a particle interacting only via nuclear absorption and F_{EM} is the fraction of real hadron energy deposited via electromagnetically interacting shower products, electrons and photons [9]. The functional form for F_{EM} is $\sim c \cdot \ln(E)$, giving an expected pion response of

$$R_\pi = [e/\pi]^{-1} = a + b \cdot \ln(E) \tag{8}$$

relative to that of an electron. Because the test beam data are well-described by this functional form, we use Equation 8 for our jet response fits.

To compare Monte Carlo and data we remove EM scale effects and measure the response of the probe jet *relative to* the photon (ie. r *vs.* E^{jet}_{meas}, not R^{probe} *vs.* E^{jet}_{meas}). This is shown in Figure 5 for both samples. The Monte Carlo reproduces both the shape and overall normalization of our *in situ* measurement well within our systematic errors. Also shown is the fit to the Monte Carlo points. An alternate method to predict jet response using test beam particles input into ISAJET and HERWIG particle jets [10] also agrees within errors.

5 Jet Scale Correction and Verification

The cumulative correction factor is shown in Figure 6 as a function of uncorrected E_T for central jets. The upper and lower dashed lines correspond to 1σ upward and downward excursions of the total error, calculated as the sum in quadrature of all

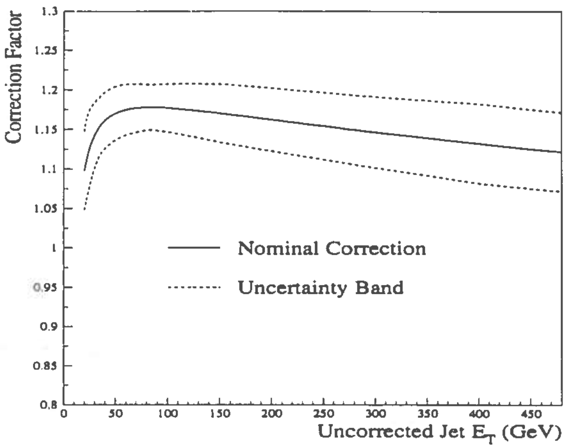

Figure 6: Total jet energy scale correction for central ($|\eta| < 0.5$) jets.

rors. These errors are dominated by systematic errors and there are substantial orrelations between errors at different energies.

We have verified that the total calibration procedure successfully obtains E^{jet}_{ptcl} from E^{jet}_{meas} using jets in the Monte Carlo sample of direct photon events. Figure shows the ratio of calorimeter and particle jet energy *vs.* particle jet energy before orrections (open circles) and after corrections (solid circles). The ratio is consistent ith unity after corrections.

Conclusions

Ve have calibrated jets in the DØ calorimeters to compensate for noise, spectator iteractions, response, and showering. The overall correction is between 10% and 8% for 0.7 cone jets above 20 GeV. The total error is about 5% below 20 GeV nd above 300 GeV, and about 2.5% at 80 GeV. The calibration is constrained by ata from 20 GeV to 350 GeV, with the portion above 150 GeV coming from EC ets. Above 350 GeV and below 20 GeV Monte Carlo data are used. Predictions f jet response in the Monte Carlo agrees with that measured in the data within rrors. An explicit comparison in Monte Carlo samples of calorimeter and matching article jet energies indicates we have correctly calculated E^{jet}_{ptcl} within errors.

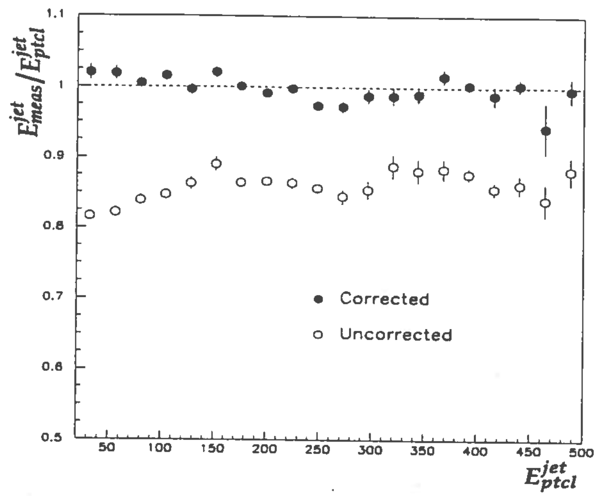

Figure 7: Ratio of reconstructed jet energy to particle jet energy *vs.* particle jet energy after (solid circles) and before corrections (open circles).

References

1. S. Abachi *et al.*, (DØ Collab.), Nucl. Instr. and Meth., **A338** (1994) 185.
2. H. Aihara *et al.*, (DØ Collab.), Nucl. Instr. and Meth., **A325** (1993) 393.
3. P. Renton, "Precision Tests of Electroweak Theories", Lepton-Photon Conference, Beijing, China (1995), OUNP-95-20.
4. S. Abachi *et al.*, (DØ Collab.), Fermilab Report No. FERMILAB-PUB-96/177-E, 1996, submitted to Phys. Rev. Lett..
   J. Kotcher, these proceedings.
5. J. Kotcher, Proc. of the 1994 Beijing Calor. Symp., IHEP - Chinese Acad. of Sci., Beijing, China, Oct. 25-27, 1994, pp. 144-158.
6. S. Abachi *et al.*, (DØ Collab.), Phys. Lett. **B357** (1995) 500-508.
7. G. Marchesini and B.R. Webber, Nucl. Phys. **B310** (1988) 461, vers. 4.6.
8. F. Paige and S. Protopopescu, Report No. BNL38034, 1986 (unpub.), vers. 7.06.
9. D. Green, Fermilab Report No. FERMILAB-TM-1958, 1996.
   C. Fabjan, Calorimetry in High Energy Physics, in Experimental Techniques in High Energy Physics, Ed. T. Ferbel, Addison-Wesley, 1987.
10. D. Stewart, Proc. of the 3rd Int. Conf. on Calor. in High Energy Phys., Corpus Christi, Texas, Sep. 29 - Oct. 2, 1992, pp. 741.

ascati Physics Series Vol. VI, (pp. 359–368)
INT. CONF. ON CALORIMETRY IN HEP – Frascati, June 8–14, 1996

ALIBRATION OF KLOE E.M. CALORIMETER MODULES WITH COSMIC RAYS: TEST SETUP AND PRELIMINARY RESULTS

Paolo Gauzzi
Dipartimento di Fisica Università La Sapienza, Roma and Sezione INFN di Roma I
for the KLOE e.m. calorimeter group*

ABSTRACT

Cosmic Ray test Stand has been setup at the Laboratori Nazionali di Frascati of IFN, to test the modules of the KLOE electromagnetic calorimeter. The massive st has started in May 1995. The results concerning 14 out of 24 barrel modules id an end-cap one show that the quality of the modules is improving and fulfils e experimental specifications: a time resolution of 55 ps/$\sqrt{E(GeV)}$ and an energy solution of 4.7%/$\sqrt{E(GeV)}$ for electromagnetic showers can be extrapolated. An jualization at 2% level of the response of the calorimeter read-out cells is performed.

Introduction

he e.m. calorimeter [1] of the KLOE experiment [2] is a sampling calorimeter made scintillating fibers embedded in lead. It consists of a barrel, 24 modules with apezoidal cross-section, approximating a cylinder of 4 m inner diameter, 4.3 m ngth and 23 cm thickness, and of two end-caps, of 4 m diameter, each consisting 32 "C" shaped modules of various lengths, and of 23 cm thickness. Scintillating bers run longitudinally in the modules, *i.e.* almost perpendicular to the direction

***The KLOE e.m. calorimeter group**: M.Antonelli,[c] F.Anulli,[c] G.Barbiellini,[j] H.Beker,[f] Bertolucci,[c] C.Bini,[f] C.Bloise,[c] G.Cabibbo,[g] R.Caloi,[f] P.Campana,[c] F.Cervelli,[e] G.De Zorzi,[f] G.Di osimo,[f] A.Di Domenico,[f] S.Di Falco,[e] O.Erriquez,[a] A.Farilla,[a] A.Ferrari,[f] P.Franzini,[f,d] A.Galli,[f] .Gauzzi,[f] S.Giovannella,[c] E.Graziani,[h] S.W.Han,[c,b] M.Incagli,[e] W.Kim,[i] G.Lanfranchi,[f] J.Lee-ranzini,[c,i] T.Lomtadze,[e] S.Miscetti,[c] F.Murtas,[c] F.Scuri,[j] E.Spiriti,[h] L.Tortora,[h] G.Venanzoni,[e] .Wölfle,[c] J.Q.Zhang.[c,b] ([a]Universitá and INFN, Bari; [b]IHEP of Academia Sinica, Beijing, China; NFN - LNF, Frascati; [d]Columbia University, New York; [e]Universitá and INFN, Pisa; [f]Universitá ıd INFN, Roma I; [g]Universitá and INFN, Roma II; [h]INFN - ISS, Roma; [i]State University of ew York at Stony Brook; [j]Universitá and INFN, Trieste/Udine.)

of the incoming particles. Two types of fibers, both emitting in the blue region of the spectrum, are used: Kuraray SCSF-81 fibers in the front half and Pol.Hi.Tech. 0046 fibers in the rear half of each module. The read-out granularity is about 4.4×4.4 cm^2. A more detailed description of the KLOE calorimeter and of the construction techique can be found in another paper in these proceedings [3].

A stand has been setup at the L.N.F. to test the calorimeter modules with minimum ionizing particles (m.i.p.s) from cosmic rays. The aim of this test is to control the module quality, to provide a first calibration and to equalize the response of the calorimeter read-out channels.

After a year's test on the full size barrel prototype (module Ø), also tested in 1994 at PSI with electron, muon and pion beams [4], a massive test of the calorimeter modules has started in May '95. Up to July '96, 14 barrel modules and an end-cap one have been tested with cosmic rays.

In this paper the stand setup is described, and the results of the cosmic ray test are presented.

2 The Cosmic Ray test Stand (CRS)

The barrel module to be tested is placed between the two halves of a telescope for cosmic rays (fig.1); each half consists of six $60 \times 7 \times 3$ cm^3 NE110 scintillator slabs and 2 planes of 310×64 cm^2 Limited Streamer Tubes (LSTs) with longitudinal and transverse coordinate read-out by means of 1 cm pitch aluminium strips. Between the barrel module and the bottom part of the telescope is placed a 5 cm thick layer of lead, to harden the spectrum of the particles triggering the apparatus. One or more end-cap modules can be placed on the top of the iron structure supporting the telescope, and tested together with a barrel one. A scintillating fiber counter, 350 cm long and 15 cm wide, can be placed above the end-cap module to improve the tracking.

The trigger requires a top-bottom coincidence of scintillators or LSTs. The trigger rate is about 20 Hz. In a Standard Calibration Run (SCR), defined as a 5 day full time data taking, about 3×10^6 events are collected.

Since the aim of the test is to study the response of the calorimeter module to m.i.p.s, a selection offline of single track events is performed. In order to have an uniform energy release in the calorimeter cells, an angular cut of 15^o around the vertical is applied, and the tracks crossing the vertical separation surface between two adjacent cells are rejected. This filtering procedure reduces the m.i.p. sample to about 3×10^5 events per SCR, corresponding to about 3×10^4 good events per calorimeter cell over the whole length (3 m) covered by LSTs.

During the test the calorimeter modules are equipped with the fine-mesh PMs Hama-

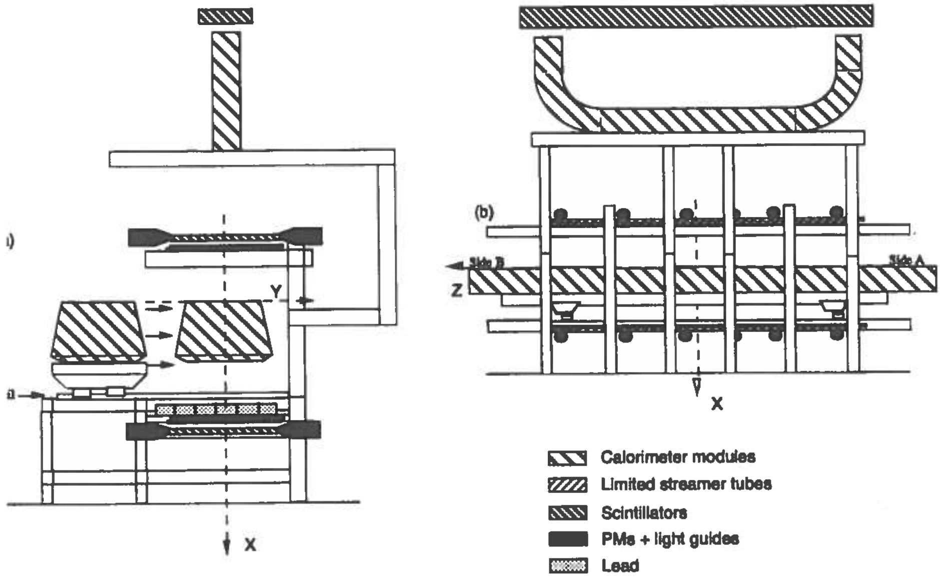

igure 1: Schematic view (not in scale) of the Cosmic Ray test Stand: (a) front iew, (b) side view.

ıatsu R5946, read-out via the KLOE front-end electronics.

Quality controls

'he pulse height and time spectra of each read-out channel are studied to control he quality of the modules. From the pulse height analysis the light yield and the ttenuation length λ are measured, while from the time spectra the light velocity in he fibers and the time and Z-coordinate (along the fibers) resolutions, σ_T and σ_Z, are btained. Since has been observed that both σ_T and σ_Z scale as $1/\sqrt{N_{pe}}$ [5], where N_{pe} is the number of collected photoelectrons, they can be taken to characterize the ght yield in an independent way from the pulse height.

.1 Pulse height

'he charge Q_{mip} collected for m.i.p.s impinging at the module center (Z=0) has been hosen to measure the light yield. In fig.2.a an example of pulse height spectrum or particles crossing a calorimeter cell in a 20 cm wide region around the center is

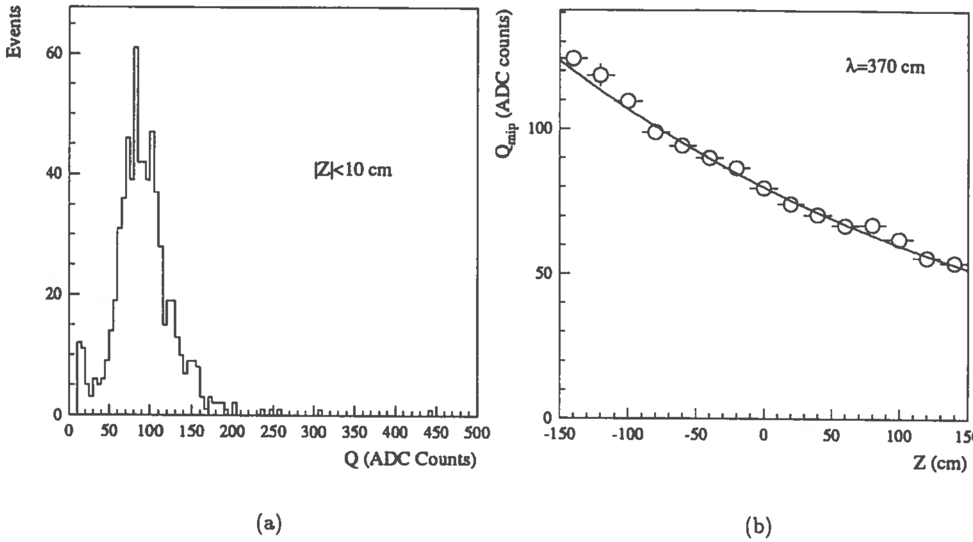

Figure 2: a) Example of ADC distribution for m.i.p.s crossing the module center, b) Q_{mip} as a function of Z.

reported. The peak of the spectrum is fitted to get Q_{mip}.

To measure λ for each calorimeter cell, an attenuation curve like that of fig.2.b is fitted to a single exponential function. The attenuation curve is obtained by looking at the signal coming from one side of the cell: the region covered by the LSTs (about 3 m long) is divided into fifteen 20 cm wide slices, for each slice the peak of the pulse height spectrum is fitted and then plotted versus the Z-coordinate of the center of the slice. This procedure is repeated also for the other side of the cell.

In a SCR Q_{mip} can be measured to an accuracy of 0.5%, corresponding to 0.5 ADC counts, and the attenuation length at 2%, corresponding to about 10 cm.

3.2 Time resolution

Since the LST trigger has a large intrinsic time jitter, the time resolution can only be evaluated by means of time differences in which the jitter cancels out. The differences ΔT_i of the mean times of two superimposed cells crossed by the same track are considered:

$$\Delta T_i = \frac{1}{2}(T_i^A + T_i^B) - \frac{1}{2}(T_{i+1}^A + T_{i+1}^B) \tag{1}$$

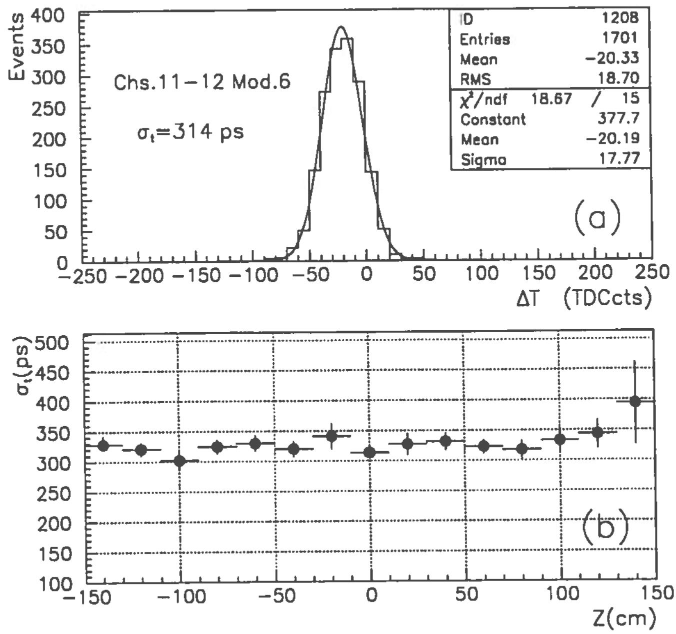

igure 3: (a) Example of ΔT_i distribution (for $i = 11$) for module 6; (b) σ_T as a ınction of Z.

and B refer to left and right sides of the *i*th and (*i+1*)th cells. Assuming that the ells have the same time response, the width of this mean time difference divided y $\sqrt{2}$ gives the time resolution σ_T. An example is shown in fig.3.

.3 Z-coordinate resolution

'he left-right time difference is directly related to the Z-coordinate of the impact oint of the particle on a calorimeter cell(fig.4.a):

$$Z = \frac{1}{2}(T_A - T_B - \Delta T_0)v_f \tag{2}$$

,here v_f is the effective velocity of light in the fibers.
n a SRC v_f can be determined to an accuracy of 0.5% and the constant ΔT_0 with a tatistical uncertainty of about 10 ps. The average value found for v_f is 16.9 cm/ns. n fig.4.b the distribution of the difference between the reconstructed Z coordinate Z_{rec}), according to eq.(2), and Z_{fit}, extrapolated from the LSTs, is shown for a ıarrel cell. Since the resolution on Z_{fit} is negligible ($\sim$ 3 mm), the width of the listribution gives the Z-coordinate resolution, that turns out to be $\sigma_Z \simeq 5 \div 5.5$ cm.

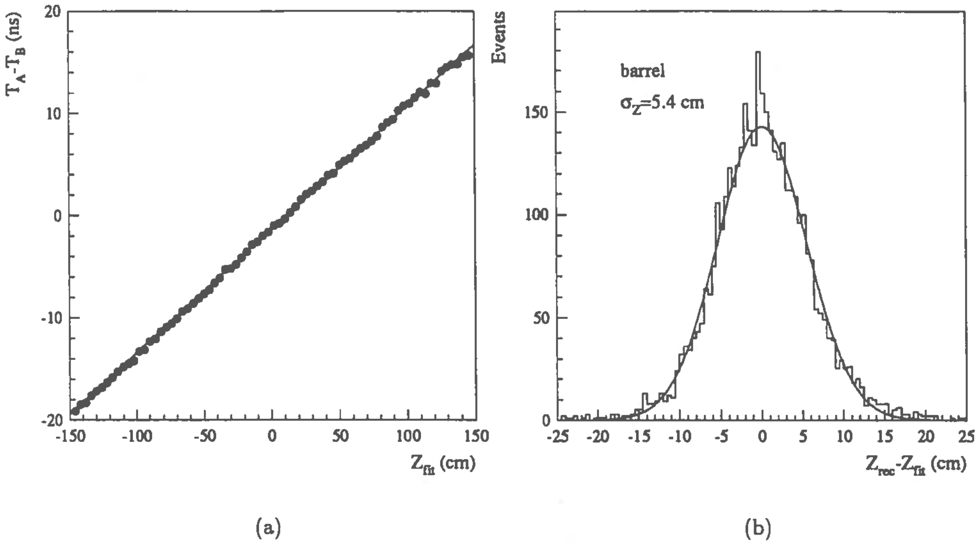

Figure 4: Examples of (a) left-right time difference vs Z_{fit}, and (b) Z-resolution for a barrel cell.

4 CRS test results

The results concerning the tested modules are summarized in fig.5, where the average values of λ and $\sigma_T(Z = 0)$ for both fiber types are plotted as functions of the barrel module construction number. Also the average λ and σ_T of module $\emptyset$ are reported for comparison. A relevant improvement can be noticed in both quantities respect to module $\emptyset$. There is a 20% improvement in λ for Kuraray fibers, mainly due to the reduction of the irradiation damage by the UV component of room-light [6], obtained by shielding with UV filters the construction halls of the modules. For Pol.Hi.Tech. λ increases of about 30%, due to a general quality improvement of the fibers. The average attenuation length is $< \lambda >$=425 cm, very close to the barrel length, for Kuraray and is $< \lambda >$=320 cm for Pol.Hi.Tech. fibers.

An analogous improvement respect to module $\emptyset$ can be observed in the light yield, by looking at the σ_T plot.

The modules from $\emptyset$ to 6 (excluding modules 2 and 5) were equipped with R5946-01 PMs, while from module 6 on, R5946-02 PMs, with improved quantum efficiency (QE), have been used. The improvement in QE has been measured with module 6, tested with both types of PMs: σ_T decreases of about 15% corresponding to a 30% rise in QE, in agreement with Hamamatsu data sheets. As expected, no

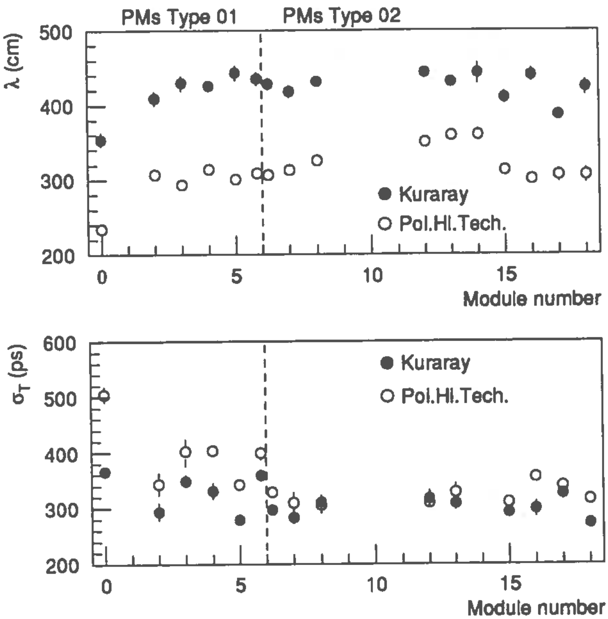

Figure 5: Average λ and $\sigma_T(Z=0)$ vs barrel module number.

ferences are observed in λ.

Since the energy deposited by a m.i.p. in a calorimeter cell is equivalent a 32 MeV photon [4], it is possible to extrapolate from the CRS results the lorimeter performance for e.m. showers. In tab.1 the extrapolations from the RS test are compared to the test-beam results on module ∅. The good quality the modules reflects in a ~25% improvement in σ_T and σ_Z. The improvement σ_E/E is less relevant, due to the fact that the energy resolution of the KLOE lorimeter is dominated by the sampling fluctuations [5]. All the figures reported tab.1 well match the KLOE specifications [1].

End-cap test

n end-cap module with a 3.4 m long straight part has been tested at the CRS. For uraray fibers $<\lambda>$=440 cm and $<\sigma_T>$=260 ps have been measured, while for ol.Hi.Tech. fibers $<\lambda>$=320 cm and $<\sigma_T>$=265 ps have been found. These easurements are in good agreement with the barrel ones, taking into account the wer length of the fibers in this end-cap module. This means that the presence the curved sections in the end-cap modules does not affect the light yield and ropagation in the fibers.

Table 1: Module performance.

	PSI test-beam (Mod.∅)	CRS tests (Mod.2÷18)
$\sigma_T(Z=0)$	72 ps/$\sqrt{E[GeV]}$	55 ps/$\sqrt{E[GeV]}$
$\sigma_Z(Z=0)$	1.2 cm/$\sqrt{E[GeV]}$	0.9 cm/$\sqrt{E[GeV]}$
σ_E/E	5.0%/$\sqrt{E[GeV]}$	4.7%/$\sqrt{E[GeV]}$

6 Equalization

In order to set a good working point for the PMs and to avoid correcting weights when summing PM analog signals for the KLOE trigger, an equalization of the response of the calorimeter cells is performed.
As equalization point an average response of 15 pC per side per m.i.p. crossing the module center has been chosen, in order to match the range of the expected signals in the experiment.
The equalization procedure is the following: (*i*) the modules are equipped with their own final PMs, (*ii*) the "step 0" high voltages (HVs) are chosen, according to the PMs' gain curves, in order to get a gain of about 2×10^6, (*iii*) a two day data taking is performed to evaluate the Q_{mip} values, and (*iv*) according to the measured Q_{mip} values the HVs are adjusted to obtain 15 pC per m.i.p.. Last two points of this procedure are repeated twice. The level of equalization reached is less than 2%, as shown in the example of fig.6.

The final HVs and calibration constants are stored in the KLOE data-base as a first calibration.

7 Long term stability

In fig.7 Q_{mip} averaged over the cells of module ∅ is shown as a function of time; the first point refers to the PSI test with 450 GeV negative pions [4]. No trends are observed in Q_{mip} and in the other calibration constants in about one year of continuous test at CRS.

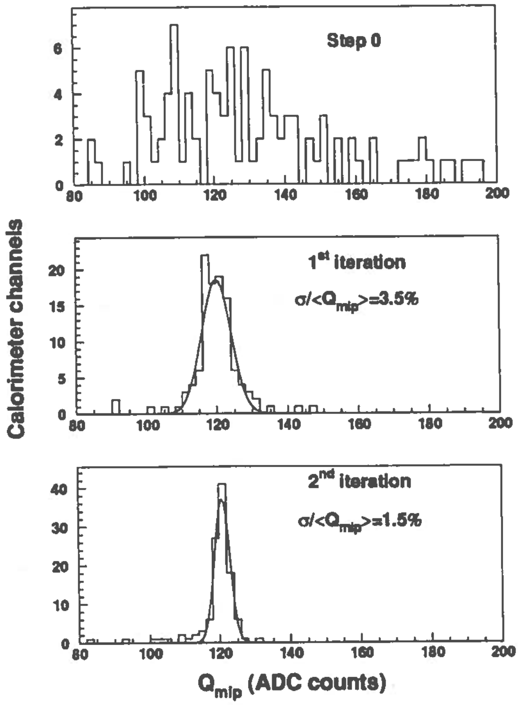

Figure 6: Example of equalization for a barrel module.

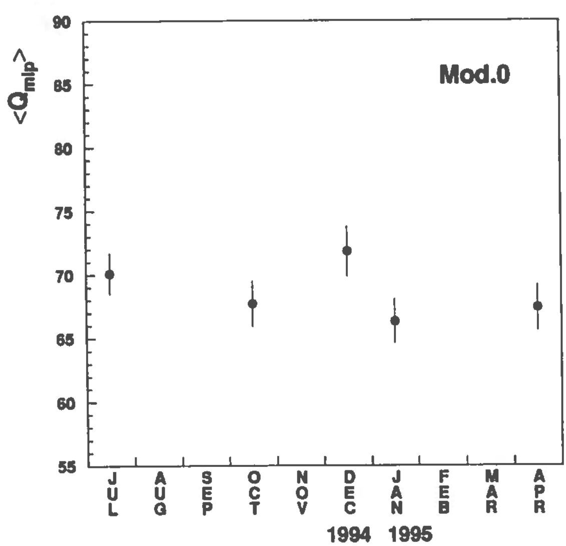

Figure 7: $<Q_{mip}>$ as a function of time for module ∅.

8 Conclusions

A massive test of the KLOE e.m. calorimeter modules is under way at the Cosmic Ray Stand facility at LNF.
This test allows to: (*i*) control the quality of the modules, (*ii*) equalize the module response at 2% level in about one week of data taking.
An improvement in the quality of the modules is observed. A time resolution of 55 ps$/\sqrt{E(GeV)}$ and an energy resolution of $4.7\%/\sqrt{E(GeV)}$ can be extrapolated from the CRS results.
The preliminary results on one end-cap module show a good quality, comparable to the barrel one.

References

1. The KLOE Collaboration, *The KLOE detector: technical proposal*, LNF-93/002 (1993).

2. The KLOE Collaboration, *A general purpose detector for DAΦNE*, LNF-92/019 (1992).

3. M.Incagli, *This conference.*

4. S.Wölfle, *Module zero, analysis of the 1994 test beam at PSI*, KLOE note No.134 (1995).

5. A.Antonelli et al., Nucl.Instr.and Meth., **A354**, 352 (1995);
J.Lee-Franzini et al., Nucl.Instr.and Meth. **A360**, 201 (1995).

6. M.Anelli et al., *Damage induced by light irradiation on blue scintillating fibers*, KLOE note No.135 (1995).

ascati Physics Series Vol. VI, (pp. 369–378)
INT. CONF. ON CALORIMETRY IN HEP – Frascati, June 8–14, 1996

A STABILITY MONITOR FOR CDF PLUG UPGRADE CALORIMETERS

D. Cauz, G. Pauletta, L. Santi
Dipartimento di Fisica dell'Università di Udine and INFN Trieste
Via delle Scienze 208, I-33100 Udine, Italy
M. Cambiaghi, G. Introzzi
Dipartimento di Fisica Nucleare e Teorica dell'Università and INFN Pavia
Via Bassi 6, I-27100 Pavia, Italy

ABSTRACT

stability monitor for the new electromagnetic and hadronic tile calorimeters for e CDF plug upgrade is described. The stability of the amplification/digitization ain will be monitored by a laser-based system, in which UV light from a pulsed, ;rogen laser is wavelength-shifted and distributed to all photomultipliers (PMT's) the calorimeters. Light pulses generated at the PMT photocathode mimic the lorimeter signal and the system power is sufficient for all ($\sim$ 2000) PMT's. Low ning jitter between remote trigger and the laser emission allows for in-beam moniring of the PMT stability. The possibility of establishing low-intensity continuous rrent in the PMT's so as to eliminate eventual rate-dependent gain instabilities the PMT's is incorporated in the design.

p to the last run, CDF plug calorimeters have been of the gas type [1]. Since the ınch crossing time in the next run (Run II) at the Fermilab collider will be as low 132 ns, their time response would be totally inadequate. New calorimeters of the intillating-tile type have been built, which will take the place of the old ones [2].

The active material in both calorimeters is scintillator SCSN38 [3], shaped tiles which are grouped together to form so-called 'megatiles'. In each tile a oove has been drilled to accomodate a Y11 wavelength shifting (WLS) fiber [3] r collecting the light produced in the tile. The fibers are then grouped together tens into optical connectors; optical cable ribbons finally transport the light into ıotomultipliers (PMT) grouped in temperature stabilized boxes.

The resolution of the calorimeters, as estimated from the engeneering prototype [2] and simulation, is expected to be:

$$\left(\frac{\sigma(E)}{E}\right)_{EM} = \frac{16\%}{\sqrt{E}} \oplus 1\% \qquad (1)$$

$$\left(\frac{\sigma(E)}{E}\right)_{HAD} = \frac{80\%}{\sqrt{E}} \oplus 5\% \qquad (2)$$

Since stability can be compromised by any of the many elements in the calorimeter, the response must be continuously monitored, preferably in a way that can distinguish between different effects. To this end, provision has been made to monitor the performance of any single tile, by means of the so-called wire source system [4], while a laser-based system will monitor the amplification/digitization chain. The system has been designed so that a single pulsed laser illuminates all of the about 2000 PMT's over both plugs and both calorimeters.

The most relevant characteristics of the monitoring system are the following

- light pulses to all PMT's are derived from a single light source
- the light pulse transmitted to the PMT's mimics the calorimeter signal
- reference detectors are redundant
- it allows stability to be monitored to better than 1% pulse-by-pulse
- it can be used to monitor stability during beam crossings
- it incorporates a means of stabilizing the PMT gain
- it can be used to check channel linearity
- it can be used to measure the PMT gain and the number of photoelectrons (n_{pe}) produced at a PMT photocathode on a pulse-by-pulse basis.

Results reported here were obtained using a pulsed nitrogen laser [5] with the following characteristics: emission wavelength: $337\,nm$, pulse width: $5\,ns$, energy stability: 3%, timing jitter: $2\,ns$. Both the emission wavelength (which can excite a scintillator) and the short pulse width are suitable for mimicking to some degree the calorimeter signals. The timing jitter, i.e. the time variability between the laser trigger and the laser emission, is sufficiently small to allow the laser-induced pulses to be synchronized (or anti-synchronized) with the the beam crossings. However energy instability is too large to satisfy our requirements and must be factorized out.

A schematic representation of the monitoring system is shown in fig.1. ght from the laser is first split in two, to feed both plugs of CDF detector. It then distributed by two primary distributors (PD, see fig.1) over 24 secondary stributors (SD), physically placed alongside of the PMT boxes (see fig.1). In fig.2, cross section of the SD is shown: we can see that the volume is divided in two ambers.

- The lower (larger) chamber has mirror-grade walls so as to maximize reflectivity. In this chamber the UV light is shifted into 430 nm blue light by means of a BC408 scintillator [6] and a part of the light reaching the chamber edge is absorbed by 90 (120 in the final design) green WLS fibers, which project into the chamber and are uniformly distributed along the circumference. These shift the blue light into 520 nm green light and feed about 4% of it to the PMT's. The exposed length of the WLS fibers can be adjusted by means of hollow screws and, by so doing, one can equalize the light signals fed to the PMT's. In fig.3 the signal uniformity over the 90 fibers of a SD, after signal equalization, is shown. The scintillator is also viewed by three PIN diodes, which serve as stable reference detectors for factoring out the laser intensity instability.

- The purpose of the upper (smaller) chamber, is that of illuminating the WLS fibers with the light of an ultra bright blue LED [7] and, by so doing, of generating a continuous current level (of the order of 2 μA at the PMT anode for initial 'burn-in' and of 100 nA during normal operation). It has been demonstrated that burn-in is necessary [8] to stabilize the PMT gain prior to data taking and that gain sensitivity to average current can be reduced by inducing a DC current of the order of 100 nA during data taking. Uniformity of the LED-induced DC current to different PMT's can be established by means of screws which shadow the WLS fibers from part of the LED light.

The fundamental redundancy in our system is obtained by the use of a ngle light-source. However one must ensure that the power of the single light urce satisfy requirements. Bench tests with our nitrogen laser show that the overall onitoring system attenuation is $A = 2.5 \times 10^8$. Given the number of photons nitted in a laser flash $n_{ph} = 4.7 \times 10^{14}$, the PMT cathode quantum efficiency $\sim 20\%$ and the maximum light yield of calorimeters $Y = 360\ pe/GeV$ [9], one ıds that the maximum number of photoelectrons at a PMT cathode can be

$$n_{pe}^{max} = \frac{n_{ph}}{A}\epsilon = 3.8 \times 10^5 \tag{3}$$

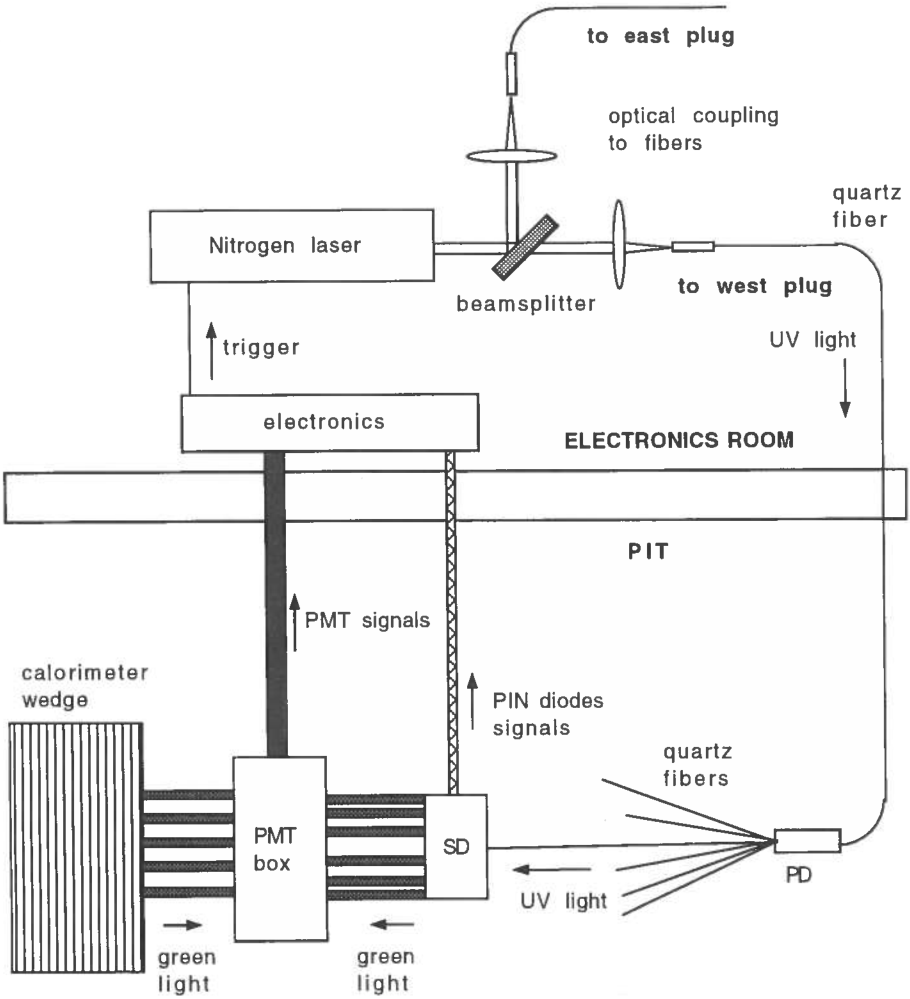

Figure 1: Schematic representation of the monitoring system

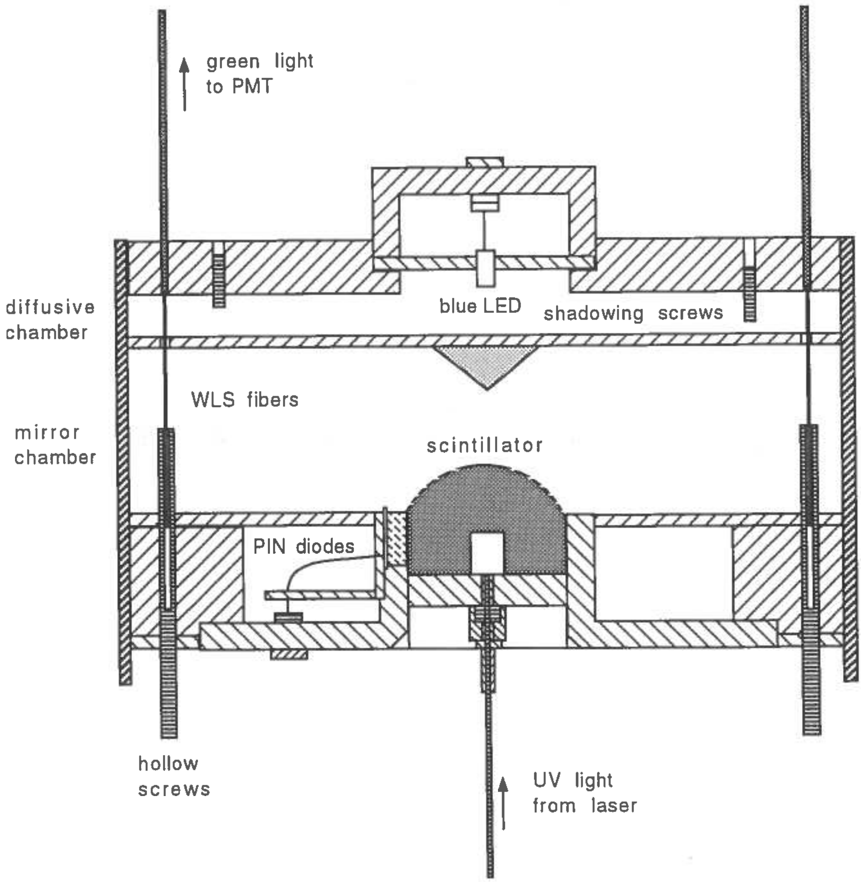

Figure 2: Cross section of the secondary distributor

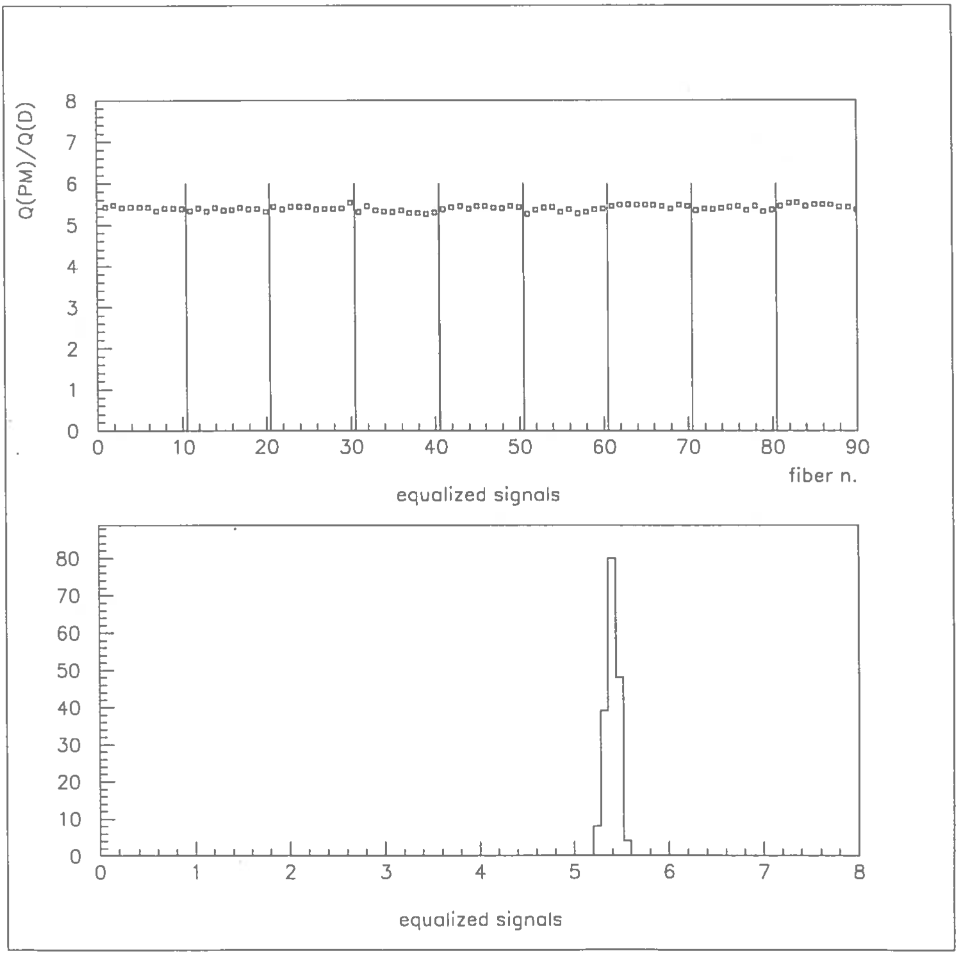

Figure 3: Azimuthal uniformity of light signals

ıich corresponds to a most energetic particle of energy

$$E_{max} = \frac{n_{pe}^{max}}{Y} = 1\ TeV \tag{4}$$

ıis is sufficient to mimic the most energetic calorimeter signals, given that the llider runs $900 + 900\ GeV$ beams and by placing a linear wedge filter downstream the laser output, we shall be able to check the channel linearity of the QIE ectronics up to $1\ TeV$.

In order to monitor stability to better than 1%, the laser instability of out 3% must be factored out. This is done by taking the ratio between the PMT ;nal and the signal of any of the three diodes (D1, D2, D3). Since both detectors the same fluctuations, the signal ratio is free of them. More precisely, let us ll S_k the integrated ADC charge of detector k measured on a laser flash: it can written as the sum of a contribution Q_k due to the laser light and the ADC edestal" P_k for detector k:

$$S_k = Q_k + P_k \tag{5}$$

ɔw consider the ratio

$$R_i = \frac{S_{PM} - \overline{P}_{PM}}{S_{D_i} - \overline{P}_{D_i}} \tag{6}$$

ıere $\overline{P}_k$ corresponds to the average charge integral, previously measured with the ser off, for detector k. This quantity must be monitored and checked for variations the order of 1%. Compare for instance figures 4a and 4b with fig 4c. The mean lue of the integrated ADC charge for both the PMT (fig 4a) and for D1 (fig 4b), ries by $2-3\%$, as both detectors feel laser instability. In fig 4c the ratio $PM/D1$ rsus time is shown, and here the fluctuations have disappeared. What remains is relatively slow trend of order of 0.3% in one hour, which is attributed to PMT gain ift (the PMT did not undergo a preliminary burn-in). Thanks to the redundancy reference diodes, this trend is confirmed by the ratios $PM/D2$ and $PM/D3$, which ow an identical pattern. We can therefore conclude that our system is capable of tecting a variation in the PMT response of less than 1%, i.e. our system meets ır stability requirement.

A final redundancy of the reference detectors is obtained by placing one MT in each PMT box in optical contact with an Americium loaded NaI crystal so .at the PM views both the light from the SD and the signal from the Americium cay. This secondary monitor will be used to verify long-term average stability.

The system can also be used to obtain an on-line evaluation of absolute MT gain. If fluctuations in the PMT signal were purely statistical, and the gain d not fluctuate, the number of photoelectrons emitted by the PMT cathode would

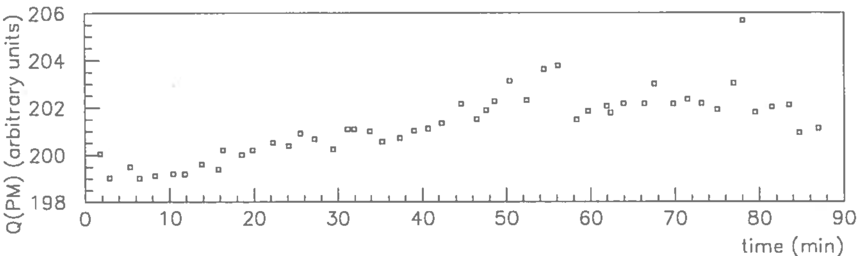

Figure 4a – integrated PM charge vs time

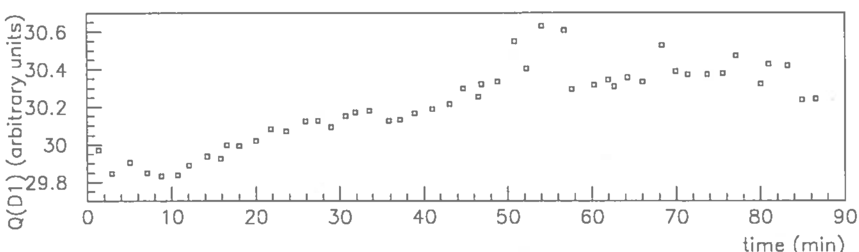

Figure 4b – integrated D1 charge vs time

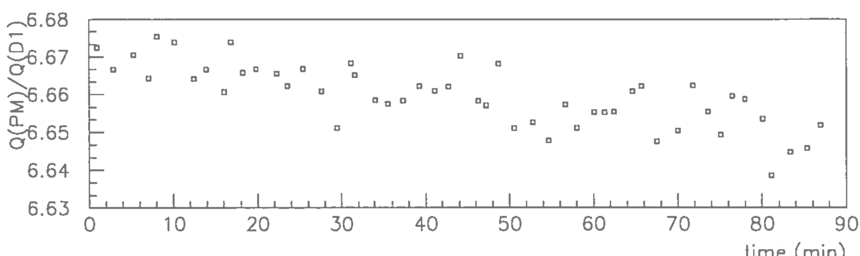

Figure 4c – PM/D1 charge ratio vs time

related to the fractional variance of the integrated PMT signal Q_{PM} by

$$n_{pe} = \frac{1}{\left(\frac{\sigma(Q_{PM})}{\overline{Q}_{PM}}\right)^2_{stat}} \tag{7}$$

our case, however, we also have a fluctuation due to the laser.

Recalling the definition of the ratio R_i, it can be shown that the statistical ıctional variance of the PMT charge can be expressed as

$$\left(\frac{\sigma(Q_{PM})}{\overline{Q}_{PM}}\right)^2_{stat} = \left(\frac{\sigma(R_i)}{\overline{R}_i}\right)^2 - PR \tag{8}$$

ıere PR represents the pedestals residuals, that can be expressed as

$$\left(\frac{\sigma(P_{PM})}{\overline{Q}_{PM}}\right)^2 + \left(\frac{\sigma(P_{D_i})}{\overline{Q}_{D_i}}\right)^2 - 2\frac{cov(P_{PM}, P_{D_i})}{\overline{Q}_{PM}\overline{Q}_{D_i}} \tag{9}$$

ɜre $cov(P_{PM}, P_{D_i})$ is the covariance between PMT and D_i "pedestals", which, as ɜll as the $\sigma(P_k)$, is previously measured with the laser off. The point is that while e left-hand part of equation 8 is not measurable (due to the laser fluctuations), e right-hand part is.

To first order, the gain is given by

$$G_0 = \frac{\overline{Q}_{PM}}{e}\left(\frac{\sigma(Q_{PM})}{\overline{Q}_{PM}}\right)^2_{stat} \tag{10}$$

ɔ take the random nature of the multiplication process into account, this expression ust be modified by including a factor $\frac{1}{1+v(G)}$:

$$G = G_0\frac{1}{1+v(G)} \tag{11}$$

here $v(G)$ is the fractional variance of the gain. This corresponds to modifying ıe equation for the number of photoelectrons by the factor $1 + v(G)$. Now the two ןuations for n_{pe} and G contain an unknown, $v(G)$, and cannot be solved any longer. /e can get around this by expressing G and $v(G)$ in terms of the n interstage mean ɪins $\overline{N}_k$ of the PMT:

$$G = \prod_{k=1}^{n} \overline{N}_k \tag{12}$$

$$v(G) = \frac{1}{\overline{N}_1} + \frac{1}{\overline{N}_1\overline{N}_2} + ... + \frac{1}{\overline{N}_1\overline{N}_2...\overline{N}_n} \tag{13}$$

'he n interstage gains are not all independent, since $n-1$ equations can be written for any $k > 1$):

$$\overline{N}_k = \left(\frac{r_{k-1}}{r_0}\right)^{p/n}\overline{N}_1 \tag{14}$$

where the r_k are the values of the resistors in the PMT amplification chain and p is the measured exponent relating the gain to the voltage applied to the PMT:

$$G = HV^p \tag{15}$$

This means that G and $v(G)$ can be expressed in terms of $\overline{N}_1$ only. So now we can express equation 11, after a small rearrangement, as a numerical equation in $\overline{N}_1$:

$$G(\overline{N}_1)(1 + v(\overline{N}_1)) = G_0 \tag{16}$$

which can be solved for $\overline{N}_1$. Hence, both G and $v(G)$ can be computed and so can n_{pe}.

To be able to perform this analysis, we need to determine the exponent p in equation 15, and this can be easily done by fitting a two-parameter curve to the mean ADC charge as a function of bias.

References

1. Y. Fukui et al., Nucl. Instr. and Meth. A267 (1988) 280.
2. G. Apollinari et al., CDF Calorimeter Upgrade Project, Proc. of the 4^{th} Int. Conf. on Calorimetry in High Energy Physics, World Scientific (1994) 200-225.
3. Kuraray International Corp., 200 Park Ave., New York, NY 10166.
4. P. de Barbaro et al., Quality Control Studies of Scintillating Tile/Fiber Megatile Production for the CDF End Plug Upgrade Hadron Calorimeter, Univ. of Rochester preprint UR-1371, CDF Note 2778 (Sep. 1994).
5. LN300C laser by Laser Photonics, Inc., Orlando, FL.
6. Bicron Inc., 12345 Kinsman Rd., Newbury OH 44065-9677.
7. BP280CWB1K LED by Ledtronics, Inc., 4009 Pacific Coast Hwy, Torrance CA 90505.
8. S. Delchamps, Shift in PMT Response to Pulsed Light as a Function of DC Anode Current, TS-DET 94-025 (May 94).
9. S. Aota et al., A Scintillating Tile/Fiber System for the CDF Plug Upgrade EM Calorimeter, CDF Note 2431 (Mar. 94).

V – Liquid Calorimeters

Convener D. Fournier
Secretary L. Bucci

Fournier	Convener's Report
Kotcher	Upgrade Plans for the DØ Calorimeter
Iconomidou–Fayard	Status of the Liquid Krypton Calorimeter of the NA48 Experiment at CERN
Seman	Optimisation of the ATLAS e.m. Calorimeter
Mansoulié	Mechanical Aspects of the ATLAS Barrel Electro–Magnetic Calorimeter
Fassnacht	ATLAS – Liquid Argon Electromagnetic Endcap Calorimetry
Stenzel	First Test Beam Results from the Liquid Argon Hadronic EndCap Calorimeter for ATLAS
N. Yakimenko	Production and Testing of Registrating Electrodes for the Liquid Argon Hadronic EndCap Calorimeter of the ATLAS Detector
S. Panin	The KEDR Liquid Krypton Calorimeter: Description and Recent Prototype Results
L. Frabetti	Measurements of Electron Drift Velocity in LKr–Methane Mixtures
Battistoni	Signal Shape Analysis as a Tool for Precision Calibration and Monitoring of the ATLAS e.m. Calorimeter

ascati Physics Series Vol. VI, (p. 381)
: INT. CONF. ON CALORIMETRY IN HEP – Frascati, June 8–14, 1996

(Convener's Report)

LIQUID CALORIMETERS

Daniel Fournier
Laboratoire de L'Accélérateur Linéaire
Université de Paris Sud – 91405 Orsay Cedex, France

Together with scintillating devices (crystals, or plastic), ionisation of noble liquids is ıe of the two main techniques for Calorimetry.

In particular, one can note that the two techniques are both present at the Tevatron, at era, and now in the planned experiments at the LHC.

With both techniques it is possible to reach high resolution by using a homogeneous ılorimeter. The use of krypton, because of its short radiation length (about 4 cm) is the 'ay chosen in the "liquid" case by KEDR (talk of V. Panin) and by NA48 (talk of . Fayard).

Concerning the large calorimeters, the session had one talk by J. Kotcher about the ıØ upgrade, and 6 talks on ATLAS (M. Seman, B. Mansoulié, P. Fassnacht, H. Stenzel, 1. N. Yakimenko, G. Battistoni). One talk was also devoted to drift speed measurements ı krypton–methane mixtures (P. L. Frabetti).

Beside the talks presented in this session, important information concerning Liquid ırgon calorimetry can be found in other sessions, in particular in the Introduction session F. Gianotti and J. Rutherfoord), in the "Non Conventional Techniques" session, in the Simulation" session, in the "Electronics" session, and finally in the "Large Systems" ession.

Since the preceding Conference (at BNL, in the fall of 1994), a good understanding ıf the prototypes for new projects has taken place (including the fast, multiple sampling eadout). Experimentalists are now engaging the construction of the full detector (NA48) or he "module zeros" (ATLAS).

rascati Physics Series Vol. VI, (pp. 383–392)
'I INT. CONF. ON CALORIMETRY IN HEP – Frascati, June 8–14, 1996

UPGRADE PLANS FOR THE DØ CALORIMETER

Jonathan Kotcher
(representing the DØ Collaboration)
Brookhaven National Laboratory
Upton, New York 11973, USA

ABSTRACT

'he DØ detector, a large collider detector located at the Fermi National Accelerator ,aboratory, has begun implementing a major detector upgrade in anticipation of the ompletion of the Main Injector project at the Fermilab Tevatron. The calorimeter eadout has been redesigned in order to accomodate the factor of $\approx$ 10 increase a instantaneous luminosity and the decrease in the inter-bunch separation. Our neans of dealing with the increased event rates, along with our plan for controlling verall noise levels in the calorimeter, are discussed. We also present a brief overview f the design for the detector upgrade, including a discussion of some of the more ogent physics topics that will be accessible with the factor of $\approx$ 20 increase over he present data sample.

Introduction

Che DØ detector, [1] located at the Fermi National Accelerator Laboratory in 3atavia, Illinois, USA, is a large hermetic detector designed to study high-p_T phe-iomena in proton-antiproton collisions at $\sqrt{s}$ = 1.8 TeV. The centerpiece of the letector is hermetic, uranium/liquid argon sampling calorimetry, designed to pro-vide high resolution energy measurements over the full solid angle. [2]

The laboratory is in the process of completing an accelerator (Main In-ector) upgrade that will increase the delivered instantaneous luminosity, $\mathcal{L}_{inst}$, by about a factor of ten (from $\mathcal{L}_{inst} \approx 10^{31}$ to 10^{32} cm^{-2}sec^{-1}). The upgraded machine s expected to begin delivering colliding beam in 1999. In order to best exploit the physics opportunities, extensive upgrades of the three major subdetectors – tracking, calorimetry, and muon – are currently underway. [3]

	Run 1	Run 2
Status	May, 1992 – Feb, 1996	$\sim$ end 1999
$\mathcal{L}_{inst}$ ($\mathrm{cm}^{-2}\mathrm{sec}^{-1}$)	$\sim 10^{31}$	$\sim 10^{32}$
$\int \mathcal{L}dt$	~ 120 pb^{-1}	~ 2 fb^{-1}
Bunch spacing	3.5 μs	396 (132) ns
Center-of-mass energy	1.8 TeV	1.8 (2.0) TeV
δM_W (MeV)	170 ($\sim$ 100)	50
δM_{top} (GeV)	11	5

Table 1: Overview of the status of the Tevatron and DØ. Representative physics benchmarks – our preliminary errors for the W boson and top quark masses – are shown for both Runs 1 and 2. (Details are in text.)

This paper is segmented into five major subsections. The first section contains a few introductory remarks. In the second section, we present an overview of the collider program at the Tevatron, a few of the physics topics accessible with the upgraded accelerator, and a short description of the overall detector upgrade. Section 3 contains a more detailed description of the internal structure of the calorimeter, including a discussion of the present readout scheme. The current and future accelerator parameters are presented in Section 4, which is followed by a description of our design for the upgrade of the calorimeter electronics. Of fundamental concern is how the noise will be affected by our design changes – this is discussed in Section 4 as well. A brief summary is presented in Section 5.

2 The DØ Upgrade

2.1 Current Status

An overview of the current status of the Fermilab collider program is shown in Table 1. We have recently completed a major collider run ("Run 1"), in which a data sample of ≈ 120 pb^{-1} was collected. Our current preliminary results for the total error on both the W mass and the top mass are as shown in the table; in parentheses is shown the W mass error we anticipate after the full analysis of the Run 1 data sample is completed. We expect to improve the precision in both of these channels by about a factor of two after the coming upgrade run ("Run 2"). The center-of-mass energy during Run 2 has not been finalized; for completeness, both of the current options are listed. Two bunch structure scenarios are anticipated (see Section 4). We note the factor of ≈ 20 increase over the current data set after Run 2.

The increase in the instantaneous luminosity, the significant decrease in the ınch spacing, and the overall physics requirements have all motivated a substantial tector upgrade. The last of these subjects is discussed in the following subsection. ıe change in the accelerator parameters has played a central role in the design of e calorimeter upgrade; we therefore defer a more detailed discussion of this subject Section 4.

2 Run 2 Physics Topics

; mentioned above, the $\approx$ 1,000 background-subtracted top candidates we expect collect should allow us to measure the top mass to $\approx$ 5 GeV. The large sample ll also allow for a measurement of the CKM matrix element $|V_{tb}|$ to $\approx$ 3%. The construction of $\approx$ 400 single top events should allow a direct measurement of the ll width of the top quark (Γ_{top}) to a precision of $\approx$ 15%.

The W and Z asymmetries will be measured to high precision, with the rward/backward asymmetry from Z decays expected to yield a $\approx$ 0.1% measure-ent of $\sin^2\theta_W$. We expect to improve the limits on the anomalous vector boson uplings by approximately an order of magnitude or more. We also anticipate a easurement of the width of the W to $\approx$ 50 MeV via the measured shape of the ansverse mass distribution.

The large b sample will allow detailed studies of $b\bar{s}$ and $b\bar{c}$ final states, as ell as enhanced searches for rare decay modes. Studies of CP violation, as statistics rmit, will also be pursued.

Monte Carlo studies have shown that the factor of $\approx$ 20 in the data set ill allow us to significantly extend our reach in searches for supersymmetry, with ass limits improving by about a factor of two over our current values. We will also ntinue to pursue searches for new, non-standard physics processes.

3 The Upgraded DØ Detector

he heart of the DØ upgrade consists of a major redesign of the tracking detectors ee Fig. 1). One of the major components will be a 2 Tesla magnetic field provided / a 2.8 m long solenoidal magnet, which will provide momentum measurements charged particles via their curvature in the field. Precision measurements of imary and secondary vertices will be provided by a silicon vertex detector (SVX), hich immediately surrounds the beampipe in the central region. Surrounding the VX is a multi-layered scintillating fiber tracker (SFT), which will provide tracking formation for charged particles in the range $|\eta| < 1.7$. [4] At the outer radius the solenoid will be a central preshower (CPS), which will provide energy and osition measurements of showering particles, enhancing electron identification over broad range in p_T. The technology for the CPS consists of triangular scintillator

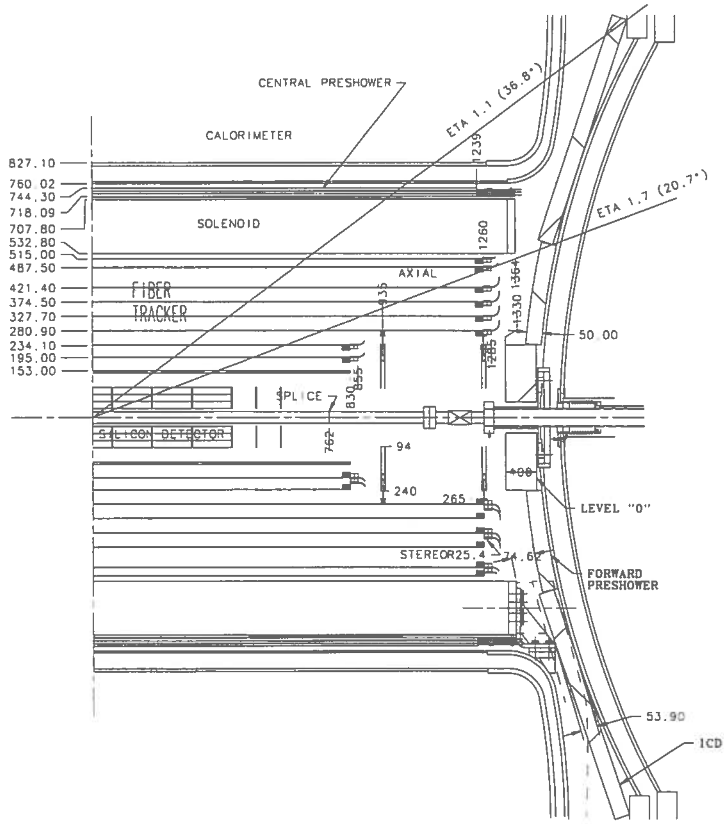

Figure 1: The view in r-z of one half of the central region of the upgraded DØ detector, showing the silicon, scintillating fiber, and preshower detectors, and the magnet solenoid.

strips with embedded wavelength shifting fibers. The speed of the SFT readout, in conjunction with new muon trigger detectors and the central preshower, will allow for fast triggering on single muons and electrons, a critical capability for exploiting the physics in Run 2.

Our design extends this capability to the forward region. A forward preshower, employing the same technology and readout as its central counterpart, will cover the range $1.6 < |\eta| < 2.5$. To complement the tracking in the central region, we have included two layers of silicon disks at more forward pseudorapidities, which extend the tracking coverage to $|\eta| \approx 3$.

Improvements in the muon system include replacing the forward drift

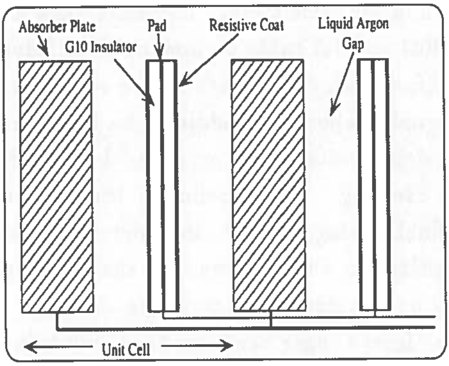

gure 2: Typical unit cell for the calorimeter, showing the gap structure, the ounded absorber plates, and the signal boards.

ambers with a version that will be more robust in the high-luminosity environ- ent, enhancing the forward shielding to reduce backgrounds, and adding both ntral and forward scintillator planes to provide fast triggering capability.

Calorimeter Structure and Readout

ıe calorimeter is housed in three cryostats – a central and forward/backward lorimeters, which together cover to $|\eta| \approx 5$ – with the inner volume consisting a series of structural modules. The readout is arranged into $\approx 5,000$ semi- ojective towers of size 0.1×0.1 in $\Delta\eta \times \Delta\phi$, and is segmented longitudinally into ectromagnetic (EM), fine hadronic (FH), and coarse hadronic (CH) sections.

Individual calorimeter modules consist of repeating sections of unit cells ch as those shown in Fig. 2, which shows a longitudinal section through a typical odule. The absorber plates vary in thickness and composition in the different lorimeter regions; the gap spacing between the signal boards and the absorber ates is 2.3 mm throughout. The substrate for the signal boards is composed of -10, which is coated with a carbon-loaded resistive epoxy to which 2.0 kV high ltage is applied. With the absorber plates at ground potential, this provides the ift field for ionization across the gap. The charge collection time is ≈ 450 ns. between the two layers of G-10 are etched copper pads, on which signals are pacitively induced by charge drifting across the gap. The G-10 plays the role of a ocking capacitor between the preamplifiers and the high voltage.

The signals are locally ganged (longitudinally) before being directed to the riphery of the modules via multi-layer boards. The details of the ganging depend on the particular location in the calorimeter. The signals are then sent to the exterior of the calorimeter via 30Ω coaxial cable to preamplifiers housed in boxes atop the cryostats. After amplification and integration, the signals are brought below the detector platform to signal shapers. In addition to performing unipolar shaping, the shapers sample the signal voltage just prior to (the "baseline") and 2.2 μs after (signal "peak") the $\bar{p}p$ crossing. The baseline is then subtracted from the peak voltage to obtain the final analog signal.[1] In order to reduce the dynamic range requirements of the digitization that follows, the shaper outputs can be amplified by 1 or by 8, depending on the size of the resulting signal.

Provided a first-level trigger has been fired (see below), the shaper output is multiplexed to analog-to-digital converters (ADC's) that have 12-bit resolution and 15-bit dynamic range. Upon receiving an appropriate signal from the software trigger, the data is then shipped to a host computer to be recorded. There are a total of 47,800 readout channels for all three cryostats.

In order to equalize the gains for all of the electronics channels (making them independent of cell capacitance), DØ employs a precision calibration pulser that injects charge directly at each preamplifier input. The pulser also monitors, and permits a correction for, any time dependence in the response of the electronics chain to charge in the system.

3.1 Relevant Accelerator Parameters

The bunch structure for Runs 1 and 2 is shown in Fig. 3. The accelerator currently delivers 6 bunches each of protons and antiprotons ("6×6" bunches), separated by a 3.50 μs gap. This gap is used to form the trigger and sample the detector baselines prior to the next crossing. The formation of this "Level 1" hardware trigger, and the subsequent transport of the signal, takes ≈ 3.0 μs, with a majority of this time (≈ 2 μs) being due to intrinsic delays in the cable that route the signals between the front end crates and the trigger framework where the decision is made.

In Run 2, the proton/antiproton bunches circulate in superbunches of 4.36 μs duration, with a 2.64 μs gap spacing between them. The laboratory expects to begin the run with a bunch spacing of 396 ns, evolving to 132 ns as the run progresses. (There will be an additional $\times 3$ more bunches per superbunch here, resulting in 108×108 rather than 36×36). This helps to reduce the number of interactions per bunch crossing, which becomes increasingly important as higher luminosities are achieved. We have been asked to design for this more restrictive 132 ns bunch spacing.

The present electronics has been designed to handle comfortably the 3.50

[1] The shapers are commonly referred to as Base-Line Subtractors, or BLS.

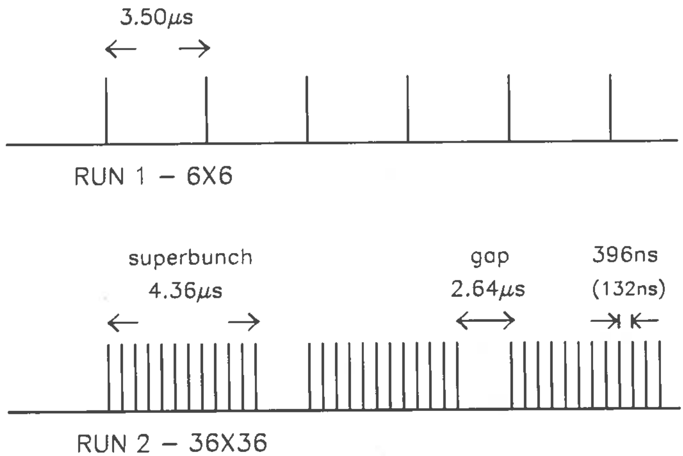

gure 3: Tevatron bunch scheme for Runs 1 and 2. Details are described in the xt. (*Diagram not to scale.*)

; inter-bunch spacing that was delivered in Run 1: the present 2.2 μs shaping time ıd 3.0 μs trigger-formation time were established with these parameters in mind. he evolution to bunch spacing times that are shorter by an order of magnitude (or ore), coupled with the increase in luminosity, dictate that major changes have to e implemented. Of most significance with regard to the calorimeter upgrade is that ıe calorimeters are welded shut and will not be changed internally. This means ıat all of the burden for adjusting to the change in accelerator parameters rests olely on the calorimeter electronics, which are external to the calorimeter cryostats.

Calorimeter Electronics Upgrade

here are two fundamental considerations that have driven the design of the upgrade ectronics:

1. Pileup noise increases with the increase in instantaneous luminosity like $\sim \sqrt{\mathcal{L}_{inst}}$. Shorter shaping times are required to reduce these effects.
2. The reduction in the minimum bunch spacing implies that some type of delay is needed to pipeline the signal.

In order to accommodate item (1), we have gone from the present 2.2 μs haping time to 400 ns. The increase in electronics noise that is associated with his decrease in the shaping time has motivated our decision to replace all 50,000 reamplifiers with a dual FET version (see Section 4.2). A low noise driver stage

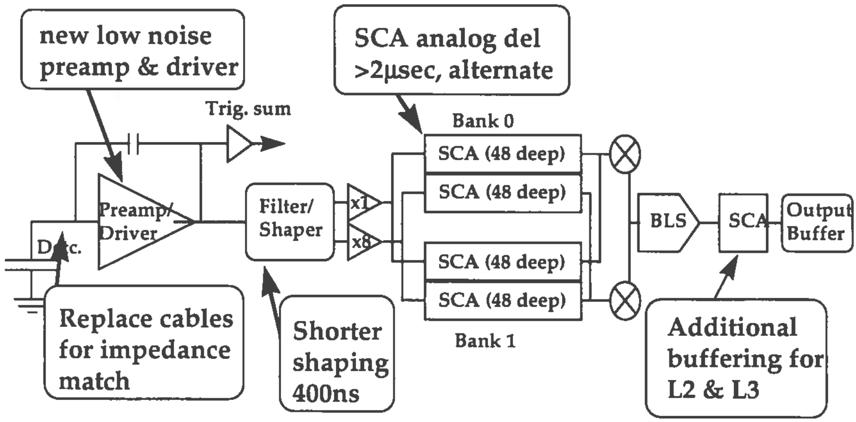

Figure 4: Schematic diagram of the calorimeter upgrade electronics.

is also being included in the preamplifier design. In response to item (2), we have opted to implement Switched Capacitor Arrays (SCA's). These are 48-element-deep analog storage devices that have been designed to provide the necessary amount of buffering capability at 132 ns crossing times. The system has been designed so that the present ADC's can be used: hence, the dynamic range and resolution of the digital readout will remain the same. A block diagram of the calorimeter electronics upgrade is shown in Fig. 4.

The $\times 1$ and $\times 8$ outputs for each channel are stored in an independent SCA element. There are two SCA banks per channel, allowing one to remain "alive" for data storage in the current crossing while the other is read out, helping to minimize dead time. An additional SCA, located just after the baseline subtraction, is used to store the data while awaiting a higher-level ("Levels 2 and 3") trigger decision. We estimate that, with the dual-bank design, there will be little or no dead time at Level 1 trigger rates up to $\approx$ 10 kHz, which is the maximum Level 1 rate we are designing for. (This assumes one trigger per superbunch). The system has also been designed to read out multiple triggers within a superbunch; this, however, is expected to result in a small but finite amount of dead time. The output SCA is used as a 48-deep buffer employed to help smooth out rate fluctuations.

4.1 *Other Modifications*

Both items (1) and (2) demand that significant infrastructure modifications be implemented as well. Approximately 1,200 110Ω cables from the cryostat feedthroughs the preamplifier inputs have been replaced with impedance-matched 30Ω cables to inimize sensitivity to reflections. A new version of the preamplifier motherboards being designed, in which pulser trace capacitances will be reduced and power feeds arranged. The BLS motherboards will be redesigned to accommodate new pinouts r SCA controls. In addition, a new timing control system, which coordinates sig-als routed between the ADC and BLS crates, is being designed. A new pulser libration system and design, which address the constraints that shorter shaping mes introduce, will also be needed for relative channel-to-channel calibration and ectronics gain monitoring.

2 *Noise Considerations*

/e have designed the upgrade electronics to provide the same noise performance as ie current readout. The electronics noise increases with shorter shaping times t as $\sqrt{t}$, but is reduced by about a factor of $\sqrt{N_{FET}}$, or $\sqrt{2}$, through the introduction f the dual FET preamplifier. Uranium noise decreases, again by $\sim \sqrt{t}$, due to ie shorter shaping times. As already mentioned, pileup noise increases by a factor $\sqrt{\mathcal{L}_{inst}}$ due to the increase in luminosity, but decreases with the shaping time by $\sqrt{t}$. As a benchmark, our current per-channel electronics noise – the *rms* width f the noise measured *in situ* that is due to electronics sources alone ($<\sigma_{el}>$) – ≈ 5 (30) MeV for the electromagnetic (hadronic) section. The *rms* width of the edestal distribution ($<\sigma_{ped}>$), which represents the contributions from uranium nd electronics noise added in quadrature, is ≈ 10 (70) MeV for each of the sections, espectively.

Using the above relations, once can compare the noise performance of the urrent electronics to that expected after the calorimeter electronics upgrade. In Run 2, the electronics (pileup) noise will increase by approximately a factor of 1.6 1.3), and the uranium noise will decrease by a factor of ≈ 2.3. The product of these ictors is about equal to unity, implying that the overall noise performance with the ew electronics at $\mathcal{L}_{inst} = 10^{32}$ cm^{-2}sec^{-1} will be comparable to that with the old lectronics at $\mathcal{L}_{inst} = 10^{31}$. A detailed simulation [5] of the pileup contribution to a enchmark measurement – the mass of the W boson – has indicated that, relative o our current W mass measurement, no additional mass or resolution bias can be xpected at the higher design luminosities with the new electronics.

.3 *Status*

Ve have developed three SCA prototypes, all of which have performed as designed. Cell-to-cell variations have been measured to be less than 0.5 mV, or ≈ 0.5 ADC ounts in our unit of readout. Ten-wafer production has recently begun, which will result in the fabrication of $\approx$ 1,000 devices. We are planning a test of a "quadrant" of electronics, which corresponds to 1/12 of the total number of channels or one preamplifier box, including the final SCA chip, this fall.

Other modifications, which include the cable replacements, BLS and preamp motherboard redesign, and preamplifier and shaper fabrication, are on track for a 1999 start date.

5 Conclusions

The upgraded DØ detector has been optimized for the physics of interest in the Main Injector era. Introduction of the silicon vertex and scintillating fiber systems, a central magnetic field, the homogeneous preshower system, and significant muon upgrades will all contribute to the accessibility of a broad range of physics at the upgraded Tevatron.

The calorimeter upgrade has been designed to respond to the challenges introduced by the increased luminosity and the change in accelerator bunch structure, enabling us to maintain the high calorimetric performance we have achieved during Run 1. The design appropriately addresses our need for data storage in the high rate environment, and controlling any associated increases in noise from the three major sources.

References

1. DØ Collaboration, S. Abachi *et al.*, *Nucl. Instr. Meth.* **A338**, 185 (1994).

2. J. Kotcher, "Design, Performance, and Upgrade of the DØ Calorimeter", *Proceedings of the 1994 Beijing Calorimetry Symposium*, IHEP - Chinese Academy of Sciences, Beijing, China, October 25-27, 1994, pp. 144-158; J. Kotcher, "Physics with the DØ Calorimeter", these proceedings.

3. DØ Collaboration, "The DØ Upgrade", DØ Internal Note # 2542 (April 17, 1995).

4. The pseudorapidity, η, is defined by the relation $\eta \equiv -\ln[\tan(\theta/2)]$, where θ is the polar angle with respect to the proton-beam direction. The z axis in the DØ coordinate system is along the beam axis, r is the distance perpendicular to that axis, and ϕ is the polar angle.

5. P. Nemethy and A. Mincer, "Pileup Effects on W Mass Measurement", DØ Internal Note # 1398 (April, 1992).

scati Physics Series Vol. VI, (pp. 393–404)
INT. CONF. ON CALORIMETRY IN HEP – Frascati, June 8–14, 1996

STATUS OF THE LIQUID KRYPTON CALORIMETER OF THE NA48 EXPERIMENT AT CERN

Lydia ICONOMIDOU-FAYARD
aboratoire de l'Accélérateur Linéaire, IN2P3 et CNRS, 91405 ORSAY FRANCE
for the NA48 Collaboration [1]

ABSTRACT

ıe NA48 detector has been designed [2] to allow the measurement of $Re(\epsilon'/\epsilon)$ in e neutral kaon system with a total error of 10^{-4}. For the detection of neutral final ıtes a Liquid Krypton calorimeter has been tested and build offering an excellent ergy, position and time resolution. In the following we present specifications of e detector, results from a small scale prototype as well as the status of the full ale apparatus.

INTRODUCTION

1 The CP symmetry

ıe non-conservation of the CP symmetry by weak interactions has been observed the system of neutral kaons in 1964, as the decay of the K_L particle to a 2 body $^+\pi^-$) final state [3]. A new formalism has been established describing the neutral .on system. Physical particles K_L and K_S, are mixtures of the two CP eigen states $_1$ and K_2. Thus the CP-forbidden decay mode becomes possible through this small ate-mixing, characterized by the mixing parameter ϵ. Since 1964, several theoreti- l works have been inspired by CP violation looking for a explanation: immediadtly ter the experimental discovery the ad-hoc Superweak Model was proposed [4] in- oducing a new force, responsible for that non-conservation. Then, in 1973, CP olation has been introduced naturally to the Standard Model [5]: in a world with families CP violation occurs due to one non vanishing phase. Thus, $K_0 \rightarrow \overline{K_0}$;cillation probability becomes different from the $\overline{K_0} \rightarrow K_0$ one. Moreover, within ıe Standard Model, a second source of CP violation would be possible: mixing excepted, a direct decay of one CP eigen state to the forbidden mode might occur through the so-called penguin diagrams. Direct CP violation, characterized by the ϵ' parameter, represents in some sens the real non-conservation of the symmetry: a given CP-eigen state sometimes doesn't obey to its own symmetry.

Direct form of CP Violation is only expected within the frame of the Standard Model. Superweak theory could therefore be validated (infirmed) by the measurement of a zero value (non zero value) of ϵ'/ϵ.

1.2 Expectations on $Re(\epsilon'/\epsilon)$

Early in the nineties, important improvements have been realized on the theoretical calculation of $Re(\epsilon'/\epsilon)$, governed by penguin contributions. First, it has been shown that electromagnetic (γ and Z) penguins dominate with respect to gluon penguins [6]. This implies that $Re(\epsilon'/\epsilon)$ value would globaly decrease when top mass increases, through γ and Z penguin contribution. Secondly, computation of hadronic matrix elements has been made up to higher orders and checked by different methods and groups [7]. Finally, the top quark has been constrained by LEP and then discovered at Fermilab having a high mass. Thus, all involved theory groups, agree today [8] to prefere a low value for $\Re(\epsilon'/\epsilon)$ ($\leq 10^{-3}$).

1.3 Recent experimental results

First generation precise experiments published their final results early in the ninenties. NA31 at CERN and E731 at FERMILAB measured $Re(\epsilon'/\epsilon)$ with precisions of the order of 7 10^{-4}. They both detect the four relevant modes $K_L,K_S \rightarrow \pi^+\pi^-$ and $\pi^0\pi^0$ and deduce $Re(\epsilon'/\epsilon)$ as follows.

$$\Re(\epsilon'/\epsilon) \approx \frac{1}{6} \times (1 - \frac{|\eta_{00}|^2}{|\eta_{+-}|^2}) = \frac{1-R}{6} \qquad (1)$$

where :

$$\eta_{00} = \frac{A(K_L \rightarrow \pi^0\pi^0)}{A(K_S \rightarrow \pi^0\pi^0)} \qquad \eta_{+-} = \frac{A(K_L \rightarrow \pi^+\pi^-)}{A(K_S \rightarrow \pi^+\pi^-)} \qquad (2)$$

It is interesting to notice that the sources of systematic effects of these experiments were quite different due essentially to the conception of K_L and K_S beams. Their respective results are compatible at 8% level: NA31 gave $(2.3\pm.7)10^{-3}$ [9] which would mean a non zero direct violation at more than 3 standard-deviations. E731's result is $(.7\pm.6)10^{-3}$, compatible with zero [10]. New generation fixed target experiments have then been studied and currently are starting to run in order to obtain more precise results (NA48 and E832 [11]) with a total error of $\approx 2\ 10^{-4}$. KLOE experiment [12] in Frascati Φ factory will also determine $Re(\epsilon'/\epsilon)$ with similar ecision in a different way. Thus, before the end of the century, one should have a tter idea about the strength of direct CP violation in the system of neutral Kaons.

THE NA48 EXPERIMENT

ıe NA48 experiment is based in the concurrent detection of four modes. Quasi llinear K_L and K_S beams of 100 GeV average energy, are produced by the 450 eV proton beam of SPS hitting beryllium targets. For a given detected decay one stinguishes between K_L or K_S origin using time information of a dedicated tagging tector [13] signing protons producing K_S beam. Tiny coincidences are then made ith the particle passage time as measured by detectors. Several detectors offer good solution time information in order to allow high final tagging efficiency through dundace use.

Unwanted 3-body charged decays are rejected down to 10^{-3} level by the use a magnetic spectrometer reconstructing Kaon mass with a resolution of 2.8 MeV. dditional rejection is offered by muon vetos and an hadronic calorimeter. The tector signes particles escaping the fiducial volume, using 7 annular scintillators aced along the decay region.

1 Specifications for the calorimeter

he electromagnetic calorimeter for NA48 has been designed in order to fulfill several nditions:

- The detector has to work in high rates environment (1MHz) due to the intense K_L beam. A fast response is therefore needed (to minimize pileup effects) as well as good stability with time.

- The detector should reject the dominant $K_L \rightarrow 3\pi^0$ decays down to 10^{-3} under the $2\pi^0$ signal in order to achieve the desired precision on $Re(\epsilon'/\epsilon)$. For that, it has to offer a good energy and position resolutions to allow the π^0 mass reconstruction with a accuracy of 1 MeV. Let us describe the way in which neutral decays are reconstructed: assuming that a kaon has decayed one imposes the total invariant mass of the event. Then the decay vertex is found using all photons energies E_i and positions (x_i, y_i) as follows:

$$Z_{K^0} = Z_{CAL} - \frac{1}{M_{K^0}} \times \sqrt{\sum_{i=1,j>i}^{4} E_i \times E_j \times [(x_i - x_j)^2 + (y_i - y_j)^2]}$$

Then, π^0's are reconstructed by making all photon combinations:

$$M_{\gamma_i\gamma_j} = \frac{1}{Z_{K^0}} \times \sqrt{E_i \times E_j \times [(x_i - x_j)^2 + (y_i - y_j)^2]}$$

The correct photon association gives π^0 mass. The precision of its reconstruction depends therefore on energy (E_i) and position (x_i, y_i) resolutions. Good granularity is thus required and a quasi-homogeneous calorimeter as well.

- The detector should also give a precise time information for the particle passage in order to distinguish K_S from K_L neutral decays making coincidences with the tagger. This implies fast response and as much as possible uniform calorimetric signal.

3 THE LIQUID KRYPTON CALORIMETER

A quasi-homogeneous Liquid Krypton Calorimeter has been finally chosen fulfilling the previous conditions. A small stochastic term can thus be obtained, free from sampling effects. The ionization signal offers the possibility to measure only the initial current [15] and to get in that way a fast response. Moreover, one can obtain precise calibration through known charge injection to the front-end electronics. The radiation length of the Liquid krypton is 4.7cm. 127cm of liquid are therefore needed to achieve a complete longitudinal containment of a shower ($27X_0$). Its Molière radius (R_M) is 4.7cm too.

3.1 The Cell structure

Electrodes are made from a Copper(98%)-Beryllium(1.8%)-Cobalt(.2%) alloy. They are 127cm long, 18mm large and 40μm thick (see figure 1) and they are held at the front and the back frames of the calorimeter with a tension of 2N.

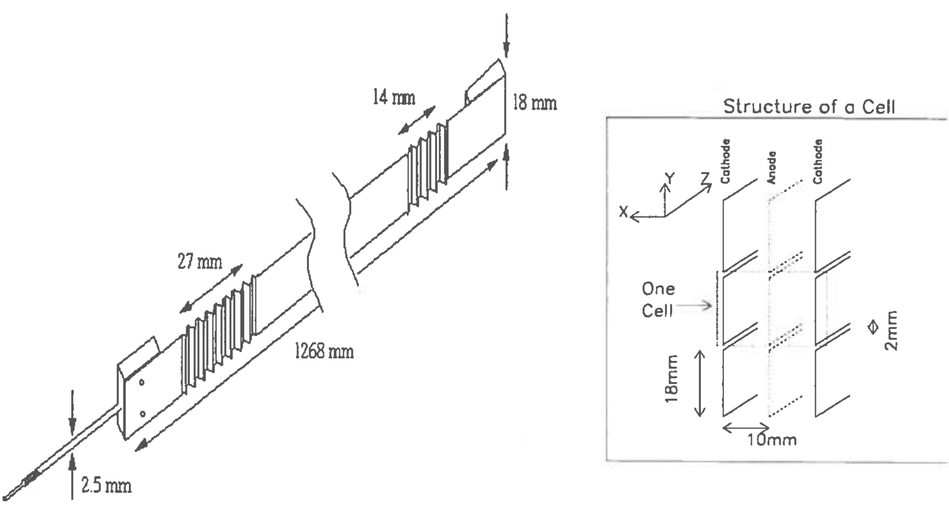

Figure 1: *One ribbon (in left). Cell definition (in right).*

Strict specifications are required for the ribbons: flatness has to be precise ±50μm, the width to ±10μm and the edges to ±100μm. During their manu- :turing two springs are formated, one on each electrode extremity, whose role is ree-fold: compensate thermal deformations during warm-up and cool-down of the uid, distribute uniformely the stretching force and enlarge positionning tolerances. ıe HV is brought through a pin threaded in the back of the electrode, which also ows the electrode readout. A cell is then defined by 3 electrodes (figure 1 right), thode-anode-cathode, with dimensions 2cm×2cm×127cm. A 2mm gap separates rticaly two cells. The gap stability is enforced by 5 spacer planes, made by 5mm G10, placed every 20.8mm longitudinaly. The second role played by these spacers to apply a small (±48mrad) angle to the ribbons (figure 2 left).

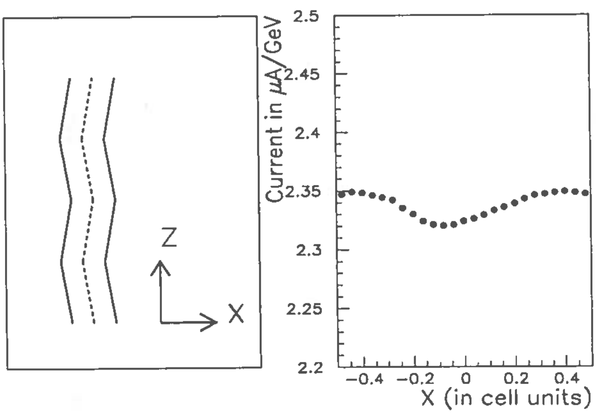

igure 2: *Longitudinal zig-zag of the cell (a). Remaining anode effect for a 48mrad g-zag.*

This *zig-zag* minimizes the region where the shower core can cross the ıode: indeed, in this case, only a part of the induced current is collected due to the nite peaking time. A remaining effect is still seen when looking at the reconstructed ıergy of a shower as a function of the impact point from the anode (figure 2 right). his so-called 'anode-effect' can be corrected offline. However, a degradation of the :solution is observed for showers crossing the cell near the anode.

.2 Readout electronics.

'his item is developped in [16] and [14]. In figure 3 a schematic view of the alorimeter readout is shown. The ionization signal is almost triangular with a uration of 2.8μs corresponding to the electron drift time at 5KV. Plugged on the lectrodes back-end, cold Si-amplifiers [15] integrate the signal with a characteristic .me of 150ns. On the feedthroughs, the signal is sent to the tranceivers [16] which

accelerate the signal (τ=10ns) and drive it differentially. Then, positive and negative signals are travelling along 16m shielded twisted cable pairs to CPD's (Calorimeter Pipelined Digitizer) [17]. There the signal is shaped (bipolar shaping as it is shown in figure 4.a) with a time τ=19ns (FWHM$\approx$ 92ns) and then sampled by a 40MHz asynchronous w.r.t the trigger 4-gain 10 bits FADC. A fast signal is needed at the CPD entrance in order to allow a fast selection of the gain to be used by the FADC. In this way the most energetic samples of the pulse will be all measured by the same gain. This assures a perfect pulse reconstruction, blinding the measurement against gain-switching imperfections.
The total dynamic range goes from -1.8GeV to 60GeV [1]. The negative range is necessary for the measurement of the undershoot part of the signal resulting from the bipolar shaping (its depth is 3% of the pulse energy).

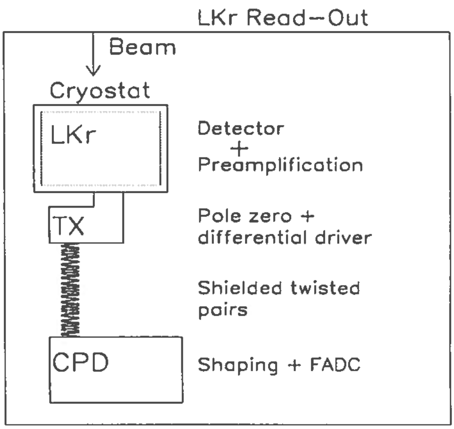

Figure 3: *Schematic view of the readout.*

3.3 Pulse reconstruction on a single cell

In figure 4.a, a typical pulse on a cell is shown as comes out from the shaping. Its positive part contains energy and arrival time information while the undershoot length is directly proportionnal to electron drift time. What one measures after FADC sampling are pulseheights every 25ns (40MHz) as is shown in figure 4.b. For energy and time reconstruction we use the three more energetic samples and fit them by a parabola whose maximum determine the energy and time. These values need to be corrected for phase dependance, since FADC sampling is asynchronous with the trigger. We point out that more elaborated algorithms, like optimal or digital [19]

[1]The average photon energy is 25 GeV. One has to detect photons from 2GeV up to 100GeV. Moreover, the most energetic cell of a shower in the calorimeter contains at most 45% of the particle energy. An additionnal contribution could be arise from pileup with accidental showers.

ers are also used, but do not improve resolution of the reconstruction since we are rking in a no-noise dominant regime. Moreover, filters require perfect knowledge pulseshape, which in our case become a heavy procedure since the pulseshape is ·ying with the distance from the anode due to the anode effect.

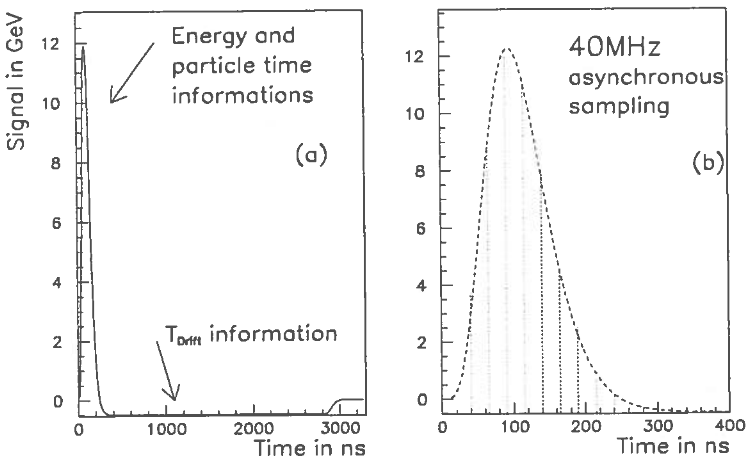

Figure 4: *Signalshape in (a). Sampled signal (b).*

PROTOTYPE RESULTS

small scale calorimeter with ≈200 channels has been build and tested under ·ctron beams. This prototype had almost the final geometry (parallel electrodes stead of projective ones converging to a point 100m far from the final detector). ·lls of the center of the prototype were equipped with CPD's (under optimization) d the rest with peak sensing ADC's. In front of the prototype, $.6X_0$ of material ıs placed to simulate final running conditions. In the following we present results ncerning energy, position and time resolution obtained during all test periods (see rresponding publications [18]).

1 Energy resolution

figure 5, the energy resolution is presented as a function of electron beam en- gy. Electron showers are reconstructed in a 11x11 cells shower box. Experimental ›ints are adjusted by the function $\sqrt{(A^2/E + (B/E)^2 + C^2)}$ with A=3.25% (sam- ing term), B=40MeV (noise term) and C=.42% (constant term). In the following, veral remarks are presented concerning the origine of A, B and C terms.

- **A term:** it is dominated by lateral leakage outside the 11x11 shower box (corresponding to $\pm 2.3 R_M$ around the impact cell) and losses in the material in front ($.6X_0$). Indeed, as it has been confirmed by Monte Carlo studies, the A term can improve by enlarging the shower reconstruction area. This shower box is however a compromize between resolution optimization and minimization of the pileup probability and electronic noise increasing with box area.

- **B term:** it is completely defined by the characteristic shaping time $\tau_{shaping}$, varying like $\tau_{shaping}^{-3/2}$. The obtained 40MeV total noise term for 11x11 cells corresponds here to a τ=22ns (FWHM≈150ns).

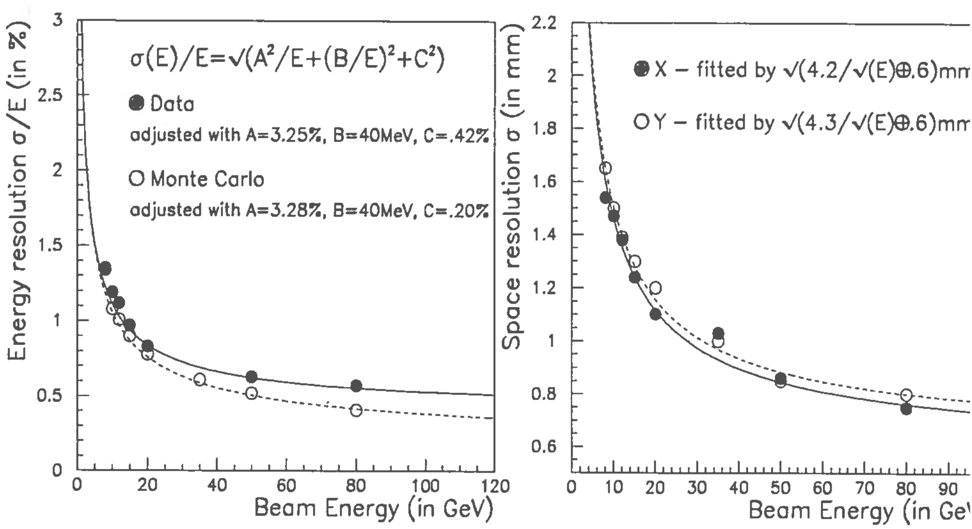

Figure 5: *Energy (left) and position (right) resolution as a function of electron beam energy.*

- **C term:** it comes from several effects. First the so-called "physics term" related to energy fluctuations. It turns out that this term depends also on $\tau_{shaping}$ through the anode effect: fast shaping limits somehow the sensitivity of the measurement to the distance of the impact point from the anode. Shaping time value has therefore opposit effects on noise (decreasing with τ) and constant (increasing with τ) terms. Secondly, calibration imperfections. From Monte Carlo studies one found that 1% spread on calibration constants implies a .4% constant term. Finally, geometry non-uniformities like gap variations from cell to cell.

A complete Monte Carlo simulation, with shower generation, realistic field maps, current collection and front end electronics simulation, describes well the ɔlution curve for 40MeV noise. For higher energies the MC constant term, taking ɔ account only physics term, is .2% to be compared to .4% adjusted to the data. s would indicate non perfect calibration constants knowledge and (or) small metry non-uniformities.

Position Resolution

ɛ Center of Gravity of electron shower is calculated using 3x3 cells around the st energetic one and compared to the track trajectory measured by small chams placed in front of the prototype. COG is then corrected for its dependence the impact point within the cell. The position resolution is shown in figure 5 ıt. For all energies above 8GeV the resolution is better than 1.6mm. The slight 'erence between x and y directions comes from crosstalk between vertical strips.

Time resolution

e arrival time of the particle can be defined as the time of the pulse maximum $_{AX}$) in the impact cell. This time can be evaluated by a parabolic fit of the ee most energetic samples. In figure 6, the time resolution is shown for two data iods (1994 and 1995) differing only by the characteristic time of the shaper. A ıstant term of 160ns, due to the trigger resolution, has to be unfolded.

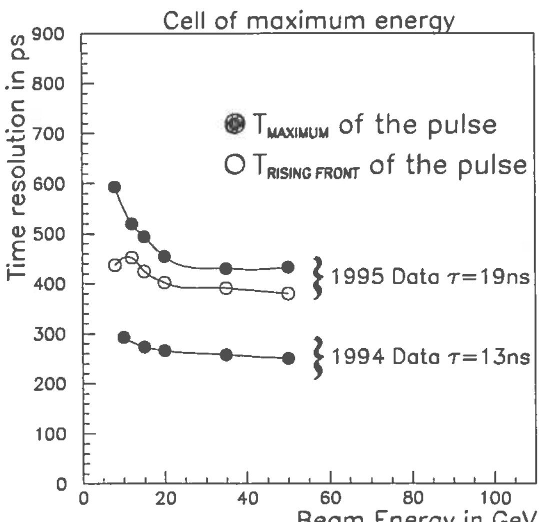

Figure 6: *Time resolution obtained for two different shaping times.*

For our frontend electronics T_{MAX} is related to the electron drift time t_{drift} d the shaping time $\tau_{shaping}$ in the following way:

$$T_{MAX} \approx 5 \times t_{drift}/(1 + t_{drift}/\tau_{shaping}) \Rightarrow \partial T_{MAX}/\partial t_{drift} = 5 \times (\tau_{shaping}/t_{drift})^2$$

For two different shaping times $\tau^1_{shaping}$ and $\tau^2_{shaping}$, fluctuations on T_{MAX} are then given by:

$$\partial T^1_{MAX} / \partial T^2_{MAX} = (\tau^1_{shaping} / \tau^2_{shaping})^2$$

Time resolution is therefore varying like $(\tau_{shaping})^2$. This is easy to understand from a phenomenological point of view and it is again related to the anode effect: the current deviates from its triangular form from one event to the other, as a function of the impact distance from the anode. Short shaping minimizes the sensitivity of the measurement to current fluctuations and therefore the constant term (as well as a part of the constant term of energy resolution too). In 1994, $\tau_{shaping}$ was 13ns while for 1995 data it was 19ns. The observed corresponding constant terms are well described by that difference: their ratio is 2.1, equal to the square of shaping times ratio (after subtraction of the common trigger resolution). For both data periods time reconstruction is precise to better than 600 psec for particle energies greater than 8GeV. One can improve the resolution by choosing another time estimator, namely T_{rising}. It corresponds to the time at the middle of the rising front of the signal and it is even less sensitive to signal fluctuations, simulating a earlier shaping (figure 6 for 1995 data).

5 STATUS OF THE CALORIMETER

The full scale calorimeter is since last May in the experimental area, joining the rest of the NA48 subdetectors. It represents a structure of 2.5m×2.5m×127cm, containing ≈13000 cells. Cold electronics is completely equipped and the cryostat is being filled (July 1996) with Liquid Krypton (≈10m^3). Tranceivers and CPD's will be installed beginning of August. Due to a limited delivery of CPD's at that time, sums of 2x8 cells will be readout for the upcoming August-September run under Kaon beams. In addition, single cells will be tested with electron beam in order to study pulseshape and resolution with the final electronics. The first 'physics' run with fully equipped calorimeter (all single channels) is foreseen for April 1997.

ferences

NA48 is a Cagliari, Cambridge, CERN, Dubna, Edinburgh, Ferrara, Firenze, Mainz, Orsay, Perugia, Pisa, Saclay, Siegen, Torino, Vienna, Warsaw collaboration.

G.Barr et al., 'Proposal for a precision measurement of ϵ''/ϵ in CP violating $K^0 \rightarrow 2\pi$ decays', CERN/SPSC/90-22 SPSC/P253, 20 July 1990.

J.H. Christenson, J.W. Cronin, V.L. Fitch and R. Turlay, Phys. Rev. Lett. **13**, 138 (1964).

L.Wolfenstein, Phys. Rev. Lett. **13**,562 (1964).

M.Kobayashi and K.Maskawa, Prog. Theor. Phys. **49**, 652 (1973).

J.M.Flynn and L.Randall, Phys. Lett. **224B**, 22 (1989),

G.Buchalla,A.J.Buras and M.K.Harlander, Nucl. Phys. **B337**, 412 (1990).
A.Buras, M.Jasmin and M.K.Lautenbacher, CERN-TH-6821/93.
M.Lusignoli, L.Maiani, G.Martinelli and L.Reina, Nucl.Phys. **B369**, 139 (1992).
S.Bertolini, J.O.Eeg and M.Fabbrichesi, SISSA 103/95/EP.
E.A.Paschos and Y.L.Wu, Mod.Phys.Lett. **A6**, 93 (1991).

Round table on computation of $Re(\epsilon'/\epsilon)$ at the Workshop on Kaon Physics, Orsay May 30-June 4rth 1996.

G.Barr et al., Phys. Lett. **B317**, 233 (1993).

L.K.Gibbons et al., Phys. Rev. Lett. **70**, 1203 (1993).

K.Arisaka et al., KTeV Design Report, FN-580.

V.Patera, 'KLOE status report', Workshop on Kaon Physics, Orsay May 30-June 4rth 1996.

P.Grafström et al., CERN-PPE/94-11.

C.Cerri, contribution to the proceedings of this conference.

V.Radeka et al., NIM **A265**, 228 (1988).
C.Cerri et al., NIM 227, 227 (1984).

G.Martin-Chassard, C.de la Taille, N.Seguin-Moreau, contribution to the proceedings of this conference.

17. B.Hallgren et al., NA48 note 96-4.
F.Bal et al., NA48 note 96-1.

18. V.Fanti et al., NIM **A344**, 507 (1994).
G.D.Barr et al., CERN-PPE/95-64.

19. W.E.Cleland and E.Stern, NIM **A338**, 467 (1994).
S.J.Inkinen, FIROSMIN 3.2, CERN-ECP-RD12 94.

OPTIMISATION OF THE ATLAS e.m. CALORIMETER

M. Seman
stitute of Experimental Physics, Slovak Academy of Sciences, Košice, Slovak Republic

Written contribution not received

ascati Physics Series Vol. VI, (pp. 407–416)
I INT. CONF. ON CALORIMETRY IN HEP – Frascati, June 8–14, 1996

MECHANICAL ASPECTS OF THE ATLAS BARREL ELECTRO-MAGNETIC CALORIMETER

Bruno Mansoulié
DAPNIA-SPP, CE-Saclay, FRANCE

ABSTRACT

he design of the barrel electro-magnetic calorimeter for ATLAS is well advanced. his paper presents the design from the point of view of mechanics, emphasizing the ɔints which were particularly studied for their relevance to the physics performance. he construction scenario shown here will be put at work in the summer of 1996 for aking the module 0, which should be completed in the fall of 1997.

General features.

general description of the detector can be found in the ATLAS Technical Proposal) and in the talks by F. Gianotti and M. Seman at this conference. The main ements for mechanics are summarized in this paragraph.

1 The barrel cryostat

s all the electro-magnetic calorimetry in ATLAS, the barrel is based on accordion ıaped absorbers and electrodes immersed in liquid argon used as the detection edium. It is housed in toroidal cryostat of internal radius 1150 mm, external dius 2250 mm, and length 6900 mm. The cryostat is vacuum insulated, with both ıells in aluminum. At the inner radius, in front of the calorimeter, the insulating ıcuum contains the thin superconducting solenoid which provides the magnetic eld in the inner detector cavity. The calorimeter signals are routed outside the yostat by 32 feed-throughs distributed evenly in azimuthal angle ϕ at each end of ıe barrel.

1.2 The detector

The design of the detector for ATLAS follows largely from the experience gained from the construction and operation of the "2m" prototype since 1992 [2].

In ATLAS, the central electromagnetic detector is made of two *identical* half-barrels ($z < 0, z > 0$). The accordion calorimeter contains 1024 stainless steel coated lead absorbers distributed in ϕ, alternating with the same number of multi-layered read-out electrodes. For practical reasons, it is constructed in 16 modules of 64 elementary sets (absorber + electrode + connectics). In front of the accordion calorimeter, just behind the cryostat inner cold wall, there is a pre-sampler used to measure and correct for energy losses in the inner detector, coil, and cryostat walls. This presampler is also divided in ϕ, into 32 modules.

1.3 Structures and services

The accordion modules are not consistent enough to be made alone into a barrel. For each half-barrel, 7 external rings provide the necessary structure. They are segmented in ϕ to allow each module to be assembled with its ring segments early in the assembly scenario. At the inner radius, 7 internal belts (also segmented) connect the modules together.

The currents induced by the ionization on the electrodes are summed by printed circuit boards tiled all over the inner and outer faces of the calorimeter. They are then driven to the feed-throughs by cables which run on the inner and outer faces. Cooling pipes flowing liquid nitrogen run along the barrel on its outer face. Fig.1 shows a view of one module with its external rings segments and the presampler modules installed (the absorbers other than first and last have been removed for clarity).

2 Absorber design

The absorber (fig.2) is made of a lead sheet sandwiched between two thin (0.2 mm) stainless steel sheets, glued with pre-impregnated fiberglass cloth (pre-preg). The sandwich is shaped as an accordion with 13 folds parallel to the barrel axis, with the edges at the inner and outer radii encased into G10 bars. These very precisely machined bars ($R \times \phi$ thickness accurate to better than 10 μ) locate the absorber in space.

Detailed simulations of the high energy response have shown that the total thickness seen by particles must be at least 24 X0. On the other hand, the resolution at medium energies is better if the sampling fraction is higher, meaning less X0's in the same radial space. One would thus like to adjust the lead sheet thickness

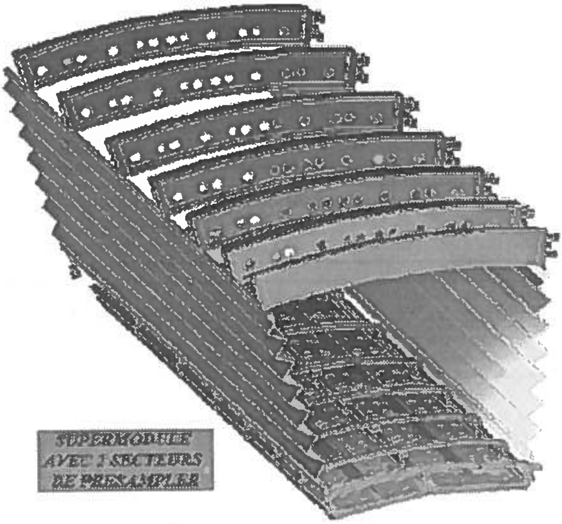

Figure 1: View of a module with external rings and presampler modules

ith the pesudo-rapidity η, to provide always 24 X0's. For simplicity, only two ıicknesses are used: 1.5 mm for $\eta < 0.8$ and 1.1 mm for $\eta > 0.8$. Assuming for moment that the accordion folds were sharp, it is easy to see that the material aversed by a particle would be uniform in ϕ if the ϕ opening of the accordion ould be an integer multiple of $2\pi/1024$, the pitch between absorbers. The chosen ultiple is 4, which corresponds to the number of gaps summed in ϕ to make a ad-out cell. However, the folds have a 2 mm radius of curvature, which introduces non-uniformity in ϕ. This effect is minimised by tuning the actual opening angle $(1+\epsilon) \times 2\pi/1024$, with $\epsilon = 0.017$.

The thermal and mechanical behaviour of the accordion absorber has been udied with care. Due to its composite structure, the folding angles close during ɔol-down, hence the radial width of the absorber shrinks more than a solid material: mm over the 500 mm width. This has to be taken into account : the shape is ɔtimised at cold temperature, then the shape at ambient temperature is computed ır fabrication (also the shape at the polymerisation temperature for designing the uing press).

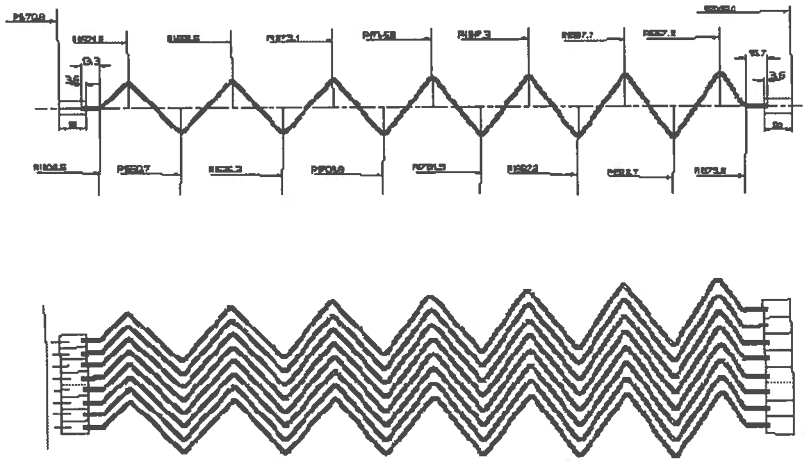

Figure 2: Geometry of the absorbers in the $R \times \phi$ plane

3 Electrode design

In between two absorbers there is a 3-layer electrode, which makes two 2 mm gaps, maintained by an honeycomb spacer. The electrode has three layers (fig.3): on each face, the high-voltage layer is made of resistive coating (copper in the folds); inside, the signal layer is made of copper. For practical reasons, the electrode is made in two parts along the length, with the separation along the $\eta = 0.8$ line. The cell granularities in η and in R are obtained by etching the pattern on each layer, according to the optimisation from physics simulation and signal analysis. At the inner and outer radii, the signals are routed by strips on the electrode, between the absorbers G10 bars to the connectors, then the printed circuit boards, and cables. Today, 5 prototypes of a large electrode have been made, showing good geometry for the patterns and their relative alignment.

4 Presampler design

The presampler is a 1 cm cylindrical liquid argon active layer located just behind the cryostat cold wall. It is read-out by electrodes almost perpendicular to the layer, with a 2 mm gap between them. To get a uniform signal over the presampler area, the particles must cross completely at least one gap. To do so, for $\eta > 0.4$,

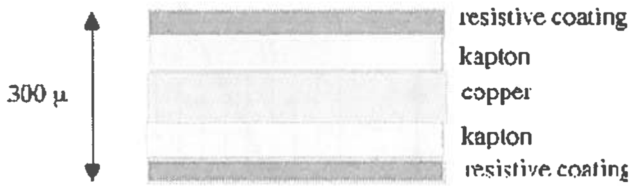

Figure 3: Structure of the 3-layer electrode

e electrodes can be just perpendicular to the beam axis, whereas for $\eta < 0.4$, ey have to be slanted (fig.4). The front face of the calorimeter is covered with esampler modules: for each half-barrel 32 modules in ϕ and 7 in η (each module ing $\Delta\eta = 0.2$ long). Each module is made simply by stacking electrodes together d gluing them with prepreg, cured in an autoclave. A prototype of the largest odule ($1.2 < \eta < 1.5$) has been realised by this method and cold-tested.

Structures and ancillaries

ıe support of a half-barrel is made by 7 external rings, located on the outer face ery $\Delta\eta = 0.2$. These are stainless steel I-beams made into a circle, and cut into 16 gments, with a strong linking feature between two segments. Special segments in e horizontal plane accomodate the support rail from the cryostat cold wall. The formation of the barrel under its load in the $R \times \phi$ plane has been computed, taking to account the weakening due to the non-continuous rings: it should amount to 5 mm maximum. The printed circuit boards of the outer face sit in-between these ngs. The cables run through holes in the rings , as well as the cooling pipes.

On the inner face, belts located every $\Delta\eta = 0.2$ secure the absorbers gether. The final material is still under study to best match the thermal properties the accordion. Connection boards sit in-between the belts, and the cables run er them. The presampler modules are fixed to these belts.

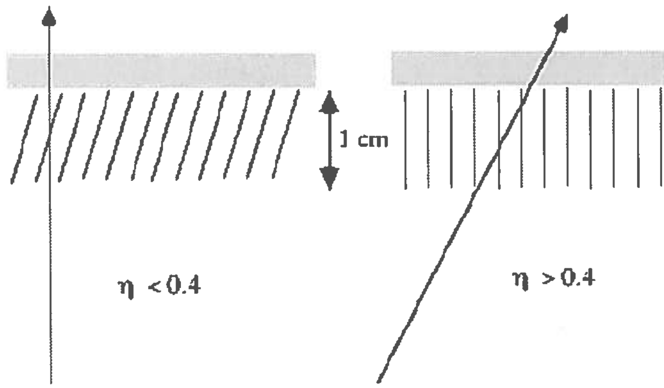

Figure 4: Schematic of the presampler electrode orientation along the barrel.

6 Lead production and control

The production of the lead sheets will be made in industry by cold-rolling. The thickness uniformity is of prime importance since the signal response depends strongly on it (as shown in fig.5):

$$\delta(signal)/signal = -0.5 \times \delta(thickness)/thickness \quad (1)$$

This dependence is also predicted by the simulation. For a contribution to the energy resolution constant term smaller than 0.3%, we need a lead uniformity of $\sigma < 0.6\%$, i.e. 10 μ for 1.5 mm plates. An on-line measurement system based on X-ray absorption will be used at the lead processing plant,to control the rolling and to mark the plates, with an accuracy of about 4μ (fig.6).

The plates will then be measured again off-line with an ultra-sound probe, and sorted in such a way that neighbour absorbers provide an homogeneous average thickness. The steel sheets are much thinner (0.2 mm) and thus contribute less to the energy loss, however, the signal response is as sensitive to an additional thickness of steel as of lead. We thus need an accuracy of steel plates thickness better than 7μ. This is about the best currently available from industry. If this is not actually achieved, we would also sort the steel sheets.

7 Absorbers production and control

The sandwich is prepared with the pre-preg cloth not cured, and bent in the *bending press.* The jaws of this press are mobile along the accordion width to follow the

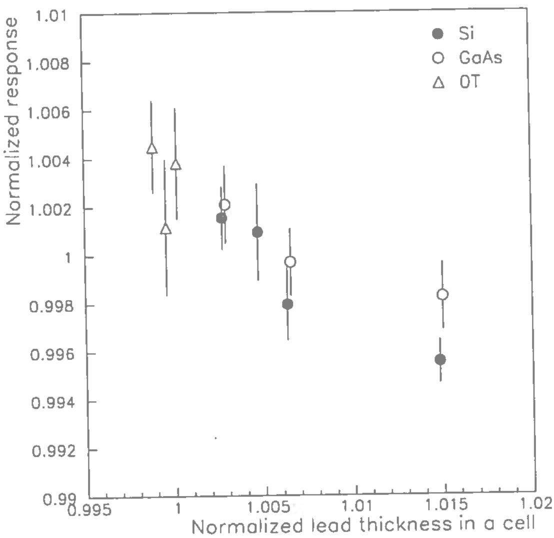

igure 5: Dependance of the signal on the lead thickness (measured on the 1992 rototype)

ecreasing width during the bending of the folds. Then the shaped sandwich is ured in the *gluing press* which presses while heating at 120 deg.C to polymerize, nd gives the final geometry. Both these large tools are now designed and will be eady beginning of '97. The absorbers will then be controlled by measuring their hape on a 3-D bench. A precision of 20 μ has been achieved by the same method n the total thickness of the "2 m" prototype's absorbers. The expected overall ccuracy on the gap thickness between two absorbers is about 50 μ. Because of the ast shaping time, approximately one tenth of the total drift time, the effect of the ap thickness dispersion on the constant term is only 0.15%.

3 Modules assembly and tests(fig.7)

The 32 modules will be assembled at two laboratories. In order to guarantee the geometry of the modules, and to ensure the assembly of the full barrel without cracks,

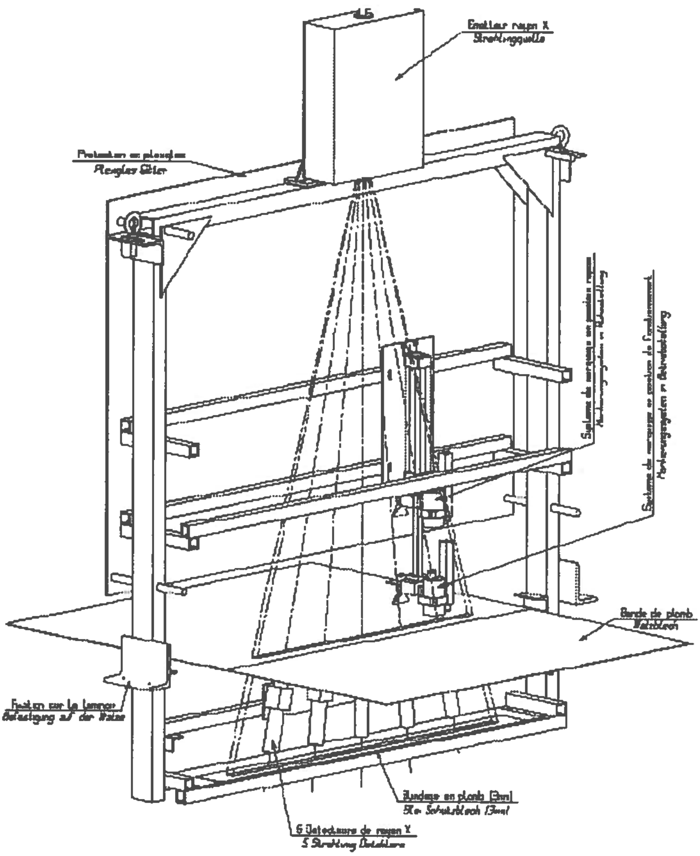

Figure 6: X-ray system for on-line lead thickness measurement

a cylindrical set of 16 frames has been designed.This set of frames is first fabricated and assembled. The external support rings (assembled) are mounted inside the cylinder of frames; their inner face is machined on a vertical lathe, making it a good circle. The ring segments are then disconnected and the frames disassembled, keeping the 7 ring segments fixed to their corresponding frame. At this time, a test of re-assembling the barrel will be done with fictive loads to simulate the modules, and check that the overall geometry is indeed mastered. Then a module is assembled (in a clean room) by stacking absorbers and electrodes using the frame and rings as a backbone, and the geometry is controlled. The module is equipped with its full connectics: p-c boards, cables for signals, calibrations, high-voltage. The module undergoes a series of tests, first in the ambient air during its assembly and once

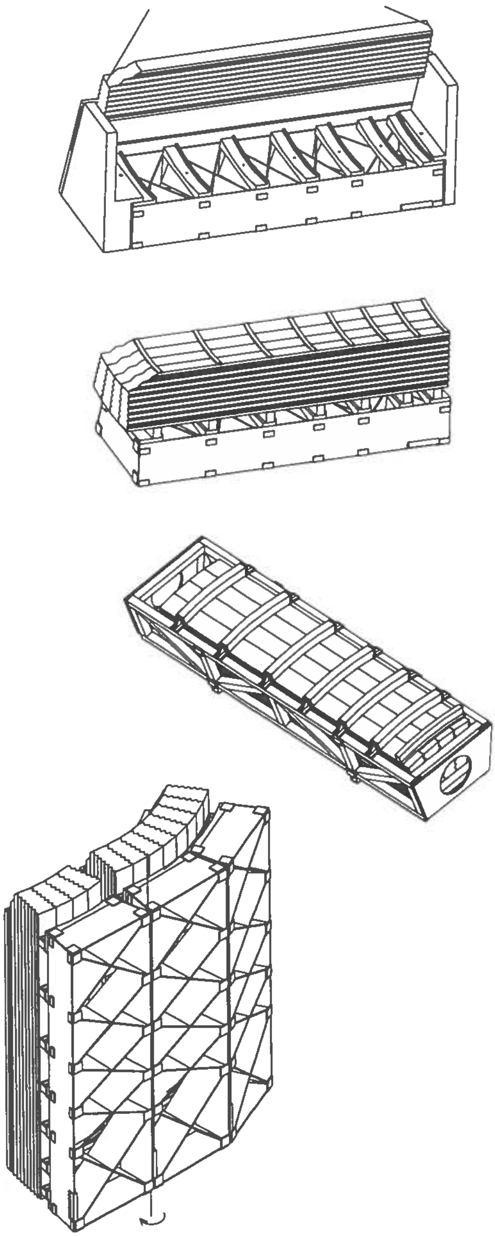

Figure 7: Some sequences of the module and barrel assembly

completed, then in a vertical cryostat with liquid argon, with all channels connected.

9 Barrel assembly (at CERN)

The 16 modules on their frames are set vertical and assembled to form a barrel. Two "sliding beams" are installed in contact with the external rings. This barrel is rotated, and laid onto a support in front of the cryostat rails. The barrel is then shoved into the cryostat by pushing on the sliding beams which slide on the cryostat rails. This way, no shearing force is applied to the external rings.

10 Conclusion

The mechanics of the barrel electro-magnetic calorimeter for ATLAS is defined to a large extent. All the elements of the complete construction scenario are known, and are being designed in details. The whole chain will get started with the construction of module 0, 1/32 th of the final detector, beginning this summer. Module 0 should be ready for tests in a beam by the fall of '97.

11 Acknowledgements

I sincerely thank the members of the barrel mechanics team for their help in the preparation of the material for this talk.

References

1. ATLAS Technical Proposal, CERN /LHCC/94-43 (15 Dec 1994).

2. D. Gingrich et al.,RD3 collaboration, Nucl. Inst. Meth. A 364 (1995) 290

ıscati Physics Series Vol. VI, (pp. 417–426)
INT. CONF. ON CALORIMETRY IN HEP – Frascati, June 8–14, 1996

ATLAS - LIQUID ARGON ELECTROMAGNETIC ENDCAP CALORIMETRY

ATLAS LAr Calorimeter Subsystem
Presented by **P. Fassnacht**
CPPM – Marseille

ABSTRACT

ı a first part, we describe the main performances obtained with the Electromagnetic ndcap calorimeter prototype, the so-called "Spanish Fan". It was tested at CERN sing electrons in the range of 20 to 300 Gev. Energy and position resolution s well as linearity and uniformity results are in good agreement with the results btained on the "2m" barrel prototype. In a second part, we present the actual esign of the ATLAS Electromagnetic Endcap calorimeter, with some emphasis on ıe latest modifications concerning the geometry and the consequences in terms of erformances as obtained from the simulation.

"Spanish Fan" prototype: Test beam results

.1 Detector description

'he prototype (1/6 of a flat disk perpendicular to the beam axis) covers the pseuorapidity range from 2.17 to 2.88. It is fully pointing toward a vertex point located t 2.8 m from the front face. All the plates, converters and electrodes are accordion ıaped and are arranged radially like wheel spokes with the waves direction parallel › the beam axis. Fig.1 shows the prototype during the assembly operation.

Each absorber plate consists of a sandwich of five elements : stainless steel (0.2 ım), prepreg adhesive, lead (the converters are plates with a linearly increasing ıickness from 1.3 to 2.3 mm in the radial direction) , prepreg adhesive, stainless ;eel. The lead thickness variation is obtained with conventional machining with a recision of 0.02 mm. The plates were sorted in such a way that the overall rms ispersion of the lead weight from plate to plate was about 0.25%. This contributes

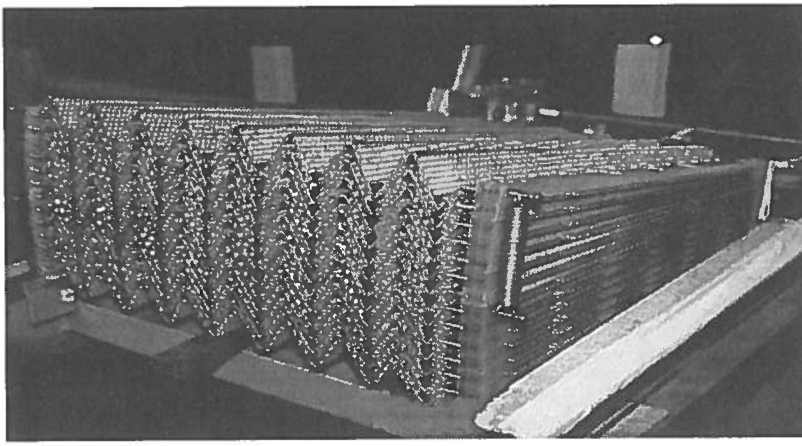

Figure 1: *Prototype during assembly*

to a signal dispersion of approximately 0.2% [1] [2].

The electrodes are multilayer copper-kapton boards of thickness 0.3 mm and are divided into 24 projective strips of $\Delta\eta = 0.03$. These electrodes are separated from the converters by a LAr gap varying from 1.65 to 2.65 mm with increasing radius.

In the azimuthal direction, three strips from consecutive electrodes boards are ganged together and thus define cells with a constant $\Delta\phi = 0.05$. Each strip has a longitudinal segmentation in three depth regions of $9X_o, 9X_o$ and $6X_o$. The readout cells are defined by $\Delta\eta \times \Delta\phi = 0.03 \times 0.05$ for the two first samplings. For the third sampling, the η strips are larger by a factor of two.

The pointing structure in ϕ is achieved by opening up the absorber and readout plates around the beam line. The lead sheet thickness and the gap between electrodes and converters increases with the radius as quoted above and the wave angle increases from 57^o to 110^o with the radius. With this geometry, as shown with a detailed Monte Carlo simulation [3], the sampling fraction can be kept nearby constant in both η and ϕ direction.

The response can be kept constant by radially increasing the high voltage on the electrodes boards. Thus, in our standard operating conditions, twelve different voltages for the first sampling zone and twelve others for the second and third zones were defined. They ranged typically from 1000 V at low radius to 2500 V at the largest, according to Monte Carlo studies.

This continuous variation of the detector geometry in the radial direction is the main difference with respect to the barrel accordion prototype [4].

The readout electrodes are multilayer boards consisting of two (one double-sided and one single sided) copper-clad kapton sheets glued together. The copper layers e etched into projective strips separated by 1 mm gap for insulation, which define e longitudinal and the η segmentation of the detector.

ıe ionization charge drifting in the LAr gap induces by capacitive coupling a ırrent on the inner conductive layer, which is DC coupled to the input of the eamplifier at the beginning of the readout chain. The two outer conductive layers e at high voltage and produce the electric field over the gap.

ɔneycomb strips, glued in a few points, were used to center the kapton readout ɛctrodes. However, in order to cope with the variable gap between kapton and nverter plates, these honeycomb strips were machined to have a variable thick- ɛss.

ıe mechanical uniformity was then estimated by measuring the capacitance C_{gap} of veral double gaps consisting of one electrode and two absorber plates on its oppo- ;e sides. We measured an rms dispersion of 2.6 % which corresponds to 1.3% rms ı the signal of the readout electrodes. After grouping readout electrodes to form lls and grouping cells to form an electromagnetic cluster, this gap non-uniformity anslates into a dispersion of 0.4% in the response to an electron shower.

ıe front-end electronics consist of a warm current preamplifier placed outside the yostat through a 50 Ω cable. The preamplifier output was shaped with a CRRC^2 ıipolar filter. The peaking time $t_p(\delta)$ of the shaped response to a short current ılse was 18 ns, corresponding to about 35 ns for the triangular ionization signal ɔm the detector. The shaper was followed by a track-and-hold (T&H) circuit whose ning was adjusted to sample the shaper signal near the maximum. The output ıs digitized by 12-bit charge integrating ADC. The coherent noise, usually associ- ed with improper shielding and ground loops has been measured to be 6 MeV, 6 eV and 7 MeV per channel in the first, second and third samplings, respectively. ıe incoherent noise observed in the calorimeter comes mainly from the preamplifier ise and varies with η due to the capacitance variation. It has been measured to between 46 and 52 MeV per channel in the first sampling, between 46 and 56 eV in the second and third sampling.

ıe cross talk between adjacent cells has been estimated using the calibration data d found to be at the level of 1% between neighbours.

2 Simulation and Test Beam results

ıe data have been taken in the H8 beam line of the CERN SPS using electrons ɔm 20 to 300 GeV. The calorimeter was installed in the back of the RD3 cryostat order to simulate an interaction point, in collider mode, at 2.8 m. Rohacell foam ıs put in front as argon excluder. The total amount of passive material in front the prototype was about 0.9 X_0 at the innermost radius. The rotation in ϕ was achieved with a motor operating in the liquid argon.

1.2.1 Response variation across a cell

Due to the change of the geometrical parameters with η, a special investigation was made to study the dependence of the corrections with η. In the η direction, the parabolic shape reflects the lateral leakage at the separation between two cells. We observed a signal response variation over several cells in η which reflects the shower containment variation with the radius.
In the ϕ direction, the modulations correspond to the variations of the accordion shape: from the Monte Carlo simulation, it has been shown that the calorimeter response as a function of ϕ has periodical modulations due to two effects : non-uniformity of the sampling fraction near the absorber fold and non-uniformity of the electric field near the absorber or the electrode fold. The sum of these two effects produces two sets of peaks with different amplitudes and widths at the position of the absorber and the electrode folds. Nice agreement between simulated data (fig.2) and test beam data has been obtained.

1.2.2 Energy resolution, linearity and uniformity

The response was corrected for the above mentioned variations across a cell as well as for energy losses due to early showers (material in front of the prototype). This later correction used the information of the Preshower [5]. The energy resolution as a function of the beam energy has been measured for four different η values, the contribution of the beam momentum spread has been subtracted (fig.3). At a given η value, the energy resolution values were parameterized with the quadratic sum : $\frac{\sigma_E}{E} = \frac{a}{\sqrt{E}} \oplus \frac{b}{E} \oplus c$ where the three terms are the sampling, the noise and the local constant term, respectively, and E is expressed in GeV. The values of the three coefficients, for the four different η values, are very similar [1]: typically a=10.2%(±0.3), b=550Mev and c=.30%(±.04).

The energy resolution obtained with the detailed Monte Carlo simulation of the prototype [3], after correction for the ϕ modulations and the backward leakage, gives a sampling term of 10% and a constant term of 0.25%. From data, the sampling term (a) is of the order of 10-11%; it is in good agreement with the simulation. The noise term (b) has been checked using random triggers and was found to be larger than the electronic noise by about 70-100 MeV. Using the preshower information, this excess has been attributed to the degradation of the energy resolution at small energy due to the material in front of the prototype. The constant term (c) reflects mainly the residual modulations in both ϕ and η directions.

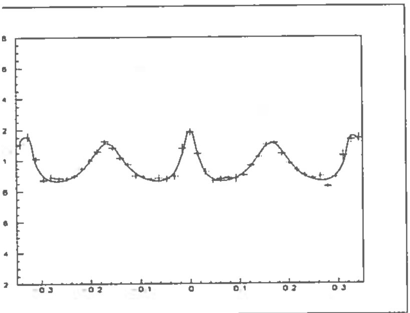

gure 2: *Modulations of the signal ɔng the ϕ direction at N_η = 22 as tained by Monte Carlo simulation. ɪe curve is a parameterization of the onte Carlo data.*

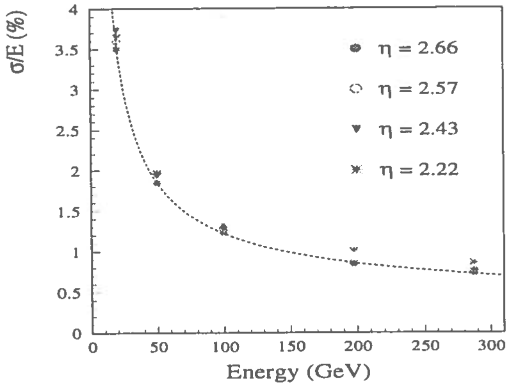

Figure 3: *Energy resolution as a function of the incident beam energy at four different η values. The dashed line is the best fit to the data at η=2.66*

The linearity has been studied with the same data and the same correcɔns used to determine the energy resolution. The pedestal value, extracted from the ents triggered randomly, is subtracted from the mean value of the fitted calorimer response. The resulting value is then divided by the nominal beam energy and ɪrmalized at 100 GeV. The non-linearity is within $\pm$ 1.0% in the range 20 to 300 eV at the four selected η values.

The response uniformity has been studied in both η and ϕ directions with :dicated sets of data, using 200 GeV electrons. The resulting global response dis:rsion is 0.55($\pm$.08)%. The overall energy resolution over 48 cells is 1.14%, taken ɔm a Gaussian fit. After subtracting quadratically from this value the contribution the sampling term (0.76%) and the noise term (0.26%), we obtain a global conant term of 0.79($\pm$.04)%. This global constant term isn't very different from the ɪadratic sum (0.65($\pm$.11)%) of the cell-to-cell dispersion and of the local constant rm. Among the various sources of instrumental non-uniformity, a large part of the ɔnstant term can be attributed to well understood mechanical effects [1].

2 Design of the ATLAS EM Endcap calorimeter

2.1 Latest design modifications

2.1.1 Constant lead thickness

Based on simulation results, which reproduced well the test beam data [1], the Atlas collaboration decided to choose the constant lead thickness option [6]. The energy resolution for simulated electrons as well as the response linearity were similar for both options. Looking at the intrinsic performances, with no corrections for leakage and modulations, we obtained a sampling term of 8.2%(±.3) and a constant term of .2%(±.1) for both options. The linearity was better than 0.5% [7].
The HV varies with the radius in order to compensate for the gap opening. In the constant lead thickness option , this variation is limited to a factor of 2.5 compared to 8.0 in the Technical Proposal design. Moreover this option is mechanically easier and cheaper (less raw material: -10 tons of lead). Nevertheless the total amount of material is larger than 25 X_0 for $\eta \geq 1.45$. The material distributions versus η in front of the calorimeter and of the calorimeter itself are shown on fig.4 and fig.5.

In the present design of the outer wheel ($1.375 \leq \eta \leq 2.5$), the total amount of absorbers and electrodes is 768, the lead thickness is 1.7mm and each absorber has 9 waves. For the inner wheel ($2.5 \leq \eta \leq 3.2$) the numbers are respectively 256, 2.2mm and 6. The opening angles of the folds vary with radius from 59^0 (54.5^0) at the outermost radius to 122.5^0 (107^0) at the innermost radius for the outer wheel (respectively the inner wheel).

2.1.2 Electrode design

Following the recommendations of the Descoping Task Force [8], which concerning the EM Endcap are the following :
- no precision physics in the region $\eta \geq 2.5$, ie only two samplings and a coarse granularity of $\delta\eta.\delta\phi$=0.1x0.1,
- in the region $1.5 \leq \eta \leq 2.4$, reconsider the fine granularity layout in order to minimize the number of channels while keeping the γ/π^0 rejection factor better than 3,
- no strip sampling at $\eta \leq 1.5$, since the amount of material is so large in this region making the γ/π^0 separation almost impossible,

the layout of the electrodes was modified.
In the region $1.5 \leq \eta \leq 2.4$, the strip granularity is now of $\delta\eta$=.025/8 up to η=1.8, $\delta\eta$=.025/6 up to η=2.0 and $\delta\eta$=.025/4 up to η=2.4. This new layout is also a consequence of some mechanical constraints in the design of the electrodes (pitch between two strips has to be larger than 4mm). With such a design of the kaptons,

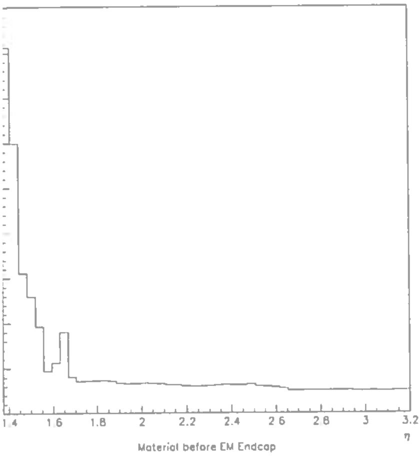

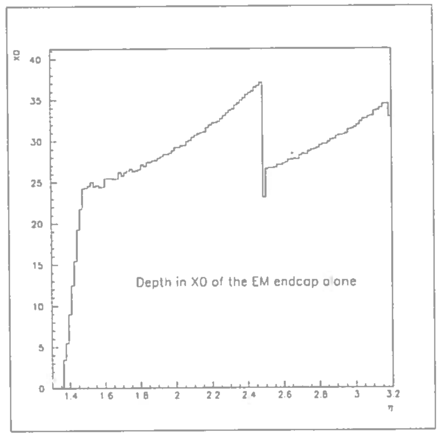

;ure 4: *Material distribution in nt of the EM Encap*

Figure 5: *Material distribution of EM Endcap itself*

e γ/π^0 separation ratio is kept near R=3 (when using the Tracker information) ith a γ efficiency of 90%. The longitudinal segmentation varies with η. Presently, is of 6, 18 and 12 X_0 for S(ampling)1, S2 and S3 respectively, at η=2.5 for a total fective active thickness of the calorimeter of 51cm. The final optimization of the ngitudinal segmentation is still under study.

With such a new design of the electrodes, the total noise, which is very uch dominated by the pile-up in this forward region, varies from 500 Mev at the ıtermost radius to 3 Gev at η=3.2 inside a 3x7 cluster (see fig.6). The electronic ›ise contribution, calculated using 0T electronics and 50Ω cables [9], is shown on ;.7. The noise varies like the capacitance which in S1 is constant ($\simeq$ 100pF) and ›es like a+b.tan$(\theta)^2$ for S2 and S3.

2 Status and progress in the design and fabrication

2.1 Absorbers, bars and spacers

he final geometry of the absorbers for both the internal and the external wheels :e now frozen. The geometrical parameters have already been mentioned. Each bsorber will consist of a sandwich of five elements : stainless steel (SS), prepreg dhesive (PA), lead, PA and SS. The lead and SS are bend together and glued. The etailed description of the cold geometry, as it is described in the DICE simulation

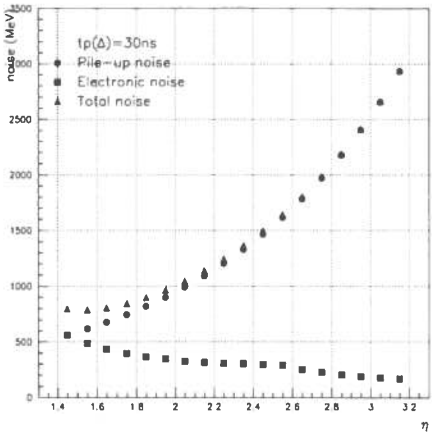

Figure 6: *Pile-up, electronic and total noise performances for a 3x7 cluster*

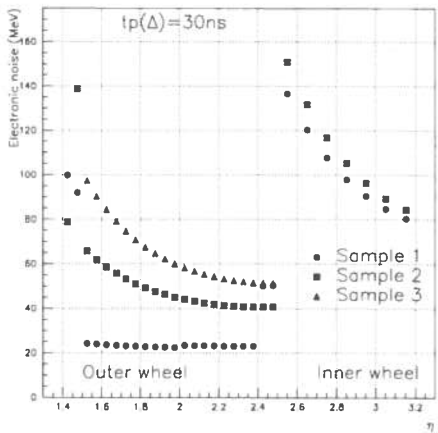

Figure 7: *Electronic noise per cell for the three samplings of the two wheels*

program, is used by a 3-dim CAD program (EUCLID) to compute the surfaces. For each 1/4 of a wave, the precise map of the coordinates of the five characteristic points which describe the wave was then obtained as a function of radius. The flat shapes of the absorbers at room temperature were obtained after unfolding of the accordion and the positioning of the knives was precisely defined in the X,Y plane. The fabrication of the lead sheets used for the construction of the Module "0" will start before the end of summer 1996.

The bars, on which the absorbers are glued, maintain the distance in between two consecutive converters. The machining of these epoxy glass bars is very demanding since the precision in the positioning has to be of the order of 10μm. Drilled holes in the bars are used to assemble the wheels and to fix the absorbers on the fixation rings. The design of the bars is finished and the orders will be placed very soon.

Due to the particular geometry of the EC, the variation of the Larg gap isn't linear. The gap varies from 1 to 2.7mm in the outer wheel with a maximum deviation from linearity of 260μm. To minimize this distance, it was decided to cut the spacers into two parts. In this case, the maximum distance between the spacer and the electrode becomes 70μm. First tests to produce a spacer with linearly variable thickness were done successfully at Cern, machining the Honeycomb strips with a saw. First orders were placed for the fabrication of the spacers.

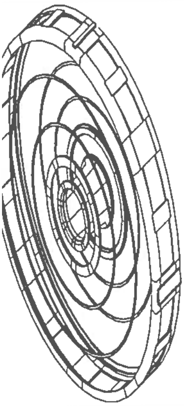

:e 8: *EM Endcap* ɔ*rting frame*

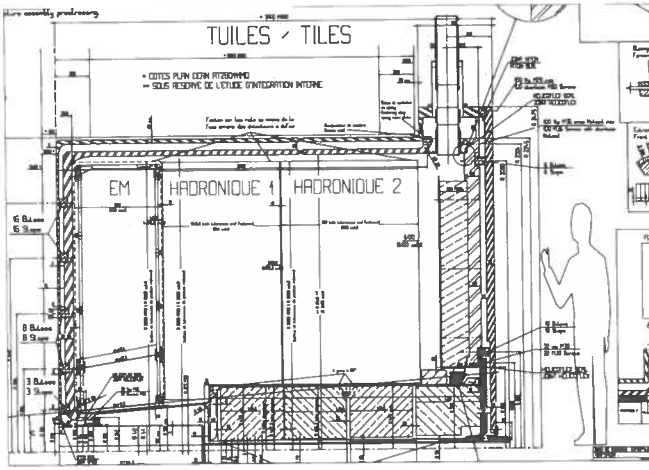

Figure 9: *ATLAS Endcap : Electromagnetic, Hadronic and Forward detectors*

.2 Assembly, supporting structure and integration

ıdules (1/8 of a wheel) of the internal and the external wheels will be assembled :ether using supporting rings. The structure (see fig.8) , made of aluminium and :mali E730, consists of three main rings (inner, intermediate and outer) of about n in radius and two smaller rings placed in between the intermediate and the ;er rings. Between the front and the back face of the calorimeter, internal spacers ass epoxy) are regularly distributed in ϕ. Laterally, two supports are mounted on ›se spacers in order to introduce the detector inside the endcap cryostat. During s operation, the calorimeter will slide on two rails and be steered using a guide ich is located on top of the overall structure, at the junction of two modules.

tensive deformation calculations have been done, both for cold and warm conions. The axial displacement of the outer front ring under the gravity load was culated (modelization by finite elements (Systus)) to be less than 1mm. Mea·ements of stresses and rupture limits at cold have also been performed.

e final envelops of the detector are now well defined as well as the tolerances 1 clearances. Common effort together with the other subdetectors has converged the final integration schema. On fig.9 the positioning of the different endcap orimeters is shown as well as a cross-section of one out of the 28 feedthroughs. ese feedthroughs are identical to the ones used in the barrel (1920 channels per ') and the distribution among the different calorimeters is now frozen.

2.2.3 Organisation and schedule

The design and the construction of the EM endcap is distributed over five laboratories : CERN, CPPM (Marseille), LAL (Orsay), Madrid and Novosibirsk. Concerning the schedule, it's our goal to have the module "0" in the beam before the end of 1997. The design of the different tools for the fabrication of the absorbers, bars and spacers is now finished and we plan to start with the production of the converters by October 1996. In parallel we will produce the tools for the assembly (rings, stacking device, ...). The stacking itself will start beginning of 1997 when the first electrodes will be delivered.
Detailed informations and drawings can be found on the WEB under the following path:
http://marpix1.in2p3.fr/calo/mechanics/mechanics.htlm

References

1. D.M.Gingrich et al, Performance of an endcap prototype of the ATLAS Accordion Electromagnetic Calorimeter,Nucl. Inst. and Meth. in preparation and CERN-PPE/95.

2. A.Cravero and F.Gianotti, Uniformity of response and energy resolution of a large scale prototype of the Barrel Accordion calorimeter, ATLAS Internal note CAL-No-33 (1994).

3. A.Cheekhtman, The endcap accordion calorimeter prototype simulation, ATLAS Internal Note LARG-No-41 (1996).

4. D.M.Gingrich et al, Performance of a Large Scale Prototype of the ATLAS Accordion Electromagnetic Calorimeter, Nucl. Inst. and Meth. A364 (1995) 290.

5. R.A. Davis, Construction and test of a fine-grained liquid argon preshower prototype,Nucl. Inst. and Meth. in preparation and CERN-PPE/95

6. S.G. Klimenko and al., The design of Endcap EM calorimeter with constant thickness of the absorber plates, ATLAS Internal Note LARG-No-025.

7. C. Scheel, Simulation results comparing constant and variable thickness lead plates in the em endcap calorimeter, ATLAS Internal Note CAL-No-079.

8. Report of the global descoping Task Force, ATLAS Internal Note GEN-No-014.

9. C. de la Taille, New noise figures for the Atlas EM calorimeter, ATLAS Internal Note Larg-No-035.

scati Physics Series Vol. VI, (pp. 427–433)
[NT. CONF. ON CALORIMETRY IN HEP – Frascati, June 8–14, 1996

?ST TEST BEAM RESULTS FROM THE LIQUID ARGON HADRONIC ENDCAP CALORIMETER FOR ATLAS

The HEC Community

Alberta, British Columbia, Dubna, Kosice, Mainz, Montreal, Moscow, Munich, Ottawa,Protvino, Seattle, Vancouver, Victoria

presented by

Hasko Stenzel

Max-Planck-Institiut für Physik
Föhringer Ring 6, D-80805 München

ABSTRACT

·st results of the hadronic endcap calorimeter (HEC) using an electron beam from ; SPS facility at CERN are presented. The recorded data are analyzed in order to 'e a preliminary estimation of energy resolution and linearity of the calorimeter.

The HEC prototype

Introduction

order to guarantee containment of jets expected at LHC [1], a total amount material of 10 λ is required to be placed within the available depth of 1.9 m. ıe HEC covers a pseudo-rapidity range of $1.5 \leq \eta \leq 3.2$, this corresponds to a ometrical diameter of 4 m (Fig. 1). One endcap is mechanically subdivided into front wheel and a back wheel, each wheel is built of 32 identical modules.

2 Mechanics of the Prototype

ıe prototype module presented here is of the front type. It consists of 24 parallel pper plates of 25 mm thickness with a total gap of 8 mm between plates. The gap :tween two plates is filled with an electrode structure. The transverse granularity the prototype is $\Delta\eta \times \Delta\phi = 0.1 \times 0.1$ and groups of 8 gaps each are connected to rm 3 longitudinal readout sections.

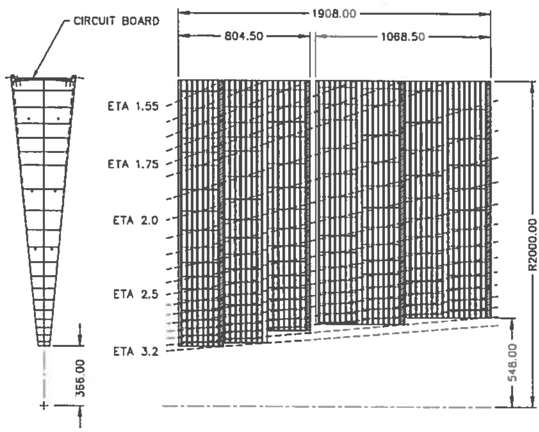

Figure 1: A side view of two modules, the front one being investigated here

1.3 Electrode Structure and Read-Out

In order to achieve a good signal-to-noise ratio, a low detector capacitance is required. Therefore, the read-out board is placed in between two electrostatic transformer (EST) boards (Fig. 2), yielding an EST ratio of two. Both EST boards and pad boards are made of copper cladded kapton, which are equipped with resistors for protection against high voltage discharges. This will be replaced by a high resistive coating [2] solution in the further modules. The read-out board is connected via 50 Ω transmission lines to a preamplifier built in GaAs technology. The front-end electronics board containing preamplifiers, summing amplifiers and line drivers is located at the outer radius of the wheel, in the liquid argon. Details of the electronics system are given in Ref. [3]. It has been verified [4] that the electronics will not be affected by radiation damages during an expected operation period of ten years. A fast signal shaping with a peaking time of 43 ns is done inside the cryostat, and the reshaped signals are digitized and transferred to the data acquisition system.

2 Test Beam Results

The prototype module has been tested with electrons, the module beeing too small to contain hadronic showers. In order to measure the energy resolution and the linearity of the calorimeter response, electron beams in the energy range between 10 GeV and 120 GeV have been used. Data were recorded at two different impact positions of the beam at the calorimeter front face. Electromagnetic showers are contained in 4 read-out channels, these are added to form a read-out tower.

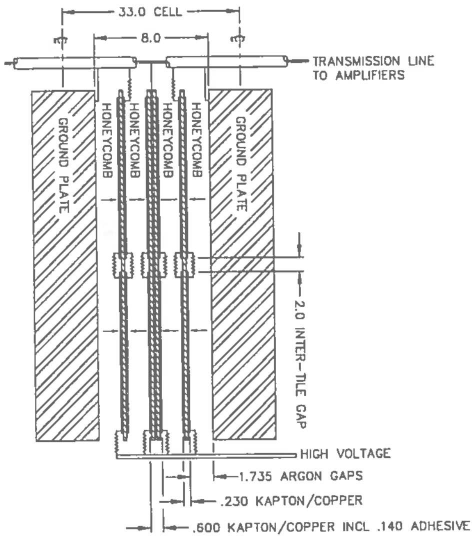

Figure 2: Details of the electrode structure placed in a liquid argon gap

1 Calibration and electronic Noise

calibration system has been set up which injects voltage pulses of different amlitudes at the preamplifier board, some channels being pulsed directely at the pad. 'his procedure allows corrections for crosstalk (measured to be less than 1 %, in greement with the geometrical crosstalk between pad boundaries) and the deterination of the calibration parameters. These parameters P_i are obtained form a t and are used to compute the charge Q from ADC counts N :

$$Q = P_0 + P_1 N + P_2 (P_0 + P_1 N)^2 + P_3 (P_0 + P_1 N)^3 \tag{1}$$

n a next step, a single calibration constant C is determined to pass from charge to nergy. The calibration constant is obtained from the normalization of the of the harge distribution to the nominal beam energy, and its uncertainty takes the varition from different beam energies into account : $C = (3.38 \pm 0.02) 10^{-3} [GeV/fC]$. random trigger is used to measure the ADC-pedestal. In Fig. 3 a) the mean of the DC distribution is shown for runs taken over a period of one week. The pedestals re very stable, no shift is observed. The electronic noise has been estimated from he width of the pedestal distribution. It is found to be about 500 MeV with a ypical uncertainty of 30 MeV per read-out channel. The stability of the level of oise can be seen in Fig. 3 b).

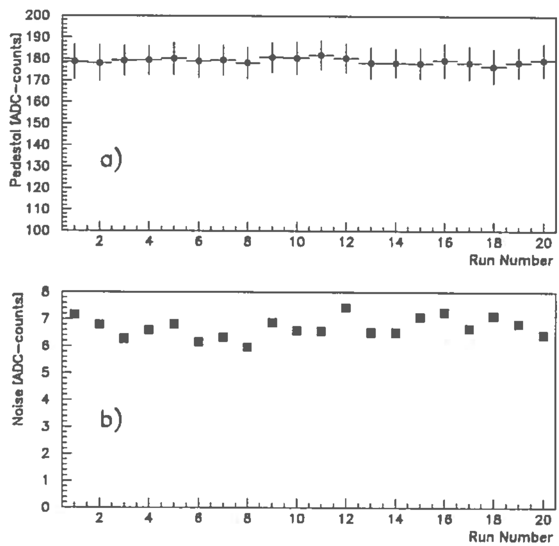

Figure 3: The pedestal (ADC-counts) a) and the level of noise b), as function of the run number

2.2 Energy Resolution and Linearity

The energy depositions for electrons in a read-out tower are shown in Fig. 4. A gauss fit has been applied in order to determine the mean $< E >$ and the sigma σ_E of the distributions. The results are summarized in Table 1. The energy resolution $\sigma_E / < E >$ has been parameterized in the usual way :

$$\frac{\sigma_E}{E} = \sqrt{\frac{A^2}{E} + B^2 + \left(\frac{C}{E}\right)^2} , \tag{2}$$

where A is the sampling term, B the constant term and the noise term C has been set to the value of (1.015$\pm$0.047) GeV, measured from random triggers. The parameters A and B have been determined from a fit shown Fig. 5, yielding the following result: $A = (21.5 \pm 0.4\%)[GeV^{-1/2}]$, $B = (1.1 \pm 0.1)\%$.
It has been verified that compatible results are obtained at a different position of the beam.
Finally, the linearity of the energy response $< E > / E_{BEAM}$ is measured to be better than 2 %, as can be seen in Fig. 6.

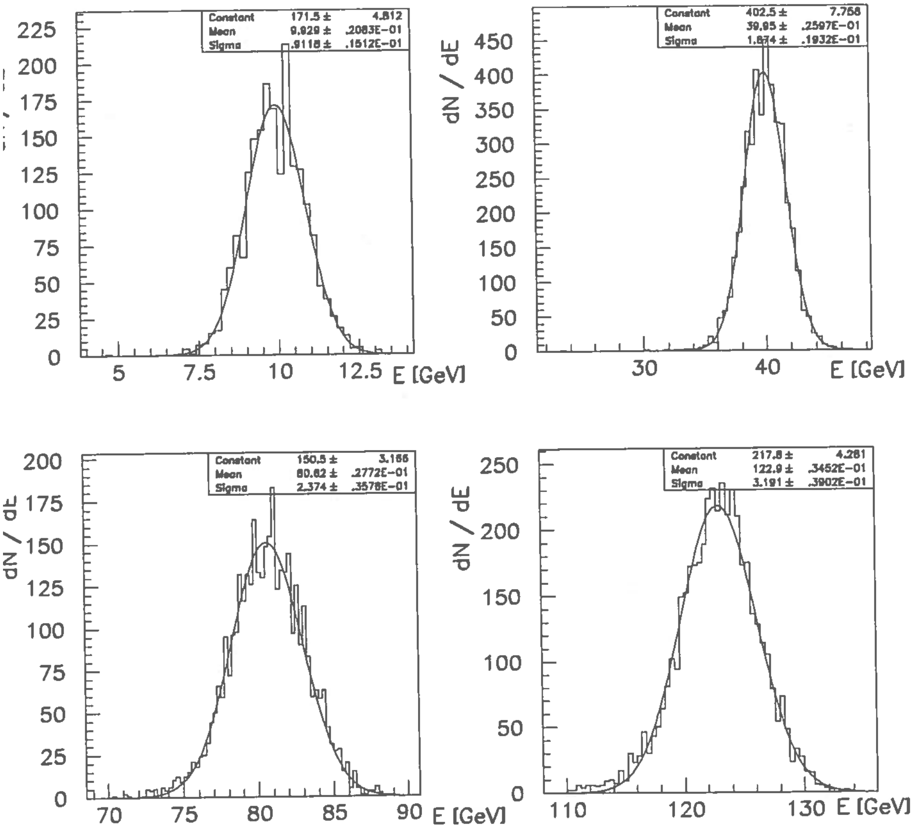

Figure 4: Distributions of energy deposit for electrons of 10, 40, 80 and 120 GeV

Beam Energy	$< E >$	σ_E
10 GeV	9.929 ± 0.021	0.9118 ± 0.015
20 GeV	19.933 ± 0.022	1.216 ± 0.016
40 GeV	39.951 ± 0.026	1.674 ± 0.019
60 GeV	60.199 ± 0.027	2.085 ± 0.029
80 GeV	80.622 ± 0.028	2.392 ± 0.033
100 GeV	101.723 ± 0.031	2.675 ± 0.035
120 GeV	122.909 ± 0.035	3.191 ± 0.039

Table 1: Results from the energy scan

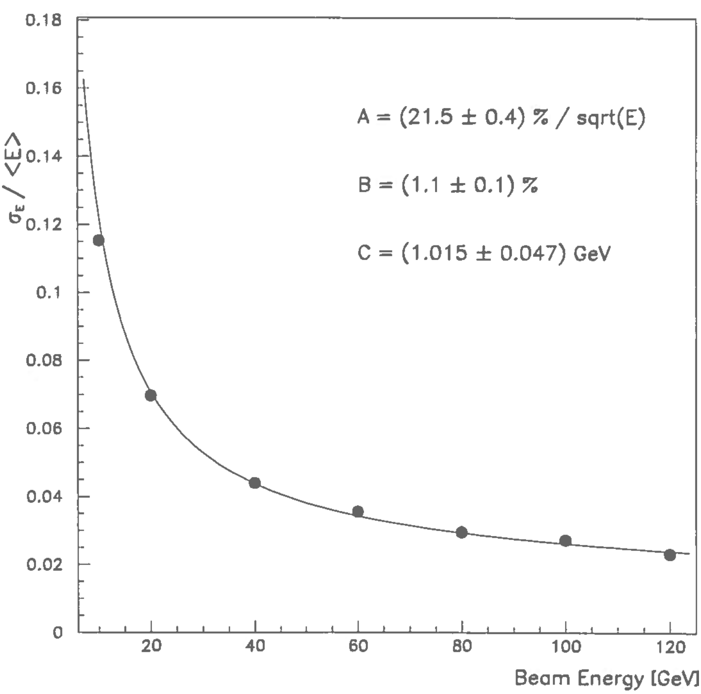

Figure 5: The energy resolution.

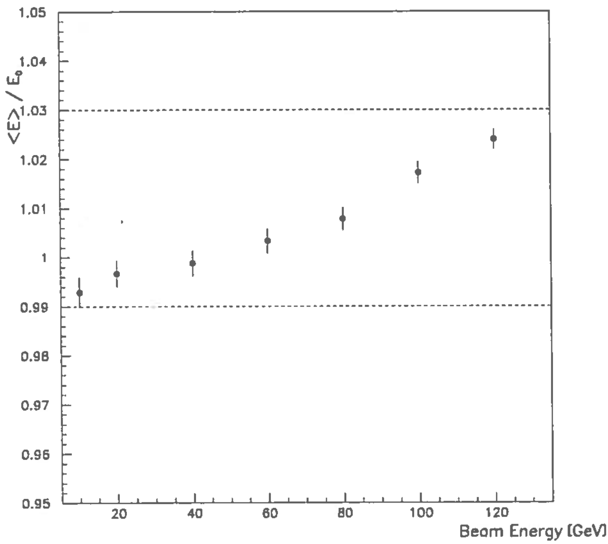

Figure 6: The linearity of the calorimeter response.

Conclusion

prototype of the front module of the hadronic endcap calorimeter for ATLAS s been built and tested with electrons. Good agreement between the measured rformance and the expectation from Monte Carlo simulation is observed. The ergy resolution is measured to be 22 $\%/\sqrt{E}$ for the sampling term with a constant rm of 1 %. The electronic noise has been determined to 500 MeV per read-out annel. Finally, the linearity of the calorimeter response is better than 2 %.

eferences

. ATLAS collaboration, ATLAS Technical Proposal, CERN/LHCC/94-43, 27 (1994).

. M.N. Yakimenko, Production and testing of registrating plates for the liquid Argon hadronic end-cap calorimeter for the ATLAS detector, these Proceedings.

. C. Berger et al. , Study of a novel electromagnetic liquid argon calorimeter - the TGT, Nucl. Instr. and Meth. **A 357** (1995), 333.

. K. Jakobs, Radiation Hardness of GaAs preamplifiers for Liquid Argon Calorimetry at LHC, these Proceedings.

rascati Physics Series Vol. VI, (pp. 435–440)
I INT. CONF. ON CALORIMETRY IN HEP – Frascati, June 8–14, 1996

PRODUCTION AND TESTING OF REGISTRATING ELECTRODES FOR THE LIQUID ARGON HADRONIC ENDCAP CALORIMETER OF THE ATLAS DETECTOR

M. I. Blagov, A. A. Komar, A. A. Snesarev, M. N. Speransky, V. V. Sulin, M. N. Yakimenko
Lebedev Physical Institute, Moscow, Russia

ABSTRACT

Production and pre-testing procedure of registrating electrodes for the liquid argon Hadronic End-Cap calorimeter (LAr HEC) of the ATLAS detector for the LHC are described. The set of the registrating electrodes in each gap of the calorimeter between the absorbing copper plates consists of one registrating electrode itself — Readout Board (ROB) — and two electrostatic transformer plates (EST). The ROB presents a sandwich composed of a readout electrode structure (divided in pads) glued between two thin films of kapton. The external surfaces of these films are covered with High Resistive Coating (HRC). The EST plates are kapton films which are also covered from both sides by HRC. Two types of plates mentioned above (ROB and EST) are very thin (about 250 and 100 microns respectively) and flexible. They are more than 1.5 m long and have borders of complex configuration, which have to be held to within an accuracy of 0.5 mm. To fix ROB and EST position thin sheets (about 2mm) of separating honeycomb material were used. For Readout Boards production large-scale lithography has been applied. Special methods of mechanical treatment, gluing and new HRC application technique have been developed. Some details of them are described.
This research has been carried out under financial support and competent direction of Max-Planck-Institute (Munich) and in close collaboration with groups of Electric Isolating Foiled Materials, Research Institute of Electro-Carbon products (Moscow district), Joint Institute of Nuclear Research (Dubna) and Institute of High Energy Physics (Protvino).

1. Introduction

LPI group in cooperation with Russian industrial firms had developed technology and manufactured this spring the registrating electrodes for the prototype module of the Hadronic End-Cap Calorimeter to be used in the ATLAS detector. Experience that we got during this work allowed us to see more clearly the peculiarities of each technological operation and plan some improvements in them for further work on HEC Calorimeter.

One of the lessons also was the understanding that only close collaboration of physicists with industry engineers can guarantee positive results.

2. The Structure of HEC Module and Registrating Gaps

The HEC module consists of 40 copper absorber plates (25mm thick) divided by 8mm registrating gaps, filled with LAr. In the median plane of each gap there is a readout-board divided in pads (ROB, registrating plate itself); in the median plane of every half-gap between copper plate and ROB there is a EST (Electro-Static Transformer). plate. Altogether there are 40 ROB's and 80 EST-plates per module.

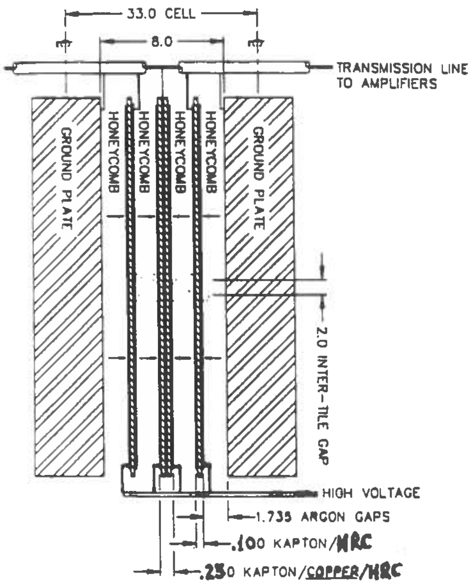

Fig 1. The structure of the registrating gap.

The space between copper plates is fixed by SS spacers, and the intervals between copper plates, EST electrodes and ROB's are defined by honeycomb layers (Fig. 1).

Pad-board presents a five-layer sandwich with copper foil pad-structure in the center glued from both sides by kapton films and then covered by High Resistive Coating (HRC) to which HV is supplied.

Each EST-plate is a 100 micron single-layer kapton film covered from both sides with HRC.

3. Short Description of Electrode Production Technology

3.1 Material

At the beginning to increase the HV hardness we planned to use sheets of two 40 micron kapton films glued together: one such sheet clad by copper and one plain sheet for ROB's and one such plain sheet of kapton for EST's.

Actually we used 100 micron kapton film with full HV pre-checking of it. Now we understand that such pre-checking could be important only for EST's, because for ROB's gluing process cures all defects of the primary kapton material, as well as defects obtained during the treatment before gluing.

In all cases we used polyurethane glue and we plan to use this glue in future.

The 100 micron kapton is very flexible material and it is very difficult to work with it. Mechanical hardness of 100 micron copper clad kapton is mainly defined by the copper thickness.

3.2 Lithography

Large-scale lithography has been done at the Research Institute of Radiotechnics, which has equipment for the lithography operation on the samples with the dimensions 0.5m x 8.0m. Unfortunately sheets of ROB's obtained after lithography operation had some waviness. In this respect it was very important to use for control prepared beforehand templates (reference specimens) made on the basis of 200 micron film of rather rigid material ("mylar") which had almost ideal flatness.

3.3 Gluing

We encountered a lot of difficulties while gluing additional layer of kapton film on ROB after lithography operation. All problems with gluing have been solved only after building in LPI workshops a mechanical press with help of which samples with dimensions 0.5mx2.4m can be glued using pressures up to 30 bars and heating up to 170°C. Cross-section of the press (not in scale) is shown on Fig.2. Using this press we could glue simultaneously up to 5 working samples (each of two ROB's), assembling them in stack.

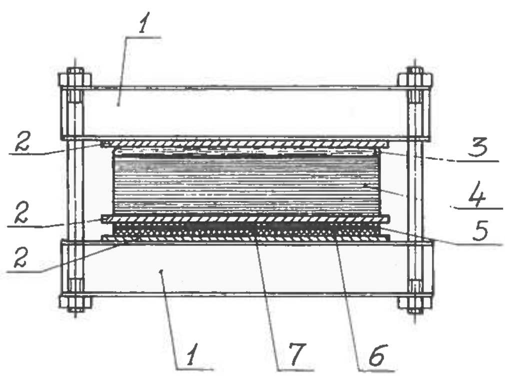

Fig 2. Cross-section of press (not in scale): 1 - I-beams, 2 - metal plates, 3 , 7 - thick layer of thermo-isolation, 4 - stack of glued samples, 5 - thin layer of isolation, 6 - heater.

Another difficulty with gluing and pressing operation was connected with the waviness of our working samples after passing lithography operation. To avoid appearance of wrinkles on the ROB's we had to stretch our samples before pressing/gluing.

3.4 Mechanical treatment

We developed a special punching technology to make step-shaped borders of the plates and use it for EST production. It was a very tedious handwork, in which operator mistakes were possible.
ROB borders have been cut out by the knives using the special template.

3.5 HRC application

ROB and EST-plates were covered with the special High Resistive Coating (HRC). HRC was developed for LPI group by Research Institute of Electro-Carbon

products. Our requirements to HRC properties were good adhesion to kapton, prescribed range of surface resistivity and good homogeneity.
To form the guard zones protected from HRC on the plates we used sticky masks, which were cut out using cutting plotter from a duplex plastic film with glue (like scotch).
In future we plan to use for these purposes rigid masks. This can be considered as a rather expensive tooling, but in this way we will get rid of very complicated hand-made operations (putting and removing sticky masks, washing out uncovered guard zones and so on).
HRC was applied by spraying. In this case homogeneity of the resulting layer was defined by many factors especially when spraying was made by hand. To improve the quality of the obtained layer a simple mechanical device was manufactured.
As a result we obtained the following values of the resulting homogeneity:

Table 1: **SUMMARY STATISTICS OF EST AND ROB HOMOGENEITY**

EST HOMOGENEITY STATISTICS

	SUMMARY	FAMILY 1	FAMILY 2	FAMILY 3	FAMILY 4	FAMILY 5
R. avrg. [MOhm/□]	1,739	1,604	1,690	2,109	1,648	1,703
r.m.s. [MOhm/□]	0,605	0,563	0,449	0,671	0,487	0,724

ROB HOMOGENEITY STATISTICS

	SUMMARY	FAMILY 1	FAMILY 2	FAMILY 3	FAMILY 4	FAMILY 5
R. avrg. [MOhm/□]	1,266	1,151	1,304	1,343	1,375	1,157
r.m.s. [MOhm/□]	0,437	0,362	0,429	0,539	0,418	0,363

4. Investigation of HRC properties

Properties of HRC have been studied in some details.

4.1 This material is a rather good absorber. Its resistivity increases with the humidity. On the Figure 3 the time dependence of resistivity is shown after dipping the sample into the distilled water. The heating of a wet sample to 100 °C restores the previous value of the resistivity (Fig 4). Drying of a sample by pumping is even more effective than heating.

Only water absorption and deabsorption can explain the temperature dependence of its resistivity (Fig.5). Reproduction of the form of this curve is rather good. On this Fig. the point of liquid nitrogen LN is also shown. Tested sample was dipped into LN. When

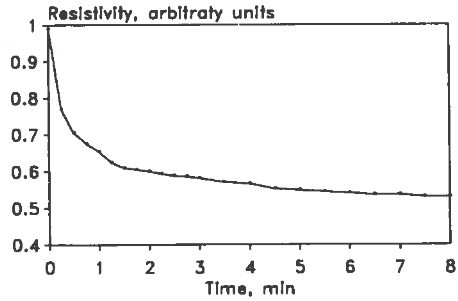

Fig 3. The time dependence of resistivity after dipping the sample into the distilled water.

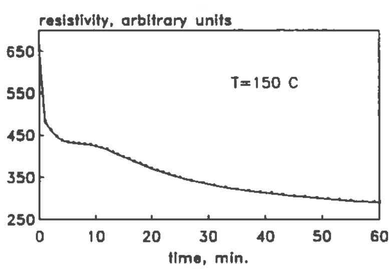

Fig 4. The time dependence of resistivity during the drying.

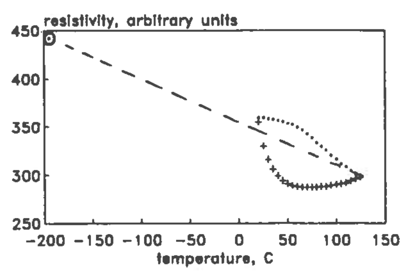

Fig 5.The resistivity versus temperature.

temperature decreased from 20 °C down to -195 °C the resistivity increased by the factor ~1.2. The cooling of tested sample in vacuum increases this factor to 1.4 - 1.5.

4.2 This material can sustain large radiation doses. The radiation tests have been carried out in Dubna by Dubna group collaborating with LPI. The results are shown in the Table2. There are no signs of the radiation influence on the HRC properties.

Table 2: **RESULTS OF RADIATION TEST (RESISTIVITY)**

neutron fluence (n/cm^2)		0	$6x10^{13}$	$1.1x10^{14}$	$4.2x10^{14}$	$6.6x10^{14}$
sample	side					
11	1	1746	1821	1797	1826	1794
	2	1870	1868	1835	1877	1832
12	1	1829	1788	1795	1789	1794
	2	1838	1823	1838	1808	1868

4.3 This material does not pollute the liquid argon. This result is obtained in Mainz University (private communication).

5. Testing of the produced electrodes

We had carried out the HV tests of all produced electrodes. The test voltage was 2.5 kV. To implement this testing special bench have been made which imitated the electrical connections of the electrodes in calorimeter module. Important element of this bench is a steel grounded plate on which brass model analogs of spacers are fixed in the positions corresponding to those in the real module. On this bench the following measurements have been made:

5.1 Isolation resistance between external surfaces of each EST plate (one of which was grounded);

5.2 Isolation resistance between two surfaces of each EST (both under HV) and grounded spacers. The leakage current of all produced EST plates was less than 50 nA.

5.3 Isolation resistance between each grounded pad of the ROB and external surfaces (both under HV, spacers are grounded). In most cases leakage current for pads was less than 25 nA. In a few cases we have discovered larger currents which were due to the defects on the external surfaces. The last could be cured by removing a small area (d = 5mm) of HRC layer.

Resuming we can say that the obtained experience has given us more certainty in planning work on HEC Calorimeter module 0.

Acknowledgments

Authors would like to thank Dr.H.Oberlack for his competent direction and Max-Planck-Institute (Munich) for financial support . They also would like to acknowledge colleagues from MPI, RIECP, ELIFOM, JINR and IHEP.

rascati Physics Series Vol. VI, (pp. 441–448)
I Int. Conf. on Calorimetry in HEP – Frascati, June 8–14, 1996

THE KEDR LIQUID KRYPTON CALORIMETER: DESCRIPTION AND RECENT PROTOTYPE RESULTS

V.M. Aulchenko, A.K. Barladyan, A.E. Bonder, S. Ganzhur, A. Krasnov, G.Ya. Kezerashvili, S.G. Klimenko, G.M. Kolachev, V.M. Malyshev, A.L. Maslennikov, A.M. Milov, N.Yu. Muchnoi, A.P. Onuchin, V.S. Panin, S.V. Peleganchuk, S.G. Pivovarov, Yu.A. Pogorelov, G.E. Pospelov, L.V. Romanov, Yu.A. Tikhonov, V.I. Yurchenko, V. Zhilich
Budker Institute of Nuclear Physics, Novosibirsk 630090, Russia

F. Lanni, F. Palumbo
Dipartimento di Fisica dell'Università and Sezione INFN, Milano, Italy

P. Cantoni, P.L. Frabetti, L. Stagni
Dipartimento di Fisica dell'Università and Sezione INFN, Bologna, Italy

P.F. Manfredi, V. Re, V. Speziali
Dipartimento di Elettronica Università di Pavia and Sezione INFN, Pavia, Italy

ABSTRACT

iquid krypton calorimeter for *KEDR—VEPP-4M* experiment is described. The ‹perimental results with a prototype, obtained at the tagged photon beam of *'EPP-4M* in the photon energy region between 50 and 4500 MeV are presented. he results on the energy resolution are in a good agreement with the Monte-Carlo ‹pectations and equals to 6% and 2% at 100 and 1000 MeV respectively. The ›ace resolution is about $1 - 1.5$ mm in a wide energy region and agrees also with ıe expected one.

Introduction

.n electromagnetic calorimeter based on liquid krypton is under construction for the *:EDR* detector at e^+e^- collider *VEPP-4M* with a maximum energy of 6 GeV [1]. . LKr calorimeter gives the possibility to obtain an energy resolution in the en- rgy range $30 \div 5000$ MeV comparable with that of NaI or CsI calorimeters and ıuch better position resolution for photons, due to the possibility of measuring the hoton conversion point. Furthermore the fine granularity of the calorimeter pro- ides information for particle identification based on dE/dx method as well as e/π ›paration using the shower longitudinal structure.

2 LKr calorimeter design

The endcaps of the KEDR calorimeter are made of CsI crystals. The barrel part is based on ionization chambers with LKr as a working media [2)-8)]. The inner radius of the barrel is 75 cm, the thickness is 68 cm $(15 \cdot X_0)$. The total amount of LKr is 30 tons. Due to the small electrodes thickness the calorimeter is practically homogeneous.

The electrode system is inserted into a hermetic aluminium vessel, which is located inside another one made of stainless steel for thermoinsulation purposes. The space between these two vessels is occupied by shield-vacuum thermoinsulator. The cooling of the cryostat is realized with liquid nitrogen flowing at a pressure of 20 bar through the tubes welded to the walls of the internal vessel. The thickness of the entrance wall is 1 mm of stainless steel and 14 mm of aluminium for a total thickness of $0.2 \cdot X_0$.

The signal is read out from high voltage electrodes, divided into rectangular pads, forming towers, oriented to the interaction point. The entrance size of the towers is 10×10 cm^2. The eight grounded electrodes of the first $6X_0$ are divided into strips of about 5 mm width for z and ϕ coordinates measurements. The layout of the calorimeter is shown in fig. 1.

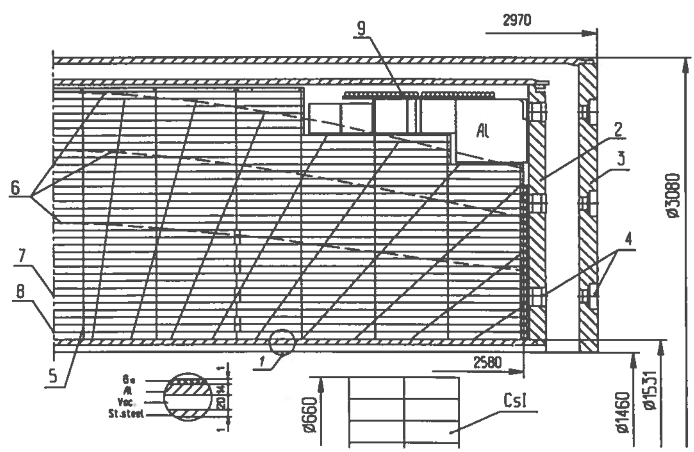

Figure 1: Layout of the LKr calorimeter. 1 – entrance wall; 2 – cold flange; 3 – warm flange; 4 – multipin connectors; 5 – spacers; 6 – lines of equal thickness; 7 – strip elecrode; 8 – tower electrode; 9 – high voltage board.

The ionization chambers of the calorimeter are operated in the electron-lse mode. The electrons drift time at the working electric field of 0.5 kV/cm is ιs. The measurement of the collected charge is provided by the charge sensitive eamplifiers, simple RC–$2CR$ shaper with a time constant of 1 μs and 12-bit ADC. ıe typical value of the equivalent noise charge is about 2000 electrons. The total mber of the electronics channels is 7240; 2304 are connected with the towers, 1864 with z-strips and 3072 – with ϕ-strips.

Expected parameters

1 Energy resolution

he energy resolution of the LKr calorimeter is mainly determined by the following ctors:

- Longitudinal (L) and transverse (T) energy leakage fluctuations;
- Sampling fluctuations in the dead material (S);
- Geometric (induction) effect (G);
- Variation of the gap (V);
- Electronic noise (N);
- Radioactivity of LKr (R);
- Calibration uncertainty, electronics instability;
- Algorithm of energy reconstruction.

Showers produced in LKr have been simulated by Monte-Carlo method ır the real structure of the calorimeter in the presence of a magnetic field of 1.8 T.

The Monte-Carlo data for the longitudinal leakage and sampling fluctua-ons ($L+S$) are well fitted by the simple formula

$$(\sigma_E/E)_{L+S} = 0.8\% + 0.3\%/\sqrt{E(GeV)}.$$

The contribution of the transverse leakage (T) depends on the acceptable ze of the block containing one photon and can be made negligible for a single hoton.

The geometric (induction) effect (G) arises from the dependence of the ollected charge on the ionization distribution inside the gap. The contribution of this effect is decreased with the ratio (r) of the charge integration time to the electron drift time. For real situation $r = 0.1$ and

$$(\sigma_E/E)_G = 1.16\%/\sqrt{E(GeV)}.$$

The contribution of the gap size variation (V) depends on the ratio σ_d/d, where d is a gap width, and σ_d – its rms variation. This contribution $(\sigma_E/E)_V = 1.7\%$ at the energy 0.1 GeV and 0.8% at 0.5 GeV when $\sigma_d/d = 5\%$. It means that the necessary mechanical accuracy of the gap width should be not worse than 1 mm.

The electronic noise has to be treated together with the LKr radioactivity. The natural krypton contains small admixture of the β–radioactive isotop ^{85}Kr with a spectrum bound of 0.67 MeV, half-life of 11 yr and activity of 300 $decays/sec$ in 1 cm^3 of LKr. The events of β-decay produce point-like ionization in the gap of the chamber. It results in the random consequence of rectangular current pulses in the input circuit of the preamplifier and can be treated as an extra source of noise. Their common contribution depends slightly on the electron capture length and results in 0.8 MeV for the typical tower with an electric capacitance of 480 pF and LKr volume of 5000 cm^3 [2, 8, 12, 13].

The calculated energy resolution is well approximated by the simple formula:

$$\sigma_E/E = 1.9\%/\sqrt{E(GeV)}.$$

3.2 Space resolution

In contrast to the crystal calorimeters where the space resolution is limited by the fluctuations of the shower center of gravity, in LKr calorimeter the position of the first point of the photon conversion into pair of charged particles can be measured, that results in a considerably better space resolution.

At low photon energy (less than 300 MeV) the space resolution is determined by the multiple scattering, at higher energy it depends on the readout method. For the anode readout the space resolution is determined by a strip width at high energy i.e. 1.4 mm in our case. For the cathode readout the resolution obtained for high energy photons using of the center of gravity technique is fractions of millimeter [2].

3.3 Particle identification

Pulse height measurements from the strips can be used for charged particles identification by the dE/dx method. The calculation shows that π/K separation could be done at the level $> 2\sigma$ up to the momentum of 1 GeV/c.

Prototype experiment at the tagged photon beam

he experiment was performed at the facility *ROKK-1M* [9] at *VEPP-4M* e^+e^- ollider. High energy photons are produced in the Compton scattering of the laser hotons (2.34 eV) on the electron beam.

The scattered electrons are detected by means of the detector *KEDR* Tag- ing System (TS) [10] with energy resolution for photons of 1.3%. The layout of ie *ROKK-1M* and *VEPP-4M* experimental area is shown in fig. 2.

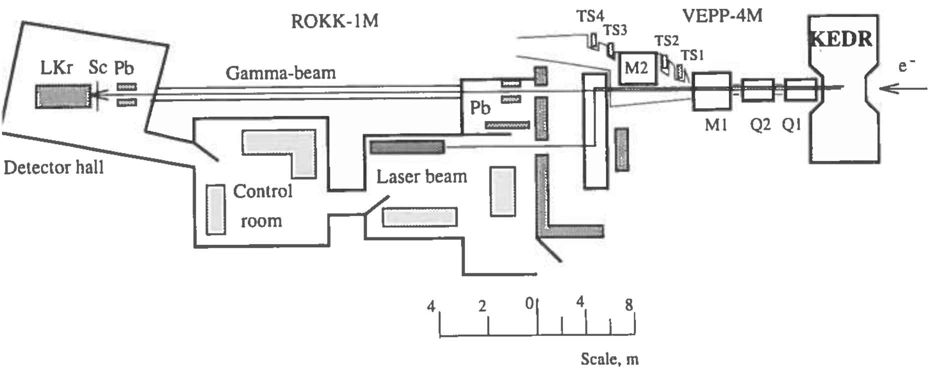

Figure 2: The layout of the $ROKK-1M$ and $VEPP-4M$ experimental area.

The prototype of the LKr calorimeter (prototype-400/3) contains 400 kg f liquid krypton, has the electrode system similar to that of the *KEDR* calorimeter lescribed above and the same electronics. Total number of electronics channels is 6. The detailed description of the cryostat and cryogenic system design is published lsewhere [2, 13].

The measurements of the energy resolution were made in two independent nethods [13]. In the energy region covered by the Compton spectrum we selected the amples of monochromatic photons by means of TS-system and fitted the measured pectra by the logarithmic normal distribution:

$$\frac{dp}{dx} = \frac{1}{\sqrt{2\pi}} \cdot exp\left\{-\frac{1}{2}\cdot\left[\frac{ln^2(1+ax)}{a^2}+a^2\right]\right\},$$

$$x = \frac{f(E-E_p)}{\sigma}, \quad \sigma = \frac{FWHM}{2.36}, \quad f = \frac{sh(a\sqrt{ln4})}{a\sqrt{ln4}},$$

vhere E is the energy parameter, E_p is the most probable energy, a is conventional asymmetry.

Another method is based on the analysis of the edges of Compton and single bremsstrahlung spectra. The convolution of the theoretical spectrum with the same logarithmic normal function describes the edge very well and allows one to find the energy resolution.

The data obtained in whole energy region between 40 and 4500 MeV are shown in fig. 3.

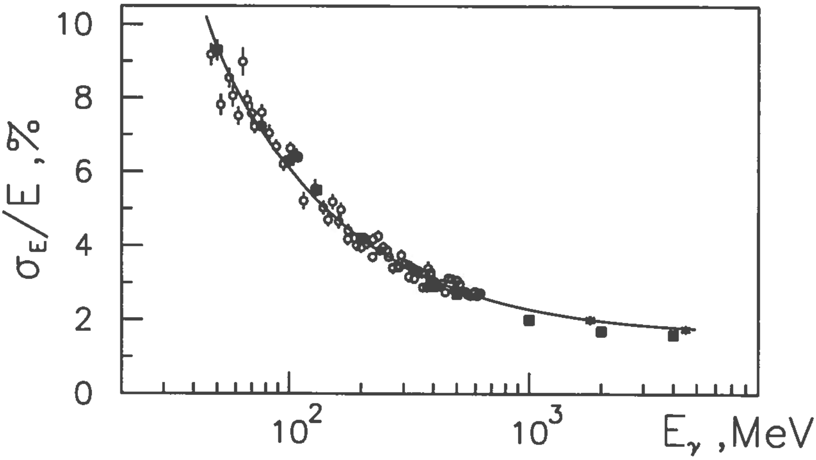

Figure 3: Energy resolution. Points – experimental data obtained with tagging system – opened circles, Compton spectra – black circles, bremsstrahlung spectra – asterisks. Black squares – MC simulation, curve – the fit of experimental data.

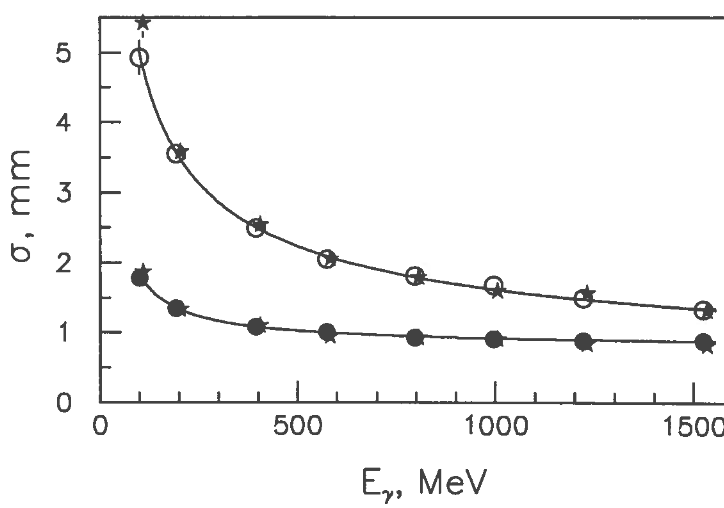

Figure 4: The space resolution. Black, opened circles – the experimental data for 1-st and 2-d layers respectively, asterisks – MC simulation, curves – the fits.

All experimental data are well-fitted by the function:

$$((\sigma_E/E)\%)^2 = (a/E(MeV))^2 + (b/\sqrt{E(MeV)})^2 + c^2,$$

ith $a = 305\ MeV$, $b = 50.2\ MeV^{1/2}$, $c = 1.61$.

For the experimental study of the space resolution for photons several runs ith the collimated photon beam were performed.

For coordinate measurements we defined the function of the pulse heights om three adjacent strips – so called "generalized" center of gravity. This function epends on the photon coordinate in a continuous and monotonous way and was easured in 10 points with 1 mm step between centers of two strips [13].

The resolution depends slightly on the coordinate across the strip. Averg- g the data taken in 10 points on the collimator position we have determined the verage space resolution for the first and second gaps counting from that gap, where e photon conversion occurred. The results are plotted in fig. 4 versus the photon ergy.

Conclusions

he described calorimeter is a part of the multipurpose detector *KEDR* at e^+e^- ollider *VEPP-4M* at Novosibirsk. It combines the high energy resolution proper o the crystal calorimeters with high space resolution for photons in a wide energy egion. The energy resolution was measured in the prototype experiment at the agged photon beam in the energy range between 40 and 4500 MeV. The results re in a good agreement with Monte Carlo expectations. The preliminary results n the space resolution for photons show the possibility of coordinate measurements ith accuracy considerably better than the width of strip.

Acknowledgments

he authors would like to express their gratitude to professor A.N.Skrinsky and rofessor V.A.Sidorov for a support and to *VEPP-4M* staff whose efforts made his work possible and to V.M.Katkov and V.M.Strakhovenko for the assistance in he analysis of the bremsstrahlung spectra.

References

1. V.M.Aulchenko et al. Proc. of the 24 Int. Conf. on High Energy Physics (conrtib. paper, Munich, 1988) V.V.Anashin et al. Proc. of the Int. Symp. on Position Detect. in High Energy Physics (Dubna, 1988)
2. V.M.Aulchenko et al. Nucl.Instr.and Meth. **A289**, 468 (1990)
3. V.M.Aulchenko et al. Proc. of the 5th Int.Conf. on Instr. for Coll.Beam Phys. (Novosibirsk, 1990)
4. V.M.Aulchenko et al., Proc. Int.Conf. on Calorimetry at High Energy Physics (FNAL, 1990).
5. V.M.Aulchenko et al., Proc. 4-th Topical Seminar on Exp. Apparatus for High Ener. Part. Phys. and Astrophys. (San Miniato, 1990)
6. P.Cantoni et al., Proc. Fifth Pisa Conf. on Calorimetry at High Energy Phys. (Pisa, 1991)
7. V.M.Aulchenko et al. Nucl.Instr.and Meth. **A316**, 8 (1992)
8. V.M.Aulchenko et al. Nucl.Instr.and Meth. **A327**, 194 (1993)
9. G.Ya.Kezerashvili et al. Nucl.Instr.and Meth. **A328**, 506 (1993)
10. A.E.Bondar et al., Proceed. of XXII International Conference on the Accelerators of High Energy Charged Particles, **1**, 309 (Dubna, 1992)
11. V.M.Aulchenko et al., Preprint INP 88-29 (Novosibirsk, 1988)
12. V.S.Panin, S.V.Peleganchuk, Preprint Budker INP 95-26 (Novosibirsk, 1995)
13. V.M.Aulchenko et al., Preprint Budker INP 95-96 (Novosibirsk, 1995)

EASUREMENTS OF ELECTRON DRIFT VELOCITY IN LKr-METHANE MIXTURES

P. L. Frabetti
Dipartimento di Fisica dell'Università and Sezione INFN, Bologna, Italy

Written contribution not received

ıscati Physics Series Vol. VI, (pp. 451–458)
INT. CONF. ON CALORIMETRY IN HEP – Frascati, June 8–14, 1996

SIGNAL SHAPE ANALYSIS AS A TOOL FOR PRECISION CALIBRATION AND MONITORING OF THE ATLAS EM CALORIMETER

G. Battistoni*
INFN, Sezione di Milano, Via Celoria 16, 20133 Milano, Italy

(*for the Liquid Argon Unit of the ATLAS Collaboration)

ABSTRACT

ccuracy of calibration using electronic signals is one of the strong points of the e.m. quid Argon calorimetry of the ATLAS experiment. Limitations associated, at fast aping, with residual inductances in the layout are analyzed. Another aspect, the pendence of the signal shape on the liquid temperature, has been analyzed, and correction method for temperature variation effects is proposed.

Introduction

ne of the most challenging goals for the Liquid Argon electromagnetic calorimetry ATLAS is to achieve a global constant term in the energy resolution smaller than 7% [1]. Such term arises mostly from non uniformities, which may come from fferent contributions. Two of these sources of non uniformity can, in principle, be rrected by means of an accurate analysis of the signal waveform. One source is lated to the systematic differences between the real physical signal, as generated a particle in the calorimeter, and the signal used for calibration. We shall see w these differences, in the case of short shaping times, as those foreseen for LHC eration, affect the signal shape, and how they depend on the residual inductance the path from the detector cell to the preamplifier. The second effect (a long nge one) may come from possible non uniformity of the liquid argon temperature, ith consequent non uniformity in the drift velocity. Again, the signal waveform rns out to be sensitive to that effect. Therefore, in principle, a measurement of ift time for each cell of the calorimeter can be envisaged.

The possibility to devise a successful correction method for both effects depends on the accuracy in the knowledge of the behaviour of the readout chain, and in the ability of reproducing it at calculation level.

Here we present the results of the first experimental investigation of these topics. After a description of the readout and calibration chain, we shall discuss the question of residual inductance in the connection between electrodes and readout. Then, the differences between calibration and physical signal will be analyzed. After, we shall discuss the question of the dependence of drift velocity on the liquid argon temperature, and the resulting effects on the signal shape.

2 The readout chain of the e.m. calorimeter of ATLAS

A general description of the electromagnetic calorimeter of ATLAS is given in ref. [1] and references therein. Specific reports on the details of the calorimeter design, optimization and performances are also presented at this conference [2]. In the following we shall refer to the barrel calorimeter, unless differently specified.

In Fig.1 the scheme for the readout of signal from an individual cell of the liquid argon calorimeter is shown. It will serve as reference for all the following discussion. The physical signal is expected to be a current pulse of triangular shape, with negligible rise time and base duration of about 420 ns (which is the drift time for the ionization electrons in the liquid argon gap in the barrel calorimeter, at the typical electric field of 10 kV/cm). The amplitude is proportional to the energy released in the gap (*i.e.* on the number of ionization electrons). The detector element (one cell) is represented by an equivalent capacitance. Its value depends on the longitudinal compart of the calorimeter to which the cell belongs, and to its pseudorapidity coordinate (η). For the discussion reported on this paper, the most relevant case for the barrel calorimeter is that of the cells in the middle and back longitudinal compart (where most of the energy of an e.m. shower is released). There, the capacitance ranges from 1 to 2 nF, depending on the η value of the cell. We remind here that a cell is obtained by ganging together in the ϕ coordinate 4 adjacent cells. According to the most recent design of the electronic readout, the signal is transferred outside the cryostat by means of a special coaxial cable, where it is terminated on a current preamplifier which acts as line receiver (denominated as "0T", since in this solution no active elements are used at cold [3]). In the quoted high capacitance regions, this transmission line will have a 25 Ω characteristic impedance. In principle, a residual inductance may exist between the equivalent capacitance and the coaxial cable, as discussed later. The signal is the shaped by a "CR-RC^2" filter. The internal time constant, optimized for the operation at the maximum luminosity of LHC, is τ =15.8 ns, which gives the signal output presented in Fig. 2, having a peaking time (from 5% to 100%) at about 46 ns.

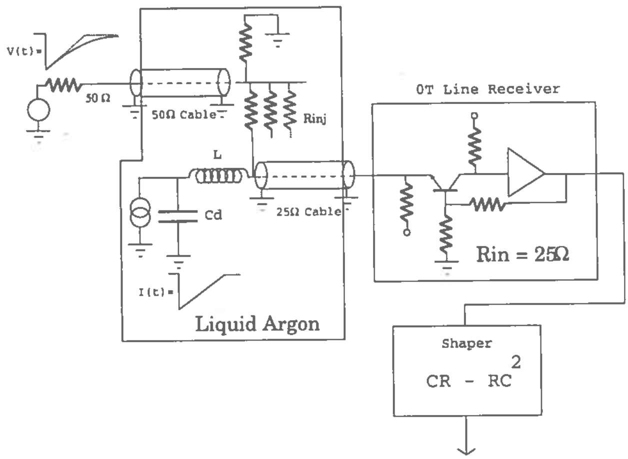

gure 1: The scheme for the readout of signal from an individual cell of the liquid gon calorimeter in the middle and back compart of the barrel.

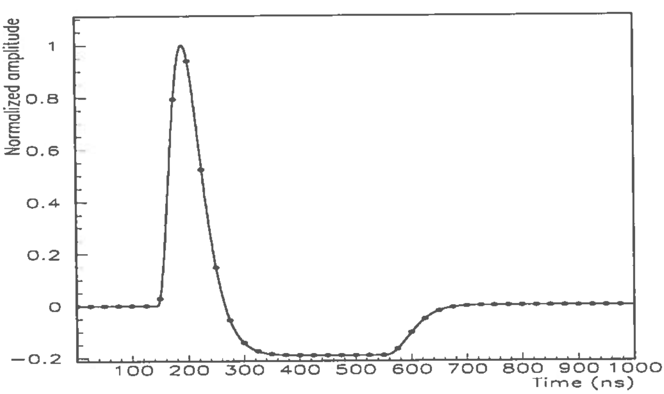

Figure 2: Typical pulse shape response of the ATLAS calorimeter.

The system for the electronic (inter)calibration of the calorimeter channels nakes use of a precise voltage generator producing an exponential falling pulse, whose time constant has the the same value of the base duration of the physical urrent pulse. The voltage calibration signal is injected through a proper resistor network, thus simulating a real current pulse, just near the connection to the coaxial cable driving out the detector signal. Therefore, there are two main reasons that make the calibration signal different from the physical one:

1. The chosen exponential shape of calibration can reproduce the triangular pulse only at very short times

2. The calibration pulse cannot see the detector capacitance at very short time (very high frequencies) because of the possible residual inductance shown in Fig.1

2.1 The residual inductance

The readout electrodes of the front and back comparts of the calorimeter allow a very short connection between the electrode itself and the coaxial cable. This is not true for the middle longitudinal compart, where the signal is transmitted to the coaxial cable through a very narrow strip running parallel to the strips of the back compart. This narrow strip introduces an additional, residual inductance, whose value ranges in the tens of nH. Furthermore, the electrodes of all comparts are connected to the signal cables by means of pin connectors which also introduce additional inductance. First measurement performed on the electrode prototypes showed that relevant local variation in the product $C_{detector} \times L_{residual}$ can be achieved: from about 1 $nF\times$ 8 nH to about $2nF\times$ 36 nH, depending on η.

3 Differences between Calibration and Physical Signal

The behaviour of the readout chain for both the physical and the calibration signal can be analytically calculated or simulated. Fig. 3 show an example of simulated physical and calibration pulse (for the same peak current value) superimposed, for the detector parameters expected at η=0 (C_d = 1.5 nF, L = 20 nH), as measured at the output of the preamplifier and at the output of the shaper.

The spike in the preamplifier output, in the case of the calibration signal, is due to the already mentioned effect of the residual inductance which makes the detector capacitance invisible at short times. After shaping this remains visible as a bump. We see that, at peaking time, the calibration pulse is systematically smaller than the physical pulse having the same peak current. At longer times, the difference in the two signals are dominated by the increasing departure between the exponential pulse from the triangle.

Fig.4 shows the calculated percentage deviation between calibration and physical signal, for a detector cell having C_d=1.5 nF, as a function of the residual

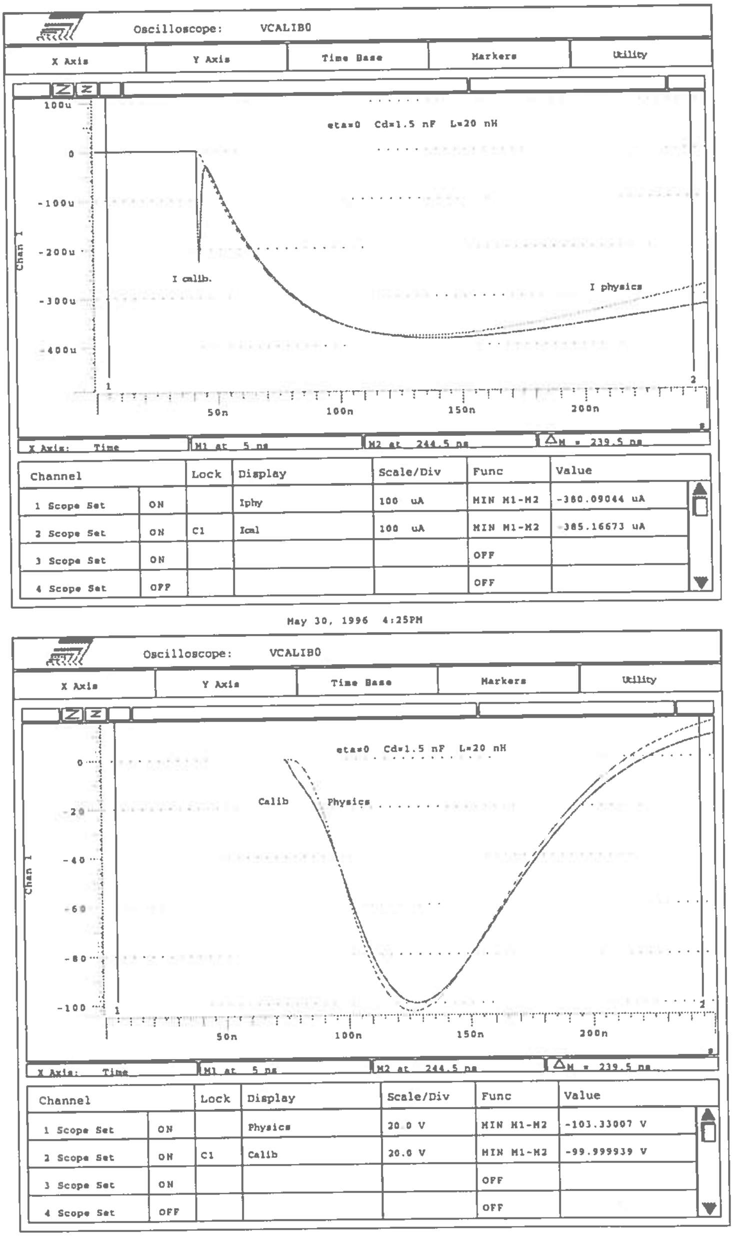

gure 3: Above: Example of simulated calibration and physical signal at the output the preamplifier. Below: Example of simulated calibration and physical signal at e output of the shaper

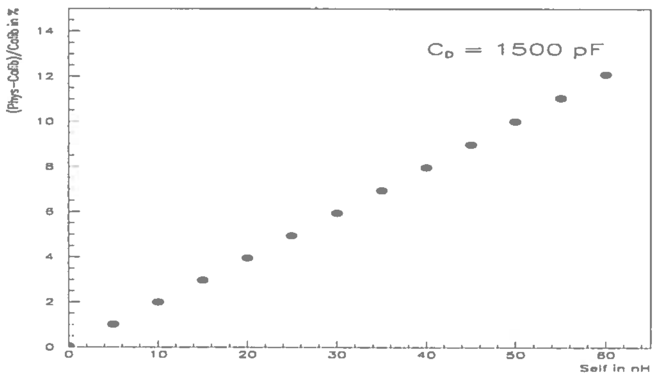

Figure 4: Calculated percentage deviation between calibration and physical signal, for a detector cell having C_d=1.5 nF, as a function of the residual inductance measured in nH

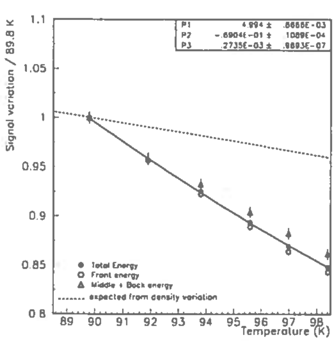

Figure 5: Measured signal variation as a function of the temperature in Liquid Argon. The dashed line is the expectation from density variation alone.

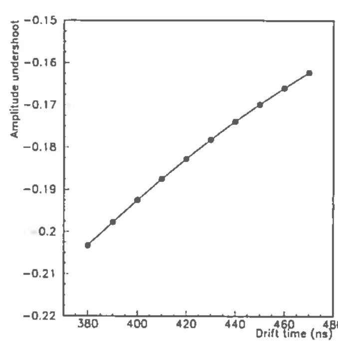

Figure 6: Correlation between the amplitude of the undershoot of the shaped signal (normalized at the peak) with the drift time

luctance measured in nH. This kind of relation can be used in data analysis correct for this systematic difference. This topic is still under investigation, in ticular by means of precision measurements on a bench test, and the correction thod is at present under test.

Temperature Variations and Signal Shape

temperature scan over about 10 °K was performed with the 2 m prototype of e Accordion calorimeter [4], taking data with a 200 GeV electron beam. The nperature was monitored by means of the pressure above the liquid at the front d back face of the calorimeter. Fig. 5 shows the signal variation, relative to the ta collected at 89.8 °K, as a function of the temperature of the liquid, for the total ergy and also for different longitudinal comparts. A clear dependence can be seen %/°K), and only part of it is accounted by the associated density variation. Most the variation is then due to a change in the drift velocity. After subtracting the ntribution of density variation, we estimated that the drift velocity changes by 55% per degree around 89.8°K [5].

An accurate measurement of drift time could bring information on the non iformity of drift velocity and gap non uniformity as well. While the first effect is pected to be rather smooth and long range, the second should be more localized or instance at the transition between different modules of the calorimeter). As far the temperature non uniformity is concerned, if one aims to a 0.1% control on e effect on the signal, this requires an accuracy of 0.075% on the the drift time, e. 300 ps for a typical calorimeter pulse, and this is quite challenging. As far the gap non uniformity is concerned, it can be calculated that the drift time is out 3 times more sensitive to the gap variation than the signal. ATLAS requires 1%control on gap uniformity (which results in 0.5% in signal uniformity) and this plies an accuracy of 1.3% on the drift time measurement, *i.e.* 5.2 ns for a typical lse.

In order to understand the possibility of performing a measurement of the ift time, we have to refer again to the shaped signal waveform (normalized at e peak) shown in Fig.2. In the case of an ideal dominant pole amplifier, such a aveform can be easily calculated, and it turns out that the amplitude of the negative be is almost flat, and sensitive to the drift time t_D through the approximate roportionality to τ/t_D. The full waveform of the shaped signal will be sampled in TLAS every 25 ns (the black dots in Fig.2). Fig.6 shows the resulting amplitude the undershoot of the shaped pulse (normalized at the peak), as obtained from a t, as a function of drift time.

The precision of the measurement is limited by different factors: i) electronic noise; for a 40 GeV signal in a cell the rms noise is 0.1% of the amplitude; ii) jitter on the bunch crossing clock; iii) cross–talk from neighbour cells: it introduces distortions since the shape of the cross–talk signal is proportional to the time derivative of the signal. Simulations show that the 300 ps goal is in principle achievable, but the conditions are the following: cross-talk must not exceed 2–2.5% in order not to be dominated by systematic errors. Furthermore, jitter can be tolerated but this increases the number of pulses needed to perform the measurement: for 200 ps jitter and 0.1% noise contribution, 40 signals/cell are necessary at 40 GeV.

Preliminary measurements were performed on the RD3 prototype, simulating the variation of drift speed by means of high voltage variation. Taking into account the introduced recombination effects which depend on the modulus of the electric field in the gap, the feasibility of the proposed method could be studied. The main difficulties in the analysis are due to some features in the shape of the physics pulse, which turns out to be slightly different with respect to the ideal calculation. The investigation of this problem is under progress. However, the first results confirmed that an accuracy better than 1 ns on the measurement of drift time can be achieved integrating a limited number of pulses.

5 Acknowledgements

C. De la Taille, N. Seguin–Moreau and L. Serin provided the essential material for this contribution.

References

1. ATLAS technical proposal CERN/LHCC/94-43.
2. see, in these proceedings, the talks from F. Gianotti, M. Seman, B. Mansoulie, P. Fassnacht, I. Vichou
3. R.L. Chase, C. de la Taille, N. Seguin–Moreau, Nucl. Instr. and. Meth., **A343** 598 (1994).
4. D.M. Gringrich et al., Nucl. Instr. and. Meth., **A364** 290 (1995).
5. C. de la Taille, L. Serin, ATLAS internal note LARG-NO-029

VI – Simulation and Analysis Techniques

Convener T. S. Virdee
Secretary F. Anulli

S. Virdee	Convener's Report
/ichou	Particle ID with the ATLAS e.m. Calorimeter
Tisserand	The 2–Photon Higgs Decay in the ATLAS Detector
Lassila–Perini	Reconstruction of Higgs $\rightarrow \gamma\,\gamma$ in CMS
:fthymiopoulos	Comparison Between the ATLAS/TileCal Hadron Barrel Calorimeter Prototype Test Beam Data and Hadronic Simulation Packages
Bonomi	Simulation of Hadronic Showers Using a Real Data Shower Library
C. Fouz	An Iron/Gas Sampling Calorimeter Based on Parallel Plate Chambers: Measured Performance and its Reproducibility by Montecarlo
Nikitenko	Simulation of the CMS Level–1 Calorimeter Trigger
Zallo	A Study of Transverse Energy Trigger Utilizing the Outer e.m. Calorimeter of FOCUS at Fermilab
Morselli	A Lead/Scintillating Fibres Calorimeter for the Measurement of Gamma Energy and Direction
Fan	A New Technique for Determining Charge and Momentum of Electrons and Positrons Using Calorimetry and Silicon Tracking
R. Sala	Study of Radiative Muon Interactions at 300 GeV

ascati Physics Series Vol. VI, (pp. 461–463)
I INT. CONF. ON CALORIMETRY IN HEP – Frascati, June 8–14, 1996

(Convener's Report)

SIMULATION AND ANALYSIS TECHNIQUES

T. S. Virdee

PPE Division, CERN and

Imperial College of Science Technology and Medicine, London, UK

ABSTRACT

An attempt is made to bring into perspective some of the presentations made in this session.

Introduction

ıe design phase of the general purpose pp LHC experiments is essentially over. Detailed st beam measurements of large scale prototypes will be almost completed by the end of)97. Comparison of the data from beam tests of these prototypes and from the mulation codes is being carried out. Detailed simulation of the response to final state ırticles of the overall detectors, including the mechanical description, is being carried ıt. It is crucial that we have confidence in these simulation studies as there is still time to ake small modifications to optimize the sub-detector designs. The detailed design work ır the electromagnetic calorimeters has benefited from the accurate reproduction by the mulation code of the electron test beam data. However the comparison when using pion ›ams suggests that the present simulation codes are not fully reproducing the test beam ıta. It is important that this is remedied soon.

/e present below a personal impression of the session (apologies to the speakers in the ›ssion whose talks are not discussed here).

Electromagnetic Calorimetry

.t the LHC the reaction that serves as the benchmark for assessing the performance ›quirements for e. m. calorimetry is the intermediate-mass Higgs decaying to two hotons. In this region the observed width of a H $\rightarrow \gamma\gamma$ signal will be entirely dominated y the instrumental two-photon mass resolution. For the best mass resolution the need for good photon energy and angular resolution is obvious. Results from detailed simulations of this channel were presented by V. Tisserand and I. Vichou on behalf of the ATLAS group and K. Lassila-Perini on behalf of the CMS group. The parameters that are studied are the di-gamma or multi-electron mass resolution, the efficiency of electron or photon identification and π^0/jet rejection. The material in front of the e.m. calorimeters has been better described in these simulations and the extent of the recovery of conversions in this material has been quantified. A judicious choice of the clustering algorithm enables recovery of a large fraction of the conversions.

In ATLAS and CMS further study and optimization is required of the barrel and endcap transition region. The non-uniform amount of material from cryostat walls and/or tracker cables in front of the calorimeters may lead to rapidly varying response and hence worse energy resolution.

3 Hadronic Calorimetry

Parameters such as pion energy resolution, e/π response and linearity were used to compare data with FLUKA, GHEISHA and CALOR hadronic simulation codes embedded in GEANT (I. Efthymiopoulos). The data come from the ATLAS Tilecal calorimeter. None of these measured parameters are satisfactorily reproduced by these codes and improvement of the code is necessary.

The performance of gas sampling calorimeters is difficult to repoduce by simulation as the sampling fraction is very small. Results from an iron/CO_2 filled PPCs (Parallel Plate Chambers) were compared with simulation code comprising GEANT + FLUKA + MICAP together with special avalanche simulation code (M.C. Fouz). Neutrons below 20 MeV were transported by MICAP. Good agreement was attained in reproducing absolute charge and energy resolutions using electron and pion beams. This was used to predict the response, especially to slow neutrons, of such a calorimeter placed in the very forward region at the LHC.

The above suggests that the low energy end of the hadronic cascade needs to be described better.

P. Sala showed that an improvement of momentum resolution is possible for low momenta muons if the energy lost in the ATLAS hadronic calorimeter (Tilecal) can be taken into account. The aim of this work was to quantify the improvement when the inner tracker information is not used.

cknowledgements

would like to thank the organizers for an enjoyable and a well organized conference. I ould also like to thank the speakers in my session for giving instructive talks.

scati Physics Series Vol. VI, (pp. 465–473)
INT. CONF. ON CALORIMETRY IN HEP – Frascati, June 8–14, 1996

PARTICLE ID WITH THE ATLAS e.m. CALORIMETER

Irene Vichou
IFAE - Universitat Autonoma de Barcelona, Spain

for the ATLAS/LARG Collaboration

ABSTRACT

›bust and efficient particle identification capability is needed in the difficult LHC vironment. The ATLAS detector, in particular the EM calorimeter, has been timised to efficiently extract the (rare) events containing genuine electrons and otons from the large jet background. Hereafter several particle identification ıdies are described, performed with detailed simulations of the ATLAS detector. ırticular emphasis is given to the performance of the electromagnetic calorimeter.

Introduction

[LAS is one of the two experiments designed for the LHC [1], whose environment ll be particularly demanding and imposes stringent requirements on the detector rformance. The electromagnetic calorimeter is a vital part of the detector [2], ıying the basic role for energy measurements and particle identification. The esent paper is focused on electron and photon identification studies emphasizing e role of the EM calorimeter in tagging the signal and rejecting the relevant ckgrounds. It has to be mentioned that full detector simulation is exploited taking ;o into account detector noise and pile-up of minimum bias events. The paper is ganised as follows: Section 2 makes an account on the physics motivation for good ırticle-ID performance and gives a brief description of the EM calorimeteter of [LAS. Section 3 is about the photon identification against jet and π^0 rejection ıdies. Section 4 refers to electron identification against jets and tagging of soft ›tons in b-jets and finally section 5 presents the summary and the conclusions.

2 Physics motivation and EM Calorimeter of ATLAS

The interesting physics chapters to explore at LHC are really a lot. We can imagine of too many signals to search for, which are unfortunately rare and difficult to extract in the high-rate LHC environment. A critical issue for the detector design is the particle-ID capability which will allow us to maximize detectable rates over backgrounds.

Some of the relevant physics issues are:

- The Higgs discovery in its decay mode to $\gamma\gamma$. This search needs good γ-identification and high background rejection of QCD jets and fast π^0's. The EM calorimeter holds the principal role for this study.

- The inclusive electron production is a vast domain since it comprises Higgs and top physics as well as W and Z production. Good electron identification is thus essential with the calorimeter assisting the role of the tracker. Especially for b-physics the calorimeter can help in tagging low p_T leptons in b-jets and reject non b-jets.

The ATLAS experiment has chosen a liquid ionisation calorimeter filled with liquid Ar as active medium and accordion shaped absorber (Pb) plates and electrodes with their zig-zags running parallel to the incident particle direction [3]. Its coverage extends down to $|\eta| < 3.2$ consisting of a barrel ($|\eta| < 1.4$) and two endcap ($1.4 < |\eta| < 3.2$) parts. The longitudinal and lateral segmentation of the calorimeter is shown in table 1. The first very fine in η sampling of the calorimeter, plays also the role of a preshower device while the presampler is used for recovery of the energy lost in the upstream material [1]. The design optimisation has been decided upon benchmark physics performance considerations [4].

3 Photon Identification

3.1 Photon ID and jet rejection

One of the principal reasons for powerful photon ID with the EM calorimeter at LHC is the detection of the Higgs boson in its decay mode to two γ's in the mass range 80 to 130 GeV. The main backgrounds are the irreducible $\gamma\gamma$ continuum and the reducible QCD jj and γj backgrounds in the case that one or both jets fake a photon on the detector. In the di-photon mass range of 70 to 170 GeV the ratios of jj and γj cross sections to the irreducible $\gamma\gamma$ continuum are 2×10^6 and 8×10^2

[1] tracker and cryostat with the embedded in it superconducting coil

Table 1: EM calorimeter granularity.

	Barrel	Endcap
η-range	$\lvert\eta\rvert < 1.4$	$1.4 < \lvert\eta\rvert < 3.2$
samples in depth	3	3 $(1.4 < \lvert\eta\rvert < 2.4)$
		2 $(2.4 < \lvert\eta\rvert < 3.2)$
granularity $\Delta\eta \times \Delta\phi$	S1: 0.03×0.1	S1: $0.003 \times 0.1(\lvert\eta\rvert < 2.4)$
	S2: 0.025×0.025	S2: 0.025×0.025
	S3: 0.05×0.025	S3: 0.05×0.025
		S1/S2: $0.1 \times 0.1(\lvert\eta\rvert > 2.4)$
presampler	1 layer	–
presampler $\Delta\eta \times \Delta\phi$	0.025×0.1	–

;pectively. To be on the safe side for the Higgs search we need a jet rejection of 00 in the p_T range 25 to 75 GeV.

A detailed study of the ATLAS capability in identifying photons and re- :ting jets has been performed exploiting the full simulation of the detector [5]. ıe samples used to extract the results are:

- 10^6 jets with $p_T{}^{parton} > 17$ GeV/c and 1500 photons with $p_T = 20$ GeV/c d uniform $|\eta|$ distribution down to 2.5.
- 2×10^5 jets with $p_T{}^{parton} > 35$ GeV/c and 3000 photons with $p_T = 40$:V/c [2].
- 2000 $H \rightarrow \gamma\gamma$ events of $m_H = 100$ GeV.

The photon and $H \rightarrow \gamma\gamma$ samples were used to study the photon detection iciency and set cuts on discriminating variables and the jet samples to conse- .ently study the jet rejection.

In this study calorimeter variables relevant to the shape of the shower are ed with the aim to recognise between EM clusters coming from γ's or jets, exploit- g the longitudinal segmentation and the high granularity of the EM calorimeter. ıts are set on the hadronic leakage behind the EM cluster (E_T^{had} in an area of $\eta \times \Delta\phi = 0.2 \times 0.2$ behind the EM cluster), on the isolation on the EM calorime- r (R^{isol}, the ratio between the energy leaking out of the 3×5 cluster to a 7×7 gion [3] and the 3×5 cluster energy) and on the transverse shape (R^{core}, the ratio :tween the energy of the four hottest EM towers and the 3×5 cluster energy) ıd width ($\sigma_w = \sqrt{\sigma_\eta{}^2 + \sigma_\phi{}^2}$) of the shower. The shape of these variables in the ses of clusters originating from γ's and jets are shown in fig. 1. The jet rejections ıtained by the calorimetric cuts are:

$$R_{jet} = 1200 \text{ for } \varepsilon_\gamma = 90\% \text{ for the low } p_T \text{ sample}$$

[2]The first jet sample will be referred to as low-p_T sample and the second one as high-p_T sample.
[3]number of EM cells in $\eta \times \phi$

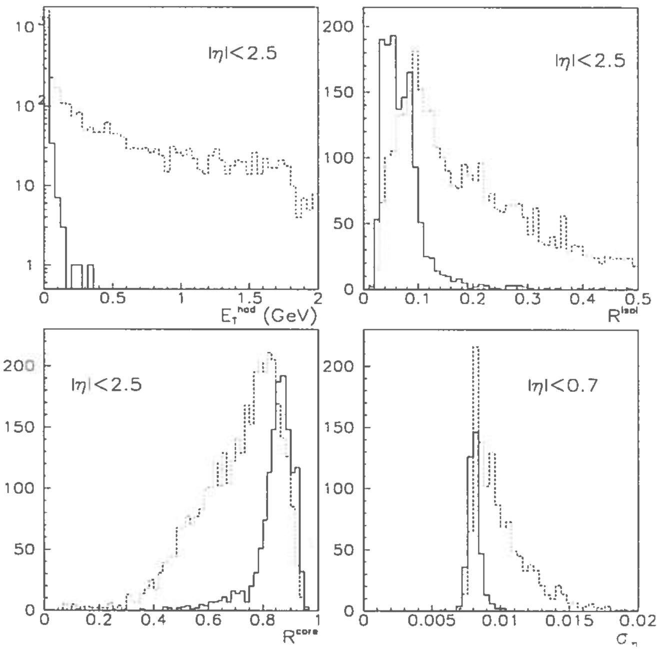

Figure 1: Discriminating calorimeter variables for clusters coming from photons (full line) and jets (dashed line).

$$R_{jet} = 2500 \text{ for } \varepsilon_\gamma = 90\% \text{ for the high } p_T \text{ sample}$$

The remaining population of jets faking photons on the calorimeter consists of 80% of meson resonances decaying into two photons (π^0, η, ω, η''s) among which 60% come from isolated π^0's. From the rest, 12% come from quark bremsstrahlung, 4% are direct photons and the remaining are due to e's from b, W or Z decays or due to single hadrons.

It is now clear that to achieve the desired rejection of the reducible Higgs background the π^0's have to be well separated from the photons on the calorimeter system. This study is presented in the following section.

3.2 Photon ID and π^0 rejection

As seen from the result on jet rejection a suppression factor of 3 is needed against π^0's to assess the required QCD background rejection for the $H \rightarrow \gamma\gamma$ search. The device having the key role for that is the first sampling (strips) of the EM calorimeter which has a very fine granularity and is shallow enough to act as a preshower [7]. For this study π^0's and photons were generated with E_T= 25, 50 and 80 GeV down to $|\eta| = 2.4$ and fully simulated through the ATLAS detector. The variables

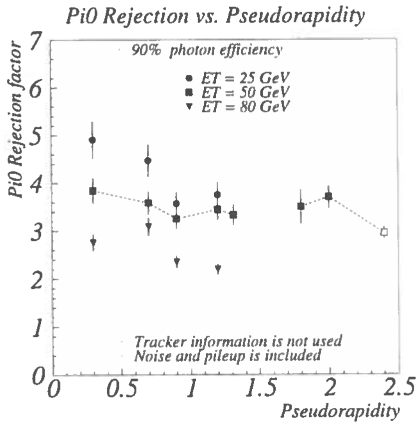

'igure 2: The π^0 rejection vs. $|\eta|$ using the strip section of the EM calorimeter.

scriminating π^0's from photons on the strip section of the calorimeter are the shape the cluster width .vs. the position in the strip, the area of the "valley" between o neighbouring energy depositions and the ratio between the energy out of the ree maximum energy strips and the energy sum in the three maximum energy rips 4).

The performance of those selections in rejecting π^0's can be seen in figure for various $|\eta|$ points. One can see that even for high-p_T the rejection stays above e desired factor of 3.

The performance expected from the full simulation of the detector has been mpared to testbeam results but for two preshower options that are now obsolete , i.e. a two layer separate preshower and a two-views integrated preshower (UV) hich is closer to what ATLAS has adopted as final solution. The comparison can seen in fig. 3, where the π^0 rejection vs η is presented. The strength of the above sults lies in the fact that the predicted performance by the detector full simulation verified in real life by the detector setup at the testbeam [4].

3 Final QCD background rejection

ombining the above measurements of performance we can extract the final rejection jets faking em showers using the EM calorimeter with its first section as preshower, as to suppress the bulk of the QCD hadronic jets by the former and the π^0's by

[4] Only non-converted photons have been considered since in the testbeam the absence of material .g. a tracker) upstream the calorimeter doesn't allow γ materialisation

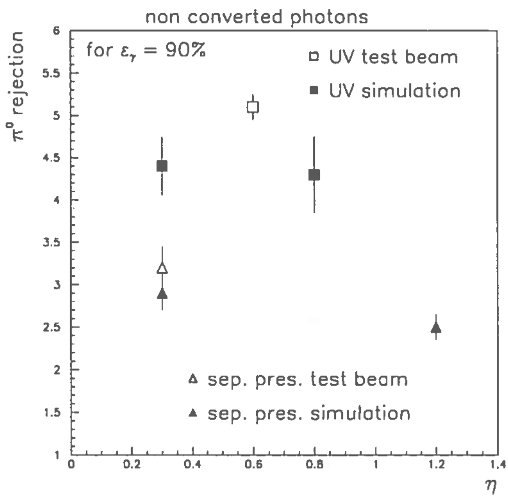

Figure 3: Comparison of the π^0 rejections vs $|\eta|$ between the detector simulation and the prototype exposure to the testbeam.

the latter. The resulting performance for the ATLAS calorimeter system is :

$$R_{jet} = 3600 \pm 150 \text{ for } \varepsilon_\gamma = 80\% \text{ for the low } p_T \text{ sample}$$
$$R_{jet} = 7500 \pm 380 \text{ for } \varepsilon_\gamma = 80\% \text{ for the high } p_T \text{ sample}$$

This shows that the convolution of cuts on EM and preshower can drive to the desired jet suppression. The above rejections are also verified if we apply the π^0 rejection criteria to the full sample of em jets remaining after the EM calo criteria (instead of using rejections extracted from single π^0's).

In the above samples photons converted in the tracker material before the calorimeter are present, but not treated separately. Their pattern on the calorimeter has a deteriorating effect on the π^0 rejection, since they may resemble to π^0's. The tracker can be used in combination with the calorimeter, since it can reconstruct the γ's materialised before the calorimeter face. In this case the rejection can be significantly improved.

The impact of this result on the Higgs search can be summarised in fig. 4. It is clear that the sum of γj and jj backgrounds after their suppression by the EM calorimeter stays below 20% of the irreducible QCD background in the mass region relevant for the $H \to \gamma\gamma$ discovery.

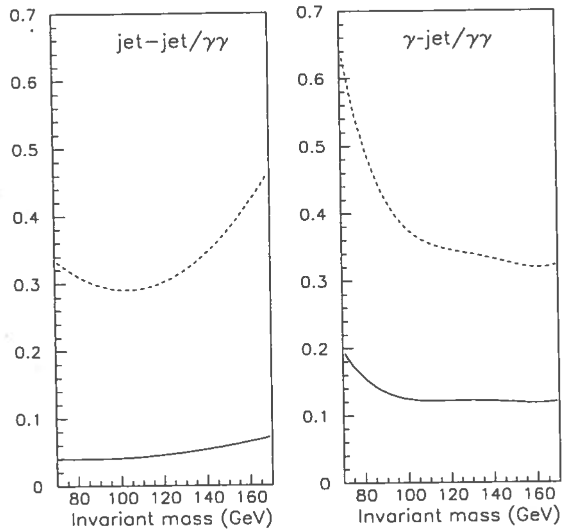

gure 4: The ratio of jj and γj to the irreducible $\gamma\gamma$ continuum after the EM ashed line) and after the preshower (full line) cuts.

Electron Identification

Electron ID vs jet rejection

ie inclusive electron identification with good reconstruction efficiency is the pre- quisite for many interesting channels of LHC physics. This implies again the need : large QCD background rejection. In this case the calorimeter plays a comple- entary role to the tracking devices. Its role is valuable since the calorimeter cluster rves as the "seed" for the track finding and also defines the energy for the E to p atching.

For the study of e/jet separation the low p_T sample of QCD jets described section 3.1 was used, testing cuts on a single e's sample of similar p_T [9]. The tained rejections after calorimeter and tracker selections is shown in fig. 5. At e calorimeter level the selections used for the study of γ/j separation were used so here to enhance EM type energy deposition. We can see that after all cuts a jection of

$$R_{jet} = 5 \times 10^5 \text{ for } \varepsilon_e = 75\%$$

obtained, which is an order of magnitude bigger than the jet/e production rates tio. To this result, the calorimeter alone has contributed as much as the initial 3 ders of magnitude of jet rejection.

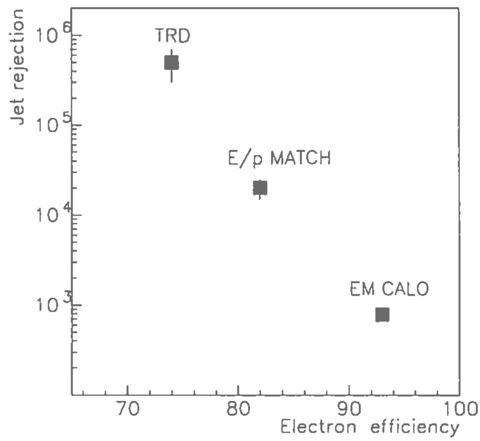

Figure 5: Jet rejection against e efficiency for different stages of selections.

4.2 Soft lepton tag

The tagging of b-jets is very interesting for many studies such as b-physics, top quark physics or Higgs through its $b\bar{b}$ decay. The basic tool is the b-vertex tag, but the calorimeter with its ability to detect low energy electron clusters can also be useful. In this spirit the role of the calorimeter here is to identify low p_T e's from $b \to e$ decays and reject light quark hadron jets. This further implies good electron(from b)/hadron(from non-b) separation capability down to calorimeter energies of 1 or 2 GeV.

For this study [10] the samples used were $H \to b\bar{b}$ events (signal) of $m_H = 80$ GeV and $H \to gg$ events (background) of the same mass. The p_T cutoff was 2 GeV/c for the single e's and hadrons which show a mean p_T of $\approx$7 GeV/c and $\approx$5 GeV/c respectively.

The variables to discriminate between e's and hadrons of such low energy on the calorimeter, were the longitudinal shape of the cluster, the energy deposited on the preshower and the E and position match between calo and tracker. The obtained hadron rejection combining calorimeter and tracker information is 450 (the initial rejection of 80 coming from the calorimeter variables) for ε_e of 75% , implying a gluon-jet rejection of $\approx$ 50 for 10% b-tagging efficiency. This result looks more attractive if we combine it with the vertex b-tagging capability (reasonably assumed to be 50%), in which case it raises the overall b-tagging efficiency by an extra $\approx$10%.

Summary and Conclusions

e ATLAS particle identification capabilities using the EM calorimeter as a basic ıl, is satisfactory in the following aspects:

- photon identification

  $R_{jet} = 7500$ and $R_{\pi^0} > 3$ keeping $\varepsilon_\gamma = 80\%$

- electron identification

  $R_{jet} = 5 \times 10^5$ keeping $\varepsilon_e = 75\%$ and $R_{non-b} = 50$ with $\varepsilon_b = 10\%$

is performance has been extracted by full simulation studies of the ATLAS de- :tor taking into account noise and pile-up and they can be considered as rather ılistic.

The above satisfactory results are mainly due to the fact that the ATLAS .orimeter system has been very well optimised in longitudinal segmentation and ınularity providing powerful tools for particle identification. Moreover, the above ɜntioned predicted performances comply with the requirements for a LHC detector.

ɜferences

. ATLAS Technical Proposal, CERN/LHCC/94-43.

. F. Gianotti, in these Proceedings.

. D.M. Gingrich et al., NIM **A364** (1995) 290.

. M.Seman, in these Proceedings.

. F. Gianotti and I. Vichou, ATLAS Internal Note, PHYS-NO-078/CAL-NO-86.

. V. Tisserand, in these Proceedings.

. D. Froidevaux et al., ATLAS Internal Note, CAL-NO-72.

. B. Aubert et al., NIM **A330** (1993) 405.
O. Linossier, private communication.

. T. Pal et al., ATLAS Internal Note, INDET-NO-127.

. F. Gianotti, ATLAS Internal Note, PHYS-NO-49.
F. Gianotti, talk at the Physics+ ATLAS Workshop, Trest-June 1995.

ıscati Physics Series Vol. VI, (pp. 475–486)
INT. CONF. ON CALORIMETRY IN HEP – Frascati, June 8–14, 1996

THE 2–PHOTON HIGGS DECAY IN THE ATLAS DETECTOR

Vincent Tisserand
Laboratoire de l'Accélérateur Linéaire
IN2P3-CNRS et Université Paris XI
91405 Orsay CEDEX - FRANCE
ATLAS collaboration [1], [2].

ABSTRACT

ıe two photon decay channel is the most clear and promising way to detect a Higgs LHC in the mass window $90 < m_{H^\circ} < 140$ GeV/c^2. As the Higgs mass is narw in this range, the observation of this channel relies heavily on the performance the electromagnetic calorimeter. A full simulation study has been performed ıth the liquid Argon ATLAS calorimeter. The simulation includes different conıbutions such as : sampling term, electronic and pile-up noise, constant term and ıgular measurement of the two photon opening angle. The level of the irreducible ıckground such as prompt diphoton production and reducible background such as ıoton-jet and jet-jet with leading π° have been estimated, taking into account the jection capability of the calorimeter. Finally the discovery potential of $H^\circ \to \gamma\gamma$ in TLAS has been computed.

Interest of the Higgs to two photon decay channel and production rate

.1 Interest of the $H^\circ \to \gamma\gamma$

'he study of the nature of the Electroweak (EW) symmetry breaking mechanism the primary goal of the future LHC proton-proton collider. The discovery of the [iggs boson would be the last major test of the standard model (SM).

The limit on the Higgs mass, from the four experiments at LEP I, is 5.2 GeV/c^2 [3]. A direct search at LEP II will be possible up to 95 GeV/c^2 and lightly lower, $\sim$ 90 GeV/c^2, in the case of the lightest CP-even Higgs boson h° of he minimal supersymetric model (MSSM) [4]. A search at TeVatron is limited due to the lack of luminosity. Recent fits of EW theory to the most recent data collected in running experiments are consistent with a Higgs mass of 70^{+111}_{-45} GeV/c^2, and 103^{+161}_{-68} GeV/c^2 if one excludes measurements of R_b and R_c, that deviate from SM predictions [5]. These values support an intermediate Higgs mass hypothesis. The precision on these fits will improve by the LHC running time : $\Delta m_W \sim 40$ MeV/c^2 (LEP II and TeVatron), $\Delta m_{top} \sim 5$ GeV/c^2 (TeVatron).

The LHC will operate at a maximum energy of 14 TeV in the mass of center with a luminosity of 10^{34}cm^{-2}s^{-1}, leading to an integrated luminosity per year of 10^5pb^{-1}. This will offer the opportunity to explore the complete allowed spectrum for the Higgs mass up to ~ 1 TeV/c^2.

In the mass window $80 < m_H < 150$ GeV/c^2, the channel $H^\circ \rightarrow b\bar{b}$ is favoured by its branching ratio, but due to the large jet background at LHC, the search for the Higgs in this mode is extremely difficult. In this context the search for the Higgs decaying in two photons is the most clear and promising way to detect the Higgs in this mass range. Moreover, this overlaps quite well LEP II domain. Above 130 GeV/c^2, the four leptons final decay mode at LHC will be competitive.

1.2 Production rate

The cross-sections (σ) and the kinematics of signal and backgrounds are generated with PYTHIA 5.7 and JETSET 7.4. The branching ratio (Br) of $H^\circ \rightarrow \gamma\gamma$ is of the order of 10^{-3}. The $\sigma \times$ Br is plotted in Fig. 1 as a function of the Higgs mass. In one year at high luminosity (100 fb^{-1}) around 4000 events are expected.

The following study has been performed with and without including higher order QCD corrections (K-factors). These corrections increase the signal cross-section by a factor of 1.5 to 1.7 [6], but are not yet fully available for all backgrounds contributions.

For the Higgs sector of MSSM, the search for the lightest Higgs boson h°, in the decay mode $h^\circ \rightarrow \gamma\gamma$ at LHC and above 90 GeV/c^2, appears as the natural complement of a search at LEP II. The MSSM predicts a maximum value for h° mass of 150 GeV/c^2, including radiative corrections. The analysis remains the same as in the case of the SM, but the rate for the signal is significantly reduced by up to a factor of 10. In Fig. 1 mass isolines for h° and corresponding $\sigma \times$Br isolines for $h^\circ \rightarrow \gamma\gamma$, are given in the usual plane (m_{A°,tan(β)), with same conditions as quoted in reference [4]. The equivalent SM rate for $h^\circ \rightarrow \gamma\gamma$ is only attained at high A° masses. As a consequence, this channel requires a large LHC integrated luminosity in order to explore the region $m_{A^\circ} < 200 - 300$ GeV/c^2 and tan(β) > 4.

In both cases, SM or MSSM, the natural Higgs width is very narrow : $\sim 10 - 20$ MeV/c^2, well below the detector resolution. In order to separate a

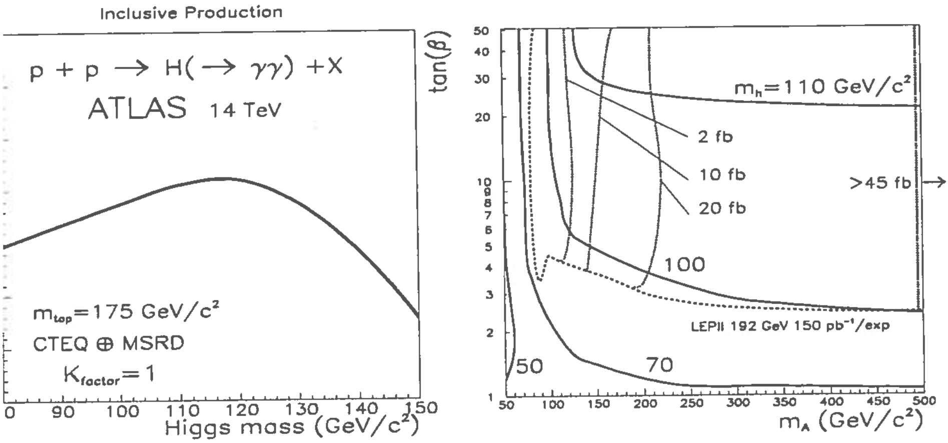

Figure 1: σ.Br of H° $\rightarrow \gamma\gamma$: SM (left), MSSM (right).

gnal from the background, an excellent mass resolution ($\Delta m_{\gamma\gamma}$) for photon pairs is ıandatory. This decay mode is taken as a benchmark signal for LHC calorimetry.

Backgrounds rejection

'he search for a H° $\rightarrow \gamma\gamma$ signal at LHC has to treat two types of backgrounds : reducible one, mainly due to jets that fake γ's in calorimeters and an irreducible ne, due to direct photon pair production. These backgrounds are predicted to be 'ell above the signal before selection by around 8 orders of magnitude. The high fficiency required to reject the backgrounds puts strong constraints on ATLAS ubdetectors. The main part of background reduction is based on the identification f isolated γ's of high transverse energy.

It is of prime importance to keep in mind that LHC will give access to nergies 10 times higher than the ones we explore today. As a consequence the ackground levels have to be evaluated with safety factors incorporated.

:.1 Reducible backgrounds

[he reducible background comes from jet-jet and γ-jet events which simulate a hoton pair. The amount of this background is 2×10^6 and 8×10^2 times the $\gamma\gamma$ continuum (cuts for $\gamma\gamma$ continuum are included at this level and the pseudo hoton pair is required to be in range $70 < m_{\gamma\gamma} < 170$ GeV/c^2). The rejection of his background is based on the use of calorimeters in a stand-alone mode. A full simulation, with GEANT 3.21, of 10^6 jets and of dedicated samples of π° and γ's, in the ATLAS detector, has been performed. The rejection of these backgrounds relies heavily on the longitudinal segmentation of the ATLAS EM CALO and on its lateral granularity [7]. The different behaviour of jets and γ's in the electromagnetic calorimeter (EM CALO) is used. A cut on the activity in the hadronic calorimeter behind the EM CALO selected cluster is also applied. An integrated preshower in EM CALO with a fine granularity (strips of $\sim$ 4 mm at a radius of 1.5 m) is used to identify the $\pi^\circ \rightarrow \gamma\gamma$ whose clusters are unresolved. More details can be found in these proceedings [8].

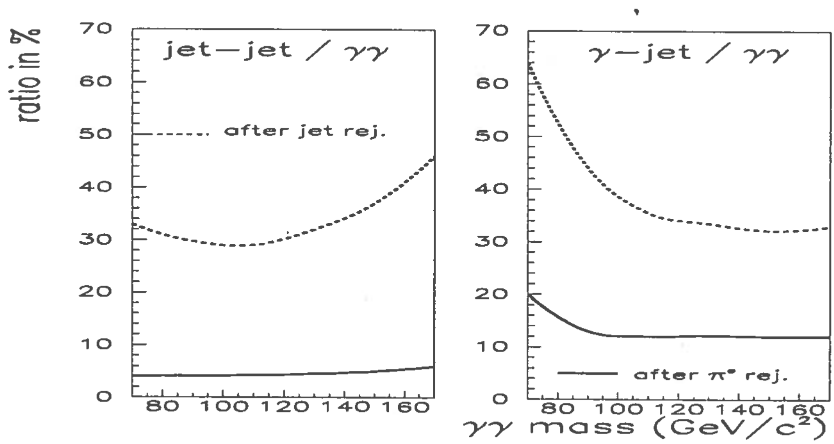

Figure 2: ratio of jet-jet (left) and γ-jet (right) backgrounds over $\gamma\gamma$ continuum after rejections.

In Fig. 2 the relative amount of this background compared to the $\gamma\gamma$ continuum is given after the shower shape analysis with the calorimeters (dashed lines). The major part of the background is already removed at this stage. The prompt isolated π°'s dominate the remaining reducible background sample. The effect of the π°/γ identification (ID) can be seen in Fig. 2 (solid lines). The integrated preshower gives a rejection factor of more than 3 for π°'s of E_T = 50 GeV (> 4 at 25 GeV). The resulting value for the rejection of jets is : $R_{jet} \sim 3600$ for P_T= 20 GeV and $R_{jet} \sim 7500$ for P_T= 40 GeV. The efficiency for the γ's of the $H^\circ \rightarrow \gamma\gamma$ signal due to this ID is fixed at 80 %.The γ-jet background dominates the sample of the reducible background at the end. Finally, the reducible background is reduced so that : $(jet - jet + \gamma - jet) < 20\% \times \gamma\gamma_{continuum}$. This safety factor of 5 is necessary due to limited knowledge of jet production and the limited power of prediction of the nulation at this level of accuracy (final detector design, unknown material effects, ysics of the generator simulating interactions of particles through the detector, :).

At the Z° mass, the $Z^\circ \to e^+e^-$ rate is 2.5×10^4 more abundant than the ' $\to \gamma\gamma$. To remove this background, a high efficiency for the ATLAS tracker to sociate a charged track with a cluster in the EM CALO is mandatory, especially high luminosity. It has been demonstrated that a rejection factor for electrons of 0 is achievable. This means that the visible rate for $Z^\circ \to e^+e^-$ can be reduced to level of 20 % compared to the $H^\circ \to \gamma\gamma$ rate at the Z° mass, at a price of a lower lative reconstruction efficiency ($\varepsilon_{H^\circ} \to \gamma\gamma \sim 75\%$).

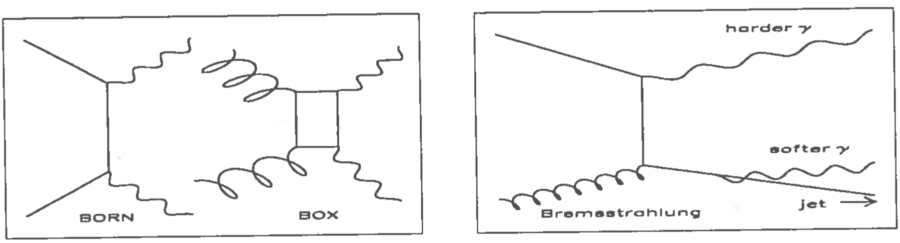

igure 3: diagrams of the contributions to the $\gamma\gamma$ continuum : Born and box (left), uark bremsstrahlung (right).

.2 Irreducible backgrounds

ıfter rejection of the reducible background, the irreducible background dominates. 'he $\gamma\gamma$ continuum has a cross section $\frac{d\sigma_{\gamma\gamma}}{dm_{\gamma\gamma}} \sim 5 \to 0.5$ (pb/GeV/c^2) in the range 0 $< m_{\gamma\gamma} <$ 150 GeV/c^2, equivalent to 10 $\to$ 100 times the rate of the sig- al. Three main processes contribute to the $\gamma\gamma$ continuum (Fig. 3). By requiring $P_T^1 > 40$GeV/c, $P_T^2 > 25$GeV/c and by only selecting central γ's, $|\eta_{1,2}| < 2.5$, the ontinuum can be reduced by a factor of 10. Above $|\eta_{1,2}| = 2.5$, the $\gamma\gamma$ background trongly dominates. So that it is not necessary to equip the ATLAS EM CALO vith a fine granularity integrated preshower beyond this limit. This limit also cor- esponds to the end of the tracking system. The relative efficiency of this selection o the signal is around 50%. After these cuts, the contribution from the box is :quivalent to the one from the Born.

The full NLO QCD calculation to the $\gamma\gamma$ continuum must be done at order $O(\alpha_s^3\alpha_{QED}^2)$ due to the box diagram, but for the moment this is not available and :his seems to be very difficult.

The third process contributing to $\gamma\gamma$ continuum is the quark bremsstrahlung. This is not fully irreducible as the softer γ is produced in the close vicinity of the jet coming from the fragmentation of the radiating parton. By requiring that there is no jet with $P_T > 15$ GeV in a cone $\Delta R = 0.7$ around the direction of the γ's[1], an additional factor 3 is obtained. After this isolation cut the quark bremsstrahlung contribution is around 50 % of the Born+box contribution.

3 Signal reconstruction : mass resolution

The $\Delta m_{\gamma\gamma}$ resolution is given by the following formula :

$$\frac{\Delta m_{\gamma\gamma}}{m_{\gamma\gamma}} = \frac{1}{2}\left(\frac{\Delta E_1}{E_1} \oplus \frac{\Delta E_2}{E_2} \oplus \frac{\Delta\theta_{\gamma\gamma}}{\tan\left(\theta_{\gamma\gamma}/2\right)}\right) \tag{1}$$

The required precision in measuring the photon energies and the two photon opening angle puts strong constraints on the ATLAS EM calorimetry. The EM CALO has been optimized with a full simulation of the ATLAS detector [7], including in particular a precise description of the LArg EM CALO with the accordion geometry of the absorbers. This simulation is in good agreement with the data obtained in test beam, with the RD3 2 meter prototype [9].

3.1 Energy resolution

The energy resolution, for single γ's of $E_T = 50$ GeV, is displayed in Fig. 4, as a function of the calorimeter pseudo-rapidity. It is parametrized as : $\frac{\Delta E}{E} = \frac{a}{\sqrt{E}} \oplus \frac{b}{E} \oplus c$, where a is the stochastic term, b the contribution of electronic and pile-up noise and c is the constant term.

3.1.1 Stochastic term

This contribution varies from 8.5 %$\mathrm{GeV}^{1/2}$ at $\eta = 0$ (90° from the beam axis) to 11 %$\mathrm{GeV}^{1/2}$ at the transition between the barrel and the endcaps, and is typically 10 %$\mathrm{GeV}^{1/2}$ in the endcaps. The energy of unconverted γ's is reconstructed in an equivalent cluster size $\eta \times \phi = 3 \times 5$ cells of the second sampling (granularity : $\Delta\eta \times \Delta\phi = .025 \times .0245$). This cluster size was found to be an optimal compromise between intrinsic resolution and sensitivity to pile-up and electronic noises, which increases with larger clusters areas.

The converted γ's are tagged in the tracker. As the e^+e^- pair opens in ϕ, due to the 2 Tesla solenoidal magnetic field, a 3×7 cluster size is used to reconstruct the energy. The presampler is used to correct for the energy lost in the

[1] $\Delta R = \sqrt{\Delta\eta^2 + \Delta\phi^2}$

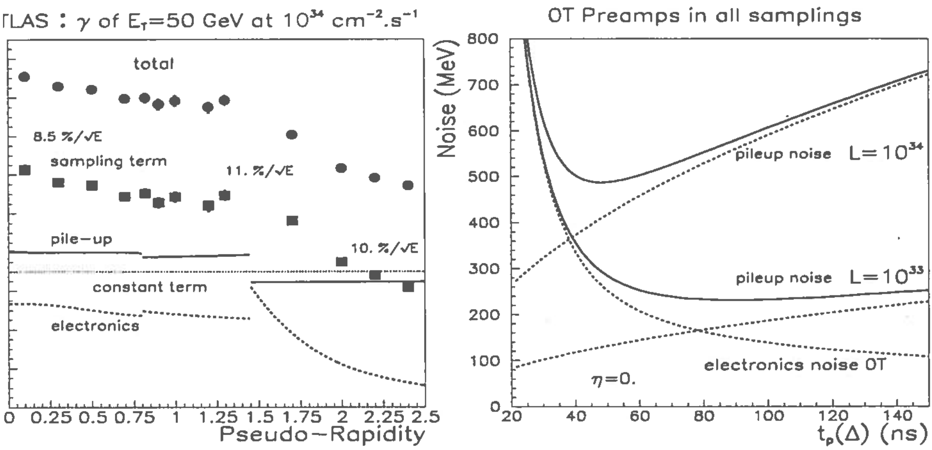

igure 4: contributions to energy resolution (left). Pileup and electronic noise as a ınction of peaking time response to signal (right).

ıperconducting coil and in the cryostat walls located in front of the EM CALO. 'he fraction of $H^\circ \rightarrow \gamma\gamma$ events with at least one converted γ is 18%.

.1.2 *Constant term*

)ue to the high energy of the γ's from Higgs decay, this contribution must be kept elow 1 %, with the goal of 0.7 % over a very large number of channels (190,000). A onstant term of 0.7 % has been achieved over 150 towers of the 2 meters prototype ı the RD3 test beam [9]. This is equivalent to 20 % of one ATLAS EM supermodule $\Delta\eta \times \Delta\phi = 1.4 \times .4$). In ATLAS, a value of 0.4 % is expected in areas of $\Delta\eta \times \Delta\phi =$ $2 \times .4$ (mechanics + electronic). It has been estimated that five days at $10^{33}\mathrm{cm}^{-2}\mathrm{s}^{-1}$ hould be enough to intercalibrate these areas with $Z^\circ \rightarrow e^+e^-$ events to an accuracy evel of 0.4 %, leading to a total constant term of 0.6 %. To be conservative in the imulation 0.7 % is taken.

.1.3 *Electronic and pileup noise*

'he pileup contribution is due to 23 events of minimum biased which are produced n average at each bunch crossing, every 25 ns, at high luminosity. This includes the ,HC bunch structure (20 % of bunches are empty). A proton inelastic cross section f 70 mb is assumed. A full simulation of the response of the ATLAS EM CALO to ileup events has been performed [10]. The $CR - RC^2$ bipolar shaping response to he triangular signal in LArg has been taken into account. The electronic noise is extracted from recent experimental measurements [11].

It has been demonstrated that, after shaping, the pileup noise sensitivity is equivalent to 1.5 times the pileup noise from one bunch crossing. Fig. 4 shows that at the optimum shaping time response to signal the electronic and pileup noise is around 500 MeV in transverse energy at high luminosity. This is the worst case as a 3×7 cluster is used (adapted to converted γ's).

3.2 Direction measurement and $\gamma\gamma$ angle reconstruction.

At high luminosity, due to the superimposed minimum biased events, the longitudinal vertex position is ambiguous. The vertex diamond size around the geometrical center of the detector is : $\Delta z \times \Delta x \times \Delta y = 5.3\ cm \times (15\ \mu m)^2$.

Techniques to determine the vertex position based on the recognition of $H^\circ \rightarrow \gamma\gamma$ events exist [12]. The $H^\circ \rightarrow \gamma\gamma$ events have typically a multiplicity of charged tracks 30% higher than the minimum biased events, moreover these tracks have higher P_T. Nevertheless the knowledge of pileup events is restricted, and a method, using the EM CALO in stand-alone, has been developped to measure the longitudinal vertex position. This method relies on the lateral and longitunal segmentation of the calorimeter.

By calculating the lateral and longitudinal centroids of the shower in sampling 1 and samplings 2 and 3, the slope of the shower can be computed and its intersection with the beam axis is determined. In Fig. 5 the resolution on the z vertex reconstruction is displayed in the case of single γ's. This corresponds to a resolution on the photon azimutal angle θ of $\Delta\theta \simeq 50$ mrad$/\sqrt{E}$ (geometric effects dominate in the endcap).

By combining the two photon measurements, the longitudinal vertex is found with a precision better than 2 cm. At low luminosity, this accuracy is estimated to be sufficient to identify the tracks coming from the $H^\circ \rightarrow \gamma\gamma$ vertex. When a γ converts in the tracker, the position of conversion is used to increase the lever arm for pointing, leading to a better vertex reconstruction.

3.3 Mass peak resolution

In Fig. 5, the mass spectrum of the signal is displayed after a full simulation of the detector response for a generated mass of 100 GeV/c^2 at high luminosity. The resolution is 1.24 GeV/c^2 and a fit over the whole mass window gives 1.26 GeV/c^2. The distribution is nicely Gaussian : 82 % of the distribution is contained in $\pm 1.4\sigma$ around 100 GeV/c^2, when the expectation is 83.8%.

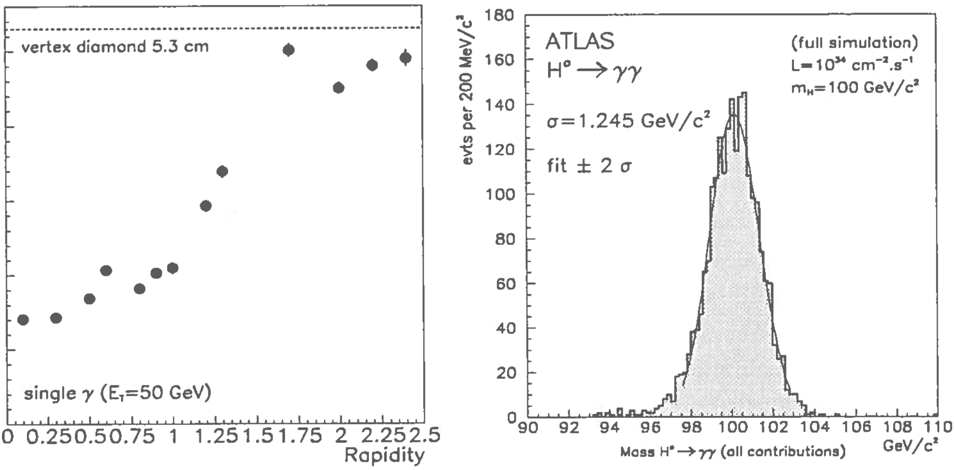

igure 5: resolution of the z vertex reconstruction versus rapidity for single γ's (left). Iass resolution for the signal (right).

Sampling term	820. MeV/c^2
Constant term (.7%)	490. MeV/c^2
Pileup $\oplus$ noise	585. MeV/c^2
$\Delta\theta_{\gamma\gamma}$ (effective RMS.)	590. MeV/c^2 (370. fit to a Gaussian)
total high Lumi. $\pm 2\sigma$ $\pm\infty$	 **1.24** GeV/c^2 1.26 GeV/c^2
total low Lumi. (vertex unambiguous) $\pm 2\sigma$ $\pm\infty$	 **1.02** GeV/c^2 1.04 GeV/c^2

Table 1: contributions to mass resolution (Higgs mass is 100 GeV/c^2).

Table 1 give the details of the contributions to the mass resolution. As xpected the sampling term dominates the resolution. At low luminosity both the ıetter knowledge of the vertex position and the smaller contribution of pileup allow o improve the resolution by 20%. For events with at least one converted γ, at .igh luminosity, a fit at $\pm 2\sigma$ gives a mass resolution equal to the resolution of the nclusive sample of events. A fit over the whole window gives 1.4 GeV/c^2. The tails .re due to early conversions in the tracker. Finally if the 0.7% constant term is modified to 0.5% (1.%), the resolution becomes 1.19 GeV/c^2 (1.35 GeV/c^2).

4 Discovery potential

Let us assume that an excess of events in the mass distribution $m_{\gamma\gamma}$, will be considered as a discovery, if it is larger than a fluctuation of the background by more than 5 standard deviations ($S/\sqrt{B} > 5$).

For a mass of 100 GeV/c^2, the total efficiency of the signal is 24% : 53% from kinematics and acceptance cuts, 81% per γ for the γ/jet ID, 87% for fiducial cuts (mainly the transition between barrel and endcap), and 80.7% for an optimized mass bin (high lumi. : 3.44 GeV/c^2, low lumi. : 2.74 GeV/c^2). The details of the numbers of signal and background events in the mass bin are given in table 2. The statistical significance is displayed as a function of the Higgs mass in Fig. 6. It turns out that the Higgs boson can be discovered already at 100 GeV/c^2 in the 2 photon decay channel, for one year of ATLAS running at the LHC high luminosity. An overlap with LEP II at 80 GeV/c^2 requires an integrated luminosity of 3.10^5pb^{-1}.

signal events in mass bin	1100
$\gamma\gamma$ background	45980
jet-jet background	1800
jet-γ background	5400
$Z \rightarrow e^+e^-$ background	-
$S/\sqrt{B}$ for 10^5pb^{-1}	**4.8**
LHC years for 5σ	**1.09**
$S/\sqrt{B}$ for 3.10^4pb^{-1}	**3.1**

Table 2: number of signal and background events for one year at 10^{34}cm^{-2}s^{-1} and statistical significance of the signal for one year at high luminosity and for 3 years at 10^{33}cm^{-2}s^{-1} (the Higgs mass is 100 GeV/c^2).

In Fig. 6, the statistical significance is also presented taking into account the K-factor. An arbitrary factor of 1.5 is applied to the box contribution. At 100 GeV/c^2, the σ.Br increases to 68 fb (instead of 47.4 fb). The significance is now 6.5 in one year at high luminosity and 4.2 in 3 years at low luminosity. As previously mentioned, the $K_{bgd.}$ is not fully calculated, but, as long as its value remains lower than $K^2_{sig.}$ ($2.3 \rightarrow 2.9$), its effect can be kept under control.

In the case of the $h^\circ \rightarrow \gamma\gamma$ search in MSSM, Fig. 6 shows that the full luminosity is required to cover the SUSY Higgs sector plane with a reasonable complementarity to LEP II. The remaining hole at $m_{A^\circ} \sim 100 - 175$ GeV/c^2 and $\tan(\beta) > 4$ will be filled using others channels such as $A^\circ \rightarrow \tau\tau$.

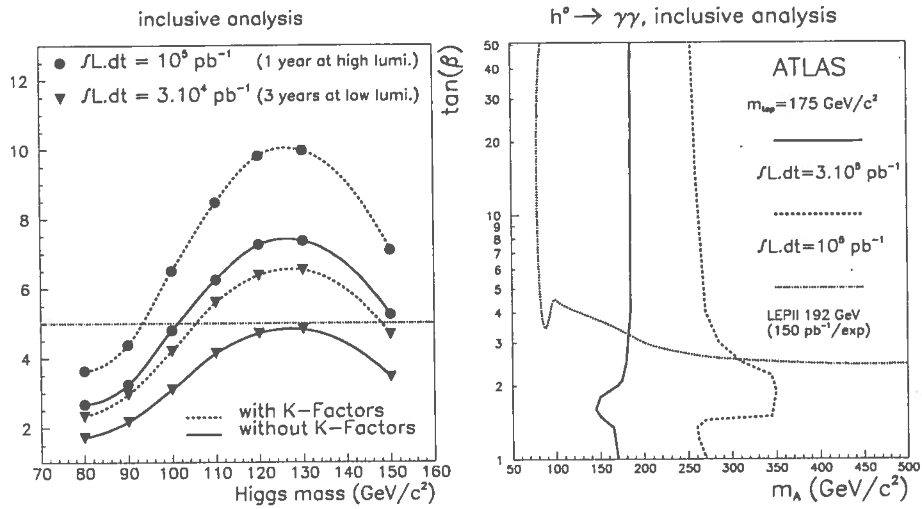

gure 6: statistical significance for different integrated luminosities and with or ithout K-factors (left). Potential for search of h° $\rightarrow \gamma\gamma$ for 2 different integrated minosities (right).

Conclusions and perspectives

has been demonstrated that the ATLAS detector has a good discovery potential r the H° $\rightarrow \gamma\gamma$. The full simulation of the ATLAS detector response to the Higgs ecaying in two photons has been performed in the most difficult conditions expected LHC. The complete background rejection capability has been studied.

Some work is still under way to a better estimation and optimisation of ie H° $\rightarrow \gamma\gamma$ discovery potential. A full simulation of 10^7 jets with the latest esign of all subdetectors is planned. The electronic front-end has been choosen be warm preamplifier outside of the cryostat, and the electronic noise value is iore precisely known. For this reason, the cluster sizes will be reoptimized : 3×3 r unconverted γ's, and 3×5 for converted γ's (better total energy resolution, asier γ-JET ID). The study of the conversion identification with the tracker at igh luminosity is in progress. For the $\gamma\gamma$ continuum, a complete NLO calculation r Born and bremsstrahlung background will be soon available [13]. Bremsstrahlung vents have been fully simulated in order to tune the isolation criteria. An up to ate study of backgrounds and signal in the associated production looking for a hoton pair with a lepton of high transverse energy, or with jets of high energy, is lso in progress.

References

1. ATLAS Collaboration, Technical Proposal, CERN/LHCC 94-93 (1994), and references therein.
2. Complete list of recents ATLAS technical internal notes used for this report is available at "http://atlasinfo.cern.ch/Atlas/GROUPS/notes.html", thanks to my colleagues.
3. J.F. Grivaz, New Particle Searches, LAL 95-83 (1995) and proceedings of IECHEP '95 conference at Brussels (Belgium), (Ed. J. Lemonne, C. Van der Velde and F. Verbeure, World scientific 1996), and references therein.
4. Results of LEP II workshops, Physics at LEP II, CERN 96-01 (ed. G. Altarelli, T. Sjöstrand and F. Zwirner).
5. D. Piccolo, Higgs Mass from Electroweak Fit, 31^{st} Rencontres de Moriond QCD, march '96, Les Arcs (France).
6. M. Spira et al., CERN TH 95-30.
7. Contributions to these proceedings from M. Seman.
8. Contributions to these proceedings from I. Vichou.
9. B. Aubert et al. (RD3 Collaboration), Nucl. Instrum. Methods **A 364** (1990) 290.
10. L. Serin and V. Tisserand, ATLAS Internal Note, CALO-073.
11. C. de La Taille, ATLAS Internal Note, LARG-035.
12. R.Y. Zhu and H. Yamamoto, GEM Internal Note, GEM TN-92-126.
13. J.P. Guillet and E. Pilon, private communication.

ascati Physics Series Vol. VI, (pp. 487–496)
I INT. CONF. ON CALORIMETRY IN HEP – Frascati, June 8–14, 1996

RECONSTRUCTION OF HIGGS → $\gamma\gamma$ in CMS

Kati Lassila-Perini
Institute of Particle Physics (IPP), ETHZ, CH-8093 Zürich, Switzerland

ABSTRACT

he mass resolution of Higgs decaying into two photons in the CMS electromagnetic ılorimeter for m_H=100 GeV has been simulated for the low luminosity phase of HC. Emphasis is put on events with a photon converting in the material in front ' the electromagnetic calorimeter. The events where a photon converts after the easuring layers of the tracker do not degrade the energy measurement noticeably. ıcluding these events, the mass resolution is shown to be 0.66 GeV. In the techniıl proposal tracker design, 18.4% of events have a conversion in the tracker, 53% ' which can be recovered with a simple algorithm. If a more sophisticated dyımic algorithm is applied for the remaining events 87% of conversion events can e recovered with only a small increase in the mass resolution.

Introduction

etecting Higgs in the decay H → $\gamma\gamma$ at the LHC in the mass range of 80-130 eV requires the best possible resolution of the electromagnetic calorimeter. To btain that, the CMS experiment will use lead tungstate crystals ($PbW0_4$) with xpected energy resolution of $2\%/\sqrt{E} \oplus 0.5\%$. CMS has a powerful inner tracking ystem which introduces material (20% X_0 at $\eta = 0$) in front of the electromagnetic alorimeter. This material causes a high probability of photon conversions and the roduced e^+e^--pair will separate in the 4 T solenoidal magnetic field which could ead to a degradation of the photon energy measurement.

The purpose of this work is to evaluate different contributions to the mass esolution using a detailed detector simulation and to study the possibility of recovring events with a photon converting into a e^+e^--pair before the electromagnetic calorimeter without degrading the mass resolution. This requires a detailed description of the detector geometry and a full shower simulation of the Higgs events.

2 CMS lead tungstate calorimeter

The CMS barrel electromagnetic calorimeter [1] consists of tapered lead tungstate crystals of 20.5 x 20.5 mm^2 front face and of 23 cm length (25.8 X_0) positioned on a cylinder of 144 cm radius from the beam axis. There are 432 crystals in the ϕ direction and 2x108 crystals in the η direction, resulting in a total of 93312 crystals for the barrel ($|\eta| < 1.56$). The crystals are arranged in baskets and the simulation setup consists of 2x4 baskets in η and 18 baskets in ϕ. The gap between crystals is 0.5 mm.

In ϕ the crystals are pointing 7.5 cm off the beam axis giving a 3 degree tilt of the crystal axis with respect to the radius in order to avoid pointing cracks. In the 3M design [2] the crystals are ordered such that each crystal has a 3 degree off-pointing in η as well.

The longitudinal light yield uniformity has been measured for the crystals used in the 1995 test beam matrix [3], showing a rise of the light yield towards the rear of the crystal which compensates for the back leakage. The measured light yield curve of one of the crystals has been included in the simulation.

3 Simulation setup

The GEANT [4] based CMS008 package [5] has been used as a framework for the simulation.

3.1 Event generation

The CMS008 package contains an interface to the physics generators [6]. The Higgs $\rightarrow \gamma\gamma$ events are generated with PYTHIA [7] including the Higgs production via gluon-gluon and vector boson fusions. Both photons should have the pseudorapidity $|\eta| < 1.4$ (only barrel region). The transverse energy of the two photons should be $E_{T,1} > 40$ GeV and $E_{T,2} > 25$ GeV respectively, corresponding to typical analysis thresholds. The vertex of the event is smeared with a 5.3 cm Gaussian σ in the z (beam) direction and 15 μm in the x and y directions.

3.2 Detector simulation

The two photons from the Higgs decay are passed through a full GEANT simulation, using the calorimeter geometry described above. Particles of the underlying event e not simulated but they are recorded for the vertex reconstruction. The cutoff lues in the simulation are set to 100 keV. Lowering the cutoff value to 10 keV es not change the results. The energy deposit in the crystals is weighted using e measured longitudinal light yield curve.

3 Analysis methods

r the Higgs mass reconstruction, the energy and the direction of the two decay otons have to be measured. The energy measurement can be done in a different y for the non-converted and converted photons depending on the available tracker formation. In the technical proposal tracker geometry [1], 18.4% of the Higgs $\rightarrow \gamma\gamma$ $|\eta_\gamma| < 1.4$) events have a conversion in the tracker and the e^+ and e^- tracks can be tected. In this case, an optimised algorithm can be used to measure the energy these converted photons. Moreover, 29% of the events have a conversion in the acker cables, placed just in front of the electromagnetic calorimeter. These late nversions must be treated like non-converting photons.

3.1 *Energy measurement - no conversions in the tracker*

hen the two photons from Higgs decay do not convert in the sensitive part of the acker, the photon energy is summed in 5x5 crystals around the maximum energy posit (a 5x5 crystal array contains approximately 96% of the photon energy).

The fluctuation in the energy measurement given by the GEANT simulaon is only due to the front, side and back leakage from the area where the energy measured. The fluctuations in the light generation, transmission and detection calibration are not reproduced by GEANT. Therefore the energy deposition obined after simulation is smeared in addition using $2\%/\sqrt{E} \oplus 0.5\%$ to take into count the above mentioned effects. For each crystal a Gaussian electronics noise th $\sigma = 25$ MeV is added.

At high η, less energy is contained in the 5x5 crystal array, and a simple rrection depending on the η direction of the photons is applied. The energy easurement can be further improved by additional corrections, e.g. a correction r the side leakage depending on the impact point on the crystal front face and the rtex point. This has not been included.

The maximum energy deposit is not allowed to be on two crystal rows adjant to a basket border. Separate studies have shown that only a very narrow region ound the basket borders has to be excluded [8] and that the energy measurement n be corrected close to the borders [9].

3.3.2 Energy measurement - conversion in the tracker

When a photon converts in the tracker the energy deposit pattern in the crystals is different from that of non-converting photons and different algorithms should be used to measure the photon energy. Only the photons converting before r=115cm are considered (the sensitive part of the tracker ends at r=120cm) as only in these cases can the two electrons be recognised as a conversion using the tracker information. The electron and positron paths bend in the magnetic field and they arrive on the calorimeter front face some distance from each other in ϕ direction (figure 1). The radius of curvature of the track depends on the electron energy. Any Bremsstrahlung photon radiated from the electron will arrive on the crystals between the two electron impact points and therefore the area of energy deposition of the converted photon is limited by the distance between the two electron impact points.

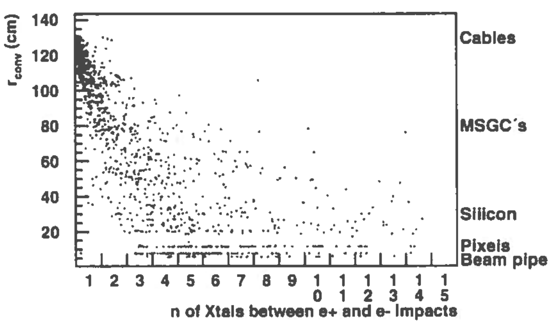

Figure 1: The radius of conversion versus the number of crystals in ϕ direction between the e^+ and e^- impact points on the crystal front face. The size of the crystal front face is 20.5 x 20.5 mm^2 ($\Delta\eta \times \Delta\phi = 0.0145 \times 0.0145$).

Two algorithms are used to measure the energy of the converted photon. A simple algorithm measures the energy in a 5x9 crystal array around the crystal with the maximum energy deposit in the direction of the e^+e^- pair ("5x9 algorithm"). This algorithm is applied if the impact points have less than four crystals between them or if one electron of the pair carries most of the photon energy. The energy distribution between the electrons is estimated by measuring the energy deposited in 3x3 crystals around the impact points and the ratio between the minimum of the two electron energies and the total measured photon energy is allowed to be in range 0.3% to 4%. The 5x9 algorithm recovers conversions where the energy deposit is concentrated in a small area.

When the criteria for applying the simple algorithm are not satisfied a namic algorithm is used. It finds the local maxima between the two impacts $_{dep} > 1$ GeV) and sums around these maxima in 5x5 crystals if the local maximum arger than 20 GeV and in 3x3 crystals in the other cases. If the number of crystals the cluster becomes large, the noise contribution increases. Using this algorithm, e average number of crystals in the cluster is 36.4 (less than 45 crystals in the 5x9 gorithm) so the contribution of noise will not increase. The energy measurement optimised when the number of summed crystals is more than 25, therefore events th less than 26 crystals in the cluster are excluded.

The measured energy is corrected using the dependence on the η direction the photon mentioned previously. When the the 5x9 algorithm is applied, a pendence of the energy on the distance between two impacts is corrected.When e dynamic algorithm is used, a correction is applied as a function of the number summed crystals.

For both algorithms, the noise and the additional fluctuation are added as the case of the non-converted photons. The events which have a maximum energy posit in one of the two crystal rows close to a basket border are excluded as for e non-converting photons.

3.3 *Angular measurement*

ithout the preshower detector the photon direction will be measured from the ıpact point on the crystals and the vertex point. The impact point is measured ing the shower centre of gravity [10]. The vertex of the Higgs is found with the help additional tracks from the same Higgs event [11]. A number of pile-up events is ded according to a Poisson distribution around the mean value of 1.7. This number rresponds to the low luminosity phase of LHC ($\mathcal{L} = 10^{33} cm^{-2} s^{-1}$). The pile-up ents are generated with PYTHIA. The tracks with $p_T > 1.5$ GeV are accepted th 95% efficiency and the point on the beam line where maximum number of acks are pointing ($\sigma_z = 2$ mm) is chosen as the vertex value. This procedure gives non-Gaussian contribution to the mass resolution: when the correct vertex point chosen the error is very small but when a wrong vertex from a pile-up event or vertex is found the error is large.

If a photon converts, its direction can be found using the reconstructed e^- tracks and the error is assumed to be negligible.

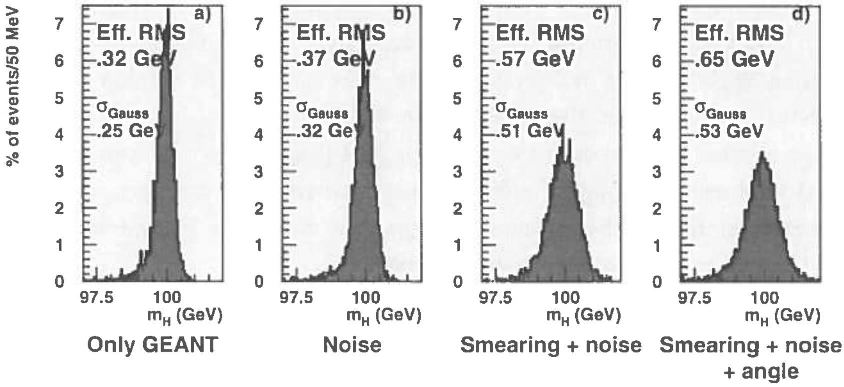

Figure 2: Contributions to the Higgs mass resolution for the events where there are no conversions before the electromagnetic calorimeter: a) fluctuation in the energy deposit in 5x5 crystals, b) noise, c) smearing to take into account photostatistics and calibration, and d) angular measurement.

4 Results

4.1 Mass resolution for events with no conversions in the tracker

The mass resolution for the events with no conversions before the crystals is shown in figure 2. The contributions to the mass width are a) fluctuation in the energy deposit in 5x5 crystals, b) 25 MeV Gaussian noise in each crystal, c) the estimated $2\%/\sqrt{E} \oplus 0.5\%$ smearing to take into account photostatistics and calibration, and d) the angular measurement. Taking all these effects into account, the effective root mean squared (half the width which contains 68.3% of the events; for a perfect Gaussian distribution the effective RMS is equal to the sigma) is found to be 0.65 GeV and the Gaussian σ is 0.53 GeV.

However, 29% of the events have a conversion in the tracker cables after the sensitive part of the tracker and before the crystals. These conversions cannot be distinguished from the non-converted photons. When the tracker cable configuration[1] is optimised [12)] the effect of these late conversion on the mass resolution is almost negligible. Figure 3 shows the mass resolution for a sample of events which includes the conversions after r=115cm. The effective RMS is found to be

[1]The cables should be uniformly distributed in ϕ to minimise the probability of showering and the space between the cables and the start of the crystals should be as small as possible to minimise the leakage of the low energy particles curling away in the air gap in high magnetic field.

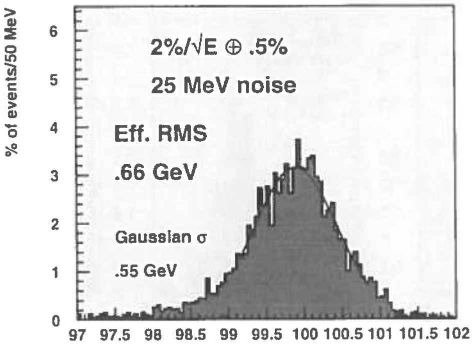

;ure 3: Higgs mass resolution for the event sample that includes the conversions er r=115cm. Using an optimised cable geometry, the late converting photons can measured almost as well as the non-converting photons and they do not degrade ; mass resolution.

6 GeV indicating only a slight degradation compared to 0.65 GeV of the events ;h non-converting photons.

! Mass resolution for events with conversion in the tracker

the technical proposal tracker geometry 18.4% of events have one or two conver- ns before r=115cm in the tracker. The goal is to recover the maximum number these events without degrading the mass resolution. First, the 5x9 algorithm is plied and it accepts 53% of the converted events. For the events not satisfying the teria (distance in ϕ between the impacts < 4 crystals, 0.3% < $E_{e,min}/E_\gamma$ < 4%) e dynamic algorithm is applied. Accepting only events where the number of mmed crystals is more than 26 removes events in the low mass tail of the mass stribution. With this cut 34% of all conversions are accepted. The mass distribu- ns of the converted events are shown in figure 4 for both algorithms separately d combined. The Gaussian width of the peak is as narrow as for the events with conversions in the tracker; nevertheless a small tail at low mass is introduced as own by the increased effective RMS.

} Mass resolution for all events

ıe effect of including the conversion events in the mass reconstruction is shown in ure 5. Table 1 shows the effective RMS of the reconstructed Higgs mass when no nversion events, 53% of conversion events and 87% conversion events are recov- ed. Including the conversion events causes only a slight degradation in the mass solution.

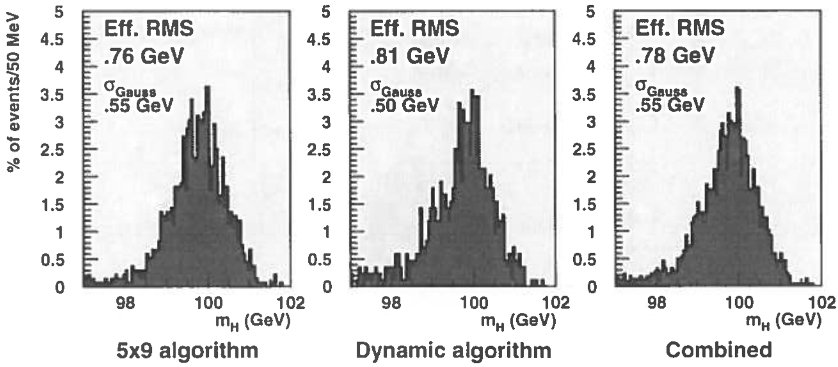

Figure 4: Higgs mass resolution for the events where at least one photon converts in the tracker before r=115cm. To the left the events accepted by the criteria of 5x9 algorithm (53% of conversions), in the middle the events to which the dynamic algorithm has been applied (34% of conversions), and to the right the two algorithms combined.

Table 1: Mass resolution for Higgs $\rightarrow \gamma\gamma$ with and without conversion events

Algorithm to recover the converted photons	% of conversion events recovered	Effective RMS
No conversions recovered	0%	0.66 GeV
5x9 algorithm	53%	0.67 GeV
5x9 algorithm + dynamic algorithm	87%	0.69 GeV

These numbers correspond to the technical proposal tracker geometry where 18.4% of events have a conversion in the tracker at $|\eta| < 1.4$ and before r=115 cm. A simple study has been performed to investigate the effect on the mass resolution if the amount of material in the tracker increases. For example, if the number of events with a conversion inside the tracker would be doubled, the effective RMS would increase to 0.69 GeV when 53% of conversion events are included (5x9 algorithm) and to 0.70 GeV when 87% conversion events are included in the analysis (5x9 algorithm + dynamic algorithm). Even under this assumption the degradation of mass resolution is small.

Pile-up at the low luminosity phase should not worsen the performance of the reconstruction algorithms. However, the algorithms need to be tested against the π^0 background and special care is needed to understand the behaviour of the dynamic algorithm.

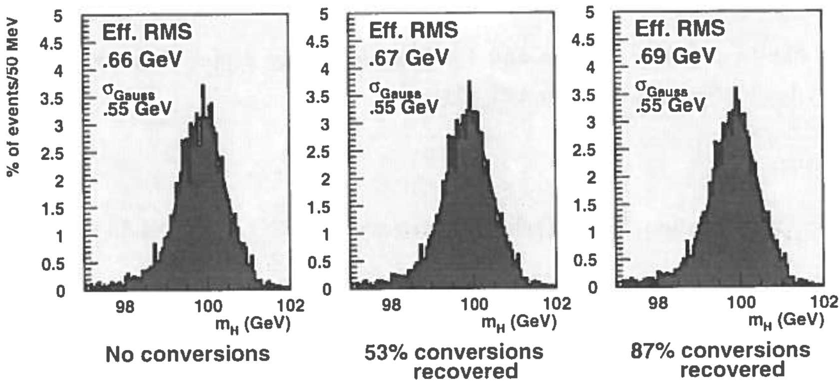

gure 5: Reconstructed m_H when all the conversions in the tracker are excluded the left), when 53% of conversion events are recovered with 5x9 algorithm and ded to the events with no conversion in the tracker (in the middle), and when ditional 34% of conversion events are recovered with the dynamic algorithm (to e right).

Any changes in the tracker geometry and material will effect the conversion obability. The opening angle between the two electrons depends on the radius iere the photon converts as shown in figure 1 and therefore the efficiency of the 9 algorithm and the dynamic algorithm will change if the material distribution in e tracker changes.

Summary

r the CMS crystal calorimeter the Higgs $\rightarrow \gamma\gamma$ mass resolution for m_H=100 GeV is own to be 0.66 GeV for the events with no conversions within the central tracker, suming the low luminosity phase of LHC. The event sample includes the photons at convert late in the tracker cables and they cause only a small degradation in solution. Recovering 53% of the 18.4% of events with a conversion within the acker volume with an algorithm measuring the energy of the converted photon in :9 crystals increases the mass resolution to 0.67 GeV and recovering an additional % of conversions with the help of a dynamic algorithm increases the mass width 0.69 GeV. Thus, a good fraction of conversion events can be recovered with only small degradation of the mass resolution.

6 Acknowledgements

I would like to thank T. Virdee and F. Pauss for many useful discussions. I also acknowledge C. Seez for his help and advice.

References

1. CMS Collaboration, CMS Technical Proposal, CERN/LHCC 94-38 (1994)
2. J.-P.Vialle, M. Lebeau, A. Givernaud, M. Maire, CMS TN/95-151 (1995)
3. P. Denes, D. Renker, private communication
4. CERN Program Library Long Writeup W5013
5. C. Charlot, V. Genchev, V. Karimäki, M. Pimiä, P. Moissenz, A. Rosowsky, G. Wrochna CMS TN/93-63 (1993)
6. V. Karimäki, A. Khanov CMS/TN 94-162 (1994)
7. T. Sjöstrand, CERN-TH.7112/93 (1993)
8. B.W. Kennedy, CMS TN/96-043 (1996)
9. A. Givernaud, E. Locci, CMS TN/96-014 (1996)
10. S. Shevchenko, CMS TN/94-299 (1994)
11. C. Seez CMS TN/93-115 (1993), D.J. Graham CMS TN/95-115 (1995)
12. K. Lassila-Perini, CMS Note/1996_101 (1996)

ıscati Physics Series Vol. VI, (pp. 497–507)
INT. CONF. ON CALORIMETRY IN HEP – Frascati, June 8–14, 1996

COMPARISON BETWEEN THE ATLAS/TileCal HADRON BARREL CALORIMETER PROTOTYPE TEST BEAM DATA AND HADRONIC SIMULATION PACKAGES

Ilias Efthymiopoulos
CERN/PPE, Geneva Switzerland

for the ATLAS/TileCal Collaboration

ABSTRACT

:omparison between the test beam data of the ATLAS/TileCal hadronic calorime- prototype modules, in standalone and in combined mode with the Liquid Argon 1 barrel calorimeter prototype in front, and different hadronic shower simulation les (FLUKA, GHEISHA, CALOR) in the framework of the GEANT program is :sented. Comparisons are made for all packages for the general hadronic shower :ameters, as well as for the energy resolution and response linearity. From these .dies, it is shown that none of the above packages is able to describe in the desired :cision the test beam data.

Introduction

r the needs of the ATLAS/TileCal hadronic calorimeter a full simulation pack- : has been developed based on the GEANT program [1] which describes in full tail the detector prototypes that have been used for the test beam runs, and was tensively used during the R&D work for the final ATLAS detector design. Dur- ; the almost four years of the TileCal collaboration five prototype modules were ıstructed. These prototypes have been put in the CERN SPS H8 test beam line, ıich is able to provide a variety of beam energies from 10 up to 400 GeV for protons, ıons and electrons. The modules have been extensively tested both in standalone d once, in September 1994, in a combined mode with the ATLAS/LARG EM .orimeter prototype in front, aiming to reproduce as much as possible the final 'LAS setup. In order to describe this combined detector setup, the TileCal simu- ion program was merged with the similar one developed for the LARG detector ıich also describes in the best possible detail the EM prototype [2].

Comparisons between the pion and muon test beam data and simulated data using the three hadronic packages interfaced with the GEANT program (FLUKA CALOR and GHEISHA) are presented. For this comparison, the basic hadronic shower characteristics such as the longitudinal and lateral profiles, the energy resolution and response linearity are used. Special emphasis is given in the reproduction of the pion response linearity curve from the Monte Carlo data, since this will allow us to transfer safely the knowledge from the test beam to the ATLAS environment at the TeV range.

2 The Detector

The ATLAS/TileCal barrel hadron calorimeter is a sampling calorimeter with steel as the absorber and scintillating tiles as the active material, oriented in planes perpendicular to the colliding beams and staggered in depth. The iron to scintillator ratio is about 4.67:1 in volume. Each scintillating tile is read out by two wavelength shifting fibres, placed at its ends along the radial direction. Each fiver is read by one photomultiplier.

This innovative design allows a simple construction technique, very important for the large ATLAS detector dimensions, and as was shown from the test beam data and from Monte Carlo simulations in the ATLAS environment, provides good sampling homogeneity when placed behind an EM calorimeter and a coil, of about two interaction lengths in total [3].

For the test beam, five prototype modules were constructed. Each module covers $2\pi/64$ in azimuth and extends 1m long in the z direction. The radial depth, starting from an inner radius of 200cm to an outer radius of 380cm accounts to about 9 λ, divided in four segments corresponding to 1.5,2, 2.5 and 3 λ at $\eta = 0$. The five modules were stacked together giving a total front face coverage of about 100×100 cm^2.

2.1 The Combined Setup

For the combined run, the LARG EM calorimeter [1] [4] and the TileCal hadron calorimeter prototypes were put together in a setup as close as possible to the final ATLAS configuration (fig. 1). In this configuration, the distance between the active parts of the two calorimeters was about 55 cm (0.27λ), almost a factor of two from the ATLAS value. Due to the mechanical constrains of the prototypes the calorimeters were put in a fixed position, with the beam entering with an angle of

[1] a sampling calorimeter with steel plated lead absorbers folded to an accordion shape separated by 3.8mm gaps and filled with liquid argon

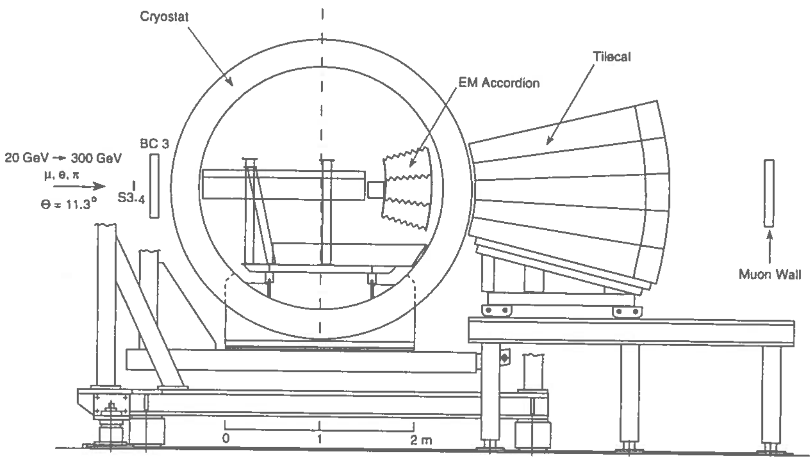

Figure 1: The combined calorimeter setup.

3^0 at $\eta \sim 0.44$, with the total active thickness of the two calorimeters being about 3λ. In front of the EM calorimeter, a $3X_0$ thick fully equiped preshower detector s put, which was used in the analysis to reject particles which give interactions the materials before the calorimeters. From the total active volume of the EM orimeter only a window of 11×11 cells (or about $25 \times 25 cm^2$) was used, centred the nominal beam incident point. The EM calorimeter is segmented in depth in ree compartments of 9, 9 and 7 X_0 at $\eta = 0$, and its fully projected cells measure 18 $\times$ 0.02 in $\eta \times \phi$ (0.036×0.02 for the last compartment). With the incident gle of this setup the calorimeter was not projective.

Standalone tests

r the standalone tests of the detector data from pions, muons and electrons of rious energies in the range from 10 to 400 GeV were used [5]. In the simulation ogram all the experimental effects (such as tile response non-uniformities, fibre fibre fluctuations, light attenuation in the fibres, noise etc..) were included thus owing the best possible description of the detector. This was indeed verified with e quality of the agreement in the simulation of the muon signal at various energies th the experimental data [6] [7].

For the study of the hadronic showers, simulated data with all the available hadronic shower packages interfaced to the GEANT program were used [1]. ie GHEISHA package does not contain any simulation of the physical processes at determine the dynamics of the interaction of hadrons with matter; instead it, is ing different parameterisations trying to reproduce directly the outcome of these reactions. The secondary particles are produced according to scaling lows, symmetry requirements, and careful tuning of the parameters to reproduce available experimental data. It was therefore of no surprise that some level of disagreement with the TileCal experimental data, was observed for this package.

The other two packages FLUKA and CALOR are actually not very different ones, at least in the way they are implemented in the GEANT code. In the FLUKA code primary interactions for particles above 5 GeV are treated according to the Dual Parton Model, while for lower energies up to 300 MeV for nucleons and 50 MeV for other particles, a resonance production model is used. For particles bellow these energies, all important nuclear effects are taken into account. In the CALOR package particles with energies above 10 GeV or particles different from pions and nucleons are treated exactly as in FLUKA. For lower energies and up to 2.5 GeV for pions and 3.5 GeV for nucleons a hybrid treatment starts, in which a fraction α of the interactions is performed as in FLUKA and the rest is simulated by the so called *scaling model.* Bellow these thresholds, the Bertini IntraNuclear Cascade (INC) code is used [8].

For the comparison the basic characteristics of the hadronic showers are used: longitudinal and lateral shower profiles, energy resolution, pion response linearity and the μ/π ratio which characterises the amount of the hadronic activity. To set the scale for both Monte Carlo and real data, electron runs were used. The shower integration time in the simulation is set to 150nsec as the ADC gate in the test beam.

3.1 longitudinal profiles

As was mentioned before in sec. 2 the TileCal calorimeter is segmented in four compartments in depth. In fig. 2 the energy for each longitudinal compartment is plotted for real and simulated data using the CALOR package. For the FLUKA package similar agreement is observed while the GHEISHA is somehow worse. All the packages reproduce quite well the average energy deposited, although they tend to predict "longer" tails at all energies.

3.2 lateral profiles

The lateral profile of the hadronic showers is strongly dependend on the production of fast neutrons and they way these are treated by the simulation code. In general for all the packages considered, the simulation tends to predict narrower showers compared to the data. The situation improves when lowering the energy cutoff values for the tracking of the neutrons.

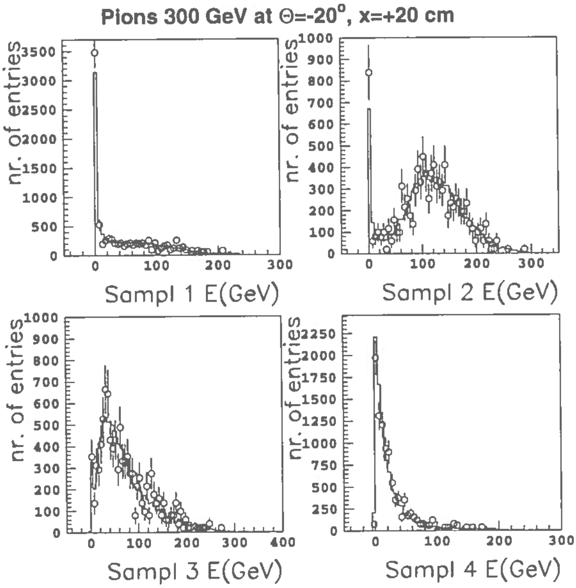

igure 2: Longitudinal shower development for 300 GeV pions. The simulated (dots) ıd experimental data (solid line) are compared.

3 energy resolution

ı fig. 3 the energy resolution for pions obtained for the experimental and the simlated data is shown. The FLUKA and CALOR packages predict almost the same ılues, with those of CALOR being closer to the data, but too optimistic. GHEISHA n the contrary seems too pessimistic.

.4 response linearity

'he TileCal calorimeter is a non compensating calorimeter, therefore the pion reponse varies with the incident particle energy, according to the formula:

$$R_h \propto (e/\pi)^{-1} = \frac{e/h}{1-(1-e/h) < f_{\pi^0}(E) >} \tag{1}$$

n fig. 4 we see this variation for both the experimental and the simulated data. It ; clear from this plot that none of the packages is able to follow the data.

As we see from eq. 1, the pion response depends on the e/h ratio of the alorimeter and of the fraction of π^0 produced. In tabl. 1 the values of the e/h are iven for two different sets of energy cutoff values. What is observed, is that the ure electromagnetic response is almost the same for all packages while the hadronic ne varies a lot, and gets smaller when the GEANT energy thresholds are increased. 'he e/h value for all the packages is anyhow far away from the 1.36 ± 0.11, the

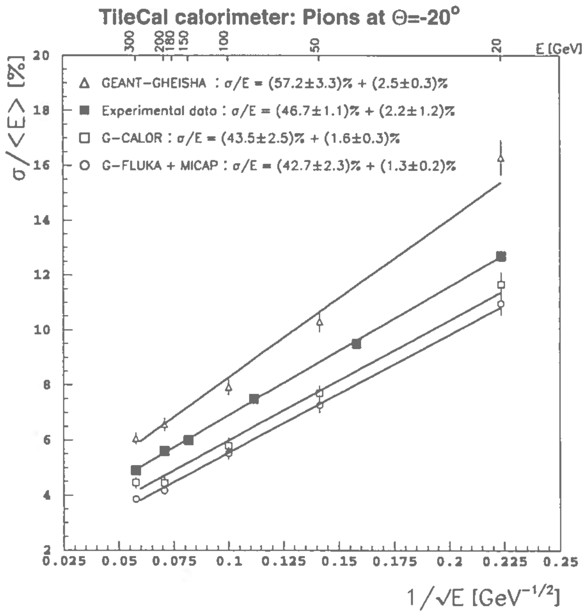

Figure 3: Energy resolution for pions from the standalone tests of TileCal calorimeter.

Table 1: The e/h values for the different hadronic simulation codes

all GEANT thresholds at 100 KeV

	CALOR	FLUKA	GHEISHA
e	2.700 ± 0.02	2.77 ± 0.02	2.69 ± 0.02
h	2.16 ± 0.02	2.32 ± 0.02	1.65 ± 0.02
e/h	1.25 ± 0.02	1.19 ± 0.02	1.63 ± 0.03

value obtained from the experimental data [3]. Correlated to the value of the e/h ratio, is the fraction of electromagnetic energy produced in a hadronic shower. For the three packages considered, FLUKA is the one that predicts much more EM part (especially at low energies) with respect to the other two who predict almost the same ammount. Once again all the packages are away from the predicted ammount according to both Wigman's and Groom's parameterisations when fitted to our data.

The low values for the e/h in the case of FLUKA and CALOR is also reflected in the value of the μ/π ratio, which is about 4% higher than the experimental data. The GHEISHA code predicts lower values by about 7%

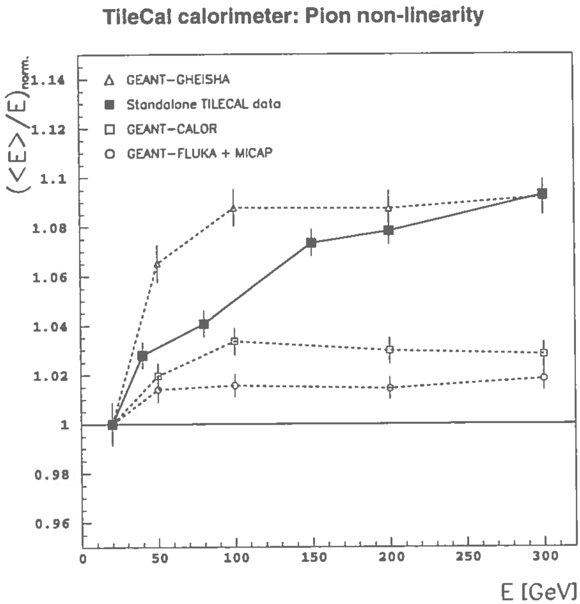

gure 4: The pion energy response linearity curve for the TileCal standalone tests.

Combined tests

or the energy reconstruction in the hybrid calorimeter case, three different algo-thms have been developed [9]. The first and simplest one, also referenced as the enchmark" approach, uses a simple formula for the total energy, keeping the elec-on energy scale for the EM calorimeter:

$$E_{total} = E_{em} + a \cdot E_{had} + b \cdot \sqrt{(E_{em}^{s3}) \cdot (a \cdot E_{had}^{s1})} + c \cdot E_{em}^2 \qquad (2)$$

he third term is a parametrisation found from the simulated data of the energy st in the materials between the calorimeters (mainly dead liquid argon and the yostat). E_{em}^{s3} and E_{had}^{s1} is the signal in the third EM in the first hadronic calorimeter epths respectively. The quadratic term in eq 2 is used in order to correct the rong dependence of the total reconstructed energy from the part released in the M calorimeter, while for the simulation due to the low e/h values (at least for ie CALOR and FLUKA packages) this dependence is much lower (fig 5). The arameters in eq. 2 are obtained by minimising the resolution at 300 GeV and are ept constant for all the energies.

The other two methods are weighting techniques, one previously used for ie standalone data and the other one was taken from a similar analysis of the [1 calorimeter [3] [10]. For the purpose of this study no weighting was applied the simulated data, instead for most of the comparisons both simulated and

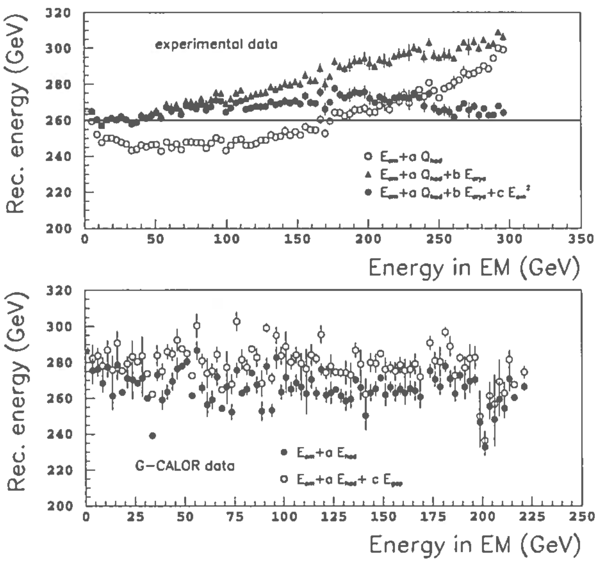

Figure 5: The dependence of the total reconstructed energy from the energy released in the EM calorimeter for experimental data (a) and simulated data with the G-CALOR package for pions at 300 GeV.

experimental data are used as "raw" quantities, adopting the electron energy scale everywhere.

4.1 longitudinal profiles

In fig. 6 the mean energy per sampling is ploted, as well as the percentage of the total energy released in the EM and the hadronic part, using raw energies. From these plots it can be seen that in general the simulation prefers showers that develop "deeper" than the experimental data, which also implies that the energy released in the hadronic calorimeter is bigger. For all the energies more than 50% of the total energy is released in the hadronic calorimeter.

4.2 energy resolution

In fig. 7 is compared the resolution for the simulated data using the "benchmark" method for the energy reconstruction and that obtained from the experimental data using all three methods.

Like before for the standalone case, FLUKA gives the best resolution, CALOR stays closer to the data and GHEISHA predicts worse values. The agreement with the experimental data is good for the high energies but for the lower ones and in particular for the 20 GeV case is quite bad. With the presend understand-

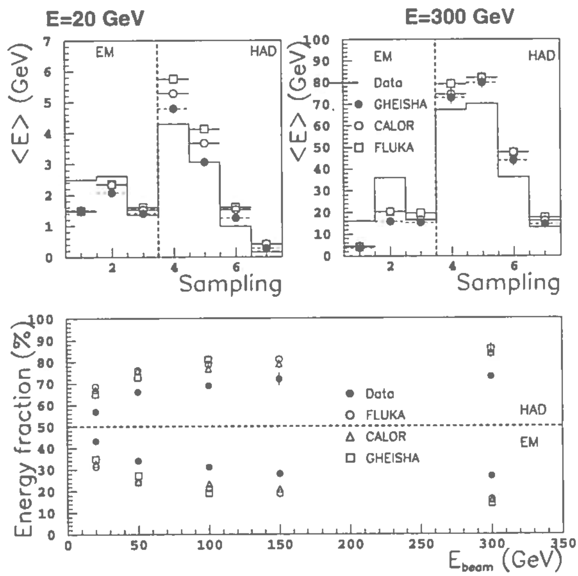

gure 6: The mean energy released in each calorimeter sampling using “raw” en-
gies for pions of 20 GeV (a), and 300 GeV (b). In (c) the ratio of the total energy
leased in the EM and in the hadronic calorimeters for different beam energies is
own.

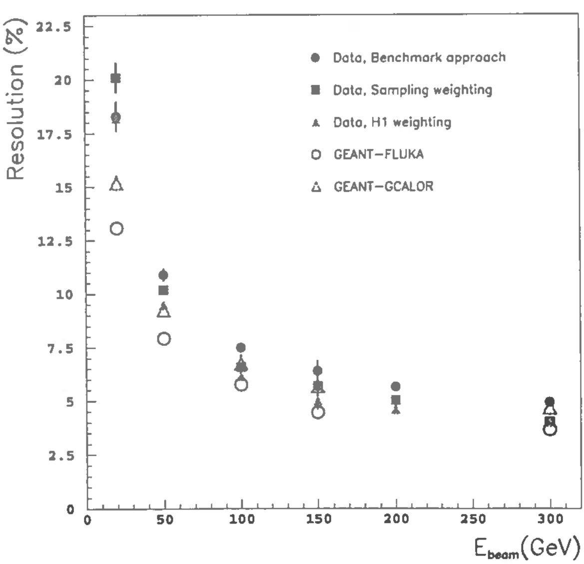

Figure 7: The enery resolution for simulated and experimental data.

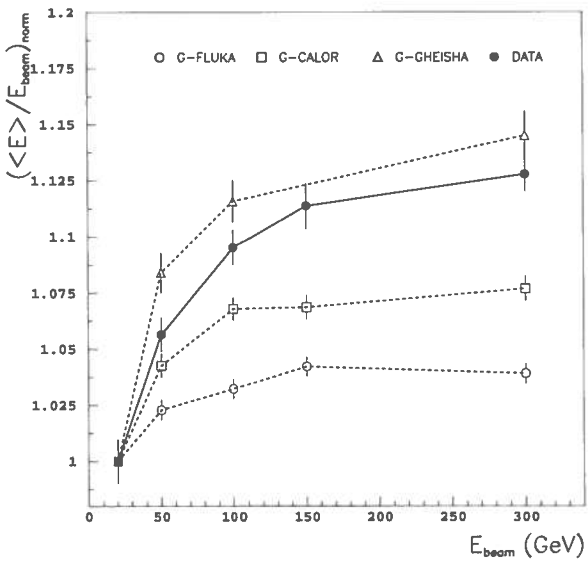

Figure 8: The pion response non-linearity for the combined case, using "raw" energies.

ing, this is due to experimental problems during the data taking such as the beam conditions and the large noise in the EM calorimeter 9).

4.3 response linearity

Since both calorimeters are non compensating it is expected that the total energy increases as the beam energy increases. This can be clearly seen in fig. 8, which is to be compared with fig. 4. The FLUKA and CALOR packages predict a much better linearity as for the standalone case, while GHEISHA seems to agree reasonably well, perhaps because its the one that describes better the EM calorimeter[2].

5 Conclusions

Summarising all the comparison studies presented, it is clear that none of the packages used is adequate to describe the experimental data for the hadron showers in both standalone and the combined setup. The major problem is the reproduction of the linearity curve which in case of FLUKA and CALOR is far away from the experimental data, a direct consequence of the wrong e/h value and the amount of the electromagnetic activity produced. Apart from linearity in the combined case

[2]to investigate further this problem a new combined run was realized in April 1996, but the data have not been analyzed yet

ıe energy released in the EM calorimeter is much lower in the simulated than the ‹perimental data.

In the years to come until the starting date of the experiment, many more ːst beam data with the actual detector modules in both standalone and in combined ıode will be taken in a big energy range from few, up to hundreds of GeV. The ˌudy of the simulation packages, not only the ones considered already but perhaps ew ones or new in environments outside of the usual GEANT one, of course will be ɔntinued and more comparison tests will be made in the single particle level as well s for the jets, where it was shown in the past that the situation is much different.

Acknowledgements

'he author would like to thank all the colleagues from the TileCal and LArgon ollaborations and especially M. Bosman, and A. Juste for their help in the work ɔr the TileCal standalone data and P. Petroff and G. Parrour for their guidance in etting up the combined simulation program.

₹eferences

1. R. Brun and F. Carminati, "GEANT Detector Description and Simulation Tool", CERN Program Library, **Long Writeup W5013**, September 1993

2. M. Lefebvre et.al., ATLAS Internal Note, RD3 No **41**, (1993)

3. F. Ariztizabal et. al.(RD34 Collaboration), Nucl. Instr. and Meth. **A 349**, (1994)
   F. Ariztizabal et. al.(RD34 Collaboration), LRDB Status Report, **CERN/LHCC 95-44**

4. D.M. Gingrich et. al. (RD3 Collaboration), Nucl. Instr. and Meth. **A 364**, 290(1995)

5. See talk of M. Bosman at the same conference

6. A. Juste, Master Thesis, **IFAE/UAB October 1995**

7. See talk of A. Henriques at the same conference

8. A. Ferrari, P.R. Sala, ATLAS Internal Note, **PHYS-No-086**, 6 June 1996 (and refs therein)

9. M. Cobal et al., ATLAS Internal Note, TILECAL No **67**, (1995)

.0. P. Casado, M. Cavalli-Sforza, ATLAS Internal Note, TILECAL No **75**, (1996)

ascati Physics Series Vol. VI, (pp. 509–518)
I INT. CONF. ON CALORIMETRY IN HEP – Frascati, June 8–14, 1996

SIMULATION OF HADRONIC SHOWERS USING A REAL DATA SHOWER LIBRARY

V. Arena, G. Boca, G. Bonomi, G. Gianini, M. Marchesotti, M. Merlo, S. P. Ratti, C. Riccardi, L. Viola, P. Vitulo
University of Pavia, and INFN

ABSTRACT

shower library to simulate the behaviour of charged and neutral hadrons inside the 687 hadron calorimeter [2] has been built. A sample of hadronic showers has been lected using protons and pions from the decays of Λ^o and K^o_s. We parameterized ıe showers depending upon impact position and momentum in 5 GeV/c intervals. omparison of simulation with data will be given.

Introduction

'he E687 experiment is a collaboration of about 20 institutions and Universities that ›ined to study the products of the interaction between a photon beam and a beryl-um target. Particular attention was given to production and decays of charmed ıesons and bosons. The experiment was held at the Fermi National Accelerator aboratory at Chicago and took data in a period that ranged from 1988 and 1991.

The E687 spectrometer [1] (shown in Fig. 1) is a large aperture fixed tar-et multiparticle spectrometer which features excellent particle identification and ertexing for charged hadrons and leptons. A photon beam is derived from the remmstrahlung of secondary electrons ($E_{max} = 450GeV$) produced from the Teva-ron proton beam. This beam impinges on a beryllium target; charged particles vhich emerge from the target are tracked by two systems of silicon microvertex de-ectors. The first system is commingled with the experimental target, the second is ust downstream of the target and consists of twelve planes of microstrips arranged n three views. These detectors provide high resolution separation of primary (pro-luction) and secondary (decay) vertices. The momentum of charged particles is

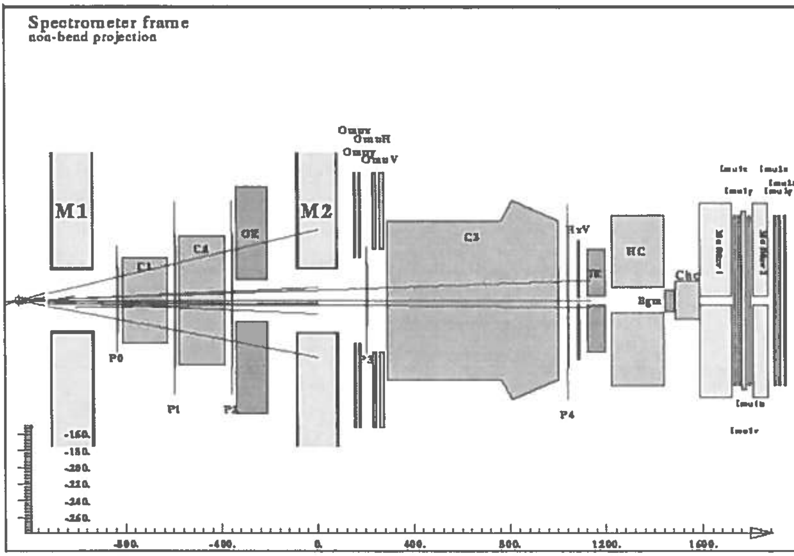

Figure 1: E687 spectrometer layout

determined by measuring their deflections in two analysis magnets of opposite polarity with five stations of multiwire proportional chambers. Three threshold multicell Cerenkov counters are used to identify electrons, pions, kaons and protons. There are two electromagnetic calorimeters. The inner calorimeter, a lead-scintillator sandwich calorimeter, covers the central solid angle and detects particles which pass through the apertures of both magnets. The outer calorimeter covers the outer angular anulus described by particles that pass through the first magnet but not the second. Muons are identified in either a fine grained scintillator hodoscope with an iron filter (covering the inner region) or in an outer system. A hadron sampling calorimeter [2)] consisting of iron and proportional tubes is used primarily in the experiment trigger but is also used to reconstruct neutral hadrons.

2 The E687 hadron calorimeter

The E687 hadron calorimeter [2)] is a sampling gas calorimeter with tower readout geometry. It consists of 28 305x103x4.45 cm^3 iron plates interspersed with planes of extruded aluminum proportional tubes. Actually the calorimeter is divided in 3 sections consisting of 5, 8 and 15 planes respectively for a total of 8 interaction lengths λ_I and 224 radiation lengths X_o. The aluminum proportional tubes have 50 μm tungsten anode wires. The working voltage has been set to around -2050 V and the gas mixture used is Argon/Ethane 50/50%. Capacitively induced signals

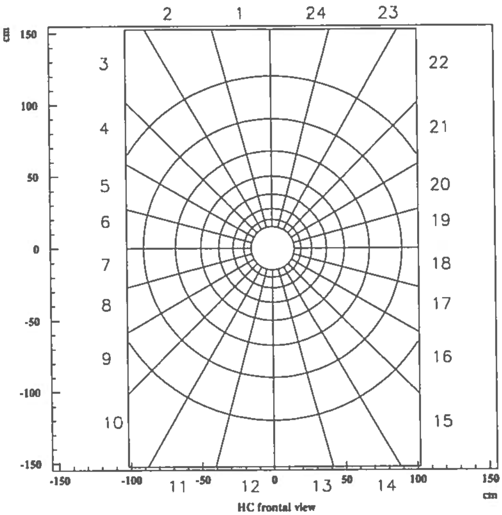

Figure 2: HC frontal schematic view

ı electrode pads with cylindrical geometry are read out. A diagram showing the ıtline of the pad geometry for each of the 3 sections is shown in Fig. 2.

The 8-ring 24-sector pad structure is clearly visible. The system has a ynamic range that spans the region from minimum ionizing particle (mip) to a w hundred mips. Calibrating the system response was done using muons, elec- onic test signals, and by recording the pulse height of an ^{55}Fe source with a :oportional counter. The HC was primarily constructed to provide information for iggering on events with hadronic final states to enhance the number of recorded vents with charm quarks. It provides a hadron energy resolution to an accuracy of 33%$/\sqrt{E}$. We have here to remind that just before the HC is placed an electro- ıagnetic calorimeter consisting of 100 scintillating fiber planes and 100 lead layers ır a total of 1 λ_I ad $25X_o$. This means that about 25% of the hadrons started to enerate a shower in the electromagnetic calorimeter prior to reaching the HC.

Working project

; is well known how is difficult simulating a hadronic shower in a calorimeter using Montecarlo. We decided to avoid the use of a Montecarlo and we created a *shower brary* using real data from the 1991 data taking period. The idea was to select a articular sample of real showers and to divide them according to their momentum nd impact position. We store shape and energy information for all of these showers.

Our goal was to have a sample that could be representative of the cinematic and geometrical range of the hadron particles.
We can divide our work in two steps: selection of the hadronic showers and creation of the *library*.

3.1 Selection of a hadron showers sample

In order to select hadronic showers the first step was to select hadronic particles. We choose charged $\pi's$ and protons coming from the decays of Λ^o and K^0_s. E687 collected a great amount of these kind of decays, of the order of 10^6. To avoid energy contamination from other showers we rejected particle closer to others. In our calorimeter the 90% of the energy of a shower was contained in a circle of 16.8 cm radius ($\simeq$ 1 interaction length). We selected isolated particle with no other charged particle inside a 33.8 cm radius. We rejected also particle not generating a shower nor in the IE or in the HC. In order to eliminate fake or bad reconstructed particles we required also an aligned energy deposition, that is an energy deposition where the particle striked the HC. Actually we required energy at least in the IE or in the first or in the second section hit pad of the HC.
During the data taking period some of the pads showed to be not perfectly working. To avoid the selection of shower comprehensive of one of these pads, we selected the so called *clean pads*. Shower originating in these *clean pads* were sure not to include not working pads. Essentially they are pads with no dead pads inside a 16.8 cm radius.

3.2 Creation of the library

All showers of hadronic tracks impacting *clean pads* were split according to their momentum and impact position. We created bidimensional virtual cells of $\Delta_p = 5GeV/c$ of momentum and $\Delta_{impact} = Ring$ of impact position. The showers inside these cells were considered equivalent. Due to the fact that our energy resolution is $133\%/\sqrt{E}$ a 5 Gev/c momentum cell seemed to be a reasonable choice. The geometric symmetry of our HC also allowed us not to discriminate between the azimuthal position of the impact point inside the same ring.
We did not store the shower generated in the 8th ring because the last ring was not completely covered by the last 2 PWC's. Due to this fact particles impacting the 8th ring can not be simulated. We have 235238 records filled with information from the associated showers. We wrote all the information in a direct access file (*shower library*). For each shower we stored 86 information: IE energy (1), HC pads energy (81 = 27x3, where 27 is the maximum number of pads interested by a shower), impact position (2), run number (1), momentum (1). We transformed each quantity

Table 1: Number of shower per cells

vs Ring	1	2	3	4	5	6	7	Total
GeV/c	458	574	1245	3658	8989	18849	15551	**49324**
5 GeV/c	1081	1589	3270	7192	10956	14678	9068	**47834**
0 GeV/c	1500	2040	3747	7414	10888	10793	3851	**40233**
5 GeV/c	1570	1943	3319	6675	8543	6995	1723	**30768**
0 GeV/c	1533	1713	2777	5394	5817	3831	691	**21756**
5 GeV/c	1274	1481	2330	3969	3503	1965	305	**14827**
0 GeV/c	1106	1191	1836	2729	2094	979	121	**10056**
5 GeV/c	878	903	1375	1777	1142	472	62	**6609**
0 GeV/c	716	717	996	1181	693	210	11	**4524**
5 GeV/c	548	534	697	755	376	137		**3047**
0 GeV/c	451	462	495	468	211	62		**2149**
5 GeV/c	307	323	334	315	92	27		**1398**
0 GeV/c	253	222	231	154	58			**918**
5 GeV/c	178	146	128	97	36			**585**
0 GeV/c	140	110	110	61	13			**434**
5 GeV/c	94	96	76	51				**317**
0 GeV/c	85	62	43	31				**221**
5 GeV/c	60	47	24	15				**146**
00 GeV/c	52	34	19					**105**
105 GeV/c	35	26	16					**77**
al	**12319**	**14213**	**23068**	**41936**	**53411**	**58998**	**31383**	**235328**

INTEGER*2. The final disk occupation was of 235238x86*2bytes $\simeq$ 40 Mbytes. ıe total number of showers per cell is shown in Tab. 1.

Simulation tests

ior to describing our simulation tests, we should explain in detail our simulation ocedure. Given a hadronic track of momentum p and impact position *Ring*, we tract randomly from the *library* an equivalent shower that belongs to the same :tual bidimensional cell. For example the shower of a pion of $p = 9.3 GeV/c$ and ıpacting the HC in Ring 3-Sector 12 can be simulated by extracting from the *li-ary* a shower generated by a proton of $p = 5.7 GeV/c$ and that impacted the HC in ng 3-Sector 23. After the extraction, we associate the extracted energy informa-ɔn to all the pads that could be interested by the shower around the hit pad. In is way we can reproduce both shape and total energy of a shower. In other words simple rotation of the extracted shower is performed.

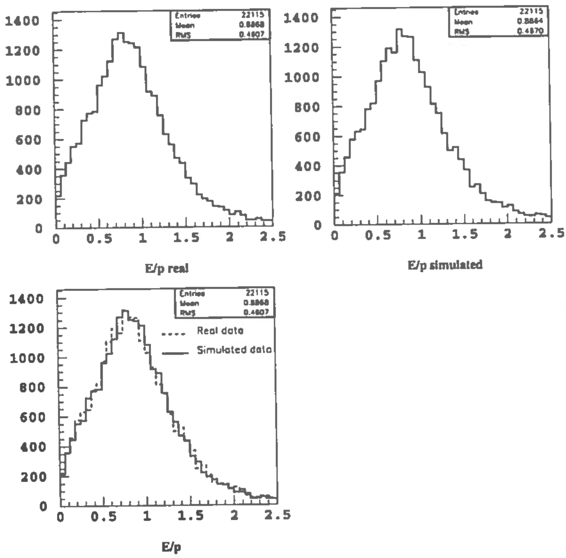

Figure 3: Self consistency test

To test the *library* and the simulation procedure we took real hadrons (again π's and protons from Λ^o and K^o_s) and extracted, for each one, a shower from the *shower library* We compared the real shower and the extracted-simulated one.

4.1 Self consistency test

To test the extraction procedure and the *shower library* cells structure (that is, the fact that we don't discriminate between particle inside the same $\Delta_p = 5GeV/c$ and $\Delta_{impact} = Ring$ interval) we created a preliminary version of *shower library* filled with around 20000 events and we reanalyzed them, simulating their showers. The result of the test is shown in Fig. 3.

The 3 plots show the E/p (energy/momentum) for real and simulated showers. The 3rd plot shows them overlapped and the agreement is very good. This means that our *shower library* cells granularity is appropriate relatively to our detector.

4.2 Simulation of showers not included in the library

After that we decided to simulate showers that were not included into the library. We chose showers selecting them the same way we selected the ones included in the

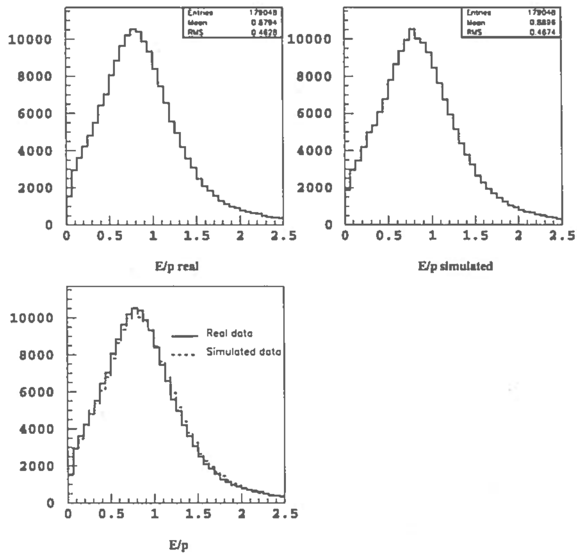

Figure 4: Simulation of showers not included in the library

rary (see 3.1). We used the same simulation method described previously and e result is summarized in Fig.4. Once again the agreement is very good. The ents were chosen inside the period of time covered by the *shower library*, that is om the 1991 data taking. To check the, let's call it, *time resolution* we divided the mulated sample in 2 subsample. The first contained events from the first half of e period (subsample A) and the second, events coming from the second half of the eriod (subsample B). The results of the simulation for the 2 subsample are shown Fig. 5 and Fig. 6. It is clear that the our HC simulation fails to reproduce e HC behaviour in a short period. That's because our *shower library* has a HC sponse mediated over all the 1991 data taking period. The same can be said if we y to simulate just a small region of the HC. That's why we choose to include in e *library* the run number and the impact position of the shower. In this way one n select the desired events in order to get a better simulation. Obviously doing is the available statistics decrease.

3 Simulation of events taken without 2nd level trigger

687 was based on a second level trigger that included information from the hadron lorimeter. Depending of the run period only events with more than 40 or 50 GeV the HC were selected. To check if the use of these events to build the *library*

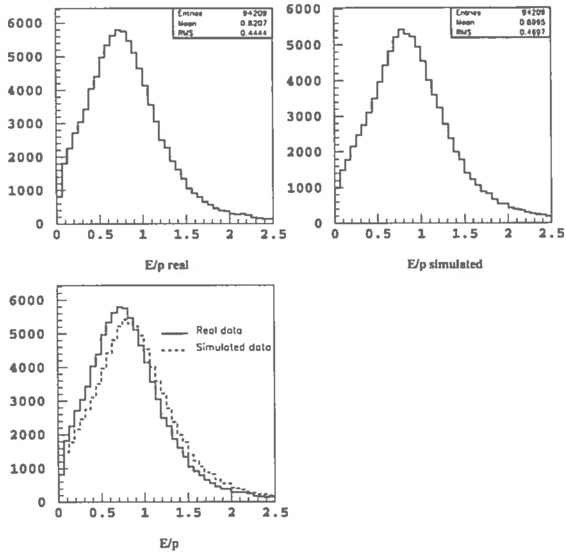

Figure 5: Simulation of the subsample A

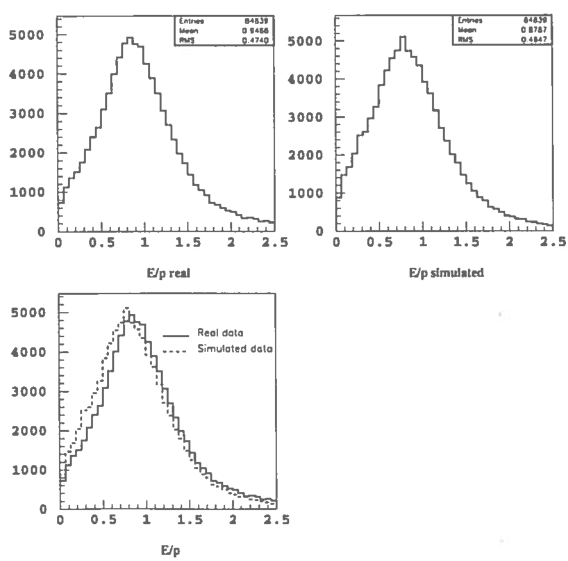

Figure 6: Simulation of the subsample B

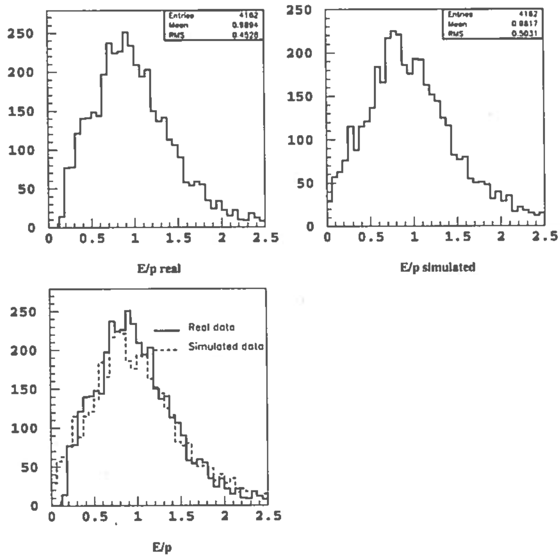

Figure 7: Simulation of events taken without 2nd level trigger

uld introduce a bias, we simulated also some events taken without the second 'el trigger. These events had a small fraction of hadronic events and our statistics quite low. Nevertheless the simulation of hadronic showers coming from these ents excluded a bias of this kind (Fig. 7).

ł Simulation of calibration pions

› check the global validity of the *library* we simulated pions from the HC calibration n. This was our more crucial test for some reasons. First of all we were absolutely rtain of the *hadronicity* of the shower and also of the *isolation* of the track (there ıs just a pion per event). Second we were avoiding all the bias that we could have troduced in our showers selection procedure. The only problem was that these .ta were taken in a single night and directing the pion beam to just a couple of .ds, and we were comparing them with data taken in all a year. Nevertheless the sult proved to be very good as shown in Fig. 8.

Summary and Conclusions

'e selected a sample of real hadronic showers and stored them in a direct access e using a $\Delta_p = 5GeV/c$ and $\Delta_{impact} = Ring$ bidimensional cells structure. We

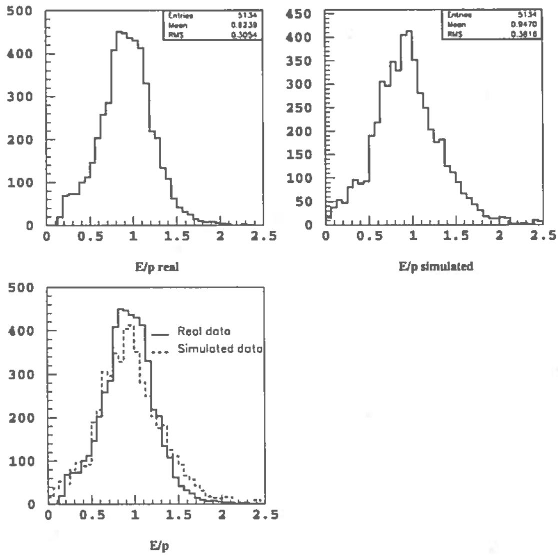

Figure 8: Simulation of HC calibration pions

tested the *shower library* and inserted it in our general Montecarlo. For every MC generated charged and neutral hadrons we extract a shower from the appropriate cell and reproduce both shower shape and energy in the HC.

This method proved to be very reliable and efficient for our hadron calorimeter. Obviously our *shower library* cannot be exported and used by other experiments because it is detector dependent. Nevertheless the idea can be also applied to other hadronic calorimeters. This method has the advantage to avoid the simulation of all particle, at all the energies, in all the materials composing a calorimeter. It gives the energy and shape information of the shower final state.

Obviously in order to be able to create a *shower library* from real data, and simulate a detector you need to have taken data first.

References

1. P.L. Frabetti et al., Nuclear Instruments & Methods in Physics Research **A320**, 519-547 (1992).

2. S. Park, D.Bucholz, C. Castoldi, D. Claes, B. Gobbi, R. Yoshida, A. Sala, V. Arena, G. Boca, A. Cotta-Ramusino, R. Diaferia, S. Ratti, P. Vitulo, Nuclear Instruments & Methods in Physics Research **A289**, 496-503 (1990).

scati Physics Series Vol. VI, (pp. 519–528)
INT. CONF. ON CALORIMETRY IN HEP – Frascati, June 8–14, 1996

AN IRON/GAS SAMPLING CALORIMETER BASED ON PARALLEL PLATE CHAMBERS: MEASURED PERFORMANCE AND ITS REPRODUCIBILITY BY MONTECARLO

Gy. L. Bencze, F. Dalla Santa, A. Iglesias
CERN

A. Ferrando, M. C. Fouz, M. I. Josa, A. Khan, L. Martinez–Laso, J. M. Salicio
CIEMAT (Madrid)

A. Bizzeti, C. Civinini, R. D'Alessandro, M. Meschini, V. Pojidaev
INFN & University (Florence)

A. Malinin
ITEP (Moscow)

V. Ivochkin
PNPI (St. Petersburg)

ABSTRACT

n iron/gas sampling calorimeter prototype based on Parallel Plate Chambers was ;posed to electron and pion beams. Performance was determined with different gh voltages. A model capable to simulate the avalanche mode of operation alws to reproduce the experimental results by Monte-Carlo, giving the possibility of aking realistic predictions for any configuration and size. Monte-Carlo simulation udies on the effect of neutrons in the gas of a low angle calorimeter based on this chnique are presented, exemplified for the CMS scenario.

Introduction

ifferent iron/gas sampling calorimeter prototypes based on Parallel Plate Chamers (PPC) were tested with electron and pion beams during the last two years [1, 2]. his type of calorimeter is specially indicated for regions of high rates of particles, emanding a fast response and a modest energy resolution, as, for instance, the low ngle areas in LHC experiments. We have developed a model capable to simulate he avalanche mode of operation in a calorimeter made of PPCs.

In the first part of this paper (sections 2 to 5) we explain the mode of peration of a single PPC and its reproduction by Monte-Carlo and we show the omparison between data and Monte-Carlo using a calorimeter prototype 6.8 λ_I ong.

In the second part (section 6) we present, as an example, the use of the hain of simulation packages: ISAJET, GEANT, FLUKA and MICAP, together ith our own avalanche simulation code, to study the effect of the neutron flux in he gas of the PPCs for the case of CMS, with LHC working at nominal luminosity.

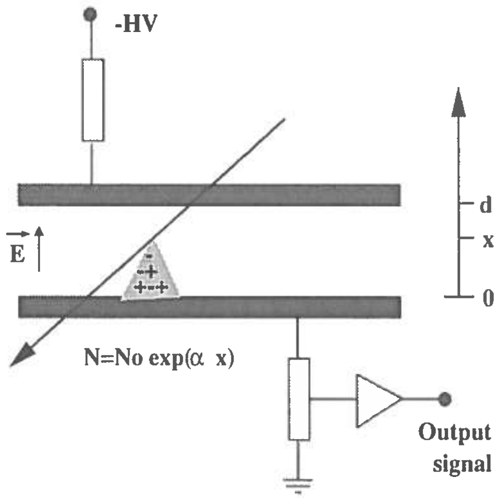

Figure 1: PPC Working Principle

2 The parallel plate chamber working principle

A Parallel Plate Chamber (PPC) is a gaseous detector [3, 4], with flat electrodes (planarity better than 5μm is needed) working in the avalanche mode. A single chamber consists of two planar metal (or metallized) electrodes kept at a fixed distance by a spacer. The gap between the electrodes is very small (1-2mm with an accurancy of 5μm) and is filled with gas which, in our case, is at atmospheric pressure. When a high voltage is applied between the electrodes, an uniform, intense electric field (50-60 kV/cm) is established inside the detector volume.

The operating principle of this detector is shown in figure 1. A particle crossing the detector can ionize the gas and produce electron-ion pairs along its path in the gas. Due to the intense electric field the electrons delivered start immediately an avalanche multiplication process.

The number of primary ion pairs can be written as [5]

$$n_0 = \Delta E/W \tag{1}$$

where ΔE is the total energy lost in the gas volume considered, and W is the effective average energy to produce one pair.

The number of electrons collected by the anode is given by [6]

$$n = n_0 e^{\alpha x} \tag{2}$$

ere n_0 is the number of primary electrons, α is the First Townsend coefficient and s the distance from the point where the primary ionization was produced to the ode. The Townsend coefficient depends on the gas mixture, on the electric field d on the atmospheric conditions [7] .The gas gain (ratio between total collected arge and primary ionization) is

$$G = e^{\alpha x} \tag{3}$$

d, integrating, the mean gain is

$$< G >= \frac{e^{\alpha d}}{\alpha d} \tag{4}$$

ere d is the distance between the electrodes.

The amplitude of the signal depends strongly on the avalanche length. izations close to the cathode give a greater contribution to the total signal than se close to the anode. As a consequence the total collected charge depends not ly on the amount of the primary ionizations but also on their location. Therefe, there is no proportionality between the energy deposited and the collected arge. The charge espectrum for minimum ionizing particles crossing the detector rpendicularly to the electrodes is not a Landau distribution [4].

Experimental conditions

l The prototype

e have tested a calorimeter prototype [2] consisting of 15 PPC layers interleaved th iron plates used as absorber. An artistic view is shown in fig 2. The total length s equivalent to about 6.8 λ_I. The PPC cells, made of metallized ceramic [8], have en assembled on one side of a multilayer printed circuit board inside a gas tight x where the gas is circulating. On the top of the enclosing box is located a HV stributor system that feeds each chamber with a single line. In this prototype each PC layer consists of 8×8 ceramic PPC , each ceramic PPC is made of two ceramic ates $50\times50\times2$ mm^3 of alumina (97 % Al_2O_3 with evaporated chromium electrodes parated by a ceramic frame, whose thickness (1.5mm in this case) determines the s gap. The sensible zone is only the 47×47 mm^2 central part of the electrode.

2 Experimental setup

he module was exposed to electron and pion beams from the CERN SPS (with ergies between 50 and 150 GeV for electrons and between 50 and 375 GeV for ons). The beam was sent to the central cell of the PPC's plane.

A gas mixture of CO_2/CF_4 (20/80) at atmospheric pressure was used and fferent high voltages were applied.

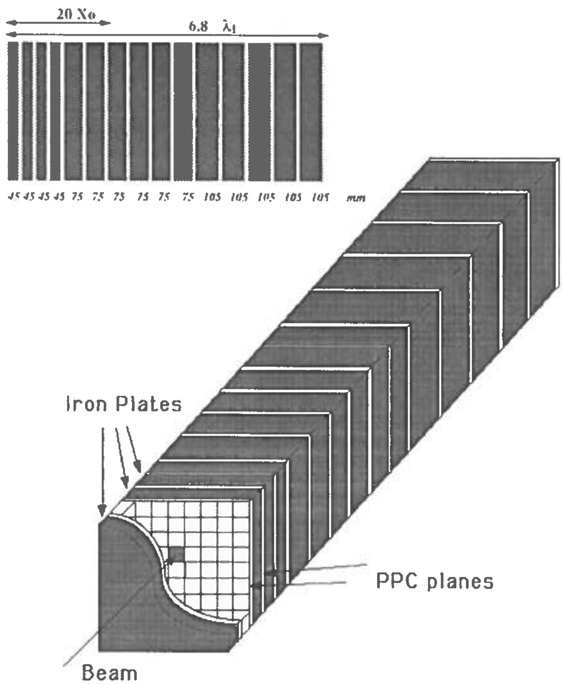

Figure 2: Sketch of an iron/PPC module

4 Montecarlo Simulation

GEANT 3.21 [9] was used to generate showers in an iron/PPC volume which reproduces the prototype tested. FLUKA [10] was used for hadron interactions inside the absorber.

Since the number of electrons collected in each cell depends on the distance between the primary ionization and the anode the gap gas in each PPC was divided in 10 subvolumes of 0.15 mm. Using the information provided by GEANT, on the energy deposited by ionization ΔE_i in each subgap, we can calculate the number of ionizations n_0^i from equation 1. As this number follow Poisson-like statistics we have approximated the number of ionizations (n_p^i) by randomly generating a number from a Poisson distribution having n_0^i as mean value. The number of collected electrons at the anode is calculated following equation 2 for each cell as

$$N = \sum_{i=1}^{10} n_p^i e^{\alpha x_i} \tag{5}$$

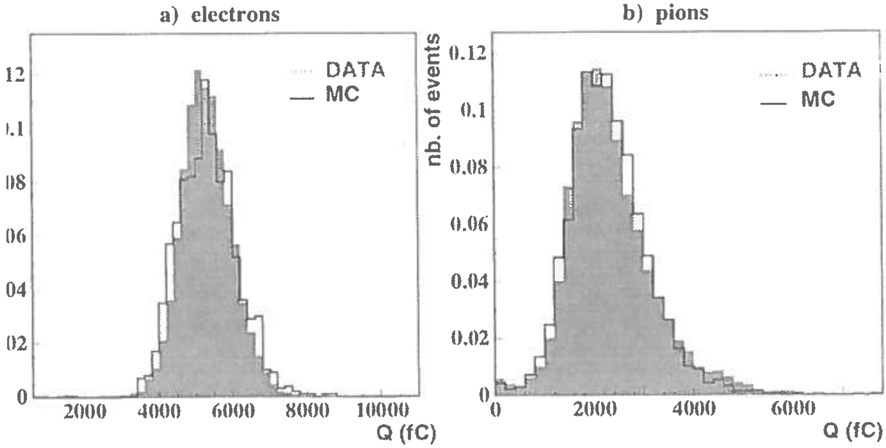

;ure 3: Normalized charge distributions for the data (shadowed) and for the ›nte-Carlo prediction (continuous line) for 100 GeV electron and pion energy at ;0 V

ere α is the first Townsend coefficient, and x_i is the distance from the i-th subgap the anode.

Comparison between Monte-Carlo and experimental data

e figure 3 shows, as an example, the collected charge distributions, normalized to ɜ, for data (shadowed) and for the Monte-Carlo prediction (continous line) for 100 V electrons and pions at 5750 V. Within the limited simulated statistics, data d Monte-Carlo distributions show a good agreement.

The comparison of measured (full circles) and predicted (open circles) col- ted charge as a function of the beam energy is given in figure 4 for electrons and ›ns at 5750 V. The slopes for the differents voltages are show in table 1.

The comparison of the energy resolution for electrons and pions at 5750 ɜ presented in figure 5. The full circles represent data points and open circles

Table 1:

	H.V	experimental	Monte-Carlo
e	5600 V	(18.2 ± 0.5) E_e (GeV)	(18.1 ± 0.8) E_e (GeV)
	5750 V	(55.4 ± 1.4) E_e (GeV)	(55.8 ± 2.5) E_e (GeV)
π	5600 V	(12.2 ± 0.5) E_π (GeV)	(12.2 ± 0.8) E_π (GeV)
	5750 V	(35.1 ± 1.4) E_π (GeV)	(34.0 ± 2.5) E_π (GeV)

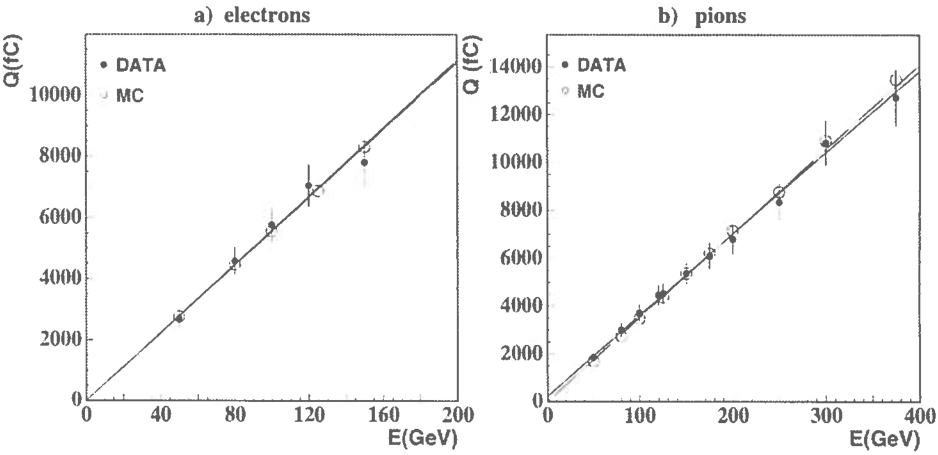

Figure 4: Comparison of measured (full circles) and predicted (open circles) collected charge as a function of the beam energy, with their corresponding linear fits, for: electrons and pions at 5750 V.

Monte-Carlo. The lines represent fits to

$$\frac{\sigma(E)}{E} = \frac{a}{\sqrt{E}} + c \tag{6}$$

the corresponding coefficients are given in table 2 for the two used voltages.

We can see that the agreement between data and Monte-Carlo is quite good and we have use this model to estimate the performance of a full size calorimeter made of 35mm thickness iron as absober interleaved with PPC planes (1.5mm gas gap). The predicted value for the single pion energy resolution is $\approx 100\%/\sqrt{E} + 3$ %. The expected level of compensation is e/$\pi \approx 1.2$

Table 2:

	H.V	experimental	Monte-Carlo
e	5600 V	$(1.03 \pm 15)/\sqrt{E_e} + (0.02 \pm 0.02)$	$(0.98 \pm 0.10)/\sqrt{E_e} + (0.03 \pm 0.02)$
	5750 V	$(0.92 \pm 0.15)/\sqrt{E_e} + (0.03 \pm 0.02)$	$(0.92 \pm 0.10)/\sqrt{E_e} + (0.04 \pm 0.02)$
π	5600 V	$(2.74 \pm 0.21)/\sqrt{E_\pi} + (0.06 \pm 0.02)$	$(1.86 \pm 0.20)/\sqrt{E_\pi} + (0.09 \pm 0.03)$
	5750 V	$(2.21 \pm 0.17)/\sqrt{E_\pi} + (0.06 \pm 0.02)$	$(1.92 \pm 0.21)/\sqrt{E_\pi} + (0.09 \pm 0.03)$

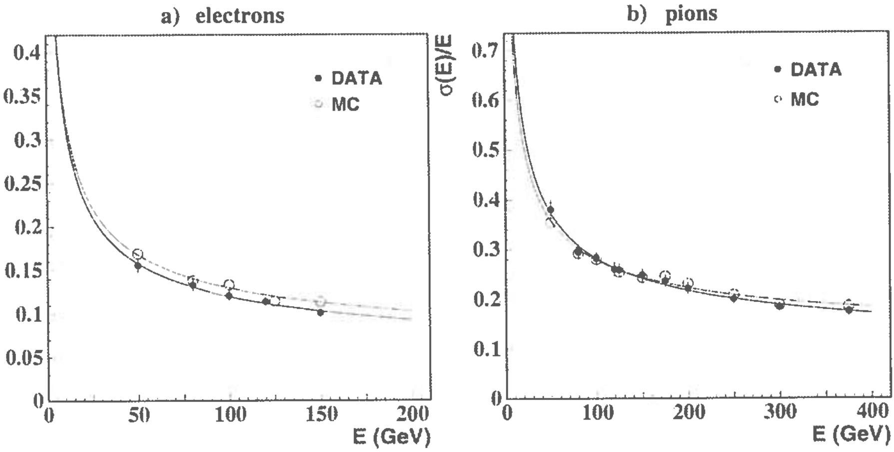

igure 5: Comparison of measured (full circles) and predicted (open circles) energy ›solutions, with their corresponding fits (see text), for electrons and pions at 5750 V

The expected effect of neutrons in the gas

.t LHC energies and luminosities the pileup of minimum bias events will be a ackground specially important in the Very Forward (VF) region. A copious neutron roduction in the development of hadronic showers will be part of it. We present Monte Carlo simulation of the effect induced by neutrons in an eventual CMS 'F/PPC calorimeter. In the following we assume the scenario described in the 'MS Technical proposal [11].

A VF/PPC calorimeter consists in 60 plates of 35mm iron absorber, in- ›rleaved with 60 planes of PPCs (1.5mm gas gap). The transverse dimensions are $\times$ 3 m^2, with an inner hole (30 $\times$ 30 cm^2) for beam pipe installation. The front ıce of the calorimeter is located at 11 m from the interaction point.

.1 Montecarlo generation of the pileup background

'ackground events have been simulated [12] with ISAJET [13]. We have considered center of mass energy per pp collision of 14 TeV, a σ_{pp}^{tot}=100mb, a Luminosity of 0^{34} $cm^{-2}s^{-1}$ and an interbunch crossing time of 25 ns.

We made the conservative hypothesis that the pp Background collisions onsists of a mixture of 60 mb two jets events ($qq \rightarrow qq$, $p_T^{jet} > 5$ GeV) and 40 mb 'linimum Bias events ($pp \rightarrow X$).

Particles are swimmed in the CMS magnetic field (4 Tesla) and those

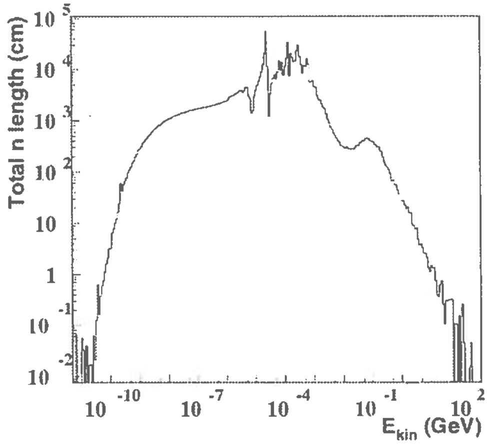

Figure 6: Kinetic energy spectrum for neutrons entering in the gas of the PPCs in the whole VF.

reaching the front face of the calorimeter are allowed to propagate inside giving rise to showers. For shower generation GEANT 3.21 was used to track particles down to 10 KeV kinetic energy except for neutrons. Hadron generation was done with FLUKA. For neutron transport we have used two different packages: MICAP [14] that describes individual neutron processes according to detailed cross section files in the range 10^{-20} eV $< E^n_{kin} <$ 20 MeV, and FLUKA, that describes all possible processes above 20 MeV.

Details of the background events and fluxes in the VF/PPC can be found elsewhere [12, 15].

6.2 Effect of the neutrons

We have made an study [17] on the effect induced by neutrons coming from pile-up background events. We studied the two gases that are currently being considered: CO_2 and CO_2/CF_4 (20/80) and compared with an hydrogeneous gas, Ar/Ethane (50/50).

Neutrons crossing the gas of the PPC cells are produced in the layers of the iron absorber. Figure 6 gives the kinetic energy spectrum of the neutron pathlength in all the detector (both sides). Te valleys observed correspond to absorption peaks in the neutron iron cross section. The integral of figure 6 gives the expected total neutron pathlength in the gas of the VF: $\approx 0.7 \times 10^6$ cm. In average one neutron travels about 4.5 mm in the gas. The highest neutron pathlength will be in the innermost region in η ($4.5 < \eta < 5.0$) and in the depth region of $2\ \lambda_I < Z < 4\ \lambda_I$.

Although the overall charge background induced by neutron interactions in e gas is negligible in the VF [17], a non zero probability exists that, in a crossing, a avy ionizing particle (mainly protons and α particles) is created in the gas followed a large energy deposition. This effect may fake a jet signal [16]. Large energy position in localized regions in gas calorimeters were already detected in the CDF rward/backward calorimeters. The effect was dubbed Texas Towers (TT.)

In the case of the VF/PPC, one of the aims is the tagging and reconstruc- on of jets [11, 16] apperaring in the V-V fussion processes having an energy larger at 500 GeV and inducing a total charge collection ≥ 50 pC if using a mean gain ≈ 700.

We found that large tails look more important in the case of α-particles d we have made an in depth study of the (n,α) process. We have generated otropically in a PPC volume, 10^6 neutrons according to the kinetic energy spectrum ven in figure 6 and forced them to undergo a (n,α) process. In this way we can tain a large sample of secondary particles that will allow to give an estimation the expected *Texas Tower* frequency. Notice that this sample is equivalent to 17.5 million LHC crossings.

We have been looking for charge depositions bigger than 50 pC to estimate e probability that a neutron, undergoing a (n,α) process, fakes a ≥ 500 GeV t. We have found that the expected number of facked jets, for the whole VF wo sides), will be $\simeq 0.29 \times 10^3$ Hz (CO_2), $\simeq 0.47 \times 10^3$ Hz (CO_2/CF_4 (20/80)) d $\simeq 0.25 \times 10^3$ Hz (Ar/Ethane (50/50)). In the case of CO_2/CF_4 mixture, the pected TT effect frequency is equivalent to $\approx 1.2 \times 10^{-5}$ per LHC crossing for e full VF (both sides).

In the experimental situation described in section 3, using a high voltage 5550 V (mean gain = 230) we have sent one million protons of 375 GeV and we ve been looking for events producing a charge larger than 12 pC in an isolated PC. We found 3 candidates. The corresponding probability is $\simeq 8.9 \times 10^{-9}$ per eV and PPC. The probability predicted by Monte-Carlo, normalized to the same nditions, is $\simeq 2.3 \times 10^{-9}$ per TeV and PPC.

Conclusions

We have found that GEANT3.21 gives a good description of the dE/dx in in gas gaps (1-2mm) and that our model describes properly the avalanche process. his allows to make predictions on the performance of iron/PPC calorimeters, for ny configuration of absorber and PPCs cells. In case of iron plates of 35mm thicknes terleaved whit PPCs planes (1.5mm gas gap) [11] we expect a single pion energy solution of about $100\%/\sqrt{(E)}$ and a level of compensation of $e/\pi \approx 1.2$.

We have made use of the package chain, ISAJET + GEANT + FLUKA + MICAP + Avalanche Simulation, to calculate the probability of production of fake jets in the gas of the PPCs. Predictions and data agree(differ) within a factor three.

References

1. A.Arefiev *et al.,* CMS TN 95-110 (1995), Nucl. Instr. and Meth. A (in press).
2. Gy.L. Bencze *et al.,* CMS TN 96-075. RD37 TN/96-16(1996)
3. A.Arefiev *et al.,* Nucl. Instr. and Meth. **A348** 318-323(1994)
4. Yu.Galaktionov *et al.,* Nucl. Instr. and Meth **A317** 116-122(1992)
5. F.Sauli CERN 77-09 (1977)
6. J.S.Townsend. Nature num 1606, vol **62**, pag 340 (1900)
7. A.Arefiev *et al.,* CERN PPE/93-82
8. V.Akimov *et al.,* Nucl. Instr. and Meth. **A344** 120-124(1994)
9. R.Brun, F.Bruant, M.Maire, A.C. McPherson and P.Zarini ERN DD/EE/84-1(1984)
10. A.Fasso *et al.,* FLUKA92. Proceedings ot the Workshop on Simulating Accelerator Radiatopm Enviroments, (Sante Fe, USA, 11-15 January 1993)
11. The CMS Collaboration, CERN/LHCC 94-38 (1994)
12. C.Burgos *et al.,* CMS TN 95-035. RD37 TN/95-4(1995)
13. F.Paige and S. Protopopescu, BNS 38774 (1986)
14. J.O. Jonhson and T.A. Gabriel. ORNL/TM-10196
15. A.Ferrando *et al.,* CMS TN 95-036. RD37 TN/95-5 (1995)
16. A.Ferrando *et al.,* CMS TN 95-61. RD37 TN/95-8 (1995)
17. A.Ferrando *et al.,* CMS TN 95-062. RD37 TN/95-9 (1995)

ıscati Physics Series Vol. VI, (pp. 529–537)
INT. CONF. ON CALORIMETRY IN HEP – Frascati, June 8–14, 1996

IMULATION OF THE CMS LEVEL-1 CALORIMETER TRIGGER

A. Nikitenko, R. Nóbrega
LIP, Lisbon, Portugal
C. Lourenço, J. Varela
CERN
S. Dasu, W. Smith
University of Wisconsin, Madison, USA

ABSTRACT

: present the baseline calorimeter trigger algorithms of the CMS experiment for ecting electrons, photons and jets as well as triggering on missing and scalar E_t. sults of the several simulation studies show that these trigger algorithms satisfy : rate and efficiency requirements both for low and high luminosity LHC running. rformance of the CMS Level 1 Calorimeter Trigger for the CMS physics program demonstrated.

Introduction

e CMS trigger system will operate at the nominal LHC design luminosity of $^{34}cm^{-2}s^{-1}$. An average of 20 inelastic events occur every 25 ns, the beam crossing erval, giving the input rate of 10^9 interactions per second. This rate must be luced by a factor of at least 10^7 to 100 Hz, which is the maximum rate that be :hived for off-line analysis. CMS has chosen to reduce this rate in two steps [1]. e Level-1 trigger system operates with the calorimeter and muon detector data lected from each LHC beam crossing. During the $3\mu s$ data storage time, the vel-1 trigger decision is taken to reduce QCD background rate below 100 kHz, ich is maximum event rate that can be accepted by the Level-2 trigger.

Rate requirements for the Level-1 Calorimeter Trigger

e uncertainties in estimates of cross-sections at LHC energy as well as uncertainties the simulations itself and in the final detector design impose a large error on the imated trigger rates. Therefore, we provide for a safety margin of a factor 3

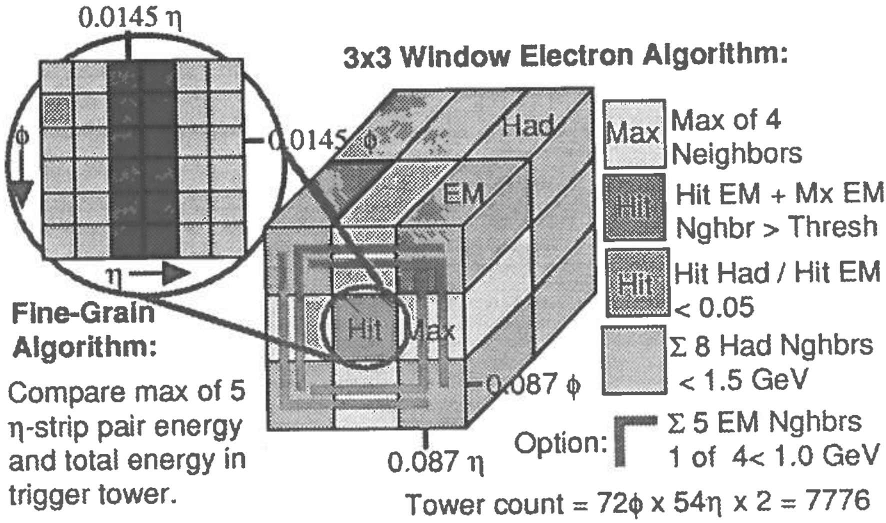

Figure 1: Scheme of the CMS electron/photon trigger

to reduce the design 100 kHz maximum Level-1 output rate to 30 kHz for design of Level-1 trigger algorithms [2]. This 30 kHz has to be shared amongst both muon and calorimeter triggers. Therefore, the nominal output rate of the Level-1 Calorimeter Trigger should not exceed approximately 15 kHz.

1.2 Geometry and definitions

Each trigger cell in the barrel and in the endcap electromagnetic (ECAL) and hadronic (HCAL) calorimeters corresponds to the size of an HCAL tower: $\Delta\eta \times \Delta\phi = 0.087 \times 0.087$ up to pseudorapidity $\eta \simeq 2.3$ and 0.180×0.087 above $\eta \simeq 2.3$. In the barrel ECAL, the trigger cell is formed by 6×6 crystals while in the endcaps a variable number of crystals form the trigger cells. In all cases, there is an exact match between the boundaries of ECAL and HCAL trigger cells. The ECAL trigger cells are also divided in strips (one crystal in η and six crystals in ϕ). The strip E_t is provided by the ECAL front-end electronics. In the VFCAL, a possible segmentation, still subject to optimization, is the following: $\Delta\eta \times \Delta\phi = 0.35 \times 0.35$ for $2.6 < \eta < 4$ and $\Delta\eta \times \Delta\phi = 1.0 \times 0.7$ for $4.0 < \eta < 5.0$.

1.3 Trigger primitives

The following trigger primitives are generated by front-end electronics for every ECAL trigger cell: transverse energy (E_t) of trigger cell and a fine grain local iso-ion bit (LI) which defines the lateral profile of the cluster. LI bit is computed m the strips by selecting the maximum E_t sum of two adjacent strips; comput- ; R, the ratio between the maximum sum of two strips and the E_t of trigger cell l comparing R with programmable thresholds to get the LI bit. For HCAL the gger primitives are the cell E_t and a MIP bit (energy compatible with mip energy posit).

Simulation tools

sults presented here were obtained with the GEANT based package CMSIM8 [3] l with a fast simulation package based on a parameterization of the hadronic and ctromagnetic showers [4].

Electron/photon trigger

high luminosity ($L = 10^{34} cm^{-2}s^{-1}$) the single electron/photon trigger is required be fully efficient (> 95%) for the isolated electrons and photons of $E_t > 35$ V and $|\eta| < 2.5$. The double e/γ trigger is required to be fully efficient for > 15 GeV for each particle in the same rapidity range. The requirement on the ible e/γ trigger provides efficiency above 95% for Higgs decays $H(80GeV) \to \gamma\gamma$ l $H(120GeV) \to ZZ^* \to 4l$. The requirement on single e/γ trigger provides ater than 50% efficiency for electrons from inclusive W production and above 60% ciency for $t \to eX$. The electron/photon trigger uses a 3x3 trigger cell sliding ndow algorithm. A scheme of the trigger is presented in fig.1. The electron/photon ntification is based:

- on the recognition of a large transverse energy given by the sum of the ntral ECAL cell ('hit cell') with the maximum of the four orthogonal neighbor cells nax cell');
- on the lateral shower profile in the 'hit cell' given by LI bit;
- on the longitudinal shower profile given by the ratio of transverse energies the hadronic and e.m. 'hit cells' (H/E in central trigger cell of 3x3 window)
- when isolated electron/photons are requested, on the e.m. isolation energy MI) as given by the smallest of the four sums of e.m. cells around the 'hit cell';
- when isolated electron/photon are requested, on the hadronic isolation rgy (HDI) as given by the sum of the eight hadronic cells surrounding the 'hit l';

The cuts on the cluster variables R(LI bit), H/E, EMI and HDI have been ed to minimize the trigger rate, while requiring the efficiency for isolated electrons l photons to be above 98%.

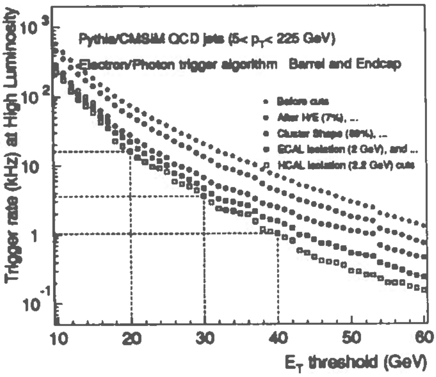

Figure 2: Rate of single e/γ trigger for $L = 10^{34} cm^{-2} s^{-1}$

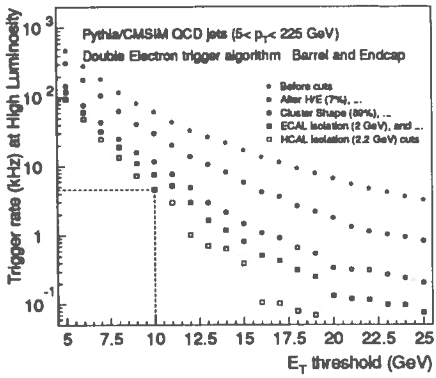

Figure 3: Rate of double e/γ trigger for $L = 10^{34} cm^{-2} s^{-1}$

For electrons and photons of 20 GeV the algorithm becomes fully efficient at a trigger threshold 5 GeV lower; for e/γ's of 40 GeV, the shift is about 10 GeV. Therefore to fulfil the physics requirements the trigger thresholds must be of the order 25 and 10 GeV for the single and double e/γ trigger respectively. The trigger rates for high luminosity, $L = 10^{34} cm^{-2} s^{-1}$ vs. E_t threshold are shown in fig.2 and fig.3 for single and double triggers. At the required thresholds of 25 GeV for single and 10 GeV for double e/γ triggers, all cuts on the cluster variables being applied together give a reduction factor for QCD background of about 5 and 10 respectively and final background rates become below 10 kHz. It was checked that trigger efficiency is uniform vs. rapidity. The trigger is efficient (about 95%) for photons converted into e^+e^- pairs in the tracker material. Therefore almost all $H \to \gamma\gamma$ events where at least one photon is converted will pass L-1 trigger.

At $L = 10^{33} cm^{-2} s^{-1}$ the electron trigger algorithm allows triggering on at single and double electrons from b-decays in the range $\mid \eta \mid < 1.6$ with momenta above 10 and 5 GeV respectively with an efficiency above 50%. The physics motivation is to increase of statistics of $B_d^0 \to \pi^+\pi^-$ events triggering on an electron from $b \to eX$ decay as well as increasing the statistics of $B_d^0 \to J/\Psi K^0$ decay using the double lepton $e - e$ and $e - \mu$ trigger. Triggering the electrons in b-jets is based on the fact that the electron is rather well isolated in a cone $R \leq 0.05$ which is the typical trigger cell size. Therefore, the cluster variables R and H/E which characterize the longitudinal and lateral cluster shape inside the hit cell can be used to identify electrons in b-jets and to suppress the background rate. The efficiency to trigger on electrons of $p_t > 10$ GeV from events $B_d^0 \to \pi^+\pi^- + b \to eX$ vs. the cut on the variable R, with a fixed cut on H/E, is shown in fig.4 for E_t threshold of 8 GeV. The rate of the single b-electron trigger is shown in fig.5.

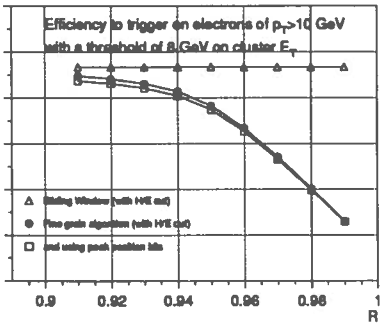

ꞡure 4: Efficiency to trigger on auty events with $p_t^e > 10$ GeV, as 'unction of R cut

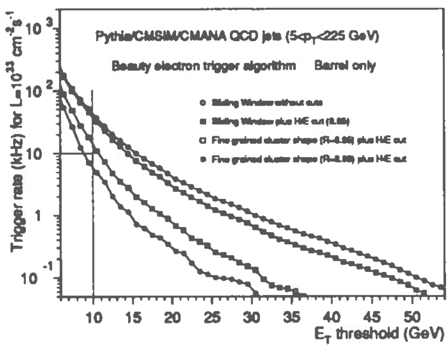

Figure 5: QCD rate of single b-electron trigger for $L = 10^{33} cm^{-2} s^{-1}$ in the barrel

Jet trigger

ıgle and multiple jet triggers at various thresholds are required to study top, SUSY ysics, compositeness as well as checking QCD. The jet trigger uses the transverse ergy sums (e.m.+ had.) computed in the calorimeter regions (4 × 4 trigger cells) $\eta \times \Delta\phi = 0.35 \times 0.35$. Two versions of the trigger were under study:

1) The jet transverse energy is given by the transverse energy in a calorime- regions.

2) The jet transverse energy is given by the transverse energy sum in 2 × :alorimeter regions, where the windows overlap center to corner.

Version 2 gives a jet trigger with a higher rate but a slightly better efficiency rve. Fig.6 shows efficiency curves for the two versions for E_t thresholds which give e same rate of 2 kHz at high luminosity for both algorithms. While giving small in in efficiency, version 2 is much more complex to build than version 1 because requires sharing of 4 × 4 trigger tower sum data across crates and complex logic filter out spurious multi-jets. Therefore, version 1 is chosen as a baseline. Rates 1 jet, ...,4 jet triggers at high luminosity vs. E_t threshold are shown in fig.7. No paration between jet regions was required for multiple jet triggers since 2 jet events e sometimes triggered by 3j and 4j triggers if the jet spreads into the adjacent gions. Requiring at least one region separation between jet regions reduces the te of 3j and 4j triggers by factors of 2 and 4 respectively. The efficiency of such quirements to trigger on multi-jet events for the physics of interest is under study.

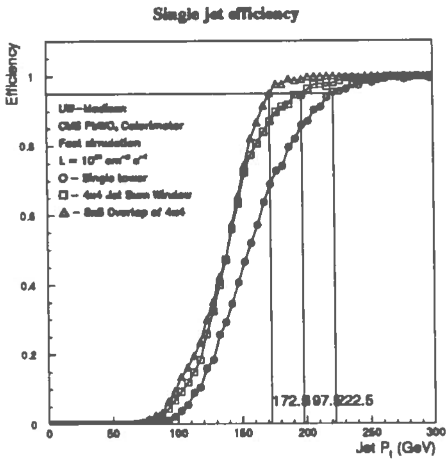

Figure 6: Single jet efficiency

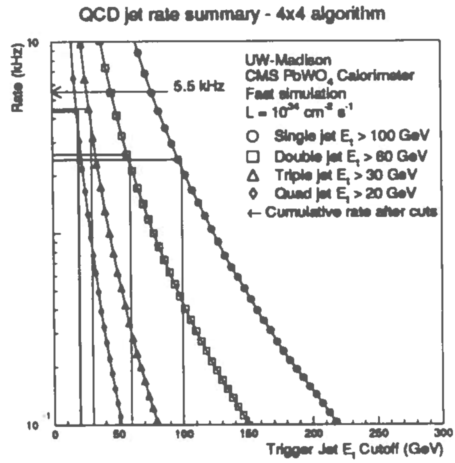

Figure 7: Jet triggers rates

4 Missing Et trigger

The missing E_t trigger is an important component in the search for SUSY events both for low and high luminosity LHC running. In particular, search for squarks and qluinos requires the identification of events with missing E_t above 150 GeV together with multi-jets [1]. The missing E_t trigger uses E_t sums (e.m.+had.) computed in fixed calorimeter regions (as for the Jet Trigger). The location of the region center is used to convert E_t to E_x and E_y. The missing E_t trigger rate at high luminosity is shown in fig.8. At a nominal threshold of 80 GeV and including the Very Forward Calorimeter, the rate is about 0.8 kHz. Removing the VFCAL from the calculation of missing E_t increases the rate by about of factor 2. Fig.9 shows the missing E_t trigger efficiency for SUSY events with multi-jet final states (Scenario A in CMS TP: $M_{LSP} = 45GeV$, $M_{spat} \approx 300GeV$) for a trigger threshold of 80 GeV. Simulated detector effects include energy resolution, loss of energy in the preshower and gaps. The dominant trigger effect is the integer scale of 1 GeV for the transverse energy (e.m.+ had.) of the trigger cells used to compute the E_t of the regions.

5 Trigger performance on physics channels

A preliminary representative set of E_t cutoffs for individual calorimeter triggers were selected both for low ($L = 10^{33}cm^{-2}s^{-1}$) and high ($L = 10^{34}cm^{-2}s^{-1}$) luminosity that satisfied the bandwidth requirement and provided good efficiency for the various physics channels studied in the CMS Technical Proposal [1]. Tab.1 presents the background rates for individual triggers and the cumulative rates as each trigger

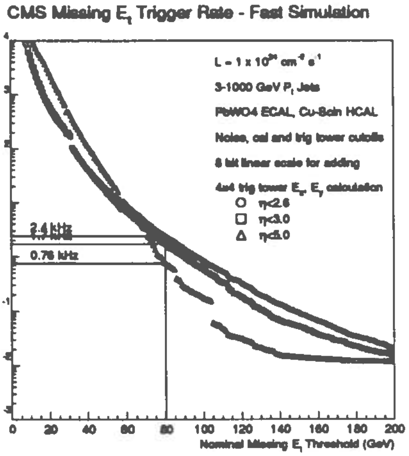

'igure 8: Missing Et triggers rates

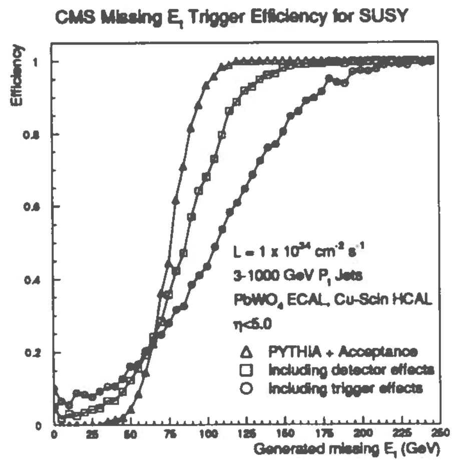

Figure 9: Missing Et trigger efficiency for SUSY

added in the order shown [1]. The cumulative efficiencies for the physics processes interest are presented in the tab.2. Efficiencies do not include the geometrical ceptance of the CMS detector. The calorimeter trigger gives very good perforance for the benchmark decays of Higgs into $\gamma\gamma$ and 4l [2] at high luminosity (for w luminosity it is better due to the lower E_t cutoffs). Top, squarks and gluinos th multi-jet final states and SUSY charged Higgs both for low and high luminosity ve a good trigger efficiency. The trigger acceptance is not very high for low mass utral Higgs decays into tau pairs due to energy cutoffs. In order to provide good igger performance at high luminosity of neutral SUSY Higgs decaying into tau irs, an independent τ trigger is being investigated.

Tau trigger

dedicated Level-1 τ - trigger is under development to improve the efficiency of e trigger system at high luminosity $L = 10^{34} cm^{-2} s^{-1}$ to the neutral SUSY Higgs cays into tau pairs. It is important to increase efficiency for the low Higgs masses 0 - 200 GeV in order to exploit the region of MSSM parameters $3 \leq tg\beta \leq 10$, 0 $\leq M_A \leq 200$ GeV, which can not be covered by $A, H \rightarrow \tau\tau$ decays at low minosity. The off-line analysis of the $e - \tau$-jet(1-prong decays) final state selects ents with $E_t^{\tau-jet} > 40$ GeV and $E_t^e > 20$ GeV for Higgs masses ≤ 300 GeV. These ents are triggered in Level-1 by the combined $e - \tau$ trigger, which was found to be ore efficient than the e-jet trigger, for the same background rate.

[1] numbers for low luminosity; numbers in parenthesis for high luminosity
[2] inclusion of muon trigger will provide full efficiency

Table 1: Individual and cumulative Level-1 Calorimeter Trigger rates for QCD jet events.

Trigger Type	Trigger Et Cutoff (GeV)	Rate (kHz) individual	Rate (kHz) cumulative
Sum Et	150 (400)	1.04 (0.48)	1.04 (0.48)
Miss Et	40 (80)	2.11 (1.29)	2.82 (1.70)
e	12 (25)	10.3 (6.84)	12.3 (8.34)
ee	7 (12)	1.54 (1.45)	13.1 (9.52)
j	50(100)	1.98 (2.06)	13.5 (10.7)
jj	30 (60)	1.63 (2.17)	13.9 (11.6)
jjj	20 (30)	1.02 (3.16)	14.1 (13.3)
jjjj	15 (20)	0.68 (2.96)	14.2 (14.3)
j-e	15-9 (50-12)	5.98 (1.35)	15.2 (14.9)

Table 2: Cumulative efficiencies for the CMS TP Physics.

Process	Efficiency (%) $L = 10^{33} cm^{-2}s^{-1}$	Efficiency (%) $L = 10^{34} cm^{-2}s^{-1}$
$H(80GeV) \to \gamma\gamma$		97.4
$H(120GeV) \to ZZ^* \to ee\mu\mu$		76.4
$pp \to t\bar{t} \to eX$	99.3	88.3
SUSY CMS TP Scenario A ($M_{LSP} = 45GeV$, $M_{spat} \approx 300GeV$)	97.8	83.0
$pp \to t\bar{t} \to H^+bWb \to \tau eX$ ($\tau \to X$)	99.0	81.7
SUSY Neutral Higgs $\to \tau\tau$ ($\tau \to$ e,hadrons; range of M, $tan\beta$)	45-98	

The τ-trigger is based on the fact that 1-prong τ decays give mainly a $\pi^{\pm}\pi^0$ final states confined in a small cone ($R < 0.1$) for E_t of τ-jet more than 40 GeV. The tau algorithm asks for a localized cluster in the ECAL, selected by the sliding window algorithm with a cut on e.m. isolation energy slightly softer than that for the e/γ trigger, associated with hadronic activity in a 3×3 HCAL matrix behind ECAL window. The τ-jet transverse energy is given by the energy of the calorimeter region where only one such cluster was selected by the sliding window algorithm. In addition, one can require isolation of this region over a bigger 3×3 calorimeter region matrix. A scheme of the τ trigger is shown in fig.10. The efficiencies of $e - j$ and $e - \tau$ triggers for $H(140GeV) \to \tau\tau \to e - jet$ vs. rate are shown in fig.11 for an E_t threshold on the electron fixed at 9 GeV. [3]. The numbers near the data points are the jet thresholds. The efficiencies were evaluated relative to events useful for

[3]pile-up is not included

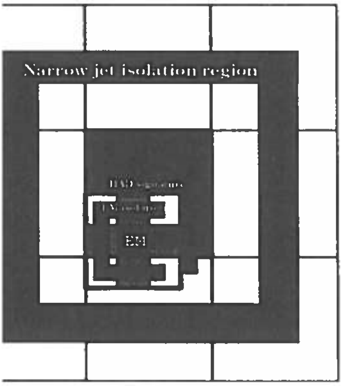

ɡure 10: Scheme of the CMS τ trig-
r

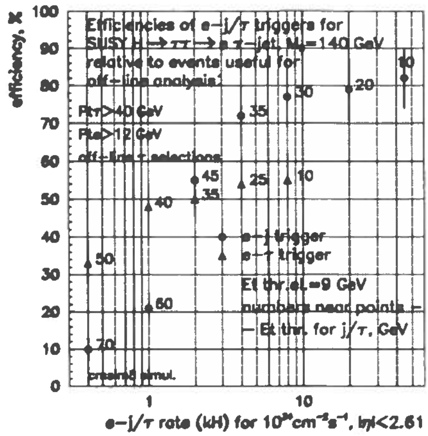

Figure 11: Level-1 e-j, e-τ triggers efficiencies for SUSY $H(M = 140GeV) \rightarrow \tau\tau \rightarrow e - jet$ v.s. rate at $L = 10^{34} cm^{-2} s^{-1}$

-line analysis ($E_t^{\tau-jet} > 40$ GeV; CMS off-line τ selections; $p_t^e > 12$ GeV). One n see that at a rate less than 2 kHz the $e - \tau$ trigger becomes more efficient than ɜ $e - j$ trigger. The simulation shows that at high luminosity the $\tau - \tau$ trigger has ːate of about 1 kHz with an E_t threshold of 40 GeV while the j-j trigger reaches ɪs rate at a higher threshold of 70 GeV. This provides the possibility to improve ɜ study of A,H decays with two τ jets in final state.

ɘferences

. CMS Technical Proposal. CERN/LHCC 94-38, 15 Dec.1994

. J. Varela at al. 'Preliminary specifications of the baseline trigger algorithms.' CMS TN/96-10

. C. Charlot at al. 'CMSIM-CMANA. CMS Simulation Facilities' CMS TN/93-63.

. S. Dasu, J. Lackey, W.H. Smith, W. Temple 'CMS Level 1 Calorimeter Trigger Performance Studies.' CMS TN/94-285.

scati Physics Series Vol. VI, (pp. 539-544)
INT. CONF. ON CALORIMETRY IN HEP - Frascati, June 8-14, 1996

A Study of a Transverse Energy Trigger Utilizing the Outer em Calorimeter of FOCUS at Fermilab

S. Bianco, F. L. Fabbri, S. Sarwar, A. Zallo
Laboratori Nazionali di Frascati dell'Infn, I-00044 Frascati, Italy.

ABSTRACT

ıe transverse energy is a powerful variable to select the production of heavy quarks. e have studied what rejection power is maintained when only the em component of e transverse energy (E_T^{em}) is used. This investigation is driven by simulation, and en applied to the data already collected by an existing experimental apparatus. ıe filtering of a low bias data sample, collected by photoproduction experiment 587, through two algorithms based on the E_T^{em} detected by the large-angle em lorimeter, is shown to provide a reduction factor of at least 2 at 80% charm ficiency. This should be compared to a factor 3 rejection attainable in the same uation if the transverse energy as measured by a hadron calorimeter (E_T^{had}) is ed. An algorithm which estimates E_T^{em} using digital variables and which could be sily implemented in DAQ triggers, has also been studied, and shown to be at least effective as the analog one.

Introduction

he total transverse energy of an event is proportional to the mass of the produced stem. Experimentally, the hadronic transverse energy has been proved to be powerful variable to select events containing heavy quarks over the light-quark ıdronic background [1], which is mainly concentrated in the forward cone. In this ork we have investigated what reduction factor, if any, could be associated to a cut plied to the em component E_T^{em} of the transverse energy. This question is mainly otivated by the following considerations:

- generally, at fixed target experiments, em calorimeters cover an angle larger than hadron calorimeters, to keep the same geometrical acceptance for charged and neutral decay products;

- em calorimeters can have a much finer space granularity than hadronic calorimeters;
- the energy resolution of em calorimeters is definitely better than hadronic calorimeters.

We have applied this exercise to a *low bias* sample of data collected by fixed-target experiment E687 at the Fermilab Tevatron [2) 3)], which studies production and decays of charmed mesons and baryons, photoproduced at high energy (250 GeV beam energy). To test the algorithms, we used an event sample selected by the second level trigger. The first level trigger requires coincidences between counters close to the experimental target, and at least two tracks outside of the e^+e^- pair region. The first level trigger by itself reduces the most copious background due to the Bethe-Heitler e^+e^- pairs produced by the conversion of the photon beam in the target and along the spectrometer. The second level trigger additionally requires a minimum total energy release in the hadron calorimeter (typically, 20 GeV). This requirement reduces by a factor of 200 the acquisition rate. The events selected by the second level trigger contain a residual 3% fraction of e^+e^- pairs, which are discarded by applying analysis selections (i.e., two-track, opposite-charge events with invariant mass under 0.002 GeV/c^2). The remaining events represent a reliable *hadronic* data sample, mostly composed of light-quark events (meson states such as ρ, ω, ϕ ...) produced mainly via vector dominance, and whose typical cross-section is 130 μb per target nucleon, to be compared to the charm photoproduction cross section, about 100 times smaller. The rejection power of an E_T^{em} based cut is given by the reciprocal of the fraction of hadronic events which survive the cut. To evaluate the efficiency of the E_T^{em} cut for charm events, we used a subset of events selected out of the hadronic data sample. The selection was made by means of the standard E687 analysis code for the search of D decays [2)], and it retains events whose mass plots for D^0 and D$^+$ in the two main charged decay channels $K\pi$ and $K\pi\pi$ are shown in fig.1, where only events with masses between 1.820 GeV/c^2 and 1.900 GeV/c^2 have been plotted. The *charm efficiency* is defined as the fraction of event yield in the peak of the mass plot of fig. 1 which survives to the cut. The event yield is determined by means of the best fit to the data of a curve composed of a gaussian (for signal) and a quadratic polynomial (for background).

2 Em calorimetry in E687

Em calorimetry in E687 is composed of two detectors, which cover the small angle and the wide angle geometrical acceptance respectively.

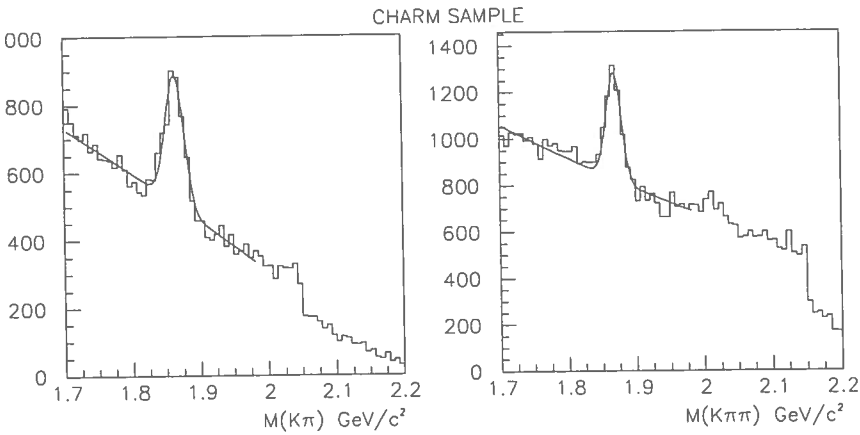

igure 1: The D^0 and D^+ invariant mass distributions for the charm background ımple used. The decay channels are $D^0 \to K^-\pi^+$ and $D^+ \to K^-\pi^+\pi^+$.

The Inner em (IE) is a Pb/SCIFI sampling calorimeter. Fibers are grouped ı 2.5 cm wide strips, for a total of about 800 readout channels, arranged in X-Y iews. The IE is located at about 20 meters from target and covers the small ngle region, up to 30 mrad. The counters are arranged in X-Y views. The energy esolution is $\sigma/E = 20\%/\sqrt{E(GeV)} \oplus 3\%$

The Outer em (OE) [4] is a Pb/scintillator sandwich sampling calorime- er, about 1200 readout channels, covering the wide-angle region from 25 mrad up to 20 mrad. Counters, 3.3-cm wide strips, are also arranged in X-Y views. The detec- or is longitudinally segmented: three main sampling modules, each one composed f interlaced horizontal (OE1H, OE2H, OE3H) and vertical (OE1V, OE2V, OE3V) ounters; two tiebreakers for solving the X-Y ambiguity; and one pre-radiator for lectron identification. The energy resolution is $\sigma/E = 13\%/\sqrt{E(GeV)} \oplus 2.5\%$.

The OE only is used to test the transverse energy algorithms discussed in his study.

3 Discriminating variables

The transverse energy of an event is :

$$E_T = \sum_{i=1}^{N_{hit}} E_i \sin\theta_i \tag{1}$$

where the energy E_i of the ith secondary is weighed by the emission angle θ_i. In the case of a finite-granularity calorimeter, the index i runs over the readout counters. We computed the transverse energy E_T^{em} deposited in the OE [1]. This quantity is a

[1] E_T^{em} is always defined in the non-bend view, i.e. only hits from vertical OE counters are considered.

measurement of the transverse energy carried by the detected em component of the event, plus a fraction of the transverse energy carried by the charged component, depending on the depth of the calorimeter in interaction lengths units. We used only the first and second longitudinal segments OE1V and OE2V[2], where em showers attains its maximum, and the contribution of the hadronic showers is small. The OE counters were gain-equalized using minimum ionizing particles. To construct E_T^{em} , raw ADC pulse heights were used. In the following, energy is expressed in minimum ionizing particles units. Such an approach is realistic, since it keeps all sources of fluctuations and systematic biases (attenuation of light in the scintillator, pedestals fluctuation, gain unbalance, etc.) that are encountered in real data taking.

Another discriminating variable was also studied. N_T is defined as the number of calorimeter counter above an energy threshold $E_{threshold}$ which varies proportional to the angle θ_i:

$$E_{threshold} = E^0_{threshold} \quad \frac{\theta_{min}}{\theta_i} \tag{2}$$

where $\theta_{min} = 25$ mrad is the minimum angle covered by the OE calorimeter.

4 Results

All results have been repeated with the threshold at small angle set to $E^0_{threshold} = 1, 2, 5\, mip$. We filtered the hadronic background sample and the charm sample through both E_T^{em} and N_T. Fig.2 shows the N_T and E_T^{em} distributions for hadronic (solid) and charm (dash) samples. Fig.3 shows the dependance of hadronic and charm efficiency as functions of the N_T and E_T^{em} cuts, while the correlation between the two efficiencies is shown in Fig.4. For the N_T variable this has been done using a few options: only hits in the first OE segment OE1V (solid), only hits in the second OE longitudinal segment OE2V (dots), and hits from both segments summed (dash). The N_T cut is at least as efficient as the E_T^{em} cut, and it provides a rejection factor better than 2, while keeping 80% of the charm sample.

These performances are compared with a cut on the E_T^{had} deposited in a typical hadron calorimeter. We simulated the effect of a E_T^{had} cut, finding for a 80% charm efficiency a factor 3 rejection of the hadronic background.

The implementation of a N_T based trigger is also been considered in the forthcoming FOCUS experiment at Fermilab [5].

[2]for a total depth of about 10 and 15 radiation lengths, and 0.5 and 0.75 interaction lengths, respectively.

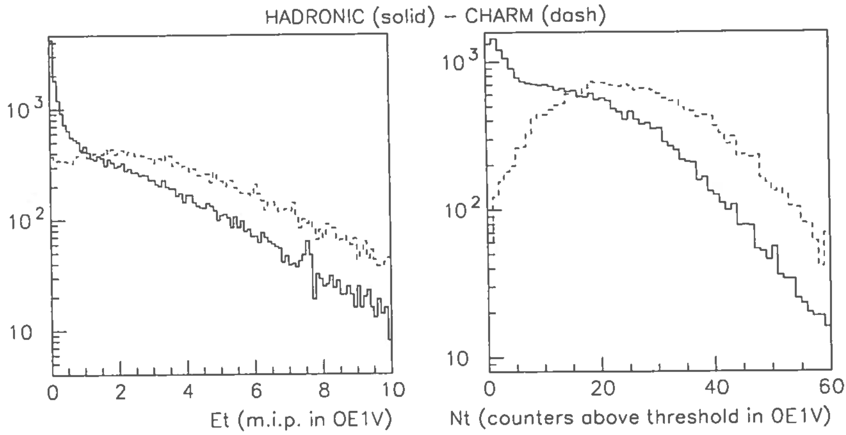

igure 2: The distribution of E_T^{em} and N_T in the Outer em for hadronic (solid) and ıarm (dash) samples. Curves are area-normalized.

Conclusions

/e have studied the performance of a cut on the em transverse energy, as a tool to ·lect heavy-quark events out of an hadronic data sample. We have demonstrated ıat a mildly-segmented em calorimeter extending at angles larger than 25 mrad pro- ides E_T^{em} information nearly as effective as a standard E_T^{had} cut. The N_T variable as effective as E_T^{em} , and simple to to implement in a DAQ system as a trigger.

Ɩeferences

1. J. R. Raab, Lifetime measurements of the three charmed pseudoscalars D-mesons, Ph. D. Thesis, Univ. of California, Santa Barbara, 1987.

2. P.L. Frabetti et al., Description and performance of the Fermilab E687 spectrometer, Nucl. Instrum. Meth. A320:519-547, 1992.

3. P. L. Frabetti et al., A wide band photon beam at the Fermilab Tevatron to study heavy flavors, Nucl. Instrum. Meth. A329:62-78, 1993.

4. P. L. Frabetti et al., Description and performance of the Fermilab E687 spectrometer, FERMILAB-PUB-90-258-E.

5. E831 Wideband Beam Photon Collaboration, A high statistics study of states containing heavy quarks using the wideband photon beam and the E687 multi-particle spectrometer, proposal to PAC, Fermilab, 1992.

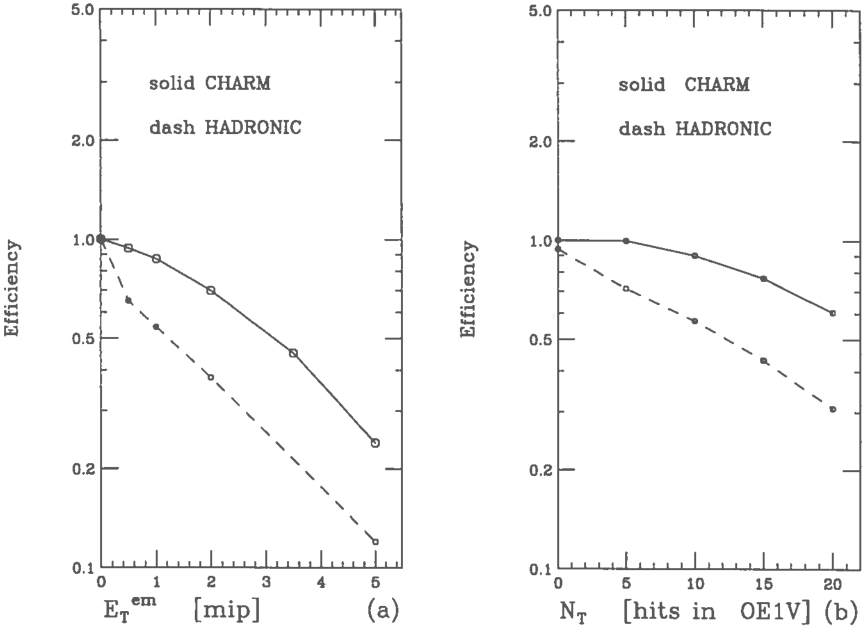

Figure 3: The charm (solid) and hadronic (dash) efficiency distributions as functions of E_T^{em} and N_T variables.

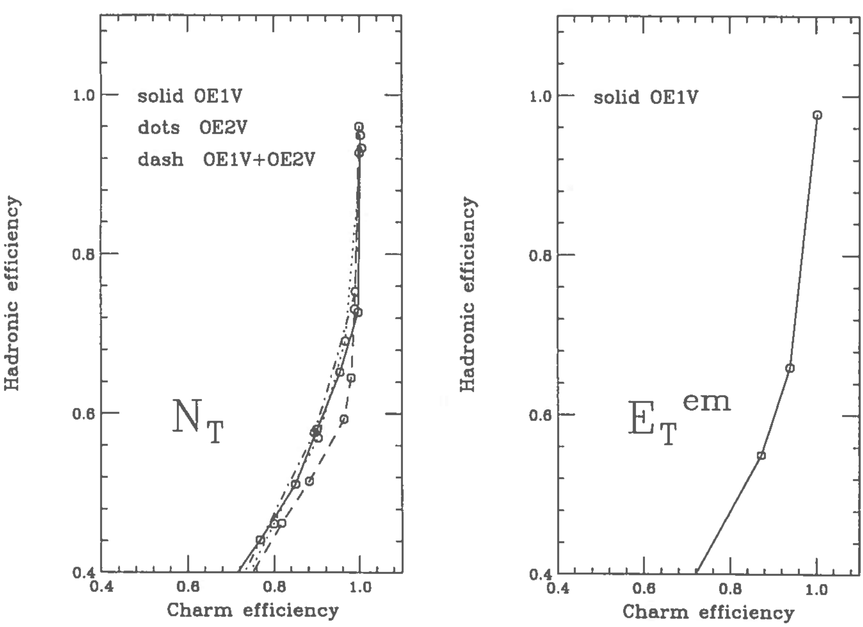

Figure 4: Charm versus hadronic efficiency for the N_T and E_T^{em} variables.

:ascati Physics Series Vol. VI, (pp. 545–552)
I INT. CONF. ON CALORIMETRY IN HEP – Frascati, June 8–14, 1996

A LEAD/SCINTILLATING FIBERS CALORIMETER FOR THE MEASUREMENT OF GAMMA ENERGY AND DIRECTION

Aldo Morselli
Dept. of Physics, Univ. of Roma "Tor Vergata" and INFN, Italy
Mirko Boezio
loyal Institute of Technology Stockholm, Sweden and sezione INFN di Trieste, Italy

ABSTRACT

ıe next generation of cosmic gamma ray detectors needs very large geometric :tor, good efficiency and good energy resolution. Here we present a study on a ıssible option for the calorimetric part of the detector based on a lead/scintillating ıer sandwich that allows not only a good energy resolution but also a measure- ənt of the gamma arrival direction and a discrimination between hadronic and ·ctromagnetic shower.

Introduction

.gh energy gamma-ray astrophysics has greatly developed in these last few years :cause of the results of the experiment EGRET [1] on the Compton Gamma Ray ɔservatory. The satellite observations have brought more detailed data about the :ll known gamma-ray sources, but also the discovery of new ones, both galactic .d extragalactic, especially Active Galactic Nuclei and gamma-ray bursts. All ese exciting results have shown the necessity of a next generation experiment with sensitivity increased by at least one order of magnitude and with better angular .d energetic resolutions that must solve the following remaining problems:

Exploring the 30 - 100 GeV Energy Range

ıe energy range between 30 and 100 GeV is completely unexplored up to now, so ere is the possibility to discover new phenomena that can be of the greatest im- ırtance in Cosmology and Particle Physics. For example the existence of gamma y lines can be the signature of the annihilation of weakly-interacting massive par- :les (Wimp's) [5], which are a prime candidate for the dark matter in the galactic halo and consequently the first evidence of the existence of the lightest supersymmetric particle [3]. Both the gravitino [4] and the photino [2], the most probable lightest supersymmetric candidates, can produce a detectable gamma line, with the difference that the gravitino can decay into a gamma ray and a quarkonium bound state, a photino also in a pair of gamma rays [6]. The free parameters in the existing theories produce great uncertainties in predictions of the gamma flux intensity, depending on the WIMP's annihilation processes, but an energy resolution around 15% could be enough to reveal the gamma lines .

- *The cosmic infrared background*

The Compton Gamma Ray Observatory (CGRO) in connection with the observations of the Whipple Observatory [7] have brought important changes in the prospect for very high energy γ-ray astronomy because it indicates that there is a strong attenuation of the γ-ray flux for objects at redshift $z \sim 1$ for energies greater than 100 GeV due to the interaction with the cosmic infrared background [8, 9]. Because of this absorption, a survey of AGN phenomena to cosmological distances may well be limited to energies below 100 GeV, requiring the development of sensitive detectors to span the region above that covered by EGRET and below the range of present-day Cerenkov telescopes .

- *Continuous monitoring*

One of the main features of observed gamma-ray sources is their strong time variability. The Active Galaxies can exhibit significant time variability on a time scale as short as 2 days. This variability means that, to understand the emission mechanisms, one needs continuous monitoring of the sources instead of a single observation.

- *Gamma ray bursts*

They are now the most interesting and mysterious objects in the sky. The theoretical models trying to understand them can be divided in two big classes: cosmological and galactic. The major difficulty for galactic models is the explanation of the complete isotropy of the bursts distribution, while for the cosmological ones is the very high value of energy that must be released at the source ($\sim 10^{51}$ ergs). All the experimental data collected up to now do not give the possibility to discriminate among these options.

Detection of the burst spectra extension can be the way to establish the distance scale, through the intergalactic absorption mechanism.

2 The next generation experiments

To solve these problems some next generation experiments has been proposed. Among these, one, GLAST [10] has been already selected by NASA and ASI for a more detailed study and GILDA [11], [12] is being studied in the framework of the iZard RIM collaboration [13].

The complete projects are presented elsewhere (see upward references), re we want to dwell upon the advantages of a possible option for the calori- tric part of the detectors made with 'active' lead-scintillating fiber absorbers w by photomultipliers (PM). This solution is now particularly attractive be- use HPK developed compact 4*4 multianode PMs (PMT R6568 series) with 4*4 n^2 anode downsized to the same dimensions as a solid state detector and housed a robust metal package 30 mm in size and 40 mm in length, while maintain- ; the same performance, high sensitivity and high speed as a conventional PM ming performances : $\sigma_t \simeq 50\, ps * E(GeV)^{-\frac{1}{2}}$). Besides the gain in thickness d power consumption with respect to CsI calorimeter, we still have a good energy solution $\left(\sigma(E)/E \leq 5\% * E(GeV)^{-\frac{1}{2}}\right)$ at least up to 1 GeV(where we have total ntainement) [15].

Moreover the tracking calorimeters have proven to be a very good tool : the separation between hadronic and electromagnetic shower (see ref. [16]) but e most relevant advantage is the possibility to use the calorimetric part as a andalone detector for the highest energy gamma rays (E >10GeV), thus with a ; improvement in geometric factor and efficiency in this particularly statistically or region of the spectrum.

So here we present the results on the angular and energetic resolution of e lead-scintillating fiber calorimeter alone.

Simulation

ie simulation for the proposed imaging calorimeter is based on the CERN GEANT) code.

ie simulated geometry is shown in fig. 1 and presented in the following table:

volume	subvolume	dimensions
calorimeter	20 planes	$25\times25\times15cm^3$
plane	5 scintillating fibers layers interleaved with 5 lead layers	$25\times25\times0.75cm^3$
scintillating fiber layer	50 strips	$25\times25\times0.1cm^3$
lead layer		$25\times25\times0.05cm^3$
scintillating fiber strip		$0.5\times25\times0.1cm^3$

ie information read in each strip in a layer is summed with the information ob- ined by the four corresponding strips in the other layers of the same plane, resulting a total of 50 strips per plane. Subsequent planes have opposite ortogonal orien- tion for set of strips giving an X and Y information, for a total of 10 X and 10 Y

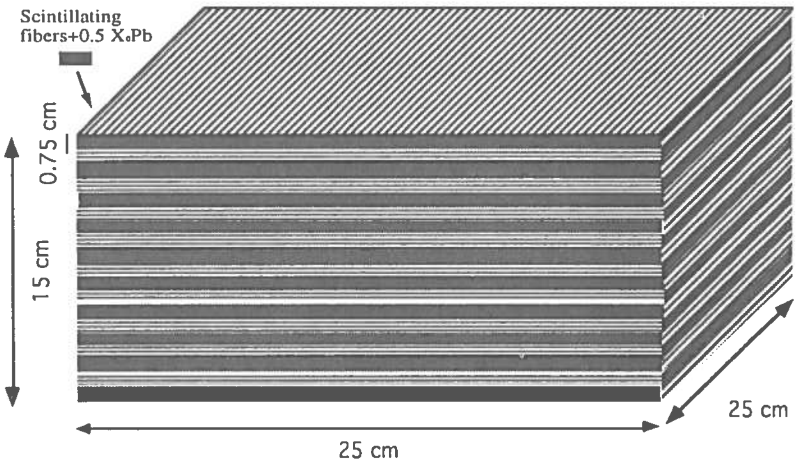

Figure 1: *The stratigraphy of lead scintillating fiber calorimeter.*

planes.
The total ammount of material corresponds to 10 radiation lenghts.

3.1 Angular reconstruction

Several thousands of photons have been simulated at three different energies: 10, 20 and 50 GeV and different orientations.
The azimuth (ϕ) and zenith (θ) angles of the incoming photons have been reconstructed through the logitudinal and trasversal sampling of the induced electromagnetic shower in the calorimeter. In fact, being the secondaries produced in an electromagnetic shower more than 100, for photons with energies greater than 1 GeV, their distribution is almost symmetric around the direction of the primary photon. This permits to assume that the direction of the incoming photon is the same of the axis of the induced shower.
For the determination of the direction we have adopted a two steps algorithm. In the first step a guess of the direction has been obtained with a straight line fit of the centers of gravity (x_c) of the detected energy in each plane for the two views:

$$x_c = \frac{\sum_{i=1}^{50} x_i \, E_i}{\sum_{i=1}^{50} E_i} \tag{1}$$

where x_i is the position of the center and E_i the energy detected of the ith strip. We have restricted the used calorimeter region to an area of $4\times4\text{cm}^2$ in the X and Y directions along the first guess fitted shower axis. Then we have performed another straight line fit of these restricted centers of gravity obtaining the final values for

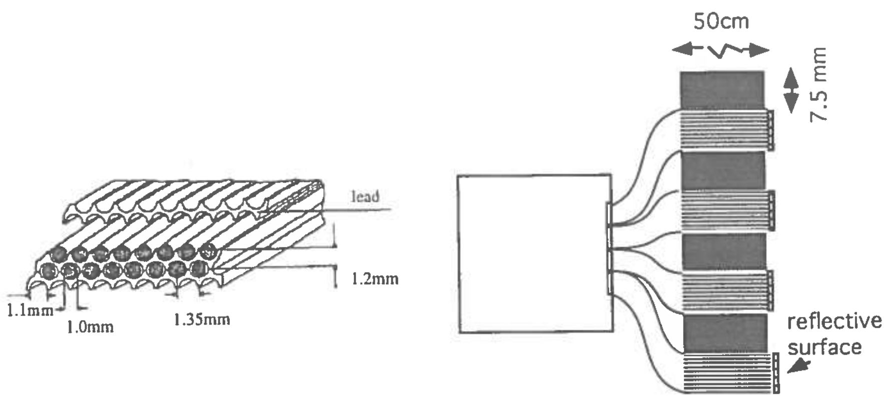

igure 2: *Structure of the lead scintillating fibers (left) and of the lateral view of the ɔnnection between the fibers and the phototube.*

ıe projected axis on the XZ and YZ plane.
'he resulting direction angles have been compared with the direction angles of the .mulated photons. The results are presented in table 1.

.2 Energy resolution

'he energy resolution is limited by the point where the incoming photon converts. : this happens in the last layers only a small fraction of the energy of the induced hower is cointained in the calorimeter, giving a worse resolution of the energy. n figure 3 is shown the total energy detected in the calorimeter for photons of 50 ;eV*. It can be noticed the long tail for low energy deposition due to the late photon onversion.
'his has led us to define the energy of the primary photon through the energy .etected in the plane of maximum. In figure 4 the energy detected in the plane of ıaximum for photons of 50 GeV.
'rom this distribution the mean detected energy and its resolution can be obtained. n table 2 is shown the results for the three simultated energies.

These results are worse than that obtained in ref. 11) because here we ccepted all the events (i.e. we have efficiency 100%). The study of new algorithms, hat use the tracking capability of the detector to improve the energy resolution vithout loss of efficiency are in progress.

*The results presented in this section have been obtained with simulated photons of incoming lirection: $\theta = 10^o$ and $\phi = 0^o$

Table 1: Direction reconstruction and its resolution

Energy [GeV]	Simulated angles [Deg]	Reconstructed angles [Deg]	Resolution [Deg]	Projected σ [Deg]
10	$\theta_S = 10$ $\phi_S = 0$	$\theta_R = 9.83$ $\phi_R = 0.2$	$\sigma_\theta = 0.85$ $\sigma_\phi = 5.6$	$\sigma_x = 0.84$ $\sigma_y = 0.97$
10	$\theta_S = 10$ $\phi_S = 45$	$\theta_R = 9.91$ $\phi_R = 45.4$	$\sigma_\theta = 0.91$ $\sigma_\phi = 5.0$	$\sigma_x = 0.84$ $\sigma_y = 0.88$
10	$\theta_S = 20$ $\phi_S = 45$	$\theta_R = 19.68$ $\phi_R = 44.94$	$\sigma_\theta = 0.83$ $\sigma_\phi = 2.6$	$\sigma_x = 0.85$ $\sigma_y = 0.90$
20	$\theta_S = 10$ $\phi_S = 0$	$\theta_R = 9.78$ $\phi_R = 0.6$	$\sigma_\theta = 0.73$ $\sigma_\phi = 4.2$	$\sigma_x = 0.65$ $\sigma_y = 0.72$
20	$\theta_S = 10$ $\phi_S = 45$	$\theta_R = 9.88$ $\phi_R = 45.8$	$\sigma_\theta = 0.79$ $\sigma_\phi = 3.7$	$\sigma_x = 0.60$ $\sigma_y = 0.66$
20	$\theta_S = 20$ $\phi_S = 0$	$\theta_R = 20.19$ $\phi_R = 0.24$	$\sigma_\theta = 0.24$ $\sigma_\phi = 2.04$	$\sigma_x = 0.60$ $\sigma_y = 0.72$
20	$\theta_S = 20$ $\phi_S = 45$	$\theta_R = 19.71$ $\phi_R = 44.87$	$\sigma_\theta = 0.74$ $\sigma_\phi = 2.2$	$\sigma_x = 0.75$ $\sigma_y = 0.68$
50	$\theta_S = 10$ $\phi_S = 0$	$\theta_R = 9.65$ $\phi_R = 0.2$	$\sigma_\theta = 0.44$ $\sigma_\phi = 5.6$	$\sigma_x = 0.45$ $\sigma_y = 0.60$
50	$\theta_S = 10$ $\phi_S = 45$	$\theta_R = 9.87$ $\phi_R = 46.1$	$\sigma_\theta = 0.56$ $\sigma_\phi = 2.8$	$\sigma_x = 0.50$ $\sigma_y = 0.49$
50	$\theta_S = 20$ $\phi_S = 0$	$\theta_R = 20.18$ $\phi_R = 0.18$	$\sigma_\theta = 0.39$ $\sigma_\phi = 1.8$	$\sigma_x = 0.50$ $\sigma_y = 0.60$
50	$\theta_S = 20$ $\phi_S = 45$	$\theta_R = 19.75$ $\phi_R = 44.88$	$\sigma_\theta = 0.56$ $\sigma_\phi = 1.8$	$\sigma_x = 0.56$ $\sigma_y = 0.55$

Table 2: Energy resolution

Energy [GeV]	Detected energy in the plane of maximum [GeV]	σ(E) [GeV]	Resolution [%]
10	0.194	0.029	14.9
20	0.357	0.045	12.6
50	0.811	0.099	12.2

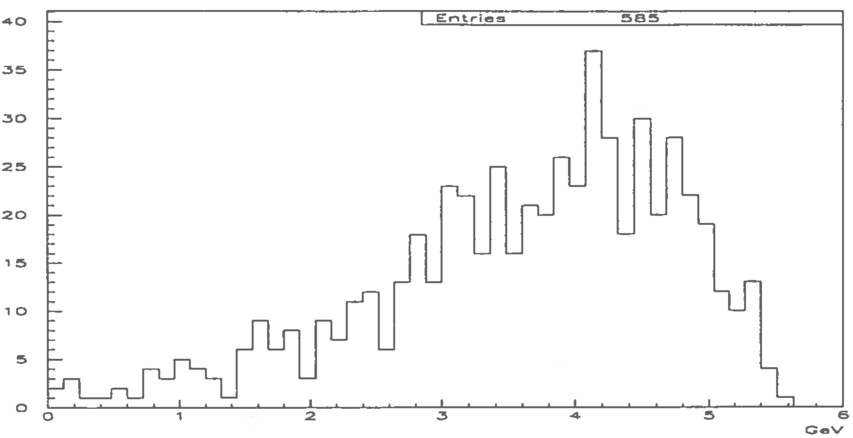

igure 1: Simulated distibution of the total detected energy in the calorimeter for) GeV primary photon.

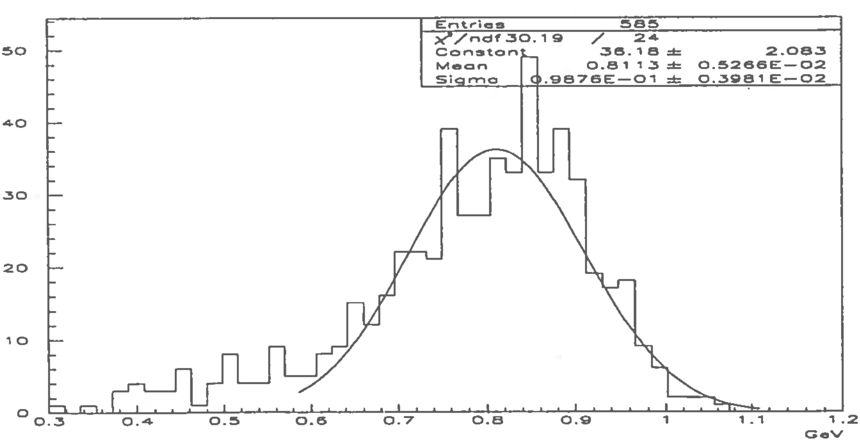

igure 2: Simulated distibution of the detected energy in the plane of maximum for) GeV primary photon.

References

1. G. Kanbach et al.,*Space Science Review*, **49**, 69,(1988).
   Fichtel C. et al., *Ap.J Supplement*, **94**, 551,(1994).

2. M. Srednicki et al., *Phys.Rev.Lett.*, **56**, 236, (1986).

3. A. Morselli, *The dark side of the Universe*, Editors: R.Bernabei & C.Tao, World Scientific Co.,127, (1984).

4. V.S. Berezinsky, *Phys. Lett. B*, **261**, 71, (1991).

5. J. Silk, M. Srednicki, *Phys. Rev.Lett.* **53**, 624, (1984).

6. L. Bergstrom, H. Snelleman, *Phys.Rev.*, **37D**, 3737, (1988).

7. M. Punch et al. , *Nature*, **358**, 477, (1992).

8. F.W. Steker, O. C. De Jager & M. H. Salamon, *Ap.J*, **L49**, 390, (1992).

9. A. Morselli, Proceedings of the "*International Symposium on cosmic ray physics in Tibet*", August 12-17, Lhasa, China, 324, (1994).

10. W.Atwood et al. NIM, **A342**, 302, (1994)

11. G. Barbiellini et al., *NIM*,**A354**,547, (1995).

12. G. Barbiellini et al., *Nuclear Physics*,**B 43**,253, (1995).

13. G. Barbiellini et al., XXIV ICRC, OG 10.3.11, v.3, 607, Roma,1995
    O.Adriani et al., XXIV ICRC, OG 10.3.7, v.3, 591, Roma,1995
    A.Morselli et al., XXIV ICRC, OG 10.3.26, v.3, 669, Roma,1995

14. R.Brun et al., "GEANT User's Guide", CERN-DD-EE **81-1** (1991).

15. The Kloe Detector Technical Proposal, LNF-93-002,(1993).

16. G. Barbiellini, et al., A&A , 309 , L15 (1996)
    Roma,1995 Roma,1995 Roma,1995

'ascati Physics Series Vol. VI, (pp. 553–560)
I Int. Conf. on Calorimetry in HEP – Frascati, June 8–14, 1996

A NEW TECHNIQUE FOR DETERMINING CHARGE AND MOMENTUM OF ELECTRONS AND POSITRONS USING CALORIMETRY AND SILICON TRACKING

Q. Fan and A. Bodek
Department of Physics and Astronomy, University of Rochester, Rochester, NY 14627

ABSTRACT

e describe the application of a new method for the determination of charge and ack parameters for electrons and positrons in both central (pseudo-rapidity [1]) $< |\eta| < 1.2$) and forward (pseudo-rapidity $1.2 < |\eta| < 2.3$) regions at CDF. ıe method uses the shower centroid position in the calorimeter in combination th a track in the inner silicon vertex detector. The use of the central tracking amber is not required. A comparison of the shower centroid in the calorimeter, th the extrapolated silicon vertex detector track determines the electron sign. This chnique has been used to measure the W asymmetry in CDF in regions beyond e pseudo-rapidity coverage of the central tracking chamber. Application to other ıysics analyses in current collider experiments at the Tevatron and in future high minosity experiments at the LHC are discussed.

Introduction

harge and momentum of electrons and positrons are typically measured inside a ntral tracking device in a magnetic field. This is particularly the case in most rge detector systems in colliding beam experiments. In the CDF experiment, r example, the central tracking chamber (CTC) plays an essential role in charge ıd momentum measurement of electrons. Figure 1 shows a cutaway view of CDF etector. In the central region, the CTC track momentum resolution is dP_T/p_T^2 0.001 $(GeV/c)^{-1}$, when the beam position constraint is included in the fit. The ıarge is determined from the bend direction of the the track.

While excellent momentum measurement is achieved in the central region, ıe CTC tracking in the forward/backward regions is compromised because the

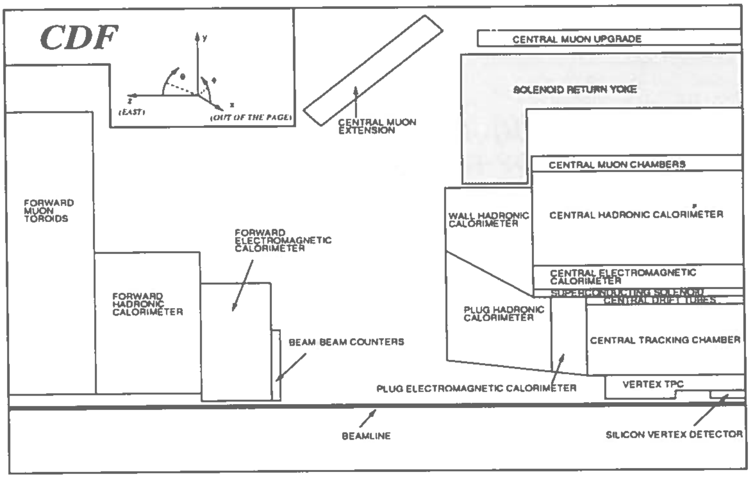

Figure 1: A cut away view of the CDF detector. Forward tracks($|\eta| > 1.1$) do not traverse the full tracking region of the CTC.

tracks traverse only a few CTC layers. The situation becomes worse at high instantaneous luminosity as the inner tracking layers suffer from higher occupancy due to increased number of soft tracks curling along the beam direction. Therefore, the central tracking chamber becomes inefficient for forward/backward electrons. Figure 2 shows that the CTC track finding efficiency falls as a function of pseudo-rapidity $|\eta|$, and is zero at $|\eta| = 1.8$.

Many physics analyses require a charge determination of electrons and positrons. In the W lepton charge asymmetry measurement [2], about half of the overall sensitivity is in the forward/backward regions. Similarly, in the dilepton analyses, e.g. Drell-Yan and Z forward-backward asymmetry, the determination of the sign of each lepton is required. The dilepton signal events are opposite sign, and the backgrounds from QCD jets are determined from the rate of same sign events. The top analysis can be also extended to forward region if a forward electron charge information becomes available for use in reducing backgrounds. Even in the central region where the CTC already provides charge determination, an independent way of determining the charge of electrons can serve as a check of central tracking efficiency at high luminosity. This will be even more important at the Large Hadron Collider (LHC) where even central tracking will be difficult at high luminosity. Therefore, an additional method for charge determination both in the central and forward direction is needed.

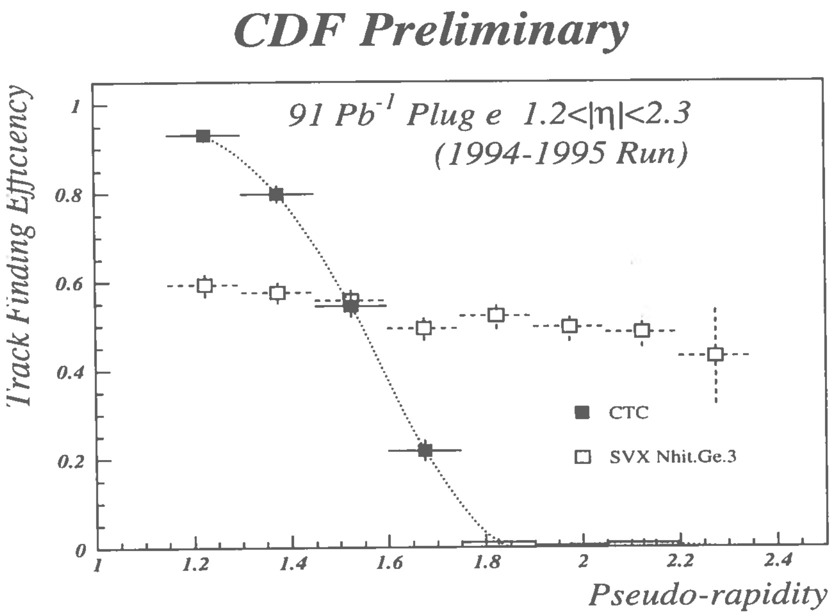

Figure 2: The track-finding efficiencies as a function of pseudo-rapidity.

The Technique

t CDF, positively (negatively) charged particles bend toward increasing (decreas-g) ϕ. The track ϕ direction can be measured near the primary vertex using sili-ɔn tracking (SVX), and at the Electromagnetic (EM) shower maximum using the ıower centroid position measurement of EM detectors. By comparing two mea-ırements, the charge of the track is determined.

A Detailed description of the CDF detector can be found elsewhere [3]. tarting at the collision points, the detector's tracking components are the Inner ilicon Vertex detector (SVX), the Vertex Tracking Chamber (VTX), and the Cen-ˑal Tracking Chamber (CTC). The Central and Plug Electromagnetic Calorimeters ᑐEM, PEM) yield both energy and also a measurement of the shower centroid osition . The SVX is a four layer, single sided device from $r \approx 3cm$ to $\approx 8cm$, ith $\approx 10\mu m$ position resolution in the $r - \phi$ plane. Inside the CEM, the EM ıower centroid is measured using strip chamber placed near the shower maximum t $r \approx 184cm$. The position measurement in the PEM is done using both the strip etector at shower maximum, and the calorimeter tower information (needed for $\eta| > 1.8$ where there is no strip coverage).

3 SVX Tracking

The track ϕ direction at SVX is measured by a standalone trackfinding using only SVX hits. A ϕ road to search for track stubs with SVX hits is defined from the electron cluster, and the collision point. The precise position resolution of the SVX device ensures low background arising from wrong combinations of hits. At least three hits are required for a stub. As shown in Figure 2, the SVX track finding efficiency in the plug region is relatively flat in contrast to the quickly falling CTC efficiency. The $\approx 60\%$ level results from the fact that SVX device is 50 cm long in z while the primary interaction has a rms $\sigma \approx 30cm$ spread in z direction. A ϕ resolution of $\approx 0.3mrad$ can be achieved from the SVX track stub. This corresponds to $\approx 550\mu m$ in position uncertainty when extrapolated to the shower maximum at the CEM, and between $120\mu m$ ($|\eta| = 2.3$) and $400\mu m$ ($|\eta| = 1.2$) at the location of the shower maximum inside the PEM. These uncertainties are small compared to the position resolution of the CEM and PEM shower centroid measurements which are described below.

4 EM Shower Centroid Measurement

The second measurement of the track direction ϕ comes from the EM shower centroid measurement. The detailed structure of the CEM is described elsewhere [4]. In the central region, the shower centroid is determined from the central strip chamber at the shower maximum. A strip cluster corresponding to each electron is formed and shower centroid is calculated from a fit using shower shape data from test beam measurements.

In the forward region, the position measurement is made using a combination of a strip detector at the shower maximum for $|\eta| < 1.8$ where it is available, and in addition the calorimeter pad information at the larger rapidities. The PEM detector is described in detail elsewhere [5]. It consists of two 2.8 m diameter and 50 cm deep round disc-shaped lead sampling calorimeters. Each is constructed using resistive plastic gas proportional tube arrays sandwiched with lead absorber panels. These are finely segmented into projective tower geometry using cathode readout based on pads and strips etched on printed circuit board in the chambers, with a precise positioning of strips and pads to $0.1mm$. The chamber high voltage is controlled from feedback of gas pressure and temperature. The gas gain is monitored by proportional tubes mounted with Fe^{55}. The gain variation is controlled to within 1% . The energy resolution (pad) is 2.8% for 100 GeV electrons. Figure 3 shows a PEM quadrant. Strips segments are 1 degree in ϕ covering $1.2 < |\eta| < 1.8$, and pads have a 5 degree segmentation. Table 1 lists the physical dimensions of the

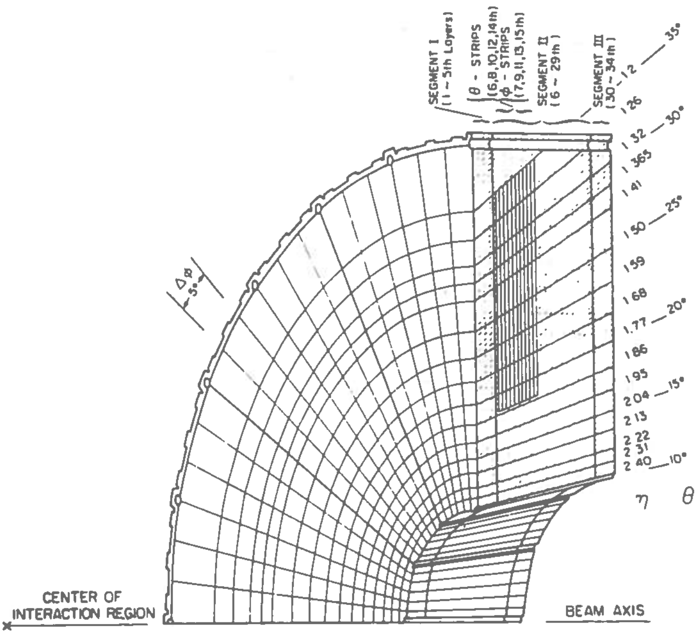

gure 3: View of a PEM quadrant. Pads are segmented in 5 degree unit in ϕ and ips in 1 degree unit covering $1.2 < |\eta| < 1.8$.

EM detector.

The transverse shape of EM showers are very stable at high energies ($E >$ GeV). Therefore, the fit function for the CEM electromagnetic shower shape from st beam can be tunned to match the data. In the plug strip case, we use similar ıstering and fitting method as for the CEM strips to extract the shower transverse ›sition. For electron clusters with $|\eta| > 1.8$, a 5x5 energy cluster is formed with the ggest energy tower in the center. To determine the ϕ position, energy is summed in blocks. The expected energy fraction for each η block is calculated and normalized the total measured energy. In the fit, the center tower energy fraction is not used

ıble 1: Summary of PEM position resolution. For electrons with $|\eta| > 1.8$, $1mm$ ›sition resolution is achieved using $4.7cm$ wide towers (bend is at mean Pt of 40 eV).

	η Range	Segmentation in ϕ	Bend	σ_{pos}
Strips	1.2-1.8	2.2-1.1 cm (1.7 cm)	0.51 cm	0.15 cm
Pads	1.8-2.3	5.6-3.4 cm (4.7 cm)	0.16 cm	0.10 cm

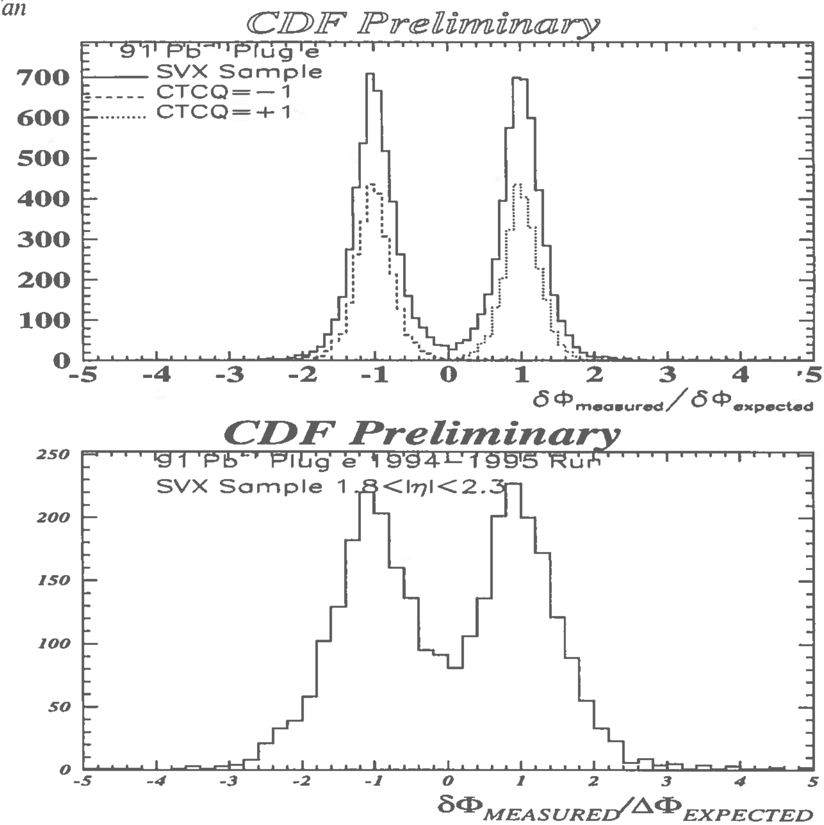

Figure 4: $\delta\phi_{measured}/\delta\phi_{expected}$ for a sample of electrons. The top and bottom plots show electrons from low η bin ($1.2 < |\eta| < 1.8$) and high η bin ($1.8 < |\eta| < 2.3$), respectively.

since it does not contain position information. For electrons with $|\eta| > 1.8$, $1mm$ position resolution is achieved using $4.7cm$ wide towers.

We differntiate between positively and negatively charged tracks by comparing the extrapolated SVX track position at EM shower maximum and the position measured by the EM calorimeter. The bending is a function of track transverse momentum P_T and the radii at shower maximum. For electrons from W decays with average $P_T = 40GeV/c$, the bending is on average $20mm, 5mm$, and $1.6mm$ for the $|\eta| < 1.2$, $1.2 < |\eta| < 1.8$, and $|\eta| > 1.8$ regions, respectively.

We take the ratio of $\delta\phi_{measured}/\delta\phi_{expected}$ where $\delta\phi$ is defined as $\phi_{PEM} - \phi_{SVX}$. The $\delta\phi_{expected}$ can be calculated using the calorimeter E_T and the radial distance that the electron travels inside magnetic field. For electrons and positrons, the average ratio peaks at -1 and $+1$ separately. Figure 4 shows the $\delta\phi_{measured}/\delta\phi_{expected}$ distribution as measured from an electron sample.

The charge misidentification rates are 0.40% and 5.0% for low and high η electrons, respectively.

Alignment of the EM Calorimeters

e alignment of the EM calorimeters is important for the shower position mea- ement. Although the internal alignment of each quadrant is controlled to within mm, the positioning of the EM calorimeters usually have on the order of $\approx 1cm$ chanical allowance in $r - \phi$ plane. Each time the EM calorimeter is pulled out shutdown maintenance and put back in, it ends up in a different $r - \phi$ posi- n. Therefore, in situ position alignment calibration is necessary in order for this hnique to work. The PEM position in $r - \phi$ plane can be described by three rameters: off-centerness in δx and δy directions and a rotation $\delta\phi_o$. The actual $_{r}$ and local ϕ are related in the following formula:

$$\phi_{cor} = \phi - \frac{\delta\ x}{R} sin\phi - \frac{\delta\ y}{R} cos\phi - \delta\phi_o, \tag{1}$$

This technique is self-calibrating in that for each local ϕ bin ϕ_{cor} corre- onds to center position of two peaks (e.g. Figure 4) and is easily determined. A mple of electrons and positrons are employed for the calibration. Figure 5 shows $_{cor} - \phi)$ as a function of ϕ for west and east PEM separately. The dashed lines e fits to the data. Using this alignment technique, the position of calorimeters is own to better than $0.5mm$.

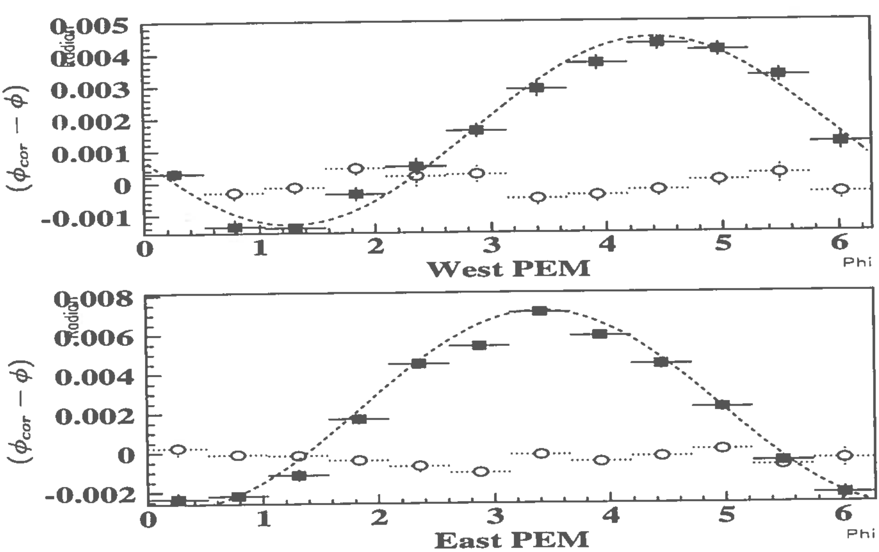

gure 5: $(\phi_{cor} - \phi)$ as a function of ϕ for west and east PEM separately. Data ints in open circles are after alignment corrections.

6 Conclusion and Outlook

We have described a new technique for charge determination of electrons in both the central and forward regions. This technique has enabled CDF to determine the charge for electrons in regions up to $|\eta| = 2.3$. As a result, the W lepton charge asymmetry measurement has been extended to high electron rapidity.

In principle a silicon vertex detector in conjunction with an electromagnetic calorimeter with good transverse segmentation can be used to do all of physics with electrons and positrons without the need for any additional tracking information either in the central or in the forward direction. This may be used at the LHC where the luminosity is high, and the central tracker is expected to have a very large number of tracks. Note that if the electromagnetic calorimeter has good transverse segmentation, the energy, η and ϕ of electrons and positrons are already well determined from the calorimetry information alone. In this technique, the silicon tracking is used only for the sign. Therefore, this use of technique should be kept in mind for future experiments, when the design of both silicon tracking and the EM calorimeters are done.

References

1. The pseudo-rapidity is defined as $\eta = -ln(tan\frac{1}{2}\theta)$, where at CDF, θ is defined as the polar angle measured from proton beam direction.
2. F. Abe *et al.*, Phys. Rev. Lett. **74** (1995) 850
3. F. Abe *et al.*, NIM A271(1988) 387-403
4. S. Bertolucci *et al.*, NIM A267(1988) 301-314
5. Y. Fukui *et al.*, NIM A267(1988) 280-300

;cati Physics Series Vol. VI, (pp. 561–570)
:NT. CONF. ON CALORIMETRY IN HEP – Frascati, June 8–14, 1996

STUDY OF RADIATIVE MUON INTERACTIONS AT 300 GEV

M. Antonelli, G. Battistoni, A. Ferrari, P.R. Sala
I.N.F.N. sezione di Milano, via Celoria 16, 20133 Milano, Italy

ABSTRACT

diative energy losses of 300 GeV muons in the prototype calorimeters (Liquid gon, e.m., and Fe+Scintillator tiles, hadronic) of the ATLAS collaboration for :C have been measured in a dedicated run. These results allow to check the sting theoretical predictions, which still have some uncertainties. The spectrum of eased energy has been measured up to the end-point, and it is has been compared detailed Monte Carlo calculations.

Introduction

From the point of view of the e.m. interactions, muons can be considered ;t as heavy electrons. Therefore they undergo all the same processes as electrons, :luding bremsstrahlung and pair production. Excellent reviews of muon e.m. in- 'actions are given in refs. [3], [4], [8]. However, it must be pointed out that while ; radiative processes by electrons and positrons are by now well understood and ecked against the QED predictions, a few uncertainties still exist for muons. The iin reasons stem both from theoretical aspects (as summarized later in this pa- r) and experimental problems: in fact one has to consider that these interactions ıst be studied with high energy muons, and a large statistics is needed. In the erature a few works can be found where high energy cosmic muon events have en analysed [1, 5], and, to our knowledge, only one [6] with a monochromatic 0 GeV beam. These analyses are appreciable, but suffer from lack of statistics in e crucial region of the radiated energy spectrum, and in the case of cosmic rays ıdies, also from the uncertainties on the knowledge of local energy spectrum. A

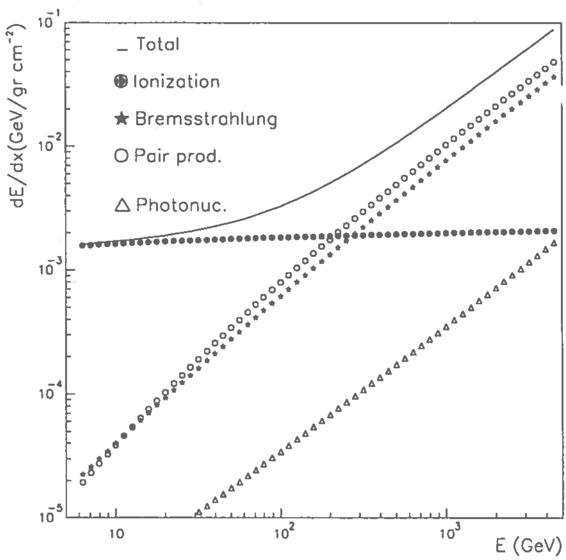

Figure 1: Total and partial energy losses for muons in lead as a function of muon energy

more precise investigation of these phenomena, using data taken in well controlled conditions, is therefore necessary, not only because it is interesting in itself, but also because of some specific experimental needs. For instance, a precise knowledge of these phenomena will allow a more reliable calculation of the survival probabilities of multi-TeV muons for large depths of soil, rock or water, and this can be essential for some non-accelerator experiments [7]. Another important example is the analysis of the systematics in muon detection at the future hadron colliders.

2 Muon Interactions

Beyond atomic ionization (including δ-ray production) and excitation processes, the most important processes that muons undergo are: bremsstrahlung, e^+e^- pair production and photo-nuclear interactions . The relative importance of these processes depends both on the target material, and on muon energy. As shown in fig1 for Lead, radiative processes start to dominate the muon $\frac{dE}{dx}$ when the muon energy exceeds a few hundred GeV. Their contribution, however, is made up by relatively rare events with significant fractional energy losses (we define, as usual, the fractional energy

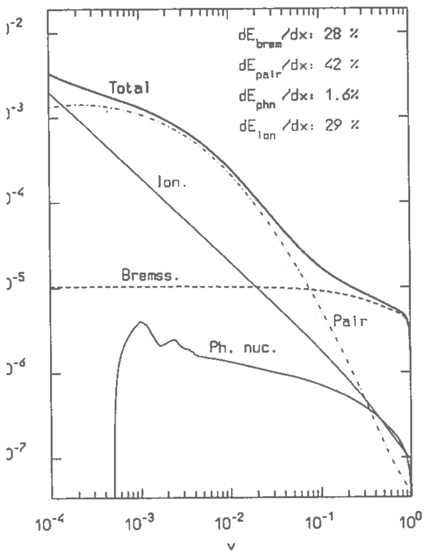

gure 2: Differential cross sections as a nction of v for the radiative processes 300 GeV muons in lead.

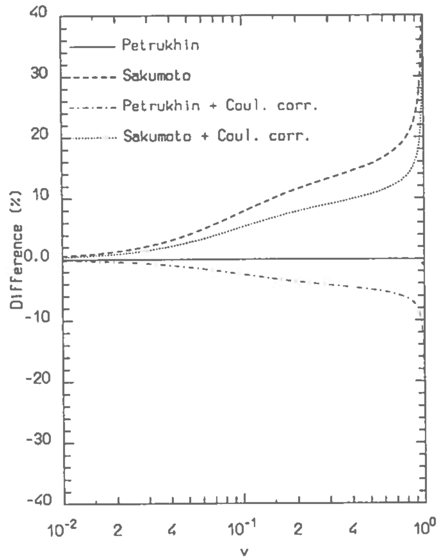

Figure 3: Energy loss difference for 300 GeV muons in lead using refs. [1] and [2] for bremsstrahlung.

ss as $v = \frac{\Delta E_\mu}{E_\mu}$), as shown in fig.2 for 300 GeV muons in Lead. Bremsstrahlung ominates the hardest part of the energy loss spectrum, while pair production the termediate part.

Most of present calculations concerning muon transport are based on the oss sections reviewed in ref. [8]; there, the formulation of A.A.Petrukhin and .V.Shestakov [2] for muon bremsstrahlung is considered. However, as already ointed out in [9, 10], a few uncertainties still exist, concerning mainly the treatent of nuclear screening, Coulomb and radiative corrections in the cross secon [9, 10, 3, 4, 11, 2, 1]. The difference in the total differential cross section as a function of v, for 300 GeV muons in lead is presented in fig. 3, assuming vo different formulations for muon bremsstrahlung: the one of Petrukhin et al. [2] nd the one of Sakumoto et al. [1].

Experimental set-up

n september 1994 the first combined test of the ATLAS hadronic and electroagnetic prototype calorimeters has been performed. The electromagnetic (e.m.) alorimeter was the Lead-Liquid Argon "2 metres" prototype built by the RD3 ollaboration [12]. It has an accordion geometry, with a $\Delta\phi \approx 0.02$, $\Delta\eta \approx 0.018$

granularity, and it is fully pointing. The total thickness is $25X_0$ at $\eta = 0$, subdivided into three longitudinal samplings. The resolution measured with electron beams is $\frac{\sigma(E)}{E} = \frac{10\%}{\sqrt{E}} \oplus 0.5\%$ plus a noise term. In this test beam it was preceeded by a separate preshower detector, also using LAr as active material [12].The need for a good coupling with the hadronic calorimeter compelled to shift the e.m. one toward the back of its cryostat, in a position that spoiled its pointing properties. Behind the e.m. calorimeter the prototype of the Tile [13] hadronic (HAD) calorimeter was placed. This is a Iron-scintillator calorimeter, with an Fe:Sci ratio around five in volume. Its total thickness is 180 cm (about 9 λ_i) and it is read-out in 4 longitudinal sections. The Tile calorimeter was followed by a "muon wall", consisting of an array of scintillator detectors. A special beam setup was prepared to obtain a 300 GeV muon beam with almost no pion contamination and a calculated momentum spread smaller than 1% [14]. The beam was impinging on the e.m. calorimeter at about 11°, and the beam spot was confined in a 3×3 cm square by a couple of scintillation detectors acting as a trigger. A total of about 700000 events have been recorded.

4 Simulations

The simulations have been performed with the standalone FLUKA code [15]. This choice has been validated by extensive comparisons with other codes about high energy muon propagation [16], and by the good agreement between simulations and test beam results on electron and pions. It is possible to choose the prescription for the effect of the nuclear form factor in muon bremsstrahlung among those of ref. [4, 1, 2], and the Coulomb correction can be optionally considered, as suggested by Tsai [3]. The treatment of photo-nuclear interactions basically follows ref. [17], with the cross section integrated down to the lowest possible q^2 values, including the existing resonances in the γN cross section. Pair-production is sampled according to the double differential cross section of ref. [18]. In the bremsstrahlung treatment, the screening factor of [2] without Coulomb correction has been chosen, since it is the most widely used formulation.

The setup and detector geometries have been modelled in great detail. The MonteCarlo calibration factors for the two detectors have been determined simulating the response to monoenergetic electrons. No other normalization factor has been applied to the simulated data. About $7 \cdot 10^5$ 300 GeV muons have been simulated. The effects of random noise and photostatistics [19] have been convoluted with MC data, while charge collection in the accordion and quenching in the scintillator have been implemented directly in the simulations.

Data analysis and comparison with simulations

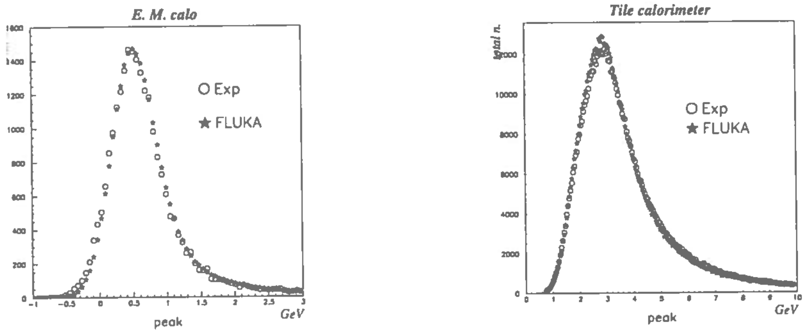

igure 4: Absolute comparison between calculated and experimental ionization eaks in the electromagnetic(left) and hadronic (right) prototypes

xperimental and MonteCarlo data have been analysed following the same algothms and applying the same cuts. Up to now, the two calorimeters have been onsidered separately, mainly because of some uncertainty in the amount of dead iaterial in between the two and of the still existing difficulties in the electromagnetic ata reduction.

The calibration issue is perhaps the most critical one in these comparisons. ny normalization factor based on the average muon energy loss or on the v specral shape would be equivalent to assuming a perfect theoretical description of the adiative processes, that is exactly what we are investigating. The endpoint is not harp enough, due to the scarcity of events, to provide a calibration. A calibration f both data and MonteCarlo on the ionization peak position would be possible, ut this would prevent any verification of the correctness of the simulations, or t least of their capability to reproduce the experimental $\frac{e}{\mu}$ ratio. Moreover, the ampling fraction for muon energy losses decreases with v, since at large v most f the energy is deposited through electromagnetic cascades indistinguishable from lectron-initiated ones, while at low v's ionization energy losses are more effectively ampled, resulting in a $\frac{\mu}{e}$ ratio larger than one. This is properly taken into account n the MonteCarlo simulation, while it is neglected in analytical calculations such s those performed in [20]. The approach followed in this work is the only self conistent one, that is an independent calibration with electrons, both of experimental nd calculated data. The e.m. calibration is well known from many beam tests [12], nd for the Tile calorimeter we used the electron calibration factor quoted in [19] : .59 pC/GeV.

As a validation of the simulations the computed and measured ionization peaks, for which no theoretical uncertainties should exist, are compared in fig. 4 (see later for details). It is worthwhile to stress that the electromagnetic energy scale has been used both for MonteCarlo and data, with no mutual normalization. The perfect agreement on the position and shape of the peak proves that the $\frac{e}{\mu}$ ratio is correctly reproduced by the simulations.

5.1 LAr calorimeter

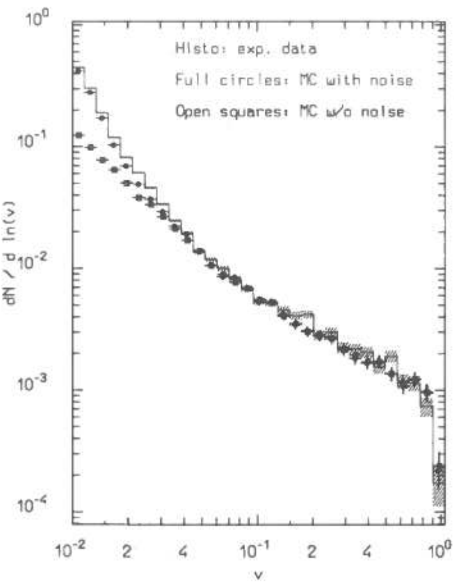

Figure 5: *300 GeV muon energy loss spectrum per incident muon in the ATLAS e.m. calorimeter prototype*

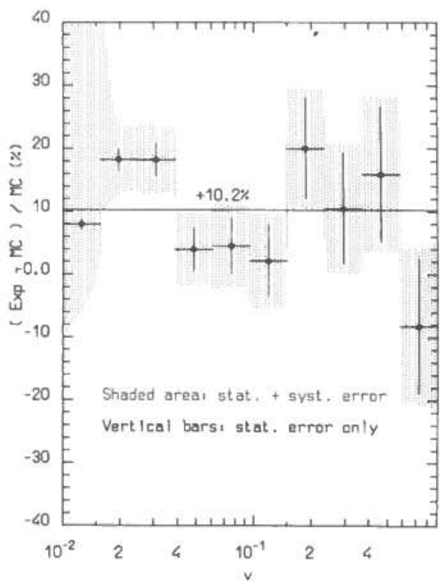

Figure 6: *Percentage difference between exp. and simulated spectra, including systematic errors.*

Due to the non optimal combined test geometry, the accordion calorimeter was hit by the beam at a non-pointing angle, i.e. 11 degree on a cell where the pointing angle is around 24 degrees. Therefore the standard clustering algorithms for electrons and muons cannot be used. An event-dependent clustering algorithm is under development: the goal is to keep the noise level as low as possible by using the minimal number of cells. The muon track position is reconstructed a priori using the beam chamber informations. The major problem we are currently facing is the presence of coherent noise, whose level and rms are not stable with time, that is hardly reproducible in the simulations. This work is still in progress, nevertheless we ɔw in fig. 4 a comparison between the MonteCarlo and experimental ionization ak in a 3×3 cluster. Only a selected (from the noise point of view) set of ta files has been used. As already said, the comparison is absolute, without any ıle normalization, and shows that the MonteCarlo reproduction of the calorimeter ucture and response is very good.

The presented radiative energy loss analysis is still a preliminary one (see o [21]), performed keeping a large, fixed window (almost 11×11 cells , bringing a noise of 1.4 GeV rms). An upper limit to the energy detected in the hadronic lorimeter was set to discriminate events with showers not fully contained in the n. calorimeter. The comparison between exp. and simulated energy loss spectra shown in fig. 5 for $v > 0.01$, before and after the convolution with noise in the nulated results. All spectra are normalized to one incident muon. The strong fluence of the noise on the soft part of the spectrum and the overall agreement MonteCarlo with data are evident. The agreement is not complete, however. fig. 6 the percentage difference between the two spectra is shown as a function v. The average difference is around 10.2%, with more energetic events in the perimental data. The main error sources are the systematic ones, which were ntatively estimated in a conservative way with a toy model. The shaded systematic us statistic errors area in fig. 6 is obtained by allowing a $\pm 1\%$ error on energy scale, ± 50 MeV error on pedestal subtraction, and ± 50 MeV on the noise rms.

2 Tile Calorimeter

wo cuts have been used to select clean primary muons: a first one on the energy deɔsited in the e.m. calorimeter, to discard muons that have already undergone hard ıergy losses, a second on the energy deposited in the muon wall, to discriminate gainst pions. The pion contamination of the beam as resulting from the muon wall ıt was very small: around 0.01%. After these cuts 743729 muon events have been ıalysed. Pedestal subtraction has been performed for each run using the random igger events.

An off-line correction has been applied to take into account the positionependence of the tile light yield. The correction has been derived from the experiıental profile, and applied only in the fourth longitudinal sampling, where tiles are ırger. No effect was visible in the other samplings. The value of noise has been exacted from the random trigger distribution, and convoluted with the MonteCarlo esults. Care has been taken in reproducing correctly both the rms (0.56 GeV) and ıe shape of the noise, that was strongly non-gaussian due to the presence of a zeable coherent noise.

The total deposited energy spectrum in the hadronic calorimeter is shown

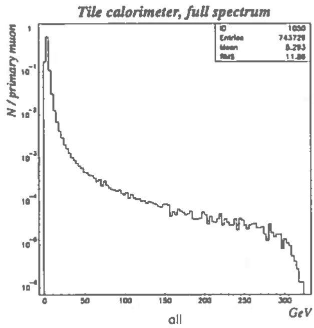

Figure 7: Total experimental spectrum in the Tile calorimeter.

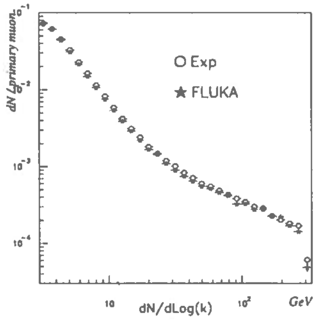

Figure 8: Comparison between calculated and experimental spectra in the tile calorimeter for $v > 0.01$

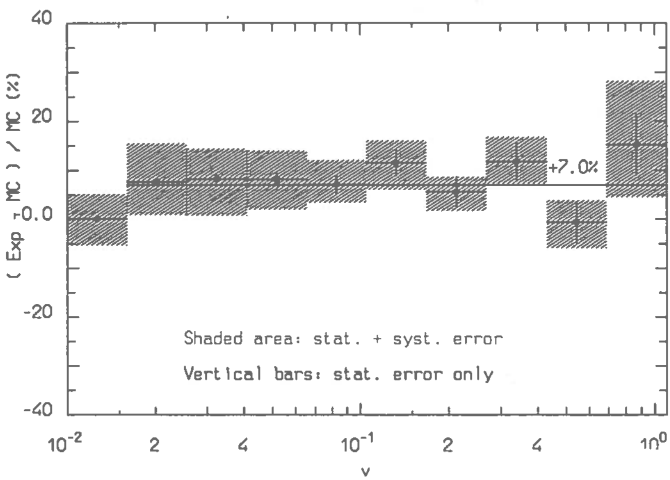

Figure 9: Percentage difference between experimental and MonteCarlo events as a function of v in the Tile calorimeter. Statistical only and statistical + systematic errors are shown.

in fig. 7. The spectra of computed and measured energy losses ($v > 0.01$) are compared in fig. 8, normalized to one primary muon. The overall shape of the spectrum and the position of the endpoint are well reproduced by FLUKA, while a small difference shows up for events above the ionization peak.

Since statistical errors are already small, an effort has been made to investigate possible sources of systematic errors. These include errors on pedestal btraction, noise evaluation, calibration constants, and on the relative effective-ss of the cut on the e.m. calorimeter. Systematic effects have been estimated by rying the aforementioned quantities in the reconstruction of the MonteCarlo data. easonable limits of variation have been chosen:

- An offset of $\pm$ 50 MeV on the pedestal values. Since pedestals are actually evaluated from out-of-burst events, this variation could be overestimated.
- A variation of $\pm 5\%$ in the noise rms. The same considerations of the previous point apply here.
- A variation of $= +4, -1$ GeV around the adopted 6 GeV cut on the e.m. energy, used to remove muons showering in the accordion This accounts for possible mismatches in the exp. and MC e.m. calibrations and noise convolution. The effect is negligible.
- A $\pm 3\%$ variation on the energy scale, as quoted in the Tile calibration [22]. This gives the largest effect, but it should be stressed that a 3% variation on the energy scale would spoil the nice agreement on the ionization peak.

he percentage difference between experimental and MonteCarlo events as a function of v is shown in fig. 9 on a condensed binning. It is consistent with a $7.0 \pm$ $4(stat) \pm 1.62(syst)$ constant difference for $v > 0.015$, that is just beyond the nization peak.

Conclusions

he experimental results show an excess of about 7–10% when compared with standard theoretical assumptions for radiative energy losses, already for $v > 0.015$. In is range both pair production and bremsstrahlung are important. These results ust be taken with care since systematic effects could be comparable to the observed screpancy; work is in progress to further reduce such effects with a more refined ta analysis.

eferences

1. W.K.Sakumoto et al., Phys. Rev. **D45**, 3042 (1992).
2. A.A. Petrukhin and V.V. Shestakov, Can. J. Phys. **46**, 5377 (1968).
3. Y.S. Tsai, Rev. of Mod. Phys. **46**, 815 (1975).
4. I.L.Rozental, Usp. Phys. Nauk, **94**, 91 (1968); Sov. Phys. Uspekhi **11**, 49 (1968).

5. C. Castagnoli et al. Phys. Rev. **D52**, 2673 (1995)

6. R. Baumgart et al., Nucl. Inst. Meth. **A258**,51 (1987)

7. P. Lipari and T. Stanev, Proc. 23rd Int. Conf. on Cosmic Rays, Calgary, **4** 411 (1993) .

8. H. Lohmann, R. Kopp and R. Voss, CERN/85-03 (1985).

9. M.J. Tannenbaum, CERN-PPE/91-134 (1991).

10. Yu.M. Andreev et al., Phys. At. Nucl.,**57**, 2066 (1994).

11. G. Battistoni et al., ATLAS Internal Note CAL-NO-041 (1994)

12. D.M. Gingrich et al. (RD3 collaboration), Nucl. Instr. Meth. **A364**, 290 (1995).

13. F.Ariztizabal et al, Nucl. Instr. Meth **A349**, 384 (1994)

14. K. Elsener, CERN, private communication, April 1994.

15. A. Fassò et al., "An update about FLUKA", Proceedings of the 2nd workshop on "Simulating Accelerator Radiation Environment", SARE-2, CERN-Geneva, October 9–11 1995. Yellow report CERN in press; A. Fassó et al, proceedings of the *Workshop on "Simulating Accelerator Radiation Environment*, Santa Fe, January 1993, A. Palounek ed., Los Alamos LA-12835-C, p. 134 (1994); A. Fassò et al., proceedings of the *IV Int. Conf. on Calorimetry in High Energy Physics*, La Biodola, (Elba), A. Menzione and A. Scribano eds., World Scientific, p. 493 (1994)

16. G. Battistoni et al., MACRO internal note 2/94 (1994)

17. L.B. Bezrukov and E.V. Bugaev, Yad. Phys. **33** (1981)

18. R.P. Kokoulin and A.A. Petrukhin, Proc. of the 12th Int. Conf. on Cosmic Rays, Hobart **6** (1971) A 2436.

19. RD-34 collaboration, ATLAS Internal Note TILECAL-NO-55 (1995)

20. R. Leitner (RD-34 collaboration) ATLAS Internal Note TILECAL-NO-53 (1995)

21. G. Battistoni et al.,Proceedings of the XXIV International Cosmic Ray Conference, August 28-September 8 (1995), Roma, Italy, Vol 1, p. 597.

22. J.A. Budagov et al., ATLAS Internal Note TILECAL-NO-72 (1995)

VII – Radiation Hardness

Convener A. Maio
Secretary S. Giovannella

Maio	Convener's Report
Y. Zhu	Lead Tungstate Radiation Damage and Cure
Y. Zhu	CsI(Tl) Radiation Damage and Quality Improvement
I. Dzhelyadin	Quartz Radiation Damage Study
Tonazzo	Performance of an Artificially Aged Module of the DELPHI HPC Calorimeter
Holm	Radiation Stability of Plastic Scintillators and the Influence on Calorimeter Performance
Dobrzynski	Radiation Hardness of a Shashlik Type Calorimeter
David	Dose Rate Effects in WLS Fibers

scati Physics Series Vol. VI, (pp. 573–576)
INT. CONF. ON CALORIMETRY IN HEP – Frascati, June 8–14, 1996

(Convener's Report)

RADIATION HARDNESS

A. Maio
LIP and FCUL, Av. Elias Garcia 14 1°, 1000 Lisbon, Portugal

Introduction

he most challenge goals for radiation hardness in HEP experiments are the detec-rs requirements for the high luminosity LHC experiments. Dose rates of a few ad/year up to 100 Mrad/year and neutron fluxes up to 10^9n cm^{-2} s^{-1}, depending 1 the η calorimeter region and distance to the beam pipe will be reached. Actual eavy Ions experiments have also very hostile radiation environments but they are ınning already and, temporarily or not, solutions have been found.

In the last Calorimetry Conferences the main topics on radiation hard-ess were focused on plastic scintillators and fibers. In this conference the *"Prima onna"* were the crystals, namely the $PbWO_4$. This session was rather short since most all presentations on calorimeters covered also the radiation hardness of the omponents and the implications on calorimeters performance. I will outline the ıain questions addressed in this session and present some of the relevant answers iven.

Inorganic crystals

bWO_4 crystals are the choice for the high performance electromagnetic calorime-ers of CMS. Crystals suffer from radiation mainly by degradation of its trans-arency. $PbWO_4$ crystals have a short radiation length, one of the reasons why hose crystals were chosen. Radiation hardness of those crystals was studied exten-ively in all aspects and benefits from previous work in other crystals, namely in aF_2, CeF_3, BGO etc. The most relevant aspects of radiation hardness of $PbWO_4$ nd $CsI(Tl)$ crystals were covered by R. Zhu talk. Exemplifications are given for he $PbWO_4$ crystals.

How to identify the causes of degradation of the crystal optical properties?)oes the spectral response change with irradiation? Do they keep their transparency n reasonable limits, up to accumulated doses of 1 Mrad? The author answered ositively to these questions and have shown how the light output, light uniformity spectra and decay kinetics change with dose. The conclusions given are the following: Scintillation mechanism is not damaged, degradation in light output is due to the color center formation. The damage in light response uniformity is small, if initial light attenuation length is long enough. Light output degrades under irradiation and recovers under room temperature.

What happen with the photodetectors? Question very relevant but not covered by this session.

Is it possible that the degradation of the optical properties of crystals recover from the damage produced by radiation? Yes. Applying the same technique foreseen to be used with the BaF_2, i.e. by optical bleaching (see Fig.1 taken from R. Zhu talk)

3 Plastic scintillator plates and fibers

Radiation damage of plastic scintillators and WLS bars and fibers and its influence on calorimeter performance was focused by three speakers.

Systematic studies on irradiated optical components were performed: transmittance and fluorescence measurements, attenuation curves for global light output of the optical chain and for selected wavelengths (U. Holm). Irradiation of polymers produces radicals that absorb fluorescent light. Radicals that are rather stable at room temperatures can react with oxygen forming peroxy radicals which do not absorb and transmission is recovered. A parametrisation based on the phenomenology is given. Although the parameters are not universal, the clear message is that permanent effects can be compared for those experiments done with the same materials, same volume and in the same kind of environment, but "transient" effects can depend on the dose rate. Based on the lab tests a computer code developed to calculate the degradation of the optical components of ZEUS and predict its performance was presented. The systematic monitorization of the calorimeter with ^{60}Co sources confirms those predictions: No degradation up to now of the ZEUS calorimeter.

Comparative tests on different types of WLS fibers were performed and low dose rate effects (from 0.55krad/h up to 1.5 Mrad/h) were investigated (M.David). Radiation effects on scintillators and WLS bars and fibers produced by a mixed field of neutrons and γ's radiation were also compared, and light yield and attenuation length measurements were presented. Typical results are shown in Fig.2 were it can be seen also that doping WLS fibers with the adequate UVA absorber it is possible to optimize the radiation hardness. No (permanent) dose rate effects were observed neither special effects due to the neutron component of the irradiation field.

Neutron vs. γ irradiation effects on SCSN-38 scintillator and WLS Y7 bars spectra were also investigated (Fig.3 from U. Holm talk): different behaviour r scintillators and WLS bars was shown, and dependency on the light wavelength. 'hy?

Finally, concerning calorimeter performance it was also shown (L. Do-

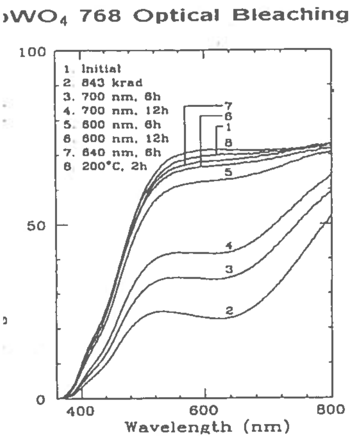

'igure 1: Optical bleaching of irradi-ted $PbWO_4$ crystals (R. Zhu).

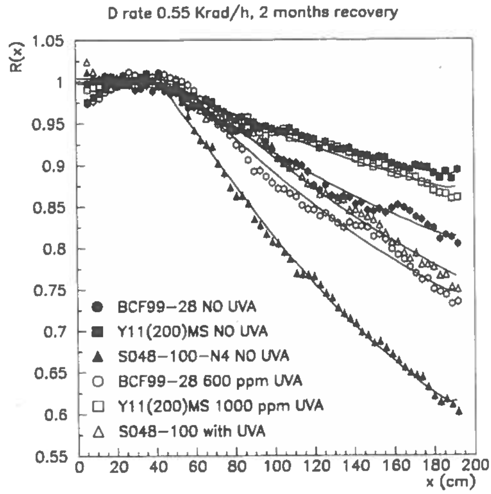

Figure 2: R(x) ratio of light output after uniform γ irradiation (from 50 cm to 200 cm) over light output before irradiation of several WLS fibers. Accumulated dose $\sim$ 140 krad (M. David).

›rezynsky) that the Shaslik type e.m. calorimeters can survive, without appreciable legradation, radiation levels of the order of 4 Mrad.

ł Cherenkov calorimeters and ionization gas chambers

›amples of crystal quartz and fused silica have been irradiated with ^{137}Cs to accumu-ate doses of about 40 Mrad and transmittance measurements have been performed. Crystal quartz does not show any visible change in properties and one of the fused juartz samples loose transparency in ultraviolet region but showed no lost above λ = 400 nm. Similar results were obtained with irradiation in accelerator. The uthor (R. Dzhelyadin) have shown, with tests in a μ beam of irradiated counters, hat inexpensive fused quartz is suitable for LHC-B calorimeter and beam counters.

DELPHI High density Projection Chamber (HPC) was affected by large ıgeing due to the natural α radioactivity of the Pb converter. A. Tonazzo has 'eported on the method to monitorise (with ^{83}Rb source) and compensate from the gain loss, by hardware (tuning the chamber High Voltage) or by software (monthly calibrations). Dedicated test module results prove the reliability of the method and n this way, ageing does not affect the HPC linearity or energy resolution.

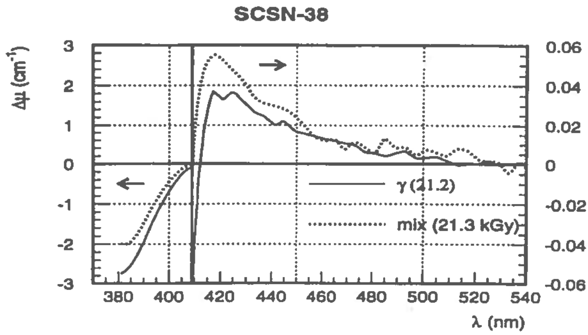

Figure 3: Change with dose of spectral absorption of SCSN38 scintillator irradiated with γ or with mixed $n + \gamma$ (U. Holm).

5 Conclusions

Great progress has been achieved in what concerns characterization, and understanding of the mechanisms that cause degradation of the optical properties of the calorimeter components.

Sometimes curing inorganic crystals from radiation damage seems to be feasible and prediction of the lifetime of plastic scintillating calorimeters works. Quartz (crystal or fused) or quartz fibers calorimeters are rather suitable to be used in high dose rate environments. The identification of criteria and materials for the construction of calorimeters to be used in LHC experiments is almost completed. It is believed that all the work done in this last decade has driven to the correct choices. However some questions remain to be answered or clarified. Some extrapolations to large quantities made from tests in a small number of samples need to be proven, such as:

i) Cure the optical degradation of the $PbWO_4$ crystals in the large scale need to built LHC electromagnetic calorimeters while maintaining the required specifications; ii) Predict the lifetime of a 10 years LHC detector based on radiation damage tests done at dose rates much higher than the reality; iii) Extrapolation to more realistic conditions of the scintillator radiation hardness results obtained with mixed fields of different types of particles, but not exactly with same energy and composition as in the final environment.

Systematic monitoring and understanding of actual running calorimeters is a very useful tool for future experiments.

ıscati Physics Series Vol. VI, (pp. 577–588)
INT. CONF. ON CALORIMETRY IN HEP – Frascati, June 8–14, 1996

LEAD TUNGSTATE RADIATION DAMAGE AND CURE

R.Y. Zhu, D.A. Ma, H. Wu, H. Newmann
California Institute of Technology, Padasena, CA 91125

C.L. Woody, J.A. Kiersteaded, S.P. Stool, P.W. Levy
Brookhaven National Laboratory, Upton, NY 11973

ABSTRACT

his report summarizes the results of a study on the radiation damage of lead ngstate ($PbWO_4$) crystals for the CMS experiment at LHC. Data are presented ı the emission, decay time, light output and response uniformity, longitudinal ›tical transmittance, radiation-induced phosphorescence and thermoluminescence. he results of damage curing with optical bleaching and thermal annealing are also esented. An in depth material study, including Particle Induced X-ray Emission 'IXE) and Glow Discharge Mass Spectroscopy (GDMS) analysis, revealed the corlations between the slow scintillation components and the Mo contamination.

Introduction

s one of two future experiments at the Large Hadron Collider (LHC) at CERN, ıe Compact Muon Solenoid (CMS) collaboration decided to construct a precision ectromagnetic calorimeter consisting of 110,000 lead tungstate ($PbWO_4$) crys- ls [1]. This decision followed extensive research and developments carried out / the physics community pursuing a precision electromagnetic calorimeter aiming searches for the Higgs boson in the intermediate mass region [2, 3, 4, 5]. Several st scintillators (BaF_2, CeF_3, undoped CsI and $PbWO_4$) were thoroughly investiıted [6, 7] for this physics motivation. $PbWO_4$ was chosen by the CMS experiment because of its high density, low cost and fast decay time.

Lead tungstate crystals are a new type of heavy scintillator which have a gh density of 8.3 g cm^{-3}, a short radiation length of 0.89 cm and a small Moliere .dius of 2.2 cm. A systematic investigation on $PbWO_4$ crystals cab be found in reference [8]. In this report, we present a study on the radiation hardness of $PbWO_4$ crystals. To realize the superb energy resolution promised by a $PbWO_4$ crystal calorimeter, the stability of the light output of $PbWO_4$ crystals *in situ* is a crucial issue. The work presented in this report is part of an ongoing effort aimed at developing fast, radiation-hard $PbWO_4$ crystals for CMS at LHC.

Section 2 describes $PbWO_4$ samples investigated. The results of radiation damage and possible curing through optical bleaching and thermal annealing are discussed in Section 3. Section 4 presents some structure and impurity analyses. Finally, conclusions and discussions are given in Section 5.

2 Samples

A total of 17 $PbWO_4$ samples were investigated, in which 8 samples were originated from the Bogoroditsk Techno-Chemical Plant (BTCP) and 9 samples were obtained from the Shanghai Institute of Ceramics (SIC). While 7 samples from BTCP are full sized CMS samples with tapered shape (2.1×2.1 cm^2 at the large end, tapering to 1.8×1.8 cm^2 at the small end, and 21.3 cm long), only one $PbWO_4$ sample from SIC (66) is close to the full size. Table 1 lists the dimensions, crystal grower and growing technology for all samples.

Table 1: $PbWO_4$ Samples Investigated in this Report

ID	Dimension (cm)	Grower	Growing Technology	Remark
478	$0.8 \times 1.0 \times 1.0$	BTCP	Czochralski	Undoped
728	$1.8^2 \times 21.3 \times 2.1^2$	BTCP	Czochralski	Undoped
767	$1.8^2 \times 21.3 \times 2.1^2$	BTCP	Czochralski	Nb-doped
768	$1.8^2 \times 21.3 \times 2.1^2$	BTCP	Czochralski	Nb-doped
1015	$1.8^2 \times 21.3 \times 2.1^2$	BTCP	Czochralski	Nb-doped
1018	$1.8^2 \times 21.3 \times 2.1^2$	BTCP	Czochralski	Nb-doped
1022	$1.8^2 \times 21.3 \times 2.1^2$	BTCP	Czochralski	Nb-doped
1031	$1.8^2 \times 21.3 \times 2.1^2$	BTCP	Czochralski	Nb-doped
4	$\phi 3 \times 4.5$	SIC	Czochralski	Early Sample
10	$2.5 \times 2.5 \times 2.5$	SIC	Modified Bridgman	Early Sample
17	$2.5 \times 2.5 \times 2.5$	SIC	Czochralski	Early Sample
34	$2.5 \times 2.5 \times 4.5$	SIC	Modified Bridgman	Vacuum Annealing
41	$2.0 \times 2.1 \times 2.5$	SIC	Modified Bridgman	O-rich Annealing
64	$1.7 \times 8.5 \times 2.0$	SIC	Modified Bridgman	Ar Annealing
65	$2.0 \times 5.4 \times 2.0$	SIC	Modified Bridgman	Air Annealing
66	$1.9 \times 17 \times 1.9$	SIC	Modified Bridgman	O_2 Annealing
67	$1.8 \times 9.8 \times 2.2$	SIC	Modified Bridgman	Vacuum Annealing

All crystals from BTCP were grown by the Czochralski method. Samples 767, 768, 1015, 1018, 1022 and 1031 were doped with niobium at a level of 10

30 ppm by weight in the melt. Most samples from SIC were grown by using e modified Bridgman method, except sample 4 and 17. All SIC samples are :perimentally prepared with special processes to investigate its consequence to the diation hardness.

All full sized BTCP samples showed a slightly yellowish color caused by ›sorption bands in the blue region. There were also macroscopic voids and scat-ring centers in some crystals which were visible to the naked eye. This seems to : a characteristic feature of crystals produced by the Czochralski method, since ystals grown by the Modified Bridgman method at SIC appear clear. All sur-ces of the samples were initially polished by the manufacturer, and no further rface treatment, other than simple cleaning with alcohol, was carried out before e measurements.

Radiation Damage

here are a number of possible effects of radiation damage in a scintillating crystal. hese include radiation induced absorption (i.e. color center formation), a possi-e effect on the scintillation mechanism, and radiation induced phosphorescence. amage to the scintillation mechanism could affect the light yield, while color center rmation would affect the light attenuation length of the crystal, and thus the light ıtput observed by the photodetector. Radiation induced phosphorescence could ıuse additional readout noise. Only damage by electromagnetic energy deposition ;ing ^{60}Co γ-rays was measured in this investigation. The irradiation was uniformely ›plied to the whole crystal.

1 Scintillation Emission

'e first looked the scintillation emission spectra. Figure 1 shows the radiolumines-:nce of BTCP samples 767 and 1015 (left) and photoluminesnce of SIC samples l, 65 and 66 (right) measured before (solid) and after (dashes) 1 Mrad (left) and krad (right) of ^{60}Co γ-ray irradiations respectively. The spectra in the figure are ·bitrarily normalized to facilitate a comparison of their shape. It is clear that there no change in the shape of the emission spectra before and after irradiation for bWO_4 crystals. However, it is more difficult to make any quantitative statement ı the possible change in the absolute amplitude of the emission spectrum, since it affected by the radiation induced absorption in samples.

We then looked the radiation effect on $PbWO_4$ decay kinetics and light ·sponse uniformity. The left side of Figure 2 shows the light yield (photoelectron ımber per MeV energy deposition) as a function of integration time for four SIC

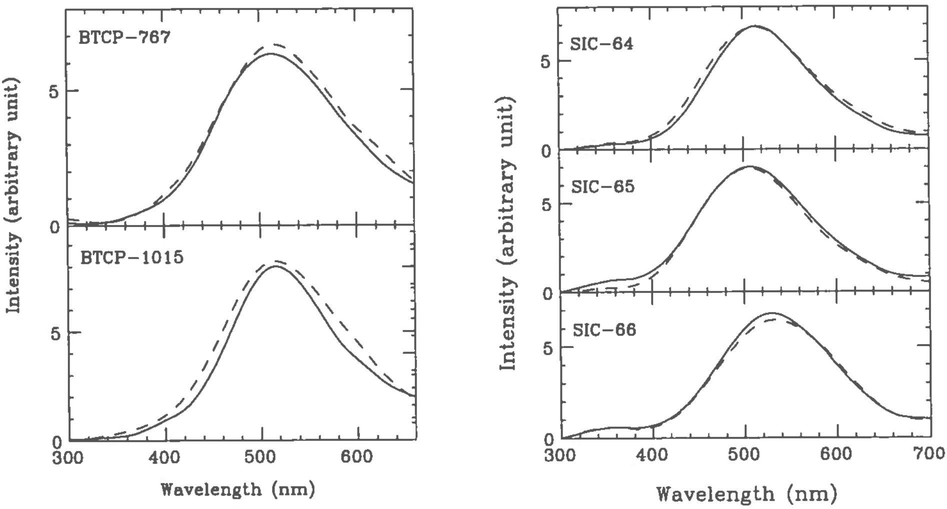

Figure 1: Radioluminescence (left) and photoluminescence (right) before and after irradiations are shown for $PbWO_4$ samples from BTCP and SIC.

samples. The result of light yield in 50, 100 and 2,000 ns gates before and after 1 krad irradiations listed in the figure indicates that the fraction of the fast decay component is not changed by the irradiation, hinting no damage in the decay kinetics.

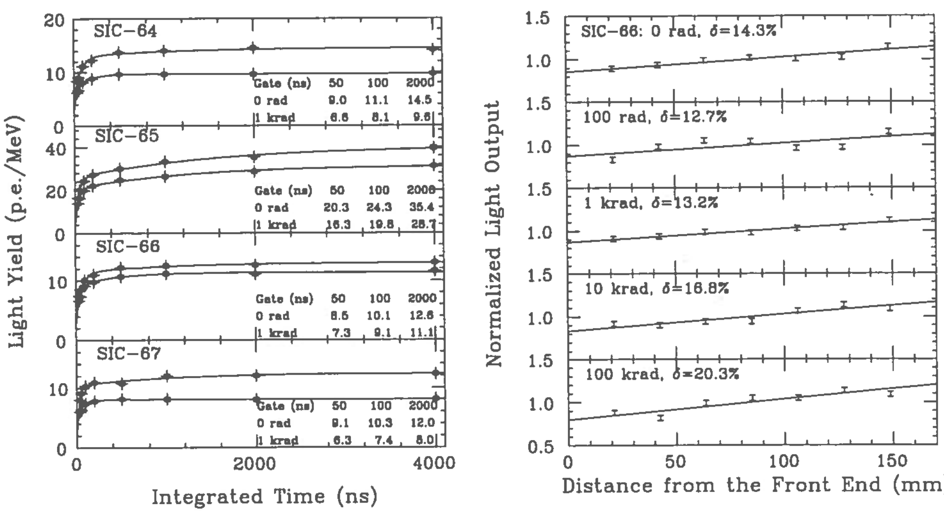

Figure 2: Light yield as a function of integration time (left) and response uniformity (right) before and after irradiations are shown for $PbWO_4$ samples from SIC.

e right side of Figure 2 shows the light response uniformity of SIC sample 66. The :asured light output as a function of longitudinal position is fit to a normalized ear function

$$LY/LY_{mid} = 1 + \delta(x - x_{mid})/x_{mid}, \tag{1}$$

ere x is the distance from the front end, LY_{mid} is the fit value of the light yield at e middle of the crystal (x_{mid}) and δ is a measure of the light response uniformity. is clear that the light response uniformity of this 17 cm long SIC sample does not ange under low dosage cumulated up to about 10 krad, although significant light tput loss is observed for this sample, as discussed in Section 3.2. The negligible mage in the light response uniformity under small dosage can be explained by the tial long light attenuation length of this crystal.

2 Radiation Induced Absorption and Light Output Loss

ıe measurements of the emission, decay kinetics and light uniformity indicate that e $PbWO_4$ scintillation mechanism is not damaged by the radiation. However, gnificant loss in the $PbWO_4$ light output was observed for all large size samples. ıe left side of Figure 3 shows the light output normalized to the unirradiated value a function of cumulated dosage, measured for four large size $PbWO_4$ samples. ıble 2 lists numerical values of the the light output degradation. Light output sses were observed at a dosage as low as 10 rad.

Since $PbWO_4$ scintillation mechanism is not damaged, the loss of light out-

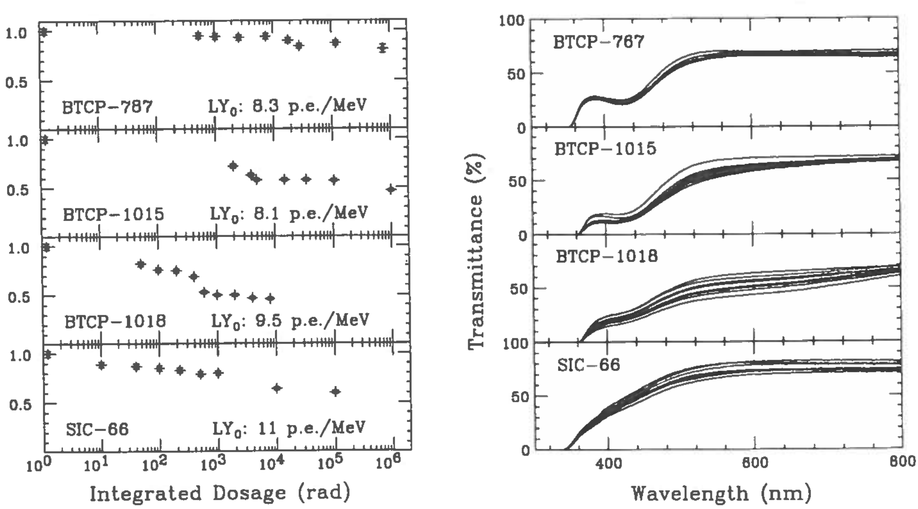

'igure 3: Light output (left) and transmittance (right) as function of cumulated osage are shown for $PbWO_4$ samples from BTCP and SIC.

Table 2: $PbWO_4$ Light Output Degradation

				BTCP-767			
Dosage (rad)	0			540	1,040	7,550	119,000
p.e./MeV	8.3			7.9	7.8	7.8	7.2
LY/LY_0	1.0			.95	.94	.94	0.87
				BTCP-1015			
Dosage (rad)	0			2,000	5,000	15,000	105,000
p.e./MeV	8.1			5.8	4.7	4.7	4.6
LY/LY_0	1.0			0.72	0.58	0.58	0.57
				BTCP-1018			
Dosage (rad)	0		50	100	1,000	8,000	
p.e./MeV	9.5		7.8	7.2	4.8	4.4	
LY/LY_0	1.0		.82	.76	.50	0.46	
				SIC-66			
Dosage (rad)	0	10	40	100	1000	10,000	100,000
p.e./MeV	11.0	9.8	9.6	9.4	8.8	7.0	6.5
LY/LY_0	1.0	.89	.87	.85	.80	0.64	0.60

put is entirely caused by the radiation-induced absorption, or color center formation. The right side of Figure 3 shows the longitudinal transmittance as a function of wavelength measured before and after a series of irradiations. The top curve in each plot represents the transmittance before irradiation, and the bottom curve represents the highest dose. For samples 767, the middle curves are difficult to distinguish from the bottom curve, indicating a very small change in the longitudinal transmittance, which is consistent with the small change of light output after a few krad of irradiation. Note, the longitudinal transmittance measurements can be used to determine the light attenuation length, as described in reference [8].

3.3 Damage Recovery and Optical Bleaching

The stability of crystal's light output in a radiation environment is affected by two factors: the degradation caused by color center formation and the spontaneous recovery caused by color center annihilation under the room temperature [9]. We looked spontaneous recovery for large size $PbWO_4$ samples. The left side of Figure 4 shows the recovery as a function of time after irradiation. The solid lines in the top two plots are a fit to an exponential recovery time with a time constant of 160 h. Note that the rightmost data points in these two plots, taken after 40 days after 1 Mrad irradiation, were also included in the fit, and the fit is shown as the horizontal bar across these two data points. Correspondingly, the transmittance and light attenuation length were also observed to recover under room temperature.

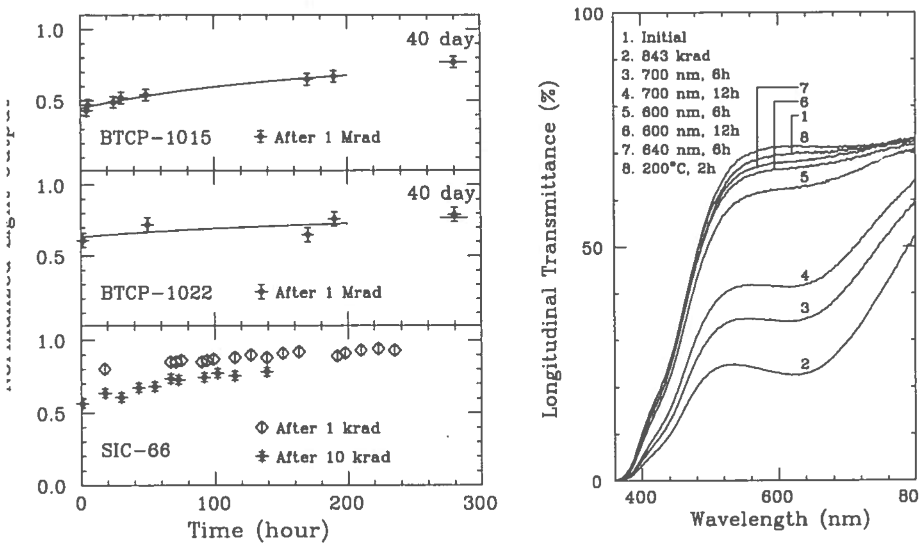

igure 4: Recovery of light output after irradiation under room temperature (left) ıd the transmittance under optical bleaching with different wavelength are shown ır $PbWO_4$ samples from BTCP and SIC.

The radiation induced absorption can also be reduced by either optical leaching or thermal annealing, and the effectiveness of the optical bleaching is nown to be wavelength dependent [10]. The right side of Figure 4 shows the ·ansmittance as a function of wavelength for sample 768. After a dose of 840 krad, leaching light at various wavelengths was applied, and then finally the crystal was laced in an oven at 200°C for two hours. It is interesting to note that the light ith a wavelength longer than 600 nm is indeed useful to bleach the sample, and ıermal annealing eliminated all radiation-induced color centers.

.4 Phosphorescence and Thermoluminescence

igure 5 shows the radiation induced phosphorescence (left) and thermolumines-ence (right) for BTCP samples 767 and 768. The phosphorescence was measured s a function of time starting approximately 10 minutes after γ-ray doses of 700 nd 1,000 krad respectively for sample 767 and 768. The apparent lower phospho-escence intensity in 768 was at least partly due to its higher induced absorption. 'he decay time of the phosphorescence intensity can be fit to two time constants: ne with a decay time of about 6 to 7 minutes, and another with a longer decay .me of about 42 minutes. For very short times after irradiation (starting within a ·w seconds), the phosphorescence intensity was observed to be considerably higher than after the first 10 minutes, but decayed away by several orders of magnitude within approximately one minute. The intensity of the phosphorescence, in terms of energy equivalent noise, was determined for times between 1 to 5 seconds after irradiation. The corresponding noise value obtained for a full sized $PbWO_4$ crystal under LHC dose rate conditions was 0.4 MeV within a 40 ns integration time, which is well below the acceptable noise limit for a precision electromagnetic calorimeter at the LHC.

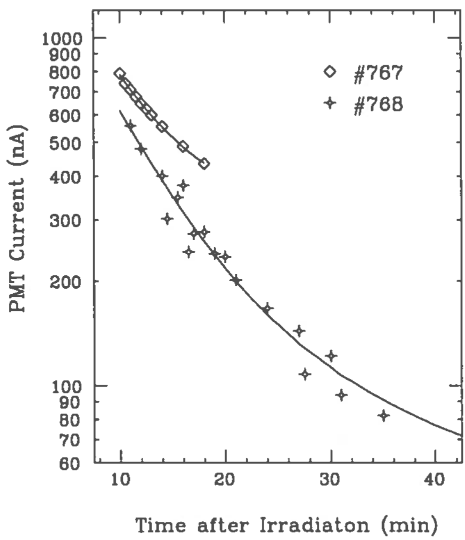

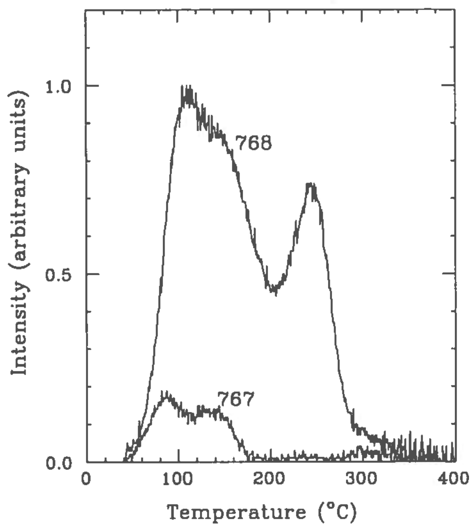

Figure 5: Phosphorescence (left) and thermoluminescence (right) measured after irradiations are shown for $PbWO_4$ samples from BTCP.

The thermoluminescence spectra were measured from 40 to 400°C at a heating rate of 2°C/sec and at 10 minutes after 1 Mrad irradiation. The result shows that sample 768 has a much stronger TL response than 767, indicating a higher concentration of trapped charge and luminescent recombination centers in sample 768. The longer lived phosphorescence observed in both crystals most likely arises from the two lowest temperature glow peaks. While sample 768 has at least three peaks at 110, 150 and 245°C, sample 767 has only two peaks at 90 and 140°C. These data indicate that the lowest temperature trap has a depth of about 0.7 eV for both crystals, but to estimate the trap depth for the other peaks would require additional measurements.

Material Characterization

shown in Section 3, the radiation hardness of $PbWO_4$ crystals vary considerably m sample to sample. Trace and defect analysis can help to find the origin [9].

Particle Induced X-ray Emission (PIXE) and quantitative wavelength dis-:sive Electron MicroProbe Analysis (EMPA) were used to identify possible devia-ns from stoichiometric $PbWO_4$ for samples 767 and 768. Both crystals were found entially pure stoichiometric $PbWO_4$. However, there was an indication that the /Pb ratio decreased by up to 5% from the small end to the large end, and 768 ; more variation than 767.

Glow Discharge Mass Spectroscopy (GDMS) was used to identify trace ment impurities for six BTCP samples and two SIC samples. A survey of 77 ments revealed impurities at the few ppm to sub-ppm level in all samples. Table 3 ;s the impurities detected in a portion of each sample, taken 3 to 5 mm below : surface of the crystal. All detected impurities at a level greater than 1 ppm are :ed, in addition to the sum of the transition metals (TM): Sc, Ti, V, Cr, Mn, Fe, , Ni, Cu and Zn, and the sum of detected rare earth elements (RE): Ce, Pr, Nd, , Sm, Gd, Tb, Dy, Ho, Er, Tm, Yb and Lu. The transition metals and rare earth ments were found to be adversely affect the radiation resistance of BGO [11] and F_2 [9], respectively.

Table 3: GDMS Analysis Result on Trace Element Concentrations (ppm)

mple	Na	Al	Si	K	Ca	Nb	Mo	Ba	TM	RE
l78	1.8	3.5	3.0	2.5	1.3	2.4	4.6	0.24	1.2	0.13
'28	3.2	<2.6	<0.7	<0.3	5.5	3.9	8.9	0.82	<1.0	0.28
'67	9.3	<0.7	42	0.50	0.97	7.8	16	0.40	<0.4	0.11
'68	1.8	<0.7	51	0.52	2.4	6.9	15	0.51	<0.4	0.12
015	2.8	3.0	1.5	1.9	5.5	7.9	120	0.16	1.8	0.11
022	3.1	3.0	1.8	1.7	7.7	10	100	0.16	1.6	0.10
34	3.0	2.0	1.3	3.3	2.7	<0.002	14	1.0	1.3	0.18
41	1.7	13	0.8	3.4	10	<0.001	18	3.8	1.4	0.15

From the GDMS analysis, the following observations can be made. All six nples from BTCP have significant Nb and Mo, while samples from SIC have no). The trace element Mo is responsible for producing the slow scintillation compo-nts. The left side of Figure 6 shows correlations between Mo contamination and e fraction of light measured in 100 ns gate for six BTCP samples. This correlation easy to be uderstood, since lead molybbate ($PbMoO_4$) is a known scintillator with w (~10 μs) decay time. However, there seem no obvious correlations between the tected trace impurities, e.g. the sum of transition metals (TM) and the sum of the rare earth elements (RE), and the susceptibility to radiation damage, indicating important role of crystal defects, such as the oxygen vacancies.

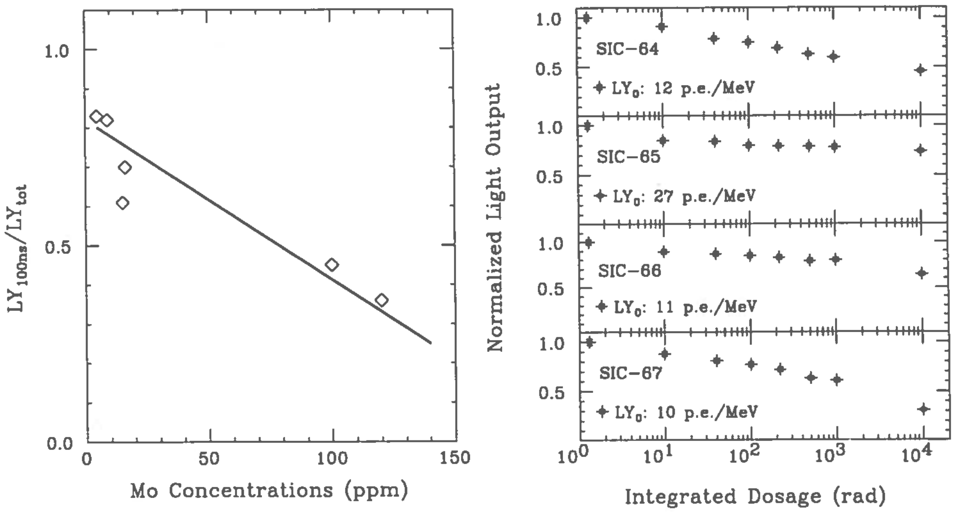

Figure 6: Left: correlation between Mo contamination and the fraction of fast scintillation component is shown for 6 BTCP samples. Right: light output as function of cumulated dosage is shown for four $PbWO_4$ samples from SIC with different annealing process.

5 Conclusions and Discussions

The quality of mass-produced crystals can be improved for high energy physics applications, if correct approach were adapted in the R&D. Previous examples are BGO [11] and BaF_2 [9]. Recent example is CsI(Tl) [12]. The work carried out in this report also led to two possitive consequences: (1) after removing Mo from the raw material, $PbWO_4$ crystals produced at both BTCP and SIC in 1996 have significant reduced slow component; and (2) significant better radiation resistance are found for crystals annealed in oxygen, indicating some compesation on $PbWO_4$ oxygen vacancy is effective to reduce color centers in the crystal. The right side of Figure 6 shows the normalized light output as a function of cumulated dosage for four $PbWO_4$ samples from SIC. As discussed in Section 2 these four samples were specially prepared with different annealing process, i.e. annealing in different atmosphere. We are particularly confident in quality improvement for $PbWO_4$ crystal, since it is intrincically radiation-hard. Negligible damage in both light yield and transmittance has been observed for a 4.5 cm long $PbWO_4$ sample from SIC [8].

In a brief summary, we have the following conclusion drawn from this estigation. First, the scintillation mechanism in $PbWO_4$ crystals is not damaged, degradation of the light output is due to the radiation-induced absorption, i.e. or cencer formation. This conclusion was drawn based on 1) no damage was ınd in the shape of the $PbWO_4$ emission spectrum; 2) no damage was found the $PbWO_4$ decay kinetics; and 3) small degradations were found in the light ponse uniformity under low dosage, if the initial light attenuation length is long ough. Second, crystal's light output degrades under irradiation and recovers under om temperature, so a **continuous inter-calibration** is necessary to realize the olution promised by $PbWO_4$ crystals. Third, optical bleaching is effective in minating color centers: crystals may be reset *in situ* during beam-off time. Last, oxygen vacancy is suspected to be responsible for color center formation: the proach to improve crystal quality is to refine the growing and annealing processes.

The final radiation hardness specification for the $PbWO_4$ crystals may ow some radiation damage, since a complete elimination of rdaiation-induced or centers in the crystal may not cost-effective for mass production. This means ne light output degradation and recovery under room temperature is allowed *in u* at LHC. However, a significant degradation of light response uniformity *in situ* is t allowed, since the degraded energy resolution caused by degraded light response iformity can not be improved with inter-calibrations. The degraded crystal light enuation length during luminosity runs is required to be long enough to maintain equate light response uniformity [9].

After $PbWO_4$ crystals with adequate quality were developed, a precision ht monitoring may be used as an inter-calibration to track the time-dependent libration, since the scintillation mechanism of $PbWO_4$ is not damaged. An example of this precision monitoring as inter-calibration is the L3 light monitoring stem used for BGO crystals in the last 7 years [13]. The monitoring has also be ınd effective for $PbWO_4$ crystals in recent CMS test beam as reported in these oceedings [14].

Continuous inter-calibrations *in situ* with monitoring may be provided by ecting light pulse to crystals in the 3.17 μs beam gap in every 88.924 μs during IC operation [15]. In addition, the same monitoring system can also be used to liver bleaching light to crystals when beam is off, so that the cumulated damage of WO_4 would not cause a degraded light attenuation length in $PbWO_4$ to an unacptable level [16]. It is expected that a $PbWO_4$ crystal electromagnetic calorimeter pable of providing a stable, precise measurement for photons and electrons with perb energy resolution at the LHC will be constructed as a result of this crystal d monitoring R&D program.

6 Acknowledgements

We would like to thank Dr. P. Lecoq for providing $PbWO_4$ samples grown in BTCP and Prof. Z.W. Yin for providing $PbWO_4$ samples grown at SIC. Many inspiring and interesting discussions with Drs. E. Auffray, P. Denes, M. Kobayashi, M. Korzhik, P. Lecoq, J.Y. Liao, M. Schneegans, C. Seez, J. Virdee and Z.W. Yin are also acknowledged. The work at Caltech is supported in part by U.S. Department of Energy Grant No. DE-FG03-92-ER40701. The work at BNL is supported in part by U.S. Department of Energy Contract No. DE-AC02-CH7600016.

References

1. *Compact Muon Solenoid Technical Proposal*, CERN/LHCC 94-38 (1994).
2. *L* Letter of Intent to the SSC Laboratory*, (1990).
3. *GEM Letter of Intent*, **SSCL SR-1184**, (1991).
4. *Compact Muon Solenoid Letter of Intent*, CERN/LHCC 92-3 (1992).
5. *L3P Letter of Intent*, CERN/LHCC 92-5 (1992).
6. R.Y. Zhu *et al.*, *Nucl. Phys.* **B44** 547 (1995).
7. S. Anderson *et al.*, *Nucl. Instr. and Meth.* **A332** 373 (1993).
8. R.Y. Zhu *et al.*, *Nucl. Instr. and Meth.* **A376** 319 (1996).
9. R.Y. Zhu, *Nucl. Instr. and Meth.* **A340** 442 (1994).
10. D.A. Ma and R.Y. Zhu, *Nucl. Instr. and Meth.* **A332** 113 (1993).
11. Z.Y. Wei *et al.*, *Nucl. Instr. and Meth.* **A297** 163 (1990).
12. R.Y. Zhu, in these proceedings.
13. A. Bay *et al.*, *Nucl. Instr. and Meth.* **A321** 119 (1992).
14. C. Seez, in these proceedings.
15. The LHC Study Group, CERN/AC/95-05 46 (1995).
16. D.A. Ma *et al.*, *Nucl. Instr. and Meth.* **A356** 309 (1995).

rascati Physics Series Vol. VI, (pp. 589–598)
I INT. CONF. ON CALORIMETRY IN HEP – Frascati, June 8–14, 1996

CsI(Tl) RADIATION DAMAGE AND QUALITY IMPROVEMENT

R.Y. Zhu, D.A. Ma, H. Wu
California Institute of Technology, Padasena, CA 91125

ABSTRACT

ıis report summarizes the results of a study on the radiation damage of thallium ıped cesium iodide crystals for the *BaBar* experiment at SLAC. Data are presented : the emission spectrum, decay time, light response uniformity, light output, lontudinal optical transmittance and damage recovery under room temperature. The ıprovement on crystal's radiation susceptibility achieved at the Shanghai Institute Ceramics and the nature of the cesium iodide radiation damage are also discussed. ıe general conclusion from this investigation is that the quality improvement for ass production crystals may be achieved with a systematic research and development program.

Introduction

ecause of its high density and light yield, the thallium doped cesium iodide, sI(Tl), crystal has been chosen by two high energy B-Factory experiments to be ıed to construct precision electromagnetic calorimeters [1, 2]. The CsI(Tl) crystal ılorimeter is the central detector subsystem of these experiments. It is an essenal detector subsystem for reconstructing the B meson, charmed meson, charmed ıryon and τ lepton at $\Upsilon(4S)$, and the B events containing CP eigenstates. The ılorimeter's intrinsic superb energy and position resolutions and detection efficiency r low energy photons provide a high reconstruction efficiency for those eigenstates compensate their small branching ratios.

The high luminosity required for these physics, however, provides a nonegligible radiation environment for the crystals. The expected dose rate for CsI(Tl) ystals at PEP-II Asymmetric Collider is 45 and 90 rad/year at $\theta = 90°$ (barrel) and 17° (endcap) respectively, during luminosity runs. Including also injections and machine study, the dose rate is estimated to be 500 and 1,500 rad/year at r = 100 (barrel) and 45 cm (endcap), respectively [1]. The corresponding radiation hardness specification for production CsI(Tl) crystals was defined for the *BaBar* experiment. It requires that crystal's light output after irradiation should be **better than 97, 90 and 80% for cumulated dosage of 10, 100 and 1,000 rad**, which corresponds to a daily degradation of crystal light output of less than 0.15 and 0.3% in the barrel and endcap, respectively.

It is known that CsI(Tl) crystals suffer from radiation damage [3, 4, 5]. The quality control for production size CsI(Tl) crystals thus is a crucial issue. In order to develop radiation-hard CsI(Tl) crystals for the *BaBar* experiment, an R&D program has been carried out at Caltech in a close collaboration with one crystal producer — the Shanghai Institute of Ceramics (SIC) [6]. This program includes two parts. The first part involves invetstigations of the radiation effect on crystal's spectroscopic properties, including (1) the emission (photo- and radio-luminescence) spectrum; (2) the scintillation light decay time; (3) the scintillation light output and the light response uniformity; (4) the longitudinal transmission spectrum; and (5) the damage recovery under room temperature. The second part of this investigation is the impurity/defect analysis, which was carried out in commercial companies. While the goal of the first part of this investigation is to learn the behavior of CsI(Tl) crystals *in situ* at PEP-II, the second part is aiming at understanding the origin of crystal's poor radiation susceptibility by looking into the correlations between crystal's radiation susceptibility and its chemical/physicsl nature. Through this R&D program, the quality of CsI(Tl) crystals produced at SIC in 1996 have significantly improved and have satisfied the *BaBar* specifications.

This report is a brief summary of this R&D program. Section 2 of this report describes CsI(Tl) samples investigated. The results of radiation damage are discussed in Section 3. Section 4 presents some structure and impurity analyses. Finally, a brief discussion and conclusion are given in Section 5.

2 Samples

A total of 14 CsI(Tl) samples were investigated. Ten full size samples were originated from four crystal producers: Crismatec [7] at France, ITC [8] at Ukrain, Beijing Glass Research Institute (BGRI) [9] at Beijing and SIC at Shanghai. All full sized samples have a tapered shape (4.5×4.5 cm^2 at the small end, tapering to 6.0×6.0 cm^2 at the large end, and >28 cm long). Table 1 lists the dimensions, crystal grower, growing technology and the origin of the raw material for all samples.

While crystals from Crismatec and ITC were grown by the Kyropoulos

Table 1: CsI(Tl) Samples Investigated in this Report

ID	Dimension (cm)	Grower	Technology	Material
rismatec	$4^2 \times 33.5 \times 6^2$	Crismatec	Kyropoulos	Chemetall
ɔvosibirsk	$4.5^2 \times 33 \times 6^2$	ITC	Czochralski	Russian
har'kov-1	$4.5^2 \times 33.5 \times 6^2$	ITC	Czochralski	Russian
har'kov-2	$4.5^2 \times 33.5 \times 6^2$	ITC	Czochralski	Russian
BGRI-1	$4.5^2 \times 29 \times 5^2$	BGRI	Bridgman	Chemetall
BGRI-2	29.5 cm long	BGRI	Bridgman	Chemetal
SIC-1	$5^2 \times 28 \times 5.5^2$	SIC	Bridgman	Chemetall
SIC-2	$5^2 \times 28 \times 6^2$	SIC	Bridgman	Chemetall
SIC-4	$4.2^2 \times 30 \times 5.4^2$	SIC	Bridgman	APL
SIC-5[a]	$4.6^2 \times 29 \times 5.8^2$	SIC	Bridgman	Chemetall
ID	**Dimension (mm)**	**Scavenger (ppm)**	**Technology**	**Material**
SIC-T1	$14^2 \times 29 \times 14^2$	0	Bridgman	Chemetall
SIC-T2	$14^2 \times 29 \times 14^2$	100	Bridgman	Chemetall
SIC-T3	$14^2 \times 29 \times 14^2$	500	Bridgman	Chemetall
SIC-T4	$14^2 \times 29 \times 14^2$	1,000	Bridgman	Chemetall

. Scanvenger (095) used in the melt.

d Czochralski method respectively, samples from SIC were grown by using the odified Bridgman method. All SIC samples were experimentally prepared with fferent processes to investigate its consequence to the radiation hardness. Sample C-5 was grown with a particular scavenger (095) [10] mixed in the melt. To ıantitatively investigate the effect of the scavenger, four small samples were grown th different amount of scavenger (095) in the melt. Table 1 also lists dimensions d the amount of scavenger in the melt for these four test samples from SIC.

Radiation Damage

ıere are a number of possible effects of radiation damage in a scintillating crystal. ıese include radiation induced absorption (i.e. color center formation), a possie effect on the scintillation mechanism, and radiation induced phosphorescence. ımage to the scintillation mechanism could affect the light yield, while color center rmation would affect the light attenuation length of the crystal, and thus the light ıtput observed by the photodetector. Radiation induced phosphorescence could use additional readout noise. Crystal radiation damage may be caused by electroagnetic energy deposition from electrons and photons, and also from neutrons and ıdrons. For applications in the *BaBar* experiment, however, dominate radiation ısage comes from 500 keV photons [1]. Only damage by electromagnetic energy position using ^{60}Co γ-rays was measured in this investigation. For full size samples, the irradiation was uniformely applied to the front (small) face of the crystal only, i.e. all side faces were shielded to simulate the situation *in situ* at PEP-II.

3.1 Scintillation Emission

The scintillation light of CsI(Tl) crystals has an emission peak at 570 nm and a decay time of about 1.3 μs. The left side of Figure 1 shows the emission, or photo-luminescence, spectra excited by UV light for six CsI(Tl) crystals from different producers. All crystals have an emission peak at about 570 nm. The right side of Figure 1 shows the CsI(Tl) emission together with quantum efficiencies of four photodetectors: Hamamatsu silicon photodiodes S2744-08 (with silicon nitrite resin) and S2744-03 (with silicon oxide resin) and Hamamatsu photomultiplier (PMT) R669 (extended-red multi-alkali cathode) and R2059 (bi-alkali cathode). The average emission weighted quantum efficiency is 82, 69, 6.5 and 6.2% for S2744-08, S2744-03, R669 and R2059, respectively. It is clear that the silicon photodiode with silicon nitrite resin (S2744-08) has about 19% higher quantum efficiency for CsI(Tl) scintillation light, as compared to silicon photodiode with silicon oxide resin (S2744-03). The R669 has a flate response over the peak of the CsI(Tl) emission.

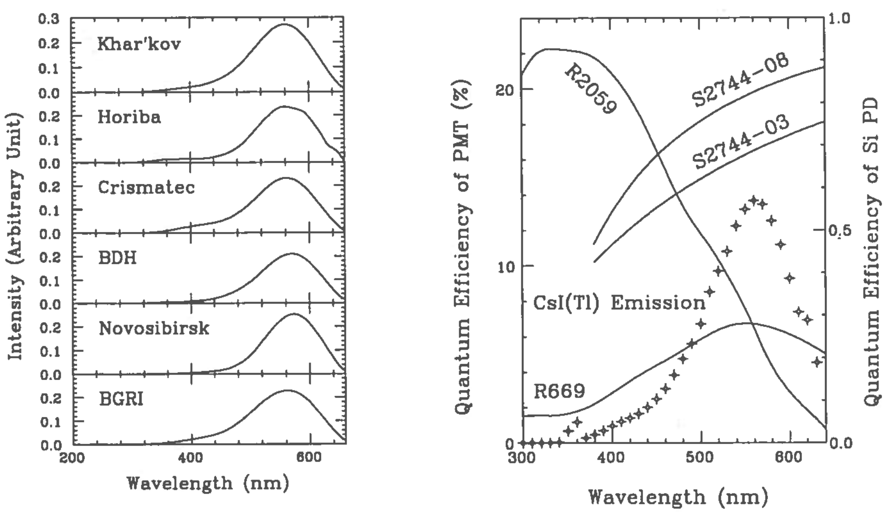

Figure 1: Left: emission spectra of six CsI(Tl) crystals. Right: quantum efficiency of S2744-08 and S2744-03 silicon photodiodes (right scale) and R669 and R2059 PMT (left scale) are shown together with CsI(Tl) emission spectrum.

It is interesting to note that the shape of the emission spectrum and the scintillation decay time are not affected by irradiation with ^{60}Co γ-rays. The left side of Figure 2 shows the photo-luminescence spectra befor and after irradiations three full size samples: Khar'kov-1, Novosibirsk and SIC-4. The right side of ;ure 2 shows the light output as a function of integration time, measured by using 69 PMT for four test samples from SIC. The photoelectron number per MeV ergy deposition as a function of integration gate width is fitted to an exponential

$$LO = S(1 - e^{-t/\tau}), \tag{1}$$

iere S is the total light yield obtained from the fit, and τ is the decay time nstant. The result of the fit is also listed in the figure. The consistency of the iision shape and decay time before and after irradiation is clearly shown in these ures. We also measured radio-luminescence, i.e. the emission spectrum excited by Co γ-rays, and find no difference btween the photo- and the radio-luminescence.

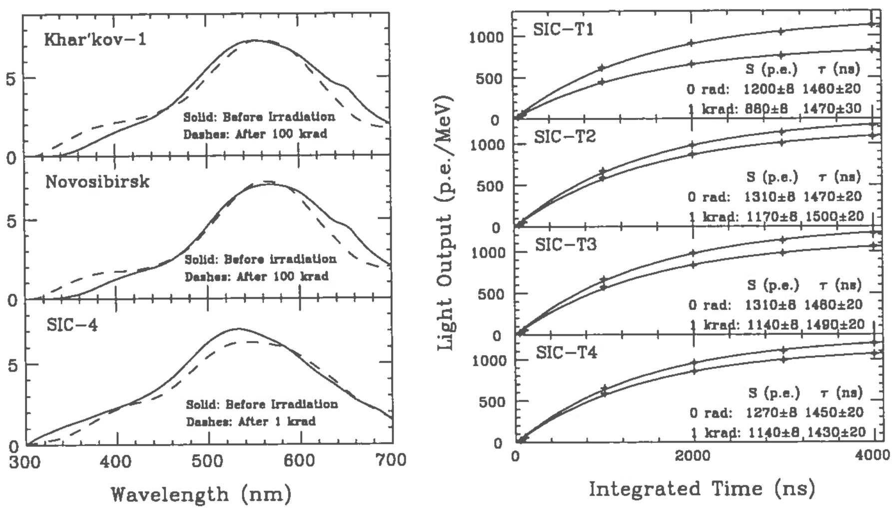

gure 2: The photoluminescence (left) and the light yield as a function of integra- on time measured by using R669 (right), before and after irradiations, are shown r CsI(Tl) samples.

The light response uniformity is also not affected by irradiation for small osages. Figure 3 shows the light response uniformity of crystal Khar'kov-2 (left) id SIC-4 (right) as a function of cumulated dosage. The pulse heights measured nine points evenly distributed along the longitudinal axis of the crystal is fit to a ormalized function:

$$LY/LY_{mid} = 1 + \delta(x - x_{mid})/x_{mid}, \tag{2}$$

here x is the distance from the small end, LY_{mid} is the fit value of the light yield at ie middle of the crystal, x_{mid}, and δ is a measure of the light response uniformity.

The figure shows clearly that the slope (δ) and the shape of the uniformity does not change very much at low dosage, although the irradiation was carried out for the front (small) face only.

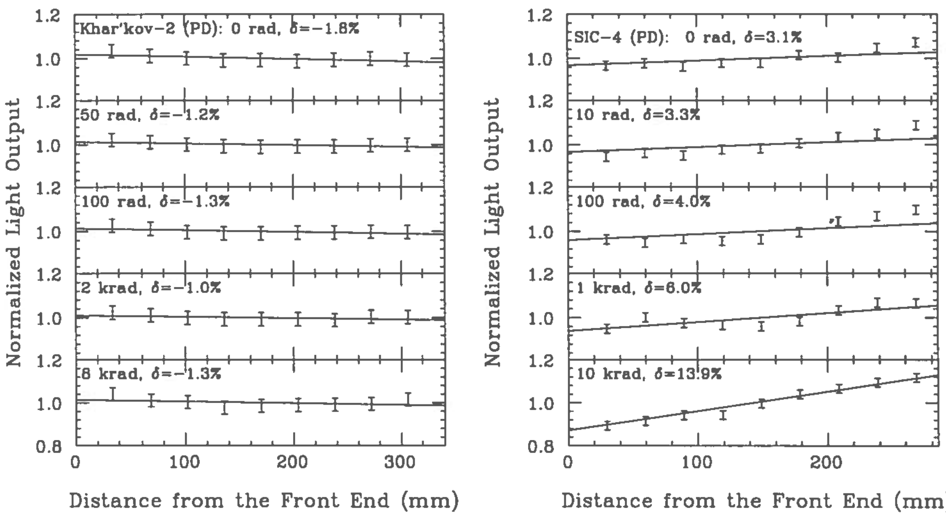

Figure 3: The light response uniformity, measured by using direct silicon photodiode readout, is plotted as a function of cumulated dosage for crystal Khar'kov-2 and SIC-4.

From this observation and the fact that the shape of the scintillation emission and its decay time do not change, we conclude that CsI(Tl) scintillation mechanism is not damaged by ^{60}Co γ-rays. The main consequence of radiation damage in CsI(Tl) is the degradation of the light output caused by the radiation-induced absorption, or color cencer formation. The radiation induced color centers cause a degradation of the transmittance and the light attenuation length, and hence the light output. However, when the initial light attenuation length is longer enough, a small degradation of light attenuation length would not affect the light response uniformity [11].

3.2 Radiation Induced Absorption and Light Output Loss

The left side of Figure 4 shows the light output as a function of cumulated dosage, measured by using 2×S2744-08 silicon diode for four full size CsI(Tl) samples: SIC-2, SIC-4, SIC-5 and Khar'kov-2. The *BaBar* radiation harness specification is also shown in the figure as a solid line. While samples Khar'kov-2 and SIC-5 satisfy the *BaBar* specification, samples SIC-2 and SIC-4 do not. The right side of Figure 4 shows the transmittance as a function of cumulated dosage for three full size nples: BGRI-2, SIC-4 and SIC-5. The radiation-induced absorption bands are arly seen in BGRI-2 and SIC-4, but not in SIC-5. The improvement of radiation rdness of crystals produced at SIC is clearly seen in these plots. This progress was iieved by improving growing process. Particular improvement was achieved for C-5 by reducing the oxygen contamination in the crystal, which was implemented introducing the scavenger (095) in the melt for sample SIC-5.

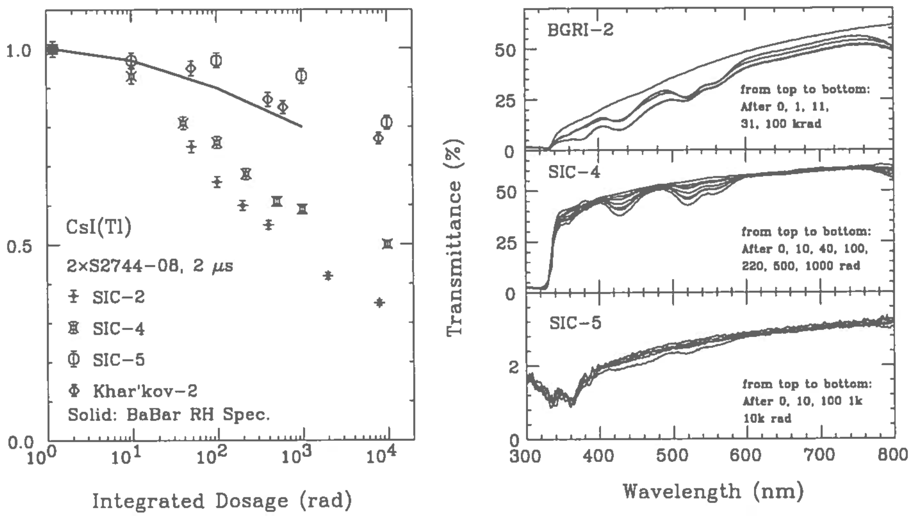

gure 4: The light output measured by using 2×S2744-08 silicon diode readout ft) and the transmittance (right) are plotted as a function of cumulated dosage r several full size samples.

The effectiveness of scavenger 095 can also be found in the left side of gure 5, showing the normalized light output as a function of cumulated dosage for ur small test samples. As seen from the figure, the degradation in light output was gnificantely reduced for samples with scavenger (095) introduced (SIC-T2, SIC-T3 id SIC-T4), as compared to the sample with no scavenger (SIC-T1). In addition, seems that the amount of scavenger in the melt is really not important, as the sult does not depend on the amount of scavenger in the melt from 100 (SIC-T2) 1,000 (SIC-T4) ppm. This is due to the fact that the function of the scavenger is form oxide with density less than CsI, so that the oxide will migrate to the top of e ingot during the growing process, similar to the zone-refining process. By doing , both oxygen and scavenger are removed from the crystal.

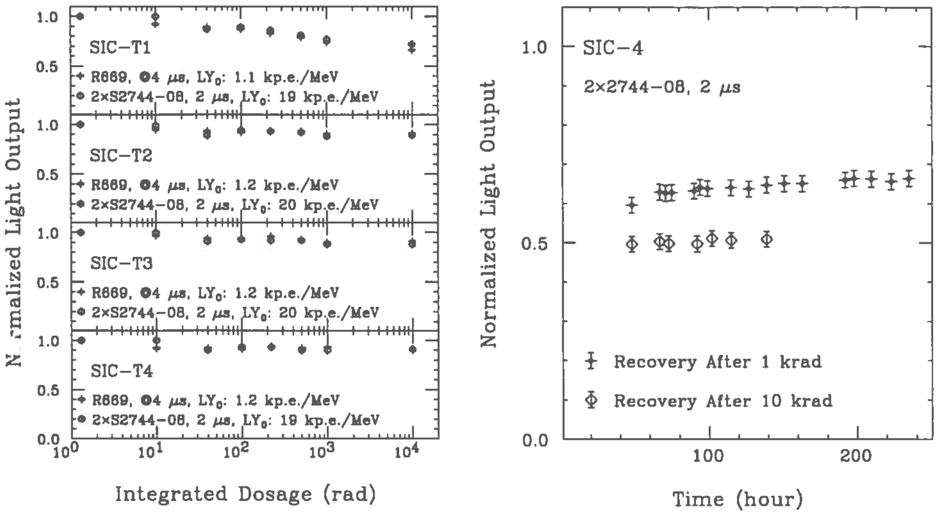

Figure 5: The light output measured by using 2×S2744-08 silicon photodiode (left), normalized to the value before irradiation, is plotted as a function of cumulated dosage for four test samples from SIC (left), and as a function of the time after irradiation for sample SIC-4 (right).

3.3 Recovery under Room Temperature

Spontaneous recovery of CsI(Tl) radiation damage is very slow under room temperature. The right side of Figure 5 shows the normalized light output as a function of time after 1 and 10 krad irradiations, measured with silicon photodiode for sample SIC-4. Measurements for all other samples show the same slow recovery. In addition, optical bleaching and thermal annealing are no effective for CsI(Tl), and high temperature annealing may introduce a phase transition, causing CsI(Tl) crystal having a milky color and no scintillation. Beacuse of this slow recovery, the inter-calibration is required to catch only the light output degradation.

4 Material Characterization

Material characterization, including determination of trace element impurities, defects and structural analysis, can help to identify key impurities and defects as the origin of crystal's poor radiation susceptibility. Previous examples are the neutron activation analysis carried out for BGO samples [12)], and the Glow Discharge Mass Spectroscopy (GDMS) analysis for BaF_2 [13)] and $PbWO_4$ crystals [14)].

An attempt is being made to identify trace element impurities by using the GDMS analysis at Charles Evans & Associates [15)]. Ten samples are being analyzed,

luding four test samples and two ends each for three full size samples: Khar'kov-
SIC-2 and SIC-4. Impurities were detected in a portion of each sample, taken 3
5 mm below the surface of the crystal. A survey of 76 elements, including all of
lanthanides, finds all trace impurities down to sub-ppm level. The result shows
obvious correlations between the crystal's susceptibility to radiation damage and
ticular impurity, e.g. the sum of transition metals, which is responsible for BGO
iation damage [16], and the sum of rare earth elements, which is harmful for
F_2 radiation damage [13]. This result indicates that there is an important role
oxygen which was unable to be measured by the GDMS analysis.

The oxygen contamination is known to cause radiation damage for other
ali halide scintillators. In BaF_2, for example, hydroxyl (OH^-) may be introduced
o crystal through a hydrolysis process, and latter decomposed to color centers of
$+ O^-_s$ or $H^-_s + O^0_i$ by radiation through a radiolysis process, where subscript i
d s refer to interstitial and susstitial centers respectively [13]. Possible means for
ce oxygen identification in alkali halide are 1) Secondary Ionization Mass Spec-
scopy (SIMS); 2) Gas Fusion (LEGO); and 3) Energy Dispersive x-Ray (EDX).
e detailed investigation on oxygen contamination in CSI(Tl) is in progress.

Conclusion

a brief summary, we have the following conclusion drawn from this R&D pro-
am. First, the scintillation mechanism in CsI(Tl) crystals is not damaged, the
gradation of the light output is due to the radiation-induced absorption, i.e. color
ncer formation. This conclusion was drawn based on 1) no damage was found in
e shape of the CsI(Tl) emission spectrum; 2) no damage was found in the CsI(Tl)
cay kinetics; and 3) small degradations were found in the light response uniformity
der low dosage.

Second, the recovery of light output under room temperature is very slow,
physics, e.g. Bhabha events at PEP-II, can be used to provide intercalibrations
situ in every few hours to track down the light output degradation.

Last, but not the least, the quality of mass production crystals can be im-
oved through systematic research. The use of scavenger (095) at SIC has improved
sI(Tl) radiation resistance. Crystals produced at SIC satisfy *BaBar* radiation
rdness specification.

Acknowledgements

would like to thank Prof. Z.W. Yin for providing CsI(Tl) samples grown at
C. Many inspiring and interesting discussions with Dr. G. Eigen, D. Hitlin, M.

Kobayashi, A. McKemey, J. Reidy, D.Z. Shen, C. Woody and Z.W. Yin are also acknowledged. The work is supported in part by U.S. Department of Energy Grant No. DE-FG03-92-ER40701.

References

1. *BaBar* Collaboration, *Technical Design Report*, **SLAC-R-95-457** (1995).
2. BELLE Collaboration, *A Study of CP Violation in B Meson Decays — Technical Design Report*, **KEK Report 95-1** (1995).
3. D. Hitlin and G. Eigen, in *Heavy Scintillators*, Editions Frontieres, ed. F. Nataristefani *et al.*, p. 467 (1992).
4. C.L. Woody *et al.*, *IEEE Trans. Nucl. Sci.* **NS-39** 524 (1992).
5. Z.Y. Wei and R.Y. Zhu, *Nucl. Instr. and Meth.* **A326** 508 (1993).
6. Shanghai Institute of Ceramics is a reasearch institution belong to the Chinse Academy of Sciences, 1295 Ding Xi Road, Shanghai 200050, China.
7. The Crismatec is a subsidiary of Sant-Gobain Ceramics Industries in France.
8. The ITC is the former Institute of Single Crystal Research in Khar'kov, Ukrain.
9. Beijing Glass Research Institute is a reasearch institution in Beijing, 1 Dongdadi Chongwenmen Wai, Beijing 100062, China.
10. Pending a patent application, SIC does not want to reveal the chemical nature of the scavenger.
11. R.Y. Zhu *et al.*, *Nucl. Phys.* **B44** 547 (1995).
12. T.Q. Zhou *et al.*, *Nucl. Instr. and Meth.* **A258** 58 (1987).
13. R.Y. Zhu, *Nucl. Instr. and Meth.* **A340** 442 (1994).
14. R.Y. Zhu *et al.*, *Nucl. Instr. and Meth.* **A376** 319 (1996).
15. Charles Evans and Associates, 301 Chesapeake Drive, Redwood City, CA 94063.
16. Z.Y. Wei *et al.*, *Nucl. Instr. and Meth.* **A297** 163 (1990).

scati Physics Series Vol. VI, (pp. 599–606)
INT. CONF. ON CALORIMETRY IN HEP – Frascati, June 8–14, 1996

QUARTZ RADIATION DAMAGE STUDY

R.I. Dzhelyadin, A.E. Ershov, A.P. Ostankov and V.I. Rykalin
Institute for High Energy Physics, Protvino, Russian Federation

ABSTRACT

ıe radiation damage was studied for three different quartz glass samples: crystal artz, fused quartz of type QU-1 and QU-2, irradiated up to maximal accumulated se of 41 Mrad. The length of these samples was 6 cm to increase the sensitivity measured transmittance to radiation damage.

The behavior of three samples was found completely different: the crystal artz does not show any change in properties. The QU-2 sample degrade sigficantly through all the spectra (200–600 nm). The QU-1 loose transparency in traviolet region, but remain almost unchanged above 400 nm.

Some possible applications for calorimetry and other detectors, to be used large radiation fields is discussed.

Introduction

he quartz is known as a high radiation resistant and transparent material. Current udy have been induced by the proposed in LHC-B Letter of Intent [1] Inner Hadron alorimeter detector with flat quartz plates as an active media for Cerenkov light. ery promising could be using of quartz as a Cerenkov radiator for charged particle ounters in high radiation environment. The advantage of extremely fast signal sponse and less sensitivity to neutrons compared to hydrogen containing plastic intillators could be utilized in future LHC detectors.

Russian industry manufactured different quartz samples were taken for the ıalysis of radiation damage. Both gamma-source and accelerator induced hadron ıower irradiation were applied.

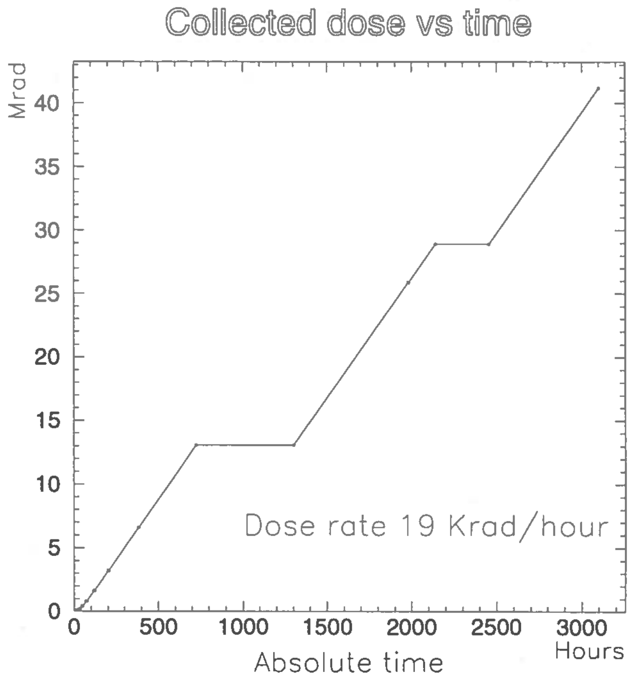

Figure 1: The accumulated dose diagram.

The Cerenkov light signal was measured using Serpukhov 70 GeV accelerator secondary beam. This was done on the pre-irradiated samples of 28 Mrad dose.

2 Quartz transmittance measurement

We choose for investigation three different quartz samples: Crystal Quartz (QU-0) and two sort of fused quartz QU-1 and QU-2. They were cut and polished at IHEP optical workshop. The length of these samples were chosen ~ 6 cm to increase the optical path and sensitivity to light absorbtion.

For reference purpose it was made two identical samples of each sort from the same raw material peace.

The measurements were performed on the SF-46 spectra-photometer within wavelength band $\lambda = 200 - 700$nm in steps of 10 nm. The Sb-Cs photo-diode current was amplified and digitized at given λ for three samples and air as a reference. The results were normalized to air transparency. During the measurement the wavelength gap was adjusted within $\Delta\lambda = 2.5 \div 6.5\,$nm to compensate variations in light

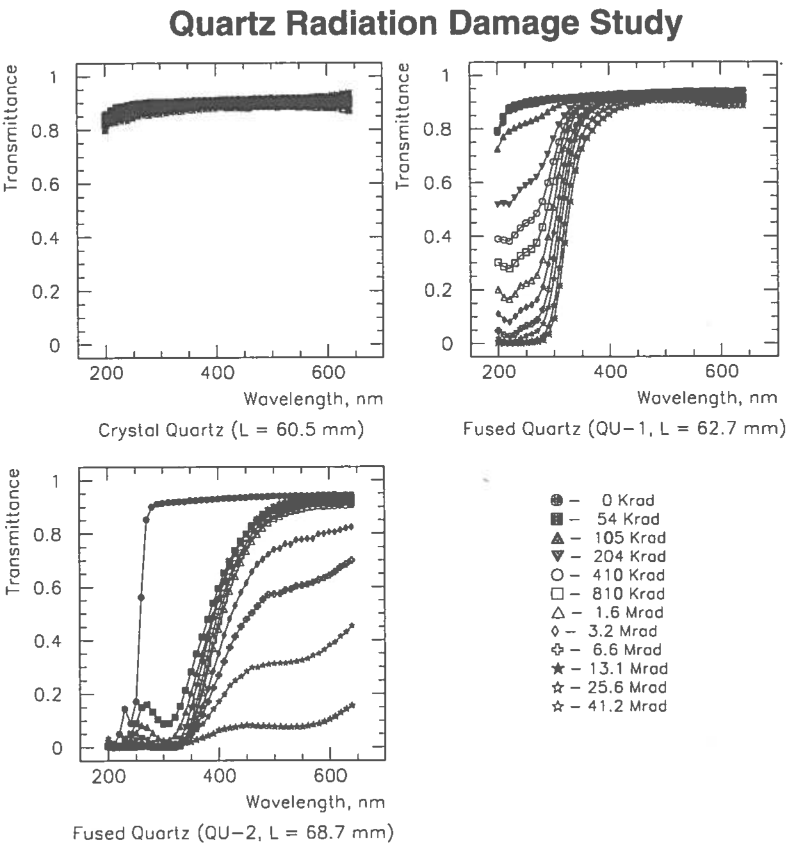

Figure 2: Three Quartz samples transmittance measurement results.

ırce intensity and photo-receiver sensitivity. Two light sources were used: the ul-ıviolet Deuterium Lamp for $\lambda = 200 - 400\,\mathrm{nm}$ and ordinary Tungsten Lamp for $= 350 - 700\,\mathrm{nm}$.

The samples were exposed by ^{137}Cs radioactive source with dose rate ~ 19 ·ad per hour. The accumulated dose as a function of astronomic time is shown on g. 1.

The results

e start the exposure with a minor dose of ~ 50 Krad and double the accumulated se for each consecutive transmittance measurement. The total radiation dose

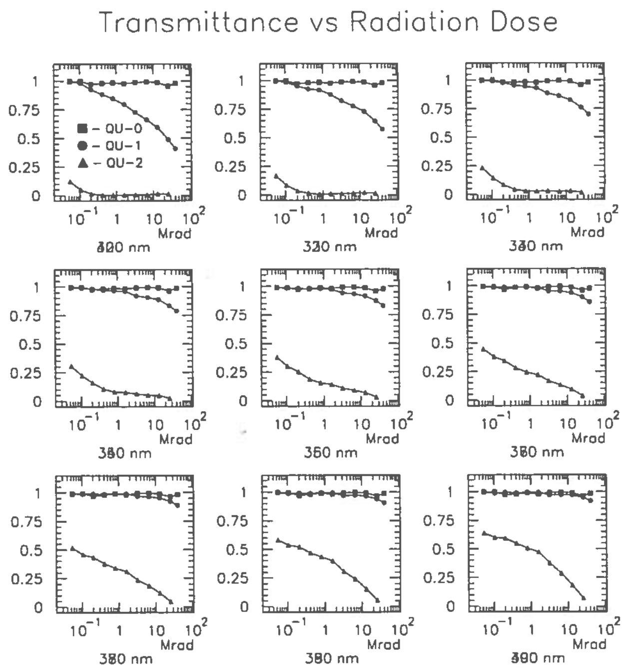

Figure 3: The quartz transparency as a function of accumulated dose. Different figures correspond to written below wavelength.

obtained was 41.2 Mrad, that corresponds to 10 year of operation for Inner part of LHC-B calorimeter.

It is remarkable that behavior of the three sort of quartz was completely different. As expected the crystal quartz show no any degradation within systematics errors of the measurement, those estimated to be of the order of 2% (see Fig. 2).

The QU-2 get dark even for visible light at 1 Mrad dose level.

The sample QU-1 show systematic decrease of transparency in the ultraviolet region, but remain unchanged for visible light above $\lambda = 400\,\mathrm{nm}$. This behavior is seen better on the Fig. 3, where the measured transmittance shown as a function of accumulated dose for different wavelength around 360 nm.

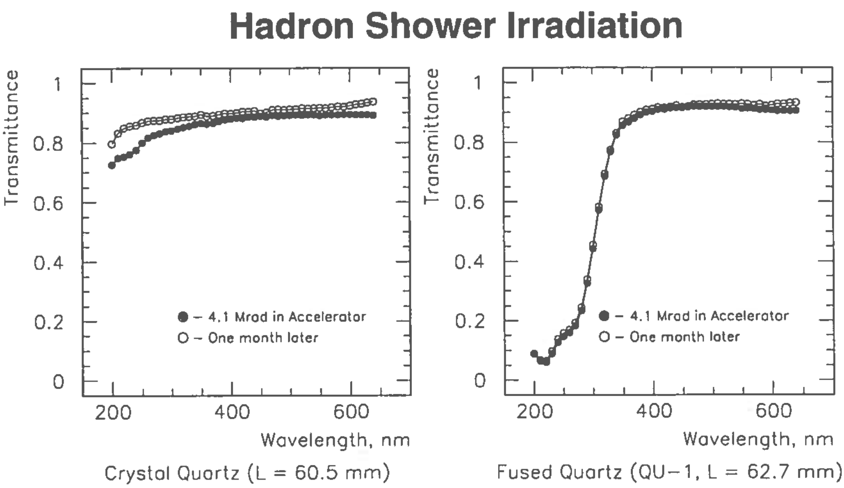

Figure 4: The Transmittance for samples irradiated on accelerator.

Irradiation on the accelerator

ring the March-April'96 run at Serpukhov 70 GeV accelerator two spare non-adiated reference samples of QU-0 and QU-1 were located in the vicinity of the ernal target station.

The accumulated dose after five weeks of exposition was measured inde-ndently as 4.1 Mrad.

Black dots on the Fig. 4 show the results of transmittance measured 3 day er accelerator shut-down, and open dots — one month later.

It worse to mention that hadron shower irradiation cause damage for QU-1 nple like gamma source does. No significant recovery in transmittance seen for J-1 after storing for one month in dark place.

The same irradiation applied to crystal quartz show small degradation of nsmittance compared to same dose of gamma-source but this affect was recovered er one month.

Quartz radiator beam tests

all set-up was assembled on the 32 GeV hadron beam behind 2 meter iron beam-mp shown on the Fig. 5. Two scintillator counter coincidence define narrow beam ot ($0.5 \times 1\text{cm}^2$) on the quartz radiator attached by optical contact to photo-

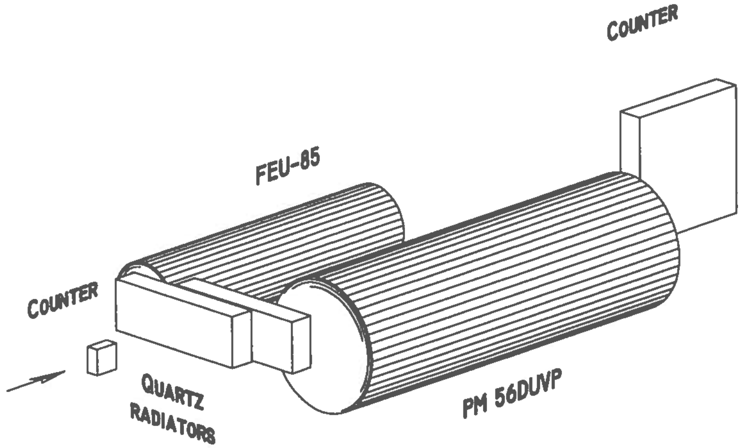

Figure 5: The beam test layout. Both quartz radiators are in optical contact with corresponding PM: crystal sample to 56DUVP (bigger tube) and fused one to FEU-85 with ordinary glass window. Two scintillator counters define beam spot of $0.5 \times 1 cm^2$.

multiplier.

The Cerenkov light from crystal quartz piece was detected by 56DUVP PM, sensitive in whole wavelength band and signal from QU-1 was detected by FEU-85 with ordinary glass window. Both quartz pieces were previously irradiated up to 28 Mrad.

Fig. 6 show the spectrum of Cerenkov light signal detected by FEU-85 on the 1 cm thick QU-1 sample. To estimate the number of photo-electrons LED calibration was performed, shown on the Fig. 7 together with average Cerenkov signal.

The dependence of the response on the distance between particle trajectory and PM's window, shown on the Fig. 7, appear to be flat within 10%. This behavior corresponds to the expectation that Cerenkov light induced by particle normally crossing the surface of rectangular radiator has to be captured inside it and as a result reach the PM's window through optical contact. The measured signal of $\sim$ 35 photo-electron per 1 cm thick radiator allows to use Cerenkov counters as a fast and

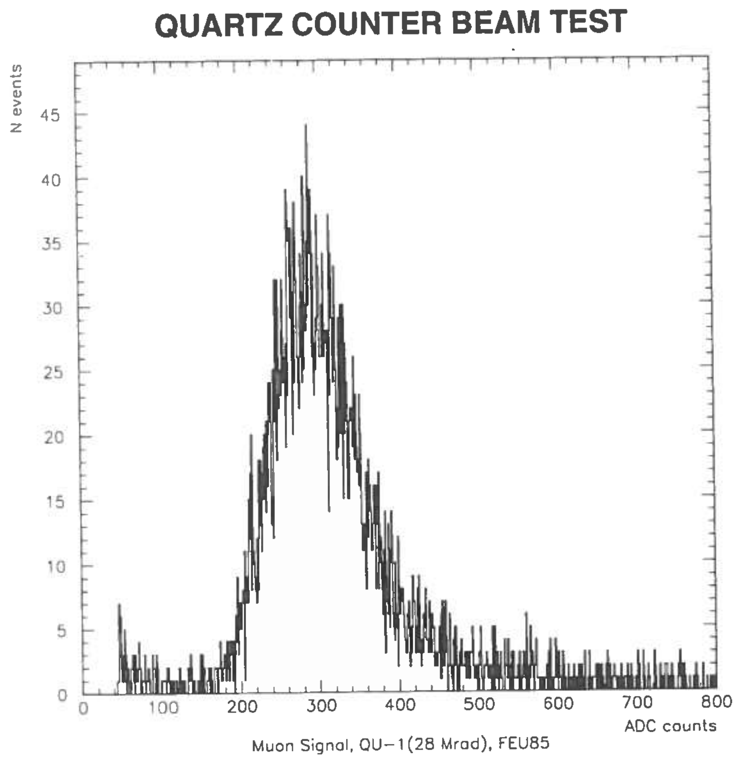

Figure 6: The Cerenkov light signal on 1 cm thick quartz.

radiation resistant particle detector, e.g. muon hodoscope, in vicinity of the LHC beam pipe.

6 Conclusions

The radiation damage for three different type of quartz were measured up to 41.2 Mrad accumulated dose. The crystal quartz does not show any visible change in properties. The QU-2 sample degraded significantly.

The QU-1 fused quartz sample loose transparency in ultraviolet region, but remain transparent above $\lambda = 400\,\mathrm{nm}$.

Accelerator induced irradiation show the same radiation damage for QU-1 as it was with ^{137}Cs gamma source. No significant recovery seen after one month keeping in the dark place.

It was found that the QU-1 fused quartz (less expensive than crystal quartz) is suitable both for calorimeter and counter applications at LHC hostile

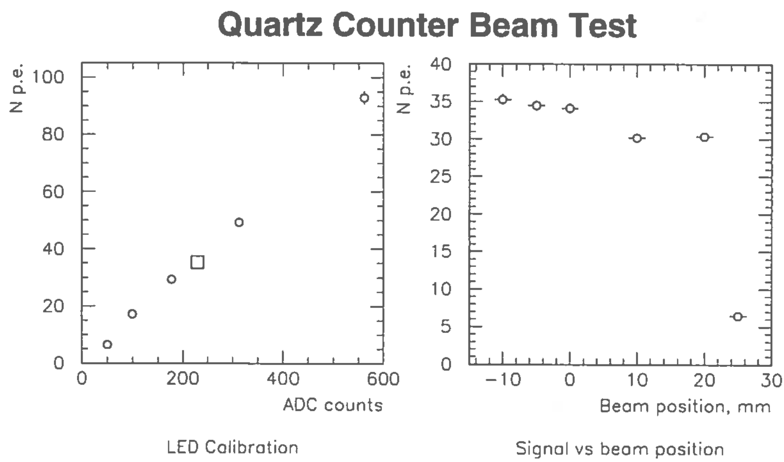

Figure 7: The LED calibration and beam particle signal, depending on beam position.

radiation environment.

7 Acknowledgements

We express our gratitude to G.I. Britvich, O.P. Gavrishchuk, A.K. Konoplyannikov, V.G. Vasilchenko for fruitful discussions and help. It is pleasure for one of us (R.D.) to express special thanks to G. Carboni and Conference Organizing Committee for support and accomodation.

References

1. LHC-B Letter of Intent, CERN/LHCC 95-5, 58 (1995).

ascati Physics Series Vol. VI, (pp. 607–616)
: INT. CONF. ON CALORIMETRY IN HEP – Frascati, June 8–14, 1996

PERFORMANCE OF AN ARTIFICIALLY AGED MODULE OF THE DELPHI HPC CALORIMETER

A. Tonazzo,
W. Bonivento, A. De Min[o], S. Ragazzi, T. Tabarelli de Fatis
University of Milan and INFN–Sezione di Milano,
Via Celoria 16, I–20133 Milan, Italy

ABSTRACT

ıe readout proportional chambers of the HPC electromagnetic calorimeter in the ELPHI experiment are affected by large ageing. In order to study the long-term haviour fo the calorimeter, one HPC module was extracted from DELPHI in 1992 ıd was brought to a test area where it was artificially aged during a period of two ars; an ageing level exceeding the one expected for the HPC at the end of the LEP a was reached. During this period the performance of the module was periodically sted by means of dedicated beam tests whose results are discussed in this paper. hese show that ageing has no significant effects on the response linearity and on ıe energy resolution for electromagnetic showers, once the analog response loss is ımpensated for by increasing the chamber gain through the anode voltage.

· The HPC Calorimeter in DELPHI

he High-density Projection Chamber (HPC) is the barrel electromagnetic calorime- ːr of the DELPHI experiment at the LEP collider.

It is composed of 144 independent units (*modules*) arranged in a cylindrical ructure around the beam interaction region. Each module, trapezoidal in shape, ɔnsists of a time projection chamber in which 41 thin layers of lead have been ıserted to act as absorber material for electromagnetic showers. The total depth f the calorimeter amounts to 17.5 X_o.

The ionization charge produced by electromagnetic showers in the 8 mm 'ide Ar-CH_4 (80-20%) gas gaps between the lead walls is drifted by an electric field

[o]Now at University of University of Padova and INFN, Sezione di Padova.

towards one end of the module, where it is collected by proportional counters and sampled at a frequency of 15 MHz. In each module the cathode of the proportional counters is segmented into 128 pads, which provide a readout granularity varying between 10 and 30 mrad in azimuthal angle as a function of depth and nine samplings along the radial coordinate.

For fast triggering purposes, a plane of plastic scintillator is inserted into one of the gaps at a depth of 4.5 X_o.

More detailed information on the HPC calorimeter construction and operation can be found in references [1) 2) 3)].

2 Ageing in the HPC

After the HPC was built, a *specific ageing* (relative amplitude loss in the chamber analog response per linear density of charge collected at the anode wire) in the readout chambers of order 10^3 cm$\cdot$C^{-1} was observed. This large specific ageing, combined with the $\sim$ 10 pA/cm average current density drawn in the HPC chambers by the natural alpha activity of the lead converter, results in an analog response loss of order 10% per year of data taking (about 5×10^6 s) [3) 4)].

This sizeable analog response loss is the most evident manifestation of ageing in the HPC and can be used to quantify the status of ageing of a module. In this paper use will be made of the *ageing factor*, defined as

$$f_a(t) = \frac{\text{analog response of the new module}}{\text{analog response at time } t}.$$

From this and the definition of specific ageing κ one can easily derive the useful relation $f_a = \exp(\kappa\lambda)$, where λ is the linear density of charge collected at the anode wire [1].

At present, the amplitude loss in each module can be accurately monitored by means of a procedure especially developed for the HPC calorimeter, based on the use of radioactive gas (^{83m}Kr) [3) 4)]. The procedure consists in adding small quantities of ^{83m}Kr gas to the gas mixture flowing in the HPC. The ^{83m}Kr gas is emitted by a ^{83}Rb source which is placed in a by-pass of the gas supply circuit. The chamber analog response is monitored analyzing the signal produced by monoenergetic electrons from internal conversion in the ^{83m}Kr decay to the ground state.

The amplitude loss is determined through monthly ^{83m}Kr runs, with a typical uncertainty of a few percent in each module, and compensated for by applying software corrections in the offline data analysis (*software equalization*). In addition,

[1] In practice, this relation holds only if κ is independent of the charge and the current density. This is true only to first order in the HPC [4)].

ce per year (usually at the beginning of the data taking period), the amplitude s in each module is compensated for by increasing the chamber gain through e anode voltage (*hardware equalization*) [3] [4] [5]. The absolute energy scale of e calorimeter is fixed with reference to the energy deposited by Bhabha events $^+e^- \to e^+e^-$), being the beam energy known with very good precision.

These software and hardware equalizations have ensured the successful eration of the HPC calorimeter since the startup of LEP in 1989.

However, side effects induced by ageing, such as worsening of the response earity and of the energy resolution, rate dependence of the analog response, and en chamber breakdown, which are widely discussed in the literature [6], could in nciple manifest themselves in the near future, affecting the detector performance the LEP200 phase. In particular, the rate dependence of the analog response and correlation with the age of the chambers was observed in HPC modules [4] and HPC-like test chambers [7]; with the same chambers a clear correlation of the solution σ_E/E at the ^{83m}Kr peak with ageing was also observed [7]. This evidence reinforced by figure 1, which shows the correlation between the resolution σ_E/E the readout chambers at the ^{83m}Kr peak and the ageing factor for the 144 HPC odules at the end of 1994 data taking. This could at least imply a progressive rsening of the precision on pulse height monitoring and chamber equalization [2].

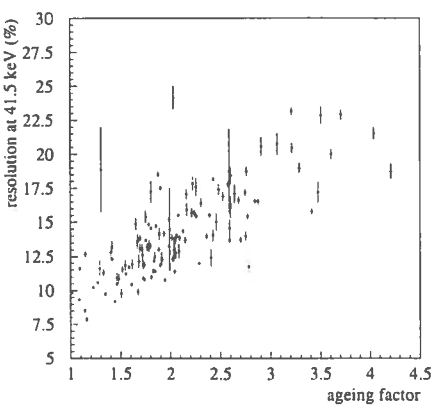

gure 1: Resolution σ_E/E at the ^{83m}Kr peak versus the module ageing factor for e 144 HPC modules at the end of 1994 data taking.

In order to evaluate the occurrence of these effects and to predict the tector performance in the years to come, a dedicated programme was pursued on unit of the HPC.

[2]At present, the precision on the HPC monitoring is limited by the systematic uncertainties ated to pressure and temperature variations and instabilities in the gas supply system [4].

3 The Ageing Programme on the Test Module

One of the most aged HPC modules that were replaced in DELPHI during the 1992/93 winter shutdown [8] was chosen as the most suitable for dedicated ageing studies. The C4 module was characterized by an ageing factor $f_a \sim 6$. This large ageing factor, compared to an average of about 2 for the rest of the HPC at that time, was due to several reasons: the module had been largely tested on electron beams in 1988, that is before the LEP startup; its readout chambers are affected by the intrinsically high specific ageing of $\sim 2.3 \times 10^3$ cm$\cdot$ C^{-1} compared to an average of $\sim 1.5 \times 10^3$ cm$\cdot$ C^{-1} for the other HPC modules; the current density drawn into its readout chambers by the alpha activity of the lead layers is about twice as much as the average current observed in the other HPC modules.

In the years 1993 and 1994 ageing was forced on the C4 module both by increasing the supply voltage of the readout chambers with respect to normal operation in DELPHI and by means of frequent calibrations with radioactive ^{83m}Kr. This caused a relative amplitude loss of about 1% per effective day [3], compared to $\sim 0.2\%$ per day for the average HPC module in normal operating conditions.

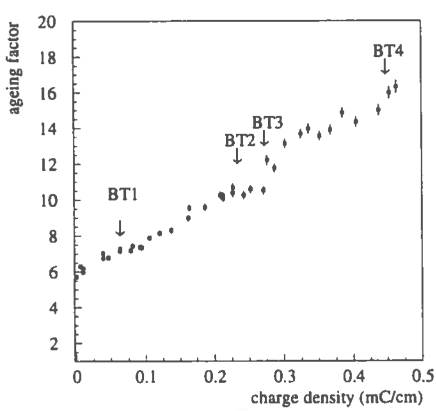

Figure 2: Ageing factor versus charge density collected at the wire for the HPC module under study after it was extracted from DELPHI: the arrows indicate the amount of charge integrated before each beam test.

Figure 2 shows the ageing factor as a function of the total charge collected on the anode wires for the C4 module after it was extracted from DELPHI. At the end of the ageing programme an ageing factor $f_a \sim 16$ was reached and a total of 0.47 mC/cm was integrated over two years, corresponding to about 8 years of operation of an average HPC module in DELPHI. A fit of the law $f_a = \exp(\kappa\lambda)$ to

[3]The *effective time* is the time with the HPC voltage on. In short, just *time* is used hereafter.

data points of the figure gives a specific ageing of $(2.3 \pm 0.1) \times 10^3$ cm$\cdot$ C^{-1}.

As indicated in the figure, the evolution of the performance of the module ; monitored in four dedicated beam tests at the CERN West Hall.

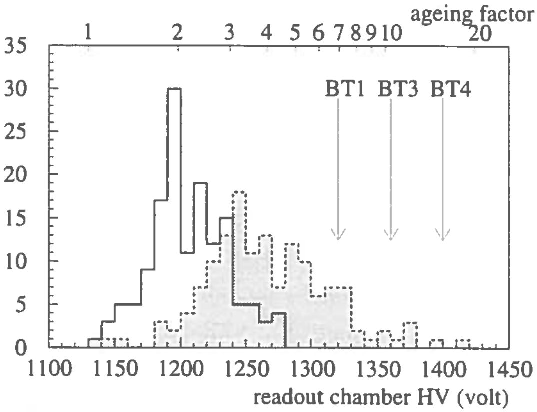

ure 3: High voltage distribution for modules equalizations in 1995 (white his-ram) and 2000 (grey histogram). The arrows indicates the anode high voltage of C4 module during the beam tests and corresponds to an ageing factor of 7, 10, respectively.

Before each beam test, a calibration with ^{83m}Kr was performed to equalize the C4 module to the same analog response of the HPC modules in DELPHI rdware equalization). This was obtained at 1320, 1360, 1360 and 1400 V anode :age respectively. For comparison, figure 3 shows the high voltage distribution ch hardware equalized the HPC modules in DELPHI at the beginning of 1995.

A conservative extrapolation of the high voltage distribution to the year 0 is also shown. Only few modules in the tail of the distribution will have an ing factor larger than the C4 module during the fourth beam test (BT4): two dules will exceed this value in the year 2000, nine modules in 2003 and half of the C in 2012. LEP is scheduled to operate until the end of 2000, thus the evolution he C4 module performance can realistically anticipate the behaviour of the HPC :he end of the LEP era.

The Beam Test Setup

: data were taken on the X7 beam line at CERN, which is a tertiary derivation :he SPS 450 GeV proton beam. Electrons and positrons are produced by the :raction of the secondary beam (mainly pions) on a lead target. The momen-ı of the beam is selected by bending magnets, while four collimators define the particle flux and the momentum dispersion; the latter was at the level of 2% and was monitored by means of a magnetic spectrometer consisting of four planes of multiwire chambers. The main backgrounds affecting the X7 beam consist of muons and pions; the relative contamination is limited to a few percent and increases with the beam energy.

The C4 module was installed in a dipole magnet providing a 0.9 T magnetic field, which is roughly 25% lower than the field intensity in DELPHI. Inside the magnet, the module was aligned with the drift field parallel to the magnetic field, by measuring the current induced in the readout chambers by the natural radioactivity of the lead as a function of the rotation angle of the module.

The position of the incident particles in the plane perpendicular to the beam axis was measured by a multiwire chamber (SFM), with 4 mm wire pitch, placed inside the magnet at a distance of ~ 10 cm from the HPC module.

For the trigger, coincidence was required between a layer of scintillators placed directly on the beam line and the SFM chamber. For beam energies above 30 GeV the coincidence with the signal from the HPC scintillator layer was also imposed, to reduce the contamination from muons and pions without affecting the efficiency for electromagnetic showers.

The drift field intensity was set at 106 V/cm which reproduces the HPC working conditions in DELPHI.

As mentioned above, before each beam test a hardware equalization of the module was performed.

5 Offline Analysis

For the final analysis the events were selected if both the impact point and the momentum of the particle were well measured in the SFM chambers and the beam spectrometer rispectively, and consistent with the average value measured in each run.

The reconstructed charge was then corrected for:

a) channel-to-channel disequalization, with coefficients determined from a dedicated ^{83m}Kr calibration run [4],

b) pressure and temperature fluctuations,

c) attenuation along the drift [9],

d) beam momentum spread, on the basis of the information from the spectrometer. This improved the overall precision on the absolute momentum to better than 1%.

e) time-dependent screening effects on anode wires. Details on such effects, related to the wire ageing, are reported in section 6.1.

The center of gravity of the reconstructed charge distribution was deterined independently for each sampling layer and, in order to minimize the contri- ıtion of path-length fluctuations in the showers, only the charge collected within a stance of ±7.5 cm from the center of gravity in the drift direction was considered.

In each run approximately 5000 events were collected, about 70% of which ıssed the fiducial cuts applied in the off-line analysis. Taking into account the ıergy resolution of the calorimeter, this sample provides a statistical accuracy uch better than 1% on the average charge deposited by the shower and at the ercent level on the resolution σ_Q/Q.

The systematic uncertainty affecting the off-line correction of the measured ıarge amounts to a few percent and is dominated by the uncertainty on the pressure ıd temperature corrections.

Results of the Beam Tests

1 Screening Effects

ı aged proportional counters, insulating material is progressively deposited on the ectrodes. Under irradiation, a layer of charge is accumulated on this material, to n extent which depend on a precarious equilibrium of different parameters, and an locally affect the charge multiplication in the gas. One of the most striking ıanifestations of this phenomenon is the rate-dependence of analog response [6]. 'his effect was also observed in HPC modules when irradiated with high intensity lectron beams [7].

This effect was seen on the C4 module during the beam tests. In this case ıe beam consisted of bunches of 50-200 electrons in two second bursts separated by en second intervals. The observed pulse height reduction during one burst in the '4 chamber was negligible for beam energies lower than 35 GeV, and ranged form % to 9% for higher energies. The time interval between two bursts was enough for he wire to recuperate the full electric field.

It should be stressed that this effect is not relevant in DELPHI, where the vent rate per module is much lower than in these beam tests. Moreover, the good nearity of the HPC for energies up to 50 GeV (see section 6.2) ensures that the creening of the charge collected during a single shower is also negligible.

.2 Linearity and Energy Resolution

'he linearity of response of the C4 module was studied by comparing the average neasured charge with the nominal beam energy in the range from 2 to 100 GeV.

The average measured charge is plotted in figure 4, as a function of the ıeam energy for the last beam test (BT4), together with a straight line fit on the

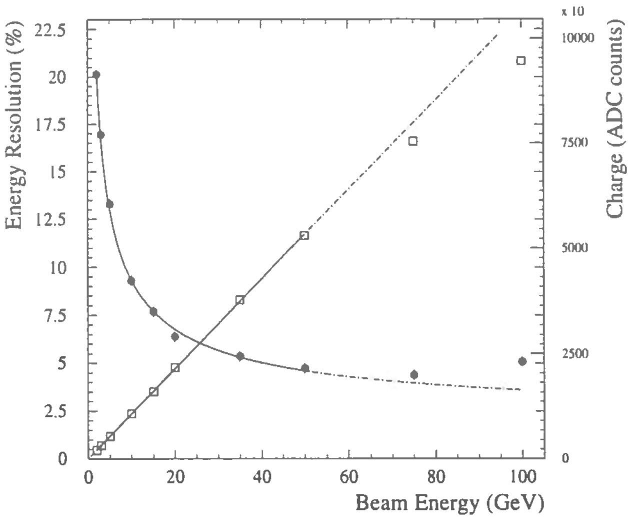

Figure 4: Average charge (open squares, right scale) and percent energy resolution (full circles, left scale) measured by the C4 HPC module in the BT4 beam test versus beam energy: the result of fits with a straight line and with the function of eq.(1) respectively, including energy points up to 50 GeV, are also shown.

points from 2 to 50 GeV.

Figure 4 shows that no significant deviation from linearity is observed for energies up to 50 GeV. This guarantees that the method of using Bhabha events ($e^+e^- \rightarrow e^+e^-$) at 45 GeV to obtain the absolute HPC calibration is reliable even with very aged chambers.

Also shown in figure 4 is the energy resolution of the C4 module in BT4. The points corresponding to beam energies from 2 to 50 GeV fit the law [4]

$$\frac{\sigma_E}{E}(\%) = \frac{28.7 \pm 0.3}{\sqrt{E\ (\mathrm{GeV})}} \oplus 2.2 \pm 0.4 \tag{1}$$

The deviations from linearity and the worsening of the energy resolution visible at higher energies are attributed to longitudinal leakage and gas gain saturation and are not induced by ageing, being observed in new modules as well.

The effect of ageing on the HPC performance can be deduced from figure 5a and 5b, where the results of the four beam tests are compared in the linearity region.

Figure 5a shows the ratio of the average charge measured in the BT1, BT2 and BT3 beam tests to the one measured in BT4 as function of the beam energy. All

[4]This result is somewhat better than the average energy resolution of the 144 HPC modules in DELPHI [2)], where the material in front of the calorimeter plays also a role.

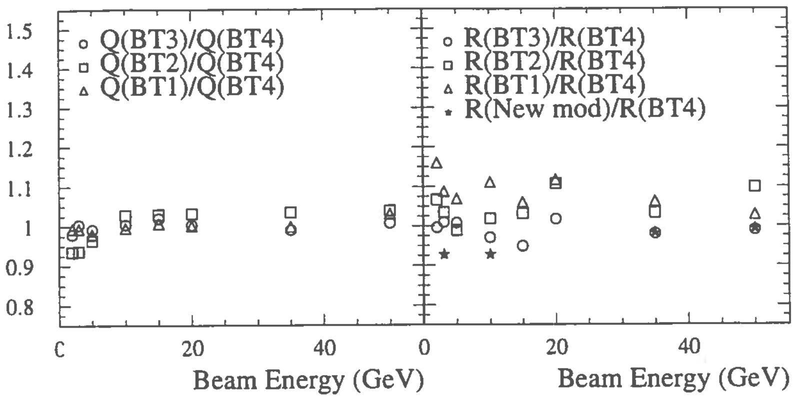

gure 5: a) Ratio of average charge (Q) measured with the HPC module under test r the BT1, BT2 and BT3 beam tests to the one measured in the BT4 beam test as function of beam energy. b) Ratio of the energy resolution $R = \sigma(E)/E$ measured the BT1, BT2 and BT3 beam tests to the one measured in the BT4 beam test, a function of beam energy. A comparison with the resolution of a new module, easured in a 1988 beam test, is also shown.

tios are compatible with unity. The spread of the experimental points is due both the uncertainties on the offline corrections to the measured charge and to the ecision of hardware equalizations: this spread can also be interpreted as an upper nit to the precision of the hardware equalizations. The hardware equalizations ppear therefore to be reliable in the recovery of the analog response loss even in e presence of large ageing and the precision of the equalization turns out to be of e same order as the one presently achieved in the HPC [4].

Finally figure 5b shows the ratio of the energy resolution measured in BT1, T2, BT3 and in a beam test in 1988 (new module) to the the one measured in e BT4 beam test as a function of beam energy. Again, good consistency with nity is found and no correlation of the resolution with the age of the module can e inferred; however, an effect of the order 5-10% cannot be excluded, though this ould not represent a serious trouble for the detector exploitation in the years to me. The somewhat better behaviour of the C4 module in 1988, particularly at low ergies, could be ascribed to the higher operating gas gain at that time, resulting a reduced importance of threshold effects [5].

[5]The gas gain has been reduced by more than a factor two with respect to its design value, in der to reduce the current density in the readout chambers and, as a consequence, the ageing [3] [4].

7 Conclusions

The expected behaviour of the DELPHI HPC calorimeter with very aged readout chambers was studied by artificially ageing one module.

From our tests we conclude that the performance of the HPC in terms of linearity of response and energy resolution is not significantly degraded by ageing.

Ageing seems to affect only the chamber analog response in amplitude, but this effect can be monitored with periodic ^{83m}Kr calibration runs and can be compensated for by both software and hardware corrections.

8 Acknowledgements

We acknowledge all the people who were involved in activities connected with this paper and especially those from the DELPHI HPC collaboration who helped us during the data taking period. In addition we would like to thank L.Gatignon of the SL division for his help in the preparation of the beam test set up.

References

1. P. Aarnio et al., DELPHI Collaboration, Nucl. Instr. and Meth. A303, 233 (1991)

2. P. Abreu et al., DELPHI Collaboration, CERN-PPE/95-194 (1995)

3. A. Algeri et al., IEEE Trans. Nucl. Sci. NS-42, 491 (1995)
A. Cattai et al., Nucl. Instr. and Meth. A367, 302 (1995)

4. A. Cattai et al., DELPHI Internal Note 93-129 CAL 108 (1993)

5. A. Cattai et al., DELPHI Internal Note 93-115 CAL 105 (1993)

6. J. Va'vra, Review of Wire Chamber Ageing, in: Workshop on Radiation Damage to Wire Chambers (ed. J.A.Kadyk, Berkeley, USA, 1986)
J.A. Kadyk, Nucl. Instr. and Meth. A300, 436 (1991)

7. A. Algeri et al., Nucl. Instr. and Meth. A338, 348 (1994)

8. A. Algeri et al., DELPHI Internal Note 93-145 CAL 100 (1993)

9. W. Bonivento et al., DELPHI Internal Note 95-3 CAL 125 (1995)

scati Physics Series Vol. VI, (pp. 617–626)
INT. CONF. ON CALORIMETRY IN HEP – Frascati, June 8–14, 1996

RADIATION STABILITY OF PLASTIC SCINTILLATORS AND THE INFLUENCE ON CALORIMETER PERFORMANCE

A. Dannemann, U. Holm, A. Meyer–Larsen, K. Wich
I. Institut für Experimentalphysik, Universität Hamburg

ABSTRACT

ıe radiation stabilities of polystyrene based scintillator SCSN38 and polymethyl-ethacrylate based wavelength shifter Y-7 have been investigated. Data are pre-nted on the dependence of the optical damage on dose, dose rate and type of diation, γ or neutrons. A computer program has been developed which predicts e influence of radiation fields on calorimeter parameters. Calculations for ZEUS ow no significant influence of the radiation background on the performance of the lorimeter. Initial results are reported.

Introduction

he high resolution compensating calorimeter of the ZEUS detector [1] at HERA is ımposed of depleted uranium and scintillator plates read out via wavelength shifter ırs by photomultipliers. The plastic scintillator used, SCSN38 [2], is polystyrene 'S) based and the wavelength shifter material is Y7 [2] in polymethylmethcrylate 'MMA) with UV absorption below 360 nm (WLS Y7). The radiation background 30 cm distance to the beampipe has been estimated [1] to be 3 kGy/10 years 0 mGy/hour) - relatively low compared to many other detectors in common use. 1995 when HERA reached about half the design luminosity, doses of about 10 y/year were measured behind the front and rear calorimeter. The influence of the ıdiation background on the quality of the optical components has been studied in etail [3]. Furthermore we have investigated the conseqences on the performance of ıe calorimeter. A computer code 'quaderatten' has been developed which allows to ılculate the radiation influence on scintillators and wavelength shifters of realistic ze.

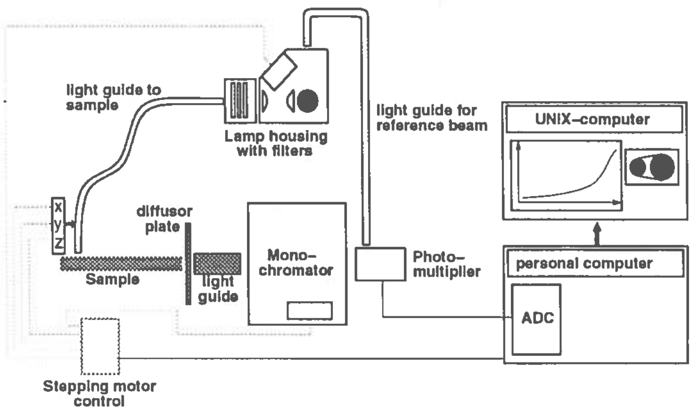

Figure 1: Scanning table.

2 Experimental Methods

Samples of scintillator and wavelength shifter materials have been investigated under various conditions concerning e.g. radiation doses, dose rates, atmospheres, temperature, composition. Most of the irradiations have been performed with a ^{60}Co source (HMI Berlin) but also in a reactor (GKSS Geesthacht). Radiation damage in this context means additional radiation induced absorption and a degradation of intrinsic fluorescence yield by destruction of the fluors.
The transmittance measured with a spectrophotometer is

$$T(\lambda) \;=\; T_0(\lambda) \cdot e^{-\mu(\lambda)\cdot d} \tag{1}$$

The radiation damage is the difference of the absorption coefficients after and before irradiation:

$$\Delta\mu(\lambda) \;=\; \mu_{irr}(\lambda) - \mu_{non}(\lambda) \tag{2}$$

Due to the small thickness of the samples (a few mm) the measurement is limited to μ smaller than about $0.1\,cm^{-1}$. To become more sensitive to longer attenuation lengths we also use a set-up (fig. 1) where an exciting light source can scan a larger sample. The light yield from the readout edge can be described by

$$I(x) \;=\; I_0 \cdot \left(e^{-\overline{\mu}\cdot x} + R \cdot e^{-\overline{\mu}\cdot(2L-x)}\right) \tag{3}$$

where x is the distance to readout edge, $\overline{\mu}$ the effective absorption coefficient, R = 0.15 the reflection coefficient at the open end, and L the sample length. For

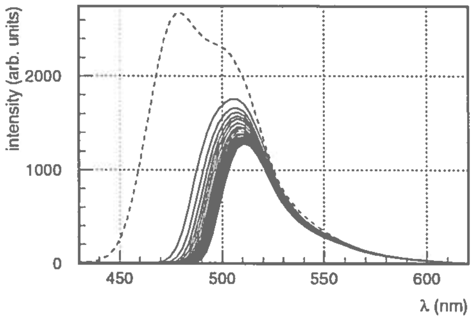

igure 2: Fluorescence spectra of WLS Y7 with different distances x of the light ›urce from the readout edge (from top to bottom: x = 0, 25, 35 ,..., 245 mm).

ıe case that the monochromator is used, $\overline{\mu}$ is replaced by the spectral $\overline{\mu}$ (λ). luorescence measurements are performed with grazing incidence of the exciting ;ht so that only light from the uppermost layers is detected. In this way one avo-s long light paths of the exciting and fluorescence light through the sample and ›tains intrinsic fluorescence spectra. Fig.2 shows the change of the fluorescence ›ectrum of WLS Y7 for different distances of the intrinsic light source to the rea-›ut edge.

Results

ı this section some especially important results of the radiation damage investiga-ons are presented.

1 Radiation damage and recovery in air

he irradiation of polymeric plastic scintillators and WLS generally leads to a forma-on of radicals which strongly absorb the intrinsic fluorescence light. The radicals ten are rather stable at least at room temperature but they react quickly with ‹ygen under the formation of peroxy radicals which do not absorb. The trans-ıittance then generally recovers to a remaining, much smaller, permanent damage. ig.3 shows the development of the damage with time. The recovery is controlled by ıe diffusion of oxygen into the sample. PMMA based materials often show a build p of the damage, the damage increases after the end of irradiation until recovery seen. Up to doses of at least 100 kGy the initial $(c \cdot D)$ and permanent damages

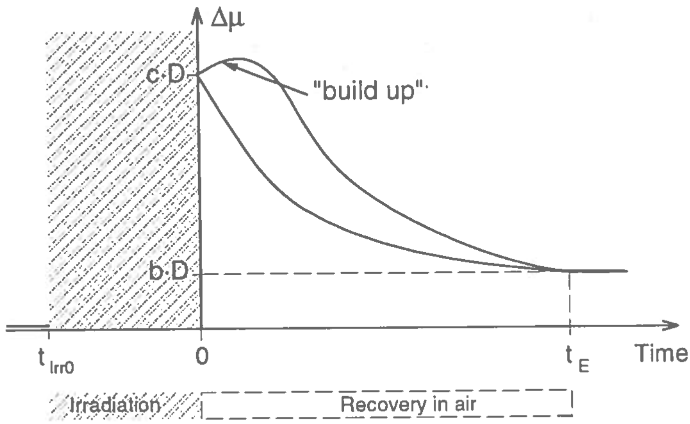

Figure 3: Development of damage with time for recovery in air. $c \cdot D$ is the initial and $b \cdot D$ the permanent damage. For very high dose rates the damage increases linearly up to $c \cdot D$ during irradiation, for very low dose rates linearly up to $b \cdot D$ if irradiation is performed in air.

Table 1: Damage parameters from γ irradiations (spectrophotometer).

Y7 damage parameters ($10^{-6}\mathrm{Gy}^{-1}\mathrm{cm}^{-1}$)					
λ	290 nm	360 nm	430 nm	460 nm	510 nm
c (λ)	675 ± 2	45 ± 7	30 ± 2	11 ± 2	6.7 ± 0.6
b (λ)	332 ± 2	-5 ± 6	7 ± 2	1 ± 1	1.1 ± 0.3
SCSN-38 damage parameter ($10^{-6}\mathrm{Gy}^{-1}\mathrm{cm}^{-1}$)					
λ	380 nm	390 nm	420 nm	430 nm	450 nm
b (λ)	-190 ± 41	-151 ± 8	1.5 ± 0.1	1.5 ± 0.1	0.8 ± 0.1

$(b \cdot D)$ have been found to be linear with applied dose D for SCSN-38 and Y7:

$$\Delta\mu(D,t) = a \cdot D \cdot f(t) + b \cdot D \tag{4}$$

where a = c - b and f(t) describes the recovery. Table 1 shows some of the damage parameters for γ irradiation of WLS Y7 and scintillator SCSN-38. Negative values are due to destruction of dyes by which the absorption is diminished.

The loss in intrinsic fluorescence light yield is

$(3 \pm 1)\%$ /10 kGy for Y7 and

$(9 \pm 1)\%$ /10 kGy for SCSN-38.

Dose rate investigations

discussed in section 3.1 the recovery of irradiated SCSN-38 and Y7 depends on : amount of oxygen in the sample compared to the number of radicals produced the radiation. Oxygen diffuses if available from outside into the material and is mediately captured by the radicals. In this way a sharp 'recovery front' moves o the sample. The penetration depth z_0 is given by

$$z_0^2 = const. \cdot \frac{p}{\dot{D}} \tag{5}$$

oxygen partial pressure, $\dot{D}$: dose rate). Measurement of the damage directly er very low dose rate irradiations (3 Gy/h) has made it possible to estimate a tical dose rate below which the material is always in the recovered state with the ıch lower damage level. For WLS Y7 of 2 mm thickness, surrounding air at normal essure and room temperature, the critical dose rate is 0.4 Gy/h (0.2 Mrad/year). r 2.6 mm thick SCSN-38 the critical dose rate is 57 Gy/h. Due to the higher fusion rate of oxygen in PS as compared to PMMA it is much higher than for Y7.

3 Neutron effects

utron irradiations of SCI and WLS have been performed in the field of the 5 MW ol type research reactor FRG-1 at GKSS Geesthacht [3) 4)]. Due to the high γ ckground (78% of dose) and temperature effects the results have large systematic rors. Nevertheless it seems to be clear that the additional radiation induced optical sorption of SCSN38 in the fluorescence emission region around 420 nm is higher r fast neutrons than for γ radiation for the same doses. For the WLS Y-7 no effect s been seen.

eutron irradiations with a very low γ background are under the way.

Computer Code Quaderatten

he aim of radiation stability investigations is to find radiation hard scintillators and 'LS and to calculate the influence of the damage on the performance of the calorieter. Most of the irradiated samples are relatively small due to practical reasons, that one has to extrapolate the results to scintillators and WLS of realistic large mensions. For this purpose a computer code 'quaderatten' has been developed [3)]. uaderatten summarizes numerically the intensities of all light rays which leave the adout face of a quadrangular prism (fig.4). The fluorescence light is excited on the cis at a distance x_e from the front face by an external (light) source. Two cones

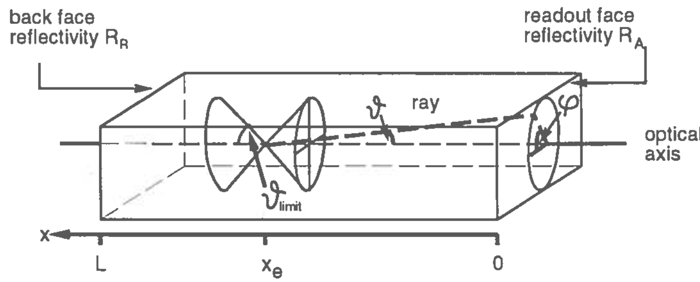

Figure 4: Sketch of quadrangular scintillator or WLS prism which is excited to fluorescence at a distance x_e from the readout edge.

of light are trapped within the totally reflecting prism: one travels in direction of the front face whereas the other propagates to the back face where it is reflected. The opening angle ϑ_{limit} is the limiting angle of total reflection. Quaderatten uses a basic data set containing all available data of geometry independent absorption coefficients, intrinsic fluorescence spectra and radiation induced additional spectral absorption coefficients for the calculation of the light propagation. It furthermore takes into consideration the exponential attenuation of monochromatic light, the Fresnel reflections at the boundaries, the surface quality of the samples by edge reflection coefficients, the refraction index, the sample dimensions and the detector spectral response.

But there also are some simplifications and assumptions: the sample must have a quadrangular prism shape, the excitation is pointlike on the axis, re-emission of self-absorbed light is not taken into account, there is no optical contact with the detector, and all light emerging the readout face is detected.

As a first step quaderatten has extended the wavelength region of the basic data set. Fig.5 shows the spectral absorption coefficient of WLS Y7 measured with a spectrophotometer. Also shown is the absorption coefficient measured with the scanning table and purified from geometrical factors by quaderatten. The agreement in the overlap region 480 nm - 520 nm is rather good.

Another comparison between attenuation curves integrated over all wavelengths measured with the scanning table, and calculations by quaderatten for WLS Y7 samples of quite different dimensions is seen in fig.6. The curves are in excellent agreement.

Fig.7 shows attenuation curves integrated over all wavelengths of SCSN-38 samples, irradiated to 21.2 kGy and non-irradiated. The calculations reproduce the measurements very well.

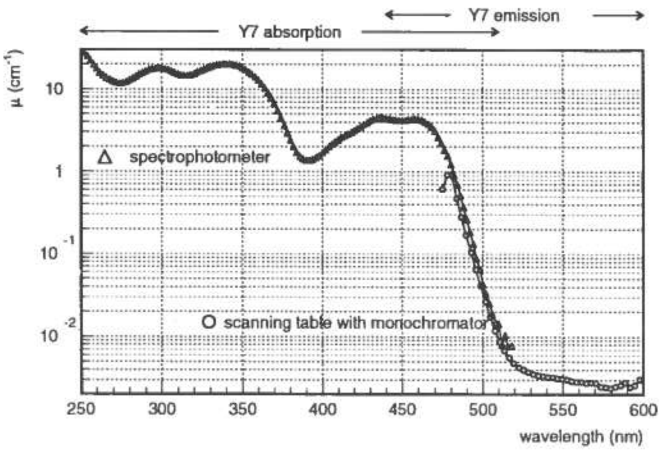

gure 5: Spectral absorption coefficients of WLS Y7, measured with a spectrophometer and calculated from spectral attenuation curves.

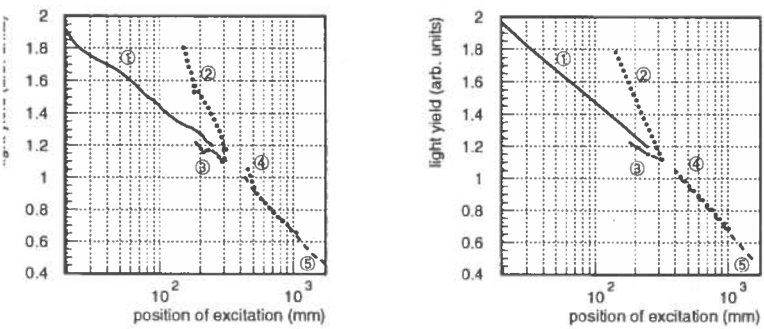

gure 6: Attenuation curves of WLS samples, measured (left) and calculated ght). Lengths and widths of the WLS are: 1) 25 cm x 4 cm, 2) 32 cm x 0.8 cm, 32 cm x 0.8 cm, 4) 109.0 cm x 20 cm, 5) 127.9 cm x 20 cm. Shown are the plane rts of the WLS. The light yields are normalized at 350 mm.

Consequences to Calorimeter

adiation of plastic scintillators and WLS effects destruction of dyes and UV absorr and generation of additional absorption centers which disturb the transport of e excitation and fluorescence light. Consequently, the performance of the calorimer is worsened: the response of scintillator becomes non-uniform in the transverse rection, the WLS becomes longitudinally non-uniform and the photoelectron yield reduced, which worsens the energy resolution.

g.8 shows the relative transverse non-uniformity of a scintillator plate of SCSN-38 0 cm x 20 cm) read out from the left and right sides assuming homogenous irraation, dose rate below critical value and surrounding air of normal pressure and

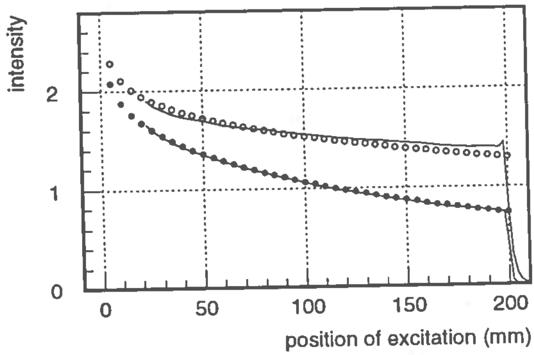

Figure 7: Attenuation curves of non-irradiated (above) and irradiated (bottom) scintillator SCSN-38. The circles denote calculations the solid lines are measurements.

temperature. For a total dose of 3 kGy the radiation induced non-uniformity is less than 2 %.

The corresponding non-uniformity of the WLS is more critical (fig.9). It amounts to 4 % at 3 kGy for the most affected WLS - well tolerable for ZEUS physics.

The consequences of light yield reduction are strongest for the electromagnetic calorimeter. Calculations by quaderatten predict a worsening of the resolution from 18 $\%/\sqrt{E/GeV}$ to 18.5 $\%/\sqrt{E/GeV}$ for a dose of 3 kGy.

As carried out above, no visible radiation damage is expected for the ZEUS calorimeter up to now. The annual scanning of the inner towers with a ^{60}Co source has given no indication of radiation damage. Other calorimeters of the ZEUS detector have suffered radiation damage: the beam pipe calorimeter, a small tungsten/SCSN-38 sampling calorimeter in direct neighbourhood of the beam pipe has accumulated a dose of at least 10 kGy in 1995. Fig.10 shows the change of response of scintillators measured with a ^{60}Co source.

The ZEUS luminosity detector, a lead/SCSN-38 sampling calorimeter, measures electrons and photons from the Bremsstrahlung process. Several scintillator plates have suffered radiation damage in the center of the beam spot. A scanning fluorescence measurement with grazing incidence measured a locally accumulated dose of 10 kGy.

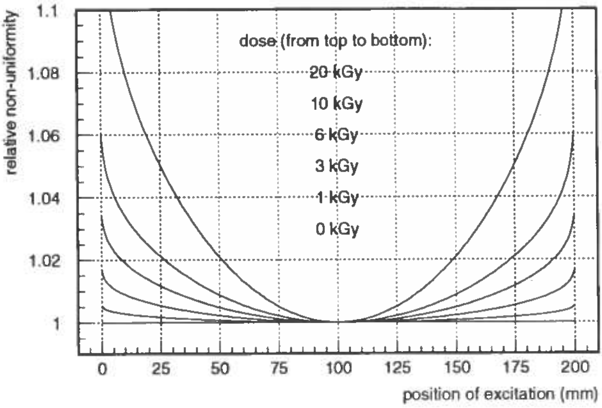

gure 8: Non-uniformity of scintillator response by irradiation, calculated by qua-
:atten.

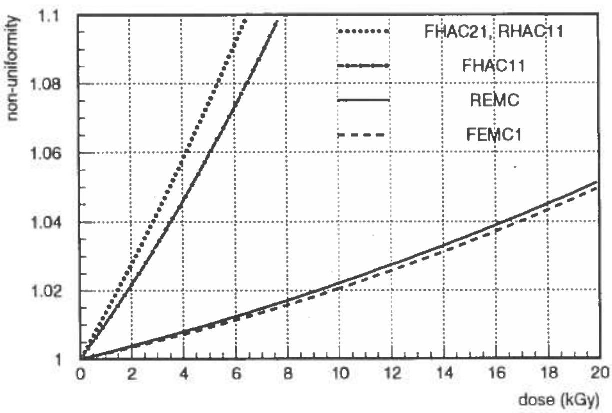

gure 9: Longitudinal non-uniformity of ZEUS WLS response due to irradiation, lculated by quaderatten. The most sensitive WLS FHAC21 and RHAC11 have a :al length of 102 cm and an active length of 64 cm.

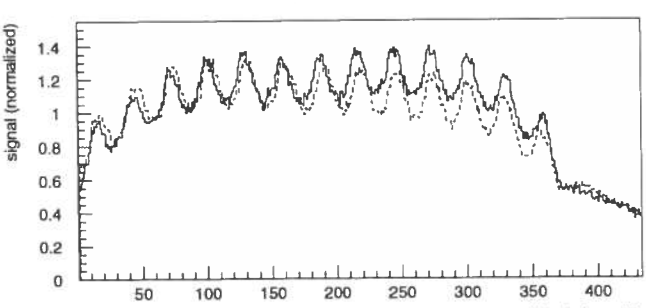

gure 10: ^{60}Co scan of a W/SCSN-38 sampling calorimeter. The scintillator plates the right show strong radiation damage.

6 Summary

The radiation stability of scintillator SCSN-38 and WLS Y7 have been studied in detail, e.g. the dose dependence of damage and loss in fluorescence yield, recovery in air and other gases, dose rate effects, γ and neutron irradiations, damage during irradiation. A computer code has been developed which calculates the influence of radiation on realistic large size pieces. With the help of this code we have demonstrated the consequences of radiation on the perfomance of the ZEUS calorimeter.

7 Acknowlegdements

We thank I. Bohnet for figure 10 and K. F. Johnson for useful discussions.
This work has been supported by the BMBF.

References

1. ZEUS Collaboration, The ZEUS Detector, Status Report 1993 (ed. U. Holm), DESY 1993.
2. T. Kamon, K. Kondo, A. Yamashita, T. Shimizu, L. Nodulman, Nucl. Instr. and Meth. **213**, 261 (1983).
3. A. Dannemann, PhD Thesis, University of Hamburg, DESY Internal Report F35D-96-06 (1996) and further references therein.
4. G. Buß, A. Dannemann, U. Holm, K Wick, IEEE Trans. Nucl. Sc. **42**, No. 4, 315 (1995).

scati Physics Series Vol. VI, (pp. 627–638)
INT. CONF. ON CALORIMETRY IN HEP – Frascati, June 8–14, 1996

RADIATION HARDNESS OF A SHASHLIK TYPE CALORIMETER

L. Dobrzynski

LPNHE, Ecole Polytechnique, Palaiseau, France

On behalf of

RD 36 Collaboration[1]

ABSTRACT

We report here test beam results obtained before and after irradiation of Shashlik towers build out of Kuraray 3HF scintillator and O2 fibres. The measured energy resolution before irradiation is defined by: a stochastic term = 8.5%/√E (E in GeV), and a constant term = 0.6%. After an irradiation with 500 MeV electrons from LiL up to 4 Mrad, the towers are affected by a light loss of ~15%. The energy resolution stochastic term is not affected by the irradiation, but its constant term reach the value of 1.6%.

Introduction

e benchmark for an electromagnetic calorimeter at LHC is the detection, at high ninosity, of an intermediate mass Higgs boson by way of its two photon decay. An cellent energy resolution must be assured with a good rapidity coverage. An ECAL tion for the CMS detector at LHC [1,2] was a lead/scintillator sandwich sampling orimeter read by wave-length-shifting (WLS) fibres, called 'Shashlik' [3,4]. This type calorimeter has been first produced by H. Fessler et al. [5], and then has been tested a IHEP/INR group [6]. Such calorimeters have also been tested at HERA [7] and are ing constructed at DESY, E865 at BNL and DELPHI [8] at CERN. There are also &D projects on Shashlik type calorimeter carried out by collaborations of

---

ist of RD36 collaboration members:

Aspell, S. Bates, Ph. Bloch, R. Grabit, P. Jarron, F. Lemeilleur, R. Loos, A. Marchioro, K. ukinas, E. Rosso *{CERN Geneva}*. S.R. Chendvankar, S.K. Gupta, S.N. Ganguli, A. Gurtu, M. ity, G. Majumder, K.Mazumdar, T. Moulik *{Tata Institute Bombay}*, R.M. Brown, D.J.A. ckerill, J. Connolly, L. Denton *{Rutherford Appleton Laboratory Didcot}*, I. Cheremukhin, I. lutvin , P. Moissenz, S. Sergueev, E. Zubarev, N. Zamiatin *{JINR Dubna}*, N. Siolios, F. Triantis *niversity of Ioannina Ioannina}*, P. Bordello, S. Ramos, J. Varela *{LIP Lisboa}*, E. Clayton, D. ler, C. Seez, T.S. Virdee *{Imperial College London}*, R. Djilkibaev, S. Gninenko, E. Guschin, Y. sienko, S. Popov, V. Popov, A. Skasyrskaya, I. Semenyuk *{INR Moscow}*, J. Badier, A. Busata, Busson, C. Charlot, L. Dobrzynski, O. Ferreira, Ch. Gregory, A. Karar, P. Manigot, R. Tanaka, Z. ı, J.Ch. Vanel *{Ecole Polytechnique Palaiseau}*, S. Bityukov, V. Obraztsov, A. Ostankov, Yu. topopov, V. Rykalin, P. Spiridonov, V. Soushkov, V. Vasil'chenko *{IHEP Protvino}*, N. dinovic, I. Puljak, I. Soric *{University of Split Split}*, P. R. Hobson, D. C. Imrie *{Brunel iversity Uxbridge}*

SPAKEBAB [9] at CERN, HERA-B [10] at DESY, PHENIX [11] at BNL and LHC-B at CERN [12].

2. RD36 Shashlik technique

A Shashlik calorimeter is based on a technique to readout the scintillation light of a lead/scintillator plate sampling calorimeter with the use of WLS fibres running perpendicular to plates through holes in the plates. Different kind of towers has been built and studied in the frame of the RD36 collaboration[13]. They differ by size, WLS fibre choice and mainly assembly technique. All these towers have been placed in high energy electron beams (10-150 GeV) at CERN SPS equipped with a 10x10mm^2 silicon PIN photodiode readout (S3590 Hamamatsu) followed by a low noise amplifier designed at INR [14]. Typically we have taken data with a shaping of 30-40 ns and a gate width of 160-200ns [15]. Light yield response of the last constructed towers (IHEP III) is typically 20 γ/MeV. Table 1 summarises the parameters for the towers which have been studied in test beam for the present study.

Table 1: Main parameters of CMS prototype Shashlik tower.

	IHEP III	IHEP IV
Number of towers	36	4
Tower lateral size	42 x 42 mm^2	42 x 42 mm^2
Number of planes	70	70
Total depth	27.5 X_0	27.5 X_0
Radiation length	16.9 mm	16.9 mm
Moliere radius	34 mm	34 mm
Lead thickness	2 ± .002 mm	2 ± .002 mm
Scintillator type	Polystyrene + .5% POPOP+2%Para-Terphenyl	3HF [(2)]
Scint. thickness	3.74 ±.01 mm	~4 mm
WLS fibres	Y11	O2 [(2)]
Number of fibres	36	36
Fibre pitch	7mm	7mm
Fibre diameter	1.0 ±.03 mm	1.0 ±.03 mm
Hole Φ in scint. (lead)	1.2 mm	1.2 mm
Front fibre Ends	Aluminised	Aluminised
Light yield	~20 γ / MeV	15 - 20 γ / MeV

In what follows, we will report the results obtained with a matrix of 6 x 6 projective towers (IHEP III and IHEP IV). The main goal of the present paper is to report the behaviour of the Shashlik towers after irradiation with 500 MeV electrons from LiL.

2 from KURARAY

Quality of the achieved towers

appreciate the quality of the towers, we have measured their response to a Cobalt 60 ioactive source.

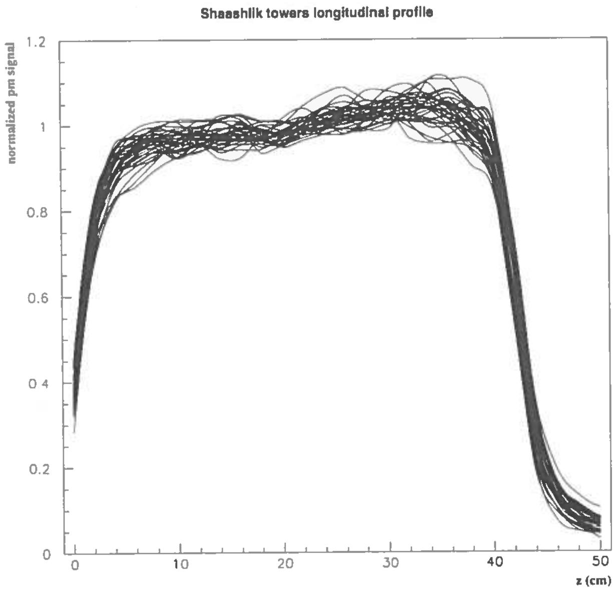

Figure 1: Longitudinal light response for the 36 IHEP III towers.

ıta have been taken every 2 cm from the front to the rear of the tower. The towers ve been readout with a PMT connected to a multimeter. The dispersion of the mean ;ht response is ±7% [13]. When the longitudinal profile of each tower is normalised to mean light response, one obtains the results presented in figure 1. One remarks the ıall dispersion of these measurements and the relative flatness of the response. This s been achieved by a relevant choice of the fibres attenuation length to compensate the ;ht loss due to the tower shape when one goes from tower front to its rear.

Main performance of Shashlik type calorimetry

1 Energy resolution of the IHEP III towers

'his section summarises published results{16} obtained with data taken in H4 SPS :am for the IHEP III 6x6 Shashlik prototype matrix. For energy resolution study, 'ents with 'wide beam' (2x2 cm^2) have been analysed and a lateral non-uniformity ırrection is applied to extract the intrinsic Shashlik energy resolution. In order to study e energy resolution the signals are summed over 9 towers. Shashlik energy resolution illustrated by figure 2 for four different towers.

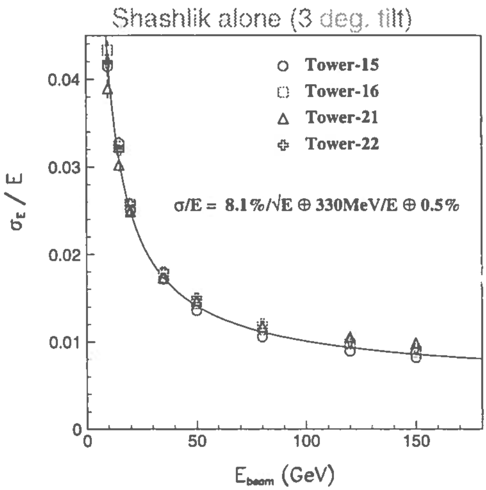

Figure 2: Energy resolution of IHEP III Shashlik prototype.

The average resolution for the 4 towers is:

$$\boxed{\frac{\sigma_E}{E} = \frac{8.1\%}{\sqrt{E}} \oplus \frac{0.330}{E} \oplus 0.5\%} \qquad \text{with E in GeV}$$

When a preshower detector is inserted in front of the calorimeter, a fraction of the energy is lost in the $3X_0$ absorber and must be corrected for the energy deposited in the Silicon planes. The average resolution is now,

$$\boxed{\frac{\sigma_E}{E} = \frac{8.5\%}{\sqrt{E}} \oplus \frac{0.330}{E} \oplus 0.5\%} \qquad \text{with E in GeV}$$

This result is in good agreement with Monte Carlo simulation and compatible with the resolution obtained for the bare towers.

Similar results have been obtained for a setup placed in a 3 Tesla magnetic field [17].

4.2 Position and Angular resolution

For the H-->$\gamma\gamma$ process at high luminosity the measurement of the emission angle of the photons is required. In order to reconstruct this angle the photon shower position has to be measured at two different depths in the electromagnetic calorimeter. In the CMS design, this is accomplished by introducing the preshower detector. The two planes of silicon strip placed after $2X_0$ and $1X_0$ absorber give the x and y of a first point and the second point is obtained from the shower barycenter in the calorimeter itself.

A resolution of ≈400μm, after unfolding of the beam chamber contribution, is measured for the position resolution of the preshower for 80 GeV electrons. The resolution varies as function of the energy. It has been found to follow:

$$\sigma_x(mm) = \frac{2}{\sqrt{E}} + .2 \qquad \text{with E in GeV}$$

ith the preshower and Shashlik tower position measurements, assuming that the ɔwer barycenter is located at the longitudinal shower average, one can estimate the gular resolution for the combined detector. Our data fit:

$$\sigma_\theta = \frac{70mrad}{\sqrt{E}} \qquad \text{with E in GeV}$$

Radiation hardness study of Shashlik towers

l Radiation environment for the CMS Electromagnetic Calorimeter

ıe LHC accelerator will produce a very high flux of charged and neutral particles due to ɜ high luminosity and the large inelastic, non-diffractive pp cross-section (~70 mb). ɔcurate simulation of the radiation environment is not simple due to uncertainties in ɜ cross-section at 14 TeV cms energy, and the exact composition of the events. Our ɔst recent analysis[18] uses DTUJET which predicts between 10% and 20% higher utron and photon fluxes than earlier simulations. The radiation dose from ɜctromagnetic energy deposited in the CMS barrel calorimeter over a ten year period ries from about 0.2 Mrad ($\eta = 0$), to 1 Mrad ($\eta = 1.5$). The neutron flux at the front ' the calorimeter is predicted to be about 300 kHz.cm^{-2} at full luminosity. Higher diation levels, up to 10 Mrad are foreseen in the detector End-Caps ($\eta = 1.5$-2.6).

2 Damage on scintillator and WLS

Γhe Shashlik construction technique demands that we use polystyrene based intillators and PMMA based WLS in order to maintain the significant cost advantage ver dense, radiation resistant homogeneous scintillators. Wide studies have been ıntinued during the last years. Further tests in the frame of RD36 have been carried out ı the polystyrene scintillator tiles and on a variety of WLS fibres. Irradiation has ːnerally been at rates much higher than those that will occur at the LHC (about 100 Rad/year at full luminosity at the ends of the barrel calorimeter). Typical rates on dividual components, carried out at IHEP[19] and INR [20, 21] have been 6 rad. s^{-1} or Cs^{137} and Co^{60} photons).

Recently[22,23] polystyrene scintillators have been considerably improved by the use ' new fluors (such as 3HF), synthesis with significant amounts of other copolymers .g. 20% of styrene by weight), or the addition of anti-radiation additives such as butl-phthalate. It has been previously reported[24] that a significant improvement ver standard polystyrene scintillator could be obtained by using an injection moulding chnique (PSM-115(A) scintillator). The most radiation resistant polystyrene based ːintillator is the one containing a high quantity of an anti-radiation additive, but which has standard fluors (pTp and POPOP). Such a scintillator has 95% of the light output of standard polystyrene based scintillator but it can withstand 5-10 Mrad suffering only 10-20% permanent reduction in light output. Partial annealing of damage after irradiation occurs with a time constant of about 20 hours.

Progress on WLS fibres has also been made, although these remain more sensitive to radiation damage. The best material (using the fluor K-27, a benzoxanthene derivative) suffers from a loss of conversion efficiency, but little decrease in attenuation length. This can be compared with the well known Y-7 fluor whose conversion efficiency is essentially unaffected by radiation, but which suffers from an enormous increase in attenuation with dose. Cladding the fibres with fluorinated PMMA allows to increase their radiation resistance. This effect has been confirmed in a Shashlik-like calorimeter built by Anzivino et al[25] and by our measurements reported here after.

Two types of towers have been irradiated. We first present results for towers using moulded Russian scintillator and Kuraray Y7 fibres. Then more extensive work has been performed on towers build out of Kuraray 3HF scintillator and O2 fibres.

5.3 Effects of radiation on towers using moulded scintillator and Y7 WLS fibres.

The effect on the performance of Shashlik modules has been studied by realistic simulation and by the irradiation of complete towers. A study of the effects of radiation damage on light collection[26] shows that in addition to the overall decrease in collected light, the non-uniformity of response across a calorimeter tower increases. This leads to an increase of the constant term in the energy resolution.

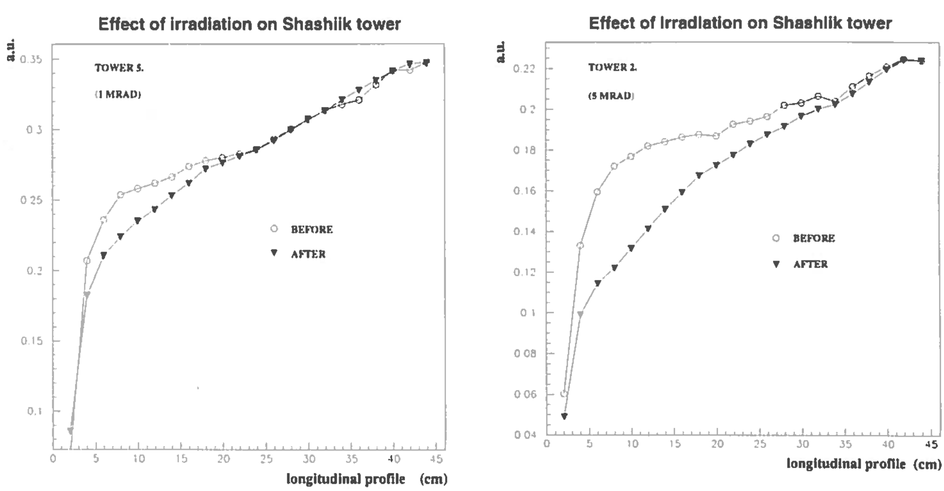

Figure 3: Longitudinal profile of the tower before and after the irradiation (effect of an irradiation of 1(5) Mrad produced at LiL by 500 MeV electrons) are shown.

ower build out of moulded Russian scintillator (the same as the one used for IHEP III) d Y7 WLS fibres from Kuraray have been irradiated in 1993 using the LiL injector to EP at CERN (up to 10^9 500 MeV electrons per second) has been carried out. The mage on the longitudinal tower profile follows closely the shower profile and is nfined to the first radiation lengths. Figure 3 shows the effects of 1 and 5 Mrad doses the longitudinal response of the tower to ^{60}Co photons.

ie consequence on energy resolution has been measured with 150 GeV electrons. It has en found that no significant effect occurs for damage up to 1 Mrad. It also appears om figure 3 that the towers studied here have not the flat response obtained for the IEP III towers (Fig. 2). This is due to the use of Y7 fibres whose attenuation length is naller to the one of Y11 used for IHEP III towers.

4 Performance of 3HF/O2 towers before irradiation.

evelopments in radiation resistant scintillators and WLS fibres have enabled the nstruction of Shashlik calorimeter towers which could withstand the full 10 years diation dose in the CMS detector with no significant deterioration of the energy solution. Currently, it is the damage to the WLS fibres as well as the scintillator tiles at are the limiting factor in using the Shashlik calorimeter in the CMS EndCaps where e dose will reach ≈8 Mrad over 10 years of LHC operation. Radiation hard material is to be developed and used. Four special towers (IHEP IV) using Kuraray 3HF intillator and O2 fibres to collect the light, have been produced for further radiation rdness studies.

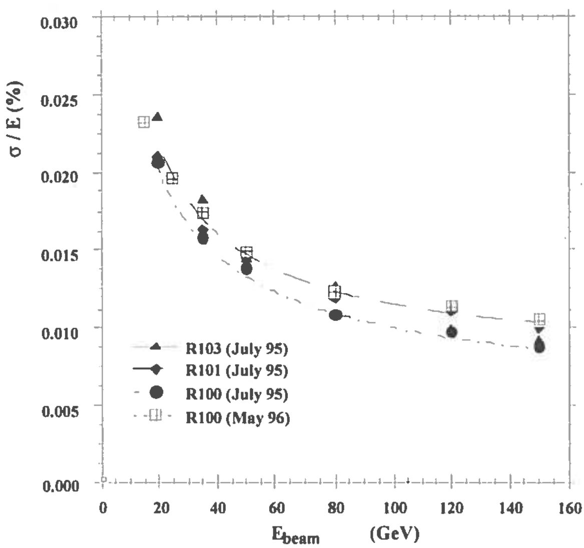

igure 4: Energy resolution for not irradiated towers using Kuraray 3HF scintillator and O2 fibres. The measurements have been performed in July 95 and in May 96.

Three out of them have been first studied in an electron beam at CERN in July 95 (R100, R101, and R103). The measured energy resolution are shown in figure 4 and given in table 2.

Table 2: Energy resolution for not irradiated towers using Kuraray 3HF scintillator and O2 fibres. The measurements have been performed in July 95 and in May 96.

Tower	Stochastic term	Constant term
R103 (July 95)	10.5 ± .2 %	0.4 ± .2 %
R101 (July 95)	8.8 ± .2 %	0.7 ± .2 %
R100 (July 95)	8.9 ± .2 %	0.5 ± .2 %
R100 (May 96)	8.7 ± .2 %	0.8 ± .2 %

One sees that these results are compatibles with what is reported in section 4. The s: all increase of the constant term for some towers is due to an non flat longitudinal profile[3] as shown in reference [13].

5.5 Effect of radiation's on 3HF/O2 towers.

Two towers have been irradiated up to 4 Mrad at the LiL with 500 MeV electrons. The 3^{d} has been kept as reference for further studies. Figure 5 gives normalised longitudinal profiles for tower R103. Just after the irradiation the loss of light is as high as 50%.

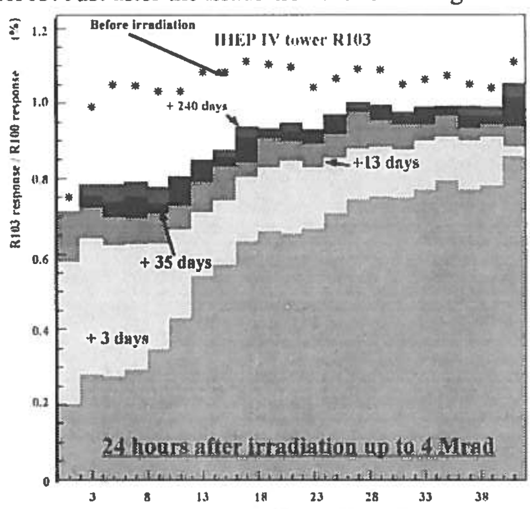

Figure 5: Tower R103 normalised longitudinal profile before and after irradiation up to 4 Mrad. The modification of the profile with time is shown.

All the longitudinal profile is affected even if the radiation damage is mainly located at ~5 X_0. This indicates that the WLS fibres are mainly responsible of the light loss. Figure

[3]We have not required any specification on attenuation length for the WLS fibres .

shows also that the tower recovers its light properties relatively fast. Two weeks after the irradiation ~ 80% of the initial response is recovered. A similar result has been obtained for the second irradiated tower (R101 not shown here).
Figure 6 gives for the two irradiated towers the light recovery as function of time.

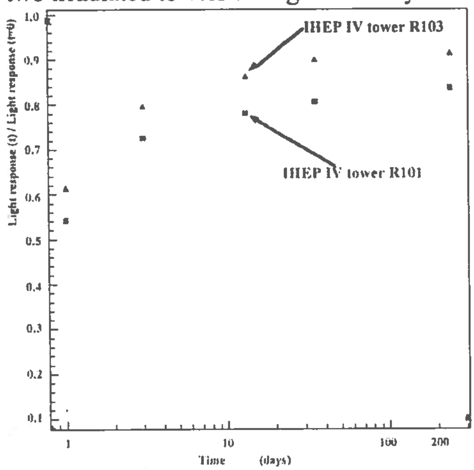

Figure 6: Tower R101 and R103 light yield recovery after irradiation.

At the time when we have put the tower again in the beam (May 96) the towers have recovered ~85-90 % of their initial light response. One also sees (Fig. 5) even after 1 month of recovery, that the light measured at the tower back side, is still below the response before irradiation. This effect come from the modification of WLS fibres transparency as well as its attenuation length. But the largest effect comes as expected, from the region (~5 X_0) where most of the electrons energy has been converted. It is clear that this will mainly affect the constant term of the energy resolution

6 Effect of radiation's on tower energy measurement

The three 3HF/O2 towers have been exposed again to electrons in the CERN-SPS H4 beam in May 96. To be able to estimate the energy resolution of these towers, they have been placed in the 6x6 matrix used by RD36 since 1994.
Figure 7 shows the energy response for 4 different towers: a IHEP III tower from the matrix (Fig. 7a), the R100 one (Fig. 7b) and the irradiated towers (R101 and R103). The last two have been irradiated up to 4 Mrad. One sees that for the 2 first the precision of the energy measurement is about the same (σ/E=~1%). But for the irradiated towers a degradation by a factor 2 is observed. The relative change of the energy peak positions[4] (Fig. 7c for R101 and Fig. 7d for R103) reflect the difference in light loss between tower R100 and the two others, respectively 10.2% and 19%, in agreement with figure 6.

[4] the distribution for the three 3HF/O2 towers have been obtained with the same readout

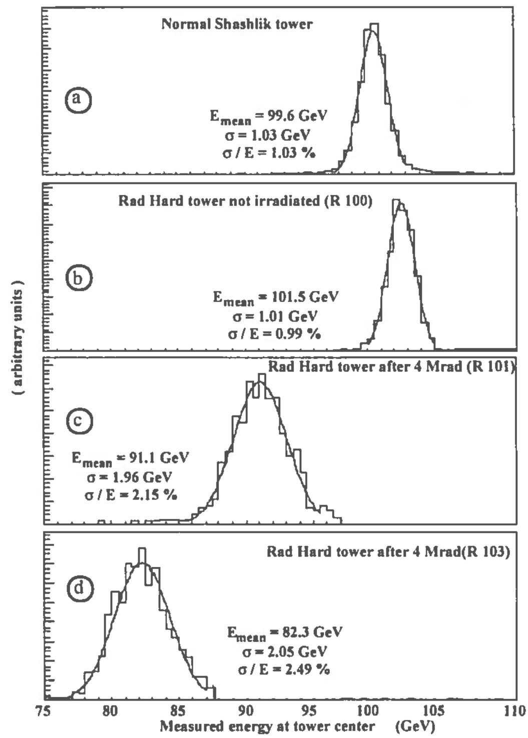

Figure 7: Energy response for single towers: a) normal IHEP III tower, b) 3HF/O2 not irradiated tower (R100), c) and d) response for the 2 irradiated towers.

5.7 Energy resolution of an irradiated tower

To verify that the towers in the matrix have not been damaged since 1994, we have first estimated the energy resolution for one IHEP III tower and of the non irradiated 3HF/O2 tower (R100). Fixing the electronic noise from an independent measurement, we measured for the IHEP III tower an energy resolution of:

$$\boxed{\frac{\sigma_E}{E} = \frac{8.5\%}{\sqrt{E}} \oplus 0.5\%} \quad \text{with E in GeV}$$

well in agreement with the results given in section 4. Figure 4 displays the 7 energy points obtained for tower R100 in July 95 and May 96. No appreciable differences can be observed. Figure 8 shows the energy resolution obtained for tower R103. The fitted curve is obtained for:

$$\boxed{\frac{\sigma_E}{E} = \frac{9.9\%}{\sqrt{E}} \oplus 1.6\%} \quad \text{with E in GeV.}$$

As expected the 10% reduction in light yield does not affect too much the stochastic term. The May 96 value is compatible with the July 95 measurement. The constant term is now 1.6% to be compared to its original value of 0.4% before irradiation.

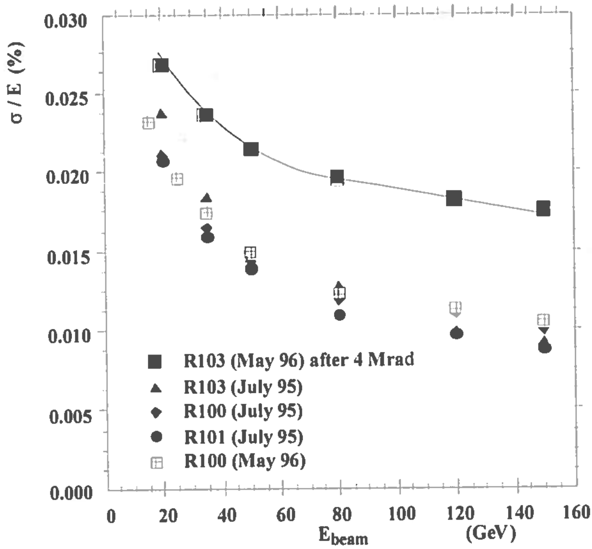

igure 8: Energy resolution of R103 tower (3HF/O2 scintillator/fibres) after irradiation. Measurements before irradiation are also given for comparison.

Conclusions

he goal of this paper is to summarise RD36 work performed on 3HF/O2 towers ‹pected to be more radiation hard as ordinary towers. It is shown that the use of ıdiation hard components like 3HF scintillator and O2 WLS fibres from Kuraray ·ovide about the same quality towers as the standard towers we studied for the CMS ırrel using polystyrene scintillator and Y7 and/or Y11 fibres.

he energy resolution measured with these towers is in agreement with the ıeasurements obtained for standard RD36 towers (IHEP III). Some improvement can ven be expected. Our O2 fibres are not multicladded and their attenuation length is too nall to properly compensate the losses due to the tower geometry.

.fter irradiation with 500 MeV electrons up to 4 Mrad, the towers performance are egraded. It is shown that the constant term is mainly affected. But it is clear that these ›wers are still on life and even with a constant term of 1.6%, they can provide decent nergy measurement in the End-Caps of a LHC calorimeter. An adequate choice of WLS bres attenuation length providing more light around 4-6 X_0 could even attenuate the ffect of the radiation and reduce the size of the constant term.

ıcknowledgements.

Ve would like to thank the CERN-SPS machine crew and N. Doble for the operation of ıe beam. We are indebted to J. Bourotte and M. Haguenauer for their work and rganisation for data taking in the SPS-H4 beam line.

References

1. CMS Letter of Intent, CERN/LHCC 92-3, LHCC/I1, 1 October 1992
2. CMS: The Compact Muon Solenoid. Technical Proposal, CERN/LHCC 94-38, LHCC/P1 (15 December 1994)
3. A combined Shashlik + Preshower detector for LHC. CERN-DRDC Proposal P50. CERN/DRDC 93-28 (1993).
4. RD36 Collaboration, Status Report, CERN/DRDC 94-47 (1995)
5. H. Fessler et al., *Nucl. Instr. and Meth.*, A228 (1985) 303, + A240 (1985) 284.
6. G.S. Atoyan et al., *Nucl. Instr. and Meth.*, A320 (1992) 144
7. B. Loehr et al., *Nucl. Instr. and Meth.*, A254 (1987) 26
8. A. Maio et al., STIC: The New DELPHI Luminosity Monitor, Proc. 4th Int. Conf. on Calorimetry in High Energy Physics, Isola d' Elba (1993) 165
9. W. Brower et al.., Test of a High Resolution Electromagnetic Calorimeter of Wavelength Shifting Fiber Readout, Proc. 5th Conf. on Calorimetry in High Energy Physics, BNL (1994) 191
10. HERA-B Proposal, DESY PRC/93-04 (1993), DESY F15-94-01 (1994)
11. G. David et al., Performance of the Phenix Shisk-Kebab EM Calorimeter, presented at the IEEE Nucl. Sci. Symp., San Francisco (1995)
12. A. Golutvin, HERA-B and LHC-B calorimetry, this conference proceedings.
13. P. Aspell et al., A Shashlik EM Calorimeter for CMS, CMS TN 94-305
14. E. Guschin, Yu. Musienko, I. Semenjuk. INR-1005/94 preprint (1994); and E.Guschin et al., CMS TN/93-108 (1993).
15. A.Karar, CERN--CMS TN/93-96(1993) and Proceedings of the IV International Conference on Calorimetry in High Energy Physics (La Biodala, Isola d'Elba,Italy,September,19-25,1993)
16. Energy and Spatial resolution of a Shashlik calorimeter and a Silicon preshower detector. CERN-PPE/95-151 (Sept 21, 1995) Submitted to NIM
17. Beam test results of a Shashlik Calorimeter in High Magnetic Field. CERN-PPE/95-152 (Sept 21, 1995) Submitted to NIM
18. Neutron and photon fluxes and shielding alternatives for the CMS detector at LHC, CMS TN/94-241, 1994
19. V. Vasilchenko et al. New results on plastic scintillators radiation damage, CMS TN 94-220, 1994
    V. Bolotov et al. Radiation hardness of WLS-fibres, CMS TN/94-221, 1994
20. Gamma-irradiation tests of Shashlik electromagnetic calorimeter injection moulding type scintillators, CMS TN/94-225, 1994
21. Britvich et al, *Nucl. Instrum. and Meth. A326* (1993) 483
22. F. Markly et al, *Radiat.Phys. and Chem.* **41** (1993) 135
    J.P. Harmon et al, *Radiat.Phys. and Chem.* **41** (1993) 153
23. J. Badier et al. Radiation hardness of Shashlik calorimeter, CMS TN/93-97, 1993
24. S. Gninenko et al. Study of the light collection in Shashlik electromagnetic calorimeter radiation damaged perforated scintillators, CMS TN/94-224, 1994
25. G.Anzivino et al, *Nucl. Instrum. and Meth.* A346 (1994) 153
26. New results on plastic scintillators radiation damage. CMS TN /94-220

ascati Physics Series Vol. VI, (pp. 639–650)
I INT. CONF. ON CALORIMETRY IN HEP – Frascati, June 8–14, 1996

DOSE RATE EFFECTS IN WLS FIBERS

M. David, A. Maio, A. Gomes
LIP, Av. Elias Garcia 14 1°, 1000 Lisbon, Portugal, and FCUL

ABSTRACT

An experiment of low dose rate irradiation of WLS fibers was performed. VLS fibers from Bicron, Kuraray and Pol.Hi.Tech doped with and without Ultra-'iolet absorber (UVA), were irradiated in a ^{60}Co γ source. A total dose of $\sim$ 140 (rad was applied. 3 dose rates were used: 0.55 Krad/h, 1.1 Krad/h and 4 Krad/h. Io low dose rate effects were observed.

BCF91A and Y11(200) fibers with single cladding and multicladding, were rradiated in a mixed field of 20% of neutrons and 80% of γ's. A total dose of Mrad was applied at a peak dose rate of 1.5 Mrad/h. The radiation effect on ingle cladding vs. multicladding fibers is compared, and are similar. The high lose rate irradiation effect on fibers is compatible with the much lower dose rate rradiation effect.

Introduction

TILECAL is the sampling hadronic calorimeter to be used in the barrel and ex-ended barrel region of the ATLAS detector. It uses iron as passive material, and cintillating tiles as active material. The tiles are readout by **WLS** which lead the ignal to the PMT's, [1] [2].

The high luminosity ($\mathcal{L} = 10^{34} cm^{-2} s^{-1}$) at which the detectors have to operate, imposes stringent requirements in the detector components concerning ra-liation damage. High dose levels of ionizing radiation are expected, especially in he inner detectors and calorimeters, as shown in the isodose map of fig. 1 obtained by Monte-Carlo simulation [3].

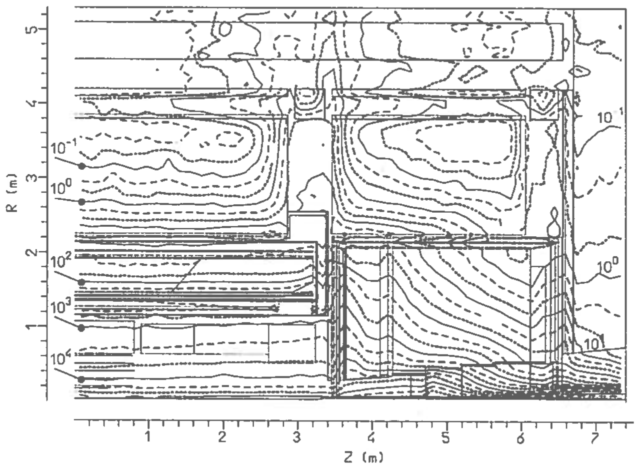

Figure 1: Yearly integrated dose ($Gy/year$) in the inner detector and calorimeters.

In the TILECAL calorimeter, the sensitive components are the scintillator tiles and WLS fibers. The estimated maximum total dose in the barrel hadronic calorimeter is of the order of 23 krad, and 36 krad in the extended barrel [4].

1.1 Low dose rate effects

Some authors observed [5], that low dose rate effects exist in plastic scintillators: the damage of some scintillators and fibers submitted to a given total dose in a short time irradiation (high dose rate), is lower than the damage due to a long time irradiation (low dose rate), for the same total dose.

This matter has been a subject of large controversy. As an example, K. Wick and U. Holm [6], did not observe low dose rate effects in SCSN38 scintillator samples, while E. Biagtan et al. [7], observed low dose rate effects in several types of scintillator samples (including the SCSN38 scintillator). It should be stressed that in both experiments the geometry of the samples tested were similar, and the total dose and dose rate were of the same order of magnitude.

1.2 Parametrization of irradiated fibers

Experimental results for different types of scintillating and WLS plates and fibers, shows that both scintillation and transmission of light decreases with increasing dose. The following parametrization describes satisfactory the radiation damage of astic scintillators and wavelengthshifters [8]:

$$\frac{I_{irr}(x)}{I_{notirr}(x)} = \exp\left(-\frac{D(x)}{\delta} - \alpha \times \int_0^x D(s)ds\right) \tag{1}$$

$D(x)$ is the total dose at a distance x from the readout end of the fiber, δ is e parameter which characterizes the loss in emission, and α characterizes the loss transmission. Radiation hard scintillators and WLS are characterized by high lues of δ and low values of α.

Dose rate studies in WLS fibers irradiated with γ's

l Dosimetry and simulation of dose profile

^{60}Co γ source was used to irradiate the fibers, and dosimetry was made with cugray alanine cables. Fig. 2 shows the dose rate profile measured for the 3 adiation positions, and also the results of a simulation with the EGS monte-carlo de [9], to predict these profiles. The dose profiles obtained are the following: a gligible dose rate between 0 and 50 cm (<200 rad/h for position A and <30 rad/h position B and C), a mean dose rate in the plateau from 50 to 200 cm of) krad/h for pos. A, 1.1 krad/h for pos. B and 0.53 krad/h for pos. C.

2 Radiation damage of WLS fibers

ne following types of WLS fibers, were irradiated [10]:

- Bicron: BCF99-28, BCF99-28 with 600 p.p.m. of UV absorber and BCF91A (all from a 1994 production).
- Kuraray: Y11(200)MS and Y11(200)MS with 1000 p.p.m. of UVA double cladding fibers (from a 1994 production).
- Pol.Hi.Tech: S048-100 N4 (1995 production) and S048-100 with UVA (1994 production, UVA concentration not specified).

All fibers have Polystyrene (PS) base, and PMMA cladding. Kuraray fibers ve a second cladding of fluorinated PMMA. The fibers are 2 m long and 1 mm ameter, and they are polished at both ends. Five fibers of each type were used for ch irradiation position.

Fig. 3 shows the light output ($I(x)$) for some typical fibers, and the fit of e experimental results to:

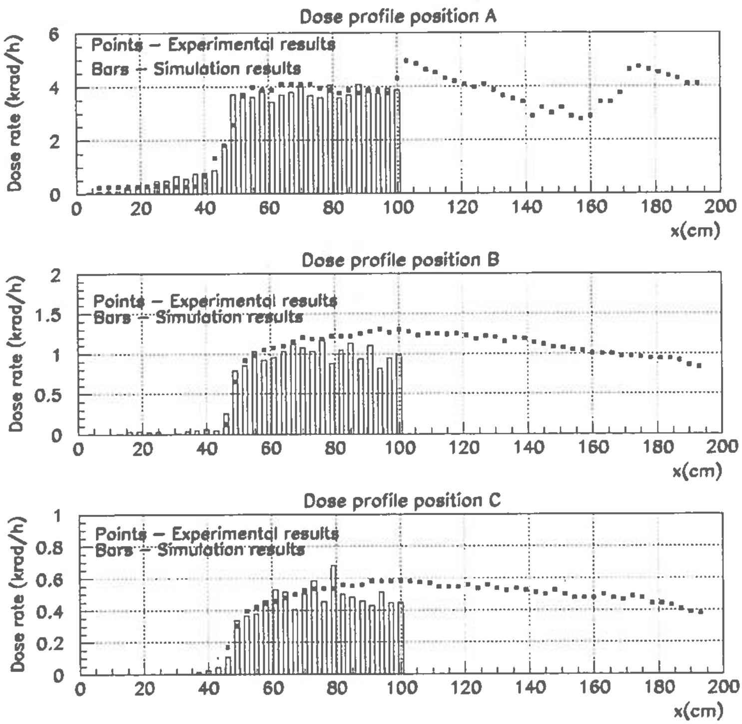

Figure 2: Dose profile for position A (top), B (middle) and C (bottom) - experimental and simulation results.

$$I(x) = I_{0S} \exp\left(-\frac{x}{L_{attS}}\right) + I_{0L} \exp\left(-\frac{x}{L_{attL}}\right) \tag{2}$$

L_{attS} is the short attenuation length, L_{attL} is the long attenuation length and $I_{0T} = I_{0S} + I_{0L}$ is the light yield. The results of this fit are summarized in table 1.

All the fibers have a short attenuation length (L_{attS}) ranging between ~15 and 20 cm. The long attenuation length (L_{attL}) is larger than 300 cm except for the Bicron BCF99-28 fibers, which is ~ 270 cm. The BCF99-28 fibers with UVA have a L_{attL} 25% lower than the corresponding fibers without UVA.

The light yield (I_{0T}) of the BCF99-28 fibers with and without UVA is similar, but the light output at $x = 180$ cm ($I(180)$) is 19% lower for the fibers with UVA. Y11(200)MS fibers with UVA have I_{0T} and $I(180)$ higher by ~ 6% than the same fibers without UVA. The fiber to fiber fluctuations are ≤3.5% in the light yield and light output.

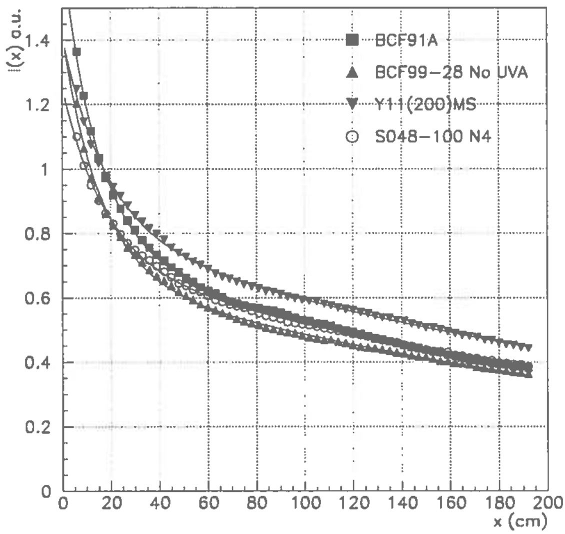

gure 3: Light output for some typical fibers. The superimposed curves are the ults from fitting the function of eq. 2 to the experimental data.

Dose rate effects and recovery of the fibers

e fibers were irradiated with an average total dose of 130 krad for position A and) krad for positions B and C. This corresponds to approximately 4 times the pected dose levels for the TILECAL at $\eta = 1.5$, for 10 years of LHC operation.

Figure 4-left shows the following ratio: $R(x) = \frac{I_{irr}(x)}{I_{notirr}(x)}$, for the fibers hout UVA, 2 months after the end of irradiation in position C (550 rad/h). An or of ±3% is estimated for $R(x)$ due to fiber to fiber fluctuations plus instrumental ects. The Y11(200)MS fibers show a light output loss of 11%, at x = 180 cm. e BCF99-28 fibers have a 18% decrease, and the S048-100 N4 a 38% light output s at x = 180 cm. Similar results are obtained for the other 2 dose rates for all fibers, except the BCF91A samples which show a 10% higher light output loss the lower dose rate position (0.55 krad/h) than in the higher dose rate positions e table 5). This can be due to some further damage in the fibers which was not ntrolled, to some global error in the measurement, or to some natural ageing after adiation.

Tables 2 and 3 show the transmission loss (α) and the emission loss (δ) rameters, respectively. Within the fibers without UVA, the Y11(200)MS fibers the ones with both the highest values of δ (5.3 Mrad) and the lowest values of 4.9$\times 10^{-3}$ (Mrad.cm)$^{-1}$.

For δ = 5.3 Mrad and a total dose of 140 krad the computed emission loss $\sim$ 3%. This means that from a total light output loss of $\sim$ 10% at $x \sim$ 200 cm.

Fiber type	L_{attS} (cm)	L_{attL} (cm)	I_{0T}	$I(180)$
BCF99-28 No UVA	14.6 ± 1.0	271 ± 2	1.674 ± 0.039	0.394 ± 0.012
BCF99-28 600 ppm UVA	15.4 ± 0.6	204 ± 8	1.673 ± 0.043	0.320 ± 0.009
BCF91-A	16.0 ± 0.7	308 ± 10	1.415 ± 0.045	0.376 ± 0.006
Y11(200)MS	18.4 ± 0.4	327 ± 5	1.410 ± 0.026	0.459 ± 0.015
Y11(200)MS 1000 ppm UVA	18.4 ± 0.8	313 ± 17	1.495 ± 0.059	0.482 ± 0.017
S048-100-N4	18.8 ± 1.3	329 ± 17	1.254 ± 0.044	0.398 ± 0.015
S048-100 with UVA	19.3 ± 1.3	333 ± 20	0.789 ± 0.018	0.243 ± 0.005

Table 1: Values obtained for L_{attS} - Short attenuation length, L_{attL} - long attenuation length, I_{0T} - light yield, $I(180)$ - light output at $x = 180$ cm. Mean and RMS of 5 fibers of each type.

Fiber type	$\alpha \times 10^3$ (Mrad cm)$^{-1}$ Position C, Time after irrad.			
	(4 hours)	(1 days)	(7 days)	(2 months)
BCF99-28 No UVA	12.1 ± 0.2	11.3 ± 1.1	11.6 ± 0.9	9.0 ± 0.7
BCF99-28 600 ppm UVA	15.3 ± 0.6	14.7 ± 1.0	15.5 ± 0.6	13.0 ± 1.3
BCF91-A	10.6 ± 0.7	10.3 ± 0.5	12.6 ± 0.3	12.2 ± 0.5
Y11(200)MS	6.7 ± 0.4	6.6 ± 0.5	6.0 ± 0.4	4.9 ± 0.3
Y11(200)MS 1000 ppm UVA	8.1 ± 0.4	7.6 ± 0.4	7.2 ± 0.5	5.8 ± 0.4
S048-100-4	27.7 ± 0.8	26.5 ± 0.4	26.0 ± 0.8	21.4 ± 0.7
S048-100 with UVA	16.9 ± 0.9	15.8 ± 0.5	15.4 ± 0.6	12.4 ± 0.5

Table 2: WLS fibers irradiated in position C (550 rad/h). Each column shows the value of the transmission loss α, after the end of irradiation. Mean and RMS for 5 fibers of each type.

about 7% is due to the transmission loss.

Figure 4-right shows $R(x)$ for the fibers with UVA. The fibers which lose less light are the Y11(200)MS with 1000 p.p.m. of UVA, with 13% decrease at $x = 180$ cm. The S048-100 fibers with UVA have a 22% light output loss, being slightly radiation harder than the BCF99-28 with 600 p.p.m. of UVA (26% of light loss).

Tables 4 and 5 summarize the values of $R(180)$ for all fiber types irradiated in the 3 positions, obtained 4 hours and 2 or 3 months after the end of irradiation, respectively. It can be seen that the addition of 1000 p.p.m. of UVA to the Y11(200)MS fibers, has a negligible effect on the radiation hardness of these fibers. The BCF99-28 fibers with 600 p.p.m. of UVA, lose $\sim$ 7% more light than the ones without UVA. We have not made a direct comparison between S048-100 N4 fibers and S048-100 UVA, since these fibers are not of the same type. S048-

Fiber type	δ (Mrad) Position C, Time after irrad.			
	(4 hours)	(1 days)	(7 days)	(2 months)
BCF99-28 No UVA	3.4 ± 0.9	2.9 ± 0.2	1.9 ± 0.3	4.1 ± 1.7
BCF99-28 600 ppm UVA	3.2 ± 1.3	2.4 ± 0.9	1.8 ± 0.7	3.1 ± 1.1
BCF91-A	2.7 ± 0.9	2.9 ± 0.4	1.2 ± 0.1	1.7 ± 0.2
Y11(200)MS	5.2 ± 1.1	6.5 ± 1.0	3.8 ± 0.6	5.3 ± 0.8
Y11(200)MS 1000 ppm UVA	4.4 ± 0.7	5.5 ± 1.1	3.7 ± 0.5	5.5 ± 1.1
S048-100-4	1.3 ± 0.2	1.6 ± 0.3	1.2 ± 0.1	1.9 ± 0.3
S048-100 with UVA	5.5 ± 2.0	5.8 ± 2.4	3.1 ± 0.9	5.9 ± 3.9

ble 3: WLS fibers irradiated in position C (550 rad/h). Each column shows the lue of the emission loss δ, after the end of irradiation. Mean and RMS for 5 fibers each type.

Fiber type	$R(180)$ 4 hours after irrad.		
	A (4 krad/h)	B (1.1 krad/h)	C (550 rad/h)
BCF99-28 No UVA	0.78 ± 0.02	0.74 ± 0.02	0.78 ± 0.01
BCF99-28 600 ppm UVA	0.72 ± 0.01	0.67 ± 0.01	0.72 ± 0.02
BCF91-A	0.84 ± 0.02	0.76 ± 0.01	0.79 ± 0.02
Y11(200)MS	0.82 ± 0.01	0.83 ± 0.01	0.86 ± 0.02
Y11(200)MS 1000 ppm UVA	0.77 ± 0.01	0.81 ± 0.01	0.84 ± 0.01
S048-100-4	0.39 ± 0.01	—	0.54 ± 0.01
S048-100 with UVA	0.58 ± 0.01	—	0.71 ± 0.01

ıble 4: Ratio $R(180)$. Fibers measured 4 hours after the end of irradiation. Mean d RMS of 5 fibers of each type.

0 UVA fibers (1994 production) are radiation harder than the S048-100 N4 fibers 995 production), which is consistent with the type of fibers used. Since shorter ıvelengths are more sensitive to ionizing radiation, the UV absorber decreases the ect of radiation on the fibers [11].

Comparing tables 4 and 5, it can be seen that all fibers recover part of e initial light output loss, except BCF91A fibers. These fibers present a higher ımage at 2 months after irradiation, than at 4 hours. The reason for this behaviour due to some uncontrolled error in the measurement or to some further damage in e fibers, as explained earlier.

Now we will look for *low dose rate effects*. This experiment was done in ch a way that the total dose and the fiber types, are the same in the 3 irradiation ›sitions. Care was taken so that the only parameter that changed was the *dose te*.

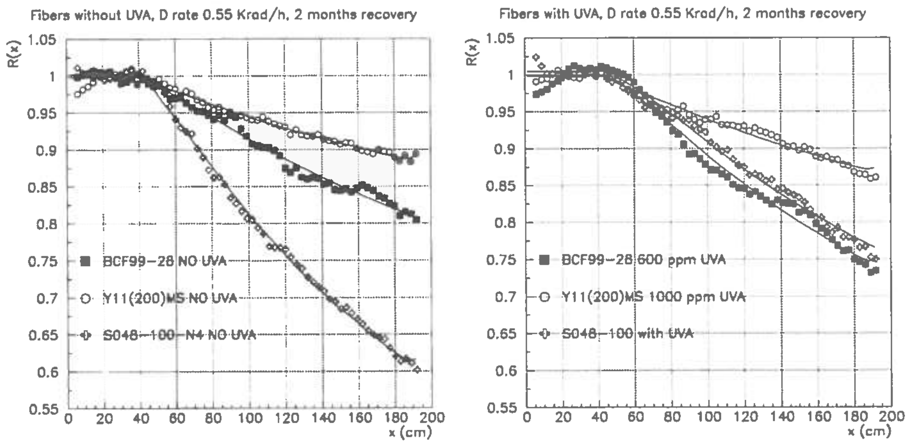

Figure 4: Light output after irradiation over light output before irradiation, for the fibers without UVA (left), and with UVA (right). Fibers irradiated in position C (550 rad/h), measured 2 month after the end of irradiation.

The BCF99-28 fibers with and without UVA, measured 4 hours after the end of irradiation (table 4), show a loss in the light output which is similar for the 3 dose rates. The light output loss of the Y11(200)MS fibers slightly decreases with decreasing dose rate. This difference is negligible for the fibers without UVA and $\simeq 7\%$ for the fibers with UVA. A much higher effect is seen in both S048-100 fibers. The light loss in dose rate A is 15% higher than in dose rate C for the S048-100 N4 fibers, and 11% for the S048-100 UVA fibers.

After 2-3 months of recovery (table 5), the BCF99-28 and Y11(200)MS fibers present a similar light loss in the 3 dose rate positions. The S048-100 fibers with UVA present a similar damage in both dose rates A and C, but the S048-100 N4 fibers show less damage at the lower dose rate C than at the higher dose rate A (difference of 6%).

The decrease in the light output loss with increasing dose rate, can be explained by the competition of two processes: The deterioration by ionizing radiation and the recovery by annealing and diffusion of oxygen into the fiber, see K. Wick in [6]. In this way, after the end of a long term (low dose rate) irradiation, the fibers can present a lower damage due to a longer recovery time, than at the end of a fast term (high dose rate) irradiation. This can explain why after 2-3 months of recovery, a similar damage for the 3 dose rates is observed, or at least a smaller difference (as is the case of S048-100 N4 fibers).

In very long term irradiations the damage due to the natural ageing of the

Fiber type	$R(180)$ 2-3 month after irrad.		
	A (4 krad/h)	B (1.1 krad/h)	C (550 rad/h)
BCF99-28 No UVA	0.86 ± 0.02	0.85 ± 0.02	0.82 ± 0.02
BCF99-28 600 ppm UVA	0.79 ± 0.02	0.77 ± 0.03	0.74 ± 0.02
BCF91-A	0.81 ± 0.01	0.83 ± 0.02	0.74 ± 0.01
Y11(200)MS	0.90 ± 0.01	0.93 ± 0.02	0.89 ± 0.01
Y11(200)MS 1000 ppm UVA	0.87 ± 0.02	0.90 ± 0.01	0.87 ± 0.01
S048-100-4	0.57 ± 0.01	—	0.62 ± 0.02
S048-100 with UVA	0.77 ± 0.02	—	0.78 ± 0.02

ble 5: Ratio $R(180)$. Fibers measured 2-3 month after the end of irradiation. ean and RMS of 5 fibers of each type.

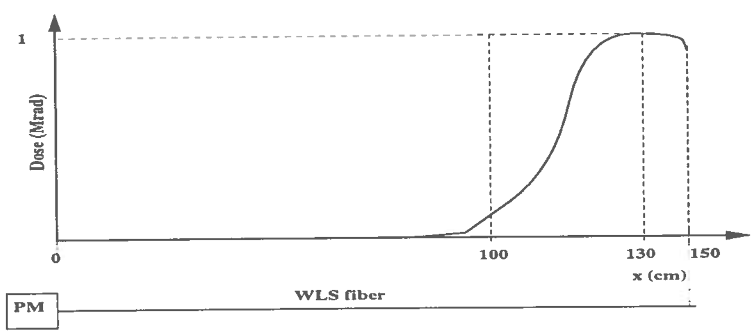

Figure 5: Estimated dose profile in the nuclear reactor.

ers can be of the same order of the damage caused by ionizing radiation, masking is effect.

Radiation damage of WLS fibers irradiated with *neutrons* + γ's

icron BCF91A (1995 production), and Kuraray Y11(200) fibers (1993 production) th with single and double cladding, were irradiated in the mixed field (80% γ's 20% *neutrons*) of a nuclear reactor. Five 150 cm long fibers of each type were sted.

A 'peak' total dose of 1 Mrad at a dose rate of about 1.5 Mrad/h was plied. An estimate of the dose profile is given in fig. 5 [12].

Table 6 summarizes the values obtained for the ratio $R(x)$ at $x = 130$ cm, rresponding to the peak of the dose profile. The recovery process was monitored etween 1 hour and 20 days after the end of the irradiation. Fig. 6-left shows

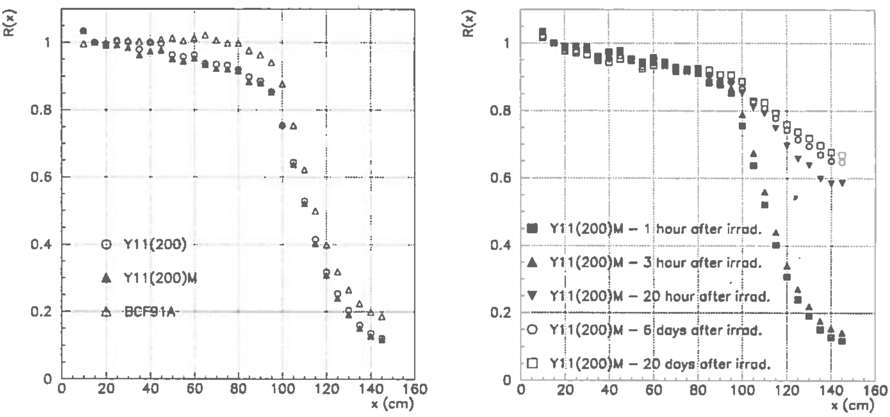

Figure 6: Light output after irradiation over light output before irradiation, for the fibers irradiated with neutrons. First measurement (1 hour) after the end of irradiation (left), fibers Y11(200), Y11(200)M and BCF91A. Recovery of Y11(200)M fibers (right).

the ratio of light output after irradiation over light output before irradiation, for the fibers Y11(200), Y11(200)M and BCF91A measured 1 hour after the end of irradiation, and fig. 6-right the recovery of Y11(200)M fibers.

It can be seen that the initial damage is very strong (of the order of 70-80%). The fibers recover in about 6 days to the permanent damage, since no difference was observed between 6 days and 20 days after the end of irradiation.

The permanent damage is 18% for the Y11(200) fibers (single and double cladding), and somewhat smaller for the BCF91A fibers (11% for double cladding and 14% for single cladding).

Experimental values obtained at high dose rate (table 6), are compared with values computed using α and δ parameters from low dose rate experiments (tables 2 and 3). Table 7 shows the values of $R(130)$ obtained experimentally in the second column, and obtained with the extrapolation from the lower dose irradiation (third column). As can be seen, the experimental and calculated values of this table have a negligible difference, no low dose rate effects are observed, neither effects from the neutron component of the irradiation field. This is consistent with results from other authors [8) 13)].

Fiber type	$R(130) \pm RMS(\%)$, time after irrad.				
	(1 hours)	(3 hours)	(20 hours)	(6 days)	(20 days)
BCF91-A	$0.26 \pm 2.8\%$	$0.30 \pm 3.2\%$	—	$0.76 \pm 0.7\%$	$0.79 \pm 0.7\%$
BCF91-A DC	$0.37 \pm 3.5\%$	$0.40 \pm 3.9\%$	—	$0.76 \pm 2.0\%$	$0.76 \pm 1.7\%$
Y11(200)	$0.20 \pm 2.8\%$	$0.22 \pm 2.8\%$	$0.60 \pm 2.8\%$	$0.70 \pm 1.2\%$	$0.72 \pm 3.7\%$
Y11(200)M	$0.19 \pm 1.6\%$	$0.22 \pm 2.1\%$	$0.64 \pm 1.8\%$	$0.70 \pm 1.0\%$	$0.72 \pm 2.8\%$

ble 6: Ratio $R(130)$. WLS fibers irradiated with *neutron* $+ \gamma$'s. Mean and RMS 5 fibers of each type.

Fiber type	$R(130) \pm RMS(\%)$	
	Experimental (high dose rate)	Calculated from low dose rate results
BCF91-A	$0.79 \pm 0.7\%$	0.73
Y11(200)M	$0.72 \pm 2.8\%$	0.75

ıble 7: Ratio $R(130)$ obtained experimentally (second column), and calculated th α and δ from the lower dose irradiation (third column).

Conclusions

ɔncerning the ^{60}Co γ irradiation we conclude that the Kuraray fibers are radiation ırder than the Bicron and Pol.Hi.Tech fibers. The UV absorber used by Kuraray ıs no effect neither in the optical properties nor in the sensitivity to ionizing ra- ation. On the other hand the UVA used by Bicron, has the effect of lowering the tenuation length and making the fibers less resistant to radiation.

We also conclude that no low dose rate effects are observed for the Polystyrene ıse WLS fibers studied, with a total dose of 130-140 krad and at dose rates rang- g between 550 rad/h and 4 krad/h. It should be emphasized that the maximum :pected dose rate in the TILECAL calorimeter is ~ 1 rad/h, which is 2-3 orders of agnitude lower than the dose rates studied in this work.

In respect to the *neutrons* $+ \gamma$ irradiation we conclude that for a total ɔse of 1 Mrad at a very high dose rate (1.5 Mrad/h), single and multicladding ɔers from the same producer, have similar light output loss. Y11(200) fibers are ightly less resistant than BCF91A fibers. The Kuraray fibers used in this study are ɔm an older production (1993), this can explain the contradiction with the ^{60}Co radiation. No low dose rate effects were observed when compared with the lower ɔse rate irradiation, neither effects due to the neutron component of the irradiation ɔld.

5 Acknowledgments

We thank Dr. E. Andrade from ITN Sacavém for providing the ^{60}Co irradiation facility. To Dr. E. Martinho and Eng.A. Craveira from the RPI Sacavém for helping in the irradiation of the fibers in the nuclear reactor. We thank to U. Holm by helpful discussions about those results. This work was supported by JNICT Portugal.

References

1. ATLAS Collaboration, *ATLAS, Technical Proposal for a General-Purpose pp Experiment at the Large Hadron Collider at CERN.* CERN/LHCC/94-43 LHCC/P2, 15 December 1994
2. F. Ariztizabal et al., Nucl. Instrum. Methods **A349** (1994) 384
3. G. Battistoni et al., ATLAS Internal Note GEN-No-010, 1994
4. A. Amorim, M. David, A. Gomes, A. Henriques, A. Maio "Study of the effect of the radiation on the TILECAL Barrel hadron calorimeter to be used in ATLAS." Presented by A. Henriques, "IV International Conference on calorimetry in High Energy Physics", La Biodola, Elba, Italy September 1993, pp. 669-673
5. Y. Sirois and R. Wigmans, Nucl. Instrum. Methods **A240** (1985) 262
6. K. Wick et al., Nucl. Instrum. Methods **B61** (1991) 472
7. E.Biagtan et al., Nucl. Instrum. Methods **B93** (1994) 296
8. A. Maio, Large Hadron Collider Workshop, vol. III, Aachen, October 1990, pp 625. CERN 90-10, ECFA 90-133, 1990
9. W.R. Nelson, H. Hirayama, D.W.O. Rogers, The EGS4 Code System, SLAC-265 (1985).
10. M. David Master Thesis, Faculdade de Ciências da Universidade de Lisboa, 1996
11. Dr. Meoni from Pol.Hi.Tech, private communication.
12. E. Martinho, "Calculation of total absorbed doses in research reactors", Kernitechnik 61 (1996) 2-3, pp 122, and private communications 1996
13. G. Bub et al., IEEE Trans. Nuc. Sci. vol. 42, No. 4, 1995, 315

VIII – Crystal and Homogeneous Calorimeters

Convener R.Y. Zhu
Co–Chair L. Maiani
Secretary S. Conticelli

Y. Zhu	Convener's Report
Fantoni	The HERMES Electromagnetic Calorimeter
E. Maas	The PbF_2 Calorimeter for the New Parity Violation Experiment at MAMI
Q. Feng	Recent Progresses on Scintillation Crystals in SIC
Novotny	The Electromagnetic Calorimeter TAPS
B. Golubev	NaI(Tl) Calorimeter for the SND Detector at the e^+e^- VEPP–2M
H. Lee	The CsI(Tl) e.m. Calorimeter for the BELLE Experiment at KEK
Seitz	The CsI(Tl) Electromagnetic Calorimeter for the BaBar Experiment at SLAC
A. Shwartz	Calorimetry with CsI Crystals in the Budker Institute of Nuclear Physics
N. Shanahan	The Performance of a New CsI Calorimeter for the KTEV Experiment at Fermilab
Di Salvo	The BGO Calorimeter for the GRAAL Beam
P. Smakhtin	Performance and Tests of the BGO Endcap Calorimeter with Phototriode Readout for the CMD–2 Detector
Diemoz	The Lead Tungstate CMS Electromagnetic Calorimeter
Lecoq	Development of Lead Tungstate Crystals for High Performance Calorimetry
Seez	Test Beam Studies of Lead Tungstate Crystal Matrices for the CMS Electromagnetic Calorimeter
Lebeau	The CMS Electromagnetic Calorimeter Mechanical Design

ıscati Physics Series Vol. VI, (pp. 653–657)
INT. CONF. ON CALORIMETRY IN HEP – Frascati, June 8–14, 1996

(Convener's Report)

CRYSTAL AND HOMOGENEOUS CALORIMETERS

R.Y. Zhu
California Institute of Technologiy, Pasadena, CA 91125

Crystal and Homogeneous Calorimetry Session

e crystal and homogeneous calorimetry session consists of fifteen presentations 'ering eleven calorimeters. It started with two calorimeters made by Cherenkov, non-scintillating, crystals: a conventional lead glass calorimeter for the HERMES ı a novel PbF_2 (lead fluoride) crystal calorimeter for the MAMI. The remain rteen presentations were devoted to calorimetry made by inorganic crystal scin- ators. It started with a presentation on crystal development by a crystal producer: anghai Institute of Ceramics (SIC), and continued with calorimeters made by al- i or alkali-earth halide crystal scintillators. This includes a BaF_2 (barium fluoride) orimeter for the TAPS, a NaI(Tl) (thallium dfoped sodium iodide calorimeter for : SND, CsI(Tl) (thallium doped cesium iodide) calorimeters for the BELLE and :*Bar*, and undoped CsI calorimeters for CMD-2 and KTeV. Finally, calorimeters ıde by oxide crystal scintillators were presented. This includes BGO ($Bi_4Ge_3O_{12}$, muth germanade) calorimeters for the LAGRANGE and CMD-2 and a PWO bWO_4, lead tungstate) calorimeter for the CMS.

Table 1 lists the speaker, his/her institution, the experiment, the type of 'stals used and a brief remark, which indicates either the energy resolution of the orimeter or the main topic of the presentation. The energy resolution ($\delta E/E$) represented in a parametrization of $(a/\sqrt{E} \oplus b \oplus c/E)\%$, where a, b and c are : stochastic, constant and noise terms respectively, E is the energy in GeV, and denotes add in quadrature. Note, the energy resolutions quoted are either the ːasured values reported in this conference or the designed target resolution for .orimeters under development.

Table 1: Crystal and Homogeneous Calorimetry Session

Speaker	Institute	Experiment	Crystal	Remark
A. Fantoni	INFN	HERMES	Lead Glass	$(5.1/\sqrt{E} + 1.5)\%$
F. Mass	Mainz U.	MAMI	PbF_2	$(4.6 \text{ to } 5.4)\%/\sqrt{E}$
X. Feng	SIC	–	–	Crystal Development
R. Novotny	Giessen U.	TAPS	BaF_2	$(0.6/\sqrt{E} + 1.9)\%$
V. Golubev	BINP	SND	NaI(Tl)	5.7% @ 500 MeV
M.H. Lee	KEK	BELLE	CsI(Tl)	$(0.7/\sqrt{E} \oplus 1.8)\%$
R. Seitz	SLAC	*BaBar*	CsI(Tl)	$(1/\sqrt[4]{E} \oplus 1.2)\%$
B. Shwartz	BINP	CMD-2	CsI	CsI Treating/Handling
P. Shanahan	FNAL	KTeV	CsI	1% @ 1 GeV
R. Disolvo	INFN	LAGRANGE	BGO	$(1/\sqrt{E} \oplus 0.4/E \oplus 0.7)\%$
V. Smakhatin	BINP	CMD-2	BGO	0.9 MeV Noise @ 1 T
M. Diemoz	Rome U.	CMS	$PbWO_4$	$(2/\sqrt{E} \oplus 0.5)\%$
P. Lecoq	CERN	CMS	$PbWO_4$	Crystals Project
C. Seez	IC	CMS	$PbWO_4$	Beam Test
M. Lebeau	CERN	CMS	$PbWO_4$	Mechanical Design

2 Crystals Used in High Energy Physics

The choice of crystals for crystal calorimetry in high energy physics is governed by its material properties (density, melting point, breaking stress, machinability and hygroscopicity), shower containment (radiation length, X_0, and Moliere radius, R_M), scintillation properties (light frequency, light yield, decay speed and temperature dependence), and radiation hardness.

Table 2 lists the basic properties of commonly used heavy crystal scintillators: NaI(Tl), CsI(Tl), undoped CsI, BaF_2, CeF_3 (cerium fluoride), BGO and $PbWO_4$. All these crystals, except CeF_3, have been successfully used in high energy physics experiments, as shown in this conference (see Table 1). Again, except CeF_3, all these crystals are available in large quantity. The expected price per cm^3 listed in the table corresponds to typical quotations for an order of more than 10^6 cm^3.

In addition to the crystals scintillators listed in Table 2, PbF_2 is another dense material (7.8 g cm^{-3}, $X_0 = 0.93$ cm $R_M = 2.21$ cm), which is easy to grow (melting point 855°C) and has good mechanical property. Pure PbF_2 is not a scintillator in its common form, and is used as a Cherenkov radiator featured with very fast response time. Attempt to grow orthorhombic structure to make it scintillating have not been successful [1]. However, a recent attempt to dope PbF_2 with rare earth element gadolinium at SIC is successful. Small size PbF_2 crystals doped with 0.15% Gd shows a light yield of 4 to 6 photoelectrons/MeV, which is 3 to 4 times that of the Cherenkov light alone [2]. As shown in Table 1, a PbF_2 calorimeter has been pursued by the MAMI experiment.

Table 2: Properties of Some Heavy Crystal Scintillators

	NaI(Tl)	CsI(Tl)	CsI	BaF_2	CeF_3	BGO	$PbWO_4$
nsity (g/cm^3)	3.67	4.51	4.51	4.89	6.16	7.13	8.3
lting Point (°C)	651	621	621	1280	1460	1050	1123
diation Length (cm)	2.59	1.85	1.85	2.06	1.68	1.12	0.9
liere Radius (cm)	4.8	3.5	3.5	3.4	2.6	2.3	2.0
eraction Length (cm)	41.4	37.0	37.0	29.9	26.2	21.8	18
fractive Index[a]	1.85	1.79	1.95	1.50	1.62	2.15	2.2
groscopicity	Yes	slight	slight	No	No	No	No
minscence[b] (nm)	410	560	420	300	340	480	510
Peak)			310	220	300		510
cay Time[b] (ns)	230	1300	35	630	30	300	50
			6	0.9	9		10
lative LY[b,c]	100	45	5.6	21	6.6	9	0.3
			2.3	2.7	2.0		0.4
.Y)/dT[b,d] (%/°C)	~0	0.3	−0.6	−2 ~0	0.14	−1.6	−1.9
ce ($/cm³)	1 to 2	2	2.5	2.5	-	7	2[e]

At the wavelength of the emission maximum.
Top line: slow component, bottom line: fast component.
Measured with a PMT with a bialkali cathode.
At Room temperature.
Quoted by russian industry to the CMS.

Crystal Calorimeters in High Energy Physics

storically, large arrays of scintillating crystals have been assembled for precision ergy measurement for photons and electrons in physics. The physics discovery tential of the crystal calorimetry was first demonstrated by the Crystal Ball de- tor [3] through its study of radiative transitions and decays of the Charmonium nily. Over the last decade, following the Crystal Ball and CUSB [5] experiments, ger crystal calorimeters have been constructed, and their use has been a key fac- in the successful physics programs of the L3 experiment at LEP [6], of the EO II at CESR [7] and of the Crystal Barrel at LEAR [8]. In this session, we many more crystal calorimeters designed and constructed for nuclear and high ergy physics. The flourish of total absorption calorimetry is due to the intrinsic tures of the calorimetry of this type: its superb energy resolution, superp detec- n efficiency and compact mechanical structure. The energy resolution achieved crystal calorimeters reported in this session can not be matched by any other hnology, especially at the low end of the energy domain.

As reported in this session, new crystal calorimeters have been designed, d are under development for the next generation of high energy physics experi- nts. Table 3 summarizes designed parameters for these crystal calorimeters. The commom physics goal of the KTeV at FNAL [9], the *BaBar* at SLAC [10] and the BELLE at KEK [11] is the nature of CP violation. This physics requires superb energy resolution and detection efficiency for photons and π^0's to reconstruct the B, charm and K mesons, charmed baryon and τ leptons. The crystal calorimeters are the key subsystem for these experiments. We are pleased to see excellent work done by these collaborations. For example, the *BaBar* and BELLE have devoted major effort in reducing the electronics noise to less than 200 keV level by using silicon photodiode readout, leading to a greatly expanded low energy reach.

Table 3: Parameters of Recently Designed Crystal Calorimeters

	KTeV FNAL	*BaBar* SLAC	BELLE KEK	CMS CERN
Crystal Type	CsI	CsI(Tl)	CsI(Tl)	$PbWO_4$
B-Field (T)	–	1.5	1.0	4.0
Inner Radius (m)	–	1.0	1.25	1.44
Number of Crystals	3,100	6,580	8,800	110,000
Crystal Depth (X_0)	27	16 to 17.5	16.2	25
Crystal Volume (m^3)	1.8	5.9	9.5	13
Light Yield. (p.e./MeV)	20	5,000	5,000	2
Photosensor	PMT	Si PD	Si PD	APD[a]
Gain of Photosensor	4,000	1	1	50
Noise/Channel (MeV)	small	0.15	0.2	30
Dynamic Range	10^4	10^4	10^4	10^5

a Avalanche photodiode.

The most challenging calorimeter reported in this session is the $PbWO_4$ crystal calorimeter for the CMS experiment at the LHC. Following extensive research and developments carried out by the physics community pursuing a precision electromagnetic calorimeter aiming at searches for the Higgs boson in the intermediate mass region [13, 14, 15, 16], the CMS collaboration decided to construct a $PbWO_4$ calorimeter consisting of 110,000 crystals of 13 m^3 [12]. As discussed by several speakers in this session, the main challenge of this calorimeter is much beyond its unprecedented scale, rather in the quality control of the mass produced crystals.

4 New Challenge for Crystal Calorimetry in Future Colliders

Despite much experience and expertise accumulated in the last decade, crystal calorimetry in high energy physics is facing a new challenge [17]. Crystals in future high energy colliders will operate in a severe radiation environment caused by increased center of mass energy and luminosity. While the dose rate for CsI(Tl) crystals at PEP-II or KEK B Factory would reach a few rad/day, the corresponding dose rate at LHC would reach 1,000 rad/day. Without a stringent quality control 'stals produced by crystal producers would suffer from significant radiation dam- : in this environment, and thus cause much degraded performance. In order to ıintain crystal's resolution *in situ*, the crystals must be radiation hard.

Much effort has been devoted to the crystal quality control, especially to : investigation and improvement of crystal's radiation resistance. In this confer- :e, both *BaBar* and BELLE experiments showed their stringent specifications CsI(Tl) crystals. Currently mass produced CsI(Tl) crystals satisfy these speci- ations. In this session, we are also pleased to see that significant progress on the ality of CsI(Tl) crystals produced at SIC has been achieved after a systematic zD program.

On the other hand, full size $PbWO_4$ crystals suffer from non-negligible ra- ıtion damage after a radiation dose as low as 10 rad. The investigations reported this conference show significant progress in our understanding on the $PbWO_4$ liation tolerance and the approach to improve its radiation susceptibility. A sys- natic research and development program, however, is certainly needed to further ntrol and improve the quality of mass produced $PbWO_4$ crystals, so that the su- rb energy resolution promised by the $PbWO_4$ crystals may be realized *in situ* at IC.

eferences

. D. Anderson *et al.*, *IEEE Trans.* **NS-43** 1303 (1996).

. C. Woody *et al.*, *Nucl. Instr. and Meth.* **A342** 347 (1994).

. M. Oreglia *et al.*, *Phys. Rev. D* **25** 2295 (1982).

. E. Bloom and C. Peck, *Ann. Rev. Nucl. Part. Sci.* **33** 143 (1983).

. T. Bõringer *et al.*, *Phys. Rev. Lett.* **44** 1111 (1980); G. Mageras *et al.*, *Phys. Rev. Lett.* **46** 1115 (1981).

. L3 Collaboration, *Nucl. Instr. and Meth.* **A289** 35 (1990).

. Y. Kubota *et al.*, *Nucl. Instr. and Meth.* **A320** 66 (1992).

. E. Aker *et al.*, *Nucl. Instr. and Meth.* **A321** 69 (1992).

. K. Arisaka *et al.*, *KTeV Design Report*, **FN-580**, January (1992).

. *BaBar* Collaboration, *Technical Design Report*, **SLAC-R-95-457** (1995).

. BELLE Collaboration, *A Study of CP Violation in B Meson Decays — Technical Design Report*, **KEK Report 95-1** (1995).

. *Compact Muon Solenoid Technical Proposal*, CERN/LHCC 94-38 (1994).

. *L* Letter of Intent to the SSC Laboratory*, (1990).

. *GEM Letter of Intent*, **SSCL SR-1184**, (1991).

. *Compact Muon Solenoid Letter of Intent*, CERN/LHCC 92-3 (1992).

. *L3P Letter of Intent*, CERN/LHCC 92-5 (1992).

. R.Y. Zhu *et al.*, *Nucl. Phys.* **B44** 547 (1995).

ıscati Physics Series Vol. VI, (pp. 659–668)
INT. CONF. ON CALORIMETRY IN HEP – Frascati, June 8–14, 1996

THE HERMES ELECTROMAGNETIC CALORIMETER

H. Avakian, N. Bianchi, G.P. Capitani, E. De Sanctis, A. Fantoni, V. Giourdjian, R. Mozzetti, V. Muccifora, M. Nupieri, A.R. Reolon, P. Rossi
\FN - Laboratori Nazionali di Frascati, P.O.Box 13, I–00044 Frascati (Roma) Italy

J.F.J. van den Brand[1,2], M. Doets[1], T. Henkes[1], M. Kolstein[1]
[1]NIKHEF, Kruislaan 411, 108 SJ Amsterdam, The Netherlands
[2]Vrije Universiteit Amsterdam, Rm. T–269, de Boelelaan 1081 hv, NL-1081 HV

A. Airapetian, N. Akopov, M. Amarian, R. Avakian, A. Avetissian, V. Garibian, S. Taroian
YPI, Alikhanian Brothers St. 2, Yerevan AM-375036, Armenia

ABSTRACT

description of the HERMES electromagnetic calorimeter is given. The measured aracteristics on the test beams and after one year data taking are presented.

Introduction: the HERMES experiment

HERMES is a new experiment at HERA (DESY) designed to study in a :cise and complete way the spin structure of the nucleon by deep inelastic scating of polarized electrons off polarized protons and neutrons [1]. The HERMES ector [2] is installed in the HERA East Hall interaction region. It consists of pectrometer magnet and a PID detector and is able to measure the scattered ctron and the total hadronic final state in a wide kinematic range and with good gular and momentum resolutions. For a detailed description of the experiment ref. 3).

By measuring the cross section asymmetry, i.e. the difference of scattering babilities of electrons off nucleons with spin parallel or antiparallel to the spin of incident electrons, HERMES determines the spin structure functions g_1 and g_2 a wide range of x and Q^2, so that fundamental sum rules are carefully evaluated. reover, by measuring semi-inclusive channels HERMES is able to disentangle the n contributions of gluons and the quarks angular momenta, with good chances of ving the spin puzzle [4].

HERMES makes use of two novel techniques: a longitudinally polarized ctron beam in a storage ring and internal polarized gas targets. The HERA beam ıaturally polarized in the transverse direction due to the Sokolov-Ternov effect [5], then spin rotators are used to rotate the spin into the longitudinal direction [6] and back to the transverse one, respectively before and after the interaction region. The internal gas targets have the important advantage of being pure atomic species, so they can be polarized to a high degree without or with only small dilution by unpolarized nuclei; they also allow for rapid polarization reversal and are therefore an ideal choice to minimize systematic errors which originate from time dependent instrumental effects.

2 The HERMES calorimeter: requirements and description

The function of the calorimeter is: *i)* to provide a first level trigger on scattered electrons, based on $\geq$3.5 GeV energy deposition in a localized spatial region; *ii)* to separate electrons from pions with a rejection factor of $\geq$10 at the first level trigger and $\geq$100 at the off-line analysis in the energy range of 4$\div$10 GeV; *iii)* to measure the energy of electrons and photons from radiative processes or from π^0 decays and *iv)* to give a coarse position measurement. The solution chosen to meet these requirements consists of 840 radiation resistant F101 lead glass (LG) blocks arranged in a two wall configuration (one wall above and the other below the beam) with PMT viewing from the rear, as shown in fig. 1.

Each wall is composed of 420 identical lead-glass blocks, which have an area 9×9 cm^2 and a length of 50 cm (about 18 radiation lengths) and are stacked in a 42×10 array. This cell size meets the requirements that $\approx$90% of the shower is contained in the cell for an axially-injected electron and that the cell occupancy is $\leq$1 for the majority of triggers. The blocks were mirror polished, wrapped with 2 mils thick aluminized mylar foil and covered with a 5 mils thick tedlar foil to provide light isolation. Each block is coupled to a 3″ photomultiplier Philips XP3461 (PMT) with a silicon glue (SILGARD 184) with refraction index 1.41.

A μ-metal magnetic shield surrounds the PMT. A surrounding aluminum tube, that is housing the μ-metal and providing light-tightness, is fixed to a flange, which is glued to the surface of the lead glass. This flange is made of titanium matching the thermal expansion coefficient of F101. Measurements of the radiation hardness of F101 LG blocks for γ rays [7] and for high energy hadrons [8] have shown that an accumulated dose of more than 10^4 rad produces a degradation of transmittance less than $1/e$ over the lead glass length. After irradiation by 10^6 rad the F101 turned visibly bright brownish with a tint of red and showed a saturation in recovery. Thus the F101 LG is 10$\div$50 times less sensitive to radiation damage than SF2 lead-glass [9], depending on dose and light wavelength. This is due to the contribution of cerium which as a drawback worsens the optical transmission characteristics. The properties of this lead glass are listed in tab. 1.

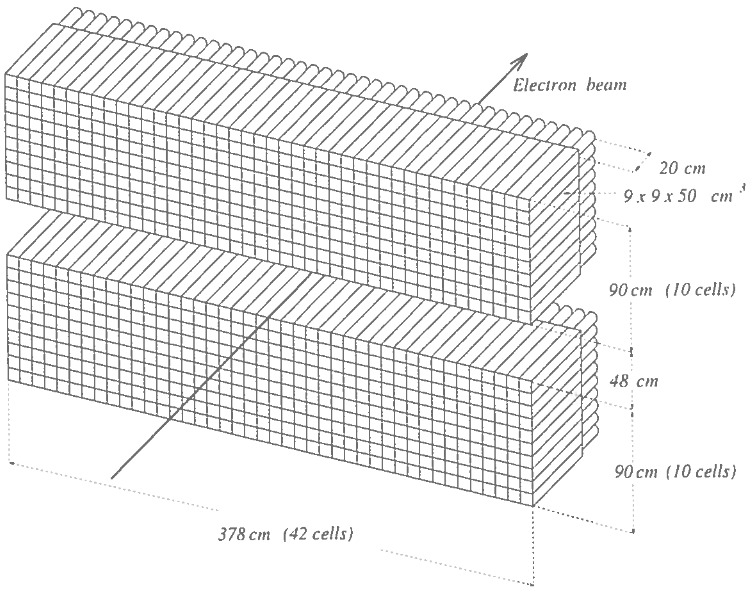

Figure 1: Isometric view of the HERMES calorimeter.

The light transmittance was measured for different F101 LG block: as the ɔrking wavelengths of light exceed 500 nm, the spectral distribution well matches e spectral response of the green extended phototube Philips XP3461 chosen.

Measured characteristics of the calorimeter

Measurements with 1÷30 GeV/c [10] electron beams have been performed CERN and DESY with a 3×3 array of counters with the addition of a preshower ɛtector, consisting of 1 cm of lead + 1 cm of plastic scintillator. This configuration ːovides information on the longitudinal development of the electromagnetic shower ıd then allows a better rejection of pions. At DESY each lead glass block was so calibrated and equalized to ≈1% in a 3 GeV/c electron beam positioned at the .odule center.

1 Linearity of the response

he absolute energy calibration measurements showed a good linearity over the hole measured energy range, as represented in fig. 2: the linear fit reproduces the ata better than 1%.

Table 1: Chemical composition and physical properties of the F101 LG.

Chemical composition (weight%)	
Pb_3O_4	51.23
SiO_2	41.53
K_2O	7.0
Ce	0.2
Radiation length (cm)	2.78
Density (g/cm^3)	3.86
Critical energy (MeV)	17.97
Moliere radius (cm)	3.28
Refraction index	1.65
Thermal expansion coefficient (C^{-1})	$8.5 \cdot 10^{-6}$

3.2 Spatial and angular dependence of the response

The energy deposition in adjacent blocks was studied as a function of the impact point for electrons hitting the front surface of the lead-glass counters at a right angle. The sum of the pulse heights obtained by the two adjacent counters resulted constant within 2%, as shown in fig. 3. The sharing of the shower into neighboring modules can be exploited to determine the impact point of the incoming photons with higher precision than expected from the lateral dimensions of the modules.

3.3 Energy resolution

In fig. 4 is shown the measured energy resolution as a function of the incident electron energy in the range 1÷30 GeV: the dotted curve is a fit of the data to the form $\sigma(E)/E\ [\%] = A/\sqrt{E\,[GeV]} + B$. The obtained values for A and B are 5.1±1.1 and 1.5±0.5 respectively, similar to the values obtained for other large lead glass calorimeters which used more transparent lead glass blocks [11].

3.4 Pion-electron identification

In fig. 5 is shown the pion rejection factor measured for a single block and for a 95% electron detection efficiency. As seen the rejection with the preshower is $\approx (4\pm2) \cdot 10^{-4}$.

3.5 Position measurement

The calorimeter provides also a coarse position measurement for the scattered electrons. In fig. 6 is shown the distribution of the difference between the position at the

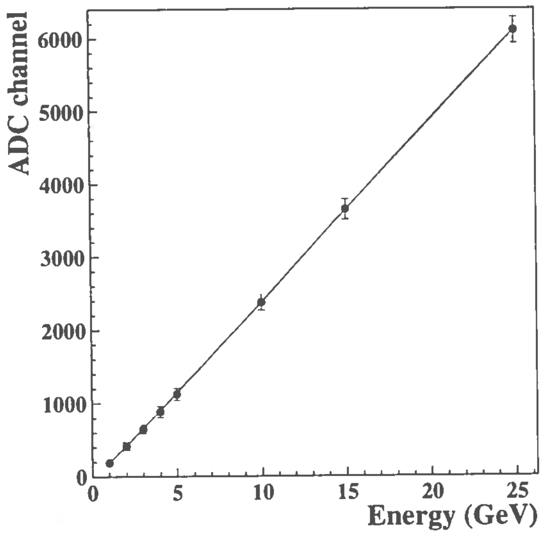

gure 2: Linearity of the LG block response versus the incident energy: the solid
.e is a linear fit to the data $E = 0.32 + 0.40 \times 10^{-2} ADC$.

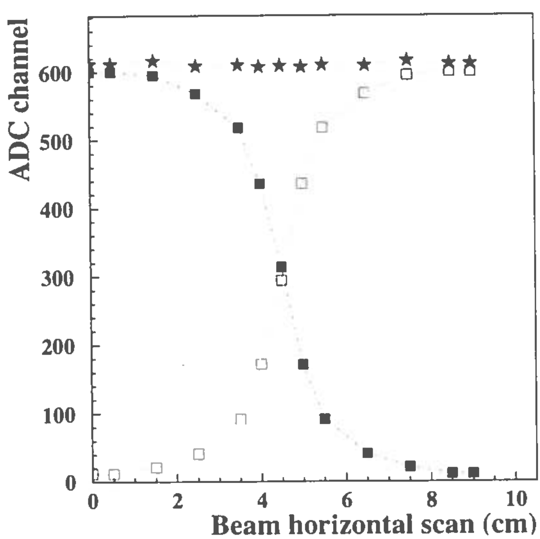

igure 3: Energy deposition in adjacent blocks. The positions 0 cm and 9 cm
›rrespond to the centers of the left and right blocks respectively. Solid squares:
ft block; open squares: right block; stars: sum of two blocks.

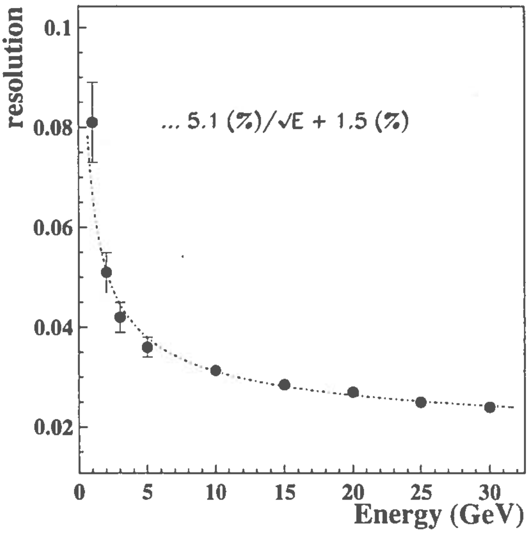

Figure 4: Energy resolution of calorimeter $\sigma(E)/E$ versus the energy: the data are compensated for the energy deposited in the preshower. The error bars take into account the statistical accuracy and the beam resolution. The line shows the parameterization described in the text.

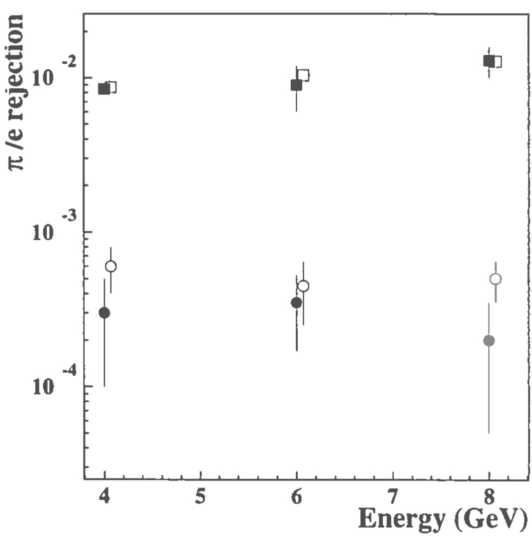

Figure 5: Pion/electron rejection in a single block of the calorimeter and preshower corresponding to an electron efficiency of 95% . Filled and empty points are experimental results and simulation respectively. Squares refer to the case of calorimeter only and circles to the case of calorimeter and preshower. The simulation results are plotted at energy values slightly shifted, to make them more visible.

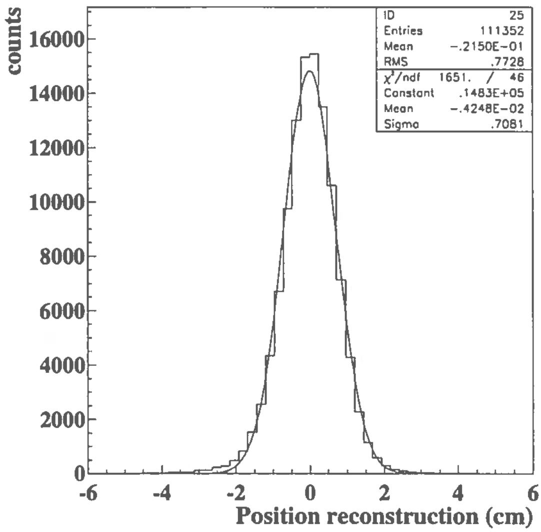

;ure 6: Distribution of the difference between the positions determined by the :ctrometer and measured by the calorimeter.

orimeter face calculated from the tracks determined by the magnetic spectrom- :r and the position of the cluster center, reconstructed from the relative energy ıring between neighboring cells. As it is shown, the resolution of the position :onstruction is $\approx$0.7 cm.

Uniformity of the response of the counters

fig. 7 is plotted the mean value of the E/p distribution, measured on each counter all the data collected in 1995, being E and p respectively the energy of electrons ›vided by the calorimeter and the momentum measured by the spectrometer. The ıtral value of the distribution is 1.003 with a rms width of 0.011, which means a iformity of response of the counters within 1%.

Stability in time and radiation damage

›m the mean value of the E/p distribution, measured for each run for the counters ırest to the beam (that have more events) it resulted a stability in time of the ponse within 1%; this value also takes in account the contribution of the radiation mage produced in one year data taking, so this means that the effect of the

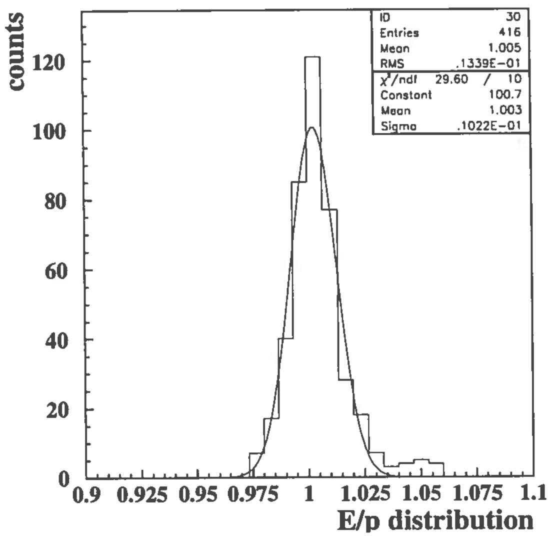

Figure 7: E/p distribution measured on each counter for all the runs collected during the first year data taking period.

radiation damage is negligible.

4 Physics results: semi-inclusive events in the calorimeter

The main physics potential of HERMES resides in the hadronic final state determination in semi-inclusive measurements. The latter yield informations on u_v and d_v, while the spin asymmetry can be used to extract various quark contributions to the nucleon spin. The following numbers of hadrons were identified in 1995 data taking: $\approx$5000 K^+ and $\approx$6000 K^-, 1000$\div$3000 K_s, $\approx$1000 Λ, $\approx$6000 ρ, $\approx$330000 π^+, $\approx$220000 π^-, $\approx$100000 π^0 and $\approx$1000 η. The calorimeter plays an important role in the identification of π^0, ρ and η, because they decays into photons which are identified as energetic clusters in the calorimeter. In fig. 8 *a*) is shown the invariant mass distribution for two cluster events in the calorimeter, with the π^0 and η peaks clearly visible. Fig. 8 *b*) shows the π^0 invariant mass obtained requiring an intercluster distance between 20 and 75 cm and a difference of the two γ energy less than 3 GeV. Fitting the distribution with a Gaussian function, the value M_{π^0}=(.1357$\pm$.0004) GeV with a σ=(.0129$\pm$.0004) GeV was obtained.

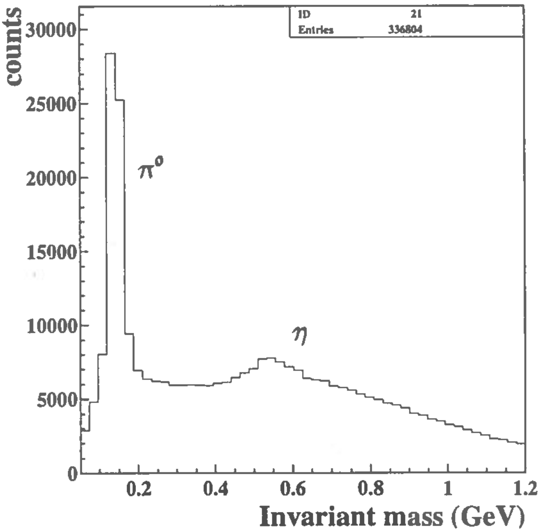

(a)

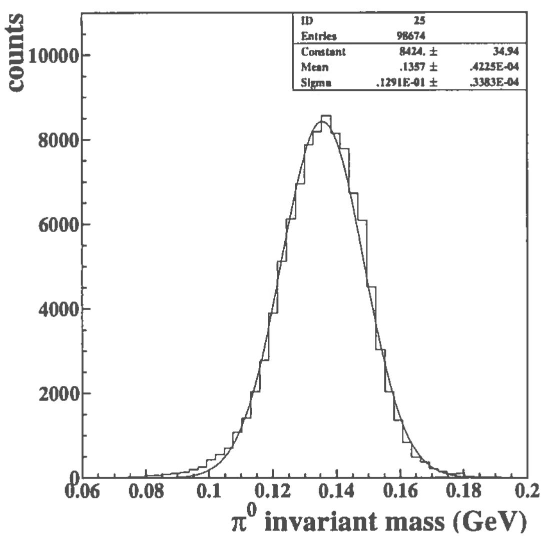

(b)

igure 8: Invariant mass distributions in the calorimeter: a) peaks of π^0 and η; b) ıass of π^0 obtained from the requirements described in the text.

5 Conclusions

The lead glass calorimeter is an essential part of the HERMES apparatus, providing the trigger of the experiment in conjunction with a scintillator hodoscope and taking part to the particle identification. Moreover, it is fundamental for neutral particles identification in semi-inclusive measurements. The measured characteristics of the calorimeter are: *i)* an energy response to electrons linear within 1%, over the energy range $1 \div 30$ GeV; *ii)* an energy resolution $\sigma(E)/E\ [\%] = 5.1/\sqrt{E\,[GeV]} + 1.5$; *iii)* a π^-/e rejection of $\approx (4 \pm 2) \cdot 10^{-4}$, in combination with a preshower, for a 95% electron detection efficiency; *iv)* a spatial resolution of the impact point of about 0.7 cm; *v)* a uniformity of the response of the counters and stability in time within 1%.

References

1. HERMES Collaboration, Proposal DESY-PRC **90/01** (1990);
2. HERMES Collaboration, Technical Design Report, DESY-PRC **93/06** (1993);
3. M. Düren, habilitation thesis, HERMES internal note **95-02** (1995);
4. V. Hughes and C. Cavata, *Symposium on the internal spin structure of the nucleon* - Yale University 1994, World Scientific (1995);
5. A.A. Sokolov and I.M. Ternov, Sov. Phys. Dokklady **8**, 1203 (1964);
6. D.P. Barber et al., Phys. Lett. **B343**, 436 (1995);
7. M. Kobayashi et al., KEK internal report **93-178** (1993);
8. A.V. Inyakin et al., NIM **215**, 103 (1983);
9. M. Holder et al., NIM **108**, 541 (1973);
10. H. Avakian et al., in print to NIM A (1996);
11. K. Ogawa et al., NIM **A243**, 58 (1986); T. Sumiyoshi et al., NIM **A271**, 432 (1988); H. Stroher et al., NIM **A269**, 568 (1988); G.T. Bartha et al., NIM **A275**, 59 (1989); H. Baumeister et al., NIM **A292**, 81 (1990); L. Bartoszek et al., NIM **A301**, 47 (1991); W. Brückner et al., NIM **A313**, 345 (1992).

ascati Physics Series Vol. VI, (pp. 669–678)
INT. CONF. ON CALORIMETRY IN HEP – Frascati, June 8–14, 1996

THE PbF_2 CALORIMETER FOR THE NEW PARITY VIOLATION EXPERIMENT AT MAMI

F.E. Maas, K. Grimm, D. v.Harrach, H. Hofmann, J. Hoffmann, P. Hartmann, T. Hammel, E. Kabuß, S. Köbis, A. Lopes Ginja
Institut für Kernphysick,Becherweg 45. D–55099 Mainz

R. Djilkibajev, V. Lobashev
Moscow Institute for Nucelar Research

I. Altarev
St. Petersburg, Institute for Nuclear Research

ABSTRACT

measurement of the parity violating asymmetry in elastic scattering of polarised ectrons on protons is currently set up at the MAMI facility in Mainz. The expected ymmetry is around 8×10^{-6} and the projected total accuracy is 4×10^{-7} (5%). ich a measurement will reveal the contribution of strange quarks to the Dirac form ctors of the nucleon to an accuracy of $\delta(F_1^s + 0.13 * F_2^s) = 0.02$.
large solid angle (0.7 sr), homogeneous crystal calorimeter will be build consisting 1022 PbF_2 crystals. The expected total event rate in the detector of about 0 MHz requires fast analogue cluster recognition with spatial and temporal pile-rejection. An energy resolution of about $3.5\%/\sqrt{E}$ with an integration time 20 ns is aimed for and will allow a discrimination of elastic scattering against elastic processes which are expected to be 10 times higher in rate. We report on cent test results concerning energy resolution and time behavior made with PWO, bF_2 and liquid xenon at the continuous 855 MeV MAMI electron beam.

Introduction

here is strong experimental evidence, that the strange quark-anti-quark pairs in e nucleon give important contributions to the properties of the nucleon: For example, the scalar density of strange quarks inside the nucleon $< N|\bar{s}s|N >$ can a complicated analysis be related to the σ_N^π term measured in pion scattering. n evaluation of the σ_N^π term yields for the contribution of the strange sea to the icleon mass $\delta m_s = m_s < N|\bar{s}s|N >$ that δm_s can be about 150 MeV [1]. Another range nucleon matrix element $< N|\bar{s}\gamma_\mu\gamma_5 s|N >$ which is directly correlated to the olarised structure function g_1 has been measured in deep inelastic muon scattering

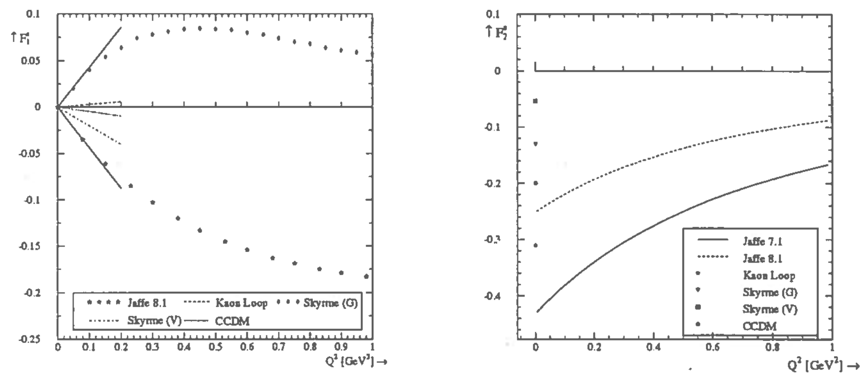

Figure 1: Theoretical prediction for the strange contribution F_1^s and F_2^s to the vector form factors. For the new Mainz parity violation experiment a sensitivity of $\delta(F_1^s + 0.13 * F_2^s) = 0.02$ at the optimum Q^2 of 0.227 GeV^2 is aimed for.

by the EMC collaboration. The contribution of the strange quark sea to the nucleon spin Σ_s has been determined to Σ_s=-0.12±0.04±0.04 [2].
The different coupling in weak and electromagnetic interaction renders the possibility to separate the strange contribution to the form factors of the nucleon, assuming strict SU(2) isospin symmetry and provided the electric (G_E) and magnetic (G_M) form factors of the proton and neutron are known precisely. Weak interaction introduces a parity violating (pv) asymmetry in the cross section of the scattering of polarised electrons on unpolarised protons. The largest contribution to the asymmetry at energies much smaller than m_Z comes from the interference of photon and Z_0 exchange and is of the order Q^2/m_Z^2. The asymmetry without a contribution of strangeness (A_0) can be calculated at tree level and has the form [3]:

$$A_0 = -\frac{G_F Q^2}{\sqrt{2}\alpha} \frac{G_E^p}{\epsilon(G_E^p)^2 + \tau(G_M^p)^2} K \tag{1}$$

$$K = \frac{1}{4}\epsilon(aG_E^p - G_E^n) + \frac{1}{4}\tau\mu_p(aG_M^p - G_M^n) + \frac{1}{2}\omega\mu_p G_A^3 \tag{2}$$

$$\delta = \frac{1}{2}a\sqrt{1-\epsilon^2}\sqrt{(1+\tau)\tau} \tag{3}$$

$$\epsilon = (1 + 2(1+\tau)\tan^2\frac{\theta}{2})^{-1} \tag{4}$$

$$a = (1 - 4\sin^2\theta_W) \tag{5}$$

Radiative corrections to equ. 2 are at the 10% level [3]. Here, as in other low energy experiments, $\sin^2\theta_W$ is taken as 0.212 [4]. The strange contribution can be written an additive correction to A_0

$$A = A_0 * (1 - \frac{(\epsilon + \tau\mu_p)F_1^s + (\tau(\mu_p - \epsilon)F_2^s + (\omega\mu_p G_A^s)}{4K}). \tag{6}$$

; the Mainzer Microtron (MAMI) the maximum electron energy is at present ound 855 MeV. At this energy, a measurement of the asymmetry at a scattering gle θ=(35 ± 5)^o or equivalently at $Q^2 = 0.227$ GeV$^2/c^2$ gives the fastest answer the question whether there is a strange contribution. The value for A_0 at 35^o 8 × 10^{-6}. At this kinematics, the asymmetry is most sensitive to F_1^s with an lmixture of 0.13×F_2^s and 0.03×G_A^s. Theoretical predictions for F_1^s and F_2^s from fferent authors are summarised in figure 1. In some cases the strange radius only :. the slope of the form factor at Q^2=0 GeV^2 has been calculated and displayed.

Experimental Setup

1 Principle of the Measurement

he parity violating experimental asymmetry A_{exp} in the scattering of polarised ectrons on unpolarised protons will be obtained by measuring the number of elastic attered electrons for left handed($N_\uparrow$) and right handed($N_\downarrow$) electrons as in equ.,7.

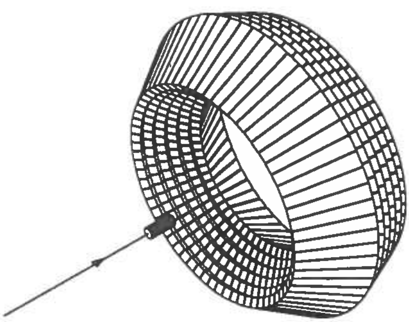

igure 2: Schematic of the calorimeter in the Mainz parity violation experiment. 'he barrel like structure will consist of 7 × 146 crystals.

$$A_{exp} = \frac{N_\uparrow - N_\downarrow}{N_\uparrow + N_\downarrow} \tag{7}$$

'or normalisation, the luminosity for each electron spin direction will be measured eparately. At an electron beam current of 20 μA and 80% electron polarisation, the rojected statistical error of 3% requires 700 h of data taking time using a 10 cm iquid hydrogen target and a detector of 0.7 sr solid angle. A technical proposal of an experimental setup has been presented in 1994 [5]. After detailed simulations and background studies it has been found, that a single arm measurement of the scattering angle and energy of the elastic scattered electron alone is sufficient to discriminate against particles from inelastic scattering which are about 10 times higher in rate [6]. The expected total rate from elastic scattered electrons on the planned detector will be $10^7 e^-/\mathrm{s}$ and the rate due to particles from inelastic scattering will be around $10^8/\mathrm{s}$.

Here we will concentrate on the description of the calorimeter and the tests with different materials we have performed in Mainz. Other parts of the experiment, like the electron source, the polarimeter, the luminosity monitor and the electron beam monitor system will not be described here.

A schematic of the planned calorimeter is shown in fig.2. It will have full azimuthal symmetry (0.7 sr solid angle) and will be formed by 7×146 single modules with a size of $\frac{4}{3}$ Molière radii (r_M) and at least 13 radiation lengths (X_0). A shower caused by an elastic scattered electron will be contained almost completely in a cluster of 3×3 modules. The high event rate and the high total number of events requires fast on-line data acquisition. Events will not be stored for off-line analysis, but will be directly sorted into histogramms. The light produced in the single modules will be read out by photomultipier tubes and the signal of every module will be summed with it's 8 neighbours in 1022 analogue preprocessor circuit boards. The board will be self triggered on the deposited energy. Temporal and spatial pile-up will veto the digitisation and the subsequent on-board histogramming. The histogramms will be read out and stored for off-line analysis. A first prototype of the electronics has been tested succesfully.

High density, high Z compact calorimeter materials which allow a small front surface (small r_M) as well as a short light decay time are necessary for the parity violation experiment in order to avoid large systematic corrections in A_{exp} due to pile up. An integration gate in the energy measurement $\sim$ 20 ns is aimed for. From the physics point of view and also from the availability (producer and price) only few materials fit to the requirements of this experiment. We have tested 2 Scintillators and one Čerenkov radiator : Lead tungstenate (PWO), which has been chosen by the CMS collaboration, liquid xenon and lead fluoride (PbF_2). A Čerenkov radiator is naturally faster than a scintillator, and in addition the rate from inelastic scattering is lower due to the Čerenkov light production threshold of slow particles like charged pions, but the light output is much less compared to a scintillator.

2.2 Lead Tungstenate (PWO)

Lead tungstenate (PWO) has a Molière radius of 2.2 cm and a radiation

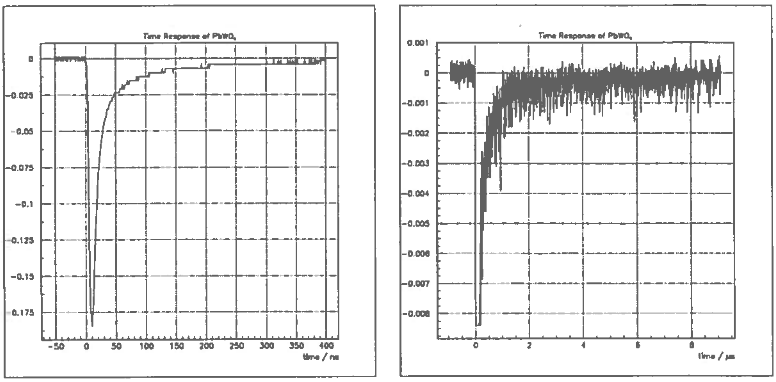

gure 3: A typical PMT signal from a 21 mm × 21 mm × 160 mm lead tungstenate WO) crystal, which has been produced beginning of 1995 in Bogorodizk. Cable ıgth between PMT and Oscilloscope has been 10 m. a) shows the signal with ns/div. b) (2 μs/div) shows a strong $\sim$ 2 μs slow component which contains -40% of the total light yield.

ıgth X_0 of 0.9 cm. About 50 PWO crystals, mainly from BTCP (Russia) and a few ›m SICCAS (China) have been tested at MAMI in Mainz partly in collaboration th R.Novotny from Giessen University (see also his contribution in this volume).

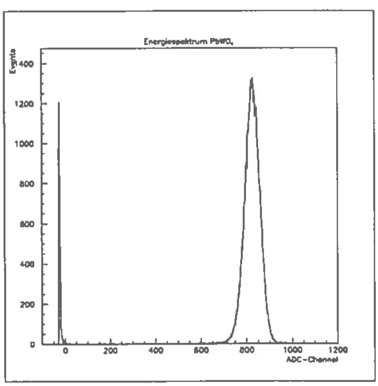

gure 4: An ADC spectrum from single 855 MeV electrons hitting the center of a ‹9 matrix of PWO crystals gives an energy resolution of (3.72±0.02)% at 855 MeV. has been measured with an integration gate at the ADC of 150 ns.

he light has been read out by Philips XP1911 photomultiplier tubes. The results ·esented here are obtained from 30 crystals, which we bought from Bogorodizk 3TCP) and have been produced in early 1995. The melt of these crystals has been ›ped with 100 ppm niobium. Figure 3 shows a typical photomultiplier signal of an ı5 MeV electron from MAMI, hitting a 21 mm×21 mm×160 mm lead tungstenate crystal from BTCP. The PMT-signal has been read out by a digitizing oscilloscope (2 GHz sampling rate, 500 MHz analogue Bandwidth) using 10 m of low attenuation RG 213 coaxial cable. As can be seen from fig 3 a) these crystals have several scintillation components, the longest one (see fig.3 b)) has ~ 2 μs decay constant and contains 30-40% of the light yield. This light decay behavior, especially the μs component, is typical not only for the crystals, which we got directly from BTCP, but for all the crystals we could test, that have been produced in 1995.

Fig. 4 shows an energy spectrum obtained by summing the signals of the inner 9 PWO crystals of a matrix of 25. The center crystal has been hit directly by single 855 MeV electrons from MAMI. The signals have been integrated and digitised with CAMAC ADC's (LeCroy 2249A) with an integration gate of 120 ns. ADC read out has been triggered by the coincidence of 2 crossed scintillators in front of the center crystal (size of plastic scintillators 2 mm×2 mm). After calibration of each of the 9 crystal with the direct electron beam from MAMI, we have measured an energy resolution of (3.72±0.02)% at 855 MeV. At the given size of the crystals, a contribution to the energy resolution of about 2% is expected according to our simulations.

2.3 Lead Fluoride (PbF_2)

Lead fluoride (PWO) has a density of 7.77 g/cm^3, a Molière radius of 2.2 cm and a radiation length X_0 of 0.9 cm and has therefore similiar compactness as PWO. Due to the Čerenkov light production threshold, the region where Čerenkov-light is produced is narrower than the real shower. An effective light production Molière radius has been obtained in simulations to 1.8 cm. We tested 25 PbF_2 crystals which have been produced by Optovac (USA) and have been lend to us by Craig Woody from Brookhaven National Laboratory. The crystals are of size 21 mm×21 mm×160 mm. Data acquisition system and photomultipliers have been identical to the test made with the PWO crystals. Figure 5 shows a typical photomultiplier signal after 10 m of cable of an 855 MeV electron from MAMI, hitting a 21 mm×21 mm×160 mm lead fluoride crystal. It can be seen very clearly that the baseline is restored very well after 20 ns. An integration gate of 20 ns is clearly possible, using these crystals, which makes this material very promising for the parity violation experiment. From the time behavior this material is clearly superior to PWO. Fig. 6 shows an energy spectrum obtained by summing the signals of the inner 9 PBF_2 crystals of a matrix of 25. Setup and data acquisition has been similiar to the PWO measurements above. After calibration, we got an energy resolution of (5.16±0.03)% at 855 MeV. When extrapolating the energy resolution to 1GeV simply by $\sqrt{E}$, we get an upper bound for the energy resolution due to the photon statistics of $4.8\%/\sqrt{E}$, which is

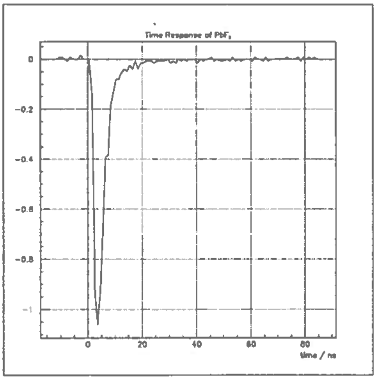

gure 5: A typical PMT signal from a 21 mm × 21 mm × 160 mm PbF_2 crystal, ıich has been produced by Optovac (USA). We did not observe any fast or slow ıntillation. The Čerenkov light signal shape is determined by the PMT and the ;ht collection geometry only.

uivalent to a lower bound on the number of photoelectrons of 0.44 PE/MeV.

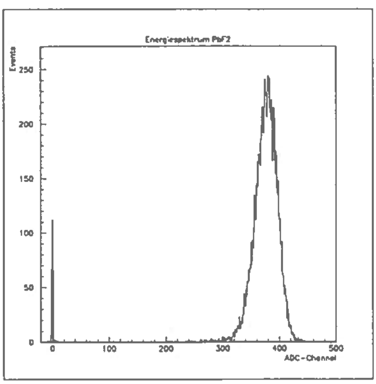

gure 6: An ADC spectrum from single 855 MeV electrons hitting the center of a ‹3 matrix of PbF_2 crystals gives an energy resolution of (5.16±0.03)% at 855 MeV.

4 Liquid Xenon

quid xenon has a Molière radius r_M of 4.1 cm and a radiation length X_0 of 2.2 cm ɜe also table 1). It scintillates by emitting 175 nm UV-light. Published values r the light output in liquid xenon are on the order of 70000 photons per MeV. ıe boiling point of liquid xenon is at 165 K at 1 bar. Since liquid xenon requires yogenic temperatures, a special test cryostat has been developed in our group, which allows quick changing of the test calorimeter setup inside with small amount of losses of the rather expensive xenon during opening. The xenon is recuperated and used again. In Fig. 7 a photomultiplier signal from 855 MeV electrons from

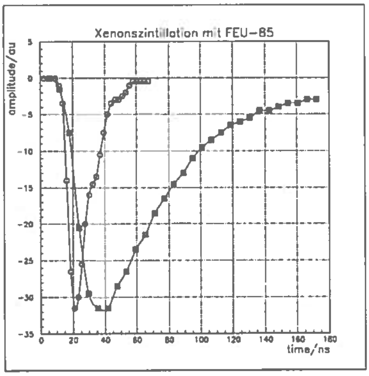

Figure 7: A typical PMT signal from a 54 mm $\times$ 54 mm $\times$ 364 mm reflector cell in a liquid xenon bath (bold squares). In order to measure the time response of the cold PMT, a Čerenkov radiator has been put into the liquid and has been read out by a PMT of the same type (open squares). For determining the liquid xenon light decay time of 41 ns the time response of the Čerenkov radiator has been deconvolved.

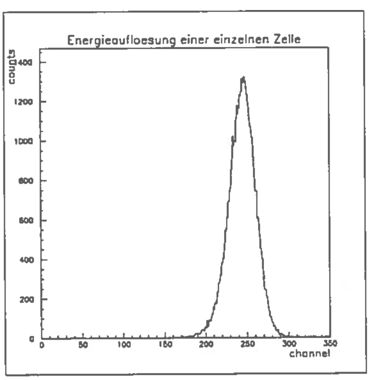

Figure 8: An ADC spectrum from single 855 MeV electrons hitting the center of a single reflector cell in a liquid xenon bath. The energy resolution is determined by the wave length shifter pattern on the surface of the reflector cell and the shower leakage. The measured resolution of (7.8±0.1)% at 855 MeV represents the best energy resolution achieved so far with liquid xenon.

MAMI which has been obtained with the test calorimeter setup is displayed. The scintillation light has been read by a UV-sensitive fast photomultiplier (rise time ns) and been recorded again with the fast digitizing storage oscilloscope. The otomultiplier is sitting in the isolation vacuum and is coupled to the liquid xenon :ough a UV transmitting fused silica window. The measured light decay constant (41±1) ns is in agreement with values obtained by other groups, which reach from ns up to 40 ns.

r a measurement of the energy resolution an 3×3 array of reflector cells coated th a special optimised pattern of wavelength shifter (size of each cell 4/3 r_m × 3 r_m × 13 X_0) has been introduced in the liquid xenon bath. The light has been ad out by a photomultiplier tube (FEU 85, russian type) sitting in the cold liquid. gure 8 shows an ADC-spectrum of single 855 MeV electrons from MAMI hitting e central module. Due to the strong variations of the signal height during the easurement, caused by a large change of the selfabsorption length in the liquid, ly the energy resolution for one single module of the required size can be given. We ve measured an energy resolution of (7.8±0.1)% at 855 MeV for a single module. ır future efforts will go into controlling the impurity level and stabilisation of the ;ht output. At this stage, our measured single module energy resolution of 7.8% 855 MeV electron energy represents the best energy resolution achieved so far th liquid xenon.

Perspectives

tab. 1 a summarizing list of materials tested in the 855 MeV MAMI electron beam given together with the results of our measurements on the time response and the ergy resolution. From this list it is obvious, that PbF_2 is the best candidate for calorimeter material, because of its excellent timing performance. The energy solution for PbF_2 can be enhanced to a great extend by rather simple measures. arger size crystals (optimised for a better coverage matching between photocathode the PMT and backsurface of the crystal) will give higher photon yield by itself. he final shape of the crystals will be tapered in order to yield a barrel like structure. he tapering angle will give an improvement for the light collection efficiency of the

able 1: Candidate materials for the Mainz parity violation experiment. The two ght most columns are the results of our measurements.

material	$r_M[cm]$	$X_0[cm]$	$\tau_{long}[ns]$	$\frac{\sigma}{E}$ at 855 MeV
Nb:PWO	2.2	0.9	2500 (30%)	3.7%
liquid Xe	4.0	2.2	41(100%)	(7.8%)
PbF_2	2.2	0.9	15 (100%)	5.2%

Čerenkov light also. In addition, the Philips XP1911 photomultiplier tubes employed have standard borosilicate windows. The PbF_2 has good optical transmission down to 250-280 nm, which means, that the Čerenkov light is produced down to that wavelength range. Since the Čerenkov light yield is proportional to $1/\lambda^2$, we expect also an enhancement of the energy resolution by using UV-sensitive photomultiplier tubes. From the production point of view, PbF_2 is also advantageous, since it has (in contrast to PWO) only two components, the whole production process can be better controlled. Also quality control is much simpler, since the Čerenkov light yield depends on the transmission only, in contrast to scintillators. We ordered 9 real size, tapered PbF_2 crystals from Shanghai Institute for Ceramics from which we expect an enhanced energy resolution.

We plan to start data taking in 1997. A measurement of the asymmetry A_{exp} with a statistical error of 3% and systematical uncertainties of 4% will be completed in 1998. Experimental values for the electric and magnetic form factors of both nucleons (relative accuracy 20%) will be available by that time, so that we can extract the strange contribution to the asymmetry. From this we can determine $(F_1^s + 0.13F_2^s)$ with an absolute error of $\delta(F_1^s + 0.13F_2^s) = 0.02$.

4 Acknowledgments

All the results presented in this work could only be achieved with the excellent electron beam of the MAMI accelerator. We are deeply indebted to K.H.Kaiser and the whole accelerator group which delivered to us everything from a few electrons per second up to 60μA. We are grateful to Craig Woody from Brookhaven National Laboratory for lending to us the 25 PbF_2 crystals, with which we have achieved the very promising results presented here. This work is supported by the Deutsche Forschungsgemeinschaft (DFG) in the framework of the Sonderforschungbereich 201.

References

1. R.Decker and U.Wiedner, Fortsch. d. Ph., **41**, 87, 1993
2. I.Adams, et al., Phys. Lett., B **329**, 399, 1994
3. M.J. Musolf et al., Phys. Rep.**239**, 1 (1994).
4. V.A. Novikov, et al., Nucl. Phys.**B 397**, 35 (1993).
5. Mainz proposal A4/1-93, D. v.Harrach, spokesperson, F.E. Maas contact person.
6. E.Heinen-Konschak, Mainz, Dissertation, 1995

'rascati Physics Series Vol. VI, (pp. 679–682)
/I INT. CONF. ON CALORIMETRY IN HEP – Frascati, June 8–14 1996

RECENT PROGRESSES ON SCINTILLATION CRYSTALS IN SIC

Zhi–Wen Yin and Xi–Qi Feng
Shanghai Institute of Ceramics, Chinese Academy of Sciences, Shanghai 200050

ABSTRACT

As an academic institution the Shanghai Institute of Ceramics has been involved n the research development and production of heavy scintillation crystals since early l980's. The Institute has collaborated with the L3 experiment at CERN, the L^+ and 3EM experiments at SSC, and is collaborating with BaBar at SLAC, BELLE at KEK ınd CMS at CERN. This report presents recent progresses on the research and levelopment for BGO, BaF_2, CeF_3,CsI (Tl) and $PbWO_4$.

The Shanghai Institute of Ceramics of the Chinese Academy of Sciences (SIC) is a specialised institute working on the inorganic non metallic materials and material sciences. The main research fields include synthetic crystals, advanced ceramics, compositional and structural analyses of above materials etc. Up to now, more than 50 kinds of crystals have been grown and studied in SIC.

Since the BGO ($Bi_4Ge_3O_{12}$) crystals were used as scintillation in the L3 experiment at CERN, a big amount of large size scintillation crystals are being needed to construct various detectors which gives us a task to develop and produce large quantity of big scintillation crystals with high quality for different applications. As above mentioned, SIC is a material institute which is much experienced in crystal growth. However it is not yet professional in high energy physics. So we would like to have extensive co–operation with high energy physics community to engage in the R&D of scintillation crystals.

About 14 years ago, SIC developed the Bridgeman method to grow large size BGO crystals. It has more advantages. Fig. 1 shows a schematic figure of set up for Bridgeman method. Firstly, the polycrystalline powder are contained in a platinum foil crucibles which has a shape of the final crystal. That is a relatively closed system which is favourable to keep crystal composition. Thus, probably it is particularly suitable for the non–stechiometric compound. Then, several crucibles are put into the chambers of furnace. This can enhance mass production efficiency. By using this method, SIC has produced 11,000 large size BGO crystals with high quality for the L3 ECAL.

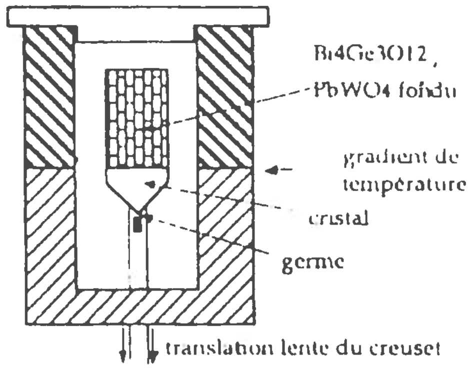

Figure 1 – Schematic diagram of the Bridgeman method.

At present, the modified Bridgeman method is used not only for BGO crystal growth, but also for other scintillation crystals such as BaF_2, CeF_3, $PbW0_4$ etc. Of course, SIC also grows many kinds of crystal by the Czochralski method which is also mature, e.g. laser crystals, photorefractive crystals, optical waveguide crystals etc. How to choose the growth method for different crystals? It depends on the physical and chemical properties of the crystals, including the consideration of production cost. Even if using the Bridgeman method, the technical details are quite different for different crystals. For example, as BaF_2 can not be grown in air, it is very important to grow fluoride crystals in high vacuum, less than 10^{-3} Pa. Concerning the CeF_3, SIC has succeeded in growing large size crystals with dimensions of 20x20x310 mm^3 without optical absorption band at 340 mm. The light yield of 310 nm long crystals has been measured about 30% in comparison to 1"–long BGO reference crystal.

Since the beginning of 1994, SIC has been in collaboration with KEK, SLAC and CALTECH to develop large size CsI crystals for the BaBar Detector. For the first time, SIC has grown large size CsI crystals using the modified Bridgeman method. Many factors including furnace design, temperature and doping level have been intensively studied which have resulted in substantial improvements on the quality of the crystal. Besides, although the CsI is a non oxide material, the large size crystals have been successfully grown at ambient atmosphere. This may lead to a big reduction in crystal production cost. This shows how SIC has the mass production capability for large size, Tl–doped, CsI crystals with high quantity.

The latest material is $PbWO_4$ (PWO). Both the Czochralski and Bridgeman methods were used for the growth experiments. After tests, it was proved how the Bridgeman method is better for growing large size PWO crystals with lower cost and high quality. Now the PWO crystals with full sized dimension for CMS have been grown and machined[1)].

Undoubtedly, SIC is making progress in PWO crystals. The light yield is increasing gradually, the super–low component has been suppressed and so on. However, there are still some problems in this material, for example, high cracking probability during growing and machining, instability of scintillating property of the crystal, etc. SIC is making a great effort to solve these problems.

Concerning the radiation hardness, special attention was focused on the BGO, BaF_2 and CsI crystals in the past years. For what concerns BGO, SIC succeeded in developing a new Europium doped BGO crystal with high radiation hardness[2)]. The crystals have been used in the endcaps of the L3 experiment. Concerning the BaF_2 crystals, it was found that the oxygen and hydroxyl are the most harmful impurities. Therefore, the elimination of these anion impurities in crystals becomes most important for the improvement of radiation hardness[3)]. It is clear that these research works have led to evident improvement in the radiation hardness of BaF_2. Besides SIC is also making good progress in the radiation hardness of CsI. Crystals produced by SIC now satisfy BaBar radiation hardness specifications.

Finally, the mechanism of radiation damage in PWO crystals is not yet clear. Some results on the SIC crystals are as follows: the light yield and decay time is not too bad, but the drop of light yield after γ–ray radiation with 500 Gy is rather high, some samples reaching even more than 40%. However for sample No. 39, the drop of light yield after the same dose is less than 15%, but its super–slow component is rather high. The latest sample No. 69 shows good radiation hardness, with drop of light yield is about 8% after beam test. Nevertheless, up to now there is a gap between the present PWO crystal performance and the requirements from CMS, especially in the regards of radiation hardness. Therefore further in depth research work is very necessary. At present, this ongoing work is supported by ETH in collaboration with PSI, CERN and the ECAL group of Caltech.

References

1. Z.W. Yin and Z.L.Xue, Proc. Intern. Conf. On Inorganic Scintillators and Their Applications, SCNT95, 1996, Delft University Press, The Netherlands, p. 490.
2. P.J. Li et al., Journal of Inorganic Materials, **8**, 15(1993).
3. Z.W. Yin and X.Q. Feng, Ferroelectrics, **151**, 287 (1994).

scati Physics Series Vol. VI, (pp. 683–692)
NT. CONF. ON CALORIMETRY IN HEP – Frascati, June 8–14, 1996

THE ELECTROMAGNETIC CALORIMETER TAPS[1]

R. Novotny
II. Physikalisches Institut, Universität Giessen, D–35392 iessen, Germany

and for the TAPS Collaboration

ABSTRACT

Two Arm Photon Spectrometer **TAPS** - comprising in its present set-up 384 vidual plastic and BaF_2 scintillation detectors - has been designed to identify and isure hard photons and neutral mesons via the reconstruction of the invariant mass n their two or three photon decay modes. The BaF_2-calorimeter detects photons up to energy of 15GeV with high resolution (σ/E=2.5% at 1GeV). Neutrons and charged icles are identified by pulse-shape (PSA) and time-of-flight techniques (TOF) with 1 efficiency. The modification into modular plastic/BaF_2-phoswich telescopes allows roved particle spectroscopy at medium energies simultaneously. For comparison, a rix of 9 $PbWO_4$ crystals has been investigated with electrons up to 855MeV energy.

Introduction and Physics Motivation

e calorimeter TAPS [1] was planned, financed and built by an European collaboration[2] investigate high energy photons as well as neutral mesons (π^0,η,ω) in relativistic and ra-relativistic heavy ion collisions or photonuclear reactions, respectively. The point impact and the total energy of the electromagnetic shower have to be determined cisely to reconstruct the invariant mass from the meson decay into two or three otons. The high multiplicity of hadronic reaction products requires a very efficient crimination against charged/neutral particles. BaF_2 is the most appropriate scintillator terial due to its high light output, fast response and intrinsic selectivity of the pulse-ipe to the nature of the impinging probe [3]. The envisaged very broad range of the ersified and rich research program at different accelerator facilities (AGOR, CERN-S, GANIL, GSI, MAMI) requires modularity of the device and high flexibility in the ometrical arrangement.

This work has been supported by BMBF, DFG (SFB 201) abd GSI.

2 The Detector Concept

2.1 The Individual Detector

Each of the almost 400 detector components consists of a 250mm long ($12X_0$) hexagonally shaped BaF_2-crystal[2] (inscribed circle Ø = 59mm). The last 25 mm are machined cylindrically in diameter (Ø = 52mm) to allow optimum magnetic shielding (see fig.1a). Laser light can be fed into each crystal by a quartzfiber for gain monitoring and calibration of the read-out electronics. The crystals are wrapped with PTFE and an additional layer of aluminum foil as UV-reflector and coupled optically to the quartz window of the photomultiplier (Hamamatsu R2059-01) with high viscosity grease. The assembly of the individual module including the base is achieved using 0.2mm thick heat shrinkable PVC-tubing [1)], which is light tight and provides the sufficient mechanical strength. The modular detectors can be grouped in blocks (see fig. 1b) arranged either on top of each other in two/three movable towers or in a ring in the horizontal plane through the target (see fig. 2). Alternatively, a large annular hexagonal supercluster can be formed. A charged-particle-veto (CPV) consisting of hexagonal plastic scintillators (5mm NE102A) read-out individually by lightguides and photomultipliers can be fixed only to the standard block geometry of 8 by 8 modules as illustrated in fig. 1b.

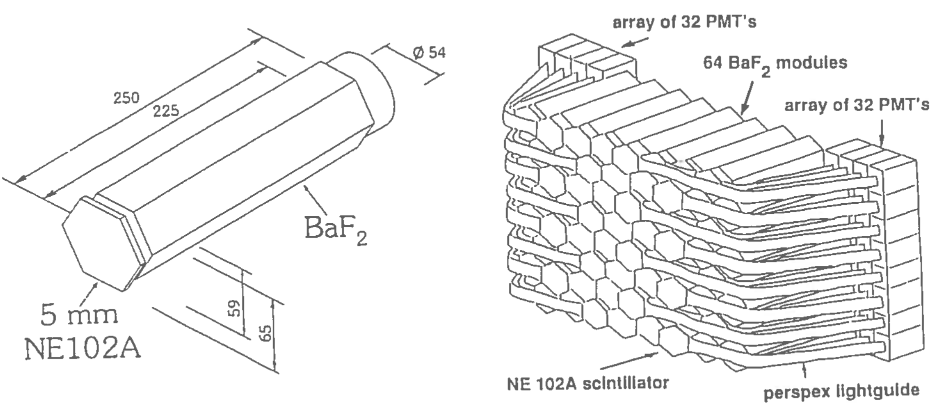

Figure 1: (a) The geometry of the individual plastic and BaF_2-scintillators (left). (b) The fully assembled detector block consisting of 64 plastic-BaF_2-scintillator telescopes (right).

[2] manufactured by Dr.Karl Korth, Kiel, Germany

optical transmission, signal shape, energy response of the fast and slow scintillation ıponent to low energy γ-sources and the contamination of α-emitting radionuclei ntified via PSA) are measured carefully for each crystal. Table 1 shows the obtained results averaged over 450 accepted crystals (in collaboration with A2 at Mainz) in ıparison to the required specification limits. Recently manufactured crystals[3] of

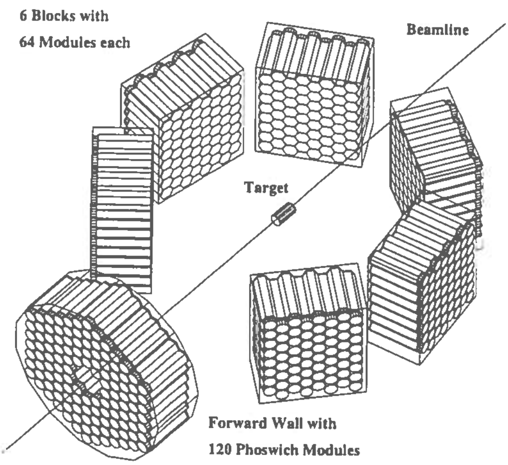

Figure 2: The TAPS set-up at the tagged photon facility of MAMI.

ıble 1: Test results obtained for 450 accepted TAPS crystals compared to the required specifications and recent samples of different geometry.

performance parameter	TAPS average	CHINA average	CHINA best results	spec.limits
absorption length Λ	[cm]	[cm]	[cm]	[cm]
at λ = 200 nm	41.7	22.8	27.5	18.0
at λ = 220 nm	76.7	41.8	56.6	28.0
at λ = 300 nm	488.7	139.2	188.6	292.0
^{137}Cs: E_γ = 662 keV				
fast: ΔE/E [%FWHM]	35.3	45.7	40.2	45.0
total: ΔE/E [%FWHM]	11.5	14.0	11.5	12.5
intensity ratio fast/slow at Δt=40ns	9.5	9.4	12.0	7.0
^{60}Co: E_γ = 1.33 MeV				
peak/valley ratio	2.28	1.61	2.30	2.00
α-activity				
dN/dt [cts s^{-1} cm^{-3}]	0.021	0.175	0.071	0.133

350mm length (quadratic diameter 35x35 mm^2) have been investigated in an identical manner. The average performance of 16 samples appears slightly worse, in particular the UV-transmission measured transverse to the symmetry axis. However, the best crystals meet very well the TAPS requirements in spite of a 40% increase in total length.

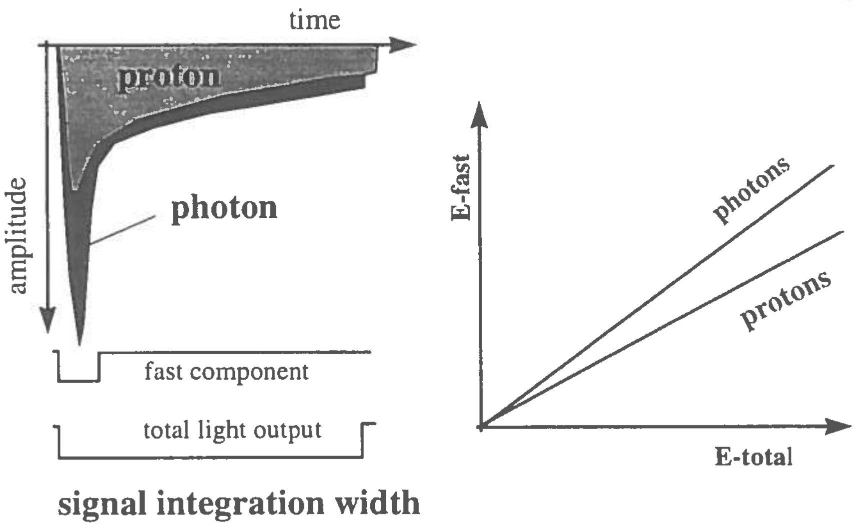

Figure 3: Left: The typical signal shape of BaF_2 for photons and charged particles. The integration gates for signal-processing are indicated. Right: Particle identification based on the correlation of the measured yield of fast and total light-output.

The processing of the BaF_2-signals foresees the determination of the time-of-impact (TOF-analysis) and the integration of the total as well as the fast scintillation component separately (integration gates 2μs and 40ns, respectively) to perform pulse-shape analysis in addition.

2.2 Particle/Photon Identification and Discrimination

The identification and discrimination of neutral and charged particles can be achieved exploiting the intrinsic properties of BaF_2 in combination with a fast plastic scintillator used either as a separate CPV system or as a phoswich detector when coupled optically

[3] manufactured by SICCAS, Shanghai, China

:he BaF_2 crystal. The short decay time and the high light output of BaF_2 allow time olutions better than σ=85ps even for the large TAPS modules [4]. Therefore, particle ntification and even energy determination can be performed based on TOF technique a typical distance of 1-2m from the vertex using a start-counter system as time erence. In particular, low and medium energy neutrons, which react via (n,γ)-ıcesses with BaF_2 and induce a signal-shape identical to that of photons, can only be ntified via TOF.

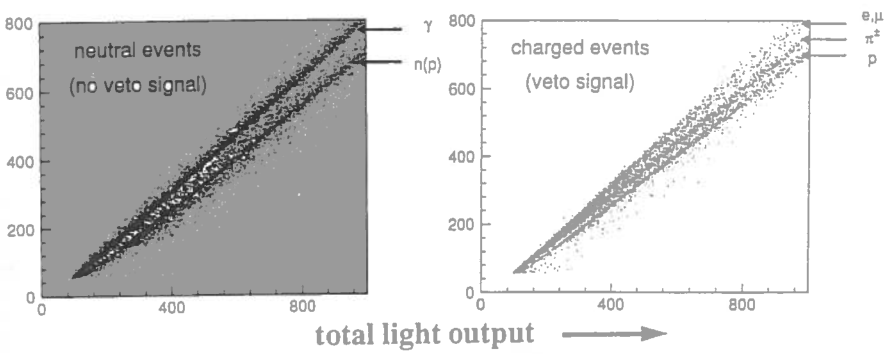

Figure 4: Scatter plot of the fast component versus the total light output shown for eutral (left) and charged (right) events in BaF_2 selected by the CPV. The shown range of the total light output corresponds to approx. 250MeV photon energy.

:stricted to the standard TAPS block geometry, the CPV system allows as well an line tagging of charged or neutral hits as the measurement of the specific energy loss : of charged particles for identification by means of ΔE-E-correlations.

ıe shape of the BaF_2-signal is extremely sensitive to the nature of the impinging rticle. The contribution of the fast scintillation components (λ=195,210nm) to the :al light output diminishes with the increase of the energy density deposited by the ıizing particles. Fig. 3 illustrates schematically the typical response of photons and otons and the crude pulse-shape analysis performed in TAPS. It has been shown that : ratio of both contributions remains constant over the full dynamic range up to :ativistic and even ultra-relativistic energies [5]. Electromagnetic and hadronic showers ntribute differently to the fast scintillation component. Fig. 4 shows as an example of : PSA two scatter plots of the fast scintillation component versus the total light output cumulated for neutral and charged events from data taken in photonuclear reactions. A dynamic range up to approx. 250MeV photon equivalent energy is covered. As marked, the distinct lines correspond to leptons, pions, protons as well as photons. The lower branch in the plot for neutral hits can be addressed to secondary protons recoiled by high energy neutrons which interact in the crystal via (n,p)-reactions. Measurements of the response function of TAPS detectors to neutrons show an efficiency which approaches a nearly constant value of 17% above 750MeV kinetic energy of the neutron.

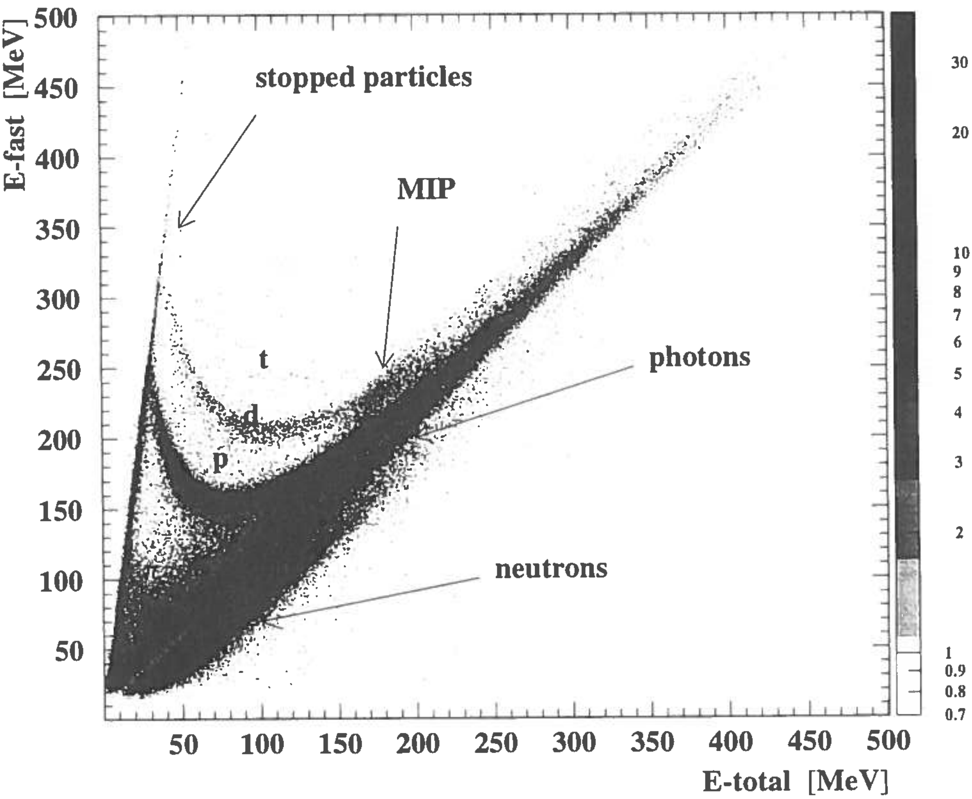

Figure 5: Pulse-shape correlation of a 15mm plastic-BaF_2 phoswich detector identifying reaction products from the collision 2GeV/u Ca+Ca.

The particle sensitivity can be further improved by a fast plastic scintillator (15mm NE102A) optically coupled to the front face of the BaF_2-crystal in phoswich technique [6)]. The energy loss of charged particles in the plastic layer leads to a substantial increase of the total fast light output. The corresponding pulse-shape correlation is illustrated in fig.5 identifying reaction products from the collision 2GeV/u Ca+Ca. Structures in the ter plot above the clearly distinct branch due to photons can be assigned to charged ticles either stopped within in ΔE-section or fully or partly stopped within the BaF_2-stal. The distinct area near E_{total} ~170 MeV is caused as an artifact by minimum izing particles generating additional Cherenkov photons within the quartz window of photomultiplier. Again, neutrons identified via (n,p) reactions can be observed ow the photon branch.

Response to Electromagnetic Probes

photon response of TAPS has been determined in the energy regime up to 800MeV ng monochromatic photons provided by the tagging facility of MAMI at Mainz [7]. excellent energy resolution for a collimated photon beam (∅=1.3cm) amounts to $E = 0.59\% E_\gamma^{-1/2} + 1.9\%$ (E_γ given in GeV) and $\sigma / E = 0.79\% E_\gamma^{-1/2} + 1.8\%$ for the component, respectively. The achieved resolution at 1 GeV of $\sigma / E = 2.5\%$ is nparable to operating 4π-calorimeters such as *L3*, *CleoII* or *Crystal Barrel*, pectively. The obtained experimental data can be well reproduced by GEANT3-ulations taking into account the exact geometry, dead material such as reflector or it tight housing and experimental thresholds.

point of impact can be reconstructed from the electromagnetic shower distribution hin the cluster of responding detectors with a resolution Δx<2cm limited due to the ge diameter of the crystals. In spite of the insufficient depth of the crystals ($12X_0$) an rgy resolution for 10GeV electrons of $\sigma / E = 5.1\%$ has been achieved within a ster of only 7 modules.

Neutral Meson Spectroscopy

thin the last few years of operation TAPS has pursued a broad and versatile research gram which covers topics such as the early phase of nuclear reactions and energy sipation mechanisms via the detection of hard photons below 100MeV/u projectile rgy. In the 1GeV regime, the investigation of baryonic excitations in nuclei via otonuclear reactions and the study of hot and dense nuclear matter via the production d propagation of neutral mesons represent the main experimental goals.

particular in heavy ion collisions, the meson reconstruction relies on the efficient utral and charged particle discrimination provided by TOF and PSA techniques as istrated in the previous sections. The very good energy resolution achieved with BaF_2 ows an invariant mass resolution of typically 8-15% (FWHM) which is necessary to ntify the weak meson signal on top of a huge combinatorial background in the variant mass spectrum. Fig. 6 shows an example taken at the so far highest bombarding energy of 450GeV/c p+Be operating TAPS assembled in a supercluster in coincidence with the dilepton spectrometer CERES at CERN-SPS [5].

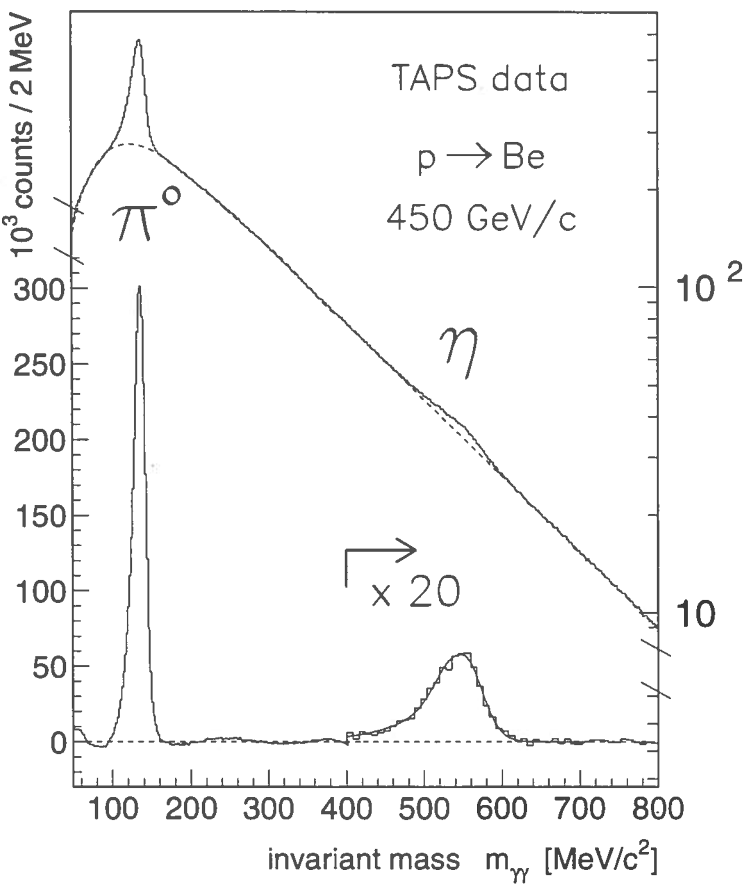

Figure 6: Invariant mass distribution measured with TAPS in the system p+Be at 450GeV/c measured at the CERN-SPS in coincident operation with the CERES dilepton spectrometer. In the lower part the combinatorial background has been subtracted.

4 Response Function of $PbWO_4$ to Electrons below 1 GeV Energy

In order to test the applicability of $PbWO_4$ in the energy regime covered by TAPS an extensive test program has been started using monoenergetic electrons between

)MeV and 855MeV, respectively, provided by the MAMI facility[4]. The time and :rgy response of a 3x3 matrix consisting of crystal samples of 150 to 210mm length rresponding to 16 to $23X_0$) with quadratic diameter ($20x20mm^2$) have been estigated. The individual crystals, delivered by suppliers from China and Russia, are ıpped with PTFE-foil as reflector and read-out individually by photomultiplier tubes ıilips XP1911). A cross of two quadratic ($2x2mm^2$) scintillating fibers mounted in nt defines the point of impact of the electrons. A cooling system allows to operate the ector at temperatures down to $T=2.5^0C$. The anode outputs are integrated in charge sitive ADCs over a gatewidth adjusted between 60ns and 220ns, respectively, to dy the influence of slow decay components of the scintillation light.

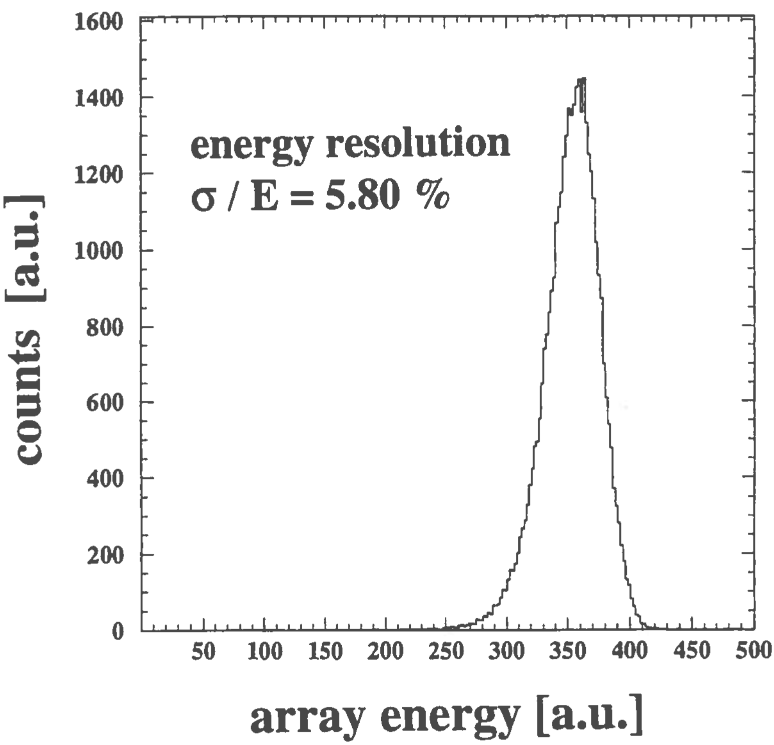

ʒure 7: Energy response of a 3x3 matrix of $PbWO_4$ crystals to 180MeV electrons. The ɛtector array has been operated at a temperature of $T=3.5^0C$. The anode signals of the photomultipliers have been integrated over 220ns.

collaboration with F.Maas et al., University Mainz, Germany

The measured energy resolutions at a operating temperature of T≈3^{0}C can be parametrized in the studied range by $\sigma / E = 2.39\% / \sqrt{E} + 0.2\%$ (electron energy E given in GeV). The achieved value at 855MeV of $\sigma / E = 2.76\%$ is only slightly above the value of 2.4% expected from GEANT3-simulations taking into account only the detector geometry and reflector material. Fig. 7 shows as an example the lineshape of the array measured at the lowest electron energy of 180MeV. The anode signal has been integrated over a gate of 220ns width.

The time response has been deduced from the relative time correlation between two adjacent detectors by impinging the beam in between these crystals. The obtained excellent resolution of $\sigma = 130ps$ per individual detector makes particle identification via TOF technique possible with high sensitivity.

5 Summary

The BaF_2-calorimeter TAPS - designed for high energy photon detection - is operating very successfully since several years with high performance and allows high resolution photon and particle spectroscopy [8]. The excellent and unique properties of the fast scintillator material BaF_2 such as time response and pulse-shape sensitivity and the combination with plastic scintillators in different concepts guarantee the required clean and selective photon detection.

First tests with $PbWO_4$ in the energy range below 1 GeV have shown very promising results. Energy and time resolution appear to be sufficient for experimental requirements at medium energies.

References

1. R.Novotny, IEEE Trans. Nucl. Sci. **38,** 379 (1991)
2. The **TAPS** collaboration: NPI, Rez (Czech Republic), GANIL, Caen (France), GSI, Darmstadt ,University Giessen, University Münster (Germany), KVI, Groningen (The Netherlands), IFIC University of Valencia (Spain)
3. R.Novotny et al., Nucl. Instr. and Meth. in Phys. Res. **A262,** 340 (1987)
4. O.Schwalb et al., Nucl. Instr. and Meth. in Phys. Res. **A295,** 191 (1990)
5. M.Franke and M.Notheisen, PhD thesis, University Giessen, (1996), to be published
6. R.Novotny et al., IEEE Trans. on Nucl. Sc. **43,** 1260 (1996)
7. A.Gabler et al., Nucl. Instr. and Meth. in Phys. Res. **A346,** 168 (1994)
8. H.Ströher, Nuclear Physics News **6,** 7 (1996)

NaI(Tl) CALORIMETER FOR THE SND DETECTOR AT VEPP–2M

V.B. Golubev
Institute of Nuclear Physics, Novosibirsk State University, Novosibirsk, 630090, Russian Federation

Written contribution not received

scati Physics Series Vol. VI, (pp. 695–704)
[NT. CONF. ON CALORIMETRY IN HEP – Frascati, June 8–14, 1996

THE CsI(Tl) E.M. CALORIMETER FOR THE BELLE EXPERIMENT AT KEK

M.H. Lee
KEK, 1-1, Oho, Tsukuba, Ibaraki 305, JAPAN

ABSTRACT

ıe BELLE detector at KEK B factory being built at KEK, Japan is now under ıstruction to clarify the long standing physics puzzle of CP violation. A highly ;mented array of CsI(Tℓ) crystals with silicon photodiode readout had been chosen the electromagnetic calorimeter and are under construction. The design and rformance of the BELLE CsI(Tℓ) crystal detector is presented.

Introduction

› study CP-violation in B-meson day, the KEK B-factory is under construction at ;ukuba, JAPAN. It consists of a high-luminosity (10^{34} $cm^{-2}s^{-1}$) and asymmetric-ergy e^-(8 GeV)e^+(3.5 GeV) collider and the BELLE detector. The collider will installed in the existing TRISTAN tunnel. The BELLE detector will be placed the Tsukuba experimental hall at the north interaction region.

The main purpose of the electromagnetic calorimeter is to detect photons ›m B-meson decays with high efficiency and good resolution. Since most of these ıotons are end-products of decay cascades, they have relatively low energy and, us, good performance below 500 MeV is especially important. Two-body decay odes such as $B \rightarrow K^*\gamma$ and $B^\circ \rightarrow \pi^\circ\pi^\circ$ produce photons with energies up to 4 GeV ıd good high energy resolution is needed to reduce backgrounds for these modes. ectron identification relies primarily on a comparison of the charged particle track omentum and the energy it deposits in the electromagnetic calorimeter. Good π^0 :tection requires the separation of two nearby photons and a precise determination their opening angle. This requires a fine-grained segmentation in the calorimeter.

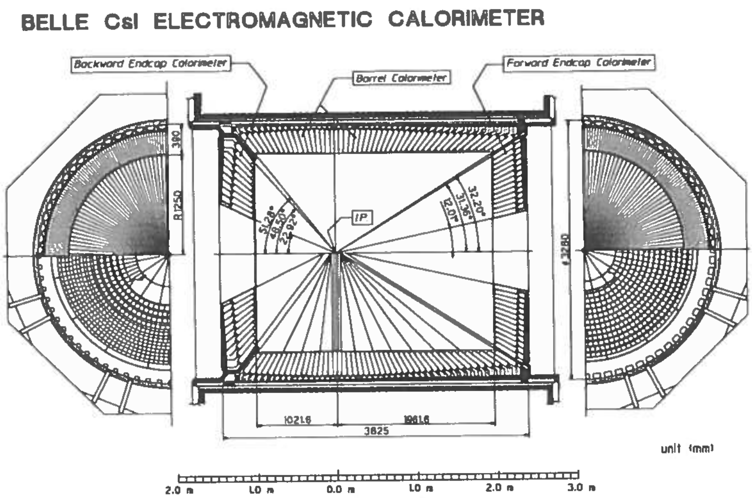

Figure 1: The overall configuration of Electromagnetic Calorimeter.

Table 1: The geometrical parameters of the CsI calorimeter.

	θ coverage	θ seg.	ϕ seg.	# of crystals
Forward Endcap	11.7° - 31.5°	13	48 - 128	1168
Barrel	32.2° - 128.7°	46	144	6624
Backward Endcap	130.8° - 158.3°	10	64 - 144	1024

In order to satisfy above requirements, a highly segmented array of CsI(Tℓ) crystals with silicon photodiode readout will be installed inside the coil of the 1.5 T solenoid magnet.

2 Overall Design of Calorimeter

The overall configuration of the calorimeter is shown in Fig.1. The complete calorimeter is comprised of a 3.0 m long, 1.25 m inner radius barrel section and annular endcaps located at z = + 2.0 m and z = − 1.0 m from the interaction point. The geometrical parameters of each section are given in Table 1.

Each crystal has a tower-like shape and is arranged so that it points almost to the interaction point; there is a small tilt angle of $\sim 1.9°$ in both θ and ϕ directions to avoid the photon escaping through the gap of crystals. The calorimeter covers the polar angle region of $17.0° < \theta < 150.0°$, corresponding to a total solid-angle coverage of 91% of 4π. Small gaps between the barrel and endcap crystals provide a pathway for cables and room for the supporting members of the inner detectors. The loss of solid angle associated with these gaps is approximately 3% of the total

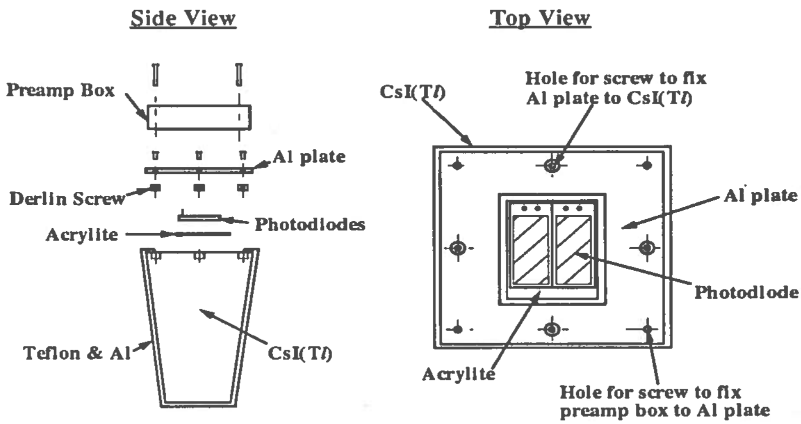

Figure 2: The mechanical assembly of the CsI(Tℓ) Counter.

ceptance. The entire system contains 8816 CsI(Tℓ) counters and weighs 43 tons.

The size of each CsI(Tℓ) crystal is determined by the condition that ap-oximately 80% of the total energy deposited by a photon injected at the center of e crystal is contained in that crystal.The 30 cm length(16.2 X_o) is chosen to avoid :terioration of the energy resolution at high energy due to the shower leakage out e rear of the counter.

The energy resolution of this system at low energy is dominated by elec-onic noise and the fluctuations of lateral shower leakage. In order to accommodate creases in the lateral shower size for low-energy photons, more counters must be ed in the summation for the energy calculation. This puts a premium on low ectronics noise for each channel. We aim at less than 200 keV incoherent thermal ise and less than 100 keV coherent pickup noise in the whole electronics chain.

Counter Assembly

ach crystal is wrapped in a diffuse reflector sheet for the best collection of scin-lation light at the end of the crystal. We tested several porous teflon sheets and illipore paper sheets with and without reflective-paint coatings. We chose a single yer of 200 μm thick Goretex teflon as the wrapping material because it gives a od light output, is easy to handle, and is expected to be stable against aging.

A single counter is assembled as in Fig. 2. All sides of crystal, except r the end face for light collection, are covered by a single layer of 200 μm thick flon. It is then covered by a layer of 25 μm thick aluminum foil lined with a thin ylar sheet for light and electrical shielding. Four tapped holes are made on the d face of the crystal and used to fix an aluminum base plate to the crystal. Small derlin pieces are screwed into the hole and the base plate is fastened to the derlin piece via tapped holes made at the center of the derlin piece. An aluminum-shielded preamplifier box is finally attached on the aluminum base plate with 4 screws. An approximately 1 cm long extra strip of aluminum foil is tacked under the base plate to provide electrical contact between the aluminum foil and the amplifier case.

Two photodiodes(Hamamatsu S2744-08), each having active area of 1×2 cm^2, are glued at the center of crystal end surface via an acrylite plate of 1 mm thickness. An acrylite buffer plate is used because direct glue joints between the photodiode and the CsI were often found to fail after temperature cycling, probably due to the different thermal expansion coefficients of silicon and CsI. After testing various glues for the strength of adherence under temperature cycling, we selected ECOBOND 24 epoxy glue from Grace Japan Co. for glueing the photodiode to the acrylite and KE-109 silicon rubber glue from Shinetsu Chemical Co. for glueing the acrylite to the CsI.

4 CsI(Tℓ) Crystal

The production of suitable CsI(Tℓ) crystals requires to meet a number of stringent optical and mechanical requirements. A summary of the technical specifications for the crystal production is listed in Table 2.

The optical properties of each crystals are tested by irradiating with a collimated ^{137}Cs source at nine points along the crystal and measuring the position of the 662 keV gamma ray photopeak. The measurement is done using a standard, bialkali phototube(Hamamatsu R1847S) at one end of the crystal. The photomultiplier output is shaped by an Ortec 570 amplifier with a 1 μs shaping time and digitized in a peak sensing ADC of Hoshin Electronics. The light output of the crystal is defined as the average of the 9 measurements with respect to the light output of a small, 2.5 cm ϕ and 2.5 cm long reference crystal. The (non)uniformity of the light collection is defined as (max.-min.)/average.

Measurements of the crystal dimensions are done with an automated device

Table 2: Specifications for the CsI(Tℓ) crystals.

Average Light Output	more than 0.27 of reference crystal for all crystals, more than 0.29 for 90 % of total crystals.
Light Nonuniformity	less than 9% for all crystals, less than 7% for 90% of total crystals.
Size(A,B,H,a,b,h)	within +0 and -200μm from specified size.
Length	within $\pm$ 1 mm from specified length.

ıt has eight linear gauges. One measurement consists of four sampling pairs, each which measures the side surface location with a pair of linear gauges. By moving : crystal length in 3 cm steps, the crystal cross section is measured at nine different ghts. The crystal dimensions are reconstructed from these data and the results : compared with the design specification. The system has a 20 μm precision for wrapped crystals.

Crystal Production

.e delivery of CsI(Tℓ) crystals from Budker Institute of Nuclear Physics(BINP) ırted in October 1994. As of the June of 1996, about 2200 pieces had been livered to KEK. Quality control and maintenance of the delivery schedule for these rstals, which are grown at the Institute of Single Crystals in Kharkov, Ukraine, is e responsibility of the BINP group. CRISMATEC had been delivered about 300 rstals. The Joint Crystal Collaboration Group(JCCG) in Shanghai and Beijing s produced more than 30 full-size crystals that satisfy the specifications for light tput and uniformity. The radiation hardness of these crystals are tested and found pass the requirement as will be explained in the next section.

Radiation Hardness

the stable physics run conditions, spent electrons and positrons from beam will duce a great number of soft γ-rays of energies up to a few MeV. They irradiate the ›nt-end surface of CsI(Tℓ) crystal and cause the decrease of light output because radiation damage. The dose of beam-induced background in the barrel region is timated to be up to 5 rad/year in the first 2 cm in depth during a steady operation the integrated luminosity of 10^{41}/cm^2/year. Based on this value with a large safety argin, the requirement for radiation hardness of the barrel crystals is set at the .lues shown in Table 3. The radiation hardness of CsI(Tℓ) crystals has been studied Tokyo Institute of Technology(TIT) and Nara Women's University(NWU). Each ystal was irradiated by γ rays from 5.8 TBq ^{60}Co source at TIT and the change light output was measured after a 5 – 30 day period of natural annealing. The ıtural annealing is shown in Fig. 3. Some crystals were uniformly irradiated and hers were irradiated from the front face, thereby simulating the actual radiation

Table 3: Requirement for radiation hardness(for Barrel part).

Dose	10 rad	100 rad	1 krad
Decrease of Light Output	< – 3%	< – 10%	< – 20%

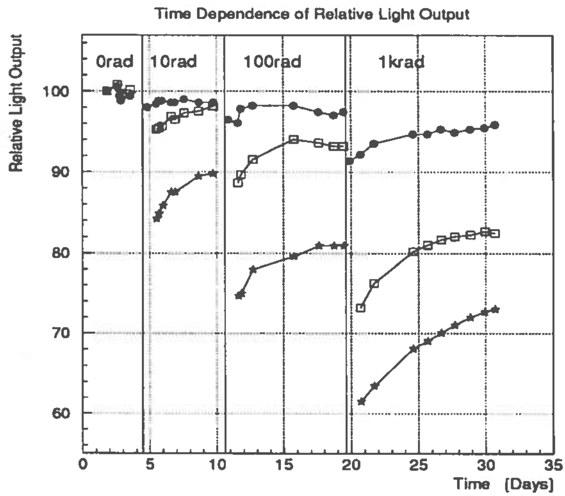

Figure 3: Time dependence of light output for uniform irradiation.

background.

At TIT, the light output was measured using a phototube with a thin air gap between the crystal and the phototube. Gamma rays from ^{137}Cs were used as the light source, which is similar to the standard light output measurement for the crystals. At NWU, the light output was measured by two photodiodes attached to the crystal with silicone grease. Cosmic-ray muons were used as the light source. The result of measurements by a photomultiplier is shown in Fig. 4, which shows the pulse height for the 662 keV photopeak from ^{137}Cs at ten points along the crystal. The measurements were done for uniform and for front face irradiation. The result shows uniform decrease of light output in both cases. The result from photodiode measurements were also consistent with that of phototube within their systematic errors. The light output change as a function of dose in the case of front face irradiation is shown in Fig.5. Here the value of light output is the average of 10 points along each crystal. Several final quality crystals from all producer's were tested and satisfy the requirement of radiation hardness up to 1krad in barrel.

7 Light Output

We have measured the light output of 16 counters produced by BINP and Quartz et Silice(QS/CRISMATEC). Two Hamamatsu photodiodes (1×2 cm^2 sensitive area) were used for light detection. Charge from the photodiodes was collected by a standard preamplifier and shaped by a Hoshin N012 shaper with $\tau = 1$ μs. The collected charge was calibrated by irradiating the photodiode using a ^{241}Am source.

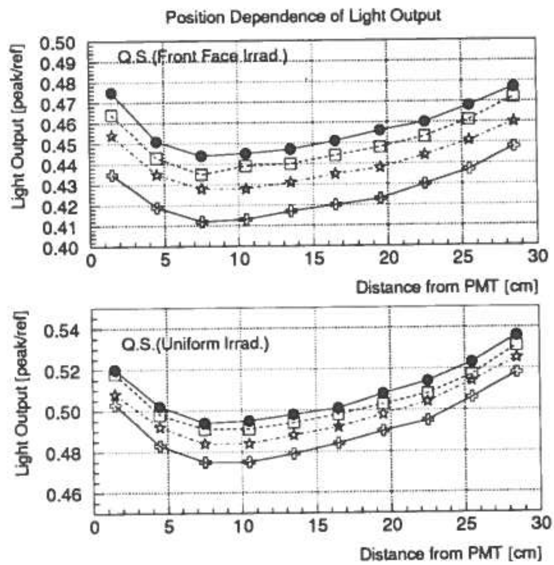

igure 4: Position dependence of light output before and after irradiation. Upper: ont face irradiation, Lower : uniform irradiation; circles, squares , stars and crosses and for the data of 0, 10, 100 and 1k rad irradiation.

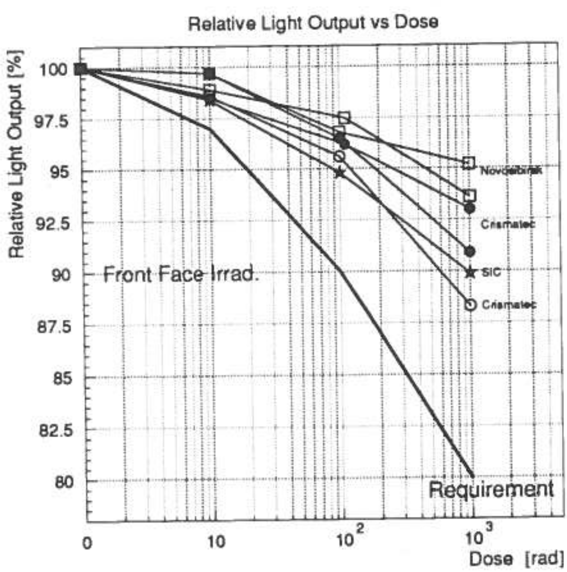

Figure 5: Light output change as a function of dose for front face irradiation.

Table 4:

Particle	Source	Energy	Comments
γ	^{60}Co	1.253 MeV	combined peaks
γ	^{88}Y	1.836 MeV	
$\mu^{\pm}$	cosmic ray	31.7 MeV	
π^{-}	beam	31.5 MeV	non-interacting pion
π^{-}	beam	185.4 MeV	non-interacting pion
e^{-}	beam	1535.3 MeV	Most probable energy loss

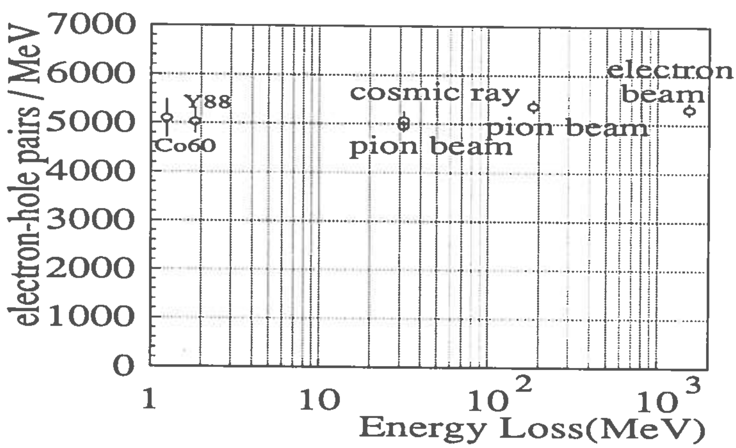

Figure 6: Average number of electron-hole pairs per MeV of deposited as detected by two Hamamatsu S2744-03 photodiodes.

We measured the light output generated from the sources listed in Table 4 and the result is plotted in Fig. 6. All measurements are consistent within 5% over a range of energies from 1 MeV to 1.5 GeV and give an average of 5060 electron-hole pairs per MeV of deposited energy. No significant difference between BINP and QS crystals was observed.

8 Readout Electronics

8.1 Overall Design

Each CsI(Tℓ) counter is read out by an independent pair of silicon PIN photodiodes and charge sensitive preamplifiers attached at the end of the crystal.The preamplifier output is transmitted on 10 m long, 50 Ω twisted pair cables to a shaping circuit where the two signals from the same crystal are summed. The summed signal is then split into two streams: one for the main ADC and the other for the trigger electronics. The main ADC signal is shaped with a $\tau = 1$ μs time constant and l into a Q-to-T converter installed on the same card. The output of Q-to-T nverter is transmitted via twisted pair to a TDC module in the electronics hut : digitization. The trigger signal is shaped with a shorter time constant and ~ 16 .es are combined to form an analog sum for the trigger logic.

2 Photodiode

ır photodiode 'S2744-08' was developed by Hamamatsu Photonics to achieve ıout 20% higher photo-sensitivity. This has 1×2 cm^2 sensitive area and its 300 μm ıfer is fully depleted at reverse bias voltage of 70 V. The reliability of the photodi- le was investigated by operating them at 70 V bias and 80°C for 500 hours, and by temperature cycles between -20°C(30 min.) and 80°C(30 min.). The long term ability was independently confirmed at KEK after the same 500 hours operation 20 samples. No failure was found and an increase of leakage current(I_d) was less an 0.3 nA. The radiation hardness was also checked by γ rays from ^{60}Co. The crease of leakage current at 6 Gy and 68 Gy exposure are less than 5% and 20%, spectively. No significant change of the capacitance and photo-sensitivity were ›served even at 68 Gy. A total of 14,000 S2744-08 photodiodes were delivered and sted. All photodiodes were burned in at 70 V reverse voltage and at 80°C for 50 ›urs and inspected before the shipping. We selected a total of 150 samples, 5 or 10 eces from each production lot, and measured the photosensitivity S(mA/W) over l wave lengths. The average photosensitivity thus obtained at the emission peak CsI(Tℓ), λ = 560 nm, is 386 ± 6(mA/W), corresponds to the quantum efficiency ϵ = 85.5 ± 1.3 %. The leakage current(I_d) and capacitance(C_j) of all photodiodes :e measured at 70 V bias voltage and at a temperature of 25°C. The averages and ns are $<I_d>$ = 3.31 ± 0.92 (nA) and $<C_j>$ = 82.8 ± 0.7 (pF). All photodiodes ıtisfy our specification.

.3 Preamplifier

ı designing the charge integration preamplifiers, we have taken care of not only the lectronic noise but also the long term reliability and dynamic range of linearity. The ircuit is realized in a 4-layer hybrid chip of 1.8×4.5 cm^2. Each photodiode output ; received by the two hybrid chips which are accommodated in an aluminum shield ase. The two chips are completely independent each other such that the failure f one readout channel does not affect the other. The mother board is equipped /ith a high luminosity LED of λ = 570 nm wave length to monitor the response f photodiodes. The shield case is placed just behind the photodiodes to reduce ›ickup noise and parasitic capacitance due to the readout cable. The measured ›erformance of the last prototype is summarized in Table 5.

Table 5: Preamplifier performance.

power consumption	125	mW
ENC with one PD($\tau = 1\ \mu$s)	620	e
decay time	65	μs
charge to voltage conversion	–1/1.3	V/pC
dynamic range of the output	–4.6	V
nonlinearity over the dynamic range	< 0.03	%

9 Beam Test

We have done beam tests of arrays of CsI(Tℓ) crystals produced by BINP, JCCG, and CRISMATEC with prototype preamplifiers and shapers using the electron and pion beams at KEK proton synchrotron. The energy resolution and pion mis-identification had been measured and reported in reference 5. Another beam test has been done at BINP by using the tagged photon beam at the VEPP-4 storage ring. The preliminary results are given in reference 6.

Acknowledgements I would like to express my gratitude to all members of the BELLE electromagnetic calorimeter group and prof. M. Fukushima for their continuous efforts.

References

1. The BELLE Collaboration, BELLE Progress Report, KEK Progress Report 96-1, March 1996.

2. The BELLE Collaboration, Technical Design Report, KEK Report 95-1, April 1995.

3. The BELLE Collaboration, Letter of Intent for A study of CP Violation in B Meson Decays, KEK Report 94-2, Apirl 1994.

4. K. Kazui *et al.*, BELLE Note 119/TIT-HPE-96-3, 1996.

5. Y. Ohshima *et al.*, KEK Preprint 96-12, May 1996.

6. B. Shwartz's talk at this conference.

ascati Physics Series Vol. VI, (pp. 705–714)
: INT. CONF. ON CALORIMETRY IN HEP – Frascati, June 8–14, 1996

THE CsI(Tl) ELECTROMAGNETIC CALORIMETER FOR THE BaBar EXPERIMENT AT SLAC

R. Seitz
Institut für Kern– und Teilchenphysik
Technische Universität Dresden, D–01062 Dresden

ABSTRACT

The BABAR-experiment at the SLAC asymmetric e^+e^- B-factory will study P-violation in B-Meson decays. This requires the detection of photons with very od angular and energy resolution. The target energy resolution is $\sigma_E/E =$ $01/E^{1/4} \oplus 0.012$.

To achieve this, a large CsI(Tl)-calorimeter consisting of 5760 crystals in e barrel and 820 crystals in the forward endcap is under construction. The crystals, cated inside the solenoidal magnet will be read out by silicon PIN-photodiodes.

Introduction

he aim of the BABAR detector at SLAC is to study CP-violation in B-meson de- ys from the $\Upsilon(4S)$ resonance. The experiment which will operate at the high minosity, asymmetric e^+e^- storage ring PEP-II, is presently under construction. he asymmetry in beam energy (electron beam 9 GeV, positron beam 3.1 GeV) osting the decaying B mesons in the laboratory frame makes time order measure- ents of B^0 $\bar{B}^0$ decays possible with present detector technology. The asymmetry beam energy translates as a forward-backward asymmetry in the design of the ABAR experiment (Fig. 1).

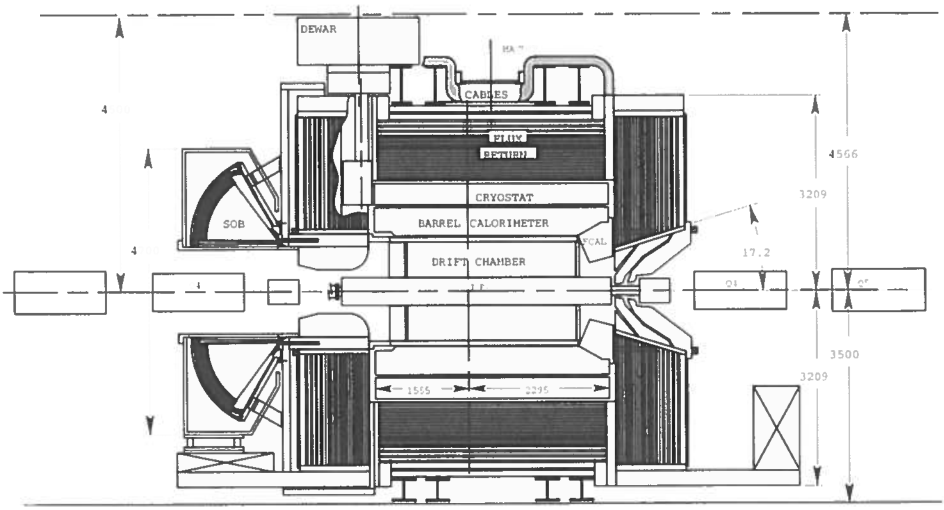

Figure 1: The *BaBar* detector in a cross-sectional view. The e^- beam comes from the left, the e^+ from the right.

Fig. 1 shows the *BaBar* detector in a cross-sectional view. The interaction point (I.P.) is surrounded by the silicon vertex tracker located inside a support tube of 20 cm diameter which traverses the experiment. A drift chamber for tracking is located outside the support tube. Particle identification is done with a Detector for Internally Reflected Cerenkov light (DIRC). The quartz bars of this detector are mounted around the drift chamber; the Cerenkov light is transported in the quartz to the photomultipliers situated at the rear of a water tank (SOB). The electromagnetic CsI calorimeter surrounds the particle identification system. All these detectors sit in a magnetic field provided by a 1.5 T superconducting coil. The magnet flux return is interleaved with Resistive Plate Chambers acting as a muon detector and hadron calorimeter. The drawing shows the beamline components Q4, Q5 as well. The overall dimensions are indicated in Fig. 1 in mm.

2 Calorimetry Requirements

To reconstruct CP eigenstates with one or more π^0, requires an excellent electromagnetic calorimeter. Generic B decays have an average of 5.5 charged tracks and 5.5 photons. For most events the photon energies are about 200 MeV or less (Fig. 2(a)).

the other hand, the kinematically most extreme channel of interest $B^0 \to \pi^0\pi^0$ ıtains photon energies higher than 4 GeV (Fig. 2(b)).

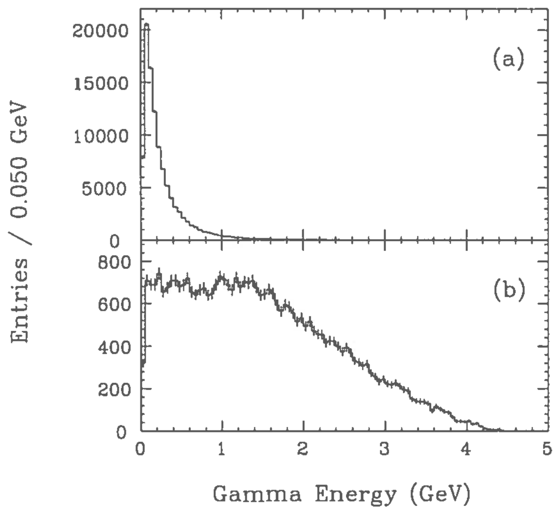

ȝure 2: Photon energy spectra for generic B decays (a) and for the kinematical ꞉reme channel $B^0 \to \pi^0\pi^0$ (b).

CsI(Tl) has a high scintillation light output (50000 p.e./MeV), thus it is ıble to reconstruct photons in the energy range of a few tens MeV. By having ficiently long crystals the target resolution extends up to about 10 GeV. Thus a I(Tl) barrel and forward endcap are the calorimeter choice for BaBar.

The CsI(Tl) Calorimeter

Overview

ıe calorimeter consists of 5760 crystals in a cylindrical barrel and 820 crystals the forward endcap (Fig. 3). The barrel is arranged in 48 rings, containing 120 ⁄stals each. The forward endcap consists of three crystal rings with 120 and 0 and two rings of 80 crystals. The crystals are truncated pyramids, having a ınt face of about 4.7 × 4.7 cm^2 and a 6 × 6 cm^2 rear surface. The beam energy ⁄mmetry requires the forward part of the detector to be longer, 180.9 cm, whereas ɜ backwards part of the barrel extends 112.7 cm from the interaction point. The ꞉lius of the barrel is 91 cm. To decrease the crystal volume, in order to save cost, ɜ crystal length varies along the barrel. In the forward endcap and the forward part of the barrel, the crystals are 32.55 cm (17.5 X_0) long, whereas in the rear part of the barrel a length of 29.76 (16 X_0) is sufficient to achieve the physics requirements.

In the laboratory frame the angular coverage of the calorimeter ranges from 15.8° to 140.8°, with the barrel-endcap interface at 26.9°. This corresponds to an angular coverage in the center-of-mass system of 88%.

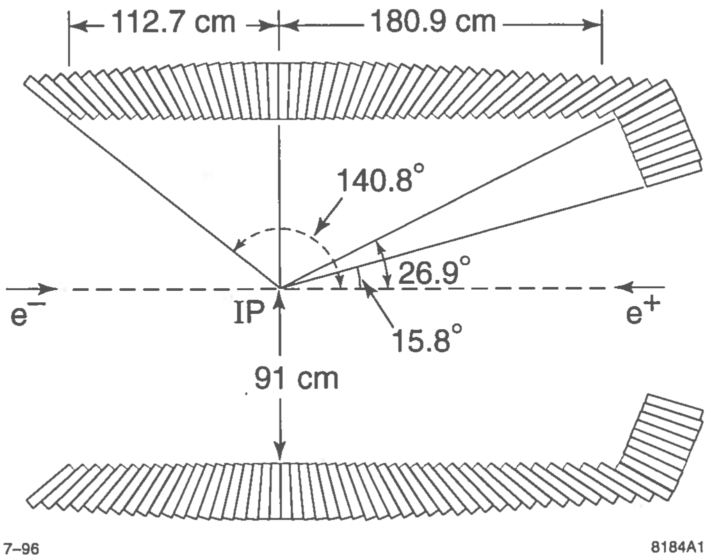

Figure 3: Cut view of the CsI calorimeter.

The material in front of the calorimeter amounts to 0.23 X_0 for the barrel, coming mainly from the DIRC (0.19 X_0) and 0.16 X_0 for the endcap.

3.2 Light Readout

The crystals are read out by two PIN photodiodes (Hamamatsu 2744-08) on the rear face, with an active surface of 1×2 cm^2 each. The diodes are coupled with epoxy to a lucite carrier plate, glued onto the crystal rear surface. Also on the rear of each crystal sits the front-end electronics, consisting of a dual range amplifier and shaper mounted on a printed circuit board.

3.3 Crystal Quality

A minimum light yield specification for every crystal is necessary to achieve the required performance, since the light yield of a crystal has direct influence on the solution and the energy equivalent electronic noise. Measurements of the light eld are done with a radioactive source, e.g. the 511 keV line of ^{22}Na or the 2 keV γ line of ^{137}Cs. To facilitate the measurement of large crystal quantities several manufacturing sites, the light yield is determined relative to a known andard crystal.

An important contribution to the constant term in the target resolution:

$$\frac{\sigma_E}{E} = \frac{0.01}{\sqrt[4]{E(\mathrm{GeV})}} \oplus 0.012,$$

the light output nonuniformity along the crystal. A GEANT simulation of increasg or decreasing light output along the length of a crystal lead to the specification own in Fig. 4 [1), 2)].

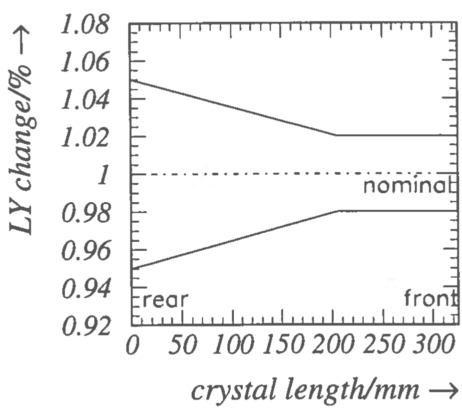

Figure 4: Crystal light output uniformity specification.

The specification is tight, (±2%) in the first part of the crystal, where the iowers start to develop, and allows a linear decrease or increase of light output as function of position in the crystal towards the rear end. For the longest crystals the detector, 17.5 X_0, the maximal nonuniformity amounts to ±5% at the crystal ear. Increasing light output along the crystal improves for high photon energies ie energy resolution since the positive nonuniformity compensates for rear leakage. his has been already observed in studies for the CLEO and L3 crystal calorimeters). Decreasing light output as a function of position in the crystal has always egative influence on the energy measurement.

3.4 Wrapping/Tuning

To maximise the light output the crystals will be individually wrapped with diffuse reflector material. A comparison of different materials [4] favours TYVEK, a spun-bonded olefin, both for reflectivity and handling properties over other candidates such as Teflon film.

The choice of TYVEK as wrapping material allows to tune the uniformity of the light output. It is possible to print a pattern directly on the material, hence changing the reflectivity of the wrapping at defined locations (Fig. 5). This procedure causes a decrease in light output, and is therefore limited by the minimum light yield requirement of 5500 photo-electrons per MeV specified for the *BaBar* crystals. An example of tuning is presented in Fig. 6, where the crystal was just out of specification at the front end. Printing a black stripe on the wrapping material takes light away (lower average light yield), but improves clearly the overal uniformity of the light output (Fig. 6(b)). The crystals will be wrapped in two layers of TYVEK, optimising dead material between crystals against the improved light collection due to additional wrapping.

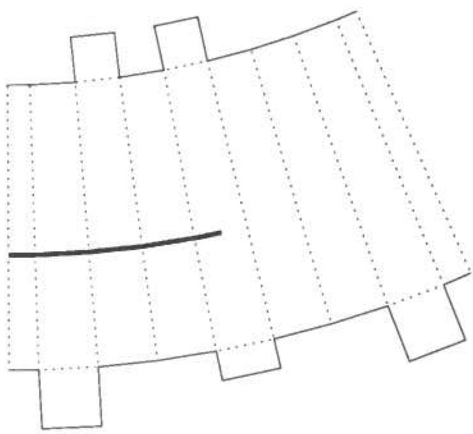

Figure 5: Wrapping material contour with tuning pattern. The material of which the contour is shown allows to wrap the crystal with two layers.

3.5 Quality Control

The high light output of CsI(Tl) permits to check light yield and light output uniformity with radioactive sources in the laboratory. The *BaBar* crystals are controlled with a ^{22}Na (511 keV photon line) source and the crystals read out with a phonultiplier. This is done at production sites and at SLAC upon arrival for each lividual crystal.

The scanning is done in a light tight box, moving a collimated source along e crystal, to obtain a position sensitive measurement of the light output. Fig. 6(a) ows the values obtained every 2 cm along the crystal, plotted normalised to the ht yield of a cylindrical standard crystal of 2.5 cm length and diameter.

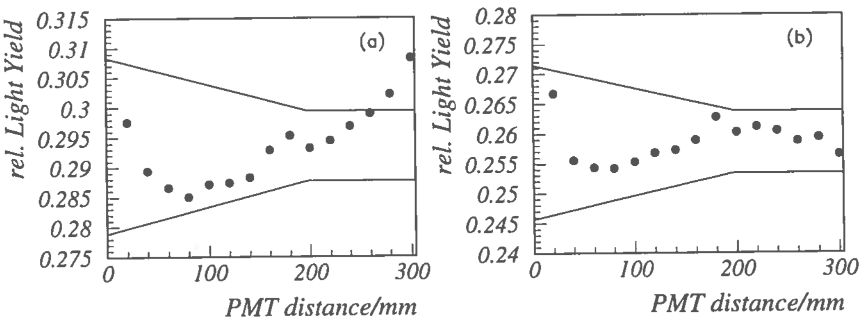

Figure 6: Longitudinal light yield uniformity before (a) and after tuning (b).

The Support Structure

1 Barrel

he basic mechanical structure of the calorimeter are so called *modules.* A module a 300 μm thick carbon fibre structure housing 3 $\times$ 7 crystals. Crystals are held ı place by an aluminium frame glued inside each carbon fibre compartment on the ·ystal rear. This frame also acts as housing for the preamplifier board which is ɔnnected to each of the two diodes.

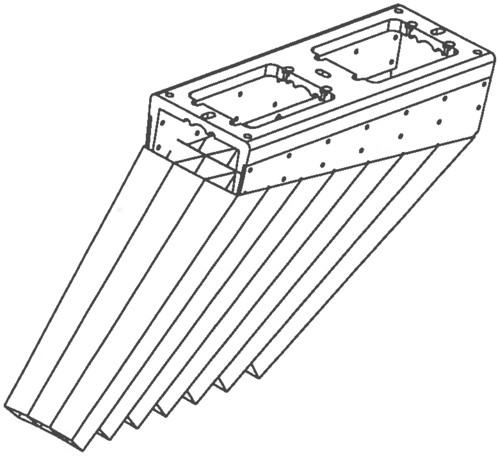

Figure 7: A barrel module housing 21 crystals.

The mechanical strongback of the modules (upper part of Fig. 7) which reaches into the carbon fibre compartments is epoxied to the inside walls of the 7 compartments on each long side of a module. A conceptional view of the loading procedure of a complete module in a strong aluminium cylinder is shown in Fig. 8. After the loading of all modules they will be aligned individually.

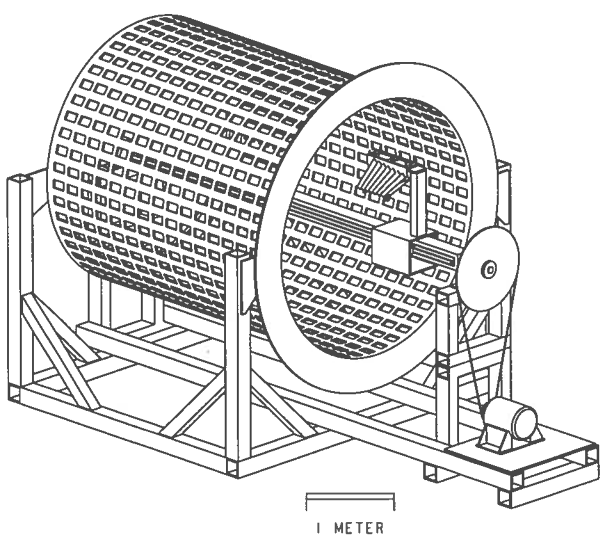

Figure 8: Conceptional drawing of the loading of modules into the barrel.

: Endcap

.e forward endcap is an arrangement of similar-sized crystals in a conic section. .is results in 8 rings of 3 times 120 and 100 followed by 2 rings of 80 crystals. .e endcap is also modular, the crystals being grouped in 20 modules containing crystals.

Beamtest Results

beamtest with crystals of 36 cm length and front faces of 5×6 cm^2 and rear :es of 6×6 cm^2 has been performed in October 1995 at PSI in Switzerland. The :ident beam, electrons and pions could be varied in energy between 100 and 400 :V.

Data was taken at five different beam momenta, 105, 135, 215, 320 and 5 MeV/c. The preliminary result for the energy resolution σ_E/E as a function of am energy is shown in Fig. 9.

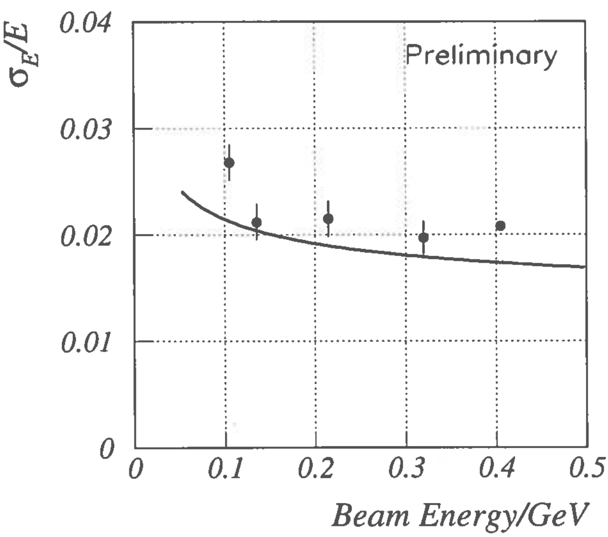

gure 9: Energy resolution as a function of incident beam energy. Drawn as line is e target resolution.

The measured energy resolution values are larger than the design target ne in Fig. 9), due to non-optimal coupling of the diodes compared to preceding boratory measurements. The electronics, which is not the final one, influences the resolution because of amplifiers with higher noise contribution. With the final electronics and optimal coupling of the diodes the beamtest suggests that the calorimeter will reach its design resolution.

6 Summary

The *BaBar* electromagnetic calorimeter for CP-physics at the SLAC *B*-factory requires large angular coverage and excellent energy resolution over a large energy range. This can be achieved with a CsI(Tl) detector. The light readout of the crystals is done with diodes glued on the crystal rear. The optimisation of the light collection due to wrapping with diffuse reflecting material, TYVEK, has been discussed. An important issue in order to reach the resolution target is crystal uniformity tuning and quality control for which procedures have been developed.

The mechanical support of the detector, barrel and forward endcap, is realised in a modular carbon fibre structure.

A first beamtest with an array of 25 crystals demonstrated the need for optimal light readout and front end electronics to reach the design resolution target.

7 Acknowledgements

I would like to thank the members of the *BaBar* calorimeter group who contributed with their work to this presentation. I would like to thank as well the local organisers in Frascati for their hospitality and effort.

References

1. The *BaBar* Collaboration, *BaBar* Technical Design Report, SLAC-R-95-457.

2. J.Brose *et al.* *BaBar*-note 175.

3. J.A.Bakken *et al.* Nucl.Instr.Meth. **A254**, 535 (1987) and E.Blucher *et al.* Nucl.Instr.Meth. **A249**, 201 (1986).

4. R.Wang *et al.* *BaBar*-note 206 and G.Dahlinger *BaBar*-note 241.

ALORIMETRY WITH CsI CRYSTALS IN THE BUDKER INSTITUTE OF NUCLEAR PHYSICS

B.A. Shwartz
Budker Institute of Nuclear Physics, Novosibirk, 630090 Russia

No written contribution received

;cati Physics Series Vol. VI, (pp. 717–726)
NT. CONF. ON CALORIMETRY IN HEP – Frascati, June 8–14, 1996

E PERFORMANCE OF A NEW CsI CALORIMETER FOR THE KTEV EXPERIMENT AT FERMILAB

P. N. Shanahan

Fermilab - MS122
P.O. Box 500
Batavia, IL 60510 USA
(Representing the KTeV Collaboration)

ABSTRACT

e KTeV experiment at Fermilab has built a new cesium-iodide calorimeter for rare K decay program (E799) and search for direct CP violation in $K^0 \to 2\pi$:ays (E832). The need for high rate, high precision electromagnetic calorimetery net by an array of 3100 undoped CsI crystals, 27 X_0 long, digitized and read-out a system of deadtimeless, multiranging pipeline ADCs, mounted directly on the ototube bases. The calorimeter is described, and its performance in cosmic ray d laser calibration tests is discussed.

Introduction

. KTeV

ıe KTeV collaboration comprises two fixed target experiments at Fermilab. E832 primarily concerned with the search for evidence of direct CP violation in $K^0 \to \pi\pi$ cays. E799 will study various rare K_L decay channels, among them the pure direct ? violating mode $K_L \to \pi^0 \nu \overline{\nu}$.

The E832 experiment will attempt to measure the direct CP violation rameter ϵ'/ϵ from the double ratio of $K^0 \to \pi\pi$ decay rates:

$$R \equiv \frac{\Gamma(K_L \to \pi^+\pi^-)}{\Gamma(K_S \to \pi^+\pi^-)} / \frac{\Gamma(K_L \to \pi^0\pi^0)}{\Gamma(K_S \to \pi^0\pi^0)}) \approx 1 + 6Re\left(\frac{\epsilon'}{\epsilon}\right) \qquad (1)$$

order to minimize systematic biases due to changing acceptances, beam fluxes, c., all four decay rates are measured simultaneously in two nearly parallel kaon :ams, using a magnetic spectrometer to analyze $\pi^+\pi^-$ decays and a CsI calorimeter analyze $2\pi^0$ decays.

1.2 Calorimetry Requirements

Monte Carlo studies and experience with a previous ϵ'/ϵ experiment, E731 [1], have led to the following requirements for the calorimeter:

Energy Resolution - < 1% at 15 GeV for photons,
Linearity - true and measured energy related by $E_T = E_M^{(1-\alpha)}$,
with $\alpha < 0.5\%$,
Position Resolution - measure center of photon clusters to 1-2 mm,
Radiation Hardness - withstand a maximum dose of 10 KRad,
Dynamic Range - physics sample covers photon energies from 2 to 80GeV,
Fast Response - expect a maximum rate of 100kHz in calorimeter, and,
e/π Seperation - reduce $K_L \rightarrow \pi e \nu$ backround to $K_L \rightarrow \pi^+\pi^-$

1.3 Description

The design of the calorimeter chosen to meet the requirements listed above has been discussed in detail in previous proceedings [2]. The KTeV calorimeter consists of 3100 crystals of pure cesium-iodide (CsI) in a $1.9 \times 1.9\text{m}^2$ array, 0.5m deep, with 2 beam holes, 15cm on a side, separated by 15cm on the horizontal axis. Each channel is read out out by a phototube, whose signal is digitized by a deadtimeless, multiranging, pipeline ADC mounted directly to the phototube base. The front end is a custom-built, VME based system which greatly reduces the data volume transfered from the calorimeter to the data acuisistion system.

Figure 1 shows the reconstructed kaon mass peak for $K_L \rightarrow 2\pi^0$ events reconstructed in the E731 lead glass calorimeter, compared to a Monte Carlo simulation for the KTeV CsI calorimeter. The normalization of the KTeV simulation is a small fraction of the expected data sample. The KTeV sample has a narrower mass peak and smaller $K_L \rightarrow 3\pi^0$ background relative to the $K_L \rightarrow 2\pi^0$ signal, indicated by the smaller wings. These improvements are due in large part to the improvement in position and energy resolution in the KTeV calorimeter.

2 Crystals

2.1 Physical Characteristics

The physical propertied of CsI most relevant to calorimetry are [4]:

Radiation Length - 1.85 cm,
Nuclear Interaction Length - 36.5cm,
Moliere Radius - 3.8cm, and
Temperature Coefficient of Response - $-1.5\%/^\circ$ C [5].

The scintillation light produced in CsI has three main components with decay times

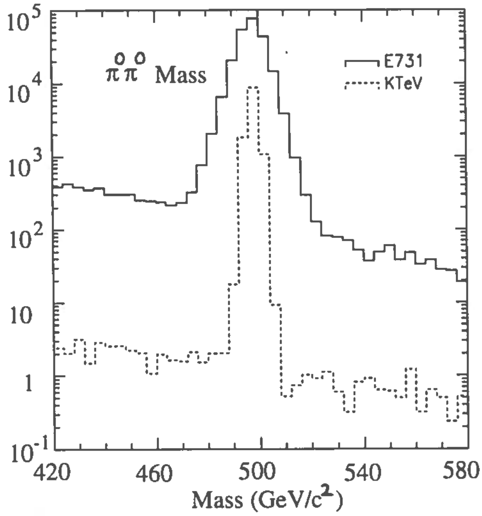

ure 1: The reconstructed K mass in the E731 lead glass calorimeter and a Monte rlo study of the reconstructed K mass in the KTeV CsI calorimeter. The normal- tion of the KTeV simulation is arbitrary.

8ns, 10ns, and 1000ns. The two fast components have a peak wavelength of 305ns the fast components and $\sim$ 480nm for the slowest [4]. A 1mm thick Schott-UG11 raviolet filter placed between each crystal and the corresponding phototube gives rompt light yield (percentage of light arriving within 100 ns) of 85%.

Geometry

ie CsI crystals have been chosen to be 50 cm (27 X_0, 1.4λ) long on the basis Monte Carlo simulations of the dependence of energy resolution on the length. optimization of the position resolution with the constraint of cost and number channels has lead to a choice of two sizes of crystals. Those within the central 2x1.2m^2 of the array have a cross section of 2.5x2.5cm^2, while the others have a oss section of 5x5cm^2.

The crystals were produced by three manufacturers. The 1674 small and 8 large crystals supplied by Bicron and Crismatec are each two 25cm crystals ied together. The 558 small crystals and 100 large crystals supplied by Horiba e single crystals. The geometric tolerances are 0.1mm on the width and 1mm on e length.

The energy resolution has been enhanced by individually wrapping each ystal with opaque and aluminized mylar to ensure a response to a radioactive

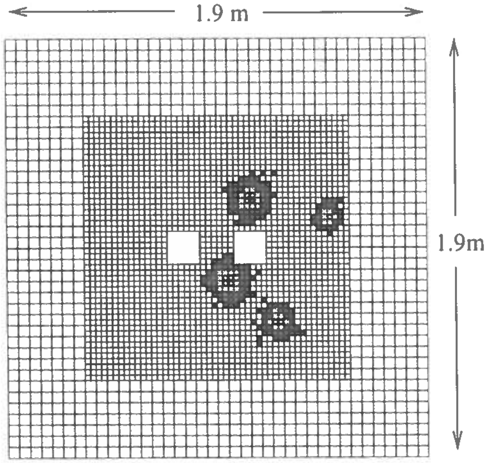

Figure 2: An event display of a Monte Carlo $K_L \rightarrow \pi^0\pi^0$ event, facing along the beams. The 4 photon clusters are seen in the right half of the array.

source (^{137}Cs) that is uniform to within 5% along the length of the crystal.

The geometry of the array is illustrated in Fig. 2, an event display of a $K_L \rightarrow \pi^0\pi^0$ event.

The array is contained within a light-tight house whose temperature is kept constant to $\pm 1°$C.

3 Phototubes

There are two sizes of phototubes corresponding to the two sizes of crystals (Table 1). The high voltage divider chain of each phototube is chosen from 5 possible types to minimize the non-linearity. The combined effect of operating at low gain and optimizing the HV divider gives a non-linearity below 1% for a 30mA peak current (with repect to the response at 7mA peak current). The rate stability of the tubes is $< 0.8\%$ for a 10mA pulse in the presence of a $5\mu A$ constant anode current. Rate effects will be stabilized by using a red LED which will give a constant anode current offset of between 10nA and 100nA.

The 25% quantum efficiency of both models, combined with the high light yield of CsI combine to yield about 15-30 photo-electrons per MeV.

Table 1: Phototube Characteristics

	Small Crystals	Large Crystals
Model	Hammamatsu R5364	Hammamatsu R5330
Diameter	0.75" (1.9cm)	1.5" (3.8cm)
Typical Gain	3750	2500
Stages	5	6

Digitization and Readout

Digitization

ιe goal of low-noise digitization of the phototube signal and the high readout ;e are met in part by the KTeV Digital Photomultiplier Base (DPMT) [2]. The ²MT is a multi-ranging, deadtimeless, pipeline ADC, comprising three principle mponents: the Charge Integrator and Encoder (QIE), a flash ADC (FADC), and e Driver/Buffer/Clock (DBC). The QIE and DBC are application specific inteated circuits (ASICs) designed by Fermilab. The DPMT is designed to continually ;itize at freqencies up to 53.104 MHz, the Tevatron RF frequency.

The QIE [3] is a fully differential device which integrates the PMT current to a set of 8 capacitors divided into 8 binary weighted ranges. The voltage of e in-range capacitor is multiplexed to the FADC, and the range is output to the 3C as a 3 bit digital number. There are 4 sets of capacitors to allow a continual, adtimeless digitization. The QIE also outputs a 2 bit number corresponding to e capacitor set, or "phase", to allow an independent calibration for each set.

The anologue multiplexed voltage from the QIE is digitized by a Harris-86 8-bit Flash ADC.

The DBC synchronizes the FADC value, QIE range, and phase data to rm a floating point representation of the charge in each integration sample. The .ta are continuously stored in a FIFO (First In, First Out buffer) 40 samples ep, 32 of which are synchronously transfered to a second FIFO upon receipt of Level-1 trigger. This 32 sample "snapshot" of the PMT signal coincident with a :vel-1 trigger is output from the DBC in byte serial mode upon receipt of a Level-2 igger. The DBC also receives the external clock signals necessary to synchronize e digitization to the arrival of energy in the detector, and provides them to the IE and FADC with the appropriate skews.

Figure 3 shows a block diagram of the DPMT design, as well as a schematic the FADC response as a function of DPMT input charge.

Figure 4 shows the average time evolution many CsI signals for a single .annel, as measured by a DPMT running at 53MHz. The data are for longitudinal

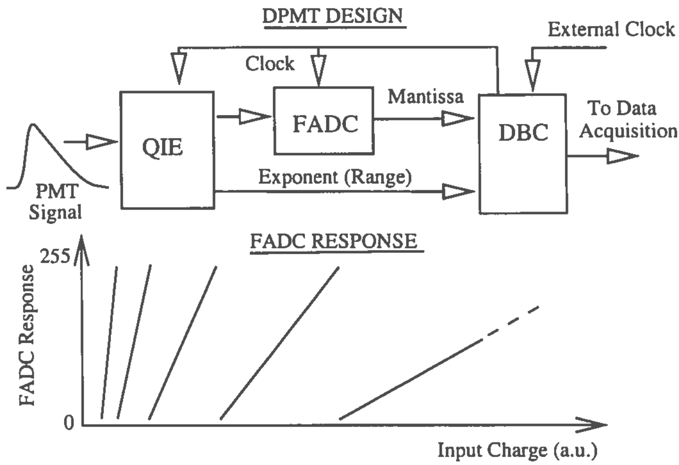

Figure 3: *Top:* Block diagram of the DPMT. *Bottom:* Schematic of the DPMT FADC response as a function of PMT charge arriving in a digitaztion sample.

cosmic rays, triggered by an analogue sum of the dynode signals from three channels. The lines are a fit to three exponential decays, giving decay times for the three components of 11, 33, and ~1000ns (c.f. Section 2.1).

4.2 Readout

The DBC data from each channel is read out for every Level-2 trigger into a custom-built VME based system. The data volume is about 200kByte per Level-2, which occur at 10-20KHz. The readout modules subject each channel to a minimum energy cut and transfer only the relevant subset of the 32 samples read out from the DBCs. This reduces the output data volume by a factor of 25 or more.

The calorimeter also provides input to the triggers. The main Level-1 triggers for the $K_{L,S} \rightarrow 2\pi^0$ mode require an analogue sum of all PMT dynode signals equivalent to a total energy of at least 28 GeV. Channels for which the dynode signal is equivalent to 1GeV or greater also contribute to a hardware search for clusters in the calorimeter. The Hardware Cluster Counter has a 1.5 μs decision time, and contributes to the Level-2 trigger.

5 Calibration Scheme

The calibration of the calorimeter can be divided into DPMT linearization and energy scale calibration. DPMT linearization is the determination of the relative gains of the 8 ranges and 4 phases within each DPMT. The energy scale for each

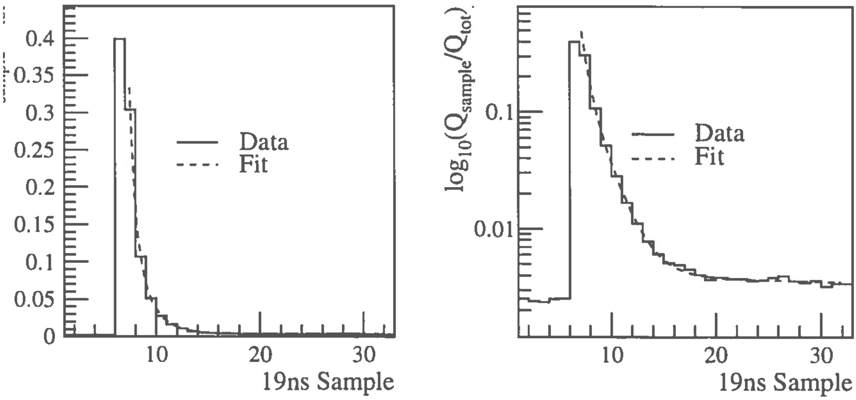

gure 4: Average fraction of charge per digitization sample for longitudinal cosmic ys, on linear (*left*) and logarithmic (*right*) scales. The fit is to a sum of three ponential decays.

annel will be set using electron showers, where the electon momentum is known m the spectrometer. The overall energy scale for photons relative to electrons ll be measured from $\pi^0 \rightarrow \gamma\gamma$ decays occuring at known positions in the beam. It expected tha the overall energy scale will be known to better than 0.02%

The DPMT linearization scheme uses light from a Nb:YAG laser with quency tripling optics, mediated by a dye of N-Methyl Carbozole (50mg/75ml) [2]. e light emitted from the dye has a peak emmision wavelength of 380nm and a cay time similar to that of CsI scintillation light. The light is carried from the e to the downstream end of each crystal by an independent quartz fiber. The libration standards are a pair of Hamamatsu 1722 P-I-N diodes per calorimeter adrant, each digitized by a Burr-Brown DDC101 20 Bit ADC.

A set of filter wheels is used to scan the light level over the dynamic range all DPMTs during calibration runs. The DPMT linearization is achieved by rforming a least squares fit between the charge in each DPMT (summed over veral digitization samples) and the corresponding pin diode. Since the DPMT sponse is modeled as a straight line within each range and phase, there are 64 rameters to be determined and stored for each channel.

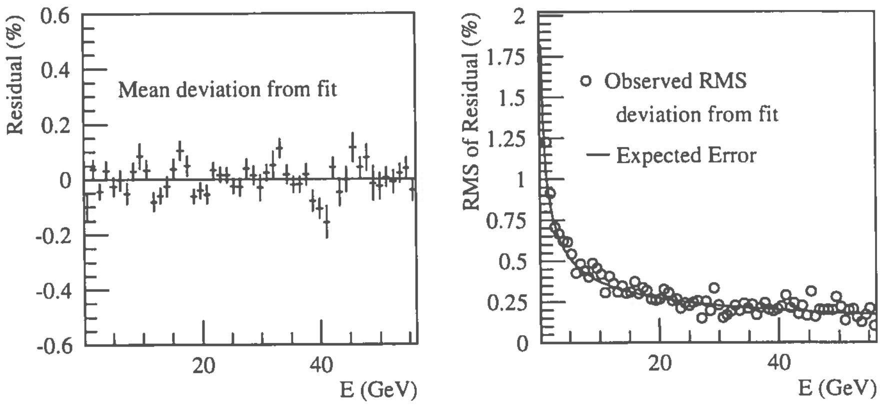

Figure 5: The results of the DPMT linearization. *Left*: The fractional residual of a fit of the DPMT response to the P-I-N diode, vs. the equivalent energy. *Right*: The expected and measured deviation of DPMT data from the fit to the P-I-N diode response.

6 Performance

The calorimeter has yet to be exposed to the nominal beam conditions, but its performance has already been partially studied using the laser calibration, a test beam at CERN, and transverse cosmic rays in the completed array at Fermilab.

6.1 Laser Data

Calibration results for a typical channel are shown in figure 5. The left plot shows the normalized residual (Fit-Data/Data) between the linearized DPMT response and P-I-N diode response, vs. equivalent energy of the DPMT response. The size of the residuals, less than 0.2%, holds for most channels. The final analysis goal of 0.1% residuals will most likely require non-linear corrections to the linear model of the DPMT response.

The right plot shows the observed RMS deviation of the data from the fit, as well as the expected error on each data point, taking into account contributions from photostatistics, digization, time jitter of the laser pulse, and the P-I-N diode noise and statistics. A overall normalization shift of 25-50% is needed to bring the expected error into agreement with the observed RMS. This is believed to be due mostly to the variation of the QIE capacitor values from the nominal, and is ultimately unimportant.

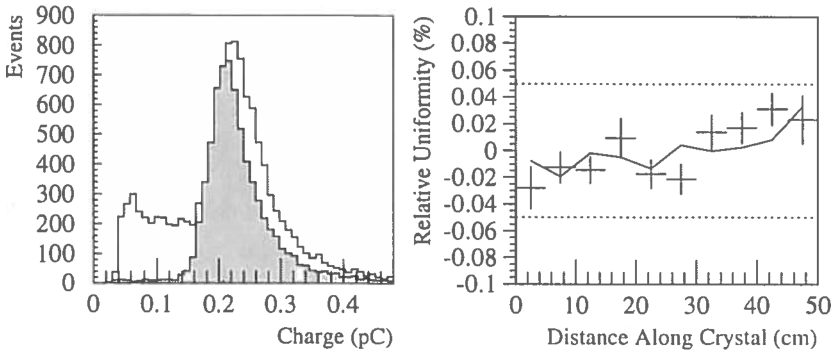

ure 6: *Left:* The transverse MIP charge distribution (lowest range only) for mic ray events for 1 CsI channel. The shaded distribution is after cuts relevant ıniformity analysis are applied. *Right:* The uniformity meaured with with cosmic s in situ (crosses), and with a radioactive source prior to installation (line).

Cosmic Ray Data

e uniformity of light response along each crystal ensured by the correct wrapping ,he crystal is continuously verified in situ using (transverse) cosmic rays tracked h a cosmic ray telescope segmented along the crystal crystal axis. The fit value the MIP peak for cosmic ray triggers in each 5cm bin along the crystal axis vides a measure of the crystal uniformity. Figure 6 shows the transverse cosmic P peak distribution for a channel, as well as the uniformity measured both in situ h cosmic rays and with a source prior to installation. Since the RMS of pedestal tributions is typically σ_{ped}=0.01 pC, the position of the 35 MeV transverse MIP .k at 0.22 pC is more than $20\sigma_{ped}$ above pedestal. This impressive result in a orimeter whose upper limit is about 80GeV is made possible by the fact that the itazation is multi-ranging, and that it is performed within 20cm of the phototube.

The uniformities in Fig. 6 are in good agreement with each other, and hin the 5% specification.

Test Beam

ub-array of 25 large crystals has been tested in pion and electron beams at CERN. analysis of those data have shown that the energy resolution of the calorimeter should be better that 1% for electromagnetic shower energies between 5 and 60GeV, and that the e/π rejection rate should be 720±75 for an 95% electron identification efficiency [5].

7 Conclusions

The KTeV collaboration has built a new CsI calorimeter for its E799 and E832 Kaon decay experiments. Earlier test beam results, and current cosmic ray and laser calibration studies indicate that the objectives of high-rate, high-precision electromagnetic calorimetry over a dynamic range of 2-80 GeV will be met. The calorimeter will be exposed to its first hadron beam in late 8/96, and is expected to run in its nominal configuration by late 9/96.

8 Acknowledgements

I would like to extend my gratitude to J. Whitmore helping me understand the DPMT, to H. Nguyen for helping me learn to use the calibration system, and to R. Tschirhart for filling many other gaps in my understanding of the calorimeter. I also thank R. Kessler for providing the cosmic ray data plot, and to Elliott Cheu for providing the event display and Kaon mass plots. This work is supported by DOE Contract No. DE-AC02-76CHO3000.

References

1. L.K. Gibbons, et al., Phys. Rev. Lett. **70**, 1203 (1993).

2. R.E. Ray, The KTeV Pure CsI Calorimeter; H.N. Nguyen, The KTeV PMT Monitoring System; J. Whitmore, A High Speed Digitizing Photomultiplier Base For the KTeV CsI Calorimeter, in: Proc. Fifth International Conference on Calorimetery in High Energy Physics (ed. H.A. Gordon and D. Rueger, Brookhaven National Laboratory, September 1994), 110, 479, and 442 (World Scientific, New Jersey, 1994).

3. T. Zimmerman and M. Sarraj., IEEE Trans. Nucl. Sci. **43**, 1683 (1996).

4. D.G. Coyne, et al., Review of Particle Properties, Phys. Rev. **D 50**, 1261 (1994), and Refs. therein.

5. R.S. Kessler, et al., Nucl. Inst. Meth. **A 368**, 653 (1996).

ascati Physics Series Vol. VI, (pp. 727–739)
INT. CONF. ON CALORIMETRY IN HEP – Frascati, June 8–14, 1996

THE BGO CALORIMETER FOR THE GRAAL BEAM

B. Girolami, F. Ghio
INFN – Sezione Sanità and Istituto Superiore di Sanità, Roma, Italy

M. Castoldi, S. Zucchiatti
INFN – Sezione di Genova, Italy

P. Levi Sandri, P. Rossi
INFN – Laboratori Nazionali di Frascati, Italy

V. Bellini
INFN– Laboratori Nazionali del Sud and Università di Catania, Italy

M. Capogni, L. Casano, L. Ciciani, A. D'Azeglio, A. D'Angelo, D. Moricciani, L. Nicoletti, C. Schaerf
INFN – Sezione di Roma II and Università di Roma "Tor Vergata", Italy

R. Di Salvo, G. Gervino
INFN – Sezione di Torino and Università di Torino, Italy

ABSTRACT

A large solid angle BGO calorimeter has been constructed and tested to measure ermediate energy (10-1000 MeV) photons. It is made of 480 crystals and covers e full solid angle with the exception of two cones in the forward and backward rections with a semiaperture of 25°. It will be used in conjunction with a polarised d tagged γ-ray beam with an energy up to 1600 MeV for the study of meson otoproduction and meson rare decays. Among the performances of the detector linear response and an energy resolution 3% (FWHM) were obtained in a test periment. A preliminary run with the Graal beam at the ESRF in Grenoble has elded a two-photon mass spectrum with peaks at the π^0 and η masses. A sixoton mass spectrum shows a clear peak at the η mass evidencing the decay of the into three π^0.

Introduction

A BGO calorimeter [1] with large solid angle has been built for the LAGRANGE paratus [2], that will operate at the GRAAL polarised and tagged photon beam cility. The BGO properties make this material one of the most suitable for the tection of low and intermediate energy photons (10-1000 MeV). The combined e of this calorimeter with a polarised and tagged γ-ray beam with energies up 1.6 GeV will provide a powerful tool to investigate the dynamical properties the nucleons in the non perturbative regime and to improve our knowledge of eudoscalar mesons neutral decays.

2 The GRAAL tagged and polarised γ-ray beam

The γ-ray beam is produced through the Compton backscattering of a laser light against the 6 GeV electrons circulating in the ESRF storage ring at Grenoble [3) 4) 5)]. The interaction takes place in one of the straight sections of the ring: an optical system allows the alignement of the Ar laser light with the electron beam with a precision of 30 μm and 3 μrad. The maximum γ energy obtained with the Argon (U.V.) laser line is 1.6 GeV. A flux of 2×10^6 γ/s over the entire spectrum has been measured with a laser power of 2.8 W.

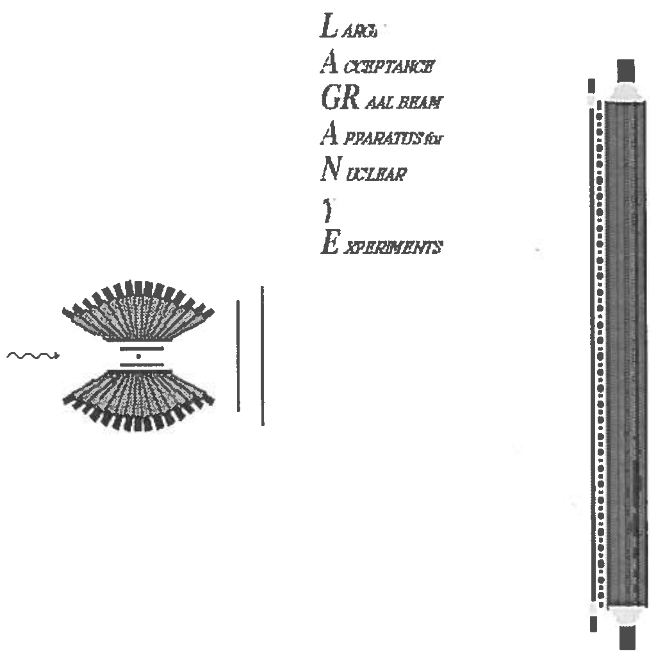

Figure 1: The LAGRANGE detector; from left to right: BGO calorimeter surrounding cylindrical MWPC and ΔE/Δx scintillators, plane MWPC, TOF scintillator wall and shower-neutron detector.

The determination of the γ energy is obtained by measuring the displacement of the scattered electron from the main orbit. The tagging detector, located inside the ring after the first bending magnet, consists of 128 micro-strips (with a 300 μm pitch) and a set of 10 plastic scintillators. The low emittance of the ESRF rage ring and the tagging detector features will allow to tag the γ-ray beam with energy resolution of about 16 MeV (FWHM).

The light emitted from the laser is linearly polarised by two Brewster win-vs and can be circularly polarised by a quarter-wave length plate. At maximum ·nergies, the laser polarisation is entirely transmitted to the backscattered γ-ray ım.

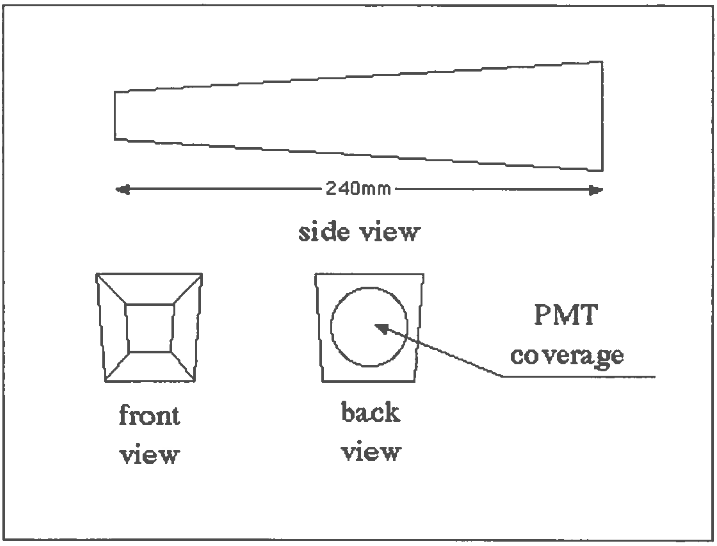

Figure 2: Cut views of BGO crystals showing PMT coverage

The GRAAL experimental set-up

Figure 1 shows the experimental set-up of the LAGRANGE detector. It consists two cylindrical and two planar MWPC to track the charged particles inside the ;O and in the forward direction respectively; a scintillator barrel and a double ntillator wall for the charged particles and photon identification; the BGO Rugby ll calorimeter and a scintillator shower detector wall for the detection of γ-rays.

The Rugby Ball calorimeter

Гhe BGO Rugby Ball covers a solid angle of 3.6 π sr. The calorimeter is composed 480 crystals, arranged in a 15 x 32 matrix covering polar angles from 25° to 155° 1 with complete azimuthal coverage. Crystals are wrapped in a thin aluminized mylar foil and are housed in 24 carbon fiber baskets, each divided into 20 cells, to keep the crystals optically and mechanically separated. The thickness of the internal walls is 0.38 mm, while the thickness of the external ones is 0.54 mm.

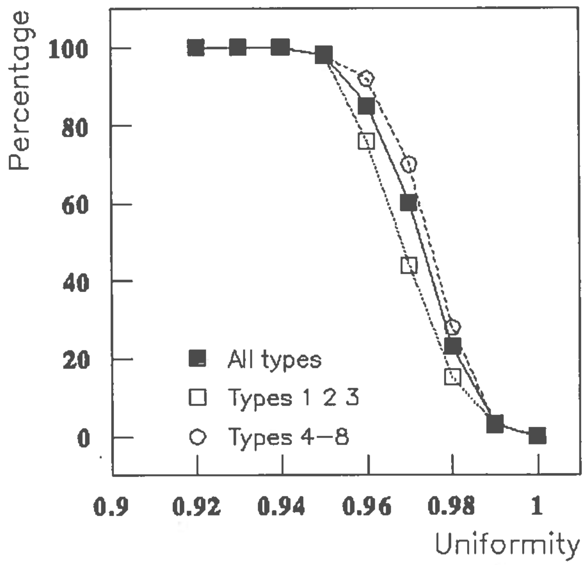

Figure 3: Percentage of crystals as a function of their uniformity

Each crystal is 24 cm long (corresponding to 21 radiation lengths) and has a pyramidal shape with trapezoidal bases, as shown in figure 2. All crystals are directly coupled with a Hamamatsu photomultiplier (R980, 1.5" diameter for $\theta = 28° \div 60.5°$ and $\theta = 119.5° \div 152.°$; R329-02, 2" diameter for $\theta = 70.5° \div 109.5°$). Signals from each detector are delayed, attenuated and split with a CAEN SY493 programmable attenuator that produces also the prompt sum of all input signals which is used for triggering: the analog signals from the crystals are digitized by linearity selected FERA-ADC. One of the most demanding features about the crystals [6] is that their uniformity pattern in the response all over the length must be at least of 95%, as shown in figure 3, and that the energy resolution must be better than 21% FWHM at 667 KeV photons from a ^{137}Cs source (see figure 4). With these limits, the contribution of non uniformities to the energy resolution of the calorimeter were found to be of the order of 0.3% (FWHM) [7].

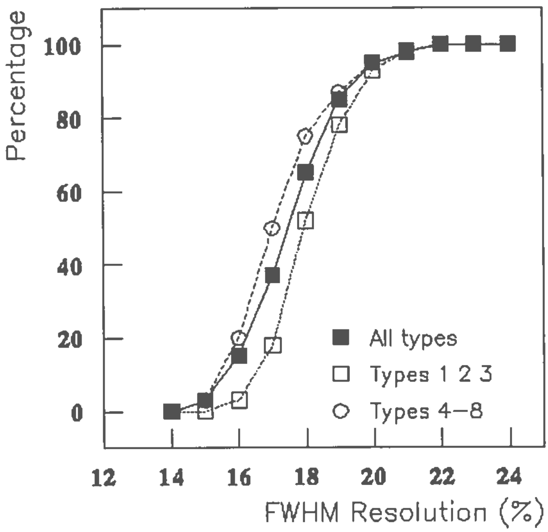

gure 4: The percentage of crystals as a function of their energy resolution at the 7 KeV photons from a ^{137}Cs source

Performances of the BGO Calorimeter

l Introduction

One of the carbon fiber baskets of the BGO Rugby Ball [8], containing 20 ƷO crystals, was exposed to the PHOENICS [9] tagged photon beam at Bonn ıiversity. Due to temperature variations, the light output of the BGO varies with a crease of about -1%/°C [10] [11]; the carbon fibre basket was thus surrounded with copper jacket with internal water circulation, keeping temperature fluctuations thin ±0.1°C. In this way the temperature contribution to the energy resolution ιs about 0.2% (FWHM).

The experimental set-up allowed only the alignement of the basket central ystal, called c_{10}, with the photon beam axis. The intercalibration between the Ms was then realized equalizing the crystals response to the added peaks of a ^{60}Co urce. As for the final experiment, this calibration procedure was rather crude and introduced a larger contribution in the energy resolution. The main results obtained concern the shower development, the linearity of the response and the energy resolution.

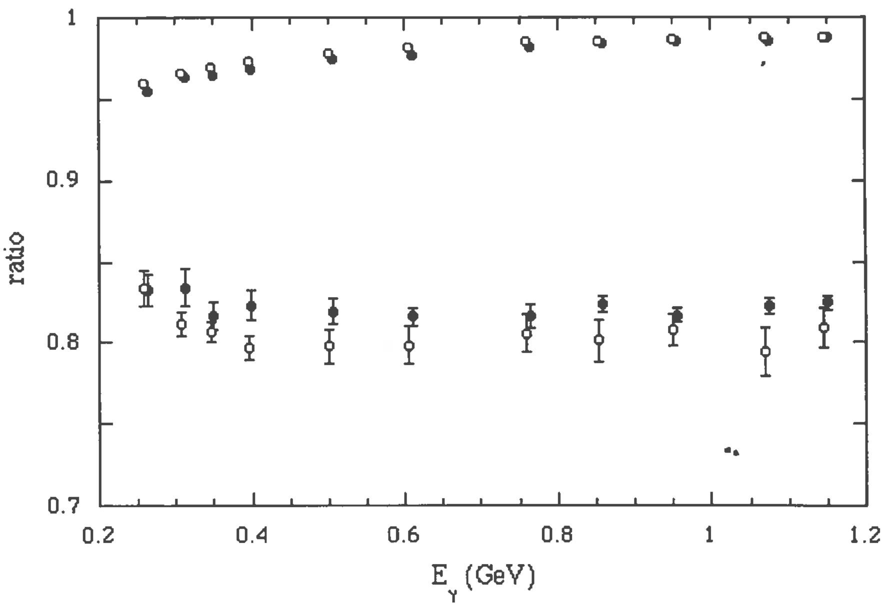

Figure 5: The ratios c_{10}/Σ_{20} and Σ_9/Σ_{20} as a function of the incident photon energy. Open points: data; full points: Monte Carlo simulation.

5.2 The shower development

We must remember that the crystals, having a length corresponding to 21 r.l., should contain more than the 99% of the e.m. shower in the longitudinal direction. This means that the energy resolution will depend essentially on the lateral energy loss. For this reason we have studied the energy dependence of the lateral containment of the shower. Figure 5 shows the behaviour of the following ratios: c_{10}/Σ_{20} between the signal c_{10} from the central crystal and the software sum Σ_{20} of the signals from the entire basket; Σ_9/Σ_{20} between the software sum of the signals coming from the 3×3 crystal matrix sorrounding the central detector and Σ_{20}. It can be seen that more than the 80% of the signal comes from the central crystal, hile the matrix 3×3 already contains more than 95% of the signal of the entire ısket. This is compatible with other similar results [12] and with the remark that ıe BGO Molière radius is 2.4 cm and the dimensions of the bases of the crystal are ×2 cm^2 on one side and 6.5×6.5 cm^2 on the other. Figure 6 shows the number of ystals with an energy greater than 6 MeV as a function of the incident photon. /e can see that the multiplicity increases by a factor 2 from 250 to 1150 MeV. This ature can be used to have a fast distinction between single photons and photons ose by.

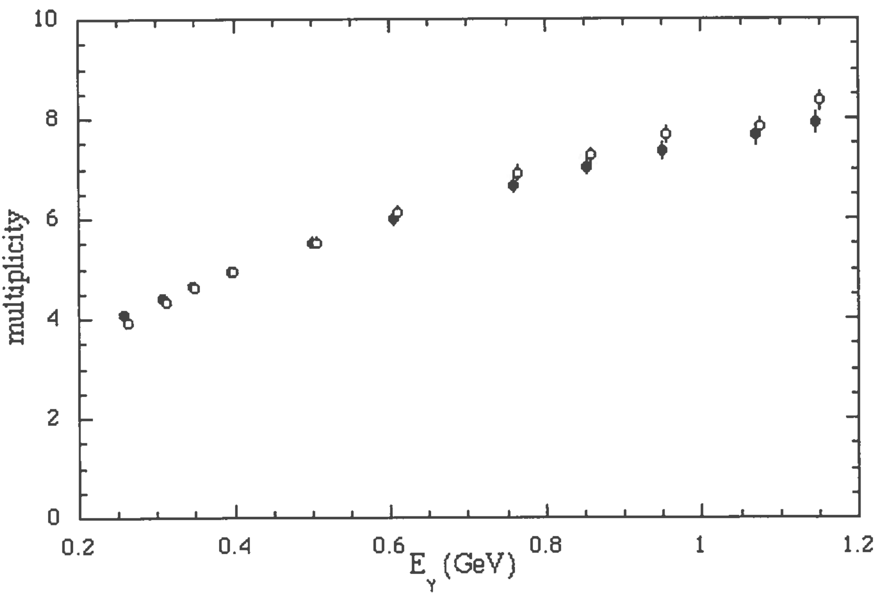

igure 6: Number of crystals with a deposited energy greater than 6 MeV as a ınction of the incident photon energy. Open points: data; full points: Monte Carlo mulation.

.3 Linearity and energy resolution

The linearity of the hardware sum of the 20 crystals has been studied and found xcellent, as shown in figure 7.

As for the energy resolution, we must remember that the total FWHM ; given by the combined contributions of the tagging detectors and of the BGO calorimeter:

$$(\Gamma_{TOT})^2 = (\Gamma_{Tag})^2 + (\Gamma_{BGO})^2$$

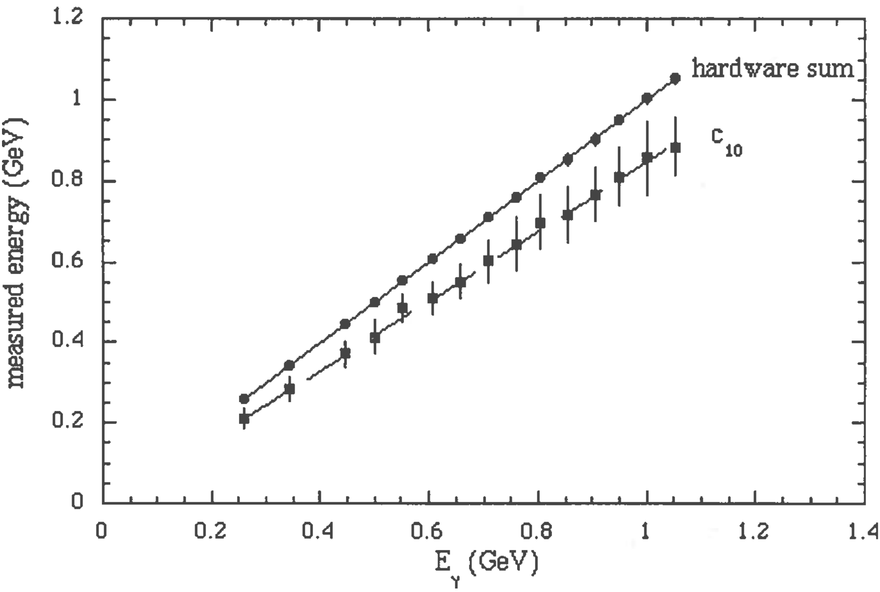

Figure 7: Linearity for the hardware sum and for a single crystal. The error bars are the standard deviations of a Gaussian fit to the peak distribution.

The tagging resolution Γ_{Tag} was well known and was then subtracted. Figure 8 shows the behaviour of $\Gamma_{BGO}(\%)$ with energy. The error bars are the standard deviations of a Gaussian fit to the peak distribution of the hardware sum. The energy resolution was parametrized in the usual way (E_γ in GeV):

$$\Gamma_{BGO}(\%) = \sqrt{a + \frac{b}{E_\gamma} + \frac{c}{\sqrt{E_\gamma}}}$$

where:

1. a is the constant term: it contains the effects not depending on energy, such as the variations of the light output due to temperature fluctuations ($\approx$0.2%), the fluctuations in the light collection due to non-uniformities of the crystals

($\approx$0.3%), the fluctuations in the energy leakage ($\approx$1.%) and the intercalibration uncertainties ($\approx$1.3%); the total contribution of these terms is: a = 1.74%; this term will be reduced during the experiment thanks to a better calibration procedure, as we will explain in the next section;

2. b represents the noise term and is well contained as we use PMs as readout devices: b=0.97%;

3. c represents the statistical term and it is also rather good considering the light output of the BGO: c=2.36%.

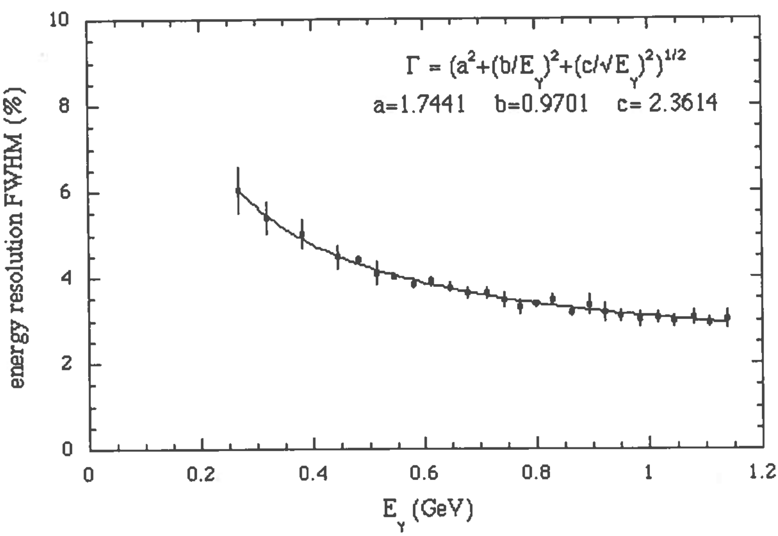

igure 8: The energy resolution Γ_{BGO} obtained with the hardware sum as a function the incoming particle energy.

The calibration procedure

Before each long run period, the response of the 480 BGO crystals is equalized ith a ^{22}Na source (E_γ = 1.275 MeV). At the same time a NaI detector, that is used as a reference, is continously calibrated with a ^{60}Co source. Here we make the assumption that it is possible to extrapolate this calibration at energies of the order of one GeV, i.e. the energies that we will detect. To do this we have measured the calibration curve for each crystal using a variable intensity light pulser.

The energy calibration of the calorimeter may vary essentially depending on two causes:

1. the variation of scintillation light output due to temperature effects;

2. the PMs gain variations.

After the initial calibration and equalization of the response of the 480 crystals, these two effects must be kept under control during the runs. In this way possible variations in the calibration constants may be corrected in the data analysis.

For the first problem, we have realized a temperature control system made of 128 platinum probes, allowing to interpolate the temperature of all the crystals. We have already pointed out that the variation of the BGO light yield is about -1%/°C if calculated at T=23°C. Due to the good thermoregulation of the experimental zone of the ESRF, we have verified that, 6 hours after the detector switch-on, very little temperature fluctuations occur, within 0.3÷0.4 °C, so that their effective contribution to the energy resolution is about 0.4% (FWHM) [13].

The PMs gain variations are kept under control with a system of optical fibers, carrying a laser light into the 480 BGO crystals and into a NaI reference detector. Before the run starts and during the dead times inside each run we can send a pulse of this laser light inside the crystals and measure the following quantities for each crystal (i) and each time (j) we repeat the operation:

$$\mathrm{L}_i^{(j)} = \frac{\text{Channel}^{(j)}\text{of the Laser peak in the BGO}_i}{\text{Channel}^{(j)}\text{of the Laser peak in the NaI}} \qquad \begin{aligned} i &= 1,\ldots,480 \\ j &= 1,\ldots,\text{n.mis.} \end{aligned}$$

The energy deposited inside the BGO reconstructed by the calibration made at the beginning of the run must be corrected by dividing it by the following term:

$$R_i^{(j)} = \frac{\mathrm{L}_i^{(j)}}{\mathrm{L}_i^{(0)}} \cdot \frac{\text{Channel}^{(j)}\text{of the }^{60}\text{Co peak in the NaI}}{\text{Channel}^{(0)}\text{of the }^{60}\text{Co peak in the NaI}} \qquad \begin{aligned} i &= 1,\ldots,480 \\ j &= 1,\ldots,\text{n.mis.} \end{aligned}$$

which keeps into account possible variations in the PMs gain and also possible variations of the NaI reference calibration constants. This ratio is obviously equal to 1 if everything remains unchanged.

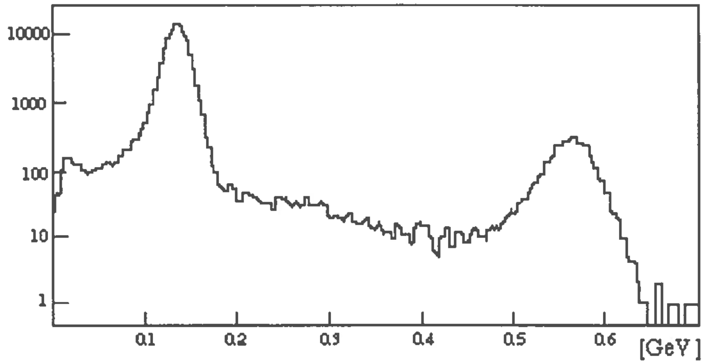

gure 9: The invariant mass spectrum reconstructed from the decay into 2 γ: we n see two clear peaks at the π^0 and η masses

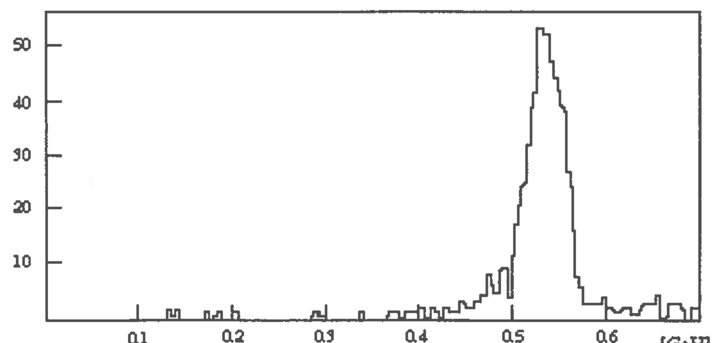

gure 10: The invariant mass spectrum as it is reconstructed from the decay into γ: it shows a very clean peak at the η mass with no background.

With this procedure, the intercalibration contribution to the energy resotion (and in particular to the constant term a) is about 0.4%, which implies that $= 1.2\%$ and that the total expected energy resolution is 2.7% (FWHM) at 1 GeV, full agreement with the requirements that the calorimeter had to satisfy.

7 First results

Since March 1996, the GRAAL group began to collect data and we can now show the first physical results.

The reactions γ+p$\rightarrow$ π^0+p and the analogous γ+p$\rightarrow$ η+p have been studied. The two reactions are detected via the decays channels: $\pi^0 \rightarrow 2\gamma$ (B.R. 98.8%); $\eta \rightarrow 2\gamma$ (B.R. 38.8%); $\eta \rightarrow 6\gamma$ (B.R. 31.9%). These results have been presented by D. Rebreyend at PANIC96 on behalf of the GRAAL collaboration.

A first level trigger is used in order to suppress the electromagnetic background (essentially composed by e^+e^- pair production) consisting in the imposition, desumed by Monte Carlo simulations [14)], of a threshold of 50 MeV on the total energy deposited inside the BGO Rugby Ball.

In figure 9 we can see the invariant mass for the two γ system detected in the BGO Ball that shows two clear maxima at the π^0 and η masses. Figure 10 also shows a six photon mass spectrum with a very clean peak at the η mass and no background.

References

1. The BGO Collaboration, LNF-90/84(R)

2. P. Levi Sandri et al., Proc. 13th PANIC Conf., Perugia-Italy 28/6-2/7, ed. A. Pascolini (1993) p.785

3. M. Preger et al., *Nucl. Instr. and Meth. in Phys. Res.* A249 (1986) 299-305

4. D. Babusci et al. Il Nuovo Cimento Vol.103 A, N.11 (Novembre 1990)

5. A. D'Angelo and D. Babusci et al., *Conference Proceedings* Vol.39 *Flavour and Spin in Hadronic and Electromagnetic Interactions* SIF, Bologna 1993

6. Crystals were manifactured by:

   -Harshaw Chemie BV, DeMeern, The Netherlands

   -Crismatec, Gières, France

7. A. Zucchiatti et al., *Nucl. Instr. and Meth. in Phys. Res.* A317 (1992) 492

8. P. Levi Sandri et al., *Nucl. Instr. and Meth. in Phys. Res.* A370 (1996) 396-402

9. P. Detemple et al., *Nucl. Instr. and Meth. in Phys. Res.* A321 (1992) 479

10. A. Zucchiatti et al., *Nucl. Instr. and Meth. in Phys. Res.* A321 (1992) 479

R. Di Salvo, Tesi di Dottorato, Torino 1996 (unpublished)

J.A. Bakken et al., L3 Collaboration, *Nucl. Instr. Meth. and Phys. Res.* A254 (1987) 535

L. Nicoletti, Tesi di Laurea, Roma 1996 (unpublished)

L. Mazzaschi et al. *Nucl. Instr. Meth. and Phys. Res.* A346 (1994) 441

PERFORMANCE AND TESTS OF THE BGO ENDCAP CALORIMETER WITH PHOTOTRIODE READOUT FOR THE CMD-2 DETECTOR

V. P. Smakhtin
Budker Institute of Nuclear Physics, Novosibirk, 630090 Russia

Written contribution not received

;cati Physics Series Vol. VI, (pp. 743–754)
NT. CONF. ON CALORIMETRY IN HEP – Frascati, June 8–14, 1996

HE LEAD TUNGSTATE CMS ELECTROMAGNETIC CALORIMETER

M. Diemoz

INFN Sezione di Roma and Università di Roma "La Sapienza", Italy

ABSTRACT

ıe CMS Collaboration is developing a high resolution electromagnetic calorimeter ıde of about 110,000 lead tungstate ($PbWO_4$) scintillating crystals to be operated the CMS detector at LHC collider at CERN. The physics motivations and the ıtus of the project are discussed.

Physics motivations and design considerations

ıe of the main goals of the LHC project is the investigation on the origin of e electroweak simmetry breaking. To this aim the CMS detector is designed to ːasure with great precision muons, photons and electrons [1].

The choice of a high resolution electromagnetic calorimeter is mainly mo- 'ated by the search of the Higgs boson via its $\gamma\gamma$ decay that is the most promising annel in the range of mass $80 < M_h < 130$ GeV. In this mass region the natu- l width of the Higgs is few MeV, thus this reaction constitutes a benchmark for e calorimeter performances. The signal width is completely dominated by the perimental $\gamma\gamma$ invariant mass resolution:

$$\frac{\sigma_M}{M} = \frac{1}{2}\left[\frac{\sigma_{E_1}}{E_1} \oplus \frac{\sigma_{E_2}}{E_2} \oplus \frac{\sigma_\theta}{\tan(\theta/2)}\right] \tag{1}$$

ıere E_1 and E_2 indicate the photon energies and θ their angular separation.

The energy resolution of a calorimeter can be parametrised as:

$$\frac{\sigma_E}{E} = \frac{a}{\sqrt{E}} \oplus b \oplus \frac{\sigma_n}{E}. \tag{2}$$

The stochastic term a of homogeneous calorimeters can be as low as 2 %/GeV$^{1/2}$ [2]. The constant term b can be mantained at the level of 0.5 %. To keep other contributions at the same order for $E_\gamma \simeq 50$ GeV (the mean photon energy for boson masses in the aforementioned range), the noise term σ_n should be around 150 MeV, and the angular resolution should stay below 50 mrad/$\sqrt{E(GeV)}$.

In the low luminosity regime of LHC, $L \sim 10^{33}$ cm^{-2}s^{-1}, the event vertex can be reconstructed by the central tracker and the photon angle can be determined with high precision using the shower center-of-gravity. At 10^{34} cm^{-2}s^{-1}, the superposition of several events from the same bunch crossing makes the association of the photons to their primary vertex very difficult. The photon direction can be determined combining the shower center of gravity with a point measured in a preshower detector located in front of the calorimeter.

Two different scenarios are then foreseen at low and high luminosity, with different partial contributions to Higgs mass resolution as detailed in Table 1. For $M_H = 100$ GeV the total $\gamma\gamma$ mass resolution can stay below 500 MeV at low luminosity and below 800 MeV at high luminosity. With such a performance in the first case a S.M. Higgs signal is detectable with more than 5 standard deviations for $95 < M_H < 150$ GeV with an integrated luminosity of 3×10^4 pb^{-1}. In the second case, the range $80 < M_H < 160$ GeV is covered keeping the same significance with an integrated luminosity of 10^5 pb^{-1} [1].

Table 1: Contributions to the $H \rightarrow \gamma\gamma$ mass resolution for $M_H = 100$ GeV.

Effect	Low luminosity $\mathcal{L} = 10^{33}$cm^{-2}s^{-1}		High luminosity $\mathcal{L} = 10^{34}$cm^{-2}s^{-1}	
Stochastic term	2 %	150 MeV	5 %	400 MeV
Constant term	0.5 %	350 MeV	0.5 %	350 MeV
Energy equiv. of noise		200 MeV		200 MeV
Angular measurement	using tracks	200 MeV	40 mrad/$\sqrt{E}$	500 MeV
Energy pileup				200 MeV
TOTAL		**475 MeV**		**775 MeV**

2 The choice of lead tungstate

Among a few other possibilities the CMS collaboration decided to use crystals of lead tungstate ($PbWO_4$ - PWO) to build a high-resolution compact homogeneous calorimeter. These crystals have many properties suited for the utilization at LHC. They present a fast scintillation emission with a large fraction of the light released within the foreseen bunch spacing of 25 ns. They have short radiation lenght (0.89 cm) and small Molière radius (2.2 cm). They are relatively easy to grow from readily ailable raw material and mass production capabilities exist in different places. The nitation of the low light-yield of the crystals can be overcome by using as readout vices Si avalanche photodiodes, immune from the high magnetic field conditions the experiment (4 T).

The actual design foresees 26 X_0 long crystals with front face of 2×2 cm^2 orresponding to $\Delta\eta\Delta\phi = 0.014 \times 0.014$). The calorimeter consists of a barrel gion covering up to $\eta = 1.56$ and two end-caps up to $\eta = 2.6$. The total number crystals is 110,000, subdivided in several modules or "baskets", cointaining about 0 crystals each [3]. A lay-out of the calorimeter is shown in fig. 1.

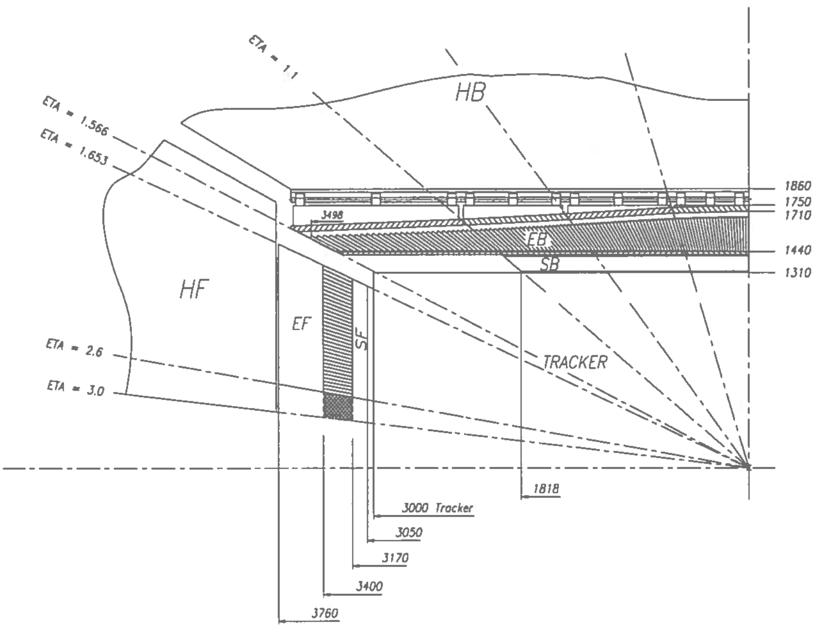

Figure 1: Lay-out of the calorimeter.

Light emission of PWO crystals

WO crystals have a composite emission spectrum [4], with two main components, e in the blue (fast, τ <10 ns, and peaking at 410-420 nm), ascribed to regular O_4^{-2} groups and a second one in the green (peaking at 480-520 nm), related to trinsic WO_3 defects associated with color centers. The latter one is partially due to slow recombination of free carriers and contributes to the slow (> 100 ns) component of the scintillation light. The relative weight of this two components can vary considerably from crystal to crystal, depending on impurities and defects, that is on raw material and growing conditions.

The R&D work on PWO was concentrated on the understanding of the scintillation mechanism in order to increase the amount of light yield and to optimize the fast component of the spectrum [5]. A first improvement of about 30% in the light emission was achieved in 1995. This was partly associated to an enhancement of the slow component. At the end of last year the clarification of the decay kinetics allowed a better definition of the requirements on the level of impurities tolerable in the raw material [6]. The 1996 crystal production shows a faster average decay time, still keeping a higher value of the light yield corresponding to ~100 γ / MeV at T=18 °C. Fig. 2 shows a typical decay-time curve for 1996 crystals together with the result of a three component fit.

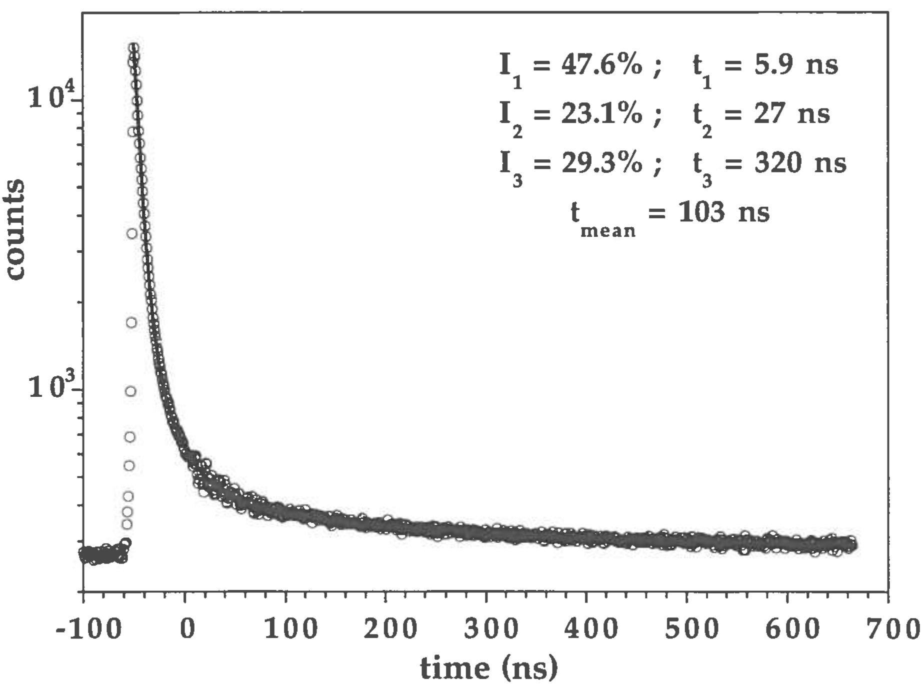

Figure 2: Scintillation decay time curve for a crystal of 1996 production. I_i (i=1,2,3) represents the fractional amount of light in percent associated to the corrisponding decay time t_i. The average scintillation time is also indicated

Radiation hardness of PWO crystals

diation environment at LHC makes radiation resistance mandatory for any detor element. In 10 years at full luminosity the electromagnetic barrel region will gamma doses up to 5 kGy and neutron fluences up to 2×10^{13} n/cm^2 [1].

The radiation resistance of PWO crystals depends on their purity and in ticular on the stability of growing conditions. Gamma irradiation is the most ıgerous one. Negligible effect is produced by neutrons [7]. Several tests and asurements were performed in many different conditions, showing some general ıres:

- Radiation damage affects light transmission rather than the scintillation mechanism as can be seen in fig. 3, that shows the exponential correlation between the light yield and the absorption coefficient induced by radiation at 440 nm. The radiation-induced absorption is associated with the formation of color centers. An important consequence is that the damage can be monitored through the measurement of crystal transparency.

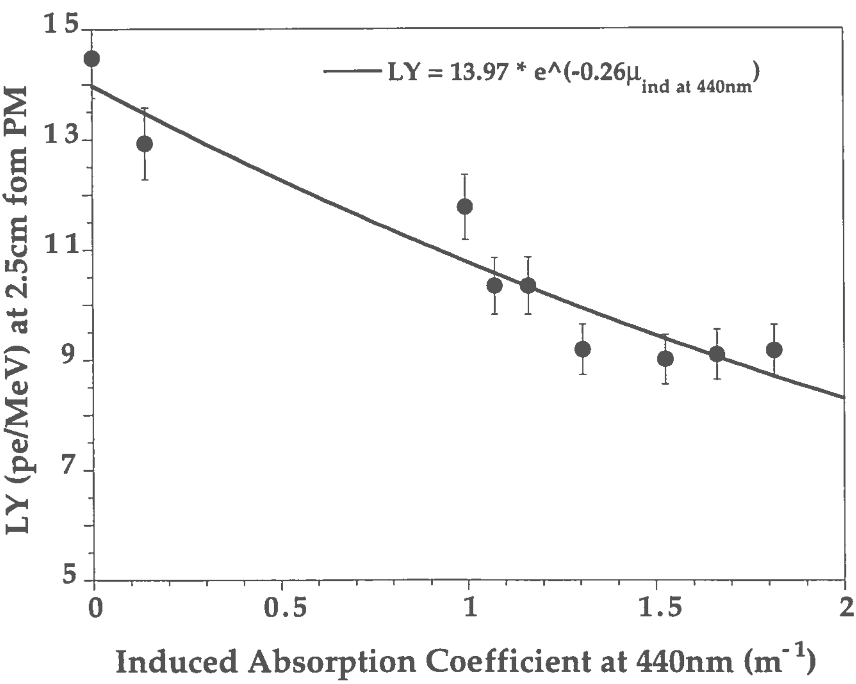

ɡure 3: Light Yield as a function of the absorption coefficent at a wavelenght of 0 nm induced by γ irradiation.

- A saturation of the damage is observed after few tens of Gy as shown in fig.4. The saturation is almost completed after 100 Gy. This indicates that the damage is due to intrinsic impurities or defects, while the radiation does not produce additional defects.
- The recovery of the damage occours in a day time scale. Fig.5 shows the amount of the recovery in terms of the reduction of the radiation induced absorption coefficient as a function of different wavelenghts for several recovery time intervals.

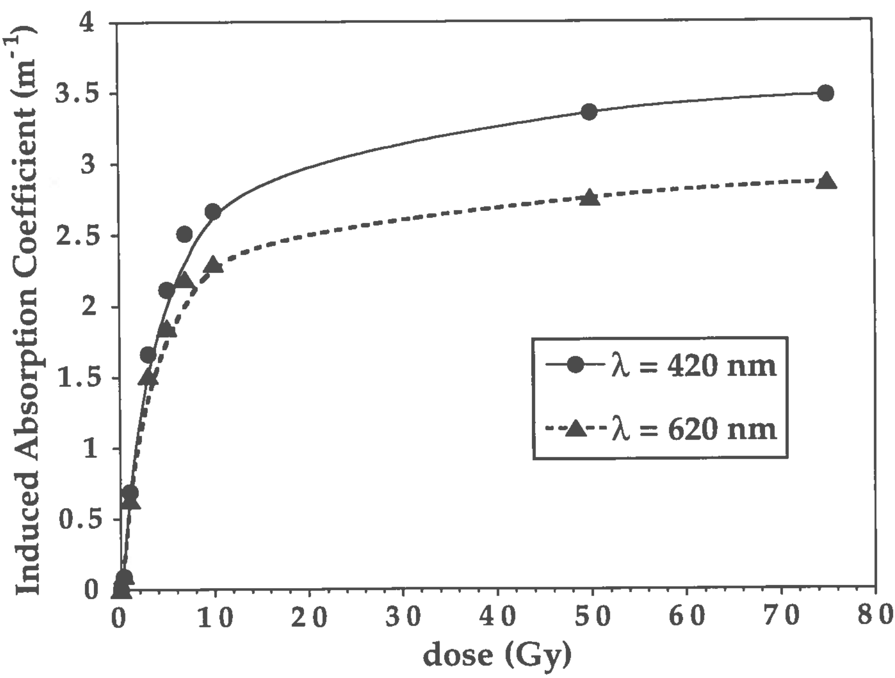

Figure 4: Induced Absorption coefficent at two different wavelenghts as a function of radiation dose.

Crystals with low radiation resistance shows a pronounced absorption band in the transmission curve around 350 nm. This correlation allows a selection of radiation resistant crystals by a measurement of their transmittance. They are usually classified in 3 types according to this measurement. Crystals of type 3 actually have a loss in light yield after irradiation that can reach 20%. This is not far from the level of variation that can be tolerated and corrected by a light transmission monitor.

Some crystals, as the one shown in fig.5, are intrinsecally radiation hard. The investigation of the reasons of such a behaviour could lead to a better under-

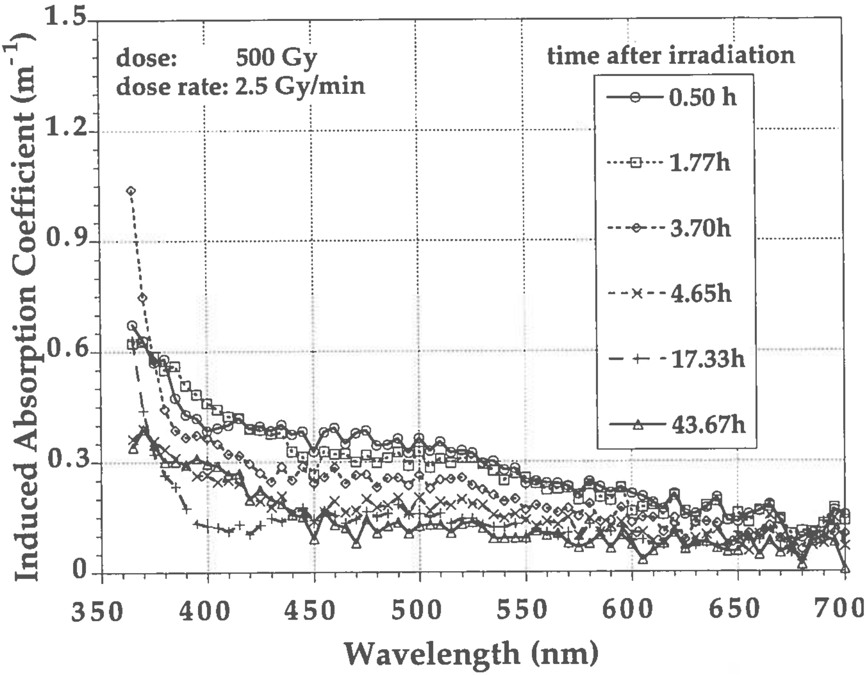

;ure 5: Absorption coefficent induced by radiation as a function of wavelenght for :erent recovery times.

nding of the mechanism of the radiation damage. An intense R&D effort is going in this direction. One interesting observation is that the radiation-induced ab- ption can be reduced by vacuum annealing at high temperature [8], through the ıporation of O^- centers partly responsible for the induced absorption. The final ıl is to identify the damage ralated impurities and defects and eventually reduce :m in the process of crystal growing.

Photoreadout devices

e choice of the photodetector devices for the CMS electromagnetic calorimeter is ven by the following considerations:

- they must work in the high magnetic field environment
- they should provide an internal gain of about a factor 50
- they should well match the PWO scintillation spectrum.

Silicon avalanche photodiodes (APD) fulfill all these requirements [9]. The crucial point for their use in the CMS electromagnetic calorimeter is the level of their noise contribution that should not degrade the intrinsic resolution of PWO crystals.

All the three terms of the calorimeter resolution (see eq. 2) are affected by an additional contribution coming from the APD:

- the term $1/E$ is affected by their capacitance and leakage current
- the term $1/\sqrt{E}$ is influenced by the excess noise factor, that is the noise contribution coming from the stochastic process of avalanche multiplication
- the constant term can receive a contribution by gain instabilities.

Compared to the low level of light emitted by PWO the "nuclear counter effect" (the direct ionization induced by charged particles traversing the active region of the photodetector) can be an additional source of degradation of the resolution. This effect can be quantified with respect to standard PIN Si diodes by an effective thickness, defined as the thickness of a PIN Si diode that gives the same signal (in units of photoelectrons) when traversed by a charged particle.

Different types of APD's have been tested up to now. EG&G APD's have a 5 x 5 mm^2 active area and are made by ion implantation and diffusion technology, Hamamatsu APD's have a 5 mm diameter active area and are made by epitaxial growth. The properties of the three types of APD's tested in 1995 are summarized in Table 2. Thanks to the R&D program under development in collaboration with the APD producers these prototypes are already close to CMS requirements in terms of noise. Further improvements are expected in global performances and radiation hardness.

Table 2: Main properties of APD's used in 1995 test beam. d_{eff} is the effective thickness, M indicates the gain.

		EG&G	Hamamatsu	
			High C	Low C
Size		5×5 mm^2	$\o$ 5 mm	$\o$ 5 mm
Capacitance	(pF)	30	325	90
$d_{eff}(M = 50)$	(μm)	7.6	3.5	13
Excess noise factor		2.8	1.8	2
$1/M \times dM/dT(M = 50)$	(% per °C)	-3.5	-2.3	-3
$1/M \times dM/dV(M = 50)$	(% per V)	2	15	5

Test beam results

1993-94 test beam [10], a stochastic term of 3.5 %/GeV$^{1/2}$ in the energy resolution s obtained using photomultipliers as photoreadout devices for PWO crystals. At ıt time the APD performances were spoiled by the nuclear counter effect. As for : angular resolution, it was shown that a preshower system consisting of 3 X_0 of d in front of the crystals ensure $\sigma_\theta = (36.5/\sqrt{E(GeV)} \oplus 4)$ mrad.

In 1995 test beam [11] the use of longer crystals and the improvements the APD's consisting in the reduction of their effective thickness allowed for : elimination of the high energy tail produced by the nuclear counter effect. An ergy resolution better than 0.6 % at 100 GeV was achieved, fulfilling the basic MS requirements. The resolution as a function of energy is shown in Fig. 6 as asured in a crystal read by one or two APD's. The stochastic term given by the n of two APD signals is consistent with the expectation coming from the increase the photon statistics.

Calibrations of the calorimeter

discussed in the CMS technical proposal [1] an absolute calibration of the calo-ıeter can be obtained at 0.3% by comparing the energy seen in the calorimeter th the momentum measured in the central tracker for electrons coming from W d Z decays. Depending on luminosity, this task would require from one to five eks of data taking. Due to the effects of radiation and recovery, this procedure not sufficient to follow the response of the calorimeter with the requested preci-n. To this purpose it will be necessary to monitor almost continuously the crystal ısparency achieving a precision of few permill. The method presently under study es laser pulses at two different wavelengths, transmitted to each crystal through ;ystem of quartz optical fibers.

Assembly of the calorimeter

order to insure a timely safe production of such a large number of crystals, veral producers will be involved. Production Centers will be located in Russia, ech Republic and in China.

The process of assembling and testing all the components of the calorimeter ll be distributed among four Regional Centers foreseen in CERN, Great Britain, otvino (Russia) and Rome (Italy). The task of a Regional Center is to check e specifications and follow the quality of the incoming crystals, to assemble tested mponents in modular entities and to verify the success of each step of the mounting

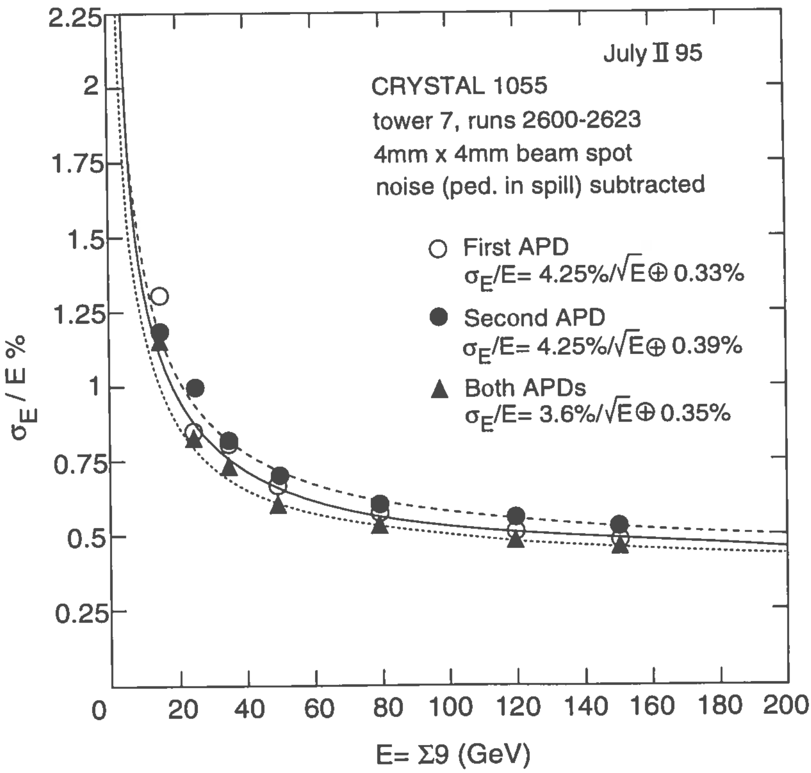

Figure 6: Energy resolution as a function of energy, measured in a 3 x 3 array of crystals. The central crystal is read by two APD's.

sequence.

Crystals will be preassembled with their photoreadout system in alveolar submodules of twelve units, mounted in modules ("baskets") made of carbon fiber, containing about 600 crystals each and equipped with light monitor and cooling systems. A basket tested and released by the Regional Center will be a complete unit ready to be operated. It will be moved to CERN for assembly in a supermodule of four baskets, exposed to test beams for calibration and finally installed in the CMS detector. Such a distributed process for production and assembly requires a high level of automation in measuring and mounting procedures and a robust system for the circulation of all the available data, from Producers and Regional Centers down to the final Data-Base of the experiment. All the required hardware and software tools are in the process of being developed or prototype testing.

Conclusions

e R&D activities of last few years on lead tungstate crystals and APD's lead several improvements that make realistic the achievement of the performances uired to the CMS electromagnetic calorimeter. Actually a great effort is going to ameliorate the radiation resistance of the whole system in order to preserve high resolution of the calorimeter in the hostile environment of LHC. This caimeter will be an unequaled instrument allowing for the detection of a low mass ggs boson at LHC and of any process involving photons and electrons.

Acknowledgements

ould like to thank all my colleagues working on the electromagnetic calorimeter d particularly E. Auffray, I. Dafinei, P. Lecoq and M. Schneegans for their help preparing this work.

ferences

CMS Technical Proposal, CERN/LHCC 94-38, (1994).

J.A. Bakken et al., "Performance of a prototype BGO calorimeter in an electron beam from 2 to 50 GeV", Nucl. Instrum. Methods Phys. Res. A **254**, 535 (1987).

See M. Lebeau contribution to this conference.

R. Grasser, A. Scharmann, K.Vlachos, "A renewed investigation of the luminescence of $PbMoO_4$ and $PbWO_4$", in Proc. 9th Int. Conf. on Luminescence, ICL '93, (Storrs, USA, 1993).

A.N. Belsky et al. "Fast luminescence of undoped $PbWO_4$ crystals" CMS TN/95-073, (1995).

See P. Lecoq contribution to this conference.

R. Chipaux and O. Toson, "Resistance of lead tungstate and cerium fluoride to low rate gamma irradiation or fast neutrons exposure", in Proc. Int. Conf. on Inorganic scintillators and their applications, SCINT95, (Delft, The Netherlands, 1995)

S. Baccaro et al., "Influence of vacuum annealing on optical and scintillation properties of $PbWO_4$ crystals", CMS TN/96-087, (1996)

9. E. Lorentz, S. Natkaniec, D. Renker, B. Schwartz, "Fast readout of plastic and crystal scintillators by avalanche photodiodes", Nucl. Instrum. Methods Phys. Res. A **344**, 64 (1994).

   See also P. Denes contribution to this conference.

10. J.P. Peigneux et al., "Results from tests on matrices of lead tungstate crystals using high energy beams", CERN-PPE-95-197 (1995), sub. to Nucl. Instrum. Methods Phys. Res. A.

11. CMS ECAL Group, CMS TN/96-04, (1996).

    See also C. Seez contribution to this conference.

ascati Physics Series Vol. VI, (pp. 755–764)
INT. CONF. ON CALORIMETRY IN HEP – Frascati, June 8–14, 1996

DEVELOPMENT OF LEAD TUNGSTATE CRYSTALS FOR HIGH PERFORMANCE CALORIMETRY

P. Lecoq
CERN, Geneva, Switzerland

ABSTRACT

The procurement of 110,000 Lead Tungstate crystals (PWO) for the CMS omagnetic calorimeter poses very challenging problems. In order to obtain a level of mance for the calorimeter which will guarantee a high discovery potential for the Higgs ing into two photons, an energy resolution of 0.5% must be reached for photon energies GeV/c and above. The first implication is that enough light can be collected from the ıls, so that the stochastic term of the resolution is kept at less than 4%. For a crystal ng in a temperature quenching mode, this means that the interplay between light yield ecay time has to be adjusted carefully. The second difficulty is to keep the performances crystal very uniform in the whole crystal volume in order to obtain a small constant of the resolution. Last but not least, these performances must remain very stable over period of time at a fraction of a percent level. In particular the radiation resistance of the ıls must be very high. In order to achieve this goal, an ambitious Research and lopment program was started in collaboration with the companies involved in the ıction of PWO crystals. The organisation of this R&D will be described, putting asis on the conditions to grow high light yield, fast and radiation hard crystals at the best ɔle cost. Results will be given showing the progression curve in the last 2 years and the tations for the future will be discussed.

TRODUCTION

The CMS experiment (Compact Muon Solenoid) to be installed at the future Large ɔn Collider (LHC) at CERN, is proposing the construction of a scintillator based high ıtion homogeneous calorimeter, to meet the performance criteria for the discovery of an nediate mass Higgs boson in its 2γ decay mode. The choice of Lead Tungstate crystals 'O4) has been made because of its high density, fast luminescence and reasonable light and radiation resistance. Similarly, the Alice experiment has decided to build a PbWO4 omagnetic calorimeter to take advantage of the very fine granularity allowed by the high ty of this material, in order to resolve the high multiplicity events generated by heavy collisions at LHC, CMS will require 110,000 crystals of trapezoidal shape x(2.4x2.4)x23cm^3 for a total volume of 13m^3, and Alice 36,608 paralellopipedic crystals .2 x20cm^3 representing 4m^3. The CMS and ALICE designs are described in more details erence[1,2]

The procurement of such a large quantity of crystals with the required quality in a relatively short period of time poses a number of problems. The examples of Silicon or high temperature supraconductors shows that the development of new materials requires a pluridisciplinary approach in a long and expensive process, involving a wide range of expertise. In the case of PbWO4 the available resources are orders of magnitude smaller than for Silicon or YBaCuO, and there is no recognised market besides High Energy Physics applications. Moreover the LHC planning allows only 2 to 3 years for R&D and 5 to 6 years for production. We need therefore to adopt a very pragmatic line based on a clear definition of the objectives, as defined by the desired detector performances, with a realistic and not too ambitious safety margin.

The present report describes the organisation of the Research and Development program as well as the chosen strategy for the production. A status of the progress already achieved and the problems remaining to be solved is also presented.

2. LEAD TUNGSTATE CRYSTAL PROPERTIES

Lead Tungstate ($PbWO_4$) is a birefringent scheelite type crystal belonging to the space group $I4\bar{a}$ with a tetragonal unit cell. It is grown from a 50%-50% mixture of Lead oxide (PbO) and Tungsten oxide (WO_3) which melts congruently at 1123°C, without phase transition during the cooling. It is particularly attractive for building a compact calorimeter because of its very high density, leading to a short radiation length and Moliere radius. Moreover, the abundance of the raw material and the relatively low melting point are important parameters for a low production cost. Being non hygroscopic and chemically inert, its handling does not give any problem. The properties of PbWO4 crystals are summarised in Table 1[3-8]

Table 1. Physical and chemical properties of PbWO4 crystals

Physical parameters

Density (g/cm^3)	8.28
Radiation length (cm)	0.89
Moliere radius (cm)	2.19
Temperature dependence %/°C	-1.98
Hygroscopicity / Chemical Stability	No / good
Mechanical Strength	1kg/mm^2
Thermal conductivity (W/°K)	3300
Specific Heat (J/kg°K)	440
Index of refraction along Z axis (λ = 500 nm)	2.3

Scintillation

Photon Yield : γ/MeV	
Best crystal, ~1cm^3, in 1µsec	200
Typical full size crystal in 1µsec	100
Typical full size crystal in 25nsec	75
After glow after 1µsec	No
Decay time	10ns(80%), 50ns(20%)
Radioluminescence peak (λ)	440-500nm
Radioluminescence spectrum at 10% of peak intensity	360 to 570nm

The mechanical resistance is somewhat lower than for BGO or Cerium fluoride, but it ves less easily than these crystals. The high index of refraction helps the light collection g the crystal but limits the photon extraction efficiency. Because of the light emission hanism character and the large number of reflections on the lateral faces before collection ıe photodetector, the birefringence of Lead Tungstate is not a problem.

The emission spectrum is rather complex, with several emission bands between 400nm 550nm, the relative amplitude of which vary from sample to sample and the chiometry. The decay time is strongly non exponential, with a mean value of about 10ns 90% of the light collected in 100ns. This results from a strong thermal quenching which s place at room temperature and which has three consequences:

- reduce the light yield to about 100 photons/MeV (large size crystals)

- shorten the decay time to about 10ns with 90% of the light collected in 100ns

-produce a strong temperature dependence of the light yield : -1.98%/°C

HE RESEARCH AND DEVELOPMENT PHASE

When the decision for Lead Tungstate crystals was made, only a few tens of crystals elatively small dimensions and modest quality had been produced in Ukraine.and Russia. CMS and LHC planning allows not more than 3 years to propose a convincing scheme he mass production of full size crystals having good properties with a small dispersion of parameters along a crystal, and from crystal to crystal. Moreover a high production yield a low production cost must be achieved to cope with the severe budgetary and planning straints of the LHC program. As the resources for this R&D stage are also limited, and in absence of a real market to amortise the development phase, a rigorous and pragmatic roach was preferred to a systematic investigation of all the PbWO4 properties.

The first task is to clearly define the specifications in order to achieve with a onable safety margin the desired performances for the calorimeter. They can be grouped categories:

a- The energy resolution must not be dominated by photostatistics. For a Higgs mass of about 100GeV, and using 25mm^2 avalanche photodiodes for the readout, it is considered that a light yield of 2 pe$^-$/MeV is a minimum, corresponding to 8 pe$^-$/MeV when measured with a 2020Q photomultiplier covering the whole back surface of the crystal, or 60 photons extracted from the same surface.

b- The radiation hardness of the crystals must be compatible with a 0.5% constant term for the energy resolution. This means that under irradiation the light yield loss must saturate at less than 10% from the initial value. Moreover the kinetics of the damage and its recovery must be compatible with the expected performances of the light monitoring system, which implies that short term variations have to be kept below 2 or 3%.

c- The non uniformity of properties along the crystal must be small enough, in order for the longitudinal shower fluctuations to not contribute to more than 0.2% to the energy resolution. Local non uniformity's depend on crystallographic defects, whereas long range non uniformity's result from a balance between the self absorption of the light and the focusing effect due to the trapezoidal shape of the crystal. It is particularly important that a uniformity of better than $0.2\%/X_0$ is maintained in the region of the shower maximum. On the other hand a small excess of the response on the back of the crystal helps for the compensation of the rear leakage.

d- The mechanical properties of the crystal must be good enough to make sure that rather tight dimensional tolerances can be obtained, in order to minimise the dead space between adjacent crystals. The highest possible yield must also be achieved during the mechanical processing phase in order to minimise the production cost.

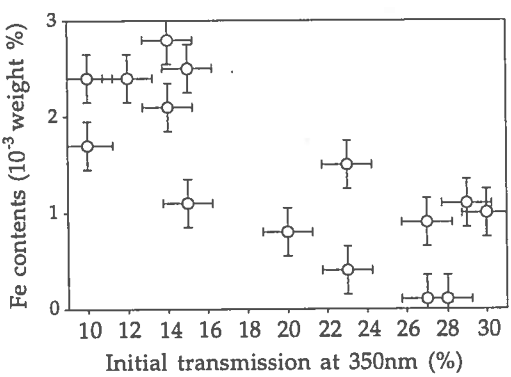

Figure 1: Influence of Fe contents on 350nm absorption band

Once the specifications are defined, one has to identify the parameters influencing them from those which are not important. This task is extremely important as it controls the cost effectiveness of the project. Contamination of Iron for instance, induces an absorption band around 350nm which reduces the light yield and seems to play an important role on the radiation hardness of the crystals (Fig.1). It is therefore mandatory to reduce the Fe contains in the raw material at the ppm level. On the other hand some divalent cations, like Ca^{++} do not significantly affect any of the above mentioned properties of PbWO4. One can therefore make the economy of expensive purification process and analytical controls for these cations. Similarly some crystallographic defects like voids, bubbles and aggregates can be tolerated, provided their concentration is low enough to not reduce the light collection efficiency. A modest surface finish, at least on the lateral faces of the crystal, is also largely sufficient for our purpose.

To organise the R&D phase in the most effective way, close collaborations have been established between the production companies and a limited number of specialised laboratories, each of them looking at a specific problem. At a second level, a quality control team including CMS physicists and outside experts is continuously monitoring the progress and controlling that the guidelines for this R&D phase are maintained. This approach allows a fast and productive feedback to the producers.

'RATEGY FOR PRODUCTION

Three constraints have to be considered to define a realistic strategy for the production ›WO4 crystals for CMS:

a- The quantity to be produced is large during a short period of time, typically 6 years. This represents a production of about 20,000 crystals, or 2.2 m^3 per year. This is nearly a factor 2 more than the whole L3 BGO detector at LEP to be produced every year during 6 years. The consequence is that important infrastructures are needed, including large number of ovens and mechanical processing machines.

b- No other applications than for High Energy Physics experiments can be expected in the frame of our present understanding of the properties of this material. There is therefore no hope to amortise infrastructure investments on a large potential market for this crystal.

c- We are aiming at a very low price which implies a high production yield and therefore high quality and dedicated machines. On the other hand a target price of 1.5$/cc does not allow any important investment to be amortised on this production only.

One has therefore to make the best possible use of existing infrastructures. By chance ıe eighties, huge production plants have been installed in Russia, in Ukraine and in the :h Republic to pull large quantities of crystals for military purpose. Among them, Lithium ›ate (LiNbO3), Lithium Tantalate (LiTaO3) and Lead Molibdate (PbMoO4) are oxides vn by the Czokralski technology which are relatively close to Lead Tungstate. These :essive installations with very high quality equipment are more or less unemployed now. :ing use of them fits also well conversion programs from military to civil use, for which ıcial resources are available.

The situation for China is somehow different. The Shanghai Institute of Ceramics has :loped about 10 years ago a modified Bridgman Stockbarger method allowing multiple ing of oxide crystals like BGO (Bismuth Germanate). One of the main achievements in 95 to prove that this technics can also be applied to PbWO4 crystals. This important result give access to this rather cheap technology and to the production infrastructure which installed for the L3 BGO detector.

The mechanical processing of such a large number of pieces to rather tight tolerances esents an important cost driver in the production of PbWO4 crystals for CMS. For this on a large effort is under way to develop cheap mechanical processing methods. One ortant aspect of it is to use simple equipment and conventional machines which will be ly converted later on to other production lines.

5. STATUS OF DEVELOPMENT

The R&D phase has started in 95 and is expected to last till the end of 97. The detailed organisation and definition of main objectives was already given in section 3. The present paragraph summarises the progress already made and describes the approach to solve the remaining problems.

5.1. Production of crystals

In 1995 more than 125 full size crystals with the tapered geometry have been produced in Russia. As already mentioned, the Shanghai Institute of Ceramics has been able to grow several full size crystals using the modified Bridgman Stockbarger method. Despite a later involvement in this project, the company Crytur in the Czech Republic has also produced 10 crystals with a length between 15 and 20cm, limited by the stroke of the pulling device. Modification of their equipment will allow them to grow full length crystals soon. Very big ingots (85mm in diameter and 250mm in length) have also been produced by the company CARAT in Lvov (Ukraine), from which at least 5 crystals can be cut.

During this period, the technology transfer of new cutting and polishing methods has led to significant improvement in the achieved tolerances. Fig. 2 and 3 shows the deviations in microns from the specified dimensions for crystals produced before and after September 95. It is clear that we are approaching the desired specification of (+0, -200μm).

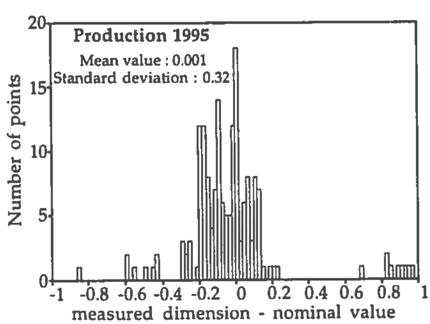

Figure 2: Deviation from specified dimensions in mm till Sept. 95

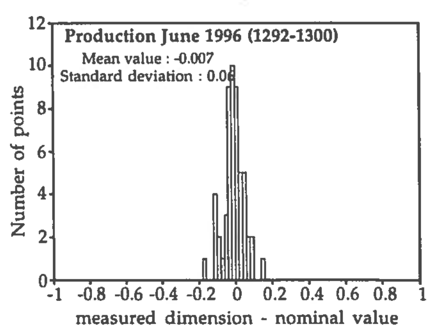

Figure 3: Deviation from specified dimensions after Sept. 95

5.2. Optical parameters

Light production is a complex mechanism in Lead Tungstate. It involves several luminescent centres working in the thermal quenching mode[9-12)]. Interband excitations create free carriers which migrate in the Pb^{2+} excited states till they recombine on one of the luminescent centres. The recombination can be either direct, producing a fast luminescence, or through one or several traps, inducing delayed light emission. In the case of the green emission band of PbWO4, several traps play a role, some of them can act as activators, asing the probability of radiative recombination. It is therefore clear that the optimisation ›WO4 results from a complex interplay between light yield and decay time.

In the first part of 95, in an attempt to increase the light yield, crystals were produced a low level (1 to 2%) but rather long afterglow (up to 100ms). A systematic investigation ıe possible origin of this afterglow led to the conclusion that a contamination by ⁄bdenum introduced local $MoO4^{2-}$ centres strongly competing with $WO4^{2-}$ centres. A effort was made to purify the raw material. An improvement by a factor of nearly 10 obtained for Mo, as well as a significant reduction of several other metallic impurities. e 2 illustrate this improvement for Russian raw material.

Table 2: Purity improvement of Russian raw material

Impurity (ppm)	Na	Al	Si	Ca	Fe	Mo
Raw material 95	7.34	4.98	2.39	3.48	2.49	160
Raw material 96	3.15	1.51	1.19	0.87	1.40	18.6

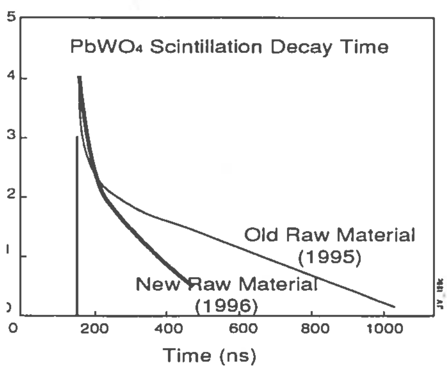

'e 4: PbWO4 decay time before and after Molvbdenum suppression

As a result of this improvement of the raw material quality the afterglow has been suppressed as can be seen on Fig. 4. Batch after batch evolution of the mean decay time defined as

$$\tau = \frac{\sum_i a_i \tau_i^2}{\sum_i a_i \tau_i}$$

is shown on Fig. 5 and 6 for Russian and Chinese crystals respectively. It must also be mentioned that this suppression of the afterglow could be achieved without any ction of the light yield. On the contrary a small light yield increase was noticed, because better transparency of the crystals resulting from the better raw material quality.

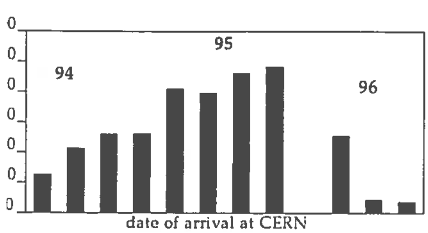

ıre 5: Mean decay time of Russian crystals versus time

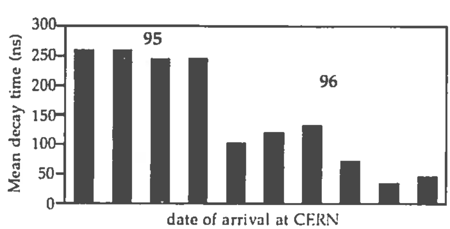

Figure 6: Mean decay time of Chinese crystals versus time

5.3. Radiation hardness

Radiation damage is one of the most important issues for a high performance calorimeter working in the LHC environment. As already mentioned in section 3, it is important that the light yield variations are kept small enough as compared to the expected performances of the monitoring and calibration system [13)] . The observed damage results from an equilibrium between the kinetics of the creation of damage centres and the kinetics of spontaneous annealing at the working temperature.

It is well established that Lead Tungstate crystals are intrinsically radiation hard, which means that colour centres are produced in the vicinity of crystal defects [11,14-16)]. One consequence is that the damage quickly saturates with increasing doses up to levels of several Megarads. The level of the saturation depends very much from the crystal growth conditions. In 95, only 30% of the produced crystals had a light yield loss of less than 10% at the saturation level, which is considered as the maximum acceptable limit. Moreover, the fact that the damage appears at low dose (from a few tens of rads up to 500 rads for the saturation) and the relatively rapid self annealing at room temperature further increases the requirements for the acceptable amplitude of the light yield variation. In a non continuous operation (as will be the case for LHC), a stability can only be reached if the number of defects is limited and if there is no recovery. This can be obtained by running the detector at low temperature, which has the negative consequence of lowering the damage saturation level. It is therefore mandatory to identify the crystal defects which are responsible for the creation of colour centres under irradiation.

Systematic investigations over the last months have led to the conclusion that the most likely defect for the creation of colour centres is a hole trapped by the Oxygen octahedron system around the Lead cation. This defect can be identified by the presence of an absorption band at 350nm which helps to recognise potentially radiation soft crystals before irradiating them[15]. Several conditions can lead to this situation. The most important ones are charge defect state on the cation and cation plus Oxygen vacancies. The origin of these two kinds of defects is quite different and requires actions at different levels. For the first ones, some impurities play the key role and the control of their level of contamination in the raw material will solve the problem. The second category of defects is more closely related to the growth technology. The cure will have therefore to be adapted the this technology. The ongoing R&D effort concentrates most of its resources on the radiation damage problem, the aim being to reach a yield of 80% for the production of radiation hard crystals.

5.4. Production yields

One of the important objectives of the R&D period is to define the conditions of a cost effective production for the 110,000 crystals for CMS.

The work in the production centres is organised around two independent teams, one for R&D and one for production. Each time a new input is given by the first team, the know-how is transferred to the production line which tries to reproduce the results at an industrial scale. This approach allows to better understand the parameters influencing the reproducibility of the parameters. It also permits to work at an early stage of the project on the factors influencing the yield at every step of the production. Impressive progress have already ı made on the production yield as is illustrated on Fig.7 which also shows the expected ·e for the production phase. Implying at an early stage the production facilities is a natural to understand the cost drivers and to adapt the production technology to reduce them. A stic monitoring of the project can be made, based on a good understanding of the nition of the production lines, manufacturing protocols as well as quality control pment and procedures.

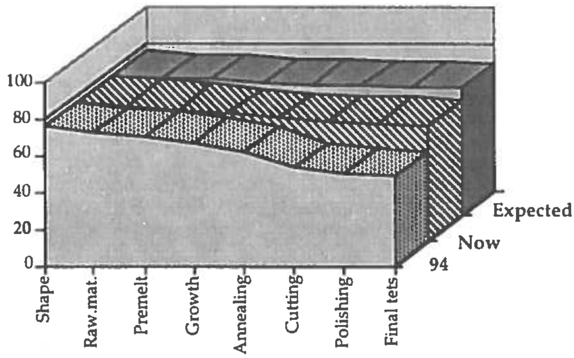

Figure 7: Evolution of Russian production yields

:ONCLUSION

The development of Lead Tungstate crystals at a high level of performance and at an ıstrial scale for LHC applications is a challenging task. The relatively short time scale en compared to the development of any other material) and the budgetary constraints ·ose a specific strategy, where the Research and Development and the industrialisation ses strongly overlap. A clear definition of the objective has to be made in a pragmatic way, rder to rapidly identify the critical parameters and to concentrate the efforts on them. Each ınical progress has to be immediately evaluated in terms of productivity and cost :ctiveness. The organisation of the production has to take realistically into account the sting infrastructures.

Halfway from the end of the R&D period and from the expected beginning of the duction phase, this report gives a status of the development of PbWO4 crystals. Impressive gress have already been made in the growth and mechanical processing of full size stals. Not only the tolerances are now very close to the specifications but the production d has significantly increased. The trade-off between light yield and decay time is now erstood and a small light yield increase could be noticed in recently produced crystals hout any afterglow. The production yield for radiation hard crystals is still low but the gin of the damage is progressively understood and several strategies to improve it at erent stages of the production process are under evaluation.

:nowledgements

The author would like to express his gratitude to all the members of the CMS/ECAL up and of the Crystal Clear collaboration for their continuous help in this collective effort. ould like to acknowledge also the production groups in China, Czech Republic and Russia their enthusiasm and very open and collaborative spirit in this difficult task.

References

[1] The Compact Muon Solenoid Technical Proposal, CERN/LHCC 94-38, 15 Dec 94

[2] The ALICE Technical Proposal, CERN/LHCC 95-38, 71 Dec 95

[3] TheRD18 Crystal Clear Collaboration status report, CERN/DRDC/94-53, Jan 95

[4] V. G. Baryshevsky et al, NIM A322 (1992) p.231-234

[5] V. A. Katchanov et al, "Beam studies of EM-calorimeter prototype built of PbWO4 crystals", Proceedings of the IV Int.Conf.on Calorimetry in High Energy, Sept.15-19, 1993 Isola Elba, Italy, A. Menzione and A. Scribano editors, p292

[6] S. Baccaro et al, Measurements of refractive index on PbWO4, Proceedings of SCINT95: International Conference on Inorganic Scintillators and their applications, Delft, August95, P. Derenbos and C.W.E. van Eijk editors, p293

[7] S. E. Derenzo, W. W. Moses, J. L. Cahon, R. C. C. Perera, Trans. Nucl. Sci. 37(1990), p.203-208

[8] L. Leciejewicz, Zeit. fur. Krist. 121 (1965) 158-164

[9] M. V. Korzhik, V. B. Pavlenko, V. A. Katchanov et al, "The scintillation mechanism in PbWO4 crystals", Proceedings of the MRS Spring Meeting '94, San Francisco, April, 1994; M.J. Weber, P. Lecoq, R.C. Ruchti, C. Woody, W.M. Yen and R.Y. Zhu editors, p 285

[10] I. Dafinei, E. Auffray, P. Lecoq, M. Schneegans, "Lead Tungstate for High Energy Calorimetry", Proceedings of the MRS Spring Meeting '94, San Francisco, April, 1994; M.J. Weber, P. Lecoq, R.C. Ruchti, C. Woody, W.M. Yen and R.Y. Zhu editors, p 99

[11] P. Lecoq, M. Korzhik et al., "Lead Tungstate (PbWO4) Scintillators for LHC EM Calorimetry" NIMA 365 (1995)291-298
CERN/CMS-TN 94-308

[12] A.N. Belsky et al, "Fast luminescence of undoped PbWO4 crystals", Chemical Physics Letters 243 (1995) 552-558

[13] C. Seez "Test beam studies of Lead Tungstate crystal matrices for the CMS electromagnetic calorimeter", Contribution to this conference

[14] E. Auffray, I. Dafinei, P. Lecoq, M. Schneegans "Local trap centres in PbWO4 crystals" Radiation effects and defects in solids, 1995, Vol. 135, 343-347

[15] E. Auffray et al., "Scintillation characteristics and radiation hardness of PWO scintillators to be used at the CMS electromagnetic calorimeter at CERN", Proceedings of SCINT95: International Conference on Inorganic Scintillators and their applications, Delft, August95, P. Derenbos and C.W.E. van Eijk editors, p282

[16] AAM. Martini, A. Vedda et al., "Trap levels in PbWO4 crystals: Correlation with luminescence decay kinetics", Submitted to Chem. Phys. Letters, May 96

ascati Physics Series Vol. VI, (pp. 765–775)
INT. CONF. ON CALORIMETRY IN HEP – Frascati, June 8–14, 1996

TEST BEAM STUDIES OF LEAD TUNGSTATE CRYSTAL MATRICES FOR THE CMS ELECTROMAGNETIC CALORIMETER

C. Seez
Imperial College of Science Technology and Medicine, London, U.K.

On behalf of the
CMS ECAL group

ABSTRACT

ı the test beam in 1995 we consistently achieved an energy resolution of better than .6% at 100 GeV and demonstrated that a lead tungstate electromagnetic calorimeter read ut by avalanche photodiodes can achieve the excellent energy resolutions necessary to ıstify its construction in the CMS detector. The small differences in performance when ıe beam is incident on different crystals can be understood in terms of the properties of ıe crystals and APDs. A study of the feasibility of following the calibration change ıduced by decrease in light yield due to radiation damage is also described.

Introduction

he first brief test-beam investigation of Lead Tungstate crystals for CMS took place in ctober 1993 using a small matrix of rectangular crystals equipped with PIN photodiode adout. The crystals were rather short, 18 cm ($\approx 20X_0$), and the large shower leakage om the rear of the crystals gave direct signals in the photodiodes of a large magnitude as ompared to the scintillation light signal. This gave an enormous tail to the signal (see Fig. (a)). A short test was made with a single crystal equipped with Avalanche Photodiode APD) readout. Due to the very short length of sensitive Si before the gain region (a w μm) the direct signals were greatly reduced in magnitude (see Fig. 1(b)). The need to se APDs rather than PIN photodiodes was clearly demonstated.

ı 1994 futher tests established more detailed requirements on the APDs and on the ıermal regulation system needed: the response of both the crystals and the APDs are ather temperature sensitive (about -1.9% per degree at 20°C for the crystals and of a imilar magnitude for the APDs). Using photomultiplier tubes it was demonstrated that the nergy resolution required by CMS could be obtained (see Fig. 2). The results of these ests have been published[1].

n 1995 we were able to demonstrate that a lead tungstate electromagnetic calorimeter read ut by avalanche photodiodes can consistently achieve the excellent energy resolutions ecessary to justify its construction in the CMS detector.

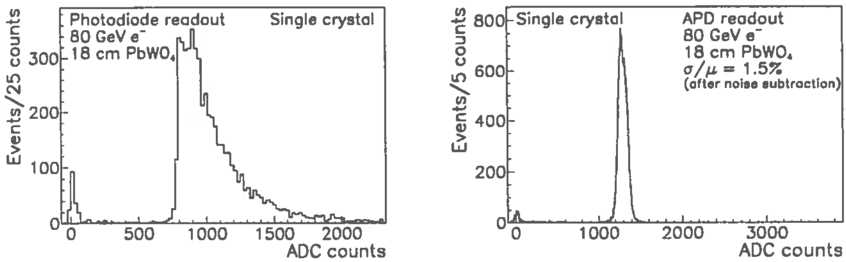

Figure 1: Response of 18 cm long rectangular crystal to 80 GeV electrons with (a) PIN photodiode readout and (b) APD readout.

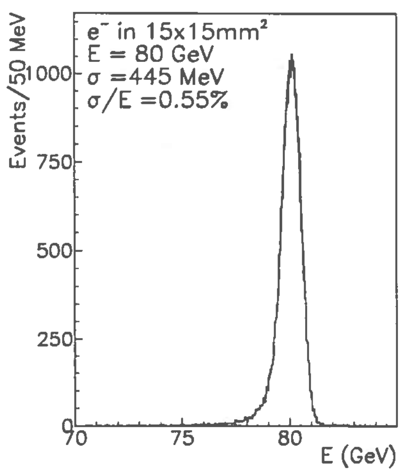

Figure 2: Energy reconstructed in 9 projective crystals with incident electrons of 80 GeV, using photomultiplier readout.

2 Test Setup for 1995

The crystals used were truncated pyramids with a length of 230 mm ($25.8X_0$) and a 20.5×20.5 mm^2 front face projective to a point about 1430 mm from the front surface, and closely approximate the crystals to be used near $|\eta| = 0$ in CMS. They were placed in a thermally insulated, light-tight, aluminium box on a remotely controlled moving table.

In front of the box were placed scintillation counters: two orthogonal planes of scintillation fingers used for adjusting the beam position, halo counters to be used offline for rejecting beam halo events, and trigger counters. The trigger used for taking the data described here was a single coincidence defining a 20×20 mm^2 spot which corresponded well to both the beam size and the front face of a crystal. Drift chambers gave a measurement of the impact point of beam particles with an error of about 195µm.

ectron beams with rates greater than 2 kHz were available in the H4 beam for momenta tween 15 and 150 GeV. With the momentum defining collimators closed to ±3 mm the omentum spread of the beam is calculated to be less than 0.2%. Pion contamination in e electron beam is generally at a level of $< 10^{-3}$ ($\approx 5 \times 10^{-4}$ at 80 GeV).

Readout and electronics

vo different APDs were used for light detection, their characteristics are shown in ole 1. The prime requirement for the 1995 beam tests was that the effective thickness of and hence the response to ionizing radiation, be sufficiently small as to not give rise to e large tails seen on the high side of the energy distributions in the 1994 data taken with PDs.

Table 1: Avalanche Photodiodes used in the H4 tests in 1995

	EG&G C30719E	Hamamatsu S5345
Size	5×5 mm^2	$\phi = 5$ mm
Capacitance [pF]	30	325
Typical operating voltage [V]	400	150
Quantum efficiency at 500nm	0.75	0.65
d_{eff} (M=50) [μm]	7.6	3.5
Excess noise factor, F (M=50)	2.8	2.0
$1/M \times dM/dT$ (M=50) [% per °C]	-3.5	-2.3
$1/M \times dM/dV$(M=50) [% per V]	2	15

ne signals went into fast, low-noise pre-amplifiers, designed around a high performance ET. These amplifiers had a peaking time of 35 ns and measured electronics noise of oout 1200 electrons when connected to an EG&G APD and about 6000 electrons when onnected to a Hamamatsu APD. These noise performance figures imply an energy quivalent noise of ≈ 15 MeV/crystal with the EG&G APDs and ≈ 75 MeV with the amamatsu APDs.

he noise seen in the standard data taking configuration was significantly larger than this hen using EG&G APDs largely because of coherent noise. Thus in the standard data king configuration the energy equivalent of noise measured for a sum of nine crystals as about 130 MeV with the EG&G APDs, and 200 MeV with the Hamamatsu APDs.

uring some of the tests two APDs were mounted on some of the crystals. In this case ach APD was followed by a complete and independent electronics chain, and read out in separate ADC channel.

.2 Monitoring the calibration

he calibration was monitored using short (≈ 30 ns) pulses of light transported to the rear of each crystal by optical fibres. The light pulses were generated by a cluster of red LEDs (Stanley Super Bright SBR5501, peak emission at 660 nm). The electronics generating the pulses used continuous feedback of the signal size, via a Si photodiode, to stabilize the pulse size. The stability of the pulse size was better than 0.1%.

2.3 Crystal preparation

On delivery to CERN crystals are inspected by eye and measured geometrically before being given an extensive series of quality checks, including tests of light yield, of optical absorption as a function of wavelength, and of longitudinal uniformity.

The crystals used in the tests were wrapped in Tyvek (type 1056, with a nominal thickness of 160 μm) on all sides except the rear, where the APDs were mounted. When using the EG&G APDs much of the remaining rear crystal surface was also covered with Tyvek. This was not possible when two APDs were mounted on each crystal, as was done with Hamamatsu APDs.

3 Energy Resolution

Data taking for energy resolution studies was generally preceded by beam calibration. Using a 50 GeV electron beam, runs of 40k events were taken with the 20×20 mm^2 trigger counter centred on each of the towers in turn. Then runs of 100k events were taken with the beam momentum set to each of 7 momenta in turn (15, 20, 35, 50, 80, 120 and 150 GeV) with the same counter centred on each of the towers to be studied, in turn.

3.1 Analysis procedure

Analysis of an electron run is begun by locating, in terms of the drift chamber coordinates, the centre of the crystal covered by the trigger. This is done by finding the point of maximum signal in that crystal. This procedure is reproducible with a precision of better than 0.1 mm. A calibration is made with the 50 GeV runs, by assuming that for electrons incident close to the centre of the crystal 40 GeV is deposited in the crystal. This gives a precise relative calibration between crystals and a rough absolute scale. The calibration is intended to be used to reconstruct energy by summing 9 crystals, and about 80% of the energy deposited in the 9 crystals is in the central crystal.

The energy reconstruction used in the energy scans is a sum of 3×3 crystals centred on the struck crystal, see figure 3. For the results presented in this section only events where the electron is incident in a 4×4 mm^2 region in the centre of the 3×3 array are used. This simplification makes the results largely insensitive to calibration errors. The large tails seen on the high side of the energy distributions in the 1994 data, due to the large APD response to ionizing radiation, are only slightly visible with the EG&G APD in 1995, and not visible when using the Hamamatsu APD.

The noise term of the energy resolution was calculated run by run. The pedestals taken th a randomly timed ADC gate during the beam spill were summed using the same libration as for the beam events. The width of this distribution was measured by a ussian fit to a region $\pm$ 1.5σ about the peak.

e noise was subtracted quadratically from the energy resolutions before fitting to obtain constant and stochastic terms. As a test, after subtracting the noise, a noise term was t as a free parameter in the fit. A value consistent with zero was found for this rameter.

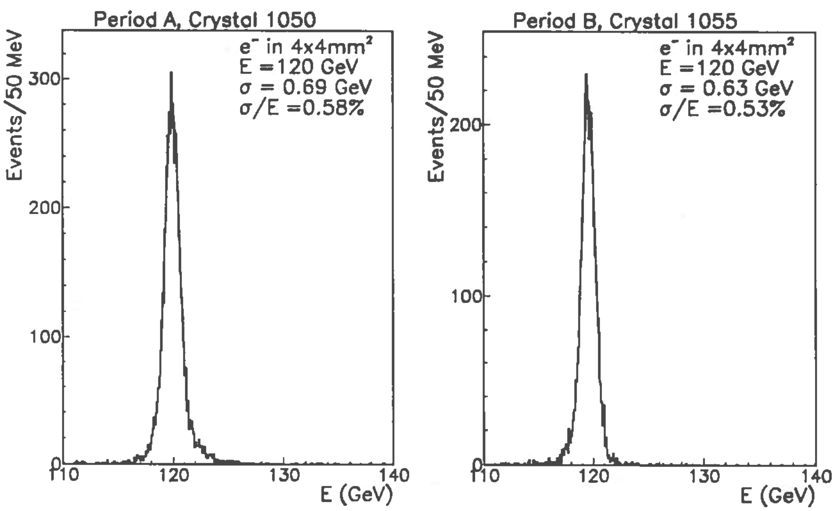

Figure 3: Energy summed in a 3×3 array of crystals for 120 GeV electrons incident in a 4×4 mm2 region about the centre of the central crystal. Spectra from two different data taking periods are shown, the first uses EG&G APDs, the second uses Hamamatsu APDs.

2 Summary of results obtained

the first July period there were 4 crystals that could be used as centres of sums of 9. In second July period and in the August period there were 9 such crystals, and each of ese crystals had 2 APDs. One can consider the resolution using the first APD, the cond APD, or both APDs together. For each of these cases (there are 40 for single PDs and 18 for double APDs, plus a few which were measured more than once) the ocedure outlined above was followed through. The results for single APDs are mmarized in table 2. The statistical errors on these values are negligible – typically out 0.1% for the stochastic term and 0.02% for the constant term. The most serious stematic uncertainty is the way in which the magnitude of the noise subtracted affects sharing of the resolution between the stochastic and constant terms in the fit. For ample: reducing the noise subtracted by 10% typically results in an increase in the fitted stochastic term by slightly more than 0.5% and a decrease in the fitted constant term by slightly less than 0.05%.

Table 2: Summary of energy resolution results (single APD)

	Stochastic term	**Constant term**
July I (4 values)	Typical: 4.5%/√E	Typical: 0.40%
July II (18 values)	Typical: 4.25%/√E 3.8 – 5.9%/√E	Typical: 0.35% 0.30 – 0.71%
August (18 values)	Typical: 4.00%/√E 3.3 – 5.4%/√E	Typical: 0.45% 0.41 – 0.65%

Such an error in the measured noise could, for example, be caused by unusual pileup conditions. The range of values given in the table is somewhat misleading because the extremes seem to be dominated by this sort of problem. The typical values given are a more reliable guide. Results using the signals from two APDs on the central crystal improved the stochastic term of the resolution function by an amount consistent with the hypothesis that doubling the APD coverage doubled the collected photostatistics. Taking all the available 18 pairs of values the mean value of the improvement factor is 1.8, although the distribution is rather wide (r. m. s. of 0.3). The two APD results were obtained by using two APDs on the central crystal only, so if doubling the APD coverage resulted in a doubling of the light collected one would have expected an improvement factor of about 1.8.

3.3 Stochastic term and light yield

Monte Carlo shower simulation predicts a stochastic term for energy reconstruction in a sum of nine crystals of about 2%/√E (due to lateral leakage). The larger stochastic term observed in our crystals can be explained by photostatistics. Here we compare the measurements of light collected in the APDs using muons passing through the APDs, and using the width of an LED pulse signal, with the values calculated from the stochastic term. In this section, and in the one that follows and discusses the constant term, we make the assumption that variations of the constant and stochastic terms are dominated by the characteristics of the central crystal, since about 80% of the energy deposited in the 3×3 array is contained in the central crystal.

Data taken with a 225 GeV muon beam provide us with a useful measure of the light collected by the APDs. Muons passing through the APDs induce a direct signal as well as the signal from scintillation light caused by the energy they deposit in the crystal. The sensitive area of the APD can be picked out by selecting events with large energy deposits. Selecting on the impact point one can obtain two peaks: one from muons ıssing only through the crystal giving only the light signal, and one from muons also ıssing through the APD and giving light plus charge. An example is shown in figure 4.

nother measure of the light collected by the APDs is provided by the LED monitoring stem. The light yield can be calculated assuming that the width of the observed LED gnal, after subtraction of noise, is due to photostatistics. The excess noise factor is sumed to be that given in table 1. In figure 5 the result of this calculation is plotted ;ainst the result coming from muon runs, for each of the 9 central crystals, each with 2 PDs, in the August period. The strong correlation suggests that the relative precision of ese results is better than 5%.

› obtain the crystal light yield from these numbers it is necessary to assume a matching ctor for the light collected into the APDs, and a quantum efficiency. Making reasonable sumptions: a matching factor equal to the area matching (i.e. 1/23 for EG&G, and 1/29 r Hamamatsu), and quantum efficiencies as given in table 1, leads to values around) γ/MeV, similar to those obtained by other measurements.

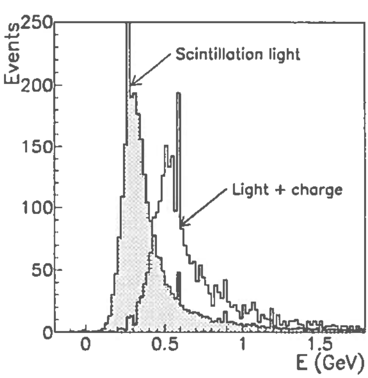

gure 4: Signals seen from muons passing ırough the crystal only haded histogram) and from muons ıssing through both crystal and APD.

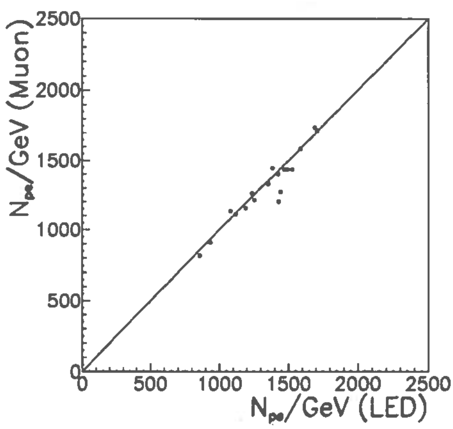

Figure 5: Photoelectron yield in 18 APDs in the August matrix as calculated from LED signals compared to photoelectron yield calculated from the muon signal. The line is drawn to help the eye.

ıe light yield as calculated by these methods can then be compared with what would be ılculated from the stochastic terms of the fitted energy resolutions, after subtracting the ɔn-photostatistics contribution (assumed to be 2%/√E). Figure 6 shows the results. In ıly three cases is the correlation poor (the point marked with a triangle is, in fact, off ale). Close examination of the cases with poor correlation shows that, in each case, the solution function fit has produced a very small stochastic term and a very large constant rm. These seem to be errors of the kind discussed in the previous section.

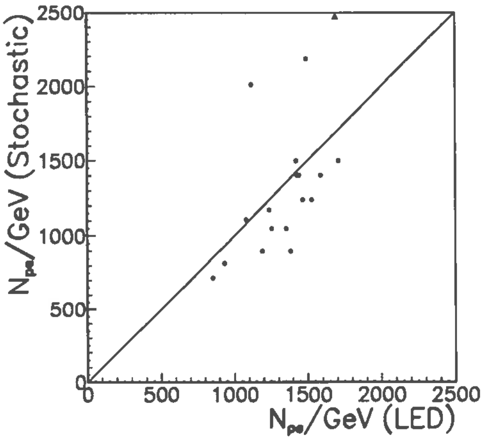

Figure 6: Photoelectron yield in 18 APDs of the August matrix as calculated from LED signals compared to photoelectron yield as calculated from the stochastic term of the measured energy resolution function. The line of is drawn to help the eye.

3.4 Constant term and longitudinal uniformity

The longitudinal uniformity of light collection has been measured using a low momentum (405 MeV, kinetic energy = 84 MeV) proton beam at the Paul Scherrer Institute. The longitudinal uniformity measurements have been used in a shower simulation Monte Carlo. It is found that the increase in response towards the back of the crystal can compensate for rear leakage and eliminate the tail on the low energy side otherwise seen in shower simulations not taking this non-uniformity into account. Severe non-uniformity, however, increases the width of the observed energy distributions. It is observed that the region around shower maximum must be particularly flat to avoid inducing a sizable constant term. Comparing the Monte Carlo predictions with the test beam data provides good agreement to the extent that the few crystals predicted by the Monte Carlo to generate large constant terms are indeed found to have large constant terms in the test beam. It should be noted that the longitudinal response measured at PSI is measured with photomultipliers tubes which cover the whole rear face whereas the APDs cover less than 1/20 of the rear face. The photomultipliers also have a rather different spectral response to the APDs. Both these factors probably mean that the longitudinal response measured at PSI is not quite the same as that seen by the APDs in the test beam.

Figure 7 shows, for the July II matrix, the predicted contribution to the constant term coming from longitudinal non-uniformity versus the fitted value after subtracting 0.3% quadratically from the fitted value. The constant terms obtained when using each of the 2 APDs are very similar, and, for this plot the mean of the 2 values has been taken. The

% subtracted from the measured constant term represents an observed floor in the ues found. The constant term predicted by a Monte Carlo of shower energy deposition :ompletely uniform crystals is about 0.2%, and results from leakage.

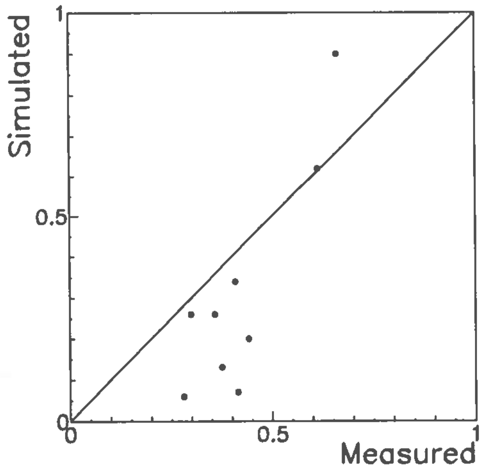

Figure 7: Constant term for event sets centred on the 9 central towers of the period B matrix (after subtracting 0.3% quadratically), compared to the contribution to the constant term from longitudinal non-uniformity of light collection as predicted by simulation. The line is drawn to help the eye.

Calibration Stability

ith the achievement of good thermal stability we hoped to have achieved good libration stability, but it was noticed that there were apparent changes in the calibration several percent – far larger than could be explained by the small residual fluctuations in nperature. A long stability study was made. The beam, set for 120 GeV electrons, was nt into the central crystal of the matrix and data were taken continuously for about 40 urs with no changes made to any conditions. The beam signal in the central crystal owed a continuous drop, which totaled slightly more than 5% over the 40 hours. The libration monitoring LED signal showed significant decreases in all the central 3×3 ystals, and smaller decreases in the surrounding ring of 16 crystals. The decrease seen r the LED monitoring signals in the central crystal is not the same as that seen for the am signal. To within the errors of the calculation procedure each APD of a pair sees the me decrease. These facts suggested that the effect was due to radiation damage of the ystals. Subsequent tests with photomultipliers confirmed this hypothesis. The damage en by the LED monitoring is less than that seen by the beam signal, due to difference in avelength between the scintillation light and the LED light.

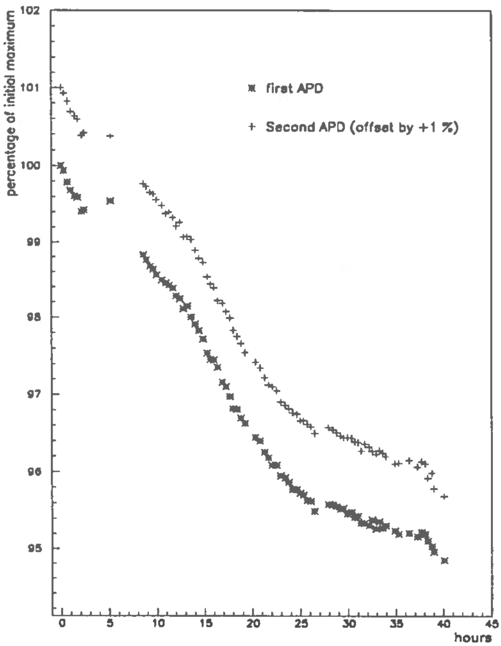

Figure 8: Signal seen in the two APDs on the central crystal, as a function of time.

The calculated dose rate during the stability study was about 5 rads/hour at shower maximum in the central crystal. Surrounding crystals received smaller doses. Few of the crystals in the matrix were classified as the radiation hard "type 3" (the classification is based on the transmission spectrum properties with which a correlation with radiation hardness has been observed). It has been known for some time that radiation damage in lead tungstate occurs rapidly and saturates. The damage consists of the formation of colour centres resulting in light transmission losses. Even type 3 crystals can suffer some damage, although it quickly saturates, so that, for example, a crystal might suffer a total loss in light output of only 15% after 5 Mrad, but most of that loss occurs during the first few hundred rads.

4.1 Use of the Calibration Monitoring System

The calibration monitoring system used in 1995 was installed as a test-beam tool, only loosely related to the final system being envisaged for CMS, but, despite the wavelength of the LED light being quite far from that of the lead tungstate scintillation light we have found it to be capable of following the changes caused by radiation damage with great precision.

The ratio of the decrease in beam signal and the decrease in LED signal, as a function of e, was observed to be constant with a value around 2.0. Using this factor of 2.0 we able to correct the calibration for the beam energy signal using the LED signal. Figure ıows the residual error after this correction. The remaining fluctuation, with a peak-to-ık magnitude of about 0.7%, is due to the uncorrected temperature variation. It seems t the calibration drift, due to radiation damage, can be corrected to better than 0.1% ng the LED signals.

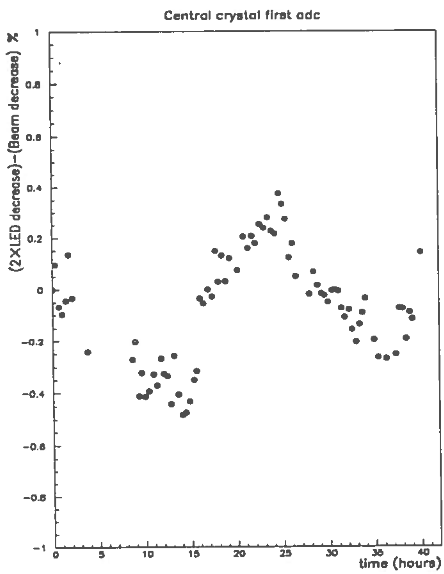

Figure 9: Residual calibration error after loss correction using LED signal

Conclusion

1995 we have demonstrated that a lead tungstate electromagnetic calorimeter read out ' avalanche photodiodes can consistently achieve the excellent energy resolutions ːcessary to justify its construction in the CMS detector. The performance achieved, and e small differences in performance when the beam is incident on different crystals, have ːen understood in terms of the properties of the crystals and APDs.

eferences

J. P. Peigneux *et al.*, Results from tests on matrices of lead tungstate crystals using gh energy beams, Accepted for publication in Nucl. Instr. and Meth.

scati Physics Series Vol. VI, (pp. 777–784)
INT. CONF. ON CALORIMETRY IN HEP – Frascati, June 8–14, 1996

THE CMS ELECTROMAGNETIC CALORIMETER MECHANICAL DESIGN

M. Lebeau
CERN, 1211 Geneva23, Swuitzerland

ABSTRACT

is paper summarises the present design status of the CMS electro-magnetic orimeter as it was worked out by the CMS ECAL Engineering Team [1] in the Spring 1996. The design is proceeding along these main lines to the Technical Design Report 1997 and ultimately to the construction of the calorimeter and its installation on LHC 2004.

CMS electro-magnetic calorimeter mechanical design problems and choices

Scale and modularity of the calorimeter

e total barrel and endcaps array sums up to 120'000 crystals of average size 2 x 2 / ! x 2,4 x 23 cm^3 = 12 m^3 (about 100 *tons*) displayed on a cylindrical inner surface of lius 2.8 *m* and length 6 *m* (fig. 1). The array is divided according to a modularity ıtching the production rates of the various components, their assembly, the calibration d the installation scheme. The CMS ECAL modularity (in the barrel part) is according the following hierarchy:

!.1 *Sub-unit*

ıe sub-unit includes the crystal,the APD, its glued capsule holding the Very Front End rt of the electronics.

!.2 *Sub-module*

ı alveolar sub-module contains 12 (2 in φ x 6 in η) crystal sub-units to be assembled d tested in the four assembly Regional Centres. This is sized to human scale to be sembled and fully testd on a workbench (fig. 2).

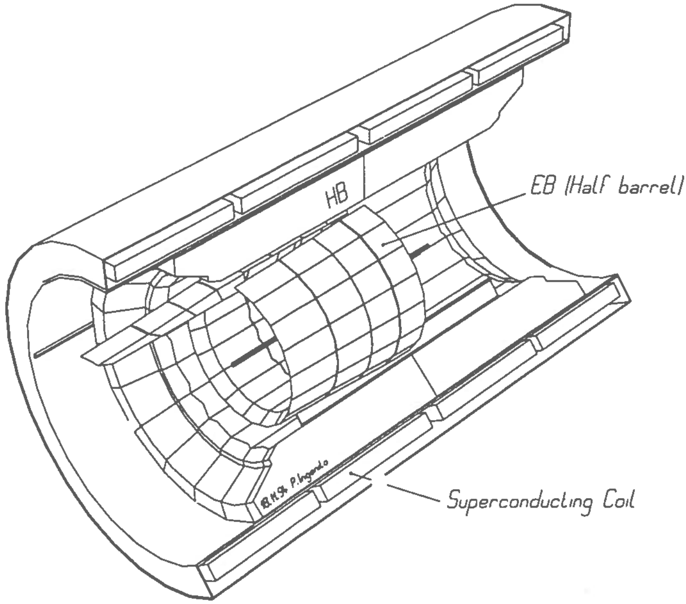

FIG.1. CMS ECAL HALF-BARREL ARRAY
SHOWN INSIDE HCAL BARREL AND SUPERCONDUCTING MAGNET
(ONE SUPER-MODULE IS REPRESENTED AS BEING INSTALLED)

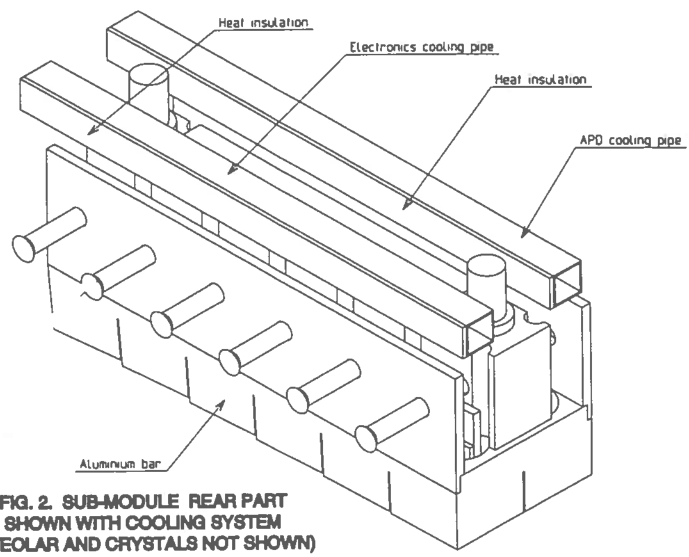

FIG. 2. SUB-MODULE REAR PART SHOWN WITH COOLING SYSTEM (ALVEOLAR AND CRYSTALS NOT SHOWN)

1.3 Module

'basket'contains 48 (12 in φ x 4 in η) sub-modules. The assembly takes place in the egional Centres before transportation to CERN (fig. 3).

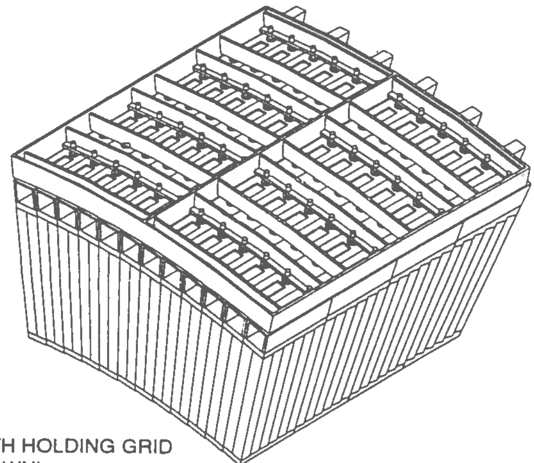

3. MODULE OF 48 SUB-MODULES WITH HOLDING GRID
(BASKET SIDE-WALLS NOT SHOWN)

.1.4 Super-module

. Super-module is a set of four modules held together by a 'spine' beam. It is ssembled at CERN as a unit for calibration and installation. The ECAL barrel consists f 36 identical super-modules with a central symmetry plane and an 18-fold symmetry ı φ (fig. 1 and 3).

.2 $PbWO_4$ crystal mechanical properties

'o cope with the low yield strength:σ_b = ca. 10 N/mm^2 and a very dissymmetrical oefficient of thermal expansion: $\alpha_a = \alpha_b = 12{,}8 \times 10^{-6}$, $\alpha_c = 29{,}5 \times 10^{-6}$ [2)] , the olution retained for the mechanical support is $PbWO_4$ crystals individually contained in lveolar sub-modules.

.3 Temperature dependence of the crystal and the APD

'he high value of the temperature coefficient of the crystal: k ($PbWO_4$) = - 0,019 /°C ' and of the Avalanche Photo Diode (APD) k (APD) = - 0,02 /°C [4)] require a careful esign of the cooling system to ensure a thermal regulation to [0,05°C] of both the rystal and the APD.

1.4 Hermeticity of the crystal array

1.4.1 Cracks between crystals

Cracks between crystal faces ≤ 0,5 *mm* produce 2,5 % dead space corrected by a 3° tilt. In φ, this tilt is achieved by a geometry scheme called the 'flat pack' [5) 6)]. In η, this tilt is achieved by a geometry scheme called the "3M" scheme [7)].

1.4.2 Cracks between modules

In η, the module boundary has a conical shape. Modules needs 2 *mm* walls for stability but a 1 *mm* module to module distance can be set in the lab. The total η crack is 6 *mm*. In φ, the module boundary has a planar shape, 1 *mm* module walls are acceptable but 3 *mm* between super-modules is required for the installation maneuvers. The total φ crack is 6 *mm*. Cracks between modules ≤6 *mm* produce 1,25 % dead space corrected by the above-mentioned 3° tilt.

1.4.3 Cracks between the barrel and the endcaps

The selected layout enables a complete crystal coverage over the rapidity range 0 < η < 3 with a sufficient gap width between barrel and endcaps in the shape of a chicane to let the tracker and pre-shower detector cables out [8)], (fig. 4).

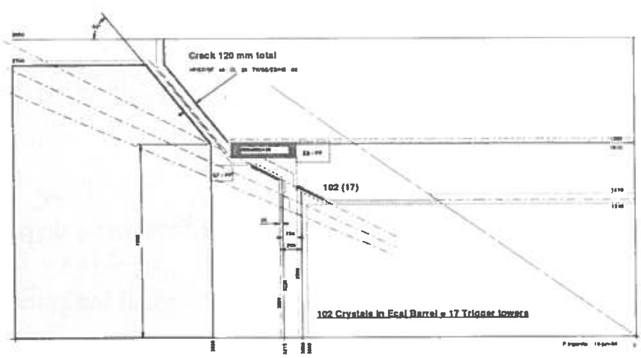

FIG.4 . ECAL BARREL / ENDCAPS TRANSITION

1.4.4 Dead material

High-strength, low Z building materials working at their optimal loading have been selected to build the support structure: glass fibre epoxy composites for the sub-module alveolar, carbon fibre epoxy composites for the module basket and super-module spine.

Description of the mechanical components of the calorimeter

1 The '2 x 6' alveolar submodule

1.1 The alveolar

he alveolar walls have been optimised to comply with the 0.5 *mm* crystal to crystal ominal distance condition. Individual cells are glued together so that middle walls have ouble thickness, and side walls simple thickness so that the 0.5 *mm* distance condition fulfilled inside an alveolar and between two alveolars. The fabrication consists in rapping crystal-like metallic mandrels with the following layers: a 100 μm reflector oating, a 70 μm glass fibre pre-preg (moulding conditions) and a 25 μm aluminium foil ight tightness). The mandrels are oversized to create a 100 μm air gap to the crystal ice (nominal), this enables elastic deformations to occur in the alveolar without ffecting the crystal. Inside its cell, a crystal is only submitted to its weight and to a ight axial compression (ca. 1 *N*). The sub-module is bearing on the module in three oints in iso-static conditions (without built-in bending moment) so that undetermined ending moment will not apply to the alveolar. In the vertical position, it hangs to its vo rear fixation points. In the horizontal position, it lies as a freely supported beam. he computed deflection of 0.04 *mm* has been verified on a full size prototype [9].

1.2 The sub-module rear part

nce the crystal sub-units are set in the 12 alveoles, the alveolar is closed by a glued luminium tablet which screens the APD and the crystals from the Very Frontend lectronics [10]. Dowels are inserted to position the crystal longitudinally. A cooling lock bearing the two rear fixation points is bolted to the tablet. Aluminium heat onducting fins are attached to heat dissipating parts. The cooling circuitry is arranged to ccurately regulate the crystal and APD temperature on its entering path (low ΔT), and cool the most dissipating items (electronics boards) on its return path (high ΔT) [11].

.2 The 'basket' module

.2.1 The 'basket'

he 'basket' acts as a modular container: it protects the fragile crystal array, it is a iermal and optical shield. Its most important function is to take the sub-module loads om the front by its bottom plate and from the back by its supporting grid so that sub-iodules are moment-free supported in all positions in the calorimeter. Basket walls of 1 *ım* in φ and 2 *mm* in η have been designed to 6 *mm* crystal to crystal nominal distance cross two baskets (both in φ and in η), using carbon fibre epoxy resin composite layup optimisation. Finite Element Analysis shows that deformations affecting the φ and η distances between modules are far smaller than the nominal distance. These distances have been defined more to comply with moulding tolerances than with deformations. For a deformation inferior to 0.3 *mm* the highest stress value of 6 *Mpa* is found in a η wall in horizontal position. It corresponds to a safety factor of 5 for the entire barrel support structure [12].

2.2.2 The module front part

The module front part (bottom plate) is a sandwich of two 2 *mm* carbon fibre epoxy resin composite skins and one 12.7 *mm* Nomex honeycomb core. The core can be filled with molten paraffin during fabrication, as a moderator. The monitoring fibres are displayed on its outer surface and reach the crystal front faces by traversing holes. To ensure the crystal thermal regulation, a thermal screen might be integrated in the sandwich inner skin. The bottom plate takes up to 50 % of the sub-modules weight in horizontal position, with a maximal 0.16 *mm* vertical and less than 0.1 *mm* radial deformation. This is compatible with the radial tolerance.

2.2.2 The module rear part

A grid-like part covers the module rear part (fig. 3). It integrates the sub-module fixation points and takes their weight, 100 % in vertical position, about 50 % in horizontal position. The grid is connected to the module side-walls and to the spine cross plates to make the load paths as short as possible. The grid integrates the crystal rear part cooling system. The grid is also a support for the digital electronics and the services placed in the spine volume.

2.3 The 'spine' beam

2.3.1 The 'spine' structure

The 'spine' is a U-shaped beam of width 600 *mm* and height 170 *mm*. The back part is an austenitic steel 20 *mm* thick plate, bolted to side parts made of 10 *mm* thick carbon epoxy resin composite. The side parts are connected to the modules φ sides. Cross plates made of 10 *mm* composite plates too, are connected to the modules η sides. Locating pins terminate the spine at the inner end, and a patch panel at the outer end.

2.3.2 The 'spine' functions

The 'spine' ensures the consistency of the super-module. It takes accurately together and bears the weight of the four modules. The spine inner volume houses the digital electronics and the cable- and pipe-work. The spine material and dimensions have been timised to ensure a maximal sag of the order of 1 *mm* in vertical position and a ıximum torsion of less than 0.1 *mm* in horizontal position [13]. This ensures the 1 *mm* p in η and the 3 *mm* gap in φ between modules not to be infringed.

3.3 Hadron Calorimeter / ECAL interfaces and the 'spine'

ıe spine transmits the super-module weight to the hadron calorimeter barrel inner bore. ılculations have verified that this load produces stresses and deformations in the ΞAL under an acceptable limit [14]. The spine material and dimensions have been timised to avoid uneven material distribution and when impossible to reduce the aterial quantity or density. This has in particular led to make the spine side walls and oss plates in carbon fibre epoxy composite.

Installation scheme

ıe ECAL barrel will be installed, super-module by super-module. The installation will oceed in parallel on both sides of the experiment. An installation device positioned on e HCAL front face will make the super-modules smoothly slide to their nominal ısition where they will be fastened to bearing fixtures accurately bolted and surveyed the HCAL inner bore face. The installation will proceed from top to bottom, ternately from right to left. The last installed super-module will be the centre bottom ıe. The movement will be motorised to cope with the experiment 1.4% slope. Each per-module will be surveyed by photogrammetry and tests of electrical continuity and pework tightness will be performed before moving the device to the next position.

CMS ECAL projected milestones:

ıpermodule preliminary integrated design	Nov. 1996
arrel design completed	Apr. 1997
ıpermodule pre-series tendering	Apr. 1997
ıpermodule pre-series orders placed	Jul. 1997
ıpermodule pre-series deliveries	Dec. 1997
DR	Dec. 1997
lounting and assembly period	Jan. 1988 to Jun. 2004
alibration periods (barrel)	Apr. to Nov. 2001, '2, '3
alibration periods (endcaps)	Apr. to Nov. 2004
ıstallation and tests (barrel)	Jan. to Sep. 2004
ıstallation and tests (endcaps)	Jun. 2004 to Mar 2005

6 References

1. The CMS ECAL Engineering Team : ÉCOLE POLYTECHNIQUE, Palaiseau, France: A. Busatta, O. Ferreira, P. Poilleux, LAWRENCE LIVERMORE NATIONALLABORATORY, USA: S. Hibbs, IPN, LYON, France: J.-C. Mabo, INFN ROME, Italy, G. Basti, A. Leone, A. Zullo, RUTHERFORD APPLETON LABORATORYU.K.: J. Connolly, L. Denton, B. Smith, CEA Saclay, France, F. Rondeaux, ETH ZURICH, Switzerland: P. Ingenito, CERN, M. Lebeau, R. Loos.

2. M. Ishii. et al., Mechanical properties of $PbWO_4$ scintillating crystals. KEK pre-print 95-106 (Sept. 1995) H submitted to NIM, A.

3. I. Dafinei et al., Lead Tungstate for High Energy Calorimetry. Mat. Res. Soc. Symp. Proc.. **348** (1994) Material Research Society.

4. Hamamatsu and EG & G Companies, constructors' data (1996).

5. B. Smith, CMS ECAL Barrel Region. Standard Crystal geometry in Phi. Rutherford Appleton Laboratory Technical Note BS-TN/96-007,(June 1996).

6. L. Denton, Flat-Pack Crystal Geometry - Geometrical Tolerances, Rutherford Appleton Laboratory internal note. (April 30, 1996), presented at CERN at the CMS ECAL Week of May 1996.

7. J.-P. Vialle, M. Lebeau, A. Giverneau and M. Maire, Barrel ECAL Simulation and Optimisation in CMS, CERN CMS technical note CMS/TN/95-151, (October 20, 1995).

8. R. Ribeiro and J. Varela, Hermetic EM Calorimetry in CMS. CERN CMS technical note CMS/TN/96-064, (May 14, 1996).

9. O. Ferreira, FEA on alveolar, presented at CERN, CMS ECAL Week of January 1996.

10. S.Hibbs and G. Johnson, Thermal Analyses by LLNL of ECAL Crystals and Very f ront End, Lawrence Livermore National Laboratory Technical Report, (May 7, 1996) presented at CERN at the CMS ECAL Week of May 1996.

11. P. Baillon, Pipes needed for cooling ECAL. CERN Internal note (June 21, 1996).

12. A. Leone, M. Marchetti, Structural Behaviour of Basket 3. Agusta S.p. A., INFN Rome, University of Rome, Aerospace Department. FEA analysis presented at CERN at the CMS ECAL Week of May 1996.

13. A. Zullo, FEA on spine. INFN Rome, FEA analysis presented at CERN at the CMS ECAL Week of May 1996.

14. I. Churin, FEA on ECAL loading of HCAL, (June 3, 1996) private communication.

IX – Readout and Electronics

Convener V. Radeka
Secretary C. Colantuono

Radeka	Convener's Report
Marroquim	Time–Digitized Signal Analysis for a Scintillator Tile Hadron Calorimeter
de La Taille	A Low Noise Transceiver for the NA48 Liquid Krypton Calorimeter
P. Mendiburu	The Electronic R&D for the Electromagnetic Calorimeter of CMS
Zoccoli	The Electromagnetic Calorimeter of the HERA–B Experiment
V. Camin	Cryogenic Front–End Electronics for Fast Noble Liquid Calorimetry
Cerri	The NA48 Liquid Krypton Calorimeter: Electrode Structure, Front–End Electronics and Calibration
Takai	Dynamic Range Compression in a Liquid Argon Calorimeter
Aspell	A Low Power, Large Dynamic Range, CMOS Amplifier and Analog Memory for Capacitive Sensors
Monnier	Analogue Optical Links for the Front–End Read Out of the ATLAS Liquid Argon Calorimeter
Savoy–Navarro	Realization and Test of a Fast Digital Readout for the LHC Calorimeters: Present Performances
Jacobs	Radiation Hardness of GaAs Preamplifiers for Liquid Argon Calorimetry at LHC

ascati Physics Series Vol. VI, (pp. 787–790)
INT. CONF. ON CALORIMETRY IN HEP – Frascati, June 8–14, 1996

(Convener's Report)

READOUT AND ELECTRONICS

V. Radeka
Brookhaven National Laboratory, Upton NY 11973

Calorimetry poses some unique requirements on readout electronics which quite different than for tracking (silicon and gas) detectors. These requirements particularly challenging in large detectors planned for the LHC, and in high ecision electromagnetic calorimetry such as in the NA48 experiment. The main tinctions are, a) the large dynamic range of the energies to be measured; and uniformity of response and accuracy of calibration over the whole detector. As most other detectors, low noise at short pulse shaping times is essential. High ninosity results in pileup effects, which are present in every measurement, and in gh radiation for front and forward parts of the calorimeter. Power dissipation is najor concern, as in any other detector subsystem, in some respects only more since all the elements of the signal processing chain require more power due to large dynamic range, speed of response, high precision, and low noise required. ie reliability of the readout electronics will have to be much higher than in most evious experiments, because the access to the electronics on the detector will be ry limited and infrequent. In the context of all these difficult requirements, the ntributions to this conference covered many interesting subjects of concern to adout electronics for calorimeters, while understandably, it was not possible to ver all of them in one session. Here are brief comments on the contributions in order they were presented:

- F. Marroquim from the University of Rio de Janeiro described "Time - Digitized Signal Analysis for a Scintillator Tile Hadron Calorimeter". This is a very valuable contribution, as it describes quantitatively the waveforms arising in scintillator tile hadron calorimeters. There have been very few published accounts of any investigations of the time dependence of the scintillation process in this type of calorimeter, and here are some specific numbers about the light (charge from the photomultiplier) as a function of time.

- G. Martin from LAL, Orsay presented a "Low Noise Transceiver for the NA48 Calorimeter". In the NA48 Calorimeter, preamplifiers based on silicon junction field effect transistors are operated in liquid krypton. This contribution describes a very compact electronic and mechanical realization of amplifier-drivers with pole-zero cancellation, which are plugged directly into the signal feedthroughs in the wall of the cryostat.

- J. P. Mendiburu from LAPP, Annecy, described some aspects of "Research and Development in Front-End Electronics for the Readout of the Electromagnetic Calorimeter of CMS". The crystal (lead tungstate) scintillator calorimeter for CMS is based on a readout with avalanche photodiodes. The questions arising in the tradeoffs between the avalanche gain and noise, and in the optimization of the performance and the parameters of the diodes are discussed in this paper.

- A. Zoccoli from INFN, Bologna, discussed some aspects of "The Electromagnetic Calorimeter of the HERA-B Experiment". In preparation for this future experiment, filtering methods for trigger from electron tracks are being considered.

- D. Camin from the University of Milano presented a summary of the results achieved in the pioneering work of his group on "A Cryogenic Front-End Electronics for Fast Noble Liquid Calorimetry". In their work they have developed monolithic preamplifiers in gallium arsenide technology. With large area input devices they have achieved a very low series noise of $\approx 0.3\ \mathrm{nV/Hz^{1/2}}$. This work has made a significant contribution to the whole area of low temperature electronics, also for applications beyond the area of calorimetry.

- C. Cerri from INFN, Pisa and CERN, gave a very thorough description of "The Front-End Electronics of the NA48 Liquid Krypton Calorimeter". This work represents an exercise in high precision readout electronics, from the current calibration to the attention devoted to minimizing coherent noise. The readout chain has been demonstrated in extensive beam tests of a prototype calorimeter.

- H. Takai from BNL described "Dynamic Range Compression in a Liquid Argon Calorimeter". This paper describes one approach to the problem of a large dynamic range, applicable when only preamplifiers (with a cable driver) can be located at the calorimeter, and the rest of the readout chain is some distance away. With dynamic range compression in the preamplifier the sensitivity to pickup noise on the cable and to the noise in the subsequent shaping amplifier is reduced. This contribution describes the data analysis, which is more demanding than in a linear system, and the results obtained in the beam tests of an accordion calorimeter are presented.

- P. Aspell from CERN presented "A Low Power, Large Dynamic Range, CMOS Amplifier and Analog Memory for Capacitive Sensors". This circuit is intended for the silicon preshower stage of the EM calorimeter in the CMS experiment. A new achievement in this work is integration of the preamplifier and an analog memory. The dynamic range is high (although not as high as in the calorimeter proper), and the challenge is to achieve all functions and many channels in a compact design.

- E. Monnier from CPPM, Marseille presented the status of the work on "Analogue Optical Links for the Front End Readout of the ATLAS Liquid Argon Calorimeter". This work, while motivated by the needs of calorimetry in the ATLAS experiment, is also of more general interest for transmission of analog signals in other detectors and experiments. If analogue optical links with linear response over a large dynamic range ($\approx 10^4$) can be realized, they will find application, whenever the problems associated with copper cables need to be avoided. In this work substantial progress has been made. The promising results presented are based on vertical cavity surface emitting laser diodes (VCSEL).

- A. Savoy-Navarro from the University of Paris (Paris VI), presented the work of her group on "Fast Digital Readout for LHC Calorimetry". In this work an approach is described, where after analog-to-digital conversion of calorimeter signals, all functions, including summation of individual channel signals for the first level trigger and the pipeline memory, are performed by digital methods.

- K. Jacobs from the University of Mainz presented an experimental study on "Radiation Hardness of Gallium Arsenide Preamplifiers for Liquid Argon Calorimetry at LHC". The results showed that, while the gallium arsenide transistors are among the most radiation resistant amplifying devices, the radiation levels at some locations in the LHC experiments may pose a challenge.

ascati Physics Series Vol. VI, (pp. 791–797)
INT. CONF. ON CALORIMETRY IN HEP – Frascati, June 8–14, 1996

TIME-DIGITIZED SIGNAL ANALYSIS FOR A SCINTILLATOR TILE HADRON CALORIMETER

J.M. Seixas, F. Marroquim, L.P. Caloba, F. Besnard
COPPE/EE/UFRJ
CERN–PPE Division

ABSTRACT

ıe signal speed of a scintillator tile hadron calorimeter is measured using time-gitized pulses. It is shown that less than 50 ns are required to collect 90% of the tal charge deposited in a detector module by 50 or 100 GeV pions hitting the nter of the module. The signal structure is also analysed on a event by event sis in terms of components that are identified with the core and tail of the shower velopment, which allows the estimation on how each part contributes to the overall lorimeter signal.

Introduction

the framework of the TILECAL collaboration 1), an iron-scintillator sampling lorimeter is being developed to perform the hadronic calorimetry for the Atlas tector on LHC environment. The measurements referred to in this paper were rformed in a prototype calorimeter composed of five sector modules, each one anning $2\pi/64$ in azimuth, with a front face of 100 x 20 cm^2 and 180 cm of radial pth. Radially oriented WLS fibers [1] are used to transport light from the tiles at th of their open edges to photomultipliers. Fibers from different tiles are grouped d readout together, so defining readout cells of 20 cm width in z direction and ur longitudinal sampling layers.

In this paper, we report on results of measurements based on samples stored a digital storage oscilloscope (DSO) [2]. The scope features eight bit amplitude

[1]Bicron BCF91A
[2]TEK TDS 520

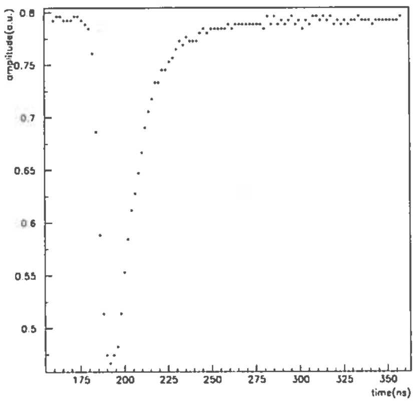

Figure 1: Typical 100 GeV pion signal.

resolution, 500 MHz bandwidth and 500 MSa/s sampling rate, or 2 ns sampling period.

The acquisition setup included a high-performance active adder [2] for combining the 40 photomultiplier signals of the central module (with respect of the beam line) of the prototype. The adder supported up to six input signals and provided two 50 Ω matched outputs. A total of eleven of such adders were used in a pyramidal acquisition topology, so that distortions resulting from possible different propagation times of the adder units could be avoided. The total signal that represents the sum of 40 PMs was sent to the DSO through a fast 50 Ω coaxial cable, in order to avoid additional tails that would distort the fast signal feature of this calorimeter. For this same reason, interconnections between the adder units were made minding the length of cables, which were kept as short as possible (typically 3 ns).

The signals for each detector layer were timed in the following way. The first layer was delayed by a 3 ns cable, the second by 2 ns and the third by 1 ns. The fourth layer was directly fed into the adders' input nodes.

The experimental data comprised pion beams of 50 and 100 GeV at 10 degrees. The beam hits the center of the module that is being linearly combined by the adders. The triggering signal was obtained by a logical combination of scintillating counters and a muon veto. The acquisition was controlled by a PC running LABVIEW.

A typical digitized pulse can be seen in Figure 1. The fluctuations on pulse shape and amplitude can be observed in Figure 2 (plot on the left), where pulses were ordered by increasing peak value and are shown inverted, as they would be positive pulses.

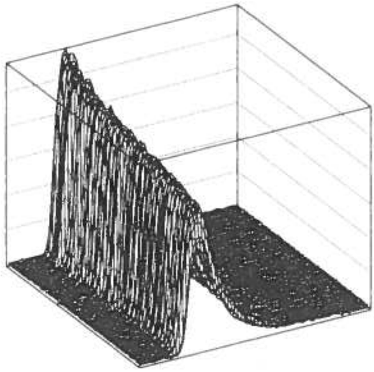

Figure 2: Fluctuations of the digitized pulses for pions of 100 GeV.

Charge Collection Curve

e charge collection curve of the calorimeter can be measured from these digitized ıals. To achieve this goal, each sampled signal was numerically integrated and time required for a given fraction of the charge to be collected was computed. ɔrder to minimize errors in the computation of the total charge collected for each nt, the pulse baseline noise was compensated for by performing an arithmetical rage on fifty points of this baseline on an event by event basis, and then subcting it from the signal. In this way, the DC level of the noise was set around o for all events.

The distribution of the time needed to collect 90% of the charge for each rgy is shown in Figure 3. It can be concluded from the figures that less than ns are required for collecting 90% of the charge deposited in the central module.

The method described so far suffers from the sampling period of the DSO. the charge curve is obtained by integrating the digitized signal, the sampling iod affects the time resolution of the crossing point at 90% of the total charge. e relatively long sampling period also makes more difficult to estimate the time tant the charge starts to be collected, as the baseline noise masks the actual ırge curve.

Due to such limitations, another way for obtaining the charge curve from itized pulses was derived. Firstly, pulses were linearly interpolated and resulting nals were fed into a low pass digital filter that is maximally flat in the passing ıd. This Butterworth filter [3)] has the cutoff frequency set to 125 MHz, in order cope with the original sampling rate of the DSO. The net effect of this filter

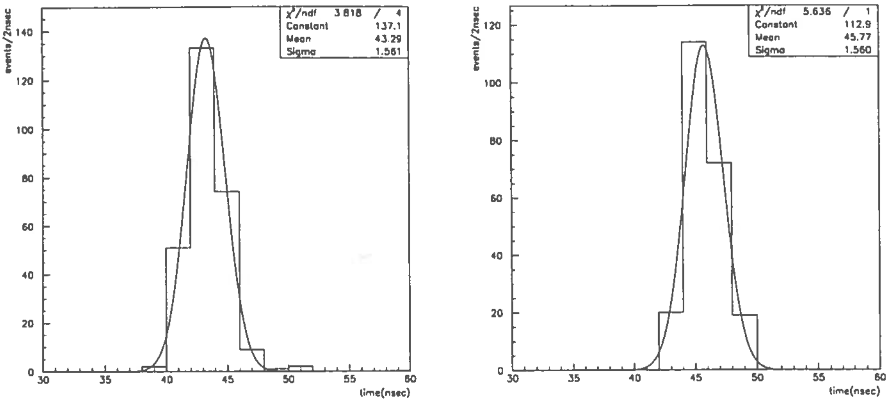

Figure 3: Time required for collecting 90% of the charge for pions of 50 (left) and 100 GeV (right).

is to preserve the original frequency contents of acquired pulses while a finer time resolution can be produced. Following this procedure, a 125 ps sampling period was obtained for interpolated pulses. Figure 4 shows how the pulse exhibited in Figure 1 gets interpolated.

After being interpolated, pulses were time aligned by means of their derivative function. A threshold value for pulse derivative was set and pulses were time aligned by the instant their derivative function crosses the threshold. As time resolution increases after interpolation, the alignment can be achieved without significant errors. In our case, the time alignment jitter was estimated to be less than 1 ns.

The time alignment of pulses allows to obtain an average pulse that can be numerically integrated. Table 1 shows the time required for charge collection for 50 and 100 GeV particles based on such averaged pulses. From this table, it can be seen that this second method fully agrees with the results obtained with the previous method.

3 Signal Structure

The understanding of the calorimeter response to hadronic showers requires the analysis of the processes occurring in all stages of the shower development. However, this becomes complicated due to the wide variety of processes involved in the hadronic shower development.

During the shower development, particles that interact electromagnetically are produced and they constitute the so called electromagnetic (e.m.) part of the

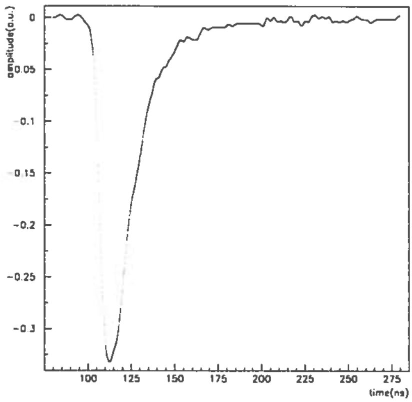

Figure 4: Interpolation of the event on Figure 1.

dronic shower. For the hadronic part of the shower, a considerable fraction of e energy is carried by neutrons. For sampling calorimeters with active readout ntaining hydrogen (as plastic scintillator), neutrons generated in the shower development deposit a large fraction of their kinetic energy in the active layers. Therefore, utrons contribute significantly to the calorimeter signals.

The time structure of the calorimeter signal can be used to estimate how n. and hadronic parts of the shower share the total charge collected. This can achieved by identifying signal components that can be related to these shower velopment parts. As the data acquisition bandwidth is high enough and cares cable lengths were taken along signal paths in order to avoid the introduction instrumental tails, the digitized signal can express reasonably well the hadronic ower components.

As the core of the shower development is expected to generate a faster sigl and the neutron component is expected to exhibit an exponential behaviour [4], e signal structure was modeled by the equation:

$$f(t) = A_1 e^{\frac{-(t-m)^2}{2\sigma^2}} + A_2 e^{\frac{-(t-t_0)}{T}} u(t - t_0) \tag{1}$$

iere $u(t)$ is the step function. In this model the e.m. part of the shower is presented by the Gaussian function and the neutron component is associated to e delayed exponential.

In our case, the time constant of the tile-fiber system can not be neglected, it has been measured as being 5.8 ns [5]. Therefore, the digitized signal is the sult of a convolution of the tile-fiber system response and the function representing e calorimeter response for pions. This means the tile-fiber response has to be

Table 1: Time required for the charge collection

Charge Fraction	Time (ns)	
	50 GeV	100 GeV
10%	9.9	10.4
20%	12.4	13.1
30%	14.6	15.5
40%	16.9	18.0
50%	19.5	20.6
60%	22.6	23.9
70%	26.9	28.2
80%	33.0	34.6
90%	43.7	46.5
95%	56.7	63.1
97%	69.7	80.7

unconvolved from the digitized signal, so that the actual neutron component can be detected. Assuming an exponential of 5.8 ns time constant for the tile-fiber response, the time constant τ of the exponential associated to the neutron component can be extracted by fitting the exponential decay of the digitized pion signal with the function

$$f(t) = \frac{A^2}{\frac{1}{\tau} - \frac{1}{5.8}}\left(e^{\frac{-t}{5.8}} - e^{\frac{-t}{\tau}}\right) \qquad (2)$$

A typical fitting is shown in Figure 5. Using this approach to signals acquired from the fourth longitudinal sampling of the central module, the neutron component was estimated to be 9.4 ns. It should be noted that the time constants of the neutron component and of the tile-fiber system are of the same order of magnitude. Thus, the time constant of the exponential part of the digitized signal can not be approximated as the square root of the sum of the individual squared time constants.

4 Conclusions

The analysis of signal speed and structure of the hadronic response of the TILECAL was performed based on time-digitized pulses from a single module. It was shown that less than 50 ns are required to collect 90% of the total charge deposited in the module by 50 and 100 GeV pions.

The digitized signal was also modeled as having Gaussian and exponential components, which were associated to the core and tail of the hadronic shower development, respectively. Using this characterization and unfolding the tile-fibre

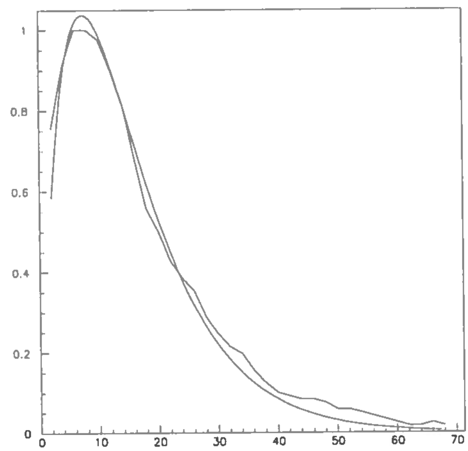

Figure 5: Fitting a typical pulse with convolution function.

stem response, a neutron component of 9.4 ns was estimated.

As acquiring signals only from the central module tends to underestimate ore significantly the tail of the hadronic shower, for the total calorimeter signal the ;nal speed and the neutron component should be slightly slower. Data acquisition r a larger fraction of the total hadronic signal are being prepared.

Acknowledgements

'e are thankful for the support that has been provided to this work by CNPq, UJB (Brazil) and CERN. We would like to thank our colleagues from the TILE-AL Collaboration for providing the experimental data, and in particular to the lermont-Ferrant group for providing data acquisition and trigger facilities. We so thank S.V. Vasconcellos for helping in parts of the analysis.

teferences

1. The RD-34 Collaboration. Construction and Performance of an Iron-Scintillator Hadron Calorimeter with Longitudinal Tile Configuration. CERN/LHCC/95-44 (1995).

2. J.M. Seixas, L.P. Caloba and M.N. Souza. NIM **A350** 300 (1994).

3. A.B. Williams. Electronic Filter Design Handbook. McGraw-Hill (1981).

4. D. Acosta et al. NIM **A(302)** pp36 (1991).

5. B. Di Girolamo and E. Mazzoni. Measurements of Scintillating Tiles. ATLAS/TILECAL-65 (1995).

scati Physics Series Vol. VI, (pp. 799–805)
INT. CONF. ON CALORIMETRY IN HEP – Frascati, June 8–14, 1996

A LOW NOISE TRANSCEIVER FOR THE NA48 LIQUID KRYPTON CALORIMETER

G. Martin–Chassard, C. de La Taille, N. Seguin–Moreau
Laboratoire de l'Accélérateur Linéaire
IN2P3-CNRS et Université Paris-Sud
91405 Orsay Cedex - France

ABSTRACT

ıe NA48 transceivers, located between the preamplifiers and the readout boards, rform a pole-zero cancellation to accelerate the preamplifier output signal from 150 to 10 ns and enable the proper gain selection in the readout. They also provide a fferential output to drive analogue signals with 14 bits dynamic range on shielded 'isted pairs. A BiCMOS ASIC and a discrete version have been developed for this ırpose and their experimental results will be presented.

Front End electronics

1 Detector and Signal

he detector is an almost homogeneous liquid krypton calorimeter, aimed at high ecision energy measurements of photons below 100 GeV. The motion of the ion-ation electrons induces a triangular current, whose initial value is typically $I_0 =$ 5 μA/GeV and which decays in the drift time $t_{dr} = 3\mu$s [1].

The electronic modelization of the detector is traditionnally done by a ırrent source in parallel with a capacitance to ground $C_d \approx 200$ pF (cf. Fig.1), though here the length of the detector makes it more similar to a transmission line 70 Ω impedance and 6 ns delay.

2 Preamplifier

ach detector tower is read out by a preamplifier, located directly at the back the calorimeter inside the LKr in order to minimize the electronic noise. The eamplifier follows the classical transimpedance architecture, as shown in Fig.1,

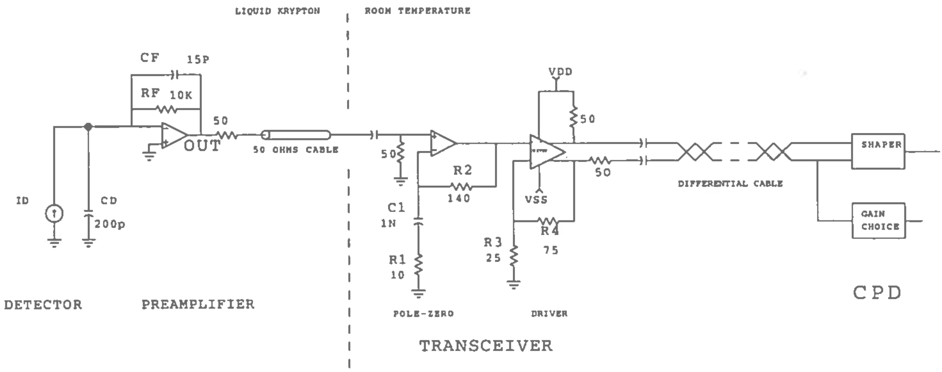

Figure 1: Schematic diagram of the front end electronics

and is optimized for operation at low temperature. The transfer function of this preamplifier is given by :

$$H_{pa}(s) = \frac{-R_f}{R_f(C_d + C_f)s^2/\omega_c + R_f C_f s + 1} \tag{1}$$

in which ω_c (=1GHz) is the unity gain frequency of the preamplifier and $s = j\omega$ the complex frequency. The stability of this second order system requires the two poles to be sufficiently separated, the quality factor being :

$$Q = \frac{1}{C_f}\sqrt{\frac{C_d + C_f}{\omega_c R_f}} \tag{2}$$

$Q < 0.5$ ensures stability and is obtained by taking $R_f > 2k\Omega$.

The transfer function can be simplified as following :

$$H_{pa}(s) = \frac{V_{out}(s)}{I_{in}(s)} = \frac{-R_f}{(1 + s\tau_f)} \tag{3}$$

where, with the notations of Fig.1, $\tau_f = R_f C_f = 150$ ns, ($R_f = 10$ kΩ, $C_f = 15$ pF).

The signal at the preamplifier output is obtained by convoluting the detector triangular current with the preamp transfer function given by Eq. 3. It looks like a rising exponential with a long time constant τ_f decaying in the typical drift time (3 μs).

This charge sensitive configuration[1] exhibits a low real input impedance

[1]The transimpedance configuration is called "charge sensitive" when $\tau_f > t_p$ where t_p is the shaping time and "current sensitive" otherwise. This simply refers to the fact that the transimpedance is constant (R_f) or decreasing with frequency ($1/j\omega C_f$) at the central frequency of the shaper.

ı, often referred to as an "electronically cooled" resistor [2],

$$R_{in} = \frac{1}{g_m}\frac{C_0}{C_f} \tag{4}$$

which g_m is the transconductance of the input transistor and C_0 is the dominant le capacitance. It can be set to terminate the detector "transmission line" in its aracteristic impedance and thereby minimize reflections which can deteriorate the ergy resolution and crosstalk. This requires a minimal value for C_f around 15 [2]. At the shaper central frequency, the dominant noise is here the series term e_n 'en by the preamplifier input FET ($e_n \approx 0.4\text{nV}/\sqrt{\text{Hz}}$ at 120K). The noise at the eamp output is obtained by multiplying e_n by the "noise gain" ($\frac{C_d+C_{pa}+C_f}{C_f}$) giving ıV/$\sqrt{\text{Hz}}$, further decreased by a 6 dB due to the cable termination at both ends. ıus, the second stage noise becomes an important consideration.

Transceiver

.e transceivers are located directly on the feedthroughs and share the Faraday cage med by the cryostat. They terminate the coaxial cables from the preamplifiers o 50Ω. A pole-zero compensation stage (cf. Fig.1) turns the preamp time constant of 150 ns into a faster value τ_1 of 10 ns, in order to enable a fast gain selection in e readout (cf. 1.4). The transfer function of this circuit is :

$$H_{pz}(s) = \frac{1 + s(R_1 + R_2)C_1}{1 + sR_1C_1} \tag{5}$$

letting $(R_1 + R_2)C_1 = R_fC_f$, the signal has a faster pole $\tau_1 = R_1C_1$. The price id for accelerating the signal is a loss of amplitude of typically τ_f/τ_1, which is npensated for by a similar amplification in the pole-zero amplifier.

The long distance between the cryostat and the readout (10 meters) and e need of precision which requires a very low coherent noise, advocates for a ferential transmission. The second stage of the transceiver is a differential line ver to send the signal on a shielded twisted pair in order to minimize crosstalk and ctromagnetic interferences. It includes an extra amplification to match the input .tage requirement from the readout, and compensate for the 6 dB attenuation due the cable termination at both ends.

Calorimeter Pipelined Digitizer (CPD)

e signal readout consists of a differential receiver for analog signals with 14 bits namic range, a fast shaper, a gain selection system on the input, a gain switching

[2] With a large NJ450 Si JFET transistors from Interfet, $g_m \approx 25$ mA/V at $I_D = 4$ mA and T 20K. $C_0 \approx 25$ pF, which leads to $C_f = 15$ pF to achieve 70 Ω input impedance.

after the shaper, a 10 bit Flash ADC and a digital pipeline, known as CPD [3]. The CPD boards are located in the electronics barracks, a few meters away from the detector.

2 Transceiver design

2.1 Requirements

From sections 1.1, 1.2, 1.3 and 1.4 the requirements for the transceiver can be summarized as follows :

•**Input impedance : 50 Ω**, in order to terminate properly the coaxial cables coming from the preamplifiers inside the cryostat.

•**Input noise : $<$ 2 nV/$\sqrt{\text{Hz}}$**, in order not to deteriorate the noise performance of the preamplifers.

•**Output rise time: $<$ 25 ns (10-90%)** corresponding to a rise time constant less than 11 ns.

•**Output amplitude : $\pm$ 1 V** after the twisted pair for a 250 μA (50 GeV) signal at the preamplifier input.

•**Linearity : $<$ 0.1 %** in order to measure accurately a signal on top of an accidental.

•**Area : 110 $\times$ 220 mm^2 for 32 channels** in order to fit right on the feedthroughs.

•**Power dissipation : as low as possible** because of the large number of channels (15,000).

2.2 ASIC version

The schematic of the ASIC transceiver is shown in Fig. 2. It consists of three almost identical operationnal amplifiers. The first one performs the pole-zero cancellation, as described in section 1.3. The other two provide the non inverting (resp. inverting) output from their voltage (resp. current) output.

The operationnal amplifier is designed in 1.2 μm AMS BiCMOS technology. In order to achieve a low noise performance, the input differential pair uses large transistors operating at rather high current. Measurements have given an open loop gain of 220, a bandwidth of 800 MHz and a very low noise (1.3 nV/$\sqrt{\text{Hz}}$). The feedback network performs the pole-zero compensation.

The differential driver is also built around this opamp : its output transistor provides a voltage and a current output of opposite polarity on its emitter and collector. Using a Darlington configuration yields a negligible base current and therefore the same current in the collector as in the emitter. This leads to an

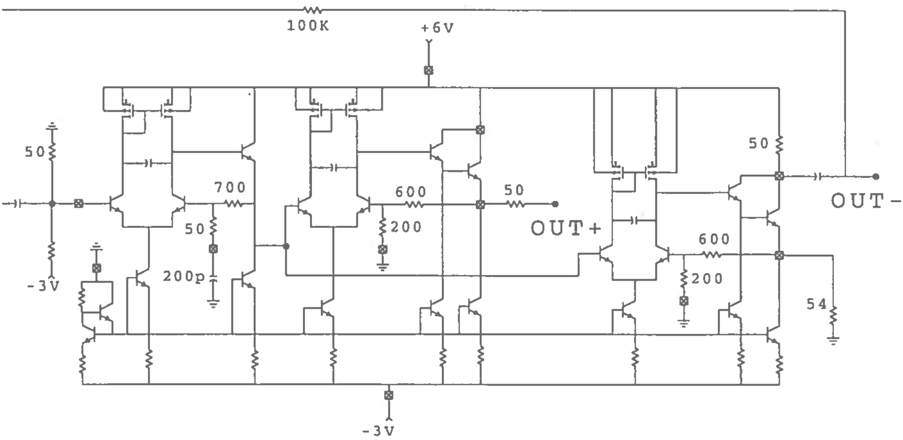

Figure 2: *Schematic diagram of the ASIC transceiver*

:ellent symmetry between the non inverting (on the emitter) and inverting (on ; collector) outputs, provided the impedances on both nodes be equal. This nciple performs a very good differential driver without PNP transistors which : not available in AMS BiCMOS 1.2 μm technology. However, there is no output ıse rejection : any pick-up on the positive output is mirrored on the negative ɜ. To overcome this problem, the output stage is duplicated so that the two ţputs (inverting and non inverting) come from two different amplifiers and noise reflections on one side do not interfere with the other one.

Integrated resistors do not have precise values, so the accuracy of the pole-ʼo compensation is obtained by putting the capacitor outside the integrated circuit well as the termination resistors. Conversely, the gain, given by a resistors ratio ide the circuit has a good accuracy. 8 channels have been housed in a 68 pins ,CC package.

; <u>Discrete version</u>

.e first stage of the discrete version is built around a low noise operationnal am-fier (CLC425) distributed by Comlinear Corporation which exhibits very good rformances such as an input noise of 1 nV/$\sqrt{}$Hz and a gain bandwidth product 1.7 GHz. This large bandwidth product allows to perform in the same stage the le-zero cancellation and the additionnal gain without sacrificing speed and linear-. The differential driver is classically obtained with two buffers built around a ,C412 dual opamp. The schematic of the discrete transceiver is shown in Fig. 3.

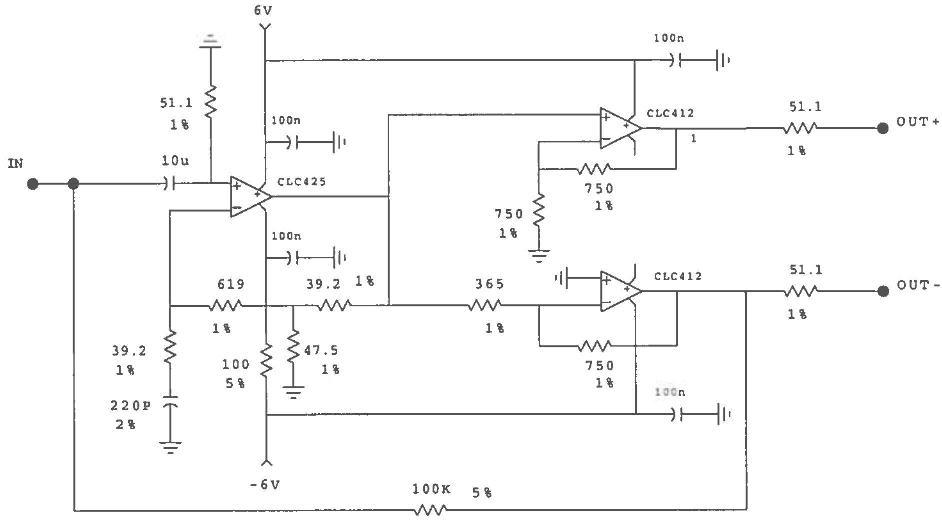

Figure 3: Schematic diagram of the discrete transceiver

2.4 Measurement results

Both versions have been tested on the H4 test beam at CERN in August 1995 [4]. They presented rather similar performances :

•**Input noise density :** = **1.9 nV/$\sqrt{\text{Hz}}$** for the transceiver alone. On the H4 test beam, the total noise was 7 MeV for the complete electronic chain with a 75 ns shaping time. It can be split among the various elements as follows : 4.5 MeV for the preamplifier, 2.4 MeV for the transceiver and 4.5 MeV for the CPD.

•**Linearity : 0.1 %** for both versions, concerning integral but also differential linearity.

•**Output rise time :** at the output of the 10 meter long cable, the rise time (10 - 90 %) is better for the discrete version **(24.4 ns)** than for the ASIC one (**29.5 ns**). The rise time of the ASIC is larger than expected, which could be traced to a parasitic resistor inside the layout (this layout problem could be fixed in a next iteration).

•**Output common mode and power supply rejection ratios :** both versions yield more than 50 dB up to 20 MHz.

•**Power dissipation :** the dissipation of the discrete circuit (**310 mW per channel**) is three times higher than the ASIC (**90 mW per channel**).

•**Cost:** a discrete channel costs around 12 CHF whereas an integrated one costs around 10 CHF.

The main problem with the ASIC transceiver has been a long delay (6 onths) in the multi-project sharing run. The iteration needed to fix the risetime d validate a series production was almost incompatible with the deadline of comete installation in august 1996. Therefore, the discrete version has been chosen by e NA48 experiment to equip the 15,000 calorimeter towers.

Conclusion

low noise integrated circuit has been designed which fulfils the NA48 requirements, it arrived too late to be installed in the experiment. A discrete version with similar rformances is now being installed and will be ready for data taking next august.

eferences

P.Calafiura and A.Ceccuci, The performance of Liquid Krypton calorimeter and the neutral reconstruction, NA48-note 1995-4.

V. Radeka, S. Rescia "Speed and noise limits in liquid ionization calorimetry" NIM A325 (1988) 228-242

F. Bal et al., Performances of the CPD prototype module, NA48-note 1996-1.

J.C. Chollet et al., Analysis of 1995 H4 data, NA48-note 1995-30.

ascati Physics Series Vol. VI, (pp. 807–816)
INT. CONF. ON CALORIMETRY IN HEP – Frascati, June 8–14, 1996

THE ELECTRONIC R&D FOR THE ELECTROMAGNETIC CALORIMETER OF CMS

J.P. Mendiburu
LAPP

ABSTRACT

The choice of CMS to invest in an electromagnetic calorimeter precise enough to tect an electromagnetic decay of the Higgs, in the region of mass between one and two ’s has rapidly become a challenge for each of the components of this calorimeter. It ıplies in particular to master the read-out at the level of precision reachable by the ›WO4 crystals. Several laboratories of the collaboration, in close connection with the dustry, are involved in R&D programs concerning the photodetectors and the front end ectronic associated to them. We describe the goals (signal/noise ratio, dynamic range, ›wer consumption, radiation hardness etc.) and the status of this R&D, as well as the ıplications on the final resolution.

– Introduction and definitions

The target resolution for the crystal calorimeter of CMS (a stochastic term ≤ 2% in the ırrel and ≤ 5% in the end caps, a calibration term ≤ 0.5% everywhere, a noise term N ≤ 50 MeV everywhere and an angle resolution on electrons ≤ 50 mrad/√E in the barrel) are al challenges for experimentalists, specially if we add that these resolutions have to be ached without deteriorating the measurements of other detectors outside ECAL, ›ecifically the hadron calorimeter and the muon spectrometer.

In order to optimize the compactness, the homogeneity and the hermeticity of the CAL, it has be decided to read the 110,000 PbWO4 crystals, by avalanche photodiodes APD’s), mounted on the rear face of the crystals, and to install the read-out electronic etween ECAL and HCAL, implying the use of low power dissipating and radiation hard chnologies. A major part of the precision of the ECAL relies in this read out electronic ıd these strategic choices have induced a very aggressive R&D to reach the ›ecifications needed at each step.

Several laboratories participate to the characterization and the improvements of the ead-out of ECAL: CEA (Saclay), CERN (Geneve), ETH (Zurich), INFN (Roma), IPN Lyon, France), LAPP (Annecy), LPNHE (Polytechnique), Oakridge (USA), Princeton JSA), PSI (Willigen), RAL (GB). They work in close connection with the producing ompanies: Advanced Photonix Inc (USA), Hamamatsu Photonix (JAPAN), EG&G)ptoelectronics (Canada), Harris (USA) and the DMILL complex.

In the following formulation, N_e ($\sqrt{N_e}$) is the number (variance) of photo-electrons that each APD receives from its crystal. This APD has a gain G, (σ_G) and produces a total number of electrons for the front end of $N_e \cdot G$, ($\sqrt{N_e(\sigma_g^2 + G^2)}$).

The resolution of the calorimeter is the quadratic sum of three terms $\frac{\sigma(E)}{E} = C \oplus \frac{S}{\sqrt{E}} \oplus \frac{N}{E}$, where

1) C is the calibration term that will dominate the high energy resolution.

2) The variance stochastic term $S = \sqrt{S_{\text{int}}^2 + \frac{F^2}{N_{Pe}^2}}$ is the statistical addition of the fluctuation in photo-electrons production before the APD and of the statistical gain fluctuation of the APD. This last one is expressed by the excess noise factor F, defined as $F = 1 + \frac{\sigma_G^2}{G^2}$

3) The noise term $N = N_s + N_P$ is the statistical sum of

- The series noise term $N_s = \frac{1}{G * N_E * \sqrt{\tau}} \{\alpha * \sum C * \sqrt{\sum R_s}\}$ which accounts for the

noise in the $\sum$C capacitance's and in the $\sum$Rs resistance's before and in the preamplifier. This series noise increases when the shaping time τ of the preamplifier is reduced.

- The parallel noise term $N_P = \frac{\sqrt{\tau}}{G * N_E} \{\beta * \sqrt{I_s + F * I_B} \oplus \varepsilon \oplus Pu\}$ which is composed

of the leakage currents in the APD and in the front transistor of the preamplifier; Pu is the pile-up contribution added as an equivalent leakage current.

The $\alpha, \beta, \varepsilon$ constants depend on the preamplifier and I_S and I_B are the surface and bulk leakage currents of the APD.

Note that this parallel noise increases with the shaping time τ of the preamplifier and that the shaping time chosen for the final set up will be a trade off between the series noise and the parallel noise components.

2 – The Avalanche Photo-Diodes (APD)

2.1 Description

The Avalanche Photodiodes are semiconductor photodetectors developed since a decade that have a built-in gain device. Their working principle is based on several layers of doping in which the photons are first converted in primary pairs; then the electrons are amplified in a junction on which is applied an electric field large enough to reach the multiplication range. These electrons are then drifted in a low doped region to a metalic cathode where they are collected.

The interesting features of APD's are their small size, their insensitivity to the magnetic field, their internal gain for low power consumption and their relatively low voltage supplies (from a few tens to a maximum of 300 V).

2 The R&D on APD's

The R&D contracted with the industry concerns the basic improvement of the aracteristics and their tailoring to our ECAL requirements:

The increase of the active surface, of the quantum efficiency in the range of the ectrum of the crystals (350-600 nm), of the stability to bias polarisation or temperature riations.

The reduction of their internal capacitance, resistance, noise dispersion (excess noise ctor), leakage current, of their sensitivity to ionizing particles and of their price.

Several important drastic improvements have been obtained on most of these rameters and the APD's have now reached a level of sophistication compatible with our eds.

3 Present Main Characteristics

	EG&G	HAMAMATSU	UNITS	COMMENT.
rea	5*5	Cercle ϕ=5	mm	
nternal capacity	30	100	pF	@M=50
nternal resistance	6	5	Ω	@M=50
uantum efficiency.	75	80	%	@500 nm
xcess noise factor	2.8	1.8		@M=50
/M*dM/dV	2	4	%	@M=50
/M*dM/dT	3.5	2.5	%	@M=50
eakage. current	10	30	nA	Before irradiation
uclear counter effect	315	220	MeV	@M=50

The final characteristics of the ECAL APD's will be the best compromise between eir qualities, some of them being antagonistic:

3.1. *The Ratio signal/noise*

The active area: the maximum active surface of ($5{\cdot}5$ mm^2) reduces our geometrical acceptance to 6%. The difficulties to get and to process large pure silicon crystal does not allow to foresee a large increase of this size at reasonable price. Different ideas are explored to increase the equivalent active surface by mounting several APD's in the same package or by focussing the light at the back face of crystals to the size of APD's.

The quantum efficiency: is now excellent, better than 80% in the region of the spectrum emission of PbWO4. (Figure 1).

- The optical coupling between the crystal and the APD (the crystal has an optical index of 2.3): this is obtained either by changing the index of the front part of the photodetector or by introducing an optical coupling between APD and the crystal. Several tests are being made in this direction.
- Gain: most of the planar structure APD's can run stable and linear devices with gain between 50 and 500 (Figure 2). The limit is due to the increasing sensitivity of the gain with the bias voltage, to the leakage current induction, and to the non uniformity of breakdown voltage over the device surface.

  We actually foresee to work at G=50.

  New types of very promising APD's developed in Russia, on Metal Resistive Semiconductor layers have reached gains as high as 10^4, for bias voltages as low as 35 V. These MRS APD's have built-in irregularities on their surface that enhance locally the electric field, up to the multiplication region. Prototypes are in preparation and will be tested in Autumn 1996.

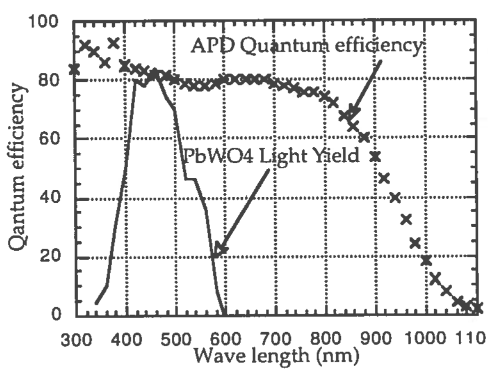

Figure 1 – Quantum efficiency of APC.

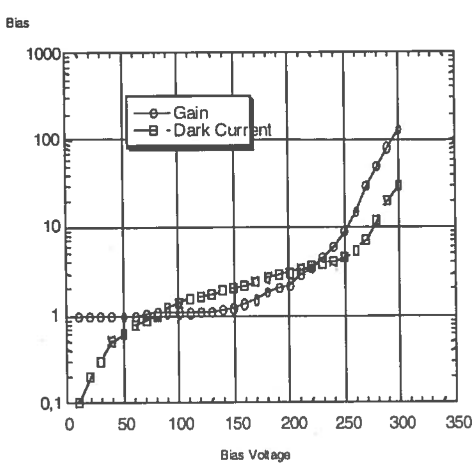

Figure 2 – Gain and Drak Current (nA).

The internal capacitance: In the resolution, the series noise term is proportional to the sum of input capacitances. The reduction the APD capacitance requires to increase the apparent width of the depleted junction. This is antagonistic with the minimization of its sensitivity to ionizing particles; the actual value of 100 pF for $5\cdot 5$ mm^2 seems to be the best actual trade off.

The leakage currents: the leakage current, due to thermal motion of charges has two components: the surface current, which does not depend on the gain and the bulk current, created by charges traversing the amplification region and which increase with the gain. These currents have been reduced by the installation of guard rings to values of the order of 10 nA (Figure 2) which represents a contribution to the resolution of 6 MeV for $N_e = 2\,\gamma\,/\,\mathrm{MeV}$.

The statistical fluctuations of the gain: the industry delivers now APD's with an excess noise factor F=2, well stabilized around G=50; this represents a contribution to the resolution of $3\%/\sqrt{E}$ for $N_e = 2\,\gamma\,/\,\mathrm{MeV}$.

3.2. *The Nuclear counter effect*

An ionizing particle passing through a silicon crystal creates 8300 electrons per 0µm of traversed depth. For electrons, this effect is canceled by the large absorption ngth of the crystals. For overlapping hadrons, the reduction of this effect has requested use only APD's where the amplification structure precedes the drift space and to reduce eir effective thickness to arround 200 µm. This effect increases with the active surface the APD's.

3.3. *The working stability*

The actual APD prototypes are stabilized in bias polarisation and temperature by tside specific electronic. Industry is able to incorporate these corrections and to deliver lf-stabilized APD's for further versions; these implants will have obviously to be diation tolerant.

3.4. *The radiation hardness*

The APD's will receive 10^{12} neutrons/cm^2 per full luminosity year. As all miconductors, these devices are sensitive to radiations; they can affect the ratio gnal/noise, the quantum efficiency spectrum, the gain, the excess noise factor and the akage currents. Several centers have measured the effects of γ and neutron radiations on PD's. They have been proved to be manageable by a precise calibration, although the akage current will increase by a factor of 1000 after 10 years (10^{13} n/cm^2) of running.

If necessary, an additional improvement of the ratio signal/noise is actually being vestigated by increasing the number of photoelectrons or by cooling the overall system ne ratio signal/noise is improved by a factor of 5 (Figure 3) when temperature deacreses om 20 to 0° Celcius).

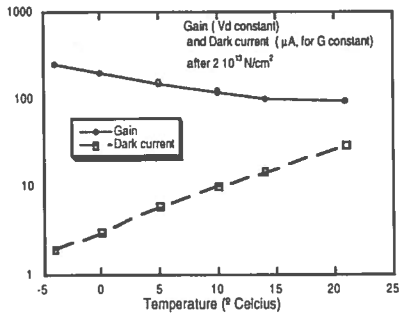

Figure 3 – APD Gain and Dark Current % Temperature (0° Celcius).

3 The Front end electronic

The main R&D issues of the front-end electronic are the ratio signal/noise, the shaping of the pulse, the dynamic range and the compression process, the stability, the radiation hardness of the circuits and the power dissipation.

In most of the projects, the front end electronic is split into a first stage directly connected to the APD, which is a low noise, large dynamic range, low dissipating transimpedance shaping-preamplifier and a further set up that compresses the signal and reduces the dynamic range (17 bits) expected for input signals to the 12 bits of the most performant fast ADC's.

3.1 <u>The shaping preamplifier</u>

The bipolar technology is known to be well adapted to low noise input stages. Today, it can be radiation hardened by ASIC- Harris technology.

A) IPN Lyon has developed a bipolar version, specifically tuned to low noise (3500 electrons for Ci = 100 pF and τ= 20 ns), large dynamic (up to 2 V), and low dissipation (20 mW). This version has been irradiated up to 0.6 10^{12} neutrons without measurable damage.

B) IPN Lyon is also developing a BiCMOS version, that combines the desirable feature of both devices (NPN and CMOS). The simulation predicts a noise of 4700 electrons for 100 pF of input capacitance and 40 ns of picking time. This preamplifier drives two amplifiers of gain 1 and 16, the second one having the possibility to be clamped.

C) LAPP is developing a low dissipation, large dynamic preamplifier based on bipolar technology, with a differential input where the complementary part is used for the stability.

3.2 <u>The Compressor</u>

The LHC physics expectations are such that energy range that the calorimeter has to asure is 17 bits; the maximum available dynamic of fast (40 Mhz) ADC's being of 12 the large signals have to be analog-compressed after the preamplification, before the itization. Two methods are explored, each using 2 to 3 stages of amplification; (this ltiplication of stage is needed to avoid the changes in rise time of the signal with large nges in amplifiers gains). Two type of projects are developped: the Gain Switched hnology and the Non Linear Amplifiers.

The Gain-Switched Technology

In this technology, the signal from the preamplifier is distributed in parallel to several plifiers of different gains. A dedicated fast logic, choose each 25 ns, to keep only the gest amplified signal that has not saturated its amplifier. A flag added to the memory icates the relevant gain for this measurement. (Figure 4).

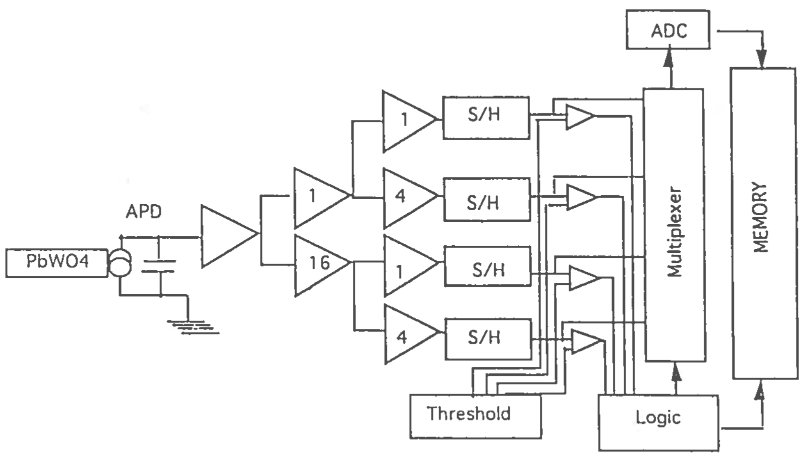

Figure 4 – Gain Switched Project.

This project, developed by Princeton, is foreseen to be connected to the preamplifier ntioned at point C) of par. 3.1. Each output of this premplifier (gain 1 and 16) is split, e being amplified by 1 and the other one by 4; at the end, the overall set up allows to oose between gains 1, 4, 16 and 64. The pulse is kept in a sample and hold device, ring the time needed for the threshold logic to indicate the relevant gain to use. This ormation (2 bits) is merged to the 12 bits of the ADC to give a 14 bits number.

The advantage of this device is that each measurement is made by a linear chain easy calibrate. The drawback is the complexity of the multi-amplifiers, the risk of noise roduced by the 40 Mhz switching circuits and the power consumption of the setup.

In order to test the difficulties of the technology, two versions of this device are being ilized by Princeton, one in 0.7μm CHFET (GaAS), and one in 0.8μm BiCMOS. The st prototypes will arrive before Summer 1996 and will be tested at CERN in the lab and en in a test beam before the end of 1996.

3.4 Active Feedback technology

This technology consists in mapping the compressor response to the detector resolution. For this purpose, an active feedback loop is added to the amplifier in parallel to the usual feedback resistance, in order to get a non linear transfer characteristic of the amplifier. For each amplitude, the gain is determined by the current flowing in this active feedback. The advantage is the simplicity and the flexibility of the system, whereas the drawbacks are the distortion of the shape of the pulse and the complexity of a calibration precise at the level needed by our calorimeter. This technology has also to prove the stability of the transfer function against irradiation.

3.4.1 *Pseudo logarithmic amplifier*

The choise of this project is to approximate a logarithmic response of the system by a succession of strait segments of decreasing slope. (A perfect logarithmic response would provide a constant resolution.)

This project, developed at LAPP, is based on 1.2 μm BiCMOS technology. The changes in slope are obtained by a series of CMOS transistors mounted in parallel on the feedback resistance of the amplifiers. The setup is made of 3 (or 4) stages, each mounted with its own compressing feedback.

The signals of low amplitude are amplified with the gain determined by the feedback resistance; when the amplitude increases, CMOS transistors, according to their polarisation, start to drive current and force the gain to decrease. Each new conducting CMOS installs a new slope in the response of the amplifier. Due to multiple stages, the peaking time remains constant (30ns within 1 ns). The project has the flexibility to install 2 to 6 slopes according to the precision needed and the difficulties of calibration.

The project is at the level of the simulation and a first prototype is planned by the end of 1996.

3.4.2. *SQRT amplifier*

CERN has developed for the preshower of ECAL an original preamplifier-shaping-compressor where the active feedback is made by MOS transistors in strong inversion that give a square root response to the device for an output swing of 1.2 V.This compression, based on a physical law, is extremely stable (polarisation and temperature) and the technique (MIETEC, 0.7 μm) is radiation tolerant. It can be adapted to the ECAL requests.

The general strategy of CMS for the read out electronics is to carry on the analogic R&D during 1996 and make a final choice during 1997.

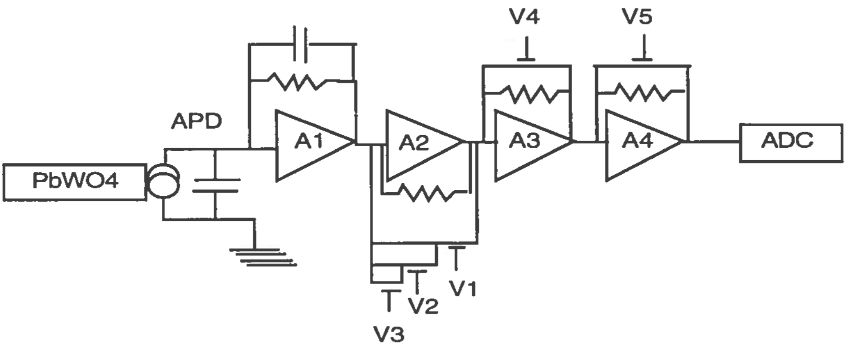

Figure 5 - Principle of the pseudo–log Ampli–shaper–compressor.

The Fermi project

Fermi is an ambitious multi-ship R&D project, developed at CERN and LPNHE aris 6) both for ATLAS and CMS since several years. It covers the decompression, the gitization, the normalisation and the pileup corrections, the first level programmable er and all the services (pipeline memory, controllers, error detection coding, zero ppression, data formatting, optical links etc...). The objective is to provide an imation of the energy of the particles, available for the first level trigger. The board first compress the signal by consulting lookup tables, calibrates each cell, then build a ister of several cells and provide the energy of the electromagnetic particle.

Several prototypes have already been tested in laboratories and used for triggering test beams.

Conclusions

LHC is foreseen to deliver beams for physics in 2005, the amplitude of the project d the industrial time scale of the construction is such that time is rather short for R&D. CMS, we will decide the final options for the read out electronic by the end of 1997. e already know that the high energy performance of ECAL will be dominated by the libration whereas the lowest energy range will be dominated by the stochastic and noise ms. Several companies producing APD's have already reached the CMS specifications d the read out electronic is still in the R&D phase. In particular, the choice of mpressor will take into account the difficulties of complex circuitry, the difficulties of ecise calibration, the price etc...

At the end, the precision of our ECAL will be, as usual, a complex tuning of its build parameters and of a long mastering of its daily characteristics.

References

CMS Technical Proposal CERN/LHCC 94-38.
Lisbonne First Workshop on electronic for LHC experiments, Lisbonne 1995.
JP Peigneux et al presented at IEE95-NSS36, Oct 1996, Preprint LAPP 95.09.
Low noise electronic Design C. D. Motchenbacher and F.C. Fitchen.
W.E.Cleland and E.G. Stern NIM A 338(1994)-467-497.
F. Anghinolfi et al CERN- ECP/95-10.

ascati Physics Series Vol. VI, (pp. 817–826)
INT. CONF. ON CALORIMETRY IN HEP – Frascati, June 8–14, 1996

THE ELECTROMAGNETIC CALORIMETER OF THE HERA-B EXPERIMENT

Benedettini, A. Bertin, M. Bruschi, A. Collamati, A. Cotta–Ramusino, D'Antone, S. De Castro, R. Donà, A. Ferretti, D. Galli, B. Giacobbe, U. Marconi, M. Piccinini, N. Semprini–Cesari, R. Spighi, S. Vecchi, A. Vezzani, F. Vigotti, M. Villa, A. Vitale and A. Zoccoli
Dipartimento di Fisica, Università di Bologna and INFN – Sezione di Bologna, Italy

ABSTRACT

After a general view of the experimental goals, of the apparatus and of e trigger requirements of the HERA-B experiment we describe the read-out and etrigger electronics designed for the electromagnetic calorimeter. We also show e results of some simulations and the subsequent criteria followed to design the etrigger system. The problematics faced to arrive to the final design are very nilar to the ones with which future high luminosity colliders have to cope.

Introduction

IERA-B is a fixed target experiment [1, 2] that will run on the HERA Proton Ring the Desy Laboratory. The main goal of the experiment is to detect CP violation the B system exploiting the so called "gold plated channel" $B_d^0 \to J/\psi\, K_S$ with e subsequent decays: $J/\psi \to l^+l^-$ and $K_S \to \pi^+\pi^-$. Furthermore the experiment ans to search CP violation also in other channels and to perform studies on B-iysics like the determination of the characteristics of the B_S system (mass, lifetime d mixing) or the detection of rare B decays.

In order to reach these goals the experiment must be capable to trigger and detect the leptons coming mainly from the J/ψ or from B semileptonic decays.

The Apparatus and the Trigger

ie HERA-B apparatus can be divided into two parts. The first one is composed the vertex detection system, placed near the wires of the nuclear target, and

Table 1: The main features of the HERA-B trigger system. In the second column is reported the number of channels involved in the trigger.

Trigger Level	Number of channels	Time scale	Input Rate → Output Rate	Gain
I	$100k$	$\sim 10\,\mu s$	$10\,MHz \rightarrow 50\,kHz$	200
II	$400k$	$\sim 10\,ms$	$50\,kHz \rightarrow 2\,kHz$	25
III	$600k$	$\sim 30\,ms$	$2\,kHz \rightarrow 100\,Hz$	20

by the tracking devices with chambers placed before, inside and after the magnet that provides a field integral of about $2.2\,Tm$. The second one is the particle identification system that is composed by a Ring Image Cherenkov (RICH), by a Transition Radiation Detector (TRD), by the Electromagnetic Calorimeter (ECAL) and by the Muon Chambers (MUON).

The HERA-B nuclear target is composed by 8 thin Aluminum wires peeling the halo of the 820 GeV proton beam. The proton interaction rate in the target is very high with a mean multiplicity of about 4 events at each Bunch Crossing (BX) of the HERA machine (1 BX every 96 ns). This means that the trigger of the experiment must be very performing, selective and fast in order to lead the acquisition rate from 10 MHz to 100 Hz without loosing in efficiency. The trigger is structured on three pipelined stages and its principal features [3] are summarized in tab.1.

- The First Level Trigger (FLT) receives lepton candidates from the electromagnetic calorimeter and from the muon detector, and, by means of a part of the tracking system performs a first pattern recognition for tracks downstream the magnet and applies cuts on the reconstructed J/ψ invariant mass or on the transverse momentum P_t in about $10\mu s$, reducing the rate to 50 kHz.

- The Second Level Trigger (SLT) exploits information from the tracking and the vertex detectors improving the back-tracking through the magnet and finding the vertex.

- The Third Level Trigger applies a full track and vertex fit and performs the particle identification and a first B reconstruction in about $30\,ms$ reducing the rate to $100Hz$.

The First Level Trigger that must provide a huge reduction of the rate (a factor ~ 200) is based on a Kalman Filtering technique [4]. First of all the electron and muon candidates are identified in the ECAL and MUON systems. Then a backward tracking toward the target is performed, requiring that each chamber

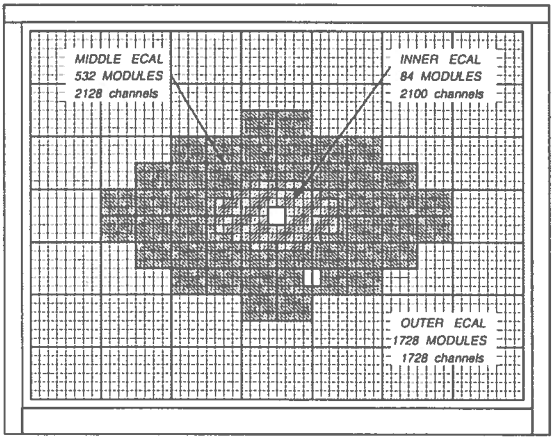

ʒure 1: The electromagnetic calorimeter geometry. The central hole is for the ɔton beam pipe, the lateral one for the electron beam pipe. The modules of the ıer section are composed by 25 towers (5×5), the ones of the Middle section by 4 vers (2×2), while the modules of the Outer section correspond to only one tower. the picture is also reported the pretrigger board partition.

ɔssed by the track is fired. Finally the track parameters are calculated imposing ertex constraint and, after the application of quality cuts, the invariant mass of .ck pairs is evaluated. As a final step the trigger decision is taken.

The electromagnetic calorimeter

.e ECAL is a sampling calorimeter of the shashlik type [5]. It must provide fast ɜtrigger signals on lepton candidates, a good hadron-electron separation as well as ɜrgy and position measurements mainly at the trigger level. The ECAL is placed meters from the interaction point and is composed by about 6000 towers. The ınularity of the detector is increasing by decreasing the distance from the beam is being the occupancies function of this quantity. The calorimeter can be divided o three sections: Inner, Middle and Outer (see fig.1). The containment depth also varying with the distance from the beam axis being 23 radiation length for ɜ Inner section and 20 for the Middle and Outer. In the Inner part the converter ɜ tungsten tiles, in order to keep low the Moliere radius, while in the Middle and ıter part, where the track density decreases, the converter is lead.

In order to avoid pile-up problems and to satisfy the trigger requirements ɜ ECAL read-out and pretrigger system have been designed in order to match the lowing characteristics:

- to provide an early digitization ($< 500\,ns$) of the signals coming from photomultipliers;
- to work with pedestal subtracted and energy calibrated data;
- to have a suitable digital pipeline for the data from the front-end (256 events for the read-out and 32 events for the pretrigger);
- to foresee debugging features both at the level of the read-out and of the pretrigger electronics;
- to calculate quickly at the pretrigger level the physical relevant quantities of an em shower.

All these features and requirements represent also an important R&D step in view of LHC.

4 The electromagnetic calorimeter read-out system

The ECAL read-out board has been designed following the prescriptions described above. It is a 9U VME standard board handling 32 channels [6]. The board can be divided into two major functional blocks:

- The Front End Driver (FED) divided into 8 ADC Sections. Each section handles 4 analog input signals fed by photomultipliers tubes and performs a fast digitization by means of a 10 MHz 12 bit flash ADC.
- The Digital Logic that processes the digitized signals handling the FLT accepted data and providing suitable interfaces to VME bus and to the SHARC based HERA-*B* experiment DAQ system [7].

The data generated by each ADC section follow two ways. On one side they are stored into a Dual Port Ram (DPRAM) organized as a circular buffer of 256 events, then, if accepted by the First level Trigger, they are sent to the DAQ system through an Event Buffer. On the other side the data are passed to a Look-Up Table (LUT) that performs the pedestal subtraction, the conversion of the ADC channels into energy and produces the 8 bit digital compressed data required by the pretrigger processor (seven bits for the energy plus one bit flag). From here these data are sent to the ECAL pretrigger by means of a two-wires (four bit per wire) serial synchronous protocol running with a 40 MHz clock, so providing the transmission of one event for each BX.

A scheme of the front end section is shown in fig.2. The signals from photomultipliers are fed into a zero pole compensation and amplifier stage in order

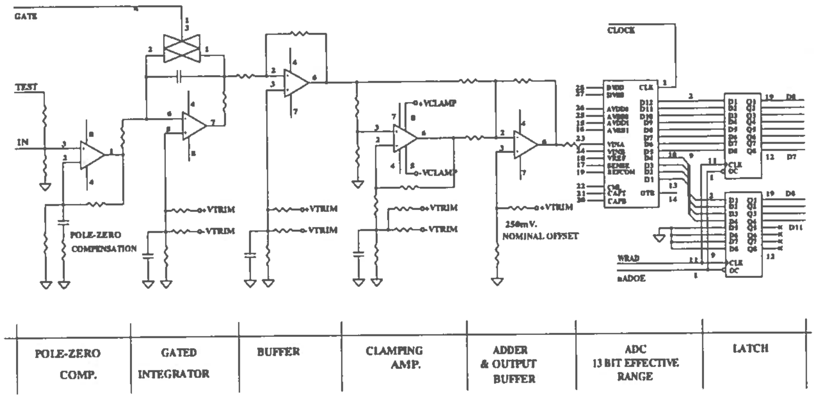

ʒure 2: The scheme of the front-end electronics for one channel. From left to right: ; zero pole stage, the integrator, a buffer, the clamping section and the ADC.

correct the bandwidth effects of cables. Then they are sent to a fast gated egrator working with an integration gate of about 60 ns followed by a buffer ,ge whose output drives two branches. On one of these branch there is a quasi- :al clamping performed by an AD8036 (400 MHz gain-bandwidth product) having ınitary gain. In this way, by summing up the signals from the two branches, we ; a dual range transfer function with a gain of two below to the clamping voltage d an unitary gain above it, so obtaining an effective 13 bit dynamic range. In fact ; Inner section of the calorimeter should measure both lepton (with energies up 250 GeV) and minimum ionizing particles (MIPS), equivalent to about 300 MeV, · calibration purposes.

The zero pole compensation and the integrator stages have been already ;ted with signals from ECAL Middle section modules prototype towers on the 'sy II electron test beam, that provides electrons in an energy range up to 4 GeV. ıe photomultipliers were supplied by means of Cockroft Walton active dividers d their gain was adjusted to cover the full dynamic range for Middle modules ɔout 120 GeV). The zero pole stage and the integrator were mounted on a 6U ΛE board and the signals were digitized by means of a of a 10 bit pipelined flash c.

The results obtained for one of the towers of the Middle section are shown fig.3. In the left side the linear response of the electronics as a function of the :ctron energy is displayed, in the right one the energy resolution is shown. In both ses the results agree very well with that obtained independently with a standard ∖MAC electronics. After these tests a quasi-final version of the read-out board

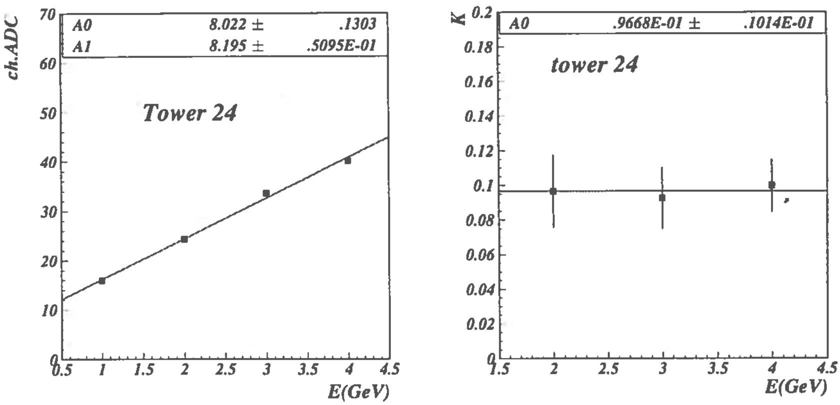

Figure 3: Left side: typical calibration curve for a tower of the Middle section. Right side: Energy resolution multiplied by the square root of the energy as a function of the electron energy for the same tower.

has been tested on the H4 facility at CERN (providing up to 150 GeV electrons, up to 50 GeV pions and 250 GeV muons). This board consisted of an SMD version of four complete read-out channels (pole-zero correction, gated integrator, compressor, 12 bit 10 MHz ADC and DPRAMs) and a VME interface logic. An auxiliary timing logic has been purposely designed in order to acquire data asynchronously (due to the continuous beam structure) with an in-built 80 MHz clock. As an example of the very promising performances we get, in fig. 4 we show the response to 250 GeV muons (seen as MIPs) as measured with a fastbus 13 bit Lecroy 1881 ADC (solid line) and with our read-out electronics (dotted line).

5 The electromagnetic calorimeter pretrigger

The main purpose of the electromagnetic calorimeter pretrigger is to provide electron/positron candidates to the first level trigger.

In order to optimize the performances and to reduce as much as possible the background the design of the pretrigger boards has based on extensive simulations. In particular we have investigated the optimization of the energy threshold, the role of the center of gravity evaluation and of the bremsstrahlung recovery as well as the possibility to handle independently the three calorimeter sections, the optimization of the pretrigger boards partition, the role of the border recovery and the effects of the digital compression of the data. In the following we describe with some details the first three items, that are the most characteristic points of this system.

The measurement of the lepton energy in the ECAL is performed by sum-

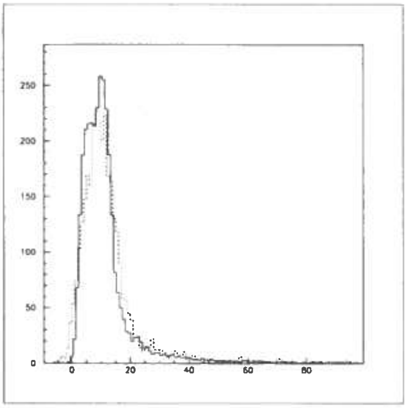

igure 4: Comparison between the response to MIPs of a fastbus 13 bit Lecroy 1881 DC (solid line) and a prototype of the read-out electronics developed for HERA-B lotted line). In abscissa are reported the ADC channels.

ing up the energies deposited on a nonet of towers and requiring that the following reshold conditions are satisfied:

$$\sum_{i=1}^{9} E_i > E_{TH} \quad ; \quad E_5 > E_{TH}/2 \tag{1}$$

$$E_{TH} = K_{TRIG}\left(\frac{1}{R} + \frac{1}{\sqrt{x^2 + |y^3|}}\right) \tag{2}$$

these equations E_5 represents the energy deposited in the central tower of the onet, R is the distance of the tower from the beam axis, x and y are the horizontal d the vertical distances from the beam axis and K_{TRIG} is a constant term (typically $K_{TRIG} = 550\, GeV\, cm$). As one can see the threshold depends on the position the cluster in the ECAL, being the occupancies function of the distance from the eam axis.

Another crucial point of the pretrigger is the capability to perform the enter of gravity calculation to determine with high precision the electron impact oint on the ECAL, following eq.3:

$$X_G = \frac{\sum_i E_i X_i}{\sum_i E_i} \quad ; \quad Y_G = \frac{\sum_i E_i Y_i}{\sum_i E_i} \tag{3}$$

fact about 50 % of the background events that could affect the FLT rate are due γs from π^0 decay detected in the ECAL and overlapped with a charged particle oming from the vertex. A precise determination of the lepton impact point can duce significantly this effect.

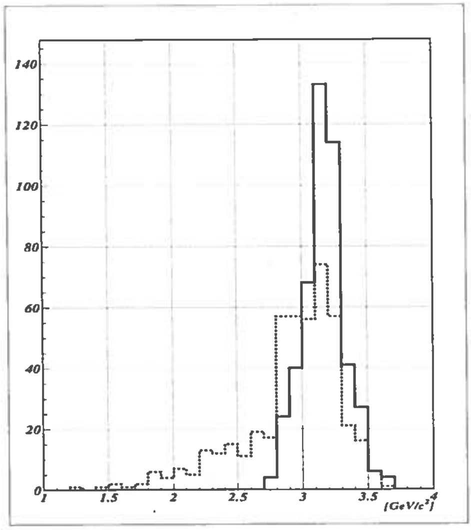

Figure 5: J/ψ invariant mass distribution reconstructed by the FLT without (dotted line) and with (continuous line) bremsstrahlung recovery.

Finally the other original feature of the ECAL pretrigger is the bremsstrahlung (BR) recovery. In fact an electron can emit a BR photon after, before and inside the magnet. In the first case the photon and the electrons travel together and hit the calorimeter nearly in the same region. In the second case the photon follows a straight line, on the contrary the electron is bent by the magnetic field and hits the calorimeter in a different point. In this case some energy information is lost and the trigger efficiency is affected. To overcome this problem the pretrigger has been designed to calculate the photon impact point from the electron energy and to recover the energy deposited in that position. The only configuration in which the recovery is not possible is when the photon is emitted in the region inside the magnet, but in this case the amount of material is little and the effect is negligible.

In fig.5 the effect of the BR recovery on the J/ψ invariant mass distribution reconstructed by the first level trigger is shown. As one can see the low mass tail (see dotted line) due to the energy losses for bremsstrahlung can be almost completely recovered (see continuous line). The improvement in the trigger efficiency obtained with this method is clear leading the efficiency from $\sim 25\%$ to $\sim 35\%$. Furthermore the bremsstrahlung recovery provides a safety margin for the experiment in the case of an unexpected increase of material in front of the magnet.

The general scheme of the pretrigger board [8)] is sketched in fig.6. It is a 9U VME standard board handling a maximum of 96 channels.

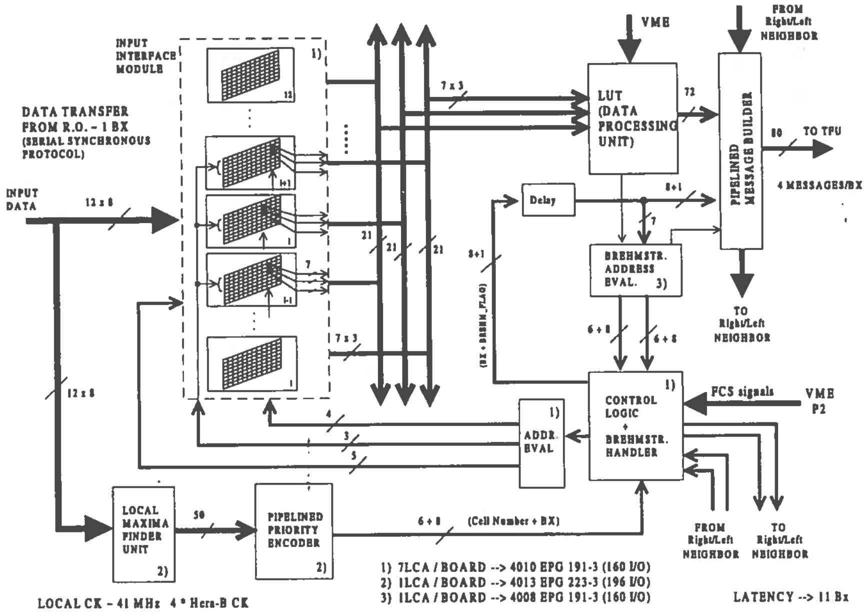

Figure 6: The logic scheme of the Pretrigger system.

Data from read-out are split into two paths. From one side they are stored a 12×8 matrix with a depth of 32 events. From the other side the data are sent to Local Maxima Finder Units that looks for the over threshold energy depositions the ECAL board. Then the data are sent, through a Pipeline, to a Control ɔgic Unit that evaluates the addresses of the nine tower belonging to the nonet. nally the data are processed from the Data processing Unit that calculates all e quantities of interest for the FLT, as the total energy deposited, the center of avity, the possible impact points of the bremsstrahlung photons.

The total latency of the pretrigger system has been evaluated in about 5 μs without the bremsstrahlung recovery algorithm and about 2.5 μs with it.

Conclusions

he HERA-B electromagnetic calorimeter read-out and pretrigger system have been scribed.

The experiment requirements led to high complexity projects. In particular e read-out system must provide an early digitization of the signals and an energy libration of the data and must handle data with a digital pipeline. Moreover the pretrigger system must provide in a short time many operations as to check energy thresholds, to calculate the cluster center of gravity and to perform bremsstrahlung recovery.

The projects are now finished and prototypes are under test at the electron test beam of the CERN and HERA laboratories.

The realization of this kind of electronics is an important development in view of the LHC experiments.

7 Acknowledgments

We would like to acknowledge G. Avoni, C. Baldanza, D. Bulgarelli and M. Zuffa for their skillful technical assistance during the development and the realization of the project. We would like also to acknowledge the full support and expertise given by the HERA-*B* ITEP group during all the phases of test of the read-out electronics for the electromagnetic calorimeter.

References

1. T. Lohse et al., An Experiment to Study CP Violation in the B System Using an Internal Target at the HERA Proton Ring, Proposal, DESY-PRC 94/02 (1994). E. Hartouni et al., HERA-B, An Experiment to Study CP Violation in the B System Using an Internal Target at the HERA Proton Ring, Design Report, DESY-PRC 95/01 (1995).

2. A. Golutvin, these Proceedings (VI International Conference on Calorimetry in High-Energy Physics, Frascati, Italy, 1996).

3. M. Medinnis, Proceedings of the III Workshop on B-Physics at Hadron Machines, Oxford, UK, Nucl. Instr. and Meth. **A368**, 161 (1995).

4. R.E. Kalman, Trans. ASME, J. Basic Engineering (1960).

5. G.S. Atoyan et al., Preprint INR 736/91 (November 1991).

6. G. Avoni et al., The ECAL read-out board, Internal Note, HERA-B/BO/96-01.

7. M. Feuerstack et al., A Common DAQ Architecture, HERA-*B* Internal Note.

8. G. Avoni et al., The ECAL pretrigger system, Internal Note, HERA-B/BO/96-02.

scati Physics Series Vol. VI, (pp. 827–839)
INT. CONF. ON CALORIMETRY IN HEP – Frascati, June 8–14, 1996

ƚYOGENIC FRONT-END ELECTRONICS FOR FAST NOBLE LIQUID CALORIMETRY

G. Battistoni, D.V. Camin, N. Fedyakin, G. Pessina and P. Sala
ipartimento di Fisica Università di Milano and Sezione INFN, I–20133 Milano, Italy

ABSTRACT

e present results obtained after evaluating a few hundred monolithic preamplifiers signed to readout, at cold, the signal of the middle and back segments of the barrel LAr lorimeter of ATLAS. Those chips have been produced in GaAs MESFET technology ing a foundry service.

Introduction

e signal generated in a noble-liquid calorimeter cell can be read-out either by a cold brid or monolithic circuit or by a warm readout. Several thousands cryogenic eamplifiers have already been used in calorimetry starting with the HELIOS (NA34) periment followed by RD3, P44 and NA48 prototypes. Good results and still better pectations in terms of noise, speed, sensitivity to pick-up noise, and cross-talk justified ıg term efforts to develop preamplifiers optimized for these applications[1, 2]. In the se of ATLAS, inaccessibility imposes severe requirements to the reliability of all the mponents inside the cryostat. Reliability of cold electronics is mainly compromised by ermal stress, possible charge trapping, and high voltage discharges and not for the mere eration at low temperatures. On the contrary, operation at very low temperatures ppresses thermal activated processes (i.e. electromigration) responsible of most failures electronic devices at room-temperature. Warm preamplifiers are connected to the tector via transmission lines of a few meters long. They have the advantage of not ssipating power inside the cryostat and that can be accessed at least once a year, but at e expense of higher electronic noise, cross-talk and pick-up noise sensitivity. In fact, ıen using cold preamplifiers the detector signal is amplified right at the cell's end before sending it out the cryostat where the risk of corruption by radiofrequency interference (RFI) or various origins is high. A warm readout circuit, instead, receives the current signal with no amplification at the outside of the cryostat. To reduce the impact of RFI, which could translate into higher coherent noise in the detector, single or double shielding technics should be used. A cold readout circuit provides input impedance of sufficiently low value, a few ohms, to reduce cross-talk effects. This can not be done in warm preamplifiers which should match the characteristic impedance of the transmission line.

To date, thousands of channels have been readout with cold preamplifiers since the very beginning of the RD3 collaboration. We have been pursuing development of monolithic preamplifiers for noble-liquid calorimetry based on GaAs MESFETs as those devices present high speed of response and low noise in a wide low-temperature range including that of LAr and LKr [3].

Recently, monolithic circuits specially designed to readout the middle and back segments of the ATLAS electromagnetic calorimeter have been fabricated. The main purpose of this fabrication run was to evaluate the feasibility of producing in the near future a large number of highly reliable chips to equip the whole detector (~ 50000 channels). We wanted to evaluate the uniformity of noise, gain and speed of the chips fabricated in the different wafers of a single foundry run. Also, we wanted to evaluate the circuit stability and its dynamic range for the nominal working conditions of the middle and back compartments of the detector which comprise a cell capacitance of 1 nF to 2 nF and a maximum detector current of 4 mA to 8 mA.

Finally, considering the severe environmental conditions imposed by the envisaged long term operation of ATLAS, about 10 years without access to the cryostat, we checked for thermal stress in passive devices and in the chips and charge trapping in the latter. Protection networks designed to limit the damage of accidental high voltage discharges have also been designed and tested.

In section 2 we describe "C4", the cryogenic monolithic chip designed for ATLAS LAr barrel calorimeter. In Section 3 we give details of the fabrication of a series of about 500 C4 chips, and in Section 4 we report the results of the independent evaluation made at BNL and INFN/Milano. In section 5 we briefly describe reliability issues and present recent results of thermal shock tests.

2 "C4": A Monolithic Dual-channel Cold Preamplifier.

The building block of the cold readout circuit is a monolithic dominant-pole amplifier (DPA) fedback as a current-to-voltage converter. The feedback network consists of a resistor R_F in parallel with a capacitor C_F, both elements external to the chip, with values optimized for each compartment and for the whole range of pseudorapidity η covered by barrel detector. The time constant C_F x R_F is set to ~20 ns and R_F is dimensioned to ndle the large input current. Its value ranges from 430 Ω to 1.5 kΩ [4]).

e chip was designed following previous experience[2]): a large MESFET, 3 x 24000 μm^2 he input followed by a cascode loaded by a current source constitutes the gain stage; it loaded by an intermediate buffer in turn followed by the output stage. The input nsistor receives its bias current from a separate power supply. In this way power sipation is kept low despite the dynamic range is high. The design was discussed with BNL team with whom we agreed sharing the burden of characterizing a large number chips in a very short time.

though simulation of the chip performance at cryogenic temperatures can be done with gh accuracy, an uncertainty always exists in a new design, in particular in what concerns ry high frequency effects which could affect circuit stability. To reduce this risk C4 is designed initially in two "flavours": SC incorporating a single transistor in the scode stage and DC having instead two devices in that stage. Simulations have shown at DC flavour had higher open-loop gain but lower phase margin. As enough space was ailable in the wafer "tile", a third flavour, LV, consisting of an SC with the output stage hifted down" to lower voltage was also incorporated. We anticipate now that all vours worked well but DC gave the best performance. Therefore, for space reasons, we ll mostly report in this paper the evaluation results of C4-DC chip whose circuit agram is presented in Fig 1.

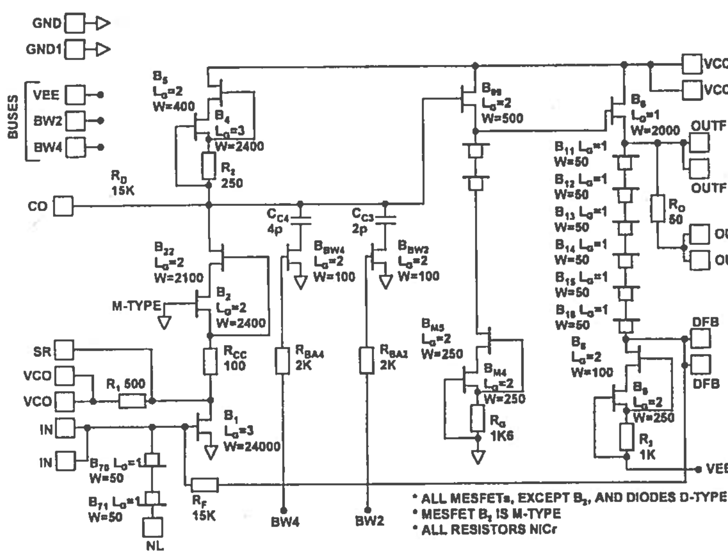

g 1: Schematic diagram of the monolithic cryogenic preamplifier C4 - DC.

3 Fabrication of a small production series

Four 4 " wafers carrying C4 dice, as well as other projects, have been fabricated using TriQuint's QED/A GaAs MESFET process. Each wafer contained 30 tiles of 15 x 13 mm^2. In each tile a set of dice (1 SC, 1 DC and 1 LV) plus one extra LV die was accomodated. Each die measures 1.5 x 2.5 mm^2 and contains two identical circuits. As explained above, the purpose of this fabrication run was to establish the uniformity of chip performance at cryogenic temperatures within a wafer and along the four wafers. In order to follow possible disuniformities within a wafer, we have received and evaluated 15 sets of chips from the first wafer (#39). Each set was identified according to their original position in the wafer. After assembly, half of those sets have been sent to BNL for independent evaluation. Fig 2 shows how the wafer is subdivided in 30 tiles tagged with their position, and the 15 tiles that have been evaluated to identify the best flavour.

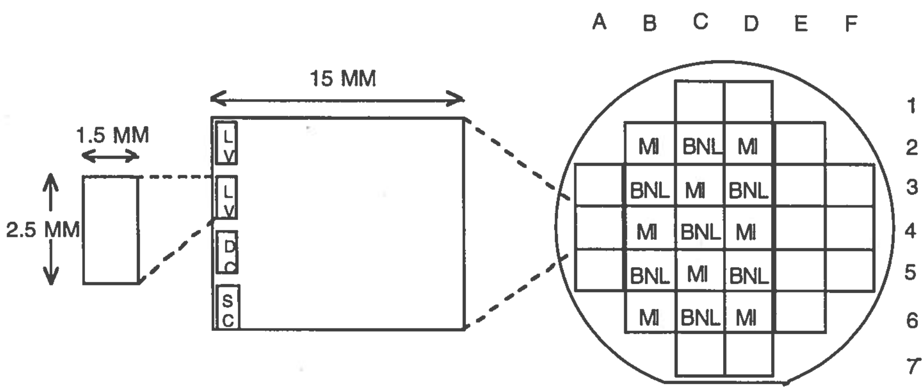

Fig 2: A wafer is subdivided in 30 tiles each one containing four dice.

Chips have been assembled into dual-in-line (DIL) 18 pin ceramic packages using silvered epoxy for die attach and 25 μm gold wire for ball-bonding. Two wires per contact have been used in almost all connections to further improve reliability. Fig 3 shows a photograph of the assembled chip taken with a scanning electron microscope. Fig 4 shows in a larger scale a detail of the die surface.

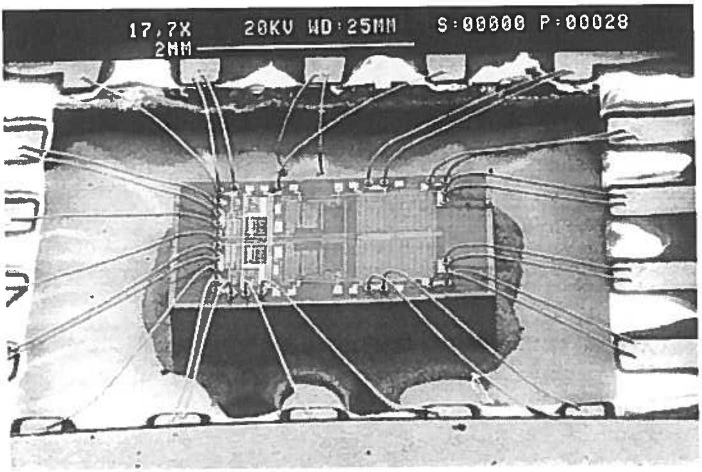

g 3: Chips have been assembled into 18 pin DIL ceramic package. The chip dimensions e 2.5 x 1.5 mm^2 and it contains two channels. Two bonding wires per pad have been ;ed in almost all contacts.

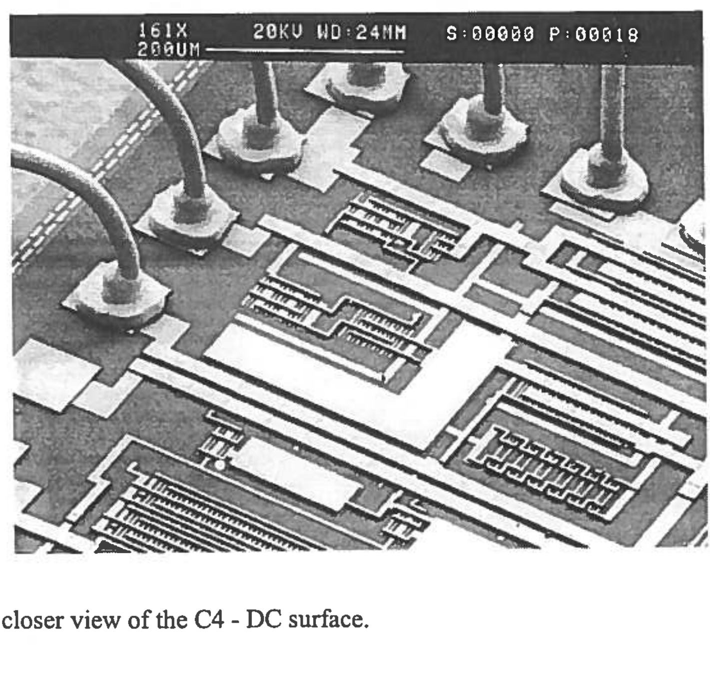

ᵓig 4: A closer view of the C4 - DC surface.

4 Evaluation of chips performance

For evaluation, tests PCB's have been prepared simulating the readout of two cells of the calorimeter. The PCB contains the feedback components, the capacitance simulating the detector and a DIL socket in which the chips under test are plugged in. One of the two channels of the chip, channel A, "sees" an external capacitance $C_D = 1$ nF and its feedbak network consists of $R_F = 820\ \Omega$ in parallel with $C_F = 22$ pF. The second channel, B, sees $C_D = 2.2$ nF and has $R_F = 430\ \Omega$ and $C_F = 56$ pF. A CR-RC^2 shaper followed the preamplifier.

An exponential current pulse with a time constant of 400 ns was applied as a test signal by using a step voltage generator and a series of a capacitor C_T and a resistor R_T. C_T-R_T values were 47 pF and 8.2 kΩ respectively during noise measurements and 470 pF 820 Ω during linearity measurements.

Results of evaluation are summarized in Table I. Amplitude and peaking time have been evaluated at shaper output.

Table 1: Results of evaluation at 87 K of the three different C4 flavours.

	Peaking Time tp [ns]		ENI at tp [nA]		Amplitude [mV]	
	C_D = 1nF	C_D = 2.2 nF	C_D = 1nF	C_D = 2.2 nF	C_D = 1nF	C_D = 2.2 nF
SC	37.7±0.80	41.3±0.73	161±20	363±35	205±4.0	94.5±1.7
DC	35±0.50	35±0.60	154±15	335±32	228±3.0	113±1.4
LV	39.3±0.60	39.9±0.59	154±8.0	327±31	200±9.8	97.9±5.7

As can be observed, DC flavour has the lowest noise (at the same tp), is the fastest and has the smallest dispersion of gain. Double cascode allows better open loop gain, and it is free from triggered oscillations that appeared in previous designs. Good agreement was obtained between the measurements done at both Labs. Table 3 summarizes the main parameters of the selected chip flavour C4 - DC.

Table 3: Main parameters of the monolithic C4-DC chip at 87 K

GBW Product (compensated)	1.7 GHz
Series White Noise	0.33 ± 0.015 to ±0.045 nV/√Hz
Corner Frequency of 1/f Noise	0.8 MHz
Dynamic Range	3 V with 0.6 % INL
Power Dissipation	70 mW

lowing determination of the best C4 flavour, we looked at all the other DC's ricated in the four wafers and visually inspected. Also additional LV's, determined to the second best , have been analized in order to complete a total number of 200 chips t added-up to the initial 50 units from the first wafer. A total number of 250 chips 0 channels) have then been evaluated of which 120 DC's. The production yield was y high: ~ 86 %. In fact, we could verify that only 17 DC chips out of 120 fabricated in four wafers presented defects; actually, 15 have been screened by visual inspection ile 2 units have been found faulty only when performing the first electrical tests. ıilar result was verified with the LV's, although we could not precisely determine the ld as we do not now how many units were screened by visual inspection.

ɔther interesting result was to found that series noise density varies as the channel bias rent I_D to the power -0.25, which demonstrates that noise in contributed only by the ut FET. In fact, noise density is inversely proportional to the square root of the FET ısconductance which in turn is proportional to the square root of I_D. Second-stage se contribution, noticeable in a previous monolithic circuit realized for LAr ɔrimetry[2] was this time strongly suppressed. Direct measurements of noise spectral sity of the input FET were in agreement with the values extracted from ENI.

ʻig 5 we present a plot of ENI vs tp for two different detector capacitances. It can be ed that the plot follows nicely the $tp^{-1.5}$ law as expected [5].

ise dispersion was evaluated at t_{ptr} = 40 ns, either at C_D = 1 nF and at C_D = 2.2 nF.

ile making noise measurements, the peaking time and amplitude at the shaper output ; monitored to also evaluate gain and speed dispersion. The results are indicated in Figs › 8.

ʒarding large signal response, measurements have been done in the following conditions: = 1nF; Imax = 4 mA and C_D = 2.2 nF; Imax = 8 mA. Integral nonlinearity was ɜrmined to be less that 0.6 %, Fig 9.

ning back to noise, the value of series noise density e_n was extracted from ENI ısurements and plotted as a function of the channel resistivity RSD, Fig 10. The ılts for this foundry run, NOV 95, are in good agreement with previous runs and firms that, at cold, noise density of MESFETs and its dependence with temperature smaller for lower channel resistivity (higher doping).

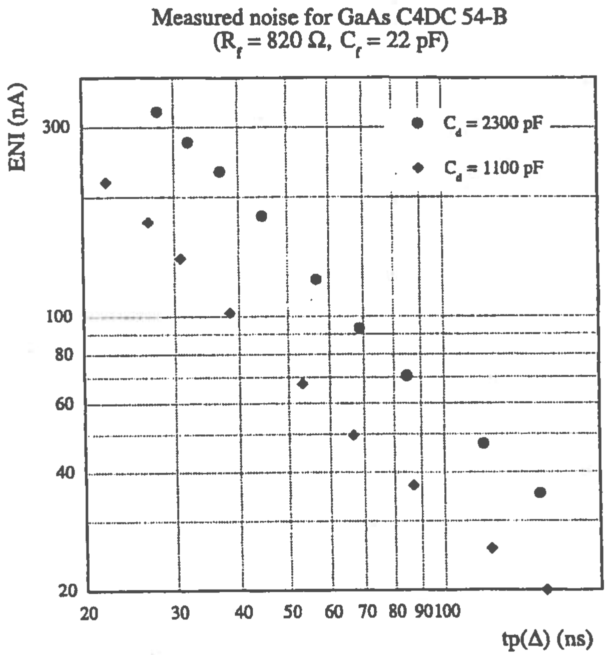

Fig 5: Equivalent Noise Current (ENI) versus peaking time for two different detector capacitances as determined by the BNL team on chip 54-B (wafer #41).

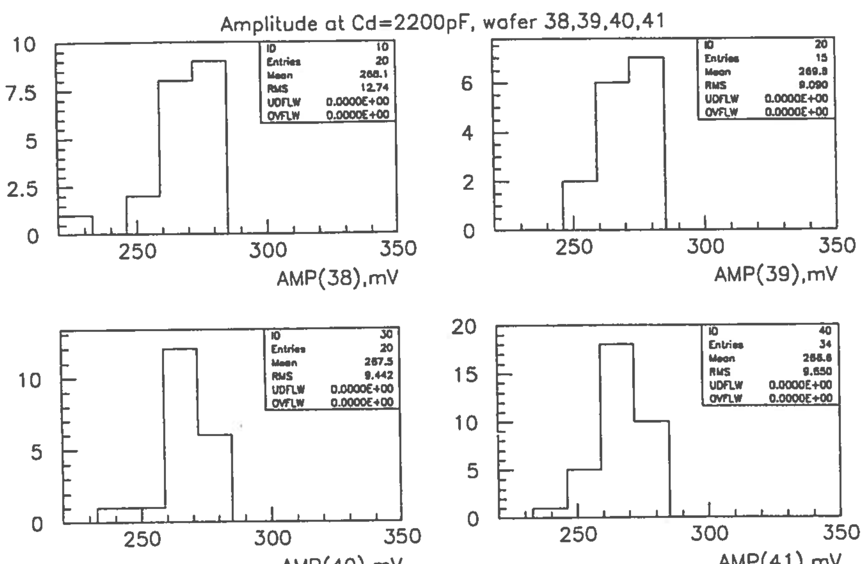

Fig 6: Amplitude distribution in the wafers # 38 to # 41. Dispersions are 4.8 %, 3.4%, 3.5% and 3.6% respectively.

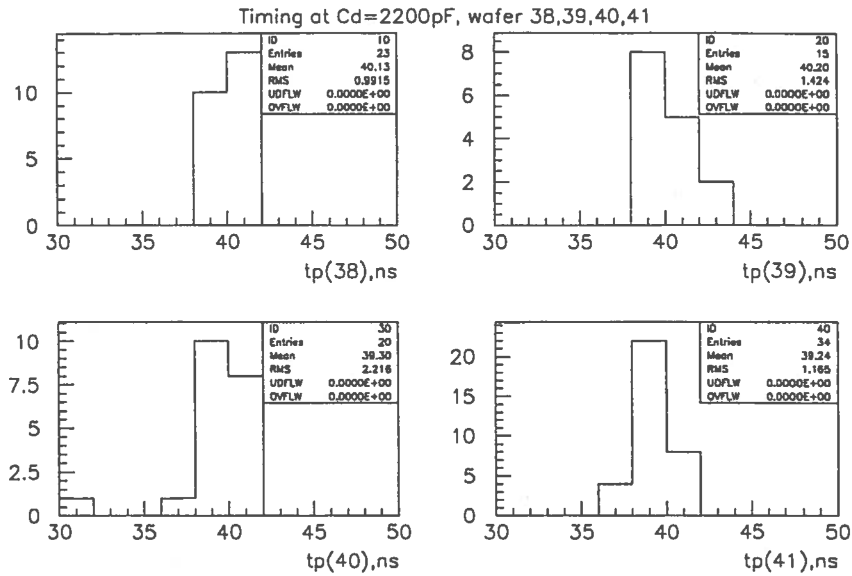

g 7: Peaking time distributions in wafers # 38 to # 41. Dispersions are
%, 3.5 % , 5.6 % and 3.0 % respectively.

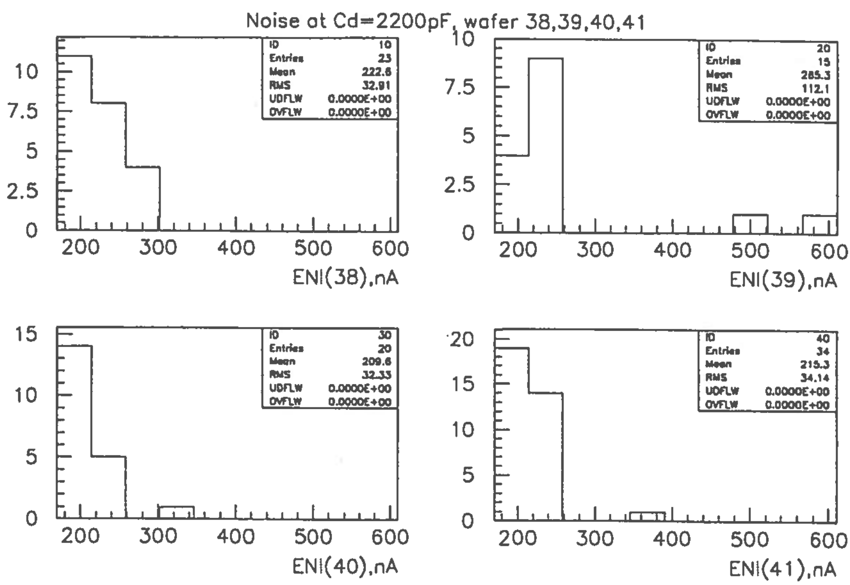

g 8 : Equivalent Noise Current distributions in wafers # 38 to # 41. Dispersions are
%, 4.5 %, 8.8 % and 9.5 % respectively. The four channels with higher noise have not
en included in the statistics.

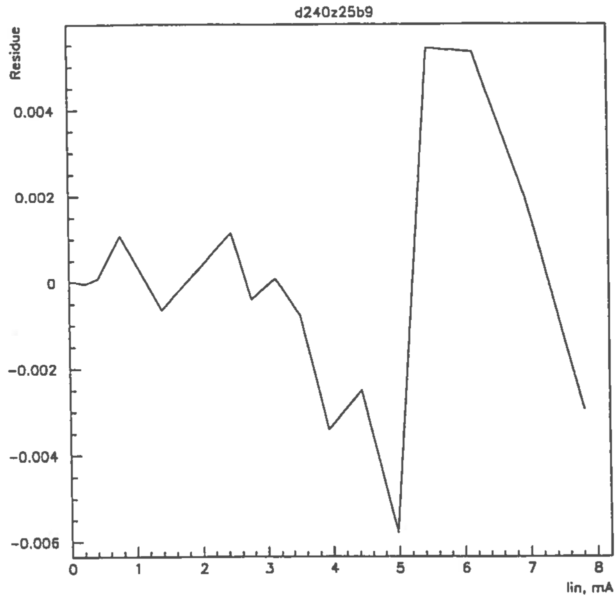

Fig 9: Residues to a linear fit, normalized to 8 mA, as a function of maximun detector current. Vcc = 9 V. Integral non-linearity is 0.6 %.

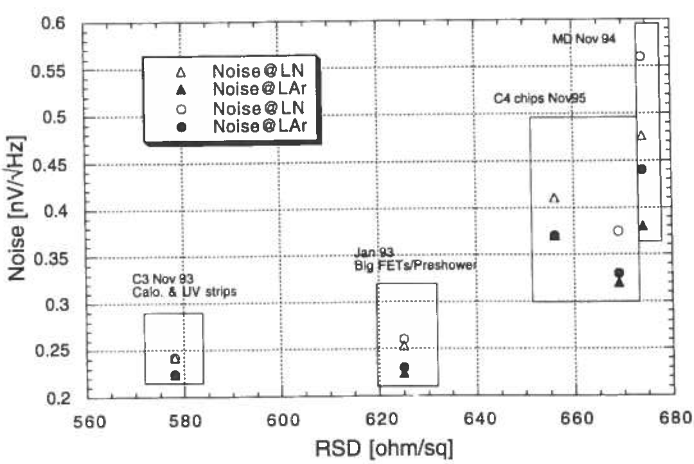

Fig 10: Noise density of MESFETs made in various foundry runs, at 77 K and 87 K as a function of channel resistivity.

Reliability issues

ıving no access to the detector components inside the cryostat for a long time, put vere requirements to system reliability. Connectors, mother boards, resistors and pacitors will be subjected to mechanical stress during thermal cycling (filling and ıptying the cryostat with LAr). Active devices must withstand thermal and also ectrical stresses that may provoke charge trapping (which evidences as a change in the vice characteristics). High voltage discharges could destroy the device if it is not otected with an adequate network. All these aspects have been given due attention.
ıarge trapping was not observed in TriQuint's FET's neither in Vitesse FETs [6] which e also ion-implanted devices of similar characteristics to TriQuint's.
echanical stress have been checked by subjecting 7 chips and a set of passive mponents to ~700 thermal shock cycles from + 50 ^{o}C to 77 K, every 50 sec. No ilures have been detected in the chips. In a few cases, at the end of the test, a tiny crack as noticed in the ceramic lid, which suggested use of metallic lid as a better solution. ost noticeable was the damage in the cables used in the test jig.
s for high voltage discharges, a protection network was designed and evaluated. Its hematic circuit is indicated in Fig 11. Tests have been performed confirming that the twork is effective to protect the chips against energy absorption of 6 mJ. In fact, 25000 discharges of a 2.2 nF (blocking) capacitor charged to 2.3 kV did not provoke gradation in chips performance.
nother aspect related to reliability is radiation damage. It was already demonstrated that ıld preamplifiers are radiation hard to the levels envisaged for 10 years operation of HC at the barrel region [7].

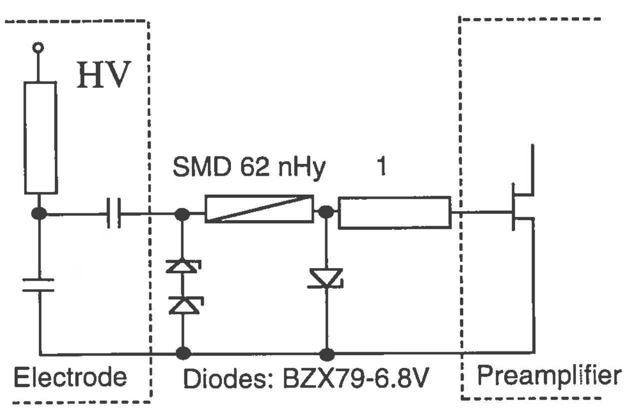

ig 11: High voltage protection network for C4 chips.

6 Concluding remarks

Recent experience of fabricating almost 500 monolithic preamplifiers using a GaAs MESFET foundry process gave positive results. More that 200 chips have been evaluated. The fabrication yield was very high: ~ 86 %. In the four wafers fabricated amplitude and timing dispersion was below 5 %. Integral-nonlinearity for the full signal excursion (8 mA , 3 V at the output) was 0.6 %. Series noise was 0.33 nV/√Hz with ± 5 to ± 15 % dispersion. The noise level agrees with the expected value according to the resistivity of the wafers.

Test to evaluate thermal stress damage showed that chips can at least survive 5000 chips x cycles. Also passive components, including electrolytic capacitors, suitable for cryogenic operation have been identified and tested for thermal stress.

We believe that the excellent performance of cold preamplifiers in terms of noise, speed, cross-talk and pick-up noise sensitivity could be safely used in noble-liquid calorimetry providing that the electrodes are designed to limit the energy delivered in case of an accidental HV discharge and/or suitable protection networks are used.

7 Acknowledgements

We thank D. Fournier and V. Radeka for stimulating the development of cold electronics for the Accordion LAr calorimeter. Discussions with J. Colas, and C. de La Taille are greatly appreciated.

We are specially grateful to M. Citterio and S. Rescia for their effort to make a large number of evaluation measurements in a very short time.

We thank G. Giudici and our students F. Barresi, P. Ramaioli, and M. Sironi for the hard work on simulations and evaluation measurements. The invaluable technical support of F. Sabatini is highly appreciated. Special thanks to E. Johansen of GIGA A/S and R. Mazzotti of Laben SPA for valuable technical advise.

References

1. V. Radeka, S. Rescia, P.F. Manfredi, and V. Speziali, Monolithic Front-End Preamplifiers for a Broad Range of Calorimetry Applications in: Proc. Fourth Intnl. Conf. on Calorimetry in HEP (eds: A. Menzione, and A. Scribano, La Biodola, 1993), 143 (World Scient., Singapore, 1994).

2. D.V. Camin, N.Fedyakin and G.Pessina, Nucl. Instr. and Meth., **A 360**, 153 (1995).

RD3 Collaboration, Performance of Monolithic Current-Sensitive Preamplifiers h an Accordion LAr Calorimeter, in : Proc. Fifth Intnl. Conf. on Calorimetry in HEP s: H.Gordon and D. Rueger, BNL, Sept.1994), 401 (World Scient., Singapore, 1995).

D.V. Camin, N.Fedyakin, G.Pessina, F.Sabatini and M.Sironi, Cryogenic Front-End ctronics in III-V Technology for Liquid Argon Calorimetry in: Proc. of the First rkshop on Electronics for LHC Experiments (Lisbon, Sept. 1995), 257 ERN/LHCC/95-96, 1995).

R.L. Chase, C. de La Taille, J.P. Richer, N. Seguin-Moreau, A Fast Monolithic aper for the ATLAS E.M. Calorimeter, ATLAS Internal Note LARG-NO-010 (1995).

Y. Christoforou, private communication.

M. Citterio, S. Rescia, and V. Radeka, Radiation Effects On Front-End Electronics r Noble Liquid Calorimetry, in: Proc. Fifth Intnl. Conf. on Calorimetry in HEP (eds: Gordon and D. Rueger, BNL, Sept.1994), 401 (World Scientific, Singapore, 1995).

'ascati Physics Series Vol. VI, (pp. 841–848)
I INT. CONF. ON CALORIMETRY IN HEP – Frascati, June 8–14, 1996

THE NA48 LIQUID KRYPTON CALORIMETER: ELECTRODE STRUCTURE, FRONT–END ELECTRONICS AND CALIBRATION

C. Cerri
INFN–Pisa / CERN, PPE Division

ABSTRACT

ne NA48 Collaboration will shortly complete and installate in its experimental paratus a 13500 channels quasi-homogeneous liquid krypton calorimeter. The ex- riment aims to measure CP violation parameter ϵ'/ϵ with an accuracy of 2×10^{-4}, d the calorimeter choice was made to guarantee the needed energy, position and ne resolutions, as precise calibration and uniformity of response. The front-end ectronics consist of charge sensitive preamplifiers based on Si-JFETs, mounted be- nd the calorimeter structure, inside the liquid krypton. The electronic calibration stem consists of a DMOS switch that generates through an RC circuit a pulse be injected in each channel. A series of eighteen layers printed circuit boards using the connectors to the preamplifiers cards, provide the necessary shielded pacitors to produce the calibration signal. The first data taking is foreseen for is summer.

ntroduction

he aim of the NA48 collaboration [1] is to measure the direct CP-violation observ- le:

$$Re(\frac{\epsilon'}{\epsilon}) = \frac{1}{6}(1 - \frac{\Gamma(K_L \to \pi^0\pi^0)}{\Gamma(K_S \to \pi^0\pi^0)}\frac{\Gamma(K_S \to \pi^+\pi^-)}{\Gamma(K_L \to \pi^+\pi^-)}) \quad (1)$$

ith a 2×10^{-4} accuracy.

The strategy adopted consists in detecting simultaneously the four decay odes by usin nearly collinear beams of K_L and K_S. Decays originated from the two eams are distinguished by the time coincidence between the decay and a proton tting the target of the K_S beam [2].

A magnetic spectrometer detects kaon decays into charged pions.

1 The electromagnetic calorimeter

The main requirements for the electromagnetic calorimeter used to detect photons from the $K_{L(S)} \rightarrow \pi^0\pi^0$ decays are:

- Sensitive area $\sim 6m^2$.
- $\sigma_E/E \sim 1\%$ at 10 GeV with a constant term lower than 0.5%.
- $\sigma_{x,y} \sim 1mm$.
- Transverse scale accurate to 0.1/1000 mm to keep at the wanted level the systematic error induced by a possible difference in energy scale for $\pi^+\pi^-$ and $\pi^0\pi^0$ decays.
- Timing accuracy $\sigma_t \leq 0.5ns$ for K_S identification.
- Single rate capability $\sim 1MHz$ to achieve statistics of the order of 10^6 for $K_L \rightarrow \pi^0\pi^0$.
- Tower structure and short sensitive time to reduce the effects of accidentals and background from the dominant decay mode $K_L \rightarrow 3\pi^0$.

To satisfy the above requirements the choice of the NA48 collaboration has been a fully sensitive liquid krypton ionization chamber [3) 4)], operating in current sensitive mode, with a tower structure segmentation in $2\times 2cm^2$ cells with electrodes parallel to the shower direction (hence ionization charge is drifting orthogonally to the shower axis).

The initial induced current is read out by using $(CR)^2(RC)^4$ shaping to get $T_{peak} \sim 1/40\ T_{DRIFT}$.

The main features of the calorimeter are:

- The use of liquid krypton with a small amount of electrodes and spacer material. This provides high density (2.45 gr/cm^3), contained showers ($X_0 \sim R_M = 4.7cm$), an almost fully sensitive volume and a high $E_{vis.}/E_{dep.}$ ratio.
- A simple mechanical structure to fill the $\sim 7m^3$ volume, namely large gaps and ribbon electrodes stretched in the longitudinal direction.
- Longitudinal tower structure to achieve high granularity.
- Initial current read-out for speed and to minimize sampling fluctuations.

The basic working principle of this detector is the measurement of the arge Q_{ion} of the electrons which are free to drift as a consequence of the ionization oduced by the shower developement in the liquid krypton. Q_{ion} is of course directly oportional to the energy deposited by shower.

We actually measure:

$$I_0 = Q_{ion} \frac{v_d}{w_{gap}} \tag{2}$$

iere v_d is the drift velocity of electrons in liquid krypton under the influence of e applied electric field between the electrodes and w_{gap} the width through which ey drift.

The Q_{ion} measurement obtained in this way offers the important advantage, ative to the more usual method of full collection of the charge, that the sensitive ne can be much shorter than the drift time. In practice the speed is limited only the charge transfer time and the electronic noise that can be accepted.

However, the w_{gap} dependence, coupled with the sharpness of the transverse ape of the electromagnetic shower developement, imposes severe constraints to e electrode geometry ($\leq 1\%$ accuracy on gap width) in order to mantain a small 0.5%) constant term in the uniformity of the ratio of the initial current to the ower energy deposition.

Concerning v_d we know, from prototype studies and direct measurements th a laser chamber [5], that its dependence on temperature of the liquid is not gligible:

$$\Delta v_d / \Delta T \sim -0.9\% / {}^\circ K \tag{3}$$

the full size calorimeter a correction for this effect is foreseen by using direct mea-rements of drift velocity, whenever temperature difference in the liquid krypton th will exceed $\sim 0.5^\circ K$.

Structure

he needed performances have been achieved in a 200 litres prototype after several am tests [6]. The use of $40\mu m$ thick Cu-Be ribbons, tensioned to $\sim 2N$ with spring obtained by corrugation at both ends, allowed a spacing of the electrodes curate to $\leq 0.1mm$ over the $10.0mm$ gap width. Transverse spacers limiting the e length of the ribbons to 20 cm prevent any electrostatic instability and allow r a $\pm 50mrad$ angle of the ribbons relative to the direction of the photons, then oiding singularity in shower developement in the Cu-Be. The pointing property o a source $\sim 110m$ in front) is obtained by increasing the pitch of separation of e ribbons (in both x and y) at each successive spacer in proportion to the distance om the source.

3 Electronic chain

The front-end cold preamplifiers and the calibration system are located at the back plane of the ribbon structure, inside the liquid krypton.

The output signals from the preamplifiers (described below) are available on warm feed-throughs at the top of the calorimeter (transmission is made by coaxial cables, 6 m long, partially cooled).

A transceiver (presented in this conference) mounted directly on the feed-through connector, performs the zero-pole cancellation and is followed by a twisted pair driver. It sends signals to the counting room, 10 m away, where a final $(CR)(RC)^4$ shaping and digitization (40 MHz FADCs, 10 bits, $\sim$ 15000 dynamic range) are performed (fig. 1).

3.1 Cold preamplifier

Various considerations pushed us to adopt a solution in which the front-end electronics together with the calibration system are working inside the cryostat very close to the electrode structure.

The main reasons for this choice are:

- To minimize the charge transfer time (for fast shaping and speed).
- To exploit a property of ordinary silicon JFET for which the noise as a function of temperature has a minimum close to the liquid krypton temperature.
- To profit of the good thermostatic properties of the liquid krypton bath to improve the long term stability, expecially important for the calibration system.

A dual hybrid version of cold charge integrating preamplifier, of BNL type [7) 8)], using silicon JFET, was designed for this project (fig. 2).

3.2 The electronic calibration system

To control the response uniformity and stability over the $6m^2$ sensitive area of the calorimeter to better than 0.5% a precise and stable calibration system was needed.

The strategy used was to distribute in the front end electronics $\sim$ 2000 pulse generators, controlled by DC reference voltages for amplitude and digital signals for trigger (fig. 3).

Calibration pulses are produced locally and then do not suffer from distortion or cross-talk due to transmission on long lines.

The generator produces an esponential voltage signal (with time constant about equal to the ionization drift time) which drives a calibration capacitor connectedd to the preamplifier input.

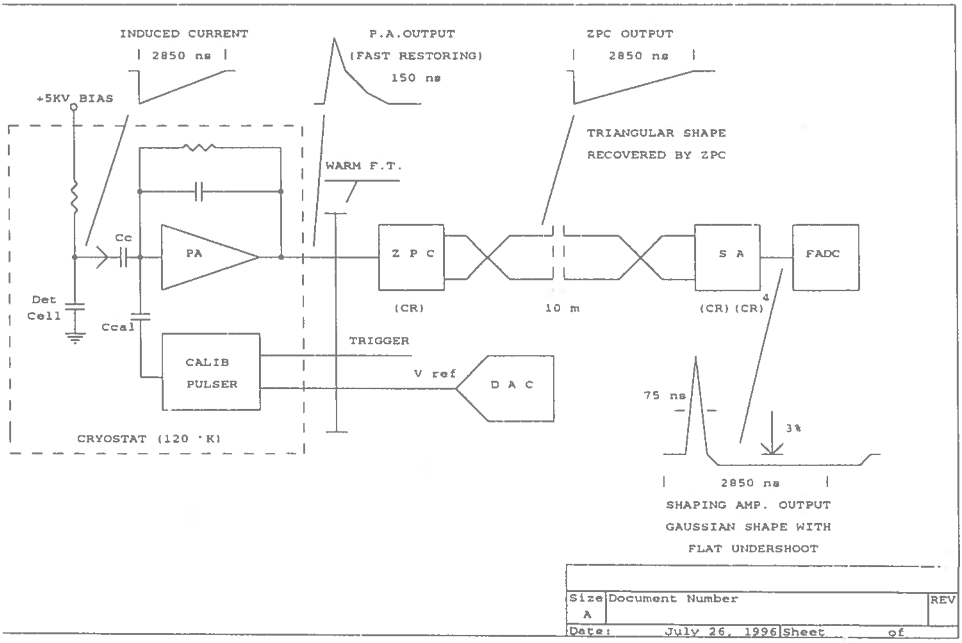

Figure 1: Read-out chain.

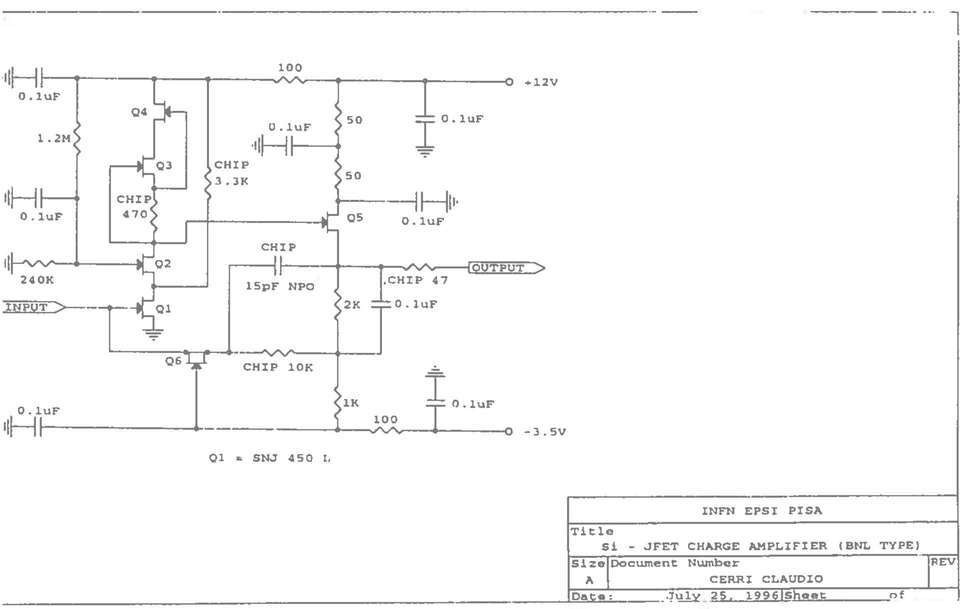

Figure 2: Hybrid.

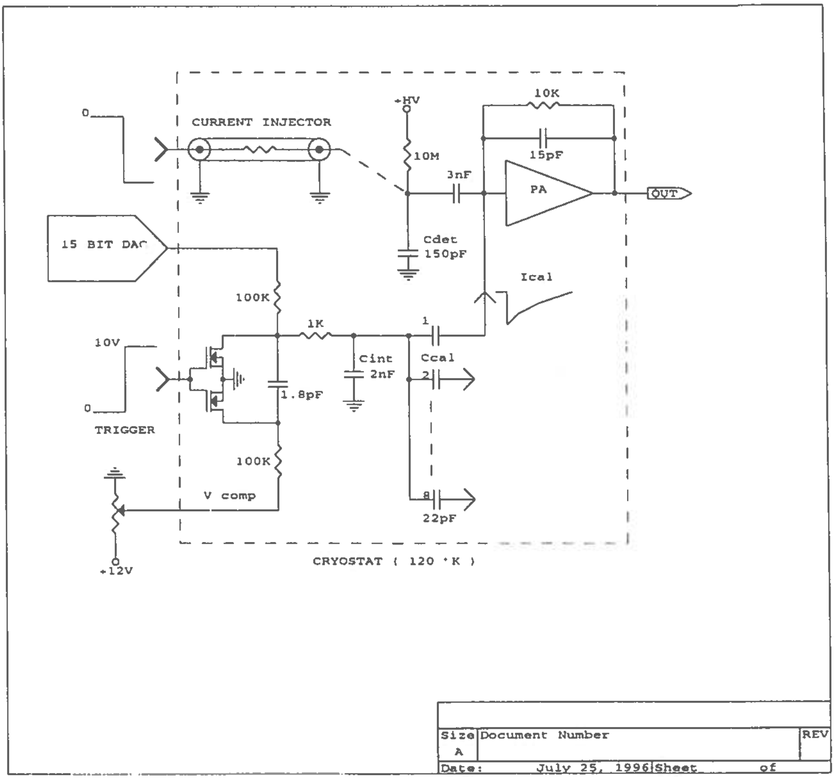

Figure 3: Calibration circuit.

The injected calibration current amplitude is controlled by a 15-bits DAC.

The calibration system is implemented, together with the power supply distribution, in a 18-layers mother board on which preamplifier cards are inseerted (8 cards $\times$ 8 channels per card = 64 channels per mother board).

For this developement the multilayer tecnology employed in printed circuit boards was particularly useful to obtain well shielded precise capacitors and strip-lines with controlled impedance and, moreover, in achieving a high deegree of immunity from temperature changes.

In each calibration pulse generator a compensation circuit [9] provides a correction for the parassitic pick-up due to the trigger signal (10 Volts amplitude). Without the correction the pick-up would have an amplitude corresponding to $3 \div 5$ times the electronic noise. The compensation reduces this effect well below the noise level.

The use of DC levels and digital signals to control the calibration system lows the implementation of a very simple multiplexer to control the calibration ıttern.

By using a very precise current injector we measured, to better than 0.5% :curacy, for each channel, at room temperature and at $120°K$, the current neces- .ry to reproduce the response corresponding to the standard on-board calibration 'stem, with 1 Volt reference voltage ($\sim$ 5 GeV). The variation of the calibration con- ant between the two temperatures was rather uniform at a value of $(1.93 \pm 0.43\%)$ The calibration constant was measured in such a way to take into account the tenuation, on the real signals, due to the coupling capacitor.

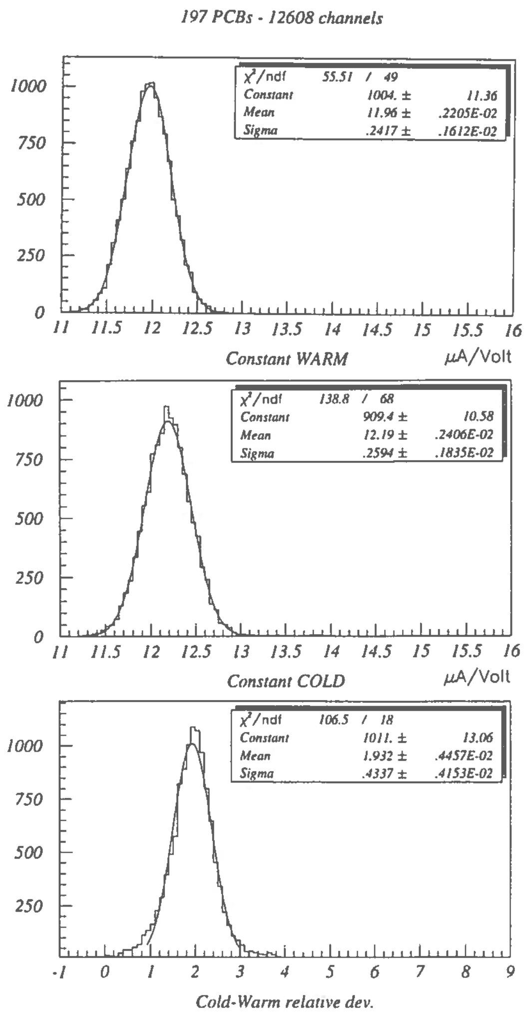

;ure 4: Calibration constants.

3.3 Read-out busses and preamplifier protection

The front-end electronics is assembled in busses containing 64 channels with their relative coupling capacitors and resistors for high voltage biasing.

The connection to the calorimeter electrode system is made by commercial connector pins inserted in a stesalite profile. It contains 64 pins for signals and 32 for a common ground connection.

The support for the 8 preamplifier cards (each containing 4 dual hybrid circuits) is a mother board (a 18-layers printed circuit board) which presents on its component side 8 calibration pulsers and 64 pads corresponding to the preamplifier inputs.

To protect the front-end electronics during the high voltage conditioning a system of switches has been implemented on each mother-board. Each set of switches consists of a long copper-beryllium spring that, once pressed, shorts all input pads to ground. When activated, due to their very low inductance and high current capability, the switches provide a complete protection for the preamplifiers, even for continuous sparking, in the electrode system up to a voltage of 7 kV.

References

1. G. D. Barr et al., CERN/SPSC/90-22/P253.
2. P. Grafström et al., NIM **A 344** (1994) 487.
3. C. Cerri et al., NIM **227** (1984) 227.
4. V. Radeka et al., NIM **A 265** (1988) 228.
5. NA48 note 96/8.
6. G. D. Barr et al. NIM **A 370** (1996), 413.
7. Private communications from S. Rescia and V. Radeka.
8. M. De Micheli et al., NIM **A 289** (1990) 418.
9. NA48 note 94/31.

ascati Physics Series Vol. VI, (pp. 849–860)
: INT. CONF. ON CALORIMETRY IN HEP – Frascati, June 8–14, 1996

)YNAMIC RANGE COMPRESSION IN A LIQUID ARGON CALORIMETER

W.E. Cleland,
University of Pittsburgh, Pittsburgh PA 15260, USA
D. Lissauer, V. Radeka, S. Rescia, H. Takai, and
Brookhaven National Laboratory, Upton NY 11973
I. Wingerter-Seez
LAPP, BP 110, 74941 Annecy-le-vieux, Cedex, France

ABSTRACT

e anticipated range of particle energies at the LHC, coupled with the need for precision, low noise ɔrimetry makes severe demands on the dynamic range of the calorimeter readout. A common ɔroach to this problem is to use shapers with two or more gain scales. In this paper we describe experience with a new approach in which a preamplifier with dynamic gain compression is used. unavoidable consequence of dynamic gain adjustment is that the peaking time of the shaper put signal becomes amplitude dependent. We have carried out a test of such a readout system in RD3 calorimeter, a liquid argon device with accordion geometry. The calibration system is used determine both the gain of the individual channels as well as to map the shape of the waveform a function of signal amplitude. A new procedure for waveform analysis, in which the fitted ameters describe the impulse response of the system, permits a straightforward translation of calibration waveform to the waveform generated by a particle crossing the ionization gap. We l that the linearity and resolution of the calorimeter is equivalent to that obtained with linear amplifiers, up to an energy of 200 GeV.

Introduction

namic range is an important consideration in the design of front end electronics for calorimeters ɔe used in LHC detectors. The ATLAS experiment has chosen for its electro-magnetic calorime- the technology of liquid argon with accordion geometry. In this calorimeter it is expected that h energy electrons will deposit up to 2 TeV per readout cell and that most of the physics will performed in the range of 10 to 100 GeV. Since the expected electronic noise levels are well ɔw 100 MeV per cell, the readout system must have a dynamic range of nearly five orders of gnitude. Also, if the readout system is linear, signals of up to 100 GeV will occupy only about of the total dynamic range.

There are several approaches to the dynamic range problem. In the more traditional of se, the output signal from the preamplifier-shaper chain is split into two or more gain ranges l digitized in an ADC of appropriate precision. We have studied a different approach, namely the dynamic compression of the signal at the preamplification stage. In this approach we use a specially designed preamplifier characterized by a response curve with two regions of different gain, joined by a smooth transition region. As the signal develops in time the compression is activated above a pre-determined level, resulting in a gain reduction. Because of the finite rise time of the preamplifier the shaper sees a signal of reduced rise time, which causes an amplitude dependence of the peaking time of its output pulse.

To evaluate the performance of such a system experimentally, we have built and tested pre-amplifiers with dynamic compression in the RD3 calorimeter. The pre-amplifiers were built with gain reduction starting at an energy of about 45 GeV. In the LHC experiment the transition would be set near 200 GeV, and, with a gain reduction of 1:4, the signals below 100 GeV would occupy about 15% of the total dynamic range. Given the effects of the compression on the shaped signal, it is necessary to sample the waveform at several points. In our case this was achieved by the use of analog switched capacitor arrays (SCA), whose output was digitized in a 14-bit ADC. A detailed knowledge of both the amplitude response and the waveform dependence on amplitude was obtained by using a precision calibration pulse injected at the preamplifier input. Using this information, data taken in an electron beam in the energy range 20 to 200 GeV were processed, and the linearity, energy resolution, and timing resolution of the system were determined. We discuss in this paper the practical aspects of implementing and analyzing data from systems with dynamic range compression of this type.

One of the important goals of this analysis is to use the calibration data to obtain information on the shape of the waveform. This is particularly important in the case of waveforms whose shape depends upon the amplitude, as this dependence can be studied in detail using the calibration system. For a large calorimetry system where the determination of the amplitude of the signal requires a knowledge of the waveform, it is important to be able to determine this waveform from the calibration signal alone, as reliance on particle data, especially for large amplitude signals, can be severely hampered by limited statistics. In order to be able to use the calibration data to calculate the waveform arising from a particle crossing the ionization gap, which we call the "signal" waveform, we have chosen to parameterize the impulse response of the system. The technique used is to make a linear expansion in terms of "basis" functions: the $\delta-$response is expanded in a set of nonorthogonal time-dependent functions with linear coefficients, and the waveforms produced with a known current waveform (either the calibration waveform or the signal waveform) are calculated as a convolution between the current waveform and this parameterized impulse response.

2 Experimental Setup

The test of the preamplifiers were carried out in the RD3 2 meter long test module at CERN. The RD3 calorimeter is described in detail elsewhere [1)] and is a prototype calorimeter for ATLAS electro-magnetic calorimeter. The calorimeter uses liquid argon as the sampling medium and lead absorber folded in the accordion geometry. It is subdivided longitudinally into 3 sections. The st two sections are 9 radiation lengths in depth, and the third section has a depth of 6 radiation ıgths. The calorimeter is segmented transversely into projective towers of $\Delta\eta \times \Delta\phi = 0.25 \times 0.25$, fined with respect to the center of projection, located at a distance of 1.2m from the front face. ır this segmentation and for the energies used approximately 50% of the beam energy is deposited a single channel in the first sampling. Thus only the first longitudinal section was equipped th preamplifiers with dynamic gain compression. The two other sections were instrumented with ιear preamplifiers. The total number of instrumented channels read out by the data acquisition stem correspond to a matrix of 6×6 towers from which a 5×5 matrix, centered on the beam, is ed in the analysis to form the total energy sum.

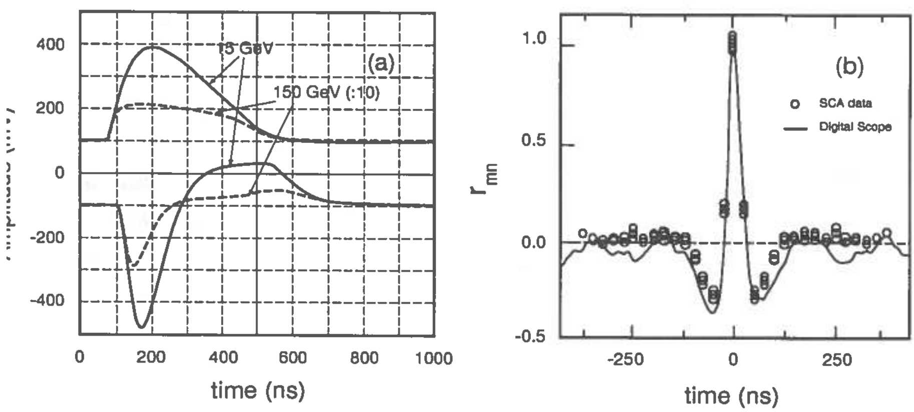

gure 1 (a) Preamplifier (upper) and shaper (lower) waveforms illustrating dynamic compression. The eamplifier is in the linear region for the 15 GeV curve. The turn-on of the dynamic compression can be ən comparing the leading edge of the 150 GeV curve with that of the 15 GeV curve. The effect of the namic compression is to present a pulse of faster rise time to the shaper input. The resulting output of e shaper is a pulse with reduced peaking time. (b)System noise autocorrelation as determined from the ;A data and digital oscilloscope

The preamplifiers, which operate at the temperature of liquid argon, were especially signed and built for this test. They are characterized by a gain curve with two linear regions th gain difference of approximately 2.5, joined by a smooth transition region (knee). For the esent test the knee was placed at approximately 45 GeV, as can be seen in Fig. 2b. In ATLAS e knee would be set at approximately 250 GeV since it is useful to make linear trigger sums for ergies below that range. The signals from the preamplifiers were shaped with dual gain shapers. ıce we used different preamplifiers, the peaking time of the signal waveforms were not the same each of the sections. In the front layer (for signals in the linear range) the 5%-100% peaking ne was approximately 55 ns, whereas in the middle and back sections it was approximately 85 .

The dynamic compression at the preamplifier has the effect of reducing the rise time pulses at the preamplifier output. Consequently the shaper output signals have an amplitude-pendent peaking time. The waveforms are sampled at at a rate of 40 MHz, giving sequential samples spaced by 25 ns The waveform sampling is done asynchronously with the beam triggers and the phase, the time between the beam trigger and the SCA clock, was recorded for each event in a TDC of 50 ps/channel precision. The SCAs sample the signals continuously until a trigger occurs. After the trigger, 16 samples corresponding to a time window of 400 ns around the peak are digitized by a 14-bit ADC. All the waveform samples, together with information (pulse height and timing) from the beam counters are recorded on tape for analysis.

3 Analysis

For the channels with dynamic compression, accurate characterization of its response, gain in both regions and the break point, are necessary. This is accomplished by means of a precision calibration system. In the present studies the existing RD3 calibration system was used. In this system a network of precision resistors is used to distribute signals with sharp rise time ($\approx$ 3 ns) followed by an exponential decay (T_C = 270 ns) to each individual channel. Calibration signals are also asynchronous with respect to the SCA sampling clock.

To process the electron signals we used the optimal filtering method to extract both amplitude and timing information. This technique relies on the detailed knowledge of both calorimeter waveform and the noise of the system. The electron waveforms were obtained by folding the experimentally determined impulse response from the calibration signals with the triangle current waveform from the liquid argon. The noise and the autocorrelation function for each channel was studied by examining random triggers interspersed with beam triggers.

3.1 Description of the Method

3.1.1 Calibration signal averaging

The first step in the analysis process is the determination of the average waveform from the calibration data. Calibration data were collected at a wide range of reference voltage values, which were provided by a precision 16-bit DAC. Each calibration run consists of a set of events in which a particular subset of the channels were pulsed N_p times, with $N_p = 100$ for most of the runs. In order to study a particular channel, it was necessary to scan through the run to select the events in which this particular channel was pulsed and to perform signal averaging on pulses with the same DAC setting.

The calibration pulser was a clock which was asynchronous with the sampling clock, and therefore each calibration "event" occurred at a particular time (which was measured in a TDC) with respect to the calibration clock. In order to determine the average waveform profile, samples were averaged in bins of 2.5 ns. However, it was found that with only 100 pulses to average, fluctuations introduced by the finite bin width contributed noticibly to the mean value. We therefore developed a two step process, in which the local slope of the waveform was measured for each bin, by the use of a cubic spline fit. On the second pass, the value of the signal waveform was corrected to the center of the bin, using the timing of the event relative to the sampling clock given by the TDC measurement. With this technique, the fluctuations in the mean value of the veform in each bin was reduced by the averaging process to approximately $1/\sqrt{N_p} \approx 1/10$ of noise level. An advantage of this method is that it also permitted the elimination of a small nber of calibration events which (for unknown reasons) had obviously incorrect amplitude or ing.

.2 *Waveform fitting in the linear region*

first consider the problem in the low energy region, where the preamplifier response is linear l the shape of the waveform is independent of amplitude. This corresponds to data taken at a m energy of 50 GeV. (Recall that only about half of the beam energy is deposited in the front tion.)

The impulse response function $h(t)$ is parameterized as a sum of basis functions $f_n(t)$ h linear coefficients d_n:

$$h(t) = \sum_n d_n f_n(t)$$

which $f_n(t)$ is the impulse response of an n-fold integrator with time constant τ_0:

$$f_n(t) = \mathcal{L}^{-1}\left(\frac{1}{(1+s\tau_0)^n}\right) = \frac{t^{n-1}}{(n-1)!}\frac{e^{-t/\tau_0}}{\tau_0^n}.$$

calculate the calibration waveform in terms of these parameters. The calibration current, which $i_C(t) = e^{-t/T_C}$, is convolved with $f_n(t)$ to produce the calibration waveform as follows:

$$g_C^{\text{lin}}(t) = \sum_{n=2}^{N_f} d_n F_n(t) \quad \text{with} \quad F_n(t) = f_n(t) * i_C(t).$$

r the waveforms used in this analysis, we have found that sufficient accuracy is obtained with $= 8$. The lower limit of $n = 2$ was chosen by observing that the value of d_1 (when included in e fit) was several orders of magnitude smaller than the other d_n.

The first step in the fitting process for the linear waveforms relies on the linearity of the lser system. For each time bin t_i, we fit the mean values of the waveform to a linear function in e DAC value. The slope of this function R_i is proportional to the amplitude of the waveform at is time value, but it is independent of any offset (*i.e.*, any contribution to the signal for a DAC lue of zero), which can be due to an offset in the DAC output voltage, but it can also vary from ne bin to time bin, due to the contribution of the "clock feed-through" signal (see below). The lues of the slopes are then used in a fit to determine the eight waveform parameters $\{d_n\}$ and

We form the χ^2 function

$$\chi^2(\{d_n\}, \tau_0) = \sum_{i=1}^{N_C} \frac{(g_C^{\text{lin}}(t_i) - R_i)^2}{\sigma^2}$$

which R_i is the slope of the calibration waveform (with respect to the DAC value) at time t_i and is the fluctuation in this value. Here N_C is the number of samples on the calibration waveform.

We used samples spaced by 5 ns from the beginning of the waveform up until a point where the trailing edge of the calibration clock signal introduced a disturbance in the shaped output, which occurred at about 220 ns after the start of the pulse. Eliminating all samples after this point gave $N_C = 43$. The correlations between the points at different times, which are very strong for an individual waveform, are reduced considerably by the processes of signal averaging and fitting for the slopes, and thus a diagonal form of the weight matrix is a good statistical representation for the mean values. Since σ is the same value for all of the time values, for simplicity we can set it equal to unity when solving for the waveform parameters.

We solve for the linear parameters d_n by the usual technique. We define the vector $\vec{B}$ and the matrix $\mathcal{A}$ as

$$B_k = \sum_i R_i F_k(t_i)$$

and

$$\mathcal{A}_{nk} = \sum_i F_n(t_i) F_k(t_i)$$

The equation which results from the minimum χ^2 condition, obtained by setting the derivative of χ^2 with respect to each of the d_n equal to zero, can be written as

$$\mathcal{A}\vec{d} = \vec{B}$$

with the solution

$$\vec{d} = \mathcal{A}^{-1}\vec{B}.$$

The parameter τ_0 is then found by varying it numerically and finding the minimum value of $\chi^2_{\rm min}$, which is the value of χ^2 found by substituting the values for d_n found from the equation above. In this way the calibration data for all DAC values of are used simultaneously to determine the values of d_n for each readout channel.

We now use the optimal filtering formalism to determine the amplitude A and time origin τ of the calibration "events" from the measured samples S_i:

$$A = \sum_{i=1}^{N_s} a_i S_i$$

$$A\tau = \sum_{i=1}^{N_s} b_i S_i,$$

where S_i are the samples spaced by 25 ns, and N_s=7. The optimal filter coefficients are determined directly from the individual calibration waveform $g_{\rm C}^{\rm lin}(t)$, its derivative, and the weight matrix $\mathcal{V}_{ij}$ [3]. The weight matrix is the inverse of the variance-covariance matrix, which is the Toeplitz matrix formed from the autocorrelation function evaluated at multiples of the sampling interval. Thus for the case of 5 samples with spacing T:

$$\mathcal{V}^{-1} == \begin{pmatrix} R(0) & R(T) & R(2T) & R(3T) & R(4T) \\ R(T) & R(0) & R(T) & R(2T) & . \\ . & . & R(0) & . & . \\ . & . & . & R(0) & . \\ . & . & . & . & R(0) \end{pmatrix}$$

which $R(t)$ is the autocorrelation function which is determined experimentally through the use randomly triggered events (see Fig. 1b). In the usual optimal filtering formalism, the values a_i are normalized, so that the units of the amplitude A are the units in which the samples S_i e measured, which are ADC counts. For each DAC value, a distribution in A gives the mean lse height in ADC counts, and a plot of this mean *vs.* DAC value yields the response curve for e system (see Fig. 2b). A linear fit of these data gives the calibration constant for the channel DC value per DAC count) in the linear region.

The particle waveforms are found by using the same basis functions but convolving with e current produced by a charged particle crossing the ionization gap:

$$g_s^{\text{lin}}(t) = h(t) * i_s(t) = \sum d_n E_n(t - t_0) \quad \text{with} \quad E_n(t) = f_n(t) * i_s(t)$$

d

$$i_s(t) = (1 - \frac{t}{T_d}),$$

which T_d is the drift time. Values of A and τ are determined as for the calibration data, solving the optimal filter constants using $g_s^{\text{lin}}(t)$, its derivative,and the weight matrix $\mathcal{V}$. The parameter is introduced to account for a relative time shift between the calibration waveform and the signal veform. Its value is determined by calculating the mean value of τ for a set of particle data. The timal filtering formalism is based on a Taylor series expansion about the point τ=0; in order t to compromise the accuracy of the determination of A, it is sufficient to adjust t_0 such that e mean value of τ is less than 2 ns. We divide the value of the amplitude A by the calibration nstant for each channel, to measure the amplitude of the energy deposited in each channel in its of DAC counts, which are of course common to all channels. Sums of the signals over the 5 matrix and over the three depth segments gives the total energy in units of DAC counts. The ean value of this peak at a known value of the beam energy establishes the DAC scale in units of cident particle energy. We obtain 34.1 MeV/DAC count for this constant. From a measurement the calibration pulse height at the input to the preamplifier for a given DAC setting, we find e relationship between the current injected into the preamplifier and the DAC value, which is .5±1.0 nA/DAC count. The ratio of these two constants yields the signal current for a given cident particle energy of 2.4 μA/GeV.

.3 *Waveform analysis in the nonlinear region*

e techniques to fit the waveforms in the energy region where the preamplifiers become nonlinear n extension of the method used for the linear region. We know that the shaper output waveform unique function of the amplitude of its input signal. Because of the finite rise time of the preamp tput, a nonlinear gain produces a signal whose rise time decreases with increasing amplitude, ich leads to a shaper output signal whose peaking time decreases with increasing amplitude, is illustrated in Fig. 1a. This behavior can be modeled as a time-varying gain function G(t). r expression for the calibration waveform then becomes $G(t) * h(t) * i_C(t)$. At low amplitudes, $t) = 1$, so the problem reduces to the linear one described above.

We parameterize the gain function as a polynomial in t:

$$G(t) = g_0 + g_1 t + g_2 t^2 + \cdots = \sum_{m=0}^{N_g} g_m t^m$$

The calibration signal then becomes

$$g_C^{\rm nl}(t) = \sum_{m=0}^{N_g} g_m \left(\sum_{n=2}^{N_f} d_n H_{mn}(t) \right) \quad \text{with} \quad H_{mn}(t) = t^m * f_n(t) * i_C(t)$$

In the low energy region $g_0 = 1$ and $g_m = 0$ for $m \geq 1$. For this case the values of d_n and τ_0 have been determined, and these values are retained for use in the nonlinear region. Thus the fit for the values g_m for a given value of the amplitude of the calibration waveform is reduced to a linear problem. The form of the gain function obtained for three different amplitudes is shown in Fig. 2a. One sees that it has a behavior which is characteristic of dynamic gain compression. It also absorbs any behavior of the waveform not predicted by the basis functions found in the linear region, which presumably explains anomalies such as the bump in the 70 GeV curve at early times where the amplitude of the output signal is quite small. We have found that an adequate representation of the waveform at all amplitudes can be obtained using 10 parameters ($N_g = 9$) or less.

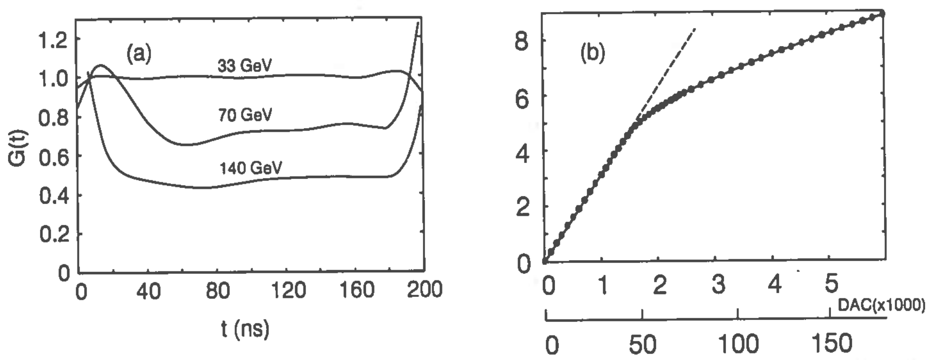

Figure 2 (a) Gain function G(t) used in the fits to the non-linear waveforms. As discussed in the text, for low energies G(t) becomes unity while at higher energies it decreases to describe the dynamic gain compression. (b) Response curve for the preamplifier with dynamic gain compression as determined from the calibration. The ordinate is the peak of the calibration signal and the abscissa is the voltage reference for the calibration pulser. The corresponding scale in incident particle energy is also shown.

As in the linear case, the optimal filtering formalism is used to treat the calibration data as events. From the value of $g_C^{\rm nl}(t)$ and its derivative, we calculate the optimal filter coefficients as a function of the fitted amplitude A, and an iterative technique is used to perform the final fit for the values of A and τ. A plot of the mean value of A as a function of the DAC value yields the full response curve for the channel in question (see Fig. 2b). A polynomial fit to this curve is obtained to give the conversion between pulse height in ADC counts and deposited energy in

AC counts. The systematic error in the method is found as a function of signal amplitude by ɔtracting the reconstructed amplitude in DAC counts from the actual DAC value used at each int in the calibration. This curve is shown (see Fig. 3a) for the channel centered on the beam the front section. It contains deviations which are clearly systematic but less than 0.5% for amplitudes. Knowing the value of g_m at each amplitude permits the calculation of the signal ·veform $g_s^{\mathrm{nl}}(t)$, in which $i_s(t)$ is substituted for $i_C(t)$ in the expression for $H_{mn}(t)$.

!.4 *Clock feed-through correction*

ıe calibration pulser delivers a pulse which is proportional to the calibration current, but in dition there is a small additional contribution to the waveform due to the capacitative coupling the clock signal through the switching transistor, the so-called "clock feed-through" pulse. In ɘ low energy (linear) region, the clock feed-through signal is automatically subtracted from the rrent-dependent part of the signal by fitting to the slopes of the waveform (with respect to the AC value) at each point in time. This is of course not possible in the nonlinear case, since the ective gain of the system changes with time. In order to correct for the clock feed-through in is case, we first find and parameterize (using another set of basis functions) the waveform for the ɔck feed-through signal in the linear region. The values of this signal are simply the offsets at AC=0 determined in the linear fits of the calibration data for each time bin. We then multiply is waveform by the time-dependent gain function $G(t)$ and subtract the result from the measured mples for the calibration signal. The corrected signal is then fit again, and $G(t)$ is re-determined. ıe maximum value of the clock feed-through signal, which occurs at a point more than half way the signal waveform, is less than 1 GeV. Since the pulses in the nonlinear region all correspond energy deposits of 50 GeV or more, the maximum size of this correction is no more than a few rcent.

Results

ıe optimal filtering coefficients for the signal waveforms were determined from the calibration ·ta as described above. Random triggers interspersed with beam triggers are processed in the me way as beam triggers and are used to determine the noise level for each channel. The energy ·d timing for each channel are reconstructed using seven samples approximately centered on the ·ak of the first lobe of the waveform. In the linear region where the waveform shape is constant an ɲplitude-independent set of coefficients is used for each channel. In the non-linear region where e coefficients are amplitude-dependent, we use an iterative technique in which the coefficients e recalculated at each step.

The present analysis employs an energy sum from a 5x5 tower matrix centered on the cident beam position. An electro-magnetic shower is fully contained in the tower since the beam ırticles which are detected by the beam scintillator elements populate only the central cell in ray. The reconstructed timing information is also obtained for each channel within the array.

4.1 Energy Reconstruction

To obtain information of linearity and energy resolution the energy is corrected for its geometrical dependence in both η and ϕ coordinates. The corrections are made using the procedure described in Ref. 1. The data is also corrected for the leakage of energy carried by particles not stopped in the full longitudinal depth and early showering due to material in front of the active region of the calorimeter. This correction is described in Ref 4.

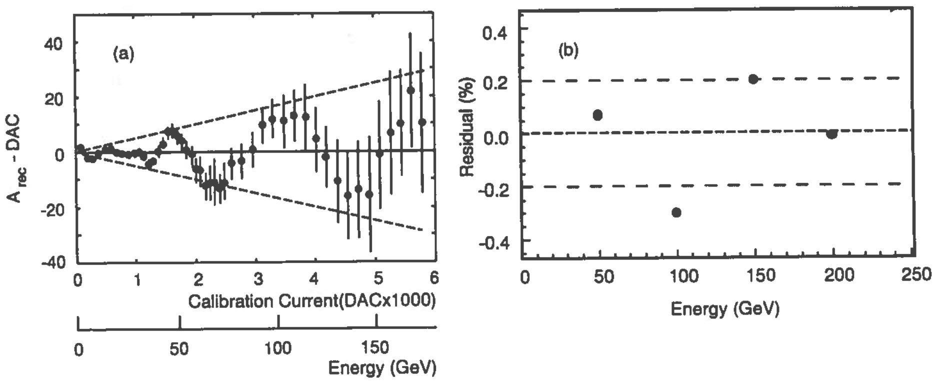

Figure 3 (a) Error in the reconstructed amplitude as a function of the amplitude of calibration signal. The dotted lines show that the systematic errors are within ±0.5%. (b) Difference between the reconstructed energy and nominal beam energy. No corrections were made for the systematic deviations in (a).

During the course of the analysis it was found that both energy and timing are dependent on the position of the samples on the waveform, which is determined by the TDC measuring the sampling clock. This dependence has not been observed in previous analysis where multiple samples were used. However this is the first analysis where complete reliance upon the calibration waveform is made to determine the signal waveform. This sample-time dependence is likely to be caused by an imperfect translation between the calibration waveform to the electron waveform. Studies carried out in recent months indicate that stray capacitances and inductances in the path of the calibration signal distort the calibration waveform, especially in the rising edge, and this effect has not been taken into account in the present analysis. This observed dependence is relatively small for the energy measurement, approximately 0.5%, but the correction for this effect is important to obtain the best resolution performance. It has a considerably larger effect on the timing measurement.

The corrected energy signals for all the electrons used in the analysis 50, 100, 150, and 200 GeV are used to determine the system linearity and resolution. The linearity is shown in Fig 3b as a fractional deviation from the nominal beam energy. Previous linearity determinations for the calorimeter show discrepancies better than 0.2% for energies between 20 and 300 GeV. Our points lie within ±0.3%. However no correction to the data for the systematic deviations shown in Fig 3a. are made, and this is probably the origin of the slightly larger non-linearity.

The energy distribution for the 200 GeV electrons is shown in Fig 4a together with the destal distribution whose width determines the noise. The Gaussian fit made in the range of $2\sigma, \infty)$ to avoid the left hand side tail is shown as an insert in the figure. The noise observed this tower geometry is 170 MeV. The noise value is lower than previously observed, by about factor of two. This reduction in comes from three causes: (1) longer shaping time was used the second and third sections; (2) use of a 14-bit ADC reduces the quantization error; and) use of multiple sampling and optimal filtering analysis essentially redefines the shaping time. iis latter effect is particularly important in the first section, which has short shaping time and nsequently high thermal noise. The resulting fractional energy resolution is shown in Fig 4b function of the electron beam momentum. The electronic noise contribution and the beam read contribution have been subtracted in quadrature for the points in the plot. A fit assuming unctional dependence

$$\frac{\sigma E}{E} = \frac{a}{\sqrt{E}} \oplus \frac{b}{E} \oplus \frac{c}{E^2}.$$

res a=10.2% and b=0.1% for a noise figure of c=170 MeV.

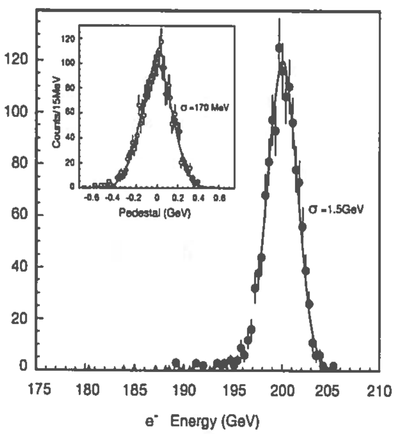

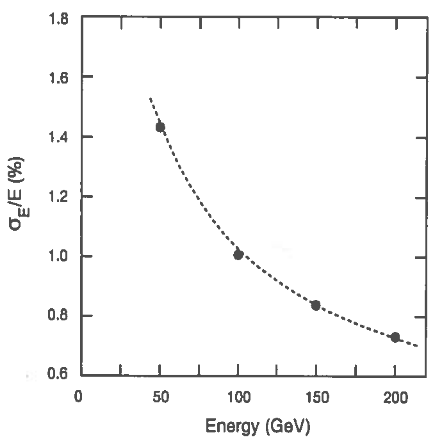

gure 4 (a) Energy spectrum for 200 GeV electrons. The width of the pedestal distribution shown in inset show the noise level for a sum of 60 channels. (b) Energy resolution as function of electron energy. e dotted curve is a function $\frac{\sigma E}{E} = \frac{a}{\sqrt{E}} \oplus \frac{b}{E} \oplus \frac{c}{E^2}$. The values of a=10.2% and b=0.1% are obtained m the fit and c=170 MeV is found from the pedestal distributions.

Timing

easurement of the time origin of calorimeter signals will be an important off-line tool to correctly ociate the events to a particular bunch crossing. Cryogenic calorimeters are known to have cellent timing properties due to the extreme constancy of the waveform. The reconstructed ning from the channel that receives the highest energy deposit shows a resolution of 260 ps. The ning resolution of the calorimeter is actually much better than this, since this value includes contribution from the beam scintillator elements which is estimated to be about the same magnitude.

5 Conclusions

This work shows that the linearity, resolution, and timing measurements are not significantly compromised in a calorimeter equipped with preamplifiers using dynamic gain compression. The fitting of waveforms with amplitude-dependent peaking times has required new techniques to be developed, but there does not appear to be any fundamental difficulty in carrying out the analysis.

In the course of the analysis several lessons were learned. The most difficult hurdle was the translation of the calibration waveform to the signal waveform, especially at the level of precision required to reach the resolution of which the calorimeter is capable. An observed dependence of the reconstructed amplitude on the position of the samples leads us to believe that small perturbations introduced in the calibration waveform by small reactive impedances are large enough to invalidate the approximation of a simple exponential for the calibration current waveform. Consequently an error is made in predicting the shape of the signal waveform. In a calorimeter system which uses multiple samples and optimal filtering, particular care must be paid to the design of the calibration system, to ensure that not only the gain of each channel but also the signal waveform is determined to an accuracy consistent with the performance goals.

6 Acknowledgments

We would like to thank the RD3 collaboration for the use of their facility in which these tests were conducted. In addition to the use of the calorimeter itself and the data acquisition system, many members of the collaboration also helped out in the process of data collection, for which we are especially thankful. This research was supported in part by the U.S. Department of Energy under contract DE-AC02-76CH 00016 at Brookhaven National Laboratory and grant DE FG02 91ER40646 at the University of Pittsburgh.

References

1. B. Aubert *et al.*, Nucl. Inst. and Methods A309(1991)438.
2. B. Aubert *et al.*, Nucl. Inst. and Methods A321(1992)467
3. W.E. Cleland and E.G. Stern, Nucl. Inst. and Methods A338 (1994) 467.
4. O.Benary *et al.*, Nucl. Inst. and Methods 344(1994)363.
5. O. Benary et al., (1996) submitted to NIM.

ascati Physics Series Vol. VI, (pp. 861–872)
I INT. CONF. ON CALORIMETRY IN HEP – Frascati, June 8–14, 1996

A LOW POWER, LARGE DYNAMIC RANGE, CMOS AMPLIFIER AND ANALOG MEMORY FOR CAPACITIVE SENSORS

P. Aspell, D. Barney, P. Bloch, J. Bourotte[1], R. Grabit, P. Jarron, S. Reynaud, A. VanHove, N. Zamiatin[2]

CERN, CH–1211 Geneva 23, Switzerland

1 LPNHE, Ecole Polytechnique, Palaiseau, France

2 Joint Institute for Nuclear Physics, Dubna, Russia

ABSTRACT

This paper has been written to announce the design of a CMOS charge to voltage amplifier and it's integration within an analog memory. Together they provide the necessary front end electronics for the CMS electromagnetic calorimeter (ECAL) preshower detector system in the LHC experiment foreseen at the CERN particle physics laboratory.

The design and measurements of the amplifier realised in a 1.5μm bulk CMOS process as a 16 channel prototype chip are presented. Results show the mean gain and peaking time of <peak_voltage> = 1.74mV/mip, <peak_time> = 18ns with channel to channel variations; σ(peak_voltage) = 8% and σ(peak_time) = 6.5%. The dynamic range is shown to be linear over 400mips with an integral non linearity (INL) = 0.05mV as expressed in terms of sigma from the mean gain over the 400mip range. The measured noise of the amplifier was ENC = 1800+41e/pF with a power consumption of 2.4mW/channel. The amplifier can support extreme levels of leakage current. The gain remains constant for up to 200μA of leakage current.

The integration of this amplifier within a 32 channel, 128 cell analog memory chip "DYN_{LDR}" is then demonstrated. The DYN_{LDR} offers sampling at 40MHz with a storage time of up to 3.2μs. It provides continuous Write/Read access with no dead time. Triggered data is protected within the memory until requested for readout which is performed at 2.5MHz. The memory is designed to have a steerable dc level enabling maximum dynamic range performance. Measurements of the DYN_{LDR} are presented confirming the original amplifier performance. The memory itself has a very low pedestal non uniformity (σ(ped)) of 0.9mV and a gain of 10mV/mip.

1 Introduction

The preshower detector consists of two planes of silicon detectors and sits respectively after 2 and 3 X_0 of lead before the ECAL endcaps. It consists of 176000 60x2mm^2 silicon strips which present an input capacitance per electronic channel of 40pF. The fine granularity of the preshower detector improves the separation of single photon electromagnetic showers from those induced by two close photons produced in the decay of a neutral pion. The measurement of the charge released in the silicon is used to measure the shower barycenter and to correct for the energy deposited in the lead radiator. It can also be used to improve electron-pion separation. The charge produced by 300μm thick silicon detectors can be from 4fC to 1600fC corresponding to 1 to 400 minimum ionising particles (mip).

The FCICON has been designed to act as the front end interface to the preshower detectors. It produces a charge to voltage conversion with linear characteristics from 4fC to 1600fC, it is robust against leakage current and operates with a large capacitive loading on the input. The amplifier is a symmetric ICON (current conveyer) structure with a folded cascode stage offering very low input impedance and high output impedance. This enables the amplifier to be directly connected to the detector reducing considerably cross coupling problems between detectors. The amplifier has a leakage current compensation system which enables the amplifier to work perfectly with many tens of micro amperes of dark current produced by the detectors.

2 The FCICON design

The FCICON shown in Figure 1, is based on the current conveyer principle[1]. It is a symmetric structure with common gate input transistors Mni and Mpi offering a very low impedance at the input node. The signal then passes symmetrically through the cascode transistors Mnc and Mpc before being transferred to two output branches through current mirrors Mp2 and Mn2. Transistors Mp1 and Mn1 are the current sources controlling I_{total} and the cascode transistors are biased in such a way as to control I_{bm}. The two input transistors therefore receive a dc current of I_{total} - I_{bm}. Transistors Mn3,4 and Mp3,4 are the current sources for the output branches each having dc current I_{bm}.

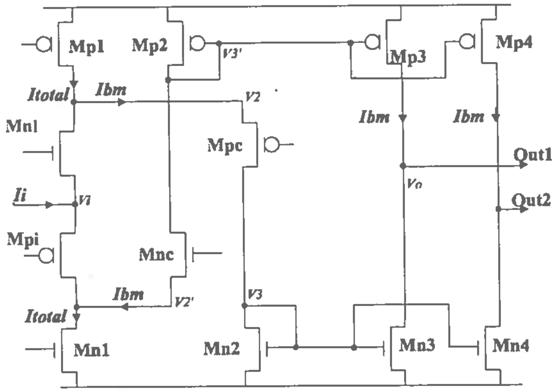

Figure 1: The FCICON.

In the frequency region of interest the noise in the amplifier is dominated by thermal white noise as opposed to 1/f noise. In order to optimise for thermal noise behaviour the input transistors have been sized such that C_i / C_{det} = 1/3[2,3] defining an input capacitance of 13pF. With 200mA of drain current the transistors are working in strong inversion with their source transconductance (gms) as given in (1)[4].

$$gms = n\sqrt{\frac{2\mu \cdot C_{ox} I_d \cdot W}{nL}} \qquad (1)$$

where n is the weak inversion slope, m is mobility, C_{ox} the capacitance of the silicon dioxide under the gate, W the transistor channel width and L the transistor channel length.

The small signal model of the circuit is shown below in Figure 2.

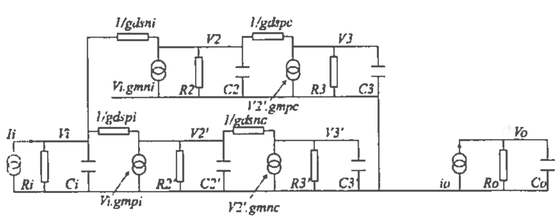

Figure 2: FCICON small signal model.

The common gate structure of the input devices together with their large W/L ratios offers a very low input impedance in the region of 124Ω as given by (2) . This together with C_i (3) produces the fast input time constant (τ) of 1.6ns.

$$R_i = \frac{1}{gms_{in} + gms_{ip}} \tag{2}$$

$$C_i = Cgs_{ni} + Cgs_{pi} \tag{3}$$

In contrast the output impedance (4) is designed to be extremely high at 2.8MW.

$$R_o = \frac{1}{gds_{p3} + gds_{n3}} \tag{4}$$

Where gds is the drain to source conductance. The load impedance then defines the voltage gain of the amplifier (5)

$$\frac{V_o}{V_i} = \left(\frac{gms_{ni} \cdot gm_{n3}}{gm_{n2}} + \frac{gms_{pi} \cdot gm_{p3}}{gm_{p2}} \right) R_o \tag{5}$$

Noise analysis has been done in order to show the equivalent noise charge (ENC)[5] in terms of equivalent series ($e_n^2 s$) (6) and parallel ($i_n^2 p$) (7) noise sources at the input[6].

$$e_n^2{}_s = \frac{8kT \cdot \Gamma}{3(gms_{ni} + gms_{pi})} \tag{6}$$

$$i_n^2{}_p = \frac{6kT}{\Gamma} \left(\sum_{x=1}^{x=3} gm_{n(x)} + \sum_{x=1}^{x=3} gm_{p(x)} \right) \tag{7}$$

Where k is the Boltsman factor, T the temperature and Γ the technology dependant excess noise coefficient.

The series component of the ENC is dominated by the channel thermal noise of the two input transistors and is shown in (8).

$$ENC^2{}_s = \frac{e_n{}^2{}_s \cdot C_i{}^2}{t_m} \tag{8}$$

Vhere t_m is the rise time after an external filter which sets a sampling window of 25ns.

'he parallel component is shown in (9) and is dominated by the noise of the current ources.

$$ENC^2{}_p = \frac{i_n{}^2{}_p \cdot t_m}{3} \tag{9}$$

3 The LDR amplifier chip

The LDR amplifier chip consists of 16 identical channels, each one as shown in Figure 3.

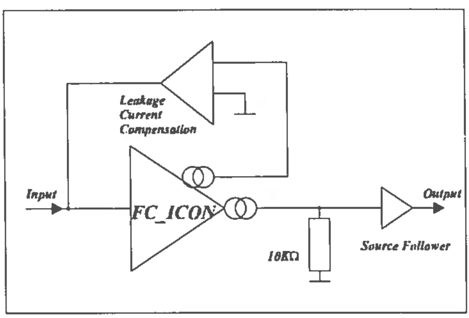

Figure 3: LDR amplifier channel

One output from the FC_ICON is fed to a leakage current compensation unit and it's output is then connected to the FC_ICON input. This enables a dc connection directly to the detector since any leakage current from the detector causes a small change in the output voltage level. This is sensed by the leakage current compensation unit and the leakage current is then diverted into the feedback device. Extremely low frequency behaviour of the feedback amplifier means that the signal current remains unaffected.

The second output from the FC_ICON is connected to a physical resistance to ground. The value of the terminating resistance has been chosen such that the integrating node at the output is completely suppressed and the voltage pulse shape follows directly the form of the detector current pulse. The gain is then determined using equation (5) with the terminating resistance (R_L) in parallel with R_O. This voltage pulse is then transferred off the chip by the voltage buffer.

4 LDR_amp Measured Results

The amplifier was biased with $I_{total} = 250\mu A$, $I_{bm} = 50\mu A$ and a 6V power supply. The overall power consumption was 2.4mW per channel.

The signal response to a 4fC input signal is shown in Figure 4. This is equivalent to the charge produced when 1 mip passes through 300μm of silicon.

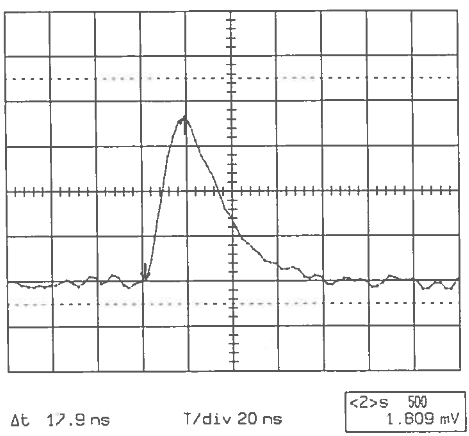

Figure 4: Signal response to 1 mip

The peak of the pulse is reached after 18ns whilst the tail takes approximately 75ns to clear completely. The value of the voltage gain is 1.8mV/mip.

The signal response is linear from -800fC to 800fC (400mips) of input charge and is shown in Figure 5. It has an integral non linearity (INL) of 0.05mV as expressed in terms of sigma from the mean gain over the 400mip range.

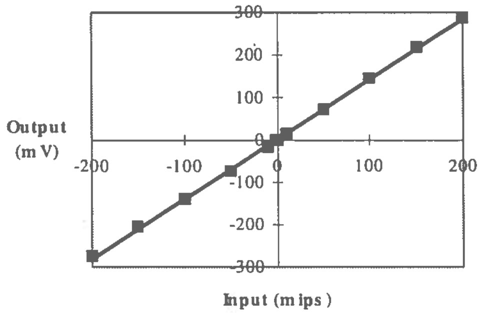

Figure 5: Linearity

The robustness to leakage current is shown in Figure 6 which shows the normalised voltage gain as a function of leakage current.

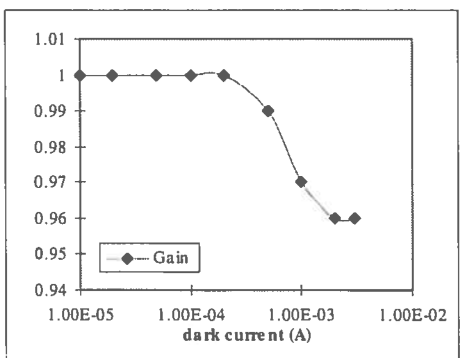

Figure 6: Signal response against leakage current

There is no apparent deteriation in signal response up to a value of 200µA of detector leakage current with less than 5% loss after 1mA. The dc output level remains constant up to 1mA with a noise increase of approximately 1e/µA.

The leakage current expected for 1.2cm^2 silicon strips is 25µA after 10Mrads(Si) of irradiation.

The noise behaviour is shown in Figure 7. The series noise can be seen to be 41e/pF, $(1.04nV(Hz)^{-1/2})$.

The parallel noise is 1800e if one assumes a linear fit to the measured data and approximately 8pF of load capacitance due to bonding, packaging and parasitic board capacitance on the inputs.

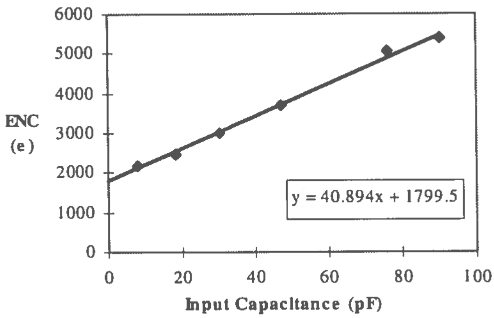

Figure 7: Measured noise of the FCICON

The standard deviation of the measured values across the 16 channels of the chip was $\sigma_{(peak\_voltage)} = 8\%$ and $\sigma_{(peak\_time)} = 6.5\%$.

5 The DYN_{LDR}

The DYN_{LDR} is a large dynamic range analog memory based on the architecture of the DYN1 analog memory chip[7]. The block diagram of the chip is shown in Figure 8.

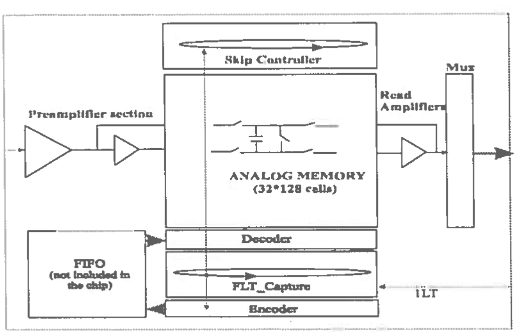

Figure 8: DYN_LDR architecture

It is capable of sampling 32 channels of sensor analog data at the full LHC bunch crossing frequency of 40MHz. 100% of the data is stored for a minimum of 3.2ms and triggered data can be stored for an indefinite time awaiting readout. Readout is performed at the lower frequency of 2.5MHz and takes the form of an analog stream of 32 multiplexed channels from a triggered time slot. The operation is continuous Write/Read and triggers with no dead time.

The chip (photograph in Figure 9) has a total area of 55mm^2.

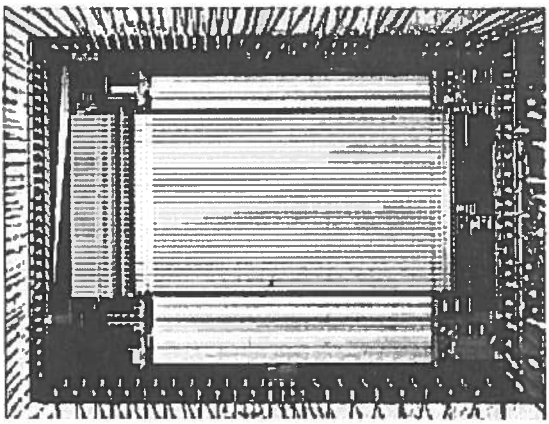

Figure 9: DYN_{LDR} photograph

The analog signal path through the memory is shown in Figure 10.

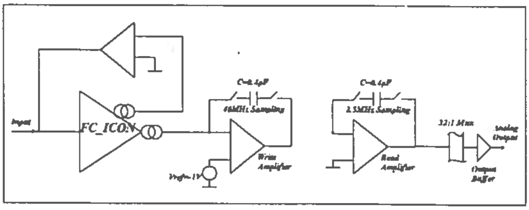

Figure 10: DYN_LDR analog signal path

A single channel consists of a FCICON preamp with a leakage current compensation feedback amplifier. The current produced is then integrated directly onto a memory capacitor by the Write amplifier. The Write amplifier itself is designed to serve both as an integrator and to control the dc level into the memory in order to obtain the maximum dynamic range. The dynamic range is determined by the virtual impedance looking into the switched capacitor memory which forms R_L for the FCICON and the linear sampling range of the switched capacitor matrix. The virtual impedance is a function of the capacitor value and switching frequency whilst the usable range is from the minimum V_{ref} setting of the Write amplifier up to the power rail minus the threshold voltage of the n_type switch transistors. The Read cycle samples the triggered capacitors and the voltage is then multiplexed and buffered out.

A data acquisition system digitises the analog data at 2.5MHz and also controls the latency of the trigger. In this way the memory can be scanned to produce a map of systematic offsets in the array. Part of this map is shown in Figure 11.

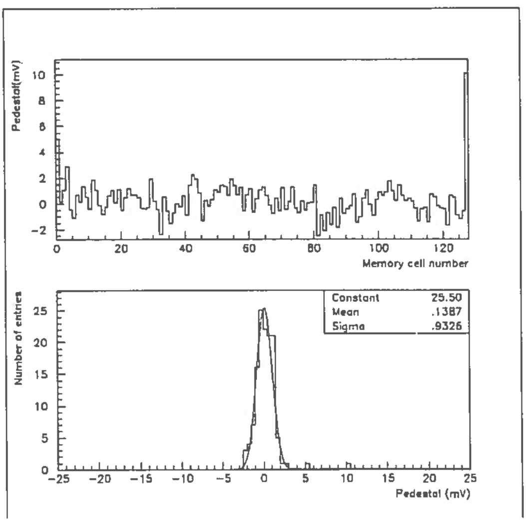

Figure 11: Pedestal variation in one channel.

The top trace shows the pedestal values of 128 cells in one channel as sampled by the ADC. There are peaks at the edge of the memory where there is a break in the symmetry of the structure. A variation in the processing at this point could play a part as could a change in dynamic parasitic pickup. The bottom trace shows the distribution of the samples. The s_{ped} is 0.9mV. These measurements have been performed without the use of common mode baseline subtraction.

The dynamic range is shown in Figure 12. It shows a gain of 9.7mV/mip with an INL of 0.37mV (3.8%) over a 400mip linear range.

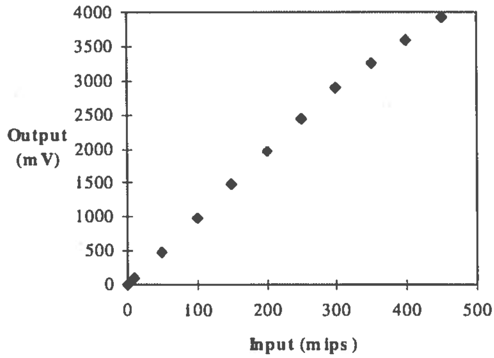

Figure 12: DYN_LDR dynamic range

6 Summary

The design and measurements of a large dynamic range amplifier and it's integration into an analog memory have been presented. The design is optimised for performance with a 40pF detector such as is foreseen for the CMS preshower development. The performance of the chip is compatible with the specifications for a linear front end system for the CMS ECAL preshower detector. The main results are condensed in Tables 1 and 2.

Table 1: LDR_amp main results

LDR_amp	
Linearity	400mips
Integral Non Linearity (INL)	0.05mV
Level of input leakage current compensation	200µA
ENC	1800e+41e/pF

Table 2: DYN_LDR main results

DYN_LDR	
σ_{ped}	0.9mV
Signal gain	9.7mV/mip
Linearity and INL	400mips (INL 0.37mV)

References

1. F.Anghinolfi, P.Aspell, M.Campbell, E.H.M. Heijne, P.Jarron, G.Meddeler, J.C.Santiard, ICON, A current mode preamplifier in CMOS technology for use with high-rate particle detectors.

2. Chang/Sansen, Low-Noise Wide-Band Amplifiers in Bipolar and CMOS Technologies, Kluwer, 1991.

3. E.Nygard, P.Aspell, P.Jarron, P.Weihammer, K.Yoshioka, CMOS low noise amplifier for microstrip readout, design and results, Nuclear Instruments and Methods **A301** (1991) 506-516.

4. E. Vittoz, CMOS VLSI Design course notes EPFL Lausanne 1989

5. Radeka, Signal, noise and resolution in position-sensitive detectors, IEEE trans. on Nuclear Science **Vol. 21** 1974.

6. P.Aspell, F.Faccio, P.Jarron, E.H.M.Heijne, A Fast, Low Power CMOS Amplifier on SOI for Sensor Applications in a Radiation Environment of up to 20Mrad(si). P1636, IEEE Transactions on Nuclear Science **Vol. 42** No 6, Dec.1995.

7. F. Anghinolfi, P.Aspell, R.Bonino, D.Campbell, M. Campbell, A.G.Clark, E.H.M.Heijne, P.Jarron, J.C.Santiard, H.Verweij, DYN1: A 66MHz front end analog memory chip with first level trigger capture for use in future high luminosity particle physics experiments, Nuclear Instruments and Methods, **A344** (1994) 173-179.

rascati Physics Series Vol. VI, (pp. 873–881)
I Int. Conf. on Calorimetry in HEP – Frascati, June 8–14, 1996

NALOGUE OPTICAL LINKS FOR THE FRONT END READ OUT OF THE ATLAS LIQUID ARGON CALORIMETER

B. Dinkespiler, M. Jevaud, E. Monnier, C. Olivetto, S. Tisserant
Centre de Physique des Particules de Marseille, CPPM
IN2P3-CNRS et Université d'Aix Marseille II, Marseille, France
J. Collot, J.Y. Hostachy, P. de Saintignon, Y. Michaud
Institut des Sciences Nucléaires, ISN
IN2P3-CNRS et Université de Grenoble I, Grenoble, France
L.O. Eek, A. Go, B. Lund-Jensen, J. Söderqvist
Royal Institute of Technology, KTH
Physics dept. Frescati, Stockholm, Sweden
J.P. Coulon, V. Tisserand
Laboratoire de l'accélérateur linéaire, LAL
IN2P3-CNRS et Université de Paris XI, Orsay, France

ABSTRACT

'e present results on the development of analogue optical links made in the frame- ork of the ATLAS experiment for the readout of the liquid argon calorimeter. The ecifications for such links and for their various components are described. A link orking in the cold designed for the readout of the liquid argon presampler is first ortly presented with some results from prototype tests. Then the amphasis is it on the presentation of a low cost link designed for the read out of the liquid gon calorimeter at room temperature. A 64 channels demonstrator is presented id preliminary performances are given and compared to specifications required for ie Atlas liquid argon calorimeter. A review of the new developments in progress is nally given.

Introduction

he Atlas liquid argon calorimeter is a highly segmented detector with roughly)0 000 channels. It is located inside a cryostat. The physic signals are transfered ırough cold cables and feedthroughs just outside of the cryostat where they are mplified and shaped. In the same cryostat, in liquid argon, a fine grain presampler also located in front of the calorimeter. In the Technical Proposal of the ATLAS kperiment [1], the physics signals from this presampler were forseen to be amplified ı the cold and then transfered to the outside world using analogue optical links. ome prototype of such links have been built and succesfully tested in test beam. Ve report here on the latest test beam results obtained with these optical link rototypes.

Recently, it has been chosen that no electronic will be located in the cold. Thus a huge number of amplifiers will be located in a reduced space taken from the hadronic calorimeter. The inner detector cables will go through the same space to the outside world. Moreover, the digital read out electronic of the liquid argon calorimeter is also forseen to be there. This high density environment may not be possible for compactness and electromagnetic noise immunity problems. Thus an alternative solution has been studied based on the use of analogue optical links working at room temperature that allow to transfer the amplified physic signals to the outside of the Atlas detector. In the following reports, this read out concept is presented with laboratory results. A 64 channel demonstrator that is under construction is also presented.

2 Cold link for the Atlas presampler

The Atlas presampler detector, located inside the cryostat in front of the liquid argon electromagnetic calorimeter was designed in the Technical Proposal in a high granularity scheme. In such a scheme, the forseen number of channels was of the order of 30000. The handling of such a large number of channels required a compact and low cost readout solution. An analogue optical link readout based on optical fibres was chosen and studied in the framework of the development made for the Atlas experiment [4)]. Such a high density scheme has now been converted to a coarse grain scheme with only 8000 channels and room temperature preamplifiers. Thus in this final version, cold links that we are describing in this section are not needed anymore.

2.1 LHC specifications of the presampler readout

In the fine grain scheme, the signals from the presampler front end preamplifiers are transferred out of the cryostat and then transmitted over several tens of meters to the shaping stage via analogue optical links (one link per channel). These low cost links should have a 12 bit dynamic range, a 2% non linearity, a 50MHz bandwidth and a power dissipation in the cold below 30mW per channel. Furthermore, the high level of radiation at LHC requires such a link (mainly its emitting stage) to withstand a radiation level of roughly 10^{14} neutrons/cm^2 and 1MRad over the 10 years of LHC running.

2.2 Description of the link and prototype results

To fulfil the LHC requirements, the use of a light emitting diode (LED) or a multi-quantum well laser diode (edge emitting) as emitter linked by optical fibres to a

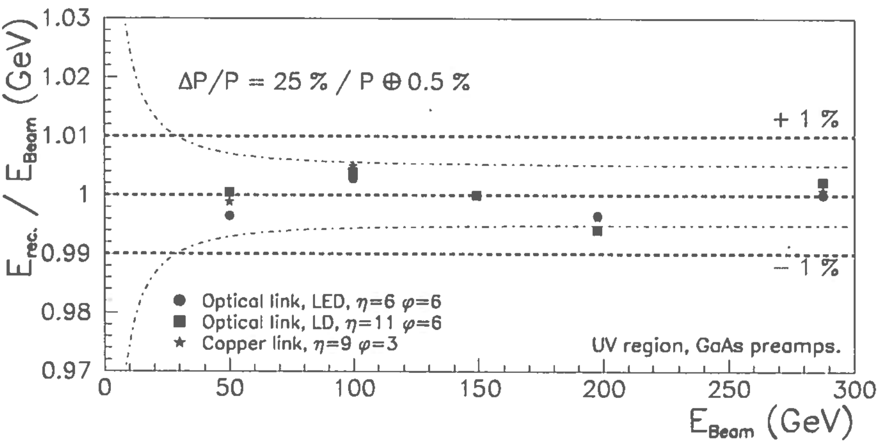

ξure 1: *Comparison of the linearity of the energy response of the so-called "2m" ·ctromagnetic calorimeter prototype and of the fine grain presampler prototype for copper read out and for an optical link read out*

N diode followed by a transimpedance amplifier as receiver has been shown to be equate to the LHC requirements [2, 3]. Several type of links have been built and ccessfully tested in laboratory [2, 3]. A first 32-channel prototype was successfully sted in september 94 during the last Atlas combined beam test (where the liquid gon presampler and electromagnetic calorimeter and the tile hadronic calorimeter re tested together) [3, 4]. Then in september 95, a 64-channel prototype aimed fulfilling the LHC requirements has been connected to a presampler module and sted in beam conditions. 32 channels were equiped with HFE4050 diodes (from oneywell) and 32 with STH51007G MQW laser diodes (1300 nm) (from Siemens). addition we have used a 4 fiber ribbon made by ACOME (with 200/245/250 n silica/fluorine dopped silica/polyimide fibres from CERAMOPTEC) for the 32 FE4050 channels and a HCS 200/230 μm silica/hard clad fibre from Spectran CR-MO200-05) for the laser diode channels. We used small ferule connectors (1 m diameter) called "Termini connectors" from RADIALL to have a more com-ct set up. With such a setup, the links worked perfectly well. No leakage were served from the optical feedthrough made in the same way as for the september test [3, 4]. For the two readout schemes (optical and copper link), the shapped ofile of test pulse signals look identical with 61ns and 63ns rise time. Minimum iising particle signals from 150 GeV muons as been analysed and compared to e noise level got for each readout system. A $S_{mip}/Noise$ ratio of 4.7 has been calculated for optical links to be compared to a ratio of 5.0 for copper links. In addition, test has been performed using electrons at various energies (50, 100, 150, 200 and 300 GeV). The energy resolution of the calorimeter using the presampler informations has been checked to be identical using copper links and optical links except the noise term that was slightly higher (by 10%) for the optical links. This increase of noise is understood. It is only due to the noise induced by the transimpedance stage that was known at that time to be not fully adequate to the PIN diode output characteristics. This can be easily corrected for future applications. The linearity of the energy response as also been measured to be identical for copper and optical links as one can see on figure 1. In conclusion of these studies at cold temperature, analogue optical links can be used in liquid argon for detector readout with very good performances comparable to the performances of copper cable with the advantage of noise imunity and compactness. More studies would have to be performed to adapt these prototype of optical link to low cost mass produced optical links but the concept is valid.

3 Room temperature link for the liquid argon calorimeter

In order to bring alternative solutions to possible compactness and noise problems, our working group is now studying room temperature optical links for the readout of the liquid argon calorimeters.

3.1 LHC specifications for the calorimeters readout

One of the possible solutions for this readout is to follow the preamplifiers, located just outside of the feedthroughs, by a four gain shaper system that reduce the physic signals dynamic range to 10 bits and an additional gain information. The signals shape is squared with a non linearity better than 1% and rise time of a few nano-second – in order to have after 10 ns a precision of a permil in the signal setting –. Then these signals are transmitted with optical links 70 meters away from the external part of the cryostat to be digitized by fast ADCs at the outside of the detector. The high number of forseen channels (i.e. 200 000 links) implies compact and very low cost solutions (a few tens of US dollars per link). Due to the protection of the calorimeter, the maximum local radiation level is relatively low. Such links will have to withstand 10 krad of gammas and 10^{12} (1MeV)neutrons.cm^2 over a period of 10 years of LHC running. But, as it is not forseen to replace dead channels, these devices need to have, in addition a very good life time to work properly for 10 years. All these specification are rather tight, though these links may be used for other less demanding applications such as the transmission of the əl one calorimeter trigger informations or the inner detector signals where for se applications, the dynamic range and the bandwidth are smaller.

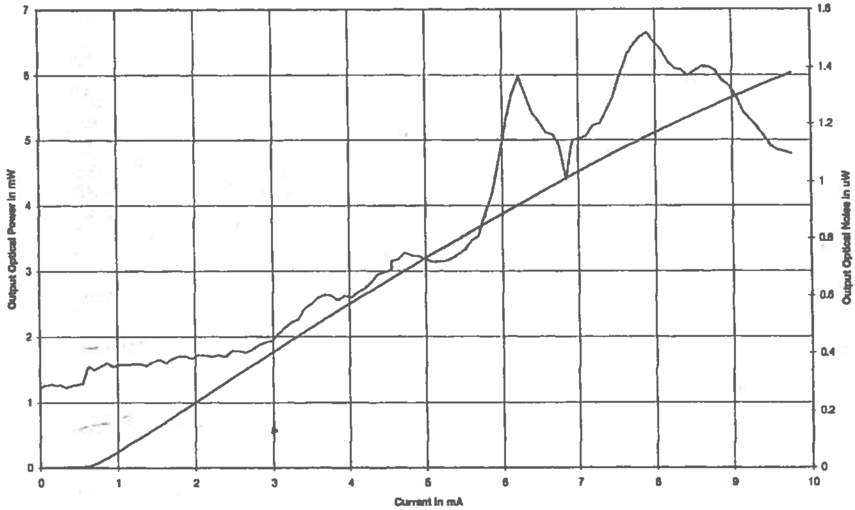

ʒure 2: *960 nm VCSEL output optical power (mW) as a funcion of the input rrent (mA) and on the left vertical axis the corresponding noise level in μW*

! <u>description of the links and laboratory results</u>

ıe forseen link is based on the use of a laser diode for the emitter stage and a PIN ɔde followed by a transimpedance amplifier for the receiver stage. The solution ed for the cold links are not suitable for the performances required now. LEDs are o slow and their power dissipation is too high. Edge emitting quantum well laser ɔdes have a too high threshold point at room temperature and they are difficult produce in array at low cost.

Thus, to reach the specified performances, we have decided to use Vertical ırface Emitting Laser diodes so-called VCSELs. These devices have the advantage be available directly in arrays that may have already been tested at the wafr level. This can reduce a lot the producing costs. The other advantage is that ey have a very low threshold current, typicaly between a few micro amperes to a w milli amperes which leads to a low power dissipation below $5mW$. Very good 'etime, uniformity [5] and radiation hardness [3] have been as well reported. In adtion one can find some that have a good linearity. This VCSELs have a wavelength between 780 nm to 960 nm. Recent published results [7, 8, 5, 6] suggested us that an optical link based on the use of such VCSELs could fulfil our requirements. Thus we have tested VCSELs coming from various manufacters (Vixel, Honeywell, HP, Motorola, Sandia Labs...) and we concluded that lateral oxidized VCSELs made by MOCVD technics from the National Sandia Laboratories are those which have the best performances. Waiting for 850 nm devices that are more suitable to our specifications, we have tested devices runing at 960 nm that behaved properly as one can see on figure 2 that represents the static output optical power (recorded through the air with a calibrated optical head (from HP)) and the corresponding noise level as a function of the input current. A typical noise level of $0.3\mu W$ just after the threshold point compared to a maximum linear level of $2mW$ shows that it is possible, with this lateral oxidized devices, to get 12 bits dynamic range. The coupling of the optical power into the fibre should not be a problem due to the small beam divergence (roughly 10%) of these devices that allow a typical 90% coupling efficiency. However, the fine effect of the coupling into a fibre has still to be fully checked on our final chip. We are now testing 850nm devices that have very recently been produced and that are claimed to have similar performances compare to 960nm devices. We have chosen to use 850nm devices for our system because, with such a wavelength, the receiving stage can be made with silicon PIN diodes that are cheaper. In addition, many tests are underway on a fair number of VCSELs (500) to measure their uniformity, their life time and their radiation hardness. Since these are long term measurements, we do not have results yet.

The choice of the wavelength allows us to use standard PIN diodes. The level of radiation is low enough to use standard graded index fibres. In order to measure all the performances of such a concept of optical link, we have started to build 64 channels demonstrator that fulfils LHC requirements and that will be available by september 96.

3.3 description of the demonstrator

This demonstrator has a modularity of 8 channels and represents in all 64 channels. The basic design of this prototype is given on figure 3. The emitter stage is based on 850 nm lateral oxidized VCSELs packaged in arrays of 8 elements that have been produced for us by the Sandia National Laboratories. The packaging is designed to handle directly a multi-fibre connector such as the MT connector (from Europtics) linked to a 8-fibre ribbon. The packaging used for the receiver stage has been produced by AME (norway) to handle MT connectors. The packaging for the emitter is under development. Other connector and packaging developments are also in progress to rich low cost and easy to mass produce solutions. The 70m ruggedised

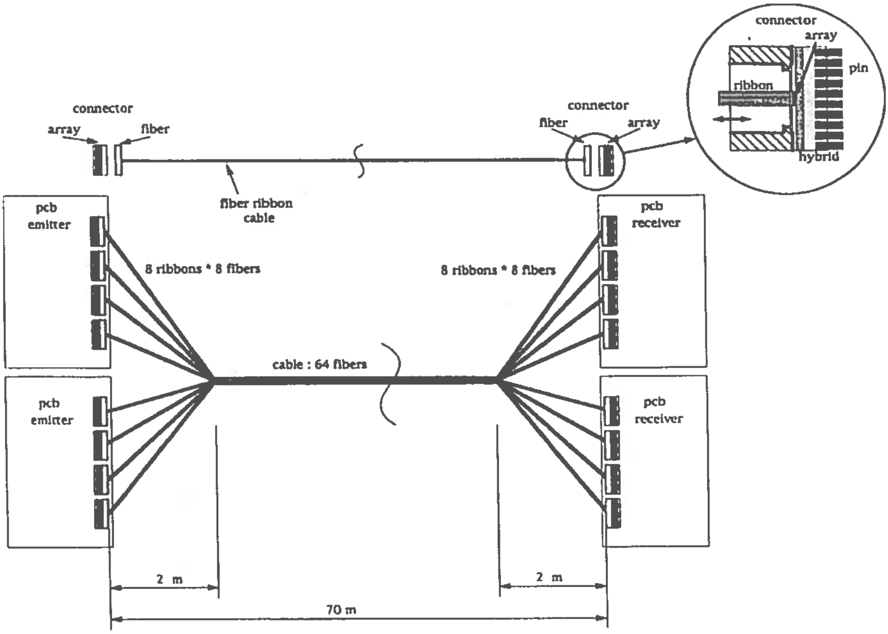

gure 3: *General design of a protype of room temperature optical links for the adout of the liquid argon calorimeters.*

›bon has been produced by ACOME with standard 62.5/125/250 μm graded index ultimode fibres, a 50/125/250 μm fibre ribbon has also been made by ACOME r evaluation. At the receiving end, the ribbons are connected with multi-fibre nnectors to remote receivers consisting of PIN diode arrays (8 elements) followed · high speed, low noise ($< 1pA/\sqrt{Hz}$) transimpedance amplifiers. The PIN diode rays have been produced by AME. The silicon chip has 8 PIN diodes with an tive area of $175\mu m^2$. A rise time below $0.7ns$ and a cross talk below 0.5% have en measured. They are mounted on a 16-pins ceramic plate equiped with a direct T connector handling as shown on the figure 4. One can see a 8-channel receiving ›ard equipped with transimpedances, PIN diode array and a fibre ribbon. The oduction of the eight receiving boards is going on and they will be available by .d of august for final tests. The emitter board is still under development and a ıal solution will be available begining of September to equip the emitting boards. he complete evaluation of the demonstrator will performed then.

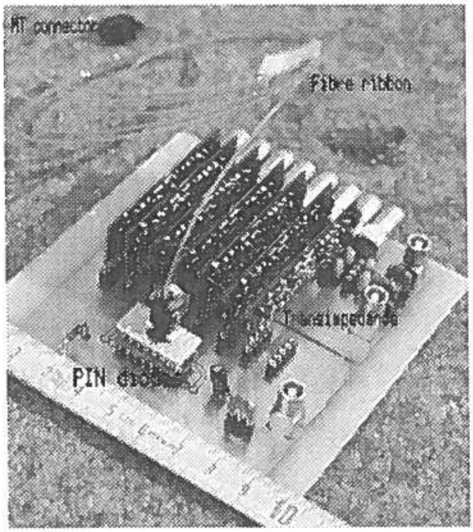

Figure 4: *Picture of one 8-channel receiving board of the demonstartor.*

4 Conclusion

An analogue optical link with more than 12 bits dynamic range and less than 2% non linearity with an emitting stage working in liquid argon has been presented. Such system has been sucessfully tested in laboratory condition as well as in test beam conditions. Among all the channels tested (more than 100 links), no bad behaviour has been observed. The test beam results showed the possibility to use such optical links for the read out of liquid argon detectors.

Room temperature optical links designed for the readout of the liquid argon calorimeters have been recently developed by our group. Laboratory measurements have demonstrated the validity of this readout concept based on the use of arrays of lateral oxided VCSEL type emitter and arrays of PIN diode type receiver. A 64-channel demonstrator is underproduction and will be available for complete evaluation in September 96. The first receiving board has already been produced and a first evaluation showed that it fulfil the specifications. In adition several developments are going on to improve the connectors and the packaging. Furthermore, uniformity, life time and radiation hardness are underway to qualify the lateral oxidized VCSEL to the LHC specifications.

We are confident that by october 1996, a 64 channel prototype will demonstrate the feasability to use analogue optical link for the readout of the ATLAS liquid gon calorimeters.

eferences

. Atlas Technical Proposal, CERN/LHCC/94-43, LHCC/P2 (December 1994).

. Analog optical links in liquid argon, Sylvain Tisserant on behalf of the RD3 Collaboration, Proceedings of the fifth international conference on calorimetry in high energy physics, BNL (Sept. 1994).

. Analogue optical links for the liquid argon calorimeters, B. Dinkespiler et al., Proceedings of the first workshop on electronics for LHC experiments, Lisbon, CERN/LHCC/95-56 (Oct. 95).

. A fine-grain liquid argon preshower detector and an analogue optical link for its read-out, L.O. Eek on behalf of the Atlas/Larg collaboration, Proceedings of the international europhysics conference on high energy physics, Brussel (July 1995).

. Fabrication, testing, and reliability of semiconductor lasers, M. Fallahi and S. C. Wang editors, Proceeding of the OE/LASE '96 conference Jan./Feb. 96, SPIE proceedings **2683**.

. Optoelectronic interconnects and packaging, R. T. Chen, P. S. Guilfoyle editors, Proceeding of the OE/LASE '96 conference Jan./Feb. 96, SPIE proceedings, Critical Reviews of Optical Science and Technology **CR62**.

. R. A. Morgan and Mary K. Hibbs-brenner, Proceeding of the IEEE workshop on optical interconnects in Santa Fe (1995), 65-93 SPIE **2398**.

. A selectively Oxidized VCSEL with 50% power coupling efficiency, K. Lear et al., Electronics Letters **31** $n^0 3$ (Feb. 95).

scati Physics Series Vol. VI, (pp. 883–892)
INT. CONF. ON CALORIMETRY IN HEP – Frascati, June 8–14, 1996

EALIZATION AND TEST OF A FAST DIGITAL READOUT FOR LHC CALORIMETERS: PRESENT PERFORMANCES

A. Savoy-Navarro
PNHE Universites de Paris VI-VII and IN2P3/CNRS, Paris, France

ABSTRACT

'ast digital readout architecture characterized by an early digitization of the in-
ɿing signals at the front-end, is a very powerful solution for the processing of
information of the LHC calorimetry. The design and the realization of such a
.llenging system are discussed here as well as the preliminary results presently
ained with the first prototypes.

Introduction

ȝeneric concept of a fast digital readout (FDR) has been initiated by the RD16 R
D Collaboration [1]. It has been developed within RD16 and also in closer and
ser contact, since about two years, with ATLAS and CMS experiments for the
C [2]. It is characterized by an early digitization of the incoming signals at the
nt-end.

The development of the readout for the calorimeters proposed for the LHC
ɔeriments is a highly challenging task as it must address a number of demanding
ues:

- a large number of channels, typically order of 10^5
- a high energy resolution, over a large dynamic range, typically from a few tens of MeV up to a few TeV

- a high acquisition speed given by the 40 MHz Bunch Crossing (BCO) rate of the collider
- a harsh environment (radiation) and lack of access to the electronics mounted on the detectors.
- the information provided by the FDR to the first-level trigger process must be precise enough to guarantee that the required reduction factor of 10^3 - 10^4 can be achieved without a significant loss of relevant physics events.

Therefore the key issues for a FDR in LHC experiments are: a fast digitization (40 MHz); a good coverage of the full dynamic range, possibly up to 17-18 bits; a powerful digital processing that includes the LV1 trigger processing working synchronously at 40 MHz and the DAQ processing in asynchronous mode and with high performances for both cases; a requirement of "applicability" to large scale detectors that implies the need for the FDR to be reliable, compact and fitting well within the overall experiment.

The design, as well as the realization of such a system are presented in Section 2. In Section 3 are discussed the preliminary results of the tests presently performed on the first prototypes. We conclude with the future prospects.

2 Design and realization of a FDR

A number of circuits with separate functionality constitutes the FDR architecture. This architecture as well as the ways to build it are discussed in this section.

2.1 Description of the main components of a FDR

The main components of the FDR architecture are schematized in the simplified block diagram shown in Fig. 1 (for more details see [3]).

A FDR is made of: *the digitizer*, i.e. a fast A/D converter that must be preceeded by an adaptation stage, located at the very front end (VFE) electronics; *the digital pipeline*, i.e. a dynamically addressed memory to store the data, plus, eventually, a look-up-table (LUT) if there is a need for expanding the data to the full dynamic range representation; *the digital processing* required to prepare the data for both the Level-1 triggering and the DAQ. It is done using Finite Impulse Response (FIR) digital filters; *a set of controllers*, including a readout controller to prepare the data for the DAQ, an address generator that handles the addressing of

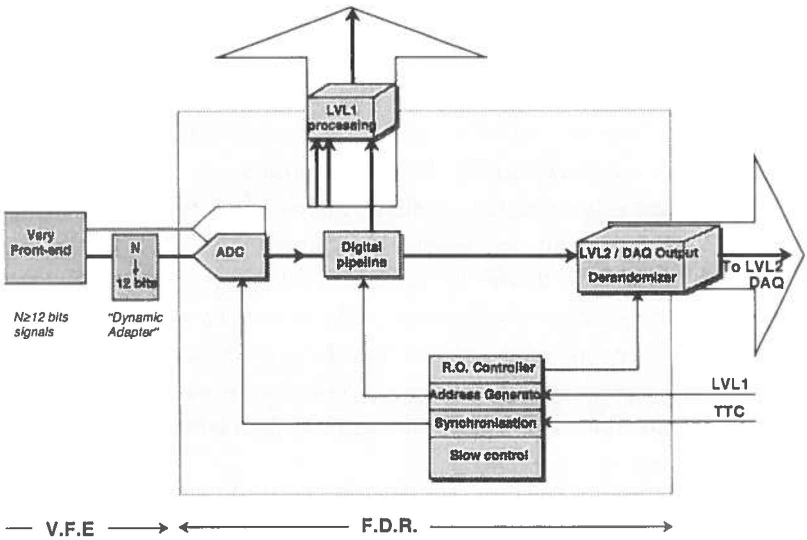

Figure 1: Simplified block diagram of the FDR architecture

ɜ pipelined memory according to the Level-1 trigger decisions, a controller for the nchronisation of the overall system and a slow control device.

!.1 *Realization of the fast digitization in the required dynamic range*

ıe two key issues for the needed A/D converter are the required high speed (40 Hz) and the possibly large dynamic range coverage (in most cases 16 bits or more). is clear that we must rely on advanced high tech industry to develop such per- ·ming devices. Due in particular to the flourishing market of cellulars, there are day, two commercially available 12 bits-40MHz ADCs: the AD 9042 (Analog De- ːe) and the ADS 800 (Burr Brown). The AD 9042 is a bipolar three steps flash ƆC specified at 20 MHz with a latency corresponding to 3 BCOs (each BCO cor- ɜponding to 25 ns). The ADS 800 is a CMOS parallel-successive approach (PSA) ƆC with a latency of 6 BCOs, thanks to the fact that it works on both the leading d the falling edges. From the point of view of signal to noise ratio, differential d integral non-linearities, the AD 9042 is better than the ADS 800. But in terms power dissipation, the ADS 800 is superior; it dissipates 390 mW per channel to compared with 600 mW for the AD 9042.

In order to tune the dynamic range to be covered by the detectors to the

actual available A/D converters, various solutions are developed at the VFE electronics, according to the specific needs of each detector (see contributions at this conference). There are two main types of such"dynamic range adaptators": the multi-gain shapers with or without fast switch and the compressors.
Deciding between these two schemes implies to choose between applying or not a compression to the incoming signals. Without compression there is no need for a LUT at the pipeline stage and the pipelined memory has to handle only 13 bits, hence less data at the output, less latency and much easier calibration. The main disadvantage is the need for twice the number of ADCs (i.e. cost and power dissipation) or a fast switch before the digitizer (difficult to make and rather expensive).
In conclusion there are different ways to handle large dynamic range (16 bits or more) with a fast digital readout, using compression or no compression schemes (according to the decision of each detector) and commercial 12 bits-40 MHz ADCs.

2.2 The VHDL design methodology to realize the digital components

The ASICs that constitute the digital components of a FDR are: the digital pipeline, the controllers and the digital processors for the Level-1 triggering and for the DAQ system. To design and build these various chips, a top-down approach making use of a complete set of ASIC design tools has been applied. This approach has proved to be very powerful and efficient.
The design methodology consists of the following main steps: the VHDL modeling and Logic simulation, the Synthesis and Dynamic Simulation, the Testability Insertion and finally the Place-Route and Post Simulation. This approach generates a VHDL model which is independent of CAD platforms and target technology

- VHDL modeling and Logic simulation: the block diagram describing the main functions of the circuit and its connections with the rest of the system are translated into a behavioural VHDL model. This model is then processed through global simulations that allow a first tuning and check.

- Synthesis and dynamic simulation: the design is synthesized according to the hierarchy of the description. The timing constraints need to be established to drive the optimizing phase. Each block written in VHDL goes through the synthesizer and is simulated with estimated delays for the logic elements. Each part is then assembled and the overall chip is finally simulated with the stimuli created by its high level VHDL model.

- Testability insertion: for modern complex circuits it is necessary to define an efficient test procedure to determine with maximum confidence if the fabricated circuits are operational. The testability procedure used is based on Built In Self Tests (BIST) for the memories and scan test chains for the surrounding logic. This ensures a coverage rate of at least 85% using about 40,000 test vectors per chip.

- Place-Route and Post Simulation: the layout consists of placing the blocks in a fashion that respects functionality and attempts to minimize the overall surface if not to fit given dimensions. Back annotation requires tools to extract actual loads on each net. With this information, the simulation netlist can be completed and the results of the Post Simulation are very close to the behaviour of the physical circuit.

2.1 *Production of the ASICs*

he design methodology described in the previous subsection, has been applied to :oduce the digital processing components of the FDR system. As a result, five ıips have been submitted to foundry, i.e. the Digital Pipeline ASIC (including the UT and the memory), the level-1 and DAQ filters, the memory and the readout ›ntroller presently assembled in a single chip and the slow control device. The size ıd complexity of the produced ASICs are summarized in Table 1. All the chips

ASIC	# of transistor	area (mm^2)	working speed (MHz)
Filters	2×10^5	30	> 40 MHz
Digital Pipeline	2.5×10^5	60	40 MHz
Memory and readout controllers	2×10^5	40	40 MHz
slow control	1×10^5	30	up to 14 MHz

Table 1: Main features of the ASICs

ave been produced in the ES2 0.7 μm CMOS process with testability leading to 00% functional chips. Moreover the used methodology provides efficient tools:

- To simulate and test the functioning of each ASIC as well as of the overall readout architecture.
- To adapt/modify the design circuits according to the specific needs of each experiment.

3 Tests and Present Performances

So far, the two main parts of the FDR i.e. the digitizer and the digital processing have been tested independently. The tests of functioning of the whole FDR system on a restricted number of channels have been performed at the VHDL simulation level and are now in progress both at the Lab test bench and in real test beam conditions. Due to the lack of space, a very brief review of the results currently obtained is given in this section; for more details we refer to [3].

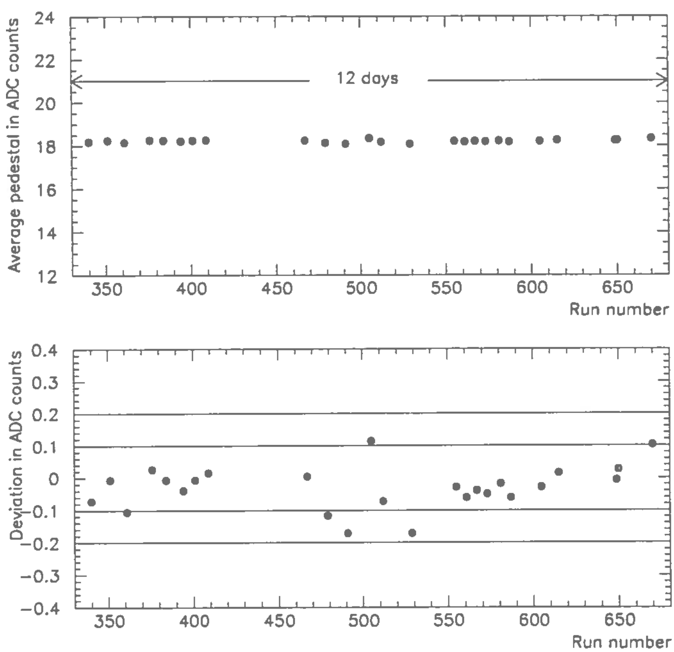

Figure 2: Pedestal stability during 12 days

3.1 Tests of the digitizer

A prototype of the digitization part of a FDR has been tested in high energy test beams (ranging from 20 to 300 GeV), at the SPS-CERN, since 1994, on various prototypes of the LHC calorimetry. The A/D prototype is a 10 bit-40 MHz PSA-ADC developed by RD16. It is preceeded by a four-gain compressor (15-16 bits to 10 ts) also developed by RD16. It has a minimal digital processing part consisting of FOs read out through VME.

The performances of this specific fast A/D converter scheme have been ıdied in terms of: noise and stability, imaging properties, linearity and calibration ues, resolution. With no additional gain at its input, the noise of the overall adout chain is in average of 1.2 ADC counts; When and extra gain of 10 is added input, the noise rises up to 1.8-2.4 ADC counts depending the channel. This timate includes the intrinsic FDR noise as well as the preamplifier and shaper noise d any external induced noise. It has been measured in very realistic test beam nditions. The pedestal data give an estimate of the stability of the electronics. ver a period of 12 days, it has been demonstrated to vary at most by ± 0.2 ADC unt (see Fig. 2).
ıe prototypes that have been tested, demonstrate very high imaging capabilities. allows to already visualize on-line, in details, the pulse shapes and even to detect erlapping events with a high accuracy (see Fig. 3).

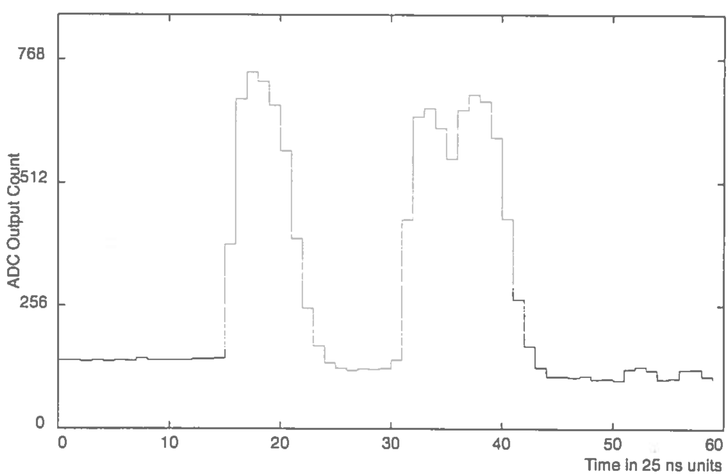

Figure 3: Online imaging properties of a fast digital readout

Moreover it permits to measure relevant parameters characterizing both e detector and its associated VFE electronics, such as drift times or shaping time nstants.
ıe linearity is another crucial parameter. The particular case that has been stud- l so far, includes a four gain compression stage. Therefore it implies four linear gions of functioning, depending on the amplitude of the signals. Each corresponds a different gain. The linearity is thus determined by the use of a LUT that con- ıns the transfer function of each channel. A way to determine the LUT is using

the test pulse data. Very detailed test pulse calibrations have been experimented, implying a large number of steps (up to 140) to cover the overall dynamic range. The analysis of these calibrations is underway. It will allow to answer the following questions about the calibration when a compression is applied to the incoming signals, namely: How many points are actually needed to determine the LUTs? Is it necessary to have one LUT per channel? How dependent is the LUT on the energy estimator? How stable are the LUTs? (monitoring and calibration issues); What is the sensitivity of the results to a detailed reconstruction of the LUTs?
All these questions are important, especially when considering the case of 10^5 or more channels...It also depends on the resolution of the detector. Therefore it is particularly crucial for the e.m. calorimeters. These calibration issues are of major importance when deciding on a scheme with or without compression at the VFE.

The expected energy resolution is achieved within the limits of the presently available prototypes, i.e. the 10 bits A/D and the compression scheme currently used. These preliminary results are very encouraging and indicate that a 12 bit A/D plus an optimized dynamic range coverage will do the job.

3.2 Tests of the digital processing part

Each digital component including the various controllers have been tested. As an example, we briefly discuss the case of the digital processor for the Level-1 trigger. It is made using FIR digital filters. The tests on the functioning of these chips have been performed so far at the Lab test bench and using detailed VHDL simulations. This is also the case for all the other digital components.
The studies have been performed on the following main issues: functioning i.e. determination of the energy, the bunch crossing identification (BCID) and the flags; contribution to the resolution; effect of the pile-up and overlapping events on the estimate of the energy and the BCID and ways to handle difficult cases such as, for example, compressed signals.
The presently built Level-1 trigger processor has been tested to work up to at least 67 MHz, with very high performances on all the above issues. Fig. 4 shows, as an example, the response of the filter ASIC to a set of input frames (signals recorded in a test beam period on a prototype of the ATLAS electromagnetic calorimeter). The upper part represents the sequence of the three input channels of the filter where, in this case, the third channel is not used. The lower part shows the corresponding output at the filter, as well as the generated flags.

The full functionality of the overall FDR system, made of the presently ·oduced ASICs, has been tested using detailed and reliable VHDL simulations. It ιs also been partially tested at the Lab test bench. The tests of the full FDR ·stem at the Lab test bench and the test beam are now underway.

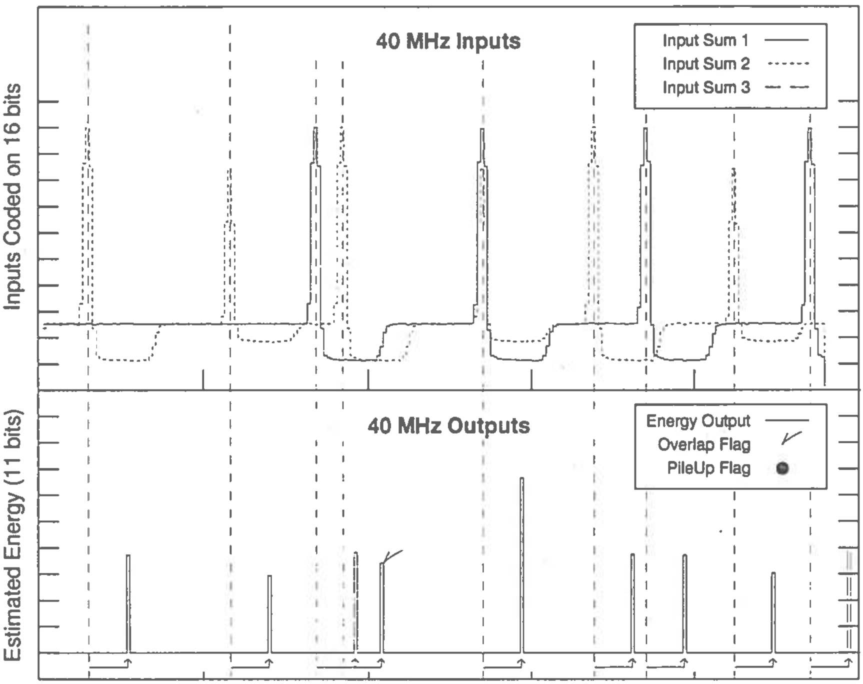

·gure 4: Level-1 filtering of Liquid Argon pulses at 40 MHz. The incoming signals e on the upper part, the output filtered data are on the lower part

Future prospects and concluding remarks

he real challenge is the "applicability" of such a FDR system to large scale LHC :periments. This means that the FDR has to fulfil the following requirements:

- *Integrability:* The FDR must fit with the design of the overall experiment, i.e. in terms of electromagnetic compatibility, cooling, mechanical positionning, power supplies, space. It must also fit with the Level-1 trigger and DAQ system architectures.
  The FDR is well suited to fulfil these integration requirements.

- *Compacticity:* Physics requires hermeticity and no dead material and there is a lack of space in the detector. As a consequence, the FDR must be as compact as possible.
  Microsystems and Multi-Chip-Module technology used to build the FDR are the most efficient way to have compact electronics.

- *Reliability:* Digital devices are easily implemented with error encoding, redundancy. They are fully programmable, thus easy to access and monitor and re-adjust whenever needed.
  Thanks to these various available facilities of the digital devices, they are very reliable.

In conclusion, commercial 12 bits-40MHz A/D converters are available now, allowing to solve the dynamic range (together with the appropriate dynamic adaptator at the VFE) and the resolution issues.
The top-down design methodology, based on an extensive use of the modern CAD tools, has proved to be the best way to build the FDR architecture. It is particularly suitable for future upgrades of both the detector and the technologies.
Modern high tech, supported by Industry, allows to fulfil the challenging requirements of the readout for calorimetry for LHC.
The strength of the digital processing allows an accurate, compact and elegant way to solve the problem of a full and efficient processing of the calorimetry signals in the harsh LHC environment. A full digital processing fits easily with the detector mechanical design, the Level-1 trigger and DAQ architectures of any experiment; Moreover it provides a high degree of reliablity and flexibility.

Digital is certainly the way to go!

References

1. H. Alexanian et al., NIM A357 (1995) 309-317
   R. Benetta et al., CERN/LHCC/95-28, April 1995 and references therein.

2. G.L. Bayatian et al., The CMS Collaboration, Technical Proposal, CERN/LHCC/94-38/LHCC/P1, Dec. 1994
   W.W. Armstrong et al., The ATLAS Collaboration, Technical Proposal, CERN/LHCC/94-43/LHCC/P2, Dec. 1994

3. ATLAS Internal Notes in preparation

ascati Physics Series Vol. VI, (pp. 893–903)
INT. CONF. ON CALORIMETRY IN HEP – Frascati, June 8–14, 1996

ADIATION HARDNESS OF GaAs PREAMPLIFIERS FOR LIQUID ARGON CALORIMETRY AT LHC

Karl Jakobs*
Max-Planck-Institut für Physik, Föhringer Ring 6, 80805 München

representing the MPI Munich - JINR Dubna Collaboration on Radiation Hardness Tests

ABSTRACT

ıld preamplifiers, designed in GaAs technology, have been proposed in the readout ain of the hadronic liquid argon end-cap calorimeter of the ATLAS experiment LHC. The preamplifiers immersed in the liquid argon must withstand the hos- radiation environment during the operation of the LHC machine at the highest ninosities for the whole expected lifetime of the experiment. The proposed pream- fiers have been exposed to a high fluence of fast neutrons and to a high dose of γ liation. No significant deterioration has been observed for a neutron fluence up $\sim 2{\cdot}10^{14}$ n cm^{-2} and up to 31 kGy, the highest γ dose rate measured. Also only noderate increase of the equivalent noise current has been seen for the radiation els relevant for the operation in the ATLAS experiment.

Introduction

ıny components of the front-end electronics of the ATLAS detector at LHC will located in the high radiation field of photons and neutrons expected at the high ninosity running. One example are the preamplifiers immersed in the cryostat of hadronic liquid argon end-cap calorimeter. At the expected high luminosity of $= 1.0 \cdot 10^{34}$ cm^{-2}s^{-1} a maximum yearly dose of 12 kGy yr^{-1} and a neutron fluence $6.1{\cdot}10^{14}$ n cm^{-2} yr^{-1} are expected in the hadronic endcaps [1]. These radiation els strongly depend on the location inside the calorimeter. They decrease signif- ntly towards central rapidity and with increasing depth inside the calorimeter. e preamplifiers of the hadronic end-cap calorimeter will be located at the circum- ence of the calorimeter wheels. At this position, at a radius of ~ 2 m from the

*now at Institut für Physik, Universität Mainz, Staudinger Weg 7, 55099 Mainz, Germany

beam line, integrated maximum radiation levels of 0.3 kGy and $0.3 \cdot 10^{14}$ n cm^{-2} are expected for an operation period of 10 years at high luminosity.

The corresponding electronics must withstand these radiation levels with a minimum deterioration of its performance in terms of gain, speed and linearity and with a small acceptable increase of noise. In the framework of the RD33 project [2)] current sensitive preamplifiers based on GaAs MESFETs have been developed. They can be considered as prototypes for the final preamplifiers which will be used in the hadronic end-cap calorimeter.

In order to address the radiation hardness question, the RD33 preamplifiers were exposed to an integrated neutron fluence of $7 \cdot 10^{14}$ n cm^{-2} and to a γ dose of 31 kGy. The irradiation was performed at nuclear power reactors at the Joint Institute of Nuclear Research at Dubna. Parameters of the preamplifiers, like the transfer function, the rise time, the linearity and the equivalent noise current, were measured before and during the irradiation. The circuits were operated at liquid nitrogen temperatures, close to their final working point in the experiment. The results of these measurements are presented in the following, after a brief description of the Dubna irradiation facilities and the measurement setup.

2 Irradiation at Dubna

The irradiation has been carried out at the pulsed nuclear reactors IBR-2 and IBR-30 at Dubna [3)]. Via a horizontal extraction channel from the reactor core the reactor IBR-2 delivered a neutron fluence of $0.9 \cdot 10^{10}$ n cm^{-2}s^{-1}. All numbers on neutron fluences quoted correspond to equivalent fluences of neutrons with an energy of 1 MeV. They have been obtained by convoluting the measured neutron energy spectrum with energy dependent correction factors as determined in Ref. [4)]. The average kinetic energy has been found to be $\sim$ 1.5 MeV with a spectrum as shown in Fig.1. The uncertainty on the evaluated neutron fluences has been estimated to be at the level of $\pm$15%. The γ radiation which is also produced in the nuclear reactions was suppressed by absorption in a 5 cm thick Pb-filter. The remaining total γ dose was measured after the irradiation to be at the level of 1.4 kGy.

The photon irradiation has been performed at the reactor IBR-30, where a stronger suppression of the neutron component was possible. The fluence of fast neutrons was attenuated by a combination of a paraffin moderator and a cadmium absorber, where neutrons were absorbed by a n-γ reaction. The deexitation of the nuclei produced on top of the prompt γ component a second one with a different energy behaviour. Folding the two components together, the average photon energy was found to be in the range between 1.5-2.0 MeV. The γ dose rate was measured to be 0.3 kGy/h. During the measurement period a total dose of (31 $\pm$ 3) kGy

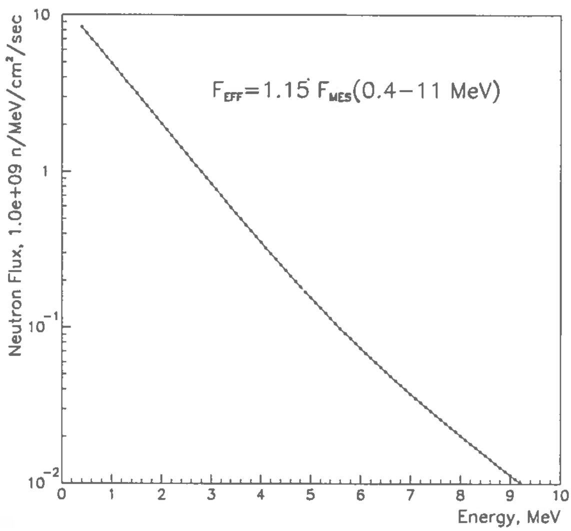

Figure 1: *Spectrum of the kinetic energy of the neutrons from reactor IBR-2.*

s collected in seven steps. At the end of the irradiation the integrated underlying utron fluence was measured to be $0.5 \cdot 10^{14}$ n cm^{-2}.

Measurement Setup

iangular pulses from a pulse generator simulating the response of a liquid argon p to the passage of a particle were sent into the GaAs preamplifiers which were iced on a board inside a cryostat close to the reactor core. The signal output from preamplifiers was fed into a shaper system [5] which allowed for the selection of iping times τ in the range between 10 ns and 10 μs. The shaper output was sent o a digital scope which was read out for further analysis by a computer system. the board in the cryostat two GaAs preamplifier chips with four channels each re mounted. In order to study the dependence of the radiation damage on the ector capacitance, three different values, 0, 125, and 330 pF, were used at the out of the preamplifiers. The value of 125 pF is typical for the operation in hadronic endcap calorimeter of the ATLAS experiment. For all channels the nsfer function, i.e. the output voltage as a function of the input current, the rise ie (τ_p) of the pulse after the shaper and the equivalent noise current (ENI) were asured. All measurements were performed as a function of the shaping time. The measured values of the equivalent noise current were compared to the expectations for a current sensitive amplifiers which is given by:

$$ENI \; = \; ENI(C_d, \tau_p) \; = \; \frac{\alpha}{\tau_p^{1.5}} \oplus \frac{\beta}{\tau_p^{0.5}} \tag{1}$$

It must be noted that the experimental setup was sensitive to pickup noise, so that the noise measurements had to be limited to shaping times below 1 μs.

4 Transfer Function and Rise Time

The transfer function was measured for each shaping time and after each radiation step. This measurement monitors the gain stability of the preamplifiers during the irradiation. The results obtained are presented in Fig.2 for both neutron and γ irradiation. Shown are the ratios of the transfer function values measured at each radiation step normalized to the ones measured before irradiation. The shaping time τ is given as a parameter on the plots. For stable operation no deviations from unity should occur. As can be seen from Fig.2a no strong deviations from the value of 1 are found in the case of γ irradiation even up to the highest γ dose values. Also for the largest detector capacitance the measured deviations from 1 do not exceed 20%. Much stronger deviations are found however under neutron irradiation beyond integrated fluences of $\sim 2{\cdot}10^{14}$ n cm^{-2}. In particular for the channels with high capacitance a significant drop in the response is observed. This could be an indication that the transconductance of the main transistor has changed under neutron irradiation.

A similar behaviour is found in the measurement of the rise time of the pulse, defined as the time needed for the pulse to go from the 5% level to the peak. In Fig.3 the measured rise time after the shaper is shown as a function of the irradiation for both photons and neutrons. Since the rise time is measured after the shaper a convolution of the rise time of the preamplifier and the shaper response is measured. In the case of γ irradiation a very stable behaviour is found with essentially no increase of the measured rise time with increasing radiation. The effect is found to be much more severe for neutron irradiation, in particular for the channels with large detector capacitance. Beyond fluence values of $\sim 2{\cdot}10^{14}$ n cm^{-2} the rise time increases drastically. It is less severe for capacitances in the order of 125 pF, which are typical for the application in the hadronic end-cap of the ATLAS calorimeter. The increase ist largest for small shaping times, where the rise time is dominated by the preamplifier response. For shaping times beyond $\sim$ 100 ns the shaper response itself dominates which is not affected by the irradiation.

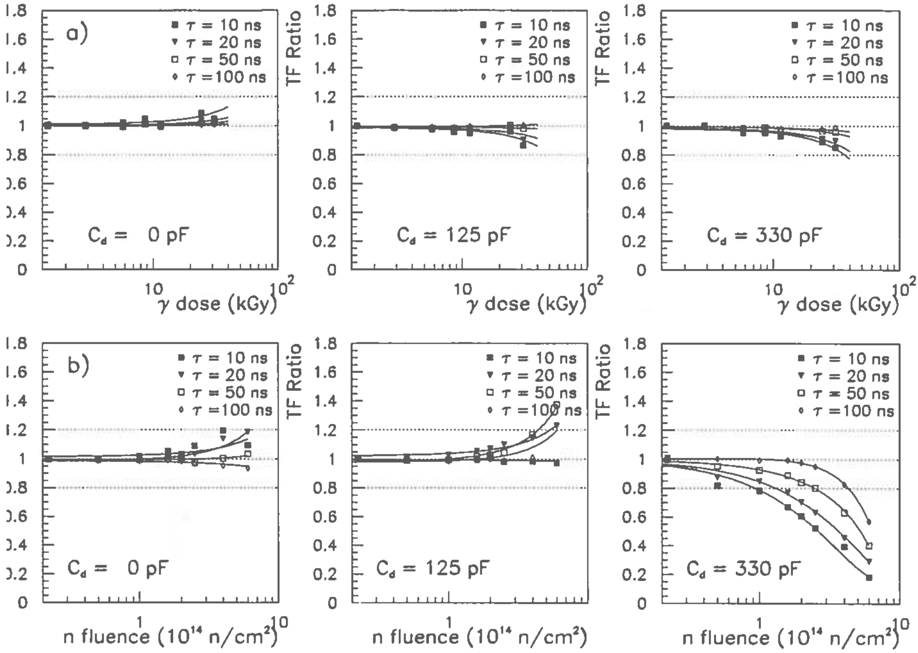

ure 2: *Ratio between the transfer function values measured after the various iation steps to the values measured before irradiation: a) γ irradiation and b) .tron irradiation. In each case three channels with different detector capacitance plotted for four different shaping times.*

Linearity

ɜ linearity of the preamplifiers was measured for some channels by injecting tri-ular pulses in the input range from 0 to 2.5 mA. Before irradiation, a linear .tion between the output voltage and the input current was observed. The same ːar fit was repeated in the interval from 0 to 0.6 mA after the various irradia-ı steps. The slope and offset parameters obtained were compared to the ones ɜrmined before the irradiation. They have been found to be stable up to an ːgrated fluence of $2.5{\cdot}10^{14}$ n cm^{-2}. In the range from 2.5 to 6 $\cdot 10^{14}$ n cm^{-2} the ɔe parameter decreased by $\sim 20\%$ for the channels with a capacitance of 330 pF . increased by $\sim 10\%$ for the channels with zero capacitance. Under γ irradiation ɜuch degradation effects have been found. For all channels the slope parameters e stable up to the highest dose values measured.

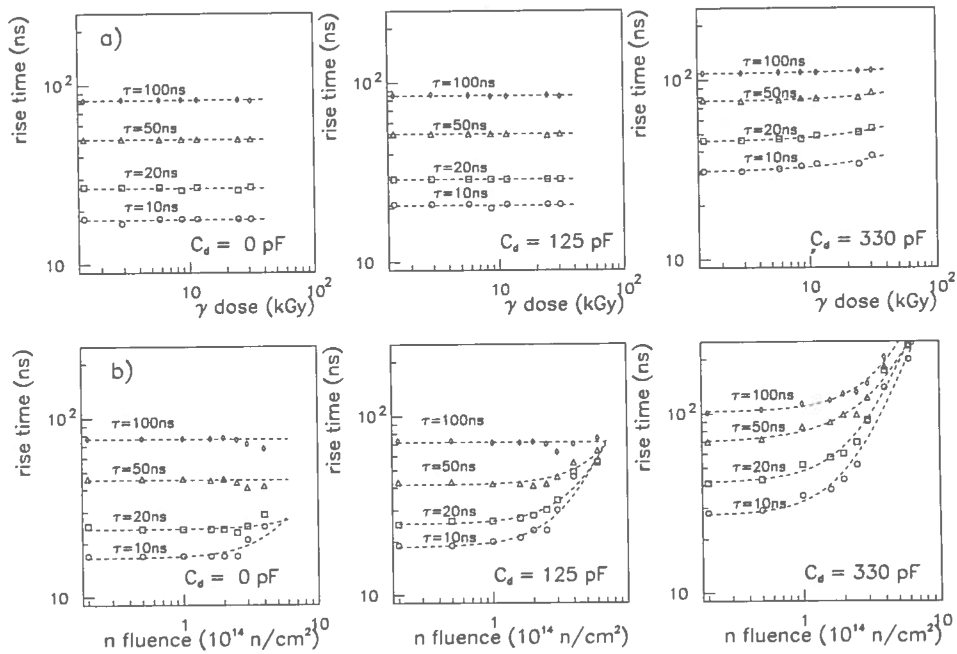

Figure 3: *The measured rise time of the pulse after the shaper as a function of irradiation: a) photon irradiation, b) neutron irradiation. The shaper time τ and the detector capacitance are given as parameters.*

6 Equivalent Noise Current

From the measured rms spread of the shaper output voltage in the absence of any input signal, the equivalent noise current was computed by using the measured transfer function. The noise values measured before the irradiation are shown in Fig.4a as a function of the measured rise time. The data from all preamplifier channels are shown on the same plot. Three groups of points, corresponding to three different detector capacitance values, are clearly visible. The data can be well described by the functional dependence given in eq.(1). The fitted values for the parameter α are shown in Fig.4b. As expected, they scale with the detector capacitance.

The dependence of the noise on the neutron irradiation is shown in Fig.5b. The data are presented for three typical channels with different capacitances. The increase of the rise time measured under irradiation for small shaping times is clearly

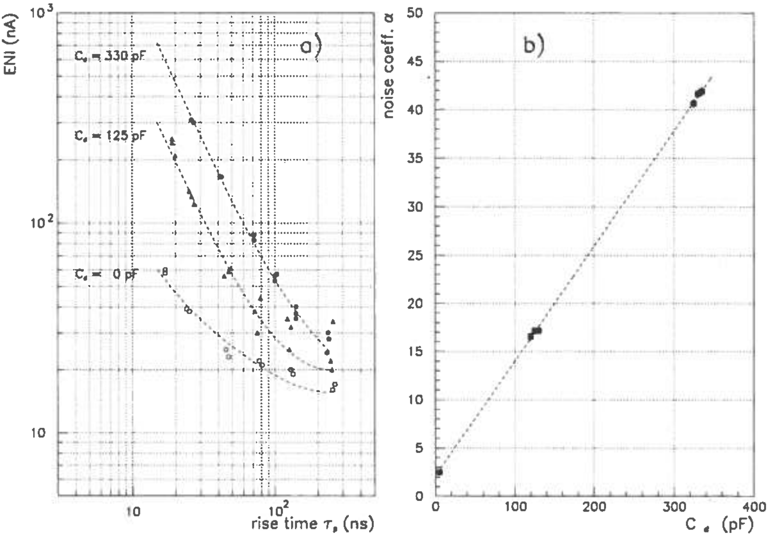

ure 4: *(a) The measured equivalent noise current before irradiation for all pream-ier channels. (b) The fitted values of the noise parameter α as defined in eq.(1).*

ble. For very high neutron fluences, exceeding $\sim 1{\cdot}10^{14}$ n cm^{-2} also an increase he equivalent noise current becomes significant, in particular for long shaping es. Under γ irradiation however, the equivalent noise current starts rising already relatively low radiation dose values. The corresponding data are shown in Fig.5a.

The increase of noise, normalized to the values measured before irradiation, hown for all channels in Fig.6. The results are given for two fixed values of the asured rise time, chosen to be 20 and 100 ns. As indicated above, the increase of se is small under neutron irradiation for small shaping times up to fluence values he order of $\sim 1 - 2{\cdot}10^{14}$ n cm^{-2}. This is found to be true for all channels inde-dent of the detector capacitance. Under photon irradiation the noise increases tinuously. For the channels with a capacitance of 125 pF an increase in the range ween 15 and 30% is seen after a collected dose of 20 kGy at a rise time of 20 ns. ıust be noted that the observed spread between the various channels is large and t the small number of irradiated preamplifier channels precludes more detailed clusions.

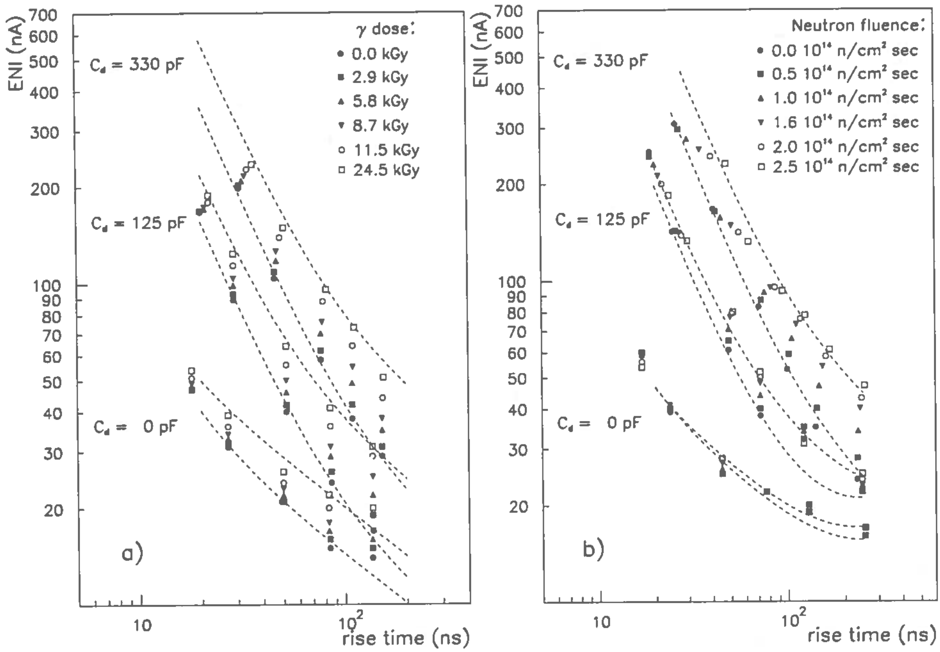

Figure 5: *The measured equivalent noise currents during irradiation for three channels with different capacitance: (a) γ irradiation, (b) neutron irradiation.*

7 Conclusions

The GaAs preamplifiers developed in the framework of the RD33 project show a stable performance in terms of transfer function, rise time and linearity up to high neutron fluences in the range of $\sim 2{\cdot}10^{14}$ n cm^{-2}. For neutron fluences exceeding this value clear deteriorations in the preamlifier performance have been observed. In particular for the channels with high detector capacitance a decreased response function together with an increased rise time have been measured. Under γ irradiation no damage of the performance has been seen up to 31 kGy, the maximum γ dose rate accumulated. The equivalent noise current has been found to increase under irradiation for both neutrons and photons. For neutrons the increase is small for short shaping times up to fluence values in the order of $\sim 1-2{\cdot}10^{14}$ n cm^{-2}. For photons a continuous increase is observed, starting already at low dose rates.

For the radiation levels expected after 10 years of operation at high luminosity in the hadronic endcap calorimeters of the ATLAS experiment (0.3 kGy and

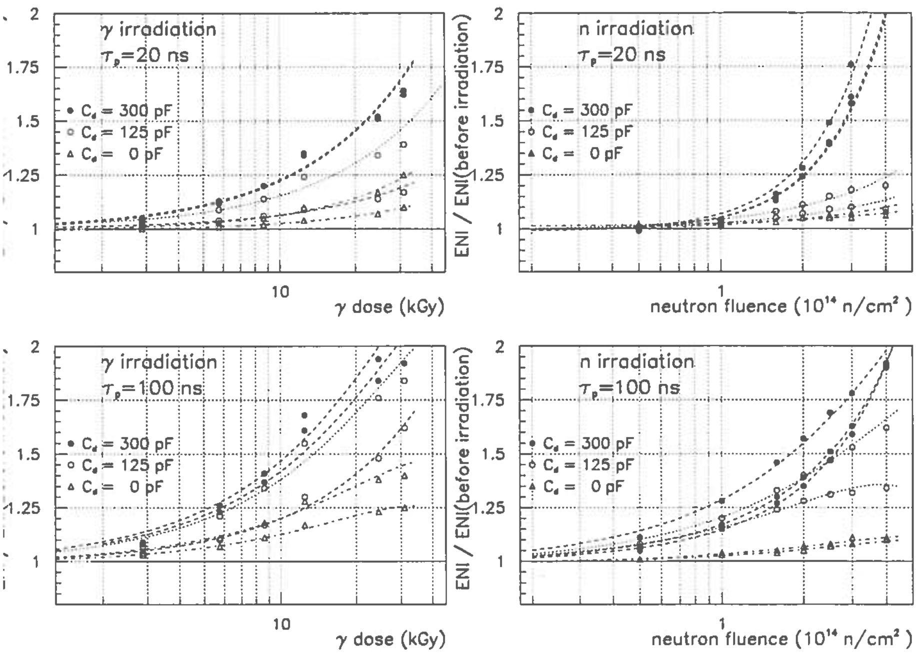

gure 6: *The measured equivalent noise currents during irradiation normalized to e values measured before irradiation for all channels.*

$3{\cdot}10^{14}$ n cm^{-2}) both the increase of the equivalent noise current and the increase the rise time are found to be small. Therefore, an application of the proposed ectronics looks uncritical from the radiation hardness point of view. However, it ıould be mentioned that the present results were obtained using high neutron fluıces and γ dose rates to evaluate on the time scale of a week the radiation damage ter 10 years of operation at LHC. The conclusions might therefore change if posble dose rate dependent effects or annealing effects exist. The present results are good agreement with previous measurements performed at different institutes [6].

cknowledgements

'e are grateful to our colleagues from the Neutron Laboratory at the Joint Institute Nuclear Research at Dubna. The continous help and support of the engineers and chnicians of the Dubna reactor group and the MPI Munich is acknowledged. We so wish to thank D.V. Camin, C. de la Taille and N. Fedyakin for stimulating and uitful discussions.

References

1. ATLAS Collaboration, Technical Proposal, CERN/LHCC/94-43 (1994).

2. RD33 Collaboration, C. Berger et al., Nucl. Instr. Methods, **A357** (1995) 333.

3. E. Shabalin, Fast pulsed and burst reactors, Pergamon Press Ltd., Oxford, 1979.

4. A.M. Ougouag et al., IEEE Trans. Nucl. Sci. **NS-37** (1990) 2219.

5. C. de la Taille, LAL/RT 92-10, Orsay preprint (1992).

6. D.V. Camin (RD3 Collaboration), Proc. IV Int. Conf. on Calorimetry in HEP, World Scientific, (1994) 618;
M. Citterio, V. Radeka and S. Rescia, Proc. V Int. Conf. on Calorimetry in HEP, Brookhaven 1994, World Scientific.

X – Calorimeter Integration in Large Systems

Convener J. A. Budagov
Chair J. Rutherfoord
Secretary P. Valente

Videau	Calorimetry at LEP. A Critical Point of View
Magill	Calorimetry at ZEUS
Fan	Doing Physics with the CDF Calorimeters
Kotcher	Physics with the DØ Calorimeter

'rascati Physics Series Vol. VI, (pp. 905–916)
'I INT. CONF. ON CALORIMETRY IN HEP – Frascati, June 8–14, 1996

CALORIMETRY AT LEP, A CRITICAL POINT OF VIEW

HENRI VIDEAU
*L.P.N.H.E. Ecole Polytechnique, Route de Saclay
Palaiseau, 91128 France.*

ABSTRACT

he phase I of LEP has now ended. This is the opportunity for a critical review of the role ıd achievements of calorimetry in this domain of physics. The goals of calorimetry are rst analysed in the perspective of LEP I physics. The different designs chosen by the LEP (periments are examined and the achieved performances described. Then a transverse ew is taken to see how the experiments brought a response to some specific problems. he emphasis is deliberately put on what would better not have been done, to suggest aces of improvement. Finally the sociology of the design decision is evoked to under-and the roots of mistakes even though this is unlikely to prevent others in the future.

. Introduction

The phase I of LEP, at the Z energy, has now ended and a large wealth of results has been ›llected in very different domains of physics. It is now time for a critical review of the role ıd achievements of calorimetry for that physics under these technical constraints. The role ıd goals are first analysed in view of the physics domain at LEP I which is quickly re-iewed. The different designs chosen by the four LEP experiments are examined and the :hieved performances described. Then a transverse view is taken to see how the experi-ıents brought a response to specific problems like separating π^0's from γ's. The success f LEP I is not to be contemplated here and the emphasis is put on what would better not ave been done to suggest places of improvement or ideas for future designs. Finally the ›ciology of the design decision is evoked to understand the roots of mistakes.

. Technical conditions for the LEP

In view of the current development of accelators, like LHC, with completely different ınning conditions, it is usefull to recall those of the LEP, an $e^+ e^-$ collider, with two phases f development. LEP phase I, now finished, where the machine was running around the Z ıass, LEP phase 2 where the energy is progressively increased above the WW threshold from 160 to 190 GeV. Up to now the backgrounds have been very low and that does not hurt much the calorimeters. The operation was first with four equally spaced bunches leaving more than 22 microsecondes between collisions, this has been susequentely reduced by a factor 2 when going to 8 bunches, but is still plenty enough for rather slow devices with long integration times. Another feature is the low cross sections. This, together with the low background gives the possibility, without generating high dead time, to use slow read outs with multiplexing. Since these considerations do not have a large impact on the physics, even though it is this possibility of multiplexing which gave to ALEPH and DELPHI their granularity, they will be discontinued. We will consider granularity, not the means to get it. At last the low angle Bhabhas are abundant providing a powerful mean to assess the luminosity to an unprecedented level of accuracy, the large angle Bhabhas are numerous enough to provide good electromagnetic calibration.

To estimate the adequacy of the calorimeters to the LEP physics we first recall the general lines of this physics. At LEP I we observe the Z decays. Due to the shape of this resonance, the initial state radiation, which plagues the electron colliders has a cut off around the Z width (1.3 GeV) and the events corresponding to a Z decay to two fermions keep generally a structure into two back–to–back jets, but the appearance of the different types of events may be dramatically different, ranging from a radiatif decay into a neutrino pair where only a low energy photon can be seen, to decays into charged lepton pairs like $e^+ e^-$ or $\mu^+ \mu^-$, to decays in pairs of taus with low multiplicities in narrow cones, to decays in high multiplicity jets where the presence of leptons or b's has to be signed. It appears that this will require good identification possibilities even in jets, this pointing toward spatial resolution. At LEP II the constraints are very different since the cross sections are very low, the radiative processes are dominant and that passing the WW threshold generates fat 4 jet events.

Role of calorimetry

Calorimetry at LEP is meant to provide four functions, trigger, measure, identify, veto. In view of the small number of events, it has to trigger on everything, with a high and well known efficiency. This implies redundant triggers. Basically three types of triggers are used, on total energy, the threshold being due to coherent noise, on localised energy, presence of photon or jet, or on energy associated with a track seen in a fast tracking system. It has to measure what is left out by the tracking, γ's and neutral hadrons but also electrons which can be better measured by calorimetry than by tracking and even charged hadrons when the tracking does not do it like in L3. The great importance of calorimetry for the energy flow measurement will be discussed later.

It has to identify γ's and π_0's, neutral hadrons, muons and electrons and consequently

Before to review the different detectors we can make some general remarks. The first one states the primacy of the detector quality in an experiment, this is not to diminish the importance of having brilliant analysts but you can steal fancy analysis methods, you are stuck with your detector. The second, quite general also says, as we will discuss later, that the aims of the design are not purely physics but politics.

The cylindrical symmetry around the beam axis of the initial state translates into symmetries for the detector. It is always structured in a cylindrical part called barrel and two end caps. The barrel contains about 70% of the events and the end caps are often not used except to veto. To preserve the symmetry in azimuth the end caps have often a radial structure which may hurt the simplicity of their design and create large dead zones. Another problem with that structure comes from the overlap between barrel and end caps which is rarely well made. Notice that this azimuthal symmetry provides a very helpful test of the data.
Does it come from "l'air du temps" but the four LEP experiments have differentiated their hadron and electromagnetic calorimeters; even more, but for L3 and SLD, all the HCAL are essentially tail catchers and muon filters, the coil just put in place to absorb the peak of the hadronic showers and destroy the particle development continuity. This is particularly interesting when it appears that a good deal of the physics comes from the study of the energy flow.

We will now try to characterise briefly each experiment calorimeters in a way to compare them.

DELPHI [3.)]

The beautiful drawing on the right does not really help to capture the possible problems in the calorimeter of such a detector. We will then avoid using this type of picture and rely on simpler tools like the two event drawings shown in the plots of figure 2.

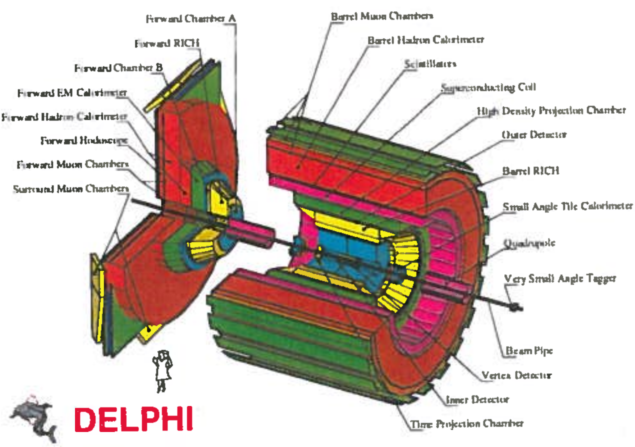

Figure 1. The DELPHI detector

The aim of DELPHI's design was clearly particle identification which goes beyond the subject of this review, and calorimetry is not their must.

charged hadrons and this for isolated particles or in jets.
t has to veto everything known but neutrinos, and this everywhere with reasonable thresholds.

Detector qualities and the experiment choices

The qualities of a detector can be described in term of qualities meaningful for physics but this has to translate into design and technical qualities. The physics qualities for a calorimeter are energy resolution, spatial and angular accuracy, spatial resolution, hermeticity and easiness to analyse and therefore to simulate very precisely. The hermeticity can be considered at the level of the veto and at the level of the measurement. These qualities will be obtained by means of the calorimeter intrinsic properties but also from the longitudinal and lateral granularity, from the absence of cracks, from the homogeneity.

The LEP calorimeters are facing some specific physics challenges. For example the hermeticity is a must for looking at supersymmetry. Simple events like τ's need measuring and identifying few particles but in a narrow cone $(\frac{m_\tau}{m_Z})$. B events need identifying leptons in jets. Complex events like 4 jets need a precise measurement of the energy flow with the identification of the jet content in leptons and b's. All these requirements may not be met by a single design and the experiments had to make their choices and bets.

The experiments

We now review the LEP experiments DELPHI, L3, OPAL and ALEPH, and mention the SLD, looking at their aims, designs, problems, successes. First have a look at the variety of technical solutions in the following table :

	ECAL barrel	ECAL end caps	HCAL barrel	HCAL end caps	Luminometer
ALEPH	Pb/wires	Pb/wires	Fe/streamers	Fe/streamers	Si/W
DELPHI	Pb/drift	Lead glass	Fe/streamers	Fe/streamers	Shashlik
L3	BGO	BGO	U/wires	U/wires	BGO
OPAL	Lead glass	Lead glass	Fe/streamers	Fe/streamers	Si/W
SLD	Liq. argon	Liq. argon	Fe/streamers	Fe/streamers	

ECAL means "electromagnetic calorimeter" and HCAL "hadronic calorimeter". Notice that, in the case of SLD, the first part of the HCAL is made homogeneous to the ECAL, in liquid argon.

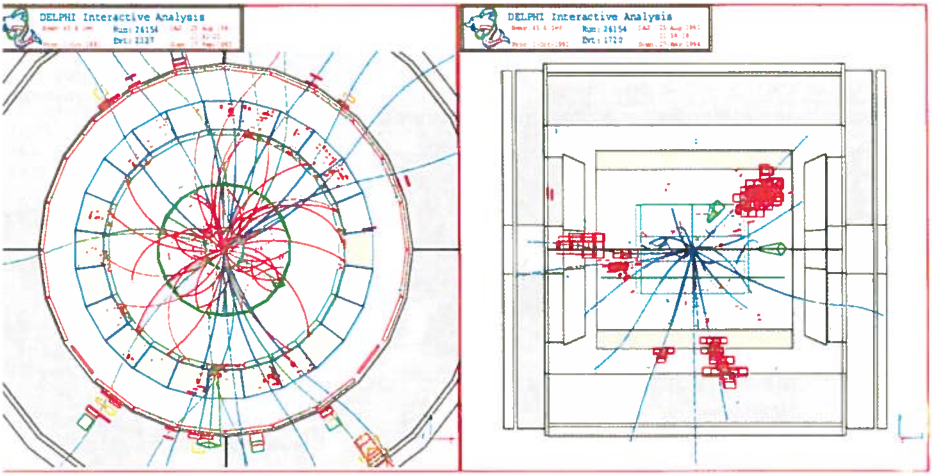

igure 2. X y cut and z y cut of the DELPHI detector with the ECAL in light gray and ıe HCAL in gray.

The ECAL uses different solutions for barrel and end–caps. These are in lead glass with ı energy resolution of 3.5% for Bhabhas at 45.6 GeV. We will develop more on the barrel hich is more original and of more use in physics. It is a HPC (heavy time projection cham- :r), sandwich of lead and long drift spaces disposed in 6 rings of 24 modules. This means lot of mechanical cracks. It is situated in front of the coil but behind the 0.8 X_0 RICH and ·ovides 18 X_0 at 90 degrees. The figures above illustrate the disconnection introduced by .e RICH between the tracking and the ECAL, and the disconnection between ECAL and CAL due to the coil. The spatial resolution is good in ϕ and excellent in θ at least when ıe showers are perpendicular to the modules. The energy resolution, lousy, is 6.5% for habhas at 45.6 GeV. The wires are aging due to the long drift which collects a lot of charge ı a wire and to the radioactivity of the lead. It corresponds to 0.12% gain loss per day but ıe gain can be readily followed using the peak of injected Krypton gas. This long drifts ın not provide a trigger which comes from special wire planes imbedded in the calorime- :r.

The HCAL is similar to the ones of OPAL and ALEPH. It is made of 21 5 cm iron abs(6.6 λ_I) interleaved with 20 layers of streamer tubes of which less than 1% has failed. is arranged in 24 modules for the barrel with a rather important dead zone in the median lane. It is read out as analog towers 20x30 cm^2 starting at 3.2 m and split into 4 storeys. . digital read–out made of 8 cm strips running on the streamer tubes has been recently add- :l. The resolution is $\frac{1.12}{\sqrt{E}} \oplus 0.21$ and the calibration stable with time.

L3 [4.)]

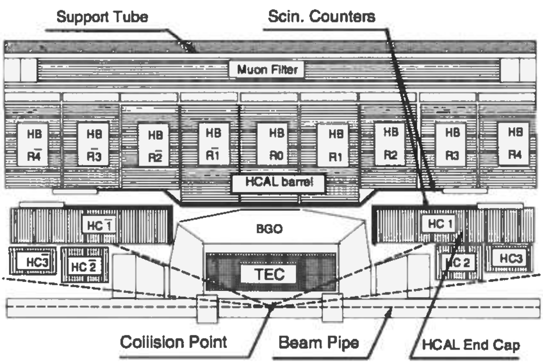

Figure 3. Structure of the inner part of L3

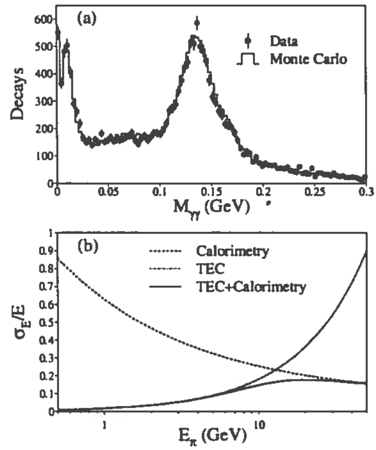

Figure 4. L3. On top π^0 in τ decays, Bottom, measurement of the pions energy from tracking and calorimetry

L3 design was aimed at the calorimetric precision. Its ECAL is identical barrel and end–caps, made of BGO ($X_0 = .1$ cm), and provides 21.4 X_0. There is nothing between the tracking and the calorimeter which starts at 52 cm from the interaction region leaving a very short space for the tracking. The ECAL is made of crystals pointing to the interaction point with a slight tilt in ϕ. This leaves a tiny 0.35% loss in the cracks. There is no sampling in depth. The resolution reaches 1.45% for Bhabhas at 45.6 GeV. A very slight loss of light has been noted, 17% over LEP life time [5.)]. The gain is thoroughly followed with Xenon lamps and RFQ. BGO needs a careful temperature control.

The HCAL is quite surprising, made of 58 5 mm uranium plates interleaved with proportional chambers. It provides 3.5 λ_I and is made out of 9 rings of 16 modules. The read out is projective in ϕ but not in θ. In the modules, the wires are stretched orthogonaly from plane to plane. This reduces the cracks to a minimum. Parallel wires are ganged together to form parallelepipeds of about 5cm in width and depth. But for the ambiguity this simulates rather tiny cells. This calorimeter yields a resolution of $\frac{0.55}{\sqrt{E}} \oplus 0.05$ equivalent to 13% on LEP I jets. The natural radioactivity of Uranium is used for the gain follow up.

It can be noticed that this a priori beautiful calorimetry interferes strongly with the tracking; in fact, above 15 GeV, the pions are better measured by calorimetry than by the tracking as can be seen on figure 4. For the energy flow, the muons energy is missed by the calorimeter, and their measurement outside the calorimeter needs corrections for energy loss. On the same figure 4. the $\gamma\gamma$ spectrum in τ to ρ decays is shown, even though the energies are ll measured the two photons are poorly disentangled in that case. In the absence of inter-ing low energy radiative decays, as was expected from toponium, the most striking re-ts using this calorimetry at its best may be negative ones, like the limits on B to $\pi^0 \pi^0$ $\eta \eta$ [6.)].

ˀAL [7.)]

ˀpal design was directed toward a safe efficiency, option strongly reinforced by the tion of the LEP committee.

ˀhe ECAL is made, barrel and end ps, in lead glass situated after the coil ˀX_0). The effect of the coil is partly unterbalanced by a presampler in ˀeamer tubes. The cells are projective the barrel, not in the end caps, which e not used in part of the physics anal-es. There is no depth sampling and e spatial resolution is rather coarse. ıe good energy resolution for Bhab-ıs, 2.5% is degraded at lower energies aking difficult to use photons below GeV. The overlap between barrel and ıd caps is delicate to use like in DEL-HI and partly ALEPH. The gain is fol-ˀwed up using Xenon lamps.

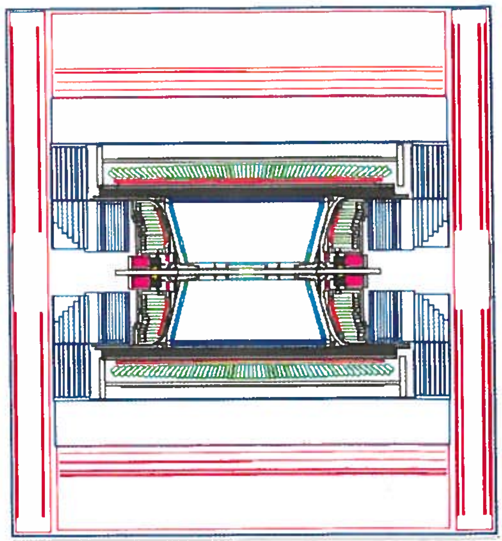

Figure 5. Structure of the OPAL detector

The trigger can be on total energy with thresholds at 6 and 4 GeV. θ and ϕ overlapping ːctors provide localised triggers at 2.5 and 1 GeV.

The HCAL is the coarsest one at LEP, this is done to match the lead glass performances ı hadronic jets, 8 10cm iron slabs interleaved with 9 layers of streamer tubes provide 6 ı . To compensate the effect of the coil, the first plane is read independently. The read out double, analog with large towers and digital, reading out each tube. The resolution is ɔout $\frac{1.20}{\sqrt{E}}$. Notice that to better ensure the hermeticity simple gamma catchers have been ıstalled to match the holes. This, and the robustness of the lead glass, yield a safe recon-ɪruction of the energy flows which has been put in evidence by the observation of the very rst Z_0 in 1989 by OPAL.

ALEPH [1.)]

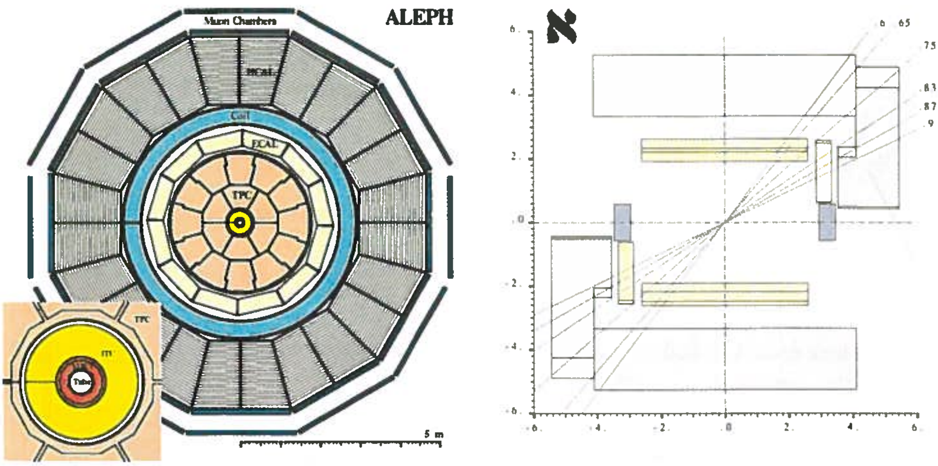

Figure 6. ALEPH transverse and longitudinal structure

Transverse and longitudinal cuts of ALEPH are shown in the figure 6. It shows clearly like in DELPHI the problem of the coil and the ECAL backing structure separating ECAL from HCAL. This makes 1 interaction length in a space of 70 cm.

The ECAL is made of stacks of lead–wire chamber sandwiches providing 21 X_0. It is inside the coil and very close to the tracking, at least for the barrel. It is tilted against the HCAL to avoid projective dead zones. It is read out in projective towers with 3 storeys, and also by planes providing some redundance. The energy resolution is 3.5% for Bhabhas and the angular precision is $\frac{2.7}{\sqrt{E}} + 0.32mrad$. The gain follow up is done with ionisation chambers. The gain loss is less than 1% a year and the fraction of dead storeys or wires is around 2 per mil.

The HCAL is made of 5 cm iron slabs interleaved with 23 layers of streamer tubes, providing with the ECAL 7.2 λ_I. The read out is triple, analog towers corresponding to groups of ECAL towers (4x4), digital tubes and analog sets of two adjacent planes. About 1% of tubes have failed.

SLD

The most remarkable is that 2 interaction lengths of the HCAL are inside the coil following just the ECAL and made in the very same technique, but inside a cryostat with a wall at some distance and after a thick CRID.

ıe transverse view

[he prime properties of calorimeters are ɜir resolution in energy and in space, that verns the capabilities in measuring and ɜentangling particles.

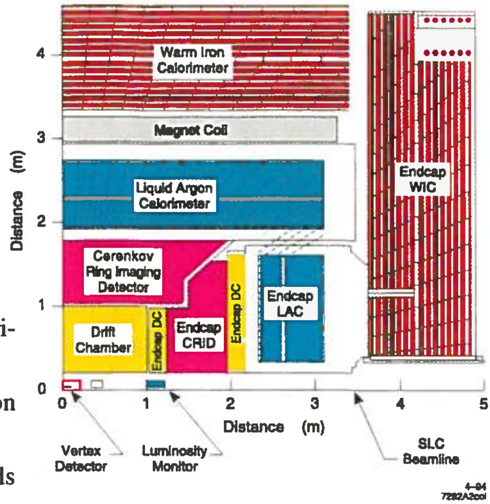

Figure 7. Structure of the SLD detector

:solution and cell sizes

[o understand properly the following ımbers it may be useful to read the experiɜnts technical publications. The question arks qualify the cases where the definition a cell size is not obvious, like in the ELPHI ECAL where the cell size depends ı the depth and polar angle or in the L3 CAL where the structures are not really 3 mensional. Depth corresponds to the number of depth subdivisions. These numbers ırrespond to the barrels.

:esolution	ALEPH	DELPHI	L3	OPAL
:CAL at 46 GeV	3.5 %	6.5 %	1.5 %	2.5 %
ICAL	100 %	112 %	55 %	120 %
'ell size				
:CAL in X_0	1.5 x 1.5	1. x 0.4 ?	1.8 x 1.8	6 x 6
in μsr	13 x 13	15 x 6 ?	34 x 34	40 x 40
depth	3 45 planes	9	1	1 presampler
ICAL in λ_I	1 x 1	1. x 1.5	0.5 x 0.5 ?	2.5 x 2.5
in μsr	52 x 52	50 x 75	42 x 42 ?	120 x 120
depth	1 / 10 planes	4	10	1
digital read–out	23 tube planes	21 strip planes		10 tube planes

lentifying the charged particles

We consider here the particles identified by means of calorimetry. For electrons the resoıtion is essential in using E/p, but the longitudinal and lateral shape are very efficient as ell as the position precision. For muons using penetration is well complemented by meaıring the lateral shape and for this the digital pattern is a must. The charged hadrons are mply neither electron nor muons. For isolated tracks like in τ decays the efficiencies in LEPH are above 99% for electrons and muons within the polar angle acceptance.

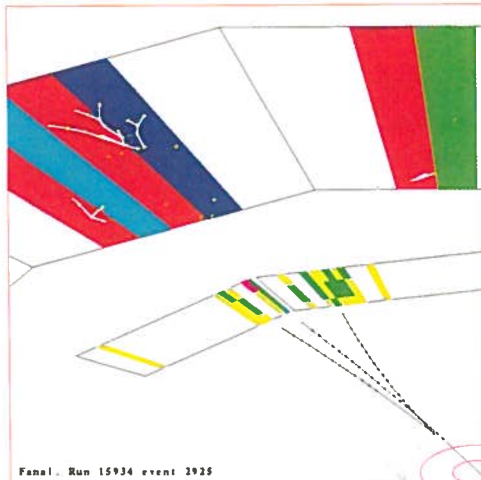

Figure 8. Display of a $\tau \rightarrow \pi\, K_s\, K_l\, \nu$ in ALEPH. The image is stretched horizontally.

The figure 8. displaying a $\tau \rightarrow \pi\, K_S\, K_l\, \nu$ seen in ALEPH (figure 8.) illustrates as well the digital pattern.

Distinguishing γ and π^0.

This is important even though the distinction can often be made from physics considerations. The energy resolution plays some role but most important is the possibility to separate the showers for a given angle between the γ's and to measure accurately this angle, this is illustrated in figure 4. The angular cell size and the angular lateral extension of the showers, characterised by the radiation length or better by the Molière radius, enter and the fine grain experiments like ALEPH are at their advantage.

But the two γ's do not need to appear in distinct cell clusters, searching for local energy maxima solves the problem in many cases and is used in all the experiments, and even when this fails, computing the transverse moments of the energy distribution measures the anisotropy of the shower and the mass of the system. These two last aspects are illustrated in figure 9. which shows how DELPHI separates photons in one cluster and in figure where the improvement brought by the moment analysis in the separation of π^0's from τ decays into ρ's for ALEPH is shown.

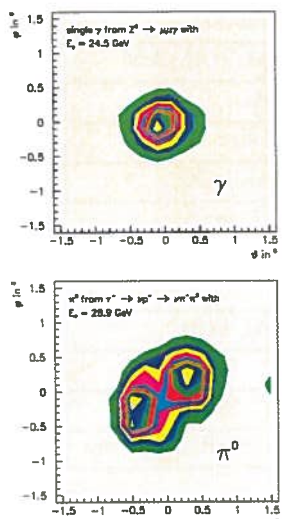

Figure 9. Profile of a γ and of a π^0 in DELPHI

Building an energy flow

For jet physics in particular it is essential to assess the energy deposited in the detector and its direction, the energy flow. It could be tempting to rely fully on precise calorimetry for this task, but the muons escape that measurement. The tracking can then be used for all the charged tracks, the sole neutrals being measured by the calorimeters. This means a proper handling of the tracking, an identification of the leptons and a good separation of neutrals from tracks.

This is not too difficult with precise posi- ɔn and proper granularity for the photons /en though they may be confused with de- ·is of charged hadronic showers but the ain problem comes from the measurement ᶠ the neutral hadronic energy which amounts ır about 15% of the total energy and has to ᵋ separated from the deposit of the charged acks. Using this method ALEPH reaches a :solution on jets of about $\frac{0.60}{\sqrt{E}}$ similar to L3. perfect separation, helped by continuity ᵋtween ECAL and HCAL, would bring that ımber down to about $\frac{0.40}{\sqrt{E}}$.

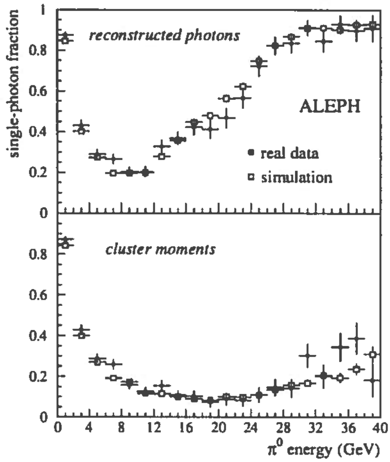

Figure 10. Proportion of π^0's from a τ decay into ρ where the γ's are not separated, on top with an energy maximum method, bottom using also a moment analysis.

ritics and wishes

You can then wonder if there are recommendations to draw. Clearly the example of L3 ıd other detectors out of our field show that space should be left for a proper tracking and good connection between tracking and calorimetry preserved. No gap should be left be- veen ECAL and HCAL, unlike in ALEPH, even if the quantity of material is negligible, ı preserve the continuity. In fact there should not be two, or more, but one calorimeter ho- ıogeneous in polar angle and in depth. To ensure the resolution it should be dense, and, we can dream, what about a 3d tracking calorimeter with a granularity below the level f an electromagnetic shower.

ociology of design

Having looked at these experiments, it appears clearly that some strange bets have been ken which raise questions and doubts. We could try to trace their origin to five sources ıd try to see how to handle them. Where they due to physics? this is the "good" reason ut mind not to bet too narrow, physics could well not be there. Did it arise from technics, om a certain lack of technical daring? isn't it true that daring has to be cautious? Was it mply from lack of money? It is probably better to stay with that than run into "politics" ı get money. There is also a less straightforward reason for strange bets which I would call aste for elegance". The design looks so cute, so astute, that it would be a sin not to incorpo- ıte it. Please stop to "bon ton". And finally there is a large source we can call politics, there ·e two domains here, you can have chosen a design in order to be approved, it may even have been imposed directly to you by a committee, what to do about it but being as firm as possible? The other domain is more troublesome, it is when the design is flawed to be complacent with possible collaborators who intend to bring their own brilliant idea. There you'd better avoid it and keep away from such collaborators.

This is what I can tell you from experience and from looking around, but do we learn from others, past, experience? Just have a look at experiments being designed now.

Conclusions

It may be tempting to compare the calorimeters. I will not do it since we know now the physics the designers just guessed, and it has no meaning to compare independently pieces of a detector. But may be the most impressive is that, even with less data than expected, LEP has reached in many domains more precision than was anticipated. And were you asked about the usefulness of four LEP experiments you would be tempted, as I am, to say they were too many. But would you cut today what you would have cut ten years ago?

Acknowledgments.
I would like to thank for their help Alessandro de Angelis and Heiner Herr, Iannis Karyotakis and Andrei Kounine as well as Tatsuo Kawamoto. They gave me all the information I needed in a very frank and helpful way. Much information used in this paper can be gathered from the experiments W3 servers: http://alephwww.cern.ch/WWW/, http://www.cern.ch/Delphi/Welcome.html, http://hpl3sn02.cern.ch/, http://www.cern.ch/Opal and http://www–sld.slac.stanford.edu/sldwww/sld–working.html for SLD.

References

1. ALEPH: a detector for electron–positron annihilations at LEP. N.I.M. **A294** (1990) 121
Performance of the ALEPH detector at LEP. ALEPH coll. N.I.M **A360** (1995) 481

2. ALEPH choices on calorimetry in the light of LEP physics. H. Videau. IInd International Conference on Calorimetry in High Energy Physics. Capri 1991. Edited by A. Ereditato

3. The DELPHI detector at LEP. DELPHI Coll. N.I.M. **A303** (1991) 233–276
Performance of the DELPHI detector. DELPHI Coll, N.I.M. **A378** (1996) 57
The performance of the DELPHI Hadron Calorimeter at LEP. DELPHI HAC Coll.

4. The construction of the L3 experiment. L3 Coll. NIM L3 N.I.M. **A289** (90) 35
Hadron calorimetry in the L3 detector. Adriani et al. N.I.M. **A302** (1991) 53–62

5. The L3 electromagnetic calorimeter. I. Karyotakis. International Calorimetry Symposium. Beijing Oct 94.

6. Search for Neutral Charmless B decays at LEP. L3 Coll. Phys.L. **B363** (1995) 137

7. The OPAL detector at LEP. OPAL Collaboration, N.I.M. **A305** (91) 275–319

CALORIMETRY AT ZEUS

S. Magill
Argonne National Laboratory, Argonne, USA

Written contribution not received

DOING PHYSICS WITH THE CDF CALORIMETERS

Q. Fan
)epartment of Physics and Astronomy, University of Rochester, Rochester, NY 14627

Written contribution not received

rascati Physics Series Vol. VI, (pp. 921–938)
I INT. CONF. ON CALORIMETRY IN HEP – Frascati, June 8–14, 1996

PHYSICS WITH THE DØ CALORIMETER

Jonathan Kotcher
(representing the DØ Collaboration)
Brookhaven National Laboratory
Upton, New York 11973, USA

ABSTRACT

.e DØ detector, located at the Fermi National Accelerator Laboratory in Batavia, nois, USA, is a large hermetic detector designed to study the products of $\bar{p}p$ colons at a center-of-mass energy of $\sqrt{s} = 1.8$ TeV. The centerpiece of the detector uranium/liquid argon sampling calorimetry, which provides high resolution de-:tion of the physics signatures of interest – electrons, photons, jets, and missing .nsverse energy – over the full solid angle. We discuss below how the calorimeter ormation is used to detect the final states relevant to the physics we are pursuing, d describe a number of physics processes and results that demonstrate the utility some of our design choices.

Introduction

.e DØ detector, located at the Fermi National Accelerator Laboratory, is a large ılti-purpose detector designed for the study of high mass and large transverse ergy (E_T) phenomena in high energy proton-antiproton collisions. The detector esses coverage over a large solid angle for electrons, muons, and jets, with the pres-:e of neutrinos inferred from the measurement of missing E_T ($\not\!\!E_T$). The heart of : device is hermetic uranium/liquid argon sampling calorimetry, designed to pro-le homogeneous, high-precision energy measurements of electrons and jets over arge range in pseudorapidity. [1] The calorimeter is complemented by a series of ıer tracking chambers that provide charged particle tracking and vertex identifica-n, and an outer 4π muon system, for identification and momentum measurement muons.

The physics program being pursued by DØ includes studies of the top quark, jet physics (including tests of quantum chromodynamics and compositeness searches), studies of the intermediate vector bosons (such as the W mass and width, vector boson self-couplings, and W/Z production in association with jets), and searches for evidence of new and exotic phenomena, including supersymmetry, fourth generation quarks, and heavy vector bosons. We have collected a total integrated luminosity of 120 pb^{-1} during the last Tevatron running cycle, which took place from May, 1992 through February, 1996.

This paper describes how the calorimeter information is integrated into the physics analyses of interest at DØ, using specific physics channels to demonstrate the methods used. It has been organized around the means of determining (or identifying) the four basic event signatures of most interest from a calorimetric standpoint: electrons, photons, jets, and $\not{E}_T$. Physics results best illustrating the design features and identification strategies in each of the categories are presented.

2 The DØ Detector

The innermost detector subsystem at DØ is the tracking system, which consists of three subsystems. Immediately surrounding the beampipe is the vertex chamber, designed for the reconstruction of primary and secondary vertices. This is followed by a transition radiation detector (TRD), employed to enhance electron identification by rejecting charged pions and photon conversions. The outermost tracking detectors consist of a central and forward/backward drift chambers, which provide charged-particle tracking and dE/dx information to $|\eta| \approx 3.2$. The calorimeters surround the tracking volume.

The muon system, consisting of five magnetized toroids together with sets of proportional drift chambers, provides momentum measurements and additional tracking information for muons to $|\eta| \approx 3.3$.

2.1 A Few Details on the Calorimeter

The calorimeters are housed in three separate cryostats: a central calorimeter (CC), and two end calorimeters (EC's). The active volume is segmented into modular structures consisting of three distinct regions: the electromagnetic (EM), fine hadronic (FH), and coarse hadronic (CH) sections. The EM and FH regions employ uranium absorber; the coarse sections, which sample the tail-end of hadronic showers, consist of either copper or steel absorber. The electromagnetic (hadronic) coverage of the calorimeter extends to $|\eta| \approx 4.1$ (5.2).

The readout is arranged into $\approx$ 5,000 semi-projective towers of size 0.1×0.1

$\Delta\eta\times\Delta\phi$. In order to enhance the position resolution for electrons and photons, the ınsverse readout segmentation at electromagnetic shower maximum (EM readout ver 3) is twice as fine in each dimension (0.05×0.05). The EM section is read out ır times – after 2, 2, 7, and 10 radiation lengths (X_0) – which provides information the longitudinal development of the shower. The hadronic section is read out e to four times, depending on the η-region.

A minimum ionizing particle (mip) liberates $\approx 20,000$ electrons in a liquid gon gap, which corresponds to about 3 femtocoulombs of charge, or $\approx$ 4 ADC unts in our unit of readout. A least count in the calorimeter is therefore equal to proximately 5,000 electrons, or 1/4 of an equivalent mip signal. The full dynamic nge of the electronics is 15 bits, or $\approx 32,000$ ADC counts. The calorimeter readout n accommodate incident electrons with energies of up to $\approx$ 400 GeV before any turation effects become relevant.

The total thickness of the calorimeter varies from $\approx$ 7 to 9 interaction ıgths (λ_0), depending on pseudorapidity. In addition to improving the jet reso- tion by containing hadronic showers, the large amount of material helps to limit dronic punch-through to the outer muon system. The EM section is a total of 21) deep.

In order to improve the energy resolution for particles that traverse the ter-cryostat region (ICR), which covers the region $0.8 < |\eta| < 1.4$, both "massless ps" and an inter-cryostat detector (ICD) have been added. The "massless gaps", named because they contain no absorber material, are located between the mod- es and the cryostat in the liquid. They sample the shower energy that is lost by rticles that traverse the module endplates and cryostat walls. The ICD, located tween the cryostats in the η-region defined above, consists of scintillator tiles that ay a similar role.

The reader is directed to Refs. [2, 3] for further details on the overall de- ctor, including the calorimeter.

Electron Identification

ectron identification at DØ relies predominantly on the calorimeter information, th complementary measurements provided by the tracking chambers. A brief scription of the process is presented below.

Electron candidates are identified in the offline reconstruction by form- g nearest neighbor clusters of electromagnetic (EM) readout towers. A series of lection criteria are then imposed:

- *Cluster (shower) shape:* The shower shape of the candidate cluster is required to be consistent with that of an electron. The determination employs a covariance-matrix technique, [4] in which 41 observables are used to determine the probability that a given electromagnetic cluster resulted from energy deposited by an electron (or photon). The variables used include the fractional energies in EM layers 1, 2 and 4, and the fractional energies in a 6×6 array in the more finely segmented EM layer 3, thereby exploiting both the transverse and longitudinal readout segmentation of the calorimeter. The covariance matrix is "trained" on Monte Carlo data at various energies, which has in turn been developed from test beam information.

- *Longitudinal isolation:* The amount of cluster energy contained within the EM portion of the calorimeter is required to exceed (typically) $\approx 90\%$ of the cluster energy in the four EM layers plus the first fine hadronic layer.

- *Transverse isolation:* The isolation fraction, f_{iso}, defined by:

$$f_{iso} = \frac{\mathrm{E}(R < 0.4) - \mathrm{EM}(R < 0.2)}{\mathrm{EM}(R < 0.2)}, \tag{1}$$

  is required to be (typically) less than 10%. Here, E (EM) is the total (electromagnetic) energy contained within a cone of radius R centered on the candidate cluster, where $R = \sqrt{(\Delta\eta)^2 + (\Delta\phi)^2}$.

- *Track match:* A suitable spatial match between the calorimeter cluster and a reconstructed drift chamber track is required. The track match significance, σ_{track}, is the figure of merit used:

$$\sigma_{track} = \sqrt{\left(\frac{\Delta\phi}{\delta_{\Delta\phi}}\right)^2 + \left(\frac{\Delta z(r)}{\delta_{\Delta z(r)}}\right)^2}, \tag{2}$$

  where the variable Δz (Δr) is used in CC (EC). The quantity δ_x is the resolution in the variable x.

- *Track ionization:* In order to reject photons that convert upstream of the calorimeter, the dE/dx energy loss as measured in the drift chambers is required to be consistent with that of an electron (*i.e.*, 1 mip vs. 2 mip tracks).

- *TRD energy deposition:* The energy deposited in the TRD is used to reject charged pion backgrounds and photon conversions.

The last two items are used optionally, depending on the demands of particular analyses. In general, cuts on the above variables are most frequently applied independently; they can, however, be applied collectively through a likelihood technique which has recently been developed. [5]

1 Absolute Energy Scale

he electromagnetic energy scale, which anchors all of the energy measurements in ie experiment, is determined by calibrating to the $Z \rightarrow ee$ resonance. The energies : all identified EM objects in physics analyses – *i.e.*, identified electrons and photons are scaled by the ratio of the Z mass as measured at LEP [6] to that measured at Ø (*i.e.*, $M_Z^{LEP}/M_Z^{D\emptyset}$). Test beam studies have demonstrated the calorimeter to e linear to better than $\approx 0.5\%$ for electron energies greater than 10 GeV, implying iat, for electrons at or above this p_T, any intrinsic non-linearity of the detector iakes a negligible contribution to the error incurred from this scaling procedure.[1]

Prior to the final assembly of the entire detector, one of the two end ılorimeter EM modules, and four prototype EM modules from the central calorime- :r, were tested in independent beam tests at the Fermilab fixed target facility. [7] series of calibration constants, such as layer-to-layer sampling weights, as well as verall ADC-to-GeV conversion factors, were carried over to the main experiment r each cryostat "type" independently. In addition, the liquid argon purity and :mperature (and therefore the response) can vary from cryostat to cryostat. Con- derations of this kind have motivated our decision to establish the Z mass, and ence the scale factor, in each of the cryostats independently.

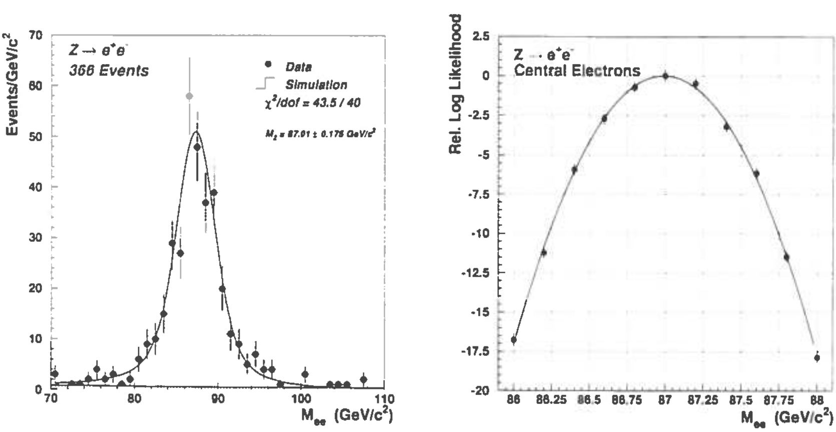

igure 1: Dielectron mass distribution, with background estimation (shaded area) ıd fitting results, for events where both electrons are central ($|\eta| < 1.0$) (left). The ·lative log likelihood as a function of mass (right). The spectra are based on the ıalysis of 12.8 pb^{-1} of data.

Our reconstructed dielectron mass distribution for central electrons is shown Fig. 1. The spectrum is fit to a relativistic Breit-Wigner line shape, convoluted

[1] This assumes that the portion of the deviation of $M_Z^{LEP}/M_Z^{D\emptyset}$ from unity that might be due an offset, rather than a pure scale factor, is negligibly small. (see Section 3.1.1)

with a Gaussian to simulate detector noise and resolutions. The relative log likelihood resulting from these fits are shown as well.

For most of the physics of interest at DØ, the accuracy of the above procedure is sufficient. An example of a measurement where a more precise determination of the energy scale is needed is the precision measurement of the mass of the W boson. [8] We discuss below our means of establishing the error associated with the energy scale in this measurement.

3.1.1 *Energy Scale Error in the Determination of the W Mass*

The W mass, which is measured from $W \rightarrow e\nu$ decays at DØ, is in practice extracted from the W to Z mass ratio, *i.e.* $M_W = (M_W^{DØ}/M_Z^{DØ}) \times M_Z^{LEP}$. A number of systematic effects common to the two measurements cancel in this ratio. Most relevant to this discussion is that, to first order, the ratio is insensitive to the electromagnetic energy scale. To establish the scale error with the precision required here, it is important to quantify the extent to which a potential offset – as opposed to a scale factor – is responsible for the deviation of the ratio $M_Z^{LEP}/M_Z^{DØ}$ from unity. We use reconstructed low energy resonances, in conjunction with the information extracted from the $Z \rightarrow ee$ resonance, to establish the energy scale with the necessary precision.

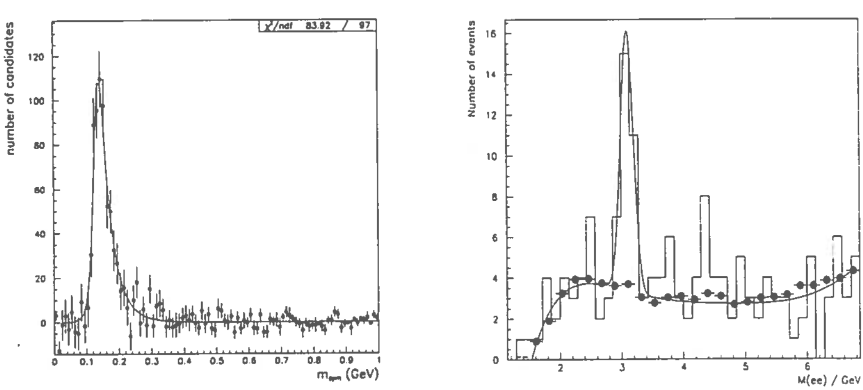

Figure 2: Background-subtracted $\pi^0 \rightarrow \gamma\gamma \rightarrow eeee$ peak, with fit. We measure $m_{\pi^0} = 134.5 \pm 10.2$ MeV/c^2 (left). Low-E_T ($E_T^e < 3$ GeV/c) dielectron invariant mass, showing the J/ψ peak and a fit to the distribution (including background). The measured J/ψ mass is $m_{J/\psi} = 3.032 \pm 0.193$ GeV/c^2 (right). (Errors quoted represent both the statistical and systematic contributions added in quadrature.)

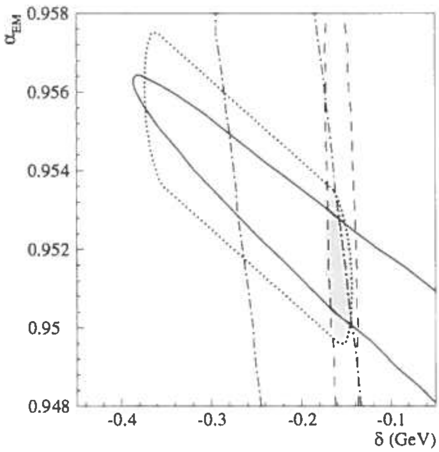

igure 3: Constraints on the scale factor α and intercept δ from observed $J/\psi \to ee$ lashed-dotted line), $\pi^0 \to \gamma\gamma$ (dashed line), and $Z \to ee$ decays (solid line). The naded inner contour shows the combined result. The dotted line indicates the llowed area when nonlinear terms, constrained from test beam measurements, are ncluded.

We assume that the measured and true calorimeter energies are related ɔ one another through the relation $E_{meas} = \alpha E_{true} + \delta$, where α and δ are the nergy scale factor and offset, respectively. Forming the invariant mass of a two-ronged decay with the above assumed functional form, and keeping terms to first rder in δ, results in an expression for the invariant mass that is given by $m_{meas} =$ $:m_{true} + \delta f$. The variable $f = \frac{2(E^1_{meas}+E^2_{meas})}{m_{meas}} \sin^2(\omega/2)$, and is determined purely :om the kinematics of the decay. The quantity ω is the opening angle between the wo electrons. The scale error on the W mass is determined by the value of, and he error on, α and δ, and the correlations between them.

We use reconstructed $\pi^0 \to \gamma\gamma$ decays, where both photons convert, and $/\psi \to ee$ decays, in conjunction with the information from the Z, to evaluate the ffset and scale factor *in situ*. The reconstructed π^0 and J/ψ peaks are shown in 'ig. 2. These resonances decay to electrons or photons with energies that are, on verage, below 10 GeV, compared with the $\approx$ 40 GeV electrons from Z decay. Each f the resonances therefore has a different sensitivity to α and δ and, taken together, rovide a powerful tool for establishing the electromagnetic scale *in situ*.

The one-sigma contours in α and δ for the three resonances, obtained from he data in conjunction with Monte Carlo simulations, are shown in Fig. 3. We btain a value for the energy scale factor $\alpha = 0.9514 \pm 0.0018^{+0.0061}_{-0.0017}$ and the offset

$\delta = (-0.158 \pm 0.015^{+0.03}_{-0.21})$ GeV. The asymmetric errors are due to possible response nonlinearities for low energy electrons, which we constrain from test beam data. From these data, we obtain a scale error on the W mass of 80 MeV/c^2 from the analysis of 76 pb^{-1} of data. This represents roughly half of the total error in the measurement, which is currently 170 MeV/c^2.

The influence of the large relative systematic error on δ on the energy scale error is suppressed (to first order) in the W-to-Z mass ratio. At this point, we find that the scale error on the W mass is dominated by the statistics of the Z.

3.2 Low p_T electrons

The importance of being able to detect electrons at low p_T and over a broad range in pseudorapidity is well illustrated in gaugino ($\tilde{W}_1\tilde{Z}_2$) searches, where we select final states consisting of three leptons and $\not\!\!E_T$. The signature of interest here is those in which the W and Z, produced in association with two non-interacting $\tilde{Z}_1$'s, both decay leptonically to final states consisting of eee, $ee\mu$, $e\mu\mu$, or $\mu\mu\mu$, along with a neutrino (or anti-neutrino). The backgrounds for this process are small; observation of a measurable signal in this distinctive SUSY channel would be quite compelling. The expected cross section times the branching ratio ($\sigma \cdot B$) for these processes, however, are also quite small, underscoring the utility of increased acceptance in this measurement.

The leptons carrying the least amount of transverse energy in these decays tend to be soft, with a large fraction of them produced in the forward direction. In the eee channel, a $\tilde{W}_1$ mass of 45 (100) GeV is expected to result in a final state in which 90 (50)% of the softest electrons (*i.e.*, the third leading electrons) have p_T below 10 GeV, with roughly 30 (25)% of these produced in the pseudorapidity range $1.5 < |\eta| < 2.5$. [2]

The overall analysis efficiency for the eee channel – which is the product of the efficiencies due to the geometric and kinematic acceptance, offline selection cuts, and the trigger – has been determined to be 2.4 (15.6)% for the lower (higher) $\tilde{W}_1$ masses quoted above. The low efficiency is, in part, an indication of the difficulty of doing physics with electrons (and muons) that are produced over a broad range in pseudorapidity, with a significant fraction of them at low p_T. We have nevertheless been able to exclude regions of the relevant parameter space via this distinctive channel, in part because of our forward calorimetry (see Fig. 4). [9)]

[2] The range $1.5 < |\eta| < 2.5$ is the region where, in practice, the forward electromagnetic calorimeter is sensitive. EM coverage in the central region extends to $|\eta| < 1.1$; the region $1.2 < |\eta| < 1.4$ lacks any EM coverage.

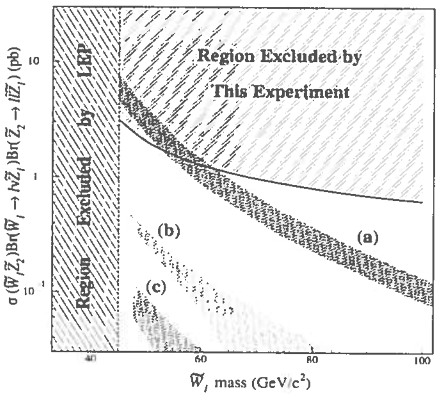

gure 4: The 95% confidence limit on cross section times branching ratio into eee, μ, $e\mu\mu$, or $\mu\mu\mu$, as a function of $M_{\tilde{W}_1}$, along with the region of $M_{\tilde{W}_1}$ excluded by :P. The bands represent the expected limits for different treatments of the theory.

Photon Identification

ιere are a number of physics signatures of interest at the Tevatron containing fi- l state photons that make photon detection an important design consideration. partial list includes the single (direct) photon cross section, the diphoton cross :tion and mass distribution, measurement of the intrinsic transverse momentum the incoming partons (k_T) in diphoton final states, and γ/jet angular distribu- ns. In addition, the $W\gamma$ and $Z\gamma$ diboson couplings are explored via their rather tinctive $e/\mu/\gamma$ final states.

The techniques and criteria applied for photon identification at DØ are alogous to those for electron identification, except that there is required to be no .ck pointing to the electromagnetic cluster. Similar cuts related to cluster shape d isolation, and electromagnetic energy fraction, are applied.

Direct Photon Cross Section

e primary experimental challenge in the measurement of the inclusive photon ›ss section is the extraction of the prompt photon signal from the copious back- ›unds due to π^0 and η meson decays to photons. We use the calorimetric quantity (EM1/E_{tot}) to determine the photon purity (or background fraction), where EM1 he energy deposited in the first electromagnetic layer, and E_{tot} is the total energy the cluster. The dominant background consists of boosted diphotons from meson :ay (*i.e.*, π^0 or $\eta \to \gamma\gamma$). Over most of the p_T regime of interest, the transverse mentation of the calorimeter is too coarse to spatially resolve the photon pair into its two components. Instead, we exploit the longitudinal readout segmentation: the meson decay backgrounds, consisting as they do of two photons, are twice as likely to convert in the first EM layer than a single photon, and will therefore shower earlier. The background is therefore expected to deposit more energy in the initial layer of the calorimeter than the single, prompt photon.

The central and forward photon cross sections, [10] spanning a photon p_T range of $\approx$ 10 to 100 GeV, are shown in Fig. 5. The dotted line represents a next-to-leading order (NLO) theoretical calculation by Baer, Ohnemus, and Owens, [11] in which CTEQ2M [12] parton distribution functions have been used. The cross section in the range $1.6 < |\eta| < 2.5$ is a new one at hadron colliders. The primary strength of DØ's contribution to physics involving photons arises from this increase in acceptance. The additional acceptance has also measurably improved our physics capability in exploring the diboson couplings. [13]

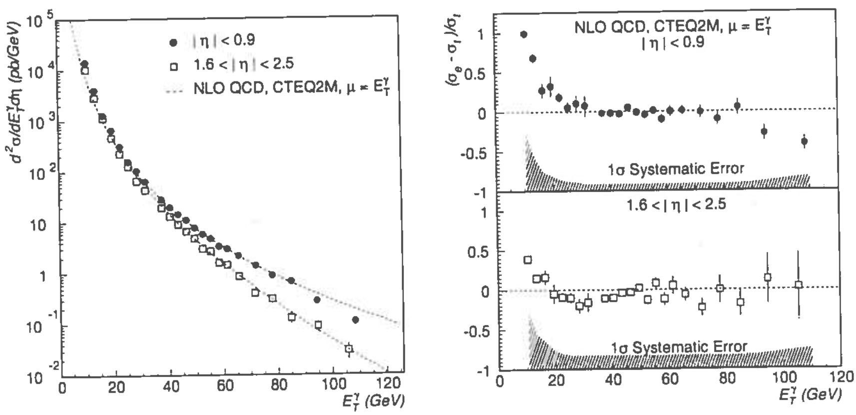

Figure 5: Direct photon cross section for the central ($|\eta| < 0.9$) and forward ($1.6 < |\eta| < 2.5$) regions, along with a theoretical calculation (left). $(\sigma_{exp} - \sigma_{theory})/\sigma_{exp}$ taken from previous plot, including the 1-σ systematic error band (right). (*DØ Preliminary*)

5 Jets

There are three basic jet-finding algorithms being employed at DØ. For the physics we have reported on to date, the fixed cone algorithm is most commonly in use. Cone sizes ΔR of 0.3, 0.5 and 0.7 are employed by default in the event reconstruction, where $\Delta R = \sqrt{(\Delta\phi)^2 + (\Delta\eta)^2}$. A nearest neighbor clustering algorithm, similar in concept to that used in our electron finding, and a k_T algorithm, are also being pursued. In the interests of space, we discuss only the cone algorithm below.

In the fixed cone algorithm, the hadronic and electromagnetic E_T in towers f size 0.1×0.1 in $\Delta\eta \times \Delta\phi$ is summed. All towers with $E_T > 1$ GeV are considered seed" towers, and jets are constructed about these towers within a cone size of a iven ΔR. The jet direction, defined in terms of the measured jet energy and its $, y$, and z components, is computed, and the process is repeated using the new jet irection as the jet center. The above is iterated until the jet direction is stable.)nly jets with $E_T > 8$ GeV are kept in the final jet list for use in offline analyses. 'he reader is referred to Ref. 14) for more detailed information on the cone algorithm sed at DØ.

Our jet calibration 15) consists of a series of steps that correct the raw ıeasured jet energy (or E_T) for a number of effects, including zero suppression of ur asymmetric pedestals, underlying energy from the spectator interaction, particle howering outside of the jet cone, and response variations correlated with jet width. 'he overall hadronic scale is derived from balancing the $\not{E}_T$ in photon-jet events. 'he minimization of dead regions and cracks in the calorimeter, the demonstrated nearity of the device, and the uniform technology have helped control the magniıde of the jet corrections that we need to apply: for central ($|\eta| < 0.5$) jets, for xample, we never correct jet energies by more than 20% for jets of any accessible $_T$ value.

.1 Jet Physics Topics

ull coverage, as well as effective control of all sources of noise (coherent and incoerent), are design features that directly impact studies of rapidity gaps between ts. We use the measurement of the energy flow between jets produced at large $|\eta|$ › distinguish between $\bar{p}p$ processes resulting from color singlet exchange, and those :sulting from exchange of a color octet (*i.e.*, a gluon). 16) Dijet events with both ts having $|\eta| > 2$ are chosen, and are classified according to the sign of the product $\cdot \eta_2 \equiv \beta$. Events with a positive (negative) value of β contain two jets produced ı the same (opposite) side(s) of the calorimeter.

Opposite-side events are expected to contain a significant component due › color singlet exchange. This component is discernible as an excess of events with :tle or no associated activity in the central region. The same-side events are exected to be dominated by color octet exchange, and are used as a control. These 'ents should result in a smooth distribution of centrally-produced particles. In ei.er case, the energy distribution of the particles produced in the central ("non-jet") gion is expected to be soft, implying that high resolution, low-noise calorimetry is particularly desirable feature here.

The number of calorimeter towers above threshold (n_{cal}) versus the number

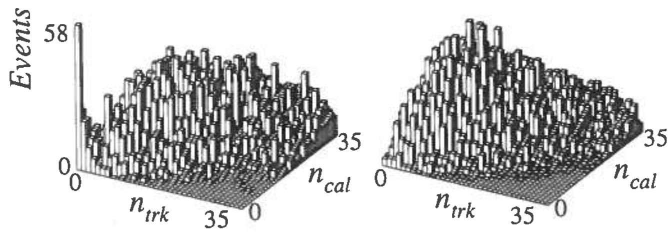

Figure 6: Number of calorimeter towers above threshold (n_{cal}) versus number of reconstructed central drift chamber tracks (n_{trk}) for $|\eta| < 1.3$ in opposite-side (left) and same-side (right) events. The excess at low track multiplicity/low number of towers above threshold is interpreted as evidence of color singlet exchange.

of tracks reconstructed in the central region (n_{trk}) is shown for the two samples in Fig. 6. The excess of opposite-side events that have small values for both n_{trk} and n_{cal} are clearly visible. The calorimeter threshold used in the analysis is 200 (400) MeV for EM (hadronic) towers, which effectively eliminates most towers containing only noise. Typical noise levels of 30 (100) MeV in an EM (hadronic) tower, and average energy deposition for minimum ionizing particles of $\approx$ 300 (1000) MeV per tower, have been measured *in situ*. Our ability to resolve small signals over noise is quite useful in analyses of this kind. From these data, we measure a fractional excess of color singlet above color octet exchange of 1.07 ± 0.10 (stat) $^{+0.25}_{-0.13}$ (syst)%.

The processes involved in rapidity gap physics help to demonstrate the importance of calorimetry that is stable and well-characterized at the low end of the dynamic range. At the other end of the scale (*i.e.*, high-E_T), shower containment is an important consideration, as it helps to mitigate the effects of fluctuations in unseen energy that can escape the calorimeter in the longitudinal direction. Broad dynamic range of the calorimeter readout is also desirable, as one would like to avoid any saturation effects that might induce biases, particularly as a function of E_T. In the central (forward) inclusive jet cross section, for example, jet energies of up to $\approx$ 450 (600) GeV are probed. Shape variations in the inclusive jet cross section can be a signature of new physics; minimization of these types of potentially E_T-dependent biases is therefore an important concern.

Our measurement of the inclusive jet cross section for $|\eta| < 0.5$ is shown in Fig. 7. Also shown is comparison of the data with a NLO theoretical calculation [17] that uses as input a few different CTEQ parton distribution functions. The cross section falls by some seven decades over the $\approx$ 450 GeV E_T interval. It is clear from the data that the theoretically predicted shape of the distribution is quite sensitive to the chosen set of parton distribution functions. The jet energy scale uncertainty

; the dominant source of systematic error, contributing up to 30% to the systematic rror at high-E_T. Efforts are underway to reduce the error in the jet energy scale, s well as the overall systematic uncertainty in the cross section.

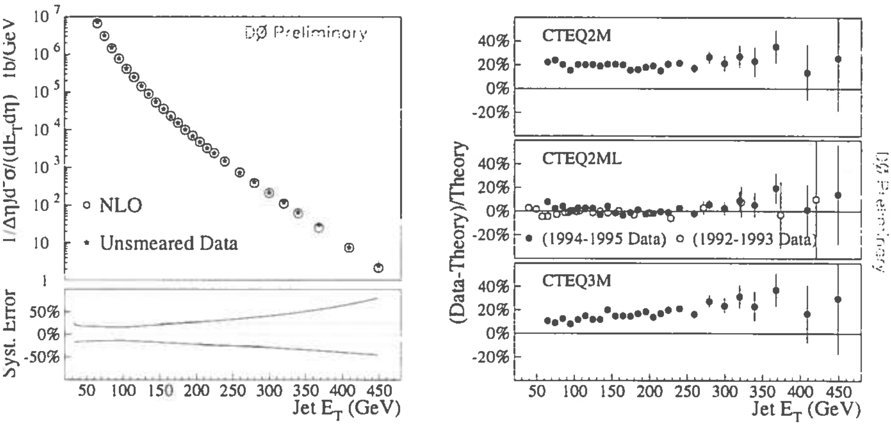

'igure 7: The central inclusive jet cross section, with a comparison to next-to-ꞓading order theory. The systematic error band is shown below (left). Comparison f the data with a few different parton distribution functions. A comparison of early nd late data sets are shown in the middle plot (right). (Errors in series of plots on ight hand side are statistical only.) (*DØ Preliminary*)

Exploiting the physics that forward $|\eta|$ coverage can provide – particularly ı jet physics – constitutes a major portion of the physics program at DØ. We direct he reader to Refs. [14, 18, 19, 20] for a description of a few of these topics.

Missing E_T ($\not\!\!E_T$)

[omogeneity of response and good resolution is also advantageous in the determi-ation of $\not\!\!E_T$, which is defined as follows:

$$\vec{\not\!\!E}_T = -\sum_{i=1}^{N_{cells}} \vec{E}_{T_i}. \tag{3}$$

'he sum is over all cells in the calorimeter. This quantity is optionally corrected for nergy detected in the inter-cryostat region, or the measured momentum of muons ı the event, or both.

Inclusion of the ICR energy has been shown to significantly enhance the esolution in $\not\!\!E_T$. We use QCD multi-jet events, where any measured $\not\!\!E_T$ results rimarily from instrumental effects, to quantify this effect (there should be little or o physics-related $\not\!\!E_T$ in these events). Computing the $\not\!\!E_T$ both with and without

ICR corrections in the same set of multi-jet events, we find a $\approx 44\%$ reduction in the number of events with $\not{E}_T > 30$ GeV after ICR corrections are applied. Cryogenic systems, which unavoidably introduce (usually sizable) inter-cryostat boundaries, invariably suffer from incomplete sampling in these regions. Global event variables, such as $\not{E}_T$, can be particularly sensitive to such dead spaces. The above number gives a semi-quantitative indication of how important recovering the energy in these detector regions can be.

Missing E_T is of course of great utility in high-p_T physics, particularly that involving final state W bosons that decay leptonically to a charged lepton and a ("invisible") neutrino. Top pair production, in which both top quarks decay to a W and a b quark, as well as a variety of electroweak topics involving W production, exploit $\not{E}_T$ in the detection of the relevant final states. $\not{E}_T$ is also particularly useful in SUSY and new phenomena searches, which are often expected to result in non-interacting final state particles, such as neutralinos or neutrinos.

The exclusion contour resulting from our squark–gluino search is shown in Fig. 8. The data for this analysis was acquired with a software trigger consisting only of a $\not{E}_T$ requirement, with a threshold that varied from 20 or 40 GeV during the run. The additional region of the parameter space that has been eliminated since our recent PRL publication [21] has resulted from a parallel ("updated") analysis in which the offline $\not{E}_T$ cut was reduced from 75 to 65 GeV, and an additional jet was required. The lower $\not{E}_T$ cut is helpful only because the variable is well-behaved – even at reasonably small values – and because fake $\not{E}_T$, which is dominated by instrumental effects and dead regions, is at some level corrected for in the DØ design.

7 Conclusion

Calorimetry, which is the heart of the DØ detector, is critical to the physics being pursued by the collaboration. The fine segmentation and superior energy resolution offer good electron and photon identification over the full solid angle, important for the broad variety of physics topics involving W and Z bosons, as well as final state photons. The uniformity of the response and technology, coupled with the full coverage, enhances many of the opportunities in jet physics, where the full shower containment, low noise, and broad dynamic range enhance the physics reach. The calorimetric energy resolution and hermeticity offer stable, high-resolution measurements of $\not{E}_T$, useful in a variety of physics processes.

With the addition of a central and forward preshower system, an improved inner tracking system (including a silicon vertex chamber and scintillating fiber tracker), and a central magnetic field, the upgraded DØ detector has been designed

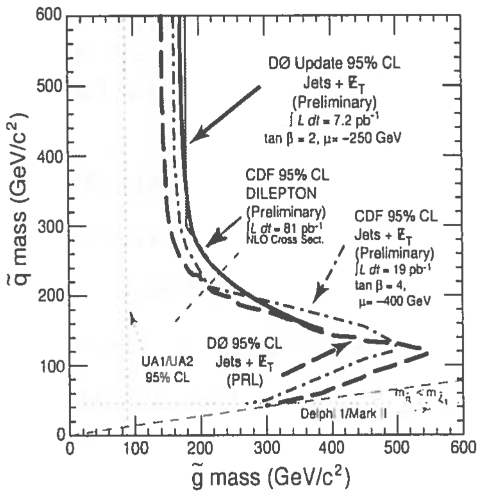

Figure 8: Squark-gluino exclusion contour.

th an eye toward continuing to exploit the detector's already-existing calorimetric rengths. We look forward to continuing our pursuit of a broad physics program ıring the coming Main Injector era at the Tevatron.

eferences

. The pseudorapidity, η, is defined by the relation $\eta \equiv -\ln[\tan(\theta/2)]$, where θ is the polar angle with respect to the proton-beam direction. The z axis in the DØ coordinate system is along the beam axis, r is the distance perpendicular to that axis, and ϕ is the polar angle.

:. S. Abachi *et al.*, *Nucl. Instr. Meth.* **A338**, 185 (1994).

;. J. Kotcher, "Design, Performance, and Upgrade of the DØ Calorimeter", *Proceedings of the 1994 Beijing Calorimetry Symposium*, IHEP - Chinese Academy of Sciences, Beijing, China, October 25-27, 1994, pp. 144-158; J. Kotcher, "Upgrade Plans for the DØ Calorimeter", these proceedings.

ı. S. Abachi *et al.*, *Phys. Rev.* **D52**, 4877 (1995).

;. M. Narain and U. Heintz, "A Likelihood Test for Electron ID", DØ Internal Note #2386 (December, 1994).

;. The value for the Z mass we use is $M_Z^{LEP} = 91.1884 \pm 0.0022$ GeV/c^2, from P. Renton, "Precision Tests of the Electroweak Theories", *Lepton-Photon Con-*

ference, Beijing, P.R. China (1995), OUNP-95-20. For reference, we quote the world value of the π^0 and J/ψ masses: $m_{\pi^0} = 0.1350 \pm 0.0006$ GeV/c^2 and $m_{J/\psi} = 3.09688 \pm 4 \times 10^{-5}$ GeV/c^2, from Particle Data Group, L. Montanet *et al.*, *Phys. Rev.* **D50**, 1173 (1994).

7. H. Aihara *et al.*, *Nucl. Instr. Meth.* **A325**, 393 (1993).

8. S. Abachi *et al.*, FERMILAB-PUB-96/177-E, submitted to *Phys. Rev. Lett.*

9. S. Abachi *et al.*, *Phys. Rev. Lett.* **76**, 2228 (1996).

10. S. Abachi *et al.*, FERMILAB-PUB-96/072-E, submitted to *Phys. Rev. Lett.*

11. H. Baer, J. Ohnemus, and J.F.Owens, *Phys. Rev.* **D42**, 61 (1990).

12. CTEQ Collaboration, J. Botts *et al.*, *Phys. Lett.* **B304**, 159 (1993).

13. S. Abachi *et al.*, *Phys. Rev. Lett.* **75**, 1028 (1995); S. Abachi *et al.*, *Phys. Rev. Lett.* **75**, 1034 (1995); S. Abachi *et al.*, FERMILAB-PUB-96/115-E, submitted to *Phys. Rev. Lett.*

14. H. Weerts, "Studies of Jet Production with the DØ Detector", *Proceedings of the 9th Topical Workshop on Proton-Antiproton Collider Physics*, University of Tsukuba, Ibaraki, Japan, October 18-22, 1993, p. 192; N. Hadley, "Cone Algorithm for Jet Finding", DØ Internal Note #904 (November, 1989).

15. B. Kehoe, "Hadronic Calibration of the DØ Calorimetry", these proceedings.

16. S. Abachi *et al.*, *Phys. Rev. Lett.* **76**, 734 (1996).

17. S.D. Ellis, Z. Kunszt, and D.E. Soper, *Phys. Rev. Lett.* **64**, 2121 (1990); F. Aversa *et al.*, *Phys. Rev. Lett.* **65**, 401 (1990); W. Giele, E.W.N. Glover, and D.A. Kosower, *Phys. Rev. Lett.* **73**, 2019 (1994).

18. S. Abachi *et al.*, *Phys. Lett.* **B357**, 500 (1995).

19. B. Abbott, "The Dijet Mass Spectrum and Angular Distributions with the DØ Detector", *Proceedings of the 11th Topical Workshop on Proton-Antiproton Collider Physics*, Padova, Italy (1996), to be published.

20. V.D. Elvira, "Inclusive Jet Cross Sections a~~t the DØ Detector",~~ *Proceedings of the 8th Meeting, Division of Particles and Fields of the American Physical Society*, University of New Mexico, Albuquerque, New Mexico, August 2-6, 1994, p. 1637.

21. S. Abachi *et al.*, *Phys. Rev. Lett.* **75**, 618 (1995).

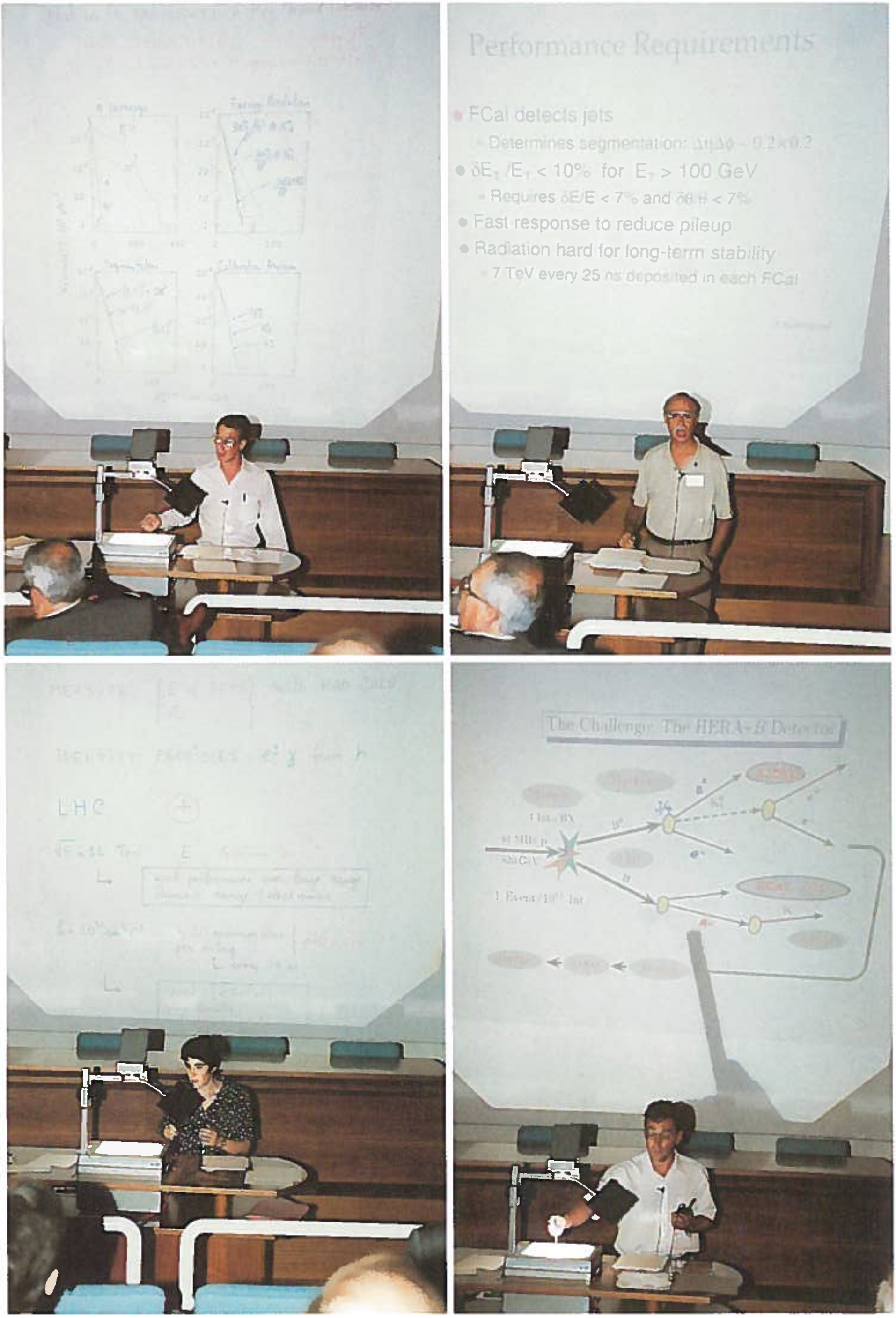

From the Overview Session (from top left, clockwise): L. Sulak, J. Rutherfoord, A. Golutvin, F. Gianotti.

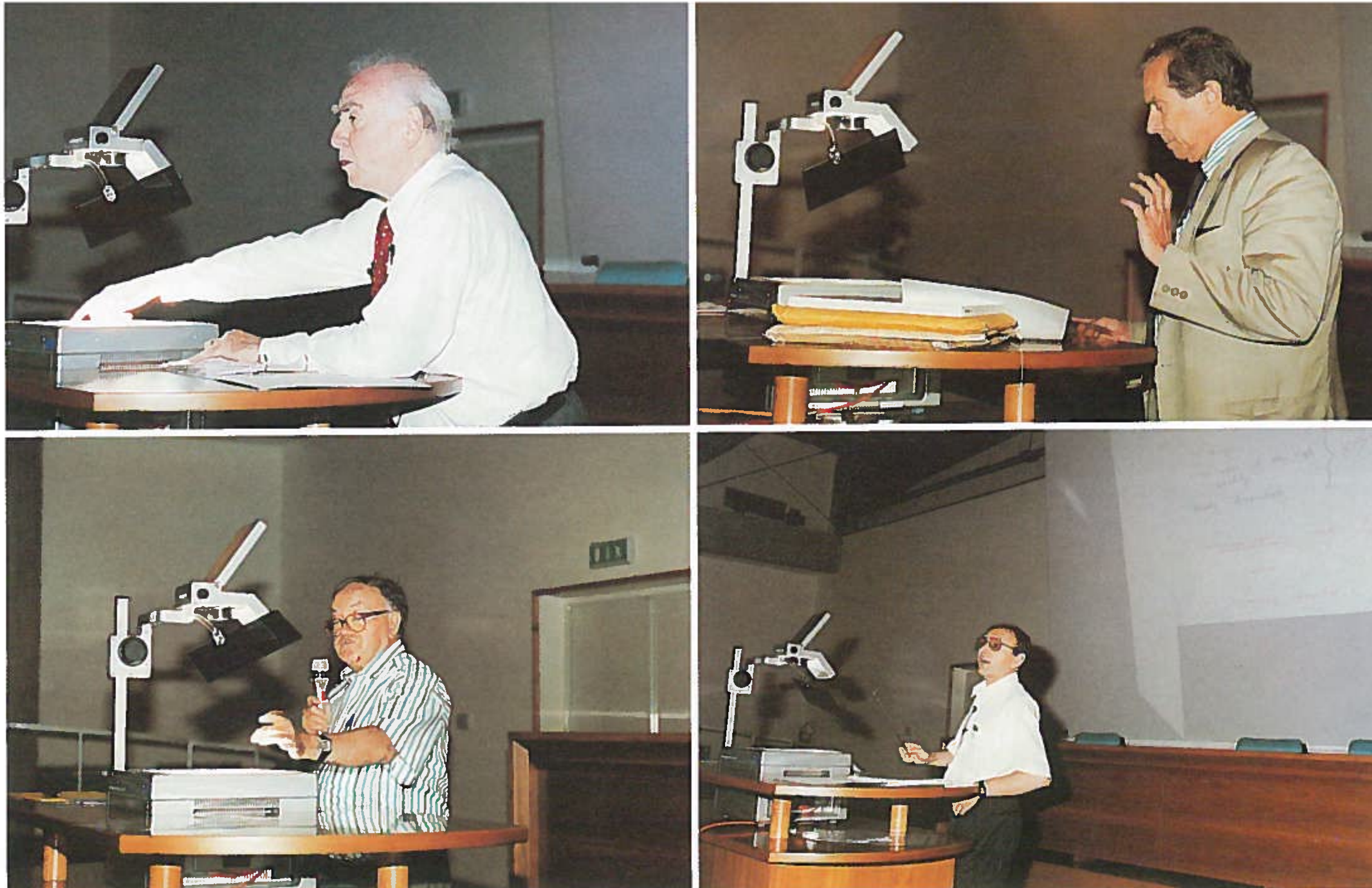

Speakers at the desk (from top left, clockwise): G. Salvini, G.Barbiellini, A. Para and B. Aubert.

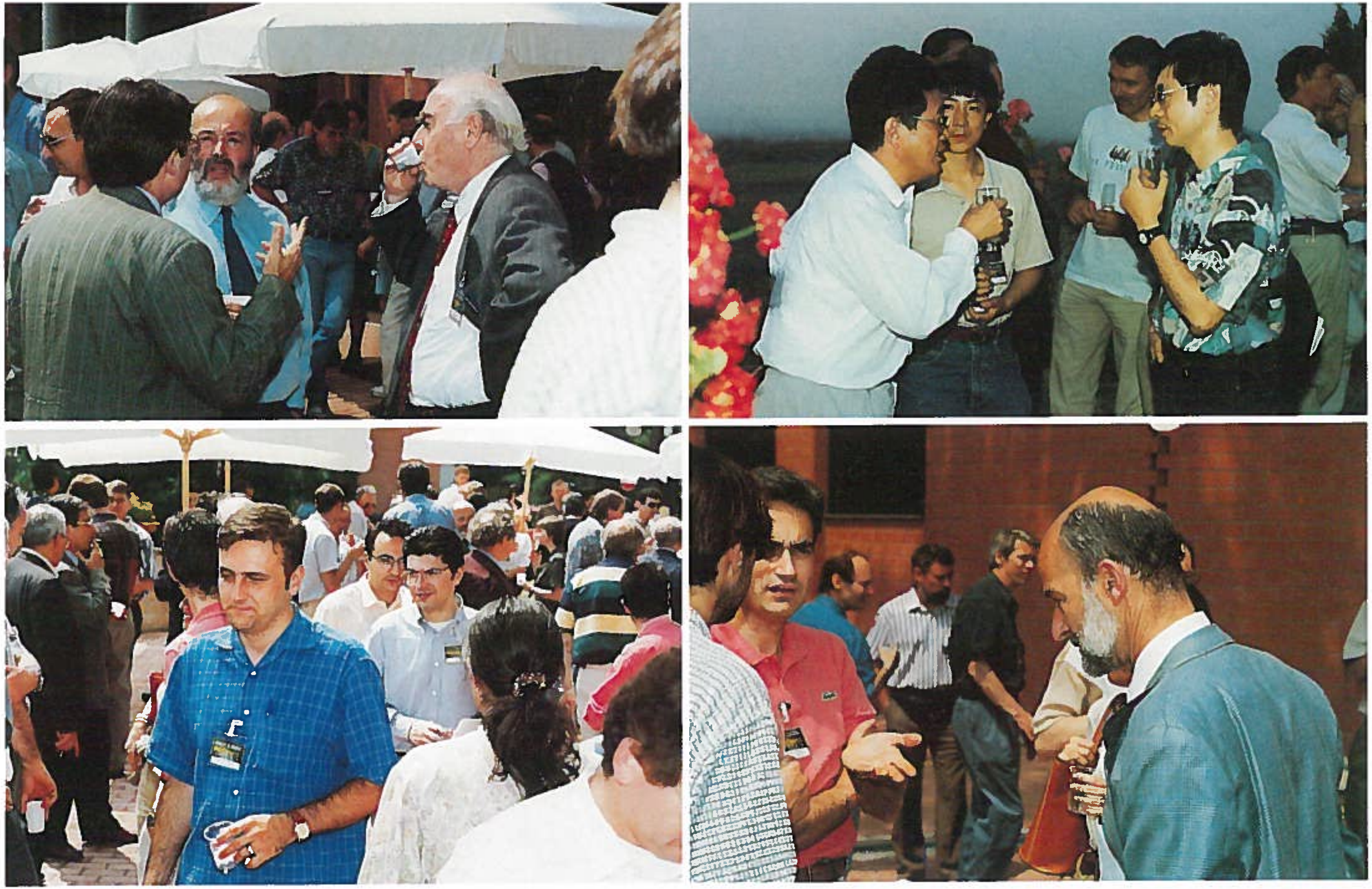

Relaxing at coffee breaks (among others): G. Salvini, F.L. Fabbri, E. Iarocci and A. Para, K. Arisaka, A. Ereditato and M. Spinetti, L. Benussi, P. Valente and L. Bucci.

In front of the new Alte Energie Building.

Lunch time (among others): K. Pretzl, L. Sulak and S. Bertolucci, G. Costa and B. Aubert, A. Antonelli. P. Shanan and V. Valente, D. Fournier and L. Dobrzynski.

Unwinding at the Social Banquet (among others): K. Lassila-Perini, L. Sulak and K. Pretzl, J. Adams, P. Gauzzi, G. Cabibbo, C. Colantuono, P. Valente, L. Bucci and S. Conticelli, R. Centioni, G. Bencivenni, and M.C. Spitalieri, P.L. Frabetti, Ms. P.L. Frabetti, S. Bianco and M. Bertani.

Author Index

uthor Index

kchurin, N. 269
ltarev, I. 669
lvsvaag, S. J. 177
nghinolfi, M. 201
ntonelli, M. 237, 359, 561
nulli, F. 237, 359
rena, V. 337, 509
rmbruster, B. 133
rrington, K. 269
spell, P. 627, 861
ubert, B. 113
ulchenko, V. M. 441
vakian, H. 201, 659
adier, J. 627
amberger, A. 209
arbiellini, G. 99, 237, 359
ari, M. 177
arladyan, A. K. 441
arney, D. 861
arreira, G. 177
ates, S. 627
attaglieri, M. 201
attistoni, G. 451, 561, 827
eetz, C. P. 269
eker, H. 359
elikov, S. V. 125
ellini, V. 727
encze, Gy. L. 519
enedettini, A. C. 177, 817
ertin, A. 817
ertolucci, S. 237, 359
esnard, F. 791
ianchi, N. 201, 659
ianco, S. 539
igi, M. 177
ini, C. 237, 359
ityukov, S. 627
izzeti, A. 519
lagov, M. I. 435
lair, I. M. 133
loch, P. 861
loch, Ph. 627
loise, C. 237, 359
oca, G. 337, 509
odek, A. 553
odmann, B. A. 133
oezio, M. 545
onder, A. E. 441
onesini, M. 177
onivento, W. 607
Bonomi, G. 337, 509
Booth, N E. 133, 269
Bordello, P. 627
Borgia, B. 347
Bornheim, A. 209
Bosman, M. 299
Bourotte, J. 861
Bozzo, M. 177
Braver, A. 269
Brown, R. M. 627
Bruschi, M. 817
Buontempo, S. 247
Busata, A. 627
Busson, Ph. 627
Cabibbo, G. 237, 359
Caloba, L. P. 791
Caloi, R. 237, 359
Cambiaghi, M. 369
Camin, D. V. 827
Campana, P. 237, 359
Camporesi, T. 177
Cantoni, P. 441
Capitani, G. P. 201, 659
Capogni, M. 727
Capone, A. 247
Carey, R. 269
Carling, H. 177
Casano, L. 727
Cassio, V. 177
Castellani, L. 177
Castoldi, M. 727
Cauz, D. 369
Cereseto, R. 177
Cerri, C. 841
Cervelli, F. 237, 359
Charlot, C. 627
Chendvankar, S. R. 627
Cheremukhin, I. 627
Chiavassa, E. 289
Chignoli, F. 177
Chung, Y. S. 337
Ciciani, L. 727
Civinini, C. 519
Clayton, E. 627
Cleland,W. E. 849
Cocco, A. G. 247
Cockerill, D. J. A. 627
Collamati, A. 817
Collot, J. 873
Conforto, G. 125

Connolly, J. 627
Corvisiero, P. 201
Cotta–Ramusino, A. 817
Coulon, J. P. 873
Crittenden, J. 209
Csabo,T. 133
D'Alessandro, R. 519
D'Angelo, A. 727
D'Antone, I. 817
D'Azeglio, A. 727
Dalla Santa, F. 519
Dannemann, A. 617
Dasu, S. 529
David, M. 219, 639
de La Taille C. 799
De Marco, N. 289
De Sanctis, E. 659
De Zorzi, G. 237, 359
De Castro, S. 817
Della Ricca, G. 177
Dellacasa, G. 289
De Min, A. 607
Denes, P. 85
Denisov, A. G. 125
Denisov, S. P. 125, 165
Denton, L. 627
Depedis, D. 247
Deppman, A. 201
de Saintignon, P. 873
De Sanctis, E. 201
Dharmasiri, D. R. 177
Di Capua, E. 247
Di Cosimo, G. 237, 359
Di Domenico, A. 237, 359
Di Falco, S. 237, 359
Diemoz, M. 743
Dinkespiler, B. 873
DiSalvo, R. 727
Djilkibaev, R. 627
Djilkibajev, R. 669
Dobrzynski, L. 627
Doets, M. 659
Donà, R. 817
Dore, U. 247
Doulas, S. 269
Drexlin, G. 133
Dushkin, A. Yu. 125, 165
Dzhelyadin, R. I. 599
Eberhard, V. 133
Edgington, J. A. 133
Eek, L. O. 873
Efthymiopoulos, I. 497
Eichner, C. 133
Eitel, K. 133
Ekimov, A. V. 125
Engler, J. 117
Ereditato, A. 247
Erriquez, O. 237, 359
Ershov, A. E. 599
Espirito Santo, M. C. 177
Fabbri, F. L. 539
Faion, S. 133
Falk, E. 177
Fan, Q. 553, 921
Fantoni, A. 659
Farilla, A. 237, 359
Fassnacht, P. 417
Fedyakin, N. 827
Feng, X. Q. 679
Fenyuk, A. 177
Ferrando, A. 519
Ferrari, A. 237, 359
Ferrari, P. 177, 561
Ferreira, O. 627
Ferretti, A 817
Ferroni, M. 247
Finckh, E. 133
Fiorillo, G. 247
Fournier, D. 381
Fouz, M. C. 519
Frabetti, P. L. 441, 449
Franzini, P. 237, 359
Freeman, J. 323
Galli, A. 359
Galli, D. 817
Gallio, M. 289
Gamba, D. 177
Ganel, O. 269
Ganguli, S. N. 627
Ganzhur, S. 441
Garufi, F. 247
Gauzzi, P. 237, 359
Gavrilov, V. 269
Gemmeke, H. 133
Gennaro, G. 125
Gershtein, Y. 269
Gervino, G. 727
Ghio, F. 727
Giacobbe, B. 817
Gianini, G. 337, 509
Gianotti, F. 65
Gilitsky, Yu. 165
Giordano, V. 177
Giourdjian, V. 201, 659
Giovannella, S. 237, 359
Girolami, B. 727
Giuliani, A. 143
Gninenko, S. 627
Go, A. 873
Godinovic, N. 627
Goerlach, U. 173
Golubev, V. B. 693

Golutvin, A. 49
Golutvin, I. 627
Gomes, A. 219, 639
Gorelov, I. V. 225
Gourlay, S. 337
Gouz, I. 177
Grabit, R. 627, 861
Grabosch, H. –J. 209
Graziani, E. 237, 359
Gregory, Ch. 627
Grimm, K. 669
Grindler, A. 133
Grothe, M. 209
Guaita, P. 289
Guerzoni, M. 177
Gumbsheimer, R. 133
Gumenyuk, S. 177
Gurtu, A. 627
Gurzhiev, S. N. 125
Guschin, E. 627
Gutnikov, Yu. E. 125
Hammel, T. 669
Han, S. W. 237, 359
v. Harrach, D. 669
Hartmann, P. 669
Hazen, E. 269
Hedberg, V. 177
Henkes, T. 659
Henriques, A. 219, 311
Hervas, L. 209
Hilger, E. 209
Hobson, P. R. 627
Hoffmann, J. 669
Hofmann, H. 669
Holm, U. 209, 617
Horstmann, D. 209
Hößl, J. 133
Hostachy, J. Y. 873
Hucker, H. 133
Iconomidou-Fayard, L. 393
Iglesias, A. 519
Imrie, D. C. 627
Incagli, M. 237, 359
Introzzi, G. 369
Ivanyushenkov, I. 177
Ivochkin, V. 519
Jacobs, K. 893
Jannakos, T. 133
Jarlskog, G. 177
Jarron, P. 627, 861
Jevaud, M. 873
Johnson, O. C. 269
Josa, M. I. 519
Kabuß, E. 669
Karar, A. 627
Karyukhin, A. 177
Kaufmann, V. 209
Kaya, M. 269
Kefford, D. 269
Kehoe, R. 349
Kezerashvili, G. Ya. 441
Khan, A. 519
Kharchilava, A. 209
Kiersteaded, J. A. 557
Kim, W. 237, 359
Kirina, T. M. 125
Kleifges, M. 133
Kleinfeller, J. 133
Klimenko, S. G. 441
Kloukinas, K. 627
Klovning, A. 177
Knapp, J. 117
Köbis, S. 669
Kochetkov, V. I. 125
Kokoulin, R. P. 125
Kolachev, G. M. 441
Kolossov, V. 269
Kolstein, M. 659
Komar, A. A. 435
Konopliannikov, A. 177
Kornmayer, H. 117
Kotcher, J. 383, 923
Kötz, U. 209
Krasnov, A. 441
Kretschmer, W. 133
Krienen, F. 269
Kronkvist, I. 177
Kuleshov, S. 269
Kummerow, D. 209
Kupta, S. K. 627
Lanceri, L. 177
Lanfranchi, G. 237, 359
Lanfranchi, M. 125
Langland, J. 269
Lanni, F. 441
Lassila–Perini, K. 487
Lebeau, M. 777
Lecoq, P. 755
Lee, K.-B. 337
Lee, M. H. 695
Lee-Franzini , J. 237, 359
Lemeilleur, F. 627
Leoni, R. 177
Levi Sandri, P. 201, 727
Levy, P. W. 557
Liguori, G. 337
Lipaev, V. V. 125
Lissauer, D. 849
Litvintsev, D. 269
Llope, W. J. 187
Lobashev, V 669
Locher, M. 117

Lomtadze, T. 237, 359
Longhi, A. 201
Loos, R. 627
Lopes Ginja, A. 669
Los, S.V. 125
Lourenço, C. 529
Loverre, P. F. 247
Lund-Jensen, B. 873
Luppi, C. 247
Ma, D. A. 557, 589
Maas, F. E. 669
Macina, D. 247
Maeland, O. A. 177
Magill, S. 919
Maity, M. 627
Majumder,G, 627
Malinin, A. 519
Mallik, U. 209
Malvezzi, S. 337
Malyshev, V. M. 441
Manfredi, P. F. 441
Manigot, P. 627
Mansanta, S. 201
Mansoulié, B. 407
Marchesotti, M. 337, 509
Marchetti–Stasi, F. 247
Marchionni, A. 125
Marchioro, A. 627
Marconi, U. 817
Marroquim, F. 791
Martelli, F. 125
Martin–Chassard, G. 799
Martinez–Laso, L. 519
Maschuw, R. 133
Maslennikov, A. L. 441
Mazumdar, K. 627
Mazza, R. 177
Mazzoni, M. A. 247
McPherson, J. 269
Melnikov, E. A. 125
Mendiburu, J. P. 807
Merlo, M. 337, 509
Meschini, M. 519
Messina, M. 247
Meyer, A. 209
Meyer–Larsen, A. 671
Michaud, Y. 873
Mielke, H. H. 117
Migliore, E. 177
Migliozzi, P. 247
Mikhailin, V. 165
Mikhailov, V. S. 125
Miller, D. 627
Miller, J. 269
Miller, M. 269
Milov, A. M 441
Miscetti, S. 237, 359
Moissenz, P. 627
Mokeev, V. I. 201
Monnier, E. 873
Moricciani, D. 727
Morselli, A. 545
Moulik, T. 627
Mozzetti, R. 659
Muccifora, V. 201, 659
Muchnoi, N. Yu 441
Murtas, F. 237, 359
Musienko, Y. 627
Musso, A. 289
Navarria, F. L. 177
Negri, P. 177
Newmann, H. 557
Nicoletti, L. 727
Nikitenko, A. 529
Nikitin, A. 269
Nòbrega, R. 529
Nossum, B. 177
Novotny, R. 683
Nowoczyn, M. 209
Nupieri, M. 659
Obraztsov, V. 177, 627
Oehler, C. 133
Olcese, M. 201
Olivetto, C. 873
Onel, Y. 269
Onofre, A. 177
Onuchim, V. 165
Onuchin, A. P. 441
Osborne, D. 269
Ossowski, R. 209
Ostankov, A. P. 599, 627
Ozel, E. 269
Ozkorucuklu, S. 269
Paganoni, M. 177
Palladino, V. 247
Palumbo, F. 441
Panin, V. S. 441
Pauletta, G. 369
Pegoraro, M. 177
Peleganchuk, S. V. 441
Peralta, L. 177
Perrotta, A. 177
Pessina, G. 827
Petrovykh, L. 177
Petrukhin, A. A. 125
Pezzetta, M. 289
Piccinini, M. 817
Piccotti, A. 289
Pietropaolo, F. 153
Pimenta, M. 177
Piredda, G. 247
Pivovarov, S. G. 441

Plischke, P.	133
Podrasky, V.	269
Pogorelov, Yu. A.	441
Pojidaev, V.	519
Polli, E.	201
Popov, S.	627
Popov, V.	627
Poropat, P.	177
Pospelov, G. E.	441
Prest, M.	177
Protopopov, Yu.	627
Pruneau, C. A.	261
Puljak, I.	627
Radeka, V.	787, 849
Ragazzi, S.	607
Ramos, S.	627
Rapp, J.	133
Ratti, S. P.	509
Ratti, S.	337
Re, V.	441
Read, A. L.	177
Rednic, I.	133
Reichenbacher, J.	133
Reolon, A. R.	201, 659
Rescia, S.	849
Reynaud, S.	861
Reznikov, M. A.	125
Riccardi, C.	337, 509
Ricci, M.	115
Ricciardi, S.	247
Ricco, G.	201
Righini, P.	247
Rininsland, A.	133
Ripani, M.	201
Roberts, B. L.	269
Rohlf, J.	269
Romanov, L.V.	441
Romero, A.	177
Rosowsky, A.	269
Rossi, P.	201, 659, 727
Rosso, E.	627
Ruf, C.	133
Rusack, R.	199
Rusinov, V.	269
Ruth, E.	269
Rutherfoord, J.	35
Rykalin, V. I.	599, 627
Saitta, B.	247
Sala, A.	337
Sala, P. R.	561, 827
Salicio, J. M.	519
Salvini, G.	3
Santacesaria, R.	247
Santi, L.	369
Sanzeni, C.	269
Sanzone, M.	201
Sapunenko, V.	201
Sarwar, S.	539
Savoy-Navarro, A.	883
Schaerf, C.	727
Schirrmann, P.	133
Schlenstedt, S.	209
Schnürer, F.	133
Scomparin, E.	289
Scuri, F.	237, 359
Seez, C.	627, 765
Seguin–Moreau, N.	799
Seitz, R.	705
Seixas, J. M.	791
Seligmann, B.	133
Seman, M.	405
Semenyuk, I.	627
Semprini–Cesari, N.	817
Sen'ko, V.	177
Sergiampieri, F.	125
Sergueev, S.	627
Shalanda, N.	177
Shanahan, P. N.	717
Shein, I. V.	125, 165
Shwartz, B. A.	715
Simonetti, L.	177
Siolios, N	627
Skaali, B.	177
Skasyrskaya, A.	627
Smakhtin, V. P.	741
Smith, W.	529
Snesarev, A. A.	435
Soave, C.	289
Söderqvist, J.	873
Soldatov, A. P.	125, 165
Soric, I.	627
Soushkov, V.	627
Spandre, G.	125
Speransky, M. N.	435
Speziali, V.	441
Spighi, R.	817
Spiridonov, P.	627
Spiriti, E.	237, 359
Stagni, L.	441
Steidl, M.	133
Stenzel, H.	427
Stolin, V.	269
Stool, S. P.	557
Strolin, P.	247
Stumm, O.	133
Sulak, L. R.	15, 269
Sulin, V. V.	435
Sullivan, J.	269
Sun, Z.	627
Sytin, A.N.	125
Sytnik, V.	165
Tabarelli de Fatis, T.	607

Taiuti, M. 201
Takai, H. 849
Tanaka, R. 627
Terranova, F. 177
Tiecke, H. 209
Tikhonov, Yu. A. 441
Tisserand, V. 475, 873
Tisserant, S. 873
Tome, B. 177
Tonazzo, A. 607
Torre, P. 337
Tortora, L. 237, 359
Trapani, P. P. 177
Triantis, F. 627
Ulyanov, A. 269
Vallazza, E. 177
van der Brand, J. F. T. 659
Vanel, J. Ch. 627
VanHove, A. 861
Varela, J. 529, 627
Vasil'chenko, V. 627
Vecchi, S. 817
Venanzoni, G. 237, 359
Vercellin, E. 289
Verkerke, W. 209
Vezzani, A. 817
Vichou, I. 465
Videau, H. 907
Vigotti, F. 817
Villa, M. 817
Viola, L. 337, 509
Virdee, T. S. 461, 627
Vitale, A. 817
Vitulo, P. 337, 509
Vlasov, E. 177
Vossebeld, J. 209
Vreeswijk, M. 209
Wang, S. M. 209
Wich, K. 617
Wigmans, R. 269, 281
Wingerter–Seez, I. 849
Winn, D. 269
Wolf, J. 133
Wölfle, S. 237, 359
Woody, C. L. 557
Worstell, W. 269
Wu, H. 557, 589
Wu, J. 209
Yakimenko, M. N. 435
Yin, Z. W. 679
Yurchenko, V. I. 441
Zaitsev, A. 177
Zallo, A. 539
Zamiatin, N 627, 861
Zeitnitz, B. 133
Zhang, J. Q. 237, 359
Zhilich. V. 441
Zhu, R. Y. 577, 589, 653
Zoccoli, A. 817
Zubarev, E. 627
Zucchelli, P. 247
Zucchiatti, A. 201
Zucchiatti, S. 727

The ATLAS Collaboration 475
The ATLAS LARG Collaboration 417, 451, 465
The ATLAS TILECAL Collaboration 299, 311, 497
The Radiation Hardness ATLAS Group 893
The CMS/ECAL Collaboration 765
The CMS Hadron Calorimeter Collaboration 323
The DØ Collaboration 923
The E864 Collaboration 261
The H1 Collaboration 225
The KTEV Collaboration 717
The NA48 Collaboration 393
The RD 36 Collaboration 627
The STAR EMC Collaboration 187
The TAPS Collaboration 683

Participants

articipants

ntonella	Antonelli	INFN LNF
abio	Anulli	INFN LNF
atsushi	Arisaka	UCLA
aul	Aspell	CERN
ernard	Aubert	CERN
uido	Barbiellini	Trieste University
iuseppe	Battistoni	INFN Milano
iovanni	Bencivenni	INFN LNF
uigi	Benussi	INFN LNF
onica	Bertani	INFN LNF
ergio	Bertolucci	INFN LNF
tefano	Bianco	INFN LNF
Valter	Bonivento	Milano University
ermano	Bonomi	Pavia University
runo	Borgia	Roma I University
artine	Bosman	IFAE Barcelona University
eo	Bucci	INFN LNF
iorgio	Cabibbo	INFN LNF
andro	Calcaterra	INFN LNF
aniel Victor	Camin	INFN Milano
iorgio	Capon	INFN LNF
runo	Caridi	SEA – LeCroy
ranco	Catarsi	CAEN S.p.A.
omano	Catolla Cavalcanti	Tecnologie Avanzate S.r.l.
iego	Cauz	Udine University
laudio	Cerri	INFN Pisa, CERN
ristiano	Colantuono	INFN LNF
imone	Conticelli	INFN LNF
ranco	Corradi	Apparecchiature Per Industrie e Laboratori
iuseppe	Costa	INFN Milano
Maria	Curatolo	INFN LNF
Mario	David	LIP Lisbona University
hristophe	de La Taille	LAL
oberto	De Nichilo	Laben S.p.A.
eter	Denes	Princeton University
ergei	Denisov	IHEP
achele	Di Salvo	INFN Torino
Marcella	Diemoz	Roma I University
Ludwik	Dobrzynski	LPNHE France
Rustem	Dzhelyadin	IHEP
lias	Efthymiopoulos	CERN
Antonio	Ereditato	INFN Napoli
Franco Luigi	Fabbri	INFN LNF
Qun	Fan	Rochester University
Alessandra	Fantoni	INFN LNF

Ada	Farilla	INFN LNF
Patrick	Fassnacht	CPPM
Giulio	Felici	INFN LNF
Xi	Feng	Shanghai Institute of Ceramics
Daniel	Fournier	LAL
Mary–Cruz	Fouz	CERN
Pierluigi	Frabetti	Bologna University
Jim	Freeman	Fermilab
Paolo	Gauzzi	Roma I University
Vladimir	Gavrilov	ITEP
Hartmut	Gemmeke	Forschungszentrum Karlsruhe
Fabiola	Gianotti	CERN
Paola	Gianotti	INFN LNF
Simona	Giovannella	INFN LNF
Andrea	Giuliani	Milano University
Ulrich	Goerlach	CRN – ULP Strasbourg
V. B.	Golubev	BINP SD RAS
Andrei	Golutvin	ITEP
Igor	Gorelov	DESY
Iouri	Gouz	INFN Torino
Hans–J.	Grabosch	DESY
Ana	Henriques	LIP
Joerg	Hoerandel	Forschungszentrum Karlsruhe
Uwe	Holm	Hamburg University
Enzo	Iarocci	Roma I University
Lydia	Iconomidou–Fayard	LAL
Marco	Incagli	INFN Pisa
Karl	Jakobs	Mainz University
Aurelio	Juste	IFAE Barcelona University
Robert	Kehoe	Notre Dame University
Jonathan	Kotcher	BNL
Kati	Lassila–Perini	ETHZ
Michel	Lebeau	CERN
Paul	Lecoq	CERN
Moohyun	Lee	KEK
Paolo	Levi Sandri	INFN LNF
W. J.	Llope	Rice University
Milos	Lokajicek	AVCR Institute Of Physics
Vincenzo	Lucherini	INFN LNF
Frank E.	Maas	University Of Mainz
Umberto	Maerna	HAMAMATSU Photonics Italia S.r.l.
Stephen	Magill	Argonne National Lab.
Amelia	Maio	LIP
Bruno	Mansoulié	CEA Saclay
Joerg	Marks	CPP Marseille
Fernando	Marroquim	Rio de Janeiro University
Giselle	Martin–Chassard	LAL
Alessandra	Masciadri	HAMAMATSU Photonics Italia S.r.l.
Jean Pierre	Mendiburu	LAPP
Massimo	Meoni	Pol.Hi.Tech. S.r.l.
Joerghans–H.	Mielke	Forschungszentrum Karlsruhe

;quale	Migliozzi	CERN
fano	Miscetti	INFN LNF
	Monnier	CPP Marseille
ɔrizio	Murtas	INFN LNF
'redo	Musso	INFN Torino
	Nikitenko	CERN
ıner	Novotny	Giessen University
S.	Panin	BINP SD RAS
am	Para	Fermilab
ıncesco	Pietropaolo	INFN Padova
ıus	Pretzl	Bern University
ıude	Pruneau	Wayne State University
ljko	Radeka	BNL
ıncesco	Raimondi	Tektronix S.p.A.
·ge	Reznikov	JINR
ırco	Ricci	INFN LNF
ger	Rusack	Minnesota University
ın	Rutherfoord	Arizona University
ɔla	Sala	INFN Milano
ɔrgio	Salvini	INFN Roma I
ahzad	Sarwar	INFN LNF
rore	Savoy–Navarro	LPNHE France
ome	Schwindling	CEA Saclay
ris	Seez	Imperial College
iner	Seitz	Technische Universität Dresden
chal	Seman	Nevis Labs Columbia University
lery	Serdiuk	INFN LNF
:er	Shanahan	Fermilab
A.	Shwartz	BINP SD RAS
	Smakhtin	BINP SD RAS
ırina	Spitalieri	INFN LNF
ısko	Stenzel	MPI
wrence	Sulak	Boston University
ıuro	Taiuti	INFN Genova
:lio	Takai	BNL
ncent	Tisserand	LAL Orsay
	Tomarelli	Tecnologie Avanzate S.r.l.
essandra	Tonazzo	INFN Milano
ncenzo	Valente	INFN LNF
olo	Valente	INFN LNF
ne	Vichou	IFAE Barcelona University
:nri	Videau	CERN
jinder	Virdee	Imperial College
olfgang	Walkowiak	Mainz University
chard	Wigmans	Texas Tech University
ikhail	Yakimenko	Lebedev Physical Institute
lriano	Zallo	INFN LNF
:n–Yuan	Zhu	Caltec HEP
ıtonio	Zoccoli	INFN Bologna

ASCATI PHYSICS SERIES

Volume I, "*Heavy Quarks at Fixed Target*"
Editors S.Bianco and F.L. Fabbri
Frascati May 31st–June 2nd, 1993, ISBN—88–86409–00–1

Volume II – Special Issue, "*Les Rencontres de Physique de la Vallée d'Aoste – Results and Perspectives in Particle Physics*"
Editor M. Greco
La Thuile, Aosta Valley, March 5th –11th, 1995, ISBN—88–86409–03–6

Volume III, "*Heavy Quarks at Fixed Target*"
Editor B. Cox
University of Virginia, Charlottesville, October7th –10th, 1994, ISBN—88–86409–04–4

Volume IV, "*Workshop on Physics and Detectors for DAΦNE*"
Editors R. Baldini, F. Bossi, G. Capon, G. Pancheri
Frascati, April 4th –7th, 1995, ISBN 88–86409–05–2

Volume V – Special Issue, "*Les Rencontres de Physique de la Vallée d'Aoste – Results and Perspectives in Particle Physics*"
Editor M. Greco
La Thuile, Aosta Valley, March 3rd –9th , 1996, in press